

Two Dimensional Polarization Independent All-dielectric Left-handed Metamaterial in Free Space

Jun Wang¹, Shaobo Qu¹, Mingde Feng¹, Bai Du², and Zhuo Xu²

¹College of Science, Air Force Engineering University, Xi'an, Shaanxi 710051, China

²Electronic Materials Research Laboratory, Key Laboratory of the Ministry of Education International Center for Dielectric Research, Xi'an Jiaotong University Xi'an, Shaanxi 710049, China

Abstract— In this paper, we proposed a type of all-dielectric metamaterial (ADM) with quasi-continuous structure, which can inspire quasi-continuous electric and magnetic responses to acquire left-handed properties in free space. The proposed model utilizing dielectric rods and cubes as sub-wavelength inclusions. A two dimensional polarization independent left-handedness can be achieved with the frequencies at C band. The rods resonant under characteristic modes can generate negative permittivity and permeability, whereas the cubes are used in the non-resonant modes to assure the continuity of the displacement currents in dielectric inclusions. The simultaneously double negative properties can be interpreted by electric and magnetic fields distributions of the dielectric inclusions near 7.6 GHz under normal incidence with polarization angle 45°. The further study on transmission spectra and effective refractive indexes of the model with different polarization angles shows that the left-handed property is insensitive to different polarization angles due to the $\pi/2$ rotation symmetry of the ADM. The proposed ADM can be easily realized at infrared and optical frequencies with dielectric inclusions.

1. INTRODUCTION

The realization of isotropic negative refractive index in two- or three-dimensional left-handed metamaterials has attracted much attention [1–5] due to the demands of realizing perfect lens [6] and other applications. Shelby et al. [1] investigated a two-dimensional isotropic left-handed metamaterial by placing SRR/wire in a square lattice. This LHM is insensitive to incident angles, but sensitive to polarization angles. Koschny et al. [2] proposed a three-dimensional left-handed metamaterials which is insensitive to incident angles, as well as insensitive to polarization angles. However, the conducting wires using in these models should have a contact on the side-walls of the waveguide or should be continuous. These features bring about difficulties in fabricating, and limit their applications in free space. On the other hand, the Ohmic losses in metallic inclusions are increased with frequency notably at the optical frequencies, where the left-handed properties will be eliminated [7].

The similarity of the conduction currents and displacement currents indicated that dielectric structures can replace metallic patterns to realize left-handed properties. Thus, an alternative way to fabricate isotropic metamaterial is proposed by using dielectric materials with high permittivity and low loss. A number of authors proposed new types of LHMs by employing dielectric materials [8–15]. Zhao et al. [9] reported that the combination of dielectric cubes and metallic wires can produce a left-handed transmission. Peng et al. [10] reported that dielectric rods contacting side-walls of a waveguide can generate negative permittivity and negative permeability simultaneously.

In this paper, we proposed a quasi-continuous structure, which can inspire quasi-continuous electric and magnetic responses to acquire left-handed properties in free space. Numerical simulations were carried out to verify the polarization insensitivity properties of the all-dielectric left-handed metamaterial (ADM) with a normal incidence of the TE wave.

2. MODEL AND SIMULATION

The proposed model is shown in Figure 1. Figure 1(a) shows the schematic of the two-dimensional polarization-free all-dielectric left-handed metamaterial (ADM). The ADM consists of a matrix ($\epsilon = 2.65$, $\tan \delta = 0.0015$) with composite cubes/rods regularly embedded within it to form a quasi-continuous network structure. The cubes and rods are made of BST ceramic, which has a permittivity of 110 and a loss of 0.0011. Figure 1(b) shows the unit cell of the ADM. The scale of the unit cell is 10 mm. The thickness of the ADM is 5 mm. The gap between the cube and rod is 0.25 mm. The numerical study of the ADM is carried out by a full-wave finite-element method simulator (Ansoft HFSS). Floquet ports and master-slave boundaries are employed to simulate free space.

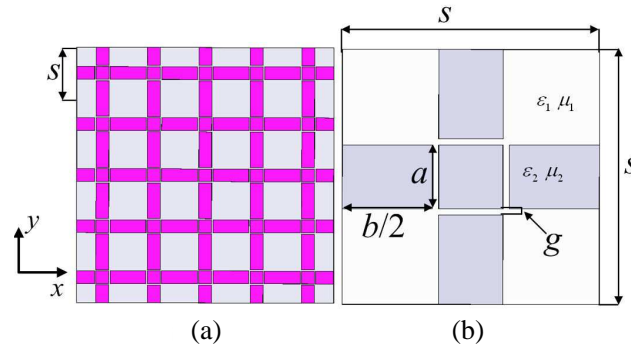


Figure 1: (a) Two-dimensional polarization-free ADM. (b) Unit cell of the 2D ADM. a is 2.5 mm, b is 7 mm, g is 0.25 mm, and S is 10 mm.

3. RESULTS AND ANALYSIS

Figure 2 shows the simulated transmission spectra and effective refractive indexes of the model subject to normal incidences with different polarization angles. The simulated transmission spectra and effective refractive indexes are stable when polarization angle changes. Note that the model has $\pi/2$ rotation symmetry; the ADM we proposed is polarization insensitive at any incident polarization angle. Figure 3(a) shows that there are three transmission peaks at 7.6, 8, and 9.5 GHz, which demonstrate three pass-bands. The investigations are focused on these three pass-bands.

The simulated scattering parameters and the retrieved effective electromagnetic parameters of the ADM are shown in Figure 3. The polarization angle of the incident TE wave is 45° . Figure 3(a) shows that there are three transmission peaks at 7.6, 8, and 9.5 GHz. Figures 3(c) and 3(d) show that negative effective permittivity and permeability are simultaneously realized at 7.6, 8, and 9.5 GHz, which demonstrate that the three pass-bands are left-handed pass-bands. The FOM (figure of merit) at 7.62 GHz is calculated to be 85.41. At this frequency, the real part of refractive index n is -3.16 , with the imaginary part 0.037 . The FOM at 8 GHz is 36.27, with the refractive index $n = -2.539 - 0.07i$. The FOM at 9.5 GHz is 19.23, with the refractive index $n = -1.538 - 0.08i$. The left-handed bands are in the range of $7.56 \sim 7.76$, $7.96 \sim 8.08$, and $9.46 \sim 9.62$ GHz, respectively. Both the magnetic resonance and electric resonance in these bands are Lorentz-type, which indicate Lorentz resonances. These resonances are generated by the rod-type dielectric resonators.

Figure 4 shows the electric and magnetic fields distributions for dielectric inclusions at 7.6 GHz. Figure 4(a) shows the distributions of the electric vector fields on the front side of the dielectric inclusions. Figure 4(b) shows the distributions of the electric vector fields on the back side of the dielectric inclusions. The resonant mode of the y -axis aligned rods is $TE_{\delta 11}^x$ mode, while the resonant mode of the x -axis aligned rods is $TE_{1\delta 1}^y$ mode. Note that the displacement current distributions for dielectric inclusions are similar to the electric field distributions. The displacement currents on the front side of the dielectric inclusions are in the same direction to the applied electric field, whereas the displacement currents on the back side of the dielectric inclusions are in the opposite direction to the applied electric field. The displacement currents in the dielectric inclusions are composed to a quasi-continuous contra-directional current pair, which can yield negative permittivity via

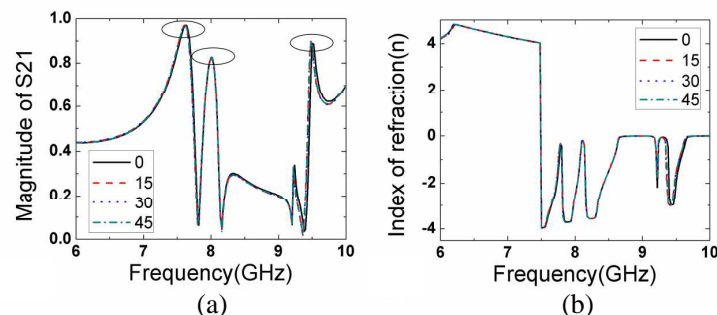


Figure 2: The simulated transmission spectra and effective refractive indexes of the model with different polarization angles. (a) Magnitude of the simulated S_{21} . (b) Real part of the retrieved refractive index.

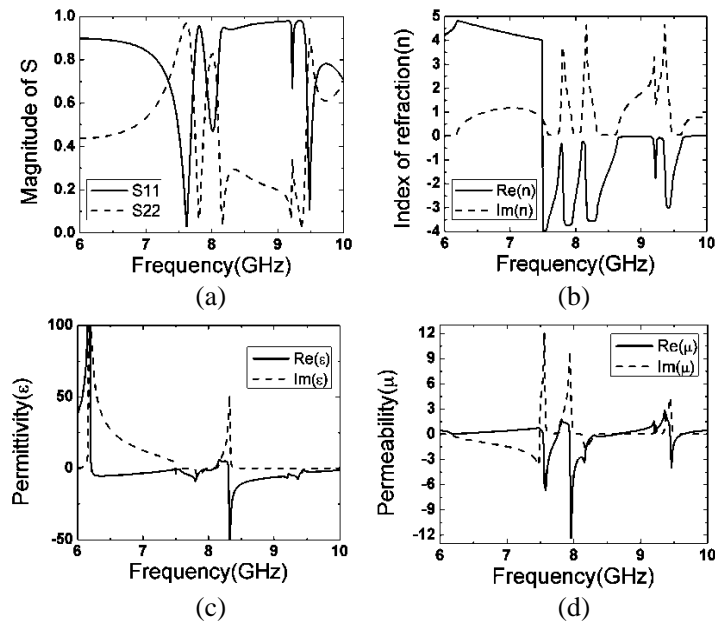


Figure 3: The simulated transmission spectra and effective parameters for the proposed model (polarization angle 45°). (a) Magnitude of the simulated S parameters. (b) Retrieved refractive index. (c) Effective permittivity. (d) Effective permeability.

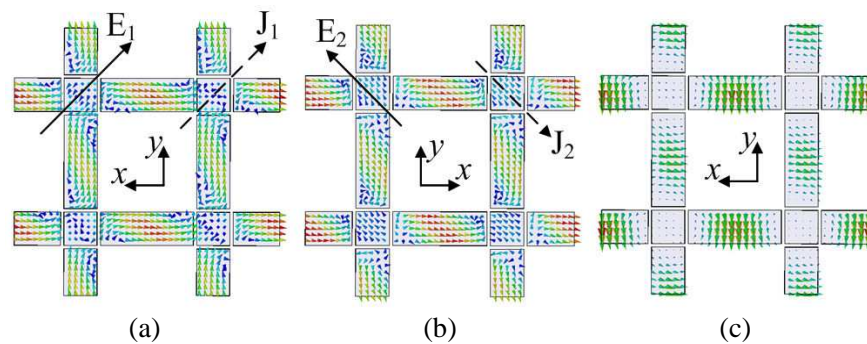


Figure 4: Electric and magnetic fields distributions of the dielectric inclusions at 7.6 GHz under normal incidence (polarization angle 45°). (a) Surface electric field distribution on the front side. (b) Surface electric field distribution on the back side. (c) Volumetric magnetic field distribution.

resonant behavior. Figure 4(c) shows the distributions of magnetic vector field of the dielectric inclusions. The combined magnetic fields, joint by the magnetic fields emerged in each rods, are equivalent to a magnetic dipole, which is oriented to the direction of the applied magnetic field. The resonant magnetic dipole can generate negative permeability. Thus, the left-handed properties can be achieved by combining a quasi-continuous contra-directional current pair and a resonant magnetic dipole.

4. CONCLUSIONS

In summary, we have proposed a method to realize 2D polarization-independent all-dielectric left-handed metamaterial in free space. The model we introduced possess $\pi/2$ rotation symmetry, which made the left-handed properties of the ADM insensitive to different polarization angles. Three left-handed pass-bands were achieved in the vicinity of 7.6, 8, and 9.5 GHz, respectively. The resonant displacement currents emerged in the high dielectric inclusions can generate negative permittivity and permeability simultaneously. The proposed ADM can be easily realized at infrared and optical frequencies with proper dielectric inclusions.

ACKNOWLEDGMENT

The authors are grateful to the supports from the National Natural Science Foundation of China under Grant Nos. 61331005, 11204378, 11274389, and 11304393.

REFERENCES

1. Shelby, R. A., D. R. Smith, S. C. Nemat-Nasser, and S. Schultz, “Microwave transmission through a two-dimensional, isotropic, left-handed metamaterial,” *Appl. Phys. Lett.*, Vol. 78, 489–491, 2001.
2. Koschny, T., L. Zhang, and C. M. Soukoulis, “Isotropic three-dimensional left-handed metamaterials,” *Phys. Rev. B*, Vol. 71, 121103(R), 2005.
3. Wang, J. F., S. B. Qu, Z. Xu, Z. T. Fu, H. Ma, and Y. M. Yang, “A broad-band three-dimensional isotropic left-handed metamaterial,” *J. Phys. D: Appl. Phys.*, Vol. 42, 155413, 2009.
4. Chen, C. H., S. B. Qu, J. F. Wang, H. Ma, J. Wang, J. B. Zhao, X. H. Wang, H. Zhou, and Z. Xu, “Wide-angle and polarization-independent three-dimensional magnetic metamaterials with and without substrates,” *J. Phys. D: Appl. Phys.*, Vol. 44, 135002, 2011.
5. Kante, B., K. O’Brien, A. Niv, X. Yin, and X. Zhang, “Proposed isotropic negative index in three-dimensional optical metamaterials,” *Phys. Rev. B*, Vol. 85, 041103(R), 2012.
6. Pendry, J. B., “Negative refraction makes a perfect lens,” *Phys. Rev. Lett.*, Vol. 85, 3966–3969, 2000.
7. Zhou, J., T. Koschny, M. Kafesaki, E. N. Economou, J. B. Pendry, and C. M. Soukoulis, “Saturation of the magnetic response of split-ring resonators at optical frequencies,” *Phys. Rev. Lett.*, Vol. 95, 223902, 2005.
8. Vendik, O. G. and M. S. Gashinova, “Artificial double negative (DNG) media composed by two different dielectric sphere lattices embedded in a dielectric matrix,” *34th European Microwave Conference*, 1209–1212, 2004.
9. Zhao, Q., L. Kang, B. Du, H. Zhao, Q. Xie, X. Huang, B. Li, J. Zhou, and L. Li, “Experimental demonstration of isotropic negative permeability in a three-dimensional dielectric composite,” *Phys. Rev. Lett.*, Vol. 101, 027402, 2008.
10. Peng, L., L. Ran, H. Chen, H. Zhang, J. A. Kong, and T. M. Grzegorzczuk, “Experimental observation of left-handed behavior in an array of standard dielectric resonators,” *Phys. Rev. Lett.*, Vol. 98, 157403, 2007.
11. Lai, Y. J., C. K. Chen, and T. J. Yen, “Creating negative refractive identity via single-dielectric resonators,” *Opt. Express*, Vol. 17, 12960–12970, 2009.
12. Zhao, Q., J. Zhou, F. L. Zhang, and D. Lippens, “Mie resonance-based dielectric metamaterials,” *Mater. Today*, Vol. 12, 60–69, 2009.
13. Lepetit, T., E. Akmansoy, and J. Ganne, “Experimental evidence of resonant effective permittivity in a dielectric metamaterial,” *J. Appl. Phys.*, Vol. 109, 023115, 2011.
14. Wang, J., Z. Xu, Z. H. Yu, X. Y. Wei, Y. M. Yang, J. F. Wang, and S. B. Qu, “Experimental realization of all-dielectric composite cubes/rods left-handed metamaterial,” *J. Appl. Phys.*, Vol. 109, 084918, 2011.
15. Wang, J., Z. Xu, B. Du, S. Xia, J. Wang, H. Ma, and S. Qu, “Achieving all-dielectric left-handed metamaterials via single-sized dielectric resonators,” *J. Appl. Phys.*, Vol. 111, 044903, 2012.

Compact SU8-silica Hybrid Thermo-optic Switch with Low Power Consumption

Wei Peng, Pengxin Chen, and Yaocheng Shi

Centre for Optical and Electromagnetic Research

State Key Laboratory of Modern Optical Instrumentation

Zhejiang University, Zijingang Campus, East Building No. 5, Hangzhou 310058, China

Abstract— We propose a novel Mach-Zehnder interferometer (MZI) type thermo-optic switch based on SU8-silica hybrid waveguide structures. The switch consists of a 1×2 power splitter, two transmission arms and a 2×1 power combiner. The input/output waveguides and the power splitter/combiner are realized by the conventional silica waveguides, while the two arms for the MZI consist of SU8 strip waveguides. Such hybrid SU8-Silica waveguide structures combines the advantages of the low propagation loss of the silica waveguides and the large thermo-optic coefficient of SU8. Due to the high thermo-optic coefficient of SU8, the length of the transmission arm can be dramatically reduced.

1. INTRODUCTION

Optical switch is one of the key devices for optical communication system. Optical switches based on planar lightwave circuits (PLCs) have attracted extensive research interests due to compact structure, being integrated easily with other devices and large-scale production. Various material systems such as silica, silicon, and polymer have been employed to realize optical switches. Among them, silica-on-silicon [1] is considered to be one of the most attractive platforms for PLCs due to its low propagation loss and high coupling efficiency to optical fibers. However, the thermo-optic coefficient of silica is very small resulting in large dimension and high power consumption. A silicon-silica hybrid waveguide structure that utilizes a silicon waveguide as a TO phase shifter has been demonstrated [2]. It exhibits an extremely low power consumption but the fabrication processes are quite complicated.

Polymer based PLCs [3, 4] have a simple fabrication technology and the merits of low cost and high thermo-optical coefficient. Therefore, it is an important branch in modern integrated optics. In this paper, we propose a novel Mach-Zehnder interferometer (MZI) type thermo-optic switch based on SU8-silica hybrid waveguide structures. Small dimension and low power consumption can be achieved since then.

2. DESIGN AND ANALYSIS

The schematic of the SU8-silica thermo-optic switch is depicted in Fig. 1. Fig. 1(a) shows the top view of the device, which consists of a 1×2 power splitter, two transmission arms, and a 2×1 power combiner. Figs. 1(b) and (c) illustrate the cross section of the silica waveguide region (AA' cross-section) and the SU8-silica hybrid waveguide region (BB' cross-section), respectively. Both the splitter and the combiner are based on multimode interference (MMI) coupler. The two transmission arms are designed to be asymmetric so that the function of switching can be realized while the two arms are heated. Buried silica waveguides which is the most popular platform for PLCs are considered in this paper. The refractive index of the substrate, core and upper-cladding are 1.45, 1.46, and 1, respectively. To be compatible with standard SMF-28 optical fiber and commercial laser diodes and photodetectors and minimize the polarization dependence, buried silica waveguides with a core size of $6 \times 6 \mu\text{m}^2$ has been considered in this work.

For the purpose of reducing the coupling loss between the silica waveguide and SU8 waveguide, we have to optimize the SU8 waveguide dimension parameters, H , W , and h_{sub} (as shown in Fig. 1(c)). Mode solution is utilized to calculate the mode distributions for the silica waveguide and the SU8-silica hybrid waveguide. Overlap integral is then used to determine the coupling efficiency. Fig. 2(a) shows the coupling efficiency for waveguide with different H and W (at each H and W , h_{sub} is optimized to obtain a highest coupling efficiency). From Fig. 2(a), we can find that the coupling efficiency decreases while the W/H increases. Besides the coupling efficiency between the silica waveguide and the SU8-silica hybrid waveguides, the ratio of the power confined in the SU8 region must be taken into account. If this ratio is very low, it will lead to a low effective thermo-optic coefficient, which causes large device dimension and high power consumption. Thus,

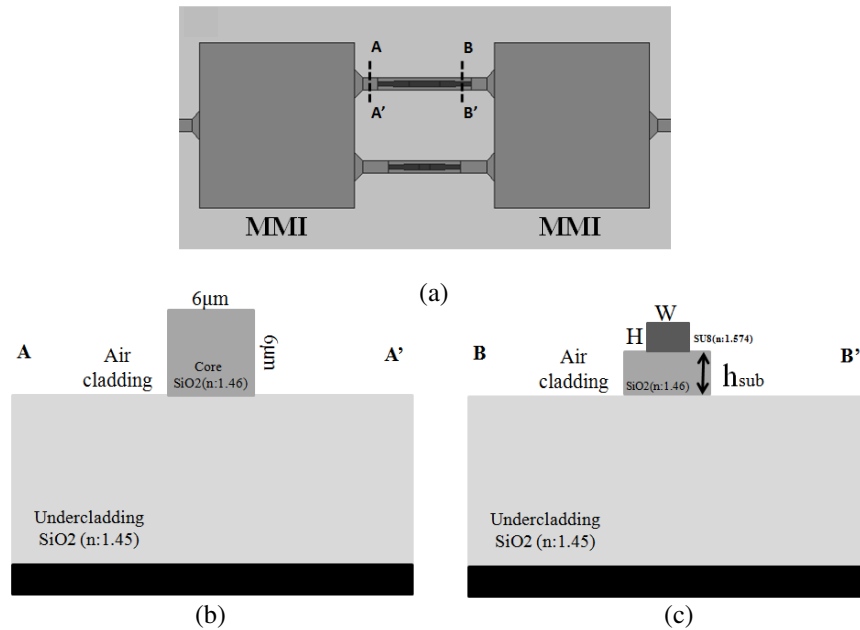


Figure 1: (a) The schematic of the SU8-silica hybrid thermo-optic switch; (b) the cross section of the silica waveguide region (AA'); (c) the cross section of the SU8-silica hybrid region (BB').

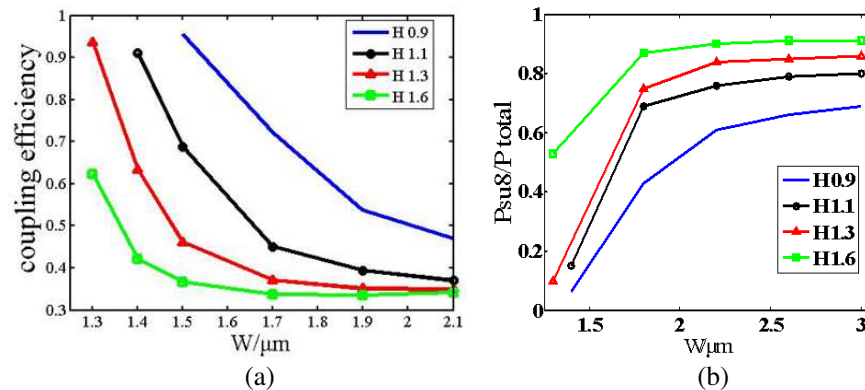


Figure 2: (a) The coupling efficiency between the buried silica waveguide and SU8-silica hybrid waveguide; (b) the ratio of the power confined in the SU8 region for the SU8-hybrid waveguides.

we also calculate the ratio of the power confined in the SU8 region for different waveguide structures. Fig. 2(b) shows the power ratios vary as the waveguide width for hybrid waveguides with different H .

From Fig. 2(b), it is obviously that the ratio of the power confined in SU8 region increases with the height of SU8. By comparing Fig. 2(a) and Fig. 2(b), we can find that it is difficult to find a waveguide structure which can provide high coupling efficiency and large power ratio simultaneously. Thus, a taper structure can be introduced. Taking into account the fabrication feasibility, width taper is preferred. According to Fig. 2(a), the height and width are determined to be $H = 1.1 \mu\text{m}$ and $W = 1.4 \mu\text{m}$. The SU8-silica hybrid waveguides are tapered from $1.4 \mu\text{m}$ to $2.3 \mu\text{m}$ to achieve a high switching efficiency. At the other side, the $2.3 \mu\text{m}$ wide waveguide is tapered linearly to $1.4 \mu\text{m}$. Three dimensional beam propagation method (3D-BPM) is utilized to verify the design. Fig. 3(a) shows the simulation light propagation from of a $1.4 \mu\text{m}$ wide and $1.1 \mu\text{m}$ high SU8-silica hybrid waveguide (h_{sub} is $4.2 \mu\text{m}$) connected with buried silica waveguide on both sides. As Fig. 3(a) indicated, the coupling efficiency is approximately 0.81 which is quite agree with the one obtained by using the overlap integral (~ 0.828). However, the ratio of the power confined in such a SU8-silica waveguide is quite low. Fig. 3(b) shows light propagation in the waveguides with tapered structures as described above. We can see that large ratio of the propagation light couples into SU8 waveguide through taper while a high coupling efficiency can be maintained.

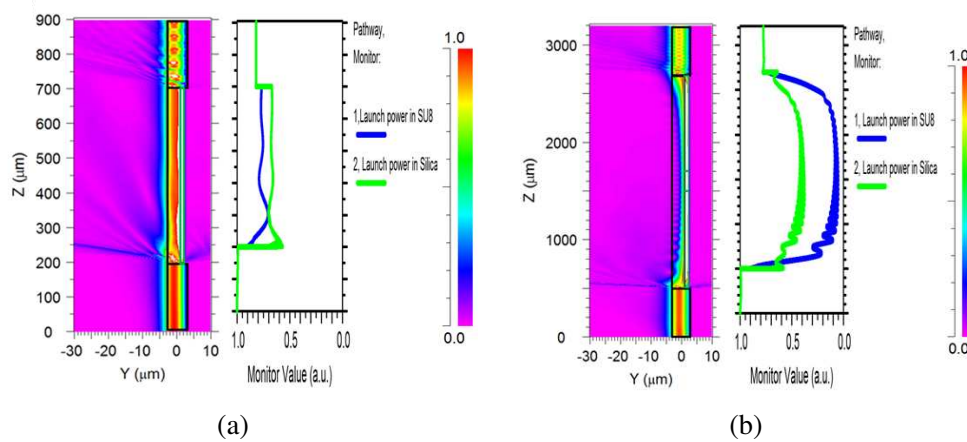


Figure 3: 3D BPM simulation shows the light propagates in (a) a $1.4\ \mu\text{m}$ wide and $1.1\ \mu\text{m}$ high SU8-silica hybrid waveguide (h_{sub} is $4.2\ \mu\text{m}$) with buried silica waveguide on both sides; (b) $1.4\ \mu\text{m}$ wide SU8-silica hybrid waveguide tapered to $2.3\ \mu\text{m}$ wide.

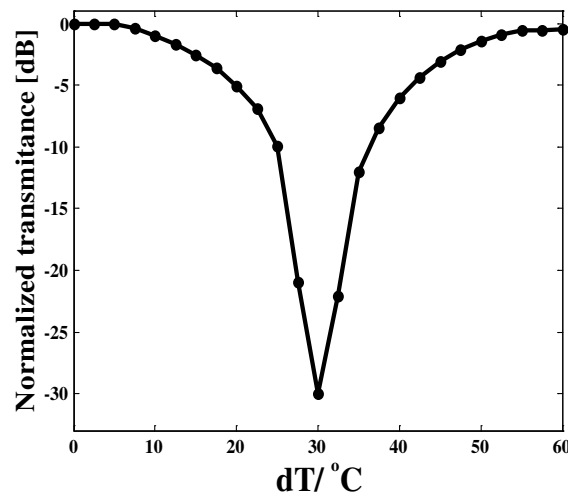


Figure 4: Simulated switching characteristics of the proposed SU8-silica hybrid waveguide switch.

Figure 4 shows the simulated switching characteristics of the proposed SU8-silica hybrid thermo-optic switch. Only 30 degree temperature change is required for a switching function.

3. CONCLUSIONS

In this paper, we propose a novel Mach-Zehnder interferometer (MZI) type thermo-optic switch based on SU8-silica hybrid waveguide structures. It combines the advantages of the low propagation loss of the silica waveguides and the large thermo-optic coefficient of the SU8. Although the design is based on the TO effect of SU8, the concept can be applied to the other type of polymers (e.g., EO polymers) to achieve high performance switches based on silica platform.

ACKNOWLEDGMENT

This work is supported by the National High Technology Research and Development Program (863) of China (No. 2012AA012201).

REFERENCES

1. Hashizume, Y., et al., *Proc. of OFC/NFOEC2007*, Paper OWO4, 2007.
2. Kasahara, R., K. Watanabe, M. Itoh, Y. Inoue, and A. Kaneko, "Extremely low power consumption thermo-optic switch (0.6 mW) with suspended ridge and silicon-silica hybrid waveguide structure," *ECOC 2008*, 2.02, Brussels, Belgium, Sep. 21–25, 2008.

3. Schiff, H., “Nanoimprint lithography: An old story in modern times? A review,” *J. Vac. Sci. Technol. B*, Vol. 26, No. 2, 458–480, 2008.
4. Tung, K. K., W. H. Wong, and E. Y. B. Pun, “Polymeric optical waveguides using direct ultraviolet photolithography process,” *Appl. Phys. A*, Vol. 80, No. 3, 621–626, 2005.

Study on Accuracy and Efficiency of the Numerical Algorithm for Electromagnetic Scattering from Targets and Rough Surface

Yu Liang¹, Li-Xin Guo², Xiang-Hua Zeng¹, Jing-Guo Hu¹, and Zhen-Sen Wu²

¹College of Physics Science and Technology, Yangzhou University, Yangzhou, Jiangsu, China

²School of Physics and Optoelectronic Engineering, Xidian University, Xi'an, Shaanxi, China

Abstract— Some studies about the accuracy and efficiency of the Propagation-Inside-Layer-Expansion (PILE) combined with the (Generalized) Forward-Backward Method ((G)FBM) hybrid scheme for electromagnetic scattering from targets and rough surface are carried out. The Relative Residual Error (RRE), that is set as the important evaluation criterion of algorithm accuracy is evaluated. The computational complexity and CPU time, acting as two key criterions for judging the efficiency are investigated. Numerical results demonstrate that, for multi-targets and rough surface cases, only needing a few iteration, the PILE and FBM hybrid scheme can reach enough accuracy, and also improve the efficiency, compared with some other classical numerical methods.

1. INTRODUCTION

Recently, scattering of electromagnetic wave in target and rough surface has been becoming an interesting topic as its important applications in electromagnetics, remote sensing, antennas theory and design, marine science, and electronic countermeasures, etc. Many analytical and numerical algorithms have been presented for this domain [1–6], such as the SPM, the KA, the MOM, the FMM, the FEM, the FDTD, etc., within which, lately, a fast and efficient numerical scheme named as the Propagation-Inside-Layer-Expansion (PILE) has been presented by N. Déchamps et al. [4]. In this paper, the accuracy and efficiency of the Propagation-Inside-Layer-Expansion (PILE) combined with the (Generalized) Forward-Backward Method ((G)FBM) hybrid scheme for electromagnetic scattering from targets and rough surface are investigated. The theory, formulations, and numerical results are given and corresponding discussions are addressed in each section.

2. BRIEF THEORY AND FORMULATIONS

When the PILE combined with (G)FBM hybrid scheme [5, 6] is applied to study the electromagnetic scattering from targets and rough surface, two important factors is needed to investigate: the accuracy and the efficiency. To validate the accuracy of EPILE+(G)FBM, the Relative Residual Error are necessarily investigated. The Relative Residual Error of using the EPILE+FBM and comparing with the MOM(LU/CGM) [5] is defined as the norm of the following form

$$\text{RRE} = \frac{\sum_{-90}^{90} |\sigma_{(\text{EPILE}+(\text{G})\text{FBM})} - \sigma_{(\text{MOM}(\text{LU}/\text{CGM}))}|^2}{\sum_{-90}^{90} |\sigma_{\text{MOM}(\text{LU}/\text{CGM})}|^2} \quad (1)$$

where, σ is the scattering coefficient. To confirm the efficiency of the EPILE+(G)FBM, the computational complexity $o(\)$ and CPU time are necessarily investigated. Take the targets both above and below rough surface case for example (be suitable for the EPILE+FBM hybrid scheme), the complexities per iteration of the terms $\mathbf{Y}_{1,2}^{(p)}$, $\mathbf{Y}_r^{(p)}$ [5, 6] are given below,

$$\mathbf{M}_r \cdot \mathbf{Y}_r^{(p-1)} = (\tilde{\mathfrak{R}}^1)^{-1} \cdot \tilde{\mathfrak{R}}^2 \cdot \underbrace{\left(\tilde{\mathfrak{R}}^3 \right)^{-1} \cdot \underbrace{\tilde{\mathfrak{R}}^4 \cdot \mathbf{Y}_r^{(p-1)}}_{\substack{o(M_{iter} 12(N_1 + N_2)^2) \\ \text{or } o(4(N_1/3 + N_2/3)^3) \text{ (b)}}}}_{\substack{o(2N_1N_3+2N_2N_3) \text{ (a)} \\ o(4(N_3)^2) \text{ (d)}}}, \quad (2)$$

$$\mathbf{M}_{1,2} \cdot \mathbf{Y}_{1,2}^{(p-1)} = \underbrace{(\bar{\mathfrak{R}}^3)^{-1} \cdot \bar{\mathfrak{R}}^4 \cdot (\bar{\mathfrak{R}}^1)^{-1}}_{o(M_{iter}12(N_1+N_2)^2) \text{ or } o(4(N_1/3+N_2/3)^3) \text{ (h)}} \cdot \underbrace{\bar{\mathfrak{R}}^2 \cdot \mathbf{Y}_{(t1,t2)}^{(p-1)}}_{o((2N_3)^2) \text{ (f)}} \cdot \underbrace{o(2N_1N_3+2N_2N_3) \text{ (g)}}_{o((2N_1N_3) \times (+2N_2N_3)) \text{ (e)}} \quad (3)$$

where, \mathbf{M}_r , $\mathbf{M}_{1,2}$ is the corresponding characteristic matrix on rough surface, and on targets above/below, N_1 , N_2 , N_3 denotes the number of sampling points for targets above/below, and rough surface, $\bar{\mathfrak{R}}^1$, $\bar{\mathfrak{R}}^2$, $\bar{\mathfrak{R}}^3$, $\bar{\mathfrak{R}}^4$ corresponds to the local interactions on the rough surface, the targets→rough surface coupling, the local interactions on the rough surface, and the rough surface→targets coupling, respectively. The CPU time refers to the computer computational time for each scattering solving. Often, considering the possible instability, the averaged CPU time that is an average value of plenty of CPU time for each computation is a more useful information for evaluating the efficiency of algorithm. Obviously, if the average CPU time is less, the efficiency of algorithm is more efficient (i.e., computationally faster), otherwise, its efficiency is lower.

3. NUMERICAL RESULTS AND DISCUSSIONS

In formulas (2) and (3), operations (a), (c), (e), and (g) are matrix-vector multiplications: their computational complexities are $o(2N_1N_3 + 2N_2N_3)$. Operations (d), (f) are the FBM iterative inversions, their complexities are $o(4(N_3)^2)$. Operations (b) and (h) are the MOM (CGM or LU scheme), whose complexities are $o(M_{iter}12(N_1 + N_2)^2)$ or $o((4N_1/3 + 4N_2/3)^3)$, where M_{iter} is the number of iterations in the CGM scheme. Therefore, the total computational complexity is $o(p(4N_1N_3 + 4N_2N_3 + M_{iter}12(N_1 + N_2)^2 + 4(N_3)^2))$ or $o(p(4N_1N_3 + 4N_2N_3 + (4N_1/3 + 4N_2/3)^3 + 4(N_3)^2))$ for both the calculation, where p is the number of iterations in the EPILE scheme, for $N_3 \gg N_1$ and $N_3 \gg N_2$, i.e., the number of samples for the rough surface is much more than those of the targets, or the size of the rough surface is far larger than that of the targets, the complexity is about $o(p(4N_3 + 4(N_3)^2)) \approx o(p(4(N_3)^2))$ (for N_3 is large enough), p is generally less than 10, so this method is much faster than the direct LU inversion, of order $o((4N_3/3)^3)$ and the CGM, of order $o(M_{iter}12(N_3)^2)$. for examples, when $N_3 = 100$, the complexity of EPILE+FBM is 4×10^4 , of LU is 2.25×10^6 , of CGM is $> 1.2 \times 10^6$; when $N_3 = 1000$, the complexity of EPILE+FBM is 4×10^6 , of LU is 2.25×10^9 , of CGM is $> 1.2 \times 10^9$, obviously, when the N_3 is larger, the complexity gap between the EPILE+FBM and the MOM(LU/CGM) is more evident.

Table 1: Comparison of different order EPILE combined with different iteration number of FBM in RRE and averaged CPU time for 100 rough surface realizations (HH polarization).

EPILE() +FBM()	(2)+(2)	(2)+(3)	(2)+(4)	(2)+(5)	(2)+(6)
RRE	8.2×10^{-3}	7.103×10^{-4}	6.645×10^{-5}	1.615×10^{-5}	1.504×10^{-5}
CPU time	≈ 35 S	≈ 40 S	≈ 45 S	≈ 50 S	≈ 55 S
EPILE() +FBM()	(3)+(2)	(3)+(3)	(3)+(4)	(3)+(5)	(3)+(6)
RRE	7.850×10^{-3}	6.814×10^{-4}	6.231×10^{-5}	1.453×10^{-5}	1.098×10^{-5}
CPU time	≈ 40 S	≈ 46 S	≈ 50 S	≈ 55 S	≈ 60 S

The 2, 3 order EPILE combined with 2, 3, 4, 5, 6 iteration number of FBM for both HH and VV polarizations of 100 rough surface realizations have also been calculated. The corresponding RRE and averaged CPU time are listed in Tables 1, 2, respectively. Comparing the data in row indicates that, for a given EPILE iteration number, the Relative Residual Error decreases as the FBM iteration number increases, and all the RRE trends to be less than 10^{-3} order of magnitudes even through the averaged CPU time increases slightly, the FBM increases one iteration step, the averaged CPU time increases about 5 seconds (S). Comparing the data in column suggests that, for a given FBM order, the RRE also decreases and trends to be less than 10^{-3} order of magnitudes as the EPILE order increases, the EPILE increases one order, the averaged CPU time also increases about 5 seconds, while the averaged CPU time of MOM is about 5 minutes, hence, it can be

Table 2: Comparison of different order EPILE combined with different iteration number of FBM in RRE and averaged CPU time for 100 rough surface realizations (VV polarization).

EPILE() +FBM()	(2)+(2)	(2)+(3)	(2)+(4)	(2)+(5)	(2)+(6)
RRE	1.386×10^{-4}	2.001×10^{-5}	1.162×10^{-5}	1.130×10^{-5}	1.115×10^{-5}
CPU time	≈ 32 S	≈ 37 S	≈ 42 S	≈ 47 S	≈ 52 S
EPILE() +FBM()	(3)+(2)	(3)+(3)	(3)+(4)	(3)+(5)	(3)+(6)
RRE	1.324×10^{-4}	1.813×10^{-5}	1.135×10^{-5}	1.086×10^{-5}	1.018×10^{-5}
CPU time	≈ 37 S	≈ 42 S	≈ 47 S	≈ 52 S	≈ 58 S

summarized that, the EPILF+FBM is efficient in a whole, increasing the order of either EPILE or FBM, the RRE decreases and is in 10^{-3} or less order of magnitudes, in fact under which, an essentially exact result have be obtained, and a slightly increased CPU time is the only cost.

4. CONCLUSIONS

In this paper, the accuracy and efficiency of the Propagation-Inside-Layer-Expansion (PILE) combined with the (Generalized) Forward-Backward Method ((G)FBM) hybrid scheme for electromagnetic scattering from targets and rough surface are studied. The numerical results demonstrate that, the EPILE+FBM hybrid scheme can provide accurate results under the premise of enough efficiency. The accuracy can be further improved by increasing the order of EPILE or the iteration step of FBM, although a rather slightly increased time is needed.

ACKNOWLEDGMENT

This work was supported by the National Natural Science Foundation of China (Grant No. 1134718 2), by the University Science Research Project of Jiangsu Province (Grant No. 13KJB140020), by the National Natural Science Foundation for Distinguished Young Scholars of China (Grant No. 61225002) and by the Science Foundation of Yangzhou University (Grant No. 2012CXJ009). If any question, please contact with Yu Liang, et al. (e-mail: liangyu@yzu.edu.cn). The authors would like to thank the reviewers for their helpful and constructive suggestions.

REFERENCES

1. Tsang, L. and J. A. Kong, *Scattering of Electromagnetic Waves-numerical Simulations*, 114–176, Wiley, New York, 2000.
2. Liu, Q. H., L. Jiang, and W. C. Chew, “Large-scale electromagnetic computation for modeling and applications,” *Proc. IEEE*, Vol. 101, No. 2, 223–226, 2013.
3. Jandhyala, V., E. Michielssen, S. Balasubramaniam, and W. C. Chew, “A combined steepest descent-fast multipole algorithm for the fast analysis of three-dimensional scattering by rough surfaces,” *IEEE Trans. Geosci. Remote Sens.*, Vol. 36, No. 3, 738–748, 1998.
4. Déchamps, N., N. De Beaucoudrey, C. Bourlier, and S. Toutain, “Fast numerical method for electromagnetic scattering by rough layered interfaces: Propagation-inside-layer expansion method,” *J. Opt. Soc. Amer. A*, Vol. 23, No. 2, 359–369, 2006.
5. Liang, Y., L. X. Guo, and Z. S. Wu, “The fast EPILE combined with FBM for electromagnetic scattering from dielectric targets above and below the dielectric rough surface,” *IEEE Trans. on Geosci. Remote Sens.*, Vol. 49, No. 10, 3892–3905, 2011.
6. Liang, Y., L. X. Guo, and Z. S. Wu, “The EPILE combined with the generalized-FBM for analyzing the scattering from targets above and on a rough surface,” *IEEE Antennas Wireless Propag. Lett.*, Vol. 9, 809–813, 2010.

Application of S-UTD-CH Model into Multiple Diffraction Scenarios at 900 MHz

Mehmet Baris Tabakcioglu¹ and Doruk Ayberkin²

¹Electrical and Electronics Engineering Department, Engineering Faculty
Bayburt University, Bayburt 69000, Turkey

²Computer Programming Department, Bayburt Vocational School
Bayburt University, Bayburt 69000, Turkey

Abstract— In this study, propagation prediction models based on ray tracing in coverage estimation for broadcasting systems are compared with respect to computation time and accuracy. Uniform Theory of Diffraction (UTD), Slope Diffraction (S-UTD) and Slope UTD with Convex Hull (S-UTD-CH) models are compared for computation time and propagation path loss. Moreover in this study, effects of transmitter height to relative path loss at the receiver are analyzed. S-UTD-CH model is optimum model with respect to computation time and relative path loss.

1. INTRODUCTION

It is vital to calculate relative path loss of electromagnetic wave reaching to the receiver in multiple diffraction scenarios for more reliable digital broadcasting. A lot of electromagnetic wave propagation models based on ray tracing technique have been developed for a long time. Base station location is vital for efficiency of field strength on receiver and computational time. For reaching to all users, predicting the coverage field accurately and quickly is most significant. Radio propagation models run for calculating electromagnetic wave strength in radio planning tools predicting coverage and field strength on the receiver. In radio planning tools, Uniform Theory of Diffraction (UTD), based on ray tracing technique, model is used due to less computation time [1]. In urban regions there are multiple diffractions and due to that the height of buildings are close to each other buildings are in the transition region of the previous one. In that case UTD model fails to calculate the electric field strength at the receiver accurately. This model can be used in rural areas not having multiple diffractions with less computation time. To remove the continuity problem on the transition region, Slope Uniform Theory of Diffraction (S-UTD) model is proposed. This model based on adding of derivative of incoming fields [2, 3]. S-UTD model gives inaccurate prediction results and require great computation time in scenarios having diffraction larger than 10. According to accuracy of predicted field and computation time, Slope UTD with Convex Hull model is optimum model [4, 5]. In this study, UTD, S-UTD and S-UTD-CH propagation models being used in broadcasting are compared with respect to accuracy and computation time. Moreover effects of transmitter height to relative path loss are discussed.

2. UTD BASED MODELS

UTD based models have been used for a long time in terrestrial broadcasting. UTD model gives inaccurate results on predicting field strength in application of multiple diffractions. UTD model can be used prediction in two cases. The first one is single diffraction case. The other one is that buildings are not in the transition zone of the previous buildings in multiple diffractions. Otherwise, UTD model fails predicting the field strength at the receiver. To remove the failure of UTD model in the transition zone, derivatives of the incoming fields are taken and added to total field. S-UTD model has large computation time and lose the accuracy due to more than 10 diffractions. To remove the failure of S-UTD model, S-UTD-CH model is proposed. In fact proposed model is not new. It is only combination of two previously proposed models. This model is combination of Convex Hull [6] and S-UTD model. In this model firstly the obstacles not having contribution to total field is excluded according to Fresnel zone concept and then convex hull constructed via remaining obstacles [7]. Next, ray tracing algorithm runs for determining all ray paths ending at the receiver. Finally, S-UTD model runs for all ray paths [8]. In this model, because of the obstacles having so little contributions are excluded from scenario, accuracy of predicted field is not compromised. Moreover, thank to less obstacle computation time reduced. Remarkably, even if only one obstacle is excluded, computation time reduce to one fifth [9].

3. COMPARISON OF UTD BASED MODELS

In the case of multiple diffraction scenario including less than 11 diffractions, S-UTD model is reference model with higher accuracy. To compare the model the scenario given in Fig. 1 is used. In this scenario, transmitting antenna height is selected as 25, 20, 15, 10 and 5 m respectively. Operational frequency assigned to 900 MHz. Average height of building 10 m and buildings' heights are randomly distributed between 10 ± 4 m. Distance between the buildings is 20 m and distances between the buildings are randomly distributed between 20 ± 5 m. Finally receiving antenna height is 1.5 m.

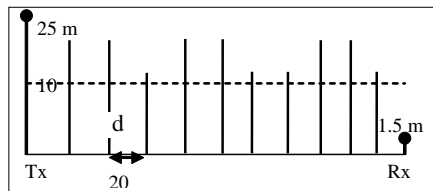


Figure 1: Scenario of comparison of UTD based models.

For given scenario, there made 20 simulations for UTD, S-UTD and S-UTD-CH models respectively. Firstly, transmitter antenna height is selected 25 m (highly elevated) and simulation results are given in Tables 1 and 2.

Table 1: Computation times for highly elevated receiver height (25 m).

UTD (s)	S-UTD (s)	S-UTD-CH (s)
1.143	223.252	0.011
0.418	73.240	0.017

As can be seen from the Table 1, leftmost column gives computation times for UTD, the second column is for S-UTD and the last column is for S-UTD-CH models, respectively. The first and second row gives the mean and standard deviations of simulations. Moreover, S-UTD model require the highest computation time. As the diffraction number increases, computation time increases, too. Because of excluding not effective buildings, computation time of S-UTD-CH model is very lower. In spite of that S-UTD and S-UTD-CH model gives almost the same results (only 0.254 dB difference); computation time of S-UTD-CH model is 0.011 s whereas computation time of S-UTD model is 223.256 s.

Table 2: Path loss for highly elevated receiver height (25 m).

UTD vs S-UTD (dB)	S-UTD-CH vs S-UTD (dB)	ELECTED
0.360	0.254	7.650
0.537	0.252	0.988

As illustrated in Table 2 leftmost column gives contribution of slope diffraction model to classical UTD model. The second column gives the difference of two slope diffraction models and the last column gives the number of elected buildings in S-UTD-CH model. Moreover, contribution of S-UTD model to UTD model is 0.360 dB resulting from adding of derivatives of incoming fields. Furthermore averagely 7.65 buildings excluded from the scenario caused by not having contribution. Secondly, transmitting antenna height is selected as 20 m (elevated) with all the same parameters and results are given in Tables 3 and 4.

As can be seen from the Table 3, leftmost column gives computation times for UTD, the second column is for S-UTD and the last column is for S-UTD-CH models, respectively. The first and second row gives the mean and standard deviations of simulations. Moreover, S-UTD model require the highest computation time. As the diffraction number increases, computation time increases, too. Because of excluding not effective buildings, computation time of S-UTD-CH model is very lower. In spite of that S-UTD and S-UTD-CH model gives almost the same results (only 0.366 dB

Table 3: Computation times for elevated receiver height (20 m).

UTD (s)	S-UTD (s)	S-UTD-CH (s)
1.539	309.089	0.024
0.587	111.851	0.049

Table 4: Path loss for elevated receiver height (20 m).

UTD vs S-UTD (dB)	S-UTD-CH vs S-UTD (dB)	ELECTED
0.267	0.366	7.050
0.470	0.249	0.999

difference); computation time of S-UTD-CH model is 0.024s whereas computation time of S-UTD model is 309.089 s.

As illustrated in Table 4 leftmost column gives contribution of slope diffraction model to classical UTD model. The second column gives the difference of two slope diffraction models and the last column gives the number of elected buildings in S-UTD-CH model. Moreover, contribution of S-UTD model to UTD model is 0.276 dB resulting from adding of derivatives of incoming fields. Furthermore averagely 7.050 buildings excluded from the scenario caused by not having contribution. Thirdly, transmitting antenna height is selected as 15 m (same) with all the same parameters and results are given in the Tables 5 and 6.

Table 5: Computation times for same receiver height (15 m).

UTD (s)	S-UTD (s)	S-UTD-CH (s)
1.462	319.442	0.695
0.582	122.972	1.192

Table 6: Path loss for elevated receiver height (15 m).

UTD vs S-UTD (dB)	S-UTD-CH vs S-UTD (dB)	ELECTED
0.626	0.153	4.950
0.904	0.205	0.999

As can be seen from the Table 5, S-UTD model require the highest computation time. As the diffraction number increases, computation time increases, too. Because of excluding not effective buildings, computation time of S-UTD-CH model is very lower. In spite of that S-UTD and S-UTD-CH model gives almost the same results (only 0.153 dB difference); computation time of S-UTD-CH model is 0.695s whereas computation time of S-UTD model is 319.442 s.

As illustrated in Table 6, contribution of S-UTD model to UTD model is 0.626 dB resulting from adding of derivatives of incoming fields. Furthermore averagely 4.95 buildings excluded from the scenario caused by not having contribution. Fourthly, transmitting antenna height is selected as 10 m (lower) with all the same parameters and results are given in the Tables 7 and 8.

Table 7: Computation times for lower receiver height (10 m).

UTD (s)	S-UTD (s)	S-UTD-CH (s)
1.351	317.003	9.667
0.428	94.830	23.921

As can be seen from the Table 7, S-UTD model require the highest computation time. As the diffraction number increases, computation time increases, too. Because of excluding not effective buildings, computation time of S-UTD-CH model is very lower. In spite of that S-UTD and S-UTD-CH model gives almost the same results (only 0.119 dB difference); computation time of S-UTD-CH model is 9.667s whereas computation time of S-UTD model is 317.003 s.

Table 8: Path loss for elevated receiver height (10 m).

UTD vs S-UTD (dB)	S-UTD-CH vs S-UTD (dB)	ELECTED
2.780	0.119	3.550
2.628	0.124	1.317

As illustrated in Table 8, contribution of S-UTD model to UTD model is 2.780 dB resulting from adding of derivatives of incoming fields. Furthermore averagely 3.55 buildings excluded from the scenario caused by not having contribution. Finally, transmitting antenna height is selected as 5 m (lower) with all the same parameters and results are given in the Tables 9 and 10.

Table 9: Computation times for lower receiver height (5 m).

UTD (s)	S-UTD (s)	S-UTD-CH (s)
0.935	231.956	10.713
0.346	83.781	23.938

As can be seen from the Table 9, S-UTD model require the highest computation time. As the diffraction number increases, computation time increases, too. Because of excluding not effective buildings, computation time of S-UTD-CH model is very lower. In spite of that S-UTD and S-UTD-CH model gives almost the same results (only 0.141 dB difference); computation time of S-UTD-CH model is 10.713 s whereas computation time of S-UTD model is 231.956 s.

Table 10: Path loss for elevated receiver height (5 m).

UTD vs S-UTD (dB)	S-UTD-CH vs S-UTD (dB)	ELECTED
1.933	0.141	3.6
1.503	0.151	1.353

As illustrated in Table 10, contribution of S-UTD model to UTD model is 1.933 dB resulting from adding of derivatives of incoming fields. Furthermore averagely 3.60 buildings excluded from the scenario caused by not having contribution.

4. CONCLUSIONS

In general, UTD model is the fastest model to predict the field strength in radio propagation. If the scenario includes less than 11 buildings, S-UTD model gives the ultimate accuracy. Despite that S-UTD model gives accurate results, this model has large computation time. With decreasing eliminated building number, S-UTD and S-UTD-CH model gives almost the same results. In the case of not eliminating buildings, these two models predict the relative path loss at the receiver similarly. As the difference between the building heights decreases, building heights close to each other. Therefore S-UTD model have the most contribution to UTD model resulted from adding derivatives of the incoming fields. In the cases of elevated and highly elevated transmitting antenna, direct fields are dominant and so contribution of derivative terms are very small and can be ignored. In these cases, UTD model can be used with higher accuracy and less computation time. As a conclusion, S-UTD-CH model is optimum model for accuracy of predicted field and relatively less computation time in multiple diffraction scenarios.

ACKNOWLEDGMENT

This work partially supported by Bayburt University Scientific Research Support Unit under grant 2013-1/14.

REFERENCES

1. Kouyoumjian, R. G. and P. H. Pathak, "A uniform geometrical theory of diffraction for an edge in a perfectly conducting surface," *Proceedings of IEEE*, Vol. 62, No. 11, 1448–1461, 1974.
2. Rizk, K., R. Valenzuela, D. Chizhik, and F. Gardiol, "Application of the slope diffraction method for urban microwave propagation prediction," *IEEE Vehicular Technology Conference*, Vol. 2, 1150–1155, 1998.

3. Tzaras, C. and S. R. Saunders, “An improved heuristic UTD solution for multiple-edge transition zone diffraction,” *IEEE Trans. Antennas Prop.*, Vol. 49, No. 12, 1678–1682, 2001.
4. Tabakcioglu, M. B. and A. Kara, “Comparison of improved slope UTD method with UTD based methods and physical optic solution for multiple building diffractions,” *Electromagnetics*, Vol. 29, No. 4, 303–320, 2009.
5. Tabakcioglu, M. B. and A. Kara, “Improvements on slope diffraction for multiple wedges,” *Electromagnetics*, Vol. 30, No. 3, 285–296, 2010.
6. Bucci, O. M., “The experimental validation of a technique to find the convex hull of scattering systems from field data,” *IEEE Antennas and Propagation Symposium*, 539–542, 2003.
7. Chung, H. K. and H. L. Bertoni, “Application of isolated diffraction edge method for urban microwave path loss prediction,” *Antennas and Propagation Symposium*, Vol. 1, 205–209, 2003.
8. Tabakcioglu, M. B. and A. Cansiz, “Comparison of S-UTD-CH model with other UTD based models,” *Mosharaka International Conference on Communications, Propagation and Electronics*, 97–101, Jordan, 2010.
9. Tabakcioglu, M. B., D. Ayberkin, and A. Cansiz, “Comparison and analyzing propagation models,” *Asia-Pacific Conference on Antennas and Propagation*, 178–179, Singapore, 2012.

Broadband Analysis and Characterization of Noise for In-door Power-line Communication Channels

M. Mosalaosi and Thomas J. O. Afullo

Department of Electrical, Electronic and Computer Engineering
University of KwaZulu-Natal, Private Bag X54001, Durban 4001, South Africa

Abstract— Powerline communication (PLC) has emerged as an alternative solution for connectivity at home and offices in recent times [1]. Its development for multimedia broadband applications thus requires an extensive knowledge of the major peculiarities which influences communication over this channel. PLC channels are susceptible to noise inherent in power networks, leading to performance degradation. In this work, we have set-up a measurement system designed to capture the noise both in frequency and time domain for real power networks. The main observable components of the indoor PLC noise are: background noise, impulsive noise, and narrowband interferences. The impulsive components of PLC noise are observed to be time variant, random in nature, have high power spectral density (PSD) and lasts for very small time durations. A greater portion of the impulsive noise has cyclostationary behaviour, though with different amplitudes and widths. The repetition rates of these impulses are synchronous with the mains harmonics of 50 Hz and 100 Hz, the supply frequency in South Africa. Others have irregular occurrences and much higher repetition rates; hence they are unpredictable in nature. This noise is referred to as asynchronous impulsive noise [2].

These noise terms are key design parameters for modulation schemes in broadband PLC, popularly orthogonal frequency division multiplexing (OFDM), with its conventional receivers assuming additive white Gaussian noise (AWGN) [3]. The time variability of PLC noise is presented alongside its statistical analysis based on a series of measurements performed on numerous power-line scenarios. The relevance of this time variance is evaluated in actual channels. The significant difference in amplitudes of the impulsive noise is observed and characterized statistically. The PSD for both the background and impulsive noise is presented. Finally, we present the results of the noise PSD captured with a parametric model and compare our results with findings from other parts of the world.

1. INTRODUCTION

The universal existence of power-line networks in buildings and residential areas present a convenient and inexpensive communication media. However, developing PLC systems turns out to be a massive challenge for the communication engineer having to deal with harsh channels [4]. The difference between power line network and other conventional media such as twisted pair and coaxial is significant in terms of topology, structure and physical properties. The transfer characteristics of PLC channels are time-varying and frequency dependent with deep fades as high as 60 dB [5]. Additionally, PLC noise cannot be described as additive white Gaussian noise (AWGN) as is the case for conventional communication Channels. With high data rates (~ 1 Gbps) in demand nowadays, the PLC band is expanded [6]. These goals can be achieved by improving the resource allocation efficiency [7], with regards to the transfer function [8, 9] and the stochastic noise detail [10]. Thus, obtaining realistic power line channel noise models remain a key goal for the PLC community worldwide. Practical modems' performance fluctuates widely and these variations are a consequence of the presence of different appliances connected to the network [11], electromagnetic interference (EMI) [12], power supplies and switching loads [13].

2. NOISE MEASUREMENTS

In this section we describe the measurement procedure and instrumentation employed throughout the measurement process. PLC noise from actual indoor channels was measured both in time and frequency domain using Tektronix TDS 2024B digital oscilloscope and Rhode & Schwartz spectrum analyser respectively. A coupling circuit is used as an interface between the PLC channel and measurement devices. The broadband coupler not only facilitates reception of the noise signals, but also provides galvanic isolation between mains and measurement equipment. The coupler as shown in Figure 1 employs a broadband 1 : 1 transformer in combination with a capacitor yielding a high pass (LC) filter. On either side of the transformer are placed transient voltage surge suppressors (TVSS) with a metal oxide varistor (MOV) on the primary and back-to-back zeners on

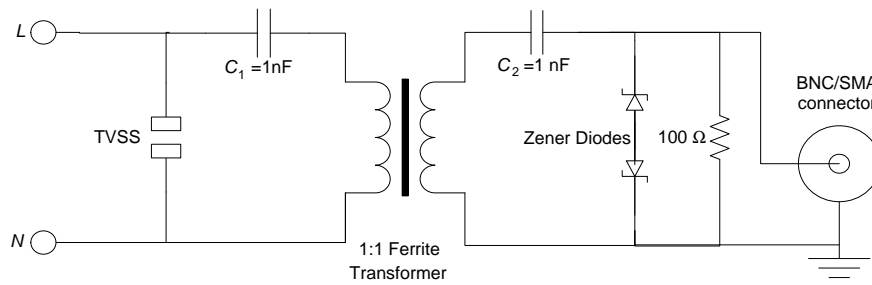


Figure 1: Coupling circuit.

the secondary. Their purpose is to suppress any voltage spikes large enough to damage the sensitive measuring equipment. The coupler transfer characteristics exhibit a reasonably flat response in the 1–30 MHz band, with the worst case loss of 1.59 dB within this band. Nonetheless, a calibration is performed prior to measurements.

PLC network noise as reported in [14] is very complex. It is resultant from electrical appliances connected to the network and external noise coupled to the network either by radiation or conduction. This noise can be classified in terms of its periodicity, randomness and cyclic nature [15].

3. IMPULSIVE NOISE

Impulsive noise can be either synchronous or asynchronous with the mains frequency. It is usually a result of switching transients peculiar with some electrical appliances in the electrical distribution network. Typical durations of impulses range from some microseconds up to a few milliseconds [16]. Typical synchronous impulsive noise is as shown in Figure 2(a) while Figure 2(b) depicts asynchronous impulsive noise. These are samples from a multitude of measurements performed in our University premises. In either case, the amplitude variability of the impulsive noise is observable. In actual PLC channels, components of both cases are present most of the time, hence in this paper; we present the behavioural statistics of impulsive noise in terms of its amplitude, duration of occurrence and time-interval between impulses. We compare our results to that of E. Liu et al. [16] which considered only the asynchronous impulsive noise. In our work, we have considered impulsive noise as that which has magnitude above a certain threshold (background noise) without cyclic classification. The results are presented in Table 1. Similar work has been done by T. Esmailian et al. [17] which presented their parameters in terms of their probability distributions.

In comparison, the disparity concerning the inter-arrival times is quite significant. This can be attributed to varied environments under study. From Table 1, the average inter-arrival time of 0.667 ms correspond to 15 impulses per half-cycle of 50 Hz mains. In our measurements, roughly 180 impulses are recorded on average every half-cycle of the mains. This is expected considering that most of our measurements are taken in laboratories running numerous electrical equipments such as electrical machines, drills, measuring equipment etc..

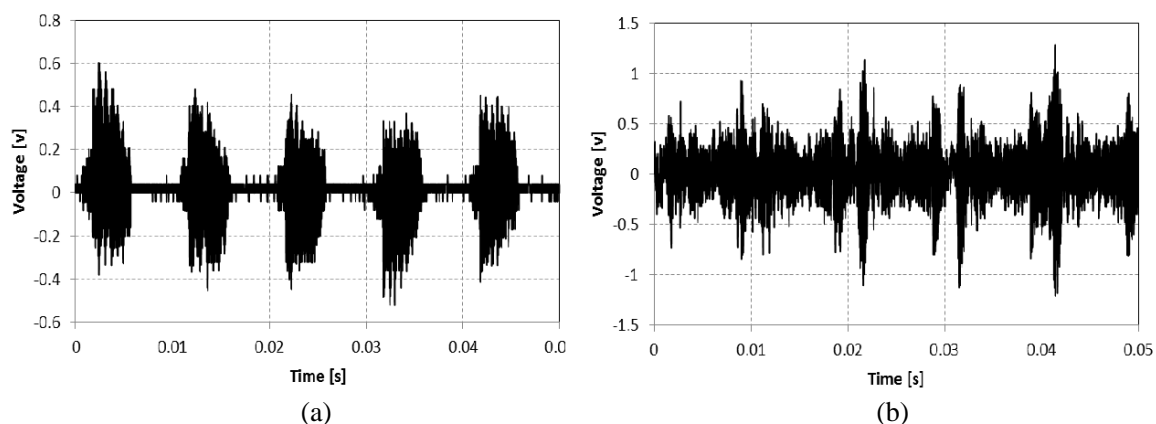


Figure 2: (a) Synchronous impulsive noise and (b) asynchronous impulsive noise.

Table 1: Statistical parameters of impulsive noise.

		Mean	Standard Deviation
Amplitude (mV)	Our Measurements	391	198
	E. Liu et al. [16]	229	121
Duration (μ s)	Our Measurements	152	139
	E. Liu et al. [16]	205	157
Interval time (ms)	Our measurements	0.0558	0.0458
	E. Liu et al. [16]	0.667	0.445

4. BACKGROUND NOISE

A power spectral density (PSD) model has been proposed by Esmalian et al. [17] for background noise as shown below:

$$\text{PSD}_{\text{noise}}(f) = A + B \cdot f^C \text{ [dBm/Hz]} \quad (1)$$

Based on the results of [17], the background noise has variability in frequency and colored. The parameter C , being less than zero, results in the background noise heavily present in lower frequencies than in higher frequencies. Guillet et al. [18] applied the same model to their measurements and obtained parameters in the same order of magnitude as that of [17]. However, [18] proposed a different approach aimed at modifying the actual description of background noise to accommodate the fact that the noise decreases as the frequency goes higher. The motivation comes from the fact that the estimated parameters are influenced by narrowband interferences and frequency located jammers inherent with the unshielded and unscreened indoor power lines [18]. They proposed an algorithm that performs a frequency sweep from low to high in order to find the minimum noise spectrum. Since their PSD is estimated from time domain data, this algorithm is embedded in their post-processing of the data. In this paper, though we still use the model of [17] to describe the PSD of background noise, we consider the proposal in [18] by tracking the minimum noise spectrum during measurements in the frequency domain. In our measurements, the new spectral magnitudes are compared to the previous data and if the new data is smaller, the new data is stored. The minimum spectral noise recorded is shown in Figure 3(b) with its mathematical model. Clearly the influence of narrowband interference and other effects are minimised, thus the background noise is not overestimated.

It is also equally important to describe the worst case scenario of the PLC channel noise. In-band spurious signals are unlikely to be intercepted even with spectrum analyzers of highest dynamic range and fast sweep capability. We apply the same algorithm to determine the minimum spectral noise, only this time the result is updated only when the new data is larger than the previous data. The maximum spectral noise recorded is shown in Figure 3(a) with its mathematical model. The model is not in good agreement with the measured results but rather presents a macroscopic capture of the measured data. The results are compared with those of Esmalian et al. [17] in Table 2 which also consider both the best and the worst case noise scenario.

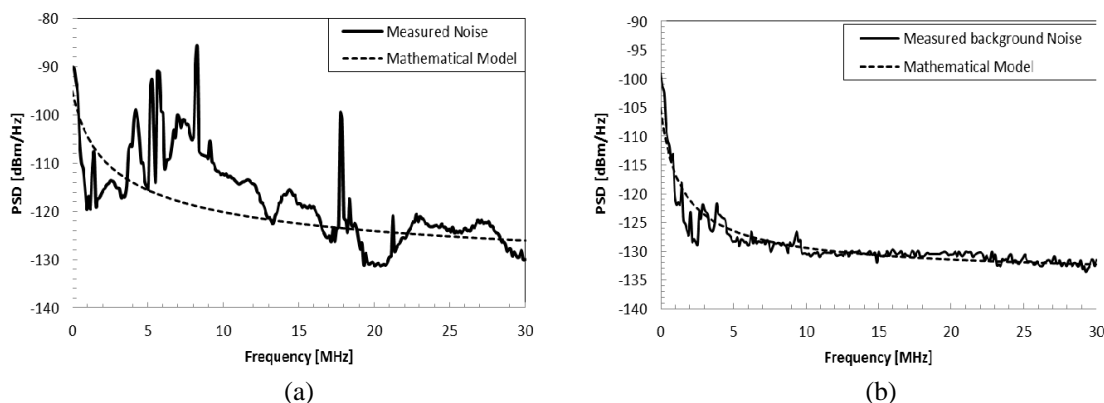


Figure 3: (a) Maximum spectral noise. (b) Minimum spectral noise.

Table 2: Parameters estimated for background noise.

		Background Parameters		
Statistics		A	B	C
Best Case	Our Measurement	-135	30.71	-0.721
	Esmailian et al.	-140	38.75	-0.72
Worst case	Our Measurement	-140	45.26	-0.341
	Esmailian et al.	-145	53.23	-0.337

5. CONCLUSIONS

In this paper, based on the measurements carried out in real indoor power line channels, the noise characteristics were investigated. The noise studies were summarised by finding the parameters of the noise statistics in terms of its amplitude, duration and interval time in time domain. Further studies were carried out in the frequency domain with a simple three parameter model used to capture its behaviour. The parameters of this model are presented. For both time and frequency domain, the parameters are compared with those of other campaigns elsewhere, a general agreement is observable, thus this statistical information can be used to aid the on-going efforts for PLC modem design and optimisation.

REFERENCES

1. Al Mawali, K. S., "Techniques for broadband power line communications: Impulse noise mitigation and adaptive modulation," Doctoral Thesis, RMIT University, Jul. 2011.
2. Cortes, J. A., L. Diez, F. J. Canete, and J. J. Sanchez-Martinez, "Analysis of the indoor broadband power-line noise scenario," *IEEE Transactions on Electromagnetic Compatibility*, Vol. 52, No. 4, Nov. 2010.
3. Lin, J. and B. L. Evans, "Cyclostationary noise mitigation in narrowband powerline communications," *Proc. APSIPA Annual Summit and Conference*, Dec. 2012.
4. Di Bert, L., P. Caldera, D. Schwingshack, and A. M. Tonello, "On noise modeling for power line communications," *Proceedings of the IEEE ISPLC 2011*, 283–288, 2011.
5. Dai, H. and H. V. Poor, "Advanced signal processing for power line communications," *IEEE Communications Magazine*, Vol. 41, No. 5, 100–107, 2004.
6. Maiga, A., J. Y. Baudais, and J. F. Herald, "Very high bit rate power line communications for home networks," *Proceedings of the IEEE ISPLC 2009*, 313–318, Dresden, Germany, 2009.
7. Sawada, N., T. Yamazato, and M. katayama, "Bit and power allocation for power-line communications under nonwhite and cyclostationery noise environment," *Proceedings of the IEEE ISPLC 2009*, 307–312, Dresden, Germany, 2009.
8. Tlich, M., A. Zeddani, F. Moulin, and F. Gauthier, "Indoor powerline communications channel characterisation up to 100 MHz — Part I: One-parameter deterministic model," *IEEE Trans. Power Delivery*, Vol. 23, No. 3, 1392–1401, 2008.
9. Tlich, M., A. Zeddani, F. Moulin, and F. Gauthier, "Indoor powerline communications channel characterisation up to 100 MHz — Part II: Time-frequency analysis," *IEEE Trans. on Power Delivery*, Vol. 23, No. 3, 1402–1409, 2008.
10. Tlich, M., H. Chaouche, A. Zeddani, and P. Pagani, "Novel approach for PLC impulse noise modeling," *Proceedings of the IEEE ISPLC 2009*, 20–25, Dresden, Germany, 2009.
11. Umehara, D., S. Denno, and M. Morikura, "The influence of compact AC adapter on PLC equipment," *IEICE 2008*, 55–60, 2008.
12. Zimmermann, M., "An analysis of the broadband noise scenario in power-line networks," *Proceedings of the IEEE ISPLC 2000*, 131–138, Limerick, Ireland, 2000.
13. Gulliet, V., G. Lamarque, P. Ravier, and C. Leger, "Improving the power line communication signal-to-noise ratio during a resistive load commutation," *Journal of Communication Magazine*, Vol. 4, No. 2, 126–132, 2009.
14. Cortes, J. A., L. Diez, F. J. Canete, and J. J. Sanchez-Martinez, "Analysis of the indoor broadband power-line noise scenario," *IEEE Trans. on Electromagn. Compat.*, Vol. 52, No. 4, Nov. 2010.

15. Zimmermann, M. and K. Dostert, “Analysis and modelling of impulse noise in broadband powerline communications,” *IEEE Trans. on Electromagn. Compat.*, Vol. 44, No. 1, 249–258, Feb. 2002.
16. Liu, E., Y. Gao, O. Bilal, and T. Korhonen, “Broadband characterization of indoor powerline channel,” *Proceedings of the IEEE ISPLC 2004*, 5, Zaragoza, Spain, 2004.
17. Esmailian, T., F. R. Kschischang, and P. G. Gulak, “Characteristics of in-building power lines at high frequencies and their channel capacity,” *Proceedings of the IEEE ISPLC 2000*, 52–59, Limerick, Ireland, 2000.
18. Guillet, V. and G. Lamarque, “Unified background noise model for power line communications,” *Proceedings of the IEEE ISPLC 2010*, 131–136, Rio de Janeiro, Brazil, 2010.

Design of All-fiber Coupled Electro-optic Sensors for High Power Microwave

Lili Song, Juntao He, Junpu Ling, Tao Jiang, and Danni Zhu

College of Optoelectronic Science and Engineering

National University of Defense Technology, Changsha, Hunan 410073, China

Abstract— A novel design of all-fiber coupled Electro-Optic (EO) sensors is introduced. Special fiber apparatus is used instead of free-space-coupling using bulk optics such as conventional lenses. The reflectance dependence on some parameters of the sensor is analyzed, such as the incident angle, the thickness of the crystal, the space between collimator and crystal, the under tested E -field, etc.. According to the analysis, the exact thickness of the LiTaO_3 crystal is calculated when attached to the collimator, which can make the reflectance and sensitivity to maximum.

1. INTRODUCTION

In the 1980s, A. Yariv gives the formula of the EO tensor coefficients. Since then, EO sensing technology has gained considerable attention due to its lower destruction [1], higher resolution [2] and broader frequency band [3] in both near-field and far-field in microwave measurement. Comparing to antenna based sensors, EO sensors present a flat response over a much broader frequency bandwidth (~ 8 decades) [2], a much higher spatial resolution on the order of the size of the laser-beam diameter or even less [4], and much less interference to the field under tested as no metal is used. Additionally, measurement in the terahertz (THz) region can be achieved when the thickness of EO crystal is on the order of $1 \sim 10 \mu\text{m}$ and the optic source is ultra-short pulse laser [4–6]. Moreover, EO sensors are independent of the mode of the microwave while antenna based sensors can only be available to special modes as the distribution of the antenna array is restricted.

Most researchers use polarizer, Wollaston prism, half-wave plates or quarter-wave plates for E -field measurement [1–7], which needs complex modulation and is immovable. Besides, the working condition is rigorous. Hence, building a sensing system with stable performance and straightforward operation is essential. This paper will show an all-fiber coupled EO sensing system which will make up these disadvantages aforementioned.

It's apparent that the design and optimization of EO sensors are crucial to achieving high-quality microwave sensing. Different sensitivities can be achieved with different structures and the enhancement of the interaction length of the crystal can improve the sensitivity [5, 8]. Fabry-Perot (F-P) cavity is efficient to improve the sensitivity, fortunately, without reduction of the spatial resolution as the volume of the crystal does not increase [5, 8, 9]. This paper displays detailed analysis and design progress of an F-P cavity based EO sensor with the application of LiTaO_3 crystal.

2. DESIGN OF ALL FIBER-COUPLED EO SENSOR SYSTEM

Instead of lens and plates, a polarization maintaining optical circulator (PMOC) and a polarization beam splitter (PBS) are used. The experimental schematic is composed of a laser, a PMOC, a PBS, an EO sensor and two photodiodes as shown in Figure 1. The laser comes out through Port ii (reflective port) after getting through the PMOC from Port i (import), and then sends to the EO crystal. The beam is reflected to Port ii by the crystal, then comes out from Port iii (export) and arrives at the PBS. The laser will be divided into 2 parts of different polarizations by the splitter, the ordinary beam and the extraordinary beam, detected by two photodiodes PD1 and PD2.

The thickness of the crystal in use should be negligible comparing to the wavelength of the E -field under tested, while it should be much larger than the wavelength of the detective laser. Figure 2 is a schematic of EO sensor whose structure is similar to an F-P cavity as the adjacent areas in both sides of the crystal are air. The EO sensor is composed of polarization maintaining fiber, a collimator (1/4 GRIN Lens), EO crystal and glass ferrule that makes the structure stable. The quasi F-P cavity configuration has drawn a lot of attention because of the following benefits. Firstly, the sensitivity is higher thanks to the enhancement of interference components [5, 8]. What's more, the Signal-to-Noise Ratio is larger [9]. Next, we take such a quasi F-P cavity structure into consideration.

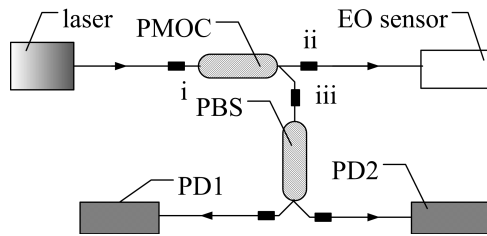


Figure 1: Schematic of all fiber-coupled EO probing system.

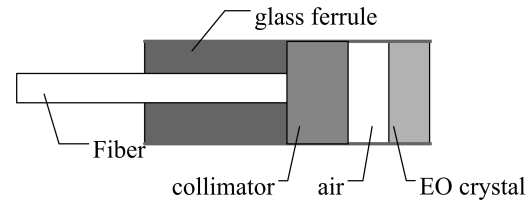


Figure 2: Schematic of EO sensor.

Suppose that the wavelength of the detective laser is λ , the thickness of the crystal is h , the thickness of the air layer between the collimator and the crystal is d , and n_o and n_e are the refractive indexes of the ordinary beam and the extraordinary beam of the crystal in the absence of E -field, respectively. r_{13} and r_{33} are EO coefficients, E_z is the Z -component of the E -field under tested, δ_o and δ_e are the phase retardations of the ordinary beam and the extraordinary beam in the appearance of E -field, respectively. The reflected beam of the F-P cavity can be expressed as in Figure 3. If $\theta_1 = 0$, we get the reflectance as Equation (1).

$$r = \sum_{n=1}^{\infty} r_n = \frac{r_1 + r_2 e^{i\delta}}{1 + r_1 r_2 e^{i\delta}} \quad (1)$$

$$R = r \cdot r^* = \frac{r_1^2 + r_2^2 + 2r_1 r_2 \cos \delta}{1 + r_1^2 r_2^2 + 2r_1 r_2 \cos \delta}$$

where r is the amplitude reflectance and R is the reflectance of the detective laser.

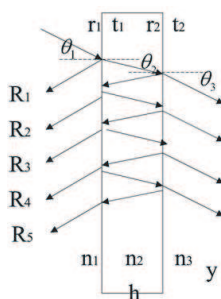


Figure 3: Schematic of reflected light in F-P cavity.

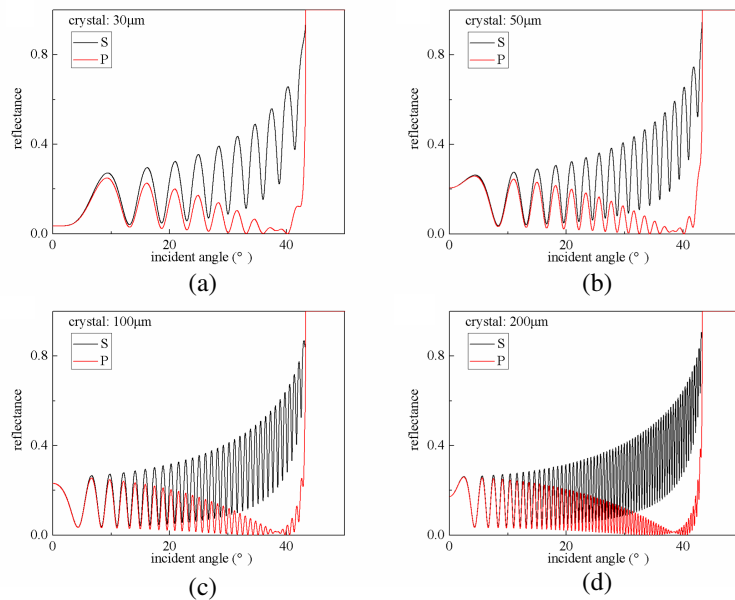


Figure 4: Reflectance dependence on incident angles with different thicknesses of crystal while $d = 0$.

3. ANALYSIS OF THE ALL FIBER-COUPLED EO SENSOR

To choose a suitable laser wavelength λ (incident wavelength), the optical communication window $\lambda = 1550 \text{ nm}$ is taken into consideration, where the attenuation is rather small. The principles of choosing the EO crystal are as following. Firstly, from Equation (1), it is obvious that the response of E_z is in proportion to either r_{13} or r_{33} . Therefore, the EO coefficients of the crystal should be large enough in the purpose of achieving higher sensitivity. Secondly, the absorption of the

crystal to the detective laser beam should be small enough. In addition, the crystal should be with low temperature effect, high optical damage threshold, good optical uniformity as well as easy to manufacture. In general, the available crystals series are mainly 3 m, 4 mm, 6 mm, 6 m⁻² and 4 m⁻³. We choose LiTaO₃ for analysis as r_{13} and r_{33} can get to 6.95×10^{-12} m/V and 27.4×10^{-12} m/V [10] respectively at $\lambda = 1550$ nm. Besides, the optical damage threshold reaches 1550 GW/m² [11]. The refractive indexes of the crystal are $n_o = 2.1186$ and $n_e = 2.1224$. Furthermore, $n_1 = 1.457$ and $n_3 = 1$, representing refractive indexes of fiber and the air, respectively [10].

3.1. Reflectance Dependence on the Incident Angle of the Laser

In general, the dominate parameters affecting the reflectance are the incident angle, the thickness of the crystal h , the space between collimator and crystal d , the under tested E -field, etc.. First, the relationship between the incident angle and reflectance is analyzed in Figure 4. For simplification, only the extraordinary beam is considered, which can be realized when the fiber is coupled to the ordinary axis, and the thickness of the air between the collimator and the crystal d is assumed to be 0. The thickness of the EO crystal h is set at four different values, 30 μm , 50 μm , 100 μm , and 200 μm , to simulate the relationship between the reflective efficiency and the incident angle of the laser ranging from 0° to 50°, as is shown in Figures 4(a)–(d). Black curves are the reflectance of the S -polarized beam and red curves are the reflectance of the P -polarized beam.

According to Figure 4, reflectance of the S -polarized beam fluctuates in localities and the maximum values rise overall. Reflectance of the P -polarized beam fluctuates in localities and the maximum values decrease at first and then increase. For all the curves, reflectance approaches 100% when the incident angle is close to 43.34° as a result of total reflectance, while the numerical value solved with the Refractive Law is 43.3385°. When the thickness of the crystal become thicker as shown in Figures 4(a) to (d), the curves fluctuate in a shorter period, which is due to the F-P effect. When the optical length of the incident wave induced by the crystal is the even multiples of half wavelength, a reflective beam in a given order is enhanced by the one in the next order, As a result, reflectance reaches maximum values in several incident angles. The minimum values appear when the optical length of the incident wave induced by the crystal is the odd multiples of half wavelength.

3.2. Reflectance Dependence on the Thickness of Crystal

The next analyzed parameter in this study is the thickness of crystal h . Figure 5 shows the reflectance dependence on the thickness of the crystal at normal incidence. The thickness of the air layer between collimator and crystal d is assumed to be 0. From the figure we can see the curves vary owing to the F-P effect. The following paragraph will give a more detailed explanation of this phenomenon. To get a maximum value, $R' = 0$, $R'' \leq 0$, that is,

$$R'(h) = 8\pi n/\lambda \frac{r_1 r_2 (1 - r_1^2)(1 - r_2^2) \sin \delta}{(1 + r_1^2 r_2^2 + 2r_1^2 r_2^2 \cos \delta)^2} = 0 \quad (2)$$

$$R''(h) = 32\pi^2 n^2 / \lambda^2 \frac{r_1 r_2 (1 - r_1^2)(1 - r_2^2)}{(1 + r_1^2 r_2^2 + 2r_1^2 r_2^2 \cos \delta)^3} (2 \sin^2 \delta + \cos \delta + \cos \delta r_1^2 r_2^2 + 2r_1 r_2 \cos^2 \delta) \leq 0 \quad (3)$$

To satisfy these two conditions, we can get Equation (4),

$$n_0 h / \lambda = \frac{k_1}{2}, \quad k_1 = 1, 2, 3, \dots \quad (4)$$

Equation (4) is in consistent with Figure 5. Sensitivity can be maximized in the condition of $R'' = 0$, then we can get Equation (7),

$$n_0 h / \lambda = \frac{1}{4\pi} ar \cos \left(\frac{(1 + r_1^2 r_2^2) \pm \sqrt{r_1^4 r_2^4 + 2r_1^2 r_2^2 - 8r_1 r_2 + 9}}{4(1 - r_1 r_2)} \right) + \frac{k_2}{2}, \quad k_2 = 1, 2, 3, \dots \quad (5)$$

According to Equation (4) and Equation (5), suitable thickness of the crystal can be chosen to realize high quality measurement, and the reflectance can reach the maximal values when $h = 365.807k_1$ (μm), $k_1 = 1, 2, 3, \dots$ when the crystal is attached to the collimator. The sensitivity can be maximized when $h = 0.1227 + 0.3658k_2$ (μm), $k_2 = 1, 2, 3, \dots$ in the same structure.

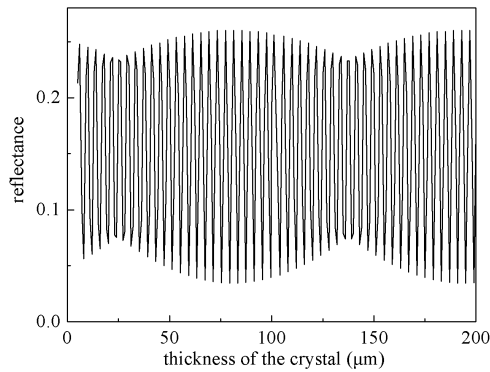


Figure 5: Reflectance dependence on the thickness of crystal at normal incidence.

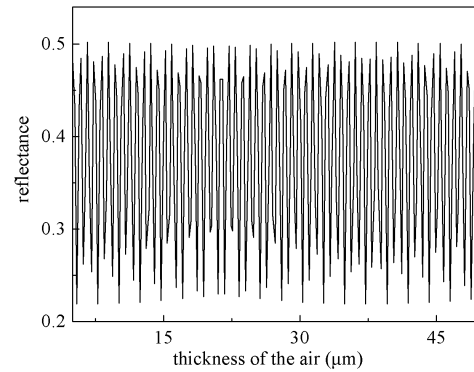


Figure 6: Reflectance dependence on d at normal incidence with $h = 100 \mu\text{m}$.

3.3. Reflectance Dependence on the Space between the Crystal and the Collimator

The reflectance dependence on the thickness of the air layer between the collimator and the crystal d is similar to that on the thickness of the EO crystal h as both are correlative to the optical length. Figure 6 is the reflectance dependence on the thickness of the air layer between collimator and the crystal at normal incidence with $h = 100 \mu\text{m}$. The reflectance increases comparing to Figure 5 in the appearance of the air between the collimator and the crystal.

3.4. Reflectance Dependence on E -field under Test

Figure 7 shows the reflectance dependence on E_z under tested with $h = 200 \mu\text{m}$ and $d = 0$. The maximum E_z is 100 MV/m in Figure 7(a) while 1 MV/m in Figure 7(b) as the damage level of the EO sensor is known to be in the order of 1 MV/m [13]. The red curves and black curves are the reflectance of the ordinary beam and the extraordinary beam, respectively.

According to Figure 7(a), the extraordinary beam has a higher sensitivity to E_z as the EO coefficient r_{33} is almost four times of r_{13} . In Figure 7(b), no repeated value occurs of the either the ordinary beam or the extraordinary beam when the E -field is smaller than 1 MV/m, which makes the operation easier in practical measurement.

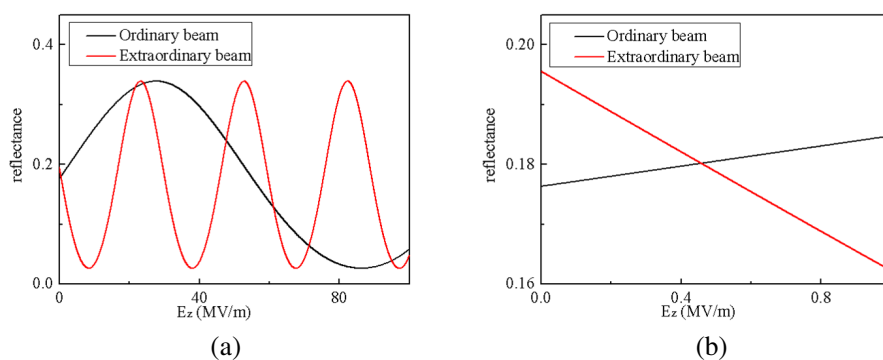


Figure 7: Reflectance dependence on E_z of ordinary beam (red) and extraordinary (black) beam in FAC structure.

4. CONCLUSION

We introduced a novel all-fiber coupled EO sensor, and analyzed the parameters which may influence the reflectance, such as the incident angle, the thickness of the crystal, the thickness of the air layer between the collimator and the crystal and the E -field under test. Based on the analysis using LiTaO_3 as the EO crystal, total reflectance appears when the incident angle is close to 43.34° . Reflectance increases in the appearance of the air between the collimator and the EO crystal. Reflectance can get the maximum value when $h = 365.807k_1 (\mu\text{m})$, $k_1 = 1, 2, 3, \dots$ when the crystal

is attached to the collimator. The sensitivity can be maximum when $h = 0.1227 + 0.3658k_2$ (μm), $k_2 = 1, 2, 3, \dots$ in the same structure.

REFERENCES

1. Bernier, M., L. Duvillaret, and G. Gaborit, "Fully-automated E -field measurement system using pigtailed electro-optic sensors for temperature-dependent-free measurements of microwave signals in outdoor conditions," *IEEE*, Vol. 9, No. 1, 61–68, 2008.
2. Bnoek, E., D. Hornbachner, E. R. Bratengeyer, et al., "Electro-optic elf field sensor," 1992.
3. Quang, D. L., D. Erasme, and B. Huyart, "Fabry-perot enhance real-time electro-optic probing of MMICs," *Elec. Lett.*, Vol. 29, No. 5, 498–499, 1993.
4. Yang, K., G. David, S. V. Robertson, et al., "Electrooptic mapping of near-field distributions in integrated microwave circuits," *IEEE*, Vol. 46, 1998.
5. Mitofanov, O., "Terahertz near-field electro-optic based on a microresonator," *Appl. Phys. Lett.*, Vol. 88, 2006.
6. Bakker, H. J., G. C. Cho, and H. Kurz, "Distortion of terahertz pulses in electro-optic sampling," *Opt. Soc. Am. B*, Vol. 15, 1795–1801, 1998.
7. Duvillaret, L., S. Rialland, and J. L. Coutaz, "Electro-optic sensors for electric field measurements. II. Choice of the crystals and complete optimization of their orientation," *J. Opt. Soc. Am. B*, Vol. 19, 2704–2715, 2002.
8. Lee, D. J., N. W. Kang, and J. H. Choi, "Recent advances in the design of electro-optic sensors for minimally destructive microwave field probing," *Sensors*, Vol. 11, 806–824, 2011.
9. Muller, P. O., S. B. Alleston, and A. J. Vickers, "An external electro-optic sampling technique based on the Fabry-Perot effect," *IEEE J. Quantum Electron*, Vol. 35, 7–11, 1999.
10. Zeng, W., D. P. Wang, and Y. H. Xu, "Growth and photoreflexive resistance properties of near-stoichiometric Zn: LiTaO₃ crystal," *Journal of Chinese Ceramic Society*, Vol. 37, No. 11, 1829–1832, 2009.
11. Yariv, A. and P. Yeh, *Optical Waves in Crystals*, Science Press, Beijing, 1991.
12. Garzarella, A., S. B. Qadri, and D. H. Wu, "Optimal electro-optic sensor configuration for phase noise limited, remote field sensing applications," *Appl. Phys. Lett.*, Vol. 94, 1–3, 2009.

Investigation of Novel Waveguide Phase Shifters for High Power Applications

Yiming Yang, Chengwei Yuan, Qiang Zhang, Danni Zhu, Shengren Peng, and Longzhou Yu

College of Optoelectronic Science and Engineering
National University of Defense Technology, Changsha 410073, China

Abstract— High-power phase shifter that can on-line adjust the transmit phase of high-power microwave (HPM) is of great interest. The traditional phase shifters can not satisfy the power capacity requirement. There is a pressing need to come up with new alternative phase shifters. In this paper, two kinds of waveguide phase shifters are investigated. To increase the power capacity, no dielectric is introduced, and they are all mechanical phase shifters. Both the phase shifters are with high transmission efficiency over 99% and high power capacity over 300 MW in the vacuum.

1. INTRODUCTION

High-power phase shifter that can on-line adjust the transmit phase of high-power microwave (HPM) is of great interest [1, 2]. It has an extensive application in mode converter, high power array antenna and others [3–6]. Ferrite phase shifter [7] and PIN diode phase shifter [8] are the two well developed phase shifters that can be applied in above mentioned fields. However, they can not be applied directly for high-power applications because ferrite and semiconductor has limited power handling capacity [9, 10]. In view of such limitation, it is a pressing need to come up with novel phase shifters for high-power applications.

In this paper, two kinds of waveguide phase shifters are investigated. To increase the power capacity, no dielectric is introduced, and they are all mechanical phase shifters. The first one named waveguide-inserting-fin phase shifter. The inserting-fin changes the transmission constant of the microwave. 360 degree phase shift can be obtained by adjusting the length of the inserting metal fin. The advantage of this phase shifter is that the microwave propagation keeps on the same direction but with longer longitudinal length. The second one named narrow side slot-waveguide phase shifter. It is designed based on 3dB power divider of waveguide Slot Bridge. The difference is using adjustable metal choke piston at the terminal position of the power divider. Then, it can realize 360 degree phase shift by adjusting the choke piston position. Both the phase shifters are with high transmission efficiency over 99% and high power capacity over 300 MW in the vacuum.

2. WAVEGUIDE-INSERTING-FIN PHASE SHIFTER

Figure 1 is the scheme of the waveguide-inserting-fin phase shifter. The rectangular waveguide is divided to four regions by metal fin 1 and fin 2 in the middle of the waveguide perpendicular to the broad wall, the input TE₁₀ mode microwave in region 1 then changes to two TE₁₀ mode in region 2 and region 3, respectively. And the two TE₁₀ modes finally combined again to TE₁₀ mode in region 4. It is known that the transmission constant in region 2 and region 3 is different from that in region 1 and region 4 [11]. Fin 1 is fixed to the waveguide, and fin 2 can be sliding in and out into fin 1 to change the transmission length L of the two TE₁₀ modes, resulting in the phase shift of the microwave. The convex 1 and 2 are used to diminish the reflections.

As an example, a phase shift operates at frequency 9.5 GHz is designed. The wide side dimension a is 40 mm, the narrow side dimension b is 20 mm; thickness of fin 1 and 2 is 5 mm and 1 mm, respectively. The dimensions of the convex 1 and 2 are optimized.

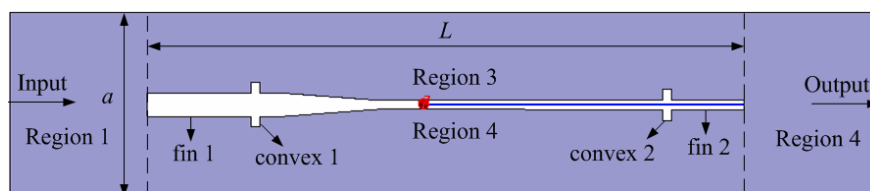


Figure 1: Scheme of the waveguide-inserting-fin phase shifter.

Figure 2 displays the electric field distribution inside the waveguide-inserting-fin phase shifter. It shows the microwave propagation process. Besides, it can be seen that there is no obvious electric field enhancement during the adjustment of the position of fin 2, the maximum field is 3.226 kV/m during the adjustment when the inject power is 1 W. It is known that the breakdown electric field is about 30 kV/cm in the normal condition, however, according to Kilpatrick criterion [12] in the vacuum condition $f = 1.643E^2e^{-8.5/E}$, where f is the frequency (MHz); E is the corresponding breakdown electric field (MV/m), so the breakdown electric field is about 80.178 MV/m for microwave at 9.5 GHz in the vacuum. Then it can be obtained that a waveguide-inserting-fin phase shifter has a power capacity larger than 864.8 kW and 617.8 MW in the atmosphere and vacuum, respectively.

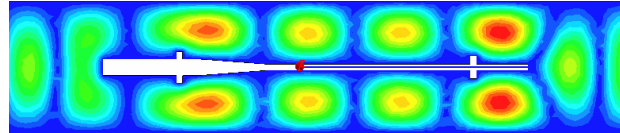


Figure 2: Electric field distribution inside the waveguide-inserting-fin phase shifter.

Figure 3 presents the phase shift and transmission coefficient versus the transmission length L changed by sliding fin 2. From the simulation results by electromagnetism software, the transmission efficiency keeps over 99% when the phase shift reaches 360 deg. The phase shift reaches 4.1 deg per millimeter. The fin 2 need to slide about 87.8 mm to achieve 360 deg phase shift, and the whole length of this phase shifter need about 200 mm. The advantage of this phase shifter is that the microwave propagation keeps on the same direction but with longer longitudinal length.

3. NARROW SIDE SLOT-WAVEGUIDE PHASE SHIFTER

Figure 4 is the structure of the narrow side slot-waveguide phase shifter. The structure is similar to the 3 dB power divider of the waveguide slot bridge and the operate mechanism is also similar. The microwave is in TE₁₀ mode in port 1, and transforms to TE₂₀ mode in the region of narrow side slot. By designing the length L of the narrow side slot and the wide side dimension of the slot region a , the power can be equally divided to port 2 and port 3. Different from the power divider, here we use the choke piston at the terminal position of the power divider. Then, the microwaves in port 2 and 3 are reflected to port 4. Optimizing the dimension L and a can obtain high transmission efficiency in port 4. Moreover, the output phase in port 4 can be changed by adjusting the length ΔL . It can realize 360 degree phase shift by adjusting the choke piston position.

Taking 14.25 GHz microwave as an example, a narrow side slot-waveguide phase shifter is designed. The wide side dimension and narrow side dimension of port 1, port 2, port 3 and port 4 is 15.8 mm and 10.16 mm, respectively. The length L of the slot is 24.14 mm, the wide side dimension a' is 30.6 mm, the wall thickness h is 2 mm.

Figure 5 displays the electric field distribution inside the narrow side slot-waveguide phase shifter. It also shows the microwave propagation process. The maximum field is 5.501 kV/m

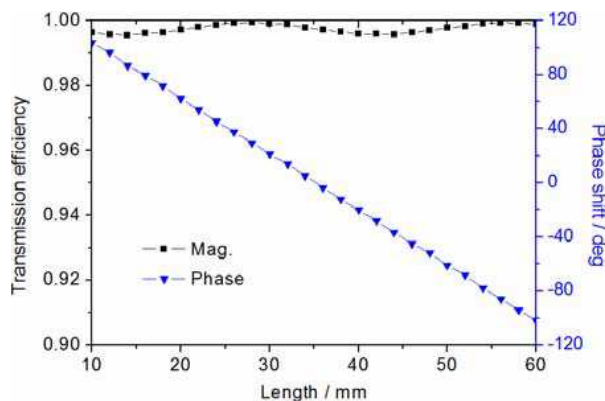


Figure 3: Phase shift and transmission efficiency versus the transmission length L .

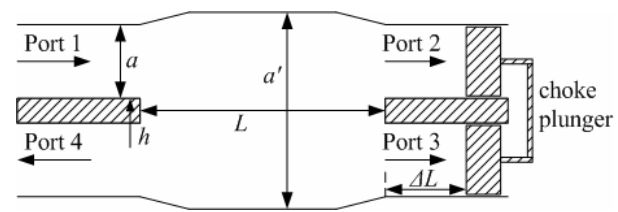


Figure 4: Scheme of the narrow side slot-waveguide phase shifter.

during the adjustment of ΔL when the inject power is 1 W. As calculated above in Section 2, it can be obtained that the breakdown threshold for Ku band 14.25 GHz in the vacuum is 97.3 MV/m. Then, such a narrow side slot-waveguide phase shifter has a power capacity larger than 297.4 kW and 312.8 MW in the atmosphere and vacuum, respectively.

Figure 6 presents the phase shift and transmission coefficient versus the length ΔL adjusted by the choke piston. From the simulation results by electromagnetism software, the transmission efficiency keeps over 99% when the phase shift reaches 360 deg. The phase shift reaches 23.12 deg per millimeter. The choke piston need to slide about 15.6 mm to achieve 360 deg phase shift, and the whole length of this phase shift structure need about 70 mm. The advantage of this phase shifter is that this kind phase shifter has high power handling capacity with relatively small size. And it is easy to be realized in engineering. The choke piston can be drive by stepper motor.

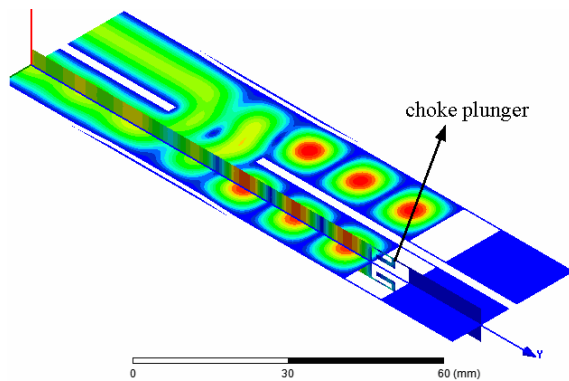


Figure 5: Electric field distribution inside the narrow side slot-waveguide phase shifter.

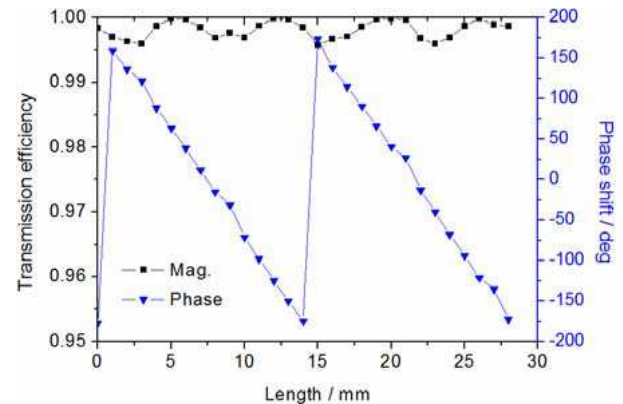


Figure 6: Phase shift and transmission efficiency versus the transmission length L .

4. CONCLUSIONS

Phase shifter, as a key device of array antenna used to adjust the output phase of HPM, is urgently needed to be investigated since the common phase shifter can not satisfy the HPM applications. In this paper, two kinds of phase shifters that adjust the output phase of HPM are put forward. Both the phase shifters are with high transmission efficiency over 99% and high power capacity over 300 MW in the vacuum. Researchers can choose a phase shifter according to their applications.

REFERENCES

1. Ge, X. J., H. H. Zhong, B. L. Qian, J. Zhang, L. G. Liang, Z. X. Jin, Y. W. Fan, and J. H. Yang, "An L-band, coaxial relativistic backward wave oscillator with mechanical frequency tunability," *Appl. Phys. Lett.*, Vol. 97, No. 10, 1503–1505, Sep. 2010.
2. Zhang, J., H. H. Zhong, Z. Jin, T. Shu, S. Cao, and S. Zhou, "Studies on efficient operation of an X-band oversized slow-wave HPM generator in low magnetic field," *IEEE Trans. Plasma Sci.*, Vol. 37, 1552–1557, 2009.
3. Yang, Y. M., C. W. Cheng, and B. L. Qian, "A novel phase shifter for Ku-band high power microwave applications," *IEEE Trans. Plasma Sci.*, Vol. 42, No. 1, 51–54, 2014.
4. Li, X. Q., Q. X. Liu, J. Q. Zhang, L. Zhao, and Z. Q. Zhang, "The high-power radial line helical circular array antenna: Theory and development," *ICMMT*, 671, 2010.
5. Li, X. Q., Q. X. Liu, X. J. Wu, L. Zhao, J. Q. Zhang, and Z. Q. Zhang, "A GW level high-power radial line helical array antenna," *IEEE Trans. Antennas Propag.*, Vol. 56, No. 9, 2943–2948, 2008.
6. Yang, Y. M., C. W. Yuan, and B. L. Qian, "Beam steering antenna for high power microwave application," *High Power Laser and Particle Beams*, Vol. 25, 2648, 2013.
7. Erker, E. G., A. S. Nagra, Y. Liu, P. Periaswamy, T. R. Taylor, J. Speck, and R. A. York. "Monolithic Ka-band phase shifter using voltage tunable BaSrTiO₃ parallel plate capacitors," *IEEE Microwave Guided Wave Lett.*, Vol. 10, No. 1, 10–12, Jan. 2000.
8. Malczewski, A., S. Eshelman, B. Pillans, J. Ehmke, and C. L. Goldsmith, "X-band RF MEMS phase shifters for phased array applications," *IEEE Microwave Guided Wave Lett.*, Vol. 9, No. 12, 517–519, Dec. 1999.

9. Wilhelm, H. and V. Aulock, *Handbook of Microwave Ferrite Materials*, Academic Press, New York and London, 1965.
10. Amitay, N. and B. Glance, “Switching performance of a 12 GHz p-i-n phase shifter/driver module for satellite communication phased array,” *IEEE Trans. Communications*, Vol. 29, No. 1, 46–50, 1981.
11. Collin, R. E., *Field Theory of Guided Waves*, McGraw-Hill, New York, 1960.
12. Jameson, R. A., “High brightness RF linear accelerators,” *NATO Advanced Study Institute on High-Brightness Accelerators Conference*, 497, Pitlochry, 1986.

Compact Microstrip Patch Antenna with Parasitic Loading for X & Ku Band Applications

Mohit Barthwal¹, Sohaib Abbas Zaidi¹, M. R. Tripathy¹, and S. S. Pattnaik²

¹Department of ECE, Amity University, Noida, India

²ETV Department, National Institute of Technical Teachers Training and Research, Chandigarh, India

Abstract— Microstrip patch antennas are becoming popular day by day because of the various advantage offered by them such as low cost, less weight, low profile and ease of fabrication [1]. Popularity of patch antenna can be known from the fact that they found their application in various fields like aircraft, space technology [2, 3], mobile communication, biomedical, broadcasting etc.. However narrow bandwidth of patch antenna is one of the major limitation, that researcher around the world have been trying to overcome. Many techniques have been suggested in the past in order to overcome this problem [4]. One such technique is employed in this paper in which parasitic elements are used along with driven patch excited with the help of coax feed for X & Ku band. An equivalent circuit of the proposed antenna is also developed and analyzed. The antenna is designed on FR4 substrate with permittivity 4.4 and having dimension of ground plane $17 \times 19 \text{ mm}^2$. The patch has a dimension of $6 \times 6 \text{ mm}^2$ which is loaded with parasitic elements. The proposed antenna is able to achieve impedance bandwidth of 1.8 GHz from 10.8 GHz to 12.6 GHz thus, covering Ku band as well and has a maximum gain of 3.9 dBi. Comparison between simulated and fabricated results would be presented. The return loss, electric field distribution, radiation pattern of the proposed antenna is presented in this paper. All simulations are done by using HFSS software.

1. RESULTS AND DISCUSSIONS

Figure 1 shows the configuration of the proposed patch antenna consisting of square patch loaded with parasitic elements with a ground plane. The complete description about parameters of proposed antenna structure is given in Table 1. The dimensions of proposed antenna are obtained by using HFSS.

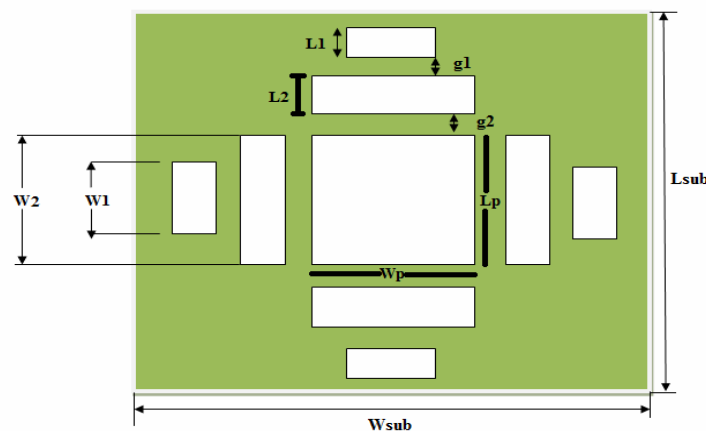


Figure 1. Configuration of the proposed antenna.

Figure 2 shows our proposed antenna from circuit point of view. When the patch antenna is loaded with parasitic elements, they get coupled with driven patch, i.e., there will be mutual coupling M between parasitic elements and patch as a result of which there will be a mutual inductance. Apart from this, patch and parasitic elements being conducting elements will possess self inductance as well. Beside inductance, there will be a mutual capacitance between the patch and parasitic elements and also between patch and ground plane that need to be taken into consideration while doing complete calculations. As the structure is being excited by coax pin so an additional inductance could be added if pin is long. However, it could be neglected if it is small.

Table 1.

L_{sub}	17 mm
W_{sub}	19 mm
L_p	6 mm
W_p	6 mm
L_1	1 mm
W_1	3 mm
L_2	1 mm
W_2	6 mm
g_1	0.5 mm
g_2	0.5 mm

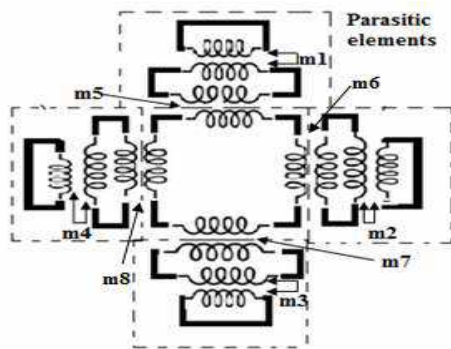
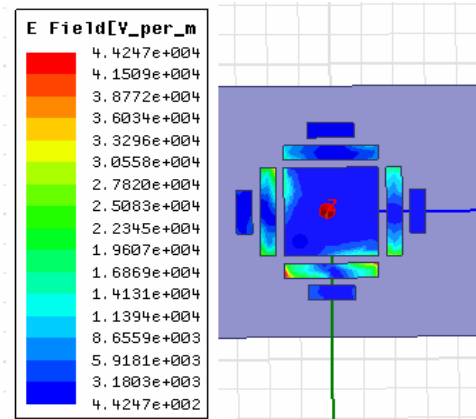


Figure 2. Showing inductive coupling in the proposed antenna.

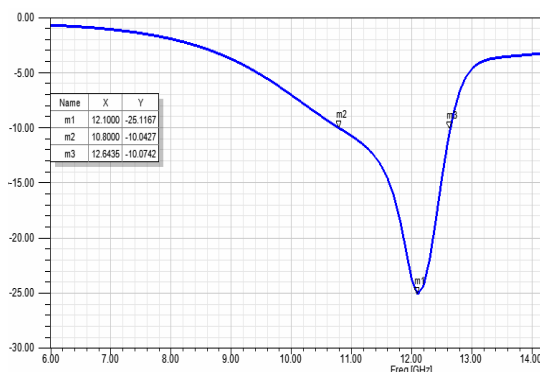
Figure 3. E field distribution.

Equations [5] given below could be used to find mutual inductance & self inductance

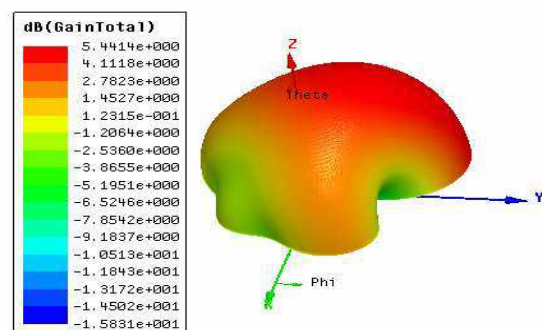
$$M = -\frac{\mu l}{2\pi} \left[\ln(1 + \sqrt{2}) + 1 - \sqrt{2} + w^2 \sqrt{2} / 24l^2 \right] \quad (1)$$

$$S = \frac{\mu l}{2\pi \left[\ln\left(\frac{2l}{w}\right) + 0.5 + \frac{w}{3l} - \frac{w^2}{24l^2} \right]} \quad (2)$$

The mutual inductance between parasitic elements is calculated using above Eq. (1) and is found as $m_1 = m_2 = m_3 = m_4 = 0.295$ nH and $m_5 = m_6 = m_7 = m_8 = 0.656$ nH. The self inductance



(a)



(b)

Figure 4. (a) Return loss of the proposed antenna. (b) 3D polar plot.

is also being calculated and is given as: $S_1 = 1.88 \text{ nH}$, $S_2 = 3.5 \text{ nH}$, $S_3 = 1.43 \text{ nH}$. The simulated return loss and polar plot of the proposed antenna are depicted in Figures 4(a) & 4(b) respectively which clearly indicates that the impedance bandwidth of antenna is 1.8 GHz for return loss less than -10 dB .

Radiation pattern of the proposed antenna is also studied and is shown in Figures 5(a) & 5(b). It is clear from the figure that a maximum gain of 3.9 dBi is achieved at resonant frequency in elevation plane and 3.2 dBi in azimuth plane.

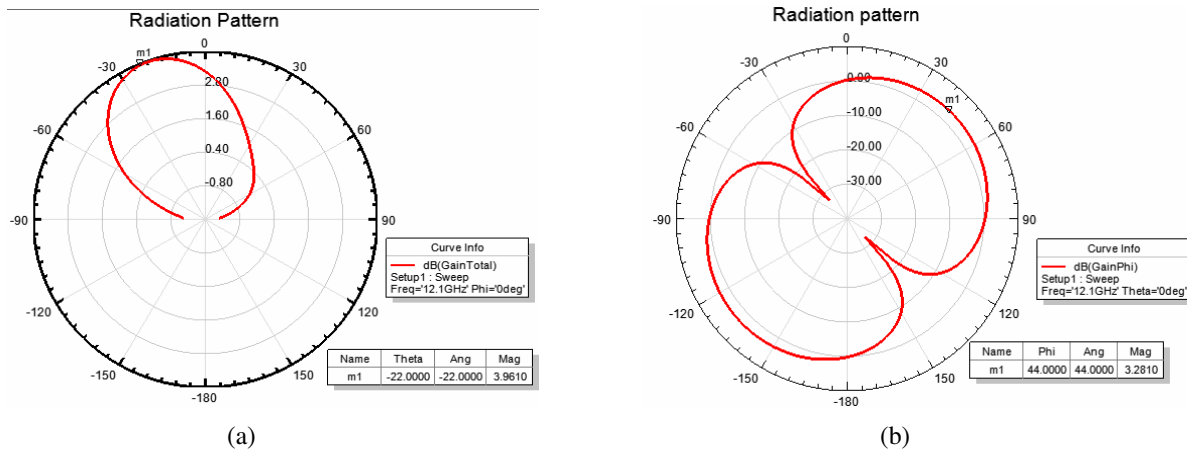


Figure 5. (a) Elevation plane. (b) Azimuth plane.

2. CONCLUSION

A compact Microstrip patch antenna for X and Ku band is successfully designed, simulated and analyzed. It has been found that the antenna achieved an impedance bandwidth of 1.8 GHz and was able to provide a maximum gain of 3.9 dBi in elevation plane and 3.28 dBi in azimuth plane. Good matching is obtained at desired frequency without any use of external tuning circuit. Further the structure can be tuned to operate at various frequencies by varying gap between parasitic elements and thus provides flexibility to our structure.

REFERENCES

1. Garg, R., P. Bhartia, I. Bahl, and A. Ittipiboon, *Microstrip Antenna Design Handbook*, Artech House Inc., 2001.
2. Bugaj, M., R. Przesmycki, L. Nowosielski, and K. Piwowarczyk, "Active microstrip antennas operating in X band," *PIERS Online*, Vol. 7, No. 3, 221–225, 2011.
3. Motin, M. A., et al., "Design and simulation of a low cost three band microstrip patch antenna for the X-band, Ku-band and K-band applications," *7th International Conference on Electrical and Computer Engineering*, Dec. 20–22, 2012.
4. Fernández González, J. M., P. Padilla, G. Expósito-Domínguez, and M. Sierra-Castañer, "Lightweight portable planar slot array antenna for satellite communications in X-band," *IEEE Antennas and Wireless Propagation Letters*, Vol. 10, 2011.
5. Joshi, J. G., S. S. Pattnaik, and S. Devi, "Geo-textile based metamaterial loaded wearable microstrip patch antenna," *International Journal of Microwave and Optical Technology*, Vol. 8, No. 1, Jan. 2013.

Accurate Numerical Solutions for Electromagnetic Scattering by Strongly Anisotropic Structures

G. Z. Yin, Y. Q. Zhang, Z. G. Zhou, J. X. Hong, and M. S. Tong

Department of Electronic Science and Technology, Tongji University, Shanghai, China

Abstract— Solving volume integral equations (VIEs) with anisotropic media usually relies on the method of moments (MoM) with the divergence-conforming Schaubert-Wilton-Glisson (SWG) basis function or curl-conforming edge basis function. However, the basis functions may not be suitable to represent unknown functions when the anisotropy of media is strong. In this work, we replace the MoM with a point-matching method to solve such problems and the method characterizes the unknown functions at discrete points with directional components and more degrees of freedoms. Also, the method allows the use of JM-formulation which does not explicitly include material property in the integral kernels. A typical numerical example is presented to demonstrate the approach.

1. INTRODUCTION

Electromagnetic (EM) analysis for anisotropic structures relies on the accurate solution of volume integral equations (VIEs) in the integral equation approach [1]. Traditionally, the VIEs are solved by the method of moments (MoM) with the divergence-conforming Schaubert-Wilton-Glisson (SWG) basis function [2] or curl-conforming edge basis function [3]. These basis functions are defined over a pair of tetrahedral elements with a common face or common edge and require conforming meshes in geometric discretization, resulting in a higher preprocessing cost. Also, the basis functions have to assume a homogeneous material in each tetrahedron and disregard the possible directional difference of material, so they may not be suitable for strongly anisotropic materials [4]. In this work, we present a point-matching method which may be more appropriate to solve such problems because of its different features. The method uses a collocation procedure to transform integral equations into matrix equations and possesses several merits, i.e., the simple mechanism of implementation, use of nonconforming meshes, and removal of basis and testing functions [5]. The method represents unknown functions at discrete points with directional components and usually includes more degrees of freedoms than the MoM. Furthermore, the method allows the use of JM-formulation which does not explicitly include material property in the integral kernels in the VIEs [6]. These characteristics indicate that it is very suitable for solving anisotropic problems and also very friendly to the incorporation of fast algorithms like multilevel fast multipole algorithm (MLFMA) [7]. Although the method has to handle the hypersingular kernels resulting from the dyadic Green's function, the robust treatment techniques developed in recent years [8, 9] make it become a good alternative to the MoM, especially for highly anisotropic problems. A typical numerical example is presented to demonstrate the method and good performance can be observed.

2. VOLUME INTEGRAL EQUATIONS

Consider the EM scattering by an anisotropic object embedded in the free space whose permittivity and permeability are ϵ_0 and μ_0 , respectively, the VIEs for governing the problem can be written as [1]

$$\mathbf{E}^{inc}(\mathbf{r}) = \mathbf{E}(\mathbf{r}) + \int_V \nabla g(\mathbf{r}, \mathbf{r}') \times \mathbf{M}_V(\mathbf{r}') d\mathbf{r}' - i\omega\mu_0 \int_V \bar{\mathbf{G}}(\mathbf{r}, \mathbf{r}') \cdot \mathbf{J}_V(\mathbf{r}') d\mathbf{r}', \quad \mathbf{r} \in V \quad (1)$$

$$\mathbf{H}^{inc}(\mathbf{r}) = \mathbf{H}(\mathbf{r}) - \int_V \nabla g(\mathbf{r}, \mathbf{r}') \times \mathbf{J}_V(\mathbf{r}') d\mathbf{r}' - i\omega\epsilon_0 \int_V \bar{\mathbf{G}}(\mathbf{r}, \mathbf{r}') \cdot \mathbf{M}_V(\mathbf{r}') d\mathbf{r}', \quad \mathbf{r} \in V \quad (2)$$

where $\mathbf{E}^{inc}(\mathbf{r})$ and $\mathbf{H}^{inc}(\mathbf{r})$ are the incident electric field and magnetic field, respectively, while $\mathbf{E}(\mathbf{r})$ and $\mathbf{H}(\mathbf{r})$ are the total electric field and total magnetic field inside the object, respectively. Also, $\bar{\mathbf{G}}(\mathbf{r}, \mathbf{r}')$ is the three-dimensional (3D) dyadic Green's function defined by

$$\bar{\mathbf{G}}(\mathbf{r}, \mathbf{r}') = \left(\bar{\mathbf{I}} + \frac{\nabla\nabla}{k_0^2} \right) g(\mathbf{r}, \mathbf{r}') \quad (3)$$

where $\bar{\mathbf{I}}$ is the identity dyad and $g(\mathbf{r}, \mathbf{r}') = e^{ik_0 R}/(4\pi R)$ is the scalar Green's function in which $k_0 = \omega\sqrt{\mu_0\epsilon_0}$ is the free-space wavenumber and $R = |\mathbf{r} - \mathbf{r}'|$ is the distance between an observation point \mathbf{r} and a source point \mathbf{r}' . In addition,

$$\mathbf{J}_V(\mathbf{r}') = i\omega [\epsilon_0\bar{\mathbf{I}} - \bar{\boldsymbol{\epsilon}}(\mathbf{r}')] \cdot \mathbf{E}(\mathbf{r}') \quad (4)$$

$$\mathbf{M}_V(\mathbf{r}') = i\omega [\mu_0\bar{\mathbf{I}} - \bar{\boldsymbol{\mu}}(\mathbf{r}')] \cdot \mathbf{H}(\mathbf{r}') \quad (5)$$

are the induced volumetric electric current density and magnetic current density inside the object, respectively, and $\bar{\boldsymbol{\mu}}_r(\mathbf{r}') = \bar{\boldsymbol{\mu}}(\mathbf{r}')/\mu_0$ and $\bar{\boldsymbol{\epsilon}}_r(\mathbf{r}') = \bar{\boldsymbol{\epsilon}}(\mathbf{r}')/\epsilon_0$ are the relative permeability tensor and relative permittivity tensor, respectively.

3. POINT-MATCHING DISCRETIZATION

The above VIEs can be solved with the point-matching method. We choose the current densities $\mathbf{J}_V(\mathbf{r}')$ and $\mathbf{M}_V(\mathbf{r}')$ inside the anisotropic media as unknowns to be solved, leading to the use of JM-formulation. The choice is more suitable than the other two choices, i.e., the DB-formulation using $\mathbf{D}(\mathbf{r}')$ and $\mathbf{B}(\mathbf{r}')$ as unknowns and EH-formulation using $\mathbf{E}(\mathbf{r}')$ and $\mathbf{H}(\mathbf{r}')$ as unknowns, for anisotropic problems [6], especially when the anisotropy is strong. Another advantage for such a choice is that we can avoid the involvement of material property, i.e., the permittivity tensor and permeability tensor inside the integrands as can be seen from Eqs. (1) and (2) since the current densities have accounted for the material property as shown in Eqs. (4) and (5), leading to much convenience in numerical implementation for anisotropic media. The material property will appear in the total fields when they are expressed in terms of current densities through Eqs. (4) and (5), namely,

$$\begin{aligned} \begin{bmatrix} E^x \\ E^y \\ E^z \end{bmatrix} = \mathbf{E}(\mathbf{r}') &= \frac{1}{i\omega} [\epsilon_0\bar{\mathbf{I}} - \bar{\boldsymbol{\epsilon}}(\mathbf{r}')]^{-1} \cdot \mathbf{J}_V(\mathbf{r}') = \frac{1}{i\omega} \begin{bmatrix} \epsilon_0 - \epsilon_{11} & -\epsilon_{12} & -\epsilon_{13} \\ -\epsilon_{21} & \epsilon_0 - \epsilon_{22} & -\epsilon_{23} \\ -\epsilon_{31} & -\epsilon_{32} & \epsilon_0 - \epsilon_{33} \end{bmatrix}^{-1} \cdot \begin{bmatrix} J_V^x \\ J_V^y \\ J_V^z \end{bmatrix} \quad (6) \\ \begin{bmatrix} H^x \\ H^y \\ H^z \end{bmatrix} = \mathbf{H}(\mathbf{r}') &= \frac{1}{i\omega} [\mu_0\bar{\mathbf{I}} - \bar{\boldsymbol{\mu}}(\mathbf{r}')]^{-1} \cdot \mathbf{M}_V(\mathbf{r}') \\ &= \frac{1}{i\omega} \begin{bmatrix} \mu_0 - \mu_{11} & -\mu_{12} & -\mu_{13} \\ -\mu_{21} & \mu_0 - \mu_{22} & -\mu_{23} \\ -\mu_{31} & -\mu_{32} & \mu_0 - \mu_{33} \end{bmatrix}^{-1} \cdot \begin{bmatrix} M_V^x \\ M_V^y \\ M_V^z \end{bmatrix}. \quad (7) \end{aligned}$$

Note that the VIEs are changed into a scalar or component form in the point-matching method. Although the permittivity tensor and permeability tensor appears in the VIEs, they are outside the integrals and only related to self-interaction terms or diagonal elements in the impedance matrix. This can greatly facilitate the implementation of fast algorithms like the MLFMA since the fast algorithms are usually designed for far-interaction terms and the self-interaction terms will be handled in a traditional way [7].

4. NUMERICAL EXAMPLE

To demonstrate the point-matching method, we consider the EM scattering by a uniaxially anisotropic sphere with a radius a as shown in Figure 1. The uniaxially anisotropic material is characterized by the following permittivity tensor and permeability tensor

$$\bar{\boldsymbol{\epsilon}} = \epsilon_0 \begin{bmatrix} \epsilon_r & 0 & 0 \\ 0 & \epsilon_t & 0 \\ 0 & 0 & \epsilon_t \end{bmatrix} \cdot \bar{\mathbf{I}} \quad (8)$$

$$\bar{\boldsymbol{\mu}} = \mu_0 \begin{bmatrix} \mu_r & 0 & 0 \\ 0 & \mu_t & 0 \\ 0 & 0 & \mu_t \end{bmatrix} \cdot \bar{\mathbf{I}} \quad (9)$$

with $\bar{\mathbf{I}} = \hat{r}\hat{r} + \hat{\theta}\hat{\theta} + \hat{\phi}\hat{\phi}$ in a spherical coordinate system. It is assumed that the incident wave is a plane wave with a frequency $f = 300$ MHz and is propagating along $+z$ direction in free space. We select $a = 0.5\lambda$, $\epsilon_r = 2.0$, $\epsilon_t = 10.0$, $\mu_r = 9.0$, and $\mu_t = 3.0$, respectively, for the object, resulting in $\epsilon_t/\epsilon_r = 5.0$ and $\mu_r/\mu_t = 3.0$. We calculate the bistatic radar cross section (RCS) observed along

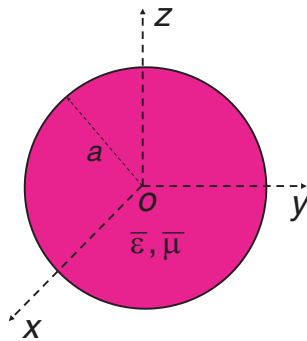


Figure 1: Geometry of a highly anisotropic object with a radius a .

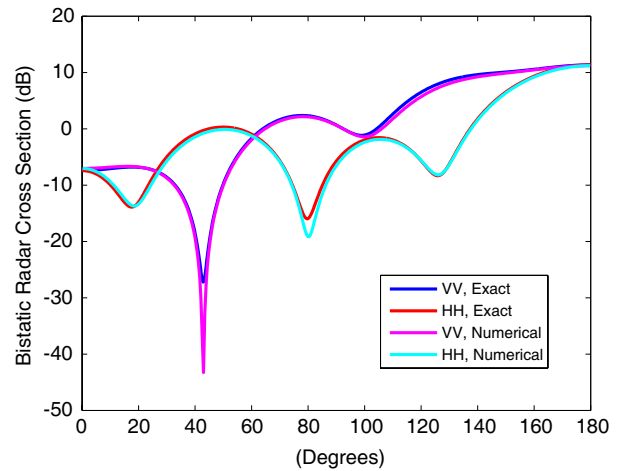


Figure 2: Bistatic RCS solutions for EM scattering by a strongly anisotropic object with a radius $a = 0.5\lambda$.

the principal cut ($\phi = 0^\circ$ and $\theta = 0^\circ - 180^\circ$) for the scatterer in both vertical polarization (VV) and horizontal polarization (HH). Figure 2 plots the bistatic RCS solutions and they are in good agreement with the corresponding analytical solutions which can be obtained using the formulas in [10].

5. CONCLUSION

The traditional MoM based on the divergence-conforming SWG basis function or curl-conforming edge basis function may not be suitable for solving the EM problems with highly anisotropic media because of the features of the basis functions. In this work, we present a point-matching method to replace the MoM for resolving such problems and the method is more flexible in implementation. In addition to its well-known merits, the method can better characterize the unknown functions at discrete points with directional components and more degrees of freedom. Furthermore, the method allows the use of the JM-formulation which can avoid the involvement of material parameters in the integral kernels. The typical numerical example has been presented to demonstrate the robustness of the method.

ACKNOWLEDGMENT

This work was supported by the opening projects of the State Key Laboratory of Millimeter Waves, Nanjing, China, under the contract K201310.

REFERENCES

1. Chew, W. C., M. S. Tong, and B. Hu, *Integral Equation Methods for Electromagnetic and Elastic Waves*, Morgan & Claypool, San Rafael, CA, 2008.
2. Schaubert, D. H., D. R. Wilton, and A. W. Glisson, "A tetrahedral modeling method for electromagnetic scattering by arbitrary shaped inhomogeneous dielectric bodies," *IEEE Trans. Antennas Propagat.*, Vol. 32, No. 1, 77–85, 1984.
3. Sun, L. E. and W. C. Chew, "A novel formulation of the volume integral equation for electromagnetic scattering," *Waves Random Complex Media*, Vol. 19, No. 1, 162–180, Feb. 2009.
4. Botha, M. M., "Fully hierarchical divergence-conforming basis functions on tetrahedral cells, with applications," *Int. J. Num. Meth. Eng.*, Vol. 71, No. 2, 127–148, Jul. 2007.
5. Yang, K., J. C. Zhou, W. T. Sheng, Z. Y. Zhu, and M. S. Tong, "Efficient Nyström solutions of electromagnetic scattering by composite objects with inhomogeneous anisotropic media," *IEEE Trans. Antennas Propagat.*, Vol. 61, No. 10, 5328–5332, Oct. 2013.
6. Markkanen, J., P. Ylä-Oijala, and A. Sihvola, "Discretization of volume integral equation formulations for extremely anisotropic materials," *IEEE Trans. Antennas Propagat.*, Vol. 60, No. 11, 5195–5202, Nov. 2012.
7. Chew, W. C., J. M. Jin, E. Michielssen, and J. M. Song, *Fast and Efficient Algorithms in Computational Electromagnetics*, Artech House, Boston, 2001.

8. Tong, M. S. and W. C. Chew, “Super-hyper singularity treatment for solving 3D electric field integral equations,” *Microw. Opt. Technol. Lett.*, Vol. 49, 1383–1388, 2007.
9. Tong, M. S., Z. G. Qian, and W. C. Chew, “Nyström method solution of volume integral equations for electromagnetic scattering by 3D penetrable objects,” *IEEE Trans. Antennas Propagat.*, Vol. 58, No. 5, 1645–1652, May 2010.
10. Wong, K.-L. and H.-T. Chen, “Electromagnetic scattering by a uniaxially anisotropic sphere,” *IEE Proc.-H*, Vol. 139, No. 4, 314–318, Aug. 1992.

Aharonov-Bohm Effect, Poincaré Lemma and Gauge Invariance

Peter A. Meleshenko^{1,2}, Hang T. T. Nguyen³,
Mikhail E. Semenov^{1,2,4}, and Alexander F. Klinskikh²

¹Zhukovsky-Gagarin Air Force Academy, Russia

²Voronezh State University, Russia

³Institute of Technology, Vietnam National University — Ho Chi Minh City, Vietnam

⁴Voronezh State University of Architecture and Civil Engineering, Russia

Abstract— In this paper we demonstrate the peculiarities of the Aharonov-Bohm effect using the theory of generalized functions. We show that the presence of the Aharonov-Bohm effect violates the Poincaré lemma (in other words the Poincaré lemma does not apply to the Aharonov-Bohm spatial geometry), moreover, such a violation is a necessary condition for the Aharonov-Bohm effect observation. The unexpected form of the Schrödinger equation for the Aharonov-Bohm effect which contains a singularity in explicit form is also obtained. These results allow to take a fresh look on the Aharonov-Bohm problem.

1. INTRODUCTION

The Aharonov-Bohm (AB) effect [1] is of more than fifty years history and remains relevant even in the present days (see, e.g., [2–7] and related references). Main object in the AB effect is an infinitely thin solenoid with the finite magnetic flux (AB flux). While the force field is absent the vector potential of the magnetic field confined in the solenoid is non-zero and can produce observable effects because the relative phase of the electron wave function depends on the AB flux. In other words, the AB flux affects the quantum state of an electron. Such an affection leads eventually to the observable effects [8, 9].

As is known, there is a close “relationship” between the AB effect and the topology of the two-dimensional space (see, e.g., [10]). One of the most important result in this field is the Poincaré lemma [11, 12] which claims that on a contractible manifold, all closed forms are exact. In other words $\mathbf{d}\mathbf{d}\omega = 0$ for any closed form ω . In this paper we show by straightforward calculations that in the presence of the AB effect the Poincaré lemma violates (the Poincaré lemma can not be applied to the AB problem due to the fact that the space is not simply-connected). Such a violation connected with the fact that the 1-form $\mathbf{d}\omega$ (see details below in Eq. (11)) is not exact.

The paper is organized as follows. In the first section we demonstrate (using the theory of generalized functions) the significant difference between the gauges of the homogeneous magnetic field and AB field. The second section is dedicated to the problem of Poincaré lemma violation. We show by the straightforward calculations that the presence of the AB solenoid leads to Poincaré lemma violation. In conclusion the main results of this paper are summarized.

2. AHARONOV-BOHM GAUGE AND MULTI-VALUED FUNCTION

In this section we would like to show the specific difference between the gauge of the vector potential in the case of the AB flux and homogeneous magnetic field. As is well known we can use the various form of the gauge for the vector potential. The most convenient is the following expression for the vector potential of a uniform magnetic field:

$$\mathbf{A}_H = \frac{Hr}{2} \mathbf{e}_\theta. \quad (1)$$

Formally, we can write

$$\mathbf{A}_H = \frac{\Phi_H}{2\pi r} \mathbf{e}_\theta, \quad (2)$$

where $\Phi_H = \pi r^2 H$ is the magnetic flux through the area of the ring with radius r .

For the vector potential of the AB solenoid (with the AB flux Φ_{AB}) we have [1]:

$$\mathbf{A}_{AB} = \frac{\Phi_{AB}}{2\pi r} \mathbf{e}_\theta. \quad (3)$$

Let us note that the AB vector potential (3) is singular at origin $r = 0$. At the same time the vector potential of the homogeneous magnetic field (see the formal expression (2)) is zero at origin due to the fact that the magnetic flux Φ_H is a quadratic function of r .

Now we can pose the following question: Does the gauge transformation (non-singular) which connects (3) and (2) exist? The answer is: no, it does not. Further calculations confirm this response.

First, we write a well known expression for the operator ∇ in cylindrical coordinates:

$$\nabla = \frac{\partial}{\partial r} \mathbf{e}_r + \frac{1}{r} \frac{\partial}{\partial \theta} \mathbf{e}_\theta + \frac{\partial}{\partial z} \mathbf{e}_z. \quad (4)$$

Next, for the homogeneous magnetic field (1) we have

$$[\nabla \times \mathbf{A}_H] = \frac{1}{r} \frac{\partial}{\partial r} [r (\mathbf{A}_H)_\theta] \mathbf{e}_z = H \mathbf{e}_z. \quad (5)$$

The situation dramatically changes when we consider the case of the AB flux. Using (4) we can rewrite (3) as [13]:

$$\mathbf{A}_{AB} = \frac{\Phi_{AB}}{2\pi} \nabla \theta. \quad (6)$$

Then, we have

$$[\nabla \times \mathbf{A}_{AB}] = \frac{\Phi_{AB}}{2\pi} [\nabla \times \nabla \theta].$$

Now we show that the expression $[\nabla \times \nabla \theta]$ is nonzero and reduces to a Dirac δ -function (this occurs because θ is a multi-valued function). In the 2D case we can write:

$$[\nabla \times \nabla \theta] = \left(\frac{\partial^2 \theta}{\partial x \partial y} - \frac{\partial^2 \theta}{\partial y \partial x} \right) \mathbf{e}_z.$$

For the azimuthal angle we know:

$$\theta = \arctan \left(\frac{y}{x} \right),$$

and

$$\frac{\partial \theta}{\partial x} = -\frac{y}{x^2 + y^2},$$

$$\frac{\partial \theta}{\partial y} = \frac{x}{x^2 + y^2}.$$

Note, that the functions $\frac{\partial \theta}{\partial x}$ and $\frac{\partial \theta}{\partial y}$ are functions with the homogeneity parameter $\lambda = -1$.

Now, let us recall some properties of the homogeneous functions. The homogeneity parameter λ is defined as follows:

$$f(\xi x_1, \xi x_2, \dots, \xi x_n) = \xi^\lambda f(x_1, x_2, \dots, x_n)$$

for all $\xi > 0$. In our case $\lambda = -n + 1 = -1$ (here $n = 2$ is a space dimension of the system under consideration). Thus, for such a function we need to use the following expression for the derivative [14]:

$$\frac{\partial f}{\partial x_i} = \left(\frac{\partial f}{\partial x_i} \right) \Big|_G + (-1)^{i-1} \delta(x_1, x_2, \dots, x_n) \times \int_\Gamma f dx_1 dx_2 \dots dx_{i-1} dx_{i+1} \dots dx_n. \quad (7)$$

Here $\frac{\partial f}{\partial x_i}$ is a derivative in terms of generalized functions, and $\frac{\partial f}{\partial x_i} \Big|_G$ is a generalized function, built on the usual derivative of f in the region G , Γ is the boundary of G , $\delta(x_1, x_2, \dots, x_n)$ is a multidimensional Dirac δ -function. Next, in our case using (7) we obtain

$$\begin{aligned} \frac{\partial^2 \theta}{\partial x \partial y} &= \frac{\partial^2 \theta}{\partial x \partial y} \Big|_G + \delta(x, y) \int_\Gamma \frac{x dy}{x^2 + y^2}, \\ \frac{\partial^2 \theta}{\partial y \partial x} &= \frac{\partial^2 \theta}{\partial y \partial x} \Big|_G + \delta(x, y) \int_\Gamma \frac{y dx}{x^2 + y^2}. \end{aligned} \quad (8)$$

Of course, $\frac{\partial^2 \theta}{\partial x \partial y} \Big|_G = \frac{\partial^2 \theta}{\partial y \partial x} \Big|_G$, then using (8) we find

$$[\nabla \times \nabla \theta] = \vec{e}_z \delta(x, y) \int_{\Gamma} \frac{x dy - y dx}{x^2 + y^2},$$

and

$$[\nabla \times \mathbf{A}_{AB}] = \mathbf{e}_z \frac{\Phi_{AB} \delta(x, y)}{2\pi} \int_{\Gamma} \frac{x dy - y dx}{x^2 + y^2}.$$

Note, that in the present case Γ can be chosen (in full analogy with an example considered in [14]), e.g., as a circle, so the contour integral can be easily calculated (in the polar coordinates) and the result is

$$\int_{\Gamma} \frac{x dy - y dx}{x^2 + y^2} = 2\pi.$$

Finally

$$[\nabla \times \mathbf{A}_{AB}] = \Phi_{AB} \mathbf{e}_z \delta(x, y). \quad (9)$$

The expressions (5) and (9) demonstrate a significant difference between the uniform magnetic field and the AB flux placed at origin (one of them is regular while another is singular)¹. Thereby, the definition of the gauge invariance of the electromagnetic potentials should be clarified, namely:

$$\mathbf{A} \rightarrow \mathbf{A} + \nabla f,$$

$$\varphi \rightarrow \varphi - \frac{\partial f}{\partial t},$$

where f is an arbitrary *single-valued* function of the spatial coordinates and time.

3. POINCARÉ LEMMA VIOLATION

Let us recall the Poincaré lemma: *On a contractible manifold all closed forms are exact*. In other words $\mathbf{d}\mathbf{d}\omega = 0$ for any closed form ω ². In this section we show that the Poincaré lemma violation takes place in the presence of the AB effect. In order to do this let us consider the 0-form $\omega = \arctan(y/x)$ that exactly corresponds to the AB gauge of the vector potential (see Eq. (6)). It should be noted one more time that the considered 0-form ω is a *multi-valued function*.

Let us expand the 1-form $\mathbf{d}\omega$ on the basis of $\mathbf{d}x$ and $\mathbf{d}y$ in the standard way [11]:

$$\mathbf{d}\omega = \frac{\partial \omega}{\partial x} \mathbf{d}x + \frac{\partial \omega}{\partial y} \mathbf{d}y,$$

and let us find the exterior derivative for this one. The result is:

$$\mathbf{d}\mathbf{d}\omega = \frac{\partial^2 \omega}{\partial x^2} \mathbf{d}x \wedge \mathbf{d}x + \frac{\partial^2 \omega}{\partial y \partial x} \mathbf{d}x \wedge \mathbf{d}y + \frac{\partial^2 \omega}{\partial x \partial y} \mathbf{d}y \wedge \mathbf{d}x + \frac{\partial^2 \omega}{\partial y^2} \mathbf{d}y \wedge \mathbf{d}y.$$

Using the general properties of the exterior derivative [12] we can write:

$$\mathbf{d}x \wedge \mathbf{d}x = \mathbf{d}y \wedge \mathbf{d}y = 0, \quad \mathbf{d}x \wedge \mathbf{d}y = -\mathbf{d}y \wedge \mathbf{d}x.$$

These properties lead to the following expression for the 2-form $\mathbf{d}\mathbf{d}\omega$:

$$\mathbf{d}\mathbf{d}\omega = \left(\frac{\partial^2 \omega}{\partial y \partial x} - \frac{\partial^2 \omega}{\partial x \partial y} \right) \mathbf{d}x \wedge \mathbf{d}y. \quad (10)$$

¹It should be noted here that the numerical solution of the Newton equation (the Lorentz force) together with the field strength (9) does not lead to some observable peculiarities. This result exactly correlates with the statement on the absence of the AB effect in classical physics.

²Here we would like to give a simple interpretation of the Poincaré lemma, namely, the last one is equivalent to the statement that *the mixed second derivatives are equal*. For the vast majority of functions that are used in physics (single-valued functions), this statement is certainly true. However, in the case of multi-valued functions (e.g., in the AB effect) this statement can be violated. The violation of this statement is presented in this section.

The expression in the brackets in (10) is nonzero because the 0-form ω is multi-valued. As a result the second derivatives in (10) should be calculated in the frame of the theory of generalized functions [14]. Using the expression (7), we obtain the following result:

$$\mathbf{d}\mathbf{d}\omega = -2\pi\delta(x, y)\mathbf{d}x \wedge \mathbf{d}y \quad (11)$$

We see that the Poincaré lemma violation takes place. Such a violation follows from the fact that the considered 0-form ω is a multi-valued function. In mathematical language this means that the 1-form $\mathbf{d}\omega$ is not exact. Physically this means that the singularity in the form of AB solenoid takes place (the space of the AB problem is multi-connected) and such a singularity affects the quantum state of an electron. Moreover, using the generalized functions technique such a singularity can be identified in the Schrödinger equation in explicit form.

4. CONCLUSIONS

In this paper we have considered the peculiarities of the AB effect in the frame of the theory of generalized functions. In particular, we have shown the significant difference between the gauges for the homogeneous magnetic field and AB field. As a result, we have pointed out that the definition of a gauge invariance should be formulated taking into account an information on the “nature” of a gauge function. Also, we have demonstrated that the Poincaré lemma violation takes place due to the presence of the AB flux. Such a violation follows from the fact that the space of the AB problem is multi-connected and the corresponding 0-form that determines the gauge of the AB field is not exact.

REFERENCES

1. Aharonov, Y. and D. Bohm, “Significance of electromagnetic potentials in the quantum theory,” *Phys. Rev.*, Vol. 115, 485–491, 1959.
2. Olariu, S. and I. I. Popescu, “The quantum effects of electromagnetic fluxes,” *Rev. Mod. Phys.*, Vol. 57, 339, 1985.
3. Peshkin, M. and A. Tonomura, *The Aharonov-Bohm Effect*, Springer-Verlag, Berlin, 1989.
4. Berry, M. V., “Asymptotics of the many-whirls representation for Aharonov-Bohm scattering,” *J. Phys. A: Math. Theor.*, Vol. 43, 354002, 2010.
5. Kaufherr, T. and Y. Aharonov, “Nonlocal quantum dynamics of the Aharonov-Bohm effect,” *J. Phys. A: Math. Theor.*, Vol. 43, 354012, 2010.
6. Klinskikh, A. F., P. A. Meleshenko, et al., “Radiative attenuation of the electron in the Aharonov-Bohm effect,” *Nuovo Ciment. B*, Vol. 125, 1161–1171, 2010.
7. Meleshenko, P. A., H. T. T. Nguyen, and A. F. Klinskikh, “Spectroscopic peculiarities in a 2D Coulomb potential under Aharonov-Bohm effect,” *Eur. Phys. J. D*, Vol. 67, 209, 2013.
8. Bayer, M., M. Korkusinski, P. Hawrylak, T. Gutbrod, M. Michel, and A. Forchel, “Optical detection of the Aharonov-Bohm effect on a charged particle in a nanoscale quantum ring,” *Phys. Rev. Lett.*, Vol. 90, 186801, 2004.
9. Caprez, A., B. Barwick, and H. Batelaan, “Macroscopic test of the Aharonov-Bohm effect,” *Phys. Rev. Lett.*, Vol. 99, 210401, 2007.
10. Evans, M. W., “Physical Optics, the Sagnac effect, and the Aharonov-Bohm effect in the evans unified field theory,” *Found. Phys. Lett.*, Vol. 17, 301–322, 2004.
11. Arnold, V. I., *Mathematical Methods of Classical Mechanics*, 2nd Edition, Springer-Verlag, New York, 1989.
12. Dubrovin, B. H., A. T. Novikov, and S. P. Fomenko, *Modern Geometry — Methods and Applications: Part III: Introduction to Homology Theory*, Springer-Verlag, New-York, 1990.
13. Ryder, L. H., *Quantum Field Theory*, 2nd Edition, Cambridge University Press, 1996.
14. Gel’fand, I. M. and G. E. Shilov, *Generalized Functions: Properties and Operations*, Academic Press, New York, 1964.

Analysis of Arrangement Structure for Metal Fiber in Blended Electromagnetic Shielding Fabric

Zhe Liu, Xing Rong, Qianxue Zheng, Ruili Sun, Yuna Chen, and Xiuchen Wang
Zhongyuan University of Technology, China

Abstract— In order to study shielding characteristics of electromagnetic shielding fabric, a method based on computer image analysis is proposed to build an arrangement model of metal fiber. At firstly, some important parameters about shielding effect are summarized, and then a new algorithm based on threshold segmentation for fabric texture extracting is put forward. By ascertaining an optimization threshold, the fabric image is divided and a feature cluster gray image is established. Furthermore, the feature matrix of metal fiber comprising only two gray values which are threshold value and feature value is founded by using normalized method. At last, calculation formulas about metal fiber content per unit area and equivalent thickness are established and the arrangement model of metal fiber is built. Experiments and analysis show that the method given in this paper is able to describe accurately the arrangement of metal fiber in fabric and it will provide a reference for studying properties of electromagnetic shielding fabric.

1. INTRODUCTION

Electromagnetic shielding fabric is an important electromagnetic shielding material. One important way in the electromagnetic shielding fabric production is using metal fiber blending with ordinary fiber, and the key factor to its shielding properties is the arrangement structure of metal fiber. So far the relationship between fabric structure and shielding properties of blended electromagnetic shielding fabric is not clear and definite, one reason is lackin **g** of the effective description of arrangement structure of metal fiber.

The literatures about arrangement structure of metal fiber in blended electromagnetic shielding fabric are few. Most literatures briefly talked about the fabric structure during their research on model [1], properties [2], measurement [3] and related products [4] of electromagnetic shielding fabric, and not involved the specific research on arrangement structure of metal fiber. However, the metal fiber arrangement is of critical importance to the shielding effectiveness. Only when it is reasonably described, can the shielding properties be exactly analyzed.

There are many ways to analysis the structure of ordinary fabric, among them, the automatic distinguish of computer is gradually become a hot research point, which mainly includes Spatial domain method and Frequency domain method [5], and has been widely used in the distinguish of many parameters such as flaws, density, texture and so on. But the application in the arrangement of metal fiber in electromagnetic shielding fabric has not been reported.

In this condition, the structure of blended electromagnetic shielding fabric is analyzed by the method of computer image analysis in this paper. On the basis of the electromagnetic shielding theory and the method of image threshold segmentation, we build a structure model of metal fiber which is suitable for the analysis of shielding effect, and extract some important parameters, providing a reference for the subsequent analysis of shielding mechanism and properties.

2. THEORETICAL ANALYSIS

Research on the arrangement structure of metal fiber in electromagnetic shielding fabric is determined by the electromagnetic shielding theory. The ideal metal shield completes its shielding effect mainly through reflection, multiple reflection and absorption, and a big part is through reflection [6]. The shielding effectiveness SE is decided by the following formula [7]:

$$SE = 168.16 - 10 \lg \frac{\mu_r f}{\sigma_r} + 1.31t \sqrt{f \mu_r \sigma_r} \quad (\text{dB}) \quad (1)$$

where t represents the thickness of the fabric, μ_r represents the relative permeability, σ_r represents the electrical conductivity, f represents the frequency.

Formula (1) shows that when the frequency is constant, the shielding effectiveness of electromagnetic shielding fabric relates to its relative permeability, electrical conductivity and thickness. According to the electromagnetic shielding theory, the three parameters essentially are determined

by the arrangement structure of metal fiber per unit area. Therefore, research on the arrangement structure of metal fiber in electromagnetic shielding fabric is of great significance, providing basis for the subsequent analysis of characteristics on electromagnetic shielding fabric.

3. RECOGNITION OF THE STRUCTURE ON ELECTROMAGNETIC SHIELDING FABRIC

3.1. Threshold Segmentation for Fabric Texture

In order to build an arrangement model of mental fiber, a new algorithm based on threshold segmentation for fabric texture feature cluster is put forward. The steps are as follows: 1) Build an image digitization matrix; 2) Determine the threshold segmentation for fabric texture; 3) Feature cluster normalization; 4) Build the feature matrix; 5) Build the arrangement model of mental fiber.

Suppose that the fabric image is composed of $N \times M$ the lower-left corner vertex o is set as the origin, the horizontal axis labeled the x axis, the vertical axis labeled the y axis and the gray value of pixels is set as the z axis, establish a three-dimensional space coordinate system. Where the values of x , y axis are natural number, the range of z axis is $[0, 255]$. Suppose the coordinate of any pixel is (x, y) , gray value is $g(x, y)$, then the gray matrix G_M of the image can be built:

$$G_M = |g(x, y)|_{N \times M} \quad (2)$$

According to knowledge of image processing, the threshold of fabric gray scale can be decided when the average value of the maximum and minimum is worked out. But the result is unreasonable because of the sporadic abnormal high or low gray level points, so the number of the pixels should be considered. This paper uses weighting method to work out the average of gray scale based on the number of all level gray pixels, so the threshold value is determined. Suppose that there are n levels of gray scale, the value of any gray scale is g_n , the number of pixels is P_n , the threshold value is G_t , then:

$$G_t = \sum_{i=1}^n \left(g_i \frac{P_i}{N \times M} \right) \quad (3)$$

3.2. The Feature Matrix Describing the Basic Arrangement of Metal Fiber

After the segmentation, the formed feature clusters describing the characteristics of fabric structure should be handled with normalized method. As shown in Figure 1, analysis area is $\Delta x \times \Delta y$, pixels are p_1, p_2, \dots, p_c , the corresponding gray scales are g_1, g_2, \dots, g_c , if $\{g_1, g_2, \dots, g_c\} > G_a$, then p_1, p_2, \dots, p_c are the point set of the feature cluster. Classify the pixels which meet formula (5) as well as adjacent to each other into k clusters and there are $m(x)$ pixels in the x cluster, then every feature cluster can be normalized as follow:

$$F(x) = \sum_{i=1}^{m(x)} g(x, i) \quad (4)$$

where in the x cluster, $F(x)$ is the normalized value, $g(x, i)$ is an arbitrary point i . The average value G_a of feature cluster can be obtained from the formula below:

$$G_a = \sum_{i=1}^k F(i) \quad (5)$$

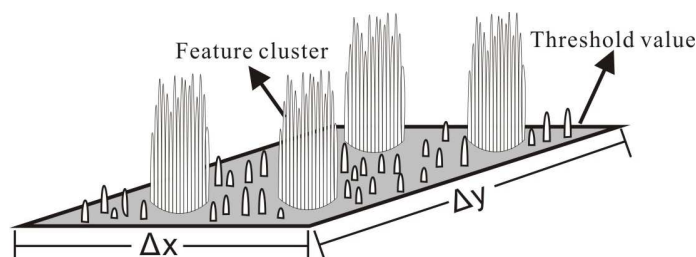


Figure 1: Diagram of texture segmentation and feature cluster.

After the normalization, the basic arrangement structure of metal fiber in electromagnetic shielding fabric can be described by the feature matrix F_M . The matrix contains two elements G_a and G_t , as described below:

$$F_M = \begin{vmatrix} G_a & G_t & \dots & G_a \\ G_t & G_a & \dots & G_t \\ \dots & \dots & \dots & \dots \\ G_a & G_t & \dots & G_a \end{vmatrix}_{N_f \times M_f} \quad (6)$$

where $N_f \times M_f$ are row and column number of the feature matrix.

4. THE BUILT OF ARRANGEMENT MODEL OF METAL FIBER

According to the electromagnetic shielding theory, there are two parameters influencing the electromagnetic parameters in fabric, which are the metal fiber content per unit area and the thickness. The two parameters can be extracted by the method given by the feature matrix (6).

Suppose T_m (g/m^2) is the metal content per unit area, then:

$$T_m = \frac{(D_w + D_v) \times tex \times P}{100} \quad (7)$$

where D_w and D_v are weft and warp densities (yarns/10 cm) recognized by the computer, tex is the fiber fineness unit, P is the metal fiber content (%) in the yarn. For the density analysis, we can consult the autocorrelation method in the literature [8].

Equivalent thickness t_e is converted by the metal fiber content computed by formula (7) and the normal metal volume density. The parameter has an important influence on the skin effect of the electromagnetic wave. If ρ respects the volume density of metal fiber, then:

$$t_e = \frac{T_m}{\rho} \quad (8)$$

5. RESULTS AND ANALYSIS

5.1. Experimental Method

Choose the 60 tex cotton/stainless steel blended yarn with 15% metal content, weave twill, plain and satin electromagnetic shielding fabrics of different densities with the small loom, and then make 15 kinds of rectangular samples each with an area of $25 \text{ cm} \times 20 \text{ cm}$. Obtain the images of the samples with Canon LiDE210 scanner. Write programs based on the method given in the paper with MATLAB7.0, we can get the gray images and arrangement model figures of metal fiber in the output, and then calculate the metal content per unit area of each sample. Take all the kinds of fabric samples, after fully burning, repeated washing and drying, the cotton ashes are filtered out, the residue is the metal fiber. Then we can work out the metal fiber content per unit area based on the weight of the metal fiber and the area of the fabric sample.

5.2. Results

Through the above experiment, we get two metal fiber contents per unit area, one is T'_m obtained by computer analysis and the other is T''_m obtained by burning test. Suppose the error is δ , then:

$$\delta = \frac{|T'_m - T''_m|}{T''_m} \times 100\% \quad (9)$$

Experiment show that error rates of all the results are less than 3%, due to the length limitation of this paper, only 3 representative samples are listed in the Table 1, in which we take the volume density ρ of the stainless-steel fiber as $7.93 \times 10^3 \text{ kg/m}^3$.

Figure 2 shows the local image of twill 1. Figure 3, processed in MATLAB7.0 based on the method given in this paper, shows the arrangement structure of metal fiber of Figure 2. In the Figure 3, we can see the texture structure and the thickness of the metal fiber clearly.

5.3. The Application of the Model

The established model in this paper is to analyze the shielding properties of electromagnetic shielding fabric. Due to the diversity of the fabric structure and complexity of the metal fiber arrangement, we can't calculate the shielding effectiveness directly with formula (1), but can analyze the shielding effectiveness by the method of FDTD in virtue of the method of dividing Yee grid. In

Table 1: Comparison results of metal fiber content per unit area with different methods and equivalent thickness of each fabric sample.

	actual warp density	actual weft density	T'_m	T''_m	t_e	δ
unit	yarns/10 cm		g/m ²	g/m ²	10 ⁻⁶ m	%
twill 1	210	182	35.53	36.07	4.45	1.5
plain 1	220	189	36.51	36.11	4.64	1.1
satin 1	198	165	32.66	33.55	4.12	2.7

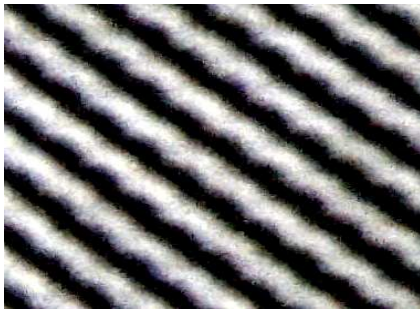


Figure 2: Local image of twill.

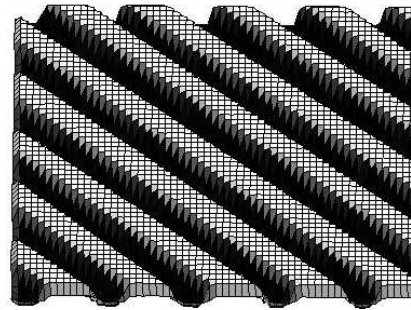


Figure 3: Arrangement structure of metal fiber in Fig. 2.

order to divide Yee grid, it is necessary to describe the geometric structure of the fabric effectively, and obtain fabric structure features related to the arrangement of metal fiber, the model is just built for the task. It extracts the fabric feature cluster, and divided them into different types according to the arrangement of metal fiber, ultimately transform the fabric into the geometric grids constituted by pore area, single yarn area and overlapping area. Based on the electromagnetic parameters of the geometric grid, build the electromagnetic shielding fabric physical model, and finally lay the foundation for analyzing the shielding effectiveness of electromagnetic shielding fabric with the method of FDTD.

6. CONCLUSION

1) The arrangement model of metal fiber, constituted by the threshold values G_t , G_a and equivalent thickness t_e , is able to describe the arrangement structure of metal fiber in electromagnetic shielding fabric better. 2) The new algorithm based on threshold segmentation for fabric texture extracting can distinguish for the plain, twill, and stain weave structure fabrics, and then build a feature matrix of metal fiber arrangement. 3) The given formula to calculate the metal content per unit area and the equivalent thickness of fabric can standardly describe the electromagnetic shielding fabric more accurately.

ACKNOWLEDGMENT

This research was supported by the National Natural Science Foundation of China (Grant No. 61471404).

REFERENCES

1. Wang, X. C., Z. Liu, and Z. Zhou, "Virtual metal model for fast computation of shielding effectiveness of blended electromagnetic interference shielding fabric," *International Journal of Applied Electromagnetics and Mechanics*, Vol. 44, No. 1, 87–97, 2014.
2. Liu, Z. and X. C. Wang, "Relation between shielding effectiveness and tightness of electromagnetic shielding fabric," *Journal of Industrial Textiles*, Vol. 43, No. 2, 302–316, 2013.
3. Wang, X. C. and Z. Liu, "A new computation of shielding effectiveness of electromagnetic radiation shielding fabric," *Progress In Electromagnetics Research Letters*, Vol. 33, 177–186, 2012.
4. Liu, Z., X. C. Wang, and Z. Zhou, "Automatic recognition of metal fiber per unit area for electromagnetic shielding fabric based on computer image analysis," *Progress In Electromagnetics Research Letters*, Vol. 37, 101–111, 2013.

5. He, F., L. Q. Li, and J. M. Xu, “Woven fabric density measure based on adaptive wavelets transform,” *Journal of Textile Research*, Vol. 28, No. 2, 32–35, 2008.
6. Qian, Z. M. and Z. J. Chen, *Electromagnetic Compatibility Design and Interference Suppression Technology*, Zhejiang University Press, Hangzhou, 2000.
7. Liu, Z. and X. C. Wang, “Influence of fabric weave type on the effectiveness of electromagnetic shielding woven fabric,” *Journal of Electromagnetic Waves and Applications*, Vol. 26, Nos. 14–15, 1–9, 2012.
8. Gao, W. D., J. H. Liu, B. J. Xu, et al., “Automatic identification of fabric texture,” *Cotton Textile Technology*, Vol. 30, No. 4, 218–220, 2002.

Shielding Effectiveness Fitting of Local Electromagnetic Shielding Clothing Based on Human Figure

Xiuchen Wang, Xing Rong, Qianxue Zheng, Ruili Sun, Yuna Chen, and Zhe Liu
Zhongyuan University of Technology, China

Abstract— This study proposes a new method of shielding effectiveness (SE) based on NURBS curve, which aim is to address current non-effective method to describe the SE distribution of electromagnetic shielding (EMS) clothing. Moreover, the SE of local clothing can be fitted with the curve to observe the distribution. A testing method of key points is introduced to test the SE of the local clothing. Some concrete functions and program steps of curve fitting are listed. And then a distribution image of the SE on arm position is drawn. Results show that the proposed algorithm can accurately draw a 3D image of the SE of the local clothing and can reveal the distribution of electromagnetic wave on the local human body.

1. INTRODUCTION

All kinds of electromagnetic radiation exist in our modern life. Many researchers have proved that the electromagnetic radiation can produce adverse reaction, and even does harm to people's health [1]. The electromagnetic radiation has been listed as pollution and must be controlled by Human Environment Conference of Unite Nations, and many national governments have warned people against electromagnetic radiation [2]. Therefore, the study on electromagnetic shielding is becoming an urgent hotspot.

Most of the research of electromagnetic shielding clothing focuses on the development and application of the fiber and fabric. These materials include metal fiber, conductive fiber, metal coating fiber, multi-ion fabric, microwave-absorbing fabric and etc. [3, 4]. Report for describing the shielding effectiveness (SE) of clothing is almost inexistent, only research about SE of fabric was found in some literatures. These studies [5, 6] mostly focus the SE of fabric on a local plane, it cannot reveal the SE rule of electromagnetic clothing. Some scholars have been aware of this problem and present some testing methods for electromagnetic shielding clothing [7], but the SE description of local body has not been reported in detail.

It is also our viewpoint that SE research between clothing and fabric is very different. Surface shape must be considered when studying the SE of clothing. At present, universal method of describing 3D shape is NURBS curve which has been applied in some fields of electromagnetic [8]. Additionally, study of EM distribution considering human figure [9] has also been reported in some electromagnetic field problems. But, these researches have not discussed SE distribution of local clothing thoroughly.

Therefore, this paper explores the laws of the SE on the local clothing. At first, fitting formulas of the SE of key points on local clothing are deduced by analyzing electromagnetic and NURBS theories. Then, an example is demonstrated to verify the curve fitting method of the SE on the local body. At last, the distribution image of the SE is drawn to reveal the SE law of electromagnetic wave. Results show that this method is effective and can express the law of SE distribution on local clothing.

2. CONCRETE METHOD

2.1. SE Acquisition

We test the SE using shielding box. The shielding box is calibrated carefully to ensure it is leakproof. The antenna is calibrated in free space. The distant between antenna and local body model reaches the regular value. Signal receivers of the body model are connected with computer data receiving system. The electromagnetic shielding clothing is coated on the local model. We can obtain the testing results of the SE by computer. The local model is shown in Figure 1.

2.2. SE Calculation for Fitting

Suppose the impedance of electromagnetic wave in the air is $Z_1(\Omega)$, the characteristic impedance of shielding clothing is $Z_2(\Omega)$, the radiation field intensity of incident wave are $E_0(N/C)$ and $H_0(N/C)$. The incident wave produces the reflection when it arrives at the interface of the clothing,

and the impedance of electromagnetic wave Z_1 is equal to impedance of a free space medium Z_0 , then [10]

$$Z_1 = Z_0 = 377 \Omega \quad (1)$$

$$Z_2 = \sqrt{\frac{2\pi f \mu_0 \mu_r}{\sigma_0 \sigma_r}} = 3.68 \times 10^{-7} \sqrt{\frac{\mu_r f}{\sigma_r}} \quad (2)$$

$$R_{HN} = 20Lg \frac{Z_1}{4Z_2} = -119.07 + 10Lg \frac{fr^2 \sigma_r}{\mu_r} \text{ (dB)} \quad (3)$$

$$A = 20Lg \frac{E_0}{E_1} = 20Lg \frac{H_0}{H_1} = 15.4t \sqrt{f \mu_r \sigma_r} \text{ (dB)} \quad (4)$$

$$B = 20Lg(1 - e^{2t/\delta}) = 20Lg(1 - e^{3.54t\sqrt{f \mu_r \sigma_r}}) \text{ (dB)} \quad (5)$$

Therefore, the theoretical model of the SE in near-field can be calculated as:

$$SE_{HN1} = R_{HN} + A + B = 14.6 + 10Lg \frac{fr^2 \sigma_r}{\mu_r} + 1.31t \sqrt{f \mu_r \sigma_r} + 20Lg(1 - e^{3.54t\sqrt{f \mu_r \sigma_r}}) \text{ (dB)} \quad (6)$$

where, t denotes the thickness of idea shield, μ_r denotes the relative magnetic permeability, σ_r denotes the relative conductivity, f denotes the frequency (H_z).

2.3. Computer Fitting

The SE of electromagnetic shielding clothing is changed with the change of the distance of signal recourse. Therefore, all SE data of clothing can be recorded by computer. The SE of each testing point is different because the position of the testing point is space distribution. We use NURBS algorithm to construct the 3D curve for the SE of key points to extract the distribution functions of the SE on the body surface. NURBS curve is described the curve and spline on the object surface using a mathematic method. It can be expressed as [11]:

$$S(u, v) = \sum_{i=0}^{i=m} \sum_{j=0}^{j=n} W_{ij} P_{ij} N_{SE, p}(u) N_j, u, v \in [0, 1] \quad (7)$$

where, P_{ij} is the low of key point of the local body model, W_{ij} is the weight factor of key point, $N_{SE, p}$, N_j and $q(v)$ are the basis function of the spline B in the order p and the order q . Here, N_{SE} is defined as:

$$N_{SE} = 14.6 + 10 \frac{pq(v)^2 N_j}{u_{ij}} + 1.31 \sqrt{p u_{ij} N_j} + 20 \left(1 - e^{3.54t \sqrt{p u_{ij} N_j}} \right) \text{ (dB)} \quad (8)$$

where, u_{ij} is the permeability of the electromagnetic shielding fabric on the sequence point $p(i, j)$.

According to above Formulas, 3D NURBS curve fitting of the SE of the local body model is made using computer analysis software. The steps are as follows:

- 1) Class the key points according to the position of testing point and the SE and determine the sequence point with same classification.
- 2) Test SE of key points.
- 3) Iterate the sequence point with same classification and determine the fitting point.
- 4) Determine the values i and j of sequence point according to the fitting point.
- 5) Calculate the SE of other points not including key points by the Formula (6) according to the position of points.
- 6) Determine the basis function of B spline.
- 7) Fitting curves of SE distribution on the local clothing.
- 8) Draw a 3D sketch demonstrating distribution laws of SE on the local clothing.

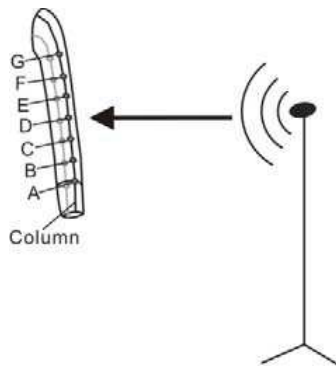


Figure 1: Local body model of SE testing.

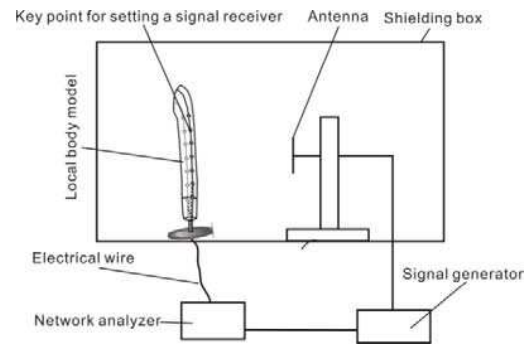


Figure 2: Experiment system for testing SE of key points in local body.

3. RESULTS AND ANALYSIS

3.1. Experimental Method

In order to test Computer Fitting method in this paper, an experiment is designed to get SE of key points in local arm. The emission frequency of signal is set as 500 MHz and the distance is set as 1 m. The testing points on the local body model are divided into six columns, three in the face of the arm, and three in the back. There are seven testing points in each column. We select ESFs with 38 dB manufactured by Shanghai Angel Textile Company as experimental samples, it were made of stainless metal fibers and cotton fibers. The experiment system is shown in Figure 2.

3.2. Results

The testing results of the SE when $f = 500$ MHz are listed in Table 1.

Table 1: The SE of each testing point on the local body model (500 MHz).

Column No. of local body	Shielding effectiveness (dB) of each key point						
	A	B	C	D	E	F	G
1	37.16	36.99	35.27	34.34	35.59	36.89	37.27
2	36.23	35.74	34.90	34.47	35.06	36.23	36.82
3	35.89	35.06	34.51	33.91	34.89	35.33	35.97
4	36.18	35.48	34.44	33.86	34.53	35.26	36.16
5	36.79	35.82	35.07	34.43	34.98	35.72	36.38
6	37.20	36.89	35.32	34.89	35.67	36.78	37.21

4. COMPUTER CURVE FITTING

4.1. Fitting According to SE of Key Points

According to Formula (7) and Formula (8), we use the MATLAB7.0 to compile a program and classify and schedule the data in Table 1. Figure 3 and Figure 5 are SE of key points according to different directions of array in Table 1. Then, we fit their SE curves by computer, as shown in Figure 4 and Figure 6.

4.2. Analysis

After the experimental verification and data analysis, we find that the SE changes have some regular changes. The SE shows linear changing along the arm axial direction. The initial value of increasing is the point of the arm model that is the nearest the radiation recourse. Otherwise, the distance from key point to emission source influences the SE distribution of the arm model. The bigger the distance is, the weaker the SE is. With the NURBS curve fitting, the farther part in the arm model is the strong SE area.

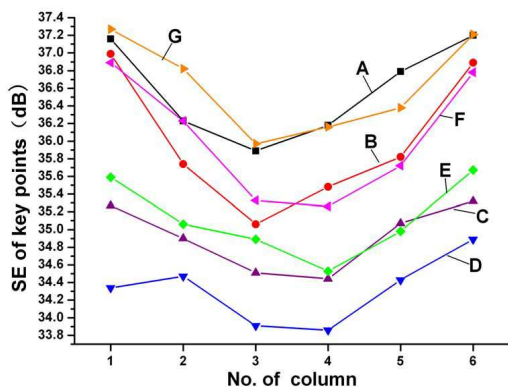


Figure 3: SE of key points with same identifier in the columns.

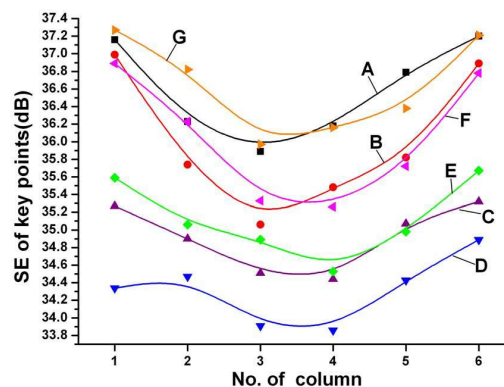


Figure 4: Fitting result of Figure 3.

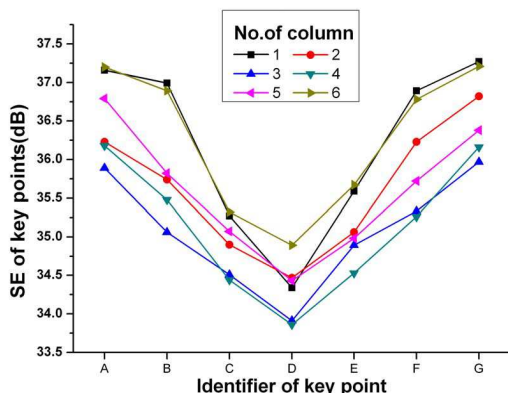


Figure 5: SE of key points in each column.

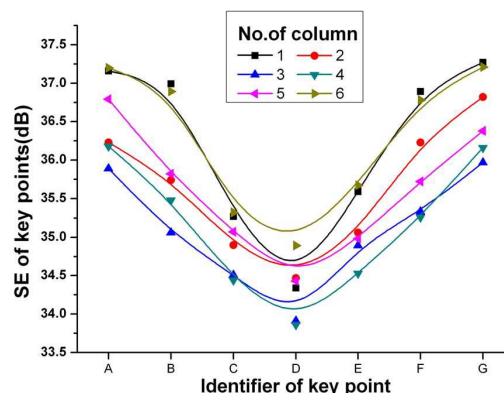


Figure 6: Fitting result of Figure 5.

5. CONCLUSION

A SE fitting analysis method on NURBS curve is proposed in this paper. With this method, the local testing points of electromagnetic shielding clothing can be classified and scheduled. A curve fitting is made by the SE of each testing point, and the 3D SE distribution of the local clothing is drawn. This image can show directly the distribution of electromagnetic wave on the body, and can provide the theoretical basis of the SE of local electromagnetic shielding clothing.

ACKNOWLEDGMENT

This research was supported by the National Natural Science Foundation of China (Grant No. 61471404).

REFERENCES

1. Wang, X. C., Z. Liu, and Z. Zhou, "Virtual metal model for fast computation of shielding effectiveness of blended electromagnetic interference shielding fabric," *International Journal of Applied Electromagnetics and Mechanics*, Vol. 44, No. 1, 87–97, 2014.
2. Wang, X. C. and Z. Liu, "Influence of fabric density on shielding effectiveness of electromagnetic shielding fabric," *Przeład Elektrotechniczny*, Vol. 88, No. 11a, 236–238, 2012.
3. Liu, Z. and X. C. Wang, "Influence of fabric weave type on the effectiveness of electromagnetic shielding woven fabric," *Journal of Electromagnetic Waves and Applications*, Vol. 26, Nos. 14–15, 1–9, 2012.
4. Liu, Z. and X. C. Wang, "Relation between shielding effectiveness and tightness of electromagnetic shielding fabric," *Journal of Industrial Textiles*, Vol. 43, No. 2, 302–316, 2013.

5. Liu, Z., X. C. Wang, and Z. Zhou, “Automatic recognition of metal fiber per unit area for electromagnetic shielding fabric based on computer image analysis,” *Progress In Electromagnetics Research Letters*, Vol. 37, 101–111, 2013.
6. Wang, X. C. and Z. Liu, “A new computation of shielding effectiveness of electromagnetic radiation shielding fabric,” *Progress In Electromagnetics Research Letters*, Vol. 33, 177–186, 2012.
7. Wang, X. C., Z. Liu, and M. L. Jiao, “Computation model of shielding effectiveness of symmetric partial for anti-electromagnetic radiation garment,” *Progress In Electromagnetics Research B*, Vol. 47, 19–35, 2013.
8. Davy, M., T. Lepetit, J. de Rosny, C. Prada, and M. Fink, “Detection and imaging of human beings behind a wall using the dort method,” *Progress In Electromagnetics Research*, Vol. 110, 353–369, 2010.
9. Moglie, F., V. M. Primiani, and A. P. Pastore, “Modeling of the human exposure inside a random plane wave field,” *Progress In Electromagnetics Research B*, Vol. 29, 251–267, 2011.
10. Qian, Z. and Z. J. Chen, *Electromagnetic Compatibility Design and Interference Suppression Technology*, Zhejiang University Press, Hangzhou, 2000.
11. Ruben, S., F. M. Sonia, and H. Antonio, “3D NURBS-enhanced finite element method (NE-FEM),” *International Journal for Numerical Methods in Engineering*, Vol. 8, No. 2, 103–125, 2011.

On the Treatment of Hypersingularity for Solving Volume Integral Equations

P. C. Wang, Z. G. Zhou, J. H. Zhou, X. F. Yin, and M. S. Tong

Department of Electronic Science and Technology, Tongji University

4800 Cao'an Road, Shanghai 201804, China

Abstract— In the meshless scheme for solving volume integral equations (VIEs), one needs to evaluate hypersingular integrals over a small cylindrical domain excluded from the whole domain for the sake of regularizing integrands. Those integrals can be evaluated semi-numerically but the implementation may not be convenient. In this work, we present some new formulas which are purely analytical for those integrals so that their evaluation can be greatly simplified. A numerical example for electromagnetic (EM) scattering is presented to demonstrate the new formulas.

1. INTRODUCTION

Volume integral equations are indispensable for solving electromagnetic (EM) problems with inhomogeneous or anisotropic media by an integral equation approach [1]. The VIEs are usually solved by the method of moments with the divergence-conforming Schaubert-Wilton-Glisson (SWG) basis function [2] or curl-conforming edge basis function [3]. These basis functions require conforming meshes for geometrical discretization, resulting in a high cost for preprocessing. Aiming to reduce the cost of meshing or remeshing geometries, point-matching methods like Nyström method and meshless methods were proposed and have been widely used in practice [4–12]. In these methods, we need to accurately evaluate singular volume integrals involving derivatives of the Green's function. Although many techniques have been developed for evaluating weakly and strongly singular integrals, the techniques for evaluating hypersingular integrals which come from the double gradient of the dyadic Green's function are very limited. Previously, we developed a treatment technique which uses a numerical integration for line integrals based on the analytical formulas of surface integrals [12]. The treatment is valid but it may not be convenient in implementation. In this work, we present new formulas for evaluating the hypersingular volume integrals over a cylindrical domain so that the implementation can be greatly simplified. We demonstrate the new formulas by solving an EM scattering problem and good results have been observed.

2. VOLUME INTEGRAL EQUATIONS

Consider the EM scattering by a dielectric (nonmagnetic) object which has a relative permittivity ϵ_r and is embedded in the free space with a permittivity ϵ_0 and a permeability μ_0 . The VIE for describing the problem can be written as [1]

$$\mathbf{E}(\mathbf{r}) = \mathbf{E}^{inc}(\mathbf{r}) + i\omega\mu_0 \int_V \bar{\mathbf{G}}(\mathbf{r}, \mathbf{r}') \cdot \mathbf{J}_V(\mathbf{r}') d\mathbf{r}', \quad \mathbf{r} \in V \quad (1)$$

where $\mathbf{E}^{inc}(\mathbf{r})$ and $\mathbf{E}(\mathbf{r})$ are the incident electric field and the total electric field inside the object, respectively, and $\mathbf{J}_V(\mathbf{r}') = i\omega\epsilon_0(1 - \epsilon_r)\mathbf{E}(\mathbf{r}')$ is the volumetric current density inside the object. Also, the integral kernel is the dyadic Green's function defined by

$$\bar{\mathbf{G}}(\mathbf{r}, \mathbf{r}') = \left(\bar{\mathbf{I}} + \frac{\nabla\nabla}{k_0^2} \right) g(\mathbf{r}, \mathbf{r}') \quad (2)$$

where $\bar{\mathbf{I}}$ is the identity dyad, $k_0 = \omega\sqrt{\mu_0\epsilon_0}$ is the free-space wavenumber, and $g(\mathbf{r}, \mathbf{r}') = e^{ik_0R}/(4\pi R)$ is the scalar Green's function with $R = |\mathbf{r} - \mathbf{r}'|$ being the distance between an observation point \mathbf{r} and a source point \mathbf{r}' . The above VIE can be solved by a meshless method as described in [12]. The method transforms the volume integral into a boundary or surface integral based on the Green-Gauss theorem so that discretizing the volume domain can be avoided, leading to a truly meshless scheme. However, this transformation is only valid for a regular integrand while the integral kernel of the VIE is hypersingular. We need to regularize the integral kernel by excluding a small cylindrical domain V_0 enclosing an observation node and the volume integral over the small cylindrical domain must be specially treated.

3. EVALUATION OF HYPERSINGULAR VOLUME INTEGRALS

The hypersingular volume integrals result from the double gradient of the dyadic Green's function and take the following form after performing a singularity subtraction

$$I_1 = \int_{V_0} \left(\frac{3u^2}{R^5} - \frac{1}{R^3} \right) dV, \quad I_2 = \int_{V_0} \left(\frac{3v^2}{R^5} - \frac{1}{R^3} \right) dV \quad (3)$$

$$I_3 = \int_{V_0} \left(\frac{3w^2}{R^5} - \frac{1}{R^3} \right) dV, \quad I_4 = \int_{V_0} \frac{uv}{R^5} dV \quad (4)$$

$$I_5 = \int_{V_0} \frac{w(-u)}{R^5} dV, \quad I_6 = \int_{V_0} \frac{w(-v)}{R^5} dV \quad (5)$$

where we have established a local coordinate system (u, v, w) as shown in Figure 1 for the integrals and the observation node is located at the origin or the center of the cylindrical domain with a radius a and a height $2h$ while the source point is located at (u, v, w) . The evaluation of those hypersingular integrals requires a numerical integration for line integrals in our original work [12] and this may not be very convenient in applications. Now we present new formulas which are purely closed-form for those integrals so as to facilitate the implementation of the meshless method. In the cylindrical domain, we also establish a polar coordinate system (ρ, ϕ) over its cross section, thus we have $\rho^2 = u^2 + v^2$ and $R^2 = \rho^2 + w^2$. The differential of cylindrical volume domain is $\rho d\rho d\phi dw$ but the integration over ϕ is just 2π because there is no dependence upon ϕ in the integrands. The above hypersingular integrals can be evaluated by the following integrals for which we have derived closed-form expressions.

$$\int_{V_0} \frac{dV}{4\pi R^3} = \int_0^h \int_0^a \frac{\rho d\rho dw}{(\rho^2 + w^2)^{3/2}} = -\ln \left[\frac{1}{w} \left(w + \sqrt{w^2 + a^2} \right) \right] \Big|_0^h \quad (6)$$

$$\int_{V_0} \frac{u^2 dV}{4\pi R^3} = \int_0^h \int_0^a \frac{\rho^3 d\rho dw}{2(\rho^2 + w^2)^{3/2}} = \frac{h}{2} \left[\sqrt{a^2 + h^2} - h \right] \quad (7)$$

$$\int_{V_0} \frac{w^2 dV}{4\pi R^3} = \int_0^h \int_0^a \frac{\rho w^2 d\rho dw}{2(\rho^2 + w^2)^{3/2}} = \frac{1}{2} \left\{ h^2 - h\sqrt{a^2 + h^2} + a^2 \ln \left[\frac{h}{a} + \sqrt{1 + \frac{h^2}{a^2}} \right] \right\} \quad (8)$$

$$\int_{V_0} \frac{u^2 dV}{4\pi R^4} = \int_0^h \int_0^a \frac{\rho^3 d\rho dw}{2(\rho^2 + w^2)^2} = \frac{1}{4} \left[h \ln \left(1 + \frac{a^2}{h^2} \right) + a \tan^{-1} \left(\frac{h}{a} \right) \right] \quad (9)$$

$$\int_{V_0} \frac{w^2 dV}{4\pi R^4} = \int_0^h \int_0^a \frac{\rho w^2 d\rho dw}{(\rho^2 + w^2)^2} = \frac{a}{2} \tan^{-1} \left(\frac{h}{a} \right) \quad (10)$$

$$\int_{V_0} \frac{u^2 dV}{4\pi R^5} = \int_0^h \int_0^a \frac{\rho^3 d\rho dw}{2(\rho^2 + w^2)^{5/2}} = -\frac{1}{6} \left\{ 2 \ln \left[1 + \sqrt{1 + \frac{a^2}{w^2}} \right] + \frac{w}{\sqrt{a^2 + w^2}} \right\} \Big|_0^h \quad (11)$$

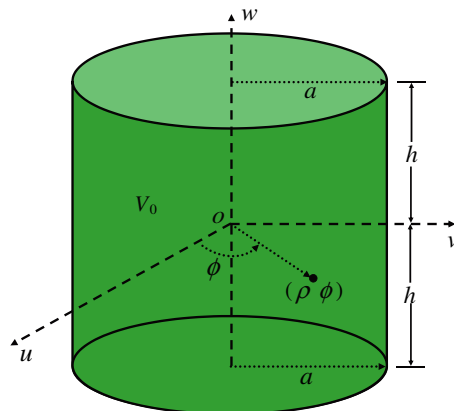


Figure 1: Cylindrical volume domain for evaluating hypersingular integrals.

$$\int_{V_0} \frac{w^2 dV}{4\pi R^5} = \int_0^h \int_0^a \frac{\rho w^2 d\rho dw}{(\rho^2 + w^2)^{5/2}} = \frac{1}{3} \left\{ \frac{w}{\sqrt{a^2 + w^2}} - \ln \left[1 + \sqrt{1 + \frac{a^2}{w^2}} \right] \right\} \Big|_0^h. \quad (12)$$

Some integrals in the above are individually divergent when $w \rightarrow 0$, but their combination will cancel the divergent terms, leading to convergent expressions, i.e.,

$$\int_{V_0} \frac{3u^2 - R^2}{4\pi R^5} dV = -\frac{h}{2\sqrt{a^2 + h^2}} \quad (13)$$

$$\int_{V_0} \frac{3w^2 - R^2}{4\pi R^5} dV = \frac{h}{\sqrt{a^2 + h^2}}. \quad (14)$$

We have omitted some integrals due to their similarity and the above integrals are representative. We have also incorporated the results of integration over ϕ and reduced the integral interval over w due to its symmetry.

4. NUMERICAL EXAMPLE

We demonstrate the new formulas by solving an EM scattering problem in which the scatterer is a homogeneous dielectric sphere with a radius r and a relative permittivity ϵ_r . It is assumed that the incident wave is a plane wave with a frequency $f = 300$ MHz and is propagating along the $+z$ direction. We calculate the bistatic radar cross section (RCS) observed along the principal cut ($\phi = 0^\circ$ and $\theta = 0^\circ - 180^\circ$) for the scatterer in both vertical polarization (VV) and horizontal polarization (HH). Figure 2 shows the solutions when $r = 0.5\lambda$ and $\epsilon_r = 4.0$ and we can see that the solutions agree with the exact Mie-series solutions very well.

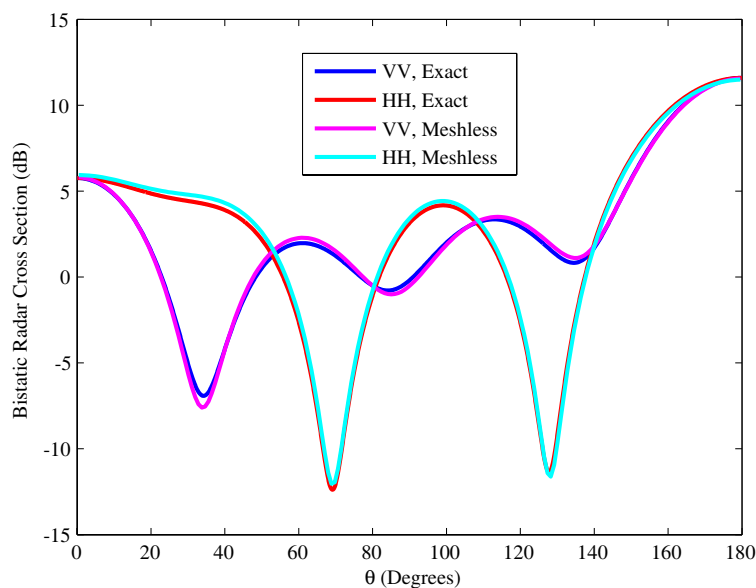


Figure 2: Bistatic RCS solutions for EM scattering by a dielectric sphere with a radius $r = 0.5\lambda$ and relative permittivity $\epsilon_r = 4.0$.

5. CONCLUSION

The accurate evaluation of hypersingular integrals is essential for using meshless methods to solve EM problems. Though they can be evaluated by performing a line integral numerically based on the analytical formulas of surface integrals, the implementation may not be convenient. In this work, we present purely analytical formulas as an alternative for evaluating those integrals and they can be easily used. A numerical example for solving EM scattering problems has been presented to verify the formulas.

ACKNOWLEDGMENT

This work was supported by the International Collaboration Foundation for Science and Technology, Shanghai, China (Project No. 13520722600).

REFERENCES

1. Chew, W. C., M. S. Tong, and B. Hu, *Integral Equation Methods for Electromagnetic and Elastic Waves*, Morgan & Claypool, San Rafael, CA, 2008.
2. Schaubert, D. H., D. R. Wilton, and A. W. Glisson, “A tetrahedral modeling method for electromagnetic scattering by arbitrary shaped inhomogeneous dielectric bodies,” *IEEE Trans. Antennas Propagat.*, Vol. 32, No. 1, 77–85, 1984.
3. Sun, L. E. and W. C. Chew, “A novel formulation of the volume integral equation for electromagnetic scattering,” *Waves Random Complex Media*, Vol. 19, No. 1, 162–180, Feb. 2009.
4. Kot, J. S., “Solution of thin-wire integral equations by Nyström methods,” *Microwave and Optical Technology Letters*, Vol. 3, 393–396, 1990.
5. Canino, L. S., J. J. Ottusch, M. A. Stalzer, J. L. Visher, and S. Wandzura, “Numerical solution of the Helmholtz equation in 2D and 3D using a high-order Nyström discretization,” *J. Comput. Phys.*, Vol. 146, No. 2, 627–663, 1998.
6. Burghignoli, P., C. Di Nallo, F. Frezza, and A. Galli, “A simple Nyström approach for the analysis of 3D arbitrarily shaped conducting and dielectric bodies,” *Int. J. Numer. Model.*, Vol. 16, 179–194, 2003.
7. Gedney, S. D., “On deriving a locally corrected Nyström scheme from a quadrature sampled moment method,” *IEEE Trans. Antennas Propagat.*, Vol. 51, 2402–2412, 2003.
8. Yang, K., J. C. Zhou, W. T. Sheng, Z. Y. Zhu, and M. S. Tong, “Efficient Nyström solutions of electromagnetic scattering by composite objects with inhomogeneous anisotropic media,” *IEEE Trans. Antennas Propagat.*, Vol. 61, No. 10, 5328–5332, Oct. 2013.
9. Maréchal, Y., “Some meshless methods for electromagnetic field computation,” *IEEE Trans. Magn.*, Vol. 34, No. 5, 3351–3354, Sept. 1998.
10. Ho, S. L., S. Yang, J. M. Machado, and H. C. Wong, “Application of a meshless method in electromagnetics,” *IEEE Trans. Magn.*, Vol. 37, No. 5, 3198–3202, Sept. 2001.
11. Zhang, Y., K. R. Shao, D. X. Xie, and J. D. Lavers, “Meshless method based on orthogonal basis for computational electromagnetics,” *IEEE Trans. Magn.*, Vol. 41, No. 5, 1432–1435, May 2005.
12. Tong, M. S., “Meshfree solutions of volume integral equations for electromagnetic scattering by anisotropic objects,” *IEEE Trans. Antennas Propagat.*, Vol. 60, No. 9, 4249–4258, Sept. 2012.

Simulation for Flat-plate Bounded Wave EMP Simulator with Distributed Terminator and Plane Source

Xiangqin Zhu¹, Jianguo Wang^{1,2}, Guowei Zhang¹, and Weiqing Chen¹

¹State Key Laboratory of Intense Pulsed Radiation Simulation and Effect (Northwest Institute of Nuclear Technology), Xi'an, Shaan'xi 710049, China

²School of Electronic and Information Engineering
Xi'an Jiaotong University, Xi'an, Shaan'xi 710049, China

Abstract— Parallelized finite-difference time-domain (FDTD) method for simulating the near-fields of flat-plate bounded wave electromagnetic pulse (EMP) simulator with distributed terminator and plane source is presented. The effect of some simulator's model-parameters to the vertical electric fields of the test points at the half-height in the simulator is simulated and analyzed.

1. INTRODUCTION

Bounded wave electromagnetic pulse (EMP) simulators, which can produce transverse electromagnetic (TEM) waves, have been widely applied to effect experiments of electromagnetic compatibility, interference and damage of complicated electronic systems. Flat-plate bounded wave EMP simulator with distributed terminator has been widely adopted because it can afford EMP with fast rise-time [1–4]. On the other hand, the size of the simulator becomes larger and larger in order to satisfy the need of general systematic experiments. So it's necessary to simulate the time-domain fields of the medium-sized or large flat-plate bounded wave EMP simulator with distributed terminator.

Parallelized finite-difference time-domain (FDTD) method has been used for simulating the near-fields of flat-plate bounded wave EMP simulator (whose height is 22 m) with distributed terminator and some different model-parameters as the simulator is fed by coaxial transmission line [5]. Considering the near-fields of the simulator fed by plane source are different with those of the simulator fed by coaxial transmission line, the effects of some simulator's model-parameters to the fields of the simulator with distributed terminator and plane source, which got by parallelized FDTD method, are presented and analyzed in this paper.

2. MODEL AND METHOD

The model of a flat-plate bounded wave EMP simulator with distributed terminator is shown in Fig. 1. The simulator includes transitional line, below perfect electric conductor (PEC) plate and distributed load. The working volume of the simulator is under the transmission line.

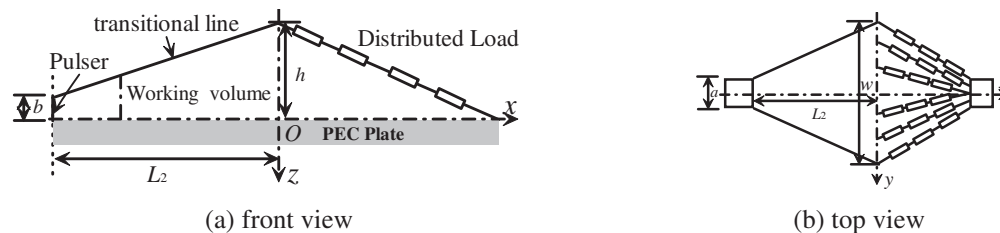
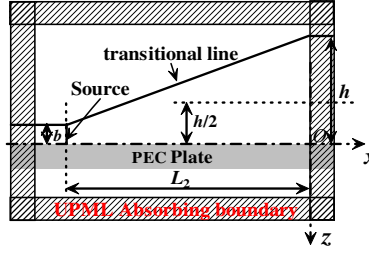


Figure 1: Configuration of flat-plate bounded wave EMP simulator with distributed terminator.

The near fields of the simulator are computed by Parallelized FDTD [6, 7]. The uniaxial perfectly matched layer (UPML) absorbing boundary is used in FDTD computing in this paper. Considering the distributed terminator at the simulator's end is used to absorb the electromagnetic waves for assuring no reflected waves returning to the working volume, the simulator's end is truncated (replaced) by UPML absorbing boundary in FDTD method, as shown in Fig. 2. On the other hand, the source pulse also propagates toward to opposite direction (the left side in Fig. 2) as it does to the direction towards working volume. Thus UPML absorbing boundary is also used in the front of the simulator, as shown in Fig. 2.


 Figure 2: Division of FDTD computing domain in xOz plane.

According to Fig. 2, there are some interfaces between UPML and the simulator's PEC plates. The FDTD expressions of electric field in y direction in UPML for lossy media are [8]

$$\begin{aligned}
 & P1_y^{n+1}(i, j + 1/2, k) \\
 = & D_u(i, j + 1/2, k)/C_u(i, j + 1/2, k)P1_y^n(i, j + 1/2, k) + ERX(i, j + 1/2, k)/C_u(i, j + 1/2, k) \\
 & \times \left\{ \left[H_x^{n+1/2}(i, j + 1/2, k + 1/2) - H_x^{n+1/2}(i, j + 1/2, k - 1/2) \right] / \delta_z \right. \\
 & \left. - \left[H_z^{n+1/2}(i + 1/2, j + 1/2, k) - H_z^{n+1/2}(i - 1/2, j + 1/2, k) \right] / \delta_x \right\} \quad (1)
 \end{aligned}$$

$$\begin{aligned}
 P_y^{n+1}(i, j + 1/2, k) &= B_z(k)/A_z(k)P_y^n(i, j + 1/2, k) \\
 &+ 1/(A_z(k) \cdot \Delta t) \times [P1_y^{n+1}(i, j + 1/2, k) - P1_y^n(i, j + 1/2, k)] \quad (2)
 \end{aligned}$$

$$\begin{aligned}
 E_y^{n+1}(i, j + 1/2, k) &= B_x(i)/A_x(i)E_y^n(i, j + 1/2, k) + 1/A_x(i) \\
 &\times [A_y(j + 1/2)P_y^{n+1}(i, j + 1/2, k) - B_y(j + 1/2)P_y^n(i, j + 1/2, k)] \quad (3)
 \end{aligned}$$

where

$$\begin{cases} C_u(i, j, k) = 1/\Delta t + \sigma(i, j, k)/(2\varepsilon_0), & D_u(i, j, k) = 1/\Delta t - \sigma(i, j, k)/(2\varepsilon_0) \\ A_x(i) = \kappa_x(i)/\Delta t + \sigma_x(i)/(2\varepsilon_0), & B_x(i) = \kappa_x(i)/\Delta t - \sigma_x(i)/(2\varepsilon_0) \\ A_y(j) = \kappa_y(j)/\Delta t + \sigma_y(j)/(2\varepsilon_0), & B_y(j) = \kappa_y(j)/\Delta t - \sigma_y(j)/(2\varepsilon_0) \\ A_z(k) = \kappa_z(k)/\Delta t + \sigma_z(k)/(2\varepsilon_0), & B_z(k) = \kappa_z(k)/\Delta t - \sigma_z(k)/(2\varepsilon_0) \\ ERX(i, j, k) = 1/\varepsilon_0 \end{cases} \quad (4)$$

and $k_v = 1 + (k_{\max} - 1)(l_v/d)^4$, $\sigma_v = (l_v/d)^4 / (30\pi\delta_v)$, $v = x, y, z$, k_{\max} is the maximum number of the layers of the interface about UPML absorbing boundary and perfect electric conductor (PEC), l_v is the distance between the PML and FDTD domain in v direction, $d = 4\delta_v$ is the depth of PML media; $\delta_v(v = x, y, z)$ is the FDTD grids' size in three directions, Δt is the time-step, and ε_0 is the dielectric parameter in vacuum. If the UPML contacts the PEC medium, $\varepsilon_r = 1$ and the conductivity $\sigma = 3.75 \times 10^7$ S/m. The FDTD expressions of the other two electric-field components are similar to the above. The FDTD expressions for magnetic fields are as same as the unlossy media.

The simulator's plane source is set at the cross section of the simulator's front-end, as shown in Fig. 2. And each electric field component in z direction (E_z) on the source plane is equal to the excited electric field at each FDTD time-step [9].

3. RESULTS AND ANALYSIS

As shown in Fig. 1 and Fig. 2, $L_2 = 80$ m, $h = 22$ m, $b = 0.4$ m and the ratio of the maximum width (w) to h is 1, 2 and 5 respectively. The width of the below PEC plate (w_d) is w or $2w$. The excited source of the simulator is

$$E_z(t) = E_0(\exp(-\alpha t) - \exp(-\beta t)) \quad (5)$$

where $E_0 = 2.31 \times 10^6$ V/m, $\alpha = 3.46 \times 10^6$ s $^{-1}$, $\beta = 5 \times 10^8$ s $^{-1}$. The rise-time of the source (t_r) is about 4 ns and the FWHM is about 221 ns. All FDTD cell sizes in three directions are 0.1 m and the time-step is $dt = \delta/(2c)$, c is the light's speed in vacuum. The total number of FDTD grids is 636 million. All test points are chosen on $y = 0$ plane and at the half-height in the simulator as shown in Fig. 2. The distance along x -axis from the test point to the source is L .

The rise-time, FWHM and peak-value of E_z changed with L at several test points in the simulator with different w_d and different w/h are shown in Figs. 3(a), (b) and (c) respectively. We can get from Fig. 3(a) that (1) when $w_d = w$ and $w/h = 1$, the rise-time of E_z increases greatly as L increases from 70 m to 80 m; (2) when $w/h = 2$, the rise-time of E_z at each test point can reach the minimum value; (3) when $w/h = 2$ (or 5), the rise-times of E_z at test points in the simulator with $w_d = w$ is almost equal to that in the simulator with $w_d = 2w$.

As shown in Fig. 3(b), when $w_d = w$ and $w/h = 2$, FWHM of E_z at each test point reaches the maximum value, while $w_d = 2w$ and $w/h = 5$, FWHM reaches the minimum value.

As shown in Fig. 3(c), we can obtain that (1) the peak-value of E_z at each test point increases with the distance from the test point to the source along x direction decreases; (2) when $w/h = 2$ (or $w/h = 5$), the peak-value of E_z at each test point in the simulator with $w_d = w$ is almost same to that in the simulator with $w_d = 2w$; (3) the peak-value of E_z at each test point as $w/h = 1$ reaches the maximum value, while that as $w/h = 5$ reaches the minimum value.

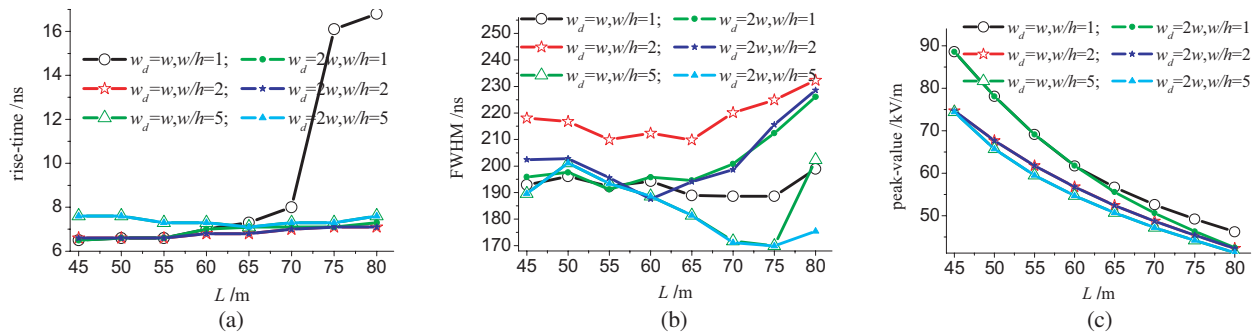


Figure 3: Rise-time, FWHM and peak-value of E_z at several points for various below PEC plate's width and various ratio of the transitional line's maximum width (w) to its maximum height (h).

From above we can get that if the ratio of the transitional line's maximum width to the maximum height (that is the simulator's ratio of width to height) is 2, the smallest rise-times of E_z at test points can be got. Let $w/h = 2$ and the width of below PEC plate is equal to w , $2w$ and infinity respectively. The rise-time, FWHM and peak-value of E_z changed with the distance from the point to the source along x -axis are shown in Figs. 4(a), (b) and (c) respectively. As shown in Fig. 4, the rise-time and peak-value of E_z at each test point are unchanged with the width of below PEC plate, that is, the width of below PEC plate has little effect on the rise-time and peak-value of E_z at each test point when $w/h = 2$, and the design of the width of below PEC plate is decided by the need of FWHM of E_z . The rise-time of E_z at the test point increases with L increased, while the peak-value decreases with L increased. When $w_d = w$, FWHM of E_z at each test point reaches the maximum value.

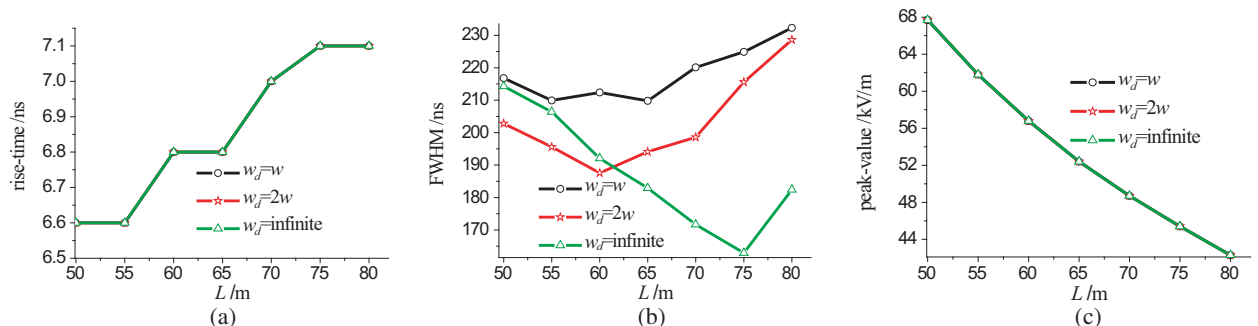


Figure 4: Rise-time, FWHM and peak-value of E_z at several points for various below PEC plate's width as the ratio of the transitional line's maximum width to its maximum height (w/h) is 2.

The electric fields changed with time at several points in the simulator with $w/h = 2$ are shown

in Fig. 5. As shown in Fig. 5, the results got by Parallelized FDTD with 80 processors ($np = 80$) are same with those by serial FDTD ($np = 1$). From Fig. 5, we also can get that there's some difference at the rear of the electric field's waveform at the same point in the simulator with $w_d = w$ or $w_d = 2w$. And the more difference, the farther the test point from the source along x -axis. That is due to the accumulation of the effect of the below PEC plate's edge become great as the distance between the point and the source increases.

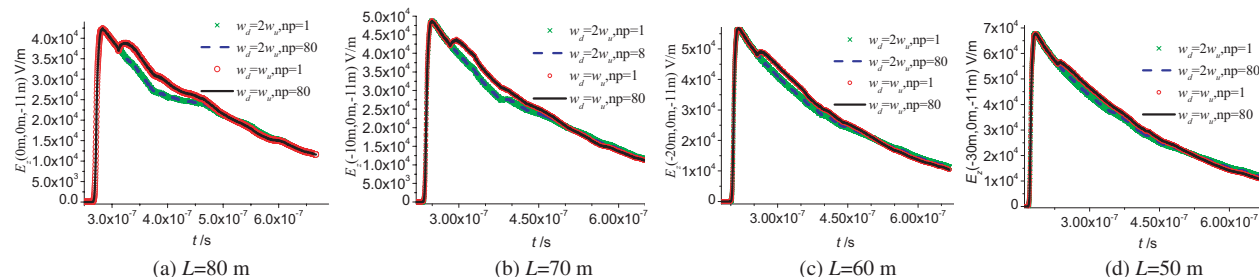


Figure 5: EMP of E_z at several points for various below PEC's width as w/h is 2.

4. CONCLUSIONS

Parallelized finite-difference time-domain (FDTD) method for flat-plate bounded wave EMP simulator with distributed terminator and plane source is shown in this paper. The distributed terminator is replaced by UPML absorbing boundary at the end of the simulator. The effect of some simulator's model parameters to the fields of several points is analyzed by the method. And the results in this paper can also be used in the design of other large simulators with distributed terminator and plane source.

REFERENCES

1. Guo, H., S. Fan, G. Wei, et al., "Study in simulation of match of loads of EMP simulation with fast rise-time," *Microcomputer Information*, Vol. 25, No. 3-1, 217–218, 2009 (in chinese).
2. Guo, H., G. Wei, S. Fan, et al., "Simulation study on vertical field distribution of EMP simulator with fast risetime," *High Power Laser and Particle Beams*, Vol. 21, No. 3, 403–406, 2009 (in chinese).
3. Klaasen, J. J. A., "An efficient method for the performance analysis of bounded-wave nuclear EMP simulators," *IEEE Trans. on Electromagnetic Compatibility*, Vol. 35, No. 3, 329–338, 1993.
4. Sun, F., X. Luo, X. Li, et al., "Theoretical analysis and experimental varification on design of transmission line for subnanosecond risetime EMP simulator," *High Power Laser and Particle Beams*, Vol. 20, No. 5, 811–814, 2008 (in chinese).
5. Zhu, X., J. Wang, W. Chen, et al., "Parallelized FDTD Simulation for flat-plate bounded wave EMP simulator with distributed terminator," *High Power Laser and Particle Beams*, Vol. 26, No. 03, 26035001, 2014 (in chinese).
6. Gropp, W., E. Lusk, and A. Skjillum, *Using MPI Portable Parallel Programming with the Message-Passing Interface*, MIT Press, Cambridge, Massachusetts, London, England, 1994.
7. Ge, D. and Y.-B. Yan, *Finite-Difference Time-Domain Method for Electromagnetic Waves*, Xidian Press, January 2005 (in chinese).
8. Gedney, S. D., "An anisotropic PML absorbing media for FDTD simulation of fields in lossy dispersive media," *Electromagnetics*, Vol. 16, No. 4, 339–415, 1996.
9. Li, Y., Z. Wang, and F. Liu, "Influence of parameters of boundary electromagnetic pulse simulator on transmitting mode," *High Voltage Engineering*, Vol. 33, No. 5, 54–57, 2007.

H-polarized Plane Wave Diffraction by an Acute-angled Dielectric Wedge: A Time Domain Solution

M. Frongillo¹, G. Gennarelli², and G. Riccio¹

¹D.I.E.M. — University of Salerno, Via Giovanni Paolo II 132, Fisciano, SA 84084, Italy

²Institute for Electromagnetic Sensing of the Environment
National Research Council, Via Diocleziano 328, Naples 80124, Italy

Abstract— This work deals with the time domain diffraction phenomenon originated by a penetrable acute-angled dielectric wedge when illuminated by a plane wave at normal incidence. In particular, the *H*-polarization case is here considered. The diffraction coefficients are determined in closed form via an inverse Laplace transform by taking advantage of the formulation of the frequency domain coefficients in terms of the transition function of the Uniform Theory of Diffraction. Then the transient diffracted field originated by an arbitrary function plane wave can be evaluated via a convolution integral.

1. INTRODUCTION

Electromagnetic wave diffraction by a penetrable wedge is an exciting canonical problem with potential applications. Moreover, time domain (TD) diffraction problems are receiving great attention from both the research community and industry interested to ultra wide band (UWB) communication and radar systems. Because of the large bandwidth of the UWB signals, the analysis of the wave propagation mechanisms in the TD framework is preferable to the frequency domain (FD) data processing. Furthermore, the analysis of transient scattering phenomena is of importance for predicting the effects of electromagnetic pulses (EMPs) on civil and military structures.

Numerical discretization techniques represent useful tools to support the research activity, but they become rapidly intractable when considering excitation pulses with high frequency content. Analytical TD solutions are not available in literature for penetrable wedges apart from those reported in [1, 2], where the TD counterparts of the frequency domain Uniform Asymptotic Physical Optics (FD-UAPO) solutions [3, 4] for the diffraction coefficients related to right- and obtuse-angled dielectric wedges were obtained.

FD-UAPO solutions for evaluating the diffracted field in the dielectric region and the surrounding free-space were recently derived in the case of a lossless acute-angled wedge illuminated by *H*-polarized plane waves at normal incidence [5]. They were expressed in closed form and given in terms of the Geometrical Optics (GO) response of the structure and the transition function of the Uniform Theory of Diffraction (UTD) [6].

2. GEOMETRY OF THE PROBLEM

The considered problem and the related geometric parameters are shown in Fig. 1. The wedge-shaped dielectric region and its surfaces are denoted by Ω_d , S_0 and S_n , respectively. It has internal apex angle $\alpha < \pi/2$ and is filled by a lossless non-magnetic ($\mu_r = 1$) material having relative permittivity ε_r . The symbol Ω_0 indicates the free-space region surrounding the wedge. The incidence direction is assumed perpendicular to the edge and defined by the angle ϕ' , which is here considered in the range from $\pi/2$ to $\pi - \alpha$, so that only S_0 is illuminated by an incident *H*-polarized plane wave having the magnetic field along the z -axis. The observation point is $P(\rho, \phi)$.

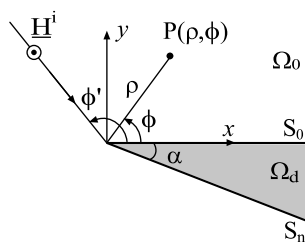


Figure 1: Geometry of the problem.

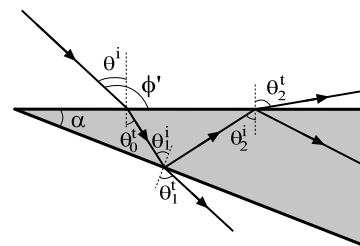


Figure 2: GO propagation mechanisms.

If $\theta^i = \phi' - \pi/2$ is the incidence angle, the wave penetrates into Ω_d according to the transmission angle $\theta_0^t = \sin^{-1}(\sin \theta^i / \sqrt{\varepsilon_r})$, and undergoes multiple reflections (see Fig. 2) until the reflection angle $\theta_p^r = \theta_p^i = p\alpha + \theta_0^t$ is greater than $\pi/2 - \alpha$. The number of total internal reflections is given by $M = \text{Int}[(\pi/2 - \theta_0^t)/\alpha]$, where $\text{Int}[\cdot]$ denotes the integer part of the argument.

Waves transmitted through S_0 and S_n define shadow boundaries in Ω_0 and exist until $\theta_p^i < \theta_c = \sin^{-1}(1/\sqrt{\varepsilon_r})$, with $p = 1, \dots, M^* = \text{Int}[(\theta_c - \theta_0^t)/\alpha] \leq M$.

3. TD-UAPO DIFFRACTED FIELD

According to [1, 2, 5], two separate problems relevant to Ω_d and Ω_0 are considered for the evaluation of the TD diffracted field

$$\underline{e}^d(P, t) = \frac{1}{\sqrt{\rho}} \int_{t_0}^{t-\rho/c} d\left(t - \frac{\rho}{c} - \tau\right) \underline{e}^i(Q, \tau) d\tau \quad \text{if} \quad t - \frac{\rho}{c} > t_0 \quad (1)$$

where in \underline{e}^i is the incident field (forcing function), $t = t_0$ is the time at the diffraction point Q when the forcing function is turned on, d is TD diffraction coefficient and c is the speed of light in the considered observation region. In the hypothesis that the material parameters are assumed independent on the frequency, the following expressions result for the TD-UAPO diffraction coefficient.

3.1. Internal Region Ω_d

$$\begin{aligned} d_{\Omega_d} &= (d_{S_0})_{\Omega_d} + (d_{S_n})_{\Omega_d} \quad (2) \\ (d_{S_0})_{\Omega_d} &= \frac{-1}{2\sqrt{2\pi}} T_0 \left\{ \frac{\sin \phi - \cos \theta_0^t}{\cos \phi + \cos(\theta_0^t + \pi/2)} g\left(2\rho \cos^2\left(\frac{(2\pi - \phi) + (\theta_0^t + \pi/2)}{2}\right), t\right) \right. \\ &\quad + \sum_{\substack{m=1 \\ m \text{ even}}}^M \left(\prod_{p=1}^{m-1} R_p \right) \frac{(1 + R_m) \sin \phi + (1 - R_m) \cos \theta_m^i}{\cos \phi + \cos(\theta_m^i + \pi/2)} g \\ &\quad \left. \left(2\rho \cos^2\left(\frac{(2\pi - \phi) + (\theta_m^i + \pi/2)}{2}\right), t\right) \right\} \quad (3) \end{aligned}$$

$$\begin{aligned} (d_{S_n})_{\Omega_d} &= \frac{-1}{2\sqrt{2\pi}} T_0 \left\{ \sum_{\substack{m=1 \\ m \text{ odd}}}^M \left(\prod_{p=1}^{m-1} R_p \right) \frac{(1 - R_m) \cos \theta_m^i - (1 + R_m) \sin(\phi + \alpha)}{\cos(\phi + \alpha) + \cos(\theta_m^i + \pi/2)} \right. \\ &\quad \left. \times g\left(2\rho \cos^2\left(\frac{\phi - (2\pi - \alpha) + (\theta_m^i + \pi/2)}{2}\right), t\right) \right\} \quad (4) \end{aligned}$$

3.2. External Region Ω_0

$$\begin{aligned} d_{\Omega_0} &= (d_{S_0})_{\Omega_0} + (d_{S_n})_{\Omega_0} \quad (5) \\ (d_{S_0})_{\Omega_0} &= \frac{-1}{2\sqrt{2\pi}} \left\{ \frac{(1 - R_0) \sin \phi' - (1 + R_0) \sin \phi}{\cos \phi + \cos \phi'} g\left(2\rho \cos^2\left(\frac{\phi \pm \phi'}{2}\right), t\right) \right. \\ &\quad \left. - T_0 \sum_{\substack{m=1 \\ m \text{ even}}}^{M^*} T_m \left(\prod_{p=1}^{m-1} R_p \right) \frac{\sin \phi + \cos \theta_m^t}{\cos \phi + \cos(\theta_m^t + \pi/2)} g\left(2\rho \cos^2\left(\frac{\phi \pm (\theta_m^t + \pi/2)}{2}\right), t\right) \right\} \quad (6) \end{aligned}$$

$$\begin{aligned} (d_{S_n})_{\Omega_0} &= -\frac{1}{2\sqrt{2\pi}} T_0 \left\{ \sum_{\substack{m=1 \\ m \text{ odd}}}^{M^*} T_m \left(\prod_{p=1}^{m-1} R_p \right) \frac{\sin(\phi + \alpha) - \cos \theta_m^t}{\cos(\phi + \alpha) + \cos(\theta_m^t + \pi/2)} \right. \\ &\quad \left. \times g\left(2\rho \cos^2\left(\frac{(\phi + \alpha) \pm (\theta_m^t + \pi/2)}{2}\right), t\right) \right\} \quad (7) \end{aligned}$$

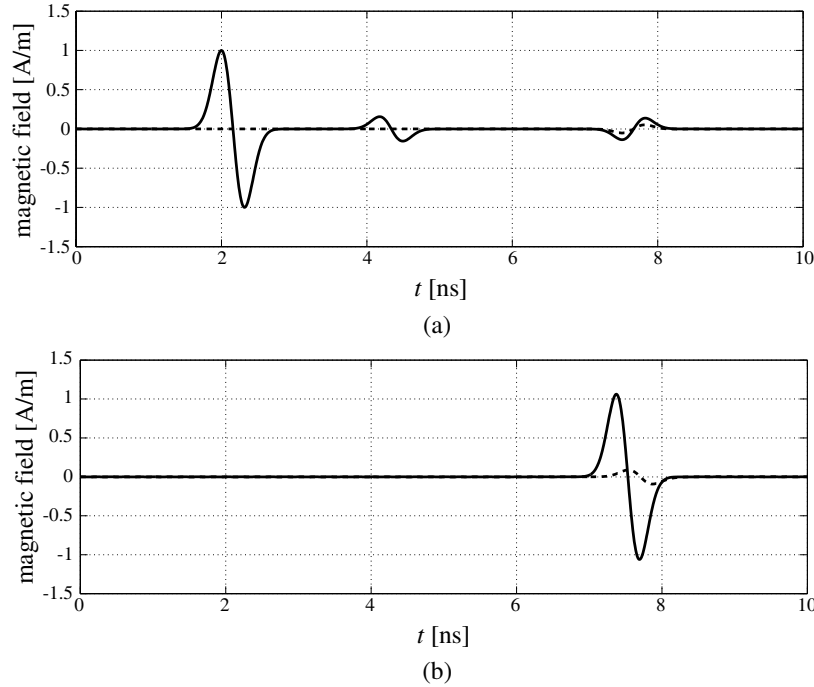


Figure 3: Magnetic field amplitude: (a) $P(2\text{ m}, 10^\circ)$; (b) $P(2\text{ m}, 310^\circ)$.

Note that the sign $+$ ($-$) must be used in (6) when $0 < \phi < \pi$ ($\pi < \phi < 2\pi - \alpha$), and in (7) when $0 < \phi < \pi - \alpha$ ($\pi - \alpha < \phi < 2\pi - \alpha$). If $\theta_p^t = \sin^{-1}(\sqrt{\varepsilon_r} \sin \theta_p^i)$, the reflection and transmission coefficients used in (3)–(4) and (6)–(7) are so defined:

$$T_0 = \frac{2 \cos \theta^i}{\sqrt{\varepsilon_r} \cos \theta^i + \cos \theta_0^t}; \quad R_0 = \frac{\sqrt{\varepsilon_r} \cos \theta^i - \cos \theta_0^t}{\sqrt{\varepsilon_r} \cos \theta^i + \cos \theta_0^t} \quad (8)$$

$$T_p = \frac{2\sqrt{\varepsilon_r} \cos \theta_p^i}{\cos \theta_p^i + \sqrt{\varepsilon_r} \cos \theta_p^t}; \quad R_p = \frac{\cos \theta_p^i - \sqrt{\varepsilon_r} \cos \theta_p^t}{\cos \theta_p^i + \sqrt{\varepsilon_r} \cos \theta_p^t} \quad (9)$$

Moreover,

$$g(X, t) = \frac{X}{\sqrt{\pi ct} (t + X/c)} \quad (10)$$

4. NUMERICAL TESTS

The reported examples refer to a lossless wedge characterized by $\varepsilon_r = 2$ and $\alpha = 15^\circ$ in the case of H -polarized plane wave impinging at $\phi' = 110^\circ$. Fig. 3(a) shows the field contributions arriving at $P(2\text{ m}, 10^\circ)$. In order of arrival, it is possible to identify the Geometrical Optics (GO) contributions (incident, specular reflection, and transmission-reflection-transmission waveforms in solid line), and the diffraction one (dashed line). Note that P is very close to the shadow boundary (10.73 degrees) for the transmission-reflection-transmission waveform. The field contributions arriving at $P(2\text{ m}, 310^\circ)$ are plotted in Fig. 3(b). Only the transmission-transmission waveform contributes to the GO field.

REFERENCES

1. Gennarelli, G. and G. Riccio, "Time domain diffraction by a right-angled penetrable wedge," *IEEE Trans. Antennas Propagat.*, Vol. 60, 2829–2833, 2012.
2. Gennarelli, G. and G. Riccio, "Obtuse-angled penetrable wedges: A time domain solution for the diffraction coefficients," *Journal of Electromagnetic Waves and Applications*, Vol. 27, No. 16, 2020–2028, 2013.
3. Gennarelli, G. and G. Riccio, "A uniform asymptotic solution for diffraction by a right-angled dielectric wedge," *IEEE Trans. Antennas Propagat.*, Vol. 59, 898–903, 2011.

4. Gennarelli, G. and G. Riccio, “Plane-wave diffraction by an obtuse-angled dielectric wedge,” *J. Opt. Soc. Am. A*, Vol. 28, 627–632, 2011.
5. Frongillo, M., G. Gennarelli, and G. Riccio, “Diffraction by an acute-angled dielectric wedge: The H -polarization case,” *PIERS Proceedings*, 846–849, Stockholm, Sweden, Aug. 12–15, 2013.
6. Kouyoumjian, R. G. and P. H. Pathak, “A uniform geometrical theory of diffraction for an edge in a perfectly conducting surface,” *Proc. of IEEE*, Vol. 62, 1448–1461, 1974.

Calculation of the Reflection and Transmission of Finite Sized Beams through Layered Uniaxial Anisotropic Media Accelerated by Plane Wave Spectrum Algorithm

Shihao Ji, Ming Bai, Zhao Liu, Yao Ma, and Xiuzhu Ye
Electromagnetics Laboratory, Beihang University, Beijing 100191, China

Abstract— In this paper, a fast method for calculating full vectorial reflection and transmission near-fields of arbitrary finite sized beams through multilayer uniaxial anisotropic media is proposed. The method combines Transfer Matrix method and optical fast-Fourier-transform based angular spectrum (FFT-AS) method. This calculation method can be used in the radome design and optical design which including multilayer anisotropic media.

1. INTRODUCTION

Calculation of electromagnetic waves through layered anisotropic media has been a problem encountered in many cases, such as radome design, optical design and ferromagnetic materials. Existing research have discussed infinite plane waves through layered anisotropic media, such as the general transmitting matrix and the Green's function method [1–3]. However, in case of finite sized beam or different orientation structured beam through layered anisotropic media, such as laser beam or antenna radiation limited in size, the calculation of reflection and transmission fields has been a problem encountered. In this case, a fast calculation method is required, especially for the design process which including large amount of parameter adjustment. For layered isotropic media, there is fast calculation method accelerated by plane wave spectrum algorithm [4]. When it comes to layered anisotropic media, this is usually performed by numerical ways, such as the Finite-Difference Time-Domain (FDTD) method [5] and the method of moment (MoM) [6], which can be time and memory consuming.

This paper proposed a method for calculating arbitrary oriented finite beams through layered uniaxial anisotropic media, as shown in Figure 1. The method combines Transfer Matrix method and optical fast-Fourier-transform based angular spectrum (FFT-AS) method. It can calculate full vectorial reflection and transmission near-fields of arbitrary finite sized beams through multilayer uniaxial anisotropic media within seconds, fully taking advantage of the FFT process.

There has been discussion on the FFT-AS method before [7], which is briefly illustrated in Section 2. The angular spectrum method also converts arbitrary oriented finite beams into superposition of plane waves with different directions. Thus the Transfer Matrix method can be used to calculate the result of every single plane wave through layered anisotropic media. Finally the transmitted plane waves and the reflected plane waves can be combined at target plane. With this method, the result of arbitrary oriented finite beams through layered anisotropic media can be

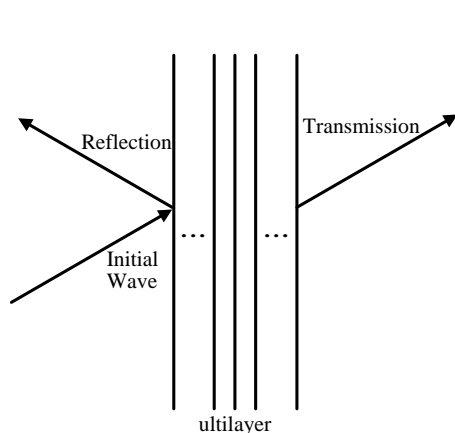


Figure 1: Schematic diagram of beam propagation through multilayer media.

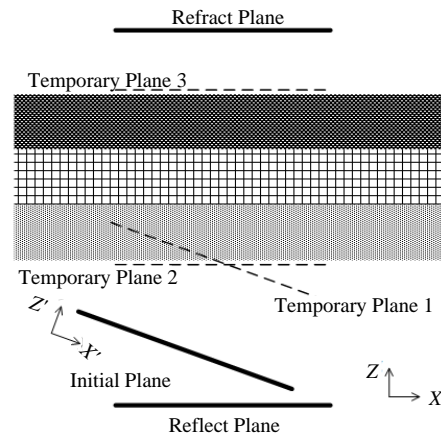


Figure 2: Model for combined method.

obtained accurately within seconds. On this basic, researchers can use this method to deal with big amount of parameter adjustment, with the complex structure and finite size of the multilayer anisotropic media involved such as radome design and optical design.

2. COMBINED METHOD OF FFT-AS AND TRANSFER MATRIX METHOD

As shown in Figure 2, the antenna in Figure 1 is replaced by an initial plane containing two orthogonal tangential field distributions. The FFT-AS method is used to calculate electromagnetic fields on temporary plane 1. Then the transfer matrix method is used to calculate transmitted beams on temporary plane 2 and reflected beams on temporary plane 3. Field distributions on arbitrary positioned target planes of the reflected and transmitted beam can be obtained by using the FFT-AS method again.

2.1. FFT-AS Method between Parallel and Tilted Planes

The Helmholtz–Kirchhoff and Rayleigh–Sommerfield diffraction formulas have been widely used to analyze the propagation and diffraction of electromagnetic wave in an isotropic medium. As in most cases the formulas cannot be solved analytically, numerical calculation of the formula has been introduced, such as the angular spectrum (AS) method accelerated by fast-Fourier-transform (FFT) [7]. The AS method treats the propagation of electromagnetic fields as a superposition of plane waves with variety of wave vectors. The initial beam and its propagation are handled in the spatial-frequency domain. The scalar field distribution $U(x, y, z)$ at distance z can be calculated as

$$U(x, y, z) = \int_{-\infty}^{\infty} \int_{-\infty}^{\infty} A(\alpha, \beta, z) \cdot \exp [j(\alpha x + \beta y)] d\alpha d\beta \quad (1)$$

The propagation of electromagnetic fields can be given as

$$A(\alpha, \beta, z) = A(\alpha, \beta, 0) \cdot G(\alpha, \beta, z) \quad (2)$$

where α, β are the direction cosines of a plane wave, $A(\alpha, \beta, 0)$ is the angular spectrum of initial field $U(x, y, 0)$ which can be computed by two-dimensional (2D) Fourier transformation, $A(\alpha, \beta, z)$ is the AS of target plane at distance z , and

$$G(\alpha, \beta, z) = \exp \left(-j \frac{2\pi}{\lambda} z \sqrt{1 - \alpha^2 - \beta^2} \right) \quad (3)$$

is the transfer function of each plane wave.

Introducing the fast-Fourier-transform, the FFT-AS method can be given as

$$U(x_m, y_n, z) = \text{IFFT} \{ \text{FFT}[U(x_m, y_n, 0)] \cdot \times G(\alpha_m, \beta_n, z) \} \quad (4)$$

where m and n mean the sampling points number of the plane, FFT2 and IFFT2 mean 2D FFT and 2D IFFT, and $\cdot \times$ stands for element-by-element multiplication.

As the wave vector of plane wave is perpendicular to electric field, the angular spectrum of electric field in z direction can be given as

$$\text{AE}_z = - \frac{\text{AE}_x \cdot k_x + \text{AE}_y \cdot k_y}{k_z} \quad (5)$$

where AE_x, AE_y is the angular spectrum of electric field in x direction and y direction calculated above and k_x, k_y, k_z is the wave vector of plane wave. Thus the full vectorial field can be calculated by FFT-AS method.

2.2. Multilayer Uniaxial Anisotropic Structure Transfer Matrix

For a multilayer structure, the transfer matrix can be written as [8]

$$M = \prod_{i=0}^N \begin{bmatrix} \cos \delta_i & (j \sin \delta_i) \cdot \eta_i \\ (j \sin \delta_i) / \eta_i & \cos \delta_i \end{bmatrix} \quad (6)$$

$$\delta_i = 2\pi n_i d_i \cos \theta_i / \lambda \quad (7)$$

where d is thickness of each layer, θ is the propagating angle of each plan wave and η is the wave impedance. The transmission coefficient T and reflection coefficient Γ are given as

$$\begin{aligned} T &= 1/M_{11} \\ \Gamma &= M_{21}/M_{11} \end{aligned} \quad (8)$$

As the wave impedance has different forms for TE and TM polarized plane wave, each plane wave should decompose to the TE and TM polarized plane wave and calculate separately.

For uniaxial anisotropic media, the permittivity tensor ε can be written as $\begin{bmatrix} \varepsilon_{\perp} & 0 & 0 \\ 0 & \varepsilon_{\perp} & 0 \\ 0 & 0 & \varepsilon_{\parallel} \end{bmatrix}$ in the principle coordinate system. For TE and TM polarized plane wave, the refractivity is given as

$$n_{\text{TE}} = \frac{c}{\sqrt{\frac{\varepsilon_{\perp}}{\varepsilon_0}}}, \quad n_{\text{TM}} = \frac{c}{\sqrt{\frac{\sin^2 \theta}{\mu \varepsilon_{\parallel}} + \frac{\cos^2 \theta}{\mu \varepsilon_{\perp}}}} \quad (9)$$

As discussed above, the initial wave is decompose to the TE and TM polarized plane wave, thus the plane of incidence is required to be parallel to the coordinate plane when using the transfer matrix method. To obtain this, a coordinate transformation matrix is adopted for each plane wave individually. The matrix $R_{i,j}$ is given as

$$R_{i,j} = \begin{bmatrix} \cos \phi_{i,j} & \sin \phi_{i,j} & 0 \\ -\sin \phi_{i,j} & \cos \phi_{i,j} & 0 \\ 0 & 0 & 1 \end{bmatrix} \quad (10)$$

$$\phi_{i,j} = \cos^{-1}(\text{sign}(\beta_{i,j}) \frac{\alpha_{i,j}}{\sqrt{\alpha_{i,j}^2 + \beta_{i,j}^2}}) \quad (11)$$

The AS method decomposes the initial wave to a series of plane wave with different directions on temporary plane 1. The AS matrices of temporary plane 2 and 3 can be obtained using the transfer matrix method. Thus the full vectorial fields on any plane can be obtained using the FFT-AS method.

3. EXAMPLES AND DISCUSSION

To verify the validity of this calculation method, an example is given. The structure of the example is shown in Figure 3 and the parameters of the structure is given in Table 1.

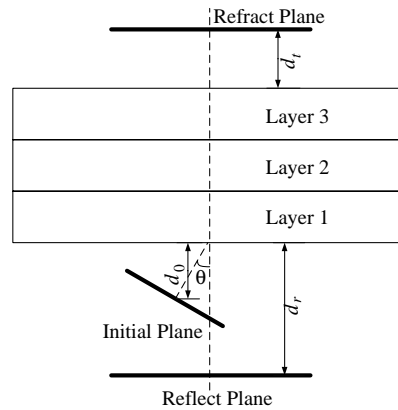


Figure 3: Simulation model of Gaussian beam propagation through layered anisotropic media.

Table 1: Structure parameters of Figure 4.

d_0	θ	d_r	d_t
45 mm	20°	75 mm	150 mm

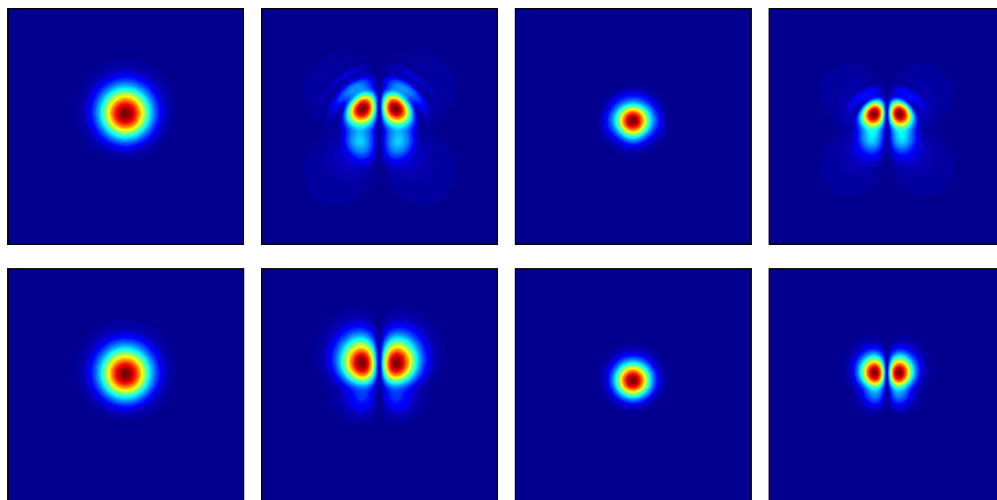


Figure 4: Amplitude of reflection and transmission fields on target plane. The first row is anisotropic media and the second row is isotropic media. The first column is main-polarization of transmitted fields. The second column is cross-polarization of transmitted fields. The third column is main-polarization of reflected fields. The fourth column is cross-polarization of reflected fields.

Table 2: Multilayer parameters of Figure 4.

	ϵ_{\perp}	ϵ_{\parallel}	Thickness
Layer 1	2.8	3.5	5 μm
Layer 2	1	1	15mm
Layer 3	2.8	3.5	5 μm

We assume the layered media be uniaxial anisotropic media such as liquid crystal. Liquid crystals are dielectric materials with anisotropic characteristics [9]. The permittivity of liquid crystal can be tuned through an external electric field. The parameters of each media is given in Table 2. The initial field is the waist of a Gaussian beam at 20 GHz. The waist of the beam is 5λ . To compare the result with isotropic media, we assume the media in layer 1 and layer 3 be an isotropic media with the permittivity tensor 2.8. The simulation process is fast and costs less than 5 minutes. The result is shown in Figure 4.

The result implies that the cross-polarization of reflection and refraction fields of the anisotropic media is different from the isotropic media. The amplitude of cross-polarization of anisotropic media is higher than isotropic media and the amplitude of main-polarization of anisotropic media is lower than isotropic media. This is because the anisotropic media has the depolarization characteristic. This characteristic can be useful in antenna design and microwave devices design.

4. CONCLUSION

A fast way to calculate reflection and refraction fields of infinite beam through multilayer uniaxial anisotropic media is proposed in this letter. This method combines FFT-AS method and transfer matrix method and can avoid the time consuming numerical solution, full vectorial near fields of reflected and transmitted can be calculated within seconds. The method provides a way for large amount parameters adjustment in design process. An example of layered liquid crystal is given and implies that the cross-polarization difference between anisotropic media and isotropic media.

ACKNOWLEDGMENT

This work was supported by the Chinese National Programs for Fundamental Research and Development (Project 2012CB315601).

REFERENCES

1. Løseth, L. O. and B. Ursin, "Electromagnetic fields in planarly layered anisotropic media," *Geophysical Journal International*, Vol. 170, No. 1, 44–80, 2007.

2. Elshafiey, T. F. and J. T. Aberle, “Green’s function for multilayer arbitrarily biased anisotropic structures — Application to phase shifters, transducers, and magnetization angle effect,” *IEEE Transactions on Microwave Theory and Techniques*, Vol. 54, No. 2, 513–521, 2006.
3. Titchener, J. B. and J. R. Willis, “The reflection of electromagnetic waves from stratified anisotropic media,” *IEEE Transactions on Antennas and Propagation*, Vol. 39, No. 1, 35–39, 1991.
4. Liang, B., M. Bai, N. Ou, M. Jin, and J. Miao, “Fast analysis of arbitrary beam through planar multilayer structures,” *Microwave and Optical Technology Letters*, Vol. 54, No. 9, 2185–2190, 2012.
5. Oh, C. and M. J. Escuti, “Time-domain analysis of periodic anisotropic media at oblique incidence: An efficient FDTD implementation,” *Optics Express*, Vol. 14, No. 24, 11870–11884, 2006.
6. Kobidze, G. and B. Shanker, “Integral equation based analysis of scattering from 3-D inhomogeneous anisotropic bodies,” *IEEE Transactions on Antennas and Propagation*, Vol. 52, No. 10, 2650–2658, 2004.
7. Shen, F. and A. Wang, “Fast-Fourier-transform based numerical integration method for the Rayleigh-Sommerfeld diffraction formula,” *Applied Optics*, Vol. 45, No. 6, 1102–1110, 2006.
8. Macleod, H. A., *Thin-film Optical Filters*, CRC Press, 2001.
9. Yaghmaee, P., O. H. Karabey, B. Bates, C. Fumeaux, and R. Jakoby, “Electrically tuned microwave devices using liquid crystal technology,” *International Journal of Antennas and Propagation*, 2013.

Impact on the Performance of Compact Antenna Test Range due to Surface Deviation of the Reflector

Zhao Liu, Ming Bai, Shihao Ji, Xiao Fang, and Xiuzhu Ye
Electromagnetics Laboratory, Beihang University, Beihang 100191, China

Abstract— The fabrication precision of designed compact antenna test range (CATR) impacts the performance of quiet zone, especially in millimeter wave range. In this paper, several surface deviations of the reflector and their influence on the quiet zone are analyzed. Comparing the data of deviated reflector with those of the ideal reflector, it is found that the sensitivity of quiet zone to the surface deviation increases with operating frequency. In addition, in order to ensure the performance of CATR, it is found that $1/560$ of wavelength is the upper limitation for mechanical production. At last, guidance for millimeter wave CATR fabrication is provided.

1. INTRODUCTION

Compact antenna test range (CATR) technology is key to measurement technology of antenna far field pattern and Radar Cross Section of targets [1, 2], the function of which is to convert the spherical wave generated from the feed to quasi-plane wave. The wave is gathered by the reflector, the ripple/taper of amplitude and phase of which should be no more than 1 dB and 10° , respectively. That zone is named as ‘quiet zone’, because the wave is considered as the uniform plane wave. With the development of microwave technology, the frequency band used increases to millimeter or even sub-millimeter range, which increases the precision requirement for the fabrication of the CATR reflector.

There are several factors that impact the performance of the quiet zone of CATR, such as the truncation of edge, the serration, clutter reflected by rear wall, the leakage of feed, deformation of reflector by gravity, surface deviation and etc. The research of the impact of surface error on parabolic dish antenna is firstly introduced by Ruze [3, 4], in which the relation between random surface error and gain lost is summarized. The model of random surface error and its impact on average power pattern are introduced by Rahmat-Samii et al. [5].

The effect on the far field pattern of antenna catches lots of eyes [6, 7], and yet, the side effect on the near field is not sufficiently studied. Indeed this topic is the key to quiet zone of the millimeter wave CATR. Therefore, in this paper, we study the effects of surface deviation on the near field distribution. According to the study, considerable guidance for further millimeter wave CATR construction is provided.

2. FORMULATION

According to Rayleigh-Sommerfeld diffraction integrals [8], propagation of microwave between two parallel planes is:

$$\vec{E} = \frac{1}{4\pi} \int_A \left[\vec{r} \times (\hat{n} \times \vec{E}_A) (1 + jkr) \frac{e^{-jkr}}{r^3} \right] ds' \quad (1)$$

When z is const, the integral is converted to two-dimension convolution as Equation (2),

$$g(x, y) = \iint f(x', y') h(x - x', y - y', z - z') dx' dy' = f(x, y) * h(x, y) \quad (2)$$

where

$$h(x, y) = (1 + jkr) \frac{e^{-jkr}}{r^3} \quad (3)$$

This algorithm is calculated by Fast Fourier Transform (FFT), which reduces time complexity to $O(N^2 \log_2(N^2))$.

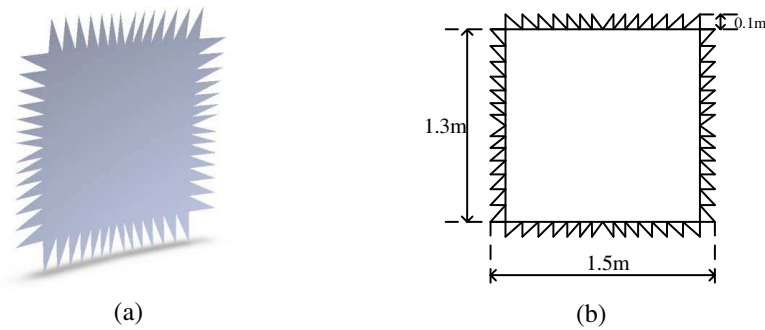


Figure 1: (a) The model of reflector; (b) The normal projection of reflector.

3. SIMULATION AND DISCUSSION

The frequency of millimeter wave CATR ranges from 50 GHz to 200 GHz. It uses a single parabolic reflector, as Figure 1. It is 1.5 m in height and 1.5 m in width, the serration edge of which is 0.1 m, and the focus of which is 2 m. The shape of ‘quiet zone’ is a cylinder, the diameter of the cross section of which is 0.8 m. The influence of machining precision is investigated.

A PASCAL program is developed based on the formulation given above. The performance of this CATR at 50 GHz to 400 GHz is evaluated. Now the situation of 100 GHz is set as the example.

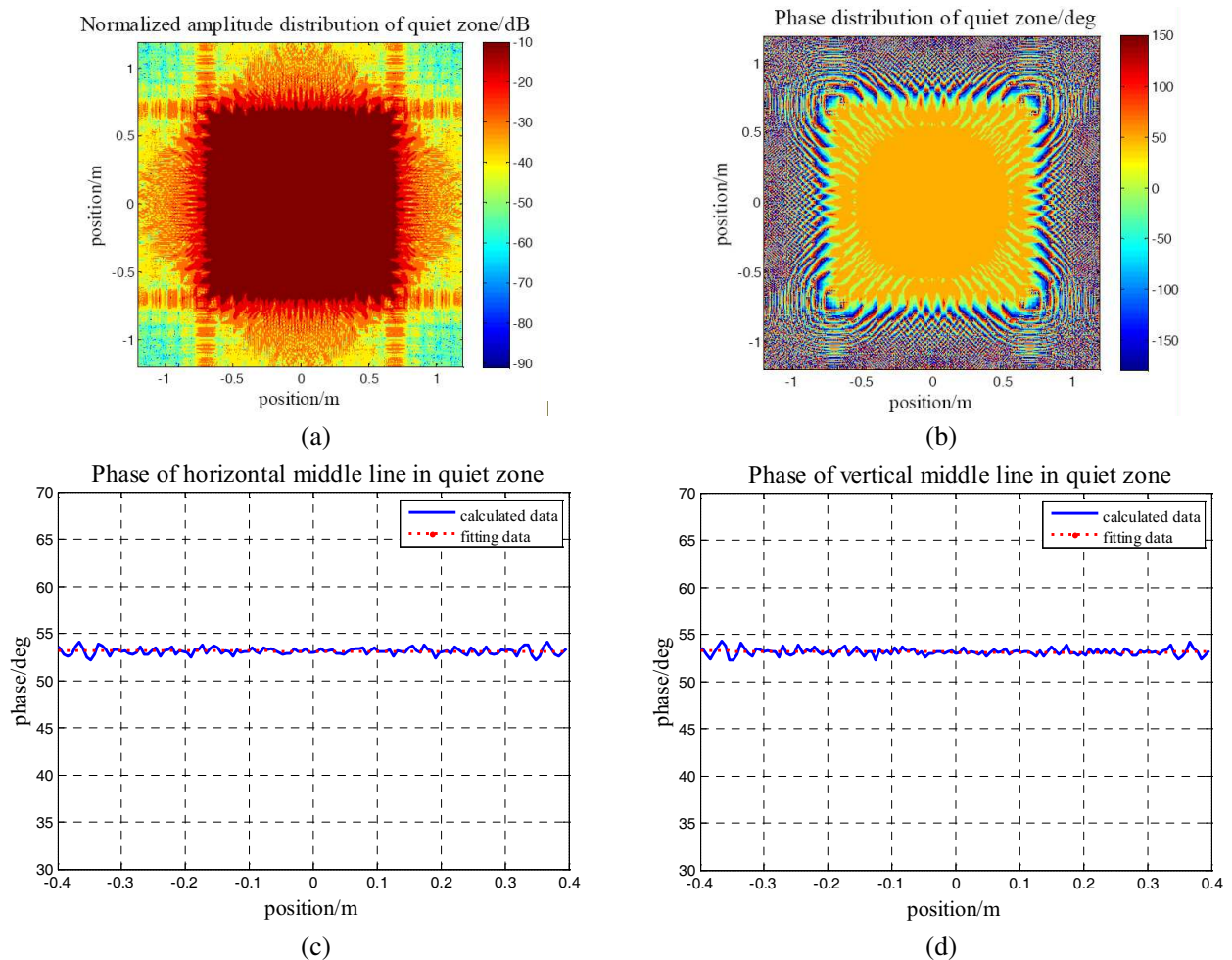


Figure 2: (a) Normalized amplitude distribution of quiet zone; (b) Phase distribution of quiet zone; (c) Phase of horizontal middle line of quiet zone; (d) Phase of vertical middle line in quiet zone.

The taper and ripple of amplitude and phase at 100 GHz are listed in the following table.

Table 1: (a) Taper and ripple of amplitude of quiet zone at 100 GHz; (b) Taper and ripple of phase of quiet zone at 100 GHz.

Result	Horizontal middle line		Vertical middle line	
	Amplitude/dB	Phase/deg	Amplitude/dB	Phase/deg
Taper	0.491	0.054	0.760	0.141
Ripple	0.214	1.908	0.282	2.036

As a matter of fact, the surface of CATR reflector cannot be absolutely smooth even in fine machining. There always is random deviation in the surface of the reflector. According to the current capacity of machining, the random deviation produces limit influence to the quiet zone of normal CATR when operating frequency is no more than 40 GHz.

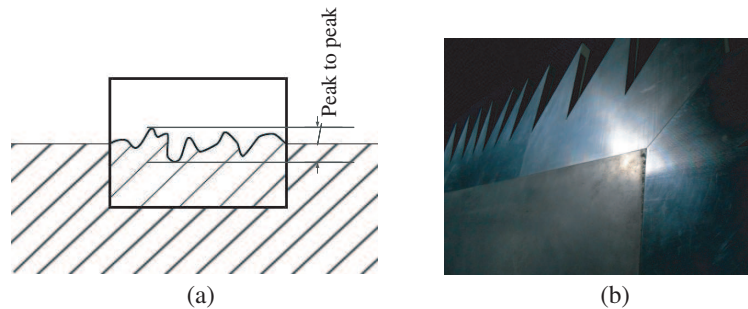


Figure 3: (a) Peak to peak value of surface deviation of reflector; (b) Surface deviation of a reflector during manufacture.

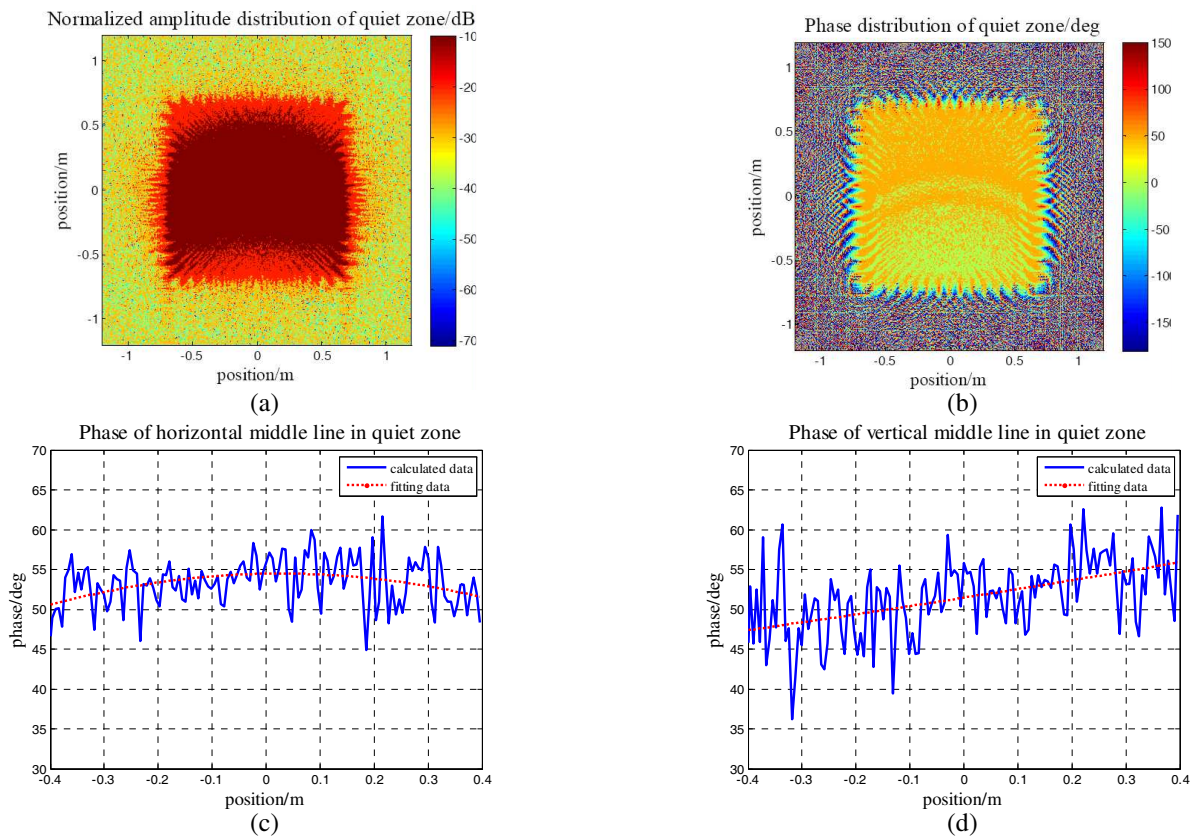


Figure 4: (a) Normalized amplitude distribution of quiet zone; (b) Phase distribution of quiet zone; (c) Horizontal middle line of quiet zone; (d) Vertical middle line in quiet zone.

The surface deviation of reflector is shown in Figure 3(a), which is described by peak to peak value. The surface deviation is clearly seen in the fabricated millimeter wave CATR reflector which needs to be polished before use. When the frequency increases to millimeter waveband, the surface error becomes comparable to the wavelength. So in this situation, the diffraction of undulating on the reflector surface cannot be ignored, and it causes depravation to the performance of quiet zone. To analyze the effects of surface deviation on the quiet zone, five cases of different surface deviation (RMS value) are calculated ($\lambda/84$, $\lambda/168$, $\lambda/280$, $\lambda/560$ and $\lambda/1400$). Here the situation of $\lambda/168$ at 100GHz is set as the example.

The taper and ripple of amplitude and phase are presented in Figure 5.

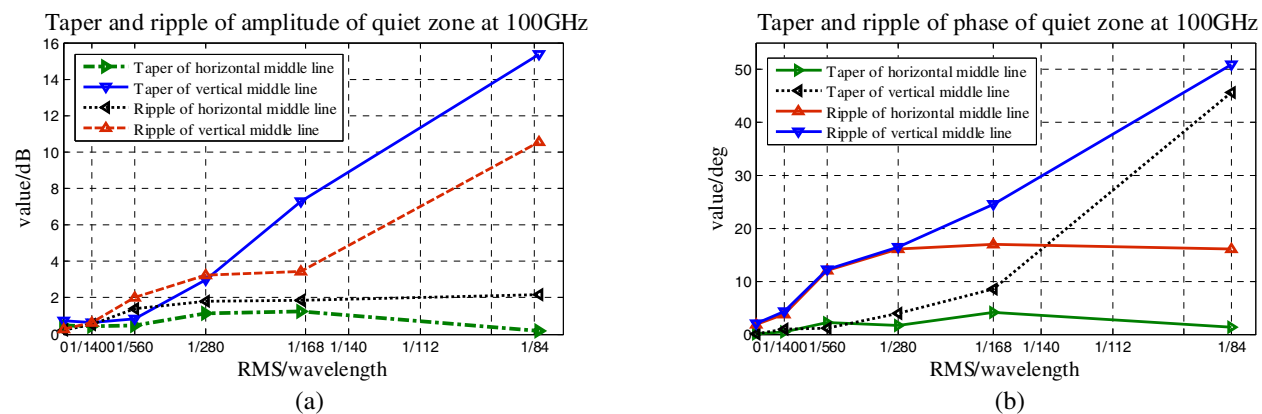


Figure 5: (a) Taper and ripple of amplitude of quiet zone at 100 GHz; (b) Taper and ripple of phase of quiet zone at 100 GHz.

From the above figures, when RMS value increases to $\lambda/168$, the ripple of amplitude and phase in quiet zone is not suitable for testing the far field pattern of antenna and the RCS of target. Besides surface deviation causes that the quiet zone is unsymmetrical in vertical direction. Coupling coefficients of different surface deviation at different frequency are presented in Figure 6.

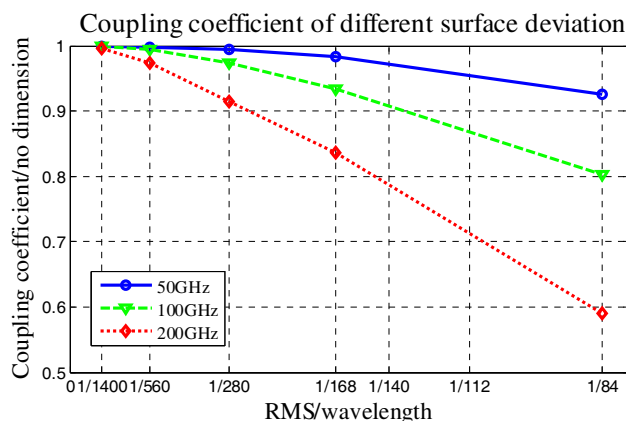


Figure 6: Coupling coefficient of different surface deviation compared to ideal surface.

Due to the result of coupling coefficient and the deterioration of taper and ripple of amplitude and phase, the precision of machining of reflector should be less than $\lambda/560$.

4. CONCLUSIONS

For millimeter wave CATR, the surface deviation exerts an obvious influence to quiet zone. It causes the scatter of energy and results in serious taper and ripple in amplitude and phase. Compared to common CATR operating frequency below 40 GHz, millimeter wave CATR is more sensitive to surface deviation. One hundred of wavelength is upper limitation for mechanical production. There are several lines of research arising from this work which should be pursued. Firstly, the evacuation of energy scatter in quiet zone is to be analyzed. Secondly, the taper and ripple in amplitude and phase of the CATR with or without polish will be test, to verify the calculation above.

ACKNOWLEDGMENT

This work was supported by the Chinese National Programs for Fundamental Research and Development (Project 2012CB315601). The authors would like to thank the reviewers for the comments.

REFERENCES

1. Goyette, T. M., J. C. Dickinson, J. Waldman, and W. E. Nixon, "1.56-THz compact radar range for W-band imagery of scale-model tactical targets," *Aero Sense 2000, International Society for Optics and Photonics*, 615–622, August 2000.
2. Teniente, J., E. Arnaud, R. Gonzalo, and C. Del-Río, "Optimized feedhorn designs for compact antenna test range at limoges university," *IEEE First European Conference on Antennas and Propagation, 2006, EuCAP 2006*, 1–6, November 2006.
3. Ruze, J., "Antenna tolerance theory — A review," *IEEE Proceedings*, Vol. 54, 633–642, April 1966.
4. Ruze, J., "The effect of aperture errors on the antenna radiation pattern," *IlNuovoCimento (1943–1954)*, Vol. 9, 364–380, 1952.
5. Rahmat-Samii, Y., "An efficient computational method for characterizing the effects of random surface errors on the average power pattern of reflectors," *IEEE Transactions on Antennas and Propagation*, Vol. 31, No. 1, 92–98, 1983.
6. Bahadori, K. and Y. Rahmat-Samii, "Characterization of effects of periodic and aperiodic surface distortions on membrane reflector antennas," *IEEE Transactions on Antennas and Propagation*, Vol. 53, No. 9, 2782–2791, 2005.
7. Wang, C. S., B. Y. Duan, and Y. Y. Qiu, "A new approach to fit the distorted reflector antenna and its computation of electrical characteristics," *The First Asia International Symposium on Mechatronics (AISM'2004)*, 27–30, Xi'an, China, September 2004.
8. Shen, F. and A. Wang, "Fast-Fourier-transform based numerical integration method for the Rayleigh-Sommerfeld diffraction formula," *Applied Optics*, Vol. 45, No. 6, 1102–1110, 2006.

Electromagnetic Waves Described with the Complex Quaternion

Zi-Hua Weng

School of Physics and Mechanical & Electrical Engineering, Xiamen University, Xiamen 361005, China

Abstract— J. C. Maxwell applied the quaternion analysis and the vector terminology to depict the electromagnetic theory. Nowadays the scholars can use the complex quaternion to study the electromagnetic feature, including the Maxwell's equations and the current continuity equation etc. Meanwhile it is able to describe the gravitational theory with the complex quaternion. On the basis of these studies, the paper separates the complex octonion into two components, the complex quaternion and the complex S -quaternion. The complex quaternion is suitable to describe the gravitational theory, while the complex S -quaternion is proper to depict the electromagnetic theory. Further the paper can apply the complex quaternion to describe the wave equation of gravitational field, and use the complex S -quaternion to depict the wave equation of electromagnetic field. The result reveals that the complex octonion is suitable to describe simultaneously the wave features of electromagnetic and gravitational fields.

1. INTRODUCTION

J. C. Maxwell represented the physical feature of electromagnetic field with the quaternion analysis and the vector terminology. In 1843, W. R. Hamilton invented the quaternion. And J. T. Graves and A. Cayley discovered the octonion independently. Later the scientists and engineers separated the quaternion into the scalar part and vector part. Maxwell mingled naturally the quaternion and the vector to describe the electromagnetic feature in his works. Making use of the complex quaternion in recent years, some scholars begin to study the Maxwell's equations [1] and the current continuity equation [2], and even the physics feature of gravitational field [3].

The ordered couple of quaternions compose the octonion. On the contrary, the octonion is able to be separated into two components, the quaternion and the S -quaternion (short for the second quaternion), while their coordinates are able to be complex numbers. The quaternion space is suitable to depict the gravitational features, and the S -quaternion space is proper to describe the electromagnetic features. Further it can directly deduce the wave equations in the electromagnetic and gravitational fields described with the complex octonion.

In the quaternion space, it is able to infer the field strength and field source etc in the gravitational field, and deduce the gravitational field equations and wave equation etc. The Newton's law of universal gravitation in the classical gravitational theory can be reduced from one of gravitational field equations described with the quaternion. And the gravitational waves are transverse waves in a vacuum. In the S -quaternion space, it is able to deduce the field strength and field source etc in the electromagnetic field. Further the Maxwell's equations and electromagnetic wave equation etc can be inferred directly also. The electromagnetic wave equation is identical with that in the classical electromagnetic theory with the vector terminology.

2. COMPLEX QUATERNION SPACE

The octonion space \mathbb{E} can be separated into two subspaces, the quaternion space \mathbb{E}_g and the S -quaternion space \mathbb{E}_e . In the quaternion space \mathbb{E}_g for the gravitational field, the basis vector is $\mathbb{E}_g = (\mathbf{i}_0, \mathbf{i}_1, \mathbf{i}_2, \mathbf{i}_3)$, the radius vector is $\mathbb{R}_g = ir_0\mathbf{i}_0 + \sum r_k\mathbf{i}_k$, and the velocity is $\mathbb{V}_g = iv_0\mathbf{i}_0 + \sum v_k\mathbf{i}_k$. The gravitational potential is $\mathbb{A}_g = ia_0\mathbf{i}_0 + \sum a_k\mathbf{i}_k$, the gravitational strength is $\mathbb{B}_g = h_0\mathbf{i}_0 + \sum h_k\mathbf{i}_k$, and the gravitational source is $\mathbb{S}_g = is_0\mathbf{i}_0 + \sum s_k\mathbf{i}_k$. In the S -quaternion space \mathbb{E}_e for the electromagnetic field, the basis vector is $\mathbb{E}_e = (\mathbf{I}_0, \mathbf{I}_1, \mathbf{I}_2, \mathbf{I}_3)$, the radius vector is $\mathbb{R}_e = iR_0\mathbf{I}_0 + \sum R_k\mathbf{I}_k$, and the velocity is $\mathbb{V}_e = iV_0\mathbf{I}_0 + \sum V_k\mathbf{I}_k$. The electromagnetic potential is $\mathbb{A}_e = iA_0\mathbf{I}_0 + \sum A_k\mathbf{I}_k$, the electromagnetic strength is $\mathbb{B}_e = H_0\mathbf{I}_0 + \sum H_k\mathbf{I}_k$, and the electromagnetic source is $\mathbb{S}_e = iS_0\mathbf{I}_0 + \sum S_k\mathbf{I}_k$. Herein $\mathbb{E}_e = \mathbb{E}_g \circ \mathbf{I}_0$. The symbol \circ denotes the octonion multiplication. $r_j, v_j, a_j, s_j, R_j, V_j, A_j, S_j, h_0$, and H_0 are all real. h_k and H_k are all complex numbers. i is the imaginary unit. $\mathbf{i}_0 = 1$. $\mathbf{i}_k^2 = -1$, $\mathbf{i}_j^2 = -1$. $j = 0, 1, 2, 3$. $k = 1, 2, 3$.

In the octonion space, $\mathbb{E} = \mathbb{E}_g + \mathbb{E}_e$, the octonion radius vector is $\mathbb{R} = \mathbb{R}_g + k_{eg}\mathbb{R}_e$, the octonion velocity is $\mathbb{V} = \mathbb{V}_g + k_{eg}\mathbb{V}_e$. The octonion field potential is $\mathbb{A} = \mathbb{A}_g + k_{eg}\mathbb{A}_e$, the octonion field strength is $\mathbb{B} = \mathbb{B}_g + k_{eg}\mathbb{B}_e$, with k_{eg} being one coefficient.

The octonion field source \mathbb{S} of the electromagnetic and gravitational fields can be defined as,

$$\mu\mathbb{S} = -(i\mathbb{B}/v_0 + \square)^* \circ \mathbb{B} = \mu_g\mathbb{S}_g + k_{eg}\mu_e\mathbb{S}_e - (i\mathbb{B}/v_0)^* \circ \mathbb{B}, \quad (1)$$

where μ , μ_g , and μ_e are coefficients. $\mu_g < 0$, and $\mu_e > 0$. $*$ denotes the conjugation of octonion. The quaternion operator is $\square = i\mathbf{i}_0\partial_0 + \Sigma\mathbf{i}_k\partial_k$. $\nabla = \Sigma\mathbf{i}_k\partial_k$, $\partial_j = \partial/\partial r_j$. $v_0 = \partial r_0/\partial t$. v_0 is the speed of light, and t is the time. $\mathbb{B} = \square \circ \mathbb{A}$. $\mathbb{B}_g = \square \circ \mathbb{A}_g$, $\mathbb{B}_e = \square \circ \mathbb{A}_e$. The gauge conditions of field potential are chosen as $h_0 = 0$ and $H_0 = 0$. In general, the contribution of the tiny term, $(i\mathbb{B}^* \circ \mathbb{B}/v_0)$, could be neglected in the weak fields.

According to the coefficient k_{eg} and the basis vectors, \mathbb{E}_g and \mathbb{E}_e , the octonion definition of the field source can be separated into two parts,

$$\mu_g\mathbb{S}_g = -\square^* \circ \mathbb{B}_g, \quad (2)$$

$$\mu_e\mathbb{S}_e = -\square^* \circ \mathbb{B}_e, \quad (3)$$

where a comparison with the classical electromagnetic and gravitational theories reveal that, $\mathbb{S}_g = m\nabla_g$, and $\mathbb{S}_e = q\nabla_e$, in the case for single one particle. m is the mass density, while q is the density of electric charge.

3. FIELD EQUATIONS

In the quaternion space \mathbb{E}_g , the definition of gravitational source, Eq. (2), can be expressed as,

$$-\mu_g(is_0 + \mathbf{s}) = (i\partial_0 + \nabla)^* \circ (i\mathbf{g}/v_0 + \mathbf{b}), \quad (4)$$

where $\mu_g = 1/(\varepsilon_g v_0^2)$, and $\varepsilon_g = -1/(4\pi G)$, with G being the gravitational constant. $\mathbf{a} = \Sigma a_k \mathbf{i}_k$, $a_0 = \varphi/v_0$, with φ being the scalar potential of gravitational field. $\mathbb{B}_g = \Sigma h_k \mathbf{i}_k = i\mathbf{g}/v_0 + \mathbf{b}$, when $h_0 = 0$. The gravitational acceleration is, $\mathbf{g}/v_0 = \partial_0 \mathbf{a} + \nabla a_0$. $\mathbf{b} = \nabla \times \mathbf{a}$. $\mathbf{g} = \Sigma g_k \mathbf{i}_k$, $\mathbf{b} = \Sigma b_k \mathbf{i}_k$. $\mathbf{s} = \Sigma s_k \mathbf{i}_k$.

The above can be expanded into the following equations,

$$\nabla^* \cdot \mathbf{b} = 0, \quad (5)$$

$$\partial_0 \mathbf{b} + \nabla^* \times \mathbf{g}/v_0 = 0, \quad (6)$$

$$\nabla^* \cdot \mathbf{g}/v_0 = -\mu_g s_0, \quad (7)$$

$$\nabla^* \times \mathbf{b} - \partial_0 \mathbf{g}/v_0 = -\mu_g \mathbf{s}. \quad (8)$$

Therefore Eqs. (5)–(8) are the gravitational field equations. Because the gravitational constant G is weak and the velocity ratio \mathbf{v}/v_0 is tiny, the gravity produced by the linear momentum \mathbf{s} can be ignored in general. When $\mathbf{b} = 0$ and $\mathbf{a} = 0$, Eq. (7) can be degenerated into the Newton's law of universal gravitation in the classical gravitational theory.

In the S -quaternion space \mathbb{E}_e , the definition of electromagnetic source, Eq. (3), is written as,

$$-\mu_e(i\mathbf{S}_0 + \mathbf{S}) = (i\partial_0 + \nabla)^* \circ (i\mathbf{E}/v_0 + \mathbf{B}), \quad (9)$$

where the electromagnetic coefficient is $\mu_e = 1/(\varepsilon_e v_0^2)$, with ε_e being the permittivity. $\mathbf{A} = \Sigma A_k \mathbf{i}_k$. $\mathbf{A}_0 = A_0 \mathbf{I}_0$, $A_0 = \phi/v_0$, with ϕ being the scalar potential of electromagnetic field. $\mathbb{B}_e = i\mathbf{E}/v_0 + \mathbf{B}$, when $H_0 = 0$. The electric field intensity is, $\mathbf{E}/v_0 = \partial_0 \mathbf{A} + \nabla \circ \mathbf{A}_0$, and the magnetic flux density is, $\mathbf{B} = \nabla \times \mathbf{A}$. $\mathbf{E} = \Sigma E_k \mathbf{i}_k$, $\mathbf{B} = \Sigma B_k \mathbf{i}_k$. $\mathbf{S}_0 = S_0 \mathbf{I}_0$. $\mathbf{S} = \Sigma S_k \mathbf{i}_k$.

The above can be expanded into the following electromagnetic field equations,

$$\nabla^* \cdot \mathbf{B} = 0, \quad (10)$$

$$\partial_0 \mathbf{B} + \nabla^* \times \mathbf{E}/v_0 = 0, \quad (11)$$

$$\nabla^* \cdot \mathbf{E}/v_0 = -\mu_e S_0, \quad (12)$$

$$\nabla^* \times \mathbf{B} - \partial_0 \mathbf{E}/v_0 = -\mu_e \mathbf{S}, \quad (13)$$

where there may be, $\nabla_e = \nabla_g \circ \mathbf{I}(\mathbf{I}_j)$, for the charged particles. And the unit $\mathbf{I}(\mathbf{I}_j)$ is one function of \mathbf{I}_j , with $\mathbf{I}(\mathbf{I}_j)^* \circ \mathbf{I}(\mathbf{I}_j) = 1$.

On the analogy of the coordinate definition of complex coordinate system, one can define the coordinate of octonion, which involves the quaternion and S -quaternion simultaneously. In the octonion coordinate system, the octonion physics quantity can be defined as $\{(ic_0 + id_0 \mathbf{I}_0) \circ \mathbf{i}_0 + \Sigma(c_k + d_k \mathbf{I}_0^*) \circ \mathbf{i}_k\}$. It means that there are the quaternion coordinate c_k and the S -quaternion coordinate $d_k \mathbf{I}_0^*$ for the basis vector \mathbf{i}_k , while the quaternion coordinate c_0 and the S -quaternion coordinate $d_0 \mathbf{I}_0$ for the basis vector \mathbf{i}_0 . Herein c_i and d_i are all real.

Table 1: The multiplication of the operator and octonion physics quantity.

definition	expression meaning
$\nabla \cdot \mathbf{a}$	$-(\partial_1 a_1 + \partial_2 a_2 + \partial_3 a_3)$
$\nabla \times \mathbf{a}$	$\mathbf{i}_1(\partial_2 a_3 - \partial_3 a_2) + \mathbf{i}_2(\partial_3 a_1 - \partial_1 a_3) + \mathbf{i}_3(\partial_1 a_2 - \partial_2 a_1)$
∇a_0	$\mathbf{i}_1 \partial_1 a_0 + \mathbf{i}_2 \partial_2 a_0 + \mathbf{i}_3 \partial_3 a_0$
$\partial_0 \mathbf{a}$	$\mathbf{i}_1 \partial_0 a_1 + \mathbf{i}_2 \partial_0 a_2 + \mathbf{i}_3 \partial_0 a_3$
$\nabla \cdot \mathbf{A}$	$-(\partial_1 A_1 + \partial_2 A_2 + \partial_3 A_3) \mathbf{I}_0$
$\nabla \times \mathbf{A}$	$-\mathbf{I}_1(\partial_2 A_3 - \partial_3 A_2) - \mathbf{I}_2(\partial_3 A_1 - \partial_1 A_3) - \mathbf{I}_3(\partial_1 A_2 - \partial_2 A_1)$
$\nabla \circ \mathbf{A}_0$	$\mathbf{I}_1 \partial_1 A_0 + \mathbf{I}_2 \partial_2 A_0 + \mathbf{I}_3 \partial_3 A_0$
$\partial_0 \mathbf{A}$	$\mathbf{I}_1 \partial_0 A_1 + \mathbf{I}_2 \partial_0 A_2 + \mathbf{I}_3 \partial_0 A_3$

4. WAVE EQUATION

4.1. Gravitational Wave Equation

In the quaternion space \mathbb{E}_g , for the gravitational wave with the angular frequency ω , the gravitational strength should be a harmonic function with respect to the time, and can be chosen as the function, $\cos(\omega t)$. In order to operate handily and cover more physics contents, it is convenient to adopt the complex vector to represent the gravitational strength,

$$\mathbf{b}(\mathbf{r}, \omega t) = \mathbf{b}(\mathbf{r}) \exp(-i\omega t), \quad \mathbf{g}(\mathbf{r}, \omega t) = \mathbf{g}(\mathbf{r}) \exp(-i\omega t), \quad (14)$$

where $\mathbf{r} = \sum r_k \mathbf{i}_k$.

For one angular frequency ω , substituting the above in the gravitational field equations in the vacuum. Deleting the time factor, $\exp(-i\omega t)$, due to the uniform transmission medium, one obtains the following equations,

$$\nabla \cdot \mathbf{b}(\mathbf{r}) = 0, \quad (15)$$

$$(-i\omega)\mathbf{b}(\mathbf{r}) + \nabla^* \times \mathbf{g}(\mathbf{r}) = 0, \quad (16)$$

$$\nabla \cdot \mathbf{g}(\mathbf{r}) = 0, \quad (17)$$

$$\nabla^* \times \mathbf{b}(\mathbf{r}) + (i\omega)\mathbf{g}(\mathbf{r})/v_0^2 = 0. \quad (18)$$

Combining with the above, the cross product of the operator ∇ with Eq. (16) yields,

$$(\omega/v_0)^2 \mathbf{g}(\mathbf{r}) - \nabla^2 \mathbf{g}(\mathbf{r}) = 0, \quad (19)$$

where $\nabla \times (\nabla \times \mathbf{g}(\mathbf{r})) = -\nabla(\nabla \cdot \mathbf{g}(\mathbf{r})) + \nabla^2 \mathbf{g}(\mathbf{r})$, and $\nabla^2 \mathbf{g}(\mathbf{r}) = -\sum \partial_k^2 \mathbf{g}(\mathbf{r})$.

Similarly the output of the curl operation of Eq. (18) produces,

$$(\omega/v_0)^2 \mathbf{b}(\mathbf{r}) - \nabla^2 \mathbf{b}(\mathbf{r}) = 0. \quad (20)$$

Equations (19) and (20) constitute the Helmholtz equations for the gravitational wave. Obviously their solutions are,

$$\mathbf{b}(\mathbf{r}) = \mathbf{b}_0 \exp(-i\mathbf{k} \cdot \mathbf{r}), \quad \mathbf{g}(\mathbf{r}) = \mathbf{g}_0 \exp(-i\mathbf{k} \cdot \mathbf{r}), \quad (21)$$

where \mathbf{b}_0 and \mathbf{g}_0 both are the constant vectors, which are independent to the coordinate and the time. The wave vector is, $\mathbf{k} = \sum k_k \mathbf{i}_k$.

Therefore the two parts, $\mathbf{g}(\mathbf{r}, \omega t)$ and $\mathbf{b}(\mathbf{r}, \omega t)$, of the gravitational wave can be written as,

$$\mathbf{b}(\mathbf{r}, \omega t) = \mathbf{b}_0 \exp(-i\mathbf{k} \cdot \mathbf{r} - i\omega t), \quad \mathbf{g}(\mathbf{r}, \omega t) = \mathbf{g}_0 \exp(-i\mathbf{k} \cdot \mathbf{r} - i\omega t), \quad (22)$$

where only the scalar part of gravitational wave is measurable in the experiment.

Further Eq. (15) and Eq. (17) deduce,

$$\mathbf{k} \cdot \mathbf{b}_0 = 0, \quad \mathbf{k} \cdot \mathbf{g}_0 = 0, \quad (23)$$

meanwhile Eq. (16) and Eq. (18) yield,

$$\mathbf{b}_0 = (1/\omega)\mathbf{k} \times \mathbf{g}_0, \quad \mathbf{g}_0 = -(v_0^2/\omega)\mathbf{k} \times \mathbf{b}_0. \quad (24)$$

The above means that the vibration direction of the gravitational wave is perpendicular to the direction of wave propagation. And the gravitational wave is the transverse wave in a vacuum. Meanwhile these three vectors, \mathbf{b}_0 , \mathbf{g}_0 , and \mathbf{k} , are perpendicular to each other, and obey the Right-handed screw rule.

On the analogy of the classical electromagnetic theory, the paper will introduce the concept of 'refractive index-like' among different transmission media for the gravitational waves. Making use of the concept of 'refractive index-like', it is able to deduce further some wave features from the above, including the 'Reflection law', 'Refraction law', 'Fresnel law', and 'Total reflection' etc for the gravitational waves.

4.2. Electromagnetic Wave Equation

In the S -quaternion space \mathbb{E}_e , for the electromagnetic wave with the angular frequency ω , the electromagnetic strength should be a harmonic function with respect to the time, and can be chosen as the function, $\cos(\omega t)$. In order to operate handily and cover more physics contents, it is convenient to adopt the complex vector to represent the electromagnetic strength,

$$\mathbf{B}(\mathbf{r}, \omega t) = \mathbf{B}(\mathbf{r}) \exp(-i\omega t), \quad \mathbf{E}(\mathbf{r}, \omega t) = \mathbf{E}(\mathbf{r}) \exp(-i\omega t). \quad (25)$$

For one angular frequency ω , substituting the above in the electromagnetic field equations in the vacuum. Deleting the time factor, $\exp(-i\omega t)$, due to the uniform transmission medium, one obtains the following equations,

$$\nabla \cdot \mathbf{B}(\mathbf{r}) = 0, \quad (26)$$

$$(-i\omega)\mathbf{B}(\mathbf{r}) + \nabla^* \times \mathbf{E}(\mathbf{r}) = 0, \quad (27)$$

$$\nabla \cdot \mathbf{E}(\mathbf{r}) = 0, \quad (28)$$

$$\nabla^* \times \mathbf{B}(\mathbf{r}) + (i\omega)\mathbf{E}(\mathbf{r})/v_0^2 = 0. \quad (29)$$

Combining with the above, the cross product of the operator ∇ with Eq. (27) yields,

$$(\omega/v_0)^2 \mathbf{E}(\mathbf{r}) - \nabla^2 \mathbf{E}(\mathbf{r}) = 0, \quad (30)$$

where $\nabla \times (\nabla \times \mathbf{E}(\mathbf{r})) = -\nabla(\nabla \cdot \mathbf{E}(\mathbf{r})) + \nabla^2 \mathbf{E}(\mathbf{r})$, and $\nabla^2 \mathbf{E}(\mathbf{r}) = -\Sigma \partial_k^2 \mathbf{E}(\mathbf{r})$.

Similarly the output of the curl operation of Eq. (29) produces,

$$(\omega/v_0)^2 \mathbf{B}(\mathbf{r}) - \nabla^2 \mathbf{B}(\mathbf{r}) = 0. \quad (31)$$

Equations (30) and (31) constitute the Helmholtz equations for the electromagnetic wave. Obviously their solutions are,

$$\mathbf{B}(\mathbf{r}) = \mathbf{B}_0 \exp(-i\mathbf{k} \cdot \mathbf{r}), \quad \mathbf{E}(\mathbf{r}) = \mathbf{E}_0 \exp(-i\mathbf{k} \cdot \mathbf{r}), \quad (32)$$

where \mathbf{B}_0 and \mathbf{E}_0 both are the constant vectors.

Therefore the magnetic field component $\mathbf{B}(\mathbf{r}, \omega t)$ and the electric field component $\mathbf{E}(\mathbf{r}, \omega t)$ of the electromagnetic wave can be written as,

$$\mathbf{B}(\mathbf{r}, \omega t) = \mathbf{B}_0 \exp(-i\mathbf{k} \cdot \mathbf{r} - i\omega t), \quad \mathbf{E}(\mathbf{r}, \omega t) = \mathbf{E}_0 \exp(-i\mathbf{k} \cdot \mathbf{r} - i\omega t), \quad (33)$$

where only the scalar part of electromagnetic wave is measurable in the experiment.

Further Eq. (26) and Eq. (28) deduce,

$$\mathbf{k} \cdot \mathbf{B}_0 = 0, \quad \mathbf{k} \cdot \mathbf{E}_0 = 0, \quad (34)$$

meanwhile Eq. (27) and Eq. (29) yield,

$$\mathbf{B}_0 = (1/\omega)\mathbf{k} \times \mathbf{E}_0, \quad \mathbf{E}_0 = -(v_0^2/\omega)\mathbf{k} \times \mathbf{B}_0. \quad (35)$$

The above means that the vibration direction of the electromagnetic wave is perpendicular to the direction of wave propagation. And the electromagnetic wave is the transverse wave in a vacuum. Meanwhile these three vectors, \mathbf{B}_0 , \mathbf{E}_0 , and \mathbf{k} , are perpendicular to each other, and obey the Right-handed screw rule.

Similar to the classical electromagnetic theory, by means of the concept of refractive index, it is able to deduce further some wave features from the above, including the Reflection law, Refraction law, Fresnel law, and Total reflection etc for the electromagnetic waves.

5. CONCLUSIONS

In the complex quaternion space, it is able to describe the field equations and wave equations in the gravitational field. Making use of the concept of ‘refractive index-like’, it is capable of inferring the ‘Reflection law’, ‘Refraction law’, ‘Fresnel law’, and ‘Total reflection’ etc among different transmission media for the gravitational waves. In the vacuum, the gravitational wave is the transverse wave. The wave vector is perpendicular to each one of two orthogonal components of gravitational wave. And they satisfy the Right-handed screw rule.

In the complex S -quaternion space, the paper can represent the Maxwell’s equations and Helmholtz equations in the electromagnetic field. These equations are respectively identical with that in the classical electromagnetic theory described with the vector terminology. One can conclude the above inferences, expressing corresponding equations into the scalar equations, and then comparing them. By means of the concept of refractive index, it is able to deduce the Reflection law, Refraction law, Fresnel law, and Total reflection etc among different transmission media for the electromagnetic waves.

It should be noted that the paper discussed only some simple features of electromagnetic and gravitational waves described with the complex octonion. But it is clear to show that the application of the complex quaternion can describe the wave feature of gravitational field, while the introduction of the complex S -quaternion can depict the wave feature of electromagnetic field. And these researches set the foundation for the further study about the wave feature. In the following study, it is going to apply the complex octonion to represent the propagation characteristics of electromagnetic and gravitational waves inside the transmission medium.

ACKNOWLEDGMENT

This project was supported partially by the National Natural Science Foundation of China under grant number 60677039.

REFERENCES

1. Honig, W. M., “Quaternionic electromagnetic wave equation and a dual charge-filled space,” *Lettere al Nuovo Cimento*, Vol. 19, No. 4, 137–140, 1977.
2. Negi, O. P. S. and B. S. Rajput, “Quaternionic formulation for electromagnetic-field equations,” *Lettere al Nuovo Cimento*, Vol. 37, No. 9, 325–329, 1983.
3. Rawat, A. S. and O. P. S. Negi, “Quaternion Gravi-Electromagnetism,” *International Journal of Theoretical Physics*, Vol. 51, No. 3, 738–745, 2012.

Methods for the Sensing and Evaluation of Ionosphere Changes and Their Impact on the Human Organism

M. Hanzelka¹, J. Dan², P. Fiala¹, M. Friedl¹, and Vladan Holcner³

¹Department of Theoretical and Experimental Electrical Engineering
Brno University of Technology, Technická 3082/12, Brno 616 00, Czech Republic

²Rector's Office, Personnel Management Office, Masaryk University
Žerotínovonám, 9, Brno 601 77, Czech Republic

³Faculty of Economics and Management, University of Defence
Kounicova 65, Brno 662 10, Czech Republic

Abstract— The impact of the environment upon living organisms constitutes a crucial problem examined by today's science. In this context, research institutes worldwide have analysed diverse positive and negative factors affecting the biological system of the human body. One such factor consists in the influence of the surrounding electromagnetic field. This paper presents the results of an investigation focused on ionosphere parameter changes and their impact on the basic function of the nervous system. It is a well-known fact that the frequency of the alpha waves of brain activity [1] ranges within 6–8 Hz. Changes in the electromagnetic and chemical structure of the Earth's surface may cause variation of signals in the above-defined frequency region of 6–8 Hz. Detailed examination of the overall impact of environmental factors upon the human organism is performed within a large number of medical disciplines. The research presented in this paper is concentrated on the sensing and detection of changes in the region of very low frequencies of the electromagnetic field; the authors use both theoretical and experimental procedures to define the effects that influence brain activity.

1. INTRODUCTION

The low-level measurement of low frequencies (0.01–10 Hz) performed to evaluate the effect of magnetic fields on the human organism can be regarded as an interdisciplinary branch of science that embraces different types of research.

The set of provinces subsumed within the discussed subject comprises elementary research disciplines such as particle physics, geophysics, astrophysics, and metrology, which are all related to the investigation of the ionosphere and magnetosphere. Moreover, medical fields and problems, for example neurology and circadian rhythms, are also included in the scope of contributing elements. By further extension, the low-level measurements are interesting from the perspectives of theoretical electrical engineering and research of magnetic fields.

At this point, it is important to consider applied research disciplines, for example the measurement and radar technology in the following ranges: the ULF (Ultra Low Frequency Band: 300 Hz–3 kHz), SLF (Super Low Frequency Band: 30 Hz–300 Hz), and ELF (Extreme Low Frequency Band: 0.1 Hz–30 Hz). The group of auxiliary subjects or activities includes mathematical modelling of electromagnetic effects, the basics of biomedical research and biological feedback, and the influence of low-level magnetic fields on the human organism. The role of the above-mentioned disciplines is complemented by the fact that human beings do not exist as solitary entities but rather live in a wider community, which is influenced by each of its members. If the external magnetic fields influenced a human being to such an extent that the man or woman would change their behaviour within the social community at a higher level of statistical significance, it would be necessary to employ various questions of economics, mainly the evolution of economic value as a market phenomenon based on human behaviour and decision-making. Scientists and researchers are currently preparing to solve special tasks related to the objectivisation of the impact of low-level magnetic fields upon the human organism; such impact will be examined from the perspective of physical harm to cells [2] and mental condition of humans [3–6]. The current status of knowledge in this field is relatively unsatisfactory, and certain hasty conclusions have been made and found application even in hygienic standards. An example of such standards is the guideline issued by the Council of Europe and implemented by the ICNIRP (International Commission on Non-Ionising Radiation Protection) in 1999 to establish the boundary values of magnetic flux in relation to the speed of magnetic field changes for very slowly changing currents. More concretely, this guideline introduces the value of 50 mT/s as the maximum magnetic flux change acceptable in an environment with a

variable magnetic field at the frequency of 1 Hz and characterised by permanent presence of humans. This value is many millions higher than the largest changes hitherto measured during the processes referred to as magnetic storms, in which the Earth was exposed to charged particles from the Sun.

2. ORIENTATION OF THE METHODS FOR DETECTING IONOSPHERE DISTURBANCES

According to the conclusions of secondary research, there is mutual interaction between low-level electric or magnetic fields irradiated both by humans and the geomagnetic system of the Earth. However, this interaction can be scientifically validated only with difficulty [4, 7]. Some of the reasons for this situation may be inadequate cohesion between the complex description of a human being, his/her biological feedback related to the internal and external electromagnetic fields, the scope of interdisciplinary scientific knowledge, and the complicated structure of devices designed for the measurement of low-level ULF, SLF, ELF of electric, magnetic, and electromagnetic fields [8]. This paper presents a portion of the research conducted in this province by the DTEEE, FEEC BUT; the research is built upon the current knowledge of low-level magnetic fields generated by the geomagnetic system of the Earth and the solar system. The authors of this article have focused their attention on examining the effect of the changes in the Earth's geomagnetic system that are due to solar activity. In this context, the research was also centered on proving the existence of the effect as a result of geomagnetic storms, which substantially influence low-level magnetic fields affecting the human organism, including its behavioural patterns and decisioning.

The detection of changes in geomagnetic field disturbances could be performed by means of the Schumann resonances. Until recently, this oscillation was at the frequency of $f_{sch} = 7.83$ Hz; this frequency changes as a result of the impact exerted by phenomena such as solar wind or greenhouse gases. In 1953, Professor W. O. Schumann of Munich university, Germany, had found out that the cavity between the ionosphere and the Earth's surface could be interpreted as a spherical resonator. After Schumann's results were published in the *Technische Physik* journal, Dr. Ankermueller, a medical specialist, immediately related the resonances to brain wave rhythm (EEG). In 1954, the measurements conducted by W. O. Schumann and Herbert Koenig, who was to become Schumann's successor, confirmed the pulsation of the Earth at the frequency of $f = 7.83$ Hz. Koenig then validated the correlation between the Schumann resonances and brain wave rhythms [12].

3. RESEARCH OF GEOMAGNETIC EFFECTS

In polar areas, the solar wind particles captured by the Earth's magnetic field travel along the lines of force to the upper layers of the atmosphere. Here, together with the ultraviolet radiation from the Sun, they excite and ionise neutral atoms. The excited atoms emit a distinctive glow, thus creating the well-known polar aurora. The ionised atoms are captured by magnetic lines of force and travel along them freely. But these are all merely traditional facts.

Ionosphere changes can be objectively measured using already known methods [Fiala, Hanzelka — PIERS2013], Fig. 1. Based on earlier observations, it is possible to demonstrate via secondary research that a connection exists between magnetic field changes and the social behaviour of groups of humans.

The effect of the environment on the human physical, emotional, mental and spiritual coherence was described by Rollin McCraty, who also proposed a link between these factors and the cardiovascular system, with its resonant frequency of 0.1 Hz (the ELF band between 0.04 and 0.26 Hz, given the condition of cardiac coherence) [16] (R. McCraty, 2011). According to Alexander Tchijevsky, 80% of the most significant events in human history occurred within the approximately five years of the maximum solar activity; this assumption is represented by the related diagram (1750–1922) [17] (A. Tchijevsky, 1971).

As further discussed below, changes in the environment can exert significant influence on the quality of decision-making, responses, and reaction times in humans. Variations (even insignificant) in geomagnetic fields are among the factors that, although generally underestimated, have the potential to change the behaviour of individuals and groups of humans. This applies to all areas of human activity, including transportation, international trade, and also the military, where the decisions and behaviour of individuals or small groups might bring major consequences of strategic character.

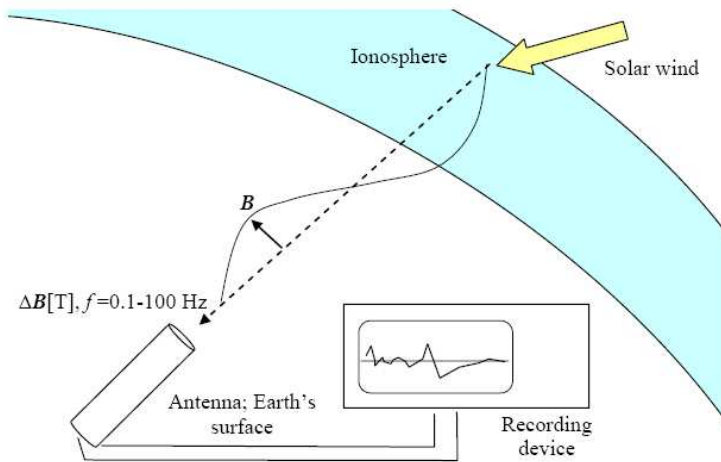


Figure 1: Schematic arrangement of the problem of detecting the changes in the Earth's ionosphere.

However, no research has been carried out thus far on a selected (homogeneous) group of humans to demonstrate the long-term effect of changes in the Earth's magnetic field and to eliminate the underlying influence of other aspects. Thus, within the preparatory stages of the investigation described in this paper, such a test group was formed in close collaboration with University of Defence in Brno, and its purpose is to facilitate the measurement and examination of psychophysiological effects exerted by geomagnetic fields upon military officers and personnel.

4. DESIGN OF THE EXPERIMENTAL MEASUREMENT

The measurement of low-level magnetic and electromagnetic signals in the ULF, SLF, and ELF bands is a unique scientific discipline. The ULF, SLF, and ELF waves exhibit wavelengths of thousands of kilometers. Generally, wavelength is expressed as $\lambda = v/f$, with units of [m; m/s, Hz], where v is the speed of the wave propagation in space, λ the length of the wave, and f its frequency. For an electromagnetic wave, v is the mean speed of light in vacuum.

In order to ensure the required sensitivity and operation in the ULF, SLF and ELF frequency bands, it is suitable to use a ferrite antenna, whose dimensions are significantly smaller than the wavelength of the incident electromagnetic wave. In such antennas, the phase φ_E of the electric field intensity E is practically identical at every point of the device, even when the incident electromagnetic wave is not planar. The directional characteristics of such antennas can be measured in the near electromagnetic field. Fig. 1 shows the experiment focused on the application of a ferrite antenna for the detection of changes in the Earth's ionosphere, its numerical model, and results otherwise introduced in Reference [15], Fig. 3.

The planned experimental research will be performed on a sample group of participants (men and women of approximately the same age), and it will consist in non-invasive physiological measurement of the human organism; this measurement process is conceived to include psychological methods sensitive to the mental changes in progress at the time of sensing.

In general terms, psychophysiological research is most often focused on factors that influence the activity of the autonomous nervous system; these factors include also parameters such as perspiration, skin temperature, pulse frequency changes, blood pressure variation, and alimentary tract contractions. In the given context, the orientation of these aspects to the central nervous system will be considered too [18] (A. Uherik, 1978).

The aim of the proposed experimental investigation consists in searching for relationships between characteristics of the ionosphere on the one hand and the examined psychophysiological or mental factors on the other. Regular connections will be sought between solar activity as a source of geomagnetic field disturbances and the variability of psychophysiological and mental characteristics.

With respect to physiological parameters, the processes to be measured involve skin impedance, muscle contraction, diaphragmatic and thoracic breathing intensity, ECG LO and HI frequencies, the perfusion of peripheral vessels, and EEG waves. The applied sensing apparatus will be Flex-Comp Infiniti, a device for physiological monitoring, bio-feedback, and the collection of psychophysiological data. The results obtained from the measurement of the physiological characteristics of

the human organism are invariably influenced by the momentary mental state of the collaborating individual, i.e., by the level of the person's positive or negative mental condition affected by life events, the environment, emotional stimuli, lunar cycles, and other aspects.

Primarily, the investigation is based on measurement models that describe the relationships between various external influences (which, in our case, are represented mainly by solar activity) and the level of physiological functions [22] G. Stemmler, 2001, p. 7.

A significant problem of the research is the identification of such physiological variables whose level variations exhibit a close relation to ionosphere changes. Secondly, we will look for the relationship between the variability of physiological characteristics and the current degree of resistance to stress; these indicators can be classified as either objectively evaluated or subjectively experienced within the binary dimension of mental stress — relaxation. In the model, psychophysiological constructs then constitute the link/bridge/between solar activity and the concrete manner of human reactions and decision-making under stress (regarding, for example, life endangering situations or the handling of principal financial problems).

The diagnostics of the current mental state can be performed using methods whose ability to determine such state has been reliably proven (which means that, in the very least, the content and predictive validities are: a) sensitive to changes within the stipulated period of days; b) relatively resistant to the effect of repeated measurement; c) used for the given purposes. Furthermore, we will utilise the ASS-SYM technique by Günter Krampen, which is defined in the paper *ASS-SYM — Änderungssensitive Symptomliste zu Entspannungserleben, Wohlbefinden, Beschwerden- und Problembelastungen*. This method is suitable for the assessment of subjective experience. To evaluate the current level of resistance to stress and the disruption of mental balance, we will make use of *Lüscher Diagnostik*, the non-verbal testing tool by Max Lüscher.

We expect to find the relationship between the variability of solar processes and the variability of the level of psychophysiological parameters. Analogously to the existing knowledge related to the effects of the environment on the level of psychophysiological characteristics, it will be possible to define the different degrees of closeness in the relationship between solar activity and the individual psychophysiological characteristics. It is assumed that the relationships between solar activity and the current subjective/objective stress resistance will be discovered.

Simultaneously with the experimental investigation of the given problem, we will pursue secondary research based on analysing the data obtained from the monitoring of solar activity throughout history [17] (A. Tchijevsky, 1971). Moreover, correlation will be sought between these historical data and socioeconomic indicators of human behaviour and decision-making, and special emphasis will be put in this context on indicators that expose the mental factor as a significant element of the decision-making process.

Historically, the formation of geomagnetic storms has been daily monitored by the Royal Observatory, Greenwich since May 1874. In 1976, the continuous measurement began to be carried out by the Solar Optical Observing Network (SOON) under support from the US National Oceanic and Atmospheric Administration (NOAA).

In addition to these facts, it is also interesting to review in the given connection the development of capital markets during recent centuries, which has been recorded via specialised indexes (such as the Dow Jones established in 1896); notably, detailed comparison of the data comprised in these indicators with registered changes of the environment could further highlight the fact that capital markets are markedly sensitive to variations in the decision-making process resulting from environmental effects.

5. CONCLUSION

The outcome of the research will be compared with the hypotheses and results already published internationally; the main aim is to demonstrably measure the differences between instantaneous condition of the Earth's ionosphere as monitored at various locations of the planet.

The prepared experiments and measurement prove the influence of the above-mentioned aspects on the human emotional system, thus pointing to the hitherto applied boundary values of magnetic flux density B in relation to the alterations of the magnetic field for very slowly changing electric currents. The experiments also highlight the impact these currents might have on human beings permanently present in such environment.

The measured dependencies will be processed mathematically and graphically and published within a specialised paper at a later time. Similarly, we will interpret and release the results obtained

from the surveys and psychological tests, which will be used as instruments to simultaneously measure and eliminate the external influences that affect the human psychophysiological structure.

ACKNOWLEDGMENT

The research described in the paper was financially supported with a grant provided by Czech Science Foundation (GACR 13-09086S), a project of the BUT science fund, No. FEKT-S-11-5/1012, and projects from the Education for Competitiveness Operative Programme (Nos. CZ.1.07.2.3.00.20.0175 and CZ.1.07/2.3.00/30.0005).

REFERENCES

1. Ferris, J., "The brain generates an electric field that influences its own activity," *Scientific American Mind*, Vol. 21, No. 10, 2010, published online: Oct. 28, 2010, doi:10.1038/scientificamericanmind1110-10a.
2. Stuchly, M. S., 2000.
3. Scorretti, R., N. Burais, L. Nicolas, and A. Nicolas, "Modeling of induced current into the human body by low-frequency magnetic field," *IEEE Transactions on Magnetics*, Vol. 41, No. 5, May 2005, Dostpná z: 10.1109/TMAG.2005.846276.
4. Carrubba, S. and A. A. Marino, "The effects of low-frequency environmental-strength electromagnetic fields on brain electrical activity: A critical review of the literature. Electromagnetic biology and medical," Vol. 27, No. 2, 83–101, Department of Orthopaedic Surgery, LSU Health Sciences Center, P. O. Box 33932, Shreveport, LA 71130-3932, United States, 2008.
5. Hashish, A. H., M. A. El-Missiry, H. I. Abdelkader, and R. H. Abou-Saleh, "Assessment of biological changes of continuous whole body exposure to static magnetic field and extremely low frequency electromagnetic fields in mice," Department of Physics, Faculty of Science, University of Mansoura, Mansoura 35516, Egypt Department of Zoology, Faculty of Science, University of Mansoura, Mansoura 35516, available online Feb. 21, 2008, Dostupná z: doi:10.1016/j.ecoenv.2007.10.002.
6. Gobba, F. M., A. Bargellini, M. Scaringi, G. Bravo, and P. Borella, "Extremely low frequency-magnetic fields (ELF-EMF) occupational exposure and natural killer activity in peripheral blood lymphocytes," Modena (MO), Italy Chair of Hygiene, Department of Public Health Sciences, University of Modena and Reggio Emilia, Via Campi 287, 41100, Modena (MO), Italy, 0048-9697/\$ — see front matter ©2008 Elsevier B.V., all rights reserved.
7. Cocco, P. and R. J. Reiter, "Urinary 6-sulfatoxymelatonin excretion in humans during domestic exposure to 50 hertz electromagnetic fields," *Neuroendocrinology Letters*, Vol. 26, No. 2, 136–142, Apr. 2005, ISSN: 0172-780X.
8. Rose, L., "Review and assessment of select US space security technology proposals," Department of Materials Engineering, University of British Columbia, 309-6350 Stores road, Vancouver, British Columbia, Canada v6t 1z4, 0265-9646/\$ — see front matter ©2008 Elsevier Ltd., all rights reserved. Dostupní z: doi:10.1016/j.spacepol.2008.09.007.
9. Cohen. M. B., "Elf/Vlf phased array generation via frequency-matched steering of a continuous hf ionospheric heating beam," Dissertation for the Degree of Doctor of Philosophy, Oct. 2009.
10. www.nasa.gov.
11. Korepanov, V., G. Lizunov, O. Fedorov, Y. U. Yampolsky, and I. Ivchenko, "IONOSAT — Ionospheric satellite cluster," Lviv Centre of Institute of Space Research, Laboratory for EM Investigations, 5-a, Naukova str., Lviv 79000, Ukraine, Received Oct. 31, 2006; received in revised form Feb. 25, 2008; accepted Feb. 27, 2008, Dostupná z: doi:10.1016/j.asr.2008.02.022.
12. Gray, J. A., *The Neuropsychology of Anxiety: An Enquiry into the Functions of the Septo-Hippocampal System*, Oxford Univ. Press, Oxford, U.K., 1982.
13. Agrimson, E., S. Kim, N. Angelo, and R. Merlino, "Effect of parallel velocity shear on the electrostatic ion-cyclotron instability in filamentary current channels," Department of Physics and Astronomy, The University of Iowa, Iowa City, Iowa 52242, Received Mar. 31, 2003; accepted Jul. 31, 2003.
14. Barchanski, A., M. Clemens, H. Gerssem, and T. Weiland, "Efficient calculation of current densities in the human body induced by arbitrarily shaped, low-frequency magnetic field sources," Received May 18, 2005; received in revised form Aug. 10, 2005; accepted Sep. 13, 2005 available online Nov. 11, 2005, Dostupná z: doi:10.1016/j.jcp.2005.09.009.
15. Steinbauer, M., P. Fiala, K. Bartusek, and Z. Szabo, "Experiments with accuracy of air ion field measurement," *PIERS Proceedings*, 1062–1066, Hangzhou, China, Mar. 24–28, 2008.

16. McCraty, R., “Coherence: Bridging personal, social and global health,” Institute of HeartMath, 14700 West Park Ave., Boulder Creek, CA 95006, USA, 2011.
17. Tchijevsky, A., “Physical factors of the historical process,” 1971.
18. Uherík, A., “Psychofyziologické vlastnosti člověka,” Psychodiagnostické a didaktické testy, n.p., Bratislava, 1978.
19. Woodworth, R. and H. Schlosberg, “Experimentálna psychológia,” Vydavateľstvo Slovenskej akadémie vied, Bratislava, 1959.
20. Lüscher, M., *Lüscher Diagnostik*, Color-Test Verlag, Luzern, 2009.
21. Krampen, G., *ASS-SYM. Änderungssensitive Symptomliste zu Entspannungserleben, Wohlbefinden, Beschwerden-und Problembelastungen*, Manual, Hogrefe Verlag, Göttingen, Bern, Wien, Toronto, Seattle, Oxford, Prag, 2006.
22. Stemmler, G., “Grundlagen psychophysiologischer Methodik,” Rösler, Frank (Hrsg.), *Grundlagen und Methoden der Psychophysiologie*, 1, vyd, Göttingen, Bern, Toronto, Seattle, Hogrefe, Verlag für Psychologie, 2001, S. 1-84. Enzyklopädie der Psychologie: Theorie und Forschung, Biologische Psychologie Bd. 4, ISBN 3-8017-0551-X.

Applications of Noise Spectroscopy in the Analysis of Periodic Material Structures

Z. Szabo, P. Drexler, J. Seginak, D. Nešpor,
M. Friedl, P. Marcoň, and P. Fiala

Department of Theoretical and Experimental Electrical Engineering
Brno University of Technology, Technická 12, Brno 616 00, Czech Republic

Abstract— The authors discuss the application of broadband noise signal in the research of periodic structures and present the basic testing related to the described problem. The aim is to find a metrological method utilizable for the investigation of metamaterials in the frequency range between 100 MHz and 10 GHz; this paper therefore characterizes the design of a suitable measuring technique based on noise spectroscopy and introduces the first tests conducted on a periodic structure (metamaterial). In this context, the applied equipment is also shown to complement the underlying analysis.

1. INTRODUCTION

In the comprehensive investigation of material structures for the micro-wave application (tensor and composite character), the properties of materials are studied by means of the classic single-frequency methods, which bring about certain difficulties in the research process [1]. In boundary changes with a size close to the wave-length there can occur wrong information concerning the examined objects [2, 3]. One of the possible ways of suppressing the negative sources of signals consists in the use of wide-band signals such as white noise, and this approach can be further reinforced by analysing the problem of absorption in the examined material. The indicated methods require a source of noise, a receiving and a transmitting antenna, and A/D conversion featuring a large bandwidth; for our purposes, the bandwidth ranged between 50 MHz and 10 GHz. Until recently, it had not been possible to design an A/D converter of the described speed or materialise devices with the above-mentioned bandwidth. Currently, high-end oscilloscopes are available with a sampling frequency of hundreds of Gsa/s.

2. NOISE SOURCE

For UWB systems, several methods enabling the generation of short pulses with large bandwidth have been developed to date, see reference [4]. However, these singly-iterative processes are not applicable for noise spectroscopy; in this respect, there is the need of a continuous noise signal source (ideally one producing white noise) with the given bandwidth.

The type of source referred to is currently being supplied by certain manufacturers operating in the given field. Importantly, for the noise spectroscopy application, we require a comparatively large output power of up to 0 dB/mW; the assumed bandwidth characteristics range up to 10 GHz. Nevertheless, at this point it is appropriate to mention the fundamental problem of finding active devices capable of performing signal amplification at such high frequencies. As a matter of fact, our requirements are thus limited by the current status of technology used in the production of commercially available devices; the highest-ranking solution for the bandwidth of up to 10 GHz can be found only up to the maximum of 0 dB/mW.

Our response to the above-discussed problem consisted in an attempt to produce a noise generator in laboratory conditions because, in principle, this type of generator can be considered as sufficient for testing and basic measurement. In view of the price and availability of noise diodes, we decided to apply thermal noise on electrical resistance as the basic noise source. The specific connection is shown in Fig. 1. The first transistor is in the CC configuration (stage), where we require mainly a high input impedance of the amplifier. The input thermal noise is given by the amplifier's input circuit element parameters. Even though the generator could operate even without a resistor at the transistor input, the unconnected input would cause a substantial deterioration of the connection stability. The second and third transistors form a cascade voltage amplifier in the CE configuration (stage); the output impedance of the third amplifier is 50 Ω .

Figure 1 shows the tested noise generator, whose output power is 0 dBm in the frequency range between 100 kHz and 10 GHz.



Figure 1: The noise generator and power amplifier.

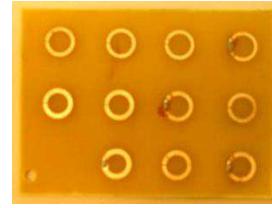


Figure 2: The first tested tuned periodic structure to verify noise spectroscopy measurement.

3. METHOD

The noise spectroscopy laboratory and the measuring instruments are shown in Fig. 3. In order to find the desired environment, we carried out several experiments in various shielded and anechoic chambers (Fig. 7). After the use of an ideal white noise (Fig. 4), a number of wideband antennas (Fig. 7), and an anechoic chamber, it became obvious that a closed, unshielded room without significant anechoic effect, Fig. 3, is fully satisfactory for the needs of noise spectroscopy. The research technique using UWB signal was tested as follows: The case to hold the examined sample (Figs. 2 and 3(c)) contained two suitably set and fixed UWB antennas, Fig. 3(b)). The first of these antennas was supplied from the noise generator and power amplifier (Fig. 1, Fig. 5), while the second one sensed the signal from both the noise generator and the adjacent electromagnetic sources; the signal spectrum was recorded iteratively. The initial stage involved repeated transmission and sensing of both the signal provided by the noise generator and the external signals. The repetition

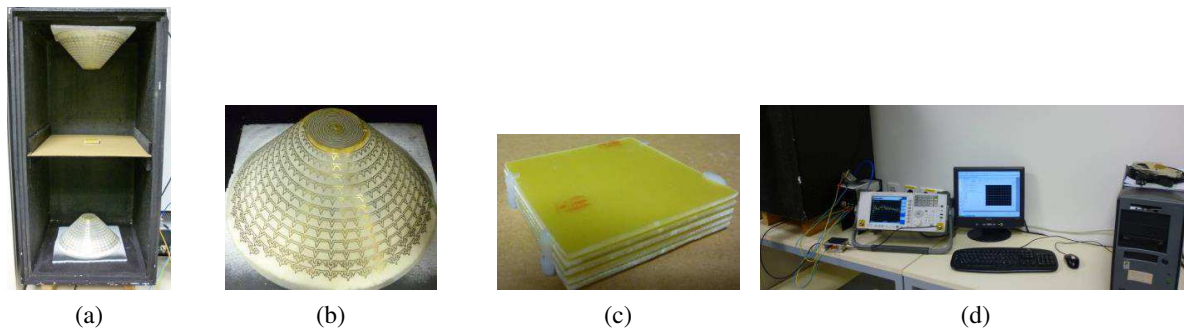


Figure 3: The measuring equipment and instruments: (a) antenna chamber; (b) antenna; (c) layered sample; (d) noise spectroscopy evaluation laboratory.

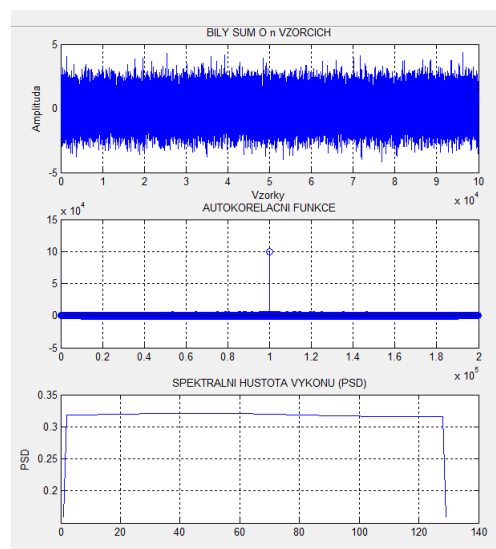


Figure 4: The spectrum of N white noise signal acquisitions.

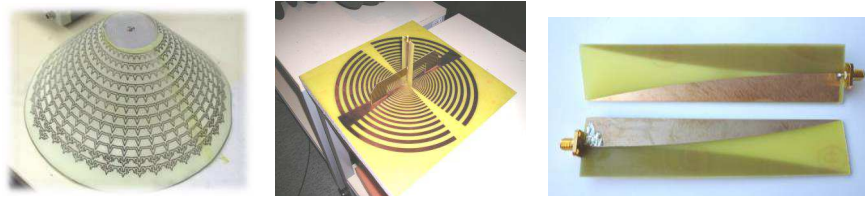


Figure 5: The tested wideband antennas.

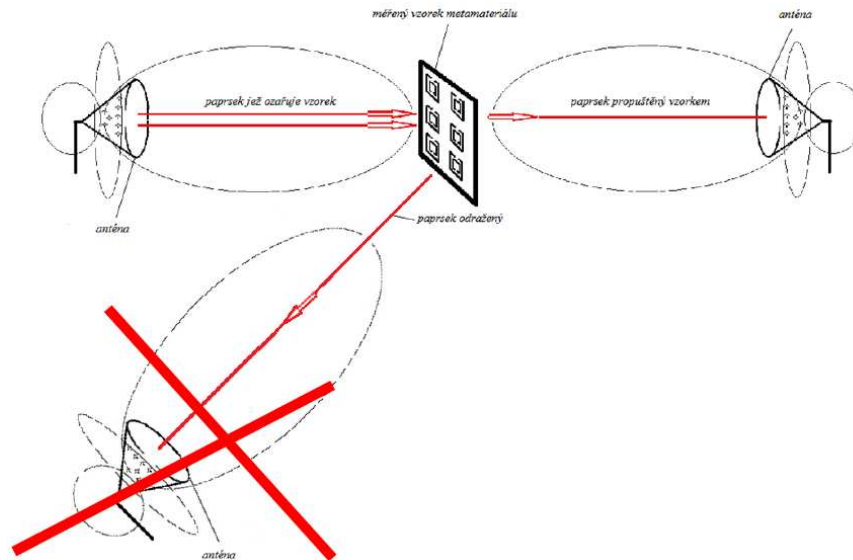


Figure 6: The irradiation of the measured sample, and signal sensing.

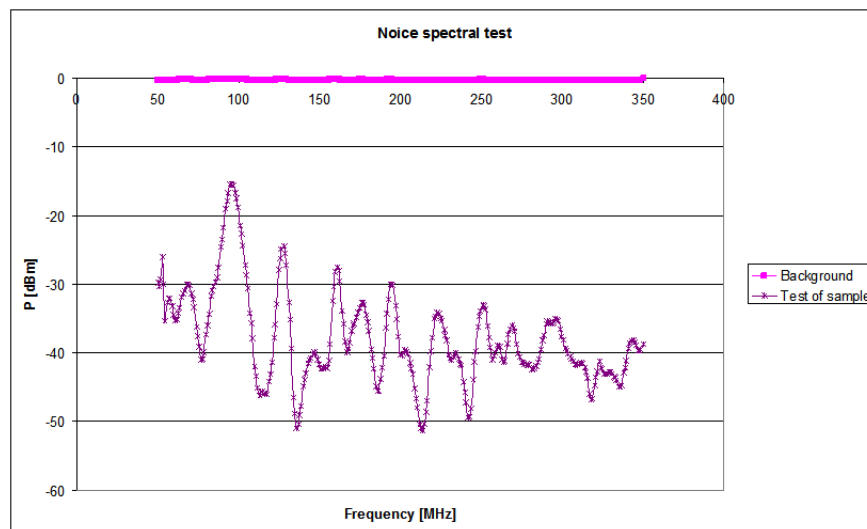


Figure 7: The waveform and spectrum of the noise generator output for the measured sample, $f = 50\text{--}350$ MHz.

was carried out for each sampled frequency, and the incident power spectrum was summed. Thus, we obtained the frequency dependence of the transmitted energy distribution. Generally, if the transmitter/receiver set is not located in a room with a defined spectral absorbance, we can expect uniform energy distribution within the whole frequency range. This record is, at its end, transformed to the frequency dependence of the specific power. In the described manner, we acquired the characteristics of the spectrum measurement background. At this point, the examined sample was placed in the support case; the sample for such application can be layered or periodic, and

it is expected to provide the assumed frequency characteristic (Figs. 2 and 3(c)). Subsequently, repeated measurement was performed observing the above-outlined procedure. In the case of a markedly frequency-dependent background, the obtained characteristic can be corrected. Fig. 7 show the frequency dependencies of the measurement setup and the multi-layer material.

4. CONCLUSION

The research paper provides an elementary overview and description of the laboratory equipment for the realization of noise spectroscopy measurement and the related experiments. Noise spectroscopy within the frequency band of between 10 MHz and 10 GHz is realizable using the currently available technologies.

The initial noise spectroscopy testing was carried out in a shielded Faraday room converted to an anechoic chamber, and the later research was confined to the laboratory shown in Fig. 3. The noise source comprised a generator (NC1108A) and an amplifier (NC1128A). The set of tested wideband antennas included conical fractal, Vivaldi, spiral, conical, and periodic dipole devices. The conical fractal antenna proved especially useful for the given purpose.

The problem of the sensitivity and accuracy of the measurement method was solved via repeated measurement and application of the stochastic model principles.

ACKNOWLEDGMENT

The research described in the paper was financially supported by Czech Science Foundation (GA 13-09086S), a project of the BUT science fund, No. FEKT-S-14-2545/2014, and a project from the Education for Competitiveness Operative Programme, No. CZ.1.07.2.3.00.20.0175 (Electro-researcher).

REFERENCES

1. Maslovski, S., S. Tretyakov, and P. Alitalo, "Near-field enhancement and imaging in double planar polariton-resonant structures," *J. Appl. Phys.*, Vol. 96, 1293, 2004.
2. Freire, M. and R. Marques, "Near-field imaging in the megahertz range by strongly coupled magnetoinductive surfaces: Experiment and ab initio analysis," *J. Appl. Phys.*, Vol. 100, 063105, 2006.
3. Machac, J., P. Protiva, and J. Zehentner, "Isotropic epsilon-negative particles," *2007 IEEE MTT-S Int. Microwave Symp. Dig.*, TH4D-03, Honolulu, USA, Jun. 2007.
4. Protiva, P., J. Mrkvica, and J. Macháč, "Universal generator of ultra-wideband pulses," *Radioengineering*, Vol. 17, No. 4, 74–79, 2008.
5. Oppenheim, A. V., R. W. Schaffer, and J. R. Buck, "Discrete-time signal processing," *Upper Saddle River*, Prentice Hall, N.J., ISBN 0-13-754920-2, 1999.
6. Brigham, E. O., *The Fast Fourier Transform*, Prentice-Hall, New York, 2002.
7. Addison, P. S., *The Illustrated Wavelet Transform Handbook*, 400, Institute of Physics Publishing, Bristol, 2002.
8. Bell, B. M. and D. B. Percival, "A two step Burg algorithm," *IEEE Transactions on Signal Processing*, Vol. 39, No. 1, 1991.

A Tunable Microwave Absorber Based on Active Frequency Selective Surface

Kainan Qi^{1,2}, Xiaofeng Yuan^{1,2}, and Yongfeng Wang^{1,2}

¹College of Information Engineering

Communication University of China, Beijing 100854, China

²Science and Technology on Electromagnetic Scattering Laboratory, Beijing 100854, China

Abstract— A novel microwave absorber is presented in this paper. The absorber is a single layer structure based on the topology of a Salisbury screen, but in which the conventional resistive layer is replaced by an active frequency selective surface (AFSS) controlled by PIN diodes. The reflectivity response of the tunable microwave absorber can be controlled by adjusting the current in PIN diodes. Experimental results are presented and prove the working mechanism of the new absorber, which show that the reflectivity response can be modulated over the frequency band from 10 GHz to 12 GHz.

1. INTRODUCTION

Stealth technology is one of the most important military technologies concerned by all the nations. Its essence is reducing radar cross section [1] (RCS) of targets. Radar absorbing materials (RAM) is the primary method of RCS reduction.

In the 1930s, there had been RAM that was used in the antenna field. After 1950s, there had been Salisbury screen [2], Dallenbach and Jaumann absorber [3] with fast development of radar technology. Passive radar absorbing material, once designed and manufactured, has fixed characteristics. If the environment of the battlefield changes the absorbing property of RAM is declined.

The tunable microwave absorber could control its reflectivity response according to threatened frequency, in order to obtain the optimal absorbing capability at its threatened frequency. In the 1990s, E. A. Parker [4] presented that the active frequency selective surface (FSS) was made by placing PIN diodes on the FSS, and the response of the active FSS could be controlled by adjusting the bias voltage or current in PIN diodes. In 2004, Barry Chambers and Alan Tennant [5] designed a single-layer tunable microwave absorber using an active FSS. Measured results proved that this absorber did well in 9–13 GHz, and the reflective response could be adjusted.

In this paper, a sample of tunable microwave absorber was designed and manufactured. At last, several microwave absorbers were optimized by genetic algorithm.

2. CONSTRUCTION

Passive radar absorbing structure involved Salisbury screen and Jaumann absorber. The tunable microwave absorber was developed based on them. The tunable absorber based on Salisbury screen was chosen through integrated advisement. Circuit analog (CA) absorber is made by adding reactance into the resistance layer of Salisbury screen. If the resistance or reactance of circuit analog absorber could be adjusted by the electricity, the tunable microwave absorber comes into being.

The tunable microwave absorber is made up of conducting plate, dielectric spacer and impedance sheet as shown schematically in Fig. 1(a). According to transmission line algorithm, the new absorber is equivalent to Fig. 1(b).

In Fig. 1(b), impedance sheet is replaced by resistance (R) and reactance (jX). So there are three methods for tuning impedance:

- (1) X fixed, R adjusted. Loading PIN diodes on FSS array, R could be controlled by adjusting the current in PIN diodes.
- (2) R fixed, X adjusted. Loading varactors on FSS array, X could be controlled by adjusting the voltage between varactors.
- (3) R and X adjusted.

In this paper, we choose an impedance sheet scheme that combines FSS and PIN diodes. The resistance of PIN diode could be tuned by adjusting the current in PIN diode, so that the whole impedance of the sheet is controlled by this way. In addition, the response time of PIN diode is several nanoseconds.

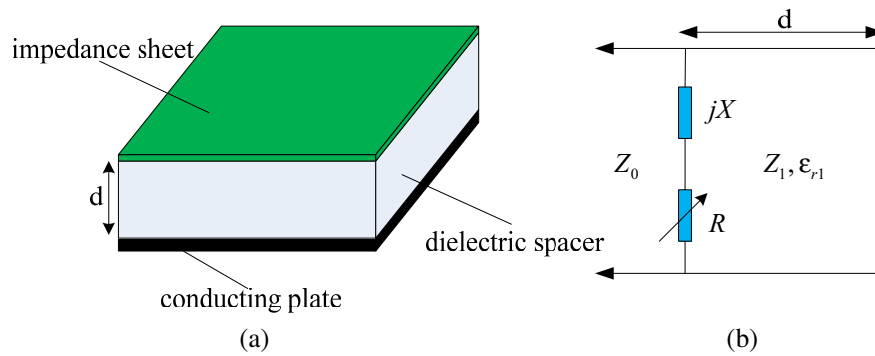


Figure 1: The tunable absorber construction and transmission line equivalent circuit model.

3. EXPERIMENTAL INVESTIGATIONS

In Fig. 2, a square ring FSS is designed to achieve a wide absorbing band, and there is a bias line between every two elements. Active control is achieved by loading a PIN diode on every leg of every element in vertical direction. To let the control current flow in the diodes, the elements are connected in parallel. In Fig. 2, the detail of an element is listed that the period is 9.44 mm, the gap between two elements is 2.76 mm, and the width of slot is 0.5 mm.

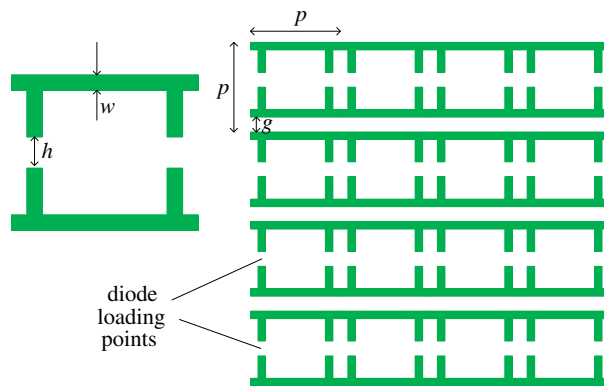


Figure 2: The geometry of FSS array.

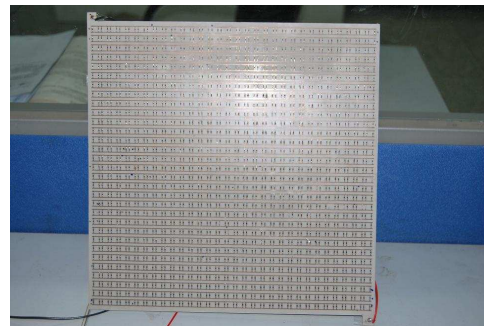


Figure 3: Manufacture of the active board.

Based on the design in Fig. 2, an active FSS is manufactured on a 1.5 mm thick dielectric board, the permittivity of which is 3.5. The board (Fig. 3) measures 300 mm by 300 mm and contains 1922 dipole elements which are loaded with commercially available surface-mount pin diodes using hand-soldering techniques.

A tunable microwave absorber is constructed by mounting the active FSS above a conducting back-plane using a 3 mm thick, foam dielectric spacer as shown in Fig. 1. The circuit surface of the board is lay downwards so that the diodes could be embedded into the foam spacer by a pressure, as a result that overall thickness is less than 5.0 mm.

The reflectivity of the absorber was measured over the frequency range of 6–18 GHz for various bias currents, and these data are presented in Fig. 4. For an applied bias current (0.02 A) the absorber is strongly reflecting. However, as the bias current is increased the reflectivity level reduces and the response frequency debases, showing a 2 GHz reflectivity bandwidth below -15 dB.

4. OPTIMIZATION

The design of tunable microwave absorber is an optimal problem. The reflectivity is a function of material parameter, thick of the spacer, shape and size of FSS element. The final intention of optimization is to search the optimal solution of all the parameters.

Genetic algorithm [6, 7] is used to an optimizing program for designing tunable microwave absorber. Applying this optimizing program, several tunable absorbers were designed. In this paper, a dual polarization tunable microwave absorber is presented. The element is cross dipole in order to achieve a dual polarization. In Fig. 5, the simulated results proved that the reflectivity response was

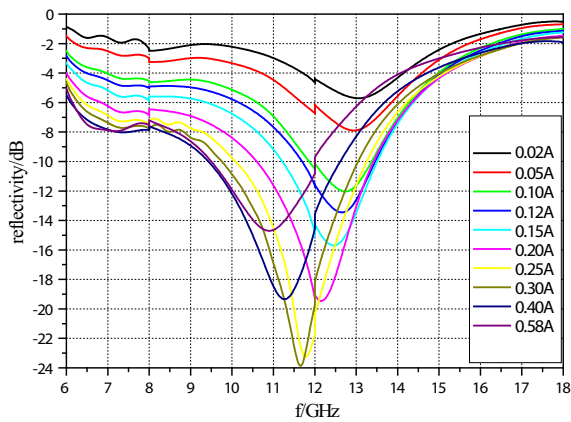


Figure 4: Measured data of the tunable absorber as various currents.

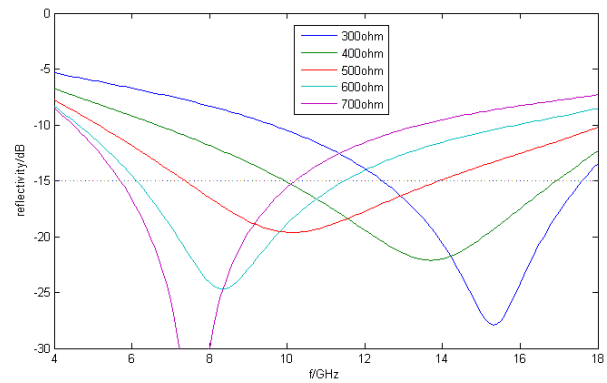


Figure 5: The simulated data of optimal result.

moved with the various resistances of the PIN diodes. From 5.6 GHz to 17.6 GHz, the reflectivity was below -15 dB, so that the absorber could achieve a 12 GHz bandwidth.

5. CONCLUSION

A new tunable microwave absorber which contains an active FSS layer has been presented. The active FSS is manufactured by loading PIN diodes onto the FSS array.

Measured data show that the absorber can be tuned to provide a variable reflectivity response over a band of frequencies from 10.6 to 12.6 GHz. A bias circuit was designed so that the PIN diodes were connected in parallel. In addition, the absorbing structure has a low weight and a thin thickness. At last, a dual polarization tunable absorber is optimized out by genetic algorithm with a 12 GHz bandwidth. And it provides an approach for a broadband, dual polarization and strongly absorbed RAM.

REFERENCES

1. Knott, E. F., *Radar Cross Section*, 2nd Edition, Artech House, Norwood, 1993.
2. Ronald, L., "Reflection properties of the salisbury screen," *IEEE Trans. A. P.*, Vol. 36, No. 10, 1443–1454, 1988.
3. Toit, L. J., "The design of Jaumann absorbers," *IEEE Trans. A. P.*, Vol. 36, No. 6, 17–25, 1994.
4. Chang, T. K., "An active square loop frequency selective surface," *IEEE Trans. Microwave and Guided Wave Letters*, 387–388, 1993.
5. Chambers, B., "A single-layer tunable microwave absorber using an active FSS," *IEEE Trans. Microwave and Wireless Components Letters*, Vol. 14, No. 1, 46–47, 2004.
6. Michalewicz, Z., "Genetic algorithms and optimal control problem," *Proc. of 29th IEEE Conf. on Decision and Control*, 1664–1666, 1990.
7. Weibe, D. S., "Genetic algorithm design of Pareto optimal broad band microwave absorbers," *IEEE Trans. Electronics Compat.*, Vol. 38, 518–524, 1996.

Nonreciprocal Perfect Absorber Consisting of Nonlinear Plasma and Matching Metamaterials

Xiang-Kun Kong^{1,2}, Shao-Bin Liu¹, Hai-Feng Zhang^{1,3}, Bo-Rui Bian¹, and Jia-Lin Yuan¹

¹Key Laboratory of Radar Imaging and Microwave Photonics, Ministry of Education
Nanjing University of Aeronautics and Astronautics, Nanjing 210016, China

²Jiangsu Key Laboratory of Meteorological Observation and Information Processing
Nanjing University of Information Science and Technology, Nanjing 210044, China

³Nanjing Branch, Artillery Academy of the PLA, Nanjing 211132, China

Abstract— A novel, compact and multichannel nonreciprocal absorber through a wave tunneling mechanism in epsilon-negative and matching metamaterials is theoretically proposed. Nonreciprocal absorption properties are acquired via the coupling together of evanescent and propagation waves in an asymmetric configuration, constituted of nonlinear plasma alternated with matching metamaterial. The absorption channel number can be adjusted by changing the periodic number. Due to the positive feedback between nonlinear permittivity of plasma and the inner electric field, bistable absorption and reflection are achieved. Moreover, compared with some designs proposed before, our design is more compact and independent of incident angle or polarization. This kind of multilayer structure offers additional opportunities to design novel omnidirectional EM wave absorbers.

1. INTRODUCTION

The metamaterial perfect absorber has been widely explored due to the fact that it can achieve unity absorptivity of electromagnetic (EM) waves. The motivation for studying metamaterial perfect absorbers comes mainly from their potential applications in emitters, sensors, spatial light modulators, spectroscopic detectors and wireless communications. The concept of perfect absorber was first proposed by Landy et al. [1] who had explored the electromagnetic response-tailorable ability of metamaterials. As a kind of metamaterials [2], plasma can have a tunable negative permittivity controlled by external parameters. Moreover, nonlinearity takes place easily in plasma metamaterials when the incident wave has a relatively high input intensity [3].

Up to now, some nonreciprocal devices have been investigated using unidirectional transmission or absorption. However, a tunable multichannel nonreciprocal perfect absorber which is insensitive to the incident angle is rare reported. In this paper, an incident angle independent unidirectional absorber with nonlinear plasma and matching double negative material is theoretically proposed. Distinct from the Tamm plasmon-polaritons, our proposed device is composed of nonlinear transparent structure with lossy double negative (DNG) substrate, which is also compact and efficient.

2. STRUCTURE MODEL AND PERFECT ABSORPTION CONDITION

In order to make the EM wave perfect transmit through one dimensional layered device without loss, we chose the plasma-DNG structure (AB^N), where A denotes the plasma, B denotes the matching metamaterial, and N represents the periodic number. The relative permittivity and permeability of layers are assumed to be

$$\varepsilon_A^L = 1 - \frac{\omega_{peA}^2}{\omega(\omega - i\nu_A)}, \quad \mu_A = 1 \quad (1)$$

and

$$\varepsilon_B = 1 - \frac{\omega_{peB}^2}{\omega(\omega - i\nu_B)}, \quad \mu_B = 1 - \frac{\omega_{meB}^2}{\omega(\omega - i\nu_B)} \quad (2)$$

where ω_{peA} , ω_{peB} , and ω_{meB} were assigned as the electronic plasma frequency and magnetic plasma frequency, respectively. ν_A and ν_B are collision frequencies for layers A and B , respectively. The working frequencies were selected to fulfill $\omega < \omega_{peA}$, ω_{peB} , and $\omega < \omega_{meB}$. Plasma is assumed to be nonmagnetic ($\mu_A = 1$) and is chosen as a material with a nonlinear Kerr effect. Considering the most powerful $|E|^2$ nonlinear dependence [2], the whole permittivity of the nonlinearity of field-dependent plasma metamaterials is expressed as

$$\varepsilon_A^{NL} = \varepsilon_A^L + \varepsilon_A^{NL} = \varepsilon_A^L + \varepsilon_0\chi |E|^2, \quad (3)$$

where χ is the nonlinear coefficient. According to the theory in nonlinear optics [4], the value of χ for gas discharge was selected at $7.7 \times 10^{-13} \text{ m}^2 \text{ V}^{-2}$ in the following calculation, which is within the range of $10^{-4} \sim 10^{-5} \text{ esu}$ ($1 \text{ m}^2 \text{ V}^{-2} \approx 9 \times 10^8 \text{ esu}$), where $|E|$ is the intensity of the electric field.

In order to absorb most of the EM wave energy transmitted from the above structure, we need to adjust the structure parameters for the last layer. The structure of the nonreciprocal absorber is designed as $AB^N A'$. Here, layer A' has the same refractive index as A but with different thickness and collision frequency. In the subsequent calculations based on the nonlinear transfer matrix method [5, 6], A and A' are nonlinear plasma layers with $\omega_{peA} = \omega_{peA'} = 100 \text{ GHz}$, $\nu_A = 0$ and $\nu_{A'} = 2.5 \text{ GHz}$. B is matching metamaterial with $\omega_{peB} = \omega_{meB} = \omega_{peA}$, $\nu_B = \nu_A$. The thicknesses $d_A = d_B = 0.5 \text{ mm}$, and $d_{A'} = 2 \text{ mm}$ are selected to study the device performance in the region from microwave to millimeter wave.

3. NONRECIPROCAL ABSORPTION PROPERTIES IN INCIDENT ANGLE INSENSITIVE PLASMA-DNG STRUCTURES

First, we demonstrate the characteristic of the perfect absorption. Without loss of generality, Fig. 1(a) shows the linear reflection, transmission and absorption of the structure ABA' as a function of the incident wave frequency. Obviously, there is a perfect absorption peak with zero transmission and zero reflection at frequency $\omega = 15.42 \text{ GHz}$. This phenomenon is attributed to the effect of the first two transparent layers [7] and the last dissipative layer. To confirm this assumption, the field distributions at $\omega = 15.42 \text{ GHz}$ are calculated and shown in Fig. 1(b). Antisymmetric electric field distribution of the propagation mode is observed in the proposed structure, and they gradually decrease within the last lossy metamaterial.

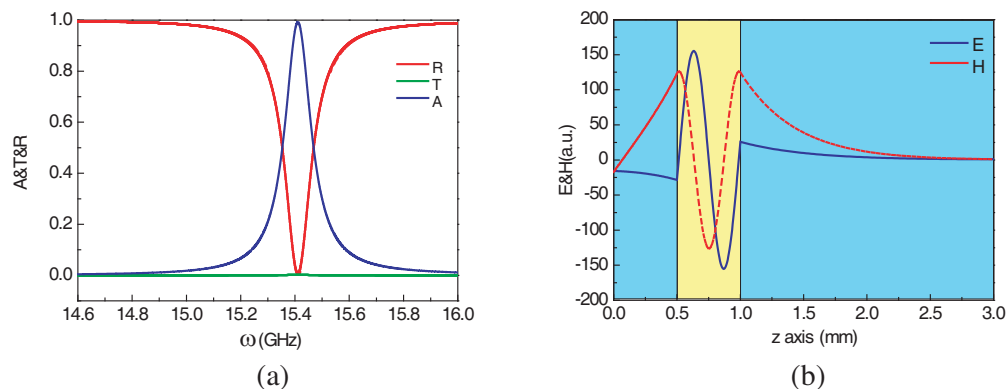


Figure 1: (a) Linear absorption (A), reflection (R), and transmission (T) spectrum of the absorber. (b) Electric (E) and magnetic (H) field distributions in the absorber at $\omega = 15.42 \text{ GHz}$.

Then we explore the nonlinear performance of the absorber to illustrate its active property since nonlinearity takes place easily in plasma. Fig. 2(a) shows the dependence of the nonlinear performance on the left side wave intensity at $\omega = 15.15 \text{ GHz}$. Not only the nonlinear absorption but also reflection are seen to exhibit bistable behaviors. Because of the nonlinearity of plasma and its loss properties, electromagnetic nonlinearity enhancement in the asymmetric structure will result in nonreciprocal transmission of EM waves. The effect of the incident wave frequency on the bistable absorption behavior is shown in Fig. 2(b). It is found that the critical frequency is 15.18 GHz , and the lower input wave frequency, the higher the critical threshold intensity.

Because of the nonlinearity traits in plasma and its loss characteristics, electromagnetic nonlinearity enhancement in the asymmetric structure leads to nonreciprocal absorption of EM waves. Fig. 3(a) shows the linear absorption spectra of the structure ABA' for both the left and right hand side incident EM waves. Near perfect absorption is observed under left incidence, but little absorption under right incidence. The maximum absorption contrast is 90.5% at $\omega = 15.18 \text{ GHz}$. In Fig. 3(b), as shown from the yellow region of the nonlinear absorption spectra, the absorption under left incidence is at the upper branch, owing to its intensity being beyond the bistable threshold, whereas the absorption under right is at the lower branch because the bistable threshold is not reached.

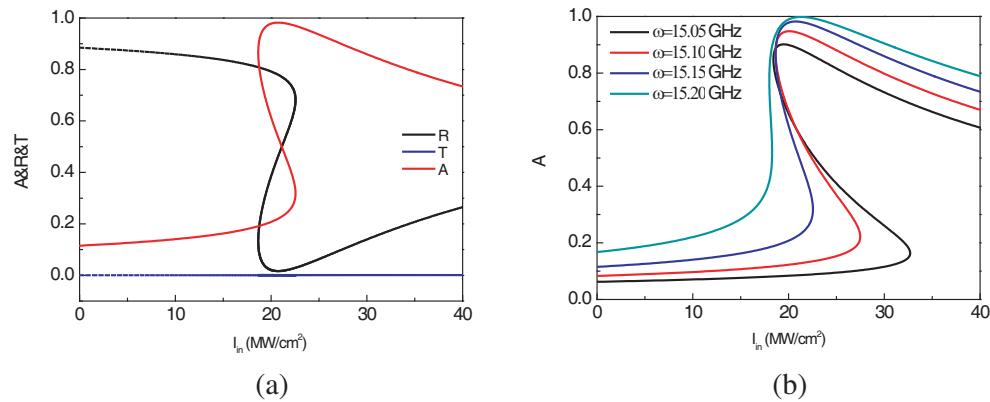


Figure 2: (a) Nonlinear absorption (A), reflection (R), and transmission (T) spectra of the absorber with structure ABA' at $\omega = 15.42$ GHz. (b) Influence of the input wave frequency to the nonlinear absorption of the absorber.

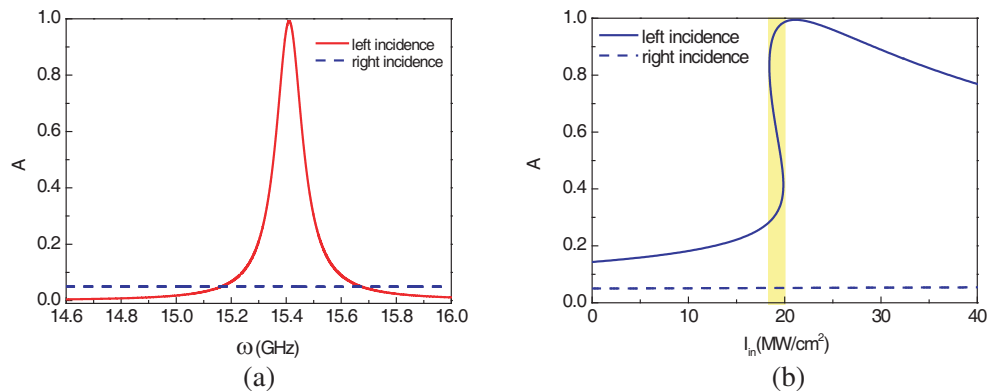


Figure 3: (a) Linear and (b) nonlinear absorption of the absorber with structure ABA' for the left and right incidence, respectively.

4. CONCLUSIONS

In this paper, a compact asymmetric nonreciprocal perfect absorber consisting of nonlinear plasma and matching metamaterials has been proposed. The linear and nonlinear absorption, reflection, and the transmission performances of the absorber have been investigated numerically, and exhibit the tunable multichannel nonreciprocal perfect absorption characteristics.

ACKNOWLEDGMENT

This work was supported by the supports from Chinese Specialized Research Fund for the Doctoral Program of Higher Education (Grant No. 20123218110017), the Jiangsu Province Science Foundation (Grant No. BK2011727), the Foundation of Aeronautical Science (No. 20121852030), Open Research Program in Jiangsu Key Laboratory of Meteorological Observation and Information Processing (Grant No. KDXS1207) and Funding for Outstanding Doctoral Dissertation in NUAA (Grant No. BCXJ11-05).

REFERENCES

1. Landy, N., S. Sajuyigbe, J. Mock, D. Smith, and W. Padilla, "Perfect metamaterial absorber," *Physical Review Letters*, Vol. 100, 1–4, 2008.
2. Sakai, O. and K. Tachibana, "Plasmas as metamaterials: A review," *Plasma Sources Science and Technology*, Vol. 21, 013001, 2012.
3. Sakai, O., "Transition between positive and negative permittivity in field-dependent metamaterial," *Journal of Applied Physics*, Vol. 109, 084914, Apr. 2011.
4. Boyd, R. W., *Nonlinear Optics*, Academic Press Inc., San Diego, CA, United States, 1992.
5. Yu, G. and Y.-T. Fang, "Achieving optical bistability through ultra-compact metal-dielectric structure," *Optics & Laser Technology*, Corrected Proof, 2010, in press.

6. Kong, X. K., S. B. Liu, H. F. Zhang, S. Y. Wang, B. R. Bian, and Y. Dai, “Tunable bistability in photonic multilayers doped by unmagnetized plasma and coupled nonlinear defects,” *IEEE Journal of Selected Topics in Quantum Electronics*, Vol. 19, 8401407–8401407, 2013.
7. Fang, Y. and S. He, “Transparent structure consisting of metamaterial layers and matching layers,” *Physical Review A*, Vol. 78, 023813, 2008.

Minimum Variance Variable Constrain DOA Algorithm

Ahmed Khairy Aboul-Seoud, Ahmed Khairy Mahmoud, Alaa Hafez, and Ali Gaballa
Faculty of Engineering, Alexandria University, Alexandria, Egypt

Abstract— This work proposes a new direction-of-arrival (DOA) estimation algorithm for Smart antenna. The proposed algorithm is based on MVDR algorithm through the introduction of a new optimization problem, which aims to maintain the array gain in the ‘look direction’, so that the DOA can be estimated correctly using Smart antenna array. To verify the performance of the proposed algorithm, computer simulations are performed and then the results obtained are compared with the MVDR algorithm. The results show that the proposed algorithm outperforms the MVDR algorithm.

1. INTRODUCTION

The use of electrostatic MEMS switches is attractive because of its advantages, such as very low power consumption and high isolation. However, MEMS switches have their share of problems, such as, high driving voltage, relatively low speed and low power handling. Many previous researches focus on RF MEMS switch, which presents a good performance at microwave frequency. This result an increasing use of RF MEMS switches for telecommunication purpose in the last ten years [1]. This paper purposes is to use RF MEMS series switch for Switched beam array creates a group of overlapping beams that together result in 0° to 180° coverage The beam pattern is generated using combines of MEMS phase shifters that feed networks into a highly integrated multifunctional chip, which can then be connected to the antenna array and T/R modules, Adaptive arrays allow the antenna to steer the beam to any direction of interest while simultaneously nulling interfering signals [2]. Beamdirection can be estimated using direction-of-arrival (DOA) estimation methods.

2. MEMS SWITCHES

MEMS refer to a 21th century technology named micro-electromechanical systems. MEMS are processes technology used to create tiny integrated devices or systems that combine mechanical and electrical components. They are fabricated using integrated circuit (IC) batch processing techniques and can range in size from a few micrometers to millimeters. These devices (or systems) have the ability to sense, control and actuate on the micro scale, and generate effects on the macro scale. In the most general form, MEMS consist of mechanical microstructures, micro-sensors, micro-actuators and microelectronics, all integrated onto the same silicon chip. Nowadays, MEMS have a diversity of applications across multiple markets like automotive, electronics, medical, communications, and defense weapons. MEMS switches are surface-micro machined devices which use a mechanical movement to achieve a short circuit or an open circuit in the RF transmission-line. RF MEMS switches are the specific micromechanical switches which are designed to operate at RF to mm-wave frequencies form 0.1 to 100 GHz [3–7]. With the recent exciting advancements in the field of microelectromechanical systems (MEMS) and micromachining technology, miniaturized MEMS phase shifters have shown to offer a superior RF performance in comparison to their semiconductor counterparts. The main objective of this research is to develop a new technique for integration at the module level that combines the MEMS phase shifters and feed networks into a highly integrated multifunctional chip, which can then be connected to the antenna array and T/R modules, RF switches are used in a wide array of commercial, aerospace and defense application areas including satellite communications systems, wireless communications systems and radar systems. The circuits are modeled and optimized using Agilent’s HP ADS circuit simulator [8]. Fig. 1 shows the equivalent circuit model of the switched Phase Shifter set up in ADS in which the “on” and “off” states of the switch obtained from decoder are used in the ADS circuit simulator to optimize and obtain the simulated response One of the key elements in the array design is the MEMS phase shifter. RF MEMS phase shifters possess many advantages such as low loss, improved power handling capability and can also be used to realize high density packages to reduce the size and weight components. 50–75% of the T/R modules can be eliminated in large phased arrays by using MEMS phase shifters. This research proposes a high resolution wide band tunable MEMS phase shifters for radar phased array antenna to steer the beam. The proposed circuit is based on dividing the tuning range which change the phase by 22.5° steps for course tuning to achieve

the desired phase. A microstrip phase shifters have been designed at 5 GHz. The phase shifter is designed, simulated and tested using Advanced Design System (ADS) software. This type of phase shifters can give high performance and resolution. Switched line phase shifters schematic diagram are illustrated in Fig. 1. It consists of nine coarse delay transmission line elements from, 0 to 180 degrees with 22.5 degrees step. A digital control circuit plays an important function during the phase change mechanism. The control circuit is a decoder circuit converts the code word to control signals open and close the MEMS switches. If the required phase is 135 degree then the control circuit chooses to close the MEMS switches of the 90 degree element and the other switch of the 45 degree element, then the total phase shift satisfied is 135 degree.

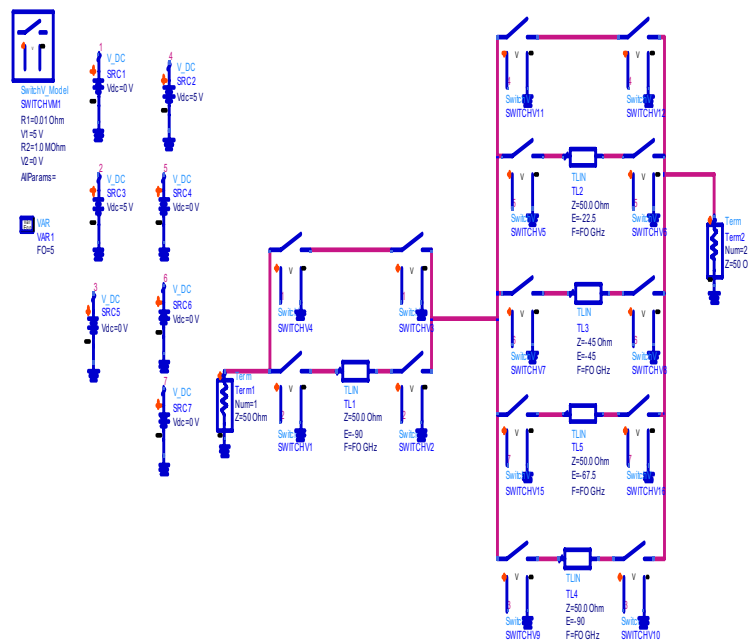


Figure 1: Switched line phase shifter schematic diagram.

3. SWITCHING-BEAM ARRAY

In the smart antenna systems, the Switching-Beam Array approach forms multiple fixed beams with enhanced sensitivity in specific area. These antenna systems will detect signal strength, and select one of the best, predetermined, fixed beams for the subscribers as they move throughout the coverage sector. Instead of modeling the directional antenna pattern with the metallic properties and physical design of a single element, a Switching-Beam Array system couple the outputs of multiple antennas in such a manner that it forms a finely directional beams with spatial selectivity [2].

3.1. Data Model

We considered an m -element array with an arbitrary geometry. The array receives narrow band signals from M spatially separated users. We ignore the multipath signals. Assume that the array response vector to a transmitted signal source from a DOA θ . Calculation of the DOA of a signal is required to track the location of the signal. We have simulated study for Capon and MUSIC DOA estimation algorithms, since those are suitable for circular array or any arbitrary shape array. Define array signal [9–12]:

$$x(t) = \sum_{i=1}^M a(\theta) s_i(t) + n(t) = As(t) + n(t) \quad (1)$$

where

$$A = [a(\theta_1), a(\theta_2), \dots, a(\theta_M)] \quad (2)$$

is signal spatial signature and:

$$s(t) = [s_1(t), s_2(t), \dots, s_M(t)]^T \quad (3)$$

is signal vector.

The covariance matrix of array signal is:

$$R = E \{x(t)x(t)^H\} = AE \{s(t)s(t)^H\} A^H + E \{n(t)n(t)^H\} = APA^H + \sigma^2 I \quad (4)$$

where P is received signal power matrix, and $\sigma^2 I$ is noise power matrix.

3.2. MVDR DOA

Minimum Variance Distortionless Response algorithm (MVDR). The key is to minimize the output power of the system except the one that pointing to the desired signal direction:

$$\min_w w^H R w \quad \text{subject to} \quad (w^H a(\theta) = 1)$$

to estimate the optimal weight vector. Solution of this minimization problem gives the optimal weight vector as [13, 14]:

$$w_{mvdr} = \frac{R^{-1} a(\theta)}{a^H(\theta) R^{-1} a(\theta)} \quad (5)$$

The MVDR minimizes the total output power while keeping the output signal constant, thus the MVDR output power spectrum is:

$$P = \frac{g^H(\theta) g(\theta)}{a^H(\theta) R^{-1} a(\theta)} \quad (6)$$

3.3. Minimum Variance Variable Constrain

The proposed algorithm is based on modified MVDR algorithm that is targeted to work with the directional antenna array. In general, the steering vector can be expressed as follows:

$$A(\theta) = [g(\theta_1)a(\theta_1) \quad g(\theta_2)a(\theta_2) \quad \dots \quad g(\theta_N)a(\theta_N)]^T \quad (7)$$

where $g(\theta_i)$ is the array gain in a specific direction θ . For antenna arrays with isotropic elements, $g(\theta_i)$ is equal to 1 for $i = 1, 2, \dots, N$. However, in the case of antenna arrays with directional elements, $g(\theta_i)$ is determined from the array gain pattern and thus significantly affect the values of $a(\theta_i)$. Furthermore, since the array response is affected by the gain pattern in a ‘look direction’, the constraint in Minimum Variance Variable Constrain MVVC can be given by:

$$\min W^H R W \quad \text{subject to} \quad w^H a(\theta) = g(\theta) \quad (8)$$

Applying Lagrange optimisation technique on the constraint in (8) yields the Lagrange multiplier, λ , and weight w given by (9) and (10) respectively.

$$\lambda = \frac{g(\theta)}{a^H(\theta) R^{-1} a(\theta)} \quad (9)$$

$$w = \frac{R^{-1} a(\theta) g(\theta)}{a^H(\theta) R^{-1} a(\theta)} \quad (10)$$

Finally, the power spectrum of the MVVC algorithm is given as:

$$P = \frac{g^H(\theta) g(\theta)}{a^H(\theta) R^{-1} a(\theta)} \quad (11)$$

4. RESULTS

Computer simulations using Matlab are conducted to evaluate the performance of the MVVC algorithm. This section compares the performance of MVVC and MVDR algorithms. The simulation results presented in this section use the Smart antenna array shown in Fig. 2. Eight uniform linear array (ULA).

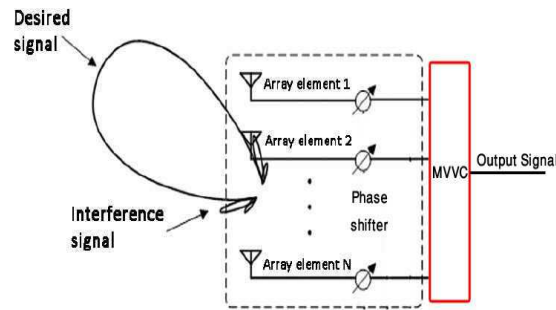


Figure 2: Switching-beam array, phase shifter and MVVC schematic diagram.

4.1. Simulation of DOA Estimation

Using the elements array shown in Fig. 2, both MVDR and MVVC algorithms are applied to estimate the DOA. Suppose there is a tin signal impinging the antenna array at 5° , 20° , 45° , 60° , 70° , 80° , 90° , 100° , 130° and 140° , signal-to-noise ratio (SNR) is fixed at 10 dB, and the number of snapshots is 10000. Fig. 3 shows a comparison of DOA estimation between the MVDR and MVVC algorithms. Clearly the MVDR algorithm yields too many spurious peaks in spatial power spectrum that could lead to inaccurate estimation. Although there is a peak appearing at 130° , but the MVVC will be estimated based on the highest peak strength, which appears at 45° . On the other hand, the MVVC algorithm manages to estimate the DOA correctly and suppress any spurious peaks. The simulation is repeated for multiple signals with the same SNR and snapshot value, Therefore, the observations in results show that the MVVC algorithm has better performance compared with the MVDR algorithm.

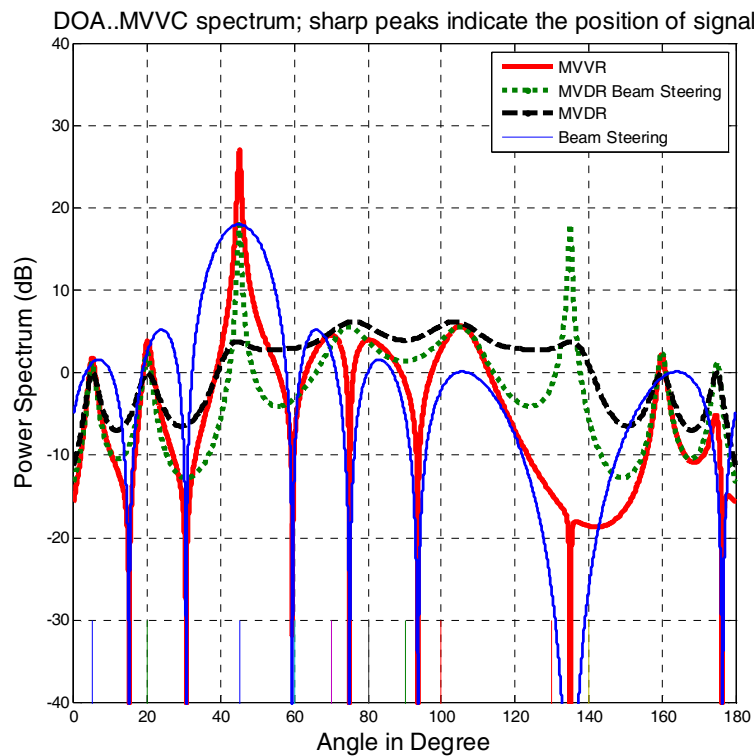


Figure 3: DOA estimation comparison between MVVC and MVDR algorithms for single signal estimation.

4.2. Accuracy

Accuracy of algorithms was tested as a function of Signal to Noise Ratio (SNR) and number of samples. Fig. 4 depicts the results obtained when RMSE is computed when SNR is varied for the algorithms of interest. Results were averaged over 200 runs and 1000 sample were used. The

number of elements used in computing the pseudo-spectrum in MVVC was 8. The results clearly show that MVVC and MVDR have comparable performance.

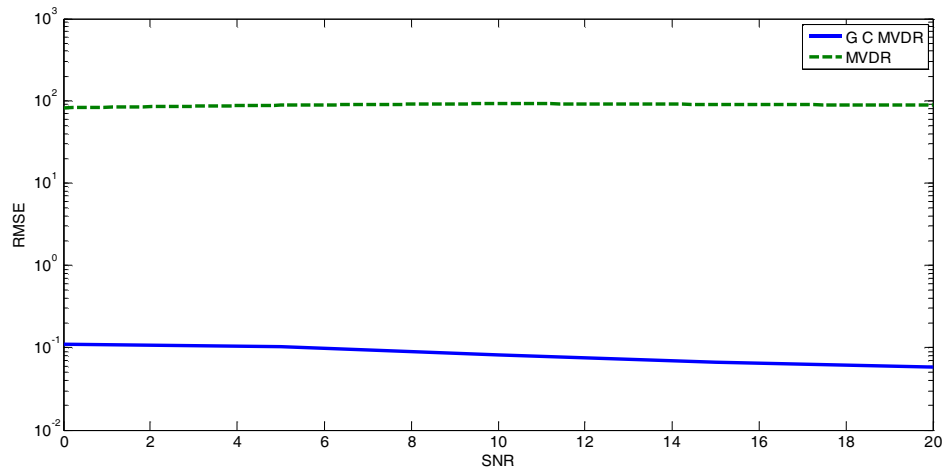


Figure 4: The convergence of estimation RMSE versus SNR for MVVC and MVDR algorithms.

Accuracy was also test as number of samples or shots were varied with a fixed SNR (10 dB). It was concluded that as the number of samples increase, RMSE was computed while varying the SNR from 0 to 20 dB in 2 dB increments. The RMSE tends to zero. MVVC RMSE seems to be slightly higher compared to MVDR but the increase is not sufficiently significant to cause a dramatic error in the DOA estimates. In a non-ideal setting, where mutual coupling was considered, RMSE was calculated for a varied mutual coupling effect (only adjacent element coupling was considered). MVVC seems to be slightly more affected. Magnitude and phase errors effects on accuracy were also investigated for the various algorithms. Results concluded that MVVC achieves a similar performance as far as robustness is concerned compared to other subspace methods.

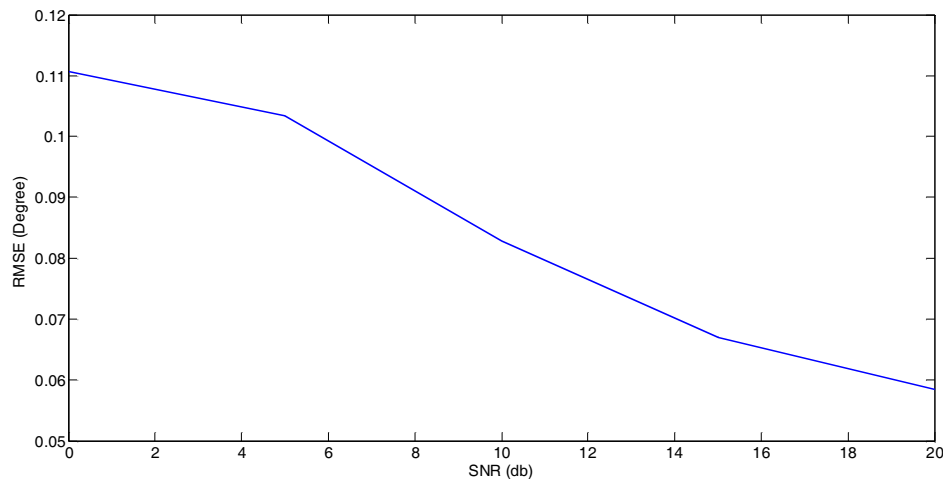


Figure 5: The convergence of estimation RMSE versus SNR for MVVC.

5. CONCLUSION

In this paper, a new algorithm (named Minimum Variance Variable Constrain) is proposed for antenna array with antenna elements. The MVVC algorithm is similar to the MVDR algorithm in one aspect, which is to minimize power from all directions subject to specific gain in the 'look direction'. However, the main difference is that while MVDR algorithm maintains unity gain at 'look direction', MVVC algorithm aims to maintain the corresponding array gain at 'look direction'. Simulations have demonstrated that the MVVC algorithm provides more accurate DOA estimations when used with antenna arrays.

REFERENCES

1. *An Introduction to MEMS*, PRIME Faraday Partnership, Loughborough University, 2002.
2. Gross, F. B., *Smart Antennas for Wireless Communications with MATLAB*, McGraw-Hill, 2005
3. Gong, Y., L. Zhang, F. Zhao, C. Meng, and L. Lv, “Design optimization of cantilever beam MEMS switch,” *International Conference on Industrial Mechatronics and Automation*, 2009.
4. Chung, D. and G. Roland, “Reduced size low voltage RF MEMS X band phase shifter integrated on multilayer organic package,” *IEEE Transaction on Components Packaging and Manufacturing Technology*, Vol. 2, No. 10, Oct. 2012.
5. Panaitov, G., N. Klien, and S. Trellenkamp, “U-saped bimorph microelectro-mechanical cantilevers with combined thermal electrostatic actuation,” *Journal of Microwave Engineering*, 2012, in press.
6. Taghavi, N. and H. Nahvi, “Pull-in instability of cantilever and fixed fixed nano switches,” *European Journal of Mechanics A/Solids*, Vol. 41, 2013.
7. Jaafar, H., F. L. Nan, and N. A. M. Yunus, “Design and simulation of high performance RF MEMS series switch,” *RSM2011 Proc.*, 349–353, Kota Kinabalu, Malaysia, 2011.
8. Internet site: <http://www.home.agilent.com/agilent>, last visited, Jan. 2014
9. Friedlander, B. and A. J. Weiss, “Direction finding in the presence of mutual coupling,” *IEEE Transactions on Antennas and Propagation*, Vol. 39, 273–284, 1991. *2011 Loughborough Antennas & Propagation Conference*, Loughborough, UK, Nov. 14–15, 2011.
10. Hwang, S., T. K. Sarkar, and S. Best, “Direction of arrival (DOA) estimation using electrically small resonant dipole antennas,” *2006 IEEE Conference on Radar*, 166–173, 2006.
11. Balanis, C. A. and P. I. Ioannides, *Introduction to Smart Antenna*, 1st Edition, Morgan and Claypool, Arizona, 2007.
12. Balanis, C. A., *Antenna Theory: Analysis and Design*, 3rd Edition, A. John Wiley & Sons Inc., New Jersey, 2005.
13. Hirata, A., E. Taillefer, H. Yamada, and T. Ohira, “Handheld direction of arrival finder with electronically steerable parasitic array radiator using the reactancedomain multiple signal classification algorithm,” *Microwaves, Antennas & Propagation, IET*, Vol. 1, 815–821, 2007.
14. Chen, Z., G. Gokeda, and Y. Yu, *Introduction to Direction-of-Arrival Estimation*, 685, Artech House, Canton Street Norwood, 2010.

Electrical Engineering Education Systems in Finnish and Chinese Universities

Jiaran Qi

Department of Microwave Engineering
Harbin Institute of Technology, Harbin 150080, China

(Invited Paper)

Abstract— Electrical engineering education systems at the university level in Finland and China are introduced in part and compared in this paper according to the author's personal education experiences in these two countries. In addition, several simple yet effective in-class demonstrative experiments or tools for undergraduate students taking my fundamental electromagnetic course are introduced.

1. INTRODUCTION

Electrical engineering is certainly one popular major that most undergraduate students are willing to choose [1–3]. As a result, it is usually one of the largest departments in an overwhelming majority of universities all over the world [4]. However, educational systems for electrical engineering may vary from country to country. It might then be interesting to make comparisons between these systems. These comparisons will possibly be helpful for the administrative personnel in universities, when there are desires to reform current educational systems, and to draw lessons from experiences and strategies of foreign universities. In Section 2 of this paper, comparisons will be conducted between electrical engineering education systems in Finnish and Chinese universities. The focus will cover curriculum design for undergraduate students, eligibility examination (trial lectures to a group of experienced educators as the audience) for new lecturers, and lecturer evaluation system. Also, responses and suggested modifications to the current educational systems from Chinese undergraduate students will be presented briefly.

Nevertheless, the very first question a reader may raise is why you choose Finnish and Chinese universities specifically. My personally educational experiences and current profession would be the straightforward explanation. Born and bred in Harbin, I was cultivated in education systems of a Chinese style from eight to twenty-five when I was granted the master degree. A new chapter of my education began in Helsinki, Finland, where I lived and worked for six years and achieved my doctoral degree, conveniently. Therefore, I am familiar with the educational systems in Finnish universities. Presently, I am an associate professor in Harbin Institute of Technology (HIT), a top 10 university in China and the largest one in northeastern China. It would then be reasonable to consider myself part of the educational systems in Chinese universities, or at least in HIT. Those are the reasons I choose Finnish and Chinese universities as the topic.

In Section 3, a rather different yet relevant issue will be discussed. I will present several simple yet effective in-class demonstrative experiments/tools for undergraduate students taking my fundamental electromagnetic course.

2. EDUCATION SYSTEM COMPARISON BETWEEN FINNISH AND CHINESE UNIVERSITIES

Electrical engineering educational system covers a very broad range of topics and issues that would be impossible to discuss thoroughly in this paper. Only a few selected yet interesting topics will be discussed in this section.

2.1. Curriculum Design

There is not any obvious divergence between the Finnish curriculum and the Chinese counterpart. The main distinction can be properly summarized with one word, i.e., freedom. In Finland, college students have more freedom to customize their curriculum in order to accumulate credit points. Indeed, courses such as Mathematics are mandatory, but they still have freedom to choose a majority of their major and minor courses, according to their own interests and advices from supervisors and instructors. Backside of such a system could be that students may avoid intentionally those 'boring' but courses of fundamental importance. Such a decision won't prevent them achieving a

degree but may have a long-term impact on their future career. On the contrary, Chinese college students do not have many choices. Academy committee in each school is responsible to design the four-year curriculum for their students. Students have to pass each course listed to complete their Bachelor degree, no matter whether they are interested or follow the specific course. It seems to me that Chinese college students resemble rare materials in a massive manufacturing factory, where they will undergo exactly the same processing. The question is how you can expect diversification from these ‘products’.

2.2. Eligibility Examination for Lecturers

According to my best knowledge, such an eligibility examination for lecturers is a peculiar characteristic in Chinese universities. The rules of this exam are as follows. For a newly employed college lecturer, who plans to give a specific lecture, he has to complete and submit the detailed lecture notes of the whole course to the teaching committee of the university, which will undergo strict inspections by a group of experienced lectures. If your lecture notes meet their requirements, the committee will randomly choose a chapter from them as the contents of your eligibility examination. Only two days are given to prepare for this trail lecture, whose audience will then be the same group of professors examining your lecture notes. This examination will be held twice annually, and the passing rate is around 80%. As far as I am concerned, such a system would effectively urge the lecturers to thoroughly prepare his lectures in advance, since you can hardly give an excellent lecture on a topic you are not extremely familiar with after a two-day preparation.

2.3. Lecturer Evaluation System

Both Finnish and Chinese universities have such a system for undergraduate students to evaluate the corresponding lecturer at the end of an academic semester. Such a system reflects from the viewpoint of a student that whether the lecturer was familiar with the lecture contents, whether he managed to present the contents logically and fluently, whether he gave enough practical examples, whether his lecture was easy to follow, etc., and most importantly, what are the suggestion to this lecturer to improve his lecture? The results of this evaluation are very helpful for lectures which point out clearly the way he should work out to improve his lectures. In particular, three overall grades (A, B, and C) exist in the lecturer evaluation system in HIT. Also, a harsh regulation is that if a lecture who received an overall evaluation grade worse than B. He will automatically lose the eligibility to give a lecture in the coming semester until he passes the eligibility exam.

2.4. Response to Current Systems from Undergraduate Students

Unfortunately, I have not done any survey regarding this point to Finnish college students. However, a recent survey, conducted in School of Electronics and Information Engineering, HIT for the third-year undergraduates, shows that there is a non-negligible demand for the redesign of current curriculum. Students ask for more rights to choose at least their minor courses according to their personal interests instead of the experiences of the academy committee. In addition, some students hope the lecturers could upgrade the textbook or at least the lecture notes to introduce more cutting-edge developments related to the lectures. A majority of students anticipate that there will be more technical training courses in the curriculum, such as Matlab programming, and training courses of popular commercial full wave simulation software. According to student’s responses, our school made the decision that each department should offer students relevant courses in the coming autumn semester in September, in order to improve their capability to manipulate useful computational software. It is believed that such a renovation in curriculum could better prepare students for their future academic or industrial careers.

3. IN-CLASS DEMONSTRATIVE EXPERIMENTS OR TOOLS

Fundamental electromagnetic courses always seem like a Himalayas to the students, both mathematically and physically. Mathematically speaking, students are not familiar with vector calculus, such as divergence and curl, leaving alone the cylindrical or the spherical coordinate systems. However, the mathematical complexities can be conquered by continuing practice [5]. The coherent difficulty of such courses for students lies in its abstract concepts and ‘invisible’ physical process to human eyes. In order to facilitate students’ understanding, lecturers could take advantages of the triple E, i.e., examples, experimental demonstrations, and electromagnetic simulations. In this section, three simple yet effective in-class demonstrative experiments or tools for undergraduate students taking my fundamental electromagnetic course will be introduced.

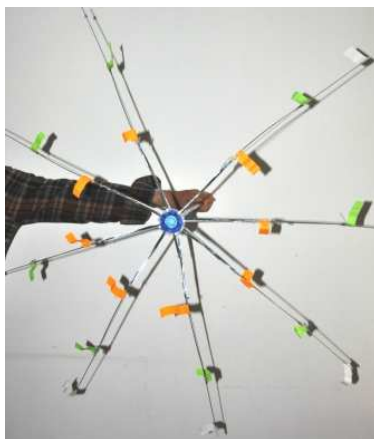


Figure 1: A foldable in-class demonstrative tool for divergence and curl.

3.1. Divergence and Curl

Divergence and Curl are mathematical operators of fundamental physical importance, as they are main operators or notations in Maxwell's Equations. Divergence of a given vector indicates the existence of a flux source or sink, while curl of a vector shows that of a rotational source. How can we impress students with the vector lines produced by different sources? A few pictures may be an easy choice, but they are still motionless and not straightforward examples. As shown in Fig. 1, a foldable in-class demonstrative tool with light weight that I constructed may solve this puzzle. It is made from a foldable broken umbrella. When held still, its shaft is the flux source and the ribs represent the vector lines. When I rotate the umbrella shaft, which is thus the rotational source, the motion of stickers of different colors will visualize the closed vector lines clearly.

3.2. Skin Depth

The skin depth is also an important concept, which quantifies the penetrable depth a wave can propagate into a lossy material including metal. By placing a cell phone in a concealed metal box, one can easily demonstrate this effect.

3.3. Modes in a Rectangular Waveguide

The mode in a rectangular waveguide is another abstract concept, and its propagation is also difficult for students to imagine. In this case, animations generated by commercial full wave computational packages could be a lifesaver. Let us take TE_{10} mode as an example. As shown in Fig. 2(a), the guided wave clearly travels along the waveguide, and forms a standing wave on the transverse plane. Figs. 2(b), 2(c), and 2(d) visualize the electrical field, the magnetic field, and the

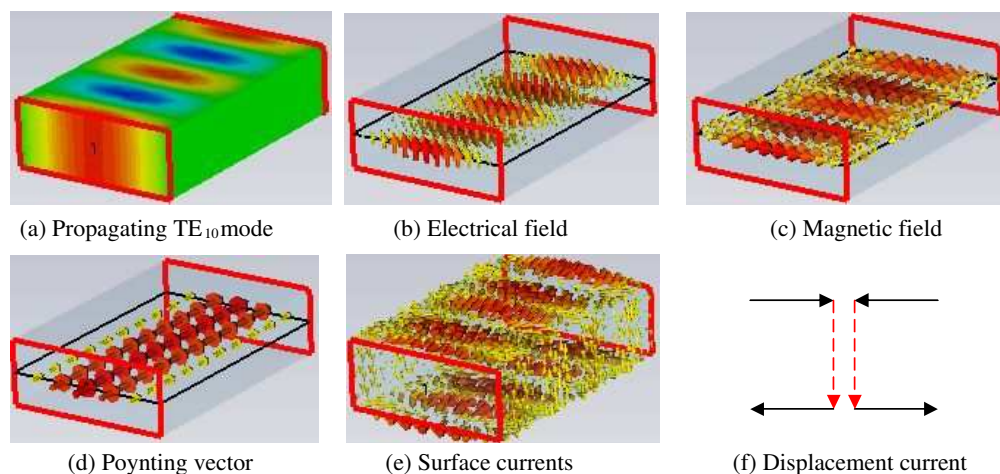


Figure 2: Simulated TE_{10} mode in a given rectangular waveguide. The conceived red-dashed displacement current (with black lines representing the surface currents) in (f) completes the physical process how a propagating TE_{10} mode is generated in the waveguide.

time averaged Poynting vector, respectively. The surface current distribution is shown in Fig. 2(e), which helps us to conceive the displacement current (red dashed lines) in Fig. 2(f). It will finally help students to understand the physical process how a propagating TE_{10} mode is generated in waveguide.

4. CONCLUSION

Electrical engineering education systems at the university level in Finland and China were introduced and compared in this paper according to the author's personal education experiences in these two countries. These comparisons would possibly be helpful for the administrative personnel in universities, when there are desires to reform current educational systems, and draw lessons from experiences and strategies of foreign universities. In addition, several simple yet effective in-class demonstrative experiments or tools for undergraduate students taking my fundamental electromagnetic course were introduced, which can facilitate the students' understanding of abstract concepts and 'invisible' physical process of electromagnetics.

REFERENCES

1. Terman, F. E., "A brief history of electrical engineering education," *Proceedings of the IEEE*, Vol. 64, 1399–1407, 1976.
2. Terman, F. E., "The electrical engineering research situation in American universities," *Science*, Vol. 65, 385–388, 1927.
3. Strassenburg, A., "Supply and demand for physicists," *Physics Today*, Vol. 23, 23–28, 1970.
4. Heuvelen, V., "Learning to think like a physicist: A review of research-based instructional strategies," *American Journal of Physics*, Vol. 59, 891–897, 1991.
5. Leppävirta, J., H. Kettunen, and A. Sihvola, "Complex problem exercises in developing engineering students' conceptual and procedural knowledge of electromagnetics," *IEEE Transactions on Education*, Vol. 55, 63–66, 2011.

Practices and Explorations on Introducing New Scientific Research Achievements into Electromagnetics Teaching for Undergraduates

Jing Liu, Jun Zhang, and Hanwu Yang

College of Optoelectronic Science and Engineering
National University of Defense Technology, Changsha 410073, China

Abstract— In accordance with the “Outline of China’s National Plan for Medium and Long-term Education Reform and Development (2010–2020)”, the raising of education quality is appointed at the heart of task for the present Chinese higher education reform and development. Furthermore, the fostering of young talents or professionals shall command a central position in college work, and no effect shall be spared to produce high-caliber professionals and top-notch innovators with steadfast faith, more integrity, rich knowledge, and superb abilities. Consequently, course teaching, as the most important activity in university, has become the top concerned and hot discussed subject. Actually, since from the beginning of the 20th century, many educational experts and scholars has suggested to introduce the latest scientific research achievement into undergraduate teaching, and then putted it into practice. This paper analyses and sums up these practices coming from some famous Chinese universities, and integrates with our own in the National University of Defense and Technology, during the past nearly 10 years. Based on these, several good ideas and reliable approaches are discussed and concluded, which we think are useful to effectively improve student’s research ability and creative thinking in the courses such as electromagnetic, electromagnetic field and wave, and electrodynamics for undergraduates. At last, some special impediments and outstanding problems are addressed with the expectation to have a deeper discussion with international colleagues.

1. INTRODUCTION

Under the guidance of the “Outline of China’s National Plan for Medium and Long-term Education Reform and Development (2010–2020)” [1], several domestic universities, such as Sun Yat-sen University, Nanjing University, Tsinghua University, Peking University and so on, have actively been involved in the wave of educational reform. Throughout these domestic teaching reform implementations in the past decade [2–10], bilingual education, computer-aided instruction, introducing the latest scientific research achievements into undergraduate curriculums have become the main directions of the reform. Besides, elementary physics curriculums like electromagnetisms, electromagnetic fields and electromagnetic waves, electrodynamics and so on, which are found on the basis of electromagnetic phenomena, always be the first choice of pilot courses.

Focus on introducing the latest scientific research achievements to promote the teaching outcomes, the electromagnetism-relating courses teaching reform has been the practice for many years in many domestic colleges and universities, receiving the widespread recognition and support from most of the educational researchers, managers and coaching staff. In the first part, this paper presents an objective summery and analysis of these practices. We pay more attention onto the ways and the approaches of which they have made use of to introduce the related scientific research achievements, as well as the effects they have achieved. At present, higher educational course reform with improvement of teaching quality at the core, aims to training high-quality talents who would be adapt to the high-speed development of national economy and national defense construction, and be adapt to the information age of science and technology changing with each passing day. For this requirement and combination with the practice of our school in this area, in the second part, this paper discusses the necessity and orientation of introducing the related scientific research achievements into teaching of those electromagnetism-related courses. Furthermore, it points out two outstanding problems encountered in the process of previous reform. One is how to solve the contradiction between the new increased content and the limited class hours, and the other is how to solve the contradiction between the new materials characterized by relativity, variability and exploratory and the textbook exiting knowledge characterized by maturity and logicity. Class discussion teaching methodology, active learning with students as the main body and research teaching, have been the hot-points in overseas education researches and become the content which domestic colleges and universities compete to study in recent years. Therefore, with the help of these new teaching ideas, in the third part, this paper addresses some special impediments and preliminary ideas, with the expectation to have a deeper discussion with international colleagues.

2. THE PRACTICES OF DOMESTIC UNIVERSITIES

Basic physics courses always become the pilot in the education teaching reform by domestic colleges and universities, and courses associated with electromagnetic phenomena, such as electromagnetism, electromagnetic field and electromagnetic wave, and electrodynamics always walk in the forefront of the pilot. On the one hand, this is because the basic status of physics and electromagnetic phenomena is one of important subjects and concepts. There are so much abstract knowledge and experimental content that it is very difficult for students to learn. So we always hope to promote students' learning effect through the teaching reform. On the other hand, this is because of the close connection between the electromagnetic theory to these technologies, such as the microwave engineering, antenna engineering, wave propagation and scattering, electromagnetic exploration, microwave remote sensing, Micro-nano electronics, vacuum electronics, microwave electronics and optics. The basic knowledge of curriculum has been widely applied in industrial applications. Scientific research put forward the realistic demand for college education, in turns, new scientific results easily put important influence on teaching. Therefore, introducing scientific research achievements in electromagnetic theory teaching is in accordance with the characteristics of the course itself.

Based on the comprehensive analysis of the domestic university reforms in the past decade, the approaches and ways of introducing new scientific research achievements to promote the teaching quality mainly reflect in the following respects.

The first measure is the textbook revision, which opens some window for the front of modern science and technology related to the course.

For example, Sun Yat-Sen University, that was chosen as the first domestic electrodynamics national fine course, rewritten the electromagnetic properties of superconductors in the new third edition teaching material of electrodynamics [8]. It duly increased the superconducting current in London theory and the theory of vector potential local relations, said London local area was given in the superconducting magnetic field penetration depth and the experimental results of deviation, increased Pippa non local modification, increased such as photonic crystal optical spatial soliton and atomic optical trap, the new research hotspot, and explained by classical electrodynamics to a certain degree of content.

Tsinghua university, focusing on cultivating students' scientific quality and from physical principle on the consciousness and ability of technology innovation. It opened Subsequent course for students with higher requirements for the physical basis, after the college course of basic physics theories. The course named as Modern physics and the physical basis of new and high technology. It focuses on the foundation and as far as possible reflect the frontier. It focuses on the physical, but appropriate contact technology. For example, except for atomic molecular nuclear and particle physics, it also talks about the general relativity and chaos. Besides, it includes the physical contents, such as solid state physics and new materials, modern optics and information processing, new energy, which are closely related to high and new technology.

Peking University writes an electrodynamics introductory tutorial. It selects material refined and pays attention to teaching skills, or artistic. It maintains the systemic of the theory and the clarity of basic concept, and at the same time it absorbs the new research results as far as possible.

Nanjing Normal University proposes to take new findings, new invention and subject forefront information into the textbook, to make it keep pace with the times. Adopt the way of the teaching material combination. As for the mature knowledge, it highlights the key part of the teaching material content. And for forefront information, it makes up as the matched reading materials.

In addition, Inner Mongolia University of Science and Technology and some other universities also stand for cut off some old content and introduce the latest scientific research achievements into the textbook, as references for students to read after class.

The second measure is redesign the experiments and practice programs, which let the students near to the real and present scientific researches.

Quite a few domestic Universities, like the Jilin University, the Taiyuan University of Technology, the Capital Normal University and the Nanjing University of Aeronautics and Astronautics University, have actively explored the methods and measures to using scientific research to improve the experiment teaching. They pay attention to transfer the professional laboratory science frontier and the scientific and technological development projects to the demonstration and practice experiments, open to the students. Comparison of representative including optical bi-stable, non steady, chaos and control, power generation using high temperature solid oxide fuel cell, the preparation of high temperature superconducting ceramics and magnetic levitation, dot matrix display based on single chip microcomputer control magnetic field distribution and the semiconductor refrigeration

demonstrations and practice experiments.

Sun Yat-Sen University designed the new ideas of new theory and new technology, in the latest scientific research achievements, as the extracurricular reading and discussion topic or in the form of lectures in the knowledge module. In addition, they encourage and guide the efficient junior students to participate in various early scientific research training, science and technology competition.

The undergraduate students' academic achievements in quality and quantity are demonstrated by the students' published academic papers.

The third measure is to establish a course online learning platform, with the new scientific achievements plentiful and easy reachable for students.

Qiqihar University and Hebei University advocates the establishment of a library or online courses for students, with learning resources, which is much less likely to involve through class but shows relation to the technology development and scientific progress. It plays the role of an auxiliary supplement classroom teaching.

The above reform proposals and initiatives does play a certain effect in the promotion of the teaching quality, but whether the textbook, website content or the practice in the experimental, need students to occupy their spare time to carry out. It failed to solve the existing difficulty that integrating the lessons with scientific research in class. Therefore, how to solve the contradiction between the increased new content and limited hours is currently a problem when we hope to take advantage of the scientific research to promote the quality of teaching. Secondly, the new results usually character with exploratory and existing classic textbook content is systematic and mature. It is difficult for students to develop their scientific discernment, and is more difficult to ensure that students are able to correctly understand and the new problem, just only be provided with lots of materials after class.

3. REFLECTIONS ON THE REFORM OBJECTIVES

Form the above analysis of the past domestic higher education reform in physics courses related to electromagnetism, we can find that the objectives of introducing new scientific research achievements are to wide students' visual field, to promote and encourage students to apply the knowledge learning in the class. However, just only through providing many materials for students to get to know, to read and to practice in their spare time, and in the classroom still making use of the traditional lecture teaching, or infusion teaching, it's difficult to get as many as students to get involved and it is almost impossible to train most of the students with the scientific way of thinking. Therefore, introducing the new scientific research achievements should be tied in closely with the innovation of teaching method. It is important to cultivate the scientific literacy and scientific spirit of students and to stimulate the interest in scientific exploration of students during the class and within the limited hours.

4. EXPLORATIONS FOR PRACTICE

Making use of the idea of discussion-based teaching, we can transfer the new thoughts, new ideas, new methods and novel application coming with new scientific research achievements to the learning materials. We need to unify the process of learning knowledge and applying knowledge with the process of thinking the research behavior coming out with new achievements repeatedly.

Around scientific research hotspot and frontier content, it is necessary to redesign the classroom examples and exercises after class. These new problems should pay attention on the raise of ability to analyzing the problem and solving the problem in the real scientific research. Besides, it is better to add some open questions for thinking, which focus on the capability of digesting the knowledge and the build of scientific thinking as well as the scientific values. Theses demand the teachers to improve their own scientific appreciation that they can grab and keep with the mainstream and frontiers in the development of science and effectively. Furthermore, teachers also need to be able to summarizes the successful application in the actual research and rise it up to the theory of education.

For students to discuss organizational issues and explore solutions to the problem together, it is better to get use of the seminars teaching style to explain examples. During the course, teacher work as guiders. Exercises explain reported by the students, and then for teachers to compare the answers between different teams, like organizers and evaluators. Open thinking questions are for voluntary students to answer freely, which can be the way of select potential researchers for the scientific program and other practice activity. Theses require teachers to improve their own seminar organizational skills. For the chosen topic, teachers need to can develop a careful plan

(includes seminar outline, discuss plans and content evaluation methods, etc.). The discussion can be arranged to start with the curriculum related knowledge, and the end result can be a return to the basics of the curriculum.

Course knowledge and concept map summary should be worked out by the students, according to their own understanding and mastery. We can image that these knowledge structures formed by the students will be Hundred Flowers picture. These knowledge structures will provide a rich learning feedback to teachers. For instance, the course difficulty and the threshold concepts from the point of students, as well as how their understanding of the knowledge is progressing.

5. SUMMARY

This paper analyses and sums up these practices coming from some famous Chinese universities during the past nearly 10 years. The approaches and ways of introducing new scientific research achievements to promote the teaching quality mainly reflect in the three respects. These are the revision of the textbook, the experiments and practice programs designed according to the achievements, and to establish a course online learning platform. Whereas, it is hard to embrace the new material within the limited class time and it is hard for students to indentify the exploratory and changeability of the new achievements. In order to solve these two problems faced by the past reform, we recommend combining the new achievements presentation with the seminar teaching method. Though redesigning the classroom examples, exercises after class, and open thinking questions, recognizing discussions on the solutions by students, and studying the course knowledge and concept maps summarized by students, we can achieve the teaching improvement benefiting from introducing new scientific achievements during the class time.

REFERENCES

1. The Ministry of Education, “Outline of China’s national plan for medium and long-term education reform and development,” 2010–2020.
2. The Ministry of Education, “On strengthening higher school undergraduate teaching work, several opinions on improving the quality of teaching,” 2001.
3. Zhang, H. and S. Gao, Vol. 1, 6–12, Jiangsu Gaojiao, 2002.
4. Lin, C. and B. You, “Teaching organization and management,” Vol. 32, 69–71, 2013.
5. Ge, M.-L., “Thinking in physics teching,” Vol. 9, 1–9, College Physics, 2013.
6. Zhang, L. and F. Liu, *Anhui Agricultural Science Bulletin*, Vol. 19, 152–154, 2013.
7. Lv, C. and Y. Yu, *Chinese Technology Innovation Herald*, Vol. 4, 105–107, 2010.
8. Guo, S., et al., *Electrodynamics*, Higher Education Press, Beijing, 2008
9. Chen, Z. *The Foundation of Modern Physics and High Technical Physics*, Tsinghua University Press, Beijing, Apr. 2001.
10. Yu, Y., *A Concise Course of Electrodynamics*, Peking University Press, Jun. 2007.
11. Jiang, X. and X. Huang, *College Physics*, Vol. 4, 52–62, 2004.
12. Liu, J., *Science & Technology Information*, Vol. 11, 2013.
13. Zhang, J., et al., *Physics Experiment*, Vol. 23, 30–36, 2003.
14. Wei, X. and Z. Yang, *Laboratory Science*, Vol. 4, 63–66, 2005.
15. Huang, Q., et al., *College Physics*, Vol. 10, 51–54, 2009.
16. Liu, X., et al., *Physics Bulletin*, Vol. 11, 20–23, 2012.
17. Xiong, W., et al., *Higher Education of Sciences*, Vol. 6, 72–75, 2003.

Random Distributed Feedback Fiber Laser Employing Erbium-doped Fibers

Lulu Wang and Xinyong Dong

Institute of Optoelectronic Technology, China Jiliang University, Hangzhou 310018, China

Abstract— A low-threshold, narrow bandwidth random fiber laser by using a short erbium-doped fiber (EDF) to provide high-efficiency gain in a FBG-formed half-opened cavity is demonstrate. Typical random laser radiation based on the resonance between the FBG reflector and distributed random Rayleigh scattering of the long-distance SMF is realized. Single- and dual-wavelength random lasing operations are realized by using one- and two-FBGs respectively, with low threshold pump power of only 10 mW, which is about two orders lower in magnitude than that of the previously reported conventional random fiber lasers amplified through distributed Raman effect.

1. INTRODUCTION

Random lasers operate without a traditional cavity but randomly distributed scattering centers, leading to the unique advantage of simple technology, i.e., without the need to engineer a precise cavity [1]. Optical fiber-based random lasers, also called random fiber lasers, have attracted lots of attention in recent years because the fiber waveguide provides one-dimensional random distributed feedback (RDFB) that can improve the laser performance significantly [2]. Normally, random fiber lasers are based on the distributed feedback of Rayleigh scattering amplified through stimulated Raman scattering (SRS) effect in a long-distance (tens of km) single-mode fiber (SMF) [2]. Their applications in sensing [3] and communications [4] have also been investigated. Improved laser performance was also achieved by using stimulated Brillouin scattering (SBS) as the gain mechanism, instead of the normally used SRS effect, because SBS has much higher gain efficiency and narrower gain bandwidth [5]. Random fiber lasers based on a randomly spaced identical FBG array recorded in rare earth-doped active fiber has also been reported with improved performance, arising from the efficient gain of the active fiber, the strong feedback and narrow reflection bandwidth of the FBGs [6].

2. LASER DESIGN AND VERIFICATION

Figure 1 shows the schematic diagram of the proposed EDF-based random fiber laser with a half-opened cavity. It consists of a 1480-nm pump laser with a maximum output power of 400 mW, two 1480/1550 nm wavelength-division multiplexers (WDMs), a FBG reflector containing one or two FBGs, a 2-m-long highly-doped EDF and a 30 km-long SMF (type G.652). The EDF has a mode field diameter of 6 μm and a high peak absorption coefficient of ~ 11 dB/m at 1480 nm. The pump laser is launched through WDM 1 into the EDF, which is followed by the long SMF. The FBG reflector is at the left of WDM 1 to reflect the selected wavelength(s) back into the EDF and the long SMF. We use one and two FBGs to achieve the single- and dual-wavelength laser operations, respectively. FBG 1 has central wavelength of 1550 nm, linewidth of 0.24 nm and reflectivity of 90%. FBG 2 has central wavelength of 1551 nm, linewidth of 0.27 nm and reflectivity of 97%. WDM 2 is used to filter out the residual pump power from the laser output. The Angled polished connectors

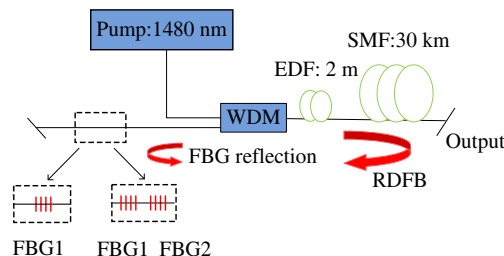


Figure 1: Proposed EDF-based random laser WDM, wavelength-division multiplexer; EDF, erbium-doped fiber; SMF, single-mode fiber; FBG, fiber Bragg grating; RDFB, random distributed feedback.

are used at the both output ends to eliminate the Fresnel reflection of the fiber ends. The laser output is measured by using an optical spectrum analyzer (OSA) with resolution of 0.02 nm and an optical power meter (OPM).

The lasing operation is supposed to be grounded on the EDF gain and the resonance between FBG reflection and RDFB through backward Rayleigh scattering in the long-distance SMF. When the EDF is pumped to generate population inversion of erbium ions, amplified spontaneous emission (ASE) is generated and then wavelength-selectively reflected by the FBG reflector and randomly backward scattered by Rayleigh scattering effect of the long SMF. With increasing power of the pump laser, resonance happens when the gain overcomes the total cavity loss.

3. LASER CHARACTERIZATION

For the single- and dual-wavelength random fiber lasers with one or two FBG(s), the output spectra, as shown in Figs. 2(a) and (b), indicate a dramatic change when the pump power reaches 10 mW. Based on previous studies [2], the generation of stochastic spikes is related to the combined effect of distributed Rayleigh scattering and cascade SBS, while nonlinear spectral broadening (NSB) arising from nonlinear interactions, such as frequency mixing and cross-phase modulation, can make the spikes broadened and superposed and further suppress the SBS process. For the single-wavelength random fiber laser, well-localized and stabilized laser spectra with narrow linewidth were observed when the pump power reaches 100 mW. For the dual-wavelength random fiber laser, the intensity increases with pump power and then stabilized and smoothed output spectrum is finally achieved when the pump power reaches about 200 mW, which is just twofold of that for the single-wavelength random fiber laser, indicating nearly the same pump power consumption for each lasing wavelength to reach the stabilized state. In addition, two new spectral peaks appear outside the two main peaks and grow up with the pump power. The wavelength separations of neighboring peaks are the same, meaning that four-wave mixing (FWM) effect in the long-distance fiber plays the key role for the generation of the new spectral peaks. It also indicates the possibility of achieving multi-wavelength random fiber laser based on this FWM effect.

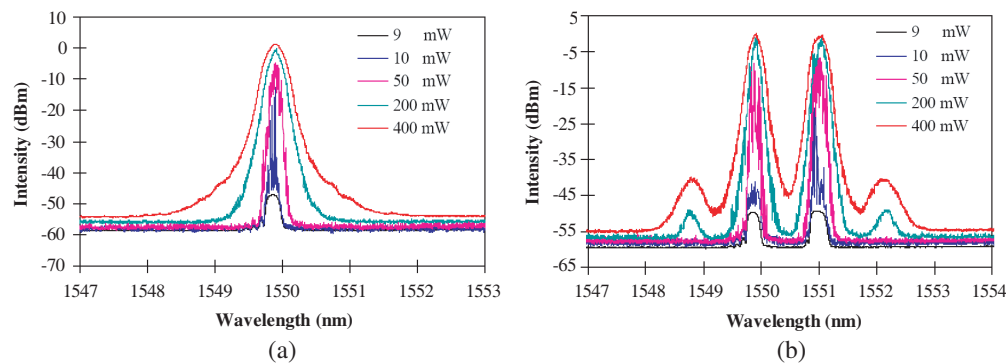


Figure 2: Output spectra of the (a) single- and (b) dual-wavelength random fiber laser for different pump powers.

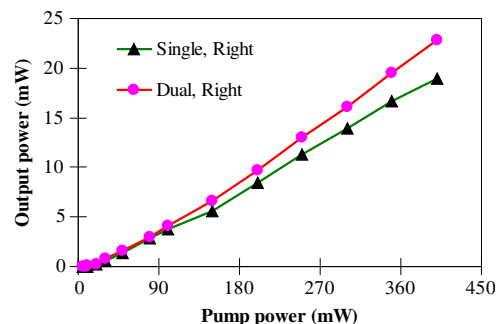


Figure 3: Output power against pump power for single- and dual-wavelength random fiber lasers.

Figure 3 shows the comparison of laser output power against pump power between the single-

and dual-wavelength random fiber lasers. It can be seen that the two lasers show the same threshold and similar output characteristic. The output powers grow nearly linearly, under maximum pump power of 400 with pump power. The maximum output powers are 19 mW and 23 mW for the single- and dual-wavelength random fiber lasers, respectively. So the pump efficiencies are up to 5.7% and 6.4% for single- and dual-wavelength output, respectively. The dual-wavelength laser has slightly higher efficiency than that of the single-wavelength one.

4. CONCLUSIONS

A low-threshold, high-efficiency and narrow linewidth random fiber laser has been demonstrated for the first time by using an erbium-doped fiber as gain medium in a FBG-formed half-opened cavity design. Due to the wavelength-selective feedback of the FBG reflector and the high-efficient gain from the pumped EDF, the threshold power of the achieved random fiber laser is as low as 10 mW, which is two orders lower in magnitude than that of the reported conventional random fiber laser amplified by distributed Raman effect. The maximum pump efficiency of single- and dual-wavelength lasers are up to 5.7% and 6.4%, which is comparable to that of normal erbium-doped fiber lasers.

ACKNOWLEDGMENT

This work was supported in part by the National Basic Research Program of China (973 Program) under Grant 2010CB327804, in part by the National Natural Science Foundation under Grant 61203205, and in part by the National Natural Science Foundation of Zhejiang Province, China, under Grant Z13F050003.

REFERENCES

1. Ambartsumyan, R., N. Basov, P. Kryukov, and V. Letokov, "Laser with nonresonant feedback," *Sov. Phys. JETP*, Vol. 3, 167–169, 1966.
2. Turitsyn, S. K., S. A. Babin, A. E. El-Taher, P. Harper, D. V. Churkin, S. I. Kablukov, J. D. Ania-Castañón, V. Karalekas, and E. V. Podivilov, "Random distributed feedback fibre laser," *Nature Photon.*, Vol. 4, 231–235, 2010.
3. Babin, S. A., A. E. El-Taher, P. Harper, E. V. Podivilov, and S. K. Turitsyn, "Tunable random fiber laser," *Phys. Rev. A*, Vol. 84, 021805, 2011.
4. Martins, H. F., M. B. Marques, and O. Frazão, "Temperature-insensitive strain sensor based on four-wave mixing using Raman fiber Bragg grating laser sensor with cooperative Rayleigh scattering," *Appl. Phys. B*, Vol. 104, 957–960, 2011.
5. Jia, X. H., Y. J. Rao, F. Peng, Z. N. Wang, W. L. Zhang, H. J. Wu, and Y. Jiang, "Random-lasing-based distributed fiber-optic amplification," *Opt. Express*, Vol. 21, 6572–6577, 2013.
6. Pang, M., S. Xie, X. Bao, D. P. Zhou, Y. Lu, and L. Chen, "Rayleigh scattering-assisted narrow linewidth Brillouin lasing in cascaded fiber," *Opt. Lett.*, Vol. 37, 3129–3131, 2012.
7. Lizárraga, N., N. P. Puente, E. I. Chaikina, T. A. Leskova, and E. R. Méndez, "Single-mode Er-doped fiber random laser with distributed Bragg grating feedback," *Opt. Express*, Vol. 17, 395–404, 2009.

Random Laser with Er/Yb-codoped Fiber Grating

Lulu Wang and Xinyong Dong

Institute of Optoelectronic Technology, China Jiliang University, Hangzhou 310018, China

Abstract— A random fiber laser is demonstrated based on a 25-mm-long multi-phase shifted fiber Bragg grating, which was fabricated in a highly Er/Yb-codoped fiber with the beam-scanning method. By inserting twenty phase errors with random amplitudes between 0 and 2π along the grating and end-pumping the Er/Yb co-doped fiber with a 980-nm laser diode, we achieved low threshold (28 mW) and almost either single or dual-wavelength random lasing operations of changeable wavelengths depending on the power of pump laser.

1. INTRODUCTION

Low threshold random fiber lasers based on optical fiber Bragg grating (FBG) technology have been reported recently by taking advantages of the effective light localization effect introduced by FBGs and high efficient gain from pumped erbium-doped fibers (EDFs) [1, 2]. Lizárraga realized the first FBG-based random fiber laser by using a randomly spaced identical FBG array recorded along a 150-cm-long Er/Ge co-doped fiber [1]. Gagne reported more compact random fiber lasers based on single FBGs, which were recorded on Er-doped fibers and of multiple phase errors randomly distributed along the whole length (20–30 cm) [2]. In this paper, we report a much more compact random fiber laser by using a 25-mm-long multi-phase-shifted FBG, which was fabricated in a highly Er/Yb-codoped fiber and pumped with a 980-nm laser diode. It is the shortest random fiber laser to the best of our knowledge if only the effective part of the fiber is under consideration. Typical random laser radiation based on the light localization behavior of the grating with randomly phase errors is realized.

2. FIBER GRATING FABRICATION

The multi-phase-shifted FBG was fabricated by using a frequency-doubled Argon laser (244 nm) with the phase mask and beam-scanning method. The highly Er/Yb-codoped fiber has a mode field diameter of $7\ \mu\text{m}$ and a high peak absorption coefficient of $\sim 500\ \text{dB/m}$ at 980 nm. A 25-mm long FBG with 20 phase shifts of random amplitude between 0.2π and 1.9π and nearly equal separation around 1.19 mm was therefore fabricated in the middle of the 40 mm-long-Er/Yb-codoped fiber. Figure 1 shows the reflection and transmission spectra of the recorded multi-phase-shifted FBG measured by using a tunable laser (AQ4321D) with resolution of 1 pm and an optical spectrum analyzer with resolution of 10 pm. The reflection spectrum has a 3-dB bandwidth around 0.95 nm centered at 1542.98 nm and reflectivity of 99.9%. Several obvious narrow transmission peaks attributed to the phase shifts are observed in the broadband reflection background.

3. LASER DESIGN AND VERIFICATION

The experimental setup is shown in Fig. 2. A 980 nm pump laser with a maximum output power of 200 mW was used to pump the multi-phase-shifted FBG through a 980/1550 nm wavelength

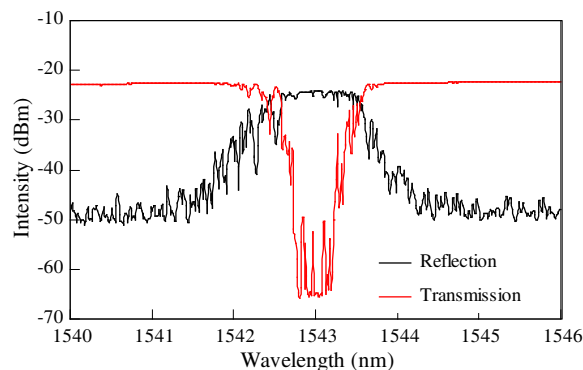


Figure 1: Reflection and transmission spectra of the phase shifted FBG.

division multiplexer (WDM). The laser output is backward in respect to the pump laser so that the residual pump laser can be avoided from the output. Angle-polished connectors or fusion splicing were used to avoid any unwanted back reflections. The multi-phase-shifted FBG was placed into water to prevent it from temperature changes arising from high power pumping because the pump generated heat can be absorbed quickly by water during the experiment. Both optical power meter and OSA were used for measurement.

The measured laser output spectra as a function of pump power are shown in Fig. 3. We measured it twice by changing the pump direction (namely injecting the pump laser from another end of the Er/Yb-codoped fiber). The threshold pump powers are 28 and 35 mW, respectively. It can be seen that the laser output spectra for the both pumping directions contain two lasing peaks when the pump power is low, a strong one on the long wavelength side and a weak one on the short wavelength side. With increasing the pump power, the weak one grows up faster than the strong one and finally exceeds the initially strong one when the pump power reaches ~ 100 mW. With further increasing the pump power, the laser output experiences different evolutions for the two pump directions: for the left end pumping case, the initially strong one shrinks quickly and disappears finally so only one peak is operating; for the right end pumping case, the two peaks keep operating together till the pump power reaches the maximum. Since each peak of the laser output may contain several randomly embedded local spatial modes and the radiation intensity of each local spatial mode depends on the local pump power, we believe that the differences in both pump threshold and spectrum evolution are related to the asymmetrical distribution of random phase errors and attenuation of the pump power along the length of the grating. The relatively broad laser linewidth and minor spectral splitting [as can be observed in Fig. 3(b)] provide the evidences that the final laser output spectrum is the sum of lots of local spatial modes that may have slightly different emission wavelengths. The laser modes for the both pumping directions have an optical signal to noise ratio (OSNR) as high as 65 dB.

The measured output powers as a function of pump power are shown in Fig. 5. For the laser pump from left end or right end of the Er/Yb-codoped fiber, it can be divided into three or two parts depends on the number of the laser peaks. The output powers grow nearly linearly with pump power increasing in different ranges, respectively. The maximum output powers of the laser for pump from left and right end are 1.18 and 1.5 mW, respectively. So the pump efficiencies are 0.7% and 0.9%, respectively. The difference of the efficiency is because the numbers of laser emission that pump from left or right ends are different. As the fusion splice between the WDM and Er/Yb-codoped fiber exhibit losses, while the reflection of the grating is high that lead to a

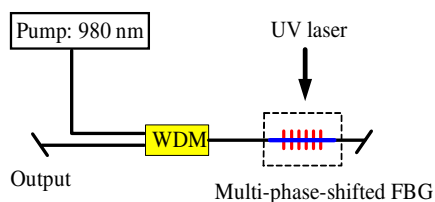


Figure 2: Schematic diagram of the experimental setup. WDM, wavelength division multiplexer; FBG, fiber Bragg grating.

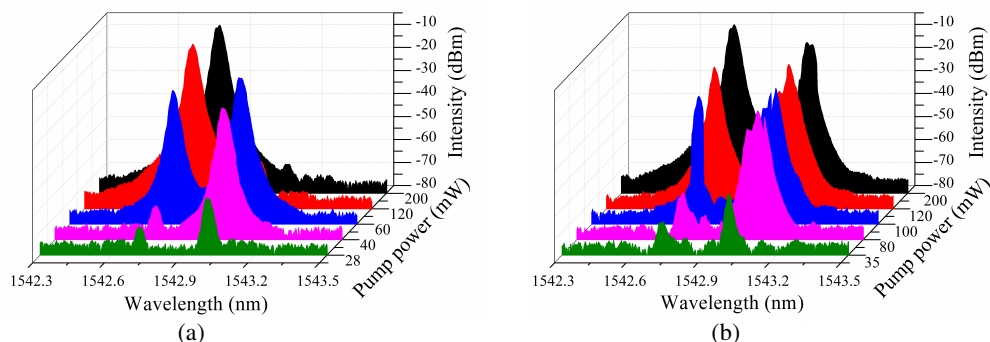


Figure 3: Laser output spectra with different pump power. (a) and (b), pump from left and right end of the Er/Yb-codoped fiber.

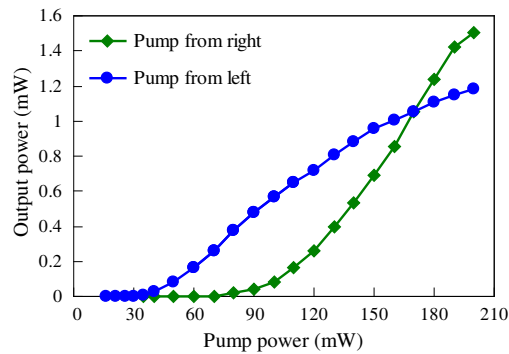


Figure 4: Laser power as a function of pump power when pumped from the left or right end of the Er/Yb-codoped fiber.

high intra-cavity flux, the efficiency is not very high.

4. CONCLUSION

To conclude, we present an ultra-short random fiber laser based on the fiber Bragg grating with multi-phase-shifts. The proposed random fiber laser exhibits the pump threshold of about 28 mW and 35 mW when pump from left and right end of the fiber. Depending on the pump power, the random laser shows almost both single and dual-wavelength operation. This proposed random fiber laser may find potential applications for sensing applications.

ACKNOWLEDGMENT

This work was supported by the National Basic Research Program of China (973 Program) under Grant No. 2010CB327804, National Natural Science Foundation under Grant No. 61203205, National Natural Science Foundation under Grant No. 61007051 and National Natural Science Foundation of Zhejiang Province, China under Grant No. Z13F050003.

REFERENCES

1. Lizárraga, N., N. P. Puente, E. I. Chaikina, T. A. Leskova, and E. R. Méndez, "Single-mode Er-doped fiber random laser with distributed Bragg grating feedback," *Opt. Express*, Vol. 17, No. 2, 395–404, 2009.
2. Gagné, M. and R. Kashyap, "Demonstration of a 3 mW threshold Er-doped random fiber laser based on a unique fiber Bragg grating," *Opt. Express*, Vol. 17, No. 21, 19067–19074, 2009.

High-performance Microcavity Optical Sensor Connected with a Waveguide

Shuai Liu¹, Zhiyuan Gu¹, Nan Zhang¹, Shumin Xiao², and Qinghai Song^{1,3}

¹Department of Electrical and Information Engineering, Shenzhen Graduate School
Harbin Institute of Technology, Shenzhen 518055, China

²Department of Material Science and Engineering, Shenzhen Graduate School
Harbin Institute of Technology, Shenzhen 518055, China

³State Key Laboratory on Tunable Laser Technology, Institute of Opto-Electronics
Harbin Institute of Technology, Harbin 158015, China

Abstract— In this letter, we have numerically demonstrated a high-performance microcavity sensor which is connected with a waveguide directly. With input light and output light transmitting in the same waveguide, we propose a robust direct coupling mechanism of the microcavity. For a circular microcavity with a diameter of 4 μm and effective refractive index of 3.3, our numerical results show that the coupled modes are excited and more than 10^6 Q -factor is calculated from the transmission spectrum. Dramatically, the spectrum shows a Fano-shape resonance at specific wavelength. Using the Fano resonance, we detected a refractive index change on the order 10^{-5} and a nanoparticle with radius 5 nm. What's more, the sensor is insensitive to waveguide width and refractive index.

1. INTRODUCTION

Highly performed sensors have been an active research area for their widely applications in biological detection and environment monitoring. The early detection of viral particles responsible for human fatal diseases makes the prevention, diagnosis, and control possible. Though labelling detection method has made excellent achievements in this area, there are also problems with its detection mechanism. The labels may produce some other unknown signals and at some time the labels can be hardly conjugated with the target sample, which limits the experiment's scope. It is evident that there is a great need to label-free detection.

Whispering-gallery-mode (WGM) optical microcavities have been proposed as a prominent example to achieve high-precision detection in real-time and label-free manner, for their compact size, small mode volume, and ultrahigh Q factors ($Q \sim \omega t$, ω is the angular frequency and t is the lifetime) [1]. In the past two decades, high- Q whispering-gallery-mode resonators have shown remarkable detection limit and been used in various important applications, e.g., the detection of protein, DNA, single molecule [2–5] and so on. What's more, the modes can be excited in various geometries and materials, such as microsphere [6], cylinder [7], microring [8], and microtoroid [9] with refractive index ranging from 1.4 to 3.5. However, both of these sensors need a tapered-fiber to excite the high- Q WGMs by means of coupling light evanescently. This means the distance between the tapered-fiber and microcavity should be precisely controlled, usually less than a few hundred nanometers, and unfortunately the distance is sensitive to environmental disturbance.

2. DISCUSSION

In this letter, we report a new direct coupling mechanism to excite high- Q WGMs of the microcavity without using the tapered-fiber. By connecting a waveguide to microdisk directly, we show that the light can easily couple in the microcavity, excite the high- Q modes, and the corresponding detection signals couple out through the same in-put waveguide. In a small microcavity with 4- μm radius, our numerical results demonstrate detection of 10^{-5} refractive index change of the surrounding medium and single nanoparticle as small as 5 nm in radius. As the thicknesses are usually much smaller than their in-plane sizes, the microdisks are treated as two-dimensional objects by applying effective index of refraction n . The cavity studied here is schematically shown in Fig. 1(a). It is a circular cavity in radius R connected with a waveguide with width w . The emissions from such structure have been thoroughly studied in microlasers and unidirectional outputs along the waveguide are reported for the relative long-lived resonances. In principle, the unidirectional emissions and high output efficiencies do make sense. At the joint position, the TIR is totally broken. Thus the leakage along the waveguide is orders of magnitude larger than the evanescent tunneling and dominates the far field patterns.

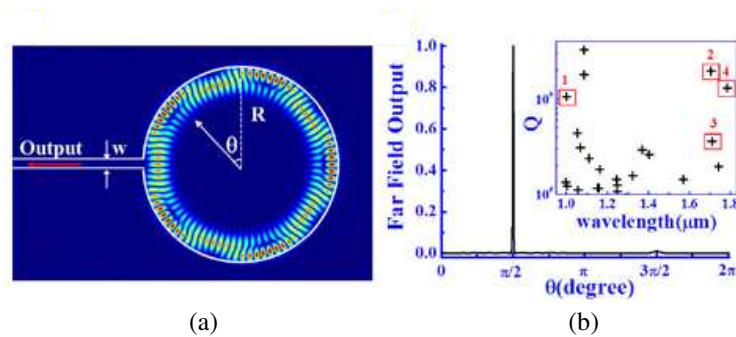


Figure 1: (a) The schematic picture of waveguide connected microdisk. $R = 4 \mu\text{m}$, $w = 300 \text{ nm}$. (b) The normalized far-field output at wavelength 1703.39 nm with Q factor marked as 2 and electric field pattern in Fig. 1(a). The picture inset (b) is the calculated quality factors more than 2×10^5 at different wavelengths ranging from $1 \mu\text{m}$ to $1.8 \mu\text{m}$.

Figure 1(b) is an example of far field output pattern of the microdisk-waveguide system and the corresponding electric field distribution is shown in Fig. 1(a) at wavelength 1703.39 nm . By exciting the high- Q modes in active devices, unidirectional outputs can be easily demonstrated. In consideration of time reversal symmetry, it is natural to think whether the high- Q modes can be efficiently excited with input light couples in through the waveguide. Below we will show that this conceive is actually true.

The microdisk-waveguide systems are numerically calculated with the Finite Element Method (Comsol Multiphysics 3.5a). Here we set the effective refractive index $n = 3.3$ (GaAs) for transverse magnetic (TM, M is in plane) polarization and ignore the material dispersion. The microdisk with radius $R = 4 \mu\text{m}$ and waveguide width $w = 0.3 \mu\text{m}$ is surrounded by air ($n = 1$). Fig. 1(b) illustrates quality factors more than 10^5 of the microdisk-waveguide systems with wavelength ranging from $1 \mu\text{m}$ to $1.8 \mu\text{m}$. Both of these modes are simulated with Comsol 3.5a eigenvalue study. We take four relative high- Q modes (marked as red rectangle 1-4) at wavelength 999.03 nm , 1703.40 nm , 1708.77 nm , and 1783.35 nm , respectively. To testify our conceive, we launch light at the waveguide around these mentioned resonance wavelengths. The light signals propagate along the waveguide and couple in the microdisk directly without using tapered-fiber. At the same time, we calculate the reflection spectrum taken at the plane marked as the dashed line in Fig. 2(e).

The normalized reflection spectrums shown in Figs. 2(a)–(d) are calculated by the reflective Poynting vector in the waveguide divided by total incident Poynting vector without the microdisk. From these spectrums, four peaks marked as red rectangle 1–4 can be easily found, which are 0.78, 0.91, 0.97, and 0.91, respectively. And the corresponding electric field patterns are shown in Fig. 2(e). The surprisingly high reflection efficiency means that almost all of the signals on resonance can easily couple out through the waveguide. In addition, the calculated Q ($Q \sim \lambda/\Delta\lambda$, λ is the resonance wavelength and $\Delta\lambda$ is the FWHM) factors are also very high, which are almost

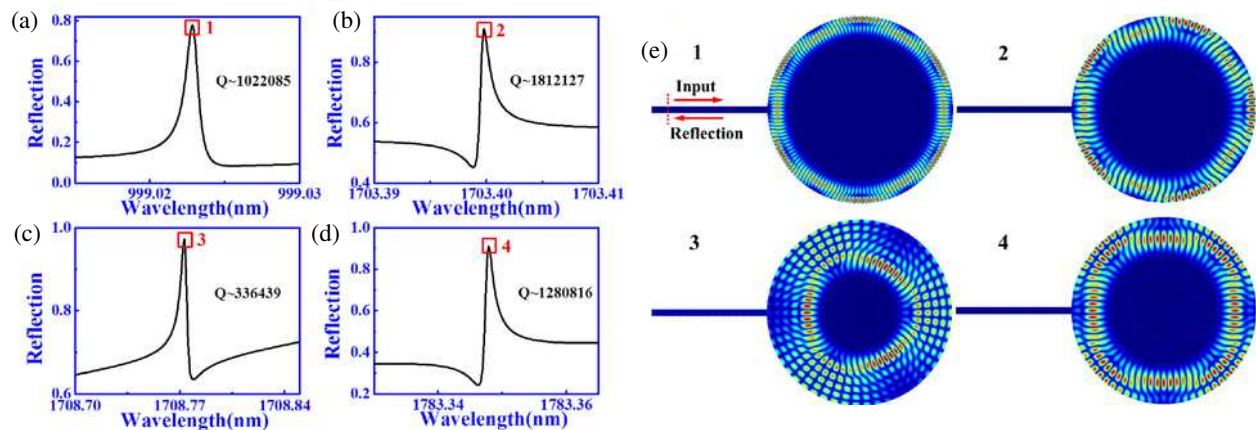


Figure 2: Calculated reflection spectra around 999.03 nm in (a), 1703.40 nm in (b), 1708.77 nm in (c), and 1783.35 nm in (d). (e) The electric field patterns of resonances marked as 1–4 in Figs. 2(a)–(d), respectively.

the same as the tapered-fiber coupling systems. So both of the resonance wavelengths, Q factors, and field patterns agree with the eigenvalue results in Fig. 1(b), demonstrating our assumption. This reveals that the direct coupling mechanism of microdisk-waveguide systems can easily excite the high Q modes as well as with high reflection efficiency, which is ‘easy come, easy go’.

The formation of high Q resonances and high reflection efficiency can be understood as the following. Below, we will take the mode 2 with the highest Q factor in Fig. 2(b) for example. Once signals are coupled to the microdisk, three different leakages occur, which are the coupling to waveguide, refractive leakage, and the scattering at the junction of microdisk and waveguide. When the wavelength close to 1703.40 nm, it is easy to see that the coupled resonance (see Fig. 2(e) marked as 2) has a pentagon-shape field pattern and is confined along period-5 stable islands. As the pentagon-shape resonance is independent to the connecting waveguide, the waveguide thus will not affect the total internal reflection within stable islands directly, making the high Q factor realized. This is also why the leakage by refractive escape is orders of magnitude smaller than the coupling to waveguide. Therefore, more than 90% signals on resonance reflect along the connecting waveguide.

In addition to the high reflection efficiencies and high Q factors at many resonant wavelengths in Fig. 2, this surprising direct coupling mechanism is also robust to the waveguide with and refractive index of microdisk, which are essential for practical fabrications. The results are summarized in Fig. 3. We can see that the reflection is kept at a high value around 90% when the width of waveguide is changed from 0.1 μm to 0.5 μm (see Fig. 3(a)). Meanwhile, the high reflection efficiency ($> 90\%$) can also be obtained with a wide range of refractive index from $n = 2.7$ to $n = 3.5$ (Fig. 4(c)). The same as reflection efficiency, the microdisk-waveguide system with different waveguide width and refractive index also demonstrates relative high Q factors shown in Fig. 3(b) and Fig. 3(d), where all of them are more than 10^5 . This means that the materials and their dispersions won't smear out the coupling mechanism.

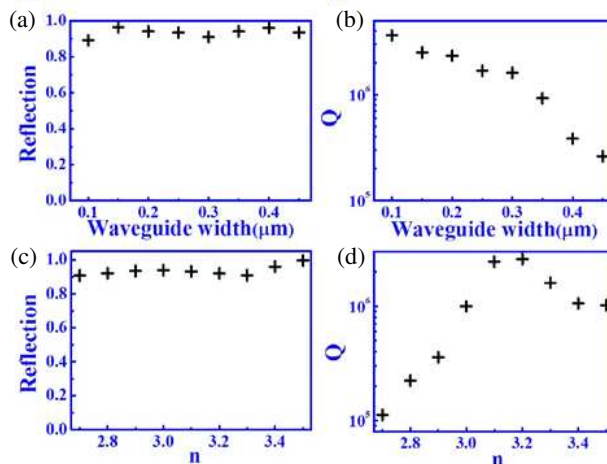


Figure 3: The maximum of reflection versus different waveguide width in (a) and refractive index in (c). (b) and (d) are the calculated quality factors versus different waveguide width and refractive index, respectively.

The resonant wavelengths of microcavity depend on the effective refractive index, which can be affected by, e.g., refractive index change of the surrounding medium and nanoparticle attached to its surface. Detection of such an effective index change can be made by either observing the shift of spectra or monitoring the change of light intensity from the output at a fixed wavelength. More interestingly, it is found that the lineshape in Fig. 2(b) is asymmetric Fano-shape resonance. The steep slope between minimum and maximal reflection makes the microdisk-waveguide system a natural highly sensitive sensor. Next, we will focus this reflection spectrum and test its detection properties.

Figure 4(a) shows the reflection spectrum of the sensor with different surrounding environment refractive indices from 1 to 1.0003 with step of 10^{-4} . The curves demonstrate an obvious red shift as the refractive index increases. Based on Fig. 4(a), the normalized reflective intensity variation at a fixed wavelength (1703.3998 nm) is plotted in Fig. 4(b) as a function of refractive index change Δn . We can see that a 10^{-5} change in refractive index can lead to almost 0.03 variation of reflective intensity. Such a high intensity variation means that Δn can be easily detected.

In addition, to test the properties of nanoparticle detection, we attach a single nanoparticle

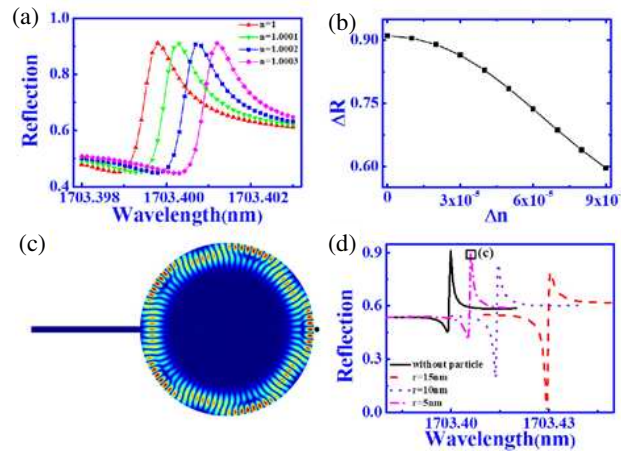


Figure 4: (a) Reflection spectra for different refractive indices n of the surrounding medium. (b) Reflection variation versus Δn at fixed wavelength of 1703.3998 nm. (c) Schematic picture of nanoparticle detection system. All the parameters are the same as Fig. 1(a). Single nanoparticle with refractive index $n_p = 3$ and radius r is attached to the microdisk at $\theta = 3/2\pi$. The electric field corresponds to the peak (marked as (c) in Fig. 4(d)) with $r = 5$ nm. (d) The calculated reflection spectra with different particle radius r .

with refractive index $n_p = 3$ to the microdisk. The schematic picture is shown in Fig. 4(c). All the parameters are the same as Fig. 1(a) except a nanoparticle is attached to the microdisk at $\theta = 3/2\pi$. Fig. 4(d) depicts the measured reflection spectrum with different particle radius r . For comparison, the black solid line in Fig. 4(d) is the reflection without nanoparticle. As a single particle in radius $r = 5$ nm is attached on the microdisk, the spectrum shows a red shift (the dash-dotted line) with both the maximal and minimal reflection decrease. And this trend keeps as the particle radius increases, demonstrating the effective nanoparticle size sensing.

3. CONCLUSION

We have demonstrated a direct coupling optical sensor which is robust to waveguide width and refractive index. Our numerical results show that light can be either easily coupled in the microcavity or easily coupled out through the same waveguide. Refractive index change on the order 10^{-5} and single nanoparticle with radius 5 nm can be detected with this sensor.

REFERENCES

1. Vahala, K. J., "Optical microcavities," *Nature*, Vol. 424, 839–846, 2003.
2. Vollmer, F. and S. Arnold, "Whispering-gallery-mode biosensing: Label-free detection down to single molecules," *Nature Methods*, Vol. 5, No. 7, 591–596, 2008.
3. Vollmer, F., D. Braun, A. Libchaber, et al., "Protein detection by optical shift of a resonant microcavity," *Applied Physics Letters*, Vol. 80, No. 21, 4057–4059, 2002.
4. Arnold, S., M. Khoshshima, I. Teraoka, et al., "Shift of whispering-gallery modes in microspheres by protein adsorption," *Optics Letters*, Vol. 28, No. 4, 272–274, 2003.
5. Vollmer, F. and L. Yang, "Review Label-free detection with high- Q microcavities: A review of biosensing mechanisms for integrated devices," *Nanophotonics*, Vol. 1, Nos. 3–4, 267–291, 2012.
6. Cai, M., O. Painter, and K. J. Vahala, "Observation of critical coupling in a fiber taper to a silica-microsphere whispering-gallery mode system," *Phys. Rev. Lett.*, Vol. 85, 74, 2000.
7. Li, H. and X. Fan, "Characterization of sensing capability of optofluidic ring resonator biosensors," *Applied Physics Letters*, Vol. 97, No. 1, 011105, 2010.
8. Yalcin, A., K. C. Popat, J. C. Aldridge, et al., "Optical sensing of biomolecules using microring resonators," *IEEE Journal of Selected Topics in Quantum Electronics*, Vol. 12, No. 1, 148–155, 2006.
9. Monifi, F., Ş. K. Özdemir, and L. Yang, "Tunable add-drop filter using an active whispering gallery mode microcavity," *Applied Physics Letters*, Vol. 103, No. 18, 181103, 2013.

Thermally-tuned Silicon Double Ring Resonator for External Cavity Tunable Laser

Lei Ding, Xianxin Jiang, Chang Yang, and Jian-Jun He

State Key Laboratory of Modern Optical Instrumentation
Centre for Integrated Optoelectronics, Department of Optical Engineering
Zhejiang University, Hangzhou 310027, China

Abstract— We designed and fabricated a thermo-optic tunable filter based on silicon double ring resonator for external cavity laser. The footprint of the device is $\sim 700 \mu\text{m} \times 400 \mu\text{m}$. The tuning range is about 16 nm and the tuning efficiency of the device is estimated to be about 0.56 nm/mW, owing to the Vernier effect.

1. INTRODUCTION

Silicon photonics has been considered a promising technology for 21st century [1]. To date, silicon photonic devices can be wafer scale produced on a silicon-on-insulator (SOI) platform, which are compatible with standard complementary metal oxide semiconductor (CMOS) technology [1–6]. SOI materials system has the inherent high-index contrast between the Si-SiO₂ ($\Delta n = 2.03$) with strong light confinement in the Si core [1, 2]. The high Δn permits to sharp bends and small sizes, thus, allowing the miniaturization of passive optical devices and leading to high-density photonic integrated circuits. The SOI optical devices offer the potential for integration with CMOS electronics in order to achieve monolithically integrated optoelectronic systems [3].

For the past decade, many research groups have demonstrated many silicon devices to process optical signals, such as coupling systems from optical fibers to optical waveguides, tunable filters and high-speed modulators [4]. These devices have been mainly focused on two major physical effects, namely, electro-optic and thermo-optic effects [5]. The electro-optic effect has the advantage of low-loss and low-power with relatively fast response time, but it required large drive voltages and tuning range is small. On the other hand, the thermo-optic effect is inherently lossless, which can be utilized to efficiently tune devices with negligible insertion loss. In addition, silicon has a relatively high thermo-optic coefficient ($1.86 \times 10^{-4}/\text{K}$) [6], which allows for wavelength tuning and switching with relatively low power. The only shortcoming of these devices is slow response time [7]. Heating of photonic devices for the utilization of the thermo-optic effect has been widely used with integration of micro-heater close to the silicon device, which can reduce the optical absorption by the metal [5].

In this paper, we present a thermally-tuned silicon double ring resonator (DRR) based on Vernier effect for hybridly integrated external cavity tunable laser. It contains cascaded double rings on SOI with micro-heaters on the top, as schematically depicted in Figure 1. The Vernier effect is an effective approach to realizing a wide tuning range.

This paper is organized as follows. In the second section, the thermal tuning of the device is mathematically analyzed. In the Section 3, the fabrication of the device is discussed. In the Section 4, the external cavity tunable laser employing the double-ring filter is presented. Finally, some conclusions are drawn in Section 5.

2. THERMAL-TUNING DESIGN

In our design, we used the thermo-optic effect in silicon, which has a relatively high thermo-optic coefficient, causing a large shift of the resonant wavelength. A change of the effective index Δn_{eff} results in a shift of the resonant wavelength $\Delta\lambda = \lambda \cdot n_{eff}/n_g$ [8]. Here, n_{eff} , n_g are the effective refractive index and the group index, respectively. The height and width of the waveguide are designed to be 250 nm and 500 nm, respectively, which was chosen for TE single-mode operation at wavelength = 1550 nm. For one ring resonator, the variation of effective refractive index of about 0.02 is achieved when the temperature changes by 100 K, corresponding to a wavelength shift in the order of 8.4 nm, which is shown in Figure 2.

To achieve thermo-optic effect, we used micro-heater. The structure of the micro-heater is shown before in Figure 1. Here, the micro-heater is placed on top of the waveguide and is separated from the waveguide by a SiO₂ upper-cladding layer, which can reduce the optical loss. The micro-heater

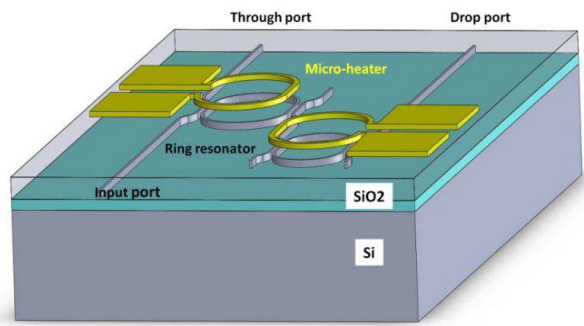


Figure 1: Schematic demonstration of the device.

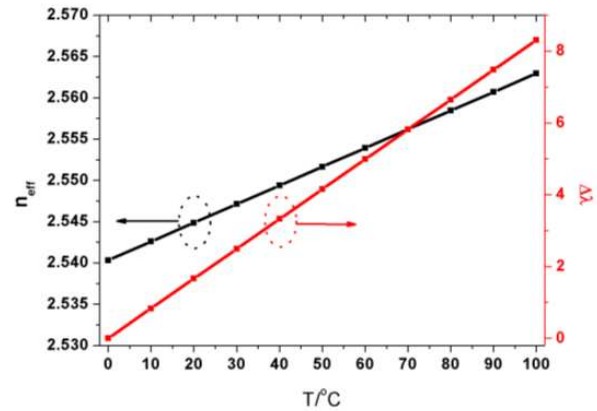


Figure 2: Variation of effective refractive index and resonant wavelength shift when the temperature changes.

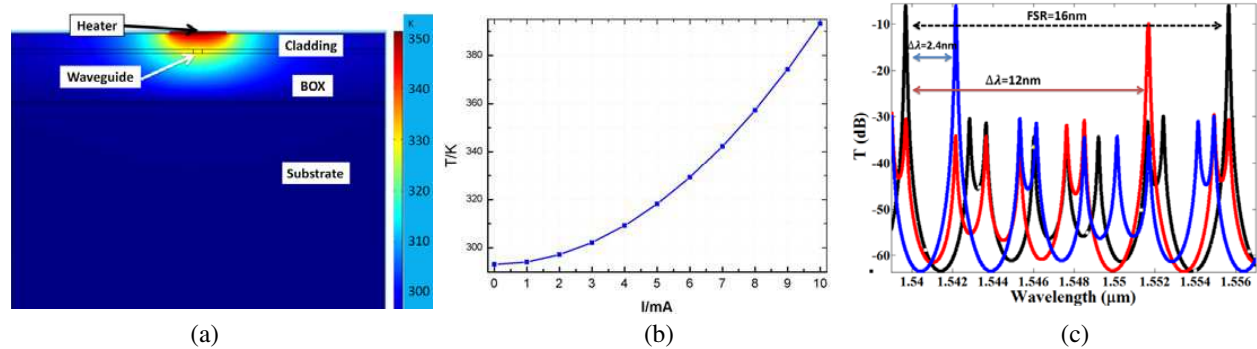


Figure 3: (a) Temperature distribution at the cross-section of the waveguide when an electrical current of 6 mA is applied on the micro-heater. (b) Temperature variation of the waveguide when applying current in the micro-heater. (c) The resonant wavelength shift when different currents are applied on the micro-heaters.

has Ω shape, which conducts most of the heat along with the ring waveguide and confines the heat to reduce thermal crosstalk. Heat transport in the device is numerically simulated based on the heat-transport equation, as follows [5]:

$$\nabla(-k\nabla T) + \rho c \frac{\partial T}{\partial t} = q_s \quad (1)$$

Here, k , c and ρ are the thermal conductivity, heat capacity and density of the material, respectively; q_s and T are the density of the heat power generation and the temperature, respectively. Using the finite-element method, the temperature distribution in the waveguide is calculated with applying 6 mA current as shown in Figure 3(a). When applying different current in the micro-heaters, a temperature variation is induced in the waveguide as shown in Figure 3(b). The free spectral ranges (FSRs) of the two racetrack ring resonators are designed to be 400 GHz and 500 GHz, respectively. In Figure 3(c), the black line is the transmission spectrum under room temperature when no electrical current is applied. The FSR of the double-ring filter is 16 nm. When 6 mA current is applied in the micro-heaters of the two resonators simultaneously, the resonant wavelength shifts by 2.4 nm, as shown by the blue line. When 6 mA current is applied in the micro-heater of the larger resonator alone, the resonant wavelength shift is 12 nm, as shown in the red line. The wavelength tuning is amplified five times by the Vernier effect. The tuning range is limited by the FSR, which is about 16 nm.

The resistance of micro-heaters of the double rings are 500 Ω , 590 Ω , respectively. When 6 mA is applied on each of the two micro-heaters, the total power consumption is about 39.2 mW and the tuning range is the same as the case with one ring resonator. The tuning efficiency in this case is about 0.06 nm/mW. With 6 mA is applied on the larger ring alone, the total power consumption is only 21.3 mW and the tuning efficiency increases to about 0.56 nm/mW, owing to the Vernier

effect.

3. FABRICATION

The device in this work was fabricated on SOI wafer with a 250 nm silicon top layer and a 3 μm buried oxide (BOX) layer. The fabrication process comprises three steps with three different photolithographic mask layers: a waveguide layer and two metal layers. The waveguide layer was fabricated by means of electron-beam lithography using ma-N 2405 photoresist to pattern the samples on the SiO_2 mask, followed by dry etching of SiO_2 and Si. Figure 4(a) shows the cross-section of the etched waveguide. The total height includes the waveguide height and the thickness of the SiO_2 mask. The ring structure and the coupler section are shown in Figure 4(b). After etching and photoresist cleaning, a one-micron-thick layer of silicon dioxide is deposited as an upper-cladding layer by plasma enhanced chemical vapor deposition (PECVD).

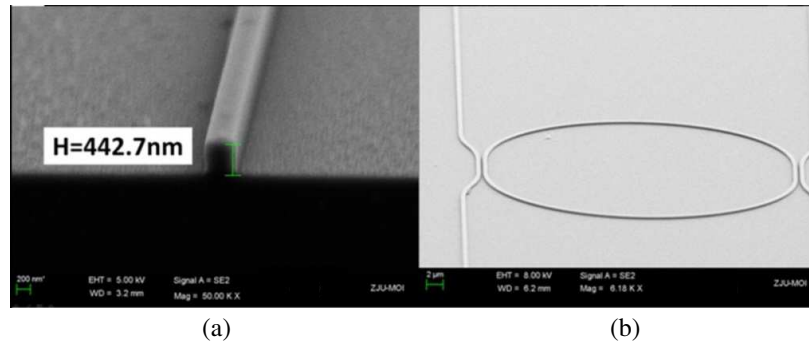


Figure 4: SEM images of (a) the waveguide cross-section and (b) the ring structure and the coupler section.

The metal was deposited in two steps using contact photolithography. The first step was photolithography of the micro-heaters and 100 nm Nichrome metal deposition, followed by lift-off. The second step consisted of photolithography of contact pads and Ti/Pt/Au (20 nm/20 nm/400 nm) deposition, followed by second lift-off. Table 1 shows the design parameters used in the fabrication of the device. The footprint of the device is $\sim 700 \mu\text{m} \times 400 \mu\text{m}$.

Table 1: Designed parameters for the fabricated device.

Waveguide cross-section	Width		Height
	500 nm		250 nm
Coupling regions	Gap		Coupling length
	300 nm		16 μm
Radii	R_1		R_2
	17.5 μm		23.2 μm
Micro-heaters	Material	Thickness	Width
	Nichrome	100 nm	3 μm
Contact pads	Material	Thickness	Width
	Ti/Pt/Au	20 nm/20 nm/400 nm	150 μm

4. EXTERNAL CAVITY LASER

Using this double ring resonator as a wavelength-tunable filter, a III-V/SOI external cavity tunable laser with narrow emission linewidth is designed, which is schematically shown in Figure 5. The laser consists of an InP based gain chip, the DRR and a free-space transmission section. The latter uses graded-index lenses to couple the gain chip with the DRR, constructing a long external cavity. The double ring resonator is used for laser mode selection. And the laser emits from the front facet of the gain chip. The fabrication of the device is currently in progress and the results will be reported later.

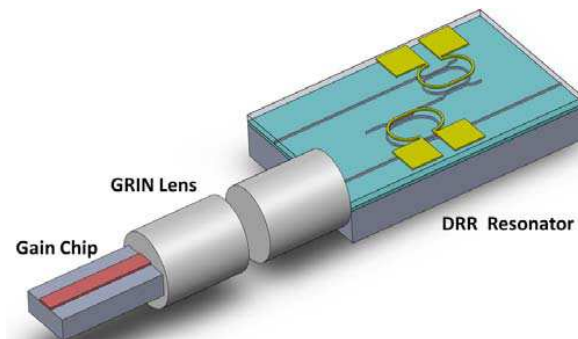


Figure 5: Schematic diagram of external cavity tunable laser.

5. CONCLUSION

In this work, numerical simulation of heat transport in micro-heater is presented for the study of thermal tuning of the silicon double ring resonator. The tuning efficiency of the device is estimated to be about 0.56 nm/mW, owing to the Vernier effect. The fabrication process of the device is discussed, and a design concept of external cavity tunable laser is presented.

REFERENCES

1. Roelkens, G., J. van Campenhout, J. Brouckaert, et al., "III-V/Si photonics by die-to-wafer bonding," *Materials Today*, Vol. 10, No. 7, 36–43, 2007.
2. Jiang, X., J. Ye, J. Zou, et al., "Cascaded silicon-on-insulator double-ring sensors operating in high-sensitivity transverse-magnetic mode," *Optics Letters*, Vol. 38, No. 8, 1349–1351, 2013.
3. Fegadolli, W. S., L. Feng, M. M. U. Rahman, et al., "Experimental demonstration of a reconfigurable silicon thermo-optical device based on spectral tuning of ring resonators for optical signal processing," *Optics Express*, Vol. 22, No. 3, 3425–3431, 2014.
4. Fegadolli, W. S., G. Vargas, X. Wang, et al., "Reconfigurable silicon thermo-optical ring resonator switch based on Vernier effect control," *Optics Express*, Vol. 20, No. 13, 14722–14733, 2012.
5. Atabaki, A. H., E. Shah Hosseini, A. A. Eftekhar, et al., "Optimization of metallic microheaters for high-speed reconfigurable silicon photonics," *Optics Express*, Vol. 18, No. 17, 18312–18323, 2010.
6. Dong, P., W. Qian, H. Liang, et al., "Thermally tunable silicon racetrack resonators with ultralow tuning power," *Optics Express*, Vol. 18, No. 19, 20298–20304, 2010.
7. Geng, M., L. Jia, L. Zhang, et al., "Four-channel reconfigurable optical add-drop multiplexer based on photonic wire waveguide," *Optics Express*, Vol. 17, No. 7, 5502–5516, 2009.
8. Nawrocka, M. S., T. Liu, X. Wang, et al., "Tunable silicon microring resonator with wide free spectral range," *Applied Physics Letters*, Vol. 89, No. 7, 071110–071110-3, 2006.

Homogenizations of Micropolar Elastic Metamaterial Using Field Averaging

C. N. Weng and T. Chen

Department of Civil Engineering, National Cheng Kung University, Tainan, Taiwan

Abstract— In this paper, we introduce an approximation in homogenization of a three dimensional elastic metamaterials by a homogeneous equivalent micropolar media whose effective parameters are determined by average theory. Formulations of averaged physical fields over the representative volume element (RVE) together with dispersion relations of plane wave propagation are presented in the text.

1. INTRODUCTION

Micropolar elasticity, also called Cosserat elasticity [1, 2], is a generalized continuum theory. In contrast to classical continuum, each material point in a micropolar medium has six degree of freedom, which often be used to describe solid materials with intrinsic microstructure effects like bone [3], porous material [4–6], brick structure [7], granular materials [8, 9] and many others. Recently, inspired by electromagnetic metamaterials [10], the research of elastic metamaterials have attracted considerable interest due to potential applications in manipulating the propagation of elastic waves [11–17]. Among them, a few reported works focus on the design of chiral microstructures which can enhance rotational resonance and thus achieve double negative effective parameters [14, 15]. The rotational motion has been observed as a fundamental mode of elastic wave propagation in phononic crystals [18–20]. However, less attention has been paid to the issues of effective micropolar constants in model analysis, the conventional effective medium theories for elastodynamics put more emphasis on Cauchy solids [21, 22] or Willis constitutive relation [23, 24]. In this paper, we attempt to propose an approximation in homogenization of heterogeneous elastic metamaterials by a homogeneous equivalent micropolar media whose effective parameters are determined by average theory. It is convince that micropolar theory is appropriate to analyze the metamaterial model than traditional continuum theory due to the complex local resonance. We illustrate a simple model with cuboid periodically arranged structures to demonstrate the calculation processes of effective parameters and the dispersion relation of plane wave propagation. Comparing to other literatures which was devoted to the modeling of two dimensional micropolar medium [7, 25–27]. the presented methodology can be applied to homogenize the three dimensional periodic structures with unit cells having micropolar effects.

2. BASIC EQUATIONS OF MICROPOLAR ELASTICITY

The key difference between a micro-polar and Cauchy medium is that each material point can not only translate but rotate independently. Additional degrees of freedom, micro-rotations ϕ_i , are introduced in linear theory of micropolar elasticity. The kinematics can be expressed as

$$\varepsilon_{ij} = u_{j,i} - e_{ijk}\phi_k, \quad \kappa_{ij} = \phi_{j,i}, \quad (1)$$

where ε_{ij} , κ_{ij} and e_{ijk} are the strain, curvature and permutation tensors, respectively. The equations of motion are

$$\sigma_{ji,j} = \rho\ddot{u}_i, \quad \mu_{ji,j} + e_{ijk}\sigma_{jk} = J\ddot{\phi}_i, \quad (2)$$

where σ_{ij} and μ_{ij} represent stress and couple-stress tensors, respectively. ρ and J are the density and rotational inertia, respectively. For a centro-symmetric micropolar medium, the constitutive relations are given as

$$\sigma_{ij} = C_{ijkl}\varepsilon_{kl}, \quad \mu_{ij} = D_{ijkl}\kappa_{kl}, \quad (3)$$

in which C_{ijkl} and D_{ijkl} are elastic tensors. It should be note that the tensor fields, ε_{ij} , κ_{ij} , σ_{ij} and μ_{ij} , are usually asymmetric in micropolar continuums, thus the constitutive moduli tensors, C_{ijkl} and D_{ijkl} , no longer possess minor symmetries but fulfill the major symmetric property. It is mention that the number of independent components of C_{ijkl} (or D_{ijkl}) is 45 for general anisotropic micropolar solids and reduces to 3 for isotropic cases.

3. HOMOGENIZATION OF MICROPOLAR MEDIUM

In this section we present a numerical homogenization procedure that relates the microscopic local fields like displacement and stresses to macroscopic quantities like rotation and couple stress. Apart from traditional models, we assume that the homogenized model behaves as a micropolar solid at macroscopic scale while each constituent remains a classical Cauchy continuum on the microscale. Consider a 3D metamaterial structure sketched in Fig. 1 whose unit cell is a rectangular cuboid with sides d_1 , d_2 and d_3 . Due to the translational symmetry, the Bloch's theorem and periodic boundary conditions are applied in our analysis. To describe the overall behavior of the model, we utilize the concept of field homogenization. The averaging process of physical fields are applied over the unit cell as

$$\bar{u}_j = \frac{1}{V} \int_V u_j dv, \quad \bar{\phi}_j = \frac{1}{V} \int_V \phi_j dv, \quad (4)$$

$$\bar{\varepsilon}_{ij} = \frac{1}{V} \int_V \varepsilon_{ij}(\vec{x}) dv, \quad \bar{\kappa}_{ij} = \frac{1}{V} \int_V \kappa_{ij}(\vec{x}) dv, \quad (5)$$

$$\bar{\sigma}_{ij} = \frac{1}{V} \int_V \sigma_{ij}(\vec{x}) dv, \quad \bar{\mu}_{ij} = \frac{1}{V} \int_V \mu_{ij}(\vec{x}) dv, \quad (6)$$

where V is the volume of the unit cell. The over bar denotes the averaged quantities. We mention that the integration of microrotations and couple stresses cannot be directly computed due to our original assumptions so that alternative approximation is demanded. In this model, the average microrotations can be approached by integrating boundary displacements as

$$\begin{aligned} \bar{\phi}_1 &= \frac{1}{8V} \int_{-\frac{d_1}{2}}^{\frac{d_1}{2}} \left(\int_{-\frac{d_3}{2}}^{\frac{d_3}{2}} u_3|_{x_2=\frac{d_2}{2}} dx_3 - \int_{-\frac{d_2}{2}}^{\frac{d_2}{2}} u_2|_{x_3=\frac{d_3}{2}} dx_2 \right. \\ &\quad \left. - \int_{-\frac{d_3}{2}}^{\frac{d_3}{2}} u_3|_{x_2=-\frac{d_2}{2}} dx_3 + \int_{-\frac{d_2}{2}}^{\frac{d_2}{2}} u_2|_{x_3=-\frac{d_3}{2}} dx_2 \right) dx_1, \\ \bar{\phi}_2 &= \frac{1}{8V} \int_{-\frac{d_2}{2}}^{\frac{d_2}{2}} \left(\int_{-\frac{d_1}{2}}^{\frac{d_1}{2}} u_1|_{x_3=\frac{d_3}{2}} dx_1 - \int_{-\frac{d_3}{2}}^{\frac{d_3}{2}} u_3|_{x_1=\frac{d_1}{2}} dx_3 \right. \\ &\quad \left. - \int_{-\frac{d_1}{2}}^{\frac{d_1}{2}} u_1|_{x_3=-\frac{d_3}{2}} dx_1 + \int_{-\frac{d_3}{2}}^{\frac{d_3}{2}} u_3|_{x_1=-\frac{d_1}{2}} dx_3 \right) dx_2, \\ \bar{\phi}_3 &= \frac{1}{8V} \int_{-\frac{d_3}{2}}^{\frac{d_3}{2}} \left(\int_{-\frac{d_2}{2}}^{\frac{d_2}{2}} u_2|_{x_1=\frac{d_1}{2}} dx_2 - \int_{-\frac{d_1}{2}}^{\frac{d_1}{2}} u_1|_{x_2=\frac{d_1}{2}} dx_1 \right. \\ &\quad \left. - \int_{-\frac{d_2}{2}}^{\frac{d_2}{2}} u_2|_{x_1=-\frac{d_1}{2}} dx_2 + \int_{-\frac{d_1}{2}}^{\frac{d_1}{2}} u_1|_{x_2=-\frac{d_1}{2}} dx_1 \right) dx_3, \end{aligned} \quad (7)$$

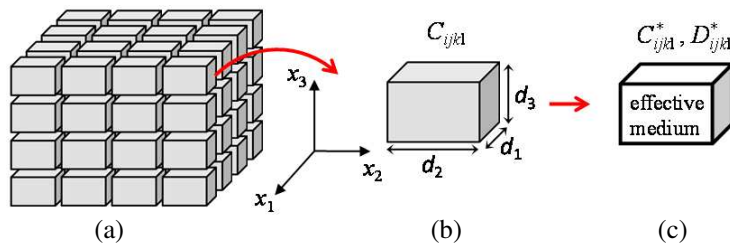


Figure 1: Illustrations of (a) 3D elastic metamaterial structure, (b) a unit cell and (c) effective model of the metamaterial. The unit cell is a traditional Cauchy medium, whereas the effective model is assumed to be a micropolar medium.

and thus Eq. (5) can be rewritten in the following form

$$\bar{\varepsilon}_{ij} = \frac{1}{V} \int_V \frac{\partial u_j}{\partial x_i} - e_{ijk} \phi_k dv = \frac{1}{V} \oint_S u_j n_i ds - e_{ijk} \frac{1}{V} \int_V \phi_k dv = \frac{1}{V} \oint_S u_j n_i ds - e_{ijk} \bar{\phi}_k, \quad (8)$$

$$\bar{\kappa}_{ij} = \frac{1}{V} \int_V \frac{\partial \phi_j}{\partial x_i} dv = \frac{1}{V} \oint_S \phi_j n_i ds = \frac{2\bar{\phi}_j}{d_i}. \quad (9)$$

Applying divergence theorem to Eq. (6) and combining Eq. (2) leads to

$$\begin{aligned} \bar{\sigma}_{ij} &= \frac{1}{V} \int_V (\sigma_{kj} x_i)_{,k} - \rho \ddot{u}_j x_i dv = \frac{1}{V} \left(\oint_S \sigma_{kj} n_k x_i ds - \int_V \rho \ddot{u}_j x_i dv \right) \\ &= \frac{1}{V} \left(d_I \int_S \sigma_{ij} ds_I - \int_V \rho \ddot{u}_j x_i dv \right), \end{aligned} \quad (10)$$

$$\begin{aligned} \bar{\mu}_{ij} &= \frac{1}{V} \int_V (\mu_{kj} x_i)_{,k} + \epsilon_{jkl} \sigma_{kl} x_i - J \ddot{\phi}_j x_i dv = \frac{1}{V} \left[\oint_S (\mu_{kj} x_i) n_k ds + \epsilon_{jkl} \int_V \sigma_{kl} x_i dv - \int_V J \ddot{\phi}_j x_i dv \right], \\ &= \frac{1}{V} \left(d_I \int_S \mu_{ij} ds_I + \epsilon_{jkl} \int_V \sigma_{kl} x_i dv - \int_V J \ddot{\phi}_j x_i dv \right). \end{aligned} \quad (11)$$

in which the capital index indicates the same number as its lower case but without summation, and s_I denote the plane with unit normal vector $n_i = 1$. The surface integration of the above equations can be reduced from over enclosed surfaces to a single plane due to each face of the proposed cuboid is normal to the coordinate axis. We introduce $m_j = m_{kj} n_k$ is the couple stress vector acting on a surface for a micropolar medium. Integrating the vector m_j over the surface normal to n_k is the total moment on that surface,

$$M_j^{(s)} = \int_s m_j ds. \quad (12)$$

In classical elasticity for Cauchy medium, the moments on a plane are caused by the non-uniformity of stress distributions, which can be expressed as

$$\begin{cases} M^{\parallel} = M_j^{(i)} = \int_S e_{ijk} \sigma_{II} x_k ds_I, \\ M^{\perp} = M_i^{(i)} = \int_S e_{ijk} \sigma_{ij} x_k ds_I, \end{cases} \quad (13)$$

in which M^{\parallel} and M^{\perp} are the parallel and perpendicular components of moment on the plane, respectively. We may assume that the moments of homogenized model and the unit cell of meta-material are equivalent on the corresponding planes, hence the first term in the parentheses of Eq. (11) can be further computed and Eq. (11) turns to

$$\bar{\mu}_{ij} = \begin{cases} \frac{1}{V} \left(d_I \int_S e_{ijk} \sigma_{II} x_k ds_I + \epsilon_{jkl} \int_V \sigma_{kl} x_i dv - \int_V J \ddot{\phi}_j x_i dv \right), & \text{for } i \neq j, \\ \frac{1}{V} \left(d_I \int_S e_{imk} \sigma_{ij} x_k ds_I + \epsilon_{jkl} \int_V \sigma_{kl} x_i dv - \int_V J \ddot{\phi}_j x_i dv \right), & \text{for } i = j. \end{cases} \quad (14)$$

Equations (8)–(10) and (14) establish the approximation of average strain, curvature, stress and couple stress from local displacements and stresses which can be conveniently obtained via numerical simulation such as FEM or others. According to these results, the effective parameters \mathbf{C}^* and \mathbf{D}^* could be obtained by solving the following equations

$$\bar{\sigma}_{ij} = C_{ijkl}^* \bar{\varepsilon}_{kl}, \quad \bar{\mu}_{ij} = D_{ijkl}^* \bar{\kappa}_{kl}, \quad (15)$$

while the effective mass density and rotational inertia are given by

$$\rho^{eff} = \frac{1}{V} \frac{F_k}{\ddot{u}_k} = \frac{1}{V} \frac{F_k}{-\omega^2 \bar{u}_k}, \quad J^{eff} = \frac{1}{V} \frac{M_k}{\ddot{\phi}_k} = \frac{1}{V} \frac{M_k}{-\omega^2 \bar{\phi}_k}, \quad (16)$$

where

$$F_k = \sum_s F_k^{(s)} = \frac{1}{V} \int_S \sigma_{jk} ds_j, \quad M_k = \sum_s M_k^{(s)} = \frac{1}{V} \int_S \mu_{jk} ds_j, \quad (17)$$

are the resultant force and moment, respectively. Note that if the independent components of \mathbf{C} or \mathbf{D} greater than 9, Eq. (15) will not sufficient to solve all material parameters unless extra conditions or constrains are taken into account.

4. PLANE WAVES IN MICROPOLAR MEDIA

Next we discuss the problems for wave propagation in micropolar media. Consider plane wave solutions

$$\begin{Bmatrix} u_i \\ \phi_i \end{Bmatrix} = \begin{Bmatrix} U_i \\ \Phi_i \end{Bmatrix} \exp[i(\mathbf{q} \cdot \mathbf{x} - \omega t)] = \begin{Bmatrix} U_i \\ \Phi_i \end{Bmatrix} \exp[i(q_1 x_1 + q_2 x_2 + q_3 x_3 - \omega t)], \quad (18)$$

where $U_i(\Phi_i)$ are the displacement(micro-rotation) amplitudes of the harmonic fields, whereas ω and \mathbf{q} are the incident frequency and wave vector, respectively. Substituting Eq. (18) and Eq. (3) into Eq. (2), we obtain

$$\begin{cases} C_{jikl} q_j q_k U_l - C_{jikl} \epsilon_{klm} q_j \Phi_m = \rho \omega^2 U_i, \\ D_{jikl} q_j q_k \Phi_l + \epsilon_{ijk} C_{jkmn} (q_m U_n - \epsilon_{mnp} \Phi_p) = J \omega^2 \Phi_i. \end{cases} \quad (19)$$

The above equations can be expanded in matrix form as

$$\begin{bmatrix} \Lambda_{3 \times 3} & \eta_{3 \times 3} \\ \xi_{3 \times 3} & \Xi_{3 \times 3} \end{bmatrix} \begin{Bmatrix} \mathbf{U}_{3 \times 1} \\ \Phi_{3 \times 1} \end{Bmatrix} = \begin{Bmatrix} \rho \omega^2 \mathbf{U} \\ J \omega^2 \Phi \end{Bmatrix}, \quad (20)$$

where

$$\begin{aligned} \Lambda_{il} &= q_j q_k C_{jikl}, & \eta_{im} &= q_j \epsilon_{klm} C_{jikl}, \\ \Xi_{il} &= q_j q_k D_{jikl} - \epsilon_{ijk} \epsilon_{mnl} C_{jkmn}, & \xi_{in} &= q_m \epsilon_{ijk} C_{jkmn}. \end{aligned} \quad (21)$$

A necessary and sufficient condition for the existence of a non-trivial solution is that the determinant of coefficient matrix vanishes, and it yields

$$\begin{vmatrix} \Lambda_{11} - \rho \omega^2 & \Lambda_{12} & \Lambda_{13} & \eta_{11} & \eta_{12} & \eta_{13} \\ \Lambda_{21} & \Lambda_{22} - \rho \omega^2 & \Lambda_{23} & \eta_{21} & \eta_{22} & \eta_{23} \\ \Lambda_{31} & \Lambda_{32} & \Lambda_{33} - \rho \omega^2 & \eta_{31} & \eta_{32} & \eta_{33} \\ \xi_{11} & \xi_{12} & \xi_{13} & \Xi_{11} - J \omega^2 & \Xi_{12} & \Xi_{13} \\ \xi_{21} & \xi_{22} & \xi_{23} & \Xi_{21} & \Xi_{22} - J \omega^2 & \Xi_{23} \\ \xi_{31} & \xi_{32} & \xi_{33} & \Xi_{31} & \Xi_{32} & \Xi_{33} - J \omega^2 \end{vmatrix} = 0. \quad (22)$$

The above equation is the dispersion relation of a general anisotropic micropolar medium. Generally, the eigenvalue problem must be solved numerically and all wave propagation modes are coupled. However, for certain high symmetric micropolar media, e.g., isotropic, the wave fields will be decoupled into pure modes so that the closed-form solutions could be obtained.

5. CONCLUSION

In conclusion, we have illustrated a numerical homogenization procedure of a 3D cuboid meta-material structure. Explicit formulations of averaged physical fields that relates the microscopic local fields to macroscopic quantities are presented in Eqs. (7)–(10) and (14). The general form of dispersion relations of anisotropic metamaterials is demonstrated as well. For further study, it is hope that the presented methodology could be extended to homogenize any periodic metamaterials with unit cells having chiral effects.

ACKNOWLEDGMENT

This work was supported by the Ministry of Science and Technology, Taiwan, under Contract No. NSC102-2221-E-006-151-MY3.

REFERENCES

1. Eringen, A. C., *Microcontinuum Field Theories: I. Foundations and Solids*, Limited, Springer, London, 2012.
2. Cosserat, E. and F. Cosserat, *Theorie Des Corps Deformables*, NASA, 1968.
3. Yang, J. F. C. and R. S. Lakes, "Transient study of couple stress effects in compact bone: Torsion," *J. Biomech. Eng.*, Vol. 103, No. 4, 275–279, 1981.
4. Lakes, R., "Size effects and micromechanics of a porous solid," *J. Mater. Sci.*, Vol. 18, No. 9, 2572–2580, 1983.

5. Lakes, R. S., “Experimental microelasticity of two porous solids,” *Int. J. Solids Struct.*, Vol. 22, No. 1, 55–63, 1986.
6. Diebels, S. and H. Steeb, “Stress and couple stress in foams,” *Comp. Mater. Sci.*, Vol. 28, No. 3–4, 714–722, 2003.
7. Sulem, J. and H.-B. Mühlhaus, “A continuum model for periodic two-dimensional block structures,” *Mech. Cohes. Frict. Mat.*, Vol. 2, No. 1, 31–46, 1997.
8. Kruyt, N. P., “Statics and kinematics of discrete Cosserat-type granular materials,” *Int. J. Solids Struct.*, Vol. 40, No. 3, 511–534, 2003.
9. Suiker, A. S. J., R. Borst, and C. S. Chang, “Micro-mechanical modelling of granular material. Part 1: Derivation of a second-gradient micro-polar constitutive theory,” *Acta Mech.*, Vol. 149, No. 1–4, 161–180, 2001.
10. Smith, D. R., W. J. Padilla, D. C. Vier, S. C. Nemat-Nasser, and S. Schultz, “Composite medium with simultaneously negative permeability and permittivity,” *Phys. Rev. Lett.*, Vol. 84, No. 18, 4184–4187, 2000.
11. Ding, Y., Z. Liu, C. Qiu, and J. Shi, “Metamaterial with simultaneously negative bulk modulus and mass density,” *Phys. Rev. Lett.*, Vol. 99, No. 9, 093904, 2007.
12. Fang, N., D. Xi, J. Xu, M. Ambati, W. Srituravanich, C. Sun, and X. Zhang, “Ultrasonic metamaterials with negative modulus,” *Nat. Mater.*, Vol. 5, No. 6, 452–456, 2006.
13. Lee, S. H., C. M. Park, Y. M. Seo, Z. G. Wang, and C. K. Kim, “Composite acoustic medium with simultaneously negative density and modulus,” *Phys. Rev. Lett.*, Vol. 104, No. 5, 054301, 2010.
14. Liu, X. N., G. K. Hu, G. L. Huang, and C. T. Sun, “An elastic metamaterial with simultaneously negative mass density and bulk modulus,” *Appl. Phys. Lett.*, Vol. 98, No. 25, 251907, 2011.
15. Liu, X. N., G. K. Hu, C. T. Sun, and G. L. Huang, “Wave propagation characterization and design of two-dimensional elastic chiral metacomposite,” *J. Sound Vib.*, Vol. 330, No. 11, 2536–2553, 2011.
16. Liu, Z., X. Zhang, Y. Mao, Y. Zhu, Z. Yang, C. T. Chan, and P. Sheng, “Locally resonant sonic materials,” *Science*, Vol. 289, No. 5485, 1734–1736, 2000.
17. Lai, Y., Y. Wu, P. Sheng, and Z. Q. Zhang, “Hybrid elastic solids,” *Nat. Mater.*, Vol. 10, No. 8, 620–624, 2011.
18. Peng, P., J. Mei, and Y. Wu, “Lumped model for rotational modes in phononic crystals,” *Phys. Rev. B*, Vol. 86, No. 13, 134304, 2012.
19. Zhao, H., Y. Liu, G. Wang, J. Wen, D. Yu, X. Han, and X. Wen, “Resonance modes and gap formation in a two-dimensional solid phononic crystal,” *Phys. Rev. B*, Vol. 72, No. 1, 012301, 2005.
20. Merkel, A., V. Tournat, and V. Gusev, “Experimental evidence of rotational elastic waves in granular phononic crystals,” *Phys. Rev. Lett.*, Vol. 107, No. 22, 225502, 2011.
21. Wu, Y., Y. Lai, and Z. Q. Zhang, “Effective medium theory for elastic metamaterials in two dimensions,” *Phys. Rev. B*, Vol. 76, No. 76, 205313, 2007.
22. Zhou, X. M. and G. K. Hu, “Analytic model of elastic metamaterials with local resonances,” *Phys. Rev. B*, Vol. 79, No. 19, 195109, 2009.
23. Willis, J. R., “Effective constitutive relations for waves in composites and metamaterials,” *Proc. R. Soc. A*, Vol. 467, No. 2131, 1865–1879, 2011.
24. Srivastava, A. and S. Nemat-Nasser, “Overall dynamic properties of three-dimensional periodic elastic composites,” *Proc. R. Soc. A*, Vol. 468, No. 2137, 269–287, 2011.
25. Casolo, S., “Macroscopic modelling of structured materials: Relationship between orthotropic Cosserat continuum and rigid elements,” *Int. J. Solids Struct.*, Vol. 43, No. 3–4, 475–496, 2006.
26. Providas, E. and M. A. Kattis, “Finite element method in plane Cosserat elasticity,” *Comput. Struct.*, Vol. 80, No. 27–30, 2059–2069, 2002.
27. Bazǎnt, Z. P. and M. Christensen, “Analogy between micropolar continuum and grid frameworks under initial stress,” *Int. J. Solids Struct.*, Vol. 8, No. 3, 327–346, 1972.

Highly Hygroscopic Polymer Microcavity Fiber Fizeau Interferometer for Humidity Sensing

Yan-Wun You, Jia-Heng Dai, and Cheng-Ling Lee

Department of Electro-Optical Engineering, National United University, Miaoli 360, Taiwan, R.O.C.

Abstract— This work demonstrates a highly hygroscopic polymer microcavity fiber Fizeau interferometer (PMFFI) that uses a single-mode fiber (SMF) tip with very little polymer attached. The polymers with specific porous structures have good hygroscopicity which is very useful for the humidity sensing application. We utilized a general laser diode (LD) with a single wavelength which is monitoring the spectral reflections of the proposed sensor. The sensing capabilities of the developed PMFFI have been experimentally investigated. Experimental results illustrate that the laser power rises when in the ascent of humidity, besides a good linear response of sensitivity and favorable spectral property are also achieved by the proposed configuration.

1. INTRODUCTION

Several fiber-optic relative humidity (RH) sensors have been developed and widely utilized in practical sensing applications, food processing, biomedical technology, electronic processing because of their many encouraging characteristics such as corrosion resistance, immunity to electromagnetic interference, high resolution, high sensitivity, small size and long distance sensing and monitoring [1–10]. Many kinds of optical fibers and fiber devices coated on different humidity-sensitive materials have been reported for the humidity sensing. They are included no core fibers [1], hollow core fibers [2], photonic crystal fibers (PCF) [3, 4], photonic bandgap fibers (PBF) [5] long period fiber gratings (LPGs) [6, 7], fiber interferometers [8, 9] and fiber Bragg gratings (FBGs) [10].

In this paper, for the first time, a simple fiber-optic RH sensor based on a highly hygroscopic polymer microcavity fiber Fizeau interferometer has been developed. The fiber sensor head using a SMF endface attaches droplet of a kind of UV-cured gel (monomer). The monomer, Norland optical adhesive 61 (NOA61) is a photo polymerizable liquid that can be cured by UV light with a maximum absorption in the range 350–380 nm. The monomer can be formed as solid and hard polymer and makes the structure permanent by the UV exposing processes. The layer of the proposed polymer NOA61 acts as a microcavity with two reflective interfaces, which reflects the optical signals back into the SMF again so that reflection interference operation is achieved. Compared with other previously reported fiber humidity sensors, our sensor structure has the advantages of easy fabrication, miniature, high sensitivity, and arbitrary structure. Experimental results demonstrate that greatly variation of the interference wavelength shift as well as highly sensitive property of the sensors can be obtained by the hygroscopic capability of the used polymer.

2. EXPERIMENTS AND RESULTS

In the experiment, the endfaces of SMFs were firstly attached little monomer NOA61 by using a particular method to control the thickness of monomer. After attaching (coating), the endface of SMF was exposed to UV light with an intensity of approximately 50 W/cm^2 for 30 s at room temperature. The refractive index of the solid polymer is around 1.56 in the measured wavelengths. The structures of the fabricated PMFFIs and reflection spectra are shown in Fig. 1. In the inset of Fig. 1, L is microcavity of the polymer. The arc shape of the fabricated polymer surface is created because the cohesion force of monomer liquid material. Adhesive force between the SMF and the polymer would be very well if it was fully cured and well aged.

We used the highly hygroscopic polymer with porous structure enables absorbing the water molecules effectively. Due to the hygroscopic capability of the polymer NOA61, the proposed PMFFI is employed to measure the surrounding RH, with the purpose of assessing the effectiveness of the sensor. In the measurement, a broadband light source (BLS) is launched into the fiber device and the reflection spectra are readily measured by using an optical spectrum analyzer (OSA). The device is placed inside a temperature and humidity controlling chamber (Resolution: 1%RH and 0.5°C) as the humidity is increased from 20 ~ 80%RH with fixed temperature of 25°C , as shown in Fig. 2. The adsorption process would expand the polymer as well as increases the effective index of microcavity to make the optical path of interference increase for shifting the interference wavelengths. Fig. 3 plots the shifts of the interference dip for a PMFFI with $L = 24 \mu\text{m}$ as

ascending humidity at wavelength around 1530 nm. The optical path of the microcavity increases as RH increases that causes a red-shift of interference fringes, as shown in Fig. 3(a). Fig. 3(b) plots

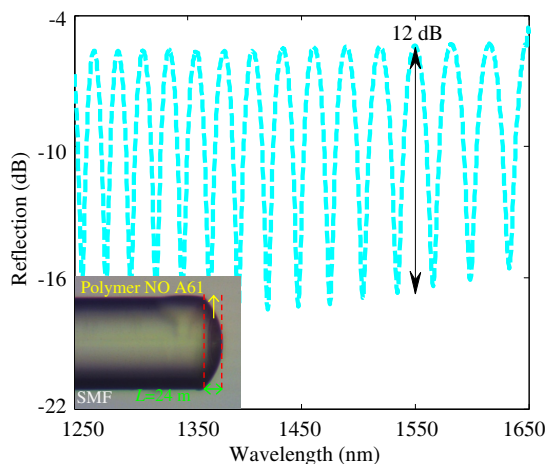


Figure 1: Interference spectra of the fabricated PMFFI. Inset presents the sensor head with microcavity of $L = 24 \mu\text{m}$.

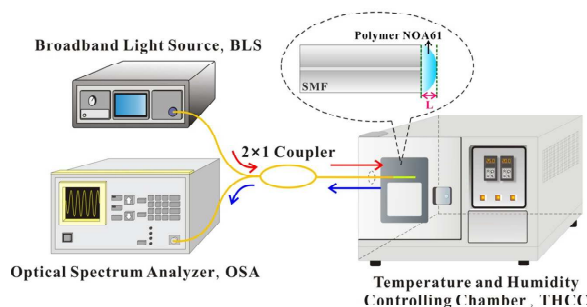


Figure 2: Experimental setup for the RH measurement. Inset shows schematic diagram of the sensor head.

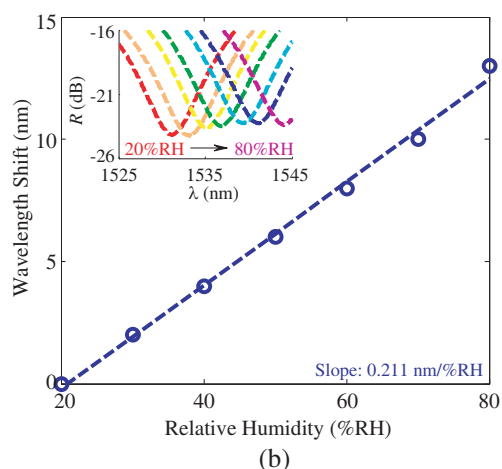
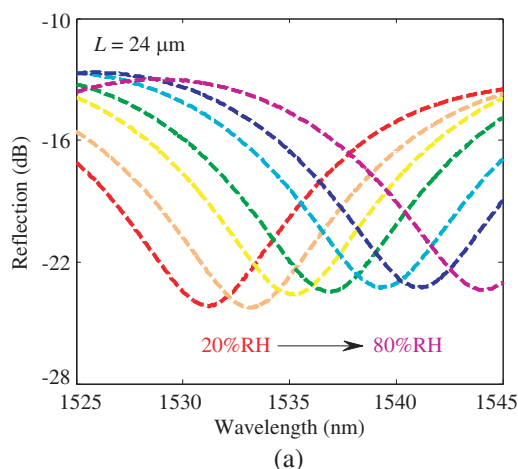


Figure 3: (a) Reflection spectra of the $L = 24 \mu\text{m}$ PMFFI with RH increase. (b) RH sensitivities for the adsorption process. Inset shows red shift of the interference wavelength dips.

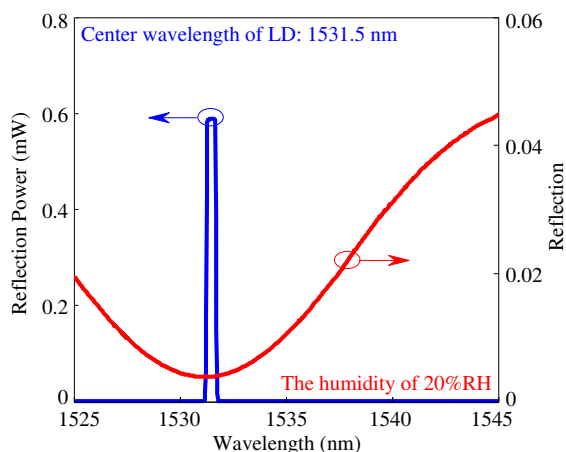


Figure 4: Wavelength location and optical power of the input LD (blue line) and spectral interference dip of the sensor when in the humidity of 20%RH (red line).

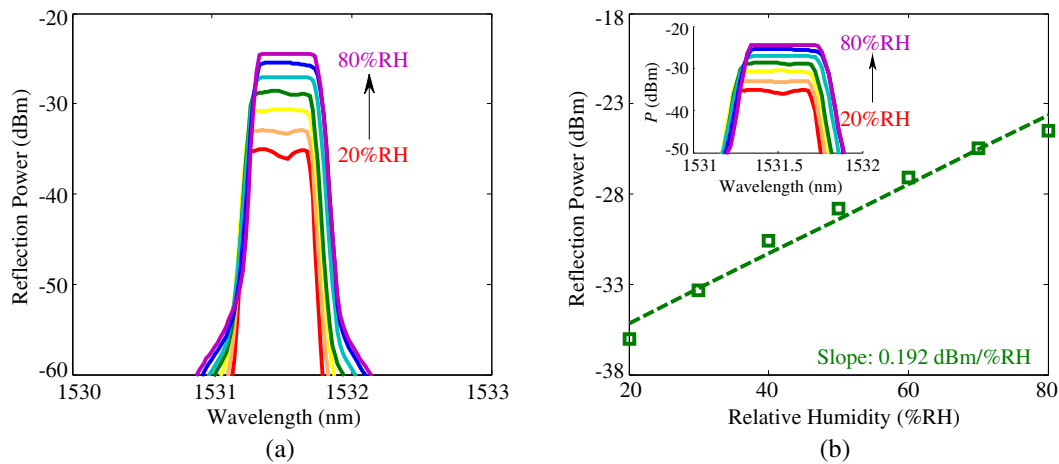


Figure 5: (a) Reflection spectra of the $L = 24 \mu\text{m}$ PMFFI with increase of humidity by using the LD light source. (b) Humidity sensitivities of the LD peak power to the increase of humidity. Inset shows the spectral variations of the LD peak power.

the linear humidity sensitivity of wavelength shift with $0.211 \text{ nm}/\%RH$ of the adsorption processes for the proposed sensor with $L = 24 \mu\text{m}$.

For reducing cost of the measurement system for the relative humidity sensor, we just utilized a general LD that replaced the former source, BLS. The LD with the optical power of about 0.58 mW and central wavelength of 1531 nm inputs the fiber sensor and the laser spectrum is shown in the blue line of Fig. 4. In Fig. 5(a), peak power of the measured laser changes with linearity when the humidity is increased. It can be predicted that a very cheap photodetector (PD) can be used to measure the optical power of the LD. The sensitivity with $0.192 \text{ dBm}/\%RH$ of peak power responses for our sensor has been achieved, as plotted in Fig. 5(b).

3. CONCLUSIONS

This study has presented a novel and miniature PMFFI based on the SMF tip with hygroscopic polymer attachment to measure the surrounding RH with high sensitivity. The used polymers with particular porous structures have good moisture absorption, so that can be used for fiber-optic RH sensing applications. A simple laser diode has been applied to monitor the spectral reflections and demonstrated the good sensing capabilities for the developed PMFFIs humidity sensor. Experimental results show that good linear response of sensitivity and the rise of peak power with the increase of the humidity have been investigated. Additionally, the ease of fabrication and lack of fiber alignment for the all-fiber devices are distinctive in the humidity sensing technology.

REFERENCES

1. Xia, L., L. Li, W. Li, T. Kou, and D. Liu, "Novel optical fiber humidity sensor based on a no-core fiber structure," *Sensors and Actuators A*, Vol. 190, 1–5, 2013.
2. Chen, L. H., T. Li, C. C. Chan, R. Menon, P. Balamurali, M. Shaillender, B. Neu, X. M. Ang, P. Zu, W. C. Wong, and K. C. Leong, "Chitosan based fiber-optic Fabry-Perot humidity sensor," *Sensors and Actuators B*, Vol. 169, 167–172, 2012.
3. Gao, R., Y. Jiang, and W. Ding, "Agarose gel filled temperature-insensitive photonic crystal fibers humidity sensor based on the tunable coupling ratio," *Sensors and Actuators B*, Vol. 195, 313–319, 2014.
4. Mathew, J., Y. Semenova, and G. Farrell, "Fiber optic hybrid device for simultaneous measurement of humidity and temperature," *IEEE Sensors Journal*, Vol. 13, 1632–1636, 2013.
5. Noor, M. Y. M., N. Khalili, and G. D. Peng, "All-fiber optic humidity sensor based on photonic bandgap fiber and digital WMS detection," *IEEE Sensors Journal*, Vol. 13, 1817–1823, 2013.
6. Miao, Y., K. Zhang, Y. Yuam, B. Liu, H. Zhang, Y. Liu, and J. Yao, "Agarose gel-coated LPG based on two sensing mechanisms for relative humidity measurement," *Applied Optics*, Vol. 52, 90–95, 2013.
7. Alwis, L., T. Sun, and K. T. V. Grattan, "Fiber optic long period grating-based humidity sensor probe using a Michelson interferometric arrangement," *Sensors and Actuators B*, Vol. 178, 694–699, 2013.

8. Santos, J. S., I. M. Raimundo, Jr., C. M. B. Cordeiro, C. R. Biazoli, C. A. J. Gouveia, and P. A. S. Jorge, “Characterisation of a Nafion film by optical fiber Fabry-Perot interferometry for humidity sensing,” *Sensors and Actuators B*, Vol. 196, 99–105, 2014.
9. Hu, P., X. Dong, K. Ni, L. H. Chen, W. C. Wong, and C. C. Chan, “Sensitivity-enhanced Michelson interferometric humidity sensor with waist-enlarged fiber bitaper,” *Sensors and Actuators B*, Vol. 194, 180–184, 2014.
10. Zhang, S., X. Dong, T. Li, C. C. Chan, and P. P. Shum, “Simultaneous measurement of relative humidity and temperature with PCF-MZI cascaded by fiber Bragg grating,” *Optics Communications*, Vol. 303, 42–45, 2013.

Optical Fiber Flowmeter Using Silver-coated FBG Cascaded by Waist-enlarged Bitaper

Xinhui Wang, Xinyong Dong, and Yan Zhou

Institute of Optoelectronic Technology, China Jiliang University, Hangzhou 310018, China

Abstract— A novel hot-wire flowmeter based on a silver-coated optical fiber Bragg grating (FBG) cascaded by waist-enlarged bitaper is proposed and experimentally demonstrated. The silver coating deposited on the surface of the FBG absorbs light of a pump laser, which is coupled into the fiber cladding by the specially-fabricated fiber waist-enlarged bitaper, to generate heat. Thus, the temperature of the FBG increases to a certain level, while air flow cools down the FBG by taking heat away. Bragg wavelength of the FBG changes with velocity of air flow according to a certain relationship. Experimental results show that a large measurement range up to 13.7 m/s is realized.

1. INTRODUCTION

Flow measurement is important for many applications in chemical engineering, in the energy and aerospace industries, and in medical equipment technology. Many approaches including differential pressure measurement, ultrasonic measurement, vortex shedding measurement and heat transfer have been proposed and employed for mass flow measurement [1–3]. Optical fiber anemometers have attracted many interests because of their advantages such as electrically passive operation, immunity to electromagnetic interference, high sensitivity, integrated structure, and the capability of remote sensing [4, 5]. In recent years, optical fiber Bragg grating (FBG) based hot-wire anemometers have been proposed by coating the FBG's surface with a metal film and heating with a high power pump laser [6–8]. To couple the laser light from the core to the cladding area of the FBG is very important in these anemometers because the metal coating can only absorb the laser light propagating in the fiber cladding area. Various coupling devices have been proposed including multimode fibers [6], no-core fibers [7] long-period fiber gratings [8], core-offset fusion splice [9] and so on.

In this paper, we propose an optical fiber hot-wire flowmeter based on a specially-fabricated fiber bitaper collaborating with a silver-coated FBG. The bitaper with an enlarged waist diameter shows high and stable coupling efficiency so that most of the pump laser power is coupled from the fiber core to the fiber cladding and absorbed by the silver coating film. That helps to improve the sensitivity by providing a relatively larger initial wavelength shift of the FBG. Furthermore, it has enhanced mechanical strength than a normal fiber so that high airflow velocity measurement is expected.

2. SENSOR FABRICATION AND PRINCIPLE

The proposed optical fiber flowmeter is schematically presented in Fig. 1. It consists of a waist-enlarged fiber bitaper and a FBG coated with a silver film. The bitaper couples laser light into the fiber cladding to heat the silver layer. Its coupling efficiency mainly depends on the length and the shape of the bitaper. The FBG is used to monitor the ambient temperature change influenced by heating from the silver absorption and airflow around. Note that the distance between the fiber grating and the bitaper should be as short as possible because there is high loss when the light propagates in the fiber cladding.

The FBG was manufactured by using a phase mask method in a hydrogen-loaded single-mode fiber (SMF-28). The achieved 4-mm-long FBG has reflectivity of 98% at the Bragg wavelength of 1549.36 nm and 3-dB bandwidth of 0.32 nm. The silver film was deposited on the surface of the FBG by the vacuum evaporating method and its thickness is ~ 120 nm, limited by the used deposition system. To prevent silver from being oxidized, a quartz film with thickness of 100 nm was then deposited over the silver film.

A waist-enlarged fiber bitaper was then fabricated 1-mm long prior to the FBG by using a fusion splicer (Fujikura FSM-60s) under the manual splicing mode, where we used a much larger overlap distance of 100 μm , instead of the commonly used setting of 10 μm , to make a waist-enlarged optical fiber bitaper [10, 11]. Given fixed fusion splicer parameter settings and good fiber tip conditions, repeatability of bitaper fabrication is achievable. The inset of Fig. 1 shows a micrograph view of

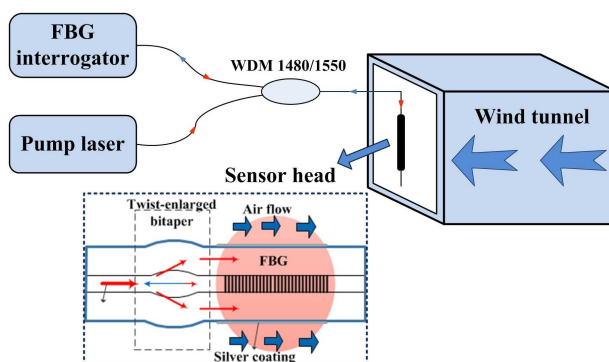


Figure 1: Schematic diagram of the proposed optical fiber flowmeter.

the formed bitaper. Its maximal diameter was increased from 125 μm to 145 μm . Its insertion loss is ~ 10 dB, which means $\sim 90\%$ of the input light can be coupled into the cladding of the fiber by the bitaper.

The silver film absorbs this part of pump laser power and generates heat, which increases temperature of the FBG. Bragg wavelength of the FBG is then shifted to a longer wavelength. When air flows by, part of the heat will be taken away and the temperature will be reduced by an amount depending on the air flow velocity, leading to a blue-shift for the Bragg wavelength of the FBG. Flow measurement is then realized by monitoring wavelength shift of the FBG. Based on the theory of hot-wire flowmeter [12], one can write the heat loss as a function of the air flow velocity as

$$P\varphi a_{\text{Ag}} = [T_{(v)} - T_e] (A + B\sqrt{v}) \quad (1)$$

where $T_{(v)}$ is the temperature of the flowmeter at airflow velocity of v , T_e is the temperature of the environment, A and B are empirical calibration constant, and v is the air flow velocity. Assuming there is equilibrium between the heat generation and loss, the following relationship can be achieved. P is the input laser power, φ is the coupling coefficient of waist-enlarged fiber bitaper, a_{Ag} is the absorption coefficient of the silver film to pump laser. Bragg wavelength of the FBG changing with temperature of the flowmeter can be described as

$$\lambda - \lambda_0 = k(T_{(v)} - T_e)\lambda_0 \quad (2)$$

where k is the FBG's temperature coefficient of sensitivity, λ_0 is the wavelength of the FBG without laser heating. The relationship between Bragg wavelength of the FBG and the airflow velocity thus can be given as

$$\lambda = \lambda_0 \left(1 + \frac{kP\varphi a_{\text{Ag}}}{A + B\sqrt{v}} \right) \quad (3)$$

Based on this equation, the airflow velocity can be determined from the measured wavelength shift of the FBG.

3. EXPERIMENTAL RESULTS AND DISCUSSIONS

The experimental setup is shown in Fig. 2. The pump laser with output power of 340 mW at 1480 nm was utilized to heat the sensor head through a 1480/1550 nm WDM coupler. A wind tunnel with cross-sectional dimension of 60 cm \times 60 cm was used to provide stable airflows. A FBG interrogator with wavelength resolution of 1 pm and scanning frequency of 500 Hz was used to monitor Bragg wavelength shift of the FBG.

Figure 2(a) presents spectral response of the FBG before and after the pump laser was turned on. It shows that the laser heating leads to the FBG a large Bragg wavelength shift of 1.19 nm. This pump laser-induced wavelength shift is just double that of our previous reported FBG flowmeter assisted by a core offset fusion splice. So the coupling efficiency is improved significantly by using the waist-enlarged bitaper. Considering temperature sensitivity of the FBG, 10.9 pm/ $^{\circ}\text{C}$, which was achieved from real testing, we can figure out that temperature of the optical fiber flowmeter would be about 109 $^{\circ}\text{C}$ higher than the room temperature when the pump laser is turned on. A high initial temperature increment is obviously helpful to increase the measurement range.

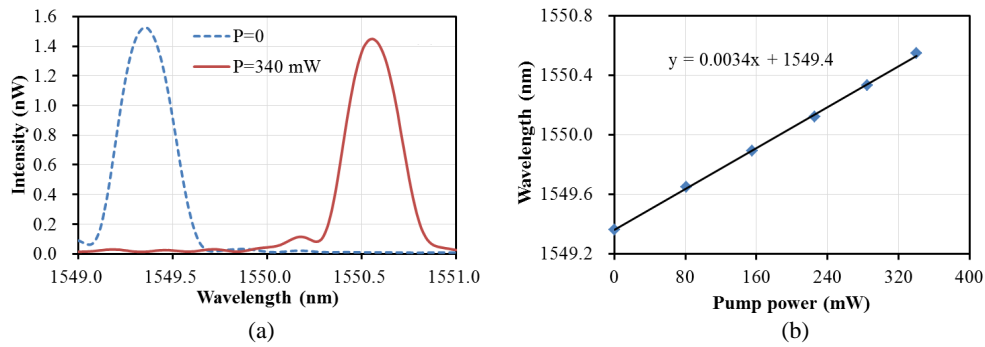


Figure 2: (a) Reflection spectra of the FBG flowmeter with and without laser heating. (b) Bragg wavelength of the FBG against power of the pump laser.

It is also noticed that reflectivity of the FBG with pump laser heating was reduced slightly by $\sim 5\%$ due to a minor chirp effect caused by a nonuniform temperature distribution along the length of the FBG. Due to continuous absorption by the sliver layer, power of the pump laser and the heating effect were reducing slowly along the FBG. This is the reason why the FBG was slightly chirped and its reflectivity was reduced. However, the influence to Bragg wavelength measurement of the FBG is totally negligible because the change of reflectivity is so small. Fig. 2(b) shows the measured Bragg wavelength of the FBG as a function of the laser power. It can be seen that the wavelength shift is proportional to the power of the laser with a slope of 3.4 pm/mW.

Airflow measurement was carried out at a fixed temperature of 20°C to avoid any possible influences caused by the environmental temperature variations. The pump laser was set at the maximum output power of 340 mW in order to achieve an as large as possible initial temperature Bragg wavelength shift of the FBG sensor. The airflow velocity in the wind tunnel was changed in a wide range from 0 to 13.7 m/s. Fig. 3 shows the reflection spectra of the flowmeter under different air flow velocities. Obviously, the Bragg wavelength shifts gradually to shorter wavelengths with the increment of the airflow velocity. It agrees well with the theoretical analysis. The total wavelength shift is 1.0 nm when the airflow velocity was changed from 0 to 13.7 m/s. It is also noticed that with increase of the airflow velocity, reflectivity of the FBG returns slightly to the original one. It is because the nonuniform temperature-induced chirp effect of the FBG is relieved gradually with the decrease of temperature.

Figure 4 shows the measured wavelength of the flowmeter as a function of the airflow velocity. It is obviously shown that the Bragg wavelength of the FBG was reduced more quickly with airflow velocity when the velocity was lower. By data fitting based on Eq. (3), we achieved a very close fitting curve, as shown in Fig. 4. The R-squared value is 0.9986. Eq. (3) is then rewritten as

$$\lambda = \frac{0.91}{0.76 + \sqrt{v}} + 1549.36 \quad (4)$$

It should be noticed that Eq. (4) is correct only under specific conditions aforementioned for our sensor and measurement setup. Any change of individual factors, including but not limited to power

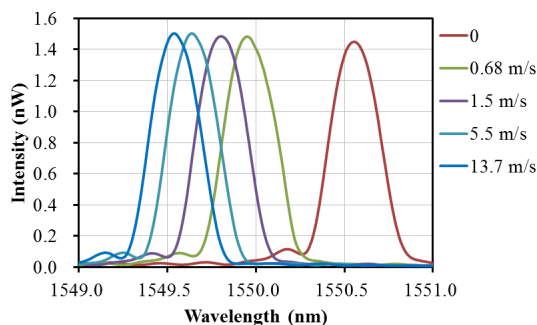


Figure 3: Reflection spectra of the flowmeter under various airflow velocities.

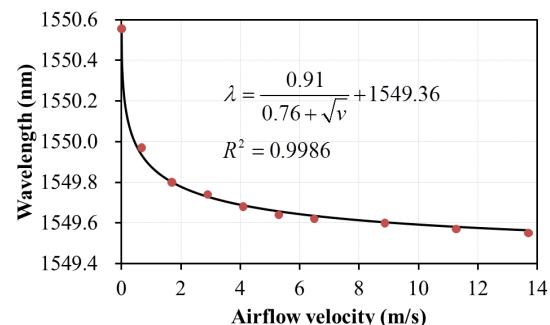


Figure 4: Resonant wavelength versus applied airflow velocity.

of the pump laser, coupling coefficient of the bitaper and environmental (or airflow) temperature, may introduce changes to the equations. It can be seen in Fig. 4, the response is close to linear when the airflow velocity is between 1.7 and 5.3 m/s. The sensitivity is ~ 47.2 pm/(m/s). Based on the wavelength resolution of 1 pm of the FBG interrogator we used, the corresponding resolution for airflow velocity measurement is up to 0.021 m/s.

4. CONCLUSION

An optical fiber thermal flowmeter has been demonstrated by using a silver-coated FBG assisted by a waist-enlarged fiber bitaper. Except for the enhanced mechanical strength than a normal fiber, the bitaper showed high and stable coupling efficiency so that most of the pump laser power was coupled from the fiber core to the fiber cladding and absorbed by the silver coating film. That helps to improve the sensitivity by providing a relatively larger initial wavelength shift of the FBG. High sensitivity of 47.2 pm/(m/s) and high resolution of 0.021 m/s have been achieved for the airflow velocity measurement.

ACKNOWLEDGMENT

This work was supported in part by the National Basic Research Program of China (973 Program) under Grant 2010CB327804, in part by the National Natural Science Foundation under Grant 61203205, and in part by the National Natural Science Foundation of Zhejiang Province, China, under Grant Z13F050003.

REFERENCES

1. Cha, J. E., Y. C. Ahn, and M. H. Kim, "Flow measurement with an electromagnetic flowmeter in two-phase bubbly and slug flow regimes," *Flow Meas. Instrum.*, Vol. 12, No. 5, 329–339, 2002.
2. Venugopal, A., A. Agrawal, and S. V. Prabhu, "Review on vortex flowmeter-designer perspective," *Sens. Actuators A, Phys.*, Vol. 170, Nos. 1/2, 8–23, Nov. 2011.
3. Oda, S., M. Anzai, S. Uematsu, and K. Watanabe, "A silicon micromachined flow sensor using thermopiles for heat transfer measurements," *IEEE Trans. Instrum. Meas.*, Vol. 52, No. 4, 1155–1159, Aug. 2003.
4. Jewart, C., B. McMillen, S. K. Cho, and K. P. Chen, "X-probe flow using self-powered active fiber Bragg gratings," *Sens. Actuators A, Phys.*, Vol. 127, No. 1, 63–68, Feb. 2006.
5. Lien, V. and F. Vollmer, "Microfluidic flow rate detection based on integrated optical fiber cantilever," *Lab Chip*, Vol. 7, No. 10, 1352–1356, Oct. 2007.
6. Cashdollar, L. J. and K. P. Chen, "Fiber bragg grating flow sensors powered by in-fiber light," *IEEE Sensors J.*, Vol. 5, No. 6, 1327–1331, Dec. 2005.
7. Wang, X., X. Dong, Y. Zhou, K. Ni, J. Cheng, and Z. Chen, "Hot-wire flowmeter based on silver-coated fiber bragg grating assisted by No-core fiber," *IEEE Photon. Technol. Lett.*, Vol. 25, No. 24 2458–2461, Dec. 2013.
8. Caldas, P., P. A. S. Jorge, G. Rego, O. Frazão, J. L. Santos, L. A. Ferreira, and F. Araújo, "Fiber optic hot-wire flowmeter based on a metallic coated hybrid long period grating/fiber Bragg grating structure," *Applied Optics*, Vol. 50, No. 17, 2738–2743, Jun. 2011.
9. Dong, X., Y. Zhou, W. Zhou, J. Cheng, and Z. Su, "Compact flowmeter using silver-coated fiber bragg grating," *IEEE Photonics Journal*, Vol. 4, No. 5, 1381–1386, Oct. 2012.
10. Meng, Q. Q., X. Y. Dong, Y. Zhou, K. Ni, Z. M. Chen, C. L. Zhao, and S. Z. Jin, "Simultaneous measurement of curvature and temperature with fiber taper-based MZI containing fiber Bragg grating," *Journal of Electromagnetic Waves and Applications*, Vol. 26, No. 17–18, 2438–2444, Dec. 2012.
11. Ni, K., X. Dong, C. Chan, T. Li, L. Hu, and W. Qian, "Miniature refractometer based on Mach-Zehnder interferometer with waist-enlarged fusion bitaper," *Optics Communications*, Vol. 292, 84–86, 2012.
12. Bruun, H. H., *Hot-Wire Anemometry: Principles and Signal Analysis*, Oxford University Press, 1995.
13. Gao, S., A. P. Zhang, H.-Y. Tam, L. H. Cho, and C. Lu, "All-optical fiber flowmeter based on laser heated fiber Bragg gratings," *Optics Express*, Vol. 19, No. 11, 10124–30, May 2011.

An Efficient Regenerator and Wavelength Assignment Approach for $1 + 1 : 1$ and $1 : 1 : 1$ Protected Lightpath Services

Gangxiang Shen¹, Chuanjun Wu², and Jixiong Dong²

¹School of Electronic and Information Engineering, Soochow University, Suzhou 215006, China

²Huawei Technologies, Shenzhen 518129, China

Abstract— We develop a waveplane-based regenerator placement algorithm for $1 + 1 : 1$ and $1 : 1 : 1$ protected lightpath services. Results indicate that the algorithm can significantly reduce the number of required regenerators and used wavelengths compared to a simple shortest-path routing algorithm.

1. INTRODUCTION

Signal regeneration is expensive because it requires a pair of transponders. Thus, minimizing signal regeneration is an important topic for the design of optical transport networks. A comprehensive survey on signal regeneration planning has been performed in [1], in which most of the studies are found to focus on planning for unprotected lightpaths. Few are dedicated to the protected services such as $1 + 1$ or $1 : 1$ services, not mentioning the services ensured with dual-failure recovery [2] such as $1 + 1 : 1$ and $1 : 1 : 1$ ones.

Network connections ensured with dual-failure recovery are important for many users that need the connections to support mission-critical services such as financial and military applications. $1 + 1 : 1$ and $1 : 1 : 1$ protection types provide good survivability for services through establishing three lightpaths between each pair of source and destination nodes. For the $1 + 1 : 1$ service, in addition to $1 + 1$ protection which provides a pair of “working” and “first protection lightpaths,” one more protection path (called “the second protection lightpath”) is also reserved in case that both the first two paths fail simultaneously. Here colon “:” means that the protection resources on the second protection path can be shared. $1 : 1 : 1$ protection is similar to $1 + 1 : 1$ protection. The only difference is that the protection resources of the first protection lightpath of a $1 : 1 : 1$ service is also allowed to be shared (note that protection resources can only be shared in the same categories; the protection resources of a first protection lightpath and a second protection lightpath cannot be shared).

For the first time, we jointly consider the lightpath routing, wavelength assignment, and regenerator placement (RWA-RP) problem for the $1 + 1 : 1$ and $1 : 1 : 1$ services. We develop an efficient waveplane-based approach that integrates the steps of lightpath routing, wavelength assignment, and regenerator placement to optimize the total numbers of required regenerators and used wavelengths.

2. RELATED CONCEPTS

Waveplane: A *waveplane* is defined as a virtual topology that is copied from a physical topology [3]. A physical topology that supports a certain number (w) of wavelengths on each fiber link can be split into w waveplanes. A node on a waveplane is defined as *wavenode*, and a link on a waveplane is defined as *wavelink*. Each wavelink corresponds to a wavelength and the wavelength indexes of all the wavelinks on a common waveplane are the same.

Regenerator placement threshold: To decide where to place necessary regenerators, we introduce an important parameter called *regenerator placement threshold*. Whenever the signal quality of a lightpath is below a predefined threshold, we place a regenerator at the nearest previous node. We may estimate the signal quality based on an accurate analytical model or a simple criterion such as physical distance. We can also use some criteria lying between the above two extremes to consider a rough optical signal-to-noise ratio (OSNR) (which is simply calculated based on the accumulated amplifier noise), or even simpler, the number of traversed optical transmission section (OTS) hops (as each OTS hop corresponds to an amplification span). Without losing generality, we use the number of traversed OTS hops as a decision criterion for regenerator placement in this paper.

3. CONDITIONS OF 1 + 1 : 1 AND 1 : 1 : 1 PROTECTION RESOURCE SHARING

For each 1 + 1 : 1 service, the first protection lightpath is assigned with dedicated protection resources, while the second protection lightpath is allowed to share protection resources in the same category subject to a certain link-disjoint condition. In this paper, protection resources include *protection wavelengths* and *regenerators* on protection lightpaths. We take Fig. 1 as an example to explain the condition of protection resource sharing on the second protection lightpath. Assume there are two 1 + 1 : 1 services with each including a working path (represented as W_i , where i is service index) and two protection paths (represented as P_{ij} , where j is protection path index). The protection resources on the second protection paths of the two services can be shared only if the condition $\overline{(W1 \otimes W2)} \cdot \overline{(P11 \otimes P21)} \cdot \overline{(W1 \otimes P21)} \cdot \overline{(P11 \otimes W2)}$ is satisfied, where the symbol \otimes denotes two paths are joint (or overlap) on some link(s) and \bar{X} represents a “NOT” operation of X . Thus, $W1 \otimes W2$ means that working paths $W1$ and $W2$ are joint, and $\overline{(W1 \otimes W2)} \cdot \overline{(P11 \otimes P21)}$ means that the working and first protection paths of the two services are *pairwise joint*, and finally $\overline{(W1 \otimes W2)} \cdot \overline{(P11 \otimes P21)} \cdot \overline{(W1 \otimes P21)} \cdot \overline{(P11 \otimes W2)}$ implies that the working and first protection paths of the two services are not pairwise joint in any way. As long as the two services are not pairwise joint in their working and first protection routes, any dual-failure would not trigger simultaneous restorations on their second protection lightpaths. Rather, at most one second protection lightpath would be triggered to use sharable protection resources, which therefore ensures 100% dual-failure recovery.

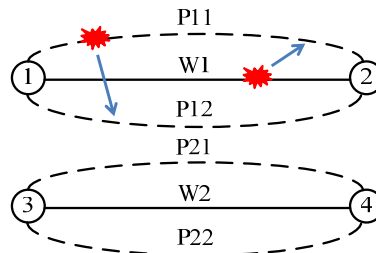


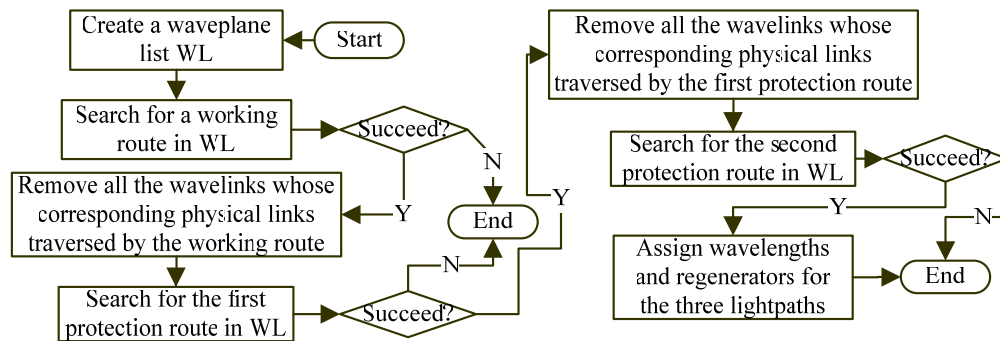
Figure 1: Conditions of protection resource sharing among protection routes.

For the 1 : 1 : 1 service, the protection resources on the first and second protection lightpaths can both be shared among the same categories. The condition of protection resources sharing on the second protection lightpath is the same as that of the 1 + 1 : 1 service, while the condition of protection resources sharing on the first protection lightpath is $\overline{(W1 \otimes W2)} \cdot \overline{(P12 \otimes P22)} \cdot \overline{(W1 \otimes P22)} \cdot \overline{(P12 \otimes W2)}$ in the context of Fig. 1.

3.1. Waveplane-based Approach for Wavelength Assignment and Regenerator Placement

We develop a new approach that integrates the steps of lightpath routing, wavelength assignment, and regenerator placement to efficiently establish 1 + 1 : 1 and 1 : 1 : 1 lightpath services. We make such integration possible with the concept of *waveplane*. Fig. 2 shows the flowchart of the approach. We employ a three-step strategy to first establish a working lightpath, then the first protection lightpath, and finally the second protection lightpath. Only if all the three lightpaths are successfully established, can the service be considered successfully established. Take a 1 + 1 : 1 service as an example. We first search for a working route; if succeeded, we then remove all the wavelinks whose physical links traversed by the found working route from the waveplane topologies (i.e., waveplane list (WL)), and then based on the updated topologies, search for the first protection route; if succeeded, then we remove all the wavelinks from the WL topology whose physical links traversed by the found first protection route, and then search for the second protection route. When searching for the second protection route, protection resource sharing (including wavelengths and regenerators) is allowed as long as the sharing condition elaborated in Section 3 is met. If we succeed in all the three route-searching steps, wavelengths and regenerators are assigned to the three lightpaths. In particular, when establishing the second protection lightpath, we should maximally share protection resources.

For a 1 : 1 : 1 service, both the first and second protection lightpaths are allowed to share protection resources. For resource sharing of the second protection lightpath, we follow the same

Figure 2: Flowchart of $1 + 1 : 1/1 : 1 : 1$ service establishment.

steps as in establishing a $1 + 1 : 1$ service. For resource sharing of the first protection lightpath, we need to step back after establishing the second protection lightpath; that is, after establishing the service in the way of $1 + 1 : 1$, which has ensured maximal sharing of protection resources on the second protection lightpath, without changing the routes of the service (so as not to destroy the resource sharing condition of the second protection lightpath), we release all the used network resources by the first protection lightpath, and reestablish it by allowing its protection resources to be maximally shared with other first protection lightpaths subject to the same sharing condition as for the second protection lightpath.

To cater to different requirements or situations, we can further extend the algorithm in Fig. 2 to incorporate new constraints. For instance, due to the *color* constraint of add/drop port in a ROADM, we may require two or all of the lightpaths of a service to use an identical wavelength. If two lightpaths are required to use an identical wavelength, the algorithm needs to search a route pair for them on a common waveplane. Likewise, if all the three lightpaths are required to use an identical wavelength, three disjoint routes should be searched on the same waveplane.

4. SIMULATIONS AND PERFORMANCE ANALYSES

To evaluate the efficiency of the proposed waveplane-based algorithm, we ran simulations for seven test networks whose topologic information and lightpath demands are shown in Table 1. The numbers of network nodes and links are listed in the second and third columns, respectively. The fourth column is the total number of lightpath demand units required between node pairs. The maximal number of wavelengths on each fiber link is assumed to be 80 in all the test networks. The threshold number of OTS hops for regenerator placement is assumed to be ten for all the test cases. In addition, because the performance of the proposed algorithm is closely related to the establishment sequence of lightpath demand units, we implemented a multi-iteration process [4] to find the minimum number of required regenerators. Specifically, we shuffled the lightpath demand units and generated 50 random demand unit lists. For each of the lists, we ran the proposed waveplane-based algorithm shown in Fig. 2 to find the total numbers of required regenerators and used wavelengths. Finally, we compare the results of the 50 iterations to choose a design that requires the smallest number of regenerators and wavelengths as our final solution.

Table 1: Test networks.

Networks	Nodes	Links	Optical channel units
1	20	40	100
2	55	90	174
3	30	55	200
4	35	70	256
5	40	70	233
6	45	90	90
7	50	100	220

Table 2: Numbers of required regenerators and used wavelengths (x, y, z : regen #, wave #, unserved lightpath unit #).

Networks	1 + 1 : 1		1 : 1 : 1	
	Shortest	Waveplane	Shortest	Waveplane
1	15, 76, 0	9, 49, 0	9, 57, 0	0, 30, 0
2	394, 80, 30	379, 80, 8	296, 80, 18	317, 78, 4
3	103, 80, 35	6, 80, 37	11, 80, 22	2, 80, 27
4	128, 80, 42	7, 66, 42	10, 76, 42	3, 61, 42
5	98, 80, 79	2, 80, 78	5, 80, 78	5, 80, 78
6	144, 80, 74	42, 80, 60	64, 80, 61	31, 80, 67
7	192, 80, 30	37, 80, 35	46, 80, 30	30, 80, 35

To evaluate the efficiency of the proposed algorithm, we compare the results of the waveplane-based algorithm (“Waveplane” in short) and the algorithm simply based on shortest physical routing (“Shortest” in short) in terms of regenerator and wavelength numbers. The algorithm based on shortest physical routing finds the working, first, and second protection paths simply based on the physical topology (not considering the waveplane topology). Table 2 shows the results of the two schemes for two different service types. Each triple (x, y, z) means that x regenerators and y (never greater than 80) waveplanes are required to establish all (except z units) of the services. For the 1 + 1 : 1 service, the second protection lightpath is required to use the same wavelength as that of either working or the first protection lightpath, while for the 1 : 1 : 1 service, all the three lightpaths are allowed to use different wavelengths.

We can see that the waveplane-based algorithm requires much smaller numbers of regenerators than those of the “shortest” algorithm. Moreover, it is found that the waveplane-based algorithm can successfully serve more traffic demands (under the constraint of 80 wavelengths on each fiber link) than the “shortest” algorithm (please compare value z in each triple between the two algorithms). Also, comparing the numbers of used waveplanes (wavelengths), we see that the proposed waveplane-based algorithm has smaller numbers of used waveplanes. For example, for the 1 + 1 : 1 service in test case 4, the proposed algorithm requires only 7 regenerators versus 128 regenerators by the “shortest” algorithm, and uses only 66 wavelengths versus 80 wavelengths by the “shortest” algorithm. For the 1 : 1 : 1 service, the proposed algorithm requires only 3 regenerators versus 10 regenerators by the “shortest” algorithm, and uses only 61 wavelengths versus 76 wavelengths by the “shortest” algorithm. The reason of better performance of the proposed algorithm is as follows: Under the waveplane-based strategy, the wavelength-continuity constraint is always ensured if a route is found on a certain waveplane; however, for the algorithm based on the shortest physical routes, in addition to placing regenerators, we have to consider wavelength collision and place wavelength converters if required. Given a limited number of wavelengths on each fiber link, more wavelength resources are consumed with the increase of lightpath demand, which leads to more wavelength collisions and therefore needs more wavelength converters (regenerators). Finally, comparing the results of the 1 + 1 : 1 and 1 : 1 : 1 services, because the latter allows the first protection lightpath to also share protection resources, we can see that much fewer regenerators and used wavelengths are required to serve all the demand units.

5. CONCLUSION

We proposed a waveplane-based lightpath routing, wavelength assignment, and regenerator placement algorithm for the 1 + 1 : 1 and 1 : 1 : 1 lightpath services. By comparing the numbers of required regenerators, used wavelengths, and unserved lightpath demand units, we show that the proposed waveplane-based algorithm is efficient to significantly outperform the algorithms simply based on shortest physical routes. In addition, allowing the first protection lightpath to also share protection resources in the 1 : 1 : 1 protection mode can further improve protection resource utilization.

REFERENCES

1. Azodolmolky, S., et al., “A survey on physical layer impairments,” *Computer Communications*, Vol. 53, No. 7, 926–944, May 2009.

2. Clouqueur, M. and W. D. Grover, “Availability analysis,” *IEEE Journal on Selected Areas in Communications*, Vol. 20, 810–821, May 2002.
3. Shen, G., et al., “Heuristic algorithm for efficient light-path routing,” *Computer Communications*, Vol. 24, No. 3–4, 364–373, Feb. 2001.
4. Shen, G., C. Wu, and J. Dong, “An almost-optimal approach for minimizing,” *Proc. OFC/NFOEC 2013*, 2013.

Towards a Framework for Small-cell Network Planning

Elaine Wong, I. Akhtar, S. Abeywickrama, C. Ranaweera, C. Lim, and A. Nirmalathas

Department of Electrical and Electronic Engineering, The University of Melbourne, Australia

(Invited Paper)

Abstract— To address the exponential growth of traffic on mobile cellular networks, heterogeneous networks have been proposed in which numerous small-radius microcells commonly referred to as “small cells” are placed alongside traditional macrocells. The practical rollout of these small cells is challenging. For example, the effects of land terrain and urban geography on cellular mobile signal propagations can significantly influence transmission quality and coverage. In this paper, we describe a small-cell planning framework that takes into consideration the effects of land terrain variation and urban geography in planning the location of the small cells. Our framework is shown to utilize fewer cells than the maximum limit of 30 cell sites/km² in urban area for LTE 1800 MHz network. We further formulate a Linear Program to obtain the optimal operating power of these small cells whilst constrained by the power and capacity requirements and subjected to daily capacity demand variations. Our preliminary results show that with our small cell power management scheme which is based on traffic and capacity demand, tangible power savings can be achieved throughout the day.

1. INTRODUCTION

The recent surge in smartphone and mobile tablet usage has placed tremendous strain on mobile bandwidth. To address this exponential growth, heterogeneous networks have been recently proposed with optical fiber technology as the backhaul solution, thereby allowing untethered bandwidth to the mobile infrastructure. In a heterogeneous network, numerous small-radius microcells commonly referred to as “small cells” (SCs), are placed alongside traditional macrocells [1]. A small cell Base Station (BS) has a much smaller coverage radius range than that of a traditional macrocell, typically at 50 m to 300 m. It is designed to achieve a small footprint with features such as low-cost and low power, and is to be deployed in a plug-and-play fashion that requires minimal regular maintenance. However, the practical rollout of small cells is not without its challenges. As discussed in the abstract, the effects of land terrain and urban geography on cellular mobile RF signal propagations significantly influence transmission quality and coverage. Varying geographical terrain posing obstructions for direct line-of-sight signal path between the transmitting BS and receiving mobile station, initiates significant signal loss and causes Non line-of-sight propagation. Further, street orientation and building blocks especially in urban areas, cause signal reflections which in turn, lead to significantly weakened signal reception for cell areas with smaller radius. The BS antenna height also influences cell positioning by affecting coverage. Thereby, appropriate cell location planning for placing small cell sites with optimal antenna height especially in urban areas, is essential. Recent studies have also shown that the BSs of cellular networks collectively contribute to ~60% of the total energy consumption [2]. Hence, considering the potentially high BS density in small-cell networks, it is imperative that rigorous studies be undertaken on energy efficient power control mechanisms which account for the radiating power and required capacity enhancements that SCs can offer.

In this paper, we review a preliminary small-cell planning framework which we have recently proposed which accounts for the effects of land terrain variation and urban geography in selecting the most appropriate locations for small cells in an urban area. For illustration purposes, we chose a part of the Melbourne Central Business District (CBD) urban area for cell planning [3]. In our proposed framework, the relatively higher geographic elevations are first selected as potential locations for a small cell deployment. A common radius for all cell sites is then chosen within the typical urban area small cell radius range. For the selected cell radius, the signal strength and coverage ability for each cell site is then tested taking into account an antenna height of just below average building height. Finally, redundant cell locations are discarded from the initial planning to satisfy the maximum limit of cell sites per km² urban area. Our framework is shown to utilize fewer cells than the maximum limit of 30 cell sites/km² in urban area for LTE 1800 MHz network [4]. A similar cell planning framework was proposed in [5], however the authors only considered terrain characteristics and discounted urban geography effect for macrocell rather than

small cell deployment. Further, we present a Linear Program (LP) to obtain the optimal operating power of SCs whilst constrained by the power and capacity requirements and subjected to daily capacity demand variations [5]. The formulation of the LP and the datasets and model parameters used in our evaluations are presented here in this paper. Even though some related studies in this area have studied energy efficiency of small-cell networks via several network models, to the best of our knowledge, a deduction to LP for the problem at hand is performed for the first time by our team.

2. TERRAIN BASED SMALL CELL PLANNING FRAMEWORK: DESCRIPTION AND EVALUATION

There are four critical steps to our proposed small-cell planning framework: (a) selecting potential small-cell site locations; (b) allocating a proper cell radius value for each cell area; (c) testing coverage and signal strength levels for all cell areas with the fixed cell area; and (d) finalizing appropriate cell locations. As discussed, a test section of the Melbourne CBD of $900\text{ m} \times 1800\text{ m}$ was chosen for our cell planning. Geographic terrain elevation information was extracted using Google Earth software. In order to select appropriate small cell locations, the case study area was divided into a two-dimensional (2D) rectangular terrain grid of multiple same-sized unit squares, having 100 m sides. The elevation value for each unit square area measured horizontally across the grid from left to right in each row, was obtained and stored in the corresponding cell of a terrain grid matrix having 9 rows and 18 columns. In this reported work, we arbitrarily chose a 200 m radius for each cell site, corresponding to the typical small-cell area range. To reflect this small cell area range in our cell planning, four square cells, starting from the first cell on top left, were grouped together to form one intended coverage block square of 200 m side. The area with highest value among each four elevations of each coverage block was then obtained as the potential candidate cell site. This process was then repeated for all coverage blocks resulting in an initial 52 small-cell locations as illustrated in Figure 1(a), whereby the pink squares are the BS location boundaries within which the small-cell BS as white diamond shape is positioned.

To evaluate the feasibility of our framework, each small-cell location was tested for sufficient coverage through path losses accounting for both Line-of-Sight (LOS) and Non-Line-of-Sight (NLoS) scenarios for a BS antenna height of 9 m and MS antenna height of 1.5 m [6]. For LoS propagation without obstructions, the Hata path loss model as described by Nissirat et al. [7] for small urban city microcells, and with an added correction factor to consider geographic terrain slope effects, was applied. In the NLoS case, a diffraction building loss of 23.73 dB accounting of for antennas just

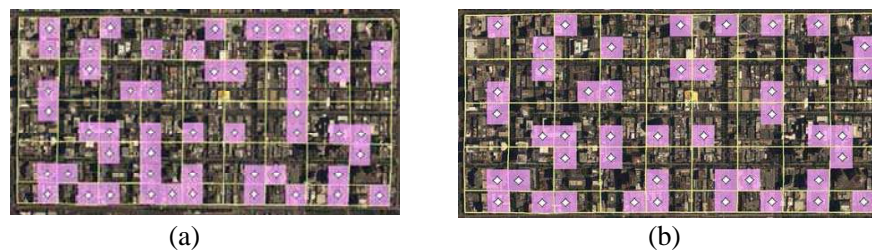


Figure 1: (a) Initial planning of 45 coverage blocks with 52 potential small cell site locations across Melbourne CBD. (b) Final selection of 45 small-cell site locations across the Melbourne CBD.

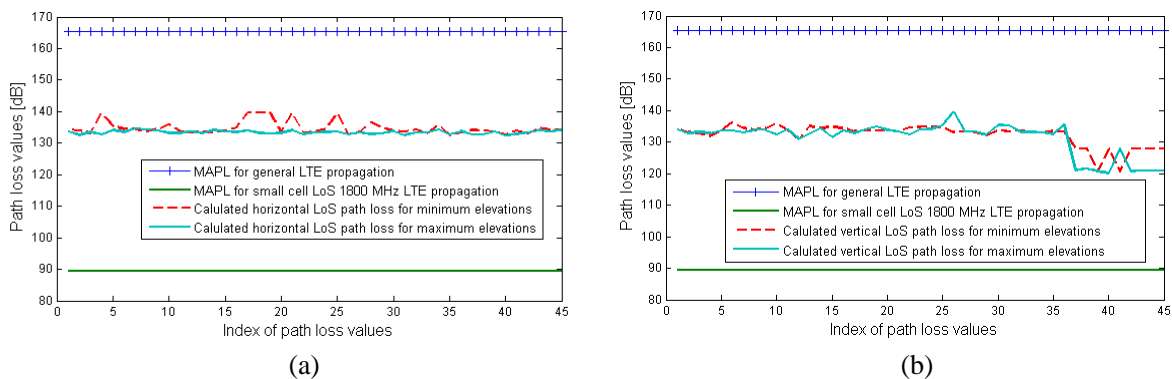


Figure 2: (a) Horizontal LoS path loss profile. (b) Vertical LoS path loss profile.

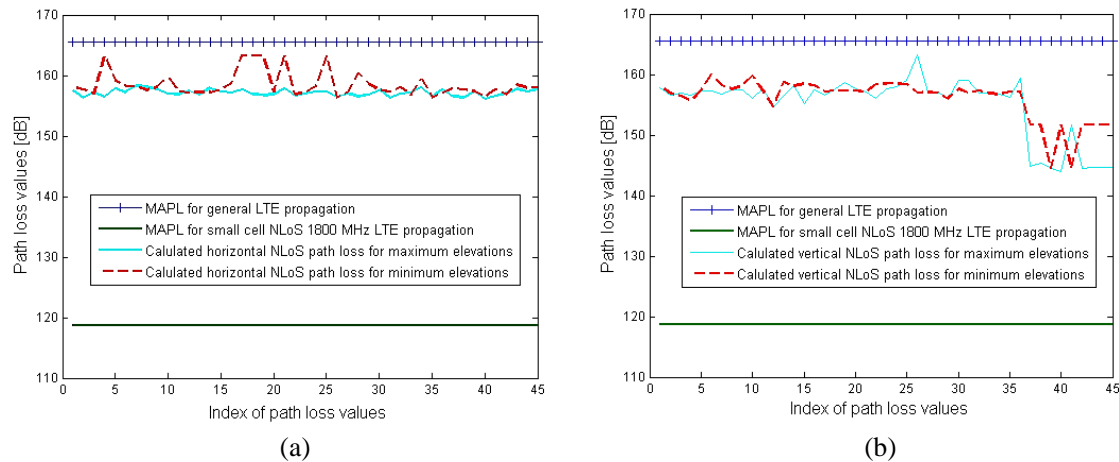


Figure 3: (a) Horizontal NLoS path loss profile. (b) Vertical NLoS path loss profile.

below rooftops [8], was added to the computed LoS path loss. For both LoS and NLoS situations, we measured the signal paths within our constructed 2D terrain grid from the farthest side of each cell location boundary (pink square) towards its cell area edges (yellow line). The corresponding path losses for the minimum elevation in each cell coverage area was similarly computed and compared to those of maximum elevations. The LoS signal loss profile when measured horizontally and vertically in the terrain grid are shown in Figures 2(a) and 2(b), respectively. Results in Figure 2(a) show that our calculated LoS propagation losses for maximum terrain elevations, remain lower in most cases and almost equal in others, to those of the minimum elevations. For Figure 2(b), in only a few cases, the maximum elevation losses are relatively higher than minimum elevation losses. Both calculated losses are also under LTE MAPL value of 165.5 dB [4].

Figures 3(a) and 3(b) illustrate the NLoS signal loss profiles of horizontal and vertical paths for the terrain grid, respectively. Results in Figure 3(a) show that LoS losses are lower for most maximum height locations, than those of the corresponding minimum ones, while almost the same for both in other occasions. Results in Figure 3(b) displays higher NLoS losses for most minimum elevations, except for a few occurrences. These NLoS losses are also below LTE MAPL. Finally, redundant site locations with the same maximum height from each coverage block are discarded from the initial planning. Here, only the highest elevation point with least path loss within each coverage block is retained, decreasing the number of final cell sites from 52 to 45 as shown in Figure 1(b), thus meeting the maximum cell site limit of 49 cells for the 1.62 km² area we studied.

3. CONTROL OF TRANSMIT POWER IN SMALL CELLS — OPTIMIZATION PROBLEM AND EVALUATION

As discussed in Section 1, recent studies have highlighted the high energy consumption of BSs, amounting to ~60% of the total energy consumption in cellular networks [2]. Care must be taken in the operation of small cell networks even though each small cell benefits from low operating powers. The main reason is that high density deployment can be expected in small cell networks since each small cell has only a small coverage area of 50 to 300 m. The collective power consumption of the network may therefore be significant. Here, a Linear Program (LP) which was formulated to optimize the transmit power of the small cells based on hourly network capacity demand of a mobile access network, is presented [8]. Our focus is on three distinct geographical areas; urban, suburban, and rural based on population density. Transmit powers of a base station is derived considering the capacity requirement of the users served. The LP is solved to optimally control the transmit power of SCs to evaluate the benefits of demand based power optimization.

Firstly, we focus on a segment of the wireless access network which includes a macro basestation and multiple randomly distributed small cell base stations. Note that in the LP, only transmit powers of base stations disregarding any other power consuming components, are optimized. Let N be the set of SCs in the network segment. Then, the objective function can be expressed as;

$$\text{minimize } P_{MC} + \sum_{i \in N} P_i \quad (1)$$

where P_{MC} is the power of the macro basestation and P_i represents the power of the i th SC bases-

tation. Then, a capacity constraint is enforced to ensure that all users connected to a SC receive required capacity, and a power constraint is enforced to represent physical equipment limitations. Let M_i be the set of users connected to the i th SC, then the capacity constraint can be shown as:

$$\sum_{m \in M_i} C_{m,i} \geq n_i C_{th} \quad \forall i \in N \quad (2)$$

where $C_{m,i}$ denotes the capacity from the i th small cell to the m th user, C_{th} denotes the capacity demand threshold per user and n_i denotes the number of users connected to the i th SC. All users connected to the SC receive the threshold capacity. This capacity constraint is then reconstructed into a power constraint using Shannon's formulae. The resulting constraint is as follows:

$$P_i \geq 2 \left[\frac{C_{th}}{B} - \frac{1}{N_i} \log_2 \left(\frac{\prod_{m \in M_i} G_{i,m}}{\prod_{m \in M_i} \left(\sum_{j \in N, j \neq i} P_{avg} G_{j,m} + \sigma^2 \right)} \right) \right] \quad \forall i \in N \quad (3)$$

In (3), N_i is the number of users connected to the i th SC base station. $G_{i,m}$ is the slow fading gain between the m th user and i th SC. P_{avg} is the average transmit power of a SC whilst σ^2 represents the interference noise power. Note that the revised constraint will now also enforce a lower bound on the transmit powers. Further, the transmit power of the SC antenna is bounded by a maximum threshold due to physical equipment limitations. This is considered as the power constraint in our formulation. The power constraint is given by:

$$P_i \leq P_{sc,max} \quad \forall i \in N \quad (4)$$

where $P_{sc,max}$ is the maximum allowable transmit power of a SC. We consider the microcell base station to operate at a constant power level of $P_{mc,max}$. The slow fading gain in constraint (3) is modeled as in [9] where:

$$G_{i,m} = K_0 \times 10^{\frac{\beta_{i,m}}{10}} \times d_{i,m}^{-\eta} \quad (5)$$

The parameter K_0 is a factor accounting for the effects of antenna gain and carrier frequency, $\beta_{i,m}$ is a Gaussian random variable with zero mean and standard deviation of 4 dB to account for log-normal shadowing effects, $d_{i,m}$ is the distance between m th user and i th SC, and η is the path loss exponent. Hourly capacity demand statistics are derived from a study that estimated network load of a mobile access network of a mobile operator [8]. Other parameters considered in this work are listed in Table 1.

Figure 4(a) shows the total transmit power of small cells against the hourly capacity demand variations throughout the day. A network segment with 50 small cell base stations was considered. Results indicate peak transmit power corresponding to the peak capacity demand at 1600 hrs. Among the three scenarios, urban and suburban environments indicate increased transmit power compared to the rural environment, due to more users being served by the small cells. The dotted horizontal lines indicate the peak transmit power in each scenario. This power level is considered as a baseline where the small cells operate continuously. We then evaluated the the small cell network with respect to this baseline in Figure 4(b). The power savings are averaged over the three population density cases. Results show maximum savings during low traffic periods and minimum

Table 1: Parameters considered in the model.

Parameters	Values
Area	1 km × 1 km
Bandwidth (B)	1.5×10^6 Hz
K_0	10^3
Path loss exponent (η) [6]	4 (urban) 3 (sub-urban), 2 (rural)
Population density [7] (inhabitants per km ²)	> 400 (urban), 150 to 400 (suburban), < 150 (rural)
σ^2	10^{-10} W
$P_{sc,max}, P_{mc,max}$ [8]	6.3 W, 80 W
$P_{sc,avg}$	5 W

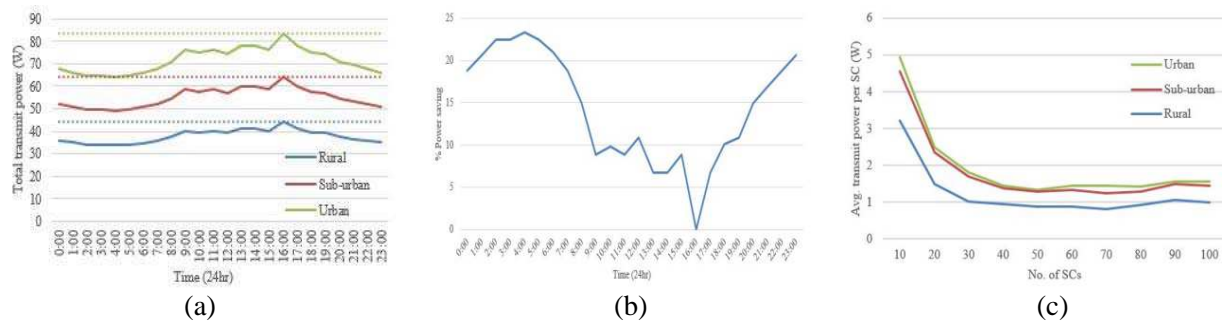


Figure 4: (a) Total transmit power under varying capacity demand throughout the day; (b) Percentage of transmit power savings, and (c) Average transmit power per SC as a function of number of SCs..

savings the peak traffic hour. Figure 4(c) presents the average transmit power per small cell as a function of number of small cells deployed at the peak traffic hour. Results show that as the number of small cells increases, the average transmit power decreases due to users being shared amongst more small cell and the increased freedom to choose a small cell with higher signal strength. We observe that the average transmit power tends to saturate when the number of small cell increases. This suggests that over-densification of small cells beyond certain a deployment number does not improve power savings though bandwidth capacity per user is increased. Further, we observe that the increase in population density will increase transmit powers. However, as population density is increased, the average power per small cell becomes less dependent on this parameter, as observed by the small difference between the urban and suburban result curves.

4. SUMMARY

In this paper, we described a small-cell planning framework that takes into consideration the effects of land terrain variation and urban geography in planning the location of the small cells. Our framework is shown to utilize fewer cells than the maximum limit of 30 cell sites/km² in urban area for LTE 1800 MHz network. Additionally, a Linear Program proposed to obtain the optimal operating power of small cells whilst constrained by the power and capacity requirements and subjected to daily capacity demand variations, was presented. The model was evaluated under urban, sub-urban and rural environments, showing tangible power savings throughout the day as compared to fully powered small cells.

REFERENCES

1. Hoydis, J., et al., *IEEE Veh. Technology Magazine*, Vol. 6, No. 1, 37–43, Mar. 2011.
2. Hasan, Z., et al., *IEEE Communications Surveys Tutorials*, Vol. 13, No. 4, 524–540, 2011.
3. Akhtar, I., et al., “Small-cell network site planning: A framework based on terrain effects and urban geography characteristics,” Accepted in *OECC/ACOFT 2014*, Jul. 2014.
4. Holma, H., et al., *WCDMA for UMTS: HSPA Evolution and LTE*, LibreDigital, 2010.
5. Abeywickrama, S., et al., “Estimation of transmit power for small cell networks, framework based on terrain effects and urban geography characteristics,” Accepted in *OECC/ACOFT 2014*, 2014.
6. Mogensen, P. E., et al., “Urban area radio propagation measurements at 955 and 1845 MHz for small and micro cells,” *Global Telecommunications Conference, GLOBECOM '91, Countdown to the New Millennium. Featuring a Mini-Theme on: Personal Communications Services*, Vol. 2, 1297–1302, 1991.
7. Nisirat, M. A., et al., “Micro cell path loss estimation by means of terrain slope for the 900 and 1800 MHz,” *2012 International Conference on Computer and Communication Engineering (ICCCCE)*, 670–674, 2012.
8. Deruyck, M., et al., *EURASIP Journal of Wireless Communications and Networking*, Vol. 2012, 248, 2012.
9. Nai, S. E., et al., *IEEE Wireless Communications and Networking Conf.*, 2261–2265, Apr. 2013.

Availability Analysis for Elastic Optical Networks with Multi-path Virtual Concatenation Technique

Xiaoling Wang¹, Limei Peng², and Gangxiang Shen¹

¹School of Electronic and Information Engineering, Soochow University, China

²Department of Industrial Engineering, Ajou University, Suwon, South Korea

Abstract— Due to high spectrum efficiency and flexibility in bandwidth allocation, elastic optical networks receive extensive research interest in recent years. Availability is one of the most important Service Level Agreement (SLA) metrics in telecommunication networks. In the paper, we apply the sub-band Virtual Concatenation (VCAT) technique to enhance the availability of elastic optical networks. Our study shows that the VCAT technique can greatly enhance the availability of the elastic optical networks, different spectrum distributions of sub-bands (i.e., numbers of frequency slots (FSs)) on multiple paths of a VCAT light path service can greatly impact the network availability, and a higher availability can be expected for a smaller VCAT sub-band granularity.

1. INTRODUCTION

Because of the unique merits, such as high spectrum efficiency and flexibility in bandwidth allocation, elastic optical networks receive extensive research interest in recent years. Availability is one of the most important SLA metrics in telecommunication networks. Different from reliability that is concerned about how likely a system will operate for a certain time period without a service-affecting failure occurring, availability considers external repair and maintenance to recover from failures, which is concerned about the state probability of finding a system in an operating state at any time when we want its service [1]. For the availability analyses of optical transport networks, the majority of existing studies focus on Wavelength Division Multiplexing (WDM) optical networks [2]. Different network protection techniques have been applied to enhance service availability in WDM networks [3–5]. However, to the best of our knowledge, there is still no study dedicated to the availability analysis for the elastic optical networks.

On the other hand, in the traditional Optical Transport Network (OTN), VCAT is an important technique to flexibly split the bandwidth of a complete service connection into multiple Virtual Containers (VCs) in the time domain, transport the VCs via different end-to-end paths, and finally recombine them at the receiver [6]. The VCAT technique can well balance the traffic load in the network, thereby significantly improving network capacity utilization. For the elastic optical network, it is also possible to extend this concatenation technique in the spectrum domain to split a complete light path into multiple sub-bands, transport the sub-bands via different paths, and finally recombine them at the receiver [7]. This technique is called *sub-band VCAT* or *spectrum split*. The distribution of sub-bands on multiple different paths enables partial bandwidth to survive when a network incurs failure(s). Thus, the sub-band VCAT technique is expected to enhance light path service availability for the elastic optical network.

This paper evaluates the benefit of applying the sub-band VCAT technique in enhancing the availability of the elastic optical networks. We develop analytical models specifically for two cases, i.e., (1) a single link-based node pair, between which multiple parallel links connect, and (2) a general mesh network, in which multiple disjoint end-to-end paths are employed for each node pair to provision light path services through the VCAT technique, and a network-wide average end-to-end connection availability is calculated. We assume that all the remaining capacity is available when one or multiple paths of a multi-path VCAT service are affected. Our study indicates that the sub-band VCAT technique can greatly enhance the availability of the elastic optical networks, and different distributions of sub-bands (i.e., numbers of FSs) on different paths of a VCAT light path service can greatly impact the network availability. For the single-link case, under the assumption of an equal link length of all the parallel links, an even distribution of FSs on the links can achieve the highest availability. For the network case, the distribution of FSs that ensures the highest network availability depends on the network topology. Also, a higher availability can be expected for a smaller VCAT sub-band granularity.

The rest of the paper is organized as follows. In Section 2, we give the assumption and a new availability definition, on which our analyses are based. In Section 3, we evaluate the availabilities

for two cases, i.e., a single link-based node pair and a general mesh network containing multiple end-to-end node pairs. We conclude the paper in Section 4.

2. ASSUMPTIONS AND NEW AVAILABILITY FORMULA

Network outages can be caused by both fiber cable cuts and invalidity of network node equipment (i.e., node failures). However, according to the statistics, the main reason for network failures is due to fiber cable cuts [2]. Thus, in this study we mainly focus on link failures (arising from fiber cable cuts) when analyzing network availability. We have the following four key assumptions for the analyses, including (1) network links are either working or in the outage state, (2) links fail independently, (3) both the in-service time and repair time of fiber cables follow independent memoryless processes with a constant mean, and (4) the repair rate is much greater than the failure rate [2].

The most widely known equation for the availability of a link is $A_l = MTTF / (MTTF + MTTR * l)$, where A_l is the link availability, $MTTF$ is the Mean Time To Failure of the link per km, and $MTTR$ is the Mean Time To Repair, l is the length of the link. FIT is the Failure In Time, which is a standard unit for measuring or specifying failure rates, and 1 FIT means 1 failure in 10^9 hours. Without losing generality, in this paper, we assume that $MTTF = 1 \text{ km} / (200 * \text{FIT})$, and $MTTR = 6 \text{ hours}$ [2].

Because a network as a whole is neither entirely available nor entirely failed, it is meaningless to directly estimate “network availability.” Rather, it is more meaningful and practical to characterize the link availability, path availability, and then based on these availabilities we can analyze a network-wide average end-to-end connection availability. If a path contains M continuous links,

the path availability is $A_p = \prod_{i=1}^M A_l^i$, which requires all the contained links are available and where A_l^i is the availability of the i th link on the path as defined before.

In the elastic optical network, the sub-band VCAT technique enables a connection (with multiple sub-bands on different paths) to survive partial bandwidth when a network incurs failure(s). Considering the partial available bandwidth with the VCAT technique, we define a new link availability as follows:

$$Ae_l = (MTTF * B_t + MTTR * l * B_r * A_r) / (MTTF + MTTR * l) * B_t \quad (1)$$

where B_t denotes the total bandwidth of the VCAT connection between a pair of source and destination nodes, B_r denotes the remaining bandwidth when link failure(s) occur, and A_r is the availability of the remaining capacity B_r . The numerator in the equation finds the total available bandwidth, in which the first part corresponds to the bandwidth when there is no failure and the second part corresponds to the remaining bandwidth when link failure(s) occur. The denominator in the equation finds total bandwidth if there is no link failure in the period of $MTTF + MTTR * l$.

3. AVAILABILITY ANALYSES

This section analyzes the availabilities for two cases: a single link-based node pair connected with multiple parallel links and a general mesh network with multiple end-to-end VCAT light path connections.

3.1. A Single Link-based Node Pair Connected by Multiple Parallel Links

3.1.1. Two Parallel Links

We first consider the case of two parallel links. Fig. 1 shows a situation where a single node pair is connected by two parallel links. Assume that B_1 is the bandwidth of first link, B_2 is the bandwidth of second link, and B_t is the total bandwidth between the two nodes, where $B_t = B_1 + B_2$, and their units are FS. When the first link fails, B_2 is the remaining capacity between the node pair. Similarly, when the second link fails, B_1 is the remaining capacity between the node pair.

Based on Equation (1), the availability for the first and second links with the VCAT technique can be calculated as (2) and (3).

$$\begin{aligned} Ae_l^1 &= (MTTF * B_t + MTTR * l_1 * A_l^2 * B_2) / (MTTF + MTTR * l_1) * B_t \\ &\approx (MTTF * B_t + MTTR * l_1 * B_2) / (MTTF + MTTR * l_1) * B_t \end{aligned} \quad (2)$$

$$\begin{aligned} Ae_l^2 &= (MTTF * B_t + MTTR * l_2 * A_l^1 * B_1) / (MTTF + MTTR * l_2) * B_t \\ &\approx (MTTF * B_t + MTTR * l_2 * B_1) / (MTTF + MTTR * l_2) * B_t \end{aligned} \quad (3)$$

where l_1 and l_2 are the physical lengths of the two links, respectively, and A_l^1 and A_l^2 are the availabilities of the two links based on the original availability definition, respectively, which are typically very close to 1.

For the two end nodes, the VCAT connection availability can be formulated as (4), and the unavailability of the connection is formulated as (5).

$$Ae_c = (Ae_l^1 * B_1 + Ae_l^2 * B_2) / B_t \quad (4)$$

$$U_c = 1 - A_c \quad (5)$$

Given the physical lengths of the two links, Equation (4) is solely dependent on the two variables B_1 and B_2 , which means that different distributions of sub-bands (i.e., numbers of FSSs) on the two links can impact the connection availability. To achieve a maximal availability, we need to find the combination of B_1 and B_2 that can make the first derivative of (4) equal zero. We find that when B_1 satisfies Equation (6), we can achieve maximal connection availability.

$$B_1 = \frac{(MTTF * MTTR * l_2 + 2 * MTTR^2 * l_1 * l_2) * B_t}{(MTTF * MTTR * (l_1 + l_2) + 2 * MTTR^2 * l_1 * l_2)} \quad (6)$$

Based on (6), we consider all the combinations of B_1 and B_2 to find maximal connection availabilities for various link length situations. Assume that the length of the first link equals 1,000 km and the total bandwidth of the connection is 10 FSSs (i.e., $B_1 + B_2 = 10$ FSSs), we find different connection availabilities considering different lengths of the second link (Len2) and combinations of B_1 and B_2 . Fig. 2 shows the connection unavailabilities for these different situations, in which each curve corresponds to a certain length of the second link and the horizontal axis shows variable numbers of FSSs on the first link. We can see that for each length of the second link, there exists minimal connection unavailability for a certain combination of B_1 and B_2 . For example, when the length of the second link is 500 km, the minimal connection unavailability occurs when the combination of B_1 and B_2 is (3, 7) FSSs, and similarly, when the length of the second link is the same as the first link, i.e., 1,000 km, the minimal connection unavailability occurs when the combination of B_1 and B_2 is (5, 5) FSSs, which means that specially for the equal link case, we should evenly split the total bandwidth onto the two links so as to achieve a maximal connection availability. Based on the above results, we can conclude that when the length of second link is longer, the maximal achievable availability is lower and the first link should be distributed with more FSSs so as to achieve higher availability. We also analyze how the range of length of the second link affect the combinations of B_1 and B_2 when achieving minimal unavailability. The results are shown in Table 1. We can see that the results are in line with those in Fig. 2, i.e., when the length of second link is longer, the first link should be distributed with more FSSs to achieve the minimal connection unavailability.

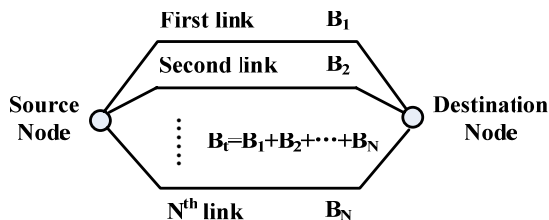


Figure 1: A simple demonstration for two nodes.

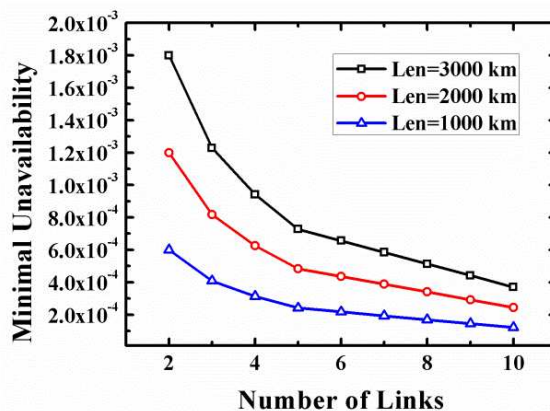


Figure 2: Connection unavailability for Len2.

3.1.2. Multiple Parallel Links

We next consider a single link-based node pair with multiple (more than two) parallel links as shown in Fig. 3. Considering the remaining capacity when a link failure occurs, the link availability

is given by Equation (7), and the connection availability is given by Equation (8).

$$Ae_l^k = \left(MTTF * B_t + MTTR * l_k * \sum_{i=1, i \neq k}^N A_l^i * B_i \right) / (MTTF + MTTR * l_k) * B_t \quad (7)$$

$$Ae_c = \sum_{i=1}^N \left(Ae_l^k * B_i \right) / B_t \quad (8)$$

where l_i denotes the length of the i th link, N denotes the number of parallel links between the two nodes, A_l^i is the availability of the i th link *not* considering the remain capacity, which can be calculated by $A_l^i = MTTF / (MTTF + MTTR * l_i)$, B_t denotes the total number of FSs, and B_i denotes the number of FSs on the i th link.

Because the connection availability is dependent on the number of parallel links and the distribution of FSs, given the set and parameters of N , $MTTR$, $MTTF$, l_i , A_l^i , and B_t as defined before, we develop an optimization model to find the maximal connection availability as follows:

Variables: Ae_l^i is the new availability of the i th link, which is calculated by (7). B_i is the number of FSs on the i th link.

Objective: Maximize $Ae_c = \sum_{i=1}^N (Ae_l^i * B_i) / B_t$. (i.e., maximize the average connection availability under different link failure situations)

Constraints: $\sum_{i=1}^N B_i = B_t$. (i.e., the sum of FSs distributed on all the parallel links equals to the total number of FSs of the connection).

Table 1: FS combinations of different ranges of Len2 for minimal unavailability.

	Range of Len2 (km)		Optimal FSs of 1st link	Optimal FSs of 2nd link
	Min	Max		
1	0	53	0	10
2	53	176	1	9
3	176	333	2	8
4	333	538	3	7
5	538	818	4	6
6	818	1222	5	5
7	1222	1856	6	4
8	1856	3007	7	3
9	3007	5699	8	2
10	5699	19419	9	1
11	19419	Infinity	10	0

Table 2: Minimal unavailability under different numbers of links.

Num Links	Minimal Unavailability	Optimal FSs distribution on different links																		
		1	2	3	4	5	6	7	8	9	10									
2	0.000599999	5	5																	
3	0.000408459	3	4	3																
4	0.000312689	3	3	2	2															
5	0.000240862	2	2	2	2	2														
6	0.000216919	2	2	2	2	1	1													
7	0.000192977	2	2	1	1	2	1	1												
8	0.000169034	2	1	1	1	1	1	2												
9	0.000145092	1	1	1	2	1	1	1	1	1										
10	0.000121149	1	1	1	1	1	1	1	1	1	1									

If the lengths of the links are different, the objective formula has quadratic components. In order to linearize the model, we assume that the lengths of all the links are the same, i.e., $l_1 = l_2 = \dots = l_N = l$, and thus $A_l^1 = A_l^2 = \dots = A_l^N = A$. We evaluate the availability of the connection between the two nodes with different parallel links. Assume that the lengths of all links are 1,000 km, $MTTR = 6$ hours, $MTTF = 5 \times 10^6$ hours*km, and $B_t = 10$ FSs, Table 2 shows the minimal unavailability to be achieved under different numbers of links and corresponding FSs distributions.

We observe that an even distribution of FSs on different links can achieve a maximal availability. In addition, we can see that a higher availability can be expected for a smaller VCAT sub-band granularity. The result is reasonable because when the length of all links are the same, and the number of links is fixed, an even distribution of FSs can make the probability of failed FSs minimal, and therefore the connection availability maximized. Also, with the increase of the number of parallel links, there are fewer FSs affected when a single link failure occurred, and thus the probability of failed FSs is lower.

Figure 4 shows the minimal unavailability of the connection between two nodes under different numbers of parallel links. Each curve corresponds to a certain link length. We observe that the shorter length of a link shows a lower unavailability. In addition, we see that a lower unavailability can be expected for a smaller VCAT sub-band granularity.

3.2. General Mesh Network

In this section, we estimate the availability of service connections for a general mesh network under the sub-band VCAT technique. We first consider a single end-to-end node pair, which is then used

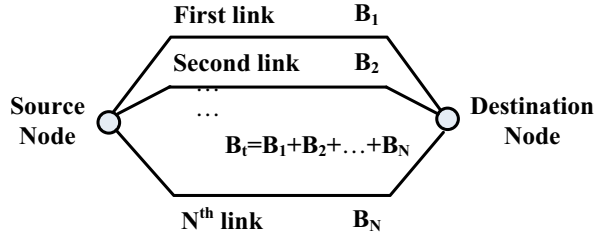


Figure 3: A single node pair connected with multiple parallel links.

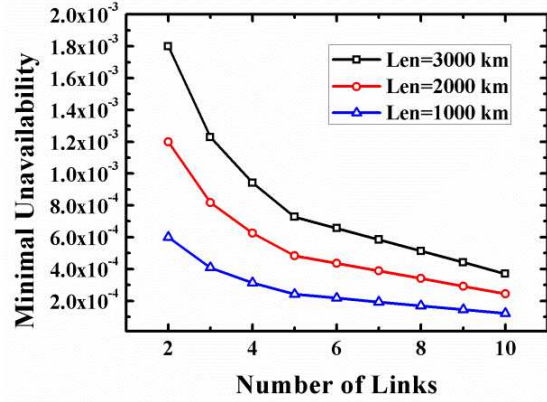


Figure 4: Minimal unavailability under different numbers of parallel links.

to calculate the availability for all the node pairs in a network. We average the availabilities of end-to-end light paths for all the node pairs to obtain average network-wide connection availability.

Figure 5 shows a single node pair connected by multiple disjoint end-to-end paths. Considering the remaining capacity upon a link failure, the availability of the i th link on the k th path is given by Equation (9), where l_{ki} denotes the length of the i th link on the k th path, N denotes the number paths between the source and destination nodes. A_p^j is the availability of the j th path not considering the remaining capacity, calculated as $A_p^j = \prod_{i=1}^{M_i^j} A_l^{ji}$, where A_l^{ji} is the availability of the i th

link on the j th path not considering the remain capacity, i.e., $A_l^{ji} = MTTF / (MTTF + MTTR * l_{ji})$, and M_i^j denotes the number links that the j th path traverses. The path availability is given by Equation (10), and the overall connection availability is given by Equation (11), where B_t is the total number of FSs, and B_k denotes the number FSs allocated on the k th path. The enhanced availability considers all the single-link failure situations and averages path availability considering the remaining capacity.

$$Ae_l^{ki} = \left(MTTF * B_t + MTTR * l_{ki} * \sum_{j=1, j \neq k}^N A_p^j * B_j \right) / (MTTF + MTTR * l_{ki}) * B_t \quad (9)$$

$$Ae_p^k = \prod_{i=1}^{M_i^k} Ae_l^{ki} \quad (10)$$

$$Ae_c = \sum_{k=1}^N (Ae_p^k * B_k) / B_t \quad (11)$$

As shown in Fig. 5, assume that there are two paths between a pair of nodes. The first path traverses two links with lengths of 500 km and 1,000 km, respectively, and the second path traverses three links with lengths of 500 km, 1,000 km, and 2,000 km, respectively. We can employ the availability calculation equations from (9) to (11) to estimate the end-to-end connection availability. The results are shown in Fig. 6, in which unavailability is considered. We compare the connection unavailability for the cases of single path and two paths. We see that the minimal connection unavailability of the two-path case with VCAT is lower than that of any single path case without VCAT. This is because the VCAT technique can integrate the sub-bands on multiple paths to make up an end-to-end light path service, which can ensure some bandwidth to survive when incurring a failure and therefore greatly enhance the connection bandwidth availability.

We apply the above end-to-end connection availability analysis approach to all the node pairs in a mesh network and calculate a network-wide average end-to-end service availability. We use a modified Dijkstra's algorithm to find two link-disjoint shortest routes between each node pair. For performance comparison, we evaluate the minimal unavailability of the first shortest path without VCAT, the second shortest path without VCAT, and the two shortest paths with VCAT. Two test networks including the n6s8 and SmallNet networks are considered for such an evaluation. Figs. 7

and 8 show the results of n6s8 and SmallNet, respectively. Because the remaining capacity can be considered available when one (or multiple) paths of a multi-path VCAT service is affected, it is easy to understand that the connection unavailability of two paths with VCAT is lower than that of any single path without VCAT.

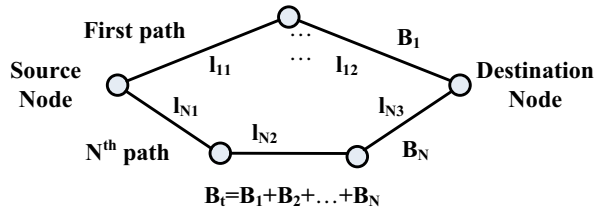


Figure 5: A single node pair connected with multiple paths.

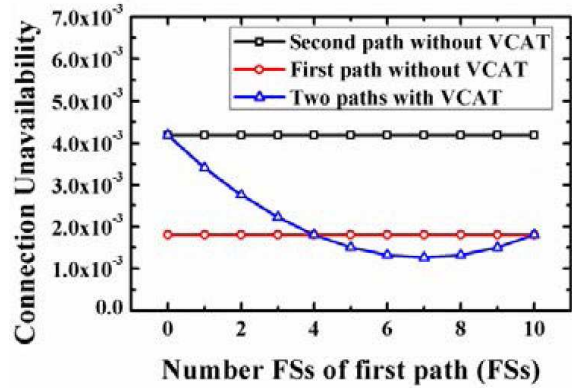


Figure 6: Unavailability comparison for a node pair.

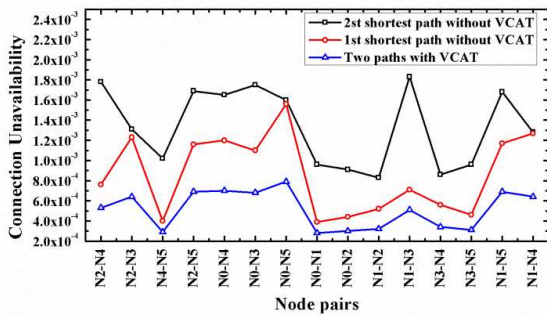


Figure 7: Unavailability comparison for the n6s8 network.

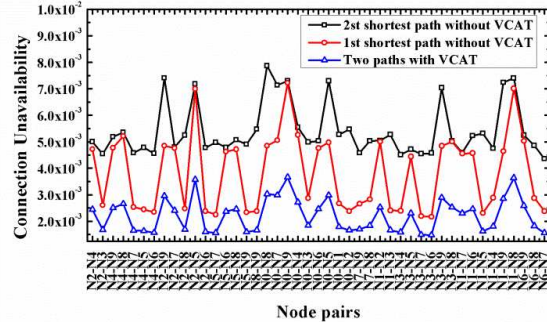


Figure 8: Unavailability comparison for the SmallNet network.

4. CONCLUSIONS

This paper evaluates the benefit of applying the sub-band VCAT technique in enhancing the availability of the elastic optical network. We made theoretical analyses for the situations of a single link-based node pair and a general mesh network. Because the distribution of FSSs on different links between a link-based node pair can affect the connection availability, we also developed an optimization model to maximize the connection availability for the node pair. We found that under the assumption that the lengths of all links are the same, an even distribution of FSSs on different links can achieve the highest availability, and a higher availability can be achieved for a smaller VCAT sub-band granularity. For the case of end-to-end paths in a mesh network, the sub-band VCAT technique can also greatly enhance the availability of service connections. It is also found that the distribution of FSSs that can achieve the highest availability depends on the network topology, and a higher availability can also be expected for a smaller VCAT sub-band granularity.

ACKNOWLEDGMENT

This work was jointly supported by the National 863 Project of China (2012AA011302), National Natural Science Foundation of China (NSFC) (61172057, 61322109), Research Fund for the Doctoral Program of Higher Education of China (20113201110005), and Natural Science Foundation of Jiangsu Province (BK2012179, BK20130003).

REFERENCES

1. Billinton, R. and R. N. Allan, *Reliability Evaluation of Engineering Systems*, 2nd Edition, Plenum Press, 1992.
2. Grover, W. D., *Mesh-based Survivable Networks: Options and Strategies for Optical, MPLS, SONET, and ATM Networking*, Prentice Hall Professional, 2004.
3. Clouqueur, M. and W. D. Grover, “Availability analysis of span restorable mesh networks,” *IEEE Journal on Selected Areas in Communications*, Vol. 20, No. 4, 810–821, May 2002.
4. Arci, D., D. Petecchi, G. Maier, et al., “Availability models for protection techniques in WDM networks,” *Proc. DRCN*, 2003.
5. Grover, W. D., “High availability path design in ring-based optical availability,” *IEEE/ACM Transactions on Networks*, Vol. 7, No. 1, 558–574, Aug. 1999.
6. Choy, L., “Virtual concatenation tutorial: Enhancing SONET/SDH networks for data transport,” *Journal of Optical Networking*, Vol. 1, No. 1, 18–29, Jan. 2002.
7. Shen, G., A. Cai, and L. Peng, “Benefits of sub-band Virtual Concatenation (VCAT) in CO-OFDM optical networks,” *Proc. ICTON*, 2012.

Optimal Time-dependent Spectrum Sharing between Neighboring Channels in Elastic Optical Networks

Xiaowei Zhao¹, Gangxiang Shen¹, and Sanjay K. Bose²

¹School of Electronic and Information Engineering, Soochow University, Suzhou, Jiangsu, China

²Department of EEE, Indian Institute of Technology, Guwahati, India

Abstract— Considering the time-dependent bandwidth characteristic of elastic optical networks, we develop two ILP models to assign spectra for lightpaths in a general mesh-network so as to maximally share optical spectra between neighboring channels and therefore minimize the total required spectrum in the whole network.

1. INTRODUCTION

In recent years, the rapid growth of high-bit-rate applications such as cloud computing and multimedia video services has led to a tremendous increase in the volume of Internet traffic. It has therefore become important to design very efficient and flexible networks which will perform better than the traditional ITU-T [1] based Wavelength Division Multiplexing (WDM) optical networks. A typical WDM optical network used for optical communications is inflexible and inefficient because of its fixed grid and coarse granularity. Elastic optical networks based on the Orthogonal Frequency Division Multiplexing (OFDM) technology can solve most of these problems and are considered promising for next-generation optical networking. The elastic optical transmission technique allows flexible bandwidth and spectrum allocation [2] along with efficient spectrum utilization. This adapts well to real networks where the traffic demand changes dynamically in different time periods. In [3], the authors proposed the concept of time-dependent optical spectrum sharing which adapts elastic optical channels to carry time-dependent traffic demands. In [4], we had applied this concept to a single fiber link and our simulation studies showed that elastic optical channels can successfully handle the time-dependent uncertainty of traffic demand on each optical channel while still achieving high spectrum efficiency.

This paper extends the concept of time-dependent optical spectrum sharing to a general mesh-network. We present two different ILP optimization models from different perspectives for efficiently assigning spectra for lightpaths in a general mesh-network so as to achieve high spectrum efficiency in supporting time-dependent traffic demands. When assigning spectra for lightpaths, one model considers a fixed center frequency of each lightpath between SD pairs in all the time slots, while the other does not consider such a constraint. The tradeoff between them is that the model with a fixed center frequency can make the reconfiguration of lightpaths simpler as we do not need to change the channel center frequency from time slots to time slots, while it may suffer from poorer spectrum utilization compared to the case without such a constraint. Both optimizations have the same objective to minimize the maximal index of the used frequency slots (FSs) on the fiber links in the entire network where we assume that the time-dependent traffic demand of each lightpath between SD pairs is given in advance.

2. CONCEPT OF TIME-DEPENDENT SPECTRUM ALLOCATION

Based on time-dependent optical spectrum sharing, we can allocate the bandwidth or spectrum of each lightpath according to the actual channel traffic demand at different time periods to better utilize the spectrum [5]. We illustrate the concept of time-dependent spectrum allocation in Fig. 1, where we show the changes in the spectrum allocation for two neighboring optical channels between two consecutive time slots. In time slot t_1 , optical channel f_1 has more traffic demand, thereby requiring more spectra, while optical f_2 has less traffic demand, thereby requiring fewer spectra. Similarly, in time slot t_2 , due to the change of traffic demand on each the two channels, optical channel f_1 may require fewer spectra while optical channel f_2 may require more spectra. This implies that we can arbitrarily allocate spectrum between the two neighboring optical channels, when the sum of the spectra used by the two channels does not exceed the total spectrum between their central frequencies. With this spectrum sharing, elastic optical networks are expected to achieve good optical spectrum utilization and efficiency. We found that the efficiency of the above spectrum sharing is closely related to the complementary status of the traffic demands of the two

neighboring channels in different time slots. If the two channels complement each other, we could assign a smaller amount of joint spectrum for them. On the contrary, if the channels always reach their peak traffic demands simultaneously or if the variation patterns of their traffic demands are always in line, there is no advantage of spectrum sharing as described above.

For a general mesh-network based on the elastic OFDM technology, with the constraints of *spectrum consecutiveness* and *spectrum continuity*, it is important to properly arrange the spectrum of each lightpath between SD pairs according to their individual time-dependent traffic demand distributions so as to achieve the best spectrum sharing. This is the key research problem that we aim to address and optimize in this paper.

3. ILP MODELS FOR SPECTRUM ASSIGNMENT IN GENERAL MESH-NETWORKS

For optimal assignment of spectrum in a general mesh-network, we develop two ILP models to minimize the total required spectrum subject to the condition that all the time-dependent channel bandwidths are satisfied. The first ILP model keeps fixed center frequencies for each lightpath between SD pairs which may be allowed to shrink its assigned bandwidth at a certain maximal percentage (for the situation where there is insufficient spectrum and therefore bandwidth squeezing [6] is required for the lightpath between a SD pair). Note that this model is generic, which by default can also be used to design for the case that does not allow for bandwidth shrinking. The second ILP model is one where the center frequencies are not fixed for each lightpath between SD pairs.

3.1. ILP Model with Fixed Channel Center Frequency

Sets and Parameters: \mathbf{V} is the set of network nodes. \mathbf{L} is the set of network links. \mathbf{NP} is the set of SD pairs in the network. \mathbf{T} is the set of the time slots. \mathbf{R}_{sd} is the set of routes for a SD pair in the network. TD_{sd}^t is the number of FSs (i.e., bandwidth) required between SD pair sd at time slot t . $X_{ij}^{sd,r}$ is a binary parameter that takes the value of 1 if the lightpath route r between SD pair sd traverses link ij ; 0, otherwise. α is the percentage that is maximally allowed for bandwidth squeezing for each lightpath. Δ is a large value.

Variables: f_{sd} is an integervariable denoting the center FS index (i.e., center frequency) of the lightpath between SD pair sd . S_{sd}^t is an integer variable denoting the starting FS index of the lightpath between SD pair sd at time slot t . E_{sd}^t is an integer variable denoting the ending FS index of the lightpath between SD pair sd at time slot t . y_{sd}^r is a binary variable that takes the value of 1 if the lightpath between SD pair sd chooses route r ; 0, otherwise. δ_{sd2}^{sd1} is a binary variable that takes the value of 1 if the starting FS index S_{sd1}^t of the lightpath between SD pair $sd1$ is smaller than the starting FS index S_{sd2}^t of the lightpath between SD pair $sd2$ at any time slot; 0, otherwise. Note that this notation makes sense only when two different lightpaths share at least one common link. c is the maximal index of used FSs on the fiber links in the entire network.

The **objective** of the ILP model is to minimize the maximal index of the used FSs in the entire network, i.e., c , and the **constraints** of the model are as follows:

$$\delta_{sd2}^{sd1} + \delta_{sd1}^{sd2} = 1 \quad \forall sd1, sd2 \in \mathbf{NP}, sd1 \neq sd2 \quad (1)$$

$$E_{sd2}^t - S_{sd1}^t \leq \Delta \cdot \left(\delta_{sd2}^{sd1} + 2 - X_{ij}^{sd1,r1} - X_{ij}^{sd2,r2} + 2 - y_{sd1}^{r1} - y_{sd2}^{r2} \right) \\ \forall ij \in \mathbf{L}, sd1, sd2 \in \mathbf{NP}, sd1 \neq sd2, r1, r2 \in \mathbf{R}_{sd} \quad (2)$$

$$\sum_{r \in \mathbf{R}_{sd}} y_{sd}^r = 1 \quad \forall sd \in \mathbf{NP} \quad (3)$$

$$S_{sd}^t = f_{sd} - 0.5 \cdot TD_{sd}^t \cdot (1 - \alpha) \quad \forall sd \in \mathbf{NP}, t \in \mathbf{T} \quad (4)$$

$$E_{sd}^t = f_{sd} + 0.5 \cdot TD_{sd}^t \cdot (1 - \alpha) \quad \forall sd \in \mathbf{NP}, t \in \mathbf{T} \quad (5)$$

$$f_{sd} \geq 0.5 \cdot TD_{sd}^t \cdot (1 - \alpha) \quad \forall sd \in \mathbf{NP}, t \in \mathbf{T} \quad (6)$$

$$c \geq E_{sd}^t \quad \forall sd \in \mathbf{NP}, t \in \mathbf{T} \quad (7)$$

$$c \geq \sum_{sd \in \mathbf{NP}, r \in \mathbf{R}_{sd}} TD_{sd}^t \cdot (1 - \alpha) \cdot X_{ij}^{sd,r} \cdot y_{sd}^r \quad \forall ij \in \mathbf{L}, t \in \mathbf{T} \quad (8)$$

Constraints (1) and (2) ensure that the spectra of two lightpaths that share common links must not overlap. Constraint (3) ensures that there is only a single route used for lightpath establishment between SD pair. Constraints (4), (5) and (6) tell the relationship of the center FS index, the starting FS index, and the ending FS index of each lightpath at time slot t (with a certain

bandwidth squeezing ratio). Constraint (7) ensures that the network-wide maximal FS index c is always no smaller than the ending FS index of any lightpath. Constraint (8) is a redundant one helping reduce the feasible solution region of the ILP model.

3.2. ILP Model with Non-fixed Channel Center Frequency

We have also developed an ILP model for the case that the channel center frequency is not fixed in different time slots. The model is extended from the one developed in [5] with the constraints and traffic demands satisfied in each time slot. Due to the page limit, we do not give the detail of the model here.

4. RESULTS AND PERFORMANCE ANALYSES

To evaluate the performance of the two ILP models, we assign spectra for the lightpaths in the SmallNet (10 nodes and 22 links) and COST 239 (11 nodes and 26 links) networks. We assume that for each lightpath between SD pairs, random hourly traffic demands (for 24 hours) are given. The traffic demand on each lightpath is assumed to vary in units of FSs, but within a certain maximal range. Specifically, we consider five ranges, from 1 to 10, 1 to 20, and maximally 1 to 50 (each number is even) units of FSs. We choose one route from multiple route options for each node pair to establish lightpaths. We minimize the total required spectra (without considering guard band) when all the time-dependent traffic demands are satisfied. In addition, for the bandwidth squeezing case, we employ the ILP model with fixed channel center frequency to minimize the total required spectra under different maximal bandwidth squeezing ratios. For this case, the required bandwidth on each lightpath between SD pairs is assumed to vary within a range from 1 to 20 units of FSs (each number is even).

Without considering bandwidth squeezing, Figs. 2 and 3 show the total number of FSs required in the SmallNet and COST239 networks with the increase of average bandwidth requirement of each lightpath, respectively. Comparing the results *with* and *without* fixed channel center frequency (i.e., “ILP 1” versus “ILP 2”), we can see that the case without fixed channel center frequency shows better performance, requiring much smaller numbers of FSs. This is reasonable since the spectrum

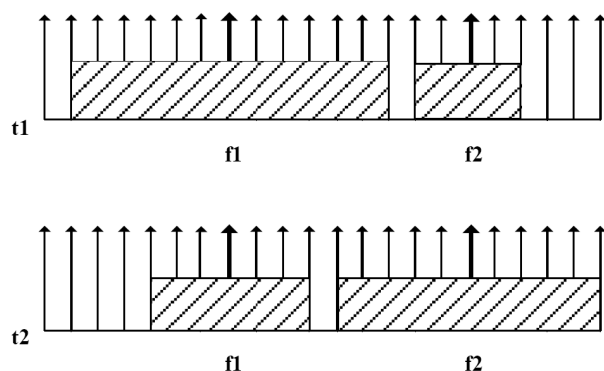


Figure 1: Time-dependent spectrum sharing between two neighboring optical channels.

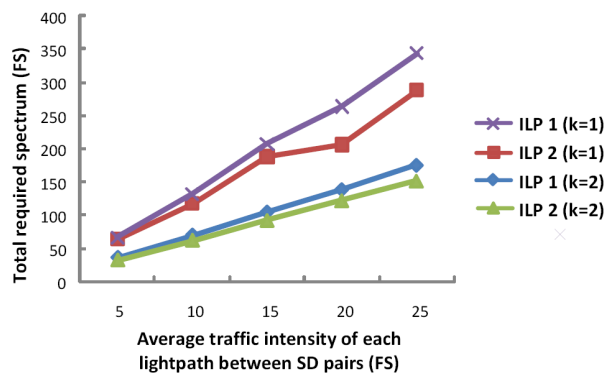


Figure 2: Total required spectra versus traffic demand intensities per node pair (SmallNet).

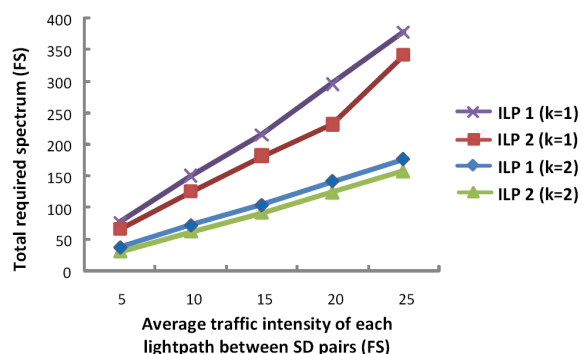


Figure 3: Total required spectra versus traffic demand intensities per node pair (COST 239).

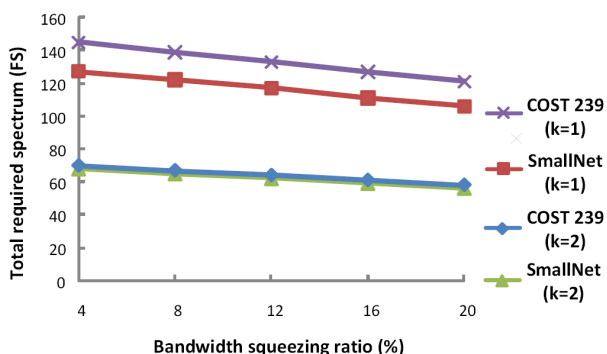


Figure 4: Total required spectra versus maximal bandwidth squeezing ratios.

assignment without fixed channel center frequency allows for different center frequency for each lightpath in different time slots, while the case with fixed channel center frequency requires each lightpath to use the same center frequency at any time slot. We also evaluate the impact of the number of routes for selection on the design performance. It is reasonable to see that the case of two routes (i.e., $k = 2$) requires a smaller number of FSs compared to the case of a single route (i.e., $k = 1$) since the former has more flexibility in route selection. Considering bandwidth squeezing, Fig. 4 shows the results of the optimal spectrum assignment under different bandwidth squeezing ratios. We have only considered the case *with* fixed channel center frequency though similar results can be obtained for the case *without* fixed channel center frequency. In Fig. 4, it is reasonable to see that with an increasing bandwidth squeezing ratio, the required spectrum decreases since a larger bandwidth squeezing ratio corresponds to more spectrum overlap between two neighboring optical channels.

5. CONCLUSION

We took advantage of flexible bandwidth and spectrum allocation of the elastic optical networks to handle time-dependent traffic demands so as to achieve the best spectrum sharing. In [4], we have evaluated the performance of time-dependent spectrum allocation for the case of a single link which has now been extended to the general mesh-network in this paper. To achieve the best optical spectrum sharing, we developed two ILP optimization models *with* and *without* fixed channel center frequency. Simulation results were reported under different combinations of experimental parameters.

ACKNOWLEDGMENT

This work was jointly supported by the National 863 Plans Project of China (2012AA011302), National Natural Science Foundation of China (NSFC) (61172057, 61322109), and Natural Science Foundation of Jiangsu Province (BK2012179, BK20130003).

REFERENCES

1. ITU-T Recommendation G694.1, "Spectral grids for WDM applications: DWDM frequency grid," v2.0, 2012.
2. Zhang, G., et al., "A survey on OFDM-based elastic core optical networking," *IEEE Commun. Surv. Tut.*, Vol. 15, No. 1, 65–87, 2013.
3. Shen, G., et al., "Maximizing time-dependent spectrum sharing between neighboring channels in CO-OFDM optical networks," *Proc. ICTON*, 2011.
4. Zhao, X., et al., "Optimal time-dependent spectrum sharing between neighboring elastic optical channels over a single link," *Proc. ACP*, 2013.
5. Klinkowski, M., et al., "Elastic spectrum allocation for time-varying traffic in flexgrid optical networks," *IEEE J. Sel. Areas Commun.*, Vol. 31, No. 1, 26–38, Jan. 2013.
6. Sone, Y., et al., "Bandwidth squeezed restoration in spectrum-sliced elastic optical path networks (SLICE)," *J. Opt. Commun. Netw.*, Vol. 3, No. 3, 223–233, Mar. 2011.

Development of Low Noise MI Sensor and Its Applications

N. Hamada, A. Shimode, C. M. Cai, and M. Yamamoto

Aichi Steel Corporation, 1 Wano-Wari Arao-machi, Tokai 476-8666, Japan

Abstract— The MI sensor is a magnetic sensor based on the MI (Magneto Impedance) effect discovered by K. Mohri et al. in 1993. A specialized low noise analog output magnetic sensor (nT sensor: MI-CB-1DK) has also been commercialized by AICHI MICRO INTELLIGENT for use in detecting AC magnetic fields. According to theoretical analysis, although the MI sensor is foreseen to show the $fT/\sqrt{\text{Hz}}$ level of noise density, MI-CB-1DK shows 20–30 pT/ $\sqrt{\text{Hz}}$ at 10 Hz. In this paper, in order to develop an MI element showing lower noise, the effect of the aspect ratio of the amorphous magnetic wire, the number of wires and the effect of electric contact on multiple wires on noise density were investigated. Then an MI element which shows 1/10 the noise density of MI-CB-1DK was developed.

1. INTRODUCTION

The MI sensor is a magnetic sensor based on the MI (Magneto Impedance) effect discovered by K. Mohri et al. in 1993 [1]. A small and highly sensitive magnetic sensor (AMI 306) based on the MI effect and used as an electromagnetic compass mainly in mobile phones and smart phones has been developed and commercialized by AICHI MICRO INTELLIGENT [2]. On the other hand, a specialized low noise analog output magnetic sensor (current nT sensor: MI-CB-1DK) has also been commercialized for use in detecting AC magnetic fields [2]. And also a research of biomagnetic measurement using MI element has been reported [3]. According to the theoretical analysis, the MI sensor is foreseen to show the $fT/\sqrt{\text{Hz}}$ level of noise density [4]. However, AMI306 shows around 7 nT/ $\sqrt{\text{Hz}}$ level of noise density at 10 Hz and the current nT sensor (MI-CB-1DK) shows 20–30 pT/ $\sqrt{\text{Hz}}$ at 10 Hz.

In this paper, in order to develop an MI element showing higher sensitivity and lower noise as compared to MI-CB-1DK, the effect of the aspect ratio of the amorphous magnetic wire, the number of wires and the effect of electric contact on multiple wires on noise density was investigated.

2. EXPERIMENT

A nearly non-magnetostrictive amorphous magnetic wire (hereafter called wire) with a diameter of 30 μm and composition Co-Fe-Si-B system produced by in-water-rotating quenching process was purchased from UNITIKA LTD. The hysteresis loop of the wire with a length of 5 mm was measured by Vibrating Sample Magnetometer (Toei Scientific Industrial Co., Ltd, type: PV-M10-5) and is shown in Fig. 1. The vertical axis shows the normalized magnetization by saturated magnetization.

The MI element using above wire was produced with photolithography and a pickup coil made of 30 μm copper wire was wound, and then the sensor characteristics were evaluated with an electric circuit which excites the wire by 80 mA as used in MI-CB-1DK [5]. The noise density of the MI element was measured by FFT analyzer (ONOSOKKI, type: CF-5220Z) at zero magnetic fields in the threefold magnetic shield box.

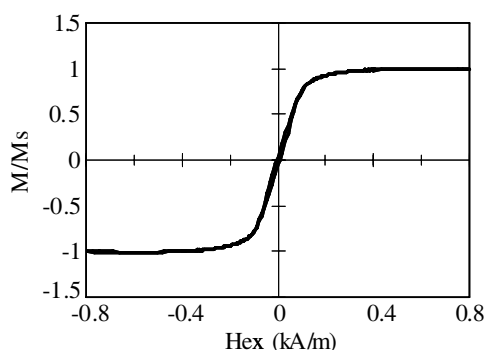


Figure 1: The hysteresis loop of wire.

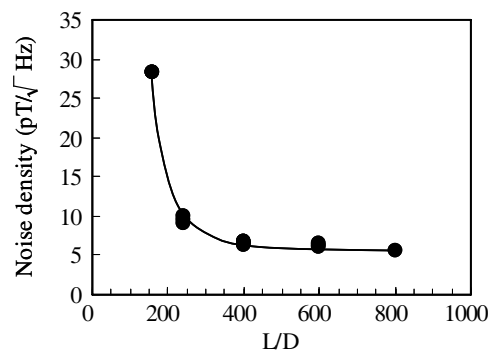


Figure 2: The effect of L/D on noise density at 10 Hz.

3. DEVELOPMENT OF LOW NOISE MI SENSOR

3.1. The Effect of Aspect Ratio, Number of Wires and Electric Contacts on Sensor Characteristics

In order to determine wire length, the effect of aspect ratio (L/D) on noise density was investigated and a sample at 10 Hz is shown in Fig. 2. Here L is defined as wire length and D is defined as diameter of wire. As shown in Fig. 2, noise density decreases as L/D increases and is saturated when L/D exceeds 400. This is because the sensitivity increases with the decrease in demagnetizing fields.

Next, in order to further reduce noise density, the effect of the number of wires on noise density was investigated. The MI element was produced with a number of wires connected in parallel and a pickup coil was wound around it. The noise density at 10 Hz is shown in Fig. 3. As shown in Fig. 3, noise density decreases as the number of wires increases. Although it was expected that the noise density decreased in inverse proportion to the square root of the number of wires, the noise density decreased almost linearly as the number of wires increased.

Thirdly, in order to further reduce noise density, the effect of electric contact with 4 wires (type A and B, shown in Fig. 4) on noise density was investigated and is shown in Fig. 5. As shown, the MI element of type B shows lower noise density compared to type A.

3.2. Development of MI Element and Its Noise Density

Based on the above investigations, an MI element with 4 wires of 10 mm with type B connections and a wound coil of 300 turns was designed. Its appearance and output property are shown in Fig. 6 and Fig. 7, respectively. The noise density of the developed MI element is shown in Fig. 8, as compared to commercialized MI-CB-1DK and AMI306. As shown in Fig. 8, the noise density of the developed MI element is about 1/10 of MI-CB-1DK. Next, with practical use in mind, sensor output of the developed MI element with ± 1 nT at 1 Hz is shown in Fig. 9, as compared to FG sensor [6] of the almost same size and MI-CB-1DK. As shown in Fig. 9, the developed MI element

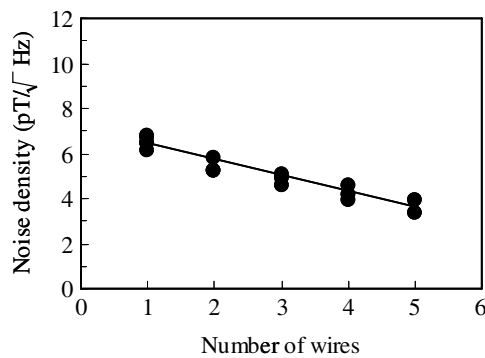


Figure 3: The effect of number of wires on noise density at 10 Hz.

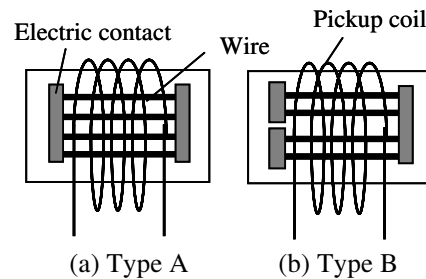


Figure 4: Electric contact type with 4 wires.

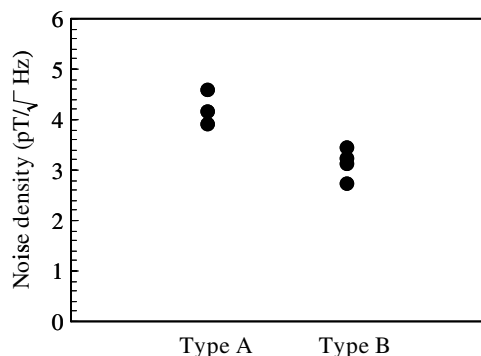


Figure 5: Comparison of the noise density at 10 Hz between type A and type B.

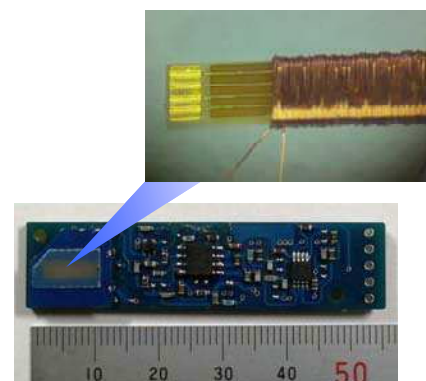


Figure 6: The appearance of developed MI sensor.

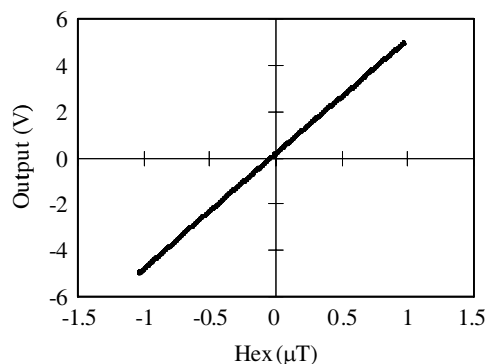


Figure 7: Output property of developed MI element.

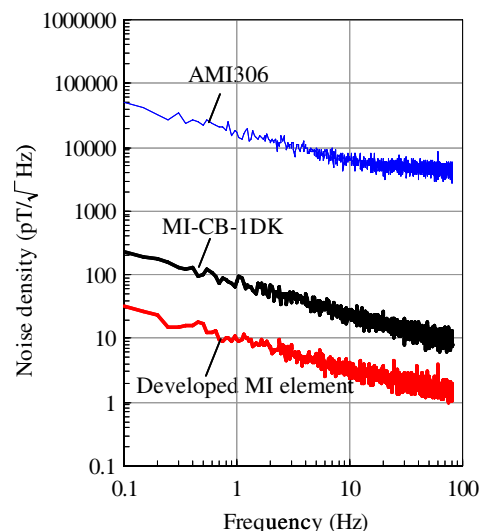


Figure 8: Noise density of developed MI sensor.

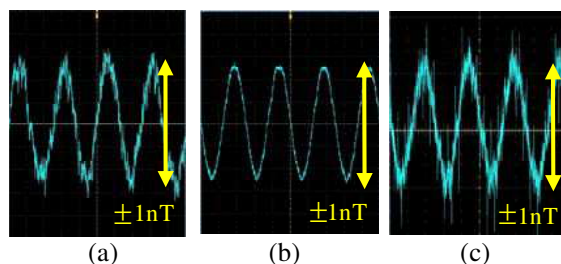


Figure 9: Sensor outputs of developed MI element. (a) MI-CB-1DK. (b) Developed MI element. (c) FG sensor.

shows sufficient magnetic resolution for detecting weak magnetic fields of 1 nT order.

4. SUMMARY

In this paper, in order to develop an MI element showing lower noise density, the effect of aspect ratio of amorphous wire, number of wires and electric contact on multiple wires on noise density was investigated. Then, an MI element showing 1/10 of the noise density of MI-CB-1DK was developed.

This developed MI element is expected to be used in various fields (foreign body detection and biomagnetic measurement etc.), due to its sub-nano-T level of noise.

REFERENCES

1. Kawashima, K., T. Kohzawa, H. Yoshida, and K. Mohri, *IEEE Trans. Magn.*, Vol. 19, 3168–3170, 1993.
2. AICHI MICRO INTELLIGENT Corporation Web site: <http://www.aichi-mi.com/>.
3. Uchiyama, T., N. Hamada, and C. M. Cai, *Digest of the 37th Annual Conference on Magnetism in Japan*, 377, 2013.
4. Melo, L. G. C., D. Ménard, A. Yelon, L. Ding, S. Saez, and C. Dolabdjian, *J. Appl. Phys.*, Vol. 103, 033903, 2008.
5. Hamada, N., A. Shimode, T. Kawano, H. Arakawa, M. Yamamoto, and Y. Honkura, *Abstract of International Magnetism Conference, Intermag*, 2011.
6. Stefan Mayer web site: <http://www.stefan-mayer.com>.

Test-production of High Sensitivity Multi-core MI Element and Its Characteristics

N. Hamada, A. Shimode, S. Tatematsu, and M. Yamamoto
Aichi Steel Corporation, 1 Wano-Wari Arao-machi, Tokai 476-8666, Japan

Abstract— The magnetic sensor is used in various fields such as industrial, automobile, IT and biomagnetism. The MI sensor is a magnetic sensor based on the MI (Magneto Impedance) effect discovered by K. Mori et al. in 1993. The MI element with a pickup coil produced by a plating process is used in electromagnetic compasses. Although it can detect 1–1000 μT level, higher performance in sensitivity and noise level is required. Here, the effect of wire length, magnetic property of the amorphous magnetic wire, the number of coil turns and number of cores on the sensor characteristics was investigated. Then based on the above investigations, the designed MI element was test produced. It was found that the designed element shows dramatically higher sensitivity and 1/100 noise, as compared to the currently used MI element (AMI306).

1. INTRODUCTION

The magnetic sensor is used in various fields such as industrial, automobile, IT and biomagnetism. The MI sensor is a magnetic sensor based on the MI (Magneto Impedance) effect discovered by K. Mori et al. in 1993 [1]. It can detect weak magnetic fields in the pT-mT order. According to theoretical analysis, the MI sensor is foreseen to show the $f\text{T}/\sqrt{\text{Hz}}$ level of noise density [2], and its performance would even be equal to SQUID.

The MI element with a pickup coil produced by a plating process (Fig. 1(a)) is used in electromagnetic compasses. Although it can detect 1–1000 μT level [3], higher performance in sensitivity and noise is required. On the other hand, a specialized high sensitivity type magnetic sensor (nT sensor) with wound coil made with copper wire of 30 μm (Fig. 1(b)) which can detect nT level [4], has also been commercialized for use in detecting AC magnetic fields and research of biomagnetic measurement using this MI element has also been reported [5].

Although the MI element (Fig. 1(b)) shows higher sensitivity the MI element (Fig. 1(a)) is more suitable for mass production in cost. Therefore in this paper, in order to develop MI element which shows higher sensitivity, with pickup coil produced by a plating process, the effect of wire length, magnetic property of the wire, coil turns and the number of cores (MI element) on sensor characteristics was investigated.

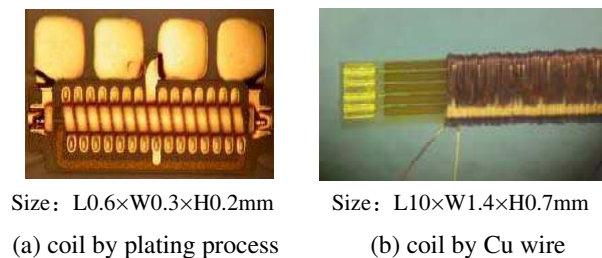


Figure 1: The aspects of MI element.

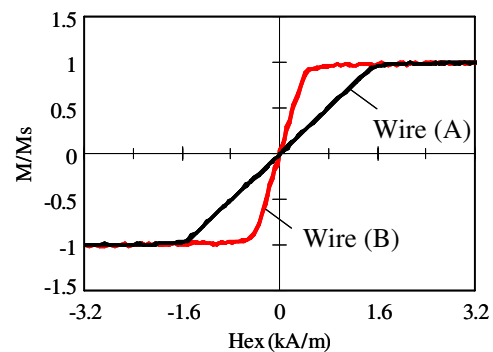


Figure 2: The hysteresis loops of wire.

2. EXPERIMENT

A nearly non-magnetostrictive amorphous magnetic wire with a diameter of 15 μm and composition Co-Fe-Si-B system produced by an in-water-rotating quenching process was purchased from UNITIKA LTD. Then two kinds of wire showing deferent magnetic properties were tailored by annealing at around 400 deg C [6]. The hysteresis loops of wire (A) and (B) with a length of 5 mm were measured by Vibrating Sample Magnetometer (Toei Scientific Industrial Co., Ltd, type: PV-M10-5) and are shown in Fig. 2. Here, in this paper, the magnetic field where the normalized

magnetization by saturated magnetization showing 90% was defined as H_k , corresponded to an anisotropy field.

The MI element was produced by photolithography and plating processes. The sensor characteristics of the MI element were evaluated with an electric circuit [4] used in the nT sensor (MI-CB-1DJ). The noise density of the MI element was measured by FFT analyzer (ONOSOKKI, type: CF-5220Z) at zero magnetic fields with magnetic shielding.

3. DESIGN OF MI ELEMENT

3.1. The Effect of Wire Length, Magnetic Property of Wire and Coil Turn on Sensor Characteristics

In order to determine the length of the MI element (wire), the effect of wire length on H_k was investigated using the wire (A). As shown in Fig. 3, H_k decreased as wire length increased and showed a trend toward saturation when the wire length exceeded 1 mm. This is because the influence of the demagnetizing field decreases. Since a demagnetizing field reduces the sensitivity of the sensor characteristics, it was found that wire length should be 1 mm or more.

Next, in order to determine the magnetic property (H_k) of wire which shows higher sensitivity as an MI sensor the output properties of MI elements produced using wire (A) and (B) were compared. The MI element consists of a wire with a length of 0.52 mm and a coil of 25 turns (17 μm coil pitch). As shown in Fig. 4, the MI element using wire (B) shows higher sensitivity compared to using wire (A). In fact, the sensitivity is strongly related to the H_k of the wire, and this is the same tendency as in the case of detecting impedance change with external magnetic fields [7].

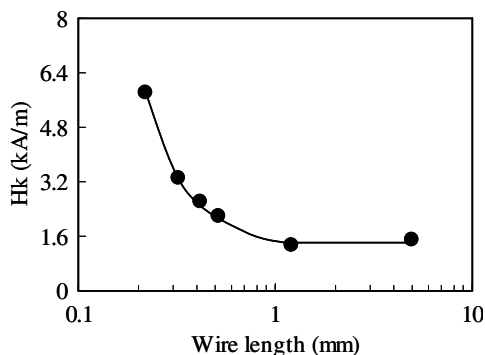


Figure 3: The effect of wire length on H_k .

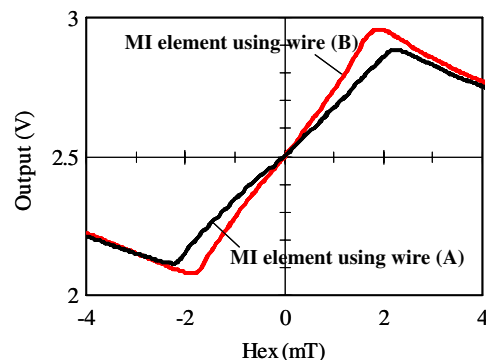


Figure 4: Output of produced MI elements.

Thirdly, in order to investigate the effect of the number of coil turns on the MI element on sensitivity, the MI elements using wire (A) of a length of 0.52 mm with 15–28 coil turns (30–15 μm coil pitch) were produced (Fig. 5). As shown in Fig. 6, although sensitivity increases as the number of coil turns increase, when the number of coil turns exceeded 21 turns, it was found that the sensitivity increase tended to be saturated. This is because the coil resistance becomes larger.

3.2. Design of MI Element

Based on the above chapters, MI elements using wire (B) were designed and a multi-core MI element was also considered. The design is shown in Table 1 and the appearance of the produced MI elements is shown in Fig. 7. Each output property is shown in Fig. 8, as compared to the commercialized MI

Table 1: Design of MI element.

	(A)	(B)	(C)
Wire length (mm)	1.2		
Number of core	1	2	4
Wire R (Ω)	12.7	25.1	50.2
Coils pitch (μm)	17		
Coil turns	66	132	250
Coil R (Ω)	6.4	11.6	23.9

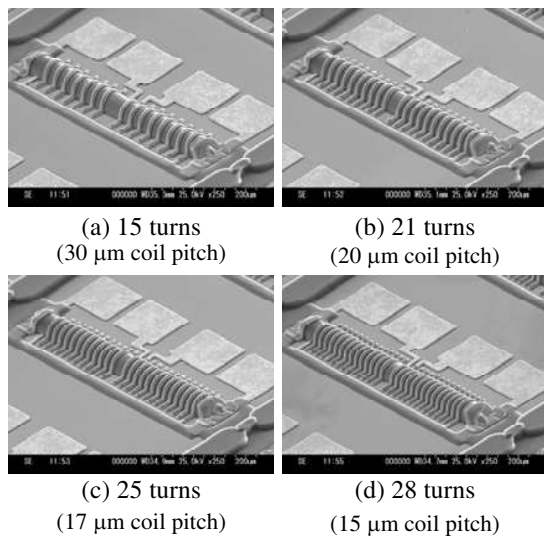


Figure 5: The appearance of MI element with several coil turn.

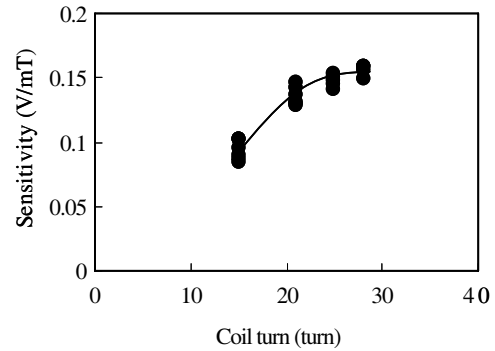


Figure 6: The effect of coil turn on sensitivity.

sensor (AMI306 [8]). As shown in Fig. 8, the sensitivity increases as the number of cores increases and it is found that the multi (4)-core MI element shows dramatically higher sensitivity than AMI 306.

3.3. The Noise Level of the Developed MI Element

The noise density of the multi (4)-core MI element was measured and it is shown in Fig. 9, as compared to AMI306 and commercialized nT sensor (MI-CB-1DJ). As shown in Fig. 9, the devel-

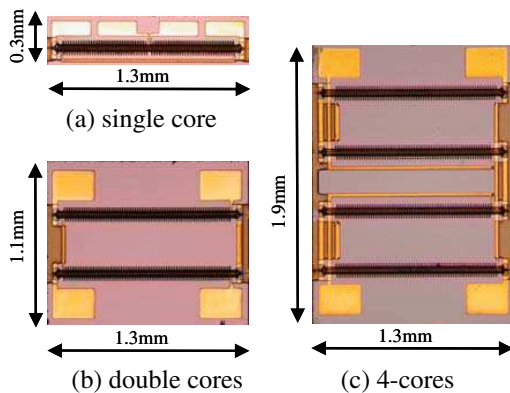


Figure 7: The appearances of designed MI elements.

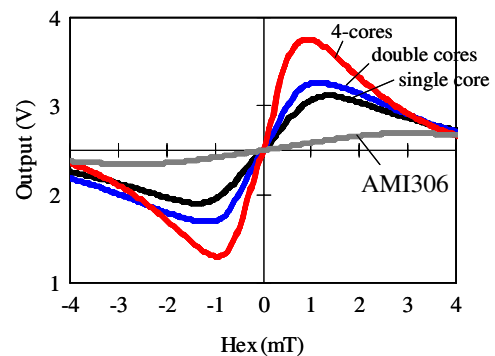


Figure 8: Output of designed MI elements.

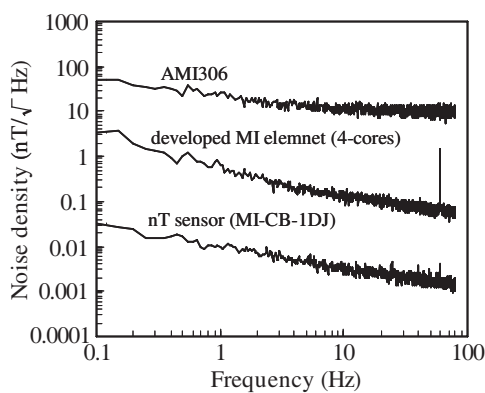


Figure 9: Noise density of 4-cores MI element.

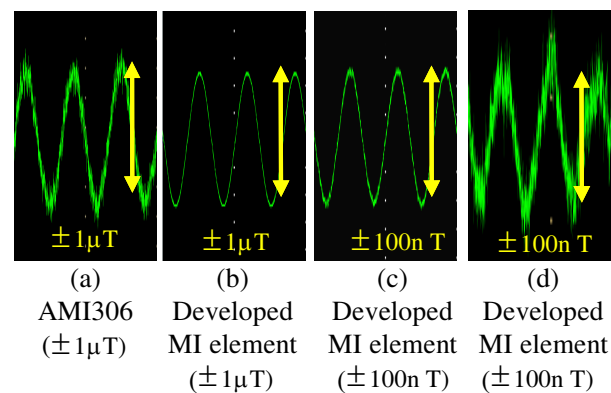


Figure 10: Sensor outputs of developed MI element corresponded to magnetic fields.

oped MI element shows 1/100 the noise level of AMI306. In addition, the sensor outputs of the developed MI element when several magnetic fields ($\pm 1 \mu\text{T}$, $\pm 100 \text{ nT}$, $\pm 10 \text{ nT}$) at 30 Hz are applied by a Helmholtz coil are shown in Fig. 10. Considering the viewpoint of each noise level, it is found that the developed MI element would have sufficient magnetic resolution in the case of $\pm 100 \text{ nT}$.

4. SUMMARY

In this paper, based on the effect of wire length, magnetic property (Hk) of wire and the number of coil turns on sensor characteristics, an MI element that could detect magnetic fields of $\pm 100 \text{ nT}$ order was developed. This developed MI element is expected to be used not only as an electromagnetic compass, for which increasingly higher levels of performance are being required, but also in automobile or industrial markets.

REFERENCES

1. Panina, L. V. and K. Mohri, *Applied Physics Letter*, Vol. 65, Vol. 9, 1189–1191, 1994.
2. Melo, L. G. C., D. Ménard, A. Yelon, L. Ding, S. Saez, and C. Dolabdjian, *J. Appl. Phys.*, Vol. 103, 033903, 2008.
3. Shimode, A., N. Hamada, M. Mori, T. Nagao, M. Yamamoto, and Y. Honkura, *Abstract of International Workshop on Magnetic Wires, IWMW2010*, 2010.
4. Hamada, N., A. Shimode, T. Kawano, H. Arakawa, M. Yamamoto, and Y. Honkura, *Abstract of International Magnetism Conference, Intermag*, 2011.
5. Uchiyama, T., N. Hamada, and C. M. Cai, *Digest of the 37th Annual Conference on Magnetism in Japan*, 377, 2013.
6. Freijo, J. J., M. Vazquez, and A. Hernando, *J. Appl. Phys.*, Vol. 85, No. 8, 5450, 1999.
7. Marin, P., J. Arcas, A. Zhukov, M. Vazquez, and A. Hernando, *Magn. Hyst. N. M. M.*, 743–748, 1997.
8. AICHI MICRO INTELLIGENT Corporation Web site: <http://www.aichi-mi.com/>.

Arousal Effect of ELF Magnetic Stimulus on Car Driver's Spine Evaluated with Occipital Electro-encephalogram and Back Magneto-cardiogram

Yoshiyuki Mohri¹, Muneo Yamada¹, Wataru Kato¹, Tsuyoshi Uchiyama², and Kaneo Mohri³

¹Faculty of Science and Technology, Meijo University, Nagoya 468-8502, Japan

²Graduate School of Engineering, Nagoya University, Nagoya 464-8603, Japan

³Nagoya Industrial Science Research Institute, Nagoya 464-0819, Japan

Abstract— We found two positive effects in the human body activity induced with an extremely low frequency (ELF) distributed magnetic field stimulus at the spine position: (1) Increasing of the defined arousal index $(\alpha + \beta)/(\theta + \delta)$ up to around 3.0 in the occipital electro-encephalogram (O-EEG), and (2) Increasing of the energy concentration in the FFT frequency spectra for the back magneto-cardiogram (B-MCG) measured with the Pico-Tesla resolution magneto-impedance sensor.

Probable correlation between the arousal center in the brainstem and the aorta with the aorta corpuscle via the vagus nerve concerning a mutual activation is discussed on the basis of the phenomena.

1. INTRODUCTION

We have developed an effective and safe method for prevention of the drowsiness during car driving with the ELF distributed magnetic stimulus on the driver's body surface at the spine [1–3] and at the pit of the stomach [4] using the magnetized olivine sintered particle train. The ELF magnetic field is applied to the blood water when the blood flows through the periodic alternating pulse distributed magnetic field generated on the sintered magnetic particle train resulting the generation of the free protons and the ATP production is promoted in the bio cells for body activation due to the magneto-protonics principle [5].

Both magnetic stimuli resupply the bio-body energy ATP on the basis of the magneto-protonics and so are not accompanied with so-called the “rebound problem” inducing a deeper drowsiness after a tentative arousal with the sensory stimuli such as the flush light, the sound or voice, the perfume shot and so on.

Thus, we tentatively concluded that the ELF magnetic stimulus on the spine position is superior for the arousal than that on the pit of the stomach after in comparison the increasing rate of the arousal index $(\alpha + \beta)/(\theta + \delta)$ between them for eleven subjects in the driving simulator test. On the basis of the results, we investigated a dependency of the EEG with the head position concerning the arousal index change after application of the ELF magnetic stimulus at the spine position for three subjects and found a remarkable arousal effect occurred at the back of the head position for all subjects. We also measured the back magneto-cardiogram of the same subjects using the pico-Tesla resolution magneto-impedance sensor [6] and found a remarkable change in the FFT frequency spectrum for the heart stroke magnetic-field time series with application of the ELF magnetic stimulus. That is, a remarkable simplification of the frequency spectrum reflecting the heart stroke system energy concentration is induced with the ELF magnetic stimulus. Thus we may consider a relationship between the arousal effect and the heart stroke activation effect with the identical ELF magnetic stimulus on the basis of the physiology showing the vagus nerve connecting mutually the brain stem and the aorta with the aorta corpuscle [7]. We also found a possibility of a visual perception activation effect with the ELF magnetic stimulus on the basis of an experimental result of a 0.5 second displayed patterns recognition test.

2. EXPERIMENTAL PROCEDURE

We use a rubber coated 9 mm diameter olivine sintered magnetized particle train belt, as illustrated in Fig. 1, which generates the bio-activation magnetic field with around 2-cm period alternating pulse distributed train for the ELF magnetic stimulus. When the human blood water runs through the magnetic field with around 30 cm/s, the water is exposed to an ELF (around 15 Hz) magnetic field and generates free protons. The serotonin production rate at the medulla is promoted with the increased ATP due to the free protons and activates the arousal function.

Rubber Coated Olivine Sintered Magnetized Particle Train Belt

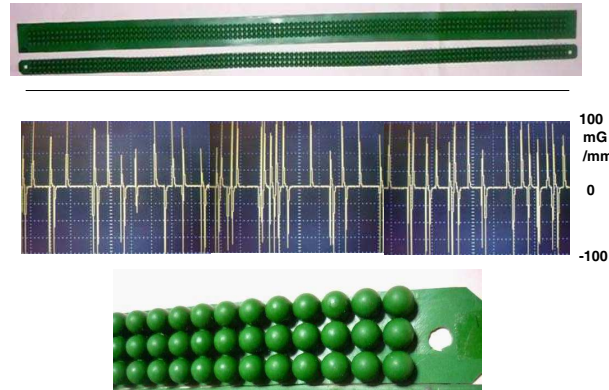


Figure 1: Rubber coated 9 mm diameter olivine sintered magnetized particle train belt generating bio-activation magnetic field with around 2-cm period alternating pulse distributed train.

3. EXPERIMENTAL RESULTS

3.1. Electro-encephalogram Measurements

Figure 2 represents measured results of the arousal index $(\alpha + \beta)/(\theta + \delta)$ for eleven subjects (22–28 years old) after 20-min. night time simple high-way driving in the driving simulator without magnetic stimulus, with the spine ELF magnetic stimulus, or with the pit of the stomach ELF magnetic stimulus. The EEG measurements were carried out for each subject in different three days in a week. Therefore, we tentatively concluded that the ELF magnetic stimulus at the spine position was the most effective for the arousal.

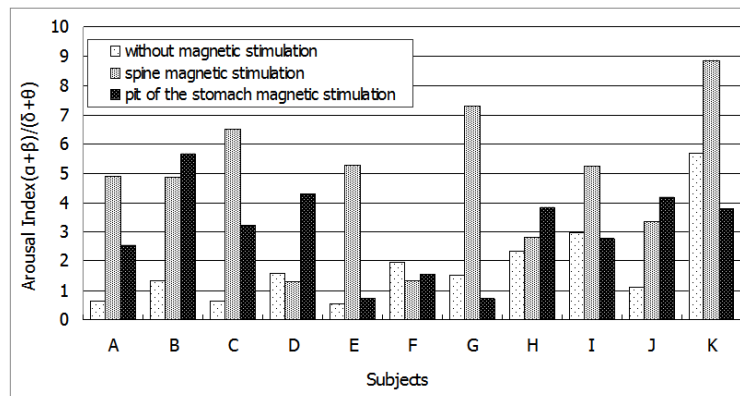


Figure 2: Arousal index of eleven subjects measured after 20-min. night time simple high-way driving in the driving simulator without magnetic stimulus, with the spine ELF magnetic stimulus, or with the pit of the stomach ELF magnetic stimulus.

Figure 3 shows the change of the arousal index for three subjects (28 year-old male (A), 73 year-old female (B), and 73 year-old male (C)) with the ELF magnetic stimulus applied to the spine position. The EEG measurement at the forehead and the occipital (back of the head) was carried out for each subject quietly sitting on a car driver's seat with closing eyes before the magnetic stimulus and after the 30-min. ELF magnetic stimulus with contacting the magnetized belt on one's spine position. We found that a remarkable arousal effect occurred in the occipital EEG with the ELF magnetic stimulus for all subjects, whilst the arousal was occurred for the two subjects and slightly decreased for the one subject in the forehead EEG.

3.2. Back Magneto-cardiogram

We detected the magneto-cardiogram at the left shoulder blade bottom position (Back-MCG) of the subject to which the amorphous wire head of the pico-Tesla resolution magneto-impedance sensor (PT-MI sensor) [6] is slightly touched via a cloth. We have found that the Back-MCG may reflect the activity of both the heart muscle and the aorta muscle referring the double-peak waveform in

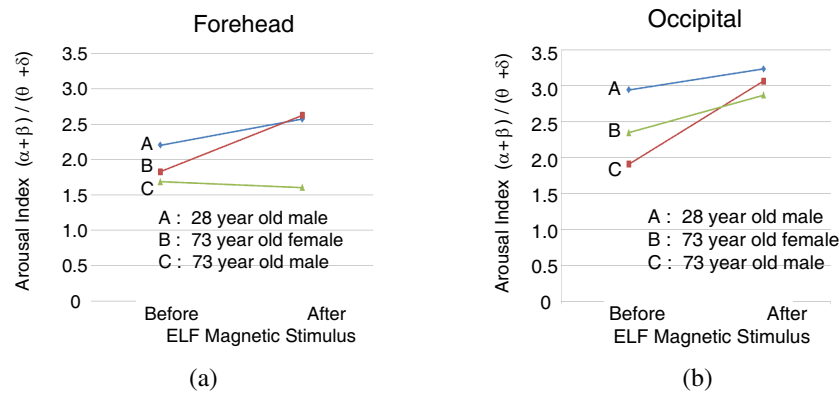


Figure 3: Change of the arousal index with application of the ELF magnetic stimulus at the spine: EEG measurement at (a) the forehead, and (b) the occipital (back of the head).

the Back-MCG, while the double-peak waveform does not appear in the Chest-MCG [8].

Figure 4 illustrates the FFT frequency spectra of the measured Back-MCG for three subjects same to the case of Figure 3 before and after application of the ELF magnetic stimulus: the 28 year-old male in (a), the 73 year-old female in (b), and 73 year-old male in (c). We found remarkable change in these spectra with the ELF magnetic stimulus showing energy concentration to the frequency f_1 which is considered as the basic heart stroke frequency of the heart-aorta blood flow system [8]. It is considered that the ELF magnetic stimulus may activate and increase the stability of the blood flow system.

Both experimental results of Figure 3 for the occipital EEG and Figure 4 for the Back-MCG suggest a relationship of the arousal center and the blood flow system and may support an activation model for the arousal center near the medulla in the brain stem and the blood flow system connected each other with the vagus nerve system with the spine ELF magnetic stimulus promoting the ATP production in the bio cells in the back of the human body.

The remarkable activation effect for the arousal in the area of the back of the head suggests a possibility of activation of the visual function. Therefore, we investigated an influence of the spine ELF magnetic stimulus for a flash displayed alphabet small characters visual recognition test as shown in Figure 5: A dotted line was before the ELF magnetic stimulus applied 30 min. at the spine and a real line was after the stimulus.

The subject (73 year-old male) has trained 7 days before the test and found almost no influence of the stimulus on the test in ordinary healthy condition. An influence appeared as in Figure 5 for the subject in a bad condition with such as a headache. The total point was improved from 73 to 91 points.

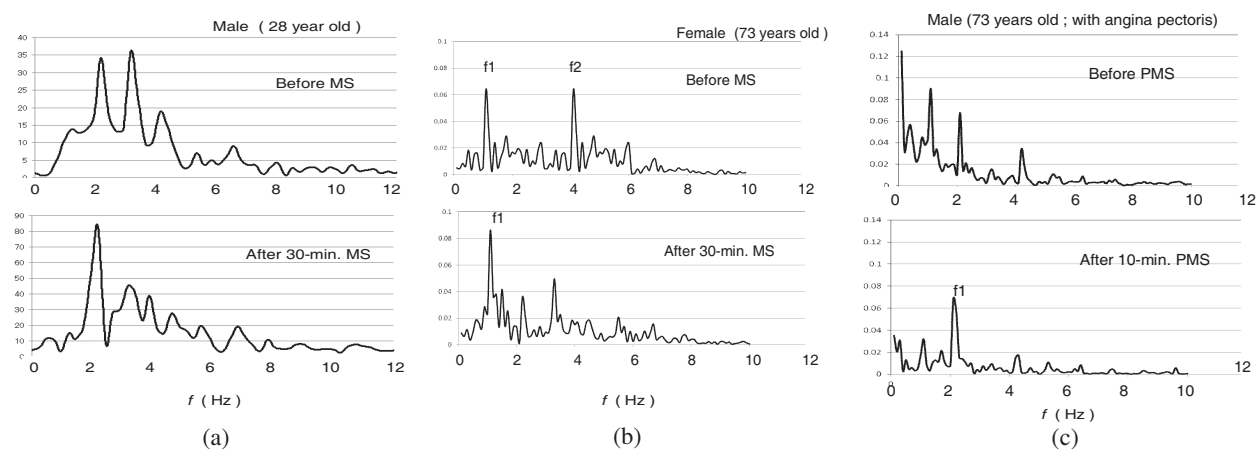


Figure 4: FFT frequency spectra of measured Back-Magnetocardiogram (Back-MCG) before and after application of the ELF magnetic stimulus: (a) the 28 year-old male, (b) the 73 year-old female, and (c) the 73 year-old male.

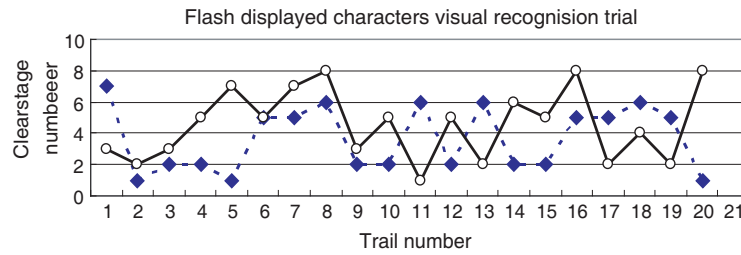


Figure 5: Improvement of a flush-displayed characters visual recognition ability with the spine ELF magnetic stimulus. The real line is after the spine ELF magnetic stimulus.

4. CONCLUSIONS

A remarkable arousal effect was obtained for the occipital EEG with the spine ELF magnetic stimulus.

Significant energy concentration appeared in the FFT frequency spectra with the spine ELF magnetic stimulus. Possible relation between them was discussed.

ACKNOWLEDGMENT

The authors wish to express their gratitude to Mr. M. Matsubara of Shinko-yogyo Ltd., Japan for his sintered particle experiments and Mr. H. Umemoto of Mitsuuma Ltd. Japan for his rubber coating experiments for the sintered particles.

REFERENCES

1. Mohri, K., T. Uchiyama, M. Yamada, T. Watanabe, Y. Inden, T. Kato, and S. Iwata, "Arousal effect of physiological magnetic stimulation on elder person's spine for prevention of drowsiness during car driving," *IEEE Trans. Magn.*, Vol. 47, No. 10, 3066–3069, 2011.
2. Mohri, K., T. Uchiyama, M. Yamada, Y. Mohri, K. Endo, T. Suzuki, and Y. Inden, "Physiological magnetic stimulation for arousal of elderly car driver evaluated with electro-encephalogram and spine magnetic field," *IEEE Trans. Magn.*, Vol. 48, No. 11, 3505–3508, 2012.
3. Mohri, Y., M. Yamada, K. Endo, T. Suzuki, and K. Mohri, "Arousal effect of physiological magnetic stimulation on car driver's spine evaluated with electro-encephalogram using driving simulator," *PIERS Proceedings*, 245–249, Kuala Lumpur, Malaysia, Mar. 27–30, 2012.
4. Mohri, Y., M. Yamada, K. Sakai, W. Kato, K. Mohri, and T. Uchiyama, "Arousal effect of physiological magnetic stimulation on car driver's pit of stomach evaluated with electro-encephalogram using driving simulator," *PIERS Proceedings*, 617, Taipei, Mar. 25–28, 2013.
5. Mohri, K. and M. Fukushima, "Milligauss magnetic field triggering reliable self-organization of water with long range ordered proton transport through cyclotron resonance," *IEEE Trans. Magn.*, Vol. 39, No. 5, 3328–3330, 2003.
6. Uchiyama, T., K. Mohri, Y. Honkura, and L. V. Panina, "Recent advances of pico-Tesla resolution magneto-impedance sensor based on amorphous wire and CMOS IC MI sensor," *IEEE Trans. Magn.*, Vol. 48, No. 11, 3833–3839, 2012.
7. Sugi, H., *Physiology of Human Body Function*, 3rd Edition, Nankodo, Tokyo, Japan, 1999 (in Japanese).
8. Mohri, Y., T. Uchiyama, M. Yamada, and K. Mohri, "Detection of back magneto-cardiogram for heart diseases at left shoulder blade bottom using pico-tesla magneto-impedance sensor," *PIERS Proceedings*, Gungzhou, China, Aug. 25–28, 2014.

Detection of Back Magneto-cardiogram for Heart Disease Using Pico-Tesla Resolution Amorphous Wire Magneto-Impedance Sensor

Yoshiyuki Mohri¹, Tsuyoshi Uchiyama², Muneo Yamada¹, and Kaneo Mohri³

¹Faculty of Science and Technology, Meijo-University, Nagoya 468-8502, Japan

²Graduate School of Engineering, Nagoya University, Nagoya 464-8603, Japan

³Nagoya Industrial Science Research Institute, Nagoya 464-0819, Japan

Abstract— We measured the magneto-cardiogram at the back of the human body (Back Magneto-cardiogram; Back-MCG) using the pico-Tesla resolution amorphous wire magneto-impedance sensor (PT-MI sensor) and found that the double-peak magnetic field waveform appeared in the healthy subject's Back-MCG only, while disappeared in the angina pectoris patient's Back-MCG. We also found that the double-peak waveform appeared for a while such as around 1 hour even in the Back-MCG of the angina pectoris patients after application of an ELF magnetic stimulus with stroking a magnetized crashed stone packed pipe on the body through 10 min.

1. INTRODUCTION

A non-invasive and sensitive detection method for heart diseases have been required on the prediction of the World Health Statistics 2012 by the WHO which predicted that the number of deaths from heart diseases per one year would increase to 25 million by 2030. We have developed a highly sensitive magnetic sensor having 1 pico-Tesla resolution using the amorphous wire CMOS IC magneto-impedance sensor named the PT-MI sensor [1,2]. We detected the Back Magneto-cardiogram (Back-MCG) at the left shoulder blade bottom position of the subject slightly touching the amorphous wire head using the PT-MI sensor and found that the double-peak magnetic field waveform appeared in the Back-MCG of the healthy subjects, which disappeared in the Back-MCG of angina pectoris patients. The double-peak waveform does not appear in the Chest-MCG for both healthy and patients with heart diseases.

We also found that the double-peak waveform appeared for a while such as one hour in the Back-MCG of the angina pectoris patients after application of an ELF magnetic stimulus with stroking a magnetized stone packed pipe on their body surface through 10 min., resulting a probable improvement of the heart diseases. Similar probable improvement was obtained after application of an ELF magnetic stimulus with touching a magnetized sintered particle train belt [3] on their spine position through 30 min..

2. MEASUREMENTS

2.1. Chest Magneto-cardiogram

Figure 1 represents simultaneous measurement results of the electrocardiogram (ECG) and the chest magneto-cardiogram (MCG) for a healthy subject (51 year old male) using the PT-MI sensor without any magnetic shielding. We found a time lag of around 150 ms of the MCG peak waveform behind the ECG peak waveform (0.4π rad. phase lag), which substantiates an assumption that the origin of the MCG peak pulse should be the Ca^{2+} ion current magnetic field flowing into the muscle cells triggered with the action potential ECG peak pulse [4, 5].

2.2. Back Magneto-cardiogram

Figure 2 illustrates measured results of the back magneto-cardiogram (Back-MCG) for five subjects: (a) healthy 51 year-old male, (b) healthy 46 year-old male, (c) healthy 73 year-old female, (d) 71 year-old male with the angina pectoris, and (e) 73 year-old male with the angina pectoris. The Back-MCG was detected using the PT-MI sensor at the left shoulder blade bottom position of each subject sitting quietly on a wooden chair without any magnetic shielding. We newly found that a double-peak waveform (DP) appeared in the Back-MCG of all healthy subjects (a), (b), and (c), while no appearance for angina pectoris patients (d) and (e).

We found a conformity of the double peaks in the Back-MCG for the healthy subjects in Figure 2 to the open and close, respectively, of the aortic valve in the time phase. Thus, it would be possible

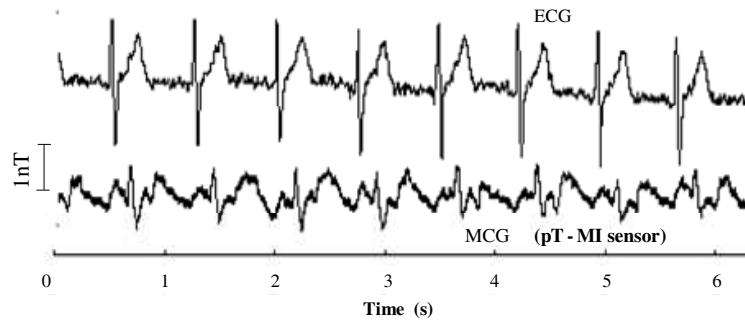


Figure 1: Simultaneous measurements of the electrocardiogram (ECG) and the chest magneto-cardiogram (MCG) for a healthy subject (51 year-old male) using the PT-MI sensor.

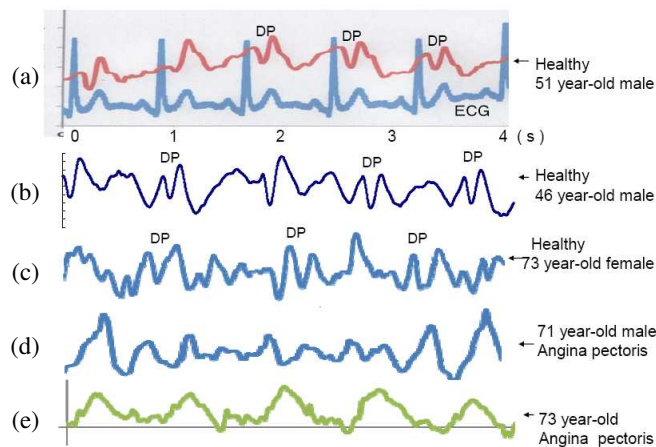


Figure 2: Back Magneto-cardiogram using the PT-MI sensor for (a) healthy 51 year-old male, (b) healthy 46 year-old male, (c) healthy 73 year-old female, (d) 71 year-old male with angina pectoris, and (e) 73 year-old male with angina pectoris.

to develop a new device for diagnosis of the arteriosclerosis measuring the time between the aortic valve open and the ascending of the pulse wave at the ankle.

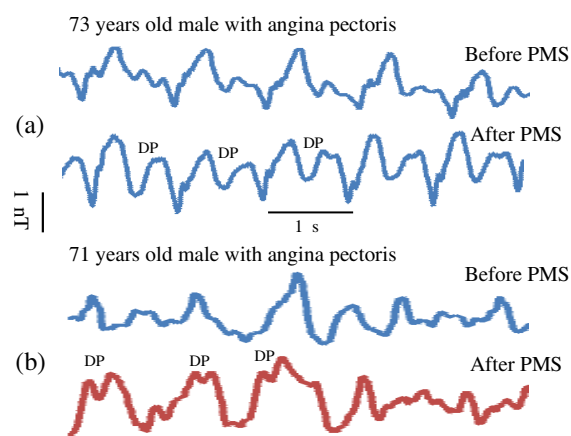


Figure 3: Change of the Back-MCG waveform for two patients with the angina pectoris after stroking a magnetized stone packed pipe on their body through 10 min.: (a) 73 year-old male, and (b) 71 year-old male.

3. CHANGE OF BACK-MCG WITH ELF MAGNETIC STIMULUS

We found that the DP magnetic field waveform appeared in the Back-MCG of the two angina pectoris patients after stroking a magnetized stone packed pipe on their body through 10 min. (we say “Physiological Magnetic Stimulus; PMS”) as represented in Figure 3. The probable improvement of the angina pectoris showing the Back-MCG DP wave with the pipe magnetic stimulus is considered due to the magneto-protonics principle, in which the free protons generated in the body water running through the periodical distributed alternating pulse magnetic field on the pipe surface activated the ATP production function of the mitochondria in the aorta muscle cells and the heart muscle cells [3, 6].

4. FFT FREQUENCY SPECTRUM OF BACK-MCG

Figure 4 shows the FFT frequency spectrum of the Back-MCG of the three subjects: (a) healthy 73 year-old female, (b) 71 year-old male with the angina pectoris, and (c) 73 year-old male with the angina pectoris.

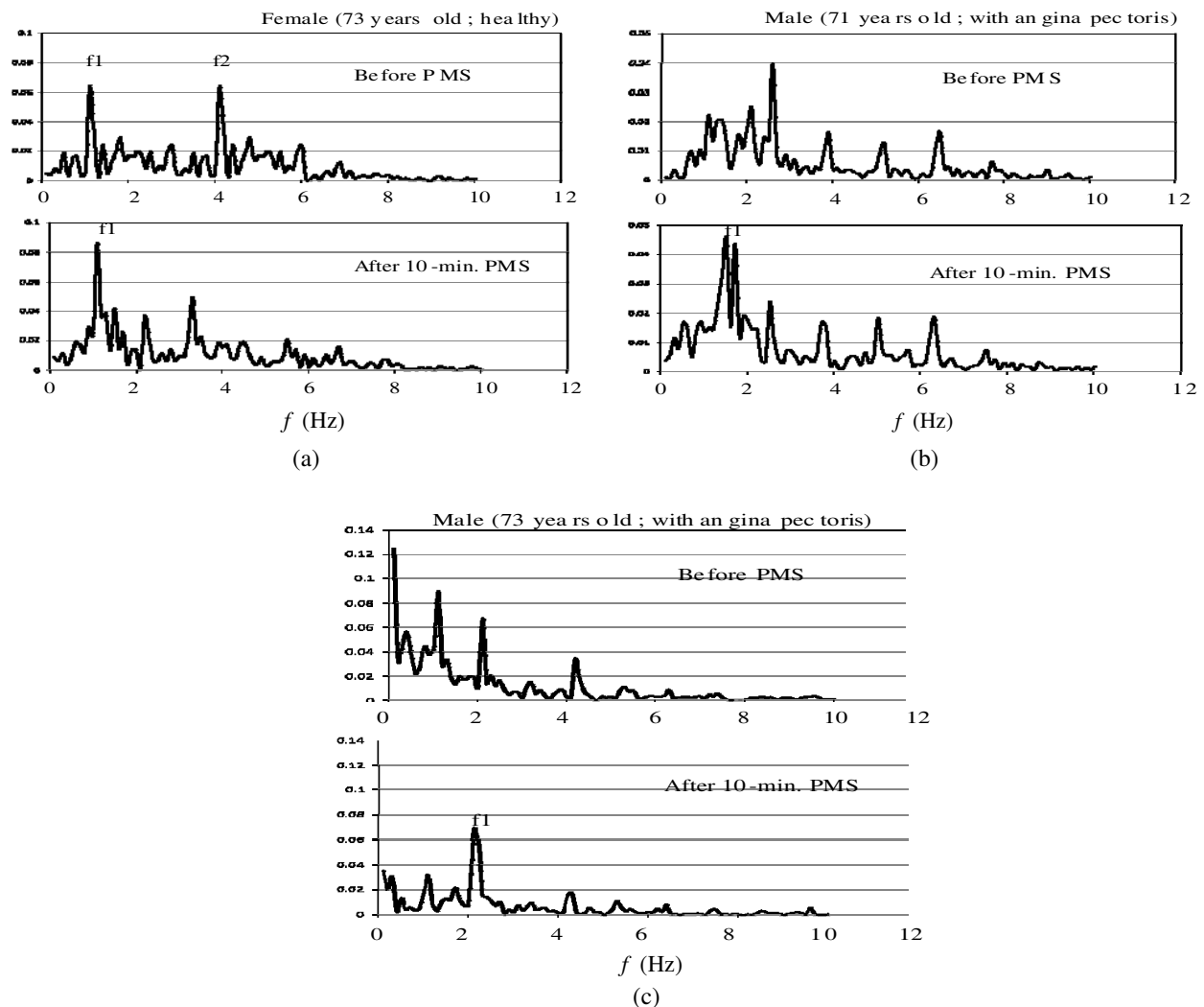


Figure 4: FFT frequency spectrum of the Back-MCG before and after the magnetic stimulus with stroking the magnetized stone packed pipe on the body through 10 min. for (a) healthy 73 year-old female, (b) 71 year-old male with the angina pectoris, and (c) 73 year-old male with the angina pectoris.

We found an energy concentration in the frequency spectra (a)–(c) to the basic stroking frequency f_1 of the heart-aorta blood circulation system with application of the ELF magnetic stimulus.

5. CONCLUSIONS

We newly found the existence of a double-peak magnetic field wave in the Back-MCG for healthy subjects whilst disappears for subjects with the angina pectoris. We may expect a new non-invasive and sensitive diagnosis method for heart diseases with measurement of the Back-MCG using the amorphous wire PT-MI sensor although we should increase the number of subjects. The ELF magnetic stimulus may effective for tentative recovery of the angina pectoris.

ACKNOWLEDGMENT

The authors wish to express their gratitude to Dr. H. Nakagawa of Aichi Steel Co. for his presentation of magnetized oxidized slag stones for making the magnetic stimulus pipe.

REFERENCES

1. Uchiyama, T., K. Mohri, Y. Honkura, and L. V. Panina, “Recent advances of Pico-Tesla resolution magneto-impedance sensor based on amorphous wire and CMOS IC MI sensor,” *IEEE Trans. Magn.*, Vol. 48, No. 11, 3833–3839, 2012.
2. Nakayama, S., K. Sawamura, K. Mohri, and T. Uchiyama, “Pulse-driven magneto-impedance sensor detection of cardiac magnetic activity,” *PLOS ONE*, Vol. 6, No. 10, 1–6, 2011.
3. Mohri, K., T. Uchiyama, M. Yamada, T. Watanabe, Y. Inden, T. Kato, and S. Iwata, “Arousal effect of physiological magnetic stimulation on elder person’s spine for prevention of drowsiness during car driving,” *IEEE Trans. Magn.*, Vol. 47, No. 10, 3066–3069, 2011.
4. Kurihara, S., “Regulation of cardiac muscle contraction by intracellular Ca^{2+} ,” *Jpn. J. Physiol.*, Vol. 44, No. 9, 591–611, 1994.
5. Uchiyama, T., K. Mohri, and S. Nakayama, “Measurement of spontaneous oscillatory magnetic field of guinea-pig smooth muscle preparation using Pico-Tesla resolution amorphous wire magneto-impedance sensor,” *IEEE Trans. Magn.*, Vol. 47, No. 11, 3070–3073, 2011.
6. Mohri, K. and M. Fukushima, “Milligauss magnetic field triggering reliable self organization of water with long range ordered proton transport through cyclotron resonance,” *IEEE Trans. Magn.*, Vol. 39, No. 5, 3328–3330, 2003.

Promotion Rate Index in ELF Magneto-protonics

Kaneo Mohri^{1,3}, Masanori Fukushima², Yuko Mohri^{1,4}, and Yoshiyuki Mohri¹

¹MI Institute, Nagoya 468-0028, Japan

²Foundation for Biomedical Research and Innovation, TRI-Kobe, Kobe 650-0047, Japan

³Nagoya Industrial Science Research Institute, Nagoya 464-0819, Japan

⁴Faculty of Science and Technology, Meijo University, Nagoya 468-8502, Japan

Abstract— An evaluation index for the promotion rate with 1–2% per week in the ELF magneto-protonics is proposed for development of the bio industry such as the cultivation and the farming on the basis of the tests for the vegetable plant cultivation, goldfish culture, and the hardening of the high strength concrete.

1. INTRODUCTION

We have proposed a new hypothetical principle named “Magneto-protonics”, since 2001 [1–3] in which the free proton generated in the water exposed to an extremely low frequency (ELF) small magnetic field. When the free protons generate in the bio-cell water, the promotion of the ATP production ability due to the proton flow in the mitochondria ATP-ase activates organisms including human [4, 5]. The magnetization of a magnetized water exposed to the ELF magnetic field has been detected using a Pico-Tesla MI sensor [6]. The magneto-protonics principle has been reviewed in detail [7]. Various evidence for the magneto-protonics bio-activation effect has been accumulated in the agricultural tests of such as the Gifu strawberry cultivation test in the Gifu prefectural agriculture research center in Japan [8].

Exposure to the ELF magnetic field in the bio body is realized using not only a conductor coil connected with the electronic oscillator but also a group of magnetized stones generating periodical alternating pulse distributed magnetic field through which the bio water such as the blood water flows [8–12]. Remarkable effects of the arousal for prevention of the drowsiness during car driving [9–11] and the health recovery for a patient with the angina pectoris [12] both would be useful for the establishment of the super-elderly sustainable society such as Japan. Therefore, we defined a promotion rate index for reasonable evaluation of the magneto-protonics effect on the bio activation such as the body growth of the crop and the domestic animal even in an early stage.

We have also found the hardening of the concrete has been promoted when using the magnetized coarse aggregate such as the magnetized olivine crashed stone and the magnetized oxidized slag crashed stone utilizing the free proton generation in the water during the concrete ingredients mixing [13]. We found that the hardening promotion effect of the magnetized aggregate concrete is also evaluated using the same promotion rate index.

2. GROWTH PROMOTION RATE INDEX: 1–2% PER WEEK IN MAGNETO-PROTONICS

Figure 1 illustrates measured results of the Japanese goldfish culture experiment through 800 days. The twenty baby goldfish showing around 4 cm long and around 2 mg weight each were separated into two groups: one in an aquarium with magnetized olivine stones floor, whilst another in an aquarium with non-magnetic stones floor. We found the average weight of the magnetized aquarium group grow faster and became around twice at 740 days. The growth promotion rate defined as $G = ((\text{Average weight of the magnetized goldfish group}) / (\text{Average weight of the control goldfish group}) - 1.0) \times 100(\%)$ for Figure 1 is represented in Figure 2, in which we tentatively illustrated a linear approximated line of “1% per week line” as the growth promotion rate index for the evaluation of the ELF magnetic field effect.

Figure 3 illustrates calculated results of the plant growth promotion rate on the basis of measured results of plant cultivation tests: A the Gifu strawberry cultivation test using ELF magnetic field generator coils [8] with A1 the average plant length, A2 the average leaf width, A3 the winter time yield amount, and A' the annual total yield amount. B and C are both for the Komatsuna vegetable plant cultivation tests setting each plant pot on a magnetized oxidized slag aggregate concrete board with B1 the total yield amount, B2 the average plant length, and B3 the average leaf width. We found these data for the plant cultivation tests of less than 22 weeks are distributed

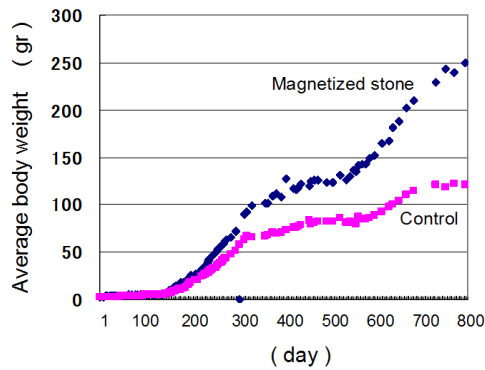


Figure 1: Rearing test for Japanese goldfish group in an aquarium with magnetized olivine stones comparing with a control group.

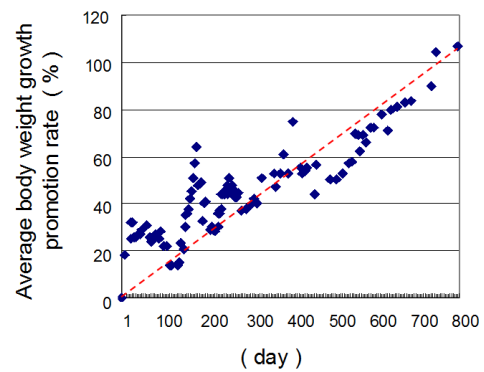


Figure 2: Goldfish growth promotion rate vs. feeding period for the group in magnetized stone set aquarium. A dotted line shows the 1% per week line.

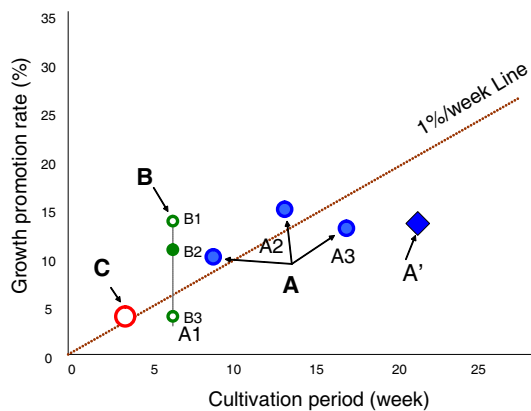


Figure 3: Plant growth promotion rate vs. cultivation period characteristics: A for Gifu strawberry cultivation using the ELF coil magnetization with A1 for the plant length, A2 the leaf width, A3 the winter-period yield amount, and A' the annual yield amount, B and C are both for the Komatsuna vegetable plant tests on the oxidized slag concrete with B1 for the total yield amount, B2 for the plant length, and B3 for the leaf width.

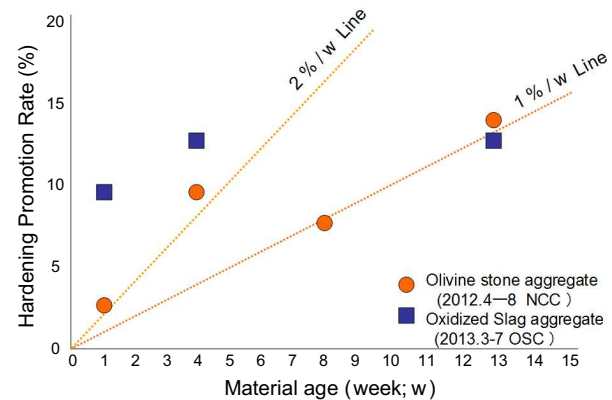


Figure 4: Concrete hardening promotion rate vs. material age using magnetized coarse aggregate: Circle marks with magnetized olivine crushed stones, and square marks with magnetized oxidized slag crushed stones comparing with non-magnetic aggregate.

roughly along the 1% per week line of the magnetized goldfish grow promotion rate as shown in Figure 2.

We found similar promotion rate versus time characteristics in the concrete hardening tests using magnetized coarse aggregate as shown in Figure 4 with measurements of the compressive strength of the concrete test pieces with the magnetized olivine crushed stones aggregate [13] and the magnetized oxidized slag crushed stones aggregate compared with test pieces with non-magnetic stones aggregate. Similarity of the organisms growth and the hardening of the concrete on the promotion rate is considered due to the free proton generation in the bio-body water and the concrete mixing water for activation of the bio-chemical reaction and the chemical reaction, respectively.

3. CONCLUSIONS

Definition of the promotion rate index “1–2% per week” makes a precise and numerical evaluation of the ELF magneto-protonics effect on the organisms growth and the concrete hardening at even short time test such as one week, that would be able to promote the new bio industries utilizing the magneto-protonics based on the intrinsic concept for the organisms with the effect accumulation. The bio-activation high strength concrete would be a basic infrastructure for the new bio industries.

ACKNOWLEDGMENT

The authors wish to express their gratitude to Mr. T. Uemura of Tsuruta Sekizai Co, Japan and Dr. H. Nakagawa of Aichi Steel Co., Japan for their presentation of the magnetized olivine stones and the magnetized oxidized slag stones, respectively.

REFERENCES

1. Mohri, K., M. Fukushima, and M. Matsumoto, "Gradual decrease of electric resistivity in water triggered by milli-Gauss low frequency pulse magnetic field," *Trans. Mag. Soc. Jpn.*, Vol. 1, No. 1, 22–26, 2001.
2. Mohri, K. and M. Fukushima, "Gradual decreasing characteristics and temperature stability of electric resistivity in water triggered with milliGauss AC field," *IEEE Trans. Magn.*, Vol. 38, No. 5, 3353–3355, 2002.
3. Mohri, K. and M. Fukushima, "Milligauss magnetic field triggering reliable self organization of water with long range ordered proton transport through cyclotron resonance," *IEEE Trans. Magn.*, Vol. 39, No. 5, 3328–3330, 2003.
4. Fukushima, M., K. Mohri, T. Kataoka, and M. Matsumoto, "MilliGauss pulsed magnetic field applied phosphate buffered saline solution elevates intracellular Ca^{2+} level and stimulates phagocytic activity in human neutrophils," *Trans. Mag. Soc. Jpn.*, Vol. 2, No. 2, 15–18, 2002.
5. Fukushima, M., T. Kataoka, N. Sugiyama, and K. Mohri, "MilliGauss magnetic field applied water exert and induce firefly luciferine-luciferase luminescence and induce intracellular calcium elevation of CHO cells without ATP," *IEEE Trans. Magn.*, Vol. 41, No. 10, 4188–4190, 2005.
6. Mohri, K., M. Fukushima, Yu. Mohri, and Y. Mohri, "Detection of magnetization of 6 Hz, 10 μT magnetic field applied water using PT-MI sensor," *PIERS ONLINE*, Vol. 6, No. 2, 145–148, 2010.
7. Davidson, R., A. Lauritzen, and S. Senef, "Biological water dynamics and entropy: A biological origin of cancer and other diseases (review)," *Entropy 2013*, Vol. 15, 3822–3876, 2013.
8. Harada, N., M. Kato, M. Suzumura, J. Yamada, K. Koshikawa, H. Matsuo, and K. Mohri, "Cultivation test of Gifu strawberry using μT , ELF magnetic field," *Annual Conf., Magnetics Soc., Jpn.*, 14aA-4, 2006.
9. Mohri, K., T. Uchiyama, M. Yamada, T. Watanabe, Y. Inden, T. Kato, and S. Iwata, "Arousal effect of physiological magnetic stimulation on elder person's spine for prevention of drowsiness during car driving," *IEEE Trans. Magn.*, Vol. 47, No. 10, 3066–3069, 2011.
10. Mohri, K., T. Uchiyama, M. Yamada, Y. Mohri, K. Endo, T. Suzuki, and Y. Inden, "Physiological magnetic stimulation for arousal of elderly car driver evaluated with electro-encephalogram and spine magnetic field," *IEEE Trans. Magn.*, Vol. 48, No. 11, 3505–3008, 2012.
11. Mohri, Y., M. Yamada, K. Endo, T. Suzuki, and K. Mohri, "Arousal effect of physiological magnetic stimulation on car driver's spine evaluated with electro-encephalogram using driving simulator," *PIERS Proceedings*, 245–249, Kuala Lumpur, Malaysia, Mar. 27–30, 2012.
12. Mohri, K., Y. inden, M. Yamada, and Y. Mohri, "Health recovery effect physiological magnetic stimulation on elder person's immunity source area with transition of EEG and ECG," *PIERS Proceedings*, 240–244, Kuala Lumpur, Malaysia, Mar. 27–30, 2012.
13. Mohri, K., M. Sasaki, T. Uemura, Y. Mohri, M. Yamada, and T. Kato, "Pulse train distributed magnetic field generated from high strength concrete using magnetized olivine stone aggregate," *PIERS Proceedings*, 1057–1060, Taipei, Mar. 25–28, 2013.

Rectangular DRA Reflectarray with an Inclined Top-loading Microstrip Patch

Eng-Hock Lim, Hong Yik Wong, and Fook Loong Lo

Department of Electrical and Electronic Engineering
Universiti Tunku Abdul Rahman, Kuala Lumpur, Malaysia

Abstract— This paper presents a dielectric resonator antenna (DRA) unit element that can be used for designing a compact reflectarray. Here, a rectangular DRA is incorporated with a top-loading metal strip where the strip inclination angle is used as the phase-shifting parameter. When modeled using the waveguide model, it is found that this DRA reflectarray unit element is able to give a reflection phase range of 162.29° . To understand further, the same unit element is also simulated using the Floquet model. It is found that the separation distance of the elements can affect the phase range and gradient of the S-curve significantly.

1. INTRODUCTION

The use of dielectric resonator antenna (DRA) in reflectarray was first proposed in 2000 [1], where the length of a rectangular DRA was varied to bring about phase shift to a scattered wave. The DRA reflectarray has many advantages such as low loss, broad bandwidth, low mutual coupling, good frequency response, and high radiation efficiency [2]. It has been found that the reflection phase range of the DRA reflectarray is usually comparable with that of the microstrip. A DRA reflectarray unit element can also be incorporated with various microstrip elements such as patches and strips for designing broadband reflectarrays. In [3, 4], a patch-loaded DRA reflectarray was proposed where a rectangular microstrip patch was stuck on the top surface of a DRA element. By varying the patch length while keeping the patch width unchanged, the reflection phase angle of the scattered wave can be easily varied.

A glass-made DRA loaded with a metallic patch on its top surface is proposed in this paper. In this case, the inclination angle of the top-loading strip is altered to provide phase shift to the scattered wave. When modelled using a waveguide, the proposed unit element is found to be able to give a reflection phase angle of greater than 160° . In this paper, the same element is also simulated using the Floquet model. It was found that the reflection phase range and gradient of the S-Curve are greatly affected by the separation distance of the elements. Simulation was done using the CST Microwave Studio software and measurements were conducted on a Vector Network Analyser (VNA). Good agreement is found between the simulated and measured results.

2. REFLECTARRAY UNIT ELEMENT

First, the waveguide model is deployed for characterizing the proposed reflectarray unit element. The simulation model places the element at one end of a rectangular waveguide (dimension: $a \times b \times l$) to receive incident wave, operating at TE₁₀ mode, coming from the waveguide port located at the other, as shown in Fig. 1. With reference to the figure, it can be seen that the incident angle (α) can be calculated as $\alpha = 90^\circ - \beta = 90^\circ - \cos^{-1} \sqrt{1 - (\frac{f_c}{f})^2}$. To demonstrate, a C-band rectangular waveguide (5.85 GHz–8.20 GHz), with a dimension of $a = 34.85$ mm, $b = 15.8$ mm, $l = 154$ mm, is used. The frequency of interest is 6 GHz, which is equal to an incident angle of $\alpha = 44.21^\circ$. The unit element here is a glass DRA ($\epsilon_r = 7$, $\tan \delta = 0.01$, $L_d = 14$ mm, and $H_d = 6$ mm) which has a top-loading metallic patch ($L_s = 13$ mm and $W_s = 2$ mm). In this case, no substrate has been used and the DRA is directly placed at the center of a ground plane. It is found that inclining the patch angle (θ) can cause the incident wave to scatter with different phases. Therefore, it can be used as the phase shifter for the reflectarray. In experiment, a waveguide section and a SMA-to-waveguide adaptor, shown in Fig. 2, are deployed for measuring the reflection characteristics. Standard OPEN-SHORT-LOAD calibration procedure is performed on the SMA port. Here, a piece of sticky copper tape is cut and stuck on the top surface of the DRA. The reflection coefficient is directly measurable through the SMA connector, and the reflection magnitude and phase are then extracted for plotting the reflection loss and S-Curves.

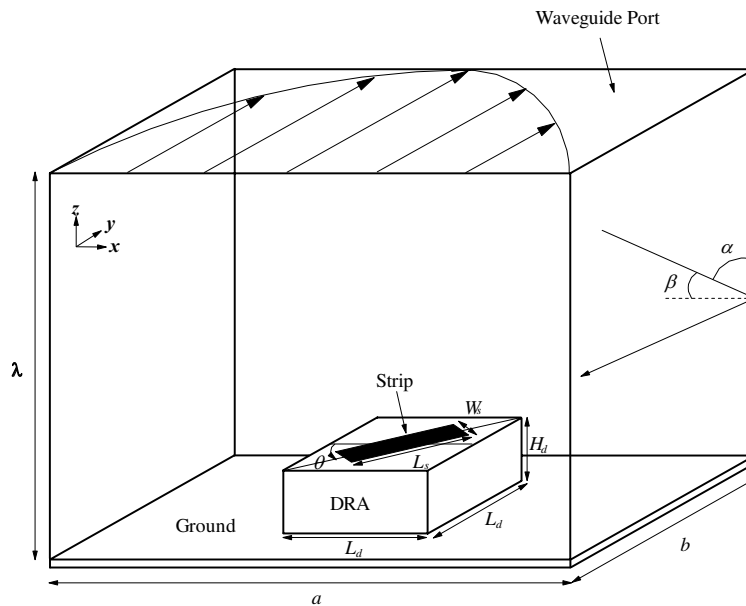


Figure 1: Waveguide model for the proposed DRA unit element with a top-loading inclined metallic patch ($L_s = 13$ mm, $W_s = 2$ mm, $0^\circ \leq \theta \leq 90^\circ$, $L_d = 14$ mm, $H_d = 6$ mm, $a = 34.85$ mm, $b = 15.8$ mm, $l = 154$ mm).

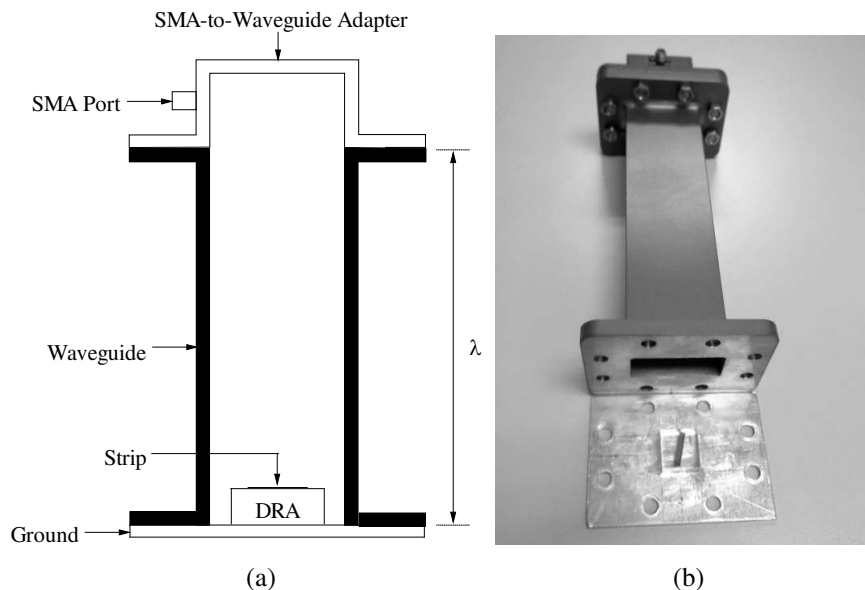


Figure 2: Experimental setup for the waveguide method. (a) Cross-sectional view. (b) Photograph.

3. RESULTS AND DISCUSSION

Figure 3(a) shows the simulated and measured reflection losses and reflection phases (S-Curve), demonstrating reasonable agreement between them. The loss peaks at -0.4 dB at the inclination angle of $\theta = 25^\circ$. This is because the resonant frequency of the strip-loaded DRA is around 6 GHz at this particular inclination angle, causing much energy dissipation. Also depicted in Fig. 3(b) is the S-Curve. The reflection phase range introducible by the strip rotation is measured to be 162.29° (simulation 147.01°). For the waveguide method, simulating as quare cell is not possible as the cell size has to follow the waveguide cross profile ($a \times b$). This creates a limitation on the spacing between the reflectarray elements.

Next, the same DRA element is simulated using the Floquet method, shown in Fig. 4. This method provides a sort of periodic boundary condition in the way that the unit element is virtually extended into an infinite array by considering the mutual coupling effect between the elements. This

makes the simulation model closer to the actual reflectarray. In this case, the angle of the incident wave does not depend on frequency. This gives much more freedom as the incident angle and operating frequency can now be chosen freely. For Floquet model, the spacing between the elements can be arbitrarily defined by simply changing the cell size ($L_1 \times L_2$). To simplify our design process, a square cell ($L_1 = L_2$) is used here. The simulated S-Curves for different element spacings are given in Fig. 5. For ($L_1 = L_2$), it can be seen that the changeable range increases when the spacing becomes smaller. The distance between the Floquet port and the unit element is not important as the port can always be de-embedded flush to the element surface.

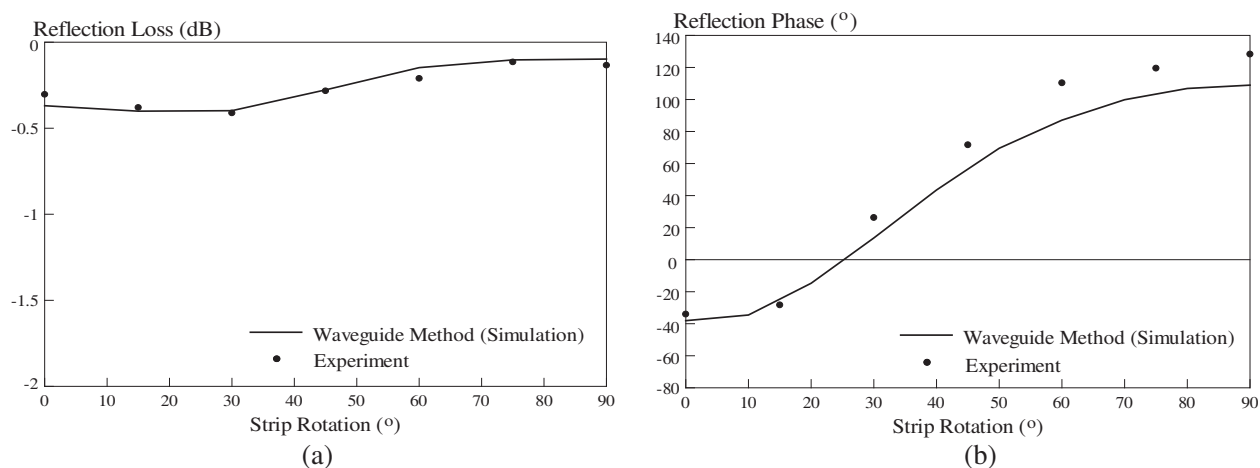


Figure 3: Simulated and measured (a) reflection loss, (b) reflection phase (S-Curve) of the proposed DRA reflectarray unit element using the waveguide method.

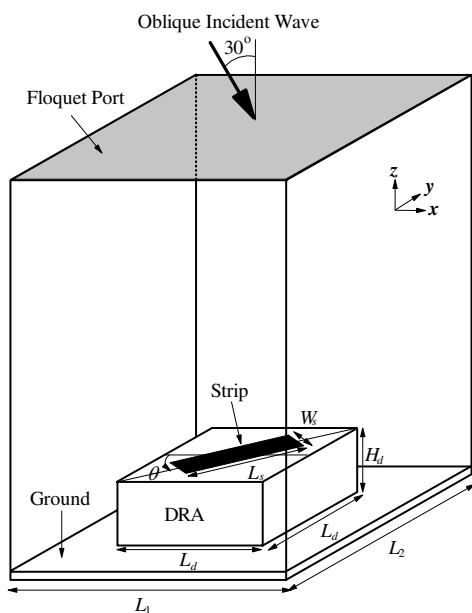


Figure 4: The Floquet model for the proposed DRA unit element.

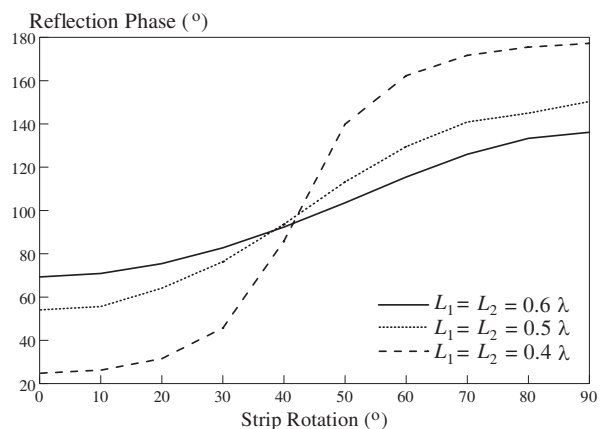


Figure 5: Simulated S-Curves for different element spacings ($L_1 = L_2$).

4. CONCLUSIONS

In this paper, the inclination angle of a top-loading patch that is stuck on top of a rectangular DRA is varied to provide reflection phase shift for designing a reflectarray. Waveguide and Floquet methods have been used to simulate this unit element. It has been found that the reflection phase range and the gradient of the S-curve are significantly affected by the spacing distance between the elements.

ACKNOWLEDGMENT

The work described in this paper was supported by a Science Fund (Project No.: 06-02-11-SF0154) provided by the Ministry of Science, Technology and Innovation, Malaysia. Part of the project was also sponsored by a UTAR Research Fund 2013 (Project No.: 6200/LA5)

REFERENCES

1. Keller, M. G., J. Shaker, A. Ittipiboon, and Y. M. M. Antar, “A Ka-band dielectric resonator antenna reflectarray,” *Proc. 30th Eur. Conf. Microw.*, 272–275, 2000.
2. Jamaluddin, M. H., R. Gillard, R. Sauleau, P. Dumon, and L. L. Coq, “Reflectarray element based on strip-loaded dielectric resonator antenna,” *Electron. Lett.*, Vol. 44, No. 11, 664–665, 2008.
3. Jamaluddin, M. H., R. Gillard, R. Sauleau, L. L. Coq, X. Castel, R. Benzerger, and T. Koleck, “A dielectric resonator antenna (DRA) reflectarray,” *European Microwave Conf.*, 025–028, 2009.
4. Jamaluddin, M. H., R. Gillard, R. Sauleau, P. Dumon, and L. L. Coq, “A low loss reflectarray element based on a dielectric resonator antenna(DRA) with a parasitic strip,” *Proc. IEEE Antennas Propag. Soc. Int. Symp.*, 1–4, 2008.

A Compact Triple-band MIMO Antenna for Wimax/WLAN Application

Huifen Huang, Yuanhua Hu, and Wei Zhao

School of Electronic and Information Engineering
South China University of Technology, Guangzhou, China

Abstract— A compact triple-band inverted-F antenna for WLAN and WiMAX multiple-input-multiple-output (MIMO) system is proposed in the paper. Its main radiation element is evolved from simple inverted-F antenna, works at 2.4 GHz, 3.5 GHz. The parasitic element works at 5.2 GHz, 5.8 GHz, In order to reduce the size of the antenna and improve the effect of the truncated ground plane on impedance match, a slot is added. A four-element array configuration of the proposed antenna for MIMO application is also studied. The simulation results of reflection coefficient, mutual coupling, and radiation pattern are presented.

1. INTRODUCTION

Multiple-input-multiple-output (MIMO) technology can enhance the data rate and reliability without sacrificing additional spectrum or transmitted power in rich scattering environment, which make it very attractive in the recent years [1]. Various types of MIMO for Wimax/WLAN Application were presented [2–5], As we all know that inverted-F antenna is widely used in mobile terminal for its low cost, compact structure and easy to fabricate [2, 6]. In this paper, a inverted-F MIMO antenna operating at WLAN and WiMAX is presented. Inverted-F antenna is dependent of the ground dimension strongly, especially at lower frequency whose electrical length is relative large, which often results in bad isolation for MIMO application, In order to reduce the coupling, each element is orthogonal to adjacent elements, Finally, the four-element MIMO antenna occupies $60 \times 60 \text{ mm}^2$, operating at the following frequency bands: 2.36–2.56, 3.45–3.74, 4.95–6.33 GHz.

2. ANTENNA DESIGN

The geometry and configuration of the proposed antenna is illustrated in Fig. 1, which is printed on a FR4 epoxy substrate with a thickness of 0.8mm, a relative permittivity of 4.4, and a loss tangent of 0.02. The antenna is comprised of a main radiation element evolved from simple inverted-F antenna and a paramistic stub, which only occupy the size of $25 \times 8 \text{ mm}^2$. Both the ground plane and the radiation element are etched on the same substrate, without vias, making the structure easily fabricated and conveniently excited. The lower resonant mode was excited by stub AB, which

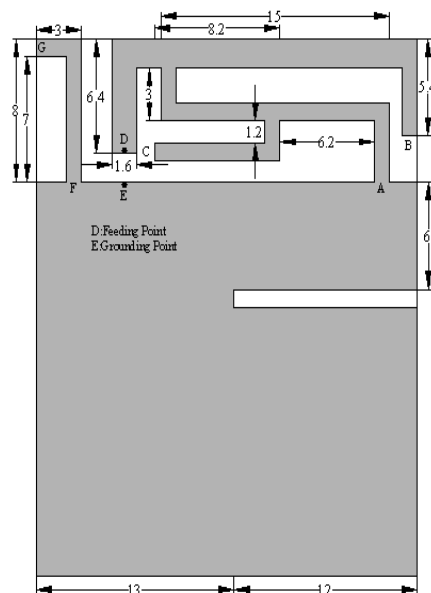


Figure 1: Geometry of the proposed antenna.

is approximately equal to a quarter-wavelength for the frequency of 2.4 GHz ($\lambda \cong c/(f \times \sqrt{\epsilon_e})$, where ϵ_e is the effective dielectric constant; the resonance in 3.5 GHz was produced by AC; The paramistic stub FG provided the upper resonance. The single-element simulated result is shown in Fig. 2.

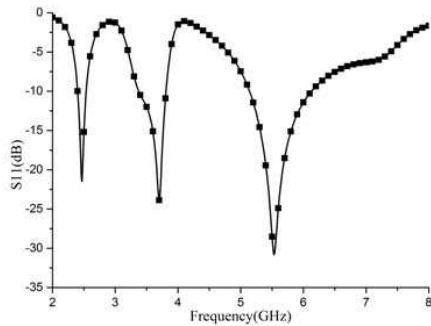


Figure 2: Reflection coefficient of the proposed antenna against frequency.

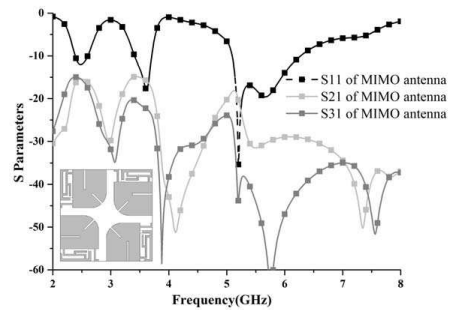


Figure 3: The MIMO antenna proposed.

3. INTEGRATION OF FOUR-ELEMENT ANTENNA

With the demand of high-quality and high-capacity data transmission, MIMO antenna become more and more important, so the trail that transform the SISO antenna into MIMO antenna will be studied in the following part. The simulated S parameters of the proposed MIMO antenna consists of four element is shown in the Fig. 3.

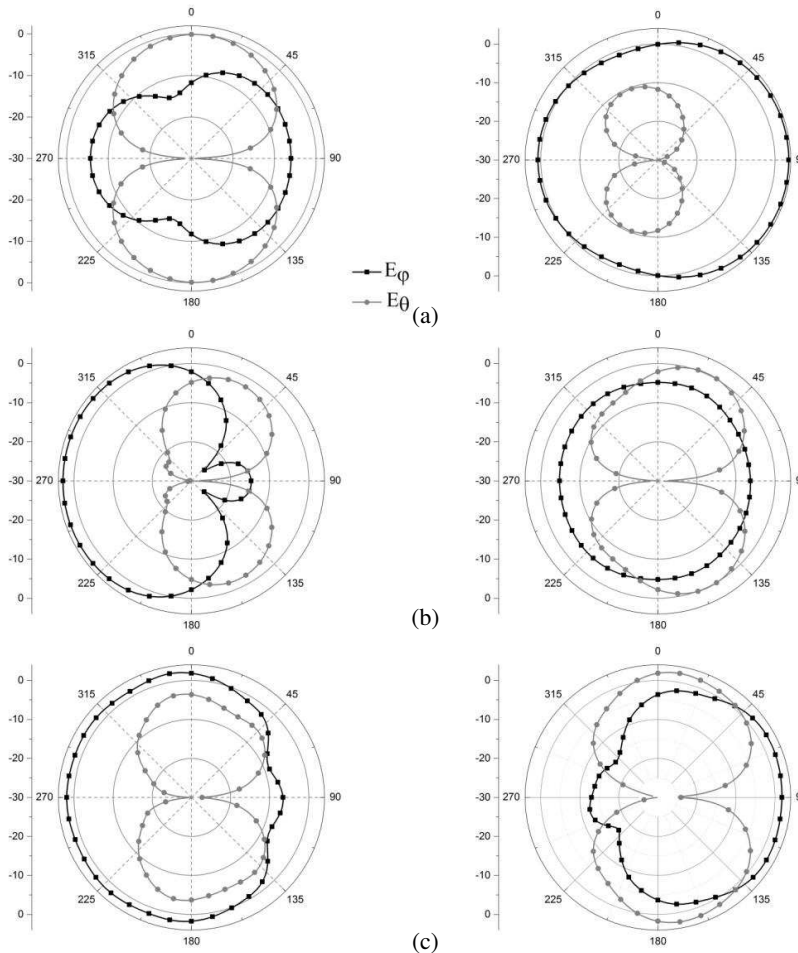


Figure 4: Radiation pattern XOZ _plane (left) and YOZ _plane (right) for (a) 2.44 GHz, (b) 3.61 GHz, (c) 5.5 GHz.

Inverted-F antenna is strong dependent of the ground. The common ground plane must cause strong mutual coupling, then make the diversity performance worse. So each element has its own ground plane, In order to further reduce the coupling, each element is orthogonal to adjacent elements. The slot and circular-corner both improve the isolation. The simulation result shows that the MIMO antenna can cover the 2.4/5.2/5.8 GHz WLAN and 3.5/5.5 GHz Wimax, within the designed frequency range, the isolation can achieved 15 dB. The radiation patterns for xoz plane and $yo z$ plane are shown in Fig. 4, nearly omnidirectional pattern can be observed in lower frequency.

4. CONCLUSION

A compact triple-band inverted-F antenna for WLAN and WiMAX multiple-input-multiple-output (MIMO) system is proposed in the paper. The four-element MIMO antenna occupies $60 \times 60 \text{ mm}^2$, operating at the following frequency bands: 2.36–2.56, 3.45–3.74, 4.95–6.33 GHz.

ACKNOWLEDGMENT

This work is supported by the National Natural Science Foundation of China under Grant 61071056.

REFERENCES

1. Foschini, G. J. and M. J. Gans, "On limits of wireless communications in a fading environment when using multiple antennas," *Wireless Personal Commun.*, Vol. 6, No. 3, 311–335, 1998.
2. Karaboikis, M., C. Soras, G. Tsachtsiris, and V. Makios, "Compact dual-printed inverted-F antenna diversity systems for portable wireless devices," *IEEE Antennas Wireless Propag. Lett.*, Vol. 3, 9–14, 2004.
3. Nezhad, S. M. A. and H. R. Hassani, "A novel E-shaped printed monopole antenna for MIMO application," *IEEE Antennas Wireless Propag. Lett.*, Vol. 9, 576–579, 2010.
4. Bhatti, R. H., J. Choi, and S. Park, "Quad-band MIMO antenna array for portable wireless communications terminals," *IEEE Antennas Wireless Propag. Lett.*, Vol. 8, 129–132, 2009.
5. Karimian, R., H. Oraizi, S. Fakhte, and M. Farahani "Novel F-shaped quad-band printed slot antenna for WLAN and WiMAX MIMO systems," *IEEE Antennas Wireless Propag. Lett.*, Vol. 12, 405–408, 2013.
6. Sim, C.-Y.-D., H.-Y. Chien, and C.-H. Lee, "Uniplanar antenna design with adhesive ground plane for laptop WLAN operation," *IEEE Antennas Wireless Propag. Lett.*, Vol. 13, 337–340, 2014.

On Frequency Optimization of Assymmetric Resonant Inductive Coupling Wireless Power Transfer Links

Nuria Egidios¹, Elisenda Bou¹, Raymond Sedwick², and Eduard Alarcon¹

¹UPC BarcelonaTech, Barcelona, Spain

²University of Maryland, College Park, MD, USA

Abstract— Resonant Inductive Coupling Wireless Power Transfer (RIC-WPT) is a leading field of research due to the growing number of applications that can benefit from this technology: from biomedical implants to consumer electronics, fractionated spacecraft and electric vehicles amongst others. However, current applications are limited to symmetric point-to-point-links. New challenges and applications of RIC-WPT emphasize the necessity to explore, predict and optimize the behavior of these links for different configurations: multi-point RIC-WPT networks and assymetrical systems. In this work a design methodology oriented towards the optimization of assymmetric RIC-WPT links is presented, resulting in a closed analytical formulation of the optimal frequency at which an assymetrical RIC-WPT link should operate. Finally, the resulting efficiency-optimized link is explored and compared to previous results obtained in RIC-WPT symmetric configurations [1, 2].

1. INTRODUCTION

Power transfer efficiency is key in wireless power transfer systems. In particular, in RIC-WPT links, the efficiency of the physical layer strongly depends upon a) the frequency of operation (resonant frequency of the link), b) the losses of the transmitter and receiver coils and c) the mutual inductance between them. Since both the losses and the mutual inductance are frequency-dependant, it is of interest to analyze the optimal frequency at which a given link should operate to maximize its efficiency. This has been previously studied for symmetric point-to-point RIC-WPT links [2], but it is still unexplored for assymetrical configurations (different transmitter and receiver sizes), in which the difference between transmitter and receiver minimum-loss frequencies emphasize the need for an optimal system co-designed frequency of operation. In this work, the power transfer efficiency of impedance-matched Assymmetric RIC-WPT links is studied in terms of frequency (Section 2) and a closed analytical expression of the optimal frequency of operation is provided (Section 3). Finally, the System Efficiency of Assymmetric Frequency-Optimized RIC-WPT links is analyzed and compared to the Symetric Frequency-Optimized Configuration (Section 4).

2. EFFICIENCY IN ASSYMETRIC RIC-WPT

The power transfer efficiency in RIC-WPT links, defined as the ratio between the power delivered to the load and the total input power, can be expressed as a function of the input frequency ω , the load R_L , transmitter and receiver losses (R_1 , R_2), and the mutual inductance between them M_{12} [5]

$$\eta = \frac{R_L(\omega M_{12})^2}{(\omega M_{12})^2(R_2 + R_L) + R_1(R_2 + R_L)^2} \quad (1)$$

If impedance matching conditions are fulfilled ($R_L = \sqrt{R_2^2 + (\omega M_{12})^2 R_2 / R_1}$ [3]), the efficiency of the system only depends upon the equivalent resistance of the coils (radiative, ohmic and dielectric losses), the mutual impedance between them and the frequency of operation, resulting in:

$$\eta_o = \frac{\sqrt{1 + \left(\frac{\omega M_{12}}{\sqrt{R_1 R_2}}\right)^2} - 1}{1 + \left(\frac{\omega M_{12}}{\sqrt{R_1 R_2}}\right)^2 + 1} = \frac{\sqrt{1 + S_a^2} - 1}{\sqrt{1 + S_a^2} + 1} \quad (2)$$

It can be observed in 2 that, to maximize efficiency, the relational factor S_a — which is equivalent to the Coupled mode Theory K/Γ [6] — has to be maximized.

$$S_a = \frac{\omega M_{12}}{\sqrt{R_1 R_2}} \quad (3)$$

To accomplish this, it is necessary to 1) Maximize the frequency of the resonators (ω), 2) maximize the mutual inductance between coils (M_{12}) and 3) minimize the transmitter (R_1) and receiver (R_2) losses, which depend upon the technological parameters of the coils and the separation between them as follows:

$$\begin{aligned} M_{12} &= f(N_1, a_1, N_2, a_2, D_{12}) \\ R_1 &= f(\omega, N_1, a_1, b_1, c_2, \sigma_1) \\ R_2 &= f(\omega, N_2, a_2, b_2, c_2, \sigma_2) \end{aligned} \quad (4)$$

where two circular loop antennas with $N_{1,2}$ turns, coil diameters $a_{1,2}$, wire radius $b_{1,2}$, inter-turn separation $c_{1,2}$, conductivity $\sigma_{1,2}$ and a distance D_{12} between them, have been assumed.

To maximize the efficiency, the frequency should be chosen so that S_a is maximized (highest frequency, maximum mutual inductance and minimum coil's losses). In the forthcoming sections, the mutual inductance as well as the coil's losses are derived for N -turn circular loop antennas.

2.1. Mutual Inductance

In the quasi-static limit, at large distances ($D_{12} \gg a_1$) the magnetic flux density at the receiver coil as a result of the transmitter coil has the form of a dipole [4].

$$B_{12} \simeq \frac{\mu_0 N_1 i a_1^2}{2 D_{12}^3} \quad (5)$$

where coaxial orientation between coils has been assumed. The mutual inductance is then found from the flux through the N_2 linkages in the receiver coil:

$$M_{12} = N_2 \frac{\partial \Psi_{12}}{\partial i} \simeq \frac{\pi}{2} N_1 N_2 \mu_0 \frac{a_1^2 a_2^2}{D_{12}^3} \quad (6)$$

2.2. Evaluation of Losses

The losses of the resonators depend upon their constituent materials ($\sigma_{1,2}, \delta_{1,2}$) and geometry ($a_{1,2}, b_{1,2}, c_{1,2}$) and can be divided into Radiative Losses (R_r), Ohmic Losses (R_o) and Dielectric Losses (R_d):

$$R_1 = R_r^1 + R_o^1 + R_d^1 \quad (7)$$

In this work, the losses of two electrically small ($a \ll \lambda$) circular loop antennas (chosen for their low radiation resistance [42]) are considered.

The radiation losses of a circular N_1 -turn loop antenna with loop radius a_1 can be found by [4]:

$$R_r^1 = 20\pi^2 N_1^2 a_1^4 \frac{\omega^4}{c_0^4} \quad (8)$$

The ohmic resistance, which is in general much larger than the radiation resistance, depends upon the proximity effect (if the spacing between the turns in the loop antenna is small) and the skin effect. The total ohmic resistance for an N_1 -turn circular loop antenna with loop radius a_1 , wire radius b_1 and loop separation $2c_1$ is given by [4]:

$$R_o^1 = \frac{N_1 a_1}{b_1} R_s^1 \left(\frac{R_p^1}{R_0^1} + 1 \right) \quad (9)$$

where $R_s^1 = \sqrt{\omega \mu_0 / 2\sigma_1}$ is the surface impedance of the conductor and R_p^1 is the ohmic resistance per unit length due to proximity effect.

Finally, if a dielectric loop antenna is considered, the dielectric losses are given by:

$$R_d^1 = \frac{\tan \delta_1}{\omega C_1} = \omega L_1 \tan \delta_1 \simeq \omega 4\mu_0 a_1 N_1^2 \tan \delta_1 \quad (10)$$

where $\tan \delta_1$ is the loss tangent of the coil and L_1 has been approximated to $L_1 = 4\mu_0 a_1 N_1^2$. Defining the ratios of asymmetry in number of turns (u_N), antenna diameter (u_a), wire radius (u_b),

inter-turn distance (u_c), conductivity (u_σ) and loss tangent (u_δ) as follows:

$$\begin{aligned} u_N &= \frac{N_2}{N_1}; & u_a &= \frac{a_2}{a_1}; & u_b &= \frac{b_2}{b_1} \\ u_\sigma &= \frac{\sigma_2}{\sigma_1}; & u_c &= \frac{c_2}{c_1}; & u_\delta &= \frac{\delta_2}{\delta_1} \end{aligned} \quad (11)$$

the losses at the receiver (assuming $u_\delta = u_c = 1$) can be expressed as:

$$R_2 = R_r^2 + R_o^2 + R_d^2 = u_N^2 u_r^4 R_r^1 + \frac{u_N u_a}{u_b \sqrt{u_\sigma}} R_o^1 + u_a u_N^1 R_d^1 \quad (12)$$

3. FREQUENCY OPTIMIZATION OF ASSYMETRIC RIC-WPT

3.1. Optimal Frequency

To find the optimal frequency at which the Assymetric RICWPT link should operate, it is necessary to take the derivative of S_a with respect to ω . To do this, the losses in the transmitter coil are expressed as:

$$\begin{aligned} R_r^1 &= C_r^1 \omega^4; & C_r^1 &= \frac{20\pi^2 N_1^2 a_1^4}{c_o^4} \\ R_o^1 &= C_o^1 \sqrt{\omega}; & C_o^1 &\simeq \frac{N_1 a_1}{b_1} \sqrt{\frac{\mu_0}{2\sigma_1}} \\ R_d^1 &= C_d^1 \omega; & C_d &\simeq 4\mu_0 a_1 N_1^2 \tan \delta_1 \end{aligned} \quad (13)$$

where C_r^1 , C_o^1 and C_d^1 are the frequency-independent coefficients corresponding to the radiation, ohmic and dielectric losses respectively. Similarly, the losses at the receiver coil can be defined as:

$$\begin{aligned} R_r^2 &= C_r^2 \omega^4; & C_r^2 &= K_r C_r^1; & K_r &= u_N^2 u_a^4 \\ R_o^2 &= C_o^2 \sqrt{\omega}; & C_o^2 &= K_o C_o^1; & K_o &= \frac{u_N u_a}{u_b \sqrt{u_\sigma}} \\ R_d^2 &= C_d^2 \omega; & C_d^2 &= K_d C_d^1; & K_d &= u_a u_N^2 \end{aligned} \quad (14)$$

where K_r , K_o and K_d model the effect of the assimetries between transmitter and receiver upon the receiver's losses. Finally, the mutual inductance can be expressed as a function of the equivalent mutual inductance obtained in a symetric link ($u_{N,a,b,c,\delta} = 1$) as:

$$M_{12}^a = K_m M_{12}; \quad K_m = u_N u_a^2; \quad (15)$$

Once this is known, both the mutual inductance (15) and the transmitter and receiver losses (13), (14) can be substituted in Equation (3) resulting in:

$$S_a = \frac{\omega K_m M_{12}}{\sqrt{(C_r^1 \omega^4 + C_o^1 \sqrt{\omega} + C_d^1 \omega)(K_r C_r^1 \omega^4 + K_o C_o^1 \sqrt{\omega} + K_d C_d^1 \omega)}} \quad (16)$$

which is then be derived with respect to ω to obtain the optimal frequency at which the assymetric link should operate. The resulting ω_o^a is the solution of:

$$6\omega^7 C_R^2 K_r + 6\omega^4 C_d C_r \left(\frac{K_d + K_r}{2} \right) + 5\omega^{\frac{7}{2}} C_o C_r \left(\frac{K_o + K_r}{2} \right) - \omega^{\frac{1}{2}} C_d C_o \left(\frac{K_o + K_d}{2} \right) - K_o C_o^2 = 0 \quad (17)$$

For illustration purposes and in order to achieve a closed analytical formulation, dielectric-less transmitter and receiver coils are assumed ($C_d^1 = C_d^2 = 0$), obtaining:

$$\omega_{opt}^a = K_\omega \omega_{opt} \quad (18)$$

where:

$$K_\omega = \left(\frac{(K_o + K_r)}{K_r} \left[\sqrt{\frac{25}{16} + \frac{6K_o K_r}{(K_o + K_r)^2} - \frac{5}{4}} \right] \right)^{\frac{2}{7}} \quad (19)$$

and ω_{opt} is the optimal frequency corresponding to a symmetric link ($u_{N,a,b,c,\sigma,\delta} = 1$):

$$\omega_{opt} = \left(\frac{C_o^1}{6C_r^1} \right)^{\frac{2}{7}} \quad (20)$$

3.2. Maximum Efficiency

Once the optimal frequency at which the link should operate is obtained, the maximum relational factor S_a and the resulting maximum efficiency η_{\max}^a can be found by substituting ω by ω_{opt} in (3):

$$S_a^{\max} = S^{\max} \frac{7K_m \sqrt{K_w}}{\sqrt{K_r K_w^7 + 6K_w^{\frac{7}{2}}(K_o + k_r) + 36K_o}} \tag{21}$$

where S^{\max} is the maximum relational factor S for a symmetric link:

$$S^{\max} = \frac{6M}{7C_o^1} \left(\frac{C_o^1}{6C_r^1} \right)^{\frac{1}{7}} \tag{22}$$

and the maximum power transfer efficiency is then obtained by:

$$\eta_a^{\max} = \frac{\sqrt{1 + (S_a^{\max})^2} - 1}{\sqrt{1 + (S_a^{\max})^2} + 1} \tag{23}$$

4. RESULTS

The results obtained above regarding the optimal frequency of the asymmetric link, the maximum relational factor $S_{a,\max}$ and the corresponding maximum efficiency $\eta_{s,\max}$ are illustrated below. First, the normalized frequency deviation due to the link asymmetry is shown in Figure 1:

$$\Delta w = \frac{w_o^a - w_o^s}{w_o^s} = k_w - 1 \tag{24}$$

where $k_w = f(K_o, K_r)$ as per Equation (19). It can be observed that, when the asymmetry between transmitter and receiver represents around a 40% of difference either in the radiation or the ohmic

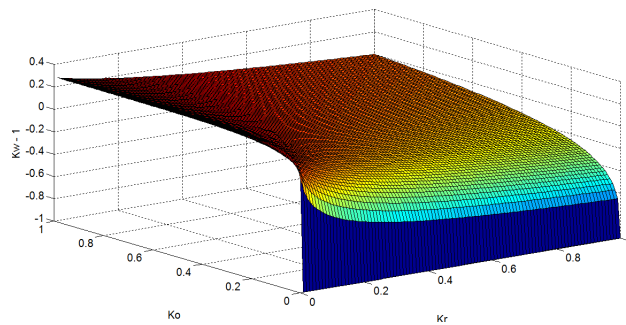


Figure 1: Normalized Frequency Deviation (Δw) with $C_o = C_r = 0.05$.

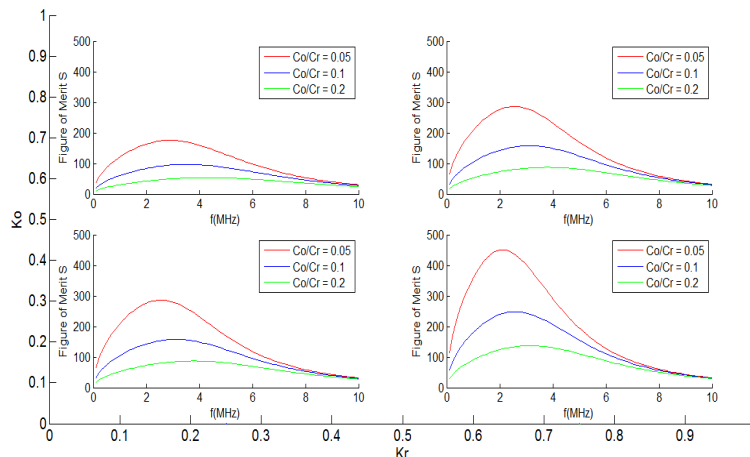


Figure 2: S_{\max}^a study for different K_o, K_r configurations.

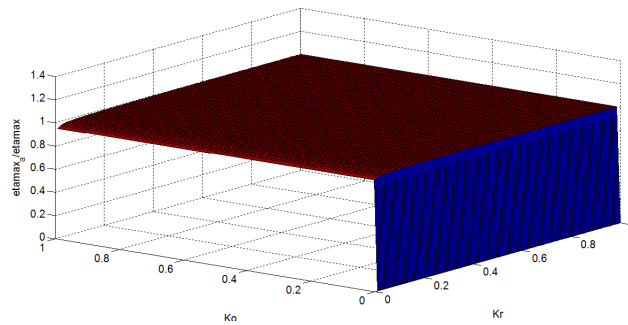


Figure 3: Normalized Maximum Efficiency for different K_o , K_r configurations. $C_o = C_r = 0.05$.

losses, the optimal frequency of operation for the asymmetric link experiments a 20% deviation from the optimal frequency in the symmetric link, showcasing the impact of this study. When assessing the effect of the asymmetry in RICWPT links, it is also of interest to study how this asymmetry (described in a compressed manner by the coefficients K_r , K_o and K_m) affects S_{\max} and the maximum achievable efficiency. To do this, Figure 4 illustrates the obtained S_{\max} for different K_o/K_r and $C_o = C_r$ coefficients as a function of frequency, where the frequency deviation explained in Figure 1 can be observed. Finally, Figure 4 shows the resulting maximum efficiency ($\eta_{\max}^a = \eta^a|_{w=w_{opt}^a}$) normalized with respect to the symmetric link maximum efficiency ($\eta_{\max}^a = \eta^a|_{w=w_{opt}^s}$).

5. CONCLUSIONS

The efficiency of Asymmetric RIC-WPT systems has been studied and presented in this work, together with a closed analytical formulation for optimal frequency in RIC-WPT Asymmetric links. Finally, the scalability of Asymmetric Frequency-Optimized RIC-WPT Links has been assessed and benchmarked with Symmetric Frequency-Optimized RIC-WPT links.

REFERENCES

1. Sedwick, R., "Long range inductive power transfer with superconducting oscillators," *Annals of Physics*, 2010.
2. Sedwick, R., "A fully analytic treatment of resonant inductive coupling in the far field," *Annals of Physics*, 2012.
3. Bou, E., E. Alarcon, and R. Sedwick, "Maximizing efficiency through impedance matching from a circuit-centric model of non-radiative resonant wireless power transfer," *Proceedings of 2013 IEEE International Symposium on Circuits and Systems*, June 2013.
4. Balanis, C. A., *Antenna Theory Analysis and Design*, Wiley, 2005.
5. Kiani, M. and M. Ghovanloo, "The circuit theory behind coupled-mode magnetic resonance-based wireless power transmission," *IEEE Transactions on Circuits and Systems I: Regular Papers*, No. 99, 1, 2012.
6. Balust, E. B., E. Alarcon, J. Gutierrez, "A comparison of analytical models for resonant inductive coupling wireless power transfer," *PIERS Proceedings*, 689–693, Moscow, Russia, August 19–23, 2012.

Application of Backscattering Models in Active-passive Microwave Remote Sensing of Ocean Salinity

J. Zhu^{1,2}, X. K. Zhang², H. Liu², and Y. J. Cai^{1,2}

¹Center for Space Science and Applied Research

University of Chinese Academy of Science, CAS, China

²The CAS Key Laboratory of Microwave Remote Sensing
Center for Space Science and Applied Research, CAS, Beijing, China

Abstract— The program of new type combined active and passive L-band sensor will meet the science needs by providing global ocean salinity distribution. Before the reconstruction of ocean salinity by brightness temperature, surface roughness must be taken into account, which is the leading part of the error sources that influences the brightness temperature. So it is a crucial step to eliminate the excess brightness temperature engendered by roughness. The elimination can be implemented by sea surface backscattering coefficient, which is directly influenced by roughness. In this paper, the sea surface is regarded as a two dimensional isotropic random process and the influence of roughness for backscattering coefficient is discussed. This can be a fundamental way to get pairs of brightness temperature and backscattering coefficient and for better inversion of ocean salinity.

1. INTRODUCTION

Ocean salinity is a key parameter to understand the interplay between the Ocean Circulation, Global Water Circle and Climate Change. The conventional way of acquiring salinity depends primarily on site measurement by ship-borne buoys, which impedes our obtainment of spatial and temporal distributions of ocean salinity. For 125 years by far, over 25% data from salinity observations of sea surface have not been acquired; moreover, the observation periods are less than 10 in almost 73 percent range of sea surface [1].

However, with the rapid development of remote sensing technologies, remote sensors can be an effective way of detecting ocean salinity. From the 1990s, some mission concepts have been proposed to measure the sea salinity from space by L band radiometers. This includes ESA's Soil Moisture and Ocean Salinity (SMOS) mission that has been launched at Nov. 2009 and NASA's Aquarius mission that has been launched at Jun. 2011 [2, 3].

In our program, a combined Passive/Active L-band salinometer has been designed [4], in which the radiometer is used to measure the brightness temperature of the ocean surface and the scatterometer is used to measure the backscattering coefficient. Since the sea surface brightness temperature is a function of SSS (Sea Surface Salinity), SST (Sea Surface Temperature) and SSR (Sea Surface Roughness), we can inverse the salinity through brightness temperature; however, the brightness temperature is influenced by various error sources at the same time, the leading part of which is sea surface roughness. Therefore, a crucial step of the inversion of SSS by brightness temperature is to eliminate the excess brightness temperature engendered by sea surface roughness. The elimination can be implemented by the sea surface backscattering coefficient, which is directly influenced by roughness.

In this paper, we show how the roughness can be described as statistical parameters of the ocean surface that is regard as a two dimensional random process with Gaussian distribution and how the backscattering coefficient is directly influenced by the sea surface roughness. This may be a fundamental way for us to build the relationship between excess temperature and backscattering coefficient and thus the inversion of ocean salinity with brightness temperature can be refined.

2. STATISTICAL DESCRIPTION FOR RANDOM SURFACES

2.1. Surface Height Standard Deviation

Suppose the average height of illuminated area S in x - y plane is \bar{z} , then the surface height standard deviation is

$$\sigma = \left(\overline{z^2} - \bar{z}^2 \right)^{1/2}$$

where

$$\bar{z} = \frac{1}{S} \iint_s z(x, y) ds \quad \bar{z}^2 = \frac{1}{S} \iint_s z^2(x, y) ds$$

2.2. Surface Correlation Length

Suppose one-dimensional condition, in the length L , the normalized surface correlation function is

$$\rho(\Delta x) = \int_l z(x)z(x + \Delta x)dx \Big/ \int_l z^2(x)dx$$

let $\rho(L) = 1/e$, then L is the correlation length.

2.3. Surface RMS Slope

The surface RMS Slope is short for the surface root mean square slope for a random process. For instance, we suppose a one-dimensional case, where $z(x)$ is a random process with average zero and standard deviation σ , and then the slope of $z(x)$ is

$$Z_x = \lim_{\Delta x \rightarrow 0} \frac{z(x + \Delta x) - z(x)}{\Delta x}$$

The second order moment of the slope is

$$\langle Z_x^2 \rangle = \lim_{\Delta x \rightarrow 0} \left\langle \frac{z^2(x + \Delta x) - 2z(x)z(x + \Delta x) + z^2(x)}{\Delta x^2} \right\rangle$$

That is

$$\langle Z_x^2 \rangle = \lim_{\Delta x \rightarrow 0} \frac{\sigma^2 - 2\sigma^2\rho(\Delta x) + \sigma^2}{\Delta x^2}$$

To find the limitation, expand $\rho(\Delta x)$ at $\Delta x = 0$, in Taylor series, upon letting $\Delta x \rightarrow 0$, we obtain the variance of the slope, which is

$$\langle Z_x^2 \rangle = \lim_{\Delta x \rightarrow 0} \frac{1 - [1 + \rho''(0)\Delta x^2/2 + \dots]}{\Delta x^2} = -\sigma^2\rho''(0)$$

Then the surface RMS slope is defined as

$$\sigma_s = \langle Z_x^2 \rangle^{1/2} = [-\sigma^2\rho''(0)]^{1/2}$$

2.4. Surface Spectrum

The surface spectrum is the two dimensional Fourier transforms of the surface correlation coefficient $\rho(x, y)$, which is:

$$W(k_x, k_y) = \int_{-\infty}^{+\infty} \int_{-\infty}^{+\infty} \rho(x, y)e^{-jk_x x - k_y y} dx dy$$

For polar coordinates:

$$W(\kappa, \varphi) = \int_{-\infty}^{+\infty} \int_{-\infty}^{+\infty} \rho(r, \phi)e^{-j\kappa r \cos(\varphi - \phi)} r dr d\phi$$

where $\kappa = \sqrt{k_x^2 + k_y^2}$, $\cos \varphi = k_x/\kappa$, $\sin \varphi = k_y/\kappa$.

3. BACKSCATTERING FROM SEA SURFACES

3.1. Backscattering Models

The scattering coefficient of an extended target in a given direction is the ratio of the total scattered power from an equivalent isotropic scatter which generates the same scattered power density in the direction to the total incident power on the illuminated area. Mathematically, the scattered coefficient can be written as [5]:

$$\sigma_{pq}^0 = \frac{4\pi R^2 \text{Re} \left\{ \left\langle \left| \vec{E}_{pq}^s \right|^2 \right\rangle / \eta_s^* \right\}}{A_0 \text{Re} \left\{ \left| E_0 \right|^2 / \eta^* \right\}}$$

The two most commonly used models for random surface scattering are Kirchhoff Approximation (KA) and Small Perturbation Model (SPM). The KA is assumed that the total field at any point on the surface can be computed as if the incident wave is impinging upon an infinite plane tangent to the point. It turned out that the surface correlation length and the curvature radius must greater than a wave length. Mathematically, that is:

$$kl > 6 \quad l^2 > 2.76\sigma\lambda$$

Here k is the wave number, σ is surface height standard deviation and l is surface correlation length. After this assumption, it is still hard to obtain the analytic results; therefore there are two simplifications: Stationary Phase Approximation of incoherent scattering for large surface height standard deviation; and Scalar Approximation with Surface RMS Slope less than 0.25 for small surface height standard deviation, which includes both coherent and incoherent scattering. In the condition when both the surface standard deviation and correlation length are smaller than the wave length, KA is not valid.

SPM is assumed that the scattered field can be represented by the superposition of the plane waves with unknown amplitudes propagating away from the interface. The unknown amplitudes can be calculated by boundary conditions. In the calculations, the unknown field amplitudes are expanded in a perturbation series and taken a first-order approximation. In fact, the first order approximation is exactly the mirror reflecting contribution from the target points, which is the mechanism of Bragg Resonance. Therefore, SPM requires the surface standard deviation to be less than about 5 percent of the electromagnetic wave length. Mathematically, that is:

$$k\sigma < 0.3 \quad \sigma/l < 0.3 \quad k^3\sigma^2l \ll 1$$

It can be summarized that KA is high frequency approximation while SPM is low frequency approximation in solving the scattered field. Since L band is used in the ocean surface detection, we next turn our attention on SPM. Mathematically, the backscattering coefficient of SPM can be written as [5]:

$$\sigma_{pq}^r = 4k^4\sigma^2 \cos^4\theta |\alpha_{pq}|^2 W(2k \sin\theta, 0) / \pi$$

where

$$\alpha_{hh} = R_{\perp}$$

$$\alpha_{vv} = (\varepsilon_r - 1) \frac{\sin^2\theta - \varepsilon_r (1 + \sin^2\theta)}{[\varepsilon_r \cos\theta + \sqrt{\varepsilon_r - \sin^2\theta}]^2}$$

This form is assumed that the random surface is isotropic in horizontal direction with Gaussian height distribution. Then the random process becomes one dimensional and for different correlation functions the surface spectra would be different. For example, the surface spectrum of Gaussian correlation function is $W(2k \sin\theta, 0) = \pi L^2 \exp[-(kL \sin\theta)^2]$. The cross polarization omitted here would be zero if only first-order approximation is considered while that would be a complex integral if we carry out to second order.

3.2. Performance of Statistical Parameters of Sea Surface

The ocean surface fluctuates when wind blows and the roughness may change. The change of surface roughness is equivalent to the variation of the surface standard deviation, surface correlation length, surface spectrum and other statistic descriptions. Then we analyzed the variation of backscattering coefficient with these parameters.

For Figure 1, we use SPM model with Gaussian distribution and Gaussian correlation function. The correlation length is 5 cm; the dielectric constant is calculated by the method of Ulaby [6] at $f = 1.4$ GHz, $T = 20^\circ\text{C}$ and $S = 30$ psu, which is $73.07 + j59.03$. We can see that the backscattering coefficients for both VV and HH polarization increases with the surface standard deviation. This is because with the increase of surface height standard deviation, it is prone to incoherent scattering and there is a higher possibility of backscattering.

For Figure 2, note that the backscattering coefficient increases with correlation length until the angle reaches about 40 degree and then decreases with the correlation length. This is because when correlation length is large, it is dominated by coherent scattering which is greatly influenced by the incident angle; when the correlation is short, the scattering is dominated by incoherent scattering which is not as sensitive as it is before.

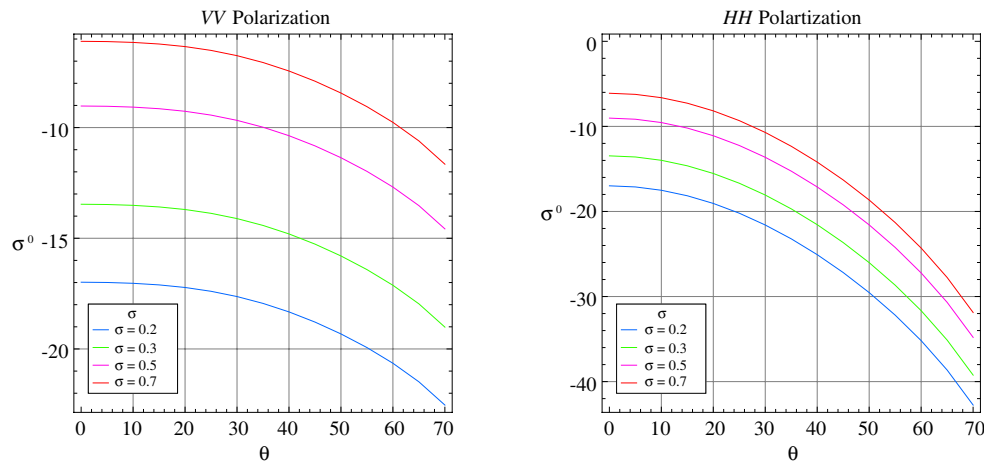


Figure 1: $L = 5$ cm, $SSS = 30$ psu at a frequency of 1.4 GHz with Gaussian correlation function.

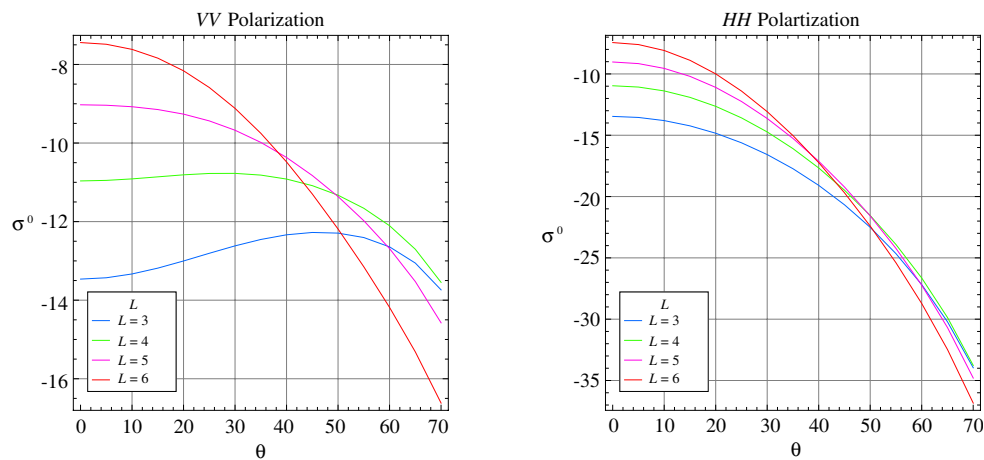


Figure 2: $\sigma = 0.25$ cm, $SSS = 30$ psu at a frequency of 1.4 GHz with Gaussian correlation function.

4. CONCLUSION

The inversion of ocean salinity by brightness temperature is impaired by the error engendered by surface roughness. The error can be eliminated by the backscattering coefficient, which is directly influenced by surface roughness. In this paper, we regard the ocean surface as an isotropic two dimensional random process and discussed the performance of backscattering coefficient with different statistical parameters which represents roughness. This can be a fundamental way for further study of building the relationship between brightness temperature and backscattering coefficient and refine the inversion of ocean salinity.

REFERENCES

1. Koblinsky, C. J., P. Hildebrand, D. Le Vine, et al., "Sea surface salinity from space: Science goals and measurement approach," *Radio Science*, Vol. 38, No. 4, 2003.
2. Kerr, Y. H., P. Waldteufel, J. P. Wigneron, et al., "The SMOS mission: New tool for monitoring key elements of the global water cycle," *Proceedings of the IEEE*, Vol. 98, No. 5, 666–687, 2010.
3. Le Vine, D. M., G. S. E. Lagerloef, F. R. Colomb, et al., "Aquarius: An instrument to monitor sea surface salinity from space," *IEEE Transactions on Geoscience and Remote Sensing*, Vol. 45, No. 7, 2040–2050, 2007.
4. Liu, H., X. K. Zhang, et al., "A combined L-band synthetic aperture radiometer and fan-beam scatterometer for soil moisture and ocean salinity measurement," *Geoscience and Remote Sensing Symposium (IGARSS)*, 4644–4647, Melbourne, Australia, Jul. 2013.
5. Ulaby, F. T., R. K. Moore, and A. K. Fung, *Microwave Remote Sensing: Active and Passive Volume II: Radar Remote Sensing and Surface Scattering and Emission Theory*, Artech House, Dedham, MA, 1982.
6. Ulaby, F. T., R. K. Moore, and A. K. Fung, *Microwave Remote Sensing: Active and Passive Volume III: From Theory to Applications*, Artech House, Norwood, MA, 1986.

Development of a Radiative Transfer Model for the Soil Media with Including Vertical Profile Effects and Its Application in AMSR2

Hui Lu^{1,2}, Toshio Koike³, and Ziwei Xu⁴

¹Ministry of Education Key Laboratory for Earth System Modeling, Center for Earth System Science
Institute for Global Change Studies, Tsinghua University, Beijing 100084, China

²Joint Center for Global Change Studies, Beijing, 100875, China

³The Department of Civil Engineering, The University of Tokyo, Tokyo 113-8658, Japan

⁴State Key Laboratory of Remote Sensing Science, School of Geography
Beijing Normal University, Beijing 100875, China

Abstract— Soil moisture plays an essential role in the Earth system. Reliable estimation of soil moisture, especially in regional and global scale, is important for climatic, meteorological and hydrological researches. This study presents a revised soil radiative transfer model (RTM) in which the vertical profile effects of soil temperature are included. In situ observations of soil moisture and temperature profile, measured during HIWater Experiment IOP, are used to formulate profile functions. The revised RTM is applied into the new AMSR2 soil moisture retrieval algorithm, in order to improve the algorithm performance in arid regions. By comparing the results of new algorithm against ground observations, the feasibility and capability of the revised algorithm and RTM were verified.

1. INTRODUCTION

Soil moisture is an essential variable in earth system science, playing a significant role in climate modeling, weather forecasting, hydrological and ecological process simulating and food production predicting. Soil moisture can be observed in point and local scales through in situ sensor networks and field survey. However, regional and global soil moisture information can be only derived from numerical model simulations or estimated from remote sensing observations. Passive microwave remote sensing has a more than 30 years history to provide earth observation which can be used to retrieve global surface soil moisture content (SMC). Besides the L-band observation provided by the current SMOS [1] and oncoming SMAP [2], the multi-band observations (C, X and K-band) provided by AMSR-E [3] and its successor AMSR2 [4] have been used to generate global SMC products from 2002 to now.

NASA, VUA and JAXA released AMSR-E SMC products independently, while JAXA is producing AMSR2 SMC data set now. The SMC retrieval algorithm of JAXA is relying on a look up table (LUT). The SMC products of JAXA gives generally reasonable soil moisture estimate in global scale, while it overestimates soil moisture in desert regions. Figure 1 gives an example of AMSR2 SMC product over Africa continent. As shown in this figure, monthly averaged soil moisture in the Sahara desert regions (15N-35N) are higher than no desert regions in southern Africa. There are two main reasons for such unreasonable overestimation: current AMSR2 algorithm does not include the temperature profile effects and volume scattering effects which are aroused when microwave penetrates into dry soil. Such overestimations are generally occurred in mid to low latitude regions where have powerful solar radiation, and could lead to the energy imbalance for its further application in atmospheric and hydrological models.

2. THE REVISED SOIL RADIATIVE TRANSFER MODEL

In microwave region, the reflectivity of the air/soil interface is generally small. The downward radiation from vegetation and rainfall, which is reflected by the soil surface, therefore, is neglected. Moreover, for the lower frequencies region of microwave, the atmosphere is transparent. Finally, after neglecting all the downward radiation and parts of upward radiation from surroundings, the radiative transfer model is written as:

$$T_b = T_{bs}e^{-\tau_c}e^{-\tau_r} + (1 - \omega_c)(1 - e^{-\tau_c})T_c e^{-\tau_r} + \int (1 - \omega_r(R))(1 - e^{-\tau_r(R)})T_r(R)dR \quad (1)$$

where T_{bs} is the emission of the soil layer, T_c is the vegetation temperature, T_r is the temperature of precipitation droplets, τ_c and ω_c are the vegetation opacity and single scattering albedo, and τ_r and ω_r are the opacity and single scattering albedo of precipitation.

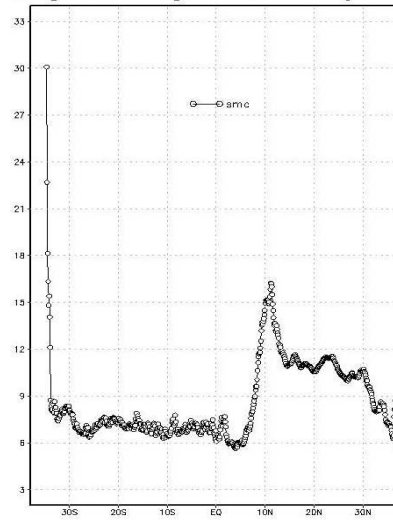


Figure 1: An example of overestimation-in-dry-religion problem of JAXA AMSR2 SMC product. Monthly averaged soil moisture over Africa continent was used to calculate the longitude average.

For the frequencies less than 18 GHz, Equation (1) can be even simplified by omitting the precipitation layer, as:

$$T_b = T_{bs}e^{-\tau_c} + (1 - \omega_c)(1 - e^{-\tau_c})T_c \quad (2)$$

For the dry regions, vegetation water content is generally very small and there is almost no vegetation attenuation effect. RTM can be further simplified as

$$T_b = T_{bs} = T_{eff}(1 - R) \quad (3)$$

where R is the surface reflectivity and can be estimated by combing Fresnel function and roughness function, T_{eff} is the effective temperature, as:

$$T_{eff} = \int_0^{\infty} T(z)\alpha(z) \exp\left[-\int_0^z \alpha(z')dz'\right] dz \quad (4)$$

$$\alpha(z) = (4\pi/\lambda)\varepsilon''(z)/2\sqrt{\varepsilon'(z)} \quad (5)$$

where $T(z)$ is soil temperature profile along the vertical direction z (cm), $\varepsilon(z)$ is the dielectric constant profile and can be estimate by inputting soil moisture and temperature profile into Dobson model.

3. STUDY REGION

We applied our RTM and algorithm [5] in the middle reach of Heihe river (38.7N-39.5N, 100.1E-100.8E), where the HIWater experiment conducted during June to September, 2012. Soil moisture and temperature at 0, 2, 4, 10 and 20 cm depth are recorded every 10 minute at Shenshawo station (38.79N, 100.49E). The location of this station is selected carefully to make it be representative for the surrounding desert. The recorded profiles are converted to three-month-averaged values and are used to calculate the effective temperature in Equation (4).

As shown in Figure 2(a), soil temperature changes obviously as depth increasing. Soil temperature profile in daytime differs from that in nighttime. After curve fitting, the soil temperature profiles shown in Figure 2(a) are formulated as:

$$T(z) = T_{surf} * [1.029 - 0.02893 * \exp(-0.355 * z)] \quad (6)$$

for descending overpass and

$$T(z) = T_{surf} * [0.9403 + 0.0595 * \exp(-0.7087 * z)] \quad (7)$$

for ascending overpass.

As shown in Figure 2(b), the soil moisture at different depths have almost same values. A uniform soil moisture profile, therefore, will be used in our RTM.

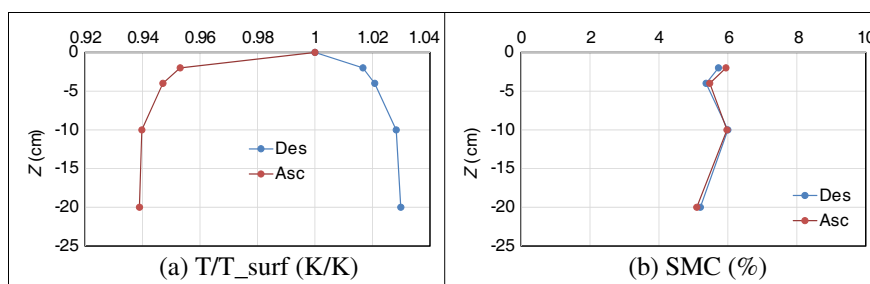


Figure 2: Averaged soil (a) temperature and (b) moisture, profile observed at Shenshawo station. “Des” denotes observations in at the time of descending overpass (around 02:00 local time); “Asc” for ascending overpass (around 13:00 local time).

4. RESULTS AND DISCUSSIONS

Figure 3 shows the comparison between soil moisture contents retrieved from new algorithm and those observed at the station. With using the new RTM, the wet-bias is partly mitigated and performance of soil moisture algorithm is improved, giving the RMSE of 4.69% with a R-square of 0.475.

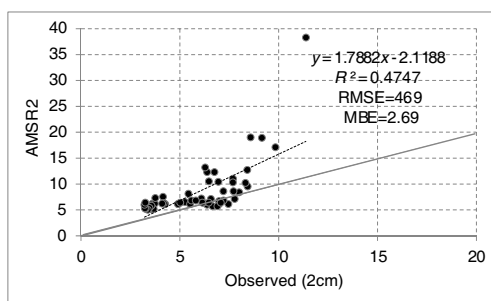


Figure 3: Comparison of retrieved soil moisture with ground observation at Shenshawo station.

5. CONCLUSION

A soil radiative transfer model with including temperature profile effects is developed to improve the accuracy of soil moisture estimation, especially in dry regions. By coupling the new RTM into AMSR2 soil moisture retrieval algorithm, algorithm performance can be improved. Further numerical and theoretical simulations will be studied.

REFERENCES

1. Kerr, Y. H., P. Waldteufel, J.-P. Wigneron, J. Martinuzzi, J. Font, and M. Berger, “Soil moisture retrieval from space: The soil moisture and ocean salinity (SMOS) mission,” *IEEE Transactions on Geoscience and Remote Sensing*, Vol. 39, 1729–1735, 2001.
2. Entekhabi, D., E. G. Njoku, P. E. O’Neill, K. H. Kellogg, et al., “The soil moisture active passive (SMAP) mission,” *Proceedings of the IEEE*, Vol. 98, 704–716, 2010.
3. Njoku, E. G., T. J. Jackson, V. Lakshmi, T. K. Chan, and S. V. Nghiem, “Soil moisture retrieval from AMSR-E,” *IEEE Transactions on Geoscience and Remote Sensing*, Vol. 41, 215–229, 2003.
4. Imaoka, K., M. Kachi, H. Fujii, H. Murakami, M. Hori, A. Ono, T. Igarashi, K. Nakagawa, T. Oki, Y. Honda, and H. Shimoda, “Global change observation mission (GCOM) for monitoring carbon, water, and climate change,” *Proc. IEEE*, Vol. 98, No. 5, 717–734, 2010.
5. Lu, H., T. Koike, H. Fujii, T. Ohta, and K. Tamagawa, “Development of a physically-based soil moisture retrieval algorithm for spaceborne passive microwave radiometers and its application to AMSR-E,” *J. Remote Sens. Soc. Jpn.*, Vol. 29, No. 1, 53–262, 2009.

Guided-mode Resonance Enhanced Near-infrared-to-visible Upconversion Fluorescence in a Resonant Waveguide Grating

Hao Yu Liou¹, Jian Hung Lin¹, Zhen-Dao Wang², Chun-Yen Tseng³,
Ching-Ting Lee³, Chu-Chi Ting², Hung-Chih Kan¹, and Chia Chen Hsu^{1,2}

¹Department of Physics, National Chung Cheng University
Ming Hsiung, Chia Yi 621, Taiwan

²Graduate Institute of Opto-Mechatronics, National Chung Cheng University
Ming Hsiung, Chia Yi 621, Taiwan

³Institute of Microelectronics, Department of Electrical Engineering
National Cheng Kung University, Tainan 701, Taiwan

Abstract— Guided mode resonance (GMR) enhanced near-infrared (near-IR)-to-visible upconversion fluorescence (UCF) from a rare-earth doped polymer resonant waveguide grating (RWG), comprised of a NaYF₄:Yb/Tm nanocrystals doped poly-methyl-methacrylate (NaYF₄:Yb/Tm-PMMA) thin layer on top of a textured SU8 substrate with a thin intervening layer of TiO₂. Strong UCF is observed by matching either incoming near-IR excitation or out-going UCF extraction to the GMR wavelengths of the rare-earth doped polymer RWG. The intensity of the UCF can be enhanced up to 10⁴ times in visible range and 10³ times in near-IR range compared with that from a flat area. According to the rigorous coupled-wave analysis calculations, high enhancement of UCF is attributed to the strong local field generated at the TiO₂ waveguide layer due to the resonance between the near-IR excitation light and the GMR. The extraction of the UPF is further promoted when the wavelengths of the UPF resonate with the GMRs.

1. INTRODUCTION

Recently, upconversion (UC) nanocrystals have attracted much attention due to their great potential applications, such as biodetection, bioimaging, solid-state lasers, three-dimensional displays, and solar cells [1–6]. The high efficient yield of UC nanocrystals are typically codoped with lanthanide, including ytterbium (Yb³⁺) sensitizer ions and activator ions such as erbium (Er³⁺), thulium (Tm³⁺) or holmium (Ho³⁺). The sensitizer of Yb³⁺ ions absorb infrared radiation and then transfer their photon energy to activator ions via multi-photon transition process. Several distinct and narrow emission bands over ultraviolet, visible, and near-infrared wavelengths can be produced from activator ions. Until now, the use of lanthanide-doped UC nanocrystals show considerable advantages [7], for example low toxicity, high chemical stability, and high signal-to-noise ratio, compared with the conventional luminescent labels, such as organic dye molecules, quantum dots, and dye-doped silica/gold nanomaterials.

Resonant waveguide grating (RWG) [8–15], that can more efficiently excite and extract the light emitted by fluorescent or nonlinear materials, are widely used in the enhancement of the traditional fluorescence and nonlinear harmonic generation. A RWG typically consists of a high refractive-index grating-waveguide layer and a low refractive-index supporting layer, which can produce very sharp reflection and near zero transmission anomalies that signature the guided mode resonance (GMR). It is very useful for enhancing excitation or extraction of fluorescence signal by aligning either the excitation wavelength or the emission fluorescent spectrum with GMR. Indeed, when the GMR occurs in the RWG, the excitation can be enhanced as a result of the strong local field generated at the surface of grating. If fluorescent molecules are in direct contact with the grating, the fluorescence signal can be improved with this strong local field. When the wavelength of the fluorescence signal overlaps with resonant mode, the extraction of fluorescence signal can be further promoted due to its high reflection.

In this work, we demonstrate an all-dielectric TiO₂ RWG covered with a NaYF₄:Yb/Tm nanocrystals doped PMMA (NaYF₄:Yb/Tm-PMMA) thin layer to enhance near-infrared (near-IR)-to-visible upconversion fluorescence (UCF). A simple and low cost two-beam interference technique and electron-beam deposition system were used to fabricate the TiO₂ RWG on the scale of mm's. Giant multiplicative enhancement in UCF, combining enhanced excitation and enhanced extraction effects, can be observed up to 10⁴ times in visible range and 10³ times in near-IR range compared with that from a flat area.

2. SAMPLE PREPARATION AND MEASUREMENT SETUP

2.1. Design and Fabrication of RWG

Figure 1(a) shows the schematic design of a 1D RWG with a NaYF₄:Yb/Tm-PMMA thin layer. The structure consists of, from top to bottom, a NaYF₄:Yb/Tm-PMMA layer, a 1D sinusoidal waveguide-grating (TiO₂), a bottom cladding layer (SU8), and a glass substrate. In order to obtain a TE GMR mode at normal incidence at around 750 nm, the TiO₂ layer was designed to be 60 nm thick (T_{TiO_2}) with periodicity (Λ) of 470 nm. A 1D SU8 grating was first fabricated by a two-beam interference technique [16, 17], and then a TiO₂ layer was deposited on top of SU8 grating by an electron-beam deposition technique. The thickness of SU8 (T_{SU8}) and TiO₂ (T_{TiO_2}) were 1400 nm \pm 100 nm and 60 nm \pm 5 nm by SEM measurement. Total area of the RWG is 6 \times 6 mm². From AFM measurement, the period (Λ) and depth (d) of grating were determined to be 466 nm and 60 nm \pm 5 nm, respectively.

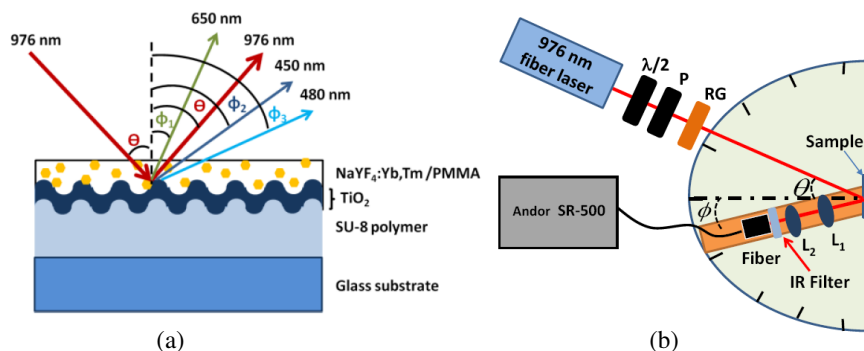


Figure 1: (a) Schematic of a 1D RWG covered with a NaYF₄:Yb,Tm doped with PMMA layer. (b) UPL measurement setup. RG: long-pass filter, P: polarizer, $\lambda/2$: half-wave plate, L₁-L₂: lenses, θ : incident angle of excitation beam, ϕ : collected angle of UPL signal, and IR Filter: short-pass filter.

The NaYF₄:20% Yb, 2% Tm nanocrystalline phosphor was chosen as the upconversion fluorescent material, which was synthesized using a co-precipitation method. The mean sizes of nanoparticles were 30 nm by transmission electron microscopy (TEM) measurement. The NaYF₄:Yb/Tm-PMMA with 20 wt% was first dissolved in toluene then spin-coated on the top of the TiO₂ RWG. The RWG with a NaYF₄:Yb/TmPMMA layer was then baked for 1 hour at 70°C on a hotplate before use. The thickness (T_N) of the NaYF₄:Yb/Tm-PMMA thin layer was 250 nm \pm 50 nm by SEM measurement. The refractive indices of NaYF₄:Yb/TmPMMA (n_N), SU8 (n_{SU8}) and TiO₂ (n_{TiO_2}) are 1.485, 2.066 and 1.581 at 0.75 μm obtained by ellipsometry measurements. The refractive index of glass substrate is 1.512 at 0.75 μm . Typical distinct emission bands of a NaYF₄:Yb/Tm-PMMA thin film are centered around 450, 480 and 650 nm excited by 976 nm. The emission bands at 450, 480, and 660 nm could be assigned to $^1D_2 \rightarrow ^3F_4$, $^1G_4 \rightarrow ^3H_6$, $^1G_4 \rightarrow ^3F_4$ and $^1G_4 \rightarrow ^3H_5$ transitions of Tm³⁺ ion [18], respectively.

2.2. Experimental Setup

In the experiment, a 0.5-W solid-state diode laser at 976 nm was employed as an excitation beam to generate upconversion signal from sample. The collimated beam with a beam size of 0.7 mm diameter was used, and its excitation power was adjusted with the combination of a half-wave plate and a polarizer. A grating spectrometer (Andor Shamrock SR-500i) adopted with one fiber detector was used to collect and analyze the upconversion signal. Before the signal reached the detector, one IR filter was used to block the excitation beam. The transmission spectra of the RWG sample were measured with a halogen white light source and a grating spectrometer (Andor Shamrock SR-500i), the sample was rotated with respect to the incident beam.

3. EXPERIMENTAL RESULTS AND DISCUSSIONS

3.1. Angle-resolved Transmission Spectra of GMR

Figure 2(a) shows the measured transmission spectra of the GMR mode in the RWG, which the transmission spectra as a function of incident angle for TE incidence. In experiment, the normal-incident GMR mode locates at 740 nm, which is closed to the prediction. As the angle increases

from the normal incidence, the GMR mode at normal incidence splits into two separate modes, by reason of first order diffraction from the grating: one red-shifts with the incident angle, and the other blue-shifts. Red-shifted dispersion can use to enhance the excitation field, which the excitation wavelength (λ_{ex}) of 976 nm falls into GMR mode when the incident angle (θ) sets 31.5° (highlight in Figure 2). Blue-shifted dispersion can use to enhance the extraction intensity, which the emission wavelength (λ_{em}) of 480 nm matches with the resonance mode at the collection angle (ϕ) of 39° (highlight in Figure 2).

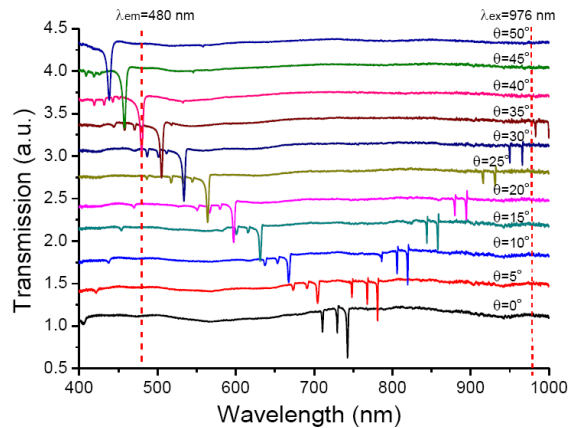


Figure 2: (a) Angle-resolved transmission spectra of the RWG covered with a $\text{NaYF}_4:\text{Yb/Tm-PMMA}$ at the different incident angle (θ) for transverse-electric (TE) mode. **Enhanced excitation:** the excitation wavelength (λ_{ex}) of 976 nm falls into GMR mode when the incident angle (θ) sets 31.5° (highlight). **Enhanced extraction:** the emission wavelength (λ_{em}) of 480 nm matches with the resonance mode at the collection angle (ϕ) of 39° (highlight).

3.2. Enhanced Excitation and Extraction

The resonant excitation for enhancing the UCF signal of the RWG was first investigated. The power of the excitation laser beam was used at 300 mW, and the collection angles (ϕ) of fiber detector set at 0° . The incident angle of illumination beam was scanned from 0° to 35° in 0.25° steps. When the incident angle of excitation beam matches with the GMR ($\theta = 31.5^\circ$), the PL intensity of upconversion spectrum has dramatically increase. Figure 3(a) shows the UCF spectra of the RWG with a $\text{NaYF}_4:\text{Yb/Tm-PMMA}$ thin layer under illuminating the excitation laser beam at the resonant angle ($\theta = 31.5^\circ$). This enhanced UCF causes from the effect of enhancement of the excitation light due to its resonant coupling to GMR mode. The UCF spectra emitted from a flat

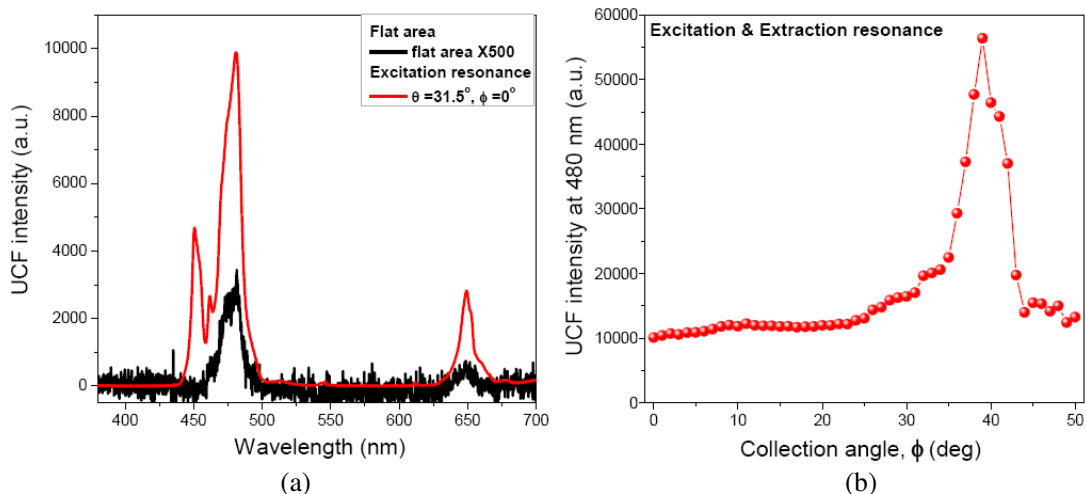


Figure 3: (a) UCF spectra emitted from the RWG with a $\text{NaYF}_4:\text{Yb/Tm-PMMA}$ thin layer under resonance on ($\theta = 31.5^\circ$) and a flat sample. (b) UCF intensity at 480 nm as a function of collecting angle.

sample, which is no grating structure, also plots in Figure 3(a) for comparison. The UCF intensity from the RWG with a $\text{NaYF}_4:\text{Yb}/\text{Tm}$ -PMMA thin layer was enhanced by a factor of 2×10^3 compared with that from the flat sample. To further enhance the UCF signal with the RWG with a $\text{NaYF}_4:\text{Yb}/\text{Tm}$ -PMMA, we next investigate the effect of enhanced extraction of the fluorescent emission. The RWG sample was illuminated with 976 nm wavelength laser beam at $\theta = 31.5^\circ$, and the collection angle of detector was varied from 0° to 50° in one-degree steps. Figure 3(b) plots UCF intensity at 480 nm as a function of collecting angle. When the collected angle was set at 39° , the UCF intensity reaches a maximum. This is the orientation where 480 nm wavelength light resonant with the RWG, as indicated by one of modes that blue shifts with incident angle in Figure 2. At this resonant condition the UCF intensity at 480 nm was enhanced nearly 6-fold enhancement compared with that collected at 0° . Compared with the UCF intensity from the flat sample, the UCF signal enhanced with both the excitation and extraction at resonance with GMR modes of the RWG produces a total enhancement factor of 10^4 times in visible range. A total enhancement in near-IR range ($\lambda_{em} = 650$ nm) can be obtained to be nearly 10^3 times.

4. CONCLUSIONS

We demonstrated that the UCF signal can be enhanced up to 10^4 times in visible range and 10^3 times in near-IR range by aligning the GMR modes with the incident excitation light and the peak emission wavelengths of a $\text{NaYF}_4:\text{Yb}/\text{Tm}$ -PMMA layer in the RWG structure. By setting the incident angle of the 976 nm wavelength laser beam at 31.5° , incident light resonates with the grating wave structure and produced strongly enhanced E -field near the TiO_2 and $\text{NaYF}_4:\text{Yb}/\text{Tm}$ -PMMA layer interface, leading to enhance excitation field and a 2×10^3 times enhancement. Furthermore, by setting the collection angle of the detection system at 39° away from the normal direction of the RWG, another 6-fold enhancement of the fluorescent signal at 480 nm wavelength was obtained due to the high reflection of the GMR mode.

ACKNOWLEDGMENT

The authors gratefully acknowledge financial support from the National Science Council, Taiwan, under grant Nos. NSC 98-2112-M194-008-MY3, NSC 99-2112-M194-008-MY3 and NSC 98-2811-M194-007.

REFERENCES

1. Downing, E., L. Hesselink, J. Ralston, and R. Macfarlane, "A three-color, solid-state, three-dimensional display," *Science*, Vol. 273, 1185–1189, 1996.
2. Parthenopoulos, D. A. and P. M. Rentzepis, "Three-dimensional optical storage memory," *Science*, Vol. 245, 843–845, 1989.
3. He, G. S., J. M. Dai, T. C. Lin, P. P. Markowicz, and P. N. Prasad, "Ultrashort 1.5- μ m laser excited upconverted stimulated emission based on simultaneous three-photon absorption," *Opt. Lett.*, Vol. 28, 719–721, 2003.
4. Heer, S., K. Kömpe, H. U. Güdel, and M. Haase, "Highly efficient multicolour upconversion emission in transparent colloids of lanthanide-doped NaYF_4 nanocrystals," *Adv. Mater.*, Vol. 16, 2102–2105, 2004.
5. Johnson, L. F., J. E. Geusic, H. J. Guggenheim, T. Kushida, S. Singh, and L. G. Van Uitert, "Comments on materials for efficient infrared conversion," *Appl. Phys. Lett.*, Vol. 15, 48–50, 1969.
6. He, G. S., P. P. Markowicz, T. C. Lin, and P. N. Prasad, "Observation of stimulated emission by direct three-photon excitation," *Nature*, Vol. 415, 767–770, 2002.
7. Schietinger, S., T. Aichele, H.-Q. Wang, T. Nann, and O. Benson, "Plasmon-enhanced upconversion in single $\text{NaYF}_4:\text{Yb}^{3+}/\text{Er}^{3+}$ codoped nanocrystals," *Nano Lett.*, Vol. 10, 134–138, 2010.
8. Ganesh, N. and B. T. Cunningham, "Photonic-crystal near ultraviolet reflectance filters fabricated by nanoreplica molding," *Appl. Phys. Lett.*, Vol. 88, 071110-1–3, 2006.
9. Ganesh, N., W. Zhang, P. C. Mathias, E. Chow, J. A. N. T. Soares, V. Malyarchuk, A. D. Smith, and B. T. Cunningham, "Enhanced fluorescence emission from quantum dots on a photonic crystal surface," *Nature Nanotech.*, Vol. 2, 515–520, 2007.
10. Katchalski, T., S. Soria, E. Teitelbaum, A. A. Friesem, and G. Marowsky, "Two photon fluorescence sensors based on resonant grating waveguide structures," *Sens. Actuators B*, Vol. 107, 121–125, 2005.

11. Muriano, A., K. N. A. Thayil, J.-P. Salvador, P. L.-Alvarez, S. Soria, R. Galve, and M.-P. Marco, “Two-photon fluorescent immunosensor for androgenic hormones using resonant grating waveguide structures,” *Sens. Actuators B: Chem.*, Vol. 174, 394–401, 2012.
12. Mathias, P. C., H.-Y. Wu, and B. T. Cunningham, “Employing two distinct photonic crystal resonances to improve fluorescence enhancement,” *Appl. Phys. Lett.*, Vol. 95, 021111-1–3, 2009.
13. Lin, J. H., C.-Y. Tseng, C.-T. Lee, H.-C. Kan, and C. C. Hsu, “Guided-mode resonance enhanced excitation and extraction of two-photon photoluminescence in a resonant waveguide grating,” *Opt. Express*, Vol. 21, 24318–24325, 2013.
14. Siltanen, M., S. Leivo, P. Voima, M. Kauranen, P. Karvinen, P. Vahimaa, and M. Kuittinen, “Strong enhancement of second-harmonic generation in all-dielectric resonant waveguide grating,” *Appl. Phys. Lett.*, Vol. 91, 111109-1–3, 2007.
15. Lin, J. H., C.-Yen Tseng, C.-T. Lee, J. F. Young, H.-C. Kan, and C. C. Hsu, “Strong guided mode resonant local field enhanced visible harmonic generation in an azo-polymer resonant waveguide grating,” *Opt. Express*, Vol. 22, 2790–2797, 2014.
16. Lai, N. D., W. P. Liang, J. H. Lin, and C. C. Hsu, “Rapid fabrication of large-area periodic structures containing well-defined defects by combining holography and mask techniques,” *Opt. Express*, Vol. 13, 5331–5337, 2005.
17. Lai, N. D., W. P. Liang, J. H. Lin, C. C. Hsu, and C. H. Lin, “Fabrication of two- and three-dimensional periodic structures by multi-exposure of two-beam interference technique,” *Opt. Express*, Vol. 13, 9605–9611, 2005.
18. Zhou, J., G. Chen, E. Wu, G. Bi, B. Wu, Y. Teng, S. Zhou, and J. Qiu, “Ultrasensitive polarized up-conversion of Tm^{3+} - Yb^{3+} doped b- NaYF_4 single nanorod,” *Nano Lett.*, Vol. 13, 2241–2246, 2013.

Novel Tunable Multi-passband Microwave Photonic Filters Based on Fiber Mach-Zehnder Interferometer and Fiber Delay Lines

Hao Chen, Zuwei Xu, Hongyan Fu*, and Dan Zhang

Department of Electronic Engineering

School of Information Science and Engineering, Xiamen University, Xiamen 361005, China

Abstract— In this article, we propose and demonstrate two new approaches to implement microwave photonic filters with multi-passband based on the sliced broadband optical source with fiber Mach-Zehnder interferometer and fiber delay lines. The proposed MPFs are simple in construction, easy to implement, and the experimental results show good tunability and reconfigurability.

1. INTRODUCTION

Microwave photonic filters (MPFs) have been under constant research in the last two decades. Compared with the traditional electronic filters, MPFs enjoy the advantages of broad bandwidth, low loss, good tunability, and the immunity to electromagnetic interference, etc. [1–3]. Many techniques have been reported to realize functional MPFs, among which MPFs based on continuous sampling of a broadband optical source and dispersive medium have drawn much attention, since its free spectrum range is infinite in the theory, and thus resulting in a single passband frequency response [4, 5]. Although the single-passband MPF has shown good application potential, in many practical applications, multi-passband MPFs with freely tunable central frequencies are more desirable. Most techniques reported in literature to realize MPFs are not applicable for this kind of multi-passband MPFs, since most of them have periodic frequency responses and their passbands move simultaneously when tuning the MPFs, while their free spectrum ranges keep the same. In this article, we propose and demonstrate two new approaches to implement MPFs with multi passbands based on the sliced broadband optical source (BOS) with fiber Mach-Zehnder interferometer (FMZI) and fiber delay lines. Dual-passband MPFs with good tunability and frequency response characteristics have been achieved in the experiment. The proposed multi-passband MPFs are easy to implement, simple in construction, and show good application potentials in fiber wireless systems and sensing systems.

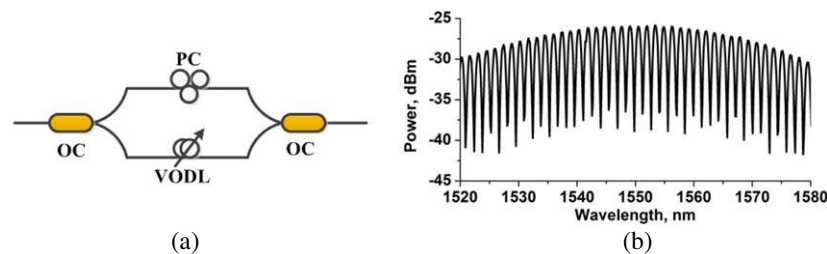


Figure 1: (a) The structure of an FMZI and (b) the sliced spectrum of the BOS after the FMZI.

2. EXPERIMENTAL SETUP AND RESULTS

The proposed multi-passband MPFs are based on the FMZI to act as a spectrum slicer for the BOS to achieve continuous optical sampling, whose structure is shown as Fig. 1(a). The FMZI is made by connecting two 3 dB optical couplers (OC) together, with a polarization controller (PC) in one arm of the FMZI in order to achieve the best extinction ratio of the sliced comb spectrum, and a variable optical delay line (VODL) in the other arm of the FMZI to tune the wavelength spacing of the FMZI. The transfer function of the FMZI can be expressed as:

$$T(\omega) = \frac{1}{2} \left[1 + V \cos \left(2\pi \frac{\omega}{\Delta\omega} \right) \right] \quad (1)$$

*Corresponding author: Hongyan Fu (fuhongyan@xmu.edu.cn).

where V is the visibility of the FMZI, and can be changed by adjusting the polarization controller in one arm of the FMZI; $\Delta\omega$ is free spectrum range of the FMZI, which is determined by the optical path difference of the two arms of FMZI, ΔL . The FMZI is an optical comb filter, and the sliced spectrum of the BOS after the FMZI is shown in Fig. 1(b).

2.1. Dual-pass MPF Based on FMZI and Dual-path Fiber Delay Line

The experimental setup of the dual-passband MPF based on an FMZI as a slicing filter and a dual-path fiber delay line is shown as Fig. 2. The light from a BOS is transmitted through the FMZI to obtain the continuous optical samples, after which the light is modulated by the electro-optic modulator (EOM) by microwave signals to be processed, and then launched into the dual-path fiber delay line which is composed of two 3 dB optical couplers and has different fiber lengths in each path. After that, the light is recombined and detected by the photodiode, and measured by the vector network analyzer (VNA).

In the experiment, after the EOM, the sliced optical source is firstly delayed by a coil of 25 km single mode fiber (SMF) which acts as the dispersive medium, and then sent to the dual-path fiber delay line composed by two 50:50 optical couplers and another coil of 25 km SMF. The modulated light is split into two branches, one of which transmits through 25 km SMF and the other one goes directly through the branch, and recombined together and detected by the PD and measured by the vector network analyzer (VNA) after the dual-path fiber delay line. The frequency responses with separate fiber delay lines and dual-path fiber delay lines are shown as Figs. 3(a) and (b), respectively. One can see that, with the dual-path fiber delay line dual-passband MPF can be realized with each passband identical to the single-passband MPF when separate dispersive fiber is used.

By adjusting the length of the VODL in one arm of the FMZI, the wavelength spacing of the FMZI can be tuned, and thus the central frequencies of both passbands, shown as the measured frequency response in Fig. 4(a). Fig. 4(b) shows the relationship between central frequencies of

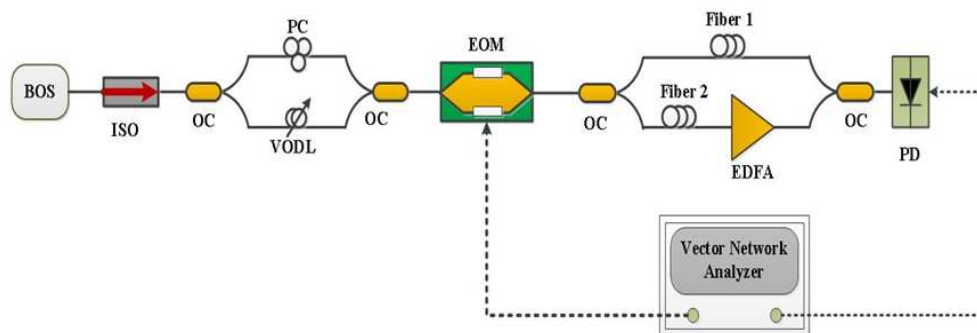


Figure 2: Experimental setup of the dual-passband MPF which utilizes an FMZI and a dual-path fiber delay line (BOS: broadband optical source, ISO: optical isolator, OC: optical coupler, PC: polarization controller, VODL: variable optical delay line, EOM: electro-optic modulator, EDFA: erbium doped fiber amplifier, PD: photodiode.)

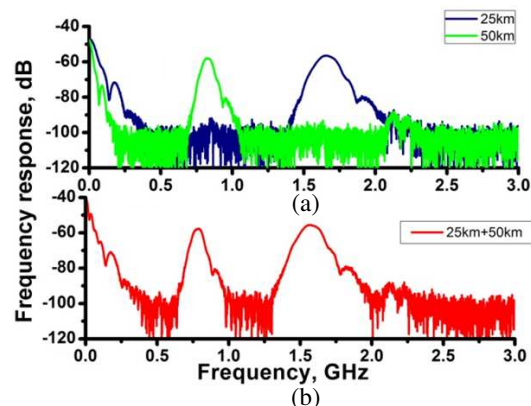


Figure 3: The frequency response with (a) single passband (with single fiber delay line) and (b) dual-passband (with dual-path fiber delay line).

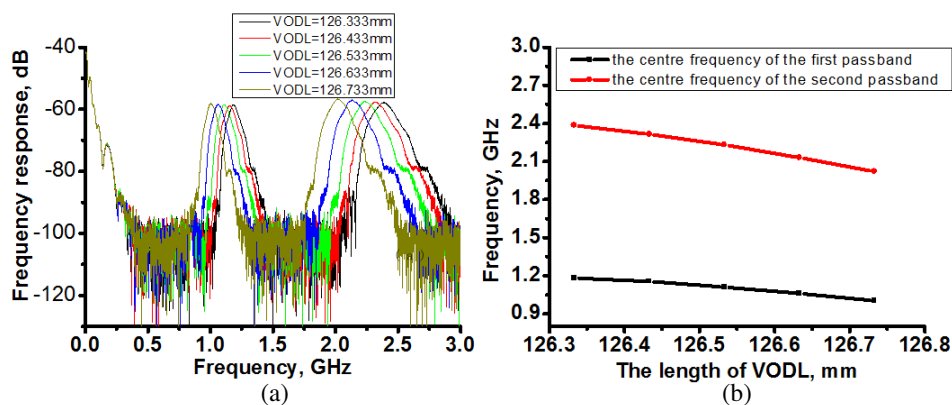


Figure 4: (a) The measured frequency responses with different length of VODL and (b) the relationship between the central frequencies of each passband and the length of VODL.

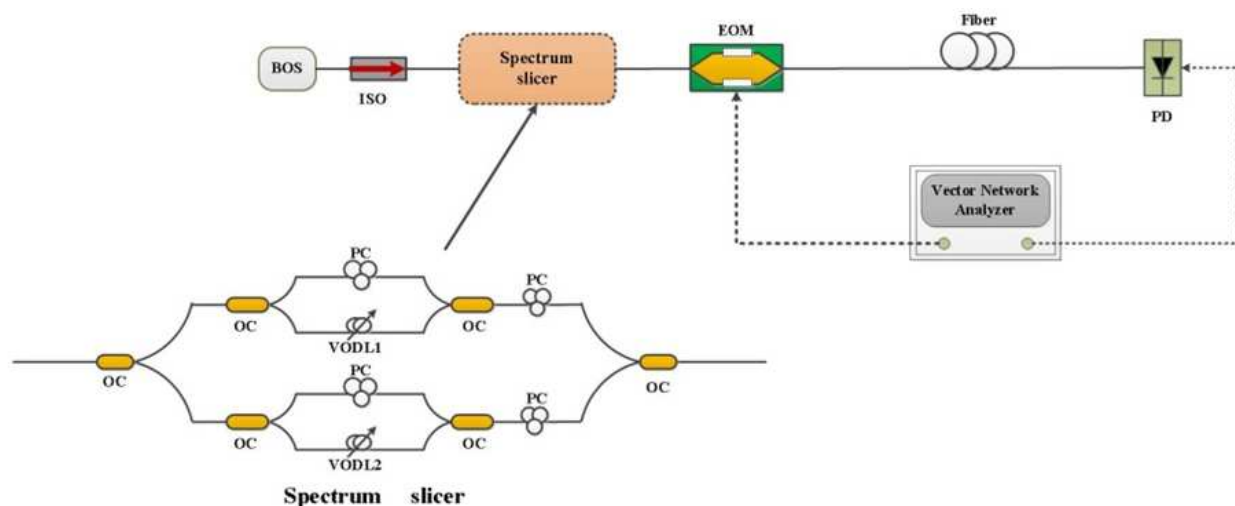


Figure 5: Experimental setup of the dual-passband MPF based on paralleled FMZIs and a dispersive medium.

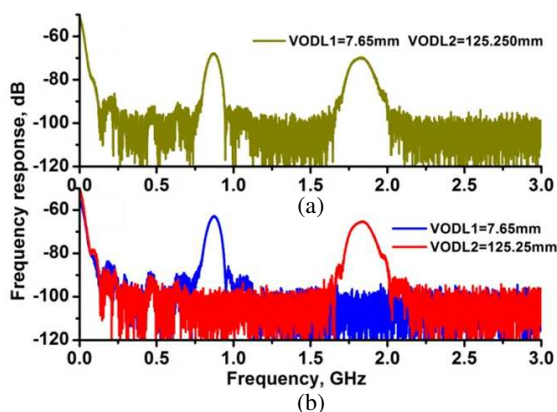


Figure 6: The frequency response of the proposed (a) dual-passband MPF (with two paralleled FMZIs) and (b) with single passband (with one FMZI).

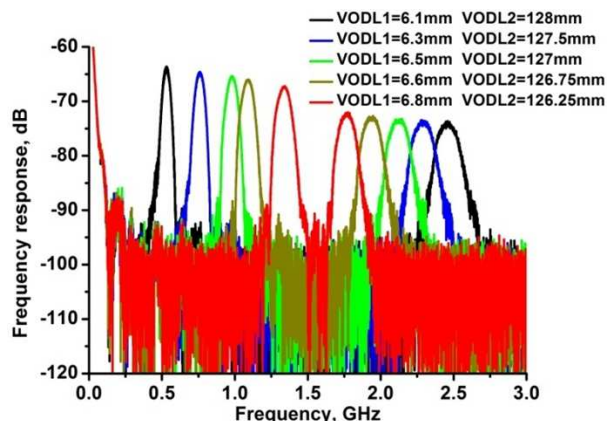


Figure 7: The frequency responses when the lengths of VODL1 and VODL2 are tuned simultaneously.

each passband and the length of VODL. The experimental results show that the central frequency of each passband has a good linear relationship with the length of VODL.

2.2. Dual-passband MPF Based on Paralleled FMZIs and a Dispersive Medium

The experimental setup of the dual-passband MPF which was realized by using paralleled FMZIs and a dispersive fiber is shown as Fig. 5. In the experiment, two paralleled FMZIs are used as

the spectrum slicing filter to obtain the optical samples, after which the light is modulated by microwave signals to be processed through an EOM. Then, the modulated light is launched into a dispersive medium which in our experiment is coil of single mode fiber, and then recovered by the high speed PD. The frequency response of the proposed dual-passband MPF was measured by the VNA.

In the experiment, when we use paralleled FMZIs ($VODL1 = 7.65$ mm $VODL2 = 125.25$ mm), dual-passband frequency response can be realized, as shown in Fig. 6(a). As a comparison, the frequency responses by using single FMZI have also been measured with the same length of VODL, as shown in Fig. 6(b). One can observe that, the passbands of the dual-passband MPF are identical to that of the separated single-passband MPF. Both passbands of the proposed MPF can be tuned by adjusting the length of the VODLs, and Fig. 7 shows the frequency responses of the proposed MPF when the length of VODL1 and VODL2 are tuned simultaneously. One can see from the experimental results that the proposed MPF shows good tunability, and both passbands can be tuned freely by adjusting the optical path difference of the corresponding FMZI.

3. CONCLUSIONS

In this article, we proposed two new approaches to implement MPFs with multi-passband based on the sliced broadband optical source with fiber Mach-Zehnder interferometer and fiber delay lines. The first approach is based on an FMZI as a slicing and a multi-path fiber delay line. In our experiment, the frequency response with dual passbands has been achieved by using a dual-path fiber delay line, and the central frequencies of both passbands can be tuned by adjusting the length of the VODL. By employing fiber delay lines with more paths, multi-passband MPF can be realized with this method. The second approach is to employ paralleled FMZIs and a dispersive medium to realize the multi-passband MPF, and in this way the central frequencies the passbands can be tuned freely by adjusting the optical path difference of each FMZI. In our experiment, dual-passband MPF has been obtained by using two paralleled FMZIs, and the central frequencies of both passbands can be tuned freely. Multi-passband MPF with desirable number of passbands can be realized by introducing more FMZIs in this technique. In conclusion, our proposed approaches to realize multi-passband MPFs are easy to implement, exhibit good tunability, flexibility, and thus show good application potential in the wireless communication and measurement systems.

ACKNOWLEDGMENT

The authors acknowledge the support from the National Natural Science Foundation of China (No. 61205059, No. 61107023), and Ph.D. Programs Foundation of Ministry of Education of China (No. 20120121120037, No. 20110121120020).

REFERENCES

1. Capmany, J., B. Ortega, and D. Pastor, "A tutorial on microwave photonic filters," *IEEE J. Lightw. Technol.*, Vol. 24, 201–229, 2006.
2. Capmany, J. and D. Novak, "Microwave photonics combines two worlds," *Nat. Photon.*, Vol. 1, 319–330, 2007.
3. Yao, J., "Microwave photonics," *IEEE J. Lightw. Technol.*, Vol. 27, 314–335, 2009.
4. Mora, J., B. Ortega, A. Díez, J. L. Cruz, M. V. Andrés, J. Capmany, and D. Pastor, "Photonic microwave tunable single-bandpass filter based on a mach-zehnder interferometer," *J. Lightwave Technol.*, Vol. 24, No. 7, 2500–2509, 2006.
5. Fu, H., K. Zhu, H. Ou, and S. He, "A tunable single-passband microwave photonic filter with positive and negative taps using a fiber Mach-Zehnder interferometer and phase modulation," *Optics & Laser Technology*, Vol. 42, No. 1, 81–84, 2010.

New Scaling of Electron Thermionic Emission from Single-layer Graphene

Shi-Jun Liang¹, L. K. Ang¹ and Gang Chen²

¹Engineering Product Development, Singapore University of Technology and Design, Singapore

²Department of Mechanical Engineering, Massachusetts Institute of Technology
Cambridge, MA 02139, USA

Abstract— In this work, a simple model is developed to explore the electron thermionic emission from a single-layer graphene. This study is based on our prior efforts in showing that electron emission mechanisms from single-layer graphene is quite different from the traditional models, such as graphene field emission, and graphene laser-induced over-barrier emission, etc.. Now, we establish a new scaling for thermionic emission from graphene, quite different from the conventional Richardson’s law responsible for bulk materials. Our analytical formula obtained in this work is demonstrated to agree well with numerical results.

1. INTRODUCTION

Electron thermionic emission describes the process of thermal electron evaporation from the surface of a hot cathode material, which is first discovered by Owen Willans Richardson in 1901 [1]. Due to this discovery, he was awarded the Nobel Prize in 1928. The mathematical description of thermionic emission is given by Richardson-Dushman equation,

$$J = AT^2 \exp \left[-\frac{\Phi}{k_B T} \right]. \quad (1)$$

where, T is the cathode temperature, Φ is the work function of metal, k_B is the Boltzmann constant, and the prefactor $A = 1.2 \times 10^6 \text{ Am}^{-2}\text{K}^{-2}$ is the Richardson constant. This equation has very important implications in the design of vacuum electronics device and the study of interface materials, as well as energy conversion. Specifically, the recent studies [2, 3] make a very promising future of the domestic application of energy converter based on thermionic emission. However, all the current applications above are based on the traditional Richardson’s law, which is derived for bulk materials.

Recently, the studies of two-dimensional materials, like graphene [4], have attracted lots of attention. Graphene has many unique properties, such as ultrahigh mobility, linear dispersion relation, etc.. Fundamentally, the single-layer graphene differs from conventional bulk materials in its linear band structure. Thus this essential difference arises an interesting question: Is the conventional Richardson’s law still valid for the thermionic emission from a single-layer graphene? In this work, we are going to answer this question.

2. MODEL

In this work, we develop a model, as shown in Fig. 1. Assume that the cathode has been heated up to a uniform temperature T_c , the electrons will be evaporated from the cathode and then condensed on the anode (which is at temperature T_a) by passing over the potential barrier as shown in Fig. 1(b).

3. RESULTS

Wallace’s electron theory of graphene provides the basis for all unique and excellent properties of graphene. The unique linear-band structure of graphene leads to massless dirac fermion electron, which obeys a 2-D dirac equation. Using this model, the density of electron states per cell in the graphene is obtained,

$$\rho(E)dE = \frac{2}{(2\pi)^2} \iint d^2k = \frac{2E}{\pi(\hbar v_f)^2} dE, \quad (2)$$

where \hbar is the reduced Planck constant and v_f (10^6 m/s) is the velocity of massless Dirac fermions in the graphene. For the thermionic emission, the current density of the emitted electrons along

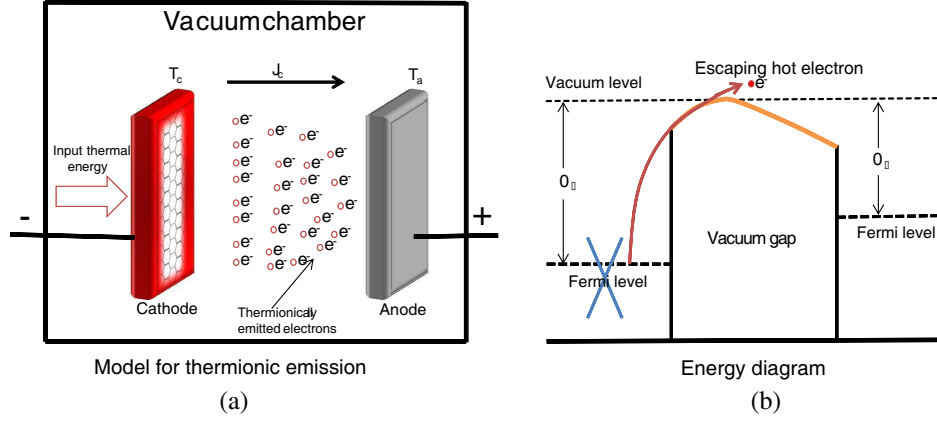


Figure 1: Schematic diagram of the (a) electron emission process of a graphene-based thermionic energy converter (TIC), where T_c and T_a are the cathode temperature and anode temperature, respectively; J_c is current ow from cathode to anode. (b) energy level for thermionic energy converter (TIC) shown in (a). Φ_c and Φ_a are the work function of cathode and of anode, respectively. The orange line represents the potential energy in the vacuum. The deep red line traces the thermionic emission process of an electron into vacuum.

the direction perpendicular to graphene plane is calculated by

$$J(E_F, T) = \int_{\Phi}^{\infty} eN(E_x)dE_x, \quad (3)$$

with

$$N(E, E_x)dEdE_x \equiv \frac{2f_{F-D}(E)^2}{2\pi} \iiint_{E, E_x} v_x d^2k dk_x = \frac{1}{\pi \hbar^3 v_f^2} E f_{FD}(E) dEdE_x. \quad (4)$$

where, $f_{F-D}(E)$ is the Fermi-Dirac distribution. To solve Eq. (4) analytically, we assume that $f_{F-D}(E)$ can be replaced with Maxwell-Boltzmann distribution $f_{M-B}(E) = \exp[-(E - E_F)/k_B T]$.

In doing so, we obtain an analytical solution to Eq. (3).

$$J(E_F, T) = \frac{ek_B^2 T^2}{\pi \hbar^3 v_f^2} (k_B T + \Phi) \exp \left[-\frac{\Phi - E_F}{k_B T} \right] \quad (5)$$

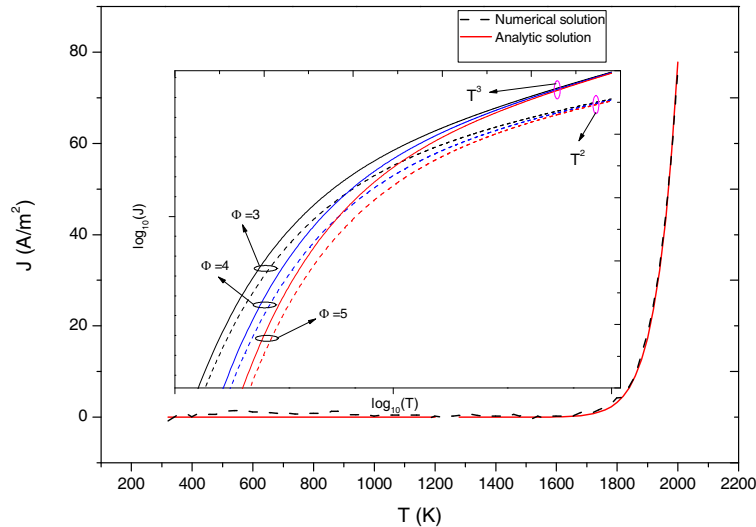


Figure 2: Comparison of our analytical results [in red line] with the numerical solution of Eq. (3) [in black dashed line] as a function of temperature. The Inset demonstrates comparison between our model (solid line) and Richardson's law (dashed line) at different work function 3 eV, 4 eV and 5 eV.

We found that Eq. (5) is completely different from the conventional Richardson's law given by Eq. (1), due to the linear band structure of graphene. And the numerical calculation of Eq. (3) is carried out to verify the analytical solution, as shown in the Fig. 2. In addition, the comparison between our results and Richardson's law is also presented in the Fig. 2. From this figure, it is found that, at high temperature limit ($k_B T \gg \Phi$), Eq. (5) also gives a new scaling of T^3 , which is different from the T^2 scaling based on the Richardson's law.

4. CONCLUSION

In the work, we study the thermionic emission from a single-layer graphene, and a new scaling of thermionic emission is established. It is found that the newly proposed scaling is quite different from the conventional Richardson's law. This finding may be very useful in the design of energy conversion devices and in the study of transport near interface.

ACKNOWLEDGMENT

This work was supported by SUTD (SRG EPD 2011014) and SUTD-MIT IDC grant (IDG21200106 and IDD21200103). L. K. Ang would like to acknowledge the support of a USA AFOSR AOSRD grant (11-4069).

REFERENCES

1. Richardson, O. W., Wexford College Press, 196, ISBN 978-1-929148-10-3, 2003.
2. Meir, S., C. Stphanos, and J. Mannhart, *Journal of Renewable and Sustainable Energy*, Vol. 5, 043127, 2013.
3. Schwede, J. W., I. Bargatin, D. C. Riley, B. E. Hardin, S. J. Rosenthal, Y. Sun, F. Schmitt, P. Pianetta, R. T. Howe, Z.-X. Shen, and N. A. Melosh, *Nature Materials*, Vol. 9, 762, 2010.
4. Novoselov, K. S., A. K. Geim, S. V. Morozov, D. Jiang, M. I. Katsnelson, I. V. Grigorieva, S. V. Dubonos, and A. A. Firsov, *Nature*, Vol. 438, 197, 2005.

1 Gbps Directed Optical Decoder Based on Two Cascaded Microring Resonators

Qiaoshan Chen, Fanfan Zhang, Lei Zhang, Yonghui Tian,
Ping Zhou, Jianfeng Ding, and Lin Yang

State Key Laboratory on Integrated Optoelectronics
Institute of Semiconductors, Chinese Academy of Sciences, China

Abstract— We report an electro-optic directed optical decoder based on two cascaded microring resonators. PN junctions embedded around the MRRs are employed to modulate the MRRs through the carrier-injection scheme. The optical decoding function from a 2-bit electrical signal to a 4-bit optical signal at the speed of 1 Gbps is performed successfully by the device.

1. INTRODUCTION

Optical directed logic is a paradigm which employs the optical switch network to perform the logical operation [1, 2]. The status of each optical switch in the network is determined by an electrical Boolean signal applied to it. The operation of each optical switch is independent of the operations of other optical switches in the network and the operation result propagates in the network at the speed of light. The overall latency of the optical directed logic circuit is very small and all optical switches perform their operations almost simultaneously [3, 4]. Therefore, the optical directed logic has a very high operation speed and low latency [1–4]. Silicon microring resonator is an attractive structure owing to its outstanding performances, such as compact size, ultra-low power consumption and CMOS-compatible fabrication process. Therefore, the optical directed logic based on silicon microring switches is easy to realize large-scale integration and low-cost manufacture in a high-volume CMOS photonics foundry. A series of optical directed logic circuits have been proposed and even demonstrated [5–9].

We have demonstrated a directed optical decoder [6], whose speed is 10 kbps due to the thermo-optic modulation scheme. In this letter, a directed optical decoder modulated by electric-field-induced carrier injection in forward biased PN junctions is demonstrated, which can perform the decoding function from a 2-bit electrical signal to a 4-bit optical signal at the speed of 1 Gbps.

2. DESIGN AND FABRICATION

The architecture of the directed optical decoder is schematically shown in Fig. 1, which consists of two cascaded electrically modulated add-drop MRRs and three waveguides. Monochromatic continuous light with the working wavelength λ_{work} is coupled into the device through its input port, and modulated by two electrical pulse sequences applied to the MRRs through electric-field-induced carrier injection in forward biased PN junctions.

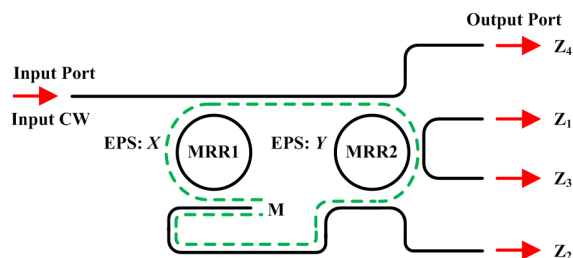


Figure 1: Schematic of the optical device. CW: continuous wave, EPS: electrical pulse signal, MRR: microring resonator.

Each MRR acts as an optical switch and two electrical signals X and Y are used to control the resonance states of two MRRs, respectively. In the previous work [11], thermo-optic effect is employed to tune the resonance state of each MRR and the MRR is on-resonance when the applied voltage is at the high level. In this work, free-carrier dispersion effect is employed to tune the resonance state of each MRR. When carriers are injected into the MRR, the refractive index of the ring waveguide is reduced and its propagation loss is increased simultaneously. In order to

achieve high contrast between optical logic 1 and 0, two MRRs are on-resonance at the working wavelength λ_{work} when the applied electrical signals are at the low level and off-resonance at the working wavelength λ_{work} when the applied electrical signals are at the high level. The high and low levels of the optical power at four output ports represent the operation result of logic 1 and 0, respectively. According to the definition above, the electrical logics applied to two MRRs, the states of two MRRs and the operation results at four output ports are summarized in Table 1. Clearly, the architecture in Fig. 1 can perform the decoding function from a 2-bit electrical signal to a 4-bit optical signal.

Table 1: Principle of the directed optical decoder.

Electrical logic of MRR1	Electrical logic of MRR2	Resonance state of MRR1	Resonance state of MRR2	Z_1	Z_2	Z_3	Z_4
0	0	ON	ON	1	0	0	0
0	1	ON	OFF	0	1	0	0
1	0	OFF	ON	0	1	0	
1	1	OFF	OFF	0	0	0	1

In Fig. 2, the waveguides are sheltered by aluminum trances and pads. The dash lines show where the waveguides are and the green arrows represent the input and output ports of the device.

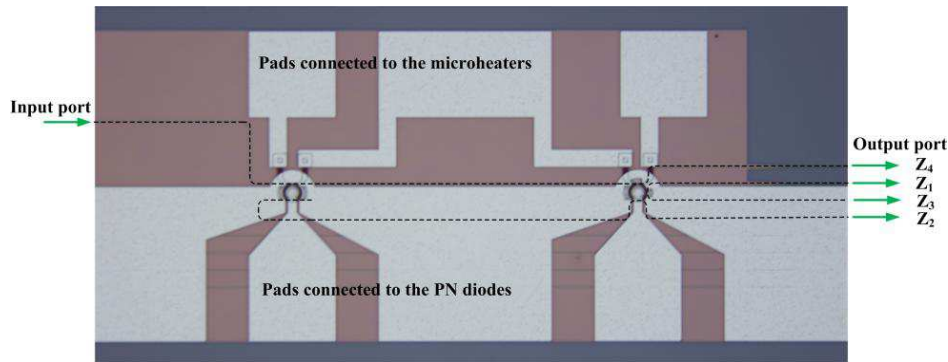


Figure 2: Micrograph of electro-optic directed optical decoder.

3. ANALYSIS OF THE STATIC RESPONSE SPECTRA

In order to determine the working wavelength of the device and the driving voltages of two MRRs, the static response spectra of the device are measured with an amplified spontaneous emission (ASE) source, an optical spectrum analyzer (OSA) and three tunable voltage sources. The light from the ASE source is coupled into the input port of the device through a lensed fiber. The light from the output port of the device is coupled into another lensed fiber and then fed into the OSA. One tunable voltage source is used to tune the microheater of the MRR with shorter initial resonance wavelength, so that its resonance wavelength matches with that of the other MRR. The left two tunable voltage sources are employed to inject carriers into the two PN diodes, respectively. With the applied voltage on the PN diode increasing, the effective refractive index decreases and the resonance wavelength of the MRR moves to the shorter wavelength.

Although two MRRs are designed to have the same structural parameters, they have slightly different initial resonance wavelengths due to the limited manufacturing accuracy. Without any tunable voltage sources applied to the device, the static response spectra at the output ports Z_1 – Z_4 are shown in Fig. 3. We can see two dips at 1551.768 nm and 1552.472 nm in the static response spectra at the output port Z_4 (Fig. 3(d)), which are caused by the resonances of MRR2 and MRR1, respectively. MRR2 has three coupling regions while MRR1 has two coupling regions. Except for this, MRR2 has the same structural parameters with MRR1 does. Therefore, MRR2 has a larger optical loss than MRR1 does and the calculated Q factor from the static response spectra is 17642 for MRR1 and 11410 for MRR2. MRR1 has an extinction ratio of 20.4 dB and MRR2 has an

extinction ratio of 14.8 dB, because MRR1 is much closer to the critical coupling than MRR2 does in the adopted structural parameters.

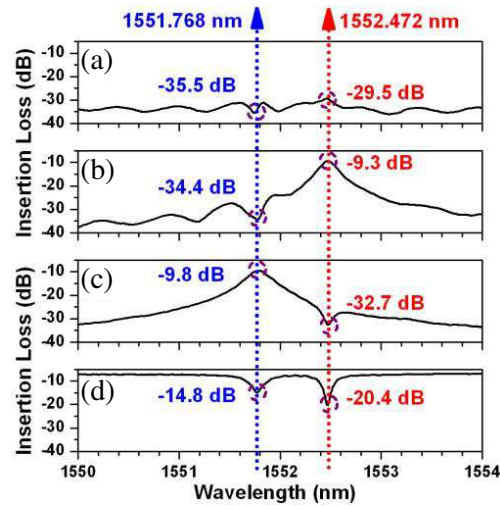


Figure 3: Static response spectra at the output ports (a) Z_1 , (b) Z_2 , (c) Z_3 , and (d) Z_4 without electrical compensating voltage applied to the device.

1552.472 nm is chosen as the working wavelength λ_{work} to achieve a relatively large extinction ratio. When MRR2 is heat up, the effective refractive index of the Si waveguide increases and the resonance wavelength of MRR2 shifts to the longer wavelength. With the voltage applied to the microheater of MRR2 being 2.1 V (the compensating voltage), the resonance wavelength of MRR2 is at the working wavelength. The static response spectra at four output ports Z_1 – Z_4 with the compensating voltage are shown in Figs. 4(a), 5(a), 6(a) and 7(a).

Noted that some ripples are observed in the static response spectra at the output ports Z_1 and Z_2 , (Figs. 3(a) and 3(b)) due to the interference effect caused by the closed cavity formed by two cascaded MRRs and the facet of port M, as shown in the green dash line in Fig. 1.

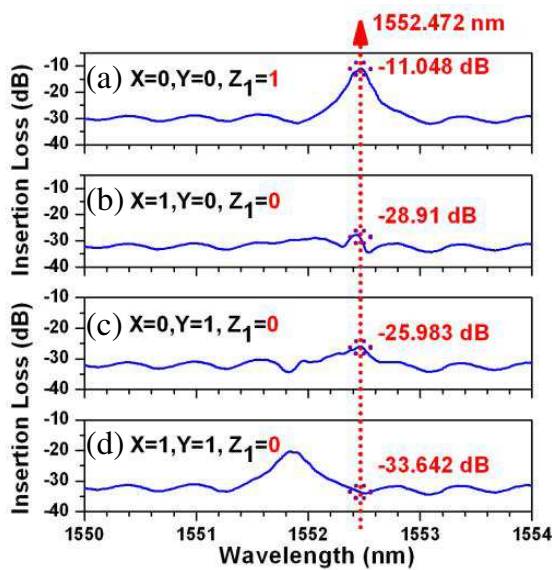


Figure 4: Static response spectra at the output port Z_1 with the voltages applied to the PN junctions of MRR1 and MRR2 being (a) 0 V and 0 V, (b) 1.5 V and 0 V, (c) 0 V and 1.4 V, (d) 1.5 V and 1.4 V.

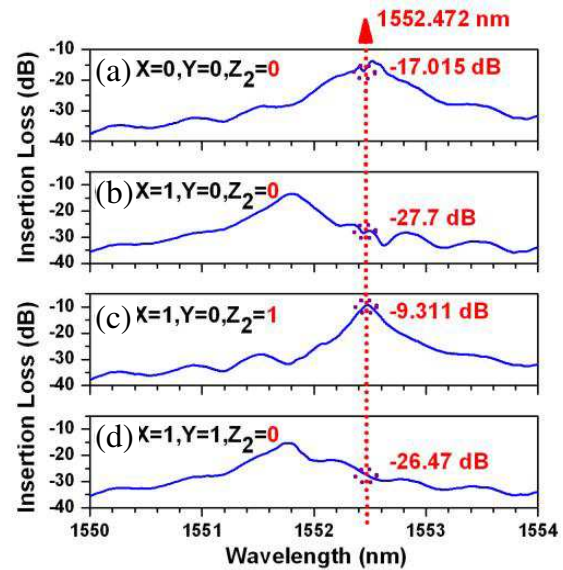


Figure 5: Static response spectra at the output port Z_2 with the voltages applied to the PN junctions of MRR1 and MRR2 being (a) 0 V and 0 V, (b) 1.5 V and 0 V, (c) 0 V and 1.4 V, (d) 1.5 V and 1.4 V.

The static response spectra at the output port Z_1 show the drop filtering characteristics of MRR1 and MRR2 (Fig. 4). According to the principle aforementioned, there is a peak when both

MRR1 and MRR2 are on-resonance at the working wavelength (Fig. 4(a)), the optical power at the output port Z_1 is at the high level (representing 1). In other three working statuses, the optical power at the output port Z_1 is at the low level (Figs. 4(b)–(d)).

The static response spectra at the output port Z_2 show the drop filtering characteristics of MRR1 and the through filtering characteristics of MRR2 (Fig. 5). The optical power at the output port Z_2 is at the high level when MRR1 is on-resonance and MRR2 is off-resonance (Fig. 5(c)). In other three working statuses, the optical power at the output port Z_2 is at the low level (Figs. 5(a), 5(b) and 5(d)).

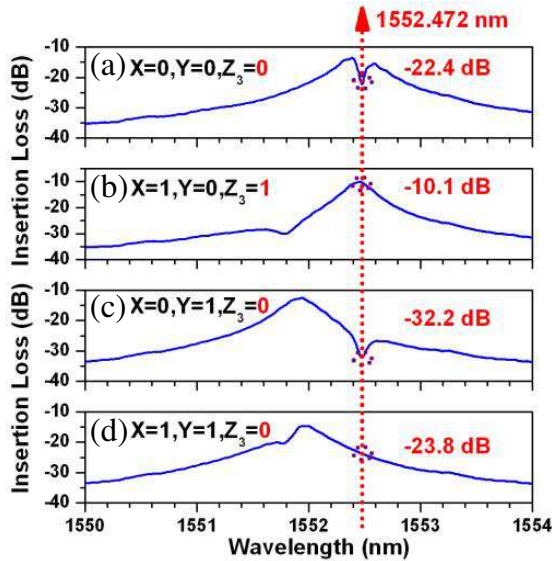


Figure 6: Static response spectra at the output ports Z_3 with the voltages applied to the PN junctions of MRR1 and MRR2 being (a) 0 V and 0 V, (b) 1.5 V and 0 V, (c) 0 V and 1.4 V, (d) 1.5 V and 1.4 V.

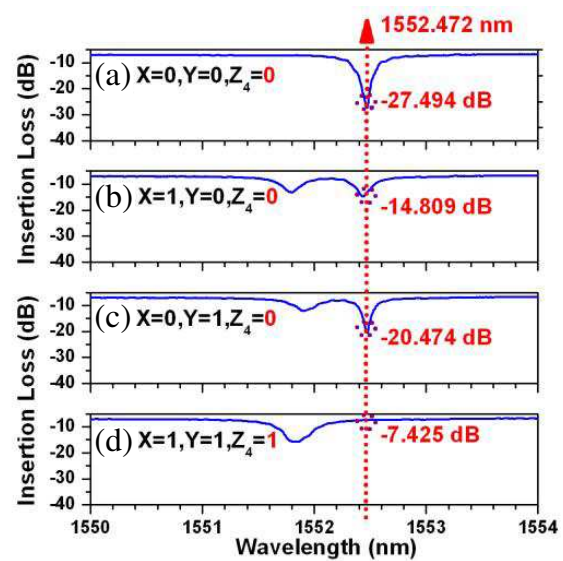


Figure 7: Static response spectra at the output ports Z_4 with the voltages applied to the PN junctions of MRR1 and MRR2 being (a) 0 V and 0 V, (b) 1.5 V and 0 V, (c) 0 V and 1.4 V, (d) 1.5 V and 1.4 V.

The static response spectra at the output port Z_3 show the through filtering characteristics of MRR1 and the drop filtering characteristics of MRR2 (Fig. 6). MRR2 has a much larger full width at half maximum (FWHM) than MRR1 does. So there is a dip in the drop filtering spectra, which can be noticed in Fig. 6(a). The optical power at the output port Z_3 is at the high level when MRR1 is off-resonance and MRR2 is on-resonance (Fig. 6(b)). In other three working statuses, the optical power at the output port Z_3 is at the low level (Figs. 6(b)–(d)).

The static response spectra at the output port Z_4 show the through filtering characteristics of MRR1 and MRR2 (Fig. 7). According to the principle aforementioned, there is a dip when both MRR1 and MRR2 are on-resonance at the working wavelength (Fig. 7(a)), the optical power is at the low level (representing 0). With only the voltage of 1.5 V applied to the PN diode of MRR1, the resonance wavelength of MRR1 shifts to the shorter wavelength (Fig. 7(b)) and the optical power is still at the low level (representing 0). With only the voltage of 1.4 V applied to the PN diode of MRR2, the resonance wavelength of MRR2 shifts to the shorter wavelength (Fig. 7(c)) and the optical power is at the low level (representing 0). The optical power at the output port Z_4 is at the high level when both MRR1 and MRR2 are off-resonance (Fig. 7(d)).

All four static response spectra at four output ports of the device are analyzed above. The results indicate that the device can implement the decoding function from a 2-bit electrical signal to a 4-bit optical signal correctly.

4. DYNAMIC EXPERIMENTAL RESULTS

A monochromatic light with the working wavelength of 1552.472 nm is coupled into a polarization rotator and the light with the TE polarization is coupled into the device by a lensed fiber. Two non-return-to-zero electrical signals with the period of 8 bits generated by two pulse pattern generators are used to modulate the PN diodes of MRR1 and MRR2, respectively. The electrical signals applied to the MRRs have the amplitude of 0.8 V with the offset of 1.1 V. The light at the output

ports Z_1 – Z_4 are fed into a wideband sampling oscilloscope (Agilent DCA-X 860100D) with an optical head for waveform observation.

The dynamic response of the device at the speed of 1 Gbps is characterized. The results are shown in Fig. 8, in which three periods (i.e., 24 bits) are shown for the input electrical signals and the output optical signals. We have measured those signals one by one and then aligned them with each other in the time axis. The device performs the decoding function from a 2-bit electrical signal to a 4-bit optical signal at the speed of 1 Gbps correctly. There are several positive spikes between two continuous outputs of ‘0s’ at the output port Z_4 , which are also observed and have been well explained in the previous work [6]. Note that the power level is same for logical ‘1’ but different for logical ‘0’ in different working statuses at the output ports Z_2 and Z_4 , which mainly results from the different extinction ratios of the dips in different working statuses. These phenomena are also observed in the static response spectra (Figs. 5 and 7), where the insertion losses for logical ‘0’ is -17.015 , -26.47 and -27.7 dB at the output port Z_2 in different cases respectively, and the insertion losses for logical ‘0’ is -14.809 , -20.474 and -27.494 dB at the output port Z_4 in different working statuses respectively.

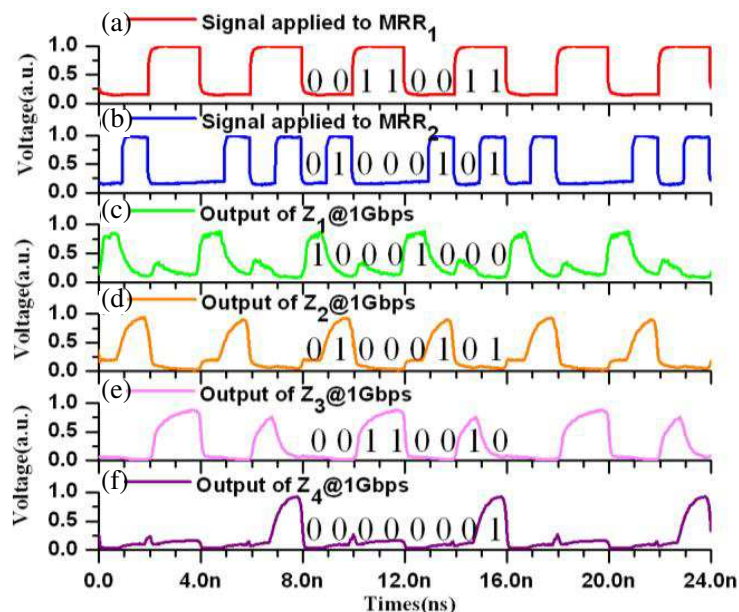


Figure 8: Dynamic operation results of the device at the speed of 1 Gbps. (a) and (b) 1 Gbps electrical signals applied to MRR1 and MRR2, respectively. 1 Gbps decoder operation results at the ports (c) Z_1 , (d) Z_2 , (e) Z_3 , (f) Z_4 respectively.

5. CONCLUSION

In conclusion, we fabricated an electro-optic directed optical decoder based on two cascaded microring resonators. PN junctions embedded around the MRRs are employed to modulate the MRRs through the carrier-injection scheme. The optical decoding function from a 2-bit electrical signal to a 4-bit optical signal at the speed of 1 Gbps is performed successfully by the device.

ACKNOWLEDGMENT

The authors thank Dr. M. B. Yu of IME for device fabrication. This work has been supported by the National Natural Science Foundation of China under grants 61204061, 61235001, and 61377067, by the National High Technology Research and Development Program of China under grants 2012AA012202 and 2013AA014203 and by Scientific and Technological Innovation Cross Team of Chinese Academy of Sciences.

REFERENCES

1. Hardy, J. and J. Shamir, “Optics inspired logic architecture,” *Optics Express*, Vol. 15, No. 1, 150–165, 2007.

2. Shamir, J., “Energy efficient computing exploiting the properties of light,” *SPIE Optical Engineering+ Applications. International Society for Optics and Photonics*, 88330J-88330J-9, 2013.
3. Caulfield, H. J. and S. Dolev, “Why future supercomputing requires optics,” *Nature Photonics*, Vol. 4, No. 5, 261–263, 2010.
4. Caulfield, H. J., R. A. Soref, and C. S. Vikram, “Universal reconfigurable optical logic with silicon-on-insulator resonant structures,” *Photonics and Nanostructures-Fundamentals and Applications*, Vol. 5, No. 1, 14–20, 2007.
5. Xu, Q. and R. Soref, “Reconfigurable optical directed-logic circuits using microresonator-based optical switches,” *Opt Express*, Vol. 19, No. 9, 5244, 2011.
6. Tian, Y., L. Zhang, R. Ji, et al., “Demonstration of a directed optical decoder using two cascaded microring resonators,” *Opt. Lett.*, Vol. 36, No. 17, 3314, 2011.
7. Tian, Y., L. Zhang, R. Ji, Lin, Yang, P. Zhou, H. Chen, J. Ding, W. Zhu, Y. Lu, L. Jia, Q. Fang, and M. Yu, “Proof of concept of directed OR/NOR and AND/NAND logic circuit consisting of two parallel microring resonators,” *Opt. Lett.*, Vol. 36, No. 9, 1650, 2011.
8. Zhang, L., R. Ji, Y. Tian, L. Yang, P. Zhou, Y. Lu, W. Zhu, Y. Liu, L. Jia, Q. Fang, and M. Yu, “Simultaneous implementation of XOR and XNOR operations using a directed logic circuit based on two microring resonators,” *Opt. Express*, Vol. 19, No. 7, 6524, 2011.
9. Zhang, L., R. Ji, L. Jia, et al., “Demonstration of directed XOR/XNOR logic gates using two cascaded microring resonators,” *Opt. Lett.*, Vol. 35, No. 10, 1620, 2010.

All-optical Wavelength Conversion Using Optical Injection Induced Wavelength Switching in V-cavity Laser

Yingchen Wu, Xiaohai Xiong, Yu Zhu, Jianjun Meng, and Jian-Jun He

State Key Laboratory of Modern Optical Instrumentation, Centre for Integrated Optoelectronics
Department of Optical Engineering, Zhejiang University, Hangzhou 310027, China

Abstract— In this paper, we present a simple, efficient, and cost-effective all-optical wavelength converter using injection-induced wavelength switching in widely tunable V-cavity laser. When an external signal beam is injected at a wavelength corresponding to one of the sidemodes with a small detuning of about 0.1 nm, the lasing wavelength is switched from the original main mode to the side mode. By filtering out the main mode of the V-cavity laser, a data-inverted wavelength conversion is achieved. This wavelength converter can offer a non-return-to-zero (NRZ) channel-to-channel conversion with converted signal approximately at 200 GHz away from the input signal. A 2.5 Gb/s non-return-to-zero (NRZ) conversion is experimentally demonstrated with an extinction ratio over 4 dB and SMSR of 36 dB.

1. INTRODUCTION

The rapid growth of high-speed data networking calls for a larger optical communication bandwidth. Without optical-to-electrical-to-optical (OEO) involved signal processing procedure, all-optical packet routing (AOPR) can overcome electrical bottleneck, which is one of the most important restriction for the optical networking bandwidth, and improve the blocking performance.

One of the major components to realize AOPR is the all-optical wavelength conversion (AOWC). So far, a lot of methods for AOWC have been published, including nonlinear optical gating based on fiber loop, cross-phase modulation, cross-gain modulation, four-wave mixing based on semiconductor optical amplifiers [1–4]. One of the goals of AOWC research is to develop simpler, amplifier-free and cost-effective chip with submilliwatt input power. The method of injection induced wavelength conversion of the single-mode laser is a promising approach. Multimode (MM) Fabry-Pérot laser diode (FP-LD) used for AOWC has been reported, which are principally based on either injection locking with an external probe light [5, 6] or transverse-magnetic (TM) mode absorption modulation which is highly-polarization-sensitive [7]. The external probe light, highly-sensitive polarization beam splitter and other associated components all increase the cost of the system and make it hard to integrate the wavelength converter as a chip.

In this paper, we demonstrate a quite simple, cost-effective WC based on V-cavity laser [8]. The V-cavity laser is a single-mode (SM) tunable laser with carefully designed tuning wavelength grid, which ensures a channel-to-channel conversion. The dominant mode of V-cavity laser works as probe light. Only -6 dBm pump signal is required. A 2.5 Gb/s non-return-to-zero (NRZ) conversion is experimentally demonstrated, the chirp-management technique is explored to increase the extinction-ratio (ER).

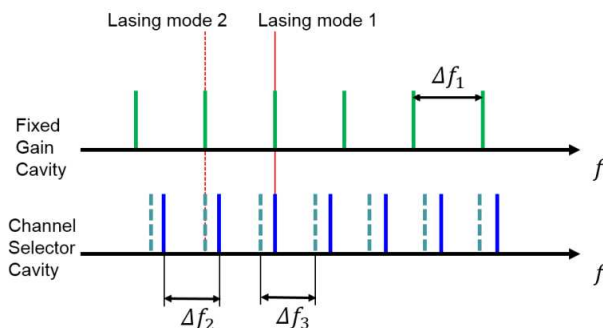


Figure 1: Schematic diagram illustrating the Vernier effect in wavelength conversion process, the dashed line is the mode comb with pump light injection, the channel spacing $\Delta f_1 > \Delta f_2 > \Delta f_3$.

2. SYSTEM PRINCIPLE

The working principle of the proposed wavelength converter is based on the injection-induced wavelength switching of the V-cavity laser. When an external pump light injected into V-cavity laser, the pump light is resonantly amplified, the process of stimulated emission consumes carrier, so the refractive index increases while carrier density decreases. In our experiment, the light is injected into the long cavity, namely the channel selector cavity. Based on Vernier effect, the mode of longer wavelength (lasing mode 2) is more likely to be stimulated, as shown in Fig. 1. In addition, the material gain spectrum is red-shift with light injection.

The injection beam needs to be TE polarized, with a longer wavelength than dominant mode, near the side mode with a small wavelength detuning instead of at the side mode to avoid unstable situation. For a stable locking, the wavelength detuning [9] can be used from 0.05 nm to 0.12 nm with a corresponding injection threshold power of -6.3 dBm to -4 dBm. Without the injection beam, power level of the dominant mode is high as logic "1". Once the injection beam is on, V-cavity laser locks to the injection beam, the original lasing mode (lasing mode 1 in Fig. 1) suppressed to a very low level as logic "0". By filtering out the dominant mode, an out-phase wavelength conversion is achieved.

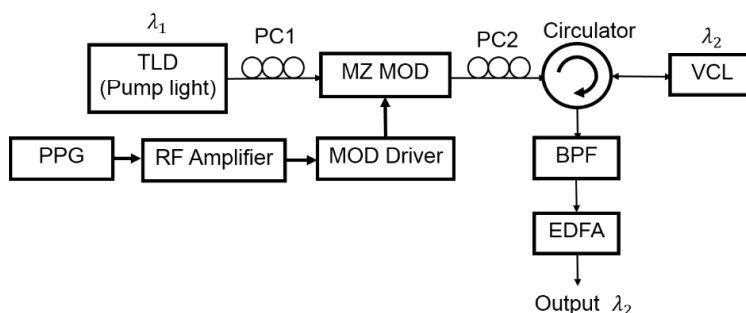


Figure 2: Experimental setup for the proposed wavelength converter based on V-cavity laser. PPG: pulse pattern generator. MZ MOD: Mach-Zehnder modulator. BPF: optical band pass filter. VCL: V-cavity laser.

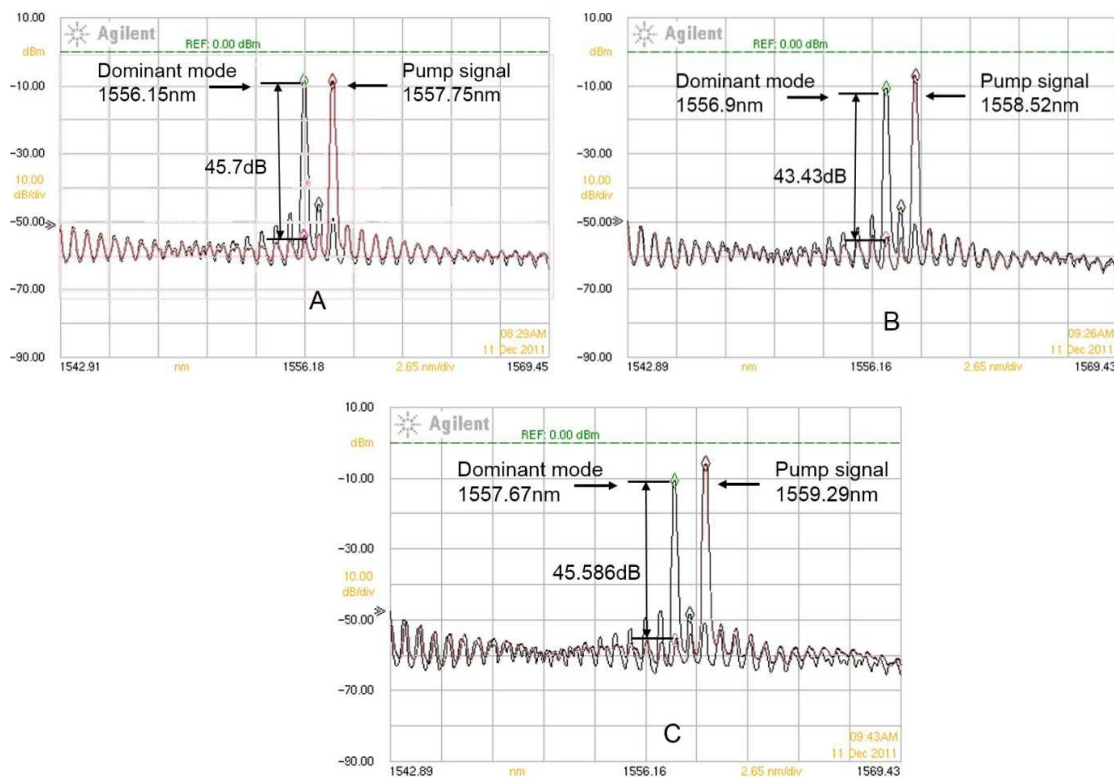


Figure 3: Optical power spectra of VCL with (red)/without (black) injection light in three conditions: A: Dominant mode is 1556.15 nm. B: Dominant mode is 1556.9 nm. C: Dominant mode is 1556.15 nm.

3. EXPERIMENTAL SETUP AND RESULTS

The experimental setup of the proposed wavelength converter is shown in Fig. 2.

The pump signal is a tunable laser (TLD) modulated by 2.5 Gb/s pseudorandom bit sequence of $2^7 - 1$. The Mach-Zehnder modulator is a polarization-dependent device, hence, the polarization controller PC1 is used to minimize power loss in the modulator. PC2 is used to ensure the TE polarized light for injection-locking of the pump signal to the VCL. The VCL is biased at 33 mA, 30 mA, 15 mA on coupler, channel selector cavity and fixed gain cavity respectively. The output power is around -6 dBm with a 6 dB chip-to-fiber coupling loss. The laser has a wide wavelength tuning range by controlling the current injection and operating temperature [8], which makes it possible to operate a wide-band wavelength conversion.

The VCL wavelength spacing of mode comb is 0.75 nm. The experiment was carried out in three cases for different dominant modes, with injection beam 0.1 nm longer than the second right-side mode of each dominant mode, as shown in Fig. 3. When the current of channel-selector cavity changes from 15 mA to 25 mA, the dominant mode is switched from 1556.15 nm, via 1556.9 nm, to 1557.67 nm. The pump signals are all approximately 1.6 nm away from the dominant mode. Thus, the V-cavity laser can offer a 200 GHz wavelength switching, fits ITU grid. The power of pump signal is a little higher in longer wavelength, which results from the deviation of material gain spectrum peak.

The dynamic measurements are shown in Fig. 4. The dominant mode of VCL is 1556.28 nm, and the pump signal is 1557.87 nm. Because of the limitation of the sweep time of optical spectrum analyzer, the optical signal is always on the screen and the integral signal power is about 3 dB less than the continuous light. The sidemode suppression ratio (SMSR) of the converted signal is

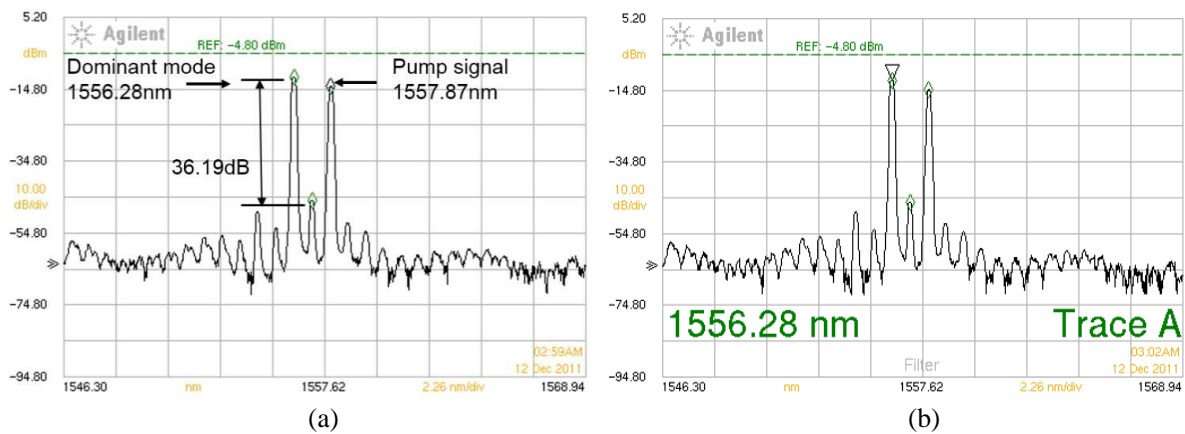


Figure 4: (a) Optical power spectra for dynamic wavelength conversion measurement. (b) The BPF is placed at the dominant mode with resolution bandwidth of 0.04 nm.

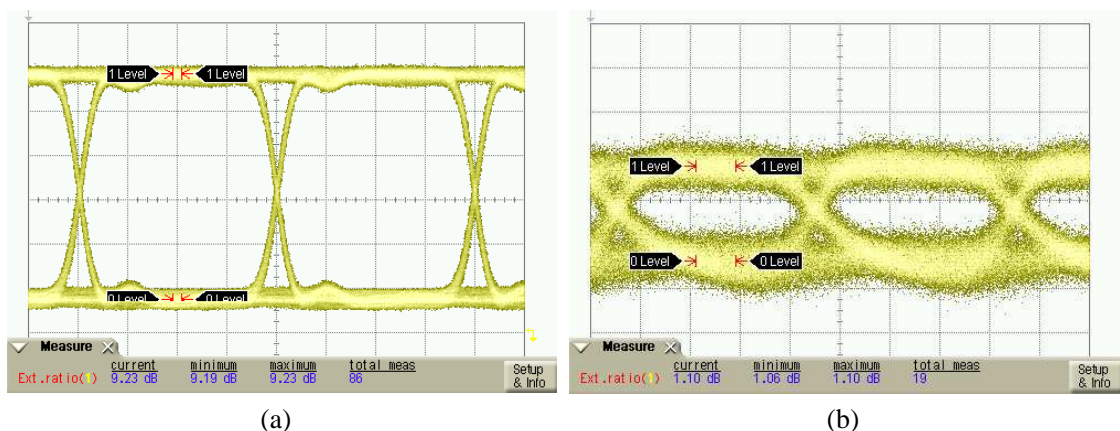


Figure 5: (a) Eye diagram of input pump signal at 2.5 Gb/s. (b) The converted eye diagram when the BPF is placed at the dominant mode.

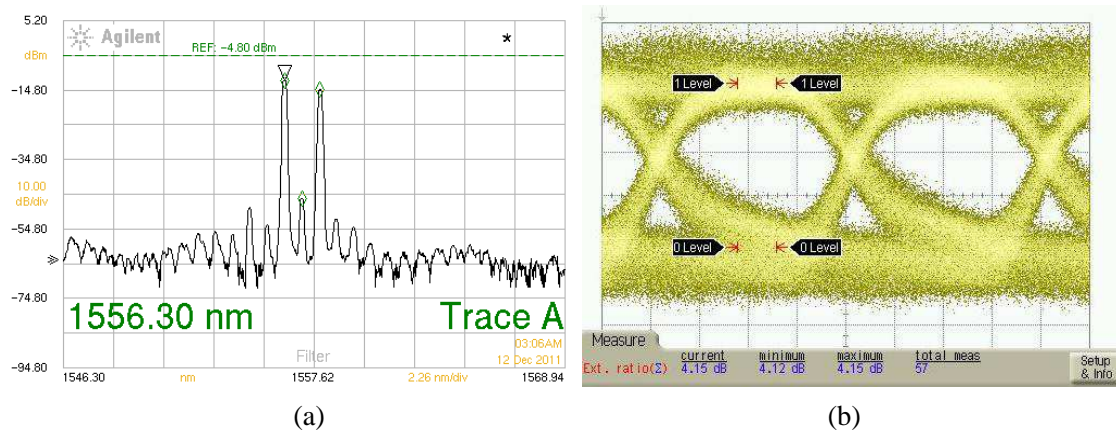


Figure 6: (a) The BPF is of 0.02 nm detuning from the dominant mode with resolution bandwidth of 0.04 nm. (b) The converted eye diagram at 2.5 Gb/s.

36.19 dB. When the BPF is placed at the dominant mode, the extinction ratio of converted eye diagram is only 1.1 dB at 2.5 Gb/s as shown in Fig. 5.

When the BPF moves a little to 1536.0 nm, the extinction ratio of converted signal increases to 4.15 dB, as shown in Fig. 6. Although the chirp of injection-locking laser is small [9, 10], chirp-management technique [11] still helps to improve the quality of converted signal.

4. CONCLUSION

A 2.5 Gb/s non-return-to-zero (NRZ) injection induced wavelength conversion is experimentally demonstrated. The V-cavity laser can accomplish a channel-to-channel wavelength conversion with 200 GHz channel spacing. It is compact, low-energy consumption and cost-effective for wavelength conversion, so is promising to work as part of optical-cross-connect with adoption of energy-band engineering to cover more communication channels.

ACKNOWLEDGMENT

This work was supported by the National High-Tech R&D Program of China (grant No. 2013AA01-4401).

REFERENCES

1. Elmirghani, J. M. H. and H. T. Mouftah, "All-optical wavelength conversion: Technologies and applications in DWDM networks," *IEEE Communications Magazine*, Vol. 38, No. 3, 86–92, 2000.
2. Segawa, T., et al., "A monolithic wavelength-routing switch using double-ring-resonator-coupled tunable lasers with highly reflective mirrors," *IEEE 2010 International Conference on Indium Phosphide & Related Materials (IPRM)*, 2010.
3. Mashanovitch, M., et al., "Photonic integrated circuits for optical routing and switching applications," *Optical Society of America Optical Fiber Communication Conference*, 2011.
4. Ueno, Y., et al., "3.8-THz wavelength conversion of picosecond pulses using a semiconductor delayed-interference signal-wavelength converter (DISC)," *IEEE Photonics Technology Letters*, Vol. 10, No. 3, 346–348, 1998.
5. Harvey, E., et al., "All-optical logic gates and wavelength conversion via the injection locking of a Fabry-Perot semiconductor laser," *SPIE OPTO, International Society for Optics and Photonics*, Vol. 8628, 2013.
6. Tsang, H. K., et al., "Experimental characterization of dual-wavelength injection-locking of a Fabry-Perot laser diode," *Optics Communications*, Vol. 156, No. 4, 321–326, 1998.
7. Yoo, H., et al., "All-optical wavelength conversion using absorption modulation of an injection-locked Fabry-Perot laser diode," *IEEE Photonics Technology Letters*, Vol. 16, No. 2, 536–538, 2004.
8. Zhang, S., et al., "Simple and compact V-cavity semiconductor laser with 50×100 GHz wavelength tuning," *Optics Express*, Vol. 21, No. 11, 13564–13571, 2013.

9. Horer, J. and E. Patzak, “Large-signal analysis of all-optical wavelength conversion using two-mode injection-locking in semiconductor lasers,” *IEEE Journal of Quantum Electronics*, Vol. 33, No. 4, 596–608, 1997.
10. Salvatore, P., P. Spano, and M. Tamburrini, “Small signal analysis of frequency chirping in injection-locked semiconductor lasers,” *IEEE Journal of Quantum Electronics*, Vol. 22, No. 1, 2219–2223, 1986.
11. Mahgerefteh, D., et al., “Chirp managed laser and applications,” *IEEE Journal of Selected Topics in Quantum Electronics*, Vol. 16, No. 5, 1126–1139, 2010.

Ultracompact Adiabatic Tapered Coupler for the Si/III-V Heterogeneous Integration

Qiangsheng Huang¹, Jianxin Cheng², Liu Liu², Yongbo Tang⁴, and Sailing He^{1,2,3}

¹Centre for Optical and Electromagnetic Research

JORCEP [Sino-Sweden Joint Research Center of Photonics]

Zhejiang Provincial Key Laboratory for Sensing Technologies, Zhejiang University, Zijingang Campus
East Building No. 5, Hangzhou 310058, China

²ZJU-SCNU Joint Research Center of Photonics

Centre for Optical and Electromagnetic Research, South China Academy of Advanced Optoelectronics
South China Normal University, Guangzhou 510006, China

³Department of Electromagnetic Engineering, Royal Institute of Technology, Stockholm 100 44, Sweden

⁴ArtIC Photonics Inc., Ottawa K2M 2C7, Canada

Abstract— An ultracompact bi-sectional tapered coupler, suitable for adiabatic mode transformation between a common single mode SOI strip waveguide and a Si/III-V hybrid waveguide, is proposed for Si/III-V heterogeneous integration. Since the bi-sectional tapered coupler mimics a semi-3D taper and avoids exciting unwanted high-order modes in the thick p-InP cladding layer (which is removed in the first tapered section), the length of the adiabatic mode coupler can be dramatically shortened. In the proposed structure, the length of the bi-sectional tapered coupler can be as short as 9.5 μm with a large fundamental mode-coupling ratio (over 95%) in a bandwidth of ~ 100 nm, and provides ± 100 nm tolerance to misalignment even when the bonding layer is as thick as 50 nm.

1. INTRODUCTION

Photonics based on Si/III-V heterogeneous integration through the DVS-BCB adhesive wafer bonding method or molecular direct wafer bonding method [1, 2] have been extensively investigated for many applications (e.g., inter-chip optical interconnects [1, 2], free-space optical communication links [3]), due to its feasibility in combining active and passive photonic submodules onto one silicon substrate. Among various Si/III-V heterogeneously integrated devices, a common critical issue is how to efficiently route light between the III-V active section and the silicon waveguide. Adiabatic taper has been considered to be a structure for this purpose due to its low insertion loss, low reflection [4], and good fabrication tolerance [5, 6].

To reduce the adiabatic taper length, optimizations of adiabatic tapered couplers have been developed in various ways. One way is to use a multi-step or complex shape tapered structure in both the Si waveguide and the III-V waveguide [5, 6]. Another way is to use a multi-level tapered structure [4]. However, the taper lengths in Refs. [4–6] are still relatively long, i.e., over 20 μm . Ref. [7] further demonstrated the shortest possible length of an adiabatic mode coupler, under the assumption of only even and odd supermodes excited in the tapered structure. However, Ref. [7] did not give a specific tapered geometrical shape to achieve the shortest taper length. Recently, Refs. [8, 9] demonstrated compact tapered couplers by using a lateral-current-injection III-V structure or a III-V membrane, where a thick p-cladding does not exist. However, these kinds of tapered structures cannot be used in a traditional vertical-current-injection III-V structure.

In this letter, we propose an ultracompact bi-sectional adiabatic tapered coupler consisting of two linearly tapered sections only in the III-V structure, and the SOI waveguide underneath is kept straight with a common dimension of 600 nm \times 220 nm. The bi-sectional tapered coupler mimics a semi-3D taper, which avoids exciting high-order modes in the thick p-cladding layer. In this way, the total taper length can be less than 10 μm even when the thickness of the intermediate bonding layer (defined as the distance between the top of the SOI structure and the bottom of the III-V structure) is relatively large, e.g., > 50 nm. We also study the influence of the bonding layer thickness and misalignment on the performance of the proposed bi-sectional adiabatic tapered coupler.

2. DESIGN OF THE BI-SECTIONAL TAPERED COUPLER

Figures 1(a)–1(c) show a schematic structure of the proposed bi-sectional tapered coupler, as well as the cross-section of the Si/III-V hybrid waveguide. In the first taper section, the optical mode

is converted from the silicon waveguide to the $0.598\ \mu\text{m}$ thick III-V waveguide [including the bottom SCH (separate-confinement heterostructure) layer, MQW (multi-Quantum-Well) layer and the upper SCH layer], without the thick p-cladding layer. At the end of the first taper, the optical mode is well-matched with the optical mode of the final Si/III-V hybrid waveguide. Thus, in the second taper section, the length can be very short. The thicknesses and the refractive indices of the materials composing the hybrid Si/III-V waveguide are shown in Fig. 1(a).

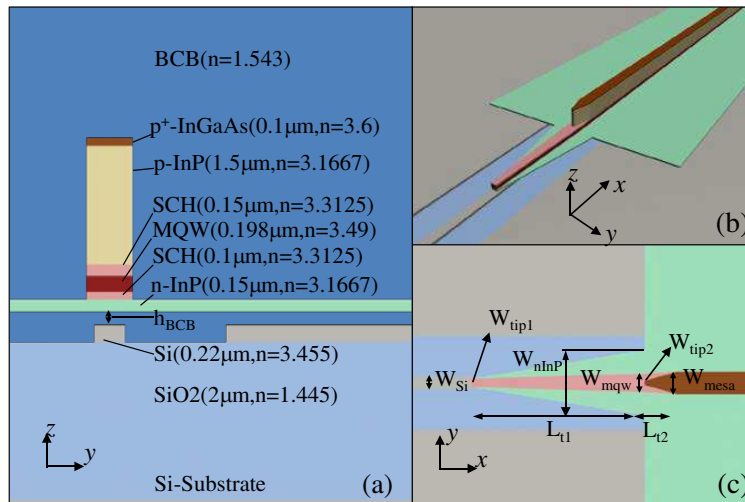


Figure 1: (a) Cross-sectional view of the hybrid Si/III-V waveguide. (b) 3D view and (c) top view of the bi-sectional adiabatic tapered coupler, respectively.

In order to reduce the complexity of the taper, we keep the silicon waveguide straight, without a tapered structure. In the present design, the width (W_{si}) and the thickness of the SOI waveguide are chosen to be $600\ \text{nm}$ and $220\ \text{nm}$ respectively. We consider a bonding layer thickness (h_{BCB}) between $0\ \text{nm}$ to $100\ \text{nm}$, which is a typical value for the adhesive or molecular bonding method. In this range, the final hybrid waveguide will present a confinement factor of 41% – 44% in the MQW layer, which is appropriate for hybrid semiconductor lasers, SOAs, and modulators.

In the present example, we choose the width of the active layer (W_{mqw}) at the end of the first taper to be $0.8\ \mu\text{m}$. The effective index of this III-V waveguide without the p-cladding layer is already well above the effective index of the silicon waveguide mode. This means that the adiabatic coupling between the silicon waveguide and the III-V waveguide mainly occurs in the first taper. At the end of the second taper, the width of the p-cladding layer and active layer (W_{mesa}) are expanded from W_{tip2} to $1\ \mu\text{m}$, in order to enhance the optical confinement in the MQW layer.

We first analyze the performance of the first taper with different values for L_{t1} , h_{BCB} , and W_{tip1} , using a three-dimensional finite-difference time-domain method [10]. Figs. 2(a) and 2(b) show the coupling efficiency as a function of the length of the first taper length (L_{t1}), when h_{BCB} and W_{tip1} vary. The coupling efficiency is defined as the fraction of power coupled to the fundamental mode of the output waveguide at the end of the taper. Note the width of the n-InP layer (in green color in Fig. 2(d)) keeps constant after the first taper in order to simplify the analysis (the reflection due to the geometrical mismatch at the end of the first taper is included in Fig. 3 below). The coupling loss mainly has two causes. The first is the coupling to the higher order mode at the entrance of the taper, since the taper tip cannot be infinitely small due to fabrication issues. The second comes from the insufficient taper length. In this case, the coupling to the higher order mode can also occur when light travels along the taper. When $W_{tip1} = 0.2\ \mu\text{m}$, and $h_{BCB} < 0.04\ \mu\text{m}$, the coupling efficiency has a large fluctuation with $L_{t1} < 11\ \mu\text{m}$, and this would require the adiabatic tapered length to increase. This fluctuation is mainly caused by the coupling between the even and odd (the first higher-order) supermodes. Here, the even supermode is the fundamental mode which should adiabatically follow the taper. For a wider taper tip or a thinner bonding layer, the odd supermode gets excited more easily at the entrance of this taper.

Figures 3(a) and 3(b) show the coupling efficiency in the second taper with $W_{tip2} = 0.2\ \mu\text{m}$ and $0.1\ \mu\text{m}$, respectively (the widths of the active waveguide and the n-InP layer at the entrance are fixed to $0.8\ \mu\text{m}$ and $3\ \mu\text{m}$, respectively). From these figures, one can see that the coupling efficiency is insensitive to both the thickness of the BCB layer and W_{tip2} . The taper length required to achieve

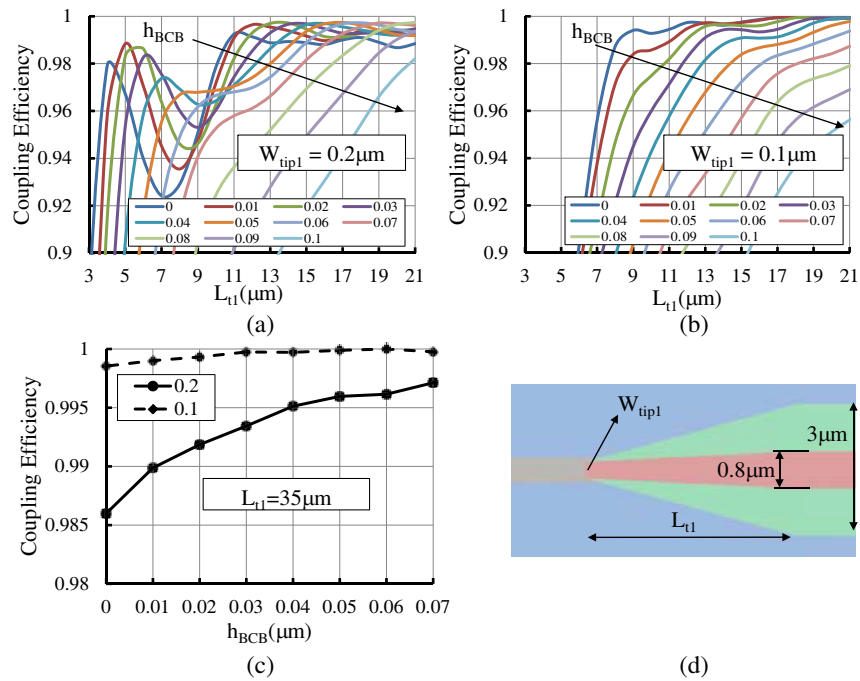


Figure 2: The coupling efficiency as L_{t1} varies under different thicknesses of BCB layer (from 0 to 0.1 μm): (a) $W_{tip1} = 0.2 \mu\text{m}$, (b) $W_{tip1} = 0.1 \mu\text{m}$. (c) The stable coupling efficiency with $L_{t1} = 35 \mu\text{m}$ as h_{BCB} varies. Solid and dashed lines in (c) show the results for $W_{tip1} = 0.2 \mu\text{m}$ and $0.1 \mu\text{m}$, respectively. (d) The structure parameter of the first section taper.

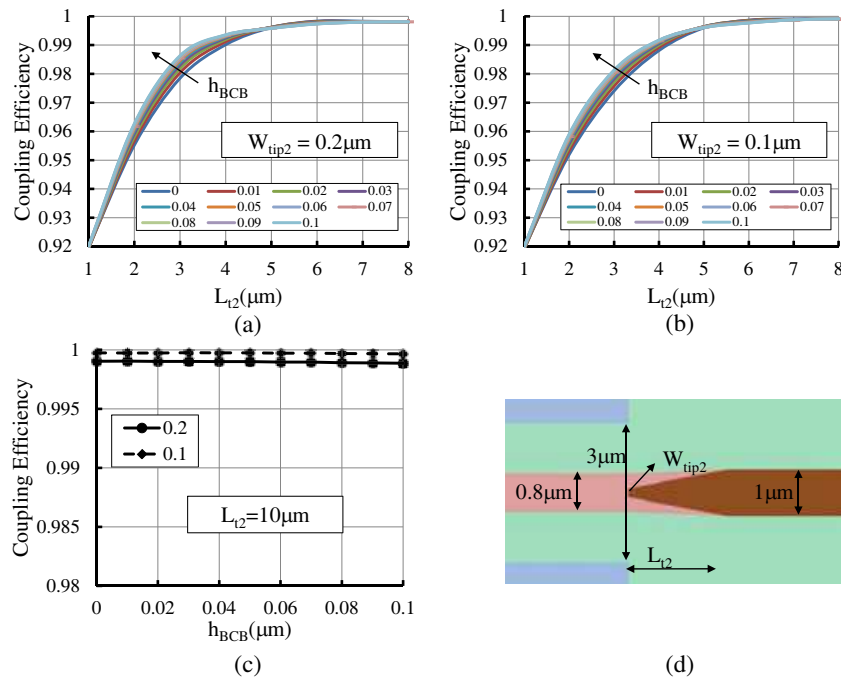


Figure 3: The coupling efficiency as L_{t2} varies under different thicknesses of BCB layer (from 0 to 0.1 μm): (a) $W_{tip2} = 0.2 \mu\text{m}$, (b) $W_{tip2} = 0.1 \mu\text{m}$. (c) The stable coupling efficiency with $L_{t2} = 10 \mu\text{m}$ as h_{BCB} varies, where the solid and dashed lines in (c) show the results for $W_{tip2} = 0.2 \mu\text{m}$ and $0.1 \mu\text{m}$, respectively. (d) The structure parameter of the second section taper.

a high coupling efficiency is also very short, as the mode input to this taper is already well-matched with that in the final Si/III-V hybrid waveguide. Moreover, Fig. 3(c) shows that the stable coupling efficiency reaches over 99% with only a 10 μm long taper for different values of h_{BCB} and W_{tip2} .

In the present paper, we propose two bi-sectional tapered couplers, with both W_{tip1} and W_{tip2} equal to 0.2 μm . For the first tapered coupler, we choose $L_{t1} = 15 \mu\text{m}$ and $L_{t2} = 4 \mu\text{m}$, and thus the total taper length is 19 μm . From Fig. 4(a), one can see that this design gives a high

coupling efficiency of over 98% at $h_{\text{BCB}} = 50$ nm for the wavelength range from 1500 nm to 1650 nm. Figs. 4(b) and (c) indicate that this 19 μm long taper also has a large fabrication tolerance to the variation of h_{BCB} and the misalignment between the silicon waveguide and III-V waveguide. When h_{BCB} varies from 0 nm to 80 nm, the coupling efficiency is still over 95% at $\lambda = 1.55$ μm , meaning that this 19 μm long taper can be applied to a relatively thick bonding layer.

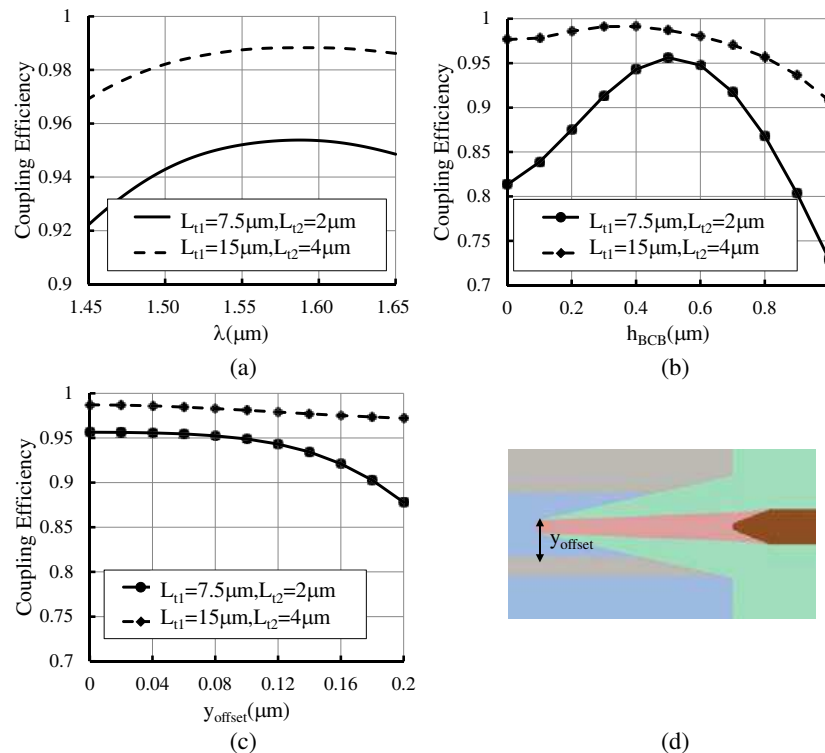


Figure 4: Wavelength dependence of the coupling efficiency and fabrication tolerance for two types of designed tapered couplers: (a) the wavelength dependence at $h_{\text{BCB}} = 50$ nm, (b) the variation of the thickness of the BCB layer at $\lambda = 1.55$ μm , (c) coupling efficiency in the presence of misalignment between the silicon waveguide and III-V waveguide (y_{offset}) with $h_{\text{BCB}} = 50$ nm and $\lambda = 1.55$ μm . (d) The structure parameter of a misaligned case.

On the other hand, another ultracompact tapered coupler is also proposed with $L_{t1} = 7.5$ μm and $L_{t2} = 2.5$ μm . In this case, the total taper length is only 9.5 μm , and the coupling efficiency of the fundamental mode can still be over 95% when $h_{\text{BCB}} = 50$ nm. The reflection of this tapered coupler from fundamental mode to (the counter-propagating) fundamental mode is lower than -40 dB when h_{BCB} varies from 0 nm to 100 nm. The bandwidth and the fabrication tolerance of the designed 9.5- μm -long tapered coupler are also analyzed, as shown in Figs. 4(a)–4(c). This ultracompact coupler demonstrates a coupling efficiency of over 95% in a wavelength range of ~ 100 nm, and a misalignment tolerance of 100 nm. Although it is more sensitive to the variation of h_{BCB} , the coupling efficiency is still above 80% when h_{BCB} varies between 0 nm to 80 nm. This ultracompact coupler is more suitable for a hybrid modulator [11], where the required coupling efficiency is not as high as a hybrid laser or SOA.

3. CONCLUSION

In conclusion, an ultracompact bi-sectional tapered coupler with a standard straight SOI strip waveguide underneath has been proposed for adiabatic mode transformation between a common single mode SOI wire waveguide and a Si/III-V hybrid waveguide in either molecular bonding or DVS-BCB adhesive bonding technology. In the first tapered section, the thick p-cladding layer is removed, which avoids exciting high-order modes. In this way, a coupling efficiency of over 95% can be achieved in a wavelength range of ~ 100 nm even when the total taper length is only 9.5 μm . Our simulation has also shown that this 9.5 μm long taper provides ± 100 nm tolerance to misalignment. We believe this ultracompact bi-sectional tapered coupler can be used in various Si/III-V heterogeneous integrated devices.

ACKNOWLEDGMENT

This work is partially supported by the National High Technology Research and Development Program (863) of China (2012AA012201), National Nature Science Foundation of China (#61107020). We thank for valuable discussions from Yaocheng Shi, Keqi Ma and Yingchen Wu.

REFERENCES

1. Roelkens, G., L. Liu, D. Liang, R. Jones, A. Fang, B. Koch, and J. Bowers, “III-V/silicon photonics for on-chip and inter-chip optical interconnects,” *Laser Photon. Rev.*, Vol. 4, No. 6, 751–779, 2010.
2. Liu, L., G. Roelkens, J. van Campenhout, J. Brouckaert, D. Van Thourhout, and R. Baets, “III-V/silicon-on-insulator nanophotonic cavities for optical network-on-chip,” *Journal of Nanoscience and Nanotechnology*, Vol. 10, 1461–1472, 2010.
3. Doylend, J. K., M. J. R. Heck, J. T. Bovington, J. D. Peters, M. L. Davenport, L. A. Coldren, and J. E. Bowers, “Hybrid silicon free-space source with integrated beam steering,” *Proc. SPIE 8629, Silicon Photonics VIII*, 862911, 2013.
4. Kurczveil, G., P. Pintus, M. J. R. Heck, J. D. Peters, and J. E. Bowers, “Characterization of insertion loss and back reflection in passive hybrid silicon tapers,” *IEEE Photon. J.*, Vol. 5, No. 2, 6600410, 2013.
5. Keyvaninia, S., G. Roelkens, and D. van Thourhout, “Engineering the heterogeneously integrated III-V/SOI tunable laser,” *Proc. 14th Ann. Symp. IEEE Photonics Benelux Chapter*, 141–144, 2009.
6. Wang, Q., D. K. T. Ng, Y. Wang, Y. Wei, J. Pu, P. Rabiei, and S. T. Ho, “Heterogeneous Si/III-V integration and the optical vertical interconnect access,” *Opt. Express*, Vol. 20, No. 15, 16745–16756, 2012.
7. Sun, X. K., H. C. Liu, and A. Yariv, “Adiabaticity criterion and the shortest adiabatic mode transformer in a coupled-waveguide system,” *Opt. Lett.*, Vol. 34, No. 3, 280–282, 2009.
8. Pu, J., Q. Wang, and S. T. Ho, “A novel type of ultra-compact lateral-current-injection III/V photonic device integrated on SOI for electronic-photonic chip application,” *Proc. SPIE 8629, Silicon Photonics VIII*, 862913, 2013.
9. Tassaert, M., H. J. S. Dorren, G. Roelkens, and O. Raz, “Passive InP regenerator integrated on SOI for the support of broadband silicon modulators,” *Opt. Express*, Vol. 20, 11383–11388, 2012.
10. Talflove, A. and S. C. Hagness, *Computational Electrodynamics: The Finite-difference Time-domain Method*, 3rd Edition, Artech House, Boston, 2005.
11. Kuo, Y. H., H. W. Chen, and J. Bowers, “High speed hybrid silicon evanescent electroabsorption modulator,” *Opt. Express*, Vol. 16, 9936–9941, 2008.

Tunable Rejections of Metamaterial Filter Based on Spoof Surface Plasmon Polaritons

Bai Cao Pan and Tie Jun Cui

State Key Laboratory of Millimetre Waves, School of Information Science and Engineering
Southeast University, Nanjing 210096, China

Abstract— According to the dispersion property, spoof surface plasmon polaritons (SPPs) can be supported within a low-pass propagating band. When the operating frequency rises to approach the asymptotic limit, which is also known as the surface plasma frequency, the spoof SPP modes vanish and the propagation cuts off. In this paper, we propose a method to achieve tunable rejections of spoof SPPs by producing independent absorptions. A spoof SPP waveguide consisting of corrugated microstrip line and matching convertors is introduced and electrically resonant metamaterials, the electric-field-coupled-LCs (ELCs), are employed and arranged along both sides of the waveguide. Since the electric field around the SPP waveguide excites strong and tight coupling to ELCs at resonant frequencies and their relative impedance keeps matching within a broadband, the propagating SPP modes are absorbed by such metamaterial particles and SPP filters with broad propagating band and significant rejection are achieved. Furthermore, the transmissions of the SPP filter with a series of ELCs scaled by different factors are investigated to clarify that the resonant frequency is directly controlled by the dimension of the metamaterial particles and that the coupling effect between different ELCs are weak enough to be ignored. As a result, it is convenient to control the absorptions by simply modulating the scaling factors of ELCs to construct a multiple rejection filter. Simulation results prove that the filter exhibits several significant rejections of -15 dB within a broad high-efficient propagating band. The proposed highly-efficient ultrathin planar filter is able to play an important role of filtering SPP waves in plasmonic circuits and systems.

1. INTRODUCTION

Surface plasmon polaritons (SPPs), the propagating electromagnetic waves along metal-dielectric interfaces [1], show the significant properties of high confinement and much shorter operating wavelength, which provide favorable conditions to overcome the diffraction limit [2]. Therefore, SPPs have been researched in areas of super-resolution imaging [3], electromagnetically induced transparency (EIT) [4], SPP circuits [5] and energy harvesting [6]. In 2004, Pendry et al. proposed an approach to achieve spoof SPPs by means of periodic holes [7]. Since then, a series of researches have been reported on spoof SPPs based on subwavelength holes or grooves [8–11]. Among the many Spoof SPPs studies, an ultrathin corrugated metallic strip waveguide fabricated on near zero thickness substrate is very promising [9]. Recently, a highly efficient broadband SPP waveguide was realized via the conversion from coplanar waveguide to the ultrathin corrugated metallic strip line [11].

In this work, we reported a convenient approach to control the rejections of spoof SPPs. When the electrically resonant metamaterials, the electric-field-coupled-LCs (ELCs), are introduced near the SPP waveguide, a strong coupling would be excited inside the ELCs and the propagating surface waves would be absorbed by the metamaterial particles. By manipulating the sizes of ELCs, the rejections of Spoof SPPs can be controlled freely. Such phenomenon could play an important role in plasmonic circuits and systems.

The proposed spoof SPP device, as is shown in Fig. 1, is composed of a meliorated corrugated metallic strip and an array of ELCs. Themeliorated SPP waveguide is fabricated on the basis of the design introduced in Ref. [11] and shows two constitutive improvements comparing with it. Firstly, we design the waveguide with grooves protruded out of the metallic strip line. Such design could provide a solution of miniaturization. Since the depth of grooves enlarges as the operating frequency shifts to a lower frequency, the width of the SPP waveguide introduced in Ref. [11] would be inconvenient for the measurement in the experiment. However, our meliorated waveguide possesses a relatively stationary width within a wide frequency band. Secondly, the ceiling of the grooves with deepening depths is beveled to better couple the excitation with spherical-like wave front coming out of the exponential slot lines.

According to the electric field distribution near the corrugated metallic strip, the ELCs with their equivalent capacitors of two inner metal lines parallel to the waveguide can provide a strong

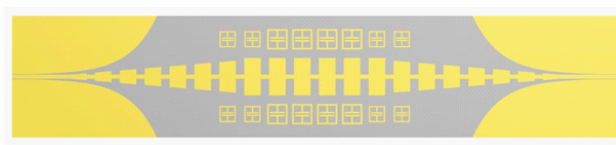


Figure 1: The schematic configuration of the DFR SPP waveguide.

resonant effect. To identify the ELCs' resonant properties and the rejections of our filters, a series of single rejection devices with different sizes of ELCs are simulated and their transmission coefficients are shown in Fig. 2. From the figure we can summarize that, by introducing such electrically resonant metamaterials, a significant rejection is obtained during the transmission and the rejecting frequencies shift along with the changes of ELCs' sizes.

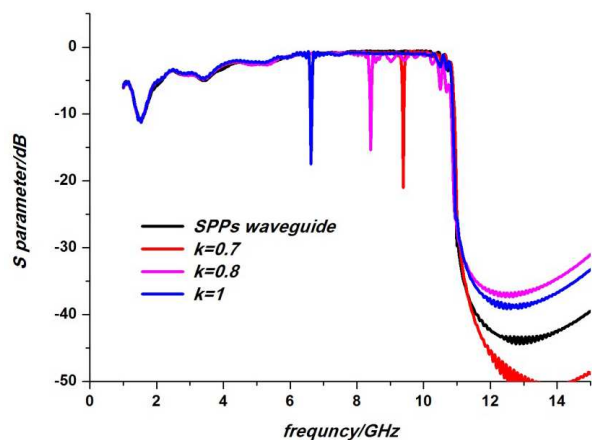


Figure 2: The transmission coefficients of the SPP waveguide with different ELC scaling factors, in which the black line stands for the spoof SPP waveguide without ELCs, while the red, pink, and blue lines represent the DFR SPP waveguides with scaling parameters $k = 0.7$, $k = 0.8$, and $k = 1$, respectively.

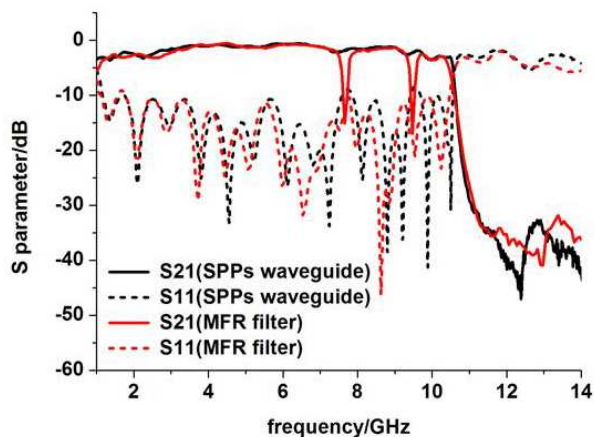


Figure 3: The measurement results of spoof SPP waveguide without ELC particles (black lines) and DFR SPP waveguide (red lines).

For the double frequencies rejection (DFR) device exhibited in Fig. 1, ELC scaling factors $k_1 = 0.7$ and $k_2 = 0.9$ are selected. The comparison of the measured results between SPP waveguide without ELCs and the DFR SPP waveguide is shown in Fig. 3, in which two clear filtering peaks at 7.65 and 9.47 GHz can be observed. Furthermore, these two rejections are in accord with the simulated results shown in Fig. 2.

We have demonstrated a double-frequency rejection device based on meliorated SPP waveguide. The filtering efficiencies of both rejections are below -15 dB and their frequencies can be designed and controlled simply by changing the sizes of ELCs, which is easy to fabricate. Our SPP rejection device has good potentials in plasmonic circuits and systems.

REFERENCES

1. Stewart, M. E., C. R. Anderton, L. B. Thompson, J. Maria, S. K. Gray, J. A. Rogers, and R. G. Nuzzo, "Nanostructured plasmonic sensors," *Chem. Rev.*, Vol. 108, No. 2, 494–521, 2008.
2. Gramotnev, D. K. and S. I. Bozhevolnyi, "Plasmonics beyond the diffraction limit," *Nat. Photonics*, Vol. 4, No. 2, 83–91, 2010.
3. Lu, D. and Z. Liu, "Hyperlenses and metalenses for far-field super-resolution imaging," *Nat. Commun.*, Vol. 3, 1205, 2012.
4. Han, Z. and S. I. Bozhevolnyi, "Plasmon-induced transparency with detuned ultracompact Fabry-Perot resonators in integrated plasmonic devices," *Opt. Express*, Vol. 19, No. 4, 3251–3257, 2011.
5. Zhao, C. and J. Zhang, "Plasmonic demultiplexer and guiding," *Acs Nano*, Vol. 4, No. 11, 6433–6438, 2010.

6. Linic, S., P. Christopher, and D. B. Ingram, “Plasmonic-metal nanostructures for efficient conversion of solar to chemical energy,” *Nat. Mater.*, Vol. 10, No. 12, 911–921, 2011.
7. Pendry, J. B., L. Martin-Moreno, and F. J. Garcia-Vidal, “Mimicking surface plasmons with structured surfaces,” *Science*, Vol. 305, No. 5685, 847–848, 2004.
8. Williams, C. R., S. R. Andrews, S. A. Maier, A. I. Fernández-Domínguez, L. Martín-Moreno, and F. J. García-Vidal, “Highly confined guiding of terahertz surface plasmon polaritons on structured metal surfaces,” *Nat. Photonics.*, Vol. 2, No. 3, 175–179, 2008.
9. Shen, X., T. J. Cui, D. Martin-Cano, and F. J. Garcia-Vidal, “Conformal surface plasmons propagating on ultrathin and flexible films,” *Proc. Natl. Acad. Sci. USA*, Vol. 110, No. 1, 40–45, 2013.
10. Gao, X., J. H. Shi, X. Shen, H. F. Ma, W. X. Jiang, L. Li, and T. J. Cui, “Ultrathin dual-band surface plasmonic polariton waveguide and frequency splitter in microwave frequencies,” *Appl. Phys. Lett.*, Vol. 102, 151912, 2013.
11. Ma, H. F., X. Shen, Q. Cheng, W. X. Jiang, and T. J. Cui, “Broadband and high-efficiency conversion from guided waves to spoof surface plasmon polaritons,” *Laser Photon. Rev.*, Vol. 8, No. 1, 146–151, 2014.

A Planar Broadband Metamaterial Absorber with the Polarization Insensitive and Omnidirectional Absorption in the Min-infrared Regime

Nan Zhang, Linbo Zhang, Guorui Zhang, Peiheng Zhou,
Xiaolong Weng, Jianliang Xie, and Longjiang Deng

National Engineering Research Center of Electromagnetic Radiation Control Materials
State Key Laboratory of Electronic Thin Film and Integrated Devices
University of Electronic Science and Technology of China, China

Abstract— In this paper, we present the design, fabrication and characterization of a polarization insensitive and omnidirectional broadband planar metamaterial perfect absorber (MPA) in the min-infrared regime. Multi-sized resonators are employed to excite the broadband absorption, and the absorption bandwidth is efficiently broadened compared with the single-sized absorber. Geometric effects on the resonance wavelengths are studied in detail by using the equivalent circuit model. Experiment result shows that greater than 70% absorption is obtained within a waveband of 0.67 μm , which is in reasonable agreement with the simulation. The electromagnetic response of the MPA is theoretically investigated to reveal the intrinsic absorption mechanism. The broadband planar MPA is polarization insensitive and the absorption retains quite high even at large incident angles. The proposed structure holds promise for many applications, such as sensitive detecting, energy harvesting, and thermal modulating.

1. INTRODUCTION

Metamaterial perfect absorbers (MPAs) have recently gained considerable attention due to their potential applications in research of sensitive sensors [1], solar cells [2], thermal emitters [3], and imaging devices [4, 5]. MPAs are artificially constructed “atoms” that composed of sandwiched multilayers, where the top layer is the metallic resonators separated from the bottom metallic film by a dielectric interlayer. The great absorption works relying on the coupling between metallic components of the sandwiched structure at the resonant frequency. The tunable and controllable effects of MPAs afford them incomparable advantages to the naturally existing materials. Nevertheless, for the resonant nature of metamaterials, most MPAs could only absorb the light in a very narrow waveband. Therefore, some efforts have gone into obtaining broadband MPAs by vertically stacking metallic resonators with different geometric dimensions [6, 7]. The complex design and fabrication process, however, have restricted their wide applications in the relevant fields.

In this paper, we design and fabricate a planar broadband metamaterial absorber in the min-infrared regime. Our design approach exhibits significant advantages to previous studies [6, 7], which does not need to precisely align metallic resonators between the layers. The absorption bandwidth is effectively broadened by the superposition of all resonances in the multi-sized planar metallic resonators. The proposed broadband MA is polarization insensitive and the absorption magnitude is still very high even at large incident angles for both transverse electric (TE) and transverse magnetic (TM) waves.

2. STRUCTURE DESIGN AND SIMULATIONS SETUP

The designed and fabricated broadband MA is shown in Fig. 1. It consist of a layer of 0.1 μm thick aluminum resonators and a 0.2 μm thick aluminum ground plane, separated by a 0.22 μm thick Al_2O_3 dielectric layer. The metallic resonators are composed of the elaborately arranged rectangular disks in a two-dimensionally symmetric structure surrounding the central square disks. The period of the planar broadband MA is $P = 4.5 \mu\text{m}$ for both the x and y directions. The Al resonators have the dimensionally dispersed geometry parameters of $t_1 = 1.7 \mu\text{m}$, $t_2 = 1.6 \mu\text{m}$, and $t_3 = 1.5 \mu\text{m}$.

Numerical simulations were performed with the CST microwave studio [8], which is based on the Finite Integration Time Domain (FITD) algorithm. In the simulations, the dielectric constant (ϵ_d) of Al_2O_3 is set to 2.28 [9], and the complex permittivity of Al is described by the Drude model with the plasma frequency $\omega_p = 2\pi \times 2895 \text{ THz}$ and the collision frequency $\omega_\gamma = 2\pi \times 15.5 \text{ THz}$ [10]. Periodic boundary conditions were employed for the x - y plane, and a plane wave of TM polarization (with magnetic field H perpendicular to the x - z plane) was normally incident upon the structure

as the excitation source. The frequency-dependent absorption was obtained from the S -parameters by $A(\omega) = 1 - T(\omega) - R(\omega) = 1 - |S_{21}|^2 - |S_{11}|^2$, where $T(\omega)$ and $R(\omega)$ are the frequency-dependent transmission and reflection, respectively. Furthermore, because the bottom metallic ground plane with a thickness of 200 nm is thick enough to suppress all the transmission light ($T(\omega) = 0$), the calculation of the absorption could be simplified as $A(\omega) = 1 - R(\omega)$.

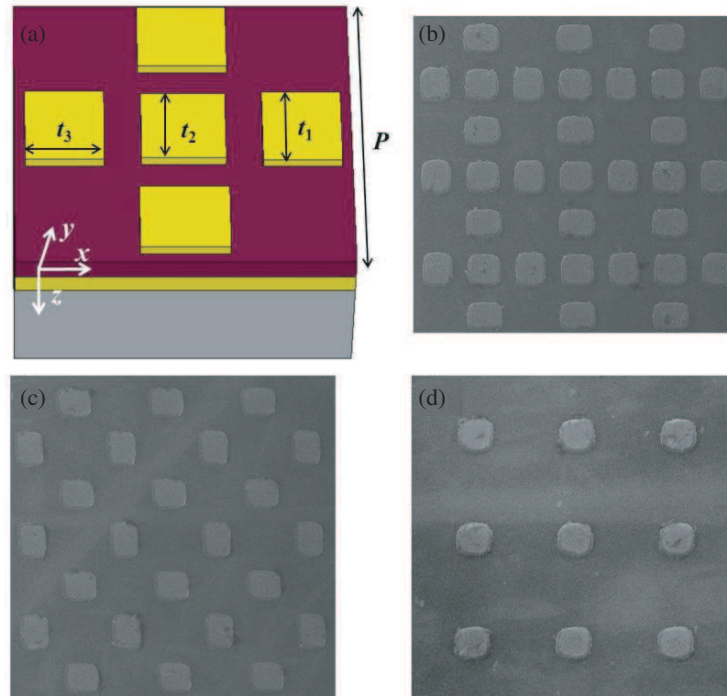


Figure 1: (a) Schematic view of the broadband MPA. Top view SEM images for (b) the structure combined of rectangular and square resonators, (c) the structure composed of separated rectangular resonators, (d) the structure composed of separated square resonators.

3. RESULTS AND DISCUSSIONS

Figure 2(a) shows the simulated absorption spectrum of the present planar broadband MA. It is seen that there are three absorption peaks aroused at $5.73 \mu\text{m}$, $5.96 \mu\text{m}$, and $6.26 \mu\text{m}$ with the absorption magnitude of 97.4%, 98.8%, and 98.1%, respectively. Because the high absorption of the three closely positioned resonant peaks, the absorption bandwidth of 97% absorptivity is up to $0.6 \mu\text{m}$. To explore the origin of the broadband absorption, absorption spectra for the structures composed of separated rectangular and square resonators were also given in Fig. 2(a). For the structure with rectangular resonators, the absorption peaks of two resonances at $5.70 \mu\text{m}$ and $6.25 \mu\text{m}$ are 99.9% and 99.5%, respectively. It is also noted that the absorption bandwidth of 80% absorptivity is $0.88 \mu\text{m}$ for this structure, and there is a deep dip at $5.98 \mu\text{m}$. For the structure with the separated square resonators, the single absorption peak resonant at $5.91 \mu\text{m}$ with the 99.5% absorption. We can see that the emergence of the central square resonators compensate the absorption dip in the structure composed of separated rectangular resonators. In other words, by combining these two separated structures together, the absorption peaks of the two structures are merged into one high absorption broadband spectrum.

Further exploring of the geometric effects on the resonant behavior of the resonator are studied in detail by using the equivalent circuit model. It is known that when the light incident upon the MPA structure, antiparallel current will be excited in the metallic resonator and bottom metal ground plane [11]. As a result, an electric current loop emerges. In this sense, one unit cell of the MPA corresponds to a “closed” wire loop. The electric current loop can be mimicked by an LC equivalent circuit model [12]. The resonance absorption is realized when the frequency of the external light equals the eigenfrequency of these resonators. The eigenfrequency of the resonator can be quantitatively described by circuit elements of the LC equivalent circuit model, which depends on the geometrical parameters and dielectric properties of the MPA. Here, we only consider the

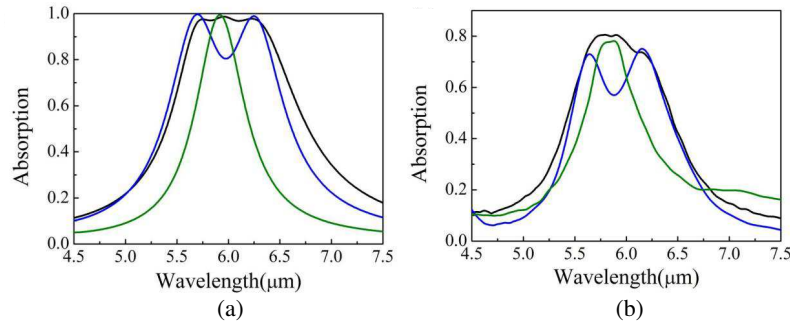


Figure 2: (Color online) (a) Simulated and (b) experimental absorption spectra of the structure combined of rectangular and square resonators (black line), the structure composed of separated rectangular resonators (blue line), and the structure composed of separated square resonators (green line).

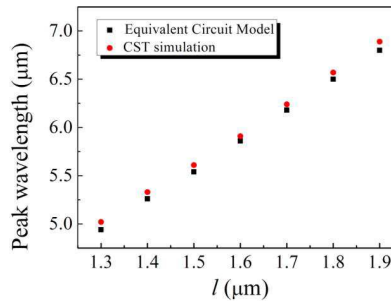


Figure 3: (Color online) Comparison between the predicted peak wavelengths by LC equivalent circuit model and results obtained from the CST simulations for different side length values.

effect of varying the resonator's side length on resonant behavior. The MPA structure discussed in our LC equivalent circuit model is composed of square resonators as the same described in Fig. 1(d) with resonator's side length l varied from 1.3–1.9 μm .

The interaction between the upper resonators and the bottom metallic film can be represented by a parallel plate capacitor of $C_m = \epsilon_0 \epsilon_r \sigma_{eff} / d$, and a parallel plate inductor of $L_m = \mu_0 l_{eff} d / (2w)$, where ϵ_0 is the permittivity of vacuum, ϵ_r is the real part of the relative permittivity of the Al_2O_3 dielectric layer, σ_{eff} is the effective area of the square resonator where charges spread, d is the thickness of the dielectric layer, μ_0 is the permeability of vacuum, l_{eff} is the effective length in the middle of the square resonator under which most of the magnetic field was trapped. The interaction between the neighboring resonators can be modeled as a gap capacitor of $C_g = 0.5 \epsilon_0 l t / g$, where g is the separate distance of the resonators, and t is the thickness of the resonators. Therefore, total impedance can be expressed as $Z_{tot} = \frac{i\omega L_m}{1 - \omega^2 L_m C_g} + \frac{2}{i\omega C_m} + i\omega L_m$, where ω is the angular frequency.

Then eigenfrequency ω_r can be deduced from $Z_{tot} = 0$, so $\omega_r = \sqrt{\frac{C_m + C_g - (C_m^2 + C_g^2)^{1/2}}{L_m C_m C_g}}$.

We then calculated the dependence of resonant peak wavelength against the side length l of the square resonator. In Fig. 3, it can be clearly seen that the resonance peak wavelength linearly rises with the increasing of side length l . Moreover, we carried out the numerical simulation for a series of samples with different side length from 1.3 μm to 1.9 μm at the step-width of 0.1 μm . The predicted peak wavelengths are in good agreement with the results indicated by the LC equivalent circuit model. So, for the present planar broadband MA, the long and short side of the rectangular resonator ($t_1 = 1.7 \mu\text{m}$ and $t_3 = 1.5 \mu\text{m}$) and the central square resonator ($t_2 = 1.6 \mu\text{m}$) could provide three resonant modes at distinct wavelengths. As a result, the superposition of all these resonances results in the broadband absorption.

To make a better understanding of the broadband absorption mechanism, we investigate the magnetic field distributions at three absorption peaks of the planar broadband MA through numerical simulation. Simulation results (Fig. 4) reveal that magnetic field at 5.73 μm , 5.96 μm , and 6.26 μm are primarily concentrated at the short side of rectangular resonator, the central square resonator and the long side of rectangular resonator, respectively. Magnetic field distributions also verified the prediction of the resonance wavelengths by the LC equivalent circuit model.

In our experiments, electron beam (e-beam) vapor deposition combined with step-and-scan

projection lithography techniques were used to prepare the MPAs. A $0.2\ \mu\text{m}$ Al metallic ground plane was first evaporated onto a silicon substrate by e-beam deposition. This was followed by the lithography to define the multiple patterned layers. The $0.22\ \mu\text{m}$ dielectric films and $0.1\ \mu\text{m}$ Al films were then deposited alternately. The pattern transfer was completed by a metal lift-off process. Scanning electron microscopy (SEM) images of the samples are shown in Figs. 1(b)–(d). A Fourier-transform infrared spectrometer (Bruker Vertex 70v) associated with the infrared microscope (Hyperion 2000) was used to measure the reflection spectra. Before measuring, the incident light was calibrated with a gold mirror. The experimentally obtained absorption spectra of the three samples are shown in Fig. 2(b). It is seen that there is a broadband absorption achieving by combining the structures of separated rectangular and square resonators together, which is in reasonable agreement with the simulation result. The absorption bandwidth of 70% absorptivity is $0.67\ \mu\text{m}$. Discrepancies between the experimental and simulated results stem from the fabrication tolerance and the inconformity of the dielectric constant of the dielectric spacing layer used in the simulation compared with the actual material parameters.

The absorption performance at non-normal incidence is quite important in practical applications. In many cases, most of possible incident light needs to be absorbed at large incident angles. So we carried out simulations to investigate the angle dependence of the absorber to evaluate its absorption performance at oblique incidence. Fig. 5 shows the absorption spectra as a function of both wavelength and incident angles under TM ($E \perp y\text{-}z$ plane) and TE ($E \perp x\text{-}z$ plane) polarization. For both configurations, the broadband absorption characteristics can be sustained with increasing the incident angle. However, when the incident angle is approach 40° , there is a decrease in the absorption magnitude and a shift in the peak position for the TM polarization waves, and there is a absorption dip for the TE polarization waves. Nevertheless, these simulations reveal that the proposed broadband absorber operates quite well for both TE and TM polarizations over a wide range of incident angles.

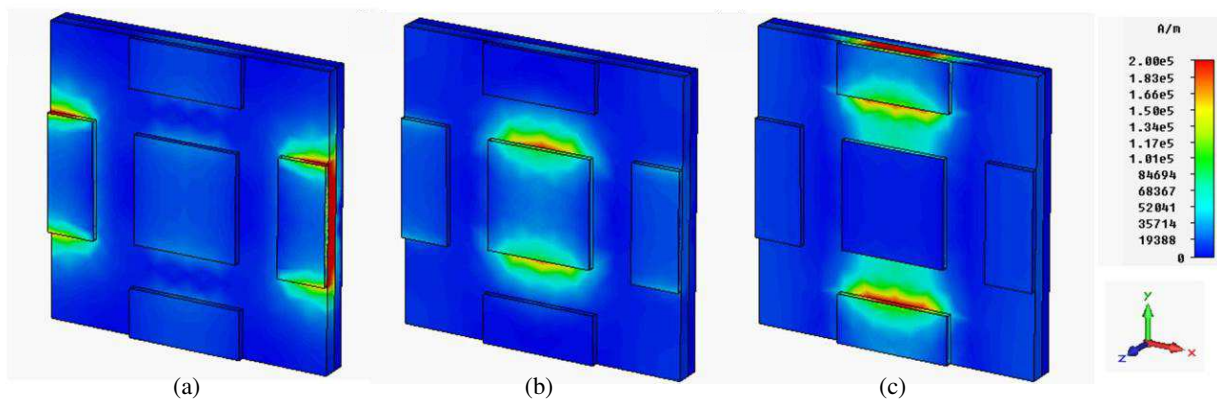


Figure 4: (Color online) Magnetic field distributions at absorption peaks of (a) $5.73\ \mu\text{m}$, (b) $5.96\ \mu\text{m}$, (c) $6.26\ \mu\text{m}$. (There are only half of the short side of rectangular resonator in the given field distributions, for the symmetry setup of the structure in the simulation).

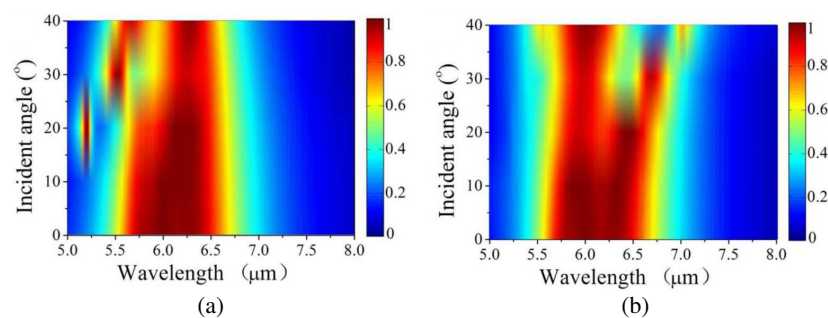


Figure 5: (Color online) Absorbance as a function of wavelength and the angle of incidence for (a) TM and (b) TE polarization incident light.

4. CONCLUSIONS

In conclusion, we have present a planar metamaterial perfect absorber worked in the min-infrared regime, which is polarization insensitive and the absorption is still high even at large incident angles. The broadband absorption originates from the superposition of multiple resonances of the multi-sized resonators. The presented design approach does not need to precisely align metallic resonators between the layers, and could simplify the fabrication process. The proposed structure may have multiple application values in the relevant fields, such as sensitive detecting, energy harvesting, and thermal modulating.

REFERENCES

1. Liu, N., M. Mesch, T. Weiss, M. Hentschel, and H. Giessen, "Infrared perfect absorber and its application as plasmonic sensor," *Nano Lett.*, Vol. 10, 2342, 2010.
2. Wang, Y., T. Sun, T. Paudel, Y. Zhang, Z. Ren, and K. Kempa, "Metamaterial-plasmonic absorber structure for high efficiency amorphous silicon solar cells," *Nano Lett.*, Vol. 12, 440, 2011.
3. Liu, X., T. Tyler, T. Starr, A. F. Starr, N. M. Jokerst, and W. J. Padilla, "Taming the black-body with infrared metamaterials as selective thermal emitters," *Phys. Rev. Lett.*, Vol. 107, 045901, 2011.
4. Mason, J. A., S. Smith, and D. Wasserman, "Strong absorption and selective thermal emission from a midinfrared metamaterial," *Appl. Phys. Lett.*, Vol. 98, 241105, 2011.
5. Liu, X., T. Starr, A. F. Starr, and W. J. Padilla, "Infrared spatial and frequency selective metamaterial with near-unity absorbance," *Phys. Rev. Lett.*, Vol. 104, 207403, 2010.
6. Ye, Y. Q., Y. Jin, and S. He, "Omnidirectional, polarization-insensitive and broadband thin absorber in the terahertz regime," *J. Opt. Soc. Am. B*, Vol. 27, 498, 2010.
7. Grant, J., Y. Ma, S. Saha, A. Khalid, and D. R. S. Cumming, "Polarization insensitive, broadband terahertz metamaterial absorber," *Opt. Lett.*, Vol. 36, 3476, 2011.
8. CST Microwave Studio 2009, (Computer Simulation Technology GmbH, Darmstadt, Germany).
9. Palik, E. D., *Handbook of Optical Constants in Solids*, Academic Press, 1991.
10. Ordal, M. A., L. L. Long, R. J. Bell, S. E. Bell, R. R. Bell, R. W. Alexander, Jr., and C. A. Ward, "Optical properties of the metals Al, Co, Cu, Au, Fe, Pb, Ni, Pd, Pt, Ag, Ti, and W in the infrared and far infrared," *Appl. Opt.*, Vol. 22, 1099, 1983.
11. Liu, N., M. Mesch, T. Weiss, M. Hentschel, and H. Giessen, "Infrared perfect absorber and its application as plasmonic sensor," *Nano Lett.*, Vol. 10, 2342, 2010.
12. Cheng, D., J. Xie, H. Zhang, C. Wang, N. Zhang, and L. Deng, "Pantoscopic and polarization-insensitive perfect absorbers in the middle infrared spectrum," *J. Opt. Soc. Am. B*, Vol. 29, 1503, 2012.

Efficient Generation of Second Harmonic from a Kind of Nonlinear Magnetic Metamaterial Composite

Shang Sun¹ and Shumin Xiao²

¹Key Lab of Micro-Optics and Photonic Technology of Heilongjiang Province
Department of Physics, Harbin Institute of Technology, Harbin 158001, China

²Department of Material Science and Engineering, Shenzhen Graduate School
Harbin Institute of Technology, Shenzhen 518055, China

Abstract— We present a numerical investigation of efficient generation of second harmonic from a kind of nonlinear magnetic metamaterial composite. The analysis is focused on a structure consisting of periodic arrays of paired thin silver strips with second-order nonlinear material filled in the gap. The sandwich shaped periodic structure exhibits remarkable advantage in the generation of second harmonic signal. We, first, make an introduction to this sandwich structure, summarize the linear resonant properties and then investigate the wavelength dependence of the field enhancement in the gap. Next, we analyze about second-harmonic generation (SHG) from composite structure doping with isotropic nonlinear material by comparing with that from single layer nonlinear material and several other conditions. The results figure out that the magnetic resonance property of this nonlinear metamaterial composite makes a great contribution to the energy localization and gives rise to strong inhomogeneous field inside the gap. As a result, the strength of SHG is almost two orders larger than that of a pure nonlinear layer with comparable dimensions. Finally, we change the material property from isotropic to anisotropic, and investigate the impact combining with field enhancement, field profiles and linear and nonlinear polarization considerations, showing that most of the fundamental-harmonic electric field in the gap polarize along y direction, which is the power giving rise to the second-harmonic generation of the composite. This work leads to deeper understanding of singular nonlinear response in metamaterials.

1. INTRODUCTION

Metamaterials are artificially structured materials, whose general electromagnetic properties are different greatly from those expressed by their individual inclusions. The scale of these composite structures is much smaller than the wavelength of interest and that makes the whole material macroscopically uniform. The electromagnetic properties can be designed at will, other than just rely on the materials exist in the natural world. Benefit from that, we can get new materials exhibiting exotic properties, such as invisibility [1] and negative refraction index [2, 3]. The study about metamaterials mostly focused on how to get all kinds of linear optical materials with interesting properties. However, utilizing metamaterials to enhance nonlinear optical response is another exciting research field. It was first reported on split-ring resonators (SRRs) [4]. Since metamaterials are always designed with considerable magnetic activity, which implies there are strongly inhomogeneous fields in them. And that gives rise to large enhancement of local field which will naturally benefit the nonlinear effects. Nonlinear metamaterial composites have been studied widely in the microwave and near-infrared regions of the spectrum [5–7]. People mainly adopt a homogenization model to describe the material, and get the closed-form expressions of nonlinear susceptibilities. And then the design of the nonlinear metamaterials can be realized [8]. Among all kinds of nonlinear optical phenomenon, the optical process that two photons in fundamental frequency convert to one photon in double frequency, namely second-harmonic generation (SHG) is the most studied. Recently, the anomalously enhanced optical transmission (EOT) through arrays of sub-wavelength apertures in metal films has attracted significant attention. Lots of researches about structures with nonlinear materials like LiNbO_3 or GaAs filled in the apertures have been made by many groups [9–13]. Besides, increasing the field enhancement brought by nano-antennas arrays is another promising way to improve the conversion efficiency of SHG [14–16].

In this letter, we introduce a nonlinear magnetic metamaterial composite, which is a structure consisting of periodic arrays of paired thin silver strips with second-order nonlinear material filled in the gap and that makes the periodic unit's cross section shapes like a sandwich, exhibiting remarkable advantage in the generation of second harmonic.

Figure 1 shows a 2D schematic of the conventional coupled silver strips which has been discussed in [17]. Each sandwich unit consists of a pair of thin silver strips with thickness t separating by an

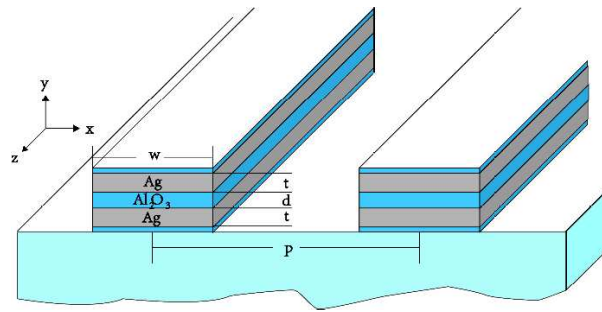


Figure 1: Structure of the coupled silver strips.

alumina layer with thickness d . The width of the sandwich stack is w , and the period is p . Two thin alumina layers of 10 nm are added to the top and bottom of sandwich stacks to make sure the fabrication is stable.

In our simulation, the analysis is performed using a FDTD model combined with analytical and numerical calculations, and the geometry parameters of the Ag- Al_2O_3 -Ag structure are set to a specified size, with the thickness of each silver layer and alumina layer being $t = d = 30$ nm, the width of the stack being $w = 170$ nm, the period of the structure being $p = 400$ nm.

The schematic of the setup and coordinates in the model is presented in Figure 2(a). According to the study in Ref. [17], only under TM illumination, this structure could exhibit resonant properties. Therefore, we set the incident field in our model to be TM polarization with the magnetic field polarized along the strips and propagating toward the structure vertically. The experimental data of Johnson and Christy in the materials database is utilized to describe the optical properties of silver. Besides, the refractive index is 1.62 for alumina and 1.52 for the substrate.

The transmission, reflection and absorption spectra of our paired-strip structure simulated under TM polarization is plotted in Figure 2(b) with the electric resonance at $\lambda_e = 615$ nm and the magnetic resonance at $\lambda_m = 1040$ nm. Furthermore, as shown in Figures 2(c) and 2(d), the magnetic field distribution is calculated at these two characteristic wavelengths (λ_e and λ_m respectively) and the field magnitude is normalized to the one in the free space. The arrows in the figures represent the electric displacement. We can note that the electric displacement is mostly aligned along one direction at the electric resonance. While around the magnetic resonance λ_m , the arrows present a loop shape and lead to an artificial magnetic moment, with a much stronger magnetic field inside

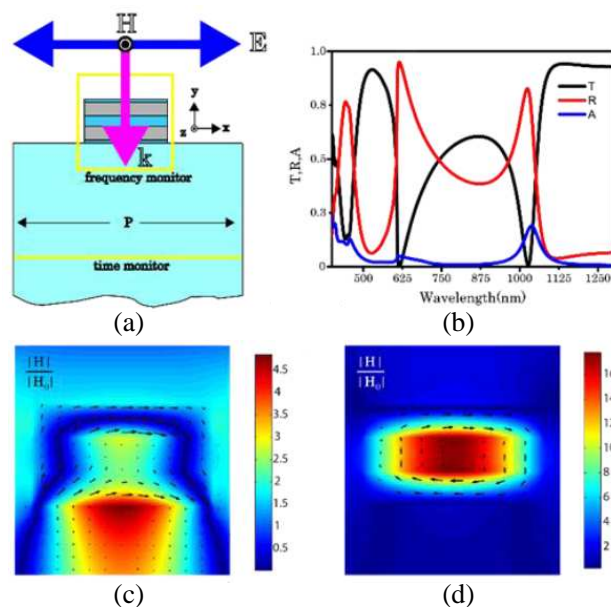


Figure 2: (a) Diagram of the model. (b) Simulated transmission (T) and reflection (R) and absorption (A) spectra of the structure for TM polarization. (c), (d) Magnetic field and the electric displacement at the electric resonance and the magnetic resonance.

the sandwich than the one at λ_e .

The strong magnetic activity at the magnetic resonance wavelength will naturally result in strong inhomogeneous fields in the stack, especially in the gap between the strips. The magnitude of the local field should be much larger than that in free space. To verify the large contribution from the magnetic resonance, we calculate the average strength of electric field and components in the gap illuminated by incident field of different wavelength, as shown in Figure 3.

In Figure 3, all the data are normalized to the magnitude of electric field in free space, which is presented as the green solid line for comparison. From the figure, we can see that curves show that all the ratios increase first and decrease after, with peaks existing around the magnetic resonance ($\lambda_m = 1040$ nm). The average strength of electric field in the gap is more than ten times larger than that in free space, which is agreed to our expectation. Note that the two curves of total electric field and the y component almost coincide, whereas the x component stay very low, which means the polarization of the local field in the gap is mainly along y direction.

Since the optical nonlinearities are greatly dependent on the electromagnetic field, it's expecting to be strengthened by field enhancement. In our study, we predict doping the structure with nonlinear material in the gap would help get enhanced nonlinearity.

In order to make a better comparison with above work, our new nonlinear magnetic metamaterial composite keep all the settings same with before but the material in the gap between paired silver strips changed from alumina to an isotropic second-order nonlinear material with refractive index $n_d = 1.62$ and $\chi^{(2)} = 3 \times 10^{-10}$ m/V (an organic nonlinear optical crystal DAST can be qualified [18]). The amplitude of the incident source is set to be 1×10^7 V/m.

First, we set the center wavelength of the fundamental harmonic (FH) source to be at the magnetic resonance 1040 nm to check if the second harmonic (SH) is generated. Figure 4(a) illustrates the SH (520 nm) electric and magnetic field distribution which are normalized to the FH ones in free space, and the arrows represent the electric displacement. It can be found that the SH electromagnetic energy is mostly concentrated in the gap with values cannot be ignored. We can also note that the second-harmonic generation result in two magnetic moments form between the paired

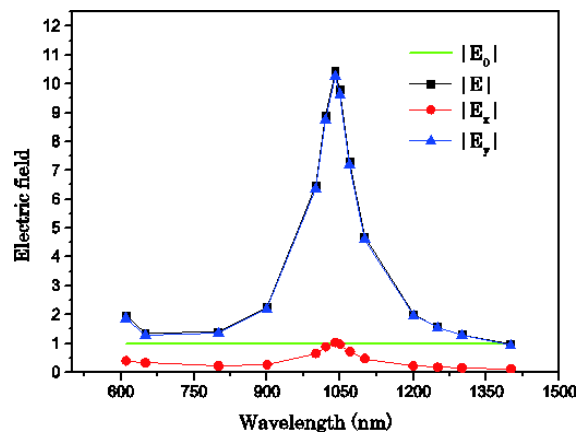


Figure 3: The dependence of the average magnitude of electric field and components on the wavelength of the incident field.

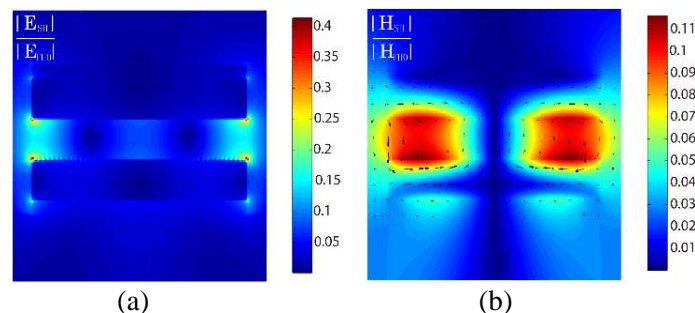


Figure 4: Simulated SH (520 nm) electric (a) and magnetic (b) field distribution with arrow representing the electric displacement.

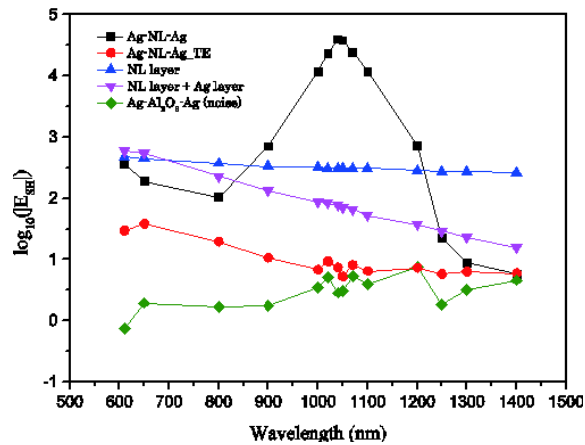


Figure 5: The average strength (\log_{10}) of SHG at the exit end of the model for different conditions.

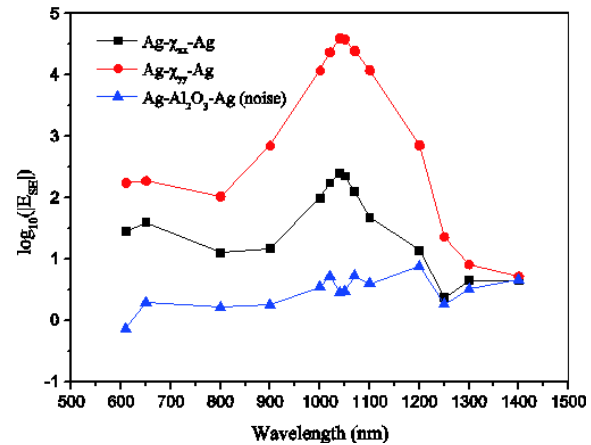


Figure 6: The average strength (\log_{10}) of SHG at the exit end of the model for two different anisotropic nonlinear composites.

silver strips.

For the purpose of verifying the advantage of our composite in the enhancement of the generation of SH, we make a comparison about the strength of SHG at exit end between different conditions, as shown in Figure 5. The figure is plotted by the wavelength of the incident FH source on the horizontal axis and the average SH electric field intensity (\log_{10}) at the exit end on the vertical.

All the data were calculated for TM polarization except the red ones. For the Ag-Al₂O₃-Ag structure, there are also SH signals existing in the numerical calculation, which are very weak and treated as noise in our analyses.

As expected, our composite (Ag-NL-Ag) shows great advantage for SHG around the wavelength of magnetic resonance (1040 nm). The SH electric field is almost two orders of magnitude larger than that from one single layer of nonlinear materials with thickness of 30 nm (NL layer) at exactly 1040 nm. The result for composite under TE polarization (Ag-NL-Ag-TE) is also presented in the figure, which is weak and display a non-resonant wavelength dependence over the spectrum range we study. Besides, the structure of one layer of nonlinear material covering one layer of silver (NL layer + Ag layer), both thickness of 30 nm, has been studied, which shows no significant benefits and gets even lower in SHG towards the longer wavelength.

For a better understanding of the generation of second-harmonic in this composite, we have made a simulation study about the structures filling with two different anisotropic nonlinear materials, assuming the second-order nonlinear susceptibility has only non-zero components of $\chi_{xx}^{(2)} = 3 \times 10^{-10}$ m/V and $\chi_{yy}^{(2)} = 3 \times 10^{-10}$ m/V respectively, as shown in Figure 6.

Thus it can be seen that it is the y -polarized FH electric field in the gap makes a large contribution to the SHG and give rise to a much better effect for structure Ag- χ_{yy} -Ag than Ag- χ_{xx} -Ag.

In summary, we have investigated the wavelength dependence of the field enhancement in the gap of paired silver strips and the SHG conversion efficiency from the structures composited with nonlinear material. We found that, the magnetic resonance property of the nonlinear metamaterial composite makes a great contribution to the energy localization and SHG, with the strength almost two orders of magnitude larger than that of a single layer of nonlinear material with comparable dimensions. We also show that most of the FH electric field in the gap polarized along y direction, which is the power giving rise to the second-harmonic generation of the composite.

REFERENCES

1. Schurig, D., J. J. Mock, B. J. Justice, et al., "Metamaterial electromagnetic cloak at microwave frequencies," *Science*, Vol. 314, No. 5801, 977–980, 2006.
2. Smith, D. R. and N. Kroll, "Negative refractive index in left-handed materials," *Physical Review Letters*, Vol. 85, No. 14, 2933, 2000.
3. Shalaev, V. M., "Optical negative-index metamaterials," *Nature Photonics*, Vol. 1, No. 1, 41–48, 2007.
4. Pendry, J. B., A. J. Holden, D. J. Robbins, et al., "Magnetism from conductors and enhanced

- nonlinear phenomena,” *IEEE Transactions on Microwave Theory and Techniques*, Vol. 47, No. 11, 2075–2084, 1999.
5. Shadrivov, I. V., A. B. Kozyrev, D. W. van der Weide, et al., “Nonlinear magnetic metamaterials,” *Optics Express*, Vol. 16, No. 25, 20266–20271, 2008.
 6. Zharov, A. A., I. V. Shadrivov, and Y. S. Kivshar, “Nonlinear properties of left-handed metamaterials,” *Physical Review Letters*, Vol. 91, No. 3, 037401, 2003.
 7. O’Brien, S., D. McPeake, S. A. Ramakrishna, et al., “Near-infrared photonic band gaps and nonlinear effects in negative magnetic metamaterials,” *Physical Review B*, Vol. 69, No. 24, 241101, 2004.
 8. Poutrina, E., D. Huang, and D. R. Smith, “Analysis of nonlinear electromagnetic metamaterials,” *New Journal of Physics*, Vol. 12, No. 9, 093010, 2010.
 9. Fan, W., S. Zhang, K. J. Malloy, et al., “Second harmonic generation from patterned GaAs inside a subwavelength metallic hole array,” *Optics Express*, Vol. 14, No. 21, 9570–9575, 2006.
 10. Fan, W., S. Zhang, N. C. Panou, et al., “Second harmonic generation from a nanopatterned isotropic nonlinear material,” *Nano Letters*, Vol. 6, No. 5, 1027–1030, 2006.
 11. Vincenti, M. A., D. De Ceglia, V. Roppo, et al., “Harmonic generation in metallic, GaAs-filled nanocavities in the enhanced transmission regime at visible and UV wavelengths,” *Optics Express*, Vol. 19, No. 3, 2064–2078, 2011.
 12. Barakat, E. H., M. P. Bernal, and F. I. Baida, “Second harmonic generation enhancement by use of annular aperture arrays embedded into silver and filled by lithium niobate,” *Optics Express*, Vol. 18, No. 7, 6530–6536, 2010.
 13. Scalora, M., M. A. Vincenti, D. De Ceglia, et al., “Second- and third-harmonic generation in metal-based structures,” *Physical Review A*, Vol. 82, No. 4, 043828, 2010.
 14. Thyagarajan, K., S. Rivier, A. Lovera, et al., “Enhanced second-harmonic generation from double resonant plasmonic antennae,” *Optics Express*, Vol. 20, No. 12, 12860–12865, 2012.
 15. Park, S., J. W. Hahn, and J. Y. Lee, “Doubly resonant metallic nanostructure for high conversion efficiency of second harmonic generation,” *Optics Express*, Vol. 20, No. 5, 4856–4870, 2012.
 16. Bar-Lev, D. and J. Scheuer, “Efficient second harmonic generation using nonlinear substrates patterned by nano-antenna arrays,” *Optics Express*, Vol. 21, No. 24, 29165–29178, 2013.
 17. Cai, W., U. K. Chettiar, H. K. Yuan, et al., “Metamagnetics with rainbow colors,” *Optics Express*, Vol. 15, No. 6, 3333–3341, 2007.
 18. Marder, S. R., J. W. Perry, and C. P. Yakymyshyn, “Organic salts with large second-order optical nonlinearities,” *Chemistry of Materials*, Vol. 6, No. 8, 1137–1147, 1994.

Design and Fabrication of Acoustic Rotator Based on Extremely-anisotropic Metamaterials

Xue Jiang, Bin Liang, and Jian-Chun Cheng

Key Laboratory of Modern Acoustics, MOE, Department of Physics
Institute of Acoustics, Nanjing University, Nanjing 210093, China

Abstract— The field rotator is a fascinating device which can be regarded as a special kind of acoustic illusion, with the capability of making the object covered by it appears like a rotated one. By exploiting acoustic metamaterials with extremely anisotropic parameters, we have theoretically designed and experimentally realized an acoustic field rotator that can be employed to rotate the acoustic wave front by a certain angle. For airborne sound, the designed field rotator simply comprises an array of identical plates made of acrylonitrile butadiene styrene plastic (ABS). Both the numerical and experimental demonstrations of the rotation effect illustrate that the resulting device has a broadband functionality. A nearly perfect agreement is observed between the numerical simulation and experimental results. The influence of the structural parameters on its performance has also been investigated. Moreover, we inspect the frequency dependence of rotation effect and it shows that the designed device can work effectively within a broad band, as long as the effective medium approximation is valid. In addition, it turns out that by elongating each plate the increase of anisotropy of metamaterial can be conveniently attained, which contributes to enhance the rotation effect. With the known relationship between the rotated angle and the structural parameters, the rotation angle can be manipulated conveniently. The application of the proposed device for non-plane wave has also been discussed and the possibility of extending the proposed scheme to three-dimensional cases has been considered. With the capability of rotating acoustic wave front in a controlled manner, the realization of acoustic field rotator has opened up a new avenue for the versatile manipulations on the acoustic waves and may have potential application in various situations that require special acoustic controls.

Recently, transformation optics [1, 2] as well as transformation acoustics [3] has aroused great attention. Numerous fantastic devices have been designed and fabricated in experiment, such as invisibility [4] and illusion cloaks [5], etc.. In this letter, we present the theory design and experimental realization of an acoustic field rotator, which can rotate the wave front a preset angle in the center, and it can be regarded as a special acoustic illusion.

We established the mapping between the virtual system and the physical system, and the mass density ρ^{-1} in the physical system should be as follows:

$$\rho^{-1} = \rho_0^{-1} \begin{pmatrix} 1 + 2t \cos \theta' \sin \theta' + t^2 \sin^2 \theta' & -t^2 \cos \theta' \sin \theta' - t (\cos^2 \theta' - \sin^2 \theta') \\ -t^2 \cos \theta' \sin \theta' - t (\cos^2 \theta' - \sin^2 \theta') & 1 - 2t \cos \theta' \sin \theta' + t^2 \cos^2 \theta' \end{pmatrix}$$

Here the background medium is chosen as air and $t = \theta_0 r / (b - a)$, which is related to the rotated angle θ_0 in the inner cylinder [6].

We proposed a reduced model for the implementability in experiment as showed in Fig. 1. The cylinder is divided into several “fanlike” cells, and a rectangle made of acrylonitrile butadiene styrene plastic (ABS) is inserted in each cell, with its macro-axis titling an angle $\tau/2$ with respect to the tangential direction of the cell. The effective mass density in two different directions ρ_u and ρ_v can be obtained.

The experimental scheme is showed in Fig. 2, where an experimental system is established by two paralleled Plexiglass plates. An array of 188 rectangles was fabricated with thermoplastics via 3D printing to meet the theoretical requirement. We detected acoustic pressure in the inner region of the device in three particular frequencies, 3400 Hz, 5700 Hz and 6700 Hz, and compare the measured results and the simulations as showed in Fig. 3. Throughout the paper, the software COMSOL MULTIPHYSICS is used for the numerical simulations. It can be clearly observed that it has an excellent agreement between the experimental result and the simulation under any particular driving frequency. The wave front inside the rotator remains a plane, almost identical as the incident wave, and it has been rotated by a certain angle as if the wave is propagating from the top-left direction.

Next we inspect the frequency dependence of rotation effect. A slice with a nearly negligible width is placed in the center of the rotator, stretching across the inner circular region. A minimum

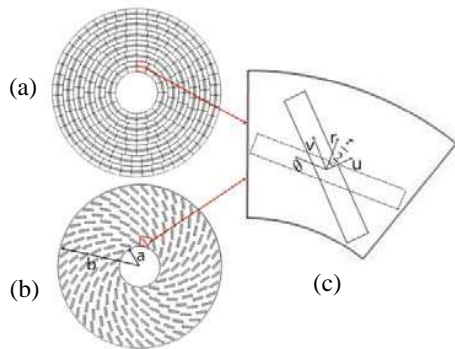


Figure 1: The pattern of the reduced model. In (a) picture the rectangle's macro-axis is parallel to the tangential direction. In (b) picture each rectangle is rotated by $\tau/2$. (c) Picture is the enlarged view of a "fanlike" cell before (dashed line) and after (solid line) rotation.

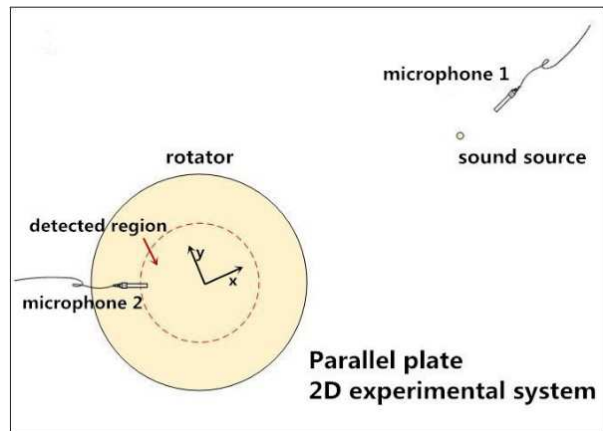


Figure 2: Schematic illustration of the experimental system. The field rotator is put 1 m away from the sound source, and the pressure in the center region (red dotted circle) is measured.

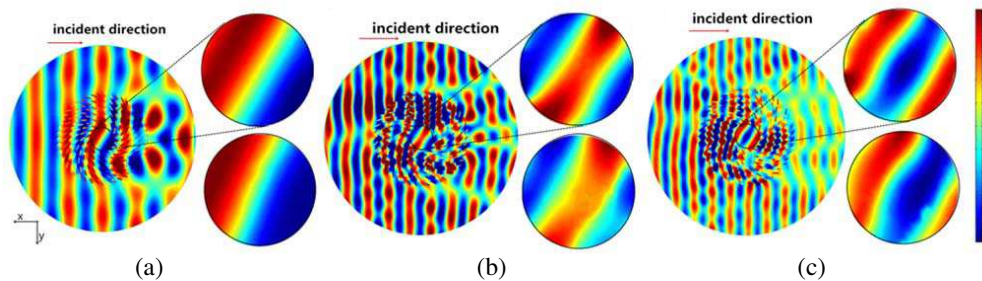


Figure 3: The comparison between the simulated and measured pressure field at (a) 3400 Hz, (b) 5700 Hz, (c) 6700 Hz. The left figure is the simulation around the rotator, the enlarged views of the simulated and measured results in the center are shown in the top-right and bottom-right figures respectively.

scattering caused by the slice can be reached when the slice is parallel to the direction of propagation. The parameter σ is defined as the integral of the scattering caused by the slice of the inner circular region. In group A, the inner radius and outer radius of the device are 3.5 cm and 14 cm, and the size of the rectangles are 2.8 mm \times 16.8 mm. The relationship between the scattering index σ and the frequency in these structural parameters is illustrated in Fig. 4, the green cycle indicates the critical frequency, and it is 6800 Hz in this group. Another two group B and C have also been carried out, in which the structural parameters are twice and half of those in group A, and the critical frequencies are 3400 Hz and 13600 Hz, respectively. We can draw a generalized conclusion that the working standard of the field rotator is $kb \leq 17.4$, with k being the wavenumber and b being the outer radius. The acoustic field rotator should have a broadband functionality due to the absence of acoustic resonance element, and the rotation effect holds within a considerably broad spectrum as long as the effective media theory is valid.

In theory, the parameters of ρ_u and ρ_v satisfy the relationship $\rho_v^{-1} - \rho_u^{-1} = t\sqrt{t^2 + 4}$, and t is related to the rotated angle θ_0 in the center of the rotator. Therefore we are able to manipulate θ_0 by changing the discrepancy between ρ_u and ρ_v , which can be obtained by using two kinds of different materials or simply by enlarging the respect ratio of the inserted rectangles. Here we keep the width unchanged and adjust the length of the rectangles, and illustrate the relationship between θ_0 and the aspect ratio of the rectangles Fig. 5 is the relationship between θ_0 and the length of the rectangles, it shows that the rotated angle increase with the increase of the length, and it has a nearly linear relationship.

It is worth noting that although the rotation performance has only been exemplified in plane

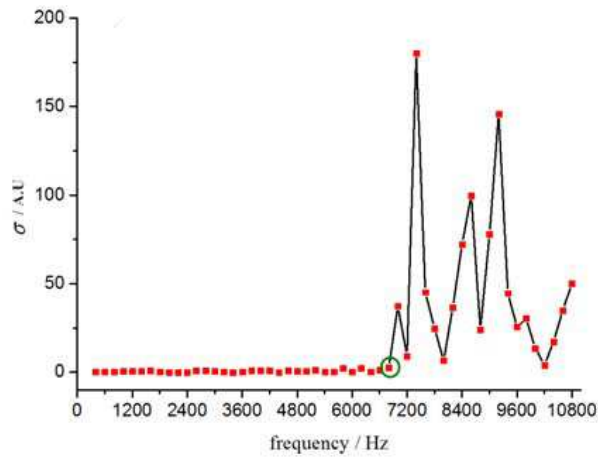


Figure 4: The relationship between the scattering index σ and the frequency in group A. The green circle indicates the critical frequency, it is 6800 Hz in these particular structural parameters.

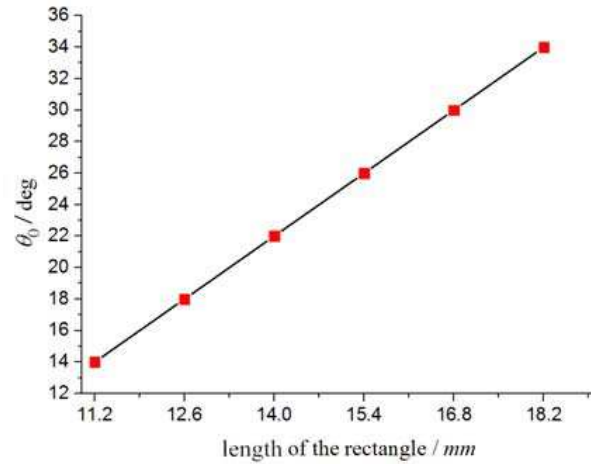


Figure 5: The rotated angle increase with the increase of the length of the rectangles.

wave, its performance should be irrelevant to the type of wavefront. Further simulations proved that it can work well in cylindrical wave. Moreover, the possibility of designing a field rotator for spherical wave in three dimensions will be anticipated in the future.

In summary, we have designed an acoustic field rotator capable of rotating the wave fronts inside it at a certain angle. It has an excellent agreement between the experimental results and simulation. We have also inspected the frequency dependence of rotation effect, it demonstrates that the device has a good performance as long as the effective media theory is valid. In addition, the rotated angle increases with the increase of the length of the rectangles, and it has a nearly linear relationship. The designed acoustic field has opened a new avenue to the special manipulation of acoustic wave.

REFERENCES

1. Pendry, J. B., D. Schurig, and D. R. Smith, *Science*, Vol. 312, 1780, 2006.
2. Leonhardt, U., *Science*, Vol. 312, 1777, 2006.
3. Cummer, S. and D. Schurig, *New J. Phys.*, Vol. 9, 45, 2007.
4. Zhu, X. F., B. Liang, W. W. Kan, X. Y. Zou, and J. C. Cheng, *Phys. Rev. Lett.*, Vol. 106, 014301, 2011.
5. Kan, W., B. Liang, X. Zhu, R. Li, X. Zou, H. Wu, J. Yang, and J. Cheng, *Scientific Reports*, Vol. 3, 1427, 2013.
6. Jiang, X., B. Liang, X. Y. Zou, L. L. Yin, and J. C. Cheng, *Appl. Phys. Lett.*, Vol. 104, 083510, 2014.

A Wideband Wide-angle Polarization-insensitive Metamaterial Absorber

Peng Cheng Zhang, Xian Qi Lin, Fei Cheng, Rui Shen, and Yong Fan

EHF Key Lab of Fundamental Science, School of Electronic Engineering

University of Electronic Science and Technology of China, Chengdu 611731, China

Abstract— In this paper, a wideband metamaterial absorber with wide-angle polarization insensitive characteristic is presented. The metamaterial absorber consists of a periodic arrangement of Jerusalem resonators lumped four resistors. Simulations demonstrate that the absorption rate is above 90% in 8–14.5 GHz, and by changing the direction angle of polarization, we achieve that this structure is polarization insensitive.

1. INTRODUCTION

Metamaterials (MM) are novel artificial materials with special properties that arise from their structure rather than their constituent materials. In recent years, much more researches on metamaterial absorber (MMA) are reported. Since the concept of a perfect MMA was proposed by Landy et al. in 2008 [1], there has been considerable attention in creating thinner and lighter MMA. Since then, many MMAs have been proposed and demonstrated with narrow-band, dual-band and multi-band absorption. More recently, several efforts have been made to improve its electromagnetic characteristics, such as polarization-insensitive [2, 3], wide incident angle [4] and wideband absorption [5].

In this paper, an efficient design is presented to achieve a wideband and polarization insensitive MMA in the gigahertz frequency region. This MMA consists of a periodic arrangement of Jerusalem resonators lumped four resistors, dielectric layer and a metallic background plane, and the whole thickness is only 2.8 mm. The simulation results indicate that lumped resistors are the chief contributor of the MMA's wideband absorption, and this structure is polarization insensitive.

2. DESIGN AND SIMULATE THE ABSORBER

2.1. Structures Design

The structure of MMA unit is illustrated in Fig. 1(a). The top layer consists of Jerusalem resonators lumped four series-parallel connection resistors set in a periodic pattern and bottom layer is a metal plane. The periodic array configuration of this unit cell is illustrated in Fig. 1(b) and is designed on a lossy dielectric board FR4 that has a dielectric constant of 4.4, tangential loss of 0.02 and thickness of 3 mm. All metals in the absorber are made of copper with a conductivity of 5.8×10^7 S/m.

2.2. Full-wave Simulation and Analysis

In more directive perspective, the absorption is defined as $A = 1 - S - T = 1 - |S_{21}|^2 - |S_{11}|^2$. To maximize the absorption rate, we can minimize the reflection and transmission simultaneously at the same frequency range. Due to the metal background of the absorber, the transmission $|S_{21}|$ is equal to zero. Full-Wave simulation is taken by using HFSS. By the master-slave boundary conditions, the simulation of the periodic array configuration of the absorber unit cell can be achieved. Through optimizing the parameters in Fig. 1(a), the simulation result is shown in Fig. 2, in which we observe a wideband absorption at about 7.8–15.5 GHz with the absorption rate of over 90%. The surface circuit at resonant frequency is shown in Fig. 3. We can see that most of the current flows through the resistors, which predicts that by tuning the value of the resistor we can match to a best absorption frequency range and rate.

2.3. Resistor Value Simulation

From the surface circuit we know that the value of the resistor is the chief contributor of the absorption. A research on wideband electromagnetic absorber loaded high impedance surfaces has been proposed by Prof. Costa [6]. It is achieved by considering the impedance of surface. In our work resistors bring the high impedance to be employed to increase the MMA's bandwidth, also can bring high loss to improve absorptivity. In Fig. 4 the absorption rates are plotted for $R = 80, 90, 100, 110 \Omega$. When $R = 100 \Omega$ the 90% absorption rate bandwidth ranges from 7.8 to 15.5 GHz.

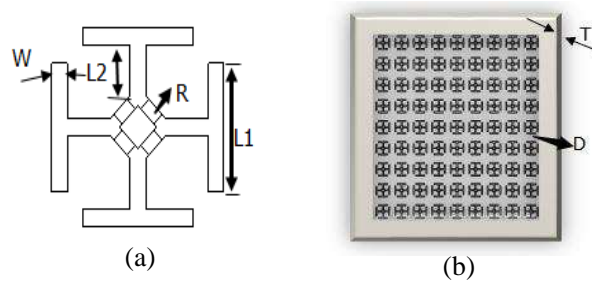


Figure 1: Structure of MMA, (a) unit cell, (b) periodic pattern cell ($L_1 = 2.8$ mm, $L_2 = 1.2$ mm, $W = 0.8$ mm, $D = 7.9$ mm, $T = 3$ mm).

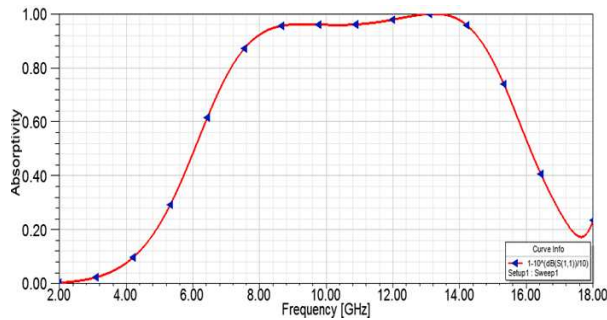


Figure 2: Simulated absorption for normal incident.

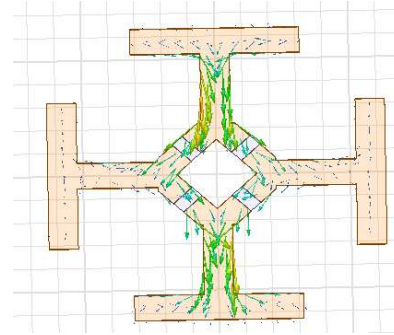


Figure 3: The surface circuit at resonant frequency.

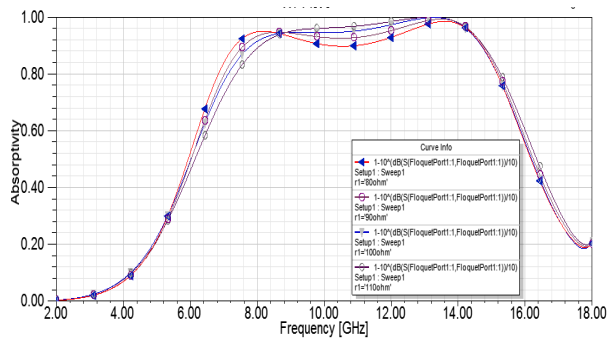


Figure 4: Simulated absorptivity for different resistors R .

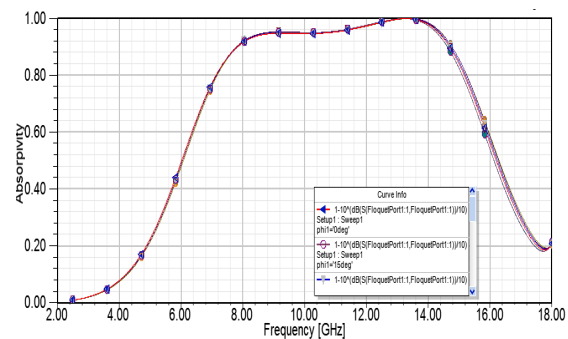


Figure 5: Simulated absorptivity for different incidence polarization angles.

2.4. Polarization Angle Simulation

Another performance we considered is MMA's polarization insensitive. Fig. 5. shows that wideband MMA remain high and stable absorptivity with wide polarization angles. We give the simulations by changing the polarization angle from 0° to 90° by 15° each step, and the results show that the absorption rates of the different polarization angles are almost at the same frequency range, which mean that the wideband MMA is polarization insensitive.

3. CONCLUSIONS

In this paper, we have presented a novel polarization-insensitive and wideband metamaterials absorber, which is composed periodic array configuration of Jerusalem resonators lumped four series-parallel connection resistors cell. The simulation results show from 7.8 to 15.5 GHz absorption rate is above 90%. The wideband absorptivity was achieved because of the series-parallel connection resistors of bringing high impedance surface to achieve wideband impedance matching. Polarization insensitivity capability results from the periodic array configuration of Jerusalem resonators.

ACKNOWLEDGMENT

This work was supported in part by the State Key Laboratory of CEMEE Foundation under Grant No. CEMEE2014Z0201A, in part by the Fundamental Research Funds for the Central Universities under Grant Nos. ZYGX2010J021 and ZYGX2012YB002, in part by the Program for New Century Excellent Talents in University under Grant No. NCET-13-****.

REFERENCES

1. Landy, N. I., S. Sajuyigbe, J. J. Mock, D. R. Smith, and W. J. Padilla, “Perfect metamaterial absorber,” *Phys. Rev. Lett.*, Vol. 100, 207402, 2008.
2. Luukkonen, O., F. Costa, C. R. Simovski, A. Monorchio, and S. A. Tretyakov, “A thin electromagnetic absorber for wide incidence angles and both polarizations,” *IEEE Trans. Antennas Propag.*, Vol. 57, No. 10, 3119–3125, 2009.
3. Bayraktar, Z., M. Gregory, D. Kern, and D. H. Werner, “Matched impedance thin composite magneto-dielectric metasurfaces,” Presented at *Antennas and Propagation Society International Symposium*, Charleston, SC, Jun. 1–5, 2009.
4. Hu, C., Z. Zhao, X. Chen, and X. Luo, “Realizing near-perfect absorption at visible frequencies,” *Opt. Express*, Vol. 17, 11039–11044, 2009.
5. Ye, Y. Q., Y. Jin, and S. He, “Omnidirectional, polarization-insensitive and broadband thin absorber in the terahertz regime,” *Opt. Soc. Am. B*, Vol. 27, 498–504, 2010.
6. Costa, F., A. Monorchio, and G. Manara, “Analysis and design of ultra-thin electromagnetic absorbers comprising resistively loaded high impedance surfaces,” *IEEE Trans. Antennas Propag.*, Vol. 58, No. 5, 1551–1558, 2010.

Design and Analysis of a Wideband Metamaterial Absorber Applied to Radome

Zhiwen Mao, Shaobin Liu, Xiangkun Kong, Borui Bian, Beiyin Wang, and Lin Chen

Key Laboratory of Radar Imaging and Microwave Photonics, Ministry of Education

College of Electronic and Information Engineering

Nanjing University of Aeronautics and Astronautics, Nanjing 210016, China

Abstract— In this paper, a detailed study of a single-layer wideband metamaterial absorber (MMA) applied to radome, which is transparent at the operating frequency and is absorption at frequencies ranging from 2.4 GHz to 7.1 GHz. The design is discussed by the unit cell and equivalent circuit model. A unit cell of the periodic structure for the absorber is designed and simulated. The MMA consists of a two-dimensional periodic array of resistor-loaded square loops and crosses. The composite structure is thoroughly analyzed by an efficient equivalent circuit approach and by full-wave numerical simulations. Simulation results show that the proposed MMA has a wideband absorption range that covering most of the C-band and S-band. A pass-band at the frequency 11.75 GHz is obtained, which is operating in X-band. It also shows that the MMA sample is polarization insensitive for TE and TM incident wave.

1. INTRODUCTION

Metamaterials (MMs) have been effectively used to produce highly absorbing structures which led the microwave engineers to research a new scientific field, with a direct impact on modern microwave systems. As an artificial medium, the permittivity and permeability of the MMs can be tuned by changing geometric dimension and shape [1]. Multi-band operation properties of MMs also can be realized by multiple-frequency resonators design [2, 3]. Generally, there will be more or less power losses occur when electromagnetic (EM) wave impinge on MMs. In 2008, Landy et al. [4], first presented a perfect metamaterial absorber (MMA) in a narrow-band which can absorb all the incident EM waves by tuning the magnetic and electrical resonances. In recent years, researchers have further studied the MMA in the GHz and terahertz (THz) frequency ranges to achieve dual working band [5, 6], broader bandwidth [7, 8], and polarization insensitive MMAs. Gu et al. [9] embedded resistors into MMA structures to lower the Q factor to increase the bandwidth in the GHz regime. Tao et al. [10] used the split-ring resonators (SRR) and bottom metallic layer structure to realize highly flexible materials in THz which can operate over wide angles of incidence for both transverse electric (TE) and transverse magnetic (TM) radiations.

In this paper, we present a novel wideband MMA based on a two-dimensional periodic array of resistor-loaded square loops and crosses. This structure is proposed using low profile single dielectric layer which shows absorption at a range that covering most of the C-band and S-band.

2. DESIGN OF THE STRUCTURE

The front and bottom view of the basic unit cell of the proposed wide-band MMA based is shown in Fig. 1. The designed MMA consists of two metallic layers separated by a dielectric substrate, each of the metallic layers is copper with frequency independent conductivity $\sigma = 5.8 \times 10^7$ S/m. The thickness and relative permittivity of the spacer are $h_1 = 12$ mm and $\varepsilon_1 = 1$, respectively. In addition to the spacer, another thin layer of substrate is introduced to facilitate the fabrication of this absorber. The thickness and relative permittivity of the spacer are $h_2 = 0.3$ mm and $\varepsilon_2 = 4.3$, respectively. The optimized geometry dimension parameters of the unit cell are as follows: $a = 24$ mm, $b = 18$ mm, $c = 12$ mm, $d = 2.6$ mm, $g = 1.5$ mm, $l = 16.8$ mm, $R_1 = 100 \Omega$, $R_2 = 800 \Omega$, $cd = 8$ mm, $wl = 2$ mm, $wc = 1$ mm, $w = 1$ mm.

The absorptivity can be found out from Eq. (1), where $A(\omega)$, $|S_{11}(\omega)|^2$, and $|S_{21}(\omega)|^2$ are the absorptivity, reflectivity and transmissivity, respectively, at an angular frequency ω ,

$$A(\omega) = 1 - |S_{11}(\omega)|^2 - |S_{21}(\omega)|^2, \quad (1)$$

3. SIMULATED RESULTS

A full wave EM simulation was performed to get the reflection parameter S_{11} based on the commercial program, CST MICROWAVE STUDIO 2010. The simulation result of the reflection and

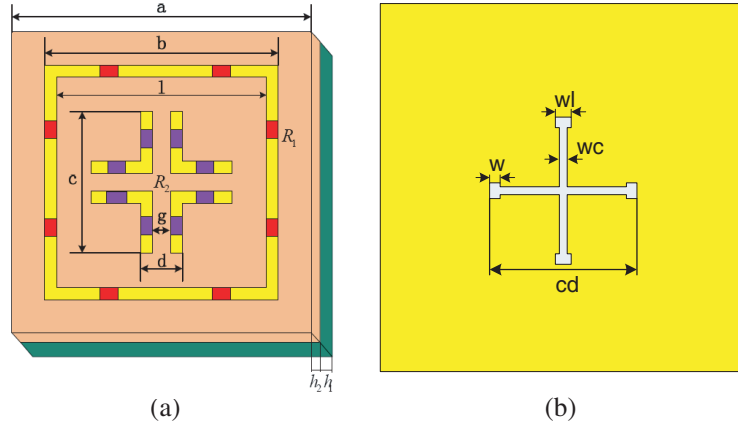


Figure 1: (a) Perspective view of the proposed MMA structure unit cell. (b) The bottom view of the basic unit cell of the proposed wide-band MMA.

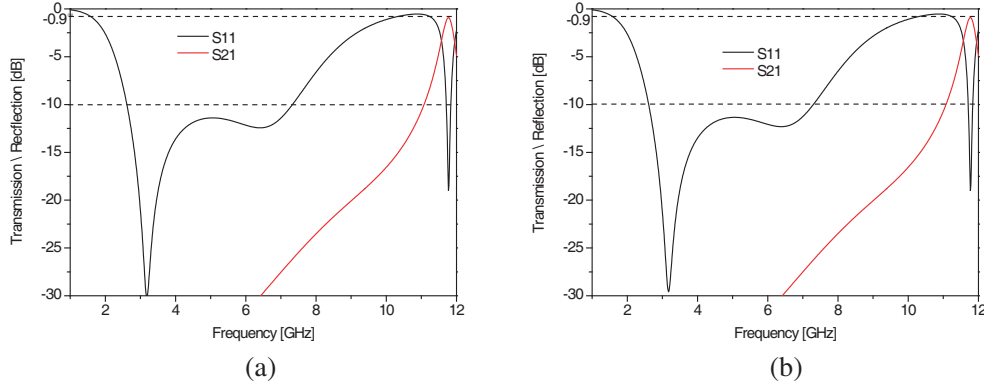


Figure 2: Simulated result of the reflection and transmission curves of wideband absorber. (a) TE and (b) TM incident radiation.

transmission curves for both TE and TM polarizations as shown in Fig. 2. The absorption curve is shown in Fig. 3. The simulation results exhibit that there have been a broad absorption band ranging from 2.4 GHz to 7.1 GHz with absorption rates of 90%. In addition, it is observed that there is a transmission peak at frequencies of 11.75 GHz with insertion loss of -0.9 dB. It indicates that the impedance of proposed MMA can be tuned to approximate match to the free space in our interested frequency range. Due to the center of symmetry, the proposed MMA is polarization-insensitive.

To better understand the physical mechanism and the origin of the five-band CSR MMA, we have studied the equivalent circuit model is shown in Fig. 4(a). It may be mentioned that R_1 , L_1 and C_1 represent the equivalent circuit of the outer loop, while R_2 , L_2 and C_2 denote the inner cross. The short-circuited transmission line section of length h_1 represents the conductor-backed spacer, while the short transmission line section of length h_2 denotes the thin substrate. The transmission line of characteristic admittance Y_0 stands for the half free space above the MMA. For the transmission line circuit shown in Fig. 2, we can obtain the reflection coefficient Γ as follows:

$$\Gamma = \frac{Y_0 - Y_{in}}{Y_0 + Y_{in}} \quad (2)$$

$$\text{where } Y_{in} = Y_{LP} + Y_{CR} + Y_d \quad (3)$$

$$Y_{LP} = \frac{1}{R_1 + j \left(\omega L_1 - \frac{1}{\omega C_1} \right)} = G_1 + jB_1 \quad (4)$$

$$Y_{CR} = \frac{1}{R_2 + j\left(\omega L_2 - \frac{1}{\omega C_2}\right)} = G_2 + jB_2 \quad (5)$$

$$Y_d = \frac{Y_{02}(Y_{02} \tan(\beta_2 h_2) - Y_{01} \cot(\beta_1 h_1))}{Y_{02} + Y_{01} \cot(\beta_1 h_1) \tan(\beta_2 h_2)} = jB_d \quad (6)$$

and $Y_{0i} = Y_0 \sqrt{\epsilon_{ri}}$, $\beta_i = 2\pi \sqrt{\epsilon_{ri}}/\lambda$, $i = 1, 2$, $\omega = 2\pi f$, Y_0 is the characteristic admittance of free space. The values of lumped resistors (R_1, R_2) are determined for optimum frequency response. The circuit model simulation in Fig. 4(b) is conducted using the following values: $R_1 = 100 \Omega$, $L_1 = 13 \text{ nH}$, $C_1 = 0.222 \text{ pF}$, $R_2 = 800 \Omega$, $L_2 = 8.25 \text{ nH}$, $C_2 = 0.065 \text{ pF}$, $R_1 = 100 \Omega$, $R_2 = 800 \Omega$, $h_1 = 12 \text{ mm}$, $h_2 = 0.3 \text{ mm}$. It is observed that the results from circuit model and CST simulations are in good agreement.

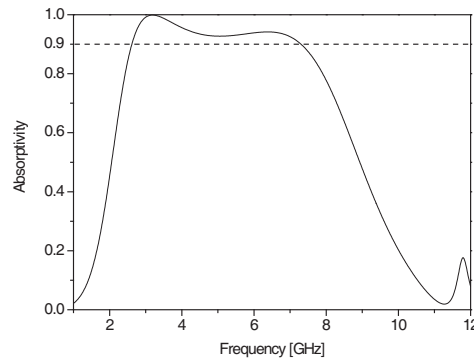


Figure 3: Simulated absorptivity of the absorber with wide-band configuration.

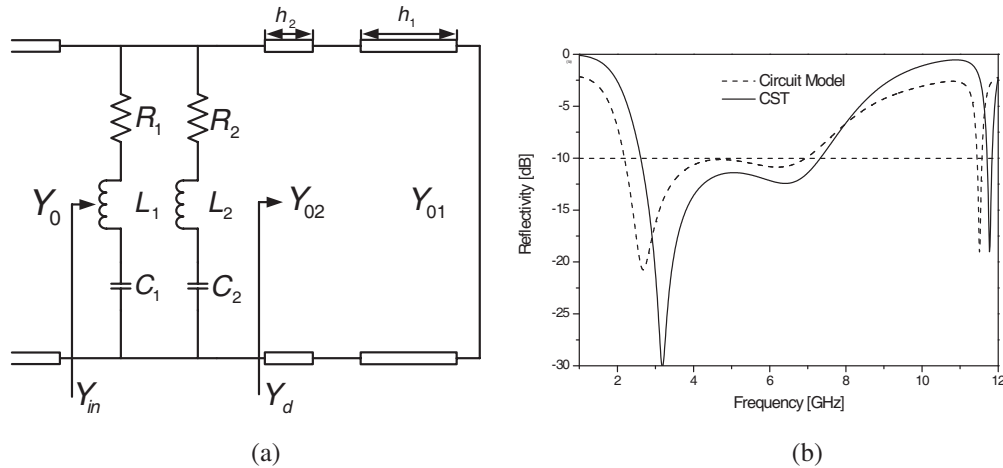


Figure 4: (a) Equivalent circuit model of the wideband MMA. (b) Reflectivity of the absorber calculated from the equivalent circuit model and CST using periodic boundaries for normal incidence.

4. CONCLUSION

In summary, the absorption properties of a single-layer wideband metamaterial absorber are studied. The CST simulation results show the absorption range can cover most of the C-band and S-band with absorptivity over 90%. In addition, there have been a transmission peak in X-band with insertion loss of -0.9 dB . Furthermore, the simulation result exhibits that the absorption of the designed MMA is nearly unchanged for different polarization angles with TE and TM modes. Such a design can have some potential applications in EM spatial filter, wavelength selective radiation and radom.

ACKNOWLEDGMENT

This work was supported by Funding of Jiangsu Innovation Program for Graduate Education (No. CXZZ13.0166), the Fundamental Research Funds for the Central Universities (No. NZ2013302), Youth Funding for Science & Technology Innovation in NUAA (NS2014039), the Chinese Specialized Research Fund for the Doctoral Program of Higher Education (No. 20123218110017), the Jiangsu Province Science Foundation (No. BK2011727), and the Foundation of Aeronautical Science (No. 20121852030).

REFERENCES

1. Gorkunov, M. V., I. V. Shadrivov, and Y. S. Kivshar, “Enhanced parametric processes in binary metamaterials,” arXiv preprint physics/0510103, 2005.
2. Chen, H., L. Ran, J. Huangfu, et al., “Metamaterial exhibiting left-handed properties over multiple frequency bands,” *Journal of Applied Physics*, Vol. 96, No. 9, 5338–5340, 2004.
3. Sydoruk, O., O. Zhuromskyy, E. Shamonina, et al., “Phonon-like dispersion curves of magnetoinductivewaves,” *Applied Physics Letters*, Vol. 87, No. 7, 072501, 2005.
4. Landy, N. I., S. Sajuyigbe, J. J. Mock, et al., “Perfect metamaterial absorber,” *Physical Review Letters*, Vol. 100, No. 20, 207402, 2008.
5. Wen, Q. Y., H. W. Zhang, Y. S. Xie, et al., “Dual band terahertz metamaterial absorber: Design, fabrication, and characterization,” *Applied Physics Letters*, Vol. 95, No. 24, 241111, 2009.
6. Li, M., H.-L. Yang, X.-W. Hou, Y. Tian, and D.-Y. Hou, “Perfect metamaterial absorber with dual bands,” *Progress In Electromagnetics Research*, Vol. 108, 37–49, 2010.
7. Cheng, Y. Z., Y. Nie, R. Z. Gong, et al., “Multi-band metamaterial absorber using cave-cross resonator,” *European Physical Journal-Applied Physics*, Vol. 56, No. 3, 4184, 2011.
8. Zhang, F., L. Yang, Y. Jin, and S. He, “Turn a highly-reflective metal into an omnidirectional broadband absorber by coating a purely-dielectric thin layer of grating,” *Progress In Electromagnetics Research*, Vol. 134, 95–109, 2013.
9. Gu, S., J. P. Barrett, T. H. Hand, et al., “A broadband low-reflection metamaterialabsorber,” *Journal of Applied Physics*, Vol. 108, No. 5, 064913, 2010.
10. Tao, H., C. M. Bingham, A. C. Strikwerda, et al., “Highly flexible wide angle of incidence terahertz metamaterial absorber: Design, fabrication, and characterization,” *Physical Review B Condensed Matter and Materials Physics*, Vol. 78, No. 24, 241103R, 2008.

Preliminary Experimental Results along a Horizontal Path for Adaptive Rate-controlled FSO

Changqi Yang¹, Juan Zhao¹, and Anqi Liu²

¹School of Science, Xi'an Shiyou University, Xi'an 710065, China

²Advanced Technology Institute, Hubei University, Hubei 430062, China

Abstract— Free-space optical communication is a focus in recent research. Because of the influence of weather conditions, the transmission channel of free-space optical communication dramatically changes. This paper describes the design of a new adaptive rate-controlled optical communication system. The rate adaptively changes through the estimation of the received signal strength. Usually estimate the channel conditions with a low rate of radio frequency feedback. Previously the author used a new technique to design an adaptive rate-controlled optical communication system. It used beacon calibration instead of radio frequency feedback. In this paper an outdoor experiment is performed along a 186 meters horizontal path. On-off Keying modulation is used. The preliminary results with adaptive rate control are compared with that of without adaptive rate control. It appears to be at least an order of magnitude decrease of the bit-error rate.

1. INTRODUCTION

For a long time, people try to communicate over long distances by free-space optical communication (FSO) [1]. Long distance communications are often faced with the problems of confidentiality and spectrum resources. Microwave and radio frequency (RF) communications tend to saturate. With the exploration of outer space, the need of communication will be stronger. In general, communication wavelength is proportional to the volume of communication equipment. Shorter wavelength means smaller volume of the equipment. So the short wave communication, such as optical communication, can use a telescope as antenna. But the longer wavelength communication needs to use larger size antenna that we usually placed on the roof. Smaller volume means less power consumption. As to the outer space satellite, it is very important.

If we count the days from the research of Soviet Union in the last century, the development of optical communications has experienced at least 60 years. If we count the days from the Baer's era, this time is even longer. Initially, the optical communication faces two major problems: one is light source, and the other is transmission medium. Free-space optical communication has not the same good luck of fiber communication. In FSO communication, the transmitter and the receiver are likely to be moving targets. This provides a great technical problem for the FSO. FSO needs to solve the technical problem of acquisition, tracking and pointing (ATP) [2]. The applications of ATP technology are generally based on a national strategy. Therefore, this technology greatly increases the cost of equipment and limits its large-scale commercial applications. FSO needs to solve another problem. Its transmission medium is extremely unstable, and can produce very bad effect. The most obvious example is the optical scintillation. There are many researches about this issue, such as Ref. [3]. As a result, FSO has a low transmission rate and a short transmission distance. High-speed and long-distance transmission leads to high bit-error rate. Due to the above difficulties, FSO has not yet received a large-scale commercial application. As to FSO, firstly promoting short distance communication between roofs is a more feasible development direction. After the market and demand are mature, it can be extended to ground-to-space or the space-to-space cases.

Due to weather conditions, even if in a 1–2 kilometers distance, FSO is difficult to communicate. The most often solution is to use radio frequency feedback technology. It uses radio frequency signal to detect channel conditions. Refs. [4–7] gives theoretical analysis and system designs of adaptive rate-controlled optical communication system.

Reference [8] use another technique to detect the channel conditions in an indoor experiment is performed. This technique is based on the beacon light calibration. The second part of the paper introduces the operation principle of the adaptive rate-controlled optical communication system. The third part introduces experimental results of outdoor 186 meters horizontal propagation.

2. OPERATION PRINCIPLE

Traditional FSO is based on direct detection. When designs and tests the circuit, this type of FSO confronts a problem: due to the channel scintillation, the optical signals are very weak and are drowned in the noise. Threshold mechanism decides that the traditional FSO can not work efficiently.

The author develops an adaptive rate-controlled FSO system. The flow chart of its operation principle is shown in Fig. 1.

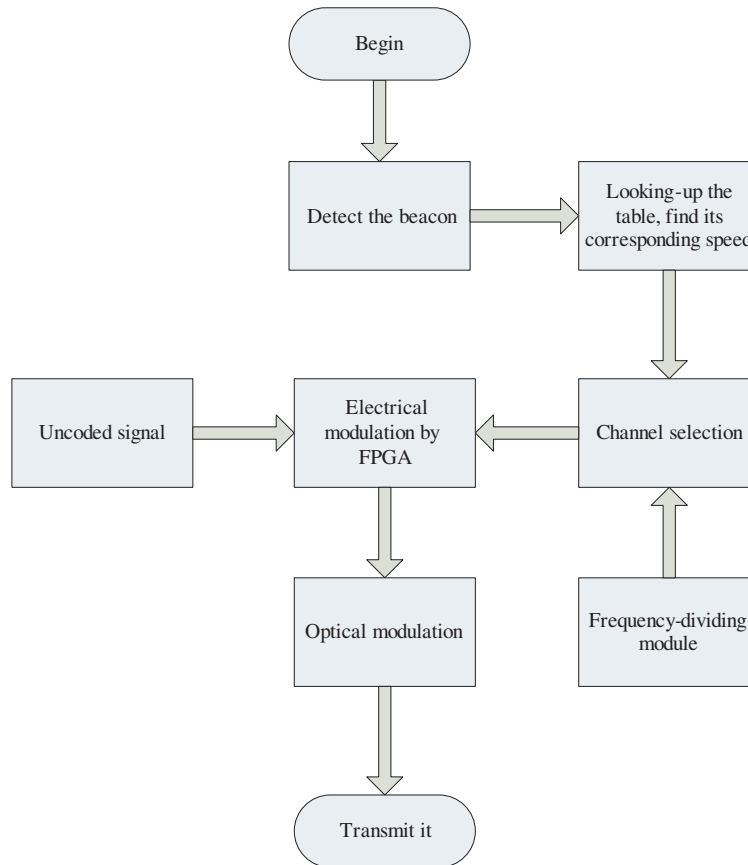


Figure 1: The operation flow chart of adaptive rate-controlled FSO.

The beacon is transmitted to the transmitter. The beacon is a cooperative laser. The transmitter detects and amplifies the beacon. Decides its optical power, looks up the table and decides its speed. Produces the same speed modulated signal, modulates the laser, and transmits it.

In other people's work, RF feedback is usually used to decide the channel conditions. Different from that, in our design, the transmitter continuously detects, amplifies and codes the beacon. In the atmospheric environment, 1 Gbit/s is a very high transmission speed. This situation usually means a very weak turbulence, such as the top of mountain. The transmitter will divide the system clock into 16 frequencies from 250 MHz–1 GHz. The FSO system designed in this paper gives 16 transmission speeds, which correspond to 16 channels from 250 Mbit/s–1 Gbit/s. Because the magnification is fixed, assuming that the detected voltage is 1.78 V, we assign that the 500 MHz channel is opened, and the other ones are closed. Then FPGA carries the encoded signal onto the open channel. The above is the process of electrical modulation. Next the electrical modulated signals are sent to the optical modulator and transmitted.

The power calibration technique of the beacon is introduced in Ref. [8].

3. 186 m HORIZONTAL PROPAGATION EXPERIMENT RESULTS

The authors perform a 186 m horizontal propagation experiment. The light propagation path is selected between the tops of two buildings of Hubei University as shown in Fig. 2.

The time of the experiment is at the mornings of August 13–15, 2013. A transmitter and a receiver are placed on the tops of two respective buildings. The distance between the beams and



Figure 2: An aerial photograph of the light propagation path (from Baidu map).

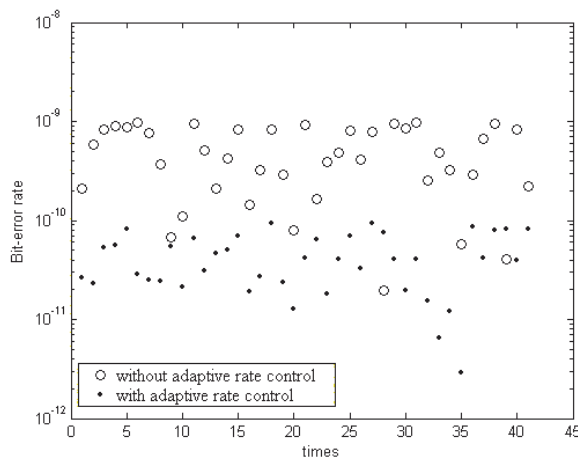


Figure 3: Comparison results.

the ground is nearly 24 meters. The diameters of the transmitter and the receiver are 10 cm. The wavelength of the beacon is 650 nm. The modulation frequency of the beacon is 5 kHz. The beacon's calibration time is at midnights. The beacon is placed at the end of the receiver and is transmitted to the transmitter. After the transmitter detects the beacon, the processing circuit decides the channel fluctuation conditions. Then an OOK (on-off keying) modulated signal is transmitted towards the receiver. The transmission speed is adjusted from 250 MHz–1 GHz according to the channel conditions.

We perform alternate measurements. The first launch is a frame of data without adaptive rate control. Its transmission rate is 500 MHz. Measure its bit-error rate. Then under the control of the beacon, we emit a frame of data with rate control according to the turbulent conditions. Also we test the bit-error rate. Repeat this process. 82 frames of data are tested alternately.

The results are plotted in Fig. 3. The number of the test times is plotted along the horizontal axis. The bit-error rate is along the vertical axis. The circles are used to show the results without adaptive rate control, and the points are used for the results with adaptive rate control.

You can see from Fig. 2 that in the adaptive rate control cases, bit-error rate has an obvious improvement. Comparing with the cases without adaptive rate control, bit-error rate decreases one order of magnitude with adaptive rate control. Sometimes the bit-error rate without adaptive rate control is less than that with adaptive rate control. But these cases are comparatively rare. Maybe it is because the turbulence changes its state during two launches.

4. CONCLUSIONS

In this paper, the authors establish a horizontal link with adaptive rate control. Under the OOK modulation, adaptive rate control shows its efficiency and bit-error rate improvement. Future research will compare different modulation modes.

ACKNOWLEDGMENT

This paper is supported by Xi'an Shiyou University research training program for university students.

REFERENCES

1. Andrews, L. C., R. L. Phillips, C. Y. Hopen, and M. A. Al-Habash, "Theory of optical scintillation," *J. Opt. Soc. Am. A*, Vol. 16, No. 6, 1417–1429, 1999.
2. Yang, C., W. Jiang, and C. Rao, "Bit-error rate for free-space optical communication with tip-tilt compensation," *Waves in Random and Complex Media*, Vol. 16, No. 3, 281–292, 2006.
3. Yang, C., X. Li, W. Jiang, and C. Rao, "Experimental validation that optical scintillation obeys the same rules of share price fluctuations," *PIERS Proceedings*, 750–753, Suzhou, China, September 12–16, 2011.
4. Zabidi, S. A., W. A. Khateeb, M. R. Islam, and A. W. Naji, *2010 International Conference on Digital Dentifier*, 1–5, 2010.

5. Tatarko, M. and L. Ovsenik, *2012 Proceedings of the 35th International Convention*, 192–195, 2012.
6. Sharma, V. and G. Kaur, *The 3rd International Conference on Digital Object Identifier*, 154–157, 2013.
7. Fatima, K., S. S. Muhammad, and E. Leitgeb, *The 8th International Symposium on Digital Object Identifier*, 1–5, 2012.
8. Yang, C., “Design of an adaptive rate-controlled FSO and its indoor experimental results,” *Hans Journal of Wireless Communications*, Vol. 3, 99–103, 2013.

A Transmission-typed Broadband Absorber

Hai-Ming Li¹, Shao-Bin Liu¹, Hai-Feng Zhang^{1,2}, and Xiang-Kun Kong¹

¹Key Laboratory of Radar Imaging and Microwave Photonics, Ministry of Education
College of Electronic and Information Engineering

Nanjing University of Aeronautics and Astronautics, Nanjing 210016, China

²Nanjing Artillery Academy, Nanjing 211132, China

Abstract— In this paper, we theoretically find that a wide, near complete absorption can be realized in a heterostructure composed of a dielectric layer and truncated photonic crystals with a lossy dielectric defect. A dielectric layer is put on the top of the truncated photonic crystals to gain a relative flatter broadband absorptions. The wide absorption band is located within transmission band gap of photonic crystals without lossy dielectric defect, which is different of some previous designs.

1. INTRODUCTION

The perfect absorption is greatly needed in photonic radiation detectors, efficient thermal emitters, and solar cells [1, 2]. Furthermore, electromagnetic (EM) absorbers with high absorption have been widely used in steal, EM shielding, darkroom, and so on.

To obtain high absorption, intensive EM field should be localized inside lossy materials. Photonic crystal with defect can enhance the intensity of the local EM field in the defect layer. Therefore, photonic crystals containing lossy dielectrics have attracted lots of attentions [3, 4]. A omnidirectional high absorption of photonic crystal consisting of negative-index material, positive-index material and defect layer is obtained in [5]. Lately, a efficient multiband absorber by using one-dimensional periodic mental-dielectric photonic crystal with a reflective substrate is reported by Wang et al. [6]. Moreover, by using metal and Bragg gap, a broadband omnidirectional absorption [7] is realized in photonic crystal heterstructure. It is noticed that all of broadband absorbers mentioned above is realized by using the forbidden band of photonic crystal. However, in this paper, we propose a transmission-type broadband absorber by using the transmission band of photonic crystal.

2. DESIGN

In order to let the all of electromagnetic (EM) wave enter the structures, a heterostructure $M(PN)^S D(PN)^K$ is designed. Fig. 1 shows the structure.

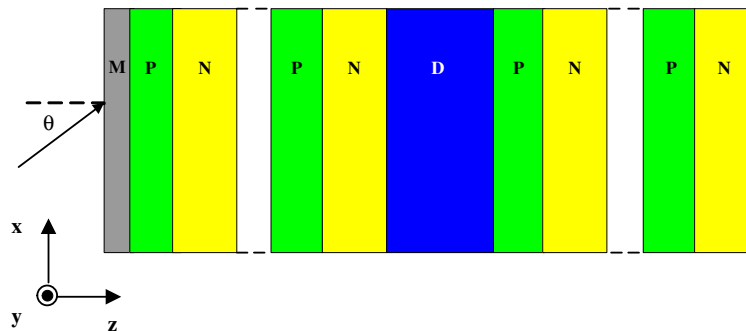


Figure 1: Schematic of the heterostructure composed of a dielectric layer (M) and a truncated photonic crystal with lossy dielectric layer (D). P and N represent positive-refractive-index and negative-refractive-index materials. S and K are the periods.

The reflectance and transmittance of the structure $(PN)^{10}$ are shown in Fig. 2. The thicknesses of P and N are denoted as d_P and d_N . The Drude model can be used to describe the property of negative-refractive-index materials, in which the relative permittivity and permeability are [8]

$$\epsilon_N = 1.21 - \omega_{ep}^2 / (\omega^2 + i\gamma\omega) \quad (1)$$

$$\mu_N = 1 - \omega_{mp}^2 / (\omega^2 + i\gamma\omega) \quad (2)$$

where ω_{ep} and ω_{mp} are the electric plasma frequency and magnetic plasma frequency, and γ is the damping factor. The transfer-matrix method [9] is used to calculate the reflectance and transmittance. For TM wave, one of the transmittance band shown in Fig. 2 is 78.6–96.7 GHz. We can find the broadband absorption frequency locate within the pass band in Fig. 3, Fig. 4.

In order to obtain absorption effect, a lossy dielectric defect layer is introduced into the $(PN)^{10}$ structure. The defect mode can remarkably enhance the fields in the defect layer, so the EM is fully absorbed by the lossy defect. dd represents the thicknesses of D . Fig. 3(a). show the reflectance, transmittance and absorbance of the structure $(PN)^5D(PN)^5$ as a function of angular frequency for TM wave. The transmittance is near zero and the reflectance is very small with the max value 0.07. The absorption is calculated by $A = 1 - R - T$. The absorption is very high (0.92–1) within the transmittance band.

The high absorption is due to remarkably enhance the local electric fields located in the defect layer, which can be seen Fig. 3(b). It is shown that the simulated distributions of the intensities of electric field ($|E|^2$) in $(PN)^5D(PN)^5$ at the frequency of complete absorption (86.5 GHz). When the electric field intensity of incident wave is taken to be 1, the intensities of electric field can reach 1.4×10^4 in the defect lossy layer. The broadband and high absorption is generated in the defect layer, which is easily understand. As shown in Fig. 3(b), the magnitude of the electric field at the left interface between the PC and $(PN)^5D(PN)^5$ is 1.01, which shows no reflection at the left interface. It indicates near all of incident TM wave can enter the structure. From Fig. 3(a), we can find that the broadband absorption is not flat, which contain five absorption peaks. In order

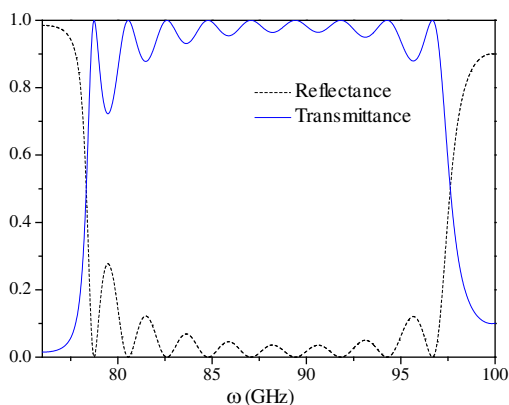


Figure 2: The reflectance (blue line) and transmittance (black dash line) of $(PN)^{10}$ as a function of frequency for TM wave. $d_P = 6.1$ mm, $d_N = 8.3$ mm, $\varepsilon_P = 1.7$, $\mu_P = 1$, $\omega_0 = 0.16\pi c/d$, $\omega_{ep} = \omega_{mp}$, $\omega_{mp} = 5.7\omega_0$ and $d = 6$ mm.

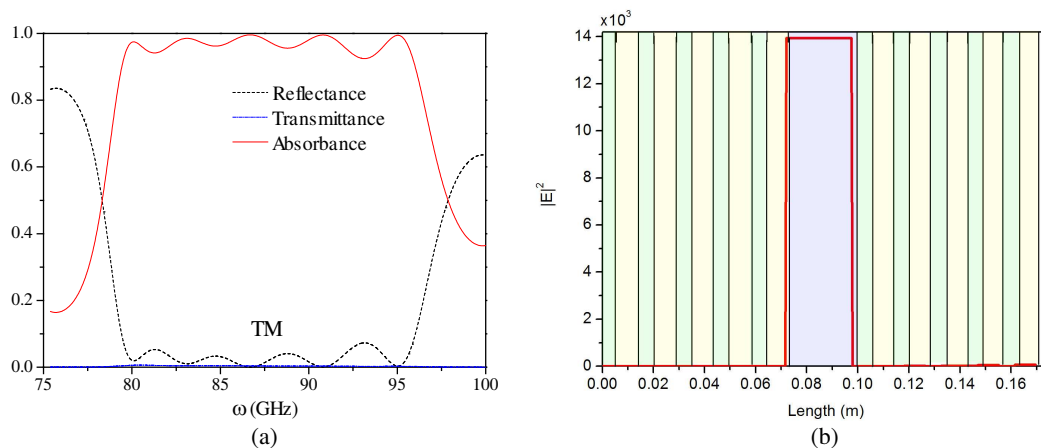


Figure 3: (a) shows the reflectance (blue line), transmittance (black line) and absorbance (red line) of $(PN)^5D(PN)^5$ as a function of frequency for TM wave. $dd = 25.6$ mm, $\varepsilon_d = 1 + 0.8i$ and $\mu_d = 1$. (b) The distributions of $|E|^2$ of $(PN)^5D(PN)^5$ at the frequency of 86.5 GHz. All of the other parameters are the same as those in Fig. 2.

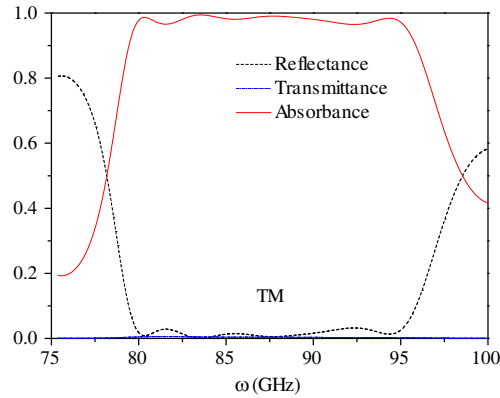


Figure 4: The reflectance (blue line), transmittance (black line) and absorption (red line) of $M(PN)^5D(PN)^5$ as a function of frequency for TM wave. $d_m = 2.8$ mm, $\varepsilon_m = 1.32$ and $\mu_m = 1$. All of the other parameters are the same as those in Fig. 3.

to obtain more flatter absorption, a match dielectric layer M is put on the top of $(PN)^5D(PN)^5$. The reflectance, transmittance and absorbance of the structure $M(PN)^5D(PN)^5$ as a function of angular frequency for TM wave is showed in Fig. 4. Here, d_m represents the thicknesses of M .

A more flatter broadband absorption is gained in Fig. 4, which is due to the weak coupling of five independent absorption peaks. We know that the relative permittivity ε_m , the thicknesses d_m and intensities of the localized EM fields can influence the coupling strength of five independent absorption peaks. Fig. 4 show a weak coupling of five independent absorption peaks. So, a more flatter broadband absorption can be obtained. The frequency range of absorption is 80–95 GHz and the value of absorption is 97–100%.

3. CONCLUSIONS

In conclusion, a broadband, nearly total absorption is realized by heterostructure containing a impedance matching dielectric layer and truncated photonic crystals with a lossy dielectric defect. A impedance matching dielectric layer is put on the top of the truncated photonic crystals to get a relative flatter broadband absorption. The width of absorption band is connected with the pass band of the $(PN)^{10}$, which is different of some previous designs [10, 11]. Our proposed transmission-typed broadband absorber offer additional opportunities to design novel optoelectronic devices.

ACKNOWLEDGMENT

This work was supported by Funding of Chinese Natural Science Foundation (Grant No. 61307052), Jiangsu Innovation Program for Graduate Education (No. CXZZ13_0166), Youth Funding for Science & Technology Innovation in NUAU (NS2014039), Open Research Program in Jiangsu Key Laboratory of Meteorological Observation and Information Processing (Grant No. KDXS1207), the Chinese Specialized Research Fund for the Doctoral Program of Higher Education (No. 20123218110017), the Jiangsu Province Science Foundation (No. BK2011727), and the Foundation of Aeronautical Science (No. 20121852030).

REFERENCES

1. Yang, Z. P., L. Ci, J. A. Bur, S. Y. Lin, and P. M. Ajayaan, "Experimental observation of an extremely dark material made by a low-density nanotube array," *Nano Lett.*, Vol. 8, No. 2, 446–451, 2008.
2. Garcia-Vidal, F. J., "Metamaterials: towards the dark side," *Nat. Photonics*, Vol. 2, 215–216, 2008.
3. Sigalas, M. M., K. M. Ho, R. Biswas, and C. M. Soukoulis, "Theoretical investigation of defects in photonic crystals in the presence of dielectric losses," *Phys. Rev. B*, Vol. 57, No. 7, 3815–3820, 1998.
4. Zhou, W., L. Chen, Z. Qiang, and G. J. Brown, "Spectrally selective infrared absorption in defect-mode photonic-crystal-slab cavity," *J. Nanophotonics*, Vol. 1, No. 1, 013515, 2007.

5. Wu, N. N., H. P. Tian, Y. H. Zhang, and Y. F. Ji, “Omnidirectional high absorption based on an asymmetric photonic crystal composed of negative-index material and positive-index material,” *J. Opt. Soc. Am. B*, Vol. 30, No. 5, 1161–1166, 2013.
6. Wang, W. Y., Y. X. Cui, Y. R. He, Y. Y. Hao, Y. Y. Lin, X. M. Tian, T. Ji, and S. L. He, “Efficient multiband absorber based on one-dimensional periodic metal-dielectric photonic crystal with a reflective substrate,” *Optics Letters*, Vol. 39, No. 2, 331–334, 2014.
7. Du, G. Q., L. W. Zhang, and H. T. Jiang, “Broadband and omnidirectional absorption in heterostructures with a highly absorptive metallic film and a dielectric Bragg reflector,” *J. Appl. Phys.*, Vol. 109, No. 6, 063525, 2011.
8. Chen, Y. H., J. W. Dong, and H. Z. Wang, “Conditions of near-zero dispersion of defect modes in one-dimensional photonic crystals containing negative-index materials,” *J. Opt. Soc. Am. B*, Vol. 23, No. 4, 776–781, 2006.
9. Born, M. and E. Wolf, *Principles of Optics*, 7th Edition, Cambridge University, 1999.
10. Watts, C. M., X. Liu, and W. J. Padilla, “Metamaterial electromagnetic wave absorber,” *Advanced Materials*, Vol. 24, No. 23, 205–213, 2012.
11. Bond, N., G. Tayeb, D. Maystre, S. Enoch, and E. Popov, “Total absorption of light by lamellar metallic gratings,” *Opt. Express*, Vol. 16, No. 20, 15431–15438, 2008.

Realization of XOR and OR Logic Gate with One Configuration in the Two-dimensional Photonic Crystals

Yuchi Jiang^{1,2}, Shao-Bin Liu¹, Hai-Feng Zhang¹, and Xiang-Kun Kong¹

¹Key Laboratory of Radar Imaging and Microwave Photonics, Ministry of Education
Nanjing University of Aeronautics and Astronautics, Nanjing 210016, China

²School of Physics and Electronic Engineering, Changshu Institute of Technology, Changshu 215500, China

Abstract— Based on the theory of light beam interference effect, a new configuration is designed to realize two types of all-optical logic gates including XOR and OR logic gate in two-dimensional (2D) photonic crystals, and the distribution of the electrical field is simulated by the Finite-difference in time-domain method. The results show that through this new configuration, not only the two types of all-optical logic gates can be realized, but the higher light contrast ratio of the logic state “1” and “0” can also be obtained. The realization of two types of all-optical logic gates in one configuration is helpful and significant to the optical device integration and potential in the optical communications. It is noticed that the logic state of “1” and “0” at output port are defined as the transmission is larger than 0.5 and less than 0.1, respectively.

1. INTRODUCTION

logic gates realized by photonic crystals have been researched and attracted much attentions recently. Logic functions are usually implemented through different ways such as using closed packed 2D photonic crystal structure, self-collimated beams in 2D photonic crystal [1], single-mode wave interference for on-off keyed signals [2] and multi-mode interference for BPSK signals [3] in the photonic crystal waveguides. Waveguides are well known for their operating frequency of the photonic band gaps (PBG) which can control the light propagation of the electromagnetic wave [4, 5]. There have been many reports about logic gates such as NOR logic gate [6], AND logic gate [7] are realized by the photonic crystal waveguides, Fu et al proposed five logic gates [8], but the scheme can implement one logic gate function almost by one waveguide configuration. This paper realize XOR and OR logic gates with one configuration in 2D photonic crystal waveguides and the design is significant to application in the integrated photonic circuits.

2. PHYSICAL MODEL

The scheme of the 2D photonic crystals is shown in Fig. 1 and the black tunnel denotes the waveguide. The Silicon rods (white circles in Fig. 1) which dielectric constant is set to 11.56 are inserted into the air background. Ports A, B, C can be chosen as input ports in logic gates design and the D ports is considered as output port. The band structure of the 2D photonic crystals shown in Fig. 2 is obtained by PWE (plane wave expansion) method [8]. The normalized frequency of the PBG is from $0.46(a/\lambda)$ to $0.57(a/\lambda)$ and we chose $0.517(a/\lambda)$ as the incident wave frequency

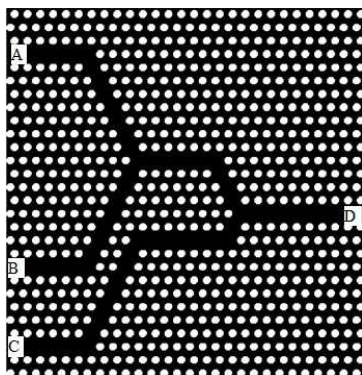


Figure 1: The scheme of the 2D photonic crystals.

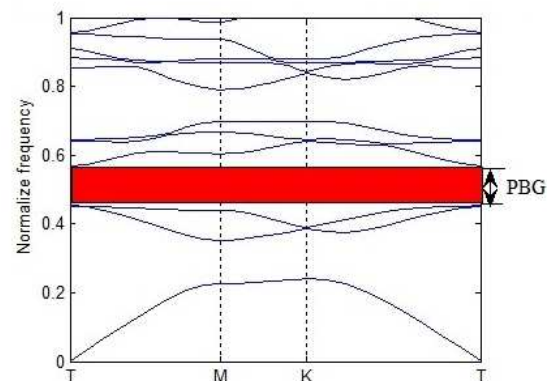


Figure 2: The band structure of the 2D photonic crystals.

which can propagate in the waveguide with little light consumption. The electromagnetic wave propagating is simulated by Finite-difference in time-domain (FDTD) method [9]. The incident wave is assumed as a continuous wave (CW) which is TM polarized in the following calculations.

3. SIMULATION OF TWO TYPES OF TWO LOGIC GATES

3.1. Realization of the XOR Logic Gate

We chose ports B and C as two input ports and the port A as an idle port. Here, we propose the amplitude of the electric field of the incident wave is 100 V/m. When the incident waves of the same amplitude and phase are simultaneously injected into both port B and C, the destructive interference will occur between the two light beams due to their phase difference equals to π . If any input port is injected into light, the higher light power can be obtained at the output port D. It is obviously that no light propagates without input waves. The distributions of the electric field are shown in Figs. 3(a)–(c), and we can conclude that the scheme realize the XOR logic gate.

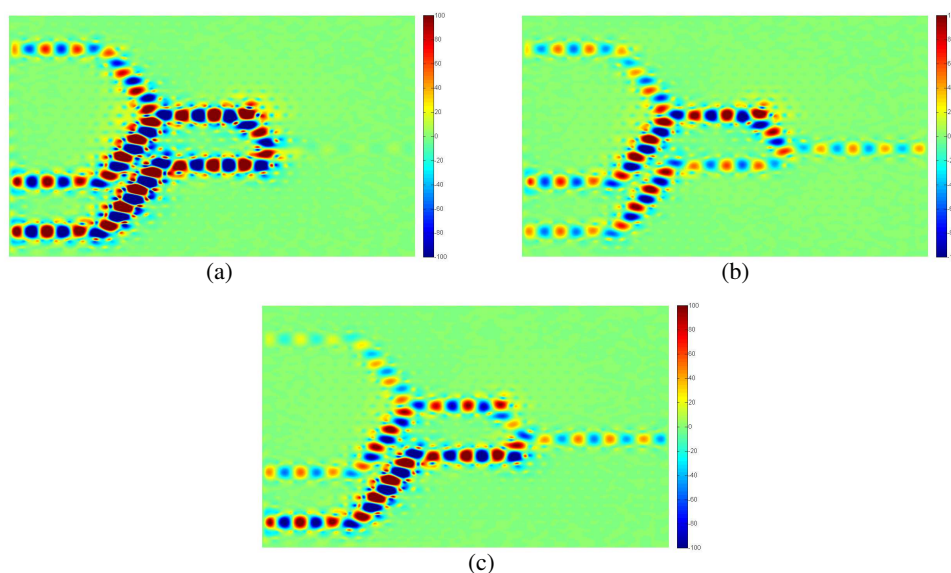


Figure 3: (a) The electric distribution as $E_C = E_B = E$. (b) The electric distribution as $E_B = E, E_C = 0$. (c) The electric distribution as $E_C = E, E_B = 0$.

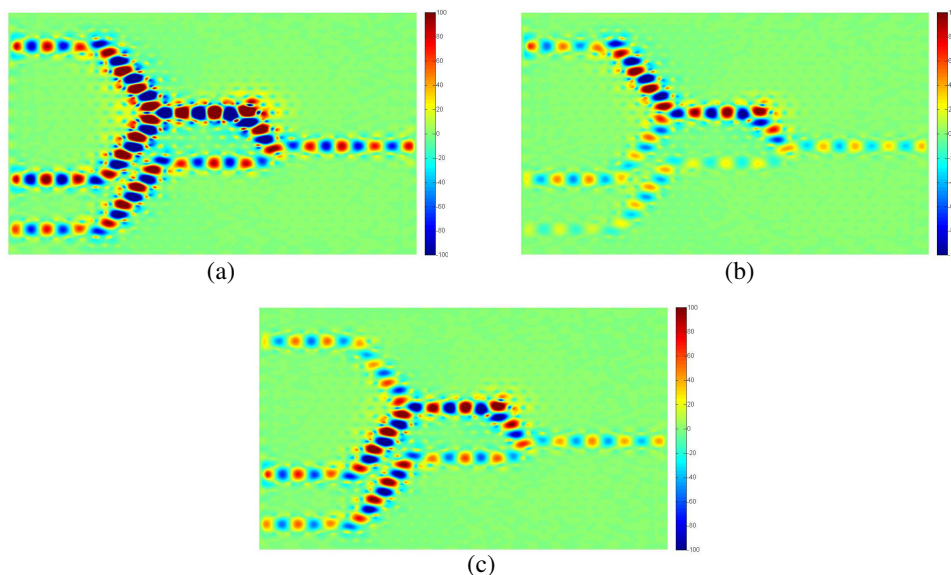


Figure 4: (a) The electric distribution as $E_A = E_B = E$. (b) The electric distribution as $E_B = 0, E_A = E$. (c) The electric distribution as $E_B = E, E_A = 0$.

3.2. Realization of the OR Logic Gate

If we consider ports A and B as two input ports and the port C as an idle port. When the two incident waves with the same amplitude and phase are excited at both port A and B, the constructive interference occurs. If any input port is injected into light, the higher light power can be obtained at the output port D. If no input wave is injected into any of the input port, there will be no light power obtained at output port D. The distributions of the electric field are shown in Figs. 4(a)–(c), and the scheme is considered as OR logic gate.

4. CONCLUSIONS

In this paper, the design of two types of logic gates in 2D photonic crystals is proposed and higher light contrast ratio between logic state “1” and “0” can be obtained by FDTD method. The results show that this configuration is helpful in optical device compactness and integration and significant to optical communications.

ACKNOWLEDGMENT

This work was supported by the supports from the National Natural Science Foundation of China (Grant No. 61307052), Chinese Specialized Research Fund for the Doctoral Program of Higher Education (grant No. 20123218110017), the Jiangsu Province Science Foundation (Grant No. BK2011727), the Foundation of Aeronautical Science (No. 20121852030) and Open Research Program in Jiangsu Key Laboratory of Meteorological Observation and Information Processing (Grant No. KDXS1207).

REFERENCES

1. Tripathy, S. K., S. Sahu, C. Mohapatro, and S. P. Dash, “Implementation of optical logic gates using closed packed 2D-photonic crystal structure,” *Optics Communications*, Vol. 285, 3234–3237, 2012.
2. Christina, X. S. and A. P. Kabilan, “Design of optical logic gates using self-collimated beams in 2D photonic crystal,” *Photonic Sensors*, Vol. 2, No. 2, 173–179, 2012.
3. Rani, P., Y. Kalra, and R. K. Sinha, “Realization for AND gate in Y shaped photonic crystal waveguide,” *Optics Communications*, 227–231, 2013.
4. Tang, C., X. Dou, Y. Lin, H. Yin, B. Wu, and Q. Zhao, “Design of all-optical logic gates avoiding external phase shifters in a two-dimensional photonic crystal based on multi-mode interference for BPSK signals,” *Optics Communications*, Vol. 316, 49–55, 2014.
5. Armenise, M. N., C. E. Campanella, C. Ciminelli, F. Dell’Olio, and V. M. N. Passaro, “Phononic and photonic band gap structures: modeling and applications,” *Physics Procedia*, Vol. 3, 357–364, 2010.
6. Sedghi, A. A., M. Kalafi, A. Soltani Vala, and B. Rezaei, “The influence of shape and orientation of scatterers on the photonic band gap in 2D metallic photonic crystals,” *Optics Communications*, Vol. 283, 2356–2362, 2010.
7. Isfahani, B. M., T. A. Tameh, N. Granpayeh, and A. R. M. Javan, “All-optical NOR gate based on nonlinear photonic crystal microring resonators,” *J. Opt. Soc. Am. B*, Vol. 26, 1097–1102, 2009.
8. Yang, Y. P., K.-C. Lin, I. C. Yang, K. Y. Lee, Y. J. Lin, W. Y. Lee, and Y. T. Tsai, “All-optical photonic crystal AND gate with multiple operating wavelength,” *Optics Communications*, Vol. 297, 165–168, 2013.
9. Zhang, H., S. Liu, X. Kong, L. Zhou, C. Li, and B. Bian, Comment on “Photonic bands in two-dimensional micro plasma array. I. Theoretical derivation of band structures of electromagnetic waves,” [*J. Appl. Phys.*, Vol. 101, 073304, 2007], *Journal of Applied Physics*, Vol. 110, No. 2, 026104, 2007.
10. Kunz, K. S. and Luebber, *The Finite Difference Time Domain Method for Electromagnetics*, CRC Press, Boca Raton, FL, 1993.

Low Reflectance GaAs Nano-cones Fabricated by Colloidal Lithography for Solar Cells

Nan Liu, Yu Hu, and Jian-Jun He

State Key Laboratory of Modern Optical Instrumentation, Centre for Integrated Optoelectronics
Department of Optical Engineering, Zhejiang University, Hangzhou 310027, China

Abstract— In this paper, we demonstrate a new method of fabricating large-area well-ordered nano-cones using colloidal lithography and inductively coupled plasma (ICP) dry etching, and discuss the anti-reflectance performance. In the fabrication, we use SiO₂ nano-particles as the mask. Its selectivity in different reacting gases in ICP can result in different shapes of nanostructures. Before the etching, we use methanol-assisted self-assembly at the air/water interface to form the patterns. Different ICP etching recipes are used to form rod-shaped and cone-shaped nanowires with the same height and period. The resultant nano-cone structures are well-shaped with smooth side walls. After the fabrication, the anti-reflection performance is measured and compared, which shows that cone-shaped nanowires can reduce the surface reflection to lower than 4% over the wavelength range of 400–900 nm, while nano-rods can only keep this value at approximately 6%. Theoretical simulations are also carried out using Comsol, which confirm that nano-cones provide better anti-reflectance performance.

1. INTRODUCTION

Semiconductor nanostructures have attracted great attention for photovoltaic applications. Solar cells with surface modified by nanowires are demonstrated to have much lower reflectance, and thus higher absorption of photons. The improved light harvesting will result in a comparatively higher power conversion efficiency (PCE).

Abundant researches have been made on Si substrates. However, considering the promising application of GaAs nanowires for solar cells [1, 2], low cost and practical nanostructuring methods on III-V materials are in great demand. Generally, III-V compound semiconductor nanowires are fabricated via chemical vapor deposition (CVD), molecular beam epitaxy (MBE), and vapor-liquid-solid (VLS) mechanism [3, 4]. However, these methods require complex procedure and expensive equipment, which have prevented the technology from wide application and mass production. Colloidal lithography is a very appealing alternative choice for patterning nanostructures without using sophisticated equipment and is far less time consuming. In our earlier work, we succeeded in fabricating nano-rods on GaAs substrates using colloidal lithography and ICP dry etching [5]. However, in practical use, the cylindrical shape makes it difficult to fill the gaps between adjacent nano-rods with other materials to form electrodes [6] or p-n junctions [1, 2]. Hence, in this paper, a cone-shaped nanostructure is introduced to mitigate this problem. As for the patterning, we also present a new method of fabricating large-area well-ordered patterns using methanol-assisted self-assembly at the air/water interface instead of spin-coating. The fabricated patterns are uniformly-distributed and the area can be as large as $2 \times 2 \text{ cm}^2$, or even larger. Lower reflection is obtained as compared to nano-rods with the same period and height.

2. FABRECAATION METHOD

We use methanol-assisted self-assembly [7, 8] to form a large-area uniformly-distributed SiO₂ nano-particle mask, as shown in Figure 1. First, we treat the cleaned GaAs substrate with oxygen plasma in ICP to improve its hydrophobicity. Then deionized water is dropped onto the wafer surface to form a 2 mm-thick water film, into which we continuously and slowly inject the well-mixed aqueous suspensions with SiO₂ nano-spheres. The methanol-water mixture carries the SiO₂ spheres to water film surface, which quickly disperse. After the sample is dried up, the nanoparticles are left self-assembled at the sample surface.

In order to obtain a well-ordered monolayer of nano-spheres, it is essential to inject an appropriate amount of the suspension liquid. The SiO₂ nano-sphere number n in unit volume of suspension liquid is given by

$$n = 6w / (\pi Q D^3) \quad (1)$$

where w is the SiO₂ sphere content (in weight) in unit volume, and Q and D are the density and diameter of the SiO₂ spheres, respectively. The needed volume V of the suspension liquid should

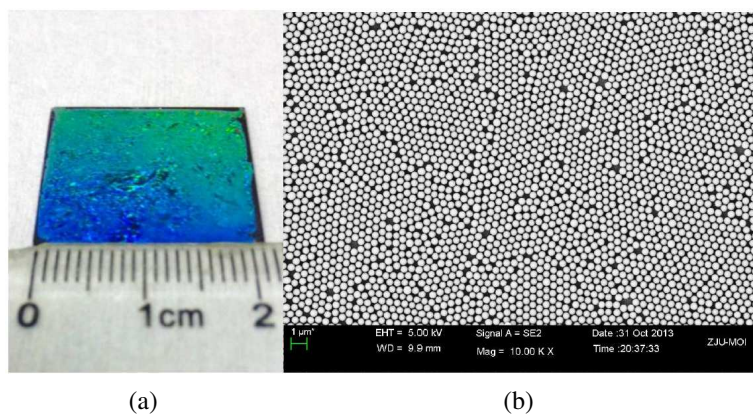


Figure 1: (a) Photo of a self-assembled SiO_2 nano-spheres sample showing iridescent color, and (b) the top view by SEM.

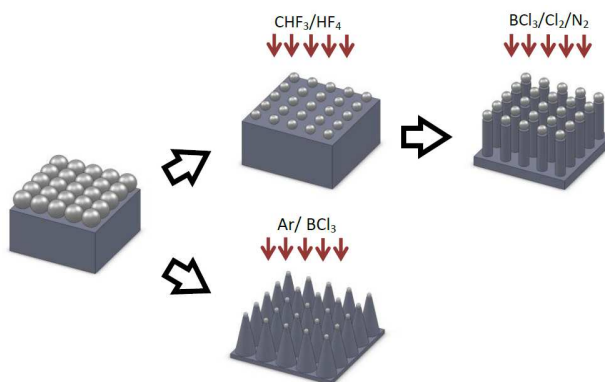


Figure 2: Different procedure of fabricating nano-rods and nano-cones.

satisfy

$$\frac{\pi SQD}{6w} < V < \frac{2SQD}{3w} \quad (2)$$

where S is the area of the wafer.

After the self-assembly process, etching of GaAs is performed by ICP (Oxford Plasmalab System 100) using Ar/ BCl_3 chemistry. BCl_3 is the main reactive gas for etching GaAs, while the accelerated Ar plasma provides a non-selective etching on both SiO_2 and GaAs. The two gases, with a ratio of 1 : 3, result in the cone-shaped nanostructure, as shown in Figure 2.

Figure 3 shows the SEM images of the fabricated nano-cones. For nano-rods, we use a $\text{BCl}_3/\text{Cl}_2/\text{N}_2$ chemistry instead to obtain vertical side walls. BCl_3 and Cl_2 provide high selectivity in etching GaAs under SiO_2 mask, while N_2 generates a passivation layer to improve smoothness and verticality [9].

3. RESULTS AND DISCUSSIONS

Figure 4 shows the simulated and measured reflectance of the nano-cone sample, compared with those of a nanorode sample and a GaAs substrate. For comparison, the etched nano-rods have the same period and height as the nano-cones. The simulation was performed using the finite element method [10]. Both the simulation and experimental results show that the nano-cone sample has lower reflectance compared to the nano-rod sample, while both exhibit significantly lower reflection compared to the GaAs substrate. The valleys of both nano-rod and nano-cone curves at 500 nm in the calculated spectra are due to the grating effect resulted from the assumption of perfect periodicity, which are absent in the measured spectra. The oscillations in the nano-rod reflection spectra are due to Fabry-Perot effect inside the cylindrical structure, with a flat top playing the role as the cavity mirror. The fact that the nano-cones exhibit better anti-reflectance performance than nano-rods can thus be attributed to the non-reflective sharp tips. In the measured spectra of

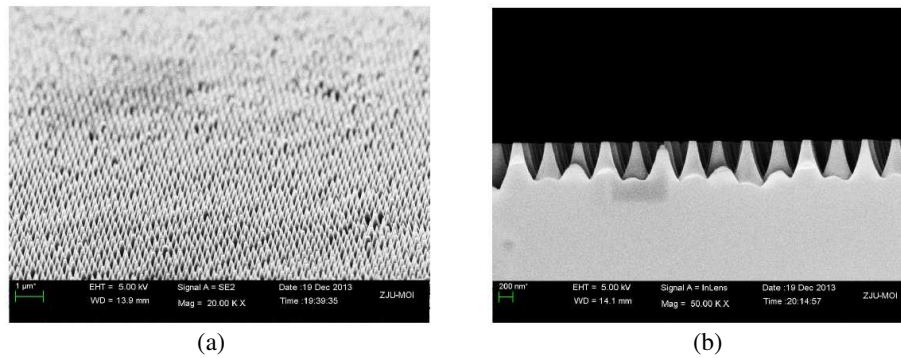


Figure 3: (a) Top view and (b) side view of fabricated nano-cones by SEM.

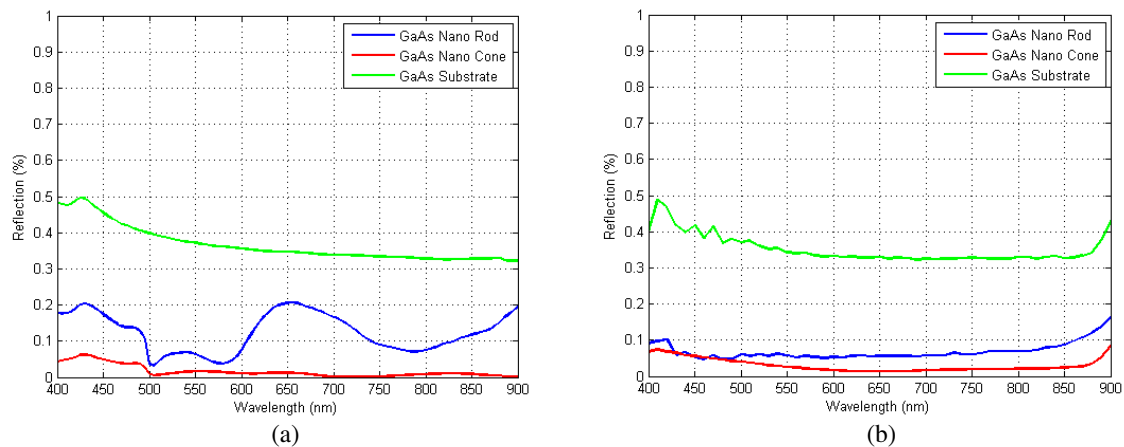


Figure 4: (a) Simulated and (b) measured reflectance of nano-cone and nano-rod modified surfaces.

Fig. 4(b), the reflectance increases after 870 nm, for which the substrates become transparent, are due to artifact of back reflection from the sample holder.

4. CONCLUSION

In conclusion, we fabricated a large-area uniformly-distributed GaAs nano-cones by colloidal lithography and ICP dry etching. The nano-cone structure has smooth side walls and provides anti-reflectance performance better than that of nano-rod structure.

ACKNOWLEDGMENT

The authors thank R. R. LaPierre of McMaster University for helpful discussions. This work was supported by the Ministry of Science and Technology of China (Grant No. 2010DFA61370).

REFERENCES

1. Bi, H. and R. R. LaPierre, "A GaAs nanowire/P3HT hybrid photovoltaic device," *Nanotechnology*, Vol. 20, No. 46, 465205, 2009.
2. Chao, J.-J., S.-C. Shiu, S.-C. Hung, and C.-F. Lin, "GaAs nanowire/poly (3,4-ethylenedioxythiophene): poly(styrenesulfonate) hybrid solar cells," *Nanotechnology*, Vol. 21, No. 28, 285203, 2010.
3. Mohseni, P. K., C. Maunders, G. A. Botton, and R. R. LaPierre, "GaP/GaAsP/GaP core-multishell nanowire heterostructures on (111) silicon," *Nanotechnology*, Vol. 18, No. 44, 445304, 2007.
4. Asoh, H., A. Uehara, and S. Ono, "Nanopatterning of Si substrate using nanospheres as a mask for localized anodization," *Japanese Journal of Applied Physics*, Vol. 43, Part 1, No. 8A, 5667, 2004.

5. Chen, K., M. Li, J.-J. He, and R. LaPierre, “GaAs nanowires fabricated using colloidal lithography and dry etching,” *IEEE Asia Communications and Photonics Conference and Exhibition*, 2011.
6. Liang, D., Y. Kang, Y. Huo, Y. Chen, Y. Cui, and J. S. Harris, “High-efficiency nanostructured window GaAs solar cells,” *Nano Letters*, Vol. 13, No. 10, 4850–4856, 2013.
7. Ngo, H. T., H. N. Wang, A. M. Fales, and T. Vo-Dinh, “Label-free DNA biosensor based on SERS molecular sentinel on nanowave chip,” *Analytical Chemistry*, Vol. 85, No. 13, 6378–6383, 2013.
8. Dai, Z., Y. Li, G. Duan, L. Jia, and W. Cai, “Phase diagram, design of monolayer binary colloidal crystals, and their fabrication based on ethanol-assisted self-assembly at the air/water interface,” *ACS Nano*, Vol. 6, No. 8, 6706–6716, 2012.
9. Volatier, M., D. Duchesne, and R. Morandotti, “Extremely high aspect ratio GaAs and GaAs/AlGaAs nanowave-guides fabricated using chlorine ICP etching with N₂-promoted passivation,” *Nanotechnology*, Vol. 21, No. 13, 134014, 2010.
10. Hu, Y., R. R. LaPierre, M. Li, K. Chen, and J.-J. He, “Optical characteristics of GaAs nanowire solar cells,” *Journal of Applied Physics*, Vol. 112, No. 10, 104311, 2012.

Experimental Analysis of Thin Graphite Periodic Structures in the THz Band

M. P. M. Colleoni and B. Vidal

Nanophotonics Technology Center, Universitat Politècnica de València
8F Building, Camino de Vera, sn, Valencia 46022, Spain

Abstract— The THz gap has attracted considerable interest in the last decade in a wide range of applications (from astronomy to biology) due to the low energy of the THz waves and their capability to provide chemical recognition and non-destructive inspection. To implement THz-based solutions, a wide range of components have been developed and efforts are being done to reduce the system cost through the use of cost effective materials.

This presentation analyzes the development of metal wire grids by using the conductive properties of graphite. The aim is drawing the wire grid using a simple graphite lead pencil on standard paper. This would reduce the cost of several wire grid base components, such as polarizers or filters.

An 8B pencil is used because of its high graphite contents. Parameters such as the pitch of the structure and its fill factor are set to study the behavior of the metal grid in a frequency range from 0.1 to 0.7 THz. An average pitch of 800 micrometers with a fill factor of 0.8 corresponds to an ER of 2dB. The samples are analyzed using a fiber-based pulsed THz Time Domain Spectrometer in transmission mode. An ultrafast laser pulse impinges on a photoconductive antenna generating the THz beam that is detected by a similar switch. Preliminary experimental results show that the increase of the angle between the horizontally-polarized incoming electric field and the graphite periodic structure corresponds to a decrease of the THz absorption, hinting at a polarizer behavior.

1. INTRODUCTION

Technology developments along the last decades allow the use of almost the whole energy range of the electromagnetic spectrum. The different features of each frequency range provide valuable tools to investigate physical processes of different energy magnitudes. The THz range, that comprises frequencies from 100 GHz to 3 THz, is quite interesting because it allows the analysis of both the macro and the microscope world by using non-invasive techniques. Many efforts are being made to explain the interaction of THz waves with matter. Recent studies demonstrated the transparency of the THz to some common materials such as cotton, wool or leather but also wood and paper [1]. THz radiation is also used to investigate biological systems, for example to define a label-free sensing approach for the characterization of genetic material. Researchers demonstrated that is possible to identify the binding DNA state, by analyzing changes in its refractive index [2]. They are also usually employ in the analysis of chemical composition of medicines or unknown compounds [3, 4], that is quite useful both in the pharmaceutical industries and in terms of security issues.

Different methods for THz generation and detection have been developed, which allow THz time-domain spectroscopy (THz-TDs) and the THz frequency spectroscopy (FDS), THz imaging and THz ad-hoc devices [5].

Such a variety of application requires suitable and cost effective tools and the implementation of quasi-optical elements working in the THz frequency range plays an important role.

Retarders, polarizers, and phase shifters, for example, are mainly produced by using complicated and expensive techniques, such as photolithography (imprinting on a photoresist layer on an infrared transmitting layer) [6] or chemical evaporation of a metal on an appropriate substrate.

With the aim of reducing the cost of the THz systems [7], we try to identify a polarizing behavior of a metal wire grid based on the conductive properties of graphite and common paper.

2. EXPERIMENTAL PROCEDURE

Due to its high graphite content ([8, 9]), an 8B lead pencil was used to deposit a thin graphite layer on common printable paper. A periodic pattern was designed and printed on the sheet and then it was used as a guide to draw a periodic structure. The key parameters that has to be taken into account when planning a wire metal grid are the pitch (from center to center), the line width and the fill factor, that is the ratio between the wire and the pitch width. The polarizing effect takes

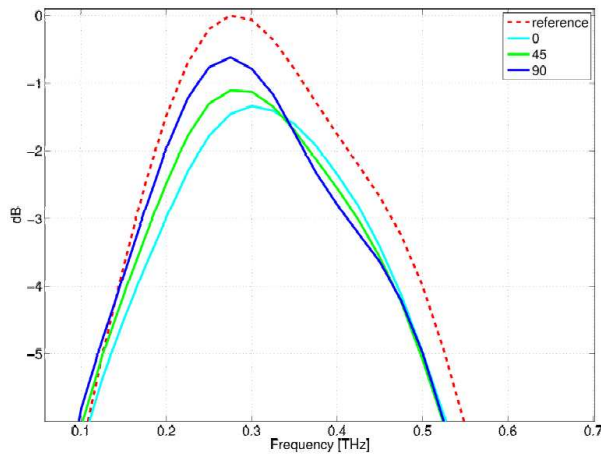


Figure 1: Frequency THz spectrum of the 0.800 mm pitch wire metal grid. The plot shows the THz power in the 0, 45, 90 degrees configuration. The dichroic effect is noticeable in the frequency range from 0.1 THz to 0.4 THz. The THz frequency amplitude decreases as the angle between the incoming THz beam and the direction of the grid decreases.

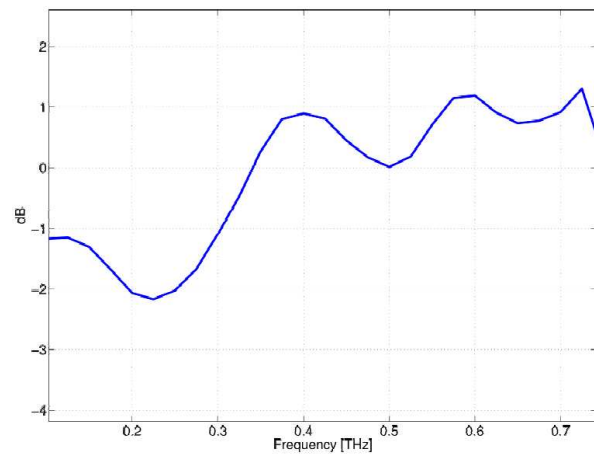


Figure 2: ER of the metal wire grid based on graphite as a function of frequency.

place as long as the pitch is a fraction of the incoming THz wavelength [10]. Otherwise, the periodic structure exhibit a diffraction effect. The sample area is $35 \times 35 \text{ mm}^2$ with a pitch of a 0.8 mm and a wire width of 0.6 mm, that lead to a fill factor of about 0.8. As the graphite deposition was hand made, it wasn't possible to ensure the deposited graphite amount, but the integrity and precision of the designed wires was checked by scanning them with an optical microscope.

To characterize the performance of the graphite-based polarizers, a transmission fiber THz-TDS setup was used. A femtosecond pulsed laser at 1550 nm provides 100 fs excitation pulses, at 100 MHz repetition rate. The pulse is split into two branches: the sampling one that impinges on a photoconductive switch that generates the THz beam, and the probe one that is used to sample the THz waveform in the photoconductive antenna that detects the THz beam. An optical delay line is used to scan the THz wave and lock-in detection is employed to improve the dynamic range of the measurement [11].

The metal wire grid was stuck with tape on an adjustable holder and placed in the optical path in the collimation area [12]. All the measurements were performed at normal incidence, while the angle θ between the incoming THz beam and the direction of the grid was changed by rotating the holder.

In Figure 1 the frequency THz spectrum is displayed. Each line is calculated by considering the blank paper sheet as reference. It can be noticed that to a decrease of the angle θ corresponds a decrease in the amplitude of the detected photocurrent signal. In particular, when the direction of the wire metal grid is perpendicular to the polarization of the incoming THz beam ($\theta = 90^\circ$) a maximum of transmission is detected, while a minimum corresponds to the parallel direction ($\theta = 0^\circ$). These results agree with the dichroism effect of selective absorption, that assets that only the components of the electric field parallel to the grid transmission axis pass the polarizer.

To evaluate the polarizing features of the graphite-based wire metal grid, its Extinction Ratio (ER) is calculated as a function of the frequency (Figure 2).

The achieved ER of 2 dB supports the idea that the wire metal grid based on graphite could be work as a polarizer.

3. CONCLUSION

A metal wire grid polarizer drawn using ordinary lead pencil based on graphite on common blank sheet paper has been experimentally demonstrated. Due to the conductive properties of the graphite, the wire grid shows a polarizing behavior based on the dichroism effect. The low-cost and the availability of the employed materials make this solution attractive in terms of cost reduction. Further studies have to be performed to achieve a better ER and to emphasize the polarizing

behavior of the wire metal grid. Methods to improve their durability and robustness are, among others, issues that play a key role in the development of a THz polarizer.

ACKNOWLEDGMENT

Spanish Ministry of Economy and Competitiveness, project TEC2012-35797.

REFERENCES

1. Gatesman, A. J., A. Danylov, T. M. Goyette, J. Dickinson, R. H. Giles, W. Goodhue, J. Waldman, W. E. Nixon, and W. Hoen, "Terahertz behavior of optical components and common materials," *SPIE Proceedings*, Vol. 6212, 2006.
2. Bolivar, P. H., M. Brucherseifer, M. Nagel, H. Kurz, A. Bosserhoff, and R. Büttner, "Label-free probing of genes by time-domain terahertz sensing," *Phys. Med. Biol.*, Vol. 47, 3815–3821, 2002.
3. Fischer, B., M. Hoffmann, H. Helm, G. Modjesch, and P. U. Jepsen, "Chemical recognition in terahertz time-domain spectroscopy and imaging," *Semicond. Sci. Technol.*, Vol. 20, S246–S253, 2005.
4. Siegel, P. H., "Terahertz technology in biology and medicine," *IEEE Transactions on Microwave Theory and Techniques*, Vol. 52, No. 10, 2004.
5. Tonouchi, M., "Cutting-edge Terahertz technology," *Nature Photonics*, Vol. 1, 2007.
6. Yamada, I., K. Takano, M. Hangyo, M. Saito, and W. Watanabe, "Terahertz wire-grid polarizers with micrometer-pitch Al gratings," *Opt. Express*, Vol. 34, No. 3, 2009.
7. Scherger, B., M. Scheller, N. Vieweg, S. Cundiff, and M. Koch, "Paper terahertz wave plates," *Opt. Express*, Vol. 19, No. 25, 1064–1076, 2011.
8. Abraham, E., A. Younus, J. C. Delagnes, and P. Mounaix, "Non-invasive investigation of art paintings by Terahertz imaging," *Appl. Phys., A Mater. Sci. Process.*, Vol. 100, No. 3, 585–590, 2010.
9. Abraham, E., A. Younus, A. El Fatmy, J. C. Delagnes, E. Nguéma, and P. Mounaix, "Broadband terahertz imaging of documents written with lead pencils," *Opt. Commun.*, Vol. 282, 3104–3107, 2009.
10. Polley, D., A. Ganguly, A. Barman, and R. K. Mitra, "Polarizing effect of aligned nanoparticles in terahertz frequency region," *Opt. Lett.*, Vol. 38, No. 15, 2013.
11. Jepsen, P. U., R. H. Jacobsen, and S. R. Keiding, "Generation and detection of terahertz pulses from biased semiconductor antennas," *J. Opt. Soc. Am. B*, Vol. 13, No. 11, 1996.
12. Grischkowsky, D., S. Keiding, M. van Exter, and C. Fattinger, "Far-infrared time-domain spectroscopy with terahertz beams of dielectrics and semiconductors," *J. Opt. Soc. Am. B*, Vol. 7, No. 10, 1990.

Analysis, Design and Simulation of a Compact Wide Band VHF High Power Tubular Band Pass Filter

Zohre Pourgholamhossein, Gholamreza Askari,
Hamid Mirmohammad Sadeghi, and Mehdi Fadaei
Information and Communication Technology Institute (ICTI)
Isfahan University of Technology (IUT), Isfahan 84156, Iran

Abstract— This paper present analysis, design and simulation of a compact VHF high power tubular band pass filter terminated with capacitor. In this analysis all effects of critical distributed and lumped structures are considered. Full wave simulator (HFSS) is used to analyze and optimize the filter performance and high power analysis done to achieve high power handling. The peak power in this filter considered above 10 kW and average power of about 1200 Watt. The insertion loss of VHF BPF filter is less than 0.6 dB and 0.2 dB bandwidth is about 10 MHz at the center frequency of 220 MHz, the stop-band attenuation is more than 30 dB at 205 MHz and 235 MHz (shape factor is 30 dB/Oct), return loss is better than 20 dB and so VSWR better than 1.2 in whole pass band. Moreover, the filter is compact in size and the dimensions are 4.5 cm \times 50 cm.

1. INTRODUCTION

Lumped element filters are used at microwave frequency to about 18 GHz [1]. Dimensions of these filters are much smaller than distributed filters, which is their major advantages. However the use of larger distributed filters is suitable when insertion loss and power handling are major concern. Actually one of the most important problems of high power transmitter is harmonic radiation and the interfering effects on other communication system. Major efforts are been done to reduce the interferences. To remove the spurious radiation various filters have been presented in [2–4]. Also various type of high power filters in [5, 6] have been proposed. These filters constructed by dielectric resonator and sinusoidal quasi periodic waveguide structures. In order to solve the large dimension and power handling difficulties, semi lumped technology was used. Several filters were realized in a semi lumped approach using both air wound inductors and coaxial transmission line or surface mounted (SMT) capacitors and microstrip lines. Tubular band pass filters are narrowband semi lumped approximation of band pass filters. Significant developments have taken place since 1998 [7]. Super conductor technology and microstrip lumped element circuits has been introduced as a tubular BPF with fractional band width about 0.6% (narrowband). Of course when power handling is important, super conducting filter technology is not employed. The later method has been presented in 2006 [8], as a wide band case which is tubular filter terminated with inductor. Generally tubular filters may be classified in two categories, one defined as a tubular filter terminated with categories, one defined as a tubular filter terminated with capacitor as shown in Fig. 1 [7, 9], and other as a tubular filter terminated with inductor, which is shown in Fig. 2 [8].

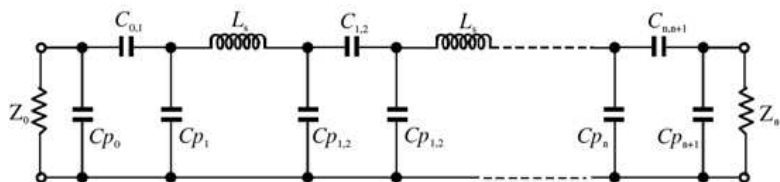


Figure 1: Semi lumped element filter terminated with capacitor [2].

In both of them each node containing a ground and all resonators are the same type. This paper present analysis, design and simulation of a VHF coaxial high power tubular band pass filter terminated with capacitor. In Section 2 basic filter designs will be introduced, filter geometry and prototype values are discussed. The realization of filter is presented in Section 3 and the physical parameters of capacitors and inductors are obtained. In Section 4 simulation and optimization of the designed filter terminated with capacitor is presented. By using the approach suggested for the study of filter terminated with inductor [8], the optimization involves computer aided optimization and full wave EM simulator. Therefore to achieve filter with high power handling and harmonic

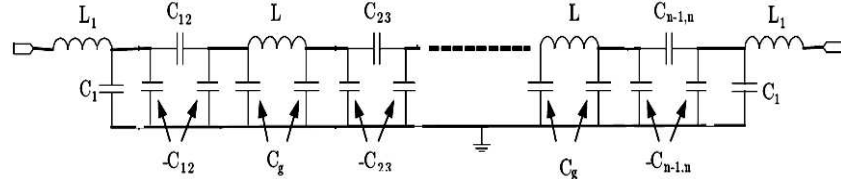


Figure 2: Semi lumped element filter terminated with inductor [8].

spurious rejection, semi lumped approach is considered. Actually the filter was realized with lumped element and transmission line segments. High power analysis is done in Section 5. In this analysis all effects of critical distributed and lumped elements are considered. Finally conclusions are drawn in Section 6.

2. BASIC FILTER DESIGN

Detailed design procedures of initial values of lumped tubular filters can be used in several texts [7, 9]. The design process of filter terminated with capacitors is summarized as follow. First typical LPF using impedance inverter (Fig. 3(a)) is transformed to corresponding BPF (Fig. 3(b)) by applying the transformation described in [10], replacing inductors L_{ai} in Fig. 3(a) with $L_{si} = (w\omega_0/\omega_c)L_{ai}$ and $C_{si} = 1/(\omega_0^2 L_{si})$ in Fig. 3(b). After that the impedance inverter values are designed based on normalized element values:

$$K_{01} = \sqrt{\frac{R_0 w \omega_0 L_S}{\omega'_1 g_0 g_1}} \quad (1a)$$

$$K_{i,i+1} = \frac{w \omega_0 L_S}{\omega'_1} \sqrt{\frac{1}{g_i g_{i+1}}} \quad (1b)$$

$$K_{n,n+1} = \sqrt{\frac{R_{n+1} w \omega_0 L_S}{\omega'_1 g_n g_{n+1}}} \quad (1c)$$

where w is the fractional bandwidth, ω_0 is normalized cut off frequency equal to 1 rad/s, L_S is inductor that specified by user, in this work the inductor chosen as 150 nH. Impedance inverter can use the tee of capacitors network. Then split the series capacitors (C_{Si}) of series resonators into two capacitors ($2C_{Si}$), one on each side of the inductors, negative capacitors between inductor in middle stages is observed and tee network capacitors converted to the exact equivalent pi . But negative capacitors at the input and output termination couldn't be realized, therefore use transformation was described in [4]. Finally the equivalent circuit of BPF is shown in Fig. 3(c).

The values of series capacitors and shunt capacitors of input and output pi networks, C_{01} and $C_{n,n+1}$ are achieved respectively.

$$C_{01} = \sqrt{\frac{Z_0 (2\omega_0 C_S K_{01})^2}{Z_0^2 + (2\omega_0 C_S K_{01})^2} \cdot \frac{(1 + Z_0^2 \omega_0^2 C_{X0}^2)}{Z_0 \omega_0^2}} \quad (2)$$

$$C_{P0} = C_{X0} - C_{01} \quad (3)$$

$$C_{P1} = \frac{1}{\omega_0} \left[\frac{Z_0^2 (2\omega_0 C_S)}{Z_0^2 + (2\omega_0 C_S K_{01})^2} - \frac{\omega_0 C_{01} (1 + Z_0^2 \omega_0^2 C_{P0} C_{X0})}{1 + (Z_0 \omega_0 C_{X0})^2} \right] \quad (4)$$

In this equations C_{X0} is chosen as that capacitors of C_{P0} and C_{P1} be realizable and is better to be equal. Therefore coupling and shunt capacitors, $C_{i,i+1}$ and $C_{Pi,i+1}$ between inductors, easily achieved by:

$$C_{i,i+1} = \frac{\left(\frac{2C_S}{1 - 2C_S \omega_0 K_{i,i+1}} \right)^2}{\frac{4C_S}{1 - 2C_S \omega_0 K_{i,i+1}} + \frac{1}{\omega_0 K_{i,i+1}}} \quad (5a)$$

$$C_{Pi,i+1} = \frac{\frac{1}{\omega_0 K_{i,i+1}} \left(\frac{2C_S}{1 - 2C_S \omega_0 K_{i,i+1}} \right)}{\frac{4C_S}{1 - 2C_S \omega_0 K_{i,i+1}} + \frac{1}{\omega_0 K_{i,i+1}}} \quad (5b)$$

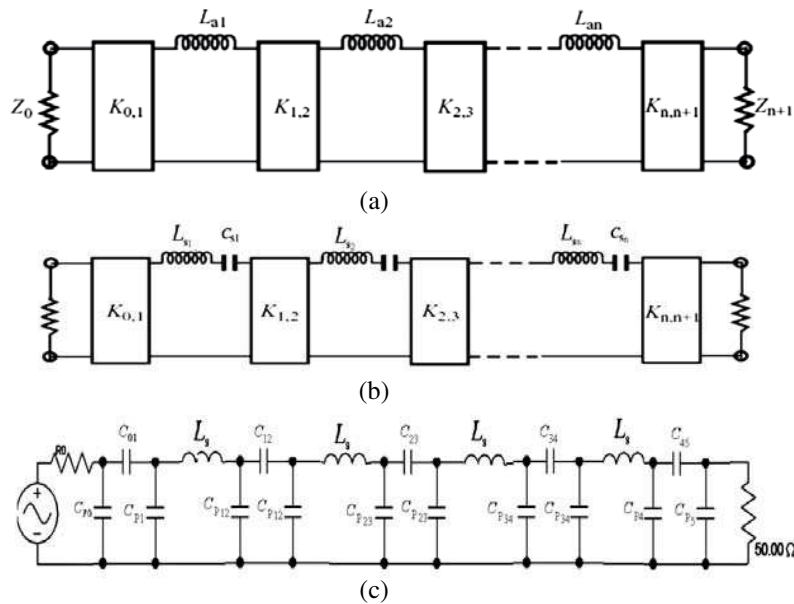


Figure 3: (a) Shunt-C coupled series resonator band pass filter, (b) band pass filter using admittance inverter, (c) equivalent circuit of tubular BPF.

Therefore all parameters of equivalent circuit are obtained. Where C_S is series capacitor in series resonance circuit and it is given by:

$$C_S = \frac{1}{\omega_0^2 L_S} \quad (6)$$

In this paper it's desired to design a filter with band ripple 0.01 dB, fractional bandwidth of 5% and a shape factor that cause 30 dBc at 10 MHz out band offset. Based on the previous equations, the obtained values of reactive elements are listed in Table 1.

Table 1: The lumped element values of equivalent circuit obtained by design.

Reactive lumped element	Designed values
$C_{P0} = C_{P5}$	3.32 (PF)
$C_{01} = C_{45}$	3.98 (PF)
$C_{P1} = C_{P4}$	3.32 (PF)
L	150 (nH)
$C_{12} = C_{34}$	0.6925 (PF)
$C_{P12} = C_{P34}$	6.35 (PF)
C'_{P12}	6.35 (PF)
C_{23}	0.506 (PF)
C_{P23}	6.5 (PF)

3. REALIZATION OF THE FILTER

For realization of the filter in coaxial form, physical parameters of distributed and lumped element should be specified. Consider the topology of four orders Chebyshev band pass filter in Fig. 4, realized by five series coupling capacitors and four resonators that constructed by lumped and distributed element. All inductors are the same value and can be chosen optionally. These inductors have been realized by wire wound air core inductors, shunt capacitors by the gap between metal disks and outer metal tube, and coupling or series capacitors by dielectric gap between cross sections of metal disks as it is shown in Fig. 5. This figure illustrated the reactive elements which are used for practical implementation of this filter. Important criteria in choosing reactive elements such as inductors, dielectric gap and air gap is considering average and peak power handling which is discussed in Section 5. As known coaxial capacitors consist of two cylinders sharing the same axis.

This coaxial capacitor will have inner radius of r_d and outer radius of b . Also the distance between plates is the distance between two radiuses $t_1 = b - r_d$. In the case of which distance of between the inner and outer radius is small, the capacitance of coaxial capacitor is equal to parallel plate capacitor that is given by (7):

$$C_{\text{Parallel}} = -\frac{2\pi\epsilon l}{\ln \frac{b}{r_d}} = \frac{2\pi l \epsilon b}{b - r_d} \approx \epsilon \frac{A}{t_1} \quad (7)$$

where, A is the area of outer radius of coaxial capacitor. Series capacitors are:

$$C_{\text{Series}} = \epsilon \frac{S}{t_S} = \epsilon_0 \epsilon_r \frac{\pi r_d'^2}{t_S} \quad (8)$$

where t_S distance between round metal plates and $r_d' = r_d - r_s$ that r_s is radius of dielectric shaft cross from elements. Serial inductors are given by:

$$L = \frac{(Rn)^2}{10l_{\text{sim}} + 9R} \text{ (}\mu\text{H)} \quad (9)$$

R , l_{sim} are mean radius of core and length of coil (in inch), n is number of turn wound wire. For realizing of physical reactive elements as Table 1, primary parameters values have to choose optionally. Chosen diameter of copper wire, length of wound wire, diameter of Teflon core, diameter of aluminum disks and diameter of shaft dielectric, are listed in Table 2. Then by using (7)–(9), length of metal disk of shunt capacitors, dielectric thickness for series capacitors and number of wound turn are found.

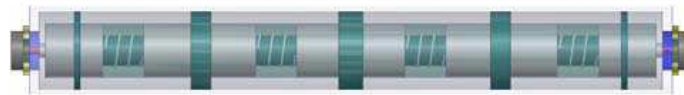


Figure 4: Configuration of a semi coaxial band-pass filter.

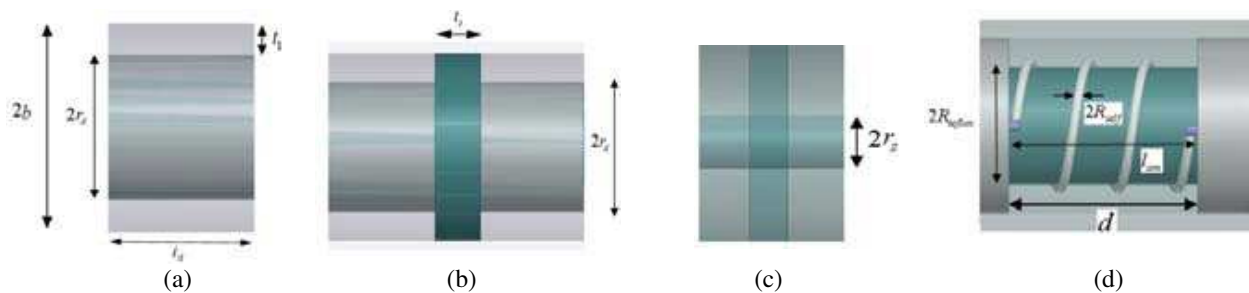


Figure 5: Physical realization of (a) reactive element, (b) shunt capacitor, (c) coupling series capacitor, (d) series inductor.

Table 2: The primary physical dimensions of elements have been chosen optionally by user (mm).

parameter	Values (mm)
Diameter of copper wire ($2R_{\text{self}}$)	1.6
Length of wound wire (L_{sim})	30
Diameter of Teflon core ($2R_{\text{tefflon}}$)	20
Diameter of coil of core (R)	$2R_{\text{tefflon}} + 2R_{\text{self}}$
Diameter of aluminum disks ($2r_d$)	35
Thickness of air (t_1)	8
Diameter of axial dielectric (r_s)	8

4. SIMULATION AND OPTIMIZATION OF THE DESIGNED FILTER

4.1. Optimization Procedure

After design and calculation of physical parameters, an electromagnetic simulation is done. To optimize the filter, due to the large number of parameters, it will be optimized by using electromagnetic simulator and computer aided design method. At the first step, all designed values of lumped element circuit of BPF, are simulated by ADS Agilent and then the frequency response is tuned. After that, designed n -order filter, will be divided into $2n + 1$ stages that consists π network capacitors or series inductors. In optimization procedure, the result of EM simulator (Ansoft HFSS) (for different physical parameters) will be compared with design analysis of ADS, to verify each other, thus exact values are determined. In this sequence, first stage will be optimized separately, and then the new stage will be added and optimized when the values of first stage remain steady and the process of increasing stage continues until $(n + 1)$ stage because of symmetrical structure of the filter. In addition, all metal disks have the same radius and thickness of dielectric sheet between metal disk and outer tube is constant along the filter so, at each step of optimization, maximum two or three parameters are changed and optimized.

4.2. Simulation Result

As described in the previous sections EM simulating by HFSS software is done. Usually frequency response of the filter structure is different from the design demands. So as mentioned, optimization should be performed. Each stages of filter one by one added to first stage. Variable parameters are length of wound wire, number of turn and length of disks. Because of symmetrical structure the processes of optimization for 6th to 8th stages are not required. Finally EM simulation is done for the whole filter by adding last stage (9th stage), (Fig. 6). As it is shown in Fig. 6, full wave analysis of the filter confirms the designed filter and performance of the full wave simulation of the complete structure, including coaxial connector and dielectric loss tangent. The filter has a center frequency of 220 MHz, 0.2 dB bandwidth of 10 MHz, insertion loss of about 0.6 dB, better than 30 dBc rejection in 10 MHz offset from the 0.2 dB bandwidth and a return loss better than 20 dB.

5. POWER-HANDLING ANALYSIS

It's necessary to use LPF or BPF filter at Output of high power microwave transmitters and receivers to prevent of harmonics in transmitting and interferences in receiving. So microwave filter in this application must be capable to handle the high power signals from high power amplifiers. Average power and peak power should be considered in high power handling. For average power, critical point is inductor, where the wire of inductors must have enough diameters to tolerate the current in the filter. The average input power is 1200 Watt and the input impedance is 50 Ohm. Thus, the average current is 5 A. Another important factor is breakdown that can destroy the filter component and performance by arcing. Breakdown voltage limit depends on RF circuit, structure geometry and RF frequency. To analysis of electrical field inside the filter, HFSS is used

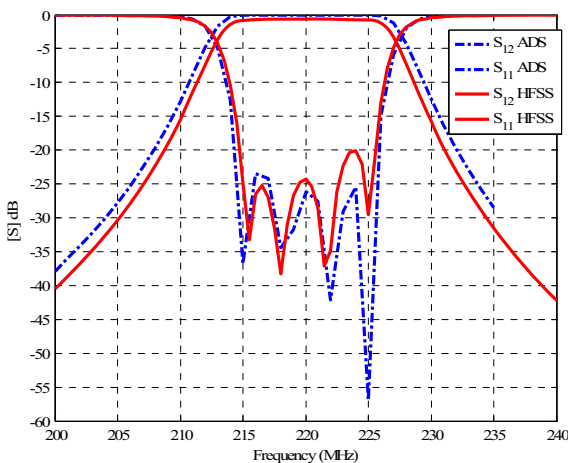


Figure 6: Simulated frequency response of the experimental band pass filter ((solid & dot-dash lines) on HFSS-ADS respectively).

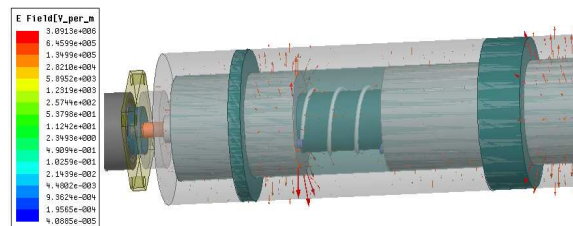


Figure 7: Vector E-field strength (V/m) across the filter in frequency 220 MHz.

as a simulator. Actually the voltage breakdown is influenced by the geometry and the dielectric strength. So for high power analysis, the critical parts across the filter should be considered. Two methods are used to enhance the breakdown voltage of the filter. The first one is using wider air gaps between disks and outer metal tube that can enhance breakdown voltages and the second method is using the thin dielectric sheet in air gaps. The Teflon (PTFE) in the gaps that can enhance the voltage breakdown to 15.74×10^6 v/m. A vector plot is used around arrows to illustrate the magnitudes and direction of electrical field which is shown in Fig. 7. It can be seen that the electric field strength in all over the filter is less than breakdown voltage in air (3×10^6 v/m) and Teflon (PTFE) with input power of 10 kW.

6. CONCLUSION

In this paper, a compact VHF semi lumped high power band pass filter is investigated based on the traditional tubular theory of the filter terminated with capacitors and Chebychev method. Analyzing of all effects of critical distributed and lumped structures were considered. The high power analysis of the filter in the realization structure was done. In the final simulation the complete practical structure were considered and optimization with the full wave analyzing software (Ansoft HFSS) were done. It is confirmed that the filter topology provides much better high power handling capability (about 10 kW). The final result are very close to design goal and filter has a center frequency of 220 MHz, 0.2 dB fractional bandwidth of 10 MHz, insertion loss of about 0.6 dB, better than 30 dBc rejection in 10 MHz offset from the 0.2 dB bandwidth, a return loss better than 20 dB and has a compact size (total length of 50 cm). Based on all experimental considerations in the full wave analysis and final results of the filter, this filter can be fabricated and use in many application which the presented in the feature works of the authors.

REFERENCES

1. Levy, R., R. V. Snyder, and G. Matthaei, "Design of microwave filters," *IEEE Transactions on Microwave Theory and Techniques*, Vol. 50, No. 3, 783, 793, Mar. 2002.
2. Stone, R. H., "High power microwave filter," *1964 General Electric Co. High Power Tube Symp.*, TWT Business Section, MD036, Palo Alto, Calif., 1960.
3. Price, V. G., "Measurement and control of harmonic and spurious microwave energy, final rept., change B," Contract AF30 (602)-1670, General Electric Microwave Lab., May 1960.
4. Yamashita, S. and M. Makimoto, "Miniaturized coaxial resonator partially loaded with high dielectric constant microwave ceramics," *IEEE Transactions on Microwave Theory and Techniques*, Vol. 31, 697–703, 1983.
5. Arregui, I., I. Arnedo, A. Lujambio, M. Chudzik, D. Benito, R. Jost, F. Gäortz, T. Lopetegi, and M. A. G. Laso, "A compact design of high-power spurious-free low-pass waveguide filter," *IEEE Microwave and Wireless Components Letters*, Vol. 20, No. 11, 595, 597, Nov. 2010.
6. Bunin, A., V. Gevorkyan, Y. Kazantsev, S. Mikhailin, and S. Vishnyakov, "Resonant section for Ku-band high-power band pass filter," *2010 IEEE Region 8 International Conference on Computational Technologies in Electrical and Electronics Engineering (SIBIRCON)*, 549, 551, Jul. 11–15, 2010.
7. Huang, Q. and J.-F. Liang, "Direct synthesis of tubular band pass filters with frequency-dependent inductors," *IEEE MTT-S, Digest*, 371–374, 1998.
8. Wu, B., T. Su, B. Li, and C.-H. Liang, "Design of tubular filter based on curve fitting method," *Journal of Electromagnetic Waves and Applications*, Vol. 20, No. 8, 1071–1080, 2006.
9. Hong, J. S. and M. J. Lancaster, *Microstrip Filters for RF/Microwave Applications*, Wiley, 2001.
10. Matthaei, G., et al., *Microwave Filters, Impedance-matching Networks, and Coupling Structures*, Artech House, 1980.

Analysis, Design and Implementation of a Broadband Coaxial-to-microstrip Transition for UWB Radars

Gholamreza Askari^{1,2}, Mahmoud Kamarei¹,
Mahmoud Shahabadi¹, and Hamid Mirmohammad Sadeghi²

¹School of Electrical and Computer Engineering, College of Engineering
University of Tehran, North Kargar St., Tehran, Iran

²Information and Communication Technology Institute
Isfahan University of Technology, Isfahan 84156, Iran

Abstract— In this paper a useful, simplex and broadband coaxial-to-microstrip transitions using GCPW, simple pre-transition, are designed and implemented. The GCPW, pre-transition section is utilized to provide a smooth transition from coaxial to microstrip. In this transition the effects of the field and impedance matching with considering possible fabrication errors in total performance are completely analyzed. Experimental results are very close with simulation results. The results of 50 mm length of Microstrip line with back-to-back transitions show that a ultra wideband transition with return loss better than -10 dB and in the worth case, total insertion loss is less than 1 dB up to 30 GHz. These good performances and its simplicity, easy fabrication and good performances make this proposed transition very useful in many applications such as UWB short range Radars up to 30 GHz and make it a very good candidate for higher frequencies.

1. INTRODUCTION

Microstrip lines are the most widely used planar transmission lines for microwave circuit applications due to their low cost and ease in circuit layouts [1]. Also in near mm-wave frequency band, some functional modules are realized by plane structure of hybrid integration, and again microstrip is the most common transmission line [2]. On the other hand, for most equipment used for microwave circuit measurements, coaxial structures are normally employed for signal inputs and outputs. Thus, coaxial-to-microstrip transitions are required [1]. Despite the impedance matching between the coaxial connectors and the microstrip lines, a discontinuity exists due to the different electromagnetic (EM) field distributions of these two transmission lines and so signal reflection and radiation are expected. These problems become worse when the operating frequencies are higher and having the same characteristic impedance does not always guarantee a good transition between two transmission lines at higher frequencies [3]. For the past few decades, many techniques have been proposed to improve the high-frequency performance of coaxial-to microstrip transitions by modifying the structures of coaxial connectors or microstrip lines for better matching of the EM field distributions at the transitions [3, 4–7]. However in some of these transitions, only the impedance is match in a narrow frequency bands and in some others, complicated structure, high cost and large size make them undesirable. Furthermore it is important to have simplex, low-cost and wideband coaxial-to-microstrip transition.

In this paper a useful, simplex and broadband transitions between Air-Coaxial SMA connector and microstrip line is designed and implemented. This transition is designed by the use of a simple and small size ground coplanar waveguide (GCPW) as a pre transition. The CPW and its various configurations such as GCPW have several attractive features in comparison with microstrip line. For example these lines have low wave propagation dispersion up to very high frequency [8]. There have been intensive studies on transition from CPW to other planner transmission lines [9–11]. However, in the conventional method that connects the coaxial inner conductor and CPW center conductor on the same plane, higher-order modes arise at the connection section. This results in the insertion of unnecessary reactance in the line at discontinuous sections in a serial or parallel manner thereby generating a large mismatch [11].

The GCPW, pre-transition section is utilized to provide a smooth transition from coaxial to microstrip. The signal and ground current paths through a transition are also critical and these paths must often be continuous and as close as possible together, to suppress radiation [4]. In this transition the effects of the field and impedance matching on the bandwidth are discussed. To study the effects of GCPW section on the transitions, electromagnetic fields of transition structure in different cut are completely analyzed with CST. Moreover the influence of the possible fabrication and assembly errors such as slightly gap, height of laminate, misalignment between microstrip

and center of SMA connector, excitation of higher order modes of SMA in connections and uncertainty of measurement instruments in total performance are completely analyzed and considered. The simulation results using CST and ADS softwares indicate that the bandwidth is increased to maximum operating frequency of SMA connector and The experimental results are in good agreement with simulation results. Insertion loss less than 1 dB and return loss better than -10 dB are obtained from 6 to 30 GHz.

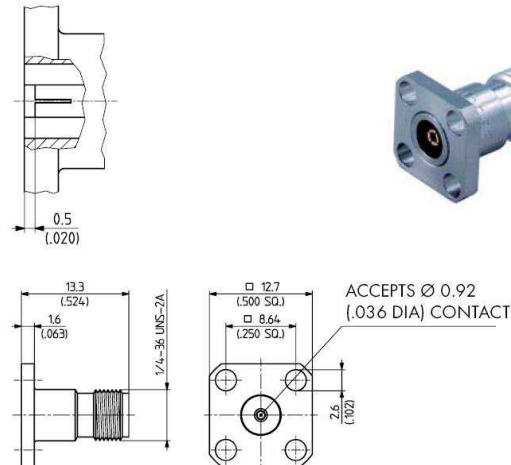


Figure 1: SMA connector [12].

2. PROPOSED TRANSITION

It is important to design a broadband coaxial-to-microstrip transition since the transition bandwidth determines the bandwidth over which the effects of the transition can properly be de-embedded from measurement results [1]. The goal of this work is to develop a coaxial-to-microstrip transition that works up to 30 GHz. The material used in the design are Rogers RT Duroid 5880 with $\epsilon_r = 2.2$ and $\tan \delta = 0.0009$, the metal thickness is 0.017 mm and the substrate thickness is 10 mil and 20 mil. There are many coaxial connectors employed to implement coaxial-to-microstrip transitions. In this work the SMA coaxial connector which is used in the design is 23_PC35-50-0-53/199_UE from Huber-Suhner Company. This connector works in a single mode up to 33 GHz [12]. As it is shown in Fig. 1, SMA conductor has inner and outer diameter of 1.52 mm and 3.5 mm consequently which should be considered in simulation structure. The width of the microstrip line is chosen 1.59 mm (20 mil) and .77 mm (10 mil) to yield characteristics impedance of 50 ohm within the desired frequency band. The length of microstrip line is 50 mm.

As it is shown in Fig. 2, return loss in the Rogers 5880 laminate with the 10 mil of height is better than of the 20 mil. After adding the SMA connectors to the 10 and 20 mil microstrip lines with direct soldering the SMA connector to the microstrip lines of back to back transition which are shown in Fig. 3 and running the full wave analysis with CST software, S -parameters are obtained

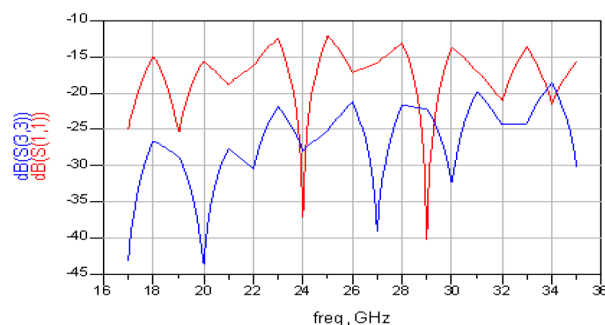


Figure 2: S -parameters of an 50 mm length Mline with ADS software, S_{11} is the return loss of the Rogers 20 mil laminate and S_{33} is for 10 mil.

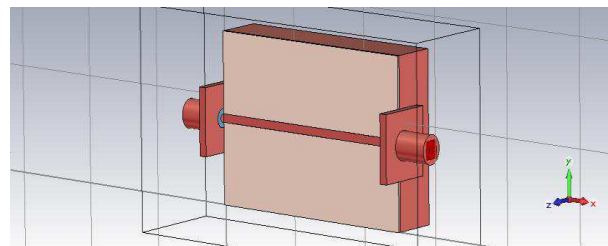


Figure 3: Proposed transition overall view.

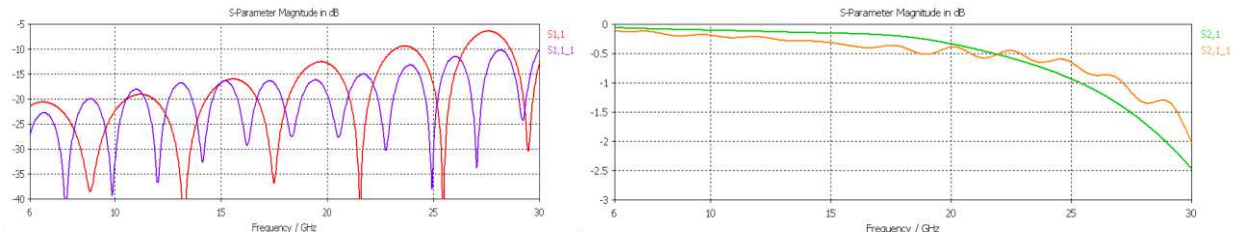


Figure 4: Scattering parameter of the 10 mil and 20 mil laminates using CST software.

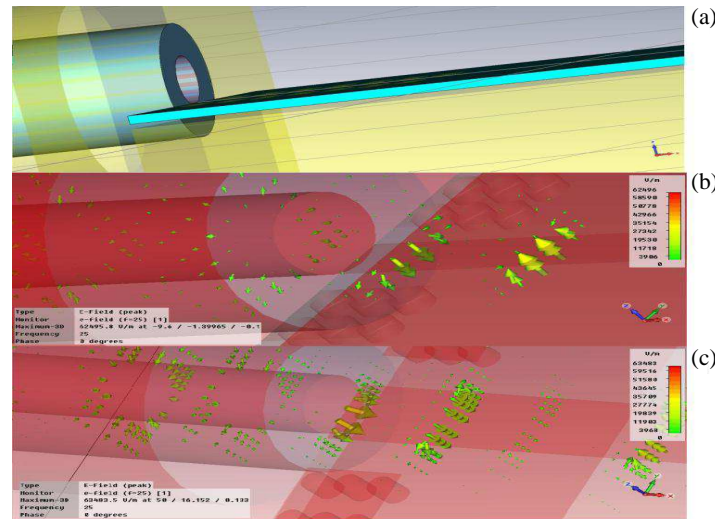


Figure 5: Electrical field in 10 and 20 mil laminate, (a) non coincidence between laminate and coaxial SMA connector in height, (b) electrical field mismatch in 10 mil laminate, (c) electrical field mismatch in 20 mil laminate.

from CST simulation.

Unlike the ADS results; CST results show that the reflection and transmission of the 20 mil height is better than 10 mil, as it is shown in Fig. 4, which S_{11} , S_{21} are the S -parameters of the 10 mil and the $S_{11} - 1$, $S_{21} - 1$ are of the 20 mil. For investigation of this confliction between CST and ADS results, Electrical field simulation with CST is run.

As could be seen in Figs. 5(b), (c), electrical fields in 10 mil laminate have more mismatches against 20 mil in contact point with the coaxial connector. This is because that there is more gap in the point contact of the 10 mil laminate with the proposed SMA coaxial connector against 20 mil laminate, because the distance between inner and outer diameters of the coaxial connector is about 1 mm. As a result the electrical fields has more mismatch in 10 mil laminate, as it is shown in Fig. 5(a). Field matching as discussed before is very important in all transitions and so for the transition design in this paper, rogers5880 laminate with 20 mil height is considered.

2.1. Transition Design

The microstrip to coaxial transition that is proposed in this work is shown in Fig. 6. The structure includes GCPW pre-transition section that ensures proper field match between coaxial and microstrip lines. The center conductor of GCPW section should has the near same width as the SMA tab contact (1.51 mm) in center conductor in order to reach good impedance matching and robust solder connection.

The length of microstrip line is 50 mm. The parameters of the transition are $W_1 = 1.57$, $W_2 = 2$, $D_1 = 3.6$, $D_2 = 1.1$, $G_1 = 0.54$, $L_1 = 2$ and $d_x = 0.54$ (all in millimeter). In the GCPW section the value of W_1 and the value of G_1 are chosen in order to yield a characteristic impedance of 50 ohm along the transition within the desired frequency band. The value of W_1 is chosen near equal to the width of microstrip line to avoid abrupt discontinuity and to minimize the reflection along the transition. In this transition also the number of via and placement of them are optimized to suppress parallel plate mode and radiation loss and to obtain maximum band width.

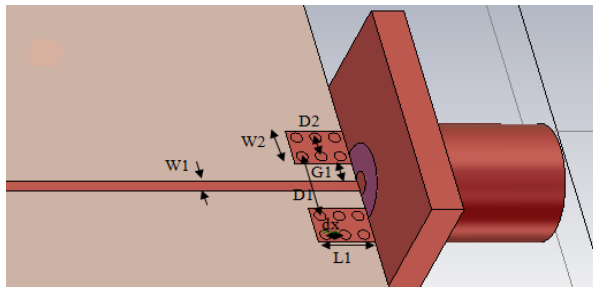


Figure 6: Proposed transition configuration.

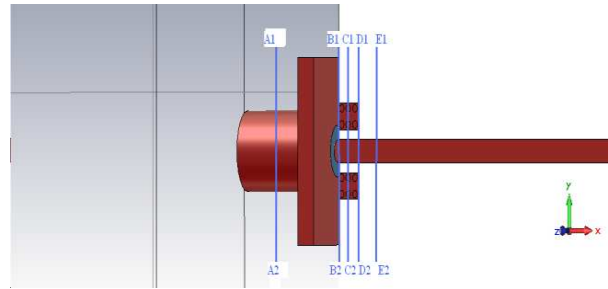


Figure 7: Proposed structure and cut plane for electrical field study.

2.2. Electromagnetic Field Matching Study

Having the same characteristic impedance does not always guarantee a good transition between two transmission line at higher frequencies and the field distributions of the transmission line must also be matched. Therefore the GCPW section used as an interface to match the electromagnetic field distributions at the coaxial-to-microstrip transition. To study the effects of GCPW section on the transitions, electromagnetic fields of transition structure which is shown in the Fig. 7 are analyzed with CST.

Figure 8 shows the magnitude and direction of the electric fields at A1-A2, B1-B2, C1-C2, D1-D2, E1-E2 cross-sections. This figure indicates that in the presence of GCPW section, the electric field distributions, step by step, from top (coaxial connector) to down (Microstrip line) figures are concentrated along the center conductor providing a good matching to the field distribution of the coaxial connector to Microstrip line.

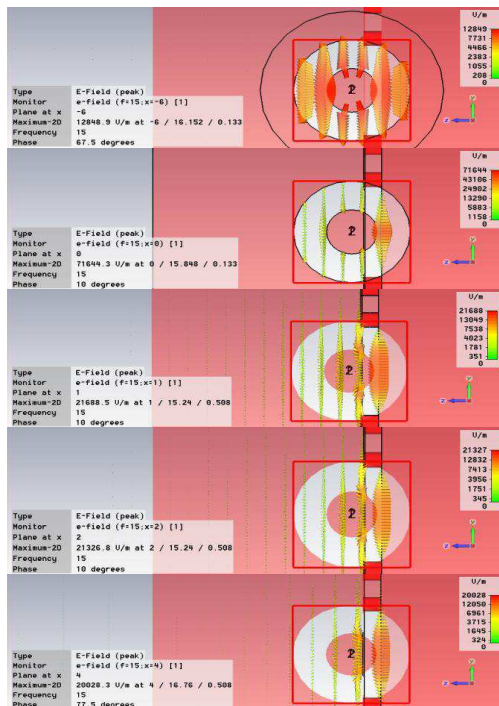


Figure 8: Magnitude and direction of the electric field at 15 GHz from top to down: A1A2: center of the coaxial connector, B1B2: coaxial to GCPW contact, C1C2: center of the GCPW, D1D2: GCPW to microstrip contact and E1E2: along microstrip transition structure shown in Fig. 7.

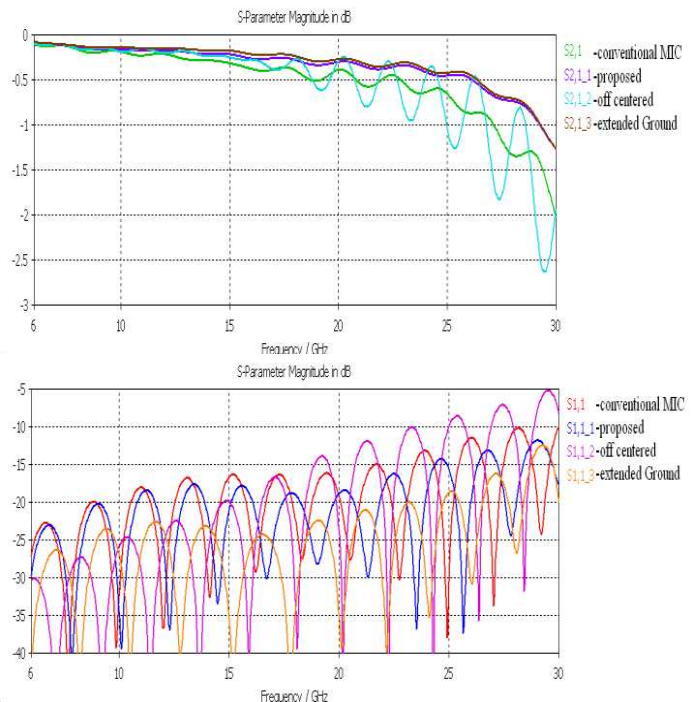


Figure 9: Scattering parameters of the proposed transition combined with a microstrip line with the length of 50 mm, against conventional coaxial to microstrip line transition, extended ground in GCPW and misalignment of the center conductor.

3. SIMULATION AND MEASUREMENT RESULTS

Figure 9 compares the S -parameters of the back to back transition structures with and without GCPW. Adding GCPW section affects the overall bandwidth of transition such that the bandwidth is wider in the presence of GCPW section. Also for better study of the proposed transition; simulation results of the transition with the extended ground in GCPW (twice in height and length) and a slightly gap (.1 mm) and misalignment between microstrip and center of SMA connector (.1 mm) in the In/Out connections are presented in Fig. 9.

As it is shown in Fig. 9, using extended ground in GCPW pre transition more than the proposed transition in the main design has no valuable effects in the performance, but the misalignment has destroying effects on the S -parameters.

The proposed transition has insertion loss less than 1.2 dB and reflection better than -12 dB up to 30 GHz. By the way it is clear that the insertion loss of the 50 mm Microstrip line in the frequency of 30 GHz is more than .6 dB (using Rogers Microwave Impedance Calculator 2014 or other software) so by removing this insertion loss from the total insertion loss, the proposed transition has less than .6 dB insertion loss up to 30 GHz.

Experimental results of the proposed transition with considering 50 mm Microstrip line is presented in Fig. 10. As can be seen from Figs. 9, 10 the measurement results are in very close with simulation results and some differences between simulation and experimental results are due to the reasons that were discussed before. In the worth case and in the worth case, total insertion loss; by removing the insertion loss of the 50 mm Microstrip line and connectors; the proposed transition has insertion loss less than 1.2 dB that can be improve to .6 dB by doing better assembly, and so can be used in many applications. Fig. 11 shows the photos of the fabricated transition with the 50 mm Microstrip line. As it is seen in Figs. 11(a), (b) there is some gap, and some misalignment respectively in the assembly. And as discussed before due to these reasons the insertion loss and resonances are increased.

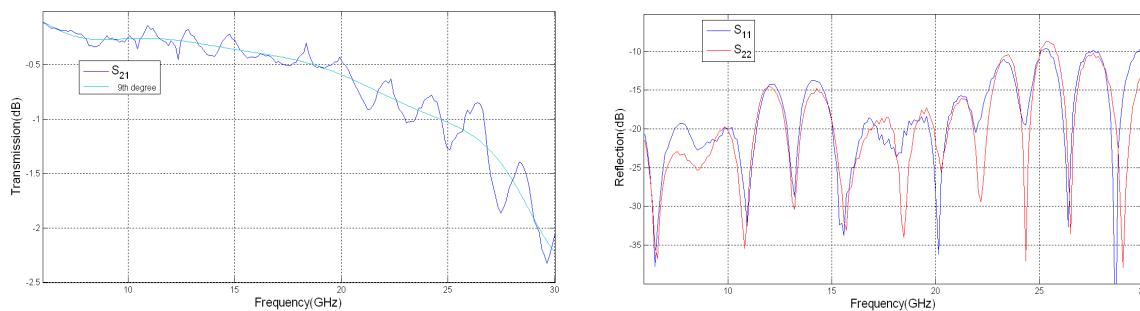


Figure 10: Experimental transmission and reflection results of the proposed transition considering 50 mm microstrip line.

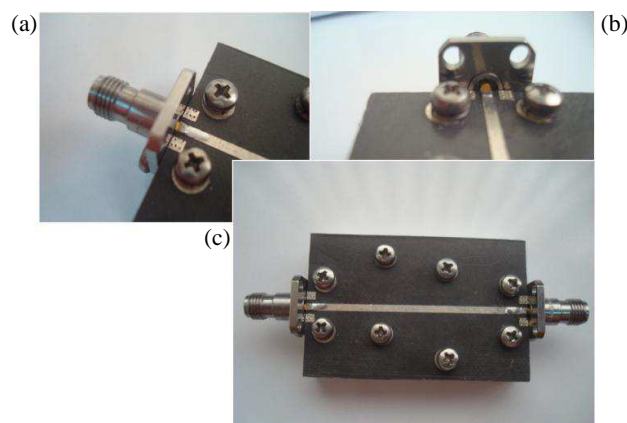


Figure 11: Photos of the proposed transition and the 50 mm microstrip line. (a) Gap view, (b) misalignment view and (c) overall top view.

4. CONCLUSION

In this paper, a very simple, low-cost, low complexity, useful and wideband coaxial-to-microstrip transition up to 30 GHz were presented. The good effects of GCPW pre transition on the overall bandwidth were discussed. In this transition the effects of the field and impedance matching with considering other practical effects in total performance were completely analyzed. The measured and simulated results of back-to-back transition were showed very good agreement. The simulation and measurement results verified that the fabricated back-to-back coaxial-to-microstrip transition can achieve a 0.6 dB insertion loss and a return loss better than -10 dB up to 30 GHz that can be improve easily by this simple structure. This low complexity low cost and easy fabrication is very useful in many application such as UWB short range Radars which work in 22–29 GHz, collision avoidance Radars in vehicular systems and UWB communications. Other transitions to improve bandwidth and other performances in UWB microwave circuits are under investigation and will be presented in the future works.

REFERENCES

1. Zhou, Z. and K. L. Melde, "Development of a broadband coplanar waveguide-to-microstrip transition with vias," *IEEE Trans. Adv. Package*, Vol. 31, No. 4, 861–872, Nov. 2008.
2. Xu, H.-J., Y.-H. Zhang, and Y. Fan, "Analysis of the connection section between K connector and microstrip with electromagnetic bandgap (EBG) structure," *Progress In Electromagnetics Research*, Vol. 73, 239–247, 2007.
3. Cheng, J.-C., E. S. Li, W.-F. Chou, and K.-L. Huang, "Improving the high-frequency performance of coaxial-to-microstrip transitions," *IEEE Trans. on Microw. Theory and Tech.*, Vol. 59, No. 6, Jun. 2011.
4. Holzman, E., *Essentials of RF and Microwave Grounding*, Artech House, Norwood, MA, 2006.
5. Gupta, K. C., R. Garg, I. Bahl, and P. Bhartia, *Microstrip Lines and Slotlines*, Artech House, Norwell, MA, 1996.
6. Agarwal, K. and R. Harlan, "Coax-to-microstrip transition," U.S. Patent, 5552753, Sep. 1996.
7. Quan, C., S. W. Drost, M. Y. Hashimoto, and R. M. Jorgenson, "Microstrip to coax vertical launcher using fuzz button and solderless interconnects," U.S. Patent, 5886590, Mar. 1999.
8. Simons, R. N., *Coplanar Waveguide Circuits, Components, and Systems*, Wiley, New York, 2001.
9. Chiu, T. and Y. Shen, "A broadband transition between microstrip and coplanar stripline," *IEEE Microw. Wireless Components. Lett.*, Vol. 13, No. 2, 66–68, Feb. 2003.
10. Nedil, M., T. A. Denidni, and A. Djaiz, "Ultra-wideband microstrip to CB-CPW transition applied to broadband filter," *IEEE Electronics Lett.*, Vol. 43, No. 8, Apr. 2007.
11. Kamei, T., Y. Utsumi, N. Q. Dinh, and N. Thanh, "Wide-band coaxial-to-coplanar transition," *IEICE Trans. Electron.*, Vol. E90-C, No. 10, 2030–2036, Oct. 2007.
12. Data sheet [On line], Available: <http://www.hubersuhner.co.th>.
13. Son, H., S. Lee, and K. Min, "FPGA implementation of UWB radar signal processing for automotive application," *Proceedings of the 3rd European Wireless Technology Conference*, Sep. 27–28, Paris, France, 2010.

A Broadband UHF RFID Tag Antenna with a Novel T-matching Network

Zhibin He¹, Te Pan¹, Hui Liu¹, Yuan Zhang¹, and Sailing He^{1,2}

¹Centre for Optical and Electromagnetic Research

Academy of Advanced Optoelectronics, South China Normal University, Guangzhou, China

²The Royal Institute of Technology, Stockholm, Sweden

Abstract— In this paper, an-ultra-high frequency (UHF) passive broadband radio frequency identification (RFID) Tag Antenna with a novel T-matching network is presented. By slightly tuned the arm lengths of the T-matching network, the impedance matching between the antenna and the chip and a broad impedance bandwidth is obtained. Thanks to the bent radiating element, the size reduction of the proposed antenna is realized. The bandwidth ($S_{11} < -20$ dB) and the corresponding 3 dB PRC bandwidth of the proposed antenna are 133 MHz (835–968 MHz) and 88 MHz (882–970 MHz) respectively, which means that both bandwidths are wide enough to cover the whole global UHF RFID frequency band. In the simulated results, a smooth and stable gain curve between 0.04 dBi to 1.86 dBi is found throughout the entire operating frequency band, and a gain of 1.38 dBi is obtained at the desired operating frequency point (915 MHz). In conclusion, the designed antenna owns the advantages of low-profile, compact size (56×56 mm²), low cost and stable gain. Based on the simple structure, the designed tag antenna can be easily manufacture and widely used in practical applications.

1. INTRODUCTION

Radio frequency identification (RFID) technology is a wireless communication technology which use radio frequency signal to read and write the data with no touching the target. RFID system consists of reader, tags and application software systems. The tags are divided into passive tags, semi-active tags and active tags according to whether there is an internal power supply. The tag is the device that carries data on the RFID systems. The tag consists of an electronic chip and an antenna. The performance of the tag mainly depends on antenna. In RFID system, the read distance of the tags is a most important index.

Nowadays, the application field of radio frequency identification (RFID) is quite extensive, such as supply chain managements, health care, manufacturing, transportation, animal identification, asset management, logistics, identifying books in library and so on [1]. RFID systems are operated at widely differing frequencies, such as LF (135 KHz), HF (13.56 MHz), UHF (840–960 MHz), and microwave Frequency (2.45 GHz and 5.8 GHz). However, according to the different standards of the globe, the ultra-high frequency (UHF) is divided into different frequency range. For instance UHF RFID applications is 840–845 MHz and 920–925 MHz in China, 865–869 MHz in Europe, 902–928 MHz in South America and North America, 908–914 MHz in Korea, 918–926 MHz in Australia, and 950–956 MHz in Japan. In order to realize cover the entire UHF RFID frequency band, a broadband folded loop tag antenna with T-matching network is presented in [2]. Its bandwidth is 220 MHz (800 MHz–1.02 GHz) covering the whole UHF RFID bandwidth and the gain of the tag antenna is -0.65 dB at 915 MHz. A Two closely spaced bent dipole tag antenna with double-T matching network is presented [3], where it presents an impedance bandwidth of 78 MHz (848–926 MHz) that not including entire UHF RFID bandwidth. Based on reference [3], a modified UHF RFID tag antenna using a double-U patch and a double-T matching network is designed [4]. Although the bandwidth of the modified tag antenna can reach 102 MHz (875–977 MHz), it can't also meet the requirement of covering the whole UHF RFID frequency band. It also has found the same problem of narrow bandwidth in [5]. The design of [5] realizes conjugate impedance matching between a dipole and three loading bars, and its bandwidth is about 6 MHz far from covering the whole global UHF RFID bandwidth.

A compact bent line UHF RFID tag antenna with novel T-matching network is proposed in the paper. The novel T-matching network is applied to improve broad impedance bandwidth. The complex impedance matching could be easily attained by slightly tuned the arm lengths of the T-matching network. Thanks to the bent radiating element, the size reduction of the proposed antenna is realized. The simulated bandwidth ($S_{11} < -20$ dB) of the proposed antenna is 133 MHz which covers the whole global UHF RFID bands. The gain of the operating frequency 915 MHz is

1.38 dBi. Based on the simple structure and the results, the tag antenna is designed as a practical application in the whole UHF RFID systems.

2. ANTENNA STRUCTURE AND DESIGN

The geometry of proposed tag antenna is shown in Fig. 1. The UHF RFID tag antenna consists of a radiating meander line, a novel T-matching network and an FR-4 layer ($\epsilon_r = 4.6$, loss tangent = 0.02, thickness = 1.6). The tag antenna (yellow part) is carved on the cheap FR-4 layer (gray part). To get the small size, the radiating part of the antenna uses a folded micro-strip line. The overall size of the tag antenna is $0.17\lambda \times 0.17\lambda$. In the paper, the UHF RFID tag antenna is designed for a tag microchip with the impedance of $(11-j143)$ at 915 MHz. The conjugated impedance matching of the microchip and the tag antenna is easy to implement by adjusting the parameter Lx of the novel T-matching network.

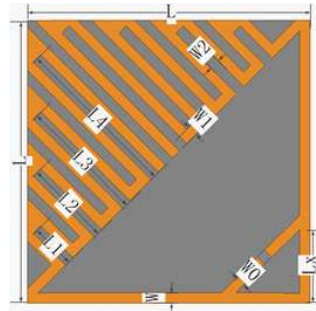


Figure 1: Structure and parameter of the proposed tag antenna.

3. ANTENNA ANALYSIS AND RESULT

In the example, the Ansoft HFSS is utilized to simulate the designed UHF RFID tag antenna. Simulated input reactance values of the tag antenna are shown in Fig. 2 with different parameter Lx . From Fig. 2, we can see that the reactance of the tag antenna increases by extending the parameter Lx at 915 MHz. The parameter Lx is adjusted to 14.6 mm to get the reactance of the proposed tag antenna equal to 143Ω at 915 MHz.

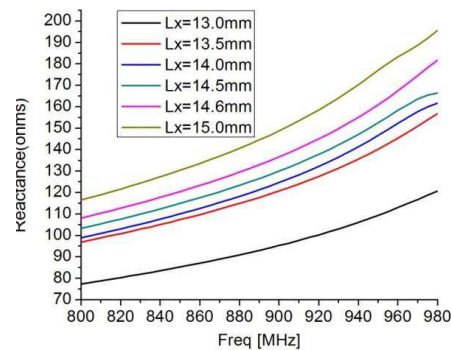


Figure 2: Reactance of antenna with each Lx .

Table 1 exhibits the final optimized design parameters of the tag antenna. The size of the antenna is only $65 \text{ mm} \times 65 \text{ mm}$ etched on a FR-4 substrate with size of $65 \text{ mm} \times 65 \text{ mm} \times 1.6 \text{ mm}$. H and H_{copper} show thickness of the FR-4 substrate and the copper, respectively.

Simulated return loss of the designed UHF RFID tag antenna is presented in Fig. 3. The simulated bandwidth is 133 MHz (835–968 MHz) under the condition of $S_{11} < -20$, which covers the whole global passive UHF RFID frequency band and Fig. 4 shows the power reflection coefficient (PRC) $\Gamma < -3 \text{ dB}$ [6] with bandwidth 88 MHz (882–970 MHz).

The simulated normalized radiation patterns of the proposed tag antenna at operating frequency of 915 MHz are shown in Fig. 5. Fig. 5(a) shows E -plane normalized radiation pattern. H -plane normalized radiation pattern is plotted in Fig. 5(b). The gain of the presented tag antenna is

Table 1: Optimized design parameters of the proposed tag antenna.

L	H	H_{copper}	ϵ_r	μ_r	$L1$	$L2$
56 mm	1.6 mm	0.035 mm	4.6	1	9 mm	17 mm
$L3$	$L4$	Lx	W	$W0$	$W1$	$W2$
25 mm	33 mm	14.6 mm	2 mm	2 mm	2 mm	2 mm

drawn in Fig. 6 from 800 MHz to 980 MHz. A stable gain curve between 0.04 dBi to 1.86 dBi is found throughout the entire operating frequency band (840–960 MHz), and a gain of 1.38 dBi is obtained at the desired operating frequency point (915 MHz), which obtains a good read distance for the proposed UHF RFID tag antenna. The performance of a stable reading range is very helpful in practice.

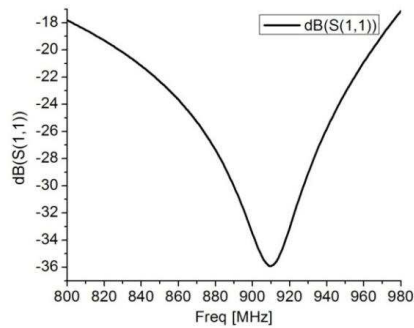


Figure 3: Return loss of the tag antenna.

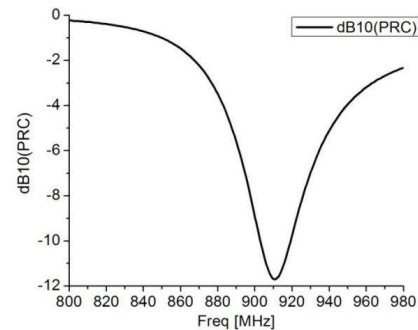


Figure 4: Power reflection coefficient of the tag antenna.

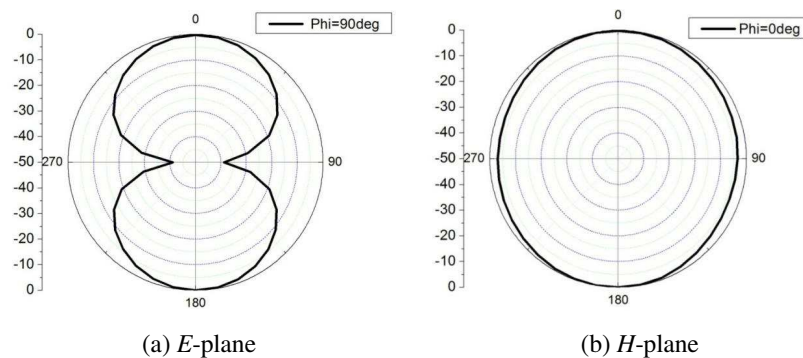
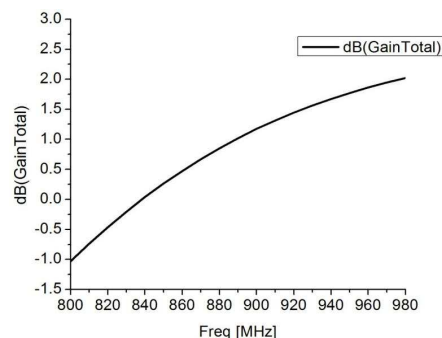
Figure 5: E -plane and H -plane of simulated normalized radiation patterns.

Figure 6: Gain curve of the tag antenna.

4. CONCLUSIONS

A broadband meander line UHF RFID tag antenna with a novel T-matching network is presented. Results demonstrate that the impedance bandwidth ($S_{11} < -20$) of the designed UHF RFID tag antenna is 133 MHz from 835 MHz to 968 MHz. Its bandwidth covers the whole UHF RFID frequency bands. At the same time, the tag antenna owns a good power reflection coefficient bandwidth 88 MHz (882–970 MHz) and a good gain 1.38 dBi at 915 MHz. Based on the simple structure and good performance, the designed tag antenna can be easily manufacture and widely used in practical applications. The UHF RFID tag antenna also has advantages of low cost, low profile, small size and high gain.

REFERENCES

1. Finkenzeller, K., *RFID Handbook: Fundamentals and Applications in Contactless Smart Cards, Radio Frequency Identification and Near-field Communication*, John Wiley & Sons, 2010.
2. Zhou, X. and G. Q. Luo, "A broadband and miniaturized UHF RFID tag antenna with T-matching network," *Microwave Workshop Series on Millimeter Wave Wireless Technology and Application (IMWS), 2012 IEEE MTT-S International*, 1–3, 2012.
3. Cho, C., H. Choo, and I. Park, "Broadband RFID tag antenna with quasi-isotropic radiation pattern," *Electronics Letters*, Vol. 41, No. 20, 1091–1092, 2005.
4. Tan, J. and X. Li, "Wideband double-UT RFID tag antenna design," *IEEE Asia Pacific Conference on Circuits and Systems, APCCAS 2008*, 1256–1259, 2008.
5. Toccafondi, A. and P. Braconi, "Compact load-bars meander line antenna for UHF RFID transponder," *First European Conference on Antenna and Propagation, 2006, EuCAP 2006*, 1–4, 2006.
6. Nikitin, P. V., K. V. S. Rao, S. F. Lam, and V. Pillai, "Power reflection coefficient analysis for complex impedances in RFID tag design," *IEEE Trans. Microw. Theory. Tech.*, Vol. 53, No. 9, 2721–2725, 2005.

Capacitively Coupled-fed Electrically Small Loop Antenna with High Efficiency for WiFi Application

Qingchong Liu¹, Yufeng Yu², and Qi Liu¹

¹Centre for Optical and Electromagnetic Research, Zhejiang University, Hangzhou 310058, China

²China Jiangnan Electronics Communication Institute, Jiaxing 314000, China

Abstract— An efficient electrically small planar loop antenna with capacitive feed is proposed for WiFi applications. The feeding element of our antenna is a printed T-shaped monopole, which is capacitively coupled to the radiating capacitively-loaded loop and good impedance matching is achieved through the capacitive coupling mechanism. Thus the capacitive feed leads to high radiation efficiency, gain and broad impedance bandwidth. The radiating element of the proposed antenna is comprised of a planar printed loop with an interdigital capacitor inserted on one side and a copper wall with height of 3 mm and thickness of 0.3 mm attached to the printed loop. The attached wall enables the antenna occupies more volume, which lowers its Q value and contributes to larger bandwidth. The proposed antenna exhibits a simulated -10 dB impedance bandwidth of 190 MHz from 2.39 GHz to 2.58 GHz, which is suitable for WiFi application.

1. INTRODUCTION

With the rapid development of mobile communication technology, the demand for electrically small antennas (ESAs) with miniaturized size, high radiation efficiency and broad bandwidth keeps increasing. Especially for modern mobile terminals, such as cell phones, laptops, and PDAs, the space available for the antenna is extremely limited. As is known to all, due to the intrinsic small radiation resistance and large reactance, electrically small antennas without external matching networks are poorly matched to 50-ohm feed lines, leading to low radiation efficiency and small bandwidth. Many methods have been taken to design ESAs with high performance, including reactive loading [1], shape meandering of wire antennas [2, 3], using dielectric substrate of high permittivity [4], etc.. In this paper, the problem of impedance matching is solved by coupled-fed technique, which have been widely used in monopoles [5], PIFAs [6], loop antennas [7], etc..

However, the other challenge in designing ESAs is to increase the bandwidth. According to the well-known relation between bandwidth and Q [8, 9], the intrinsic bandwidth of ESAs is limited due to their physical dimensions. In this paper, a copper wall (red part in Figure 1) attached to the printed loop is introduced. The attached wall enables the antenna occupies more volume, thus lowers its Q value and contributes to larger bandwidth. The proposed antenna exhibits a simulated -10 dB impedance bandwidth of 190 MHz from 2.39 GHz to 2.58 GHz, which is suitable for WiFi application.

2. ANTENNA DESIGN

The prototype and configuration of the proposed antenna is depicted in Figure 1 and detailed dimensions are given in Table 1. A substrate with size of $100\text{ mm} \times 40\text{ mm} \times 1\text{ mm}$, relative permittivity of 2.6 and loss tangent of 0.002 is used as the system circuit board in this paper. A system ground plane is printed on the top side of the circuit board, with a no-ground portion of $14\text{ mm} \times 7.5\text{ mm}$ at one corner. The antenna is mounted on the no-ground portion.

Table 1: Detailed dimensions of the proposed antenna.

Parameter	Length (mm)	Parameter	Length (mm)
L_r	11.5	H_r	7.5
W_r	1.4	L_f	7.2
W_{f1}	2.0	W_{f2}	0.5
g	0.3	L_c	1.7
W_c	0.3	g_c	0.2

Figures 1 (a) and (b) give top and 3D view of the antenna, respectively. The radiating element of the proposed antenna is a modified capacitively-loaded loop (CLL). It is comprised with a printed

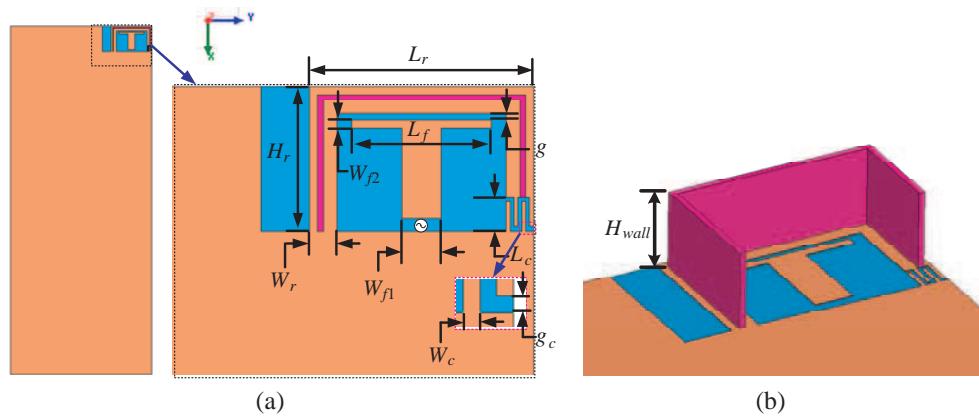


Figure 1: Geometry of the proposed planar loop antenna. (a) Top view. (b) 3D view.

half rectangular loop with an interdigital capacitor inserted on one side and a copper wall with height of 3 mm and thickness of 0.3 mm attached to the printed loop. The attached wall (red part in Figure 1) enables the antenna occupies more volume, thus lowers its Q value and contributes to larger bandwidth. The interdigital capacitor provides loaded capacitance, which allows the loop with total length of about 24 mm (about $1/5$ wavelength at 2.47 GHz) to self-resonates at 2.47 GHz. The feeding element of our antenna is a printed T-shaped monopole, which is capacitively coupled to the radiating CLL and good impedance matching is achieved through the capacitive coupling mechanism. The advantage of using this feeding technique is that the inductive impedance of the feeding line is effectively canceled by the capacitance introduced by the feed and radiating element.

3. RESULTS AND DISCUSSION

A full-wave simulation of the proposed antenna is conducted with Ansoft High Frequency Structural Simulator (HFSS). In Figure 2, the simulated reflection coefficients of the antenna are provided. The proposed antenna with wall height H_{wall} of 3 mm exhibits a simulated -10 dB impedance bandwidth of 190 MHz from 2.39 GHz to 2.58 GHz, covering the bandwidth from 2.4 GHz to 2.48 GHz for WiFi application. The simulated resonant frequency of this antenna is 2.47 GHz, where the reflection coefficient is -30.4 dB and radiation efficiency is 98.6%. The far-field properties of the proposed antenna are also simulated with HFSS and the radiation patterns on three orthogonal planes are shown in Figure 3. One sees that the maximum radiation of such an antenna is toward its opposite direction with a tilt angle, and the radiation pattern is symmetrical with respect to the plane of the planar loop, implying its potential use as electrically small radiators for pattern diversity based MIMO terminals with very small inter-element space.

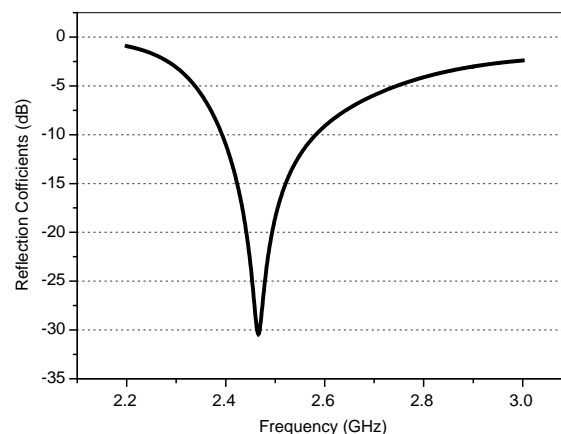


Figure 2: Simulated reflection coefficients of the proposed antenna.

Figure 4 shows the effects of the height H_{wall} of attached wall of the modified CLL. The simulated -10 dB impedance bandwidth and resonant frequency of the proposed antenna with different H_{wall}

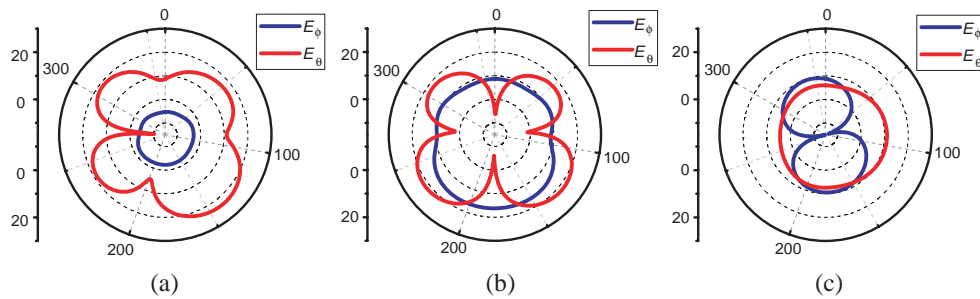


Figure 3: Radiation pattern at 2.47 GHz. (a) yoz -plane. (b) xoz -plane. (c) xoy -plane.

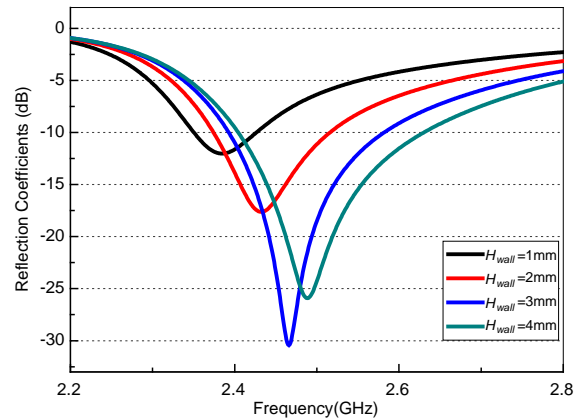


Figure 4: Simulated reflection coefficients of the proposed antenna with different values of H_{wall} .

Table 2: Simulated bandwidth and resonant frequency with respect to the height of wall H_{wall} .

H_{wall} (mm)	1	2	3	4
Bandwidth (MHz)	76 2350–2426	142 2374–2516	190 2392–2582	226 2404–2630
Resonant Frequency (GHz)	2.385	2.432	2.466	2.488

are given in Table 2. We can see that as H_{wall} increases from 1 mm to 4 mm, the bandwidth gets broader from 76 MHz to 226 MHz, and resonant frequency gets higher from 2.385 GHz to 2.488 GHz. As the antenna with larger H_{wall} occupies larger volume, it has smaller Q value and broader bandwidth. And larger H_{wall} leads to smaller current density on the radiating CLL, which lowers the loss resistance, so higher radiation efficiency is obtained. For the good of the balance between bandwidth and low-profile of the antenna, we choose $H_{wall} = 3$ mm as the optimal value of the parameter.

4. CONCLUSIONS

In this paper, we have proposed an electrically small planar loop antenna. A copper wall is attached to the CLL, which enables the antenna occupies more volume, thus lowers its Q value and contributes to larger bandwidth. The interdigital capacitor provides loaded capacitance, which allows the loop with total length of about 24 mm (about $1/5$ wavelength at 2.47 GHz) to self-resonates at 2.47 GHz. With the capacitive coupled feeding, the electrically small loop can be directly connected with a 50-Ohm feed line, and good radiation efficiency and gain have been obtained. The proposed antenna can be applied in mobile terminals for WiFi application.

REFERENCES

1. Liu, J., W.-Y. Yin, and S. He, "A new defected ground structure and its application for miniaturized switchable antenna," *Progress In Electromagnetics Research*, Vol. 107, 115–128, 2010.

2. Liao, W.-J., S.-H. Chang, and L.-K. Li, “A compact planar multiband antenna for integrated mobile devices,” *Progress In Electromagnetics Research*, Vol. 109, 1–16, 2010.
3. Li, J.-F., B.-H. Sun, H.-J. Zhou, and Q.-Z. Liu, “Miniaturized circularly-polarized antenna using tapered meander-line structure,” *Progress In Electromagnetics Research*, Vol. 78, 321–328, 2010.
4. Wong, K. L., *Compact and Broadband Microstrip Antennas*, Wiley, New York, 2002.
5. Kang, T.-W., et al., “Coupled-fed shorted monopole with a radiating feed structure for eight-band LTE/WWAN operation in the laptop computer,” *IEEE Transactions on Antennas and Propagation*, Vol. 59, 674–679, 2011.
6. Lee, C.-T. and K.-L. Wong, “Uniplanar printed coupled-fed PIFA with a band-notching slit for WLAN/WiMAX operation in the laptop computer,” *IEEE Transactions on Antennas and Propagation*, Vol. 57, 1252–1258, 2009.
7. Wong, K.-L., W.-Y. Chen, and T.-W. Kang, “On-board printed coupled-fed loop antenna in close proximity to the surrounding ground plane for penta-band WWAN mobile phone,” *IEEE Transactions on Antennas and Propagation*, Vol. 59, 751–757, 2011.
8. Chu, L. J., “Physical limitations of omni-directional antennas,” *J. Appl. Phys.*, Vol. 19, 1163–1175, 2004.
9. Yaghjian, A. D. and S. R. Best, “Impedance, bandwidth and Q of antennas,” *IEEE Transactions on Antennas and Propagation*, Vol. 53, No. 4, 1298–1324, Apr. 2005.

25 G/s Passive Current Board Design of PRBS Generator

Chih-Wei Yu, Jia-Jin Wu, C. L. Chiu, Jau-Ji Jou, and Tien-Tsorng Shih

Department of Electronics Engineering, National Kaohsiung University of Applied Sciences
No. 415 Chien Kung Road, Kaohsiung, Taiwan, R.O.C.

Abstract— The 25 Gb/s BER test set comprises a signal generator that drives an passive current board including micro-strip line (R6C) through Gennum GN2426A IC and SEMTECH GN2426A chip generated with a Pseudo Random Binary Sequence (PRBS) of digital 1's and 0's, representing a random data stream. The simple 25 Gb/s testing of passive current board converts the PRBS data stream from electrical to optical components. The R6C's price for 25 Gb/s passive current board of a PRBS generator is almost 1/400 times than the measuring equipment price. R6C board is a structure for four layers. Its feature of eye diagram is a jitter of 12.614 ps, a bit rate of 25.35 Gb/s, a fall time of 14.5 ps and a rise time of 12.5 ps. R6C has a useful role under mass production. It is very cheap and simple high speed testing for 25 Gb/s.

1. INTRODUCTION

Today short reach optical communications development require low cost and high speed transceivers. Internet and consumer electronics products flourish, and promote the development of cloud computing and processing large data [1–3]. Enhance the data processing speed and high capacity optical transport network (OTN) is the current trend, Therefore, the development of 100 Gb/s transfer several times even faster optic transceiver [4]. Using vertical cavity surface emitting lasers (VCSEL) coupled to multimode fibers (MMF) are best solution [5]. The high-frequency signal transceiver used micro-strip circuit will be necessary to be matched with dependent resistant and then operate under the reliable communication [6]. PRBS can be considered of the well suited to the bit error rate (BER) testing and eye diagram analysis in communications system [7, 8].

Between chip and printed-circuit-board (PCB) bit rates and frequency are increased. Testing the signal integrity effect of PRBS as well as validating the impedance matching of micro-strip is important when using micro-strip transmission line and connector. Micro-strip is measure impedance by time domain measurement. Also, the communication system measurement costs are high since PRBS equipment is expensive and bulky. The authors proposed a 25 Gb/s PRBS generator circuit board.

The PRBS generator chip connects the PCB using micro-strip transmission line to achieve high-speed bit rates. PRBS circuit board was combine two micro-strip type, one is the differential micro-strip, and another is the single-end. Hence, using the micro-strip and PRBS generator IC, it is possible to Performance the signal integrity property at 25 Gbps. This paper is organized as follows. In Section 2, In Section 3, the test PRBS circuit board is demonstrated to property the signal integrity. The Section 4 is conclusion.

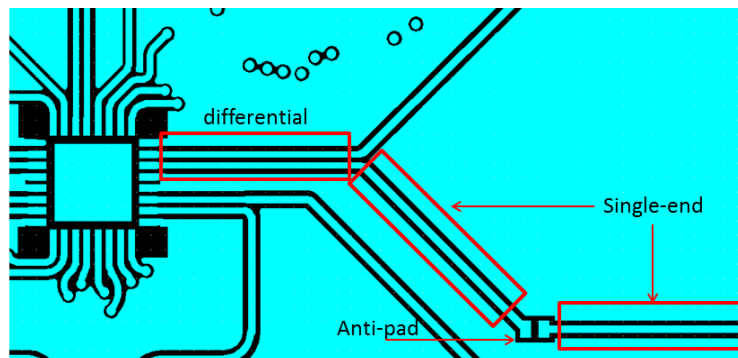


Figure 1: Micro-strip layout of top-layer.

2. DESIGN AND EXPERIMENT

In a dual-channel, each channel 25~28 Gb/s programmable PRBS generator is designed at R6C generator, and the circuit is used to ATMEGA 328P microcontroller unit to control GN 2426A

Chip. The program is written by ATMEGA 328P or the usage of the computer trigger in GN 2426A chip generates a PRBS signal. GN 2426A chip is operated at reference free clock and data recovery (CDR) [9] and PRBS generator and PRBS signal length is up to $2^9 - 1$. GN 2426A chip is two input and output, and each port is connected with the differential and single-end output shown in Figure 1 [10].

R6C board is used four-layer PCB, and reduced two-layer than standard evaluation board (EB-GN2426A). R6C board volume at a wide of 6.35 cm and height of 6.7 cm. Table 1, which R6C circuit board structure of four layers, and each layer was Top-layer, Ground-layer, Vcc-layer and Bottom-layer, between the IC and K-type connector transmit the signal by micro-strip. Micro-strip is layout on the Top-layer. The GN 2426A chip transmits Serial data by differential output, and the signal-end connects R6C board and K-type connector. Using Rogers 4350B PCB in top-layer due to the required of best transmission efficiency. Micro-strip width and impedance calculate by Polar software. The micro-strip transmission line width was 9.9 mils in differential and 12 mils in single-end, which the micro-strip width was very close proximity provides better impedance matching and reduced interconnection losses. Micro-strip impedance calculate differential of 99.94 ohm, single-end of 49.85 ohm and Anti-pad of 50.47 ohm. The R6C micro-strip is impedance matching.

3. MEASURING RESULTS

Figure 3 shows the measured results of micro-strip impedance by Time-Domain Reflectometry (TDR). Compare the R6C board with standard evaluation board (EB-GN2426A) in the 25 Gb/s. The R6C board micro-strip impedance curve is smooth and approximation to 50 ohm. Figure 4 shows the 25.35 Gb/s bit rate of the R6C board. The eye diagram shows a clear eye opening and width of 29.1 ps, height of 70 mV, jitter of 12.614 ps, fall time of 14.8 ps and rise time of 12.5 ps. System reaches for 25.35 Gb/s passive current board of a PRBS generator has been successfully demonstrated.

Table 1: R6C circuit board structure of four layers.

Layer	Material	Thickness	Dielectric Constant	Dielectric Loss Tangent
Top	Cu 0.5 ounce(oz.)	0.03 mm	1	0
	Rogers 4350B	6.6 mils	3.66	0.004
Ground	Cu 0.5 oz.	0.017 mm	1	0
	PP	10 mils	4.2	0.017
Vcc	Cu 0.5 oz.	0.017 mm	1	0
	FR4	6 mils	4.2	0.02
Bottom	Cu 0.5 oz.	0.017 mm	1	0

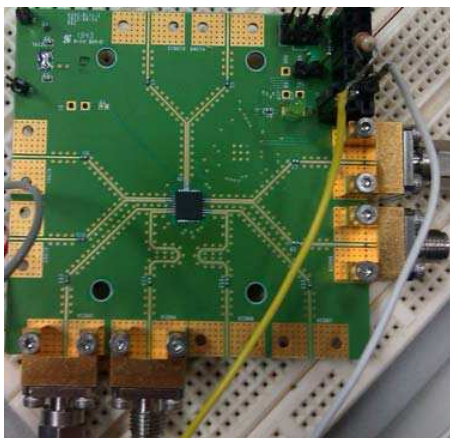


Figure 2: Passive current board of R6C.

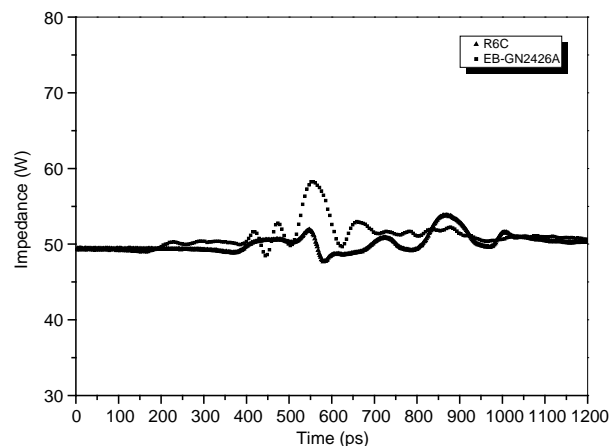


Figure 3: Comparing R6C board to a standard evaluation board (EB-GN2426A) of the measurement of impedance and time using a 25 Gb/s for time-domain reflectometry (TDR).

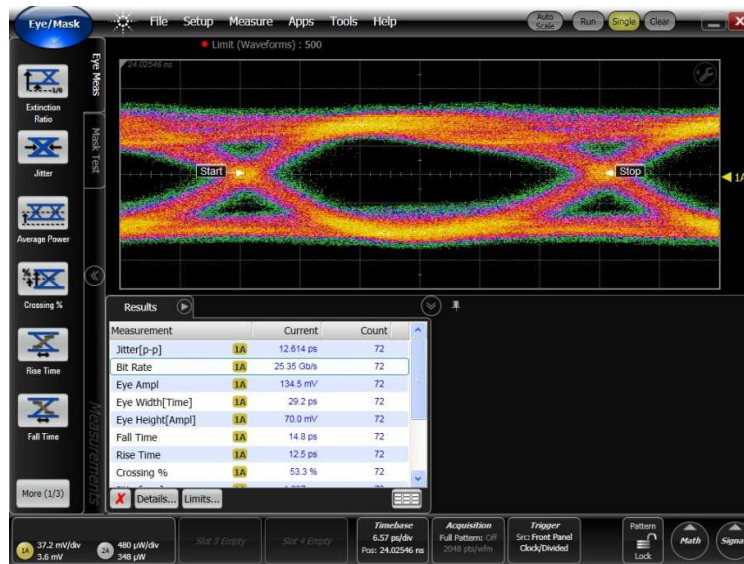


Figure 4: Eye diagram in R6C circuit board gets the bit rate of 25.35 Gb/s.

4. CONCLUSION

This paper uses differential, anti-pad, single-and and via layout impedance matching techniques match almost 50 ohm. The price of R6C board for 25 Gb/s passive current board of a PRBS generator was almost 1/400 times than the measuring equipment price and 1/4 times than the standard evaluation board (EB-GN2426A) price. R6C circuit board dimension was smaller than the standard evaluation board (EB-GN2426A). The R6C board has better eye diagram at 25.35 Gb/s bit rate, and its Jitter of 12.614 ps. A PRBS generator was up to $2^9 - 1$ R6C has a useful role under mass production. It is very cheap and simple high speed testing for 25 Gb/s.

REFERENCES

- Xu, X., "From cloud computing to cloud manufacturing," *Robotics and Computer-integrated Manufacturing*, Vol. 28, No. 1 75–86, Feb. 2012.
- Guan, Q., C.-C. Chiu, and S. Fu, "CDA: A cloud dependability analysis framework for characterizing system dependability in cloud computing infrastructures," *2012 IEEE 18th Pacific Rim International Symposium on Dependable Computing*, 11–20, Niigata, Japan, Nov. 2012.
- Datta, A., M. R. Islam, A. K. Mukherjee, and D. Kandar, "Cloud computing: A solution to human resource management system," *International Conference on Radar Communication and Computing*, 176–179, Tiruvannamalai, India, Dec. 2012.
- Fujisawa, T., S. Kanazdwa, Y. Ueda, W. Kobauashi, A. Ohki, T. Ito, M. Kohtoku, and H. Lshii, "Low-loss cascaded Mach-Zehnder multiplexer integrated 25-Gbit/s \times 4-lane EADFB laser array for future CFP4 100 GbE transmitter," *IEEE Journal of Quantum Electronics*, Vol. 49, No. 12, 1001–1007, Dec. 2012.
- Gholami, A., Z. Toffano, A. Destrez, S. Pellerrault, M. Pez, and F. Quentel, "Optimization of VCSEL spatiotemporal operation in MMF links for 10-Gb ethernet," *IEEE Journal of Selected Topics in Quantum Electronics*, Vol. 12, No. 4, 767–775, Jul. 2006.
- Horn, A. F., J. W. Reynolds, and J. C. Rautio, "Conductor profile effects on the propagation constant of micro-strip transmission lines," *2010 IEEE MTT-S International Microwave Symposium Digest (MTT)*, 868–871, Anaheim, America, May 2010.
- Aisawa, S., M. Suzuki, T. Ono, T. Ohara, and M. Tomizawa, "100 G high gain FEC performance measurement using 10 Gbps PRBS signal," *Opto-Electronics and Communication conference*, 170–171, Busan, Korea, Jul. 2012.
- Rasmussen, A., S. Ruepp, M. Berger, H. Wessing, J. V. Nielsen, and H. Harving, "Framed bit error rate testing for 100 G Ethernet equipment," *2010 International Conference on High Performance Switching and Routing*, 165–168, Richardson, America, Jun. 2010.
- Presi, M., N. Calabretta, G. Contestabile, and E. Ciaramella, "Wide dynamic range all-optical clock and data recovery from preamble-free NRZ-DPSK packets," *IEEE Photonics Technology Letters*, Vol. 19, No. 6, 372–374, Mar. 2007.

10. Chen, W.-Z. and G.-S. Huang, “A low power programmable PRBS generator and a clock multiplier unit for 10 Gbps serdes applications,” *2006 IEEE International Symposium on Circuits and Systems*, 3273–3276, Island of Kos, Greece, May 2006.

A Quasi-hexagon Shaped Band-stop FSS in Wideband RCS Reduction

Peng Cheng Zhang, Xian Qi Lin, Fei Cheng, Rui Shen, and Yong Fan

EHF Key Lab of Fundamental Science, School of Electronic Engineering
University of Electronic Science and Technology of China, Chengdu 611731, China

Abstract— In this paper, a quasi-hexagon shaped band-stop frequency selective surface with a wideband RCS reduction is proposed. In terms of structural mode scattering, we design a kind of band-stop FSS as a substitute for the traditional metal reflection board grounded on a hexagon FSS prototype and the typical Koch fractal curve. Patch dipole antenna is used to confirm the validity of this method and the result of simulation shows that relative RCS of the patch antenna with metal ground, there is a considerable out-of-band RCS of the antenna with band-stop FSS ground plane about 11.3 dB reduction on average, and 27.3 dB reduction on 5.8 GHz.

1. INTRODUCTION

Frequency selective surface (FSS) is the free-space counterparts of microwave filters in a transmission line. FSS has been widely applied in microwave antenna, radar and satellite communications [1–3]. For example, FSS has been used traditionally in stealth technology for reducing the radar cross section (RCS) of communication and radar antennas as well as protecting receivers of such systems from interfering signals and jamming [4]. Over the years, a variety of FSS elements were introduced for band-pass and band-stop applications.

Band-stop FSS is from time to time used as antenna reflection ground [5] to improve the antenna gain [6] as well as reduce the out-of-band RCS. In this paper, an efficient design is present to achieve the traditional hexagon shaped band-stop FSS miniaturization, and effective harmonic suppression. By these excellent electromagnetic characteristics, our new quasi-hexagon shaped band-stop FSS can get great wideband RCS reduction.

2. DESIGN AND SIMULATED RESULTS

2.1. Structures Design

Figure 1(a) shows the traditional hexagon shaped band-stop FSS unit cell. The top layer consists of hexagon with length of l and width of w set in a periodic pattern, and the dielectric board consists of the F4B material with $\epsilon_r = 2.45$, $\tan \sigma = 0.001$ and thickness 0.8 mm is used as the dielectric substrate. All metals in the FSS are made of copper with a conductivity $\sigma = 5.8 \times 10^7$ S/m. According to the particularity of hexagon, we target by the following way of fractal. Fig. 1(b) shows the first-order fractal structure, the method is from each vertex of hexagon, generate inside a bend line with the width of the hexagon. From first-order to second-order and the higher order fractal are adopts similar to the structure of the Koch curve method [7]. Second-order fractal structure is illustrated in Fig. 1(c).

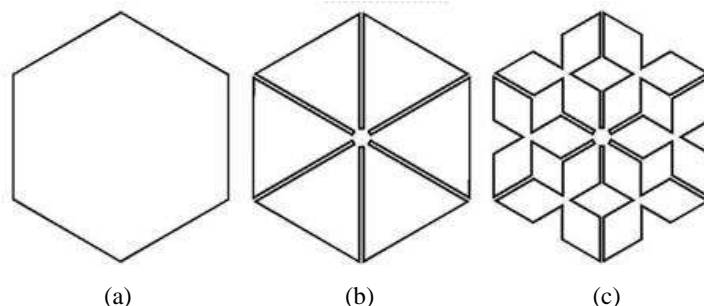


Figure 1: Structures of band-stop FSS unit: (a) traditional hexagon; (b) first-order fractal; (c) second-order fractal. ($l = 6$ mm, $w = 0.1$ mm).

2.2. Second-order Fractal Simulate and Analysis

We make full-wave simulations by using the commercial software HFSS. The simulation results of these three structures are shown in Fig. 2. for the normal incident, in which we observe the Transmission coefficient zeroes are 1 GHz, 2 GHz, 3 GHz. Compared with the traditional hexagon shaped band-stop FSS, the second-order fractal FSS with same length is almost 2 times miniaturization. These three structures have 2 times, 3.5 times, and 5 times respectively higher harmonic resonant frequency, which verify the second-order fractal FSS has effective harmonic suppression.

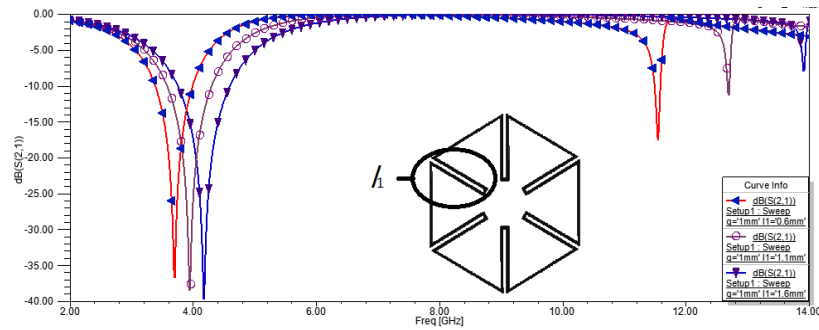
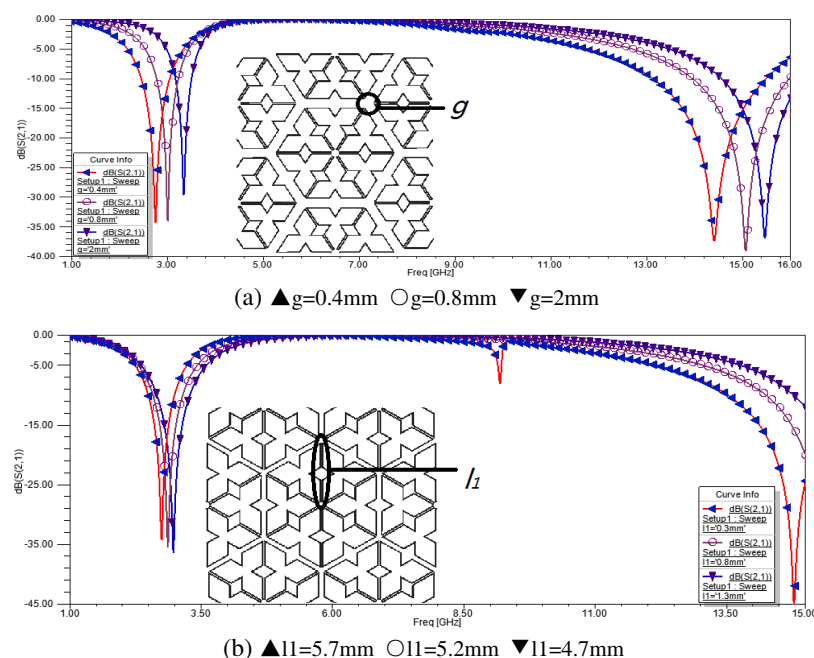


Figure 2: Simulations of the three structures FSS.

Figure 3 illustrates the simulation of the parameters of the design second-order fractal FSS including g unit interval, l_1 as the length of the bend line, l_2 as the length of Koch curve fractal line, and the gap width of the bend line. Fig. 3(a) shows the transmission coefficients with different g , in which we observe increasing the g increases the center frequency, a result of a larger capacity coupling. Fig. 3(b) and Fig. 3(d) show the transmission coefficients with different l_1 and l_2 , in which we observe increasing the l_1 or l_2 decrease the center frequency for the larger electrical length. Fig. 3(d) shows the transmission coefficients with different g_1 . It is worth mentioning that increasing the value of g_1 , the higher harmonic resonant frequency in not monotonous changing subsequently.

2.3. RCS Simulate

In order to verifying the RCS reduction of the new hexagon FSS, we design two working at the same frequency 2.9 GHz patch dipole antennas with metal ground and second-order fractal FSS ground. Through optimizing the parameters of the second-order fractal FSS, the simulation result is shown in Fig. 4, in which we observe the refraction index pole at 2.9 GHz and zero at 5.8 GHz.



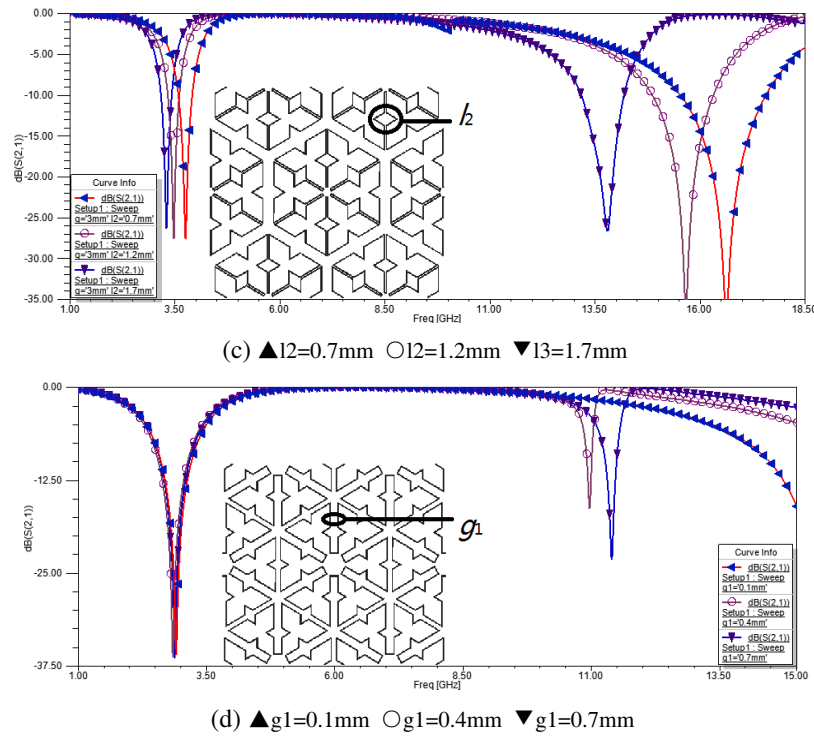


Figure 3: Free-space simulations of second-order fractal band-stop FSS; (a) g ; (d) l_1 ; (c) l_2 ; (d) g_1 .

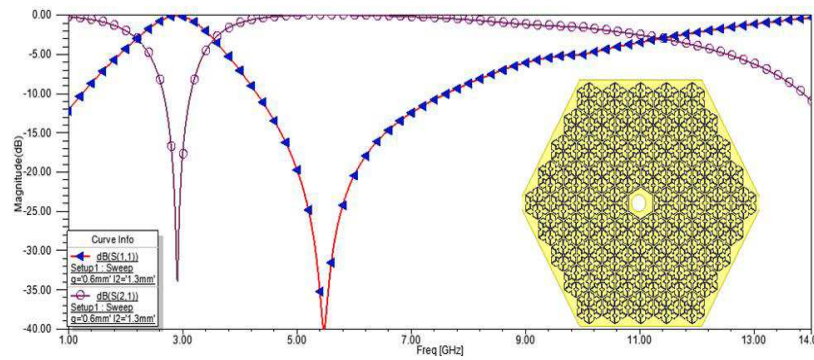


Figure 4: Free-space simulation of the second-order fractal band-stop FSS for the antenna ground.

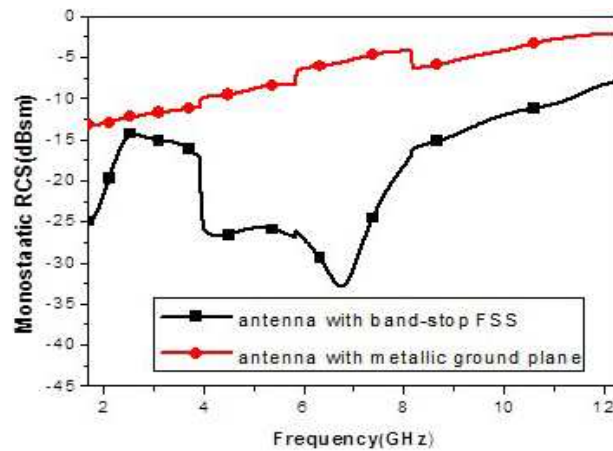


Figure 5: Simulation of RCS of the patch antenna with band-stop FSS and metal ground.

Fig. 5 illuminates the RCS of the antennas with metal ground and FSS ground, in which we observe comparing the antenna with metal ground, RCS of the antenna with FSS ground at out-of-band

about 11.3 dB reduction on average from 1 GHz to 12 GHz, and the most reduction 27.3 dB at 5.8 GHz.

3. CONCLUSIONS

In this article, design of a quasi-hexagon shaped band-stop FSS in RCS reduction is presented. The quasi-hexagon structure is designed by a new fractal method, which effectively achieves the FSS miniaturization. The second-order fractal band-stop FSS has a great harmonic suppression, which effectively improve the RCS bandwidth.

ACKNOWLEDGMENT

This work was supported in part by the State Key Laboratory of CEMEE Foundation under Grant No. CEMEE2014Z0201A, in part by the Fundamental Research Funds for the Central Universities under Grant Nos. ZYGX2010J021 and ZYGX2012YB002, in part by the Program for New Century Excellent Talents in University under Grant No. NCET-13-****.

REFERENCES

1. Munk, B. A., *Frequency Selective Surfaces: Theory and Design*, Wiley, New York, 2000.
2. Wu, T. K., "Four-band frequency selective surface with double-square-loop patch elements," *IEEE Transactions on Antennas and Propagation*, Vol. 42, No. 12, 1659–1663, 1994.
3. Vardaxoglou, J. C., *Frequency-selective Surfaces: Analysis and Design*, Research Studies Press, Taunton, U.K., 1997.
4. Wu, T. K., "High Q bandpass structure for the selective transmission and reflection of high frequency radio signals," U.S. Patent 5103241, Apr. 7, 1992.
5. Leberer, R. and W. Menzel, "A dual planar reflectarray with synthesized phase and amplitude distribution," *IEEE Transactions on Antennas and Propagation*, Vol. 53, No. 11, 3534–3539, 2005.
6. Akalin, T., J. Danglot, O. Vanbesien, and D. Lippens, "A highly directive dipole antenna embedded in a Fabry-Perot type cavity," *IEEE Microwave and Wireless Components Letters*, Vol. 12, No. 2, 48–50, 2002.
7. Ismahayati, A, P. J. Soh, R. Hadibah, and G. A. E. Vandenbosch, "Design and analysis of a multiband koch fractal monopole antenna," *IEEE International RF and Microwave Conference (RFM)*, 58–62, 2011.

A Spiral Antenna with Integrated Planar Feeding Structure

Huifen Huang, Zonglin Lv, and Junfeng Wu

School of Electronic and Information Engineering
South China University of Technology, China

Abstract— In practical applications, the low-profile spiral antennas suffer from the lack of proper planar feeding ways. The vertical balun always has a significantly long length, inconsistent with the requirements of the low profile spiral antenna geometry. A spiral antenna with integrated planar feeding structure is proposed in this paper. The antenna used has obviously improved axial ratio compared to the equiangular spiral antenna at low frequencies. And the traditional balun in the third dimension is moved to the planar plane. The resulting structure maintains the typical radiation behavior and the broadband operation of the spiral antennas, but the vertical balun is integrated at the same plane with the antenna. The overall size of the spiral antenna is largely reduced.

1. INTRODUCTION

Planar spiral antennas have the advantages of great performance on circular polarization, easy impedance matching, and the superior radiation efficiency. However, the conventional feeding structure for planar spiral antennas is situated in the center of the spiral and extends into the third dimension [1].

Many efforts have been made to feed spiral antennas in the planar plane, but the radiation behavior always becomes worse at the same time. Feeding the spiral from the terminations on the perimeter is proposed. This method achieves a completely planar spiral antenna at the cost of limited band width [2]. The coplanar waveguide (CPW)-fed slot antenna has received considerable attention [3]. Despite the advantages of completely planar structure, the CP (circularly polarization) bandwidth is also limited.

Feeding the spiral with a transmission line that follows the metal layer beneath the spiral arm to the center point is proposed [4]. This method is used to feed equiangular spiral antenna and achieves axial ratio below 5 dB over the frequency range of 3–10 GHz, but it is impossible to feed the Archimedean spiral antenna in the same way because of its long and thin arms. However, the Archimedean spiral antenna has a noticeable advantage at axial ratio bandwidth over its equiangular counterparts. On this condition, this paper uses the similar feeding way to feed a newly designed spiral antenna. The antenna designed has largely improved axial ratio compared to the equiangular spiral antenna at comparable size, and the arms are wider and largely shorter than the Archimedean spiral antenna to make it possible to feed the antenna in similar way with [4]. The spiral antenna and a Dyson-style balun have been integrated into a multi-layer structure. The resulting structure maintains the typical radiation behavior and broadband operation of spiral antennas, and achieves good axial ratio performance without the vertical balun. The overall size of the spiral antenna is largely reduced.

2. ANTENNA DESIGN

Figure 1 shows the conventional equiangular spiral antenna, Archimedean spiral antenna and the newly designed antenna. The new spiral antenna edge is described by (1).

$$r(\varphi) = r_0 * A * \left[\frac{\arctan(\varphi - B)}{C} + D \right] \quad (1)$$

where r is the radial distance, φ is the winding angle, and r_0 is the inner radius. A , B , C and D are constants related to the defining geometrical parameters of the antennas.

As shown in Figure 1, the Archimedean spiral has thin and long arms and is impossible to be fed in the new way mentioned in [4]. However, Archimedean spiral has an obvious advantage of axial ratio bandwidth at comparable size. On this condition, the new kind of spiral antenna is designed to achieve improved axial ratio and shorted arm length. The design process of the new antenna is well explained in our former work [5].

Figure 2 shows the newly designed antenna with integrated planar feeding structure. The balun and the antenna are integrated together at the border. The spiral antenna uses one arm of the

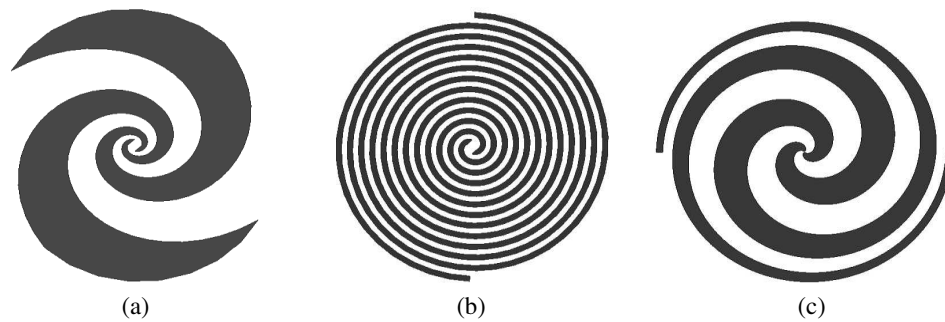


Figure 1: The antennas discussed in this paper. (a) Equiangular spiral, (b) archimedean spiral, (c) new spiral.

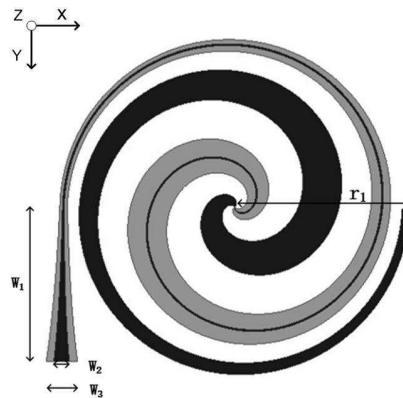


Figure 2: The geometry of the proposed antenna. Metal on the front side (black) and metal on the back side (gray).

Table 1: Parameters of the antennas.

A	B	C	D	r_0	φ_{\max}	W_1	W_2	W_3
64.1	4.6	3	1	0.2 mm	3.75π	25 mm	2.5 mm	5 mm

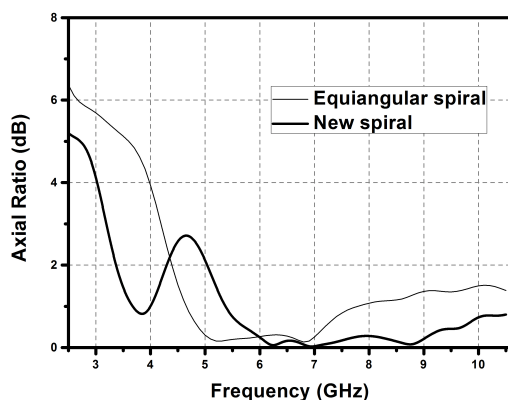


Figure 3: Simulated axial ratio for the new spiral and equiangular spiral.

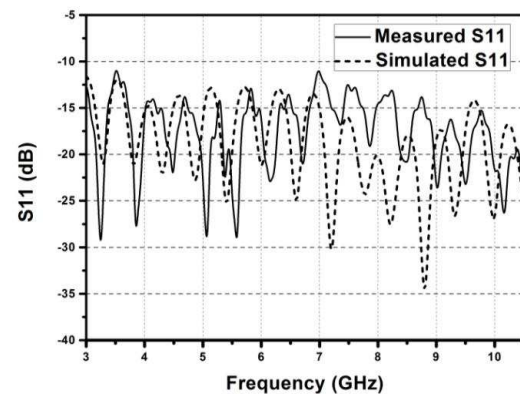


Figure 4: Measured and simulated S_{11} .

spiral antenna as ground of the stripline feed network and the center conductor of the strip line provides the other spiral arm.

The parameters A , B , C , D , r_0 , φ_{\max} , W_1 , W_2 , and W_3 are illustrated in Table 1. The antenna is constructed on the F4B substrate with the dielectric constant of 2.2, the loss tangent of 0.0009 and the thickness of 0.8 mm, occupying an area of $70 \times 70 \text{ mm}^2$.

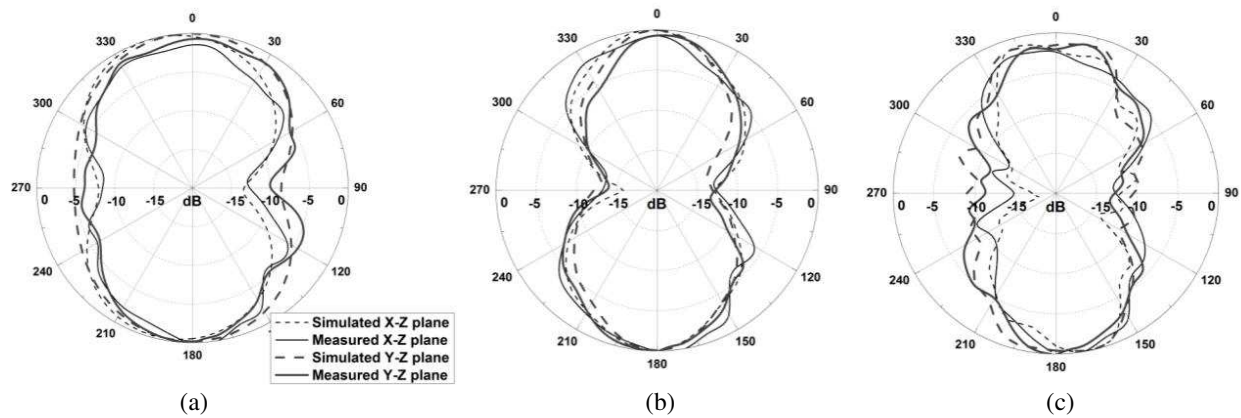


Figure 5: Measured and simulated radiation directivity, (a) 3 GHz, (b) 6 GHz, (c) 9 GHz.

3. SIMULATIONS AND MEASUREMENTS

The antenna performance is investigated by HFSS simulation software. The axial ratio of the new spiral antenna and equiangular spiral antenna are compared in Figure 3. The new antenna has a noticeable advantage of axial ratio at low frequencies compared to equiangular spiral antenna at even smaller size. The radius of the equiangular spiral antenna is 32.5 mm. The radius of the new spiral antenna is only 28 mm, and the axial ratio is largely improved at low frequencies.

Figure 4 shows measured and simulated results of S_{11} for the developed spiral antenna with feeding structure.

Figure 5 shows comparison between simulated and measured results of normalized radiation patterns for the total gain at 3 GHz, 6 GHz, and 9 GHz.

4. CONCLUSION

A new spiral antenna with a planar feeding structure is proposed in this paper. The antenna used has a noticeable advantage of axial ratio over equiangular spiral antenna. And the traditional vertical balun has been replaced by integrated planar feeding structure. The resulting structure maintains the typical radiation behavior and broadband operation of spiral antennas, and achieves good axial ratio performance without the vertical balun.

ACKNOWLEDGMENT

This work is supported by the National Natural Science Foundation of China under Grant 61071056.

REFERENCES

1. Gschwendtner, E., J. Parlebas, and W. Wiesbeck, "Spiral antenna with planar external feeding," *Proc. 29th Eur. Microwave Conf.*, Vol. 1, 135–138, 1999.
2. Wu, W. Z., T. H. Chang, and J. F. Kiang, "Broadband slot spiral antenna with external feed and microstrip-to-slotline transition," *Proc. IEEE AP-S Int. Symp.*, Vol. 1, 767–770, Jun. 2004.
3. Wang, C.-J. and D.-F. Hsu, "Studies of the novel CPW-fed spiral slot antenna," *IEEE Antennas Wireless Propag. Lett.*, Vol. 3, No. 1, 186–188, Dec. 2004.
4. Veysi, M. and M. Kamyab, "Bandwidth enhancement of low-profile PEC-backed equiangular spiral antennas incorporating metallic posts," *IEEE Transactions on Antennas and Propagation*, Vol. 59, No. 11, 4315–4318, 2011.
5. Huang, H.-F. and Z. Lv, "A new spiral antenna with improved axial ratio and shorted arm length," *Progress In Electromagnetics Research C*, Vol. 46, 83–89, 2014.

A Novel Compact UWB Antenna with Triple Band-notched Characteristics

Lin Chen¹, Shaobin Liu¹, Xiangkun Kong^{1,2}, Borui Bian¹, and Zhiwen Mao¹

¹Key Laboratory of Radar Imaging and Microwave Photonics, Ministry of Education
College of Electronic and Information Engineering

Nanjing University of Aeronautics and Astronautics, Nanjing 210016, China

²Jiangsu Key Laboratory of Meteorological Observation and Information Processing
Nanjing University of Information Science and Technology, Nanjing 210044, China

Abstract— In this article, a novel compact ultra-wideband (UWB) planar monopole antenna with tri-notched bands is presented. The proposed antenna is fed by a microstrip line and a partial ground plane. The antenna achieves an operating bandwidth ranging from 2.9 to more than 11 GHz and triple band-notched properties of 3.22–3.91, 5.15–5.44, 5.70–5.91 GHz. Throughout this article, the simulated and experimental results of impedance characteristic, gain, and radiation patterns are presented and discussed. The proposed antenna has an overall dimension of $20 \times 21.1 \text{ mm}^2$.

1. INTRODUCTION

Since the US Federal Communications Commission approved the unlicensed use of UWB from 3.1 to 10.6 GHz for commercial communications, the ultrawideband technology has drawn more and more attention for its merits such as low cost, low complexity, wide impedance bandwidth and omnidirectional radiation pattern [1]. However there still co-exists other communication protocols such as the world interoperability for microwave access (WiMAX) service (3.3–3.6 GHz) and the Wireless Local Area Network (WLAN) service (5.15–5.35 GHz, 5.725–5.825 GHz). It is necessary to avert the overlapping frequency bands.

Recently, many new antennas with band-notched function have been put forward for the UWB systems which can prevent the interference problem. There are lots of ways in which band-notched characteristics can be achieved. The common and popular method is to insert different shaped slots on the patch or the ground plane, including U-shaped, -shaped, L-shaped, C-shaped and etc. [2–4]. Apart from this, there are many other methods to create the band-notched property such as using parasitic structures, adding split ring resonator (SRR) coupled to the feed-line or adopting the complimentary split ring resonator (CSRR) structure. All of the methods mentioned above obey the same rule that is to introduce a perturbation into the antennas.

In this study, a novel compact UWB antenna with triple notched band at 3.22–3.91, 5.15–5.44, 5.70–5.91 GHz is proposed. A tapered radiating patch is designed to cover UWB working frequency band. The radiation patch and ground plane of the original antenna are all cut by arc which is for impedance matching over the whole UWB. Resonating element etched out above the ground plane generates the rejection at WiMAX band. To achieve the lower and higher WLAN band-notched characteristics, two independent curved slots is embeded into the radiation patch. Moreover, the proposed antenna here is significantly smaller and exhibits omni-directional radiation patterns which makes it a suitable candidate for the UWB system.

2. ANTENNA DESIGN

The configuration of the proposed antenna and its dimensions are exhibited in Figure 1. The microstrip-fed antenna has a compact size of $20 \times 21.1 \text{ mm}^2$ and is printed on 1.0 mm thick F4B-2 dielectric substrate with dielectric constant 2.65 and loss tangent 0.001. Because the tapered geometry of the patch and the microstrip line, the proposed antenna will have good performances at a very wide band.

As illustrated in the Figure 1, the resonant element symmetrically etched above the ground plane generates the rejection at WiMAX band and two meandering slots embedded within the patch is designed to create the notched bands at lower and upper WLAN band. The upper band-notched slot is longer in length than the lower one corresponding to the lower and higher WLAN band conversely. Furthermore, the total length of the inserted meandering quarter wavelength slot

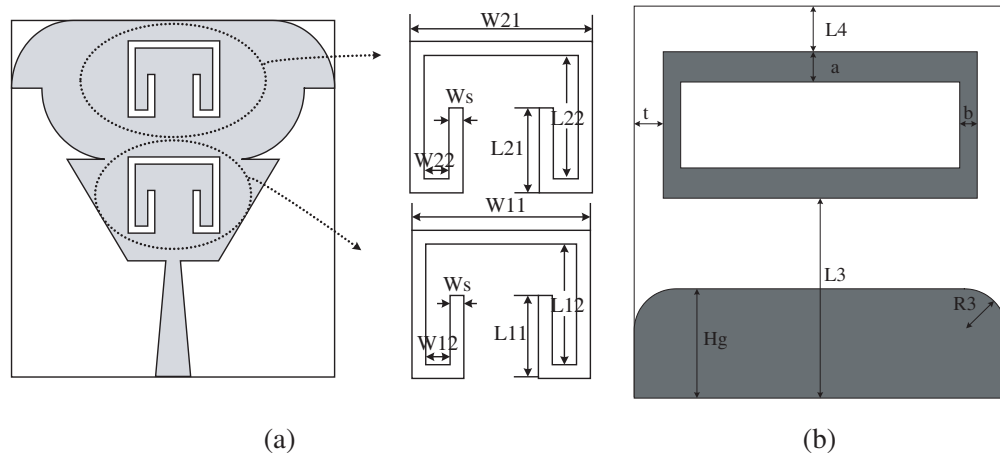


Figure 1: Configuration of the proposed antenna with triple notched-bands: (a) top view of the antenna, (b) bottom view of the antenna. (Dimensions: $W_{11} = 5.8$ mm; $W_{12} = 1.0$ mm; $W_s = 0.3$ mm; $L_{11} = 2.6$ mm; $L_{12} = 3.7$ mm; $W_{21} = 6$ mm; $W_{22} = 0.9$ mm; $L_{21} = 2.8$ mm; $L_{22} = 4$ mm; $t = 1.4$ mm; $a = 1.1$ mm; $b = 0.6$ mm; $L_3 = 9$ mm; $L_4 = 2$ mm; Unit: mm).

resonator L_i ($i = 1, 2$) can be calculated from the following formulas:

$$L_i \approx \frac{c}{4f_i \sqrt{\epsilon_{eff}}} \quad (1)$$

$$\epsilon_{eff} = \frac{\epsilon_r + 1}{2} \quad (2)$$

where c is the speed of light in free space, ϵ_r is the dielectric constant of the substrate, f_i ($i = 1, 2$) is the center frequency of notched bands and ϵ_{eff} is effective dielectric constant.

3. MEASUREMENT RESULTS

The proposed antenna structure is simulated and optimized using Ansoft High Frequency Structure Simulator. Besides, the photo of the fabricated antenna is shown in Figure 2. From the Figure 3, one can see the simulated and measured results match well which validates our design concept and theory.

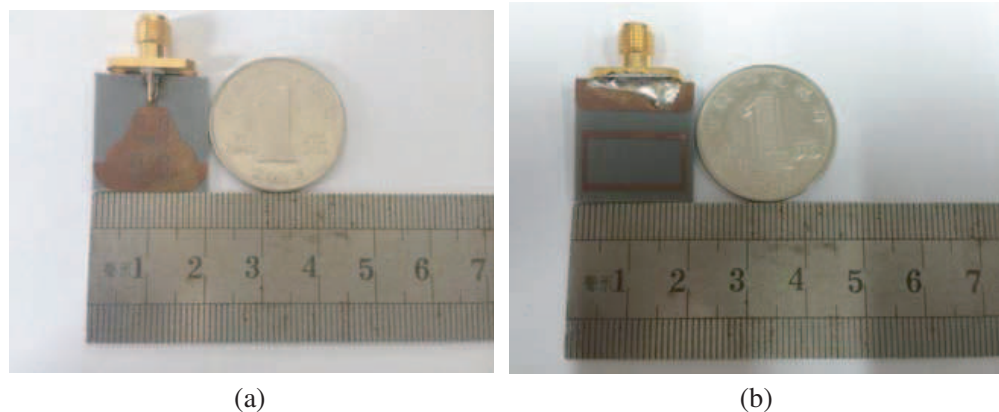


Figure 2: Photograph of the fabricated UWB antenna: (a) top view, (b) bottom view.

Figure 4 shows the far-field radiation patterns at 4, 7 and 10 GHz, the copolarization and cross-polarization in the x - z (E -plane) and y - z (H -plane) planes are given. It can be observed that the proposed antenna has an approximately omni-directional radiation patterns at these frequencies.

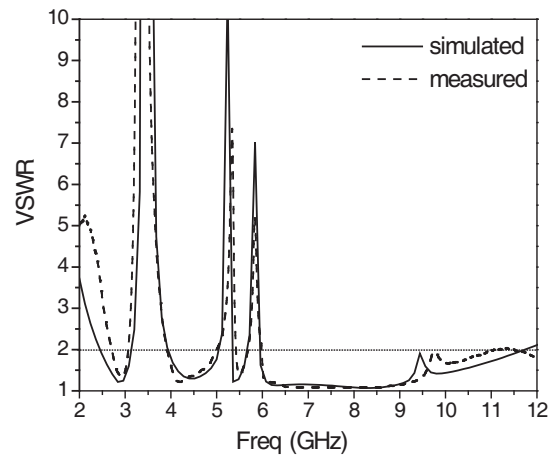


Figure 3: Simulated and measured VSWR of the proposed antenna.

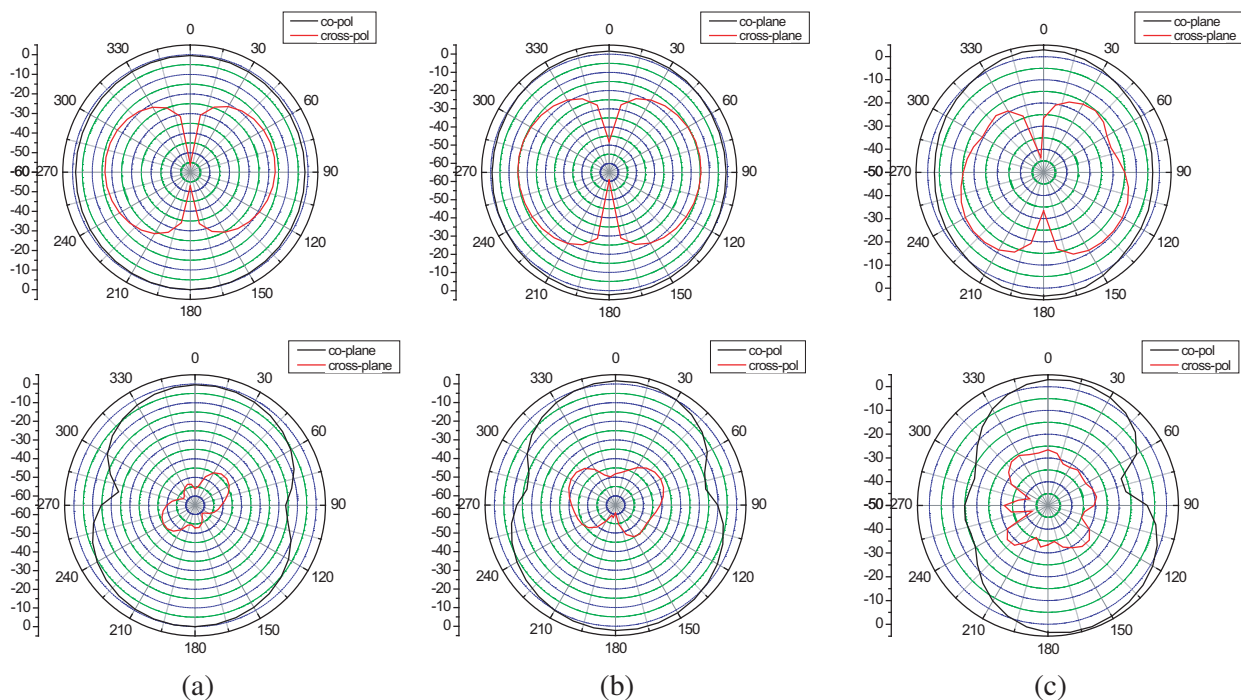


Figure 4: Radiation patterns of the antenna at (a) 4 GHz, (b) 7 GHz and (c) 10 GHz.

4. CONCLUSION

A novel compact UWB planar antenna with tri-notched bands to eliminate interfering signals from WLAN and WiMAX systems has been presented and discussed. The band notches are realized by rectangular ring above the ground plane to omit the WiMAX frequency band. To realize the WLAN notch band, two curved slots is placed into the radiation patch. It is observed from the measurement that the proposed antenna achieved good UWB performance. Therefore, the proposed antenna is suitable for UWB applications.

ACKNOWLEDGMENT

This work was supported by Funding of Jiangsu Innovation Program for Graduate Education (No. CXZZ13.0166), the Fundamental Research Funds for the Central Universities (No. NZ2013302), the Funding for Outstanding Doctoral Dissertation in NUAA (No. BCXJ11-05), the Chinese Specialized Research Fund for the Doctoral Program of Higher Education (No. 20123218110017), the Jiangsu Province Science Foundation (No. BK2011727), and the Foundation of Aeronautical Science (No. 20121852030).

REFERENCES

1. Federal Communication Commission, “Authorization of ultra-wideband technology,” First Note and Order, February 14, 2002.
2. Liu, X., Y. Yin, and P. Liu, “A compact CPW-FED UWB antenna with independent dual band-notched characteristics,” *Microwave and Optical Technology Letters*, Vol. 55, No. 5, 1126–1130, 2013.
3. Azim, R. and M. T. Islam, “Compact planar UWB antenna with band notch characteristics for WLAN and DSRC,” *Progress In Electromagnetics Research*, Vol. 133, 391–406, 2013.
4. Zhou, D., S. C. S. Gao, F. Zhu, R. A. Abd-Alhameed, and J.-D. Xu, “A simple and compact planar ultra wideband antenna with single or dual band-notched characteristics,” *Progress In Electromagnetics Research*, Vol. 123, 47–65, 2012.
5. Li, C.-M. and L.-H. Ye “Improved dual band-notched uwb slot antenna with controllable notched bandwidths,” *Progress In Electromagnetics Research*, Vol. 115, 2011.
6. Islam, M. T., R. Azim, and A. T. Mobashsher, “Triple band-notched planar UWB antenna using parasitic strips,” *Progress In Electromagnetics Research*, Vol. 29, 161–179, 2012.

Quasi-coherent Noise Jamming Based on Interrupted-sampling and Pseudo-random Serials Phase-modulation

Ning Tai, Yu-Jian Pan, Deping Zhang, Chao Wang, and Naichang Yuan

College of Electronic Science and Engineering
National University of Defense Technology, Changsha, China

Abstract— Using the idea of pseudo-random serials phase modulation for reference, an active jamming method of quasi-coherent noise suppression is proposed for countering wideband radar of pulse compression system. The basic idea is that the jammer processes interrupted-sampling in range direction and modulates phases on sampled radar signal according the values of pseudo-random serials, and then sends the jamming signal to victim radar. This method will form large amounts of noise around the pulse compression output of target echo. Simulation results shows that jammer based on this technology needs less jamming power than other non-coherent ones.

1. INTRODUCTION

Coherent radars, for example, pulse compression radar and pulse Doppler radar, can achieve high coherent processing gain by making use of the characteristics of intra pulse and inter pulse [1]. This coherent processing obviously depresses the efficiency of non-coherent electronic jamming and puts forward a great challenge for radar jammer. With the development of high-speed large scale integrated circuits and signal processing method in the electronic counter field, technologies such as digital radio frequency memory (DRFM) and direct digital synthesizer (DDS) have become popular measures to counter coherent radars [2]. After detecting radar signal, jammer with two receive-transmit antennas which work asynchronously should receive and transmit the sampled signal. But in many occasions, the high isolation between two antennas is difficulty or even unable to be implemented. To solve this problem, [3] proposes a method based on interrupted-sampling. The jammer samples a segment of radar signal and then transmits the sampled signal. A train of false targets will be achieved after the sampled signal passing through the matched filter of pulse compression radars. [4] introduces a kind of smart noise jamming technology: convolution modulation noise jamming method. This type of jamming could acquire radar processing gain but its real-time is not good and can't be applied in the jammer with only one antenna. This paper proposes a quasi-coherent jamming signal. Section 2 describes the time domain characteristic and the frequency domain characteristic of pseudo-random serials phase-modulation signal. Section 3 deals with the interrupted-sampling theory. Section 4 shows the output of pulse compression radar when the jamming signal feeds the matched filter. Section 5 gives the simulation results of jamming effect and conclusions.

2. THEORY OF PSEUDO-RANDOM SERIALS PHASE-MODULATION

Pseudo-random serials are usually applied in spread-spectrum communication and the serials can be created by a shift register under the control of oscillator. The expression of the serials in time domain is as below:

$$u(t) = \sum_{l=-\infty}^{+\infty} \sum_{i=0}^{N-1} \text{rect} \left(\frac{t - \frac{T_c}{2} - iT_c - lPT_c}{T_c} \right) a(i) \quad (1)$$

where $\text{rect}(\frac{t}{T_c}) = \begin{cases} 1 & |t| \leq \frac{T_c}{2} \\ 0 & \text{else} \end{cases}$, $a(i) = \pm 1$, T_c is the code width and P is the period of pseudo-random serials, For the pseudo-random serials created by a N bit shift register, P equals to $2^N - 1$. From expression (1) we can get the power spectral density [5].

$$G(f) = \frac{P+1}{P^2} \left(\frac{\sin(\pi f T_c)}{\pi f T_c} \right)^2 \sum_{\substack{k=-\infty \\ k \neq 0}}^{+\infty} \delta \left(f - \frac{k}{PT} \right) + \frac{1}{P^2} \delta(f) \quad (2)$$

Figure 1 illuminates the power spectral density of pseudo-random serials, of which T_c is set as $0.5 \mu\text{s}$. The result shows that the main power of pseudo-random serials is concentrated in

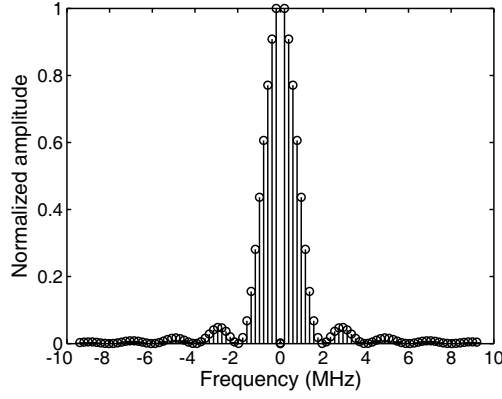


Figure 1: Power spectral density.

$[-1/T_c, +1/T_c]$. The envelope of power spectral density is determined by the code width T_c , that's to say, T_c determines the frequency spectrum width of pseudo-random serials. The shorter T_c is, the wider the frequency width will be, and the main amplitude will descend.

3. THE THEORY OF INTERRUPTED-SAMPLING AND DIRECT TRANSMITTING

This section briefly introduces the theory of interrupted-sampling and direct transmitting jamming. The basic procedure is: A serial of rectangle pulse is used for sampling the large band-time product radar signal and meanwhile the transmitting process takes place at the interval between two sampling processes. Assuming the interrupted-sampling signal noted as $p(t)$ is a rectangular envelope pulse train with pulse repeat interval T_s and pulse duration τ .

$$p(t) = \text{rec}\left(\frac{t}{\tau}\right) * \sum_{n=-\infty}^{+\infty} \delta(t - nT_s) \quad (3)$$

The corresponding frequency spectrum is given as:

$$P(f) = \sum_{-\infty}^{+\infty} \tau f_s \cdot \text{sa}(\pi n f_s \tau) \cdot \delta(f - n f_s) \quad (4)$$

where $\text{sa}(x) = \sin(x)/x$ and $f_s = 1/T_s$ means the sampling frequency of interrupted-sampling signal. A special occasion in (4) is $T_s = 2\tau$, i.e., $p(t)$ is a square pulse train, and (4) becomes

$$P(f) = \sum_{-\infty}^{+\infty} \frac{1}{2} \cdot \text{sa}\left(\frac{n\pi}{2}\right) \cdot \delta(f - n f_s) \quad (5)$$

It is obvious that when n is even except for zero, the amplitude of (5) is zero and it decreases when n increases. Assume that the radar signal intercepted by jammer is $x(t)$, so that the sampled radar signal is

$$x_s(t) = p(t)x(t) \quad (6)$$

and its frequency spectrum is

$$X_s(f) = P(f) * X(f) \quad (7)$$

Substituting (4) into (7), the expression becomes:

$$X_s(f) = \sum_{n=-\infty}^{+\infty} \tau f_s \cdot \text{sa}(\pi n f_s \tau) \cdot X(f - n f_s) \quad (8)$$

From (8) we can see that $X_s(f)$ is a weighted superposition of the shifted replicas of $X(f)$. The weighting coefficient is $\tau f_s \cdot \text{sa}(\pi n f_s \tau)$. In the situation $T_s = 2\tau$, (8) becomes

$$X_s(f) = \sum_{n=-\infty}^{+\infty} \frac{1}{2} \cdot \text{sa}\left(\frac{n\pi}{2}\right) \cdot X(f - n f_s) \quad (9)$$

When $n = 0$, $X_s(f)$ equals to the spectrum of real target echo wave. Thus this portion could form a primary false target after matched filter as same as the real target. The other parts $X(f - nf_s)$ shifting $\pm nf_s$ in frequency can be seen as jamming signals adding $\pm nf_s$ to f . For a linear frequency modulated (LFM) signal pulse compression radar, this jamming signal after pulse compression will form multiple false targets with different amplitude in the range direction. The amplitude is determined by $\tau f_s \cdot sa(\pi n f_s \tau)$. These false targets are located symmetrically around the primary false target. With the increasing of n , the mismatch after matched filter in $X(f - nf_s)$ is getting worse, and the amplitude of false target debases heavily. Thus this jamming method of interrupted-sampling and direct transmitting usually forms 3 to 5 effective false targets. The simulation parameters are set as below: The radar signal bandwidth is 10 MHz, pulse width is 48 μs , and the sample signal period T_s is 4 or 2 μs . As is shown in Fig. 2, multiple false are achieved after pulse compression and the distance between two neighboring false targets are determined by T_s . An especial instance is that is larger than the bandwidth of radar signal so that $X(f \pm nf_s)$ $n \neq 0$ is located outside the bandwidth of match filter. The jamming signal in above occasion generates only one primary false target and this is the limitation of this type of jamming.

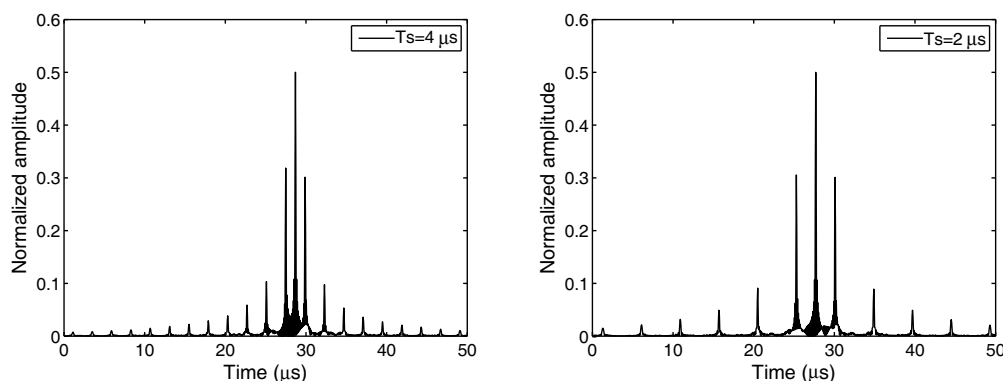


Figure 2: Pulse compression results of interrupted-sampling and direct transmitting.

4. INTERRUPTED-SAMPLING AND PSEUDO-SERIALS PHASE-MODULATION JAMMING METHOD

The pseudo-random serials phase-modulation process on sampled signal is the product of (1) and (6).

$$x_p(t) = u(t)x_s(t) \quad (10)$$

Of which the frequency spectrum is:

$$X_p(f) = U(f) * X_s(f) \quad (11)$$

From the analysis in Section 2 we know that the pseudo-random serials phase-modulation will expand the spectrum of modulated signal. Section 3 shows that interrupted-sampling jamming can form many false targets. (11) means that $X_p(f)$ is the superposition of each expanded false target. We know that phase-modulation by pseudo-random serials further wrecks the coherence between interrupted-sampling signal and radar signal, but this jamming method can still get some processing gain. Thus this jamming effect is similar to noise jamming but the frequency of jamming signal is around that of radar signal. (10) shows that when the value of pseudo-random serials changes, a 180° phase change happens in the jamming signal. This discontinuity caused by phase conversion will expand the spectrum of signal. Fig. 3 shows pulse compression outputs of target echo, Gauss noise and jamming signal. In the simulation, the interrupted-sampling period is 4 μs with a duty ratio 50%. The code width of pseudo-random serials is 0.5 μs and the length of serials is 511. The parameter of LFM signal is set as: bandwidth is 10 MHz and pulse width is 48 μs . From the results we know that jamming signal forms large amount of noise around the radar echo and Gauss noise distributes evenly in time domain. The coherence between jamming signal and original radar signal declines after phase-modulation and thus the processing gain of jamming signal will of course debase.

As is shown in Fig. 3, the ideal amplitude output of LFM signal after pulse compression is normalized to 1.00. The jamming signal output descends obviously to the value of 0.14. Meanwhile

the amplitude of Gauss noise is nearly 0.02. Compared with the non-coherent Gauss noise, this jamming signal can achieve more processing gain, which means that this method saves jamming power. Provided that the power of jammer is large enough, victim radar can't distinguish the right position of target from the jammed situation. A jammer based on this theory requires lower jamming power than other non-coherent jammers and it depresses a long distance for the covered target. Fig. 3 shows that the jamming signal covers 20 μs in time domain and depresses 6 kilometers in range direction. If code width is narrow, the cover distance is relative wide. But the processing gain decreases when code width becomes narrow, which means that the wider cover distance needs more jamming power. The simulation result indicates that with the selection of different code widths and sampling periods we can acquire different depressing distance and different pulse compression gain. To achieve a long depressing distance we need a narrow code width and large jamming power.

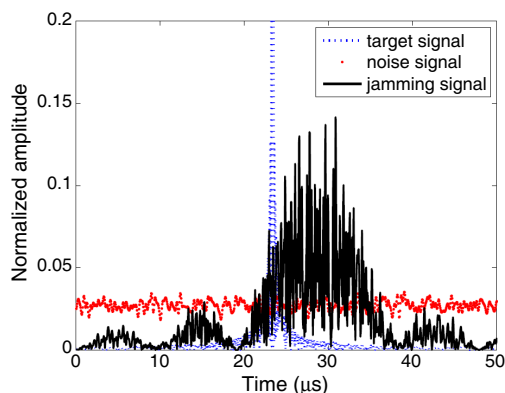


Figure 3: Pulse compression results of target echo, Gauss noise and jamming signal.

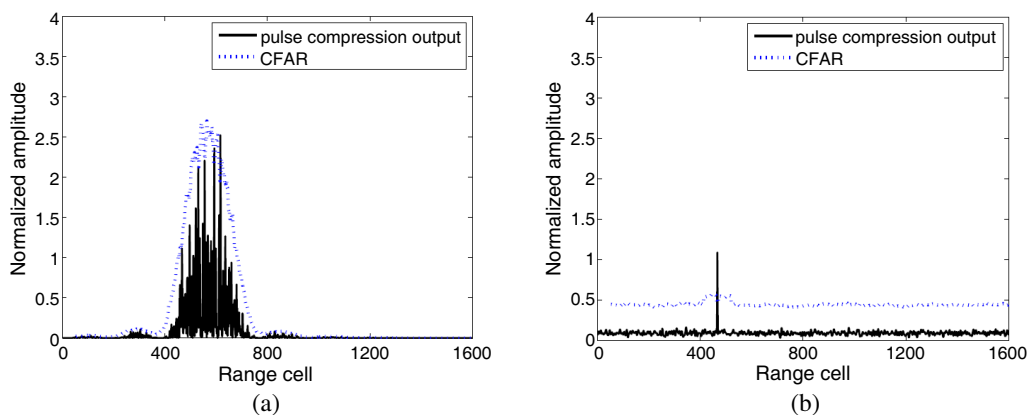


Figure 4: CFAR threshold results. (a) Jamming condition. (b) Gauss condition.

5. SIMULATION AND CONCLUSION

To validate the effect of this jamming method, we analyze the CFAR threshold of a pulse compression radar. The simulation parameters are set as: The pulse width of LFM signal is 48 μs , bandwidth is 10 MHz, pseudo-random serials code width is 0.5 μs . The period of interrupted-sampling signal is 4 μs with the duty ratio of 50%. The power of jamming signal and Gauss noise is 11.5 dB. The real target is located at the 467th range cell and the jammer is at the 534th range cell. The CFAR threshold results for quasi-coherent jamming signal and Gauss noise is shown in Fig. 4. In the simulation, the pulse compression amplitudes of jamming signal and Gauss noise are normalized to the amplitude of target. From the results we can see that Gauss noise enhances the CFAR threshold evenly but the target can be still distinguished. The quasi-coherent jamming signal forms large amount of noise around the real target and the CFAR threshold is too high for the real target so it can't be found out.

REFERENCES

1. Chen, S., D. Dai, and Y. Li, “The theory of 2-D cosinusoidal phase-modulated repeater scatter-wave jamming to SAR,” *Acta Electronica Sinica*, Vol. 37, No. 12, 2620–2625, 2009.
2. Yun, X., “An overview of modern frequency synthesizer techniques,” *Acta Electronica Sinica*, Vol. 23, No. 10, 148–151, 1995.
3. Wang, X., J. Liu, and W. Zhang, “Mathematic principles of interrupted-sampling repeater jamming (ISRJ),” *Sci. China Ser. F-Inf. Sci.*, Vol. 50, No. 1, 113–123, 2007.
4. Xu, X., Y. Bao, and H. Zhou, “Technology of smart noise jamming based on convolution modulation,” *Modern Radar*, Vol. 29, No. 5, 28–31, 2007.
5. Zhong, C., “Study on pseudorandom signal source in pseudorandom phase modulation fuze,” *Guidance & Fuze*, Vol. 26, No. 2, 14–18, 2005.

Validation Analysis and Test of Semiconductor Device Simulator GSRES

Yong Li¹, Gong Ding¹, Haiyan Xie¹, Chun Xuan¹, Hong-Fu Xia¹, and Jian-Guo Wang^{1,2}

¹Northwest Institute of Nuclear Technology, Xi'an 710024, China

²School of Electronic and Information Engineering, Xi'an Jiaotong University, Xi'an 710049, China

Abstract— Basic drift-diffusion model (DDM) of carriers in semiconductor using in a numerical simulator: General Semiconductor Radiation Effect Simulator (GSRES), is studied in order to identify and reduce the numerical errors of this semiconductor simulator. Numerical approximations of the semiconductor device EMP effect simulator is analysed. Numerical errors caused by approximation of the field distribution of lattice temperature, and approximation the of the recombination rate and generation rate are studied. Application range of this simulator is analysed according to the numerical errors caused by these approximations. Terms of the simulator that should be improved and enhanced precision are given.

1. INTRODUCTION

Numerical simulation of semiconductor devices can reflect the physical phenomena and mechanisms of devices, and is important in effect study. This simulation method is proved to be efficient and accurate as many research papers showed [1–5]. A two-dimension semiconductor device Electromagnetic pulse effect simulator GSRES (General Semiconductor Radiation Effect Simulator) is using widely in numerical simulation radiated field (EMP, HPM) effect of semiconductor device, which is developed by our research group. This simulator contains modeling modularmeshing modulardata-base of material parameters and Graphical User Interface (GUI). The numerical simulation of carriers bases on Drift-Diffusion Model (DDM). Two-dimension semiconductor device and simple circuit can be simulation numerically by this simulator [6–9].

The demand of analysis of error sources rises up while manufacturer technic of device and precision of experiments are developing [10–12]. For another reason, Verification and validation (V&V) analysis is required for engineering implementation of GSRES. Bases on these requirement, physical models (DDM) in GSRES are analysed, possible error sources are evaluated, and contemplation. of capability of upgrade version GSRES is established.

1.1. Basic Drift-diffusion Model in GSRES

Response capability of device is determined by the movement of carriers in semiconductor material [8, 13, 14]. Drift-Diffusion model is used more and more widely in numerical simulation of semiconductor device since the first use by Gummel. Drift-Diffusion model is based on this equation

$$\begin{cases} \frac{\partial n}{\partial t} = \nabla \cdot (\mu_n n \vec{E}_n + \mu_n \frac{k_b T}{q} \nabla n) - (U - G) \\ \frac{\partial p}{\partial t} = -\nabla \cdot (\mu_p p \vec{E}_p - \mu_p \frac{k_b T}{q} \nabla p) - (U - G) \\ \nabla \cdot \varepsilon \nabla \psi = -q (p - n + N_D^+ - N_A^-) - \rho_s \end{cases} \quad (1)$$

where n is the concentration of carrier electron and p for hole; N_D^+ is the concentration of effective ionic donors and N_A^- for acceptor; μ_n is mobility of electron and μ_p for hole; \vec{E}_n is the equivalent electric field intensity to electron and \vec{E}_p for hole; ψ is electrostatic potential; ρ_s is the static charge and interphase charge; U is the recombination term of carrier. G is the generation term of carrier; T is temperature; q is charge of electron.

Equation (1) is the basic and mostly used calculation model in GSRES. Analysis of error sources is base on this model in this paper.

2. APPROXIMATION IN SIMULATION MODEL

The basic DDM in Equation (9) is deduced by the solution of electromagnetic Poisson equation base on energy band and tight-banding theory. In the deduce process of basic DDM, these assumptions are taken: (a) velocity of carriers much more less than light; (b) collisions of carriers in the semiconductor material are elastic; (c) collisions of carriers do not effect gap of energy band; (d) temperatures

of carriers and lattice are equality. Approximations of calculation model in GSRES center in two: (1) the approximations induced by energy band and tight banding theory; (2) approximations induced by DDM. In this paper, our error analysis focuses on the approximations induced by DDM.

In DDM used in GSRES, approximations mostly in: (a) distribution and change of temperature; (b) recombination and generation rate of carrier; (c) mobility model.

2.1. Approximation Caused by Distribution and Change of Temperature

In Equation (9), the basic DDM takes approximations in the distribution and change of temperature, the temperature of lattice is assumed to be uniformity and invariableness and no temperature effect is taken into the model. If the gradient term of temperature is not 0, the DDM in (1) now is

$$\begin{cases} \frac{\partial n}{\partial t} = \nabla \cdot \left(\mu_n n \vec{E}_n + \mu_n \frac{k_b T}{q} \nabla n + \mu_n \frac{k_b n}{q} \nabla T \right) - (U - G) \\ \frac{\partial p}{\partial t} = -\nabla \cdot \left(\mu_p p \vec{E}_p - \mu_p \frac{k_b T}{q} \nabla p - \mu_p \frac{k_b p}{q} \nabla T \right) - (U - G) \\ \nabla \cdot \varepsilon \nabla \psi = -q (p - n + N_D^+ - N_A^-) - \rho_s \\ \rho c_p \frac{\partial T}{\partial t} = \nabla \cdot \kappa \nabla T + \vec{J} \cdot \vec{E} + (E_g + 3k_b T) \cdot (U - G) \end{cases} \quad (2)$$

The fourth equation in (2) is equation of heat generation and diffusion. ρ is mass density. c_p is heat capacity. κ is heat diffusion coefficient. E_g is gap of energy band. This equation means: thermal energy which is absorbed or released in unit volume contains three parts: induced by heat diffusion as the first term; induced by current as the second term; induced by generation and recombination of carriers as the third term.

In Equation (2), the gradient term of temperature is not 0, but temperature of carriers is set to be same with the temperature of lattice, the difference between these two is ignored. When considered the difference, the fourth term in Equation (2) must be changed, the equation current density of electron and hole and the equation of heat diffusion of lattice is

$$\begin{cases} \vec{J}_n = q \mu_n n \vec{E}_n + k_b \mu_n (n \nabla T_n + T_n \nabla n) \\ \vec{J}_p = q \mu_p p \vec{E}_p - k_b \mu_p (p \nabla T_p + T_p \nabla p) \\ \rho c_p \frac{\partial T}{\partial t} = \nabla \cdot \kappa \nabla T + (E_g + \omega_n + \omega_p) \cdot (U - G) + \frac{n(\omega_n - \omega_0)}{\tau_{\omega_n}} + \frac{p(\omega_p - \omega_0)}{\tau_{\omega_p}} \end{cases} \quad (3)$$

\vec{J}_n is current density of electron. \vec{J}_p is current density of hole. T_n is the temperature of electron. T_p is the temperature of hole. ω_0 is the balance energy of carriers (when temperature of carriers equivalent to lattice). τ_{ω_n} is the energy relaxation times of electrons and τ_{ω_p} is the energy relaxation times of holes.

The calculation model in (3) considered the energy exchange between carriers and lattice. Carriers exchange energy with lattice by collision, and can be characterized by energy relaxation times. This model is much more precise than models in (1) and (2), and cost much more computer memory resource and CPU time for numerical simulation.

2.2. Approximation Caused by Recombination and Generation Rate of Carrier

In GSRES, recombination of carriers are numerically simulated by three mechanism [8, 14]: Shockley-Read-Hall (SRH) recombination mechanism; Auger recombination mechanism; direct recombination mechanism. SRH recombination characterizes the recombination of carriers nearby impurity and defects. These impurity and defects which facilitate recombination are defined as recombination centers. Auger recombination characterizes the recombination of electron-hole pair with the help of another carrier which absorbs energy from the electron-hole pair. Direct recombination characterizes the recombination of electron-hole pair directly with the help of an electron's transition from conduction band to valence band. Commonly, SRH recombination is the mostly mechanism in semiconductor material. Auger recombination taking more and more rate as the density of carriers increasing. Direct recombination arises in high injection levels (for instance: power device) only.

In GSRES, these three recombination mechanisms are simulated separately for the difficulty form numerical simulation. Total recombination rate is the sum of these three.

$$U = U_n = U_p = U_{\text{SRH}} + U_{\text{dir}} + U_{\text{Auger}} \quad (4)$$

The term in right side means SRH recombination rate, direct recombination rate and Auger recombination rate.

$$\begin{cases} U_{\text{SRH}} = \frac{pn - n_{ie}^2}{\tau_p \left[n + n_{ie} \exp\left(\frac{\text{ETRAP}}{kT_L}\right) \right] + \tau_n \left[p + n_{ie} \exp\left(\frac{-\text{ETRAP}}{kT_L}\right) \right]} \\ U_{\text{Auger}} = \text{AUGN} (pn^2 + nn_{ie}^2) + \text{AUGN} (np^2 - pn_{ie}^2) \\ U_{\text{dir}} = \text{DIRECT} (np^2 - n_{ie}^2) \end{cases} \quad (5)$$

τ_n and τ_p are lifetime of electron and hole, which rest with density of impurity.

$$\begin{cases} \tau_n = \frac{\text{TAUN0}}{1 + N_{\text{total}}/\text{NSRHN}} \\ \tau_p = \frac{\text{TAUP0}}{1 + N_{\text{total}}/\text{NSRHP}} \end{cases} \quad (6)$$

The implicit value in Equations (5) and (6) of parameters in GSRES can be found in Reference [8].

The generation mechanism of carrier in GSRES is simulated by using an experimental equation advised by Selberherr [8, 14].

2.3. Approximation Caused by Mobility Model

Using mobility model pertinently can efficiently reduce numerical error, and extend the application of DDM. Mobility model contains three types in the main [14]: weak field model; surface model; strong field model; A integrated mobility model ordinarily combines weak field model and surface model, with modification due to the intensity of electric field.

Various mobility models are modularized in GSRES. A weak field model mostly used is Analytic Mobility Model, which is numerically fitting by experimental results. It is accurate in the simulation of diodes. Another weak field model is Philips Mobility Model, which is exactitude in the simulation of silicon triode. Lombardi surface model mostly used in simulation of silicon MOS device. Lucent model combines the modification of saturation velocity bulk mobility and surface mobility in strong field. Hewlett-Packard model can get the same precision in the simulation of MOS device as Lucent model, but can reduce CPU time efficiently.

These mobility models contains physical mechanism that not in DDM, in order to be tally with test results. For instance, enhanced diffusion effect caused by heat carriers is taken into modification of strong field. Impair effect caused surface state and letdown of carriers density caused by quantum well on Si-SiO₂ interface are both taken into surface mobility model. In fact, mobility models are modifications and complements for DDM, which improve simulation precision, extend application area, at the same time, aggrandizement instability and complicity of calculation.

3. ANALYSIS OF ERROR SOURCES

Approximation of temperature and approximation of mobility are found to be the main numerical sources of GSRES while using this simulator [10–12].

3.1. Errors Caused by Approximation of Temperature

Generation of heat happens in the same time with current. In the case when current is weak, Joule heat is small, so alteration of device's temperature is low. In that time, effect of temperature to performance of device can be ignored [10]. However, if the current is strong, the effect of the temperature to performance of device may be prominent.

In the case of strong field, insufficiency of energy exchange may happen because the velocity of carrier is too fast. Insufficiency of energy exchange may happen if the field last for a too short time. Avoidance of these case can improve simulation precision. Fig. 1 is the simulation result of 1.5KECA39 unidirectional TVS diode, which is a micron device. The numerical data is tally with test data [12].

3.2. Errors Caused by Approximation of Mobility

Mobility model is an modification and an complement for DDM. Numerical error will extremely be reduced by using pertinent mobility model contrapose to different structures and parameters. For instance, Lucent mobility model, which combines Philips Mobility Model and Lombardi surface Mobility Model, is not often used in simulation of simple device (like diode) for the reason of huge amount of calculation. But it can efficiently ameliorate numerical precision of the simulation of MOS device because the intense field in tunnel.

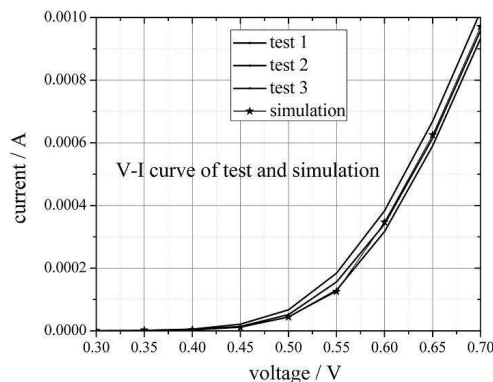


Figure 1: I-V curve of 1.5KECA39 unidirectional TVS diode.

As mentioned in part 3.1, if the scale of device on one direction is too small, simulation of thermal effect will be difficult For GSRES. Using surface Mobility model which considers quantum wall effect can extend the application of GSRES to these submicron device and nano scale device.

4. ANALYSIS OF APPLICATION SCOPE OF GSRES

In order to decide the application scope of GSRES, a validation test is taken. If the simulation error is less than that of the validation test, GSRES is indicated to be suitable. Otherwise, GSRES is indicated to be out of the application scope and inapplicable, modification should be taken in the calculation/physics model or the initial parameters.

In test, errors are mainly caused by two parts: the random error of samples and the errors of instrument. In the first, Character of TVS diodes are tested to find the random errors of these diode of same type. The errors are showed in Table 1.

Table 1: Random errors of TVS diode.

	Sample 1	Sample 1	Sample 1	errors
breakdown voltage	39.9	38.7	38.8	3.1%
junction Capacitance, $1/C_D^2$ -V curve (100 Hz)/ 10^{16} cm ² /CV	-6.676	-7.068	-6.685	5.9%
junction Capacitance, $1/C_D^2$ -V curve (1 MHz)/ 10^{16} cm ² /CV	-6.641	-7.092	-6.644	6.8%
I-V curve (0.7 V)	0.00102	0.00096	0.00093	9.2%

Random error from samples (TVS diode) is from 3.1% to 9.2%, much greater than that of the instrument. In this case, error in test process is mainly caused by random error from samples, and the range of test process error is from 3.1% to 9.2%.

As a result, if the simulation error is less than 3.1% (as shown in Fig. 1), we may say that GSRES in the right application scope, because the numerical error is much less than random error in test. But, in the other hand if the simulation error is greater than 9.2%, GSRES may be out of the application scope, and modification of numerical method and physics model must be taken.

Figure 2 gives an example of that out of application scope. Change of temperature in TVS diode under an 1.8 V voltage lasts for 4 ns is 35.2 K and under an 1.5 V voltage lasts for 15 ns is 45.7 K, 11.7% and 15.1% equally. In high voltage or long time case, basic DDM is out of application scope, it must be modified and energy balance model should be used.

Figure 3 gives another example of that out of application scope. Basic DDM can not simulates deep submicron device quite precisely as analysed in part 3. Fig. 4 gives the output characteristics and transfer characteristics of deep submicron MOSFE. Parameters of MOSFET and experiment result are download form website [15]. As Fig. 4 shows, simulation error of basic DDM is over 20%, and out of application scope, while energy balance model shows and precisely simulation result.

As simulation result shows, GSRES with basic DDM can simulate low voltage, small temperature change and micron device precisely. But high voltage, great temperature change and deep submicron device is out of application scope.

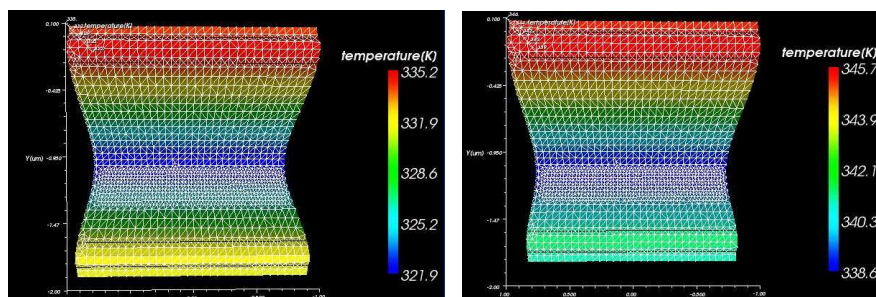


Figure 2: Change of temperature in TVS diode, parameter of diode model is same with tested sample.

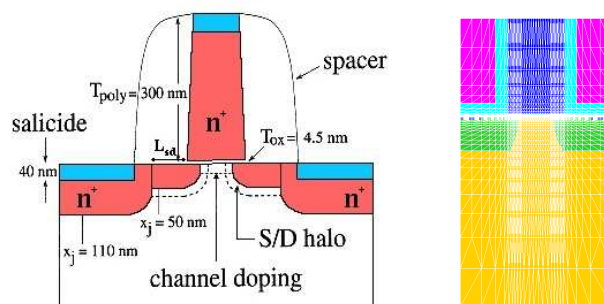


Figure 3: Deep submicron MOSFET model download from website.

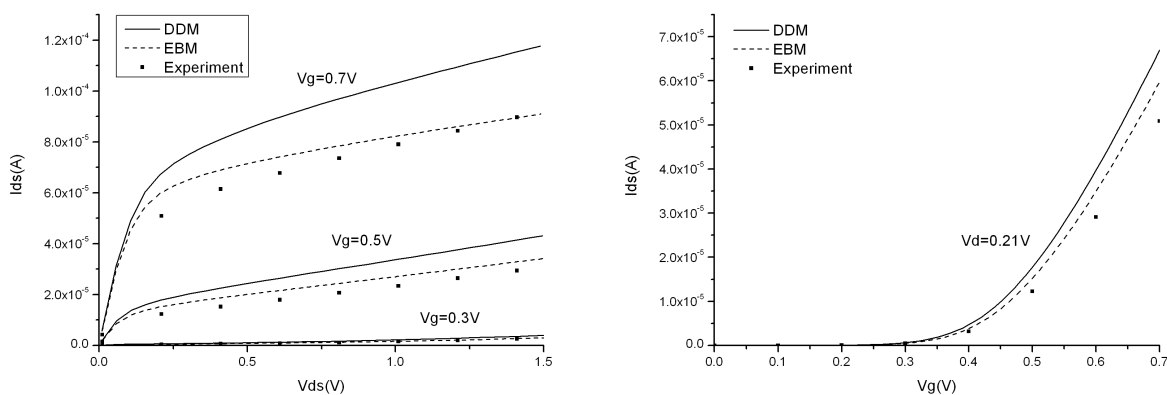


Figure 4: Output characteristics and transfer characteristics of deep submicron MOSFET.

5. CONCLUSION

In this paper, DDM in semiconductor effect simulator GSRES is analysed theoretically. For normal devices, current inside device increases as load voltage increase, which resulting in an augment of Joule heat. As a result, the temperature of device is not uniformity and invariableness, gradient term of temperature is not 0. Equation (1) is not suitability, so modification of lattice temperature and carrier temperature must be introduced into DDM. Carriers exchange energy with lattice by collision, and can be characterized by energy relaxation times or mean free path. The numerical errors will increase because the insufficiency of energy exchange in the case when the scale of device is too small, or the electric field is too strong, or the period of load voltage pulse is too short. In order to reduce error, simulations of deep submicron device and strong field should be avoided.

Mobility model is an modification and an complement for DDM. Pertinently use of mobility model can efficiently reduce numerical error. Appropriate mobility model considers strong field effect and quantum well effect can efficient reduce the error and extend the application area such as deep submicron device and nano scale device. This is the next target for our development and improvement of GSRES.

ACKNOWLEDGMENT

This work was supported in part by National Science Foundation of China (NFSC) under Grant 61201090 and 61231003.

REFERENCES

1. Gummel, H. K., "A self-consistent iterative scheme for one-dimensional steady state transistor calculations," *IEEE Trans. Electron Devices*, Vol. 9, No. 11, 455–465, 1964.
2. Yee, J. H., "Modeling of current and thermal mode second breakdown phenomenon," *Electrical Overstress/Electrostatic Discharge Symposiums Proceedings*, 76–81, 1982.
3. Orvis, W. J., "Modeling and testing for second breakdown phenomena," *Electrical Overstress/Electrostatic Discharge Symposiums Proceedings*, 108–117, 1983.
4. Zhou, H., Z. Du, and K. Gong, "Overshoot phenomena in PIN diode under EMP with fast rise time," *High Power Laser and Particle Beams*, Vol. 17, No. 5, 783–787, 2005.
5. Wang, B. and K. Huang, "Response of high power PIN diode limiter to electromagnetic pulse descending edge," *High Power Laser and Particle Beams*, Vol. 20, No. 7, 1177–1181, 2008.
6. Ding, G., F. Han, and J. Wang, "2D hydrodynamic simulation of GaAs metal-semiconductor-field-effect-transistor," *High Power Laser and Particle Beams*, Vol. 18, No. 7, 1144–1148, 2006.
7. Ding, G., J. Wang, D. Zhang, et al., "A general purpose two-dimensional semiconductor simulator," *Chinese Journal of Computational Physics*, Vol. 24, No. 2, 247–252, 2007.
8. Ding, G. and X. Zhang, *GSS User's Manual*, Northwest Institute of Nuclear Technology, Xi'an, 2008.
9. Xuan, C., D. Gong, H. Xie, et al., "Semiconductor device/circuit mixed-type simulation and its application in HPM effects," *Microelectronics*, Vol. 39, No. 3, 424–428, 2009.
10. Li, Y., C. Xuan, and J. Wang, "Study of response to electromagnetic pulse of PIN diode," *Proceedings of EME*, 280–283, 2012.
11. Li, Y., C. Xuan, H. Xie, et al., "Response of PIN diode to electromagnetic pulse," *High Power Laser and Particle Beams*, Vol. 25, No. 8, 2061–2066, 2013.
12. Li, Y., Y. Liu, C. Xuan, et al., "Study of modeling and validation of TVS diode," Submitted.
13. Sze, M., *Physics of Semiconductor Device Solid*, Suzhou University Press, Suzhou, 2002.
14. Ye, L., *Semiconductor Physics*, High Education Press, Beijing, 2007.
15. <http://www-mtl.mit.edu/researchgroups/Well/>.

A Triple-band Planar Inverted-F Antenna for WLAN Application

Huifen Huang and Yuanhua Hu

School of Electronic and Information Engineering
South China University of Technology, Guangzhou, China

Abstract— A novel tri-band PIFA antenna operating at WLAN frequency is proposed. The antenna has a two-layer structure, resembling a capital E. By folding the E-shaped structure down, it can largely reduce the size of the antenna. The antenna is fed by the probe, which extends from the ground plane to connect to the radiating strip. The short-circuit strip connects with the ground plane is realized by the probe or shorting wall. The whole structure is the three-dimension version of the simple inverted-F antenna. Three electric current paths constitute three resonant modes, corresponding to 2.4/5.2/5.8 GHz, respectively.

1. INTRODUCTION

Wireless local area network (WLAN) technology has extensively been used in commercial, medical, and industrial applications over the last decade [1]. Various antennas operating in this frequency band have been reported. Planar inverted-F antenna (PIFA) is widely applied in mobile terminals due to its low backward radiation and easily-fabricated structure. And due to the flexibility of PIFA antenna's structure, it can cover the whole WLAN frequency band conveniently. A variety of designs can be found in the literature [2–5].

In this paper, a novel tri-band E-shaped PIFA antenna for WLAN application is proposed. It can provide three frequency bands for WLAN application, covering 2.4, 5.2 and 5.8 GHz.

2. ANTENNA DESIGN

An E-shaped tri-band PIFA antenna is presented, illustrated in Figure 1. The antenna can be considered as an E-shaped plane folded to reduce the size; the antenna balances the capacitive reactance and the inductive reactance through a short pin with a length of 2 mm, which can also be replaced by a short wall, just slightly tuning the parameters. A thickness of 0.8 mm FR4 epoxy substrate is placed below the metal ground to sustain the whole structure. The first current

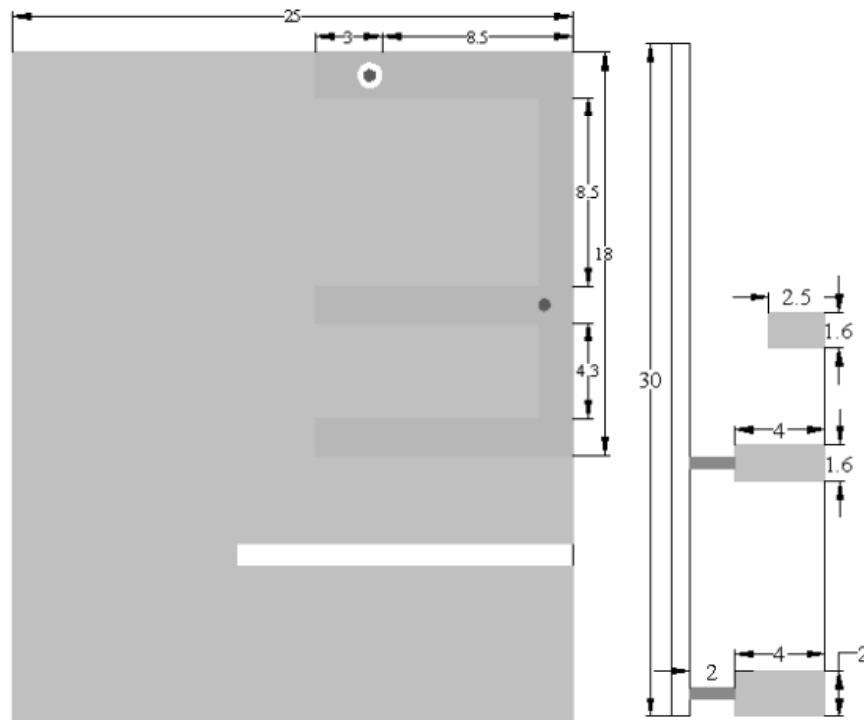


Figure 1: Geometry of the proposed antenna.

path from point A to B is 42 mm, approximately equal to quarter-wavelength in the frequency 2.4 GHz, its current distribution pattern is shown in Figure 2(a), it can be observed that the

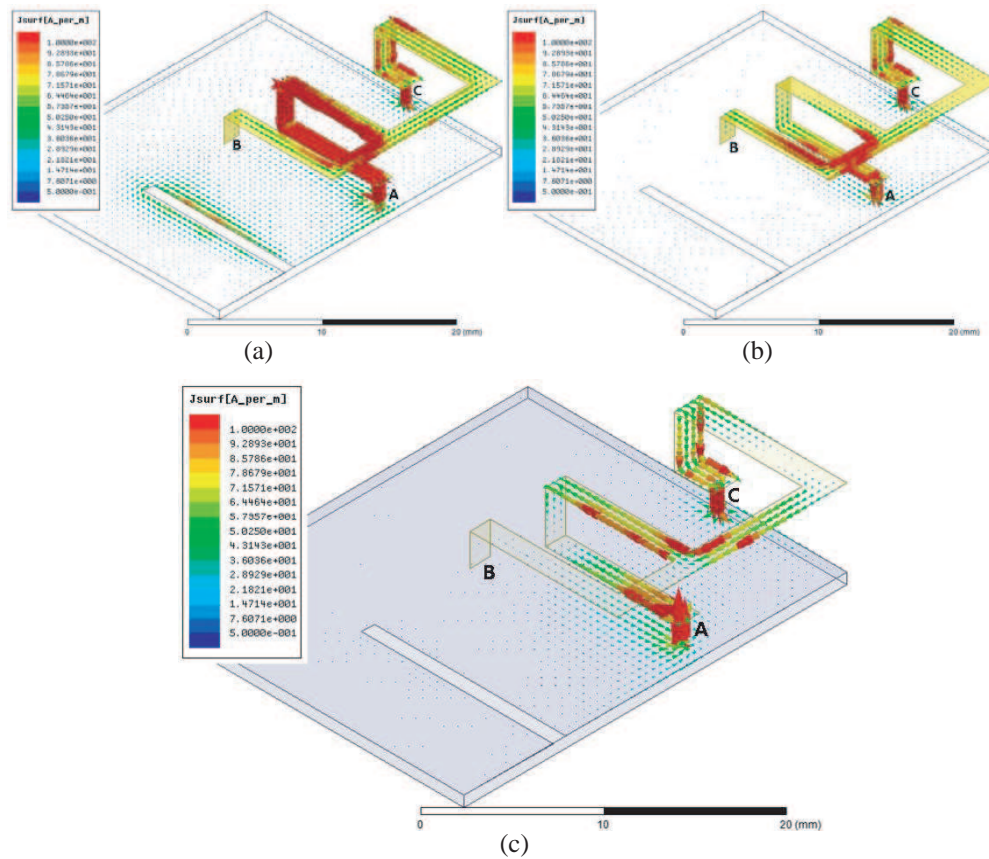


Figure 2: Simulated current distribution of the proposed PIFA antenna, (a) 2.45, (b) 5.28, (c) 5.86 G.

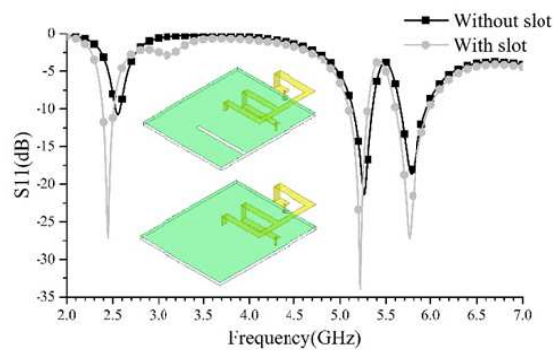


Figure 3: Comparison of the return loss for proposed antenna with/without slot.

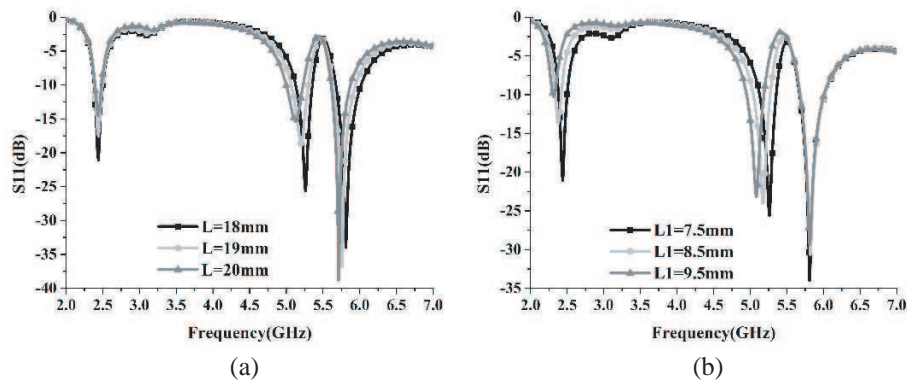


Figure 4: Return loss against frequency with different parameters. (a) L and (b) L_1 .

majority of the current is concentrated on AB at frequency 2.4 GHz, the slot extend the current path, plays a role in enhancing the impedance matching at lower frequency. The second current path composed of AC and BC parts is about 48 mm close to three quarter-wavelength at 5.28 GHz, the current distribution in Figure 2(b) verify it well. The third current path BC is about 53 mm, one-wavelength, two current nulls also verify it, at 5.86 GHz, as shown in Figure 2(c).

3. RESULT AND DISCUSSION

The return loss with/without slot are shown in Figure 3, it can be observed that the slot has slight influence on highfrequency, namely, the length of the ground is enough to excite the resonance of high-frequency. However the slot improve the impedance match of low-frequency and reduce the lowest operating frequency.

To further comprehend the working mechanism, the effect of several parameters on the proposed antenna are studied and displayed in Figure 4. Figure 4(a) implies that the variation of L barely affect the lower resonant frequency, while Figure 4(b) shows that the increment of L_1 has little impact on the upper resonant frequency.

Figure 5 display the radiation pattern of the antenna at the frequency of 2.44, 5.26 and 5.81 GHz in the xoz and yoZ planes. At the frequency of 2.44 GHz and 5.81 GHz, their omnidirectional characteristic have an advantage over that of 5.26 GHz, which may be related with the current

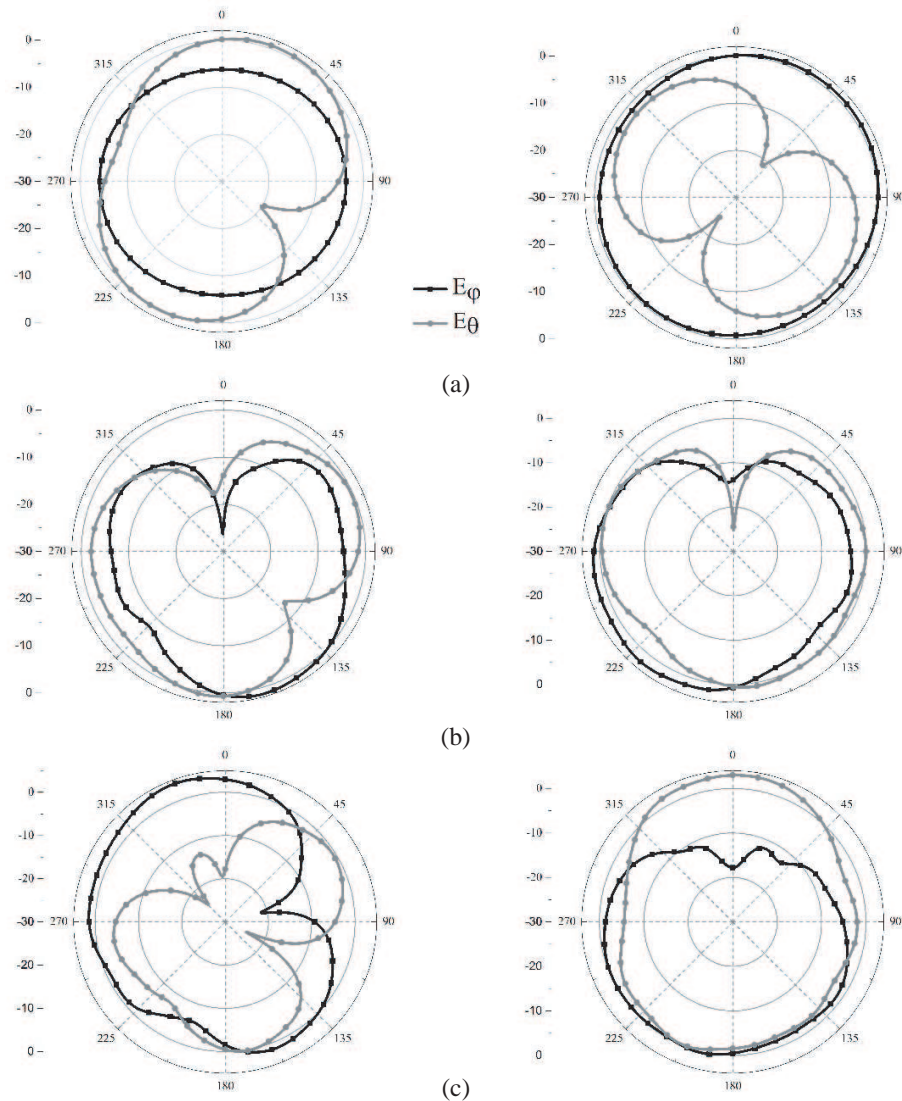


Figure 5: Radiation pattern XOZ _plane(left) and YOZ _plane(right) for (a) 2.44 GHz, (b) 5.26 GHz, (c) 5.81 GHz.

distributed along two path. The inclination of radiation pattern is related with three-dimensional structure.

4. CONCLUSION

A novel tri-band PIFA antenna operating at WLAN frequency is proposed. The tri-band PIFA only occupies $30 \times 25 \times 6 \text{ mm}^3$. Its working mechanism and radiation characteristic are studied.

ACKNOWLEDGMENT

This work is supported by the National Natural Science Foundation of China under Grant 61071056.

REFERENCES

1. Wu, Y. J., B. H. Sun, J. F. Li, and Q. Z. Liu, "Triple-band omnidirectional antenna for WLAN application," *Progress In Electromagnetics Research*, Vol. 76, 477–484, 2007.
2. AbuTarboush, H. F., R. Nilavalan, T. Peter, and S. W. Cheung, "Multiband inverted-F antenna with independent bands for small and slim mobile handsets," *IEEE Trans. Antennas Propag.*, Vol. 59, No. 7, 2636–2645, Jul. 2011.
3. See, C. H., R. A. Abd-Alhameed, D. Zhou, and P. S. Excell, "Dual frequency planar inverted F-L-antenna (PIFLA) for WLAN and short range communication systems," *IEEE Trans. Antennas Propag.*, Vol. 56, No. 10, 3318–3320, Oct. 2008.
4. Sim, C. Y. D. and Y. T. Cheng, "Quad-band PIFA design for WLAN/satellite applications," *Microw. Opt. Technol. Lett.*, Vol. 52, 2331–2336, Oct. 2010.
5. Zuo, S., Y. Yin, Z. Zhang, and W. Wu, "A compact tri-band PIFA antenna for WLAN and WiMAX applications," *Microw. Opt. Technol. Lett.*, Vol. 52, 919–922, Jun. 2010.

Design and Implementation of a New One Layer Microstrip Antenna Array with CSC2 Pattern for SSR

M. Abdolahi¹, Gh. Askari², and H. Mirmohammad Sadeghi²

¹Department of Electrical and Computer Engineering
Isfahan University of Technology (IUT), Isfahan 84156, Iran

²Information and Communication Technology Institute
Isfahan University of Technology (IUT), Isfahan 84156, Iran

Abstract— In this paper, an antenna with a cosecant squared pattern to work as a radiating vertical array of SSR antennas is designed. A simple microstrip structure is adopted to design as feed network and 11 half-wave dipoles are selected as radiating elements. In order to achieve desired pattern, amplitude and phase of elements are obtained using a synthesis pattern method. Equal and unequal Wilkinson power dividers are used to prepare desired power amplitudes to feed the elements. The designed antenna has nearly 10 dB gain and its main beam in the elevation plane is 9 degrees above the ground. Its -10 dB Beam width in elevation pattern is 50 deg. and return loss in central frequency is 22 dB. A one element and a two element array are fabricated on RT Duroid5880 ($\epsilon_r = 2.2$ and $\tan \delta = 0.0009$) with thickness of 31 mil and measured to investigate verification between simulation and measurement and considering mutual coupling.

1. INTRODUCTION

The most common beam shapes found in radar antennas are fan beams which have an upper boundary to detect small and large targets at both short and long ranges. A special case of the fan beam is cosecant squared pattern which has significant features. The cosecant squared elevation beam shape is ideal for detection of small and large targets at both short and long range, including where the antenna is mounted, on a high tower or hill side. In some radars sensitivity time control (STC) is used. STC decreases the sensitivity of the radar at short ranges and increases in long ranges. This system works quite well near the peak of the radar beam, but when used with a cosecant squared pattern, it creates a problem. It decreases the sensitivity of desired targets at high elevation angles where the antenna gain is low. The solution to this problem is to boost the antenna gain at high elevation angles to be considerably higher than requirement for the cosecant squared pattern. In other words, a desired pattern is a cosecant squared pattern which in high elevation angles its gain will be more than a typical cosecant squared pattern [1].

Synthesis of cosecant squared patterns was achieved using reflectors [2], non-uniform arrays [3] and serial fed uniform arrays [4, 5]. The use of microstrip antenna is becoming more and more common nowadays, among others in the area of aviation, telecommunication and radiolocation system. For this purpose, microstrip antennas are used to generate cosecant squared patterns. The typical microstrip implementation is a serial-fed linear array of the type described in [4] and a wideband conformal microstrip array antenna with cosecant-squared beam [6]. The main drawback of a serial fed antenna is being narrowband [4]. Any realization of the cosecant squared antenna using the planar microstrip array would exhibit a narrow bandwidth, even using a parallel-feed network. Shovel-microstrip array which was introduced in [7] is used for solving that problem. This structure has advantage of flexibility of the dielectric substrate, which can easily be shaped.

One of the most uses of cosecant squared pattern is in secondary surveillance radar's (SSR) antennas, these antennas work in two frequencies, 1030 MHz is used to send signals and 1090 MHz for receiving signals is used. A prototype integrated microstrip antenna column [8], a two-layer microstrip antenna for monopulse [9] and microstrip patch that coupling aperture is centered under the patch and feed line is positioned at right angles to the center of slot [10] are some of fabricated antennas for SSR systems. In all of above structures multi layers are used to have an acceptable bandwidth (nearly 8% bandwidth) which for this reason, their fabrication are difficult and have complicate structure. In this paper, a microstrip structure that is simple and works as a radiating vertical array, with printed dipoles as elements, is introduced and a one element and a two element array is fabricated and measured to verify results from simulation and measurement. This new and simple structure has acceptable bandwidth which is one of the most important criteria in design. In first section desired pattern is synthesized with Orchard-Elliott method and amplitude and phase of elements are specified. Next in order to provide our specification for antenna, printed dipole

is chosen as element, equal and unequal Wilkinson power dividers are used to provide specified amplitude and phase in elements. Then a special balun for matching feed network with elements is used. Finally result of designed and simulated antenna, result of measurement of fabricated element and array are shown.

2. ANTENNA DESIGN

An antenna with desired pattern (modified cosecant squared pattern) is designed in several steps, at first with a synthesis pattern method, amplitude and phase of elements must be specified. Next feed network for distributing input power to outputs must be designed, then radiating element with considering low mutual coupling and required gain and polarization must be selected and matched with feed network.

2.1. Synthesis of Desired Pattern

Several methods for synthesizing pattern (shaped pattern) can be used. In nonuniformly spaced array antenna, particle swarm optimization (PSO) [13] method and in uniformly spaced array antenna Woodward-Lawson, Fourier series [14], and Orchard-Elliott, . . . , methods are used. The pattern synthesis was performed using the Orchard-Elliott method [15]. For this goal, it has chosen to conceive a cosecant squared pattern with $\theta_0 = 9$ deg., since this case seems optimal for SSR systems [5]. An array configuration of 11 elements with $0.6\lambda_0$ distance between elements in 1060 MHz is considered in which required amplitude and phase of elements are obtained. These amplitudes and phases are listed in Table 1.

2.2. Feed Network Design

Weighted power distribution has been used to feed each of elements with specific level of amplitudes and phases. The level of excitation at the inputs for feeding the individual radiators specifies the

Table 1: Amplitude and phase of elements.

El. Num.	Amplitude	Amplitude
1	0.0975	-57.00
2	0.1025	-57.00
3	0.2000	-54.00
4	0.2450	-24.00
5	0.2630	-25.00
6	0.5070	-9.000
7	0.5710	62.00
8	0.4310	121.0
9	0.1550	173.0
10	0.0877	96.00
11	0.1025	156.5

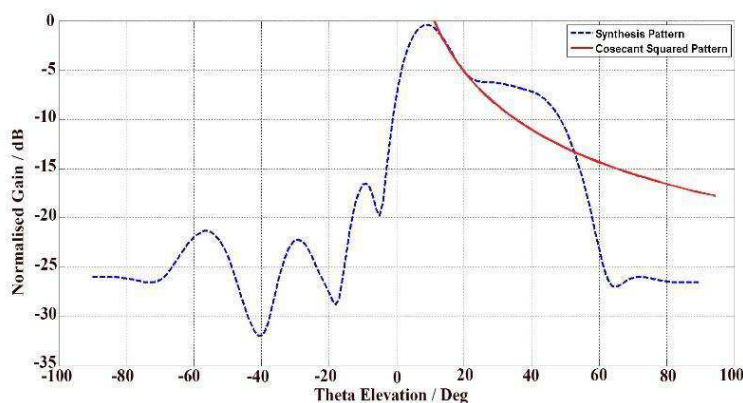
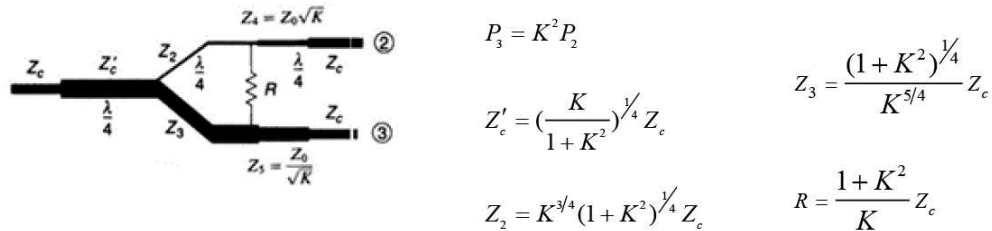


Figure 1: The ideal and synthesized cosecant squared patterns.

radiation characteristics of the array, mainly its effective pattern shape. Array factor which results from this distribution (synthesized pattern), and an ideal cosecant squared pattern are shown in Fig. 1, where beam shaping features can clearly be seen.

The required excitations to radiating elements are provided from input power through some equal and unequal Wilkinson power dividers, which shapes the column’s radiation characteristic according to modified cosecant squared function. In order to decrease size of feed network, Wilkinson power dividers from these formulas are designed, shaped and optimized to order in horizontal plane. Designed feed network is shown in Fig. 2.



The microstrip feed network have been designed for realizing the array excitations using CST Microwave Studio [12] to provide the required excitation. As it expected, this power distribution should work in two frequencies well; consequently, the output amplitudes should not change in regard to frequency (Fig. 3) and slope of output phase lines should be the same as shown in Fig. 4. These Phase lines have same slope if only length of all paths from input to outputs be the same.

2.3. Antenna Element

The choice of array element is made based on the requirement of bandwidth (10% bandwidth), beam width, desired radiation patterns in *E*- and *H*-planes, compatibility with microstrip structures and low mutual coupling for realizing an ultimate low SSL with vertical polarization. Several radiating element candidates exist which can comply with the above requirements. In array applications it is typically necessary to use elements that can be approximately 0.5λ . For this purpose, a parallel

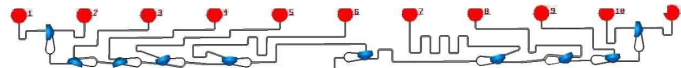


Figure 2: Designed feed network.

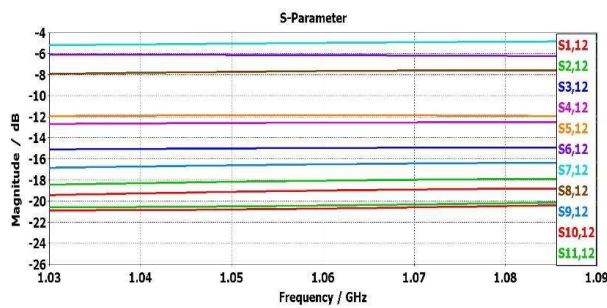


Figure 3: The amplitude distribution.

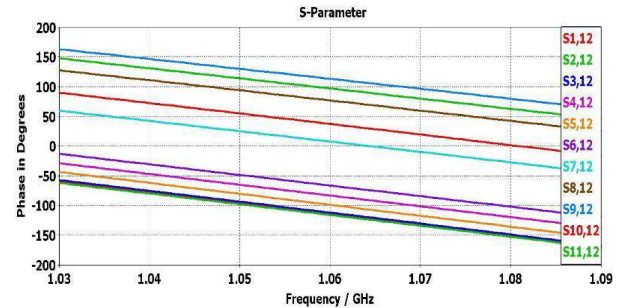


Figure 4: The phase distribution.

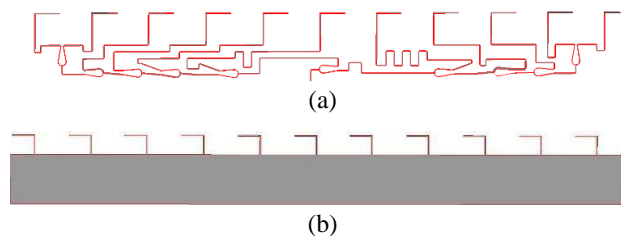


Figure 5: Designed antenna, (a) top view, (b) bottom view.

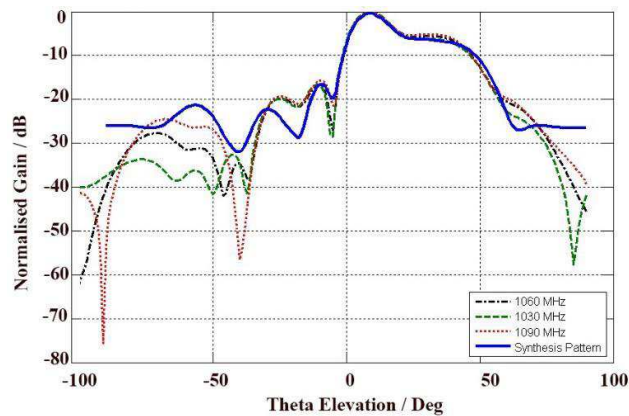


Figure 6: The simulated cosecant squared pattern.

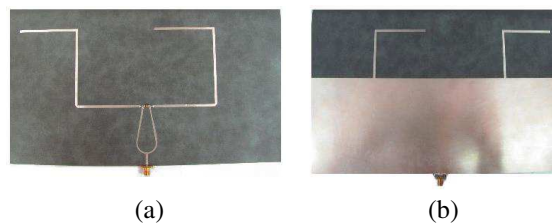
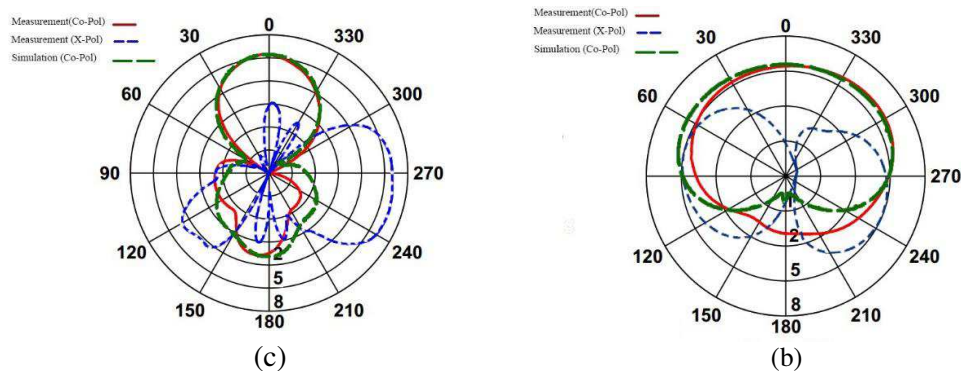


Figure 7: Fabricated elements, (a) top view, (b) bottom View.


 Figure 8: Result of simulation and measurement of fabricated elements, (a) E -plane, (b) H -plane.

strips printed dipole [11] has been chosen and designed as an array element which satisfies the above requirements. These radiation characteristics of the element are 5.57 dB gain, angular width (3 dB) of 157.5 deg. in the azimuth plane, 72.3 deg. in the elevation plane and with -10.7 dB SLL.

2.4. Microstrip to Parallel Strip Balun

Since half-wave dipole has an impedance nearly $73 + j42$ ohm and it is integrated to 50 ohm line, length of element is decreased to omit imaginary part of impedance and a balun is used for matching microstrip feed network with parallel strips dipole.

3. ANTENNA SIMULATION AND RESULTS

3.1. Analysis and Simulation of Whole Antenna

The designed antenna has been shown in Fig. 5. The feed network and the printed half-wave dipoles are fabricated on RT-Duroid 5880 substrate ($\epsilon_r = 2.2$ and $\tan \delta = 0.0009$) with 31 mil thickness. Fig. 6 shows simulated elevation pattern for center (1060 MHz) and edge frequencies (1030 MHz and 1090 MHz). It can be seen that beam shaping is obtained according to the objectives in the whole band. In this figure, the synthesized radiation pattern is also shown. It has to be noted that the synthesis was done with considering isotropic elements, therefore the differences between the synthesis and the simulated pattern at out of 10 dB beam width are due to element radiation

pattern.

3.2. Array Element Implementation

For investigating the difference between simulation and fabrication and for considering the effect of mutual coupling between elements, two element array of dipoles has been fabricated, measured and compared with simulated design. Structure of fabricated array is shown in Fig. 7 and the result for co-polarization and cross polarization of designed and fabricated array at 1060 MHz are shown in Fig. 8. In order to result be completely obvious, scale of co-pol and x -pol patterns are considered same but actually difference between them is 25 dB. As it is shown, simulated and measured results are almost same.

4. CONCLUSION

A Simple structure with modified cosecant squared pattern for SSR antenna was designed and presented in L band frequencies (1030 ± 10 MHz and 1090 ± 10 MHz). Microstrip structure usually have some limitation in bandwidth but the new structure that was introduced in this paper, solved this problem. In order to achieve specified criteria for element a simple element such as printed half-wave dipole was used in which it is compatible with microstrip structure. The array of these elements has negligible mutual coupling. The simulation results showed that beam shaping is achieved based on the objectives in the whole band.

ACKNOWLEDGMENT

The authors would like to thank ICTI (Information and communication technology institute) to support of this project.

REFERENCES

1. Skolnik, M. I., *Radar Handbook*, 3rd Edition, 2–96, 2–97, McGraw-Hill, 2008.
2. Silver, S., *Microwave Antenna Theory and Design*, Sec. 5.7, McGraw-Hill, New York, 1949.
3. Stutzman, W. L., “Synthesis of shaped-beam radiation patterns using the iterative sampling method,” *IEEE Tran. Ant. Prop.*, Vol. 19, No. 1, 36–41, Jan. 1971.
4. Jones, B., Y. M. F. Chow, and A. W. Seeto, “The synthesis of shaped patterns with series-fed microstrip patch arrays,” *IEEE Tram. Atit. Prop.*, Vol. 30, No. 6, 206–1202, Nov. 1982.
5. Freytag, L. and B. Jecko, “Cosecant-squared pattern antenna for base station at 40 GHz,” *IEEE*, 2004.
6. Madany, M., “The analysis of wideband conformal microstrip array antenna with cosecant-squared beam shaping,” *IEEE Trans.*, 2006.
7. Schrank, H. and N. Herscovici, “A simple cosecant squared microstrip array: The shovel microstrip array,” *IEEE Antennas and Propagation Magazine*, Vol. 35, No. 4, Aug. 1993.
8. Borowiec, R., A. Jankowski, and Z. Langowski, “Microstrip radio location antenna with electronically controlled beam built using composite technology,” *IEEE Trans. Microwave.*, Vol. 57, No. 4, 815–823, 2009.
9. Biswas, D. and R. Vulapalli, “A two-layer microstrip antenna to generate cosecant squared fanbeam for monopulse tracking,” *IEEE Proceeding of International Conference on Microwave*, 2008.
10. Kreczkowski, A., T. Rutkowski, and A. Buda, “The microstrip IFF antenna for the airborne radar,” *IEEE*, 2005.
11. Garg, R., *Microstrip Antenna Design Handbook*, Artech House, Inc., 2001.
12. CST Studio Suitesoftware, 2012.
13. Zhang, X., K. ManLuk, Q. Wu, and T. Ying, “Cosecant-square pattern synthesis with particle swarm optimization for nonuniformly spaced linear array antennas,” *IEEE*, 2008.
14. Stutzman, W. L., *Antenna Theory and Design*, 3rd Edition, John Wiley and Sons, Inc., 2012.
15. Orchard, H. J. and C. Eng, “Optimizingthe synthesis of shaped beam antenna patterns,” *IEEE Proceedings*, Vol. 132, No. I, Feb. 1985.

A Simple Minimized Polarization Reconfigurable Slot Antenna

Maziar Hedayati¹, Mohsen Abdolahi¹,
Gholamreza Askari², and Hamid Mirmohammad Sadeghi²

¹Department of Electrical and Computer Engineering
Isfahan University of Technology (IUT), Isfahan 84156, Iran

²Information and Communication Technology Institute
Isfahan University of Technology (IUT), Isfahan 84156, Iran

Abstract— Recent developments in the wireless communication industry continue to drive the requirements for small, compatible, and affordable reconfigurable antennas. Polarization-reconfigurable antennas can mitigate multipath fading loss and provide a double-transmission channel for frequency reuse. A polarization-reconfigurable slot antenna, for wireless communication, is presented in this paper. In the proposed design a new shape of slot antenna based on SIW structures at the center frequency 31 GHz is presented which is linear-polarization (LP)/circular-polarization (CP) switchable reconfigurable antenna while the antenna is still operable over the desired frequency band. The proposed antenna is designed and simulated using Ansoft HFSS, a Finite-Element-Method based EM solver. The computed return loss, for each case, is better than 10 dB over the 30–32 GHz frequency range. The 3 dB axial ratio BW around is 11% in the CP state.

1. INTRODUCTION

Wireless communication systems have been developed rapidly in recent years in that systems require an antenna with a wideband, good radiation performances and sometimes switchable ability. To obtain the switchable ability of the antenna, the concept of a reconfigurable antenna was proposed a few years ago [1]. Reconfigurable antennas generally have a frequency, radiation pattern, or polarization tune ability. Frequency, radiation pattern [2–5], and polarization [6–8] reconfigurable antennas are alternatives to broadband/multiband antenna, beam forming array, and dual-polarized antenna, respectively. Polarization-reconfigurable antennas are wireless link terminals that help increase the performance of communications systems through polarization diversity and frequency reuse. But few polarization reconfigurable antennas have recently been presented [9–11]. This is because it's difficult to simultaneously realize a good impedance matching for circular and linear polarizations. In this paper, a very simple polarization-reconfigurable slot antenna, for wireless communication, is proposed.

2. ANTENNA CONFIGURATION AND DESIGN GUIDELINES

The antenna is designed to have the linear and circular polarization. The substrate with $\epsilon_r = 2.33$, $\tan \delta = 0.0009$, and thickness of 0.508 mm was used for antenna. The design process consists of three parts. At first, designing of single slot then, Calculation of coupling factor and second slot length and finally, reconfigurable antenna design. An overall layout of the designed slots is shown in Fig. 1.

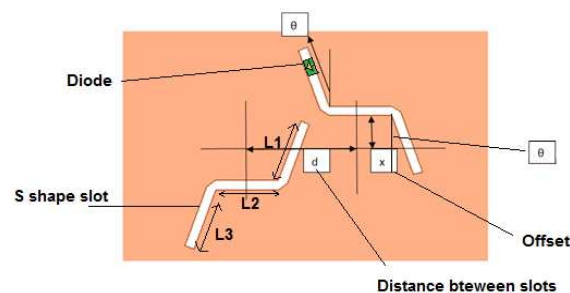


Figure 1: The layout of the designed slot.

2.1.

2.1.1. SIW Design

In the previous years, there have been attempt of different kinds to implement the waveguide in the surface because these elements are cheaper. One of the best method to construct these elements is using the two line of cylindrical conductors that works as a waveguide. The main difference between SIW and conventional waveguide is their propagation modes. In the conventional waveguide all of TM_{nm} and TE_{nm} mode are propagated, but only TE_{n0} is propagated in the SIW. To design of purposed antenna the SIW with $d = 0.8$ mm, $p = 2$ mm, $a = 7.2$ mm, $h = 0.508$ mm, $\epsilon_r = 2.33$ is used. The cut-off frequency of the SIW is 15.2 GHz that is suitable for the purposed application. All the structures implemented by SIW should be fed accurately. Since dominant modes of rectangular waveguide and microstrip line are similar. A microstrip line is usually used for SIW feeding. The optimized dimensions of feed are $a_1 = 6.096$ mm, $l = 5.588$ mm, $d_1 = 2.286$ mm, $h = 0.508$ mm, $w = 0.711$ mm. Fig. 2 shows surface current of SIW.

2.1.2. Single Slot Design

In an effort to decrease the total area occupied by the antenna, the slot configuration was altered from its standard straight form to an S-shape. From the simulated equivalent magnetic current distribution on the straight and S-shape slots [Fig. 3, antennas (a) and (b)], it is obvious that they both closely follow a sinusoidal pattern with the maximum current concentrated in the middle of the slot. As a result, the two antennas share very similar properties and they only Differ in their polarization orientation.

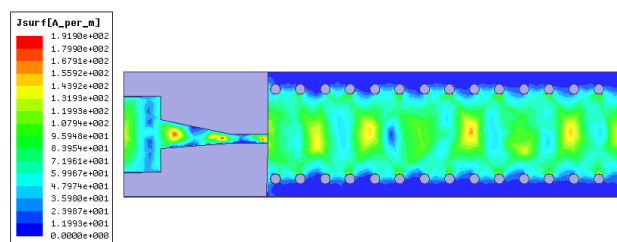


Figure 2: Surface current on SIW.

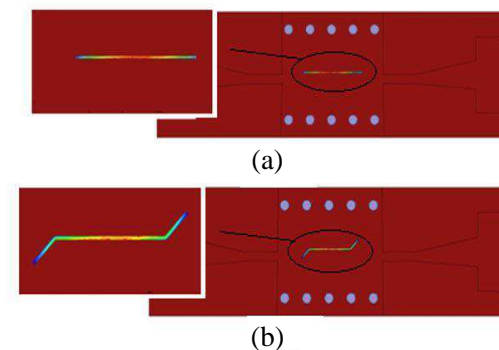


Figure 3: The equivalent magnetic current distribution on the (a) straight and (b) S-shape slots.

Table 1:

	θ	Polarization
1	20	49
2	40	63
3	60	78
4	90	90

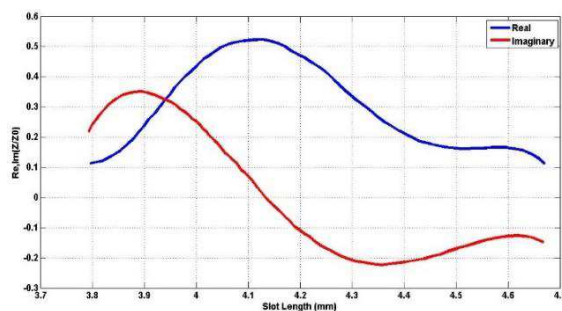


Figure 4: The real and imaginary part of normalized slot impedance vs. length of slot.

Antenna (a) is horizontally polarized, while antenna (b) slant linear polarized. The slot must be placed in a point on SIW surface which the transverse and longitudinal current distribution components of the TE_{10} mode be equal. Two values of x can be found for which $|J_x| = |J_y|$. $x = a/\pi (\tan^{-1}(\lambda_g/2a))$ is achieved according to the method that is discussed in [12] which a and λ_g are the width and guided wavelength of SIW, respectively. At the following point, the transverse and longitudinal components of the current distribution are equal in magnitude. If an s-slot be cut at the x point, the produced electric fields in the s-slot branches are equal in magnitude but the transverse and longitudinal components of the electrical field are not exactly the same in s shape slot, so it is necessary to optimize the slot to achieve 45 deg. Polarization which θ in Fig. 1 must be 20° and $\frac{L_1+L_3}{L_2} < 0.37$. Table 1 shows the effect of θ vs. polarization. HFSS software is used to simulate an isolated S shape slot to achieve its length according to the method in [13]. Fig. 4 shows the real and imaginary part of normalized slot impedance vs. length of slot. So the length of slot is obtained 4.12 mm for first slot.

2.2. Calculation of Coupling Factor

By means of the model in Fig. 5, the coupling coefficient, indicating the amount of radiation from a single slot is derived. The slot is placed in its calculated offset from previous section and the length of module is $\lambda_g/2$.

The reference planes at two ports should be shifted inward to remove the transmission line effects. This yields

$$S = \begin{pmatrix} S_{11} & S_{12} \\ S_{21} & S_{22} \end{pmatrix}$$

$$S = \begin{pmatrix} e^{2j\beta_{10}s} & 0 \\ 0 & e^{2j\beta_{10}s} \end{pmatrix} S^b \begin{pmatrix} e^{2j\beta_{10}s} & 0 \\ 0 & e^{2j\beta_{10}s} \end{pmatrix}$$

where S^b is the scattering parameters matrix calculated by the simulation software and β_{10} is the propagation constant for TE_{10} mode.

S matrix of calculated slot is shown in Fig. 7. So coupling factor is obtained as follow $|S_{21}|^2 + |S_{11}|^2 + |S_{31}|^2 = 1$, $|S_{21}| = 0.8$, $|S_{11}| = 0.079$, $|S_{31}| = \alpha = 0.59|S_{21}| = 0.8$ must be applied to the

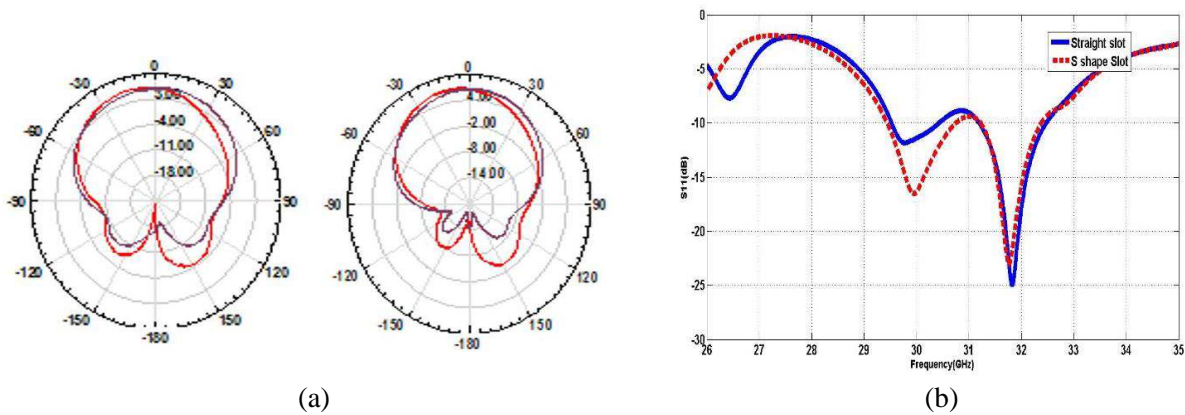


Figure 5: (a) The pattern and (b) the S parameter of straight and S-shape slot.

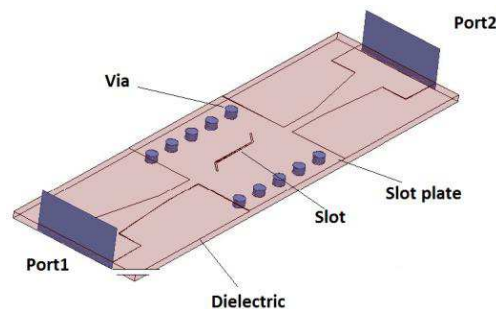


Figure 6: Structure model to calculate coupling.

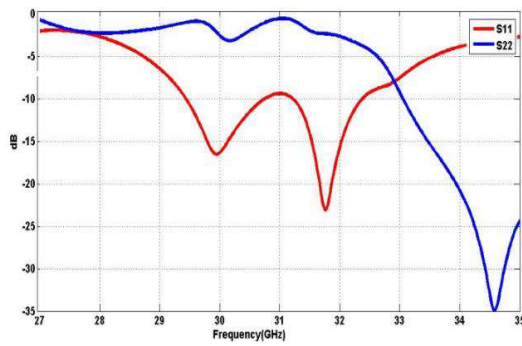


Figure 7: The S matrix of calculated slot.

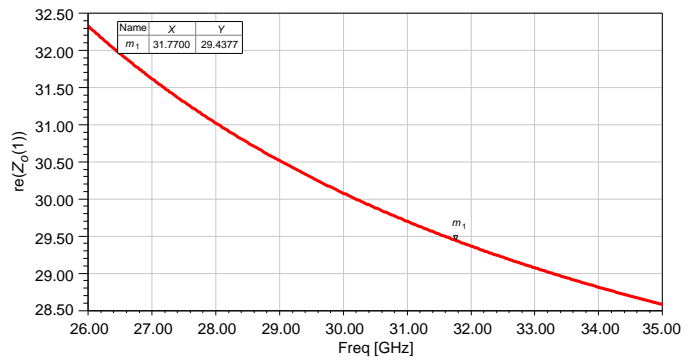


Figure 8: The input impedance of first module.

input of second slot to achieve the second slot length to have the same coupling coefficient. But the input impedance of second module is not 50 anymore. So output of first module should be applied to output of second module. Fig. 8 shows the input impedance of first module which is $29\ \Omega$ at 32 GHz. With this scenario the length of second slot is obtained 4.32 mm. So all of necessary parameters to design the antenna in Fig. 1 are obtained.

2.3. Reconfigurable Antenna Design and Simulation Result

There are various elements and techniques implemented in order to achieve the tune ability: micro electromechanical switches (MEMS), varactors, PIN diodes, FET transistors, and special substrate materials like ferroelectric or ferromagnetic materials. In this paper PIN diodes are used, because PIN diode's reliability, compact size, high switching speed, small resistance and capacitance in the ON and OFF state, respectively, make it most appropriate for the application at hand. But at first a biased circuit must be intruded for diode. The switch bias network is presented in Fig. 9. An inductor is necessary for RF signal isolation but lumped elements do not have appropriate behavior in high frequencies because their self-resonance frequency is less than 31 GHz. The Stub is designed

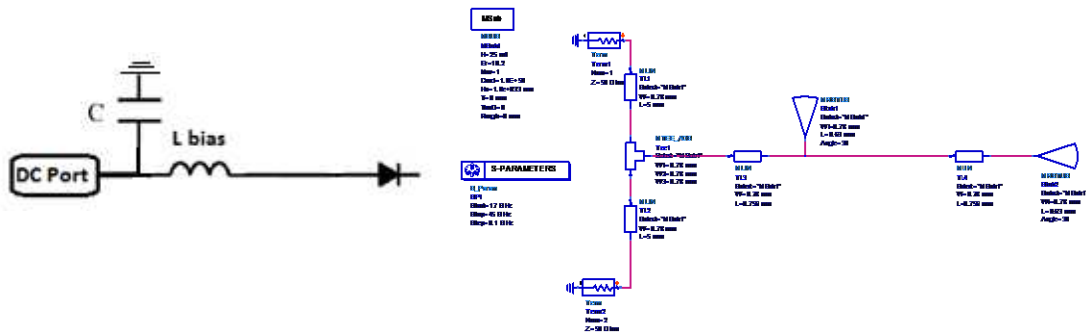


Figure 9: The biased circuit for diode.

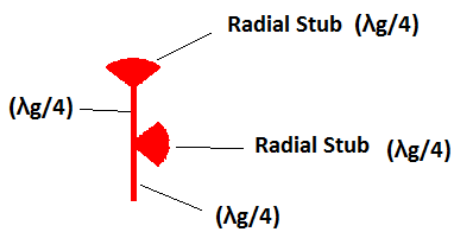


Figure 10: The stub is designed by two $\lambda_g/4$ open circuit radial stub line.

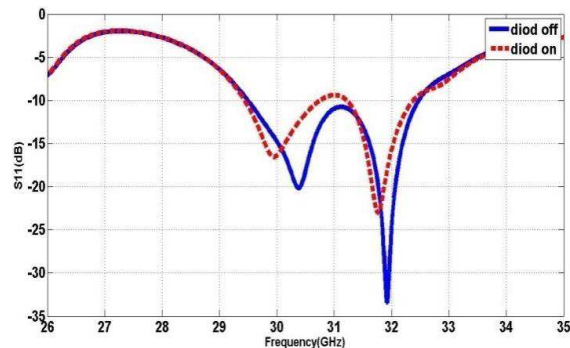


Figure 11: The S parameter of antenna.

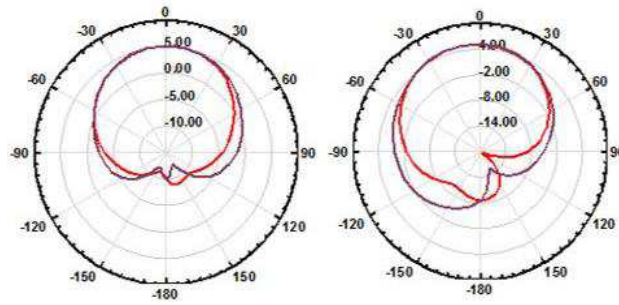


Figure 12: The computed radiation patterns, in the X - Z and Y - Z planes, at 31 GHz for diode on and off.

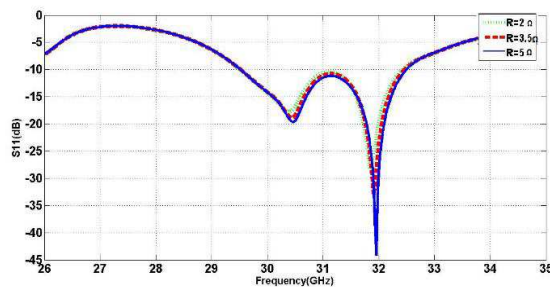


Figure 13: The simulated return loss versus the switch ON state resistance for three different cases between 2 to 5Ω .

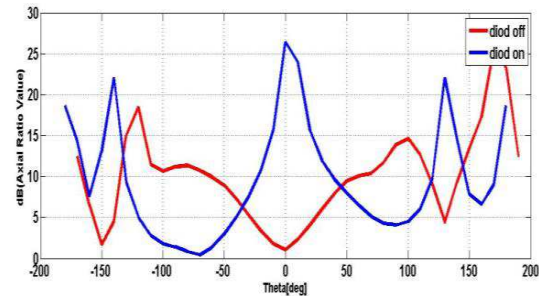


Figure 14: The axial-ratio of the proposed antenna.

by two $\lambda_g/4$ open circuit radial stub line which enhance stub bandwidth (Fig. 10). Furthermore two 2.7 pF capacitors are used to improve the DC isolation. The diode is placed on slot and its bias circuit is on a separate substrate which is connected to diode with appropriate wires. The antenna was designed and simulated using Ansoft HFSS for one switching conditions. Computed return loss plots, as depicted in Fig. 11 shows that the antenna operate in 30–32 GHz in both case (diode on and off). The return loss is acceptable in both case and there is not necessary any additional switch to tune the resonance frequency. The computed radiation patterns, in the X - Z and Y - Z planes, at 31 GHz for diode on and off, are shown in Fig. 12. The small ON state resistance also affects the Antenna performance and particularly its input impedance. Full wave analysis was used to model these effects. For a first order approximation, the diode resistance was modeled as a thin film resistor on top of the slot and the packaging parasitic elements were neglected in this analysis. Fig. 13 shows the simulated return loss versus the switch ON state resistance for three different cases between 2 to 5Ω . As it is shown in this figure, the parasite resistance does not effect on antenna performances. The radiation of the antenna is acceptably the same. However, the efficiency and the gain will be reduced compared to a half-wavelength slot due to the resistive losses caused by the diodes. When diode is on, the gain of antenna is 0.5 dB less than another one and the side lobe level is more than when diode is off. But In either case, the antenna is expected to have maximum radiation in $\theta = 0$. Accordingly, the axial-ratio of the proposed antenna is shown in Fig. 14. As it is shown in this figure when diode is off the ratio of E_x and E_y is one with 90° differences in phase but when diode is on, this ratio is not one anymore, so there is not circular polarization anymore.

ACKNOWLEDGMENT

The authors would like to thank ICTI (Information and communication technology institute) to support of this project.

REFERENCES

1. Peroulis, D., K. Sarabandi, and L. P. B. Katehi, "A planar VHF reconfigurable slot antenna," *IEEE Antennas and Propagation Society International Symposium*, Vol. 1, 154–157, Jul. 8–13, 2001.

2. Chen, S.-H., J.-S. Row, and K.-L. Wong, “Reconfigurable square-ring patch antenna with pattern diversity,” *IEEE Trans. Antennas Propag.*, Vol. 55, No. 2, 472–475, Feb. 2007.
3. Wu, S.-J. and T.-G. Ma, “A wideband slotted bow-tie antenna with reconfigurable CPW-to-slot line transition for pattern diversity,” *IEEE Trans. Antennas Propag.*, Vol. 56, No. 2, 327–334, Feb. 2008.
4. Huff, G. H. and J. T. Bernhard, “Integration of packaged RF MEMSS witches with radiation-pattern-reconfigurable square spiral microstrip Antennas,” *IEEE Trans. Antennas Propag.*, Vol. 54, No. 2, 464–469, Feb. 2006.
5. Jung, C. W., M. J. Lee, G. Li, and F. de Flaviis, “Reconfigurable scan beam single-arm spiral antenna integrated with RF-MEMS switches,” *IEEE Trans. Antennas Propag.*, Vol. 54, No. 2, 455–463, Feb. 2006.
6. Sung, Y., “Investigation into the polarization of asymmetrical-feed triangular microstrip antennas and its application to reconfigurable antennas,” *IEEE Trans. Antennas Propag.*, Vol. 58, No. 4, 1039–1046, Apr. 2010.
7. Simons, R. N., D. Chun, and L. P. B. Katehi, “Polarization-reconfigurable patch antenna using microelectromechanical-system (MEMS) actuators,” *IEEE Antennas Propag. Soc. Int.*, Vol. 2, 6–9, 2002.
8. Yang, F. and Y. Rahmat-Samii, “A reconfigurable patch antenna using switchable slots for circular polarization diversity,” *IEEE Microw. Wireless Compon. Lett.*, Vol. 12, No. 3, 96–98, Mar. 2002.
9. Qin, P.-Y., A. R. Weily, Y. J. Guo, and C.-H. Liang, “Polarization reconfigurable U-slot patch antenna,” *IEEE Trans. Antennas Propag.*, Vol. 58, 3383–3388, Oct. 2010.
10. Parihar, M. S., A. Basu, and S. K. Koul, “Polarization reconfigurable microstrip antenna,” *Proceedings of the Asia-Pacific Microwave Conference, APMC’09*, 1918–1921, Singapore, 2009.
11. Monti, G., L. Corchia, and L. Tarricone, “Patch antenna with reconfigurable polarization,” *Progress In Electromagnetics Research*, Vol. 9, 13–23, 2009.
12. Simmons, A. J., “Circularly polarized slot radiators,” *IRE Transactions on Antennas and Propagation*, Vol. 5, No. 1, 31–36, Jan. 1957.
13. Oraizi, H. and M. T. Noghani, “Design and optimization of waveguide fed centered inclined slot arrays,” *IEEE Trans. Antennas Propag.*, Vol. 57, No. 12, 3993–3997, Dec. 2009.

Microwave Radiation Interferometry High Resolution Reconstruction Based on Mixed Orthogonal Basis

Chao Song, Lu Zhu, Yuanyuan Liu, and Suhua Chen

School of Information Engineering

East China Jiaotong University, Nanchang 330013, China

Abstract— Microwave radiometry is the primary means of soil moisture remote sensing and capable of observation soil moisture all-time, all-weather. But the imaging method of traditional microwave radiometry has complex structure and low resolution, which limited largely the application in regional soil moisture remote sensing. In this paper, we propose a new inversion method for microwave radiation interferometry imaging based on compressed sensing (CS), by mining the sparse and compressible information of the microwave radiation image. The proposed method can break through the limit of the inherent spatial resolution of the imaging system which based on the Nyquist sampling, achieving the spatial resolution image closely obtained by the expensive large aperture imaging system, and reducing the complexity and the cost of the hardware of the imaging system configuration. Due to the complexity of microwave radiation image scene, it is difficult to sparsely represent the microwave radiation image by single orthogonal basis, so we make use of the sparse representation in mixed orthogonal basis and the constraint conditions of total variation regularization of microwave radiation image, and establish the optimal reconstruction model of microwave radiation image. We solve the optimal solution of reconstruction model by adopting the alternating direction method (ADM), achieve high resolution microwave radiation image reconstruction from low-dimensional measurements to high -dimensional data, and solve the contradiction between the high resolution and the complexity of the system, and establish evaluation methods of spatial resolution. The simulation results show that, compared with orthogonal the matching pursuit (OMP) algorithm, the proposed algorithm can achieve higher spatial resolution.

1. INTRODUCTION

Interferometric synthetic aperture microwave radiometry (ISAMR) integrates small aperture antenna array into large observation aperture, without mechanical scanning, can overcome the shortcomings of real aperture microwave radiometer. However, for L-Band space borne ISARM, in order to achieve a spatial resolution of 50 km, it still needs 9 meters in diameter antenna array. And with soil moisture sensing area and the fine structure in the direction of development, need increase the diameter of antenna array to satisfy the high spatial resolution requirement, the resolution of radiometer data can be enhanced by using either image processing techniques or special reconstruction algorithms. ISAMR has evolved into a large and complex system that need hundreds of millions data to imaging. In this regard, interferometry and conventional microwave radiation imaging method based on spatial Nyquist is difficult to achieve.

Compressed sensing (CS) theory [1] brought a huge breakthrough in the field of information processing in recent years, and it has changed the way people access information. The CS model is shown in Figure 1.

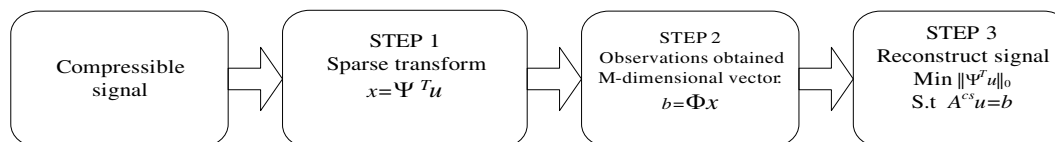


Figure 1: Compressed sensing theoretical framework.

For encoders, recent results indicate that stable reconstruction for both K -sparse and compressible signals can be ensured by *restricted isometry property* (RIP). However, it is extremely difficult to verify the RIP property in practice. Fortunately, Candes et al. show that RIP holds with high probability when the measurement matrix are random. Being under determined, the equation $b = \Phi \Psi^T u$ usually has infinitely many solutions. If we know in advance that b is acquired from a highly sparse signal, a reasonable approach would be adopted to seek the sparsest one among all solutions, i.e.,

$$\min_x \{ \|\Psi^T u\|_0 : Au = b \} \quad (1)$$

Unfortunately, this l_0 decoder is generally NP-hard and impractical in computation for almost all real problems. Candes and other studies show that we can replace the l_0 with l_1 as a signal sparse approximation measure, i.e.,

$$\min_x \{ \|\Psi^T u\|_1 : Au = b \} \quad (2)$$

We can see that the problem (2) is constrained. According to the optimization theory, it can be transformed into the following unconstrained problem.

$$\min_x \|\Psi^T u\|_1 + \mu \|Au - b\|_2^2 \quad (3)$$

where $\mu > 0$.

In literature [3], the CS theory was applied to microwave radiation interference measurement inversion imaging. By using sparse sampling methods to reduce the sampling rate to optimize the number of antenna array, and decrease the complexity of the imaging system in some certain extent. However, for image restoration, recent research [5] has confirmed that the use of total variation (TV) regularization instead of the l_1 term in CS problems makes the recovered image quality sharper, and the edges or boundaries which is essential to characterize images can be preserved accurately. Based on the disadvantage of minimum l_1 norm in computing speed and matching pursuit algorithm in the reconstruction accuracy, and according to the microwave radiation image's characteristic of multi-structure, in this paper, we propose a new model MixTV-W based on the TV and wavelet basis combined with alternating direction method (ADM) algorithm, which can overcome the above disadvantages.

2. BASIC ALGORITHM AND OPTIMALITY

2.1. The Model of MixTV-W

The greatest contribution of this literature is to propose the MixTV-W model. This model is mainly the combination of mixed orthogonal basis and augmented Lagrangian function. In our approach, u is reconstructed based on the following model:

$$\min_u \sum_i \|D_i u\|_2 + \tau \|\Psi^T u\|_1 + (1/2)\mu \|Au - b\|_2^2 \quad (4)$$

where \sum_i is taken over all pixels, $\sum_i \|D_i u\|_2$ is a discretization of the TV of u , and $\tau \|\Psi^T u\|_1$ is the l_1 -norm of the representation of u under Ψ . Ψ is the wavelet basis particularly the Haar wavelet basis in our experiments, A is a random observation matrix and $\tau, \mu > 0$ are scalars which are used to balance regularization and data fidelity.

We introduce auxiliary variables $w = [w_1, w_2, \dots, w_N]$, where each $w_i \in R^2$ and $z \in R^2$ therefore the problem (4) is equivalently transformed to the following form

$$\begin{aligned} \min_{w,z,u} \sum_i \|w_i\|_2 + \tau \|z\|_1 + (1/2)\mu \|Au - b\|_2^2 \\ \text{s.t. } w_i = D_i u, \text{ for all } i; z = \Psi^T u \end{aligned} \quad (5)$$

To tackle the linear constraints, we consider the augmented Lagrangian function of (5). Then come to our MixTV-W model:

$$\begin{aligned} \min_{w,z,u,\lambda_1,\lambda_2} \ell_A(w, z, u, \lambda_1, \lambda_2) = \sum_i \left\{ \|w_i\|_2 - (\lambda_2)_i (w_i - D_i u) + (\beta_2/2) \|w_i - D_i u\|_2^2 + \tau \|z_i\|_1 \right. \\ \left. - (\lambda_1)_i (z_i - \psi_i^T u) + (\beta_1/2) \|z_i - \psi_i^T u\|_2^2 \right\} + \mu/2 \|Au - b\|_2^2 \end{aligned} \quad (6)$$

where $\beta_1, \beta_2 > 0$, for each i $(\lambda_1)_i \in R$, $(\lambda_2)_i \in R^2$, and ψ_i is the i th column of Ψ . For simplicity, we assume $\beta_1 = \beta_2 \equiv \beta$.

2.2. Solving the MixTV-W Model by the ADM

However, each iteration of the augmented Lagrangian method (ALM) is relatively expensive. In contrast, the ADM approach has a much cheaper per-iteration cost. Supposed that w_i , z_i , and u respectively denote the approximate minimizers of (6) at the k th iteration which refers to the inner iteration while solving the subproblem

Firstly, for fixed z_i, u and (here and after $\lambda = (\lambda_1, \lambda_2)$), the minimization of (6) is equivalent to solve the so-called “w-subproblem”

$$\min_{w_i} \sum_i \|w_i\|_2 - (\lambda_2)_i(w_i - D_i u) + (\beta/2) \|w_i - D_i u\|_2^2 \quad (7)$$

According to the theory of two-dimensional shrinkage operator [5], the minimizer w_i is defined by

$$w_i = \max \left\{ \left\| D_i u + \frac{(\lambda_2)_i}{\beta} \right\|_2 - \frac{1}{\beta}, 0 \right\} \cdot \frac{D_i u + (\lambda_2)_i/\beta}{\|D_i u + (\lambda_2)_i/\beta\|_2} \quad (8)$$

Similarly, according to the theory of one-dimensional shrinkage operator, the minimizer z_i is defined by

$$z_i = \max \left\{ \left\| \psi_i^T u + \frac{(\lambda_1)_i}{\beta} \right\|_1 - \frac{\tau}{\beta}, 0 \right\} \cdot \frac{\psi_i^T u + (\lambda_1)_i/\beta}{|\psi_i^T u + (\lambda_1)_i/\beta|} \quad (9)$$

In addition, after the values of w_i and u_i is determined, u can be achieved by solving (6) which is equivalent to solve the so-called “u-sub-problem”

$$\begin{aligned} \min_u \vartheta(u) = & \sum_i -(\lambda_2)_i(w_i - D_i u) + (\beta/2) \|w_i - D_i u\|_2^2 - (\lambda_1)_i(z_i - \psi_i^T u) \\ & + (\beta/2) \|z_i - \psi_i^T u\|_2^2 + (\mu/2) \|Au - b\|_2^2 \end{aligned} \quad (10)$$

The minimizer u can be solved by the least squares method, the value of u is as follows

$$u = (\beta\psi_i^T \psi_i + \beta D_i^T D_i + \mu A^T A)^T \cdot [-(\lambda_2)_i D_i^T + \beta D_i^T w_i - (\lambda_1)_i \psi_i + \beta \psi_i z + \mu A^T b] \quad (11)$$

In summary, according to the ADM, the (6) is divided into three sub-problems, and these three sub-problems can be solved relatively simple arithmetic operations, thereby avoiding the direct solution more than 1-norm and 2-norm of hybrid optimization question.

Algorithm of MixTV-W:

Input: random observation matrix A , Observation information b , τ , μ , $\beta > 0$, tolerance ε .

Initialize $u^0, (\lambda_1)^0, (\lambda_2)^0$, $k = 0$.

While stopping criteria unsatisfied **Do**

- 1) Compute w^{k+1}, z^{k+1} by solving (8) and (9).
- 2) Compute u^{k+1} by solving (11).
- 3) Update λ_1 and λ_2 by $(\lambda_1)_i^{k+1} = -(\lambda_1)_i^k + \beta (z_i^{k+1} - \psi_i^T u^{k+1})$

$$(\lambda_2)_i^{k+1} = -(\lambda_2)_i^k + \beta (w_i^{k+1} - D_i u^{k+1})$$

- 4) $k = k + 1$.

End Do

The stopping criteria is $\|u^{k+1} - u^k\|_2 \leq \varepsilon$.

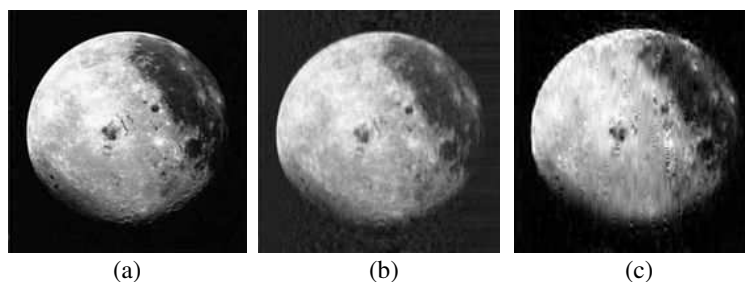


Figure 2: The result of reconstruction under the sampling rate 0.4.

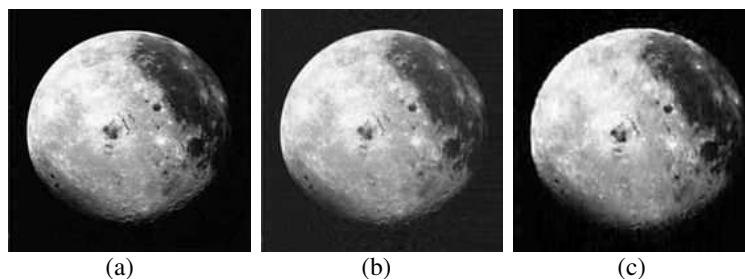


Figure 3: The result of reconstruction under the sampling rate 0.7.

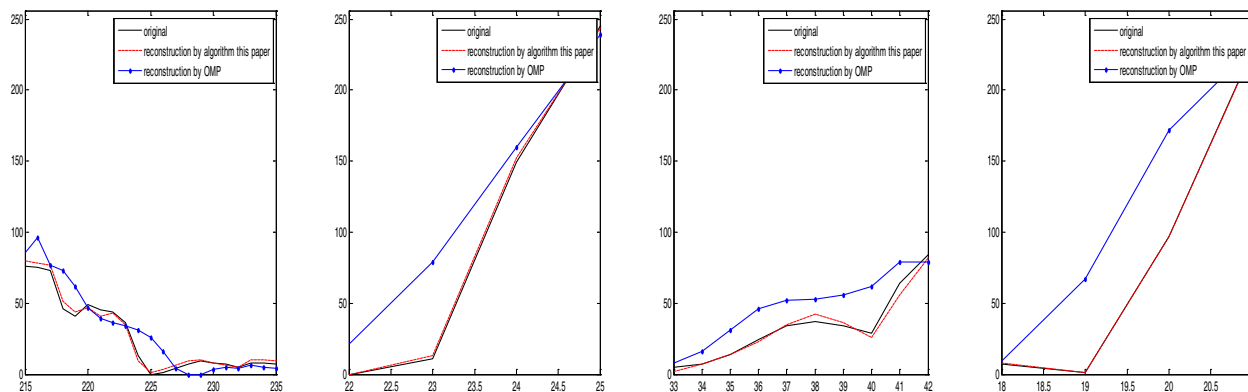


Figure 4: Gray value near the edge portion of the moon.

Table 1: The PSNR (dB) of different sampling rates and different algorithms.

	algorithm this paper		OMP	
sampling rate	0.4	0.7	0.4	0.7
Moon	28.43	33.84	25.02	30.42

3. SIMULATION EXPERIMENT

In the simulation experiment, we simulate the microwave radiation image of the Moon by the proposed algorithm based on the total variation basis and wavelet basis. Also the OMP algorithm based on the wavelet basis is adopted to simulate the result as the comparison. The two images' size are 256×256 . Sampling rate is set to 0.4 and 0.7 respectively. The reconstruction results are presented in Figure 2 to Figure 3.

In the two figures, subgraph (a) are the original, subgraph (b) are the results of the reconstruction by the algorithm this paper proposed, subgraph (c) are the results of the reconstruction by the OMP based on the signal basis. We can see that the results of the subgraph (b) in the two figures are better than the subgraph (c). According to the Simulation data in Table 1, the PSNR of subgraph (b) in the two figures are higher 2–4 db than subgraph (c).

In each subgraph of the Figure 4, black solid line represents original, red dotted line represents

reconstruction by algorithm this paper, blue dot and solid line represents reconstruction by OMP. In the Figure 4, each subgraph shows the grey value of image border and the change illustrating that the spatial resolution are high. We can see from the figure that the faster the grey value changes which is the steeper the curve changes illustrating that the spatial resolution are higher. In each subgraph of the Figure 4, black solid line represents original, red dotted line represents reconstruction by algorithm this paper, blue dot and solid line represents reconstruction by OMP. So from the Figure 4 denotes that the spatial resolution of reconstruction by our proposed algorithm is higher.

4. CONCLUSION

This paper proposed the model based on the mixed orthogonal basis and the augmented Lagrangian approach, and use the ADM reconstruct the microwave radiation images. The result of simulation of complex microwave radiation image show that the method we proposed is better than the OMP method based on the signal basis. However if the image's structure is too simple, the result used by our proposed algorithm is not as good as the result of OMP. The next step will focus on the reconstruction quality, and optimize the reconstruction algorithm.

ACKNOWLEDGMENT

The work was supported by the National Nature Science Foundation of china (No. 61162015) and (No. 31101081).

REFERENCES

1. Li, S. T. and D. Wei, "A survey on compressive sensing," *Acta Automatica Sinica*, Vol. 35, No. 9, 1369–1377, 2009.
2. Wang, L. J., G. M. Shi, and F. Li, "Compressed sensing image reconstruction in multiple sparse spaces," *Journal of Xindian University*, Vol. 40, No. 3, 73–80, 2013.
3. Chen, L., Q. Li, W. Guo, et al., "One-dimensional mirrored interferometric aperture synthesis," *IEEE Geoscience and Remote Sensing Letters*, Vol. 7, No. 2, 357–361, 2010.
4. Lenti, F., F. Nunziata, M. Migliaccio, et al., "2D TSVD to enhance the resolution of radiometer data," *2012 IEEE International Geoscience and Remote Sensing Symposium (IGARSS)*, 6091–6094, 2012.
5. Li, C. B., "An efficient algorithm for total variation regularization with applications to the single pixel camera and compressive sensing," Diss. Rice university, 2009.
6. Yang, J., Y. Zhang, and W. Yin, "A fast alternating direction method for TVL1-L2 signal reconstruction from partial Fourier data," *IEEE Journal of Selected Topics in Signal Processing*, Vol. 4, No. 2, 288–297, 2010.

Stereo-SAR Technique without Using Control Points to Estimate Terrain Height

Hsi-Tseng Chou¹, Shih-Chung Tuan², and Kung-Yu Lu¹

¹Department of Communication Engineering, Yuan Ze University, Chung-Li, Taiwan

²Department of Communication Engineering, Oriental Institute of Technology, Pan-Chiao, Taiwan

Abstract— Estimation of terrain profiles remains very interested in the applications of remote sensing. In particular, the high-resolution images obtained by the Airborne or satellite-borne synthetic aperture radars (SARs) were effectively used in conjunction with the applications of stereo techniques to perform the estimation. Many simulation models were thus developed and applied in the stereo techniques to process the optical images to estimate terrain profiles such as the digital elevation model (DEM) and digital terrain model (DTM). Some typical examples of technologies revealed in the literatures are summarized in the following. The works in proposed a new hybrid radar grammetric model as a function of terrain's slope to establish the stereo DEM without the need of using any reference cartographic data. The accuracy was examined by using the topographic 1959 DEM, and Ice, Cloud, and land Elevation Satellite (ICESat) data. It was applied to ice-covered areas with 1-sigma 25- or 18-m accuracy over less than 30° or 5° slopes, respectively. In addition, a systematic elevation lowering of around 10 m computed between 1959 DEM and recent elevation data (R-2 and ICESat) could be due to icefield wastage over the last 50 years.

1. INTRODUCTION

Estimation of terrain profiles remains very interested in the applications of remote sensing. In particular, the high-resolution images obtained by the Airborne or satellite-borne synthetic aperture radars (SARs) [1–3] were effectively used in conjunction with the applications of stereo techniques to perform the estimation. Many simulation models were thus developed and applied in the stereo techniques to process the optical images to estimate terrain profiles such as the digital elevation model (DEM) and digital terrain model (DTM). Some typical examples of technologies revealed in the literatures are summarized in the following. The works in [4] proposed a new hybrid radar grammetric model as a function of terrain's slope to establish the stereo DEM without the need of using any reference cartographic data. In [5, 6] stereo-techniques using a reference point to estimate the height difference relative to the reference point are developed. In particular, [5] employs a known profile as the reference to find the profile of desired terrain. The reference point is selected in the vicinity of the target point in an one-to-one correspondence. Instead, [6] starts with a single reference point. The target point most close to the reference point is first estimated. Afterward, this target point is used as a new reference point to estimate the next target point in a sequential order. A systematic bias [5] based on a conjecture of being proportional to the height difference between the target area and the reference area is developed to improve the accuracy. The estimated height error can be reduced to 1 m or less by correcting such bias if the target points are near the center row. The approach of using a single reference point dramatically simplifies the systematical structure at the cost of estimation accuracy.

The work presented in this paper is most related to [5, 6] by estimating the height difference between the target point and a reference point. The important progress achieved in this works is that the reference profile is established from the SAR range information of the desired terrain's profile under estimation instead of using the existing and known profiles. This approach simplifies the estimation procedure because the known profile of reference terrain may not be available at the time of processing. Beside the known profile of reference terrain might be also obtained from estimation, where the estimation errors exist in the profile. The use of such reference profile may accumulate errors in the subsequent estimation.

2. STEREO-SAR TECHNIQUE

2.1. Review of SAR Technique

The range-Doppler SAR algorithm [7, 8] used in this work is illustrated which is a two-stage processing procedure to process the range and azimuth compressions in a sequential order. According to the illustration, the received data, $s(t, \tau)$, obtained by SAR is first employed to conduct a range

compression, where t and τ denote the receiving time and variables, respectively. In this procedure, the data is first transformed in the range domain by applying the fast Fourier transform (FFT) algorithm over the variable t , $\tilde{s}(\omega, \tau) = F_t [s(t, \tau)]$.

2.2. The Developed Processing Algorithm

The algorithm is developed based on the difference of range information obtained by two receivers of SAR satellites, which can be obtained from two different satellites flying in one pass or a single satellite flying in two passes along two different paths as illustrated in Fig. 1(a). Here the altitudes of the two different flight paths are assumed to be same and equal to h so that a trigonometric relationship can be established between the receivers, S_1 and S_2 , on the two flight paths, and the target under estimation. This assumption will avoid the possibility of forming any collinear relationship between the three points, and assure the validity of algorithm. Here the coordinate system is therefore selected for S_1 and S_2 to be $(0, 0, h)$ and $(r_d, 0, h)$, respectively. Thus S_1 serves as a reference point of coordinates with the vector of $\overrightarrow{S_1 S_2}$ pointing to \hat{x} , which makes the along-track separation is zero, and the across-track separation is r_d .

As mentioned in Section 1, the algorithm presented in this work builds up its own reference profile by using the same set of SAR data obtained from the target terrain profile. The scheme is illustrated by the geometrical illustration in Fig. 1(b), where a reference point, P_r , in the same range cell of the target, P_t , is selected. The reference is at a postspacing distance, Δx to P_t with a height z_r . Fig. 1(b) also shows four dummy circular circles, which are plotted with respect to the centers at the two satellites on S_1 and S_2 . In particular, the radii of F_{1r} and F_{2r} are the distances, R_{1r} and R_{2r} measured from P_r while those of F_1 and F_2 are the distances R_1 and R_2 measured from P_t . To establish the reference, the range information, R_{1r} and R_{2r} , is considered. The processing algorithm is developed according to the differential information received between those at S_1 and S_2 . The development starts with the expressions of R_{1r} and R_{2r} by

$$R_{1r} = \sqrt{x_r^2 + y_r^2 + (h - z_r)^2} \quad (1)$$

and

$$R_{2r} = \sqrt{(x_r - r_d)^2 + y_r^2 + (h - z_r)^2}, \quad (2)$$

respectively. Note that if one considers the strip profile in the vicinity of $y_r = 0$, where in practice $x_r, h \gg y_r$, (1) and (2) can be approximated as

$$R_{1r} \cong \sqrt{x_r^2 + (h - z_r)^2} + \frac{1}{2} \frac{y_r^2}{\sqrt{x_r^2 + (h - z_r)^2}} \quad (3)$$

and

$$R_{2r} \cong \sqrt{(x_r - r_d)^2 + (h - z_r)^2} + \frac{1}{2} \frac{y_r^2}{\sqrt{(x_r - r_d)^2 + (h - z_r)^2}}, \quad (4)$$

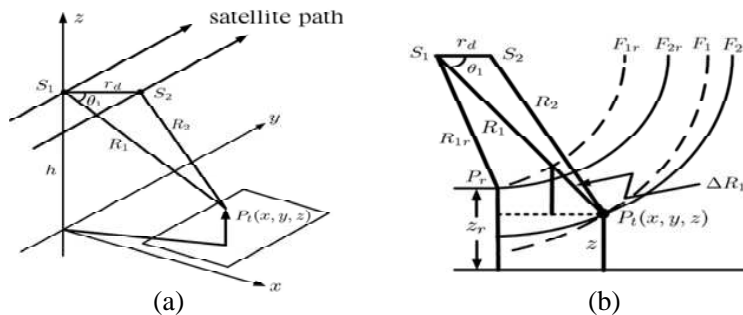


Figure 1: Configuration of dual satellite path and estimation of target height using the receiving data along two paths. (a) Configuration of dual satellite paths over a target area. (b) Estimation of θ_1 using R_1 , R_2 and r_d .

2.3. Calibration of SAR Range Information Base Two Known Terrain Profiles

The range information obtained by SAR technique experiences the estimation errors, which will affect the estimation accuracy of terrain's profile when the information is used to evaluate the height of terrain via any algorithm. It is assumed that the errors are solely caused by the SAR satellite's performance for simplification. Thus given a set of satellite's system parameters, the relative errors can be considered to be roughly the same regardless the terrain's profile under estimation. In this work, this relative error is first examined by using two known terrains' profiles, which will be used to correct the estimation errors and improve the accuracy.

3. NUMERICAL EXAMPLES

Examples are presented to demonstrate the utilization of this technique and validate the feasibility. The relevant parameters of the TerraSAR-X satellite [9], which is used in our simulations. The target area has a size of $1500 \times 150 \text{ m}^2$ with the center located at $(x_c, y_c) = (350, 0) \text{ km}$. The altitude of satellite is 750 km. Thus the angular variation of any point in the target area, when it is observed from the satellite, is significantly small and can be ignored as having been assumed in Section 2. From the satellite, a total of 8192 pulses are emitted along the track, and the pulse repetition interval is chosen to be $\Delta\tau = 43.86 \mu\text{s}$, making an effective aperture length of $L = 8192V\Delta\tau = 2560 \text{ m}$. The target area of the terrain is discretized into square cells of $\Delta x \times \Delta y$, where $\Delta x = 30 \text{ m}$ and $\Delta y = 30 \text{ m}$ are used to create 306 sample points. In this case, the range resolution of SAR is in the order of $\Delta R = c/2Bw \cong 2 \text{ m}$ while the azimuth resolution is in the order of $\Delta R_a = \lambda R/(2L) \cong 5 \text{ m}$. The three terrain profiles selected for the examinations are shown in Figs. 2(a), (b), which are the contoured maps and images of: (a) Mountain area, Highland Experimental Farm, National Taiwan University, Nantou County, Taiwan; (b) Batura Glacier, Batura Valley Passu, Gojal, Gilgit-Baltistan, Pakistan. These three regions experienced special influences by the global weather changes or were used to perform the related studies. In the simulation, six rows of height data at the sampled points are recorded, with each row containing 51 data points.

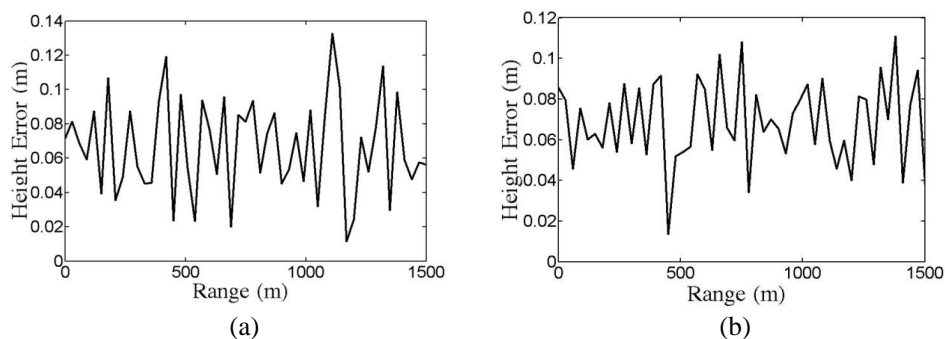


Figure 2: Height error along the center row of the strip area in (a) Mountain area, Highland Experimental Farm, National Taiwan University, Nantou County, Taiwan, (b) Batura Glacier, Batura Valley Passu, Gojal, Gilgit-Baltistan, Pakistan.

4. CONCLUSIONS

A stereo-synthetic aperture radar (stereo-SAR) technique is proposed to reconstruct the height profile of terrains, requiring only one reference point. The technical parameters of TerraSAR-X satellite is chosen to simulate over three different types of terrain. The rms error of height estimation can be reduced to one meter, making this technique practical for certain applications.

REFERENCES

1. Stimson, G. W., *Introduction to Airborne Radar*, 2nd Edition, SciTech, 1998.
2. Soumekh, M., *Synthetic Aperture Radar Signal Processing with MATLAB Algorithms*, Wiley-Interscience, 1999.
3. Cumming, I. G. and F. H. Wong, *Digital Processing of Synthetic Aperture Radar Data Algorithms and Implementation*, Artech House, 2005.

4. Toutin, T., E. Blondel, D. Clavet, and C. Schmitt, “Stereo radargrammetry with radarsat-2 in the Canadian Arctic,” *IEEE Trans. Geosci. Remote Sens.*, Vol. 51, No. 5, 2601–2609, May 2013.
5. Lu, K.-Y. and J.-F. Kiang, “Stereo-synthetic aperture radar technique with bias correction to estimate terrain height,” *IET Radar Sonar Navig.*, Vol. 7, No. 3, 225–232, Mar. 2013.
6. Lu, K.-Y. and J.-F. Kiang, “Terrain height estimation using a stereo-sar technique aided by a reference point,” *Progress In Electromagnetics Research*, Vol. 31, 1–11, May 2013.
7. Stiles, J. A., V. S. Frost, J. C. Holtzman, and K. S. Shanmugam, “The recognition of extended targets: SAR images for level and hilly terrain,” *IEEE Trans. Geosci. Remote Sens.*, Vol. 20, No. 2, 205–211, Apr. 1982.
8. Monaldo, F. M. and D. R. Lyzenga, “On the estimation of wave slope and height-variance spectra from SAR imagery,” *IEEE Trans. Geosci. Remote Sens.*, Vol. 24, No. 4, 543–550, Jul. 1986.
9. Buckreuss, S., R. Werninghaus, and W. Pitz, “German satellite mission TerraSAR-X,” *IEEE Aero. Electron. Syst. Mag.*, Vol. 24, No. 11, 4–9, Nov. 2009.

Detection of Selected Chemical Substances by Means of Nuclear Quadrupole Resonance

M. Steinbauer¹, B. Kral², I. Fiala², M. Stanek²,
M. Prochazka¹, P. Fiala¹, J. Seginak¹, and P. Drexler¹

¹Department of Theoretical and Experimental Electrical Engineering
Brno University of Technology, Technická 12, Brno 616 00, Czech Republic

²Prototypa, Hudcova 533/78c, Brno 612 00, Czech Republic

Abstract— Nuclear Quadrupole Resonance (NQR) is an advanced diagnostic method for the spectroscopy of solid state substances. NQR exploits the presence of the electrical quadrupole moment of the atomic nuclei of certain isotopes. A broad set of substances, both inorganic and organic, have their quadrupole resonance in the range of ones to tens of MHz. An important fact is that recognizable quadrupole resonance can be detected in the case of substances present in explosives, drugs, and medicaments. The utilization of NQR constitutes a promising perspective for non-contact, non-destructive diagnostics in chemical research, material science, and security applications. A compact experimental NQR spectrometer has been built at the DTEEE, Brno University of Technology. The spectrometer enables us to experimentally verify the impact of various functional blocks on the detection abilities. Selected chemical substances containing chlorine and nitrogen isotopes were analyzed with the spectrometer.

1. INTRODUCTION

The principles of NQR spectroscopy can be found in reference [1]. Although this technique seems to be very promising for the detection of explosives [2], it is presently too slow and not very suitable for field applications [3]. The detection of explosive materials via NQR is now used as a confirmatory method in airport scanners. This type of detection is mostly based on the presence of nitrogen isotope ¹⁴N. In addition to this, NQR spectroscopy can also be used to detect a variety of other chemicals, such as those based on chlorine, bromine, or lithium. In this way, it is then possible to identify drugs, which often contain some of the detectable isotopes.

The experimental NQR spectrometer in our laboratory is designed to measure within the frequency range of up to 100 MHz. Its design, which is based on paper [4], utilizes a SpinCore radioprocessor and is equipped with a 250 W rf power amplifier. A photograph of the experimental NQR setup is shown in Figure 1.

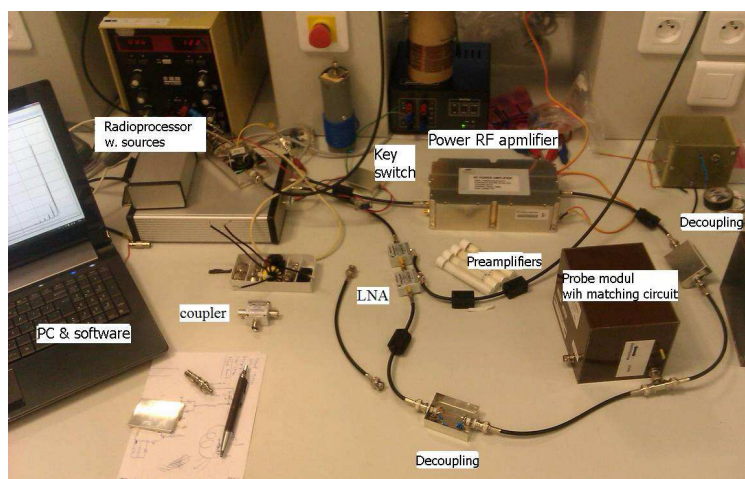


Figure 1: The NQR setup during the experiment.

We examined the possibility of detecting some of the compounds and explosive mixtures introduced in Table 1, and we also verified the minimum detectable amounts. These obviously depend on the specific design of the spectrometer, in particular on the volume of the measuring coil and the associated power of the rf amplifier. Other aspects significant in determining the minimum amounts include the sensitivity and low SNR of the amplifiers and acquisition circuitry.

Table 1: Resonant frequencies of some substances.

Substance	Resonant frequency
KClO ₃	28.09 MHz
NaClO ₃	29.93 MHz
NaNO ₂	3.6 and 4.64 MHz
RDX	3.41 and 5.192 MHz
HMX	5 and 3.5 MHz
PETN	1 MHz

2. EXPERIMENT

A key part of the spectrometer is the rf preamplifier. We tested an AU-1647 low-noise amplifier by Miteq and a cascade of two MiniCircuits ZFL-1000LN amplifiers. The best obtained SNR value was 27 dB for the pair of ZFL-1000LN and 38 dB for the AU-1647; furthermore, the cascade comprising an AU-1647 + 2 × ZFL-1000LN was examined, with the resulting SNR of 22 dB. It is therefore evident that the increasing number of amplifiers also causes the SNR to decrease.

As an example, we will now describe the results obtained from the measurements of two substances: potassium chlorate (KClO₃) and sodium nitrite (NaNO₂). The acquired FID signals are presented in the graphs in Figures 2 and 3; here, the values on the y -axis are in units of output from the A/D converter, and the x -axis shows time in seconds. The blue and red curves represent the components I and Q of the quadrature detection. The applied parameters of the NQR experiment are given in the description of the image.

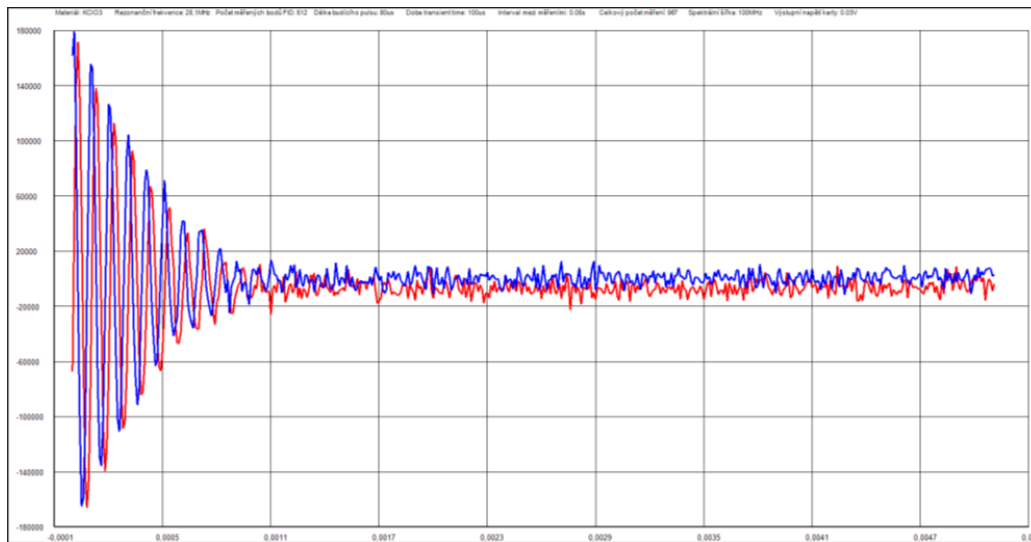


Figure 2: The FID of the KClO₃ sample at the frequency of 28.1 MHz (number of measured points: 512; excitation pulse length: 80 μ s; dead time: 100 μ s; interval between the measurements 50 ms; spectral width: 100 kHz; output voltage level: 30 mV). The response time is about 1 ms.

After the time accumulation, the signal was transformed into the frequency domain; the received spectrum can be seen in Figures 4 and 5. The x -axis is in kHz, while the y -axis is in relative units of the A/D converter. The spectrum shown here was computed from the signal accumulated from 1000 implementations.

As the resonant frequency of the LC probe slightly shifted after the insertion of the sample, it is appropriate to tune the resonant circuit only in the presence of the sample. During the measurement, the spectral response often exhibited narrowband artifacts; these unwanted components can be caused by phenomena such as nonlinearities in the circuit or interferences from nearby appliances. We also verified the impact of slight changes (within the scale of kHz) in the excitation signal frequency on the spectrum. Artifacts unrelated to the measured sample remained at the same position in the spectrum, while the response of the sample was shifted to the other frequency.

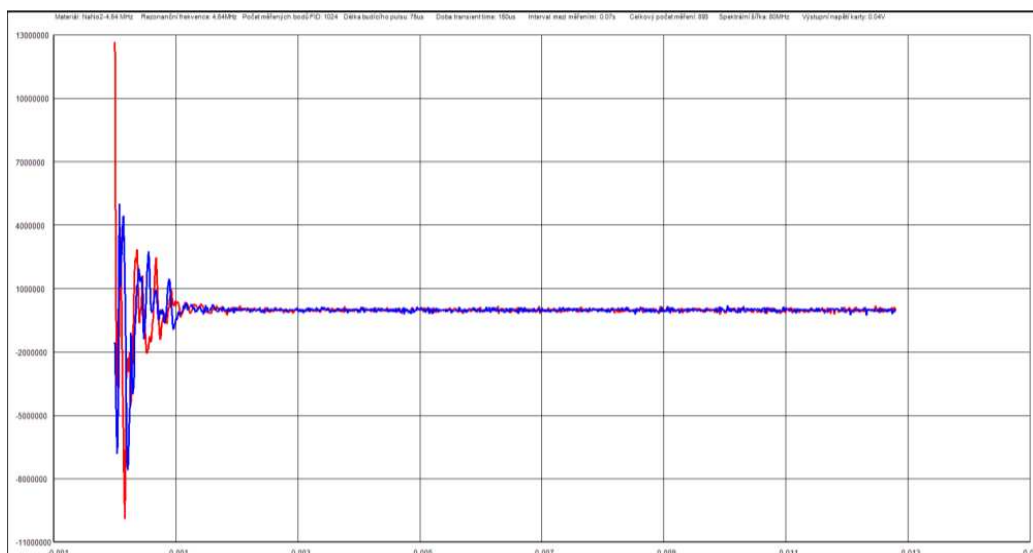


Figure 3: The FID of the NaNO_2 sample at the frequency of 4.64 MHz (number of measured points: 1024; excitation pulse length: 75 μs ; dead time: 150 μs ; interval between the measurements: 70 ms; spectral width: 80 kHz; output voltage level: 40 mV). The response time is about 1 ms.

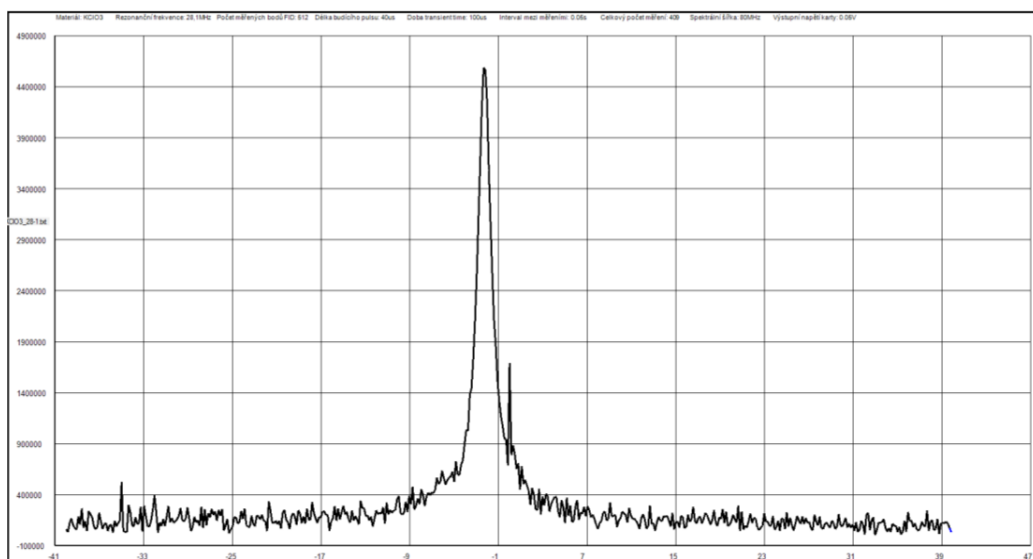


Figure 4: The spectral response of the KClO_3 sample at the excitation frequency of 28.1 MHz.

This approach can be used to identify and eliminate artifacts in the measured spectrum.

The spectral response depends on the excitation parameters, especially on the duration of the excitation pulse: for the strongest spectral response, it is necessary to find its optimal value. When measuring potassium chlorate, the intensity of the main spectral lines increased with the excitation pulse lengthening up to 80 microseconds and remained strong up to 200 microseconds. Further excitation pulse lengthening has an opposite effect, and thus the signal fades. Equally important to proper detection is the excitation level: at an excessively high level, the sample is overexcited, and weak or even no NQR response is obtained. A prerequisite for the FID acquisition is the correctly set dead time, which must be optimally selected to recover the preamplifier transients after the excitation pulse; simultaneously, the time must not be too long to preclude FID decay.

The averaging methods require us to measure n implementations of the signal. To ensure high sensibility, this value should be large enough to facilitate the visibility of even small signals; conversely, a too large n causes measurement time extension and amplifies the artifacts as well as the correlated noise, which leads to a relative decrease in the signal intensity (despite the fact that its absolute value increases). The usual number of implementations was therefore around 1000.

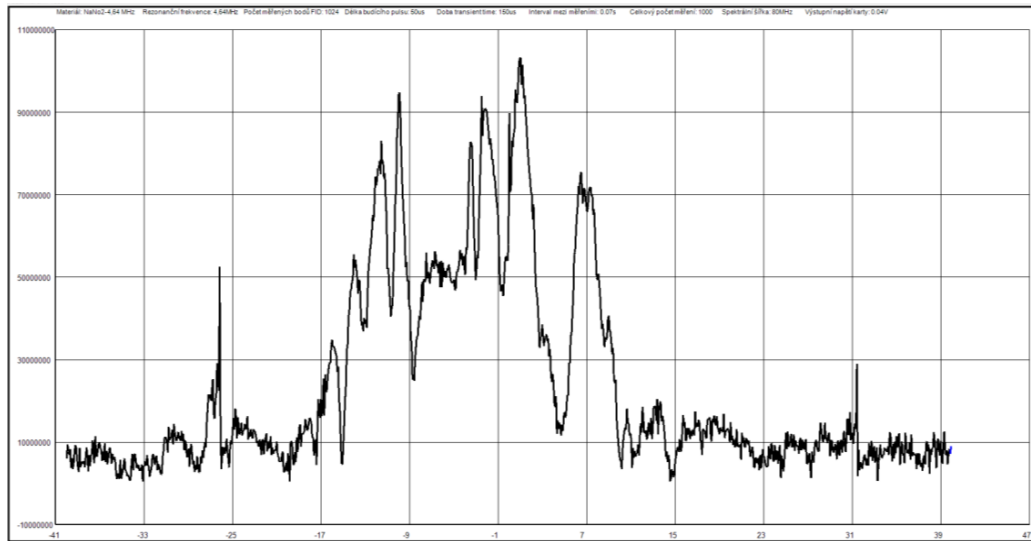


Figure 5: The spectral response of the NaNO_2 sample at the excitation frequency of 4.64 MHz.

In accordance with the theoretical knowledge, we observed the influence of the ambient temperature and atmospheric pressure on the experiment. In some cases, we failed to find the NQR response when the laboratory was too warm or when the atmospheric pressure dropped before a storm.

3. DETECTABLE AMOUNT OF SAMPLES

The basic parameters for the NQR signal strength are the probe coil volume and duty cycle, i.e., the ratio of the volume of the measured substance to the working volume of the coil. A major problem lies in the electromagnetic field distribution in such a coil; thus, the signal depends on the location of the sample in the coil. In this paper, we present the results obtained from several measurements with varying amounts of potassium chlorate (KClO_3) excited at the frequency of 28.09 MHz. The experimental arrangement of the test is shown in Figure 6. In a coil having the volume of about 30 cm^3 and with a 17 cm^3 test tube, the minimal detectable amount of KClO_3 was approximately 7 g. For substances with a weaker NQR signal, the measurement in the given configuration does not make sense. It turned out that any prior mechanical movement affecting the powder sample exerted strong influence on the NQR signal; it is therefore suitable to let each sample recrystallize for several hours before measurement.

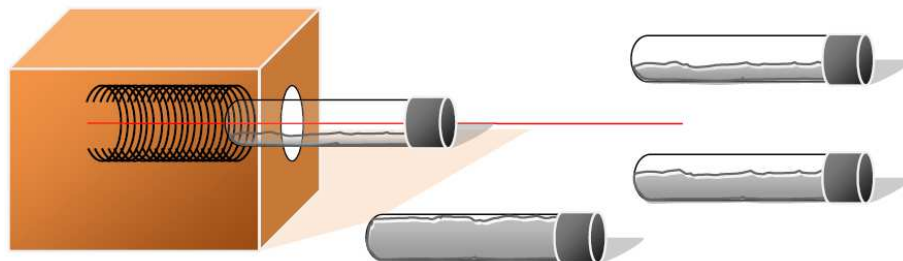


Figure 6: The experiment with the minimum detectable amount of KClO_3 . The red abscissa indicates the center of the coil with the maximum electromagnetic field; the tube filled with over a half of the volume thus exhibits a substantially higher signal value.

ACKNOWLEDGMENT

The presented activities were supported by the project No. FEKT-S-14-2545/2014, Brno University of Technology internal science fund. Further, the research utilized financial assistance from the project No. CZ.1.07.2.3.00.20.0175 within the Education for Competitiveness Operative Programme.

REFERENCES

1. Suits, B. H., “Nuclear quadrupole resonance spectroscopy,” Physics Department, Michigan Technological University, Houston, USA, D. R. VIJ, *Handbook of Applied Solid State Spectroscopy*, Springer, ISBN-10: 0387324976, July 2006.
2. American Scientist, “Explosives detection with nuclear quadrupole resonance,” Vol. 93, No. 1, 50, January–February 2005, [online] <http://www.americanscientist.org/issues/feature/explosives-detection-with-nuclear-quadrupole-resonance/1>.
3. “International journal on smart sensing and intelligent systems,” *Nuclear Quadrupole Resonance for Explosive Detection*, Vol. 1, No. 3, September 2008, [online] <http://www.s2is.org/Issues/v1/n3/papers/paper8.pdf>.
4. Hiblot, N., B. Cordier, M. Ferrari, A. Retournard, D. Grandclaude, J. Bedet, S. Leclerc, and D. Canet, “A fully homemade ^{14}N quadrupole resonance spectrometer,” *Methodologie RMN, C. R. Chimie*, Vol. 11, 568–579, Nancy-Universite, Universite Henri-Poincare, France, 2008.

Subsurface Imaging 3-D Objects in Multilayered Media by Using Electromagnetic Inverse Scattering Series Method (EISSM)

J. G. Wang¹, Z. Q. Zhao¹, Z. P. Nie¹, and Q. H. Liu²

¹School of Electronic Engineering

University of Electronic Science and Technology of China, China

²Department of Electrical and Computer Engineering, Duke University, USA

Abstract— Subsurface imaging 3-D objects buried in layered medium with electromagnetic waves has recently attracted significant interests. Due to the uncertainty of dielectric parameters of layered background media in practice, most of existing electromagnetic inverse methods reconstruct the buried objects unfaithfully. In order to accurately reconstruct the objects buried in multilayered media with unknown dielectric parameters, we develop a new imaging method named electromagnetic inverse scattering series method (EISSM) for imaging 3-D objects in multilayered media. The 3-D EISSM combines the inverse scattering series (ISS) theory with a multi-array tomographic approach. It directly reconstructs the positions of the buried objects (not their dielectric properties) solely with the dielectric parameters of free space according to the discontinuities of dielectric parameters. Moreover, the effects of multilayered media to the position error predicted by EISSM are also analyzed and discussed. Aiming to validate the feasibility of the developed 3-D EISSM, some numerical simulations are given as well as the results reconstructed by commonly used time reversal mirror (TRM) technique. Through the simulations, the EISSM is capable of positioning 3-D targets buried in multilayered media with less error than traditional TRM.

1. INTRODUCTION

Subsurface imaging 3-D objects buried in multilayered media with electromagnetic waves has recently attracted significant attentions and been extensively studied. Up to now, various algorithms have been proposed to circumvent the inherent difficulties in different application backgrounds [1–5]. However, most of existing electromagnetic inverse methods are based on the assumptions that the dielectric parameters of multilayered media are exactly known. Owing to the uncertainty of dielectric parameters of the layered background media in practice, existing methods in [1–5] will reconstruct the buried objects unfaithfully.

Aiming to accurately reconstruct the buried objects in practice conditions (the dielectric parameters of multilayered media are unknown), a modified inverse scattering series method (MISS) based on the inverse scattering series (ISS) theory was developed in hydrocarbon exploration for 1-D and 2-D scenarios [6]. The MISS method reconstructs the electric conductivity of objects with an approximation that the dielectric permittivity is constant and equal to the value of water.

Different to the MISS method, we develop an imaging method named electromagnetic inverse scattering series method (EISSM) for imaging 3-D objects buried in multilayered media. The proposed EISSM combines the ISS idea with a multi-array tomographic approach [7]. It directly reconstructs the positions of the buried objects (not their dielectric properties) solely with the dielectric parameters of free space according to the discontinuities of dielectric parameters. Moreover, the effects of multilayered media to the position error predicted by EISSM are also analyzed and discussed. In order to validate the feasibility of the developed EISSM, some numerical simulations are given as well as the results reconstructed by commonly used time reversal mirror (TRM) technique [8, 9]. Through the simulations, the EISSM is capable of positioning 3-D targets buried in multilayered media with less error than traditional TRM.

2. THEORY

Figure 1 shows the configuration of a 3-D object buried in a layered medium. In order to avoid the mutual coupling, an antenna array which consists of a sequence of monostatic pairs is applied. When a given transmitter emits an electromagnetic pulse, only the corresponding receiver is activated [7]. In addition, the transmitters are assumed as z -directed electric dipoles.

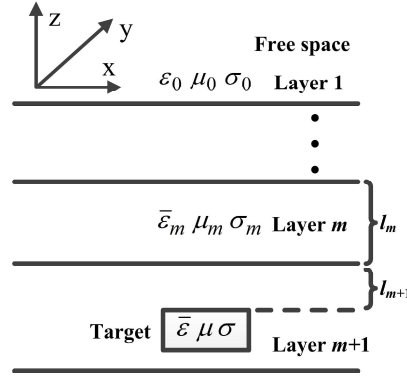


Figure 1: Typical configuration of an object in a layered medium.

For the model in Figure 1, the wave equations for electric field in the actual medium and free space are expressed as

$$(\nabla^2 + k_m^2) \mathbf{E}(\mathbf{r}, \mathbf{r}_s) = -\mathbf{J}(\omega)\delta(\mathbf{r} - \mathbf{r}_s), \quad (1)$$

$$(\nabla^2 + k_0^2) \mathbf{E}_0(\mathbf{r}, \mathbf{r}_s) = -\mathbf{J}(\omega)\delta(\mathbf{r} - \mathbf{r}_s), \quad (2)$$

where $k_m = \omega\sqrt{\bar{\varepsilon}_m\mu_m}$, $k_0 = \omega\sqrt{\varepsilon_0\mu_0}$, $(\bar{\varepsilon}_m, \sigma_m, \mu_m)$ are the permittivity, conductivity and permeability of the actual layered medium m , $(\bar{\varepsilon}, \sigma, \mu)$ are the permittivity, conductivity and permeability of the target, $(\varepsilon_0, \sigma_0, \mu_0)$ are the permittivity, conductivity and permeability of free space. \mathbf{J} is an excitation source, ω is the angular frequency, the field point $\mathbf{r} = (x, y, z)$ and the position of source $\mathbf{r}_s = (x_s, y_s, z_s)$.

Define a perturbation operator as

$$\beta = (\nabla^2 + k_m^2) - (\nabla^2 + k_0^2) = \omega^2\varepsilon_0\mu_0 [(\bar{\varepsilon}_m\mu_m/\varepsilon_0\mu_0) - 1] = k_0^2\alpha, \quad (3)$$

where the dielectric perturbation $\alpha = (\bar{\varepsilon}_m\mu_m/\varepsilon_0\mu_0) - 1$. In this paper, μ_m and μ are assumed as μ_0 .

According to the Lippmann-Schwinger equation, electric field \mathbf{E} is rewritten as

$$\mathbf{E}(\mathbf{r}, \mathbf{r}_s) = \mathbf{E}_0(\mathbf{r}, \mathbf{r}_s) + \int_D G_0(\mathbf{r}, \mathbf{r}')\beta(\mathbf{r}')\mathbf{E}(\mathbf{r}', \mathbf{r}_s)d\mathbf{r}', \quad (4)$$

where G_0 is the Green's function of free space, D is the image domain.

Assume $\mathbf{E} = \mathbf{E}_0 + \mathbf{E}_1 + \dots + \mathbf{E}_n + \dots = \sum_{n=0}^{+\infty} \mathbf{E}_n$, substitute it into (4) and therefore (4) can be successively iterated for field \mathbf{E} on the right hand side,

$$\mathbf{E}_1(\mathbf{r}, \mathbf{r}_s) = \int_D G_0(\mathbf{r}, \mathbf{r}')\beta(\mathbf{r}')\mathbf{E}_0(\mathbf{r}', \mathbf{r}_s)d\mathbf{r}' \stackrel{Denote}{\Rightarrow} (G_0\beta\mathbf{E}_0), \quad (5)$$

$$\mathbf{E}_2(\mathbf{r}, \mathbf{r}_s) = \int_D G_0(\mathbf{r}, \mathbf{r}')\beta(\mathbf{r}')\mathbf{E}_1(\mathbf{r}', \mathbf{r}_s)d\mathbf{r}' \stackrel{Denote}{\Rightarrow} (G_0\beta\mathbf{E}_1), \quad (6)$$

$$\mathbf{E}_n(\mathbf{r}, \mathbf{r}_s) = \int_D G_0(\mathbf{r}, \mathbf{r}')\beta(\mathbf{r}')\mathbf{E}_{n-1}(\mathbf{r}', \mathbf{r}_s)d\mathbf{r}' \stackrel{Denote}{\Rightarrow} (G_0\beta\mathbf{E}_{n-1}), \quad n = 1, 2, \dots, +\infty. \quad (7)$$

Then the scattered field is

$$\begin{aligned} \mathbf{E}_s &= \mathbf{E} - \mathbf{E}_0 = \mathbf{E}_1 + \mathbf{E}_2 + \mathbf{E}_3 + \dots = (G_0\beta\mathbf{E}_0) + (G_0\beta\mathbf{E}_1) + (G_0\beta\mathbf{E}_2) + \dots \\ &= (G_0\beta\mathbf{E}_0) + (G_0\beta(G_0\beta\mathbf{E}_0)) + (G_0\beta[G_0\beta(G_0\beta\mathbf{E}_0)]) + \dots \end{aligned} \quad (8)$$

Assume β and α as a sum of constituent terms,

$$\beta = \beta_1 + \beta_2 + \dots + \beta_n + \dots = \sum_{n=1}^{+\infty} \beta_n = k_0^2\alpha = k_0^2\alpha_1 + k_0^2\alpha_2 + \dots + k_0^2\alpha_n + \dots = k_0^2 \sum_{n=1}^{+\infty} \alpha_n, \quad (9)$$

where β_n and α_n are the n th part of β and α , respectively.

Substitute (9) into (8)

$$\begin{aligned} \mathbf{E}_s(\mathbf{r}_M, \mathbf{r}_s) &= \left(G_0 \left(\sum_{n=1}^{+\infty} \beta_n \right) \mathbf{E}_0 \right) + \left(G_0 \left(\sum_{n=1}^{+\infty} \beta_n \right) \left(G_0 \left(\sum_{n=1}^{+\infty} \beta_n \right) \mathbf{E}_0 \right) \right) + \dots \\ &= (G_0 \beta_1 \mathbf{E}_0) + (G_0 \beta_2 \mathbf{E}_0) + (G_0 \beta_3 \mathbf{E}_0) + \dots + (G_0 \beta_1 (G_0 \beta_1 \mathbf{E}_0)) + (G_0 \beta_1 (G_0 \beta_2 \mathbf{E}_0)) \\ &\quad + (G_0 \beta_2 (G_0 \beta_1 \mathbf{E}_0)) + \dots + (G_0 \beta_1 (G_0 \beta_1 (G_0 \beta_1 \mathbf{E}_0))) + \dots, \end{aligned} \quad (10)$$

where $\mathbf{E}_s(\mathbf{r}_M, \mathbf{r}_s)$ is the scattered field measured at the positions of receivers \mathbf{r}_M .

Match the equal order of β_n and therefore the solution of (10) is equivalent to solve following equations

$$(G_0 k_0^2 \alpha_1 \mathbf{E}_0) = \mathbf{E}_s(\mathbf{r}_M, \mathbf{r}_s), \quad (11)$$

$$(G_0 k_0^2 \alpha_2 \mathbf{E}_0) + (G_0 k_0^2 \alpha_1 (G_0 k_0^2 \alpha_1 \mathbf{E}_0)) = 0, \quad (12)$$

$$\begin{aligned} &(G_0 k_0^2 \alpha_3 \mathbf{E}_0) + (G_0 k_0^2 \alpha_1 (G_0 k_0^2 \alpha_2 \mathbf{E}_0)) + (G_0 k_0^2 \alpha_2 (G_0 k_0^2 \alpha_1 \mathbf{E}_0)) \\ &+ (G_0 k_0^2 \alpha_1 (G_0 k_0^2 \alpha_1 (G_0 k_0^2 \alpha_1 \mathbf{E}_0))) = 0, \end{aligned} \quad (13)$$

...

By using Fourier transform and inverse Fourier transform, one can solve (11) with (3) for α_1 ,

$$\alpha_1(x, y, z) = -8 \frac{\cos^3 \theta_0}{c_0} \text{Ez}_s \left(\mathbf{r}_M, \mathbf{r}_s; \frac{\cos \theta_0}{c_0} (2z - z_m - z_s) + \frac{\sin \theta_0}{c_0} \right), \quad (14)$$

where θ_0 is the incident angle, $x = (x_m + x_s)/2$, $y = (y_m + y_s)/2$, $\mathbf{r}_M = (x_m, y_m, z_m)$, $\mathbf{r}_s = (x_s, y_s, z_s)$. $\text{Ez}_s(\mathbf{r}_M, \mathbf{r}_s; t)$ is the z -directed electric field data measured by the receiver at position \mathbf{r}_M .

Then substitute α_1 into (12) to solve for α_2 , and so on. Finally, α is constructed by summing a series of constituent terms, i.e.,

$$\alpha(x, y, z) = \sum_{n=1}^{\infty} \frac{(-1/2)^{n-1}}{(n-1)! \cos^{2(n-1)} \theta_0} \cdot \left[\int_{z_s}^z \alpha_1(x, y, z') dz' \right]^{n-1} \cdot \frac{\partial^{n-1} \alpha_1(x, y, z)}{\partial z^{n-1}}. \quad (15)$$

By using the differential properties of Fourier transform over α_1 , a closed form of α is derived as

$$\alpha_{\text{EISSM}}(x, y, z) = \alpha_1(x, y, z - \Delta), \quad (16)$$

where $\Delta = (2 \cos^2 \theta_0)^{-1} \int_{z_s}^z \alpha_1(x, y, z') dz'$. Detailed derivation can be referred to [10].

In (16), α_{EISSM} is an approximate solution of actual α in (15) because it encapsulates an infinite number of terms through a manipulation of the depth variable z in α_1 . So, an error will be produced by using EISSM for positioning the buried target.

In order to well understand the error of EISSM, the position error predicted by α_1 is firstly discussed. For simplicity, the transmitters and receivers are assumed to be placed on the same plane ($z_s = z_m$). So the position predicted by α_1 is

$$\hat{z}_R = \int_{z_s}^{z_R} \frac{\cos \theta_0}{c_0 / \sqrt{\varepsilon_r(x, y, z')}} dz' \times \frac{c_0}{\cos \theta_0} + z_s = \int_{z_s}^{z_R} \sqrt{\varepsilon_r(x, y, z')} dz' + z_s, \quad (17)$$

where z_R is the real position of target. According to (14), α_1 uses c_0 of free space to position the target buried in the layered medium. The position error of α_1 is

$$\Delta \delta_{\alpha_1} = \hat{z}_R - z_R = \int_{z_s}^{z_R} \sqrt{\varepsilon_r(x, y, z')} dz' + z_s - z_R = \int_{z_s}^{z_R} (\sqrt{\varepsilon_r(x, y, z')} - 1) dz'. \quad (18)$$

From (16), the position reconstructed by EISSM is $\hat{z}_{\text{EISSM}} = \hat{z}_R + \Delta$. Then the error in position predicted by EISSM is

$$\begin{aligned} \Delta \delta_{\text{EISSM}} &= \hat{z}_{\text{EISSM}} - z_R = \underbrace{\hat{z}_R - z_R}_{\Delta \delta_{\alpha_1}} + \Delta = \int_{z_s}^{z_R} (\sqrt{\varepsilon_r(x, y, z')} - 1) dz' + \frac{\int_{z_s}^{z_R} \alpha_1(x, y, z') dz'}{2 \cos^2 \theta_0} \\ &= \int_{z_s}^{z_R} (\sqrt{\varepsilon_r(x, y, z')} - 1) dz' - \frac{4 \cos \theta_0}{c_0} \int_{z_s}^{z_R} \text{Ez}_s \left(\mathbf{r}_M, \mathbf{r}_s; \frac{\cos \theta_0}{c_0} (2z' - z_m - z_s) + \frac{\sin \theta_0}{c_0} \right) dz'. \end{aligned} \quad (19)$$

For the planar layered medium shown in Figure 1, (19) can be rewritten as

$$\Delta\delta_{\text{EISSM}} = \sum_{i=2}^{m+1} (\sqrt{\varepsilon_r(i)} - 1) l_i - \frac{4 \cos \theta_0}{c_0} \int_{z_s}^{z_R} \text{Ez}_s(\mathbf{r}_M, \mathbf{r}_S; \frac{\cos \theta_0}{c_0} (2z' - z_m - z_s) + \frac{\sin \theta_0}{c_0}) dz', \quad (20)$$

where $\varepsilon_r(i)$ is the relative permittivity of layered medium i and assumed as a constant in layered medium i ($i = 2, 3, \dots, m+1$). l_i is the z -direction thickness of layered medium i ($i = 2, 3, \dots, m$), l_{m+1} is the depth that the target embedded in layered medium $m+1$, and $\sum_{i=2}^{m+1} l_i = z_R$.

In (20), the incident angle θ_0 and the measured data Ez_s are fixed when the transmitters and receivers are given. So $\Delta\delta_{\text{EISSM}}$ relates with z_R , $\varepsilon_r(i)$ and l_i of layered medium according to (20).

3. NUMERICAL SIMULATIONS

In order to demonstrate the feasibility of the proposed method, Figure 2 shows a scenario of a 3-D target buried in the bottom of a three-layer medium. 18 z -directed electric dipole antennas are co-located to form 9 monostatic pairs with a uniformly space of 15 cm. When a given dipole transmitter emits a pulse, only the corresponding receiver is activated [7]. 9 transmitters operate sequentially until completing one full cycle of activations. Then the antenna array moves along $+x$ direction (scan line) for surveying. In the simulations, the antenna array moves 9 times evenly along $+x$ direction with an interval of 15 cm. A pulse of Blackman-Harris window (BHW) function with characteristic frequency of 1.5 GHz is used as a source signal. The dielectric constant and conductivity of the three layers and the target are $(\varepsilon_r, \sigma) = (1.0, 0.0 \text{ S/m})$, $(2.0, 0.01 \text{ S/m})$, $(3.4, 0.01 \text{ S/m})$ and $(9.0, 2.0 \text{ S/m})$, respectively. The size of the target is $20 \text{ cm} \times 20 \text{ cm} \times 5 \text{ cm}$. The synthesis data are generated by using FDTD method.

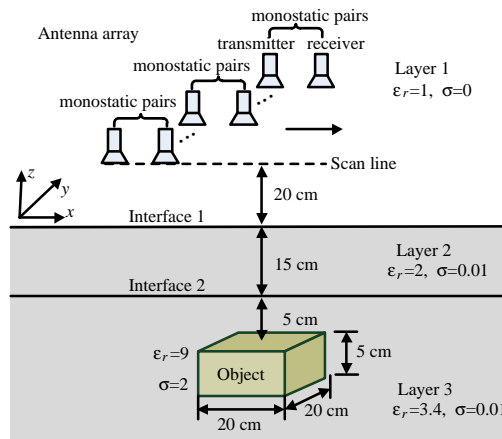


Figure 2: Configuration of an object in a three-layer medium.

With the synthesis data, the results reconstructed under different conditions are given in Figure 3. In practice conditions, the dielectric parameters of layered background medium are unknown. So, Figure 3(a) shows the result reconstructed by using time reversal mirror (TRM) technique solely with the dielectric parameters of free space. Here, Figure 3(a) is used as a reference because TRM has been widely used for surface-penetrating radar detection [8]. In Figure 3(a), the interface 1 is accurately reconstructed because the layer 1 is just free space, while the interface 2 is difficult to detect. The target reconstructed by TRM shifts about 12.9 cm downward to the actual one with the dielectric parameters of free space. Figure 3(b) gives the result reconstructed by using the EISSM under the same conditions as Figure 3(a). The interface 1 is accurately imaged and the interface 2 has a 3.6 cm error downward to the actual one. The buried target reconstructed by the EISSM deviates about 6.0 cm downward to the actual one. Compared with the TRM, the EISSM positions the buried target with more accuracy. To simulate more realistic scenario, Gaussian noise is added to the measured data. The result reconstructed by the EISSM at an SNR of 5 dB is given in Figure 3(c). From Figure 3(c), Gaussian noise does not affect the positions of subsurface scatters predicted by the EISSM and just decrease the image contrast.

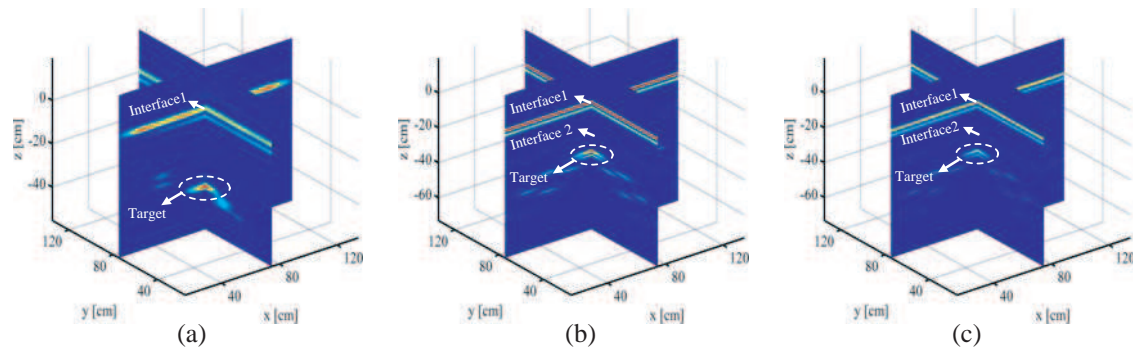


Figure 3: Results reconstructed by using (a) TRM with the dielectric parameters of free space; (b) EISSM with the dielectric parameters of free space; (c) EISSM with the dielectric parameters of free space at SNR = 5 dB.

4. CONCLUSION

This paper presents an electromagnetic inverse scattering series method (EISSM) for sensing 3-D object buried in planar multilayered media with unknown dielectric parameters. The advantage of the EISSM is that it can locate the concealed target without knowing the exact dielectric parameters of multilayered media. Numerical results demonstrate that the EISSM can position the target buried in multilayered media with more accuracy than traditional TRM by solely using the dielectric parameters of free space. For the measured data with Gaussian noise, the EISSM still obtain good results. The developed EISSM is potentially useful for subsurface sensing the concealed targets in practice conditions.

REFERENCES

1. Li, F., Q. H. Liu, and L.-P. Song, "Three-dimensional reconstruction of objects buried in layered media using Born and distorted Born iterative methods," *IEEE Geosci. Remote. Sens. Lett.*, Vol. 1, No. 2, 107–111, 2004.
2. Song, L. P., Q. H. Liu, F. Li, and Z. Q. Zhang, "Reconstruction of three-dimensional objects in layered media: Numerical experiments," *IEEE Trans. Antennas Propag.*, Vol. 53, No. 4, 1556–1561, 2005.
3. Yu, C., M. Yuan, Y. Zhang, J. Stang, R. T. George, G. A. Ybarra, W. T. Joines, and Q. H. Liu, "Microwave imaging in layered media: 3-D image reconstruction from experimental data," *IEEE Trans. Antennas Propag.*, Vol. 58, No. 2, 440–448, 2010.
4. Yu, C., M. Yuan, and Q. H. Liu, "Reconstruction of 3D objects from multi-frequency experimental data with a fast DBIM-BCGS method," *Inv. Probl.*, Vol. 25, No. 2, 024007, 2009.
5. Wei, B., E. Simsek, C. Yu, and Q. H. Liu, "Three dimensional electromagnetic nonlinear inversion in layered media by a hybrid diagonal tensor approximation stabilized biconjugate gradient fast Fourier transform method," *Waves Random Complex Media*, Vol. 17, No. 1, 129–147, Feb. 2007.
6. Kwon, M. J., "Two unconventional approaches to electromagnetic inversion-hierarchical Bayesian inversion and inverse scattering series," Master Thesis, Colorado School of Mines, 2013.
7. Soldovieri, F., G. Prisco, and R. Solimene, "A multiarray tomographic approach for trough-wall imaging," *IEEE Trans. Geosci. Remote Sens.*, Vol. 46, No. 4, 1192–1199, 2008.
8. Cresp, A., I. Aliferis, M. J. Yedlin, C. Pichot, and J. Y. Dauvignac, "Investigation of time-reversal processing for surface-penetrating radar detection in a multiple-target configuration," *Proc. 5th European Radar Conference*, 144–147, Amsterdam, Netherlands, Oct. 30–31, 2008.
9. Cresp, A. and M. J. Yedlin, "Comparison of the time-reversal and SEABED imaging algorithms applied on ultra-wideband experimental SPR data," *Proc. 7th European Radar Conference*, 360–363, 2010.
10. Shaw, S. A., "An inverse scattering series algorithm for depth imaging of reflection data from a layered acoustic medium with an unknown velocity model," Dissertation, 2005.

Data Acquisition System for Body-to-body Radio Communication Channel

H. A. Rahim¹, F. Malek¹, K. K. Goh¹, V. Ganesan¹, F. A. A. Fuad¹,
N. A. A. Talib², and F. S. Abdullah²

¹Embedded, Network and Advanced Computing Research Cluster (ENAC)
School of Computer and Communication Engineering, Universiti Malaysia Perlis
P. O. Box 77, d/a Pejabat Pos Besar, Kangar, Perlis 01000, Malaysia
²School of Electrical System Engineering, Universiti Malaysia Perlis
P. O. Box 77, d/a Pejabat Pos Besar, Kangar, Perlis 01000, Malaysia

Abstract— This paper presents a data acquisition system (DAS) for body-to-body radio communication channel by using Labview. In order to analyze the characteristics of channel fading on body-to-body radio communication channel, a real time DAS must be utilized. The software will be integrated in the measurement system that uses an Agilent Vector Network Analyzer (VNA) (model PNA E8362B), desktop and an interface buses (GPIB)-USB cable from National Instrument (NI). A computer connected to VNA will carry out the acquisition of large data. The measurement data, S_{21} -parameter, will be recorded and stored for offline processing usage. In addition, by using this software, it is more convenient and easier to collect a large data set. This software is also able to capture rapid changes of S -parameter values in dynamic human body motions that requires for further investigation. The comparison of data acquisition between without and with the integrated software is analyzed. The results demonstrate that DAS satisfies the requirement to obtain real-time data with minimum error up to 0.02 dB for magnitude and almost 0 degree for phase of S_{11} -parameter.

1. INTRODUCTION

Body-centric wireless communications (BCWC) defines as human-self and human-to-human networking with the use of wearable and implantable wireless sensors. It is a subject area combining wireless body-area networks (WBANs), Wireless Sensor Networks (WSNs) and Wireless Personal Area Networks (WPANs) [1]. In body-to-body radio communication channel experiment involving dynamic movements, data collection is very critical as a slight movement will cause changes on the output results. Therefore, to ensure the efficiency and reliability of the system, there are several requirements need to be properly investigated. Especially, for those dealing with physical layer issues and the one related to medium access and network layers [2]. Due to this reason, the significant section of the current studies on body centric networks has been focusing on the characterization and modeling of the propagation characteristics as well as the transmission channel [3]. According to the research, a variety of investigations has concerned on the characterization of the on-body channel and described how the current human body affects the communication between two or more devices laced on it [4, 5]. However, limited studies have been done on body-to-body channel [6]. The aim of this work is to design and analyze performance of DAS for data collection in dynamic body-to-body radio propagation channel investigation.

2. CHANNEL MEASUREMENT SETUP

The channel measurement system that will consist of an Agilent E8362B vector network analyzer (VNA), textile monopole antennas (TM) and computer with Lab-VIEW™ 7 software as a controller to collect the data. The transfer function measurement mode will be operated in a VNA, where port 1 is the transmitting port and port 2 is the receiving port. This corresponds to a S_{21} -parameter measurement set-up (see Figure 2). The sweep time of the network analyzer, depending on the number of frequency points within the sweep band, will be automatically adjusted by VNA. The frequency band that will be used in the measurement is from 2 GHz to 3 GHz. Two TM antennas will be required, antenna1 will be attached on the subjectA (SubA) which is the transmitter, Tx and the antenna 2 will be attached on the subjectB (SubB) as the receiver, Rx. The experiment will be carried out in a controlled indoor environment at Embedded Computer Research Cluster, Universiti Malaysia Perlis.

No other people will be present when the measurement is running, except two student subjects and the data collectors. The placement of the transmitter (Tx) will be fixed at the right side of

upper arm on the SubA and the placement of receiver (Rx) will be fixed at the left side of upper arm on the SubB. The antenna to body separation for both subjects is 10 mm air gap. Two 4 meter low loss semi-rigid coaxial cables will be used in the measurement campaign, manufactured by Huber-Suhner. At first, both of the subjects will be in a static movement for calibration purpose. During the measurement, SubA will be static and SubB will be having dynamic movement. Figure 1 shows the measurement setup utilizing TM antennas worn on two subjects' bodies in the indoor environment.



Figure 1: Measurement setup utilizing TM antennas worn on two subjects' bodies in indoor environment.

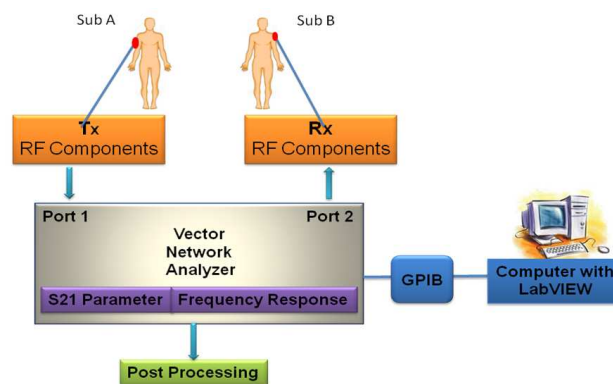


Figure 2: Measurement setup flow diagram.

3. RESULT AND ANALYSIS

The layout is created on the control panel of Labview. The graphical user interface for DAS is used to setup the instrument by using LabView interface through the GPIB card to VNA. The VISA section is the option to select the instrument model to connect with. File path is used to select the particular file location that user wants to save the data. Measurement type consists of four S -parameters; S_{11} , S_{12} , S_{21} and S_{22} , options to choose. The power level is used to select the required power to use for the particular measurement. For display trace there are two options either display phase or magnitude of S -parameter. The default setting of sweep point for this experiment is 1601 points. Besides, the frequency range setup is on the start and stop frequency. Next, the sweep time is the time range requirement to measure and collect the data. The analyzer display shows the sinusoidal graph flow of the result as shown on the screen of VNA (see Figure 3).

Table 1 presents the comparison of measured S_{11} between without and with DAS. The VNA is calibrated before the measurement starts. To validate measurement result, data is taken without DAS. First, frequency range, sweep point and sweep time are configured manually. Second, when the measuring process stops, *Save* button on PNA is pressed to save the data inside the PNA network analyzer. Finally, USB thumb drive is used to save S_{11} parameter from the instrument by connecting to the USB port of PNA and data is transferred to PC for further analysis. Data is saved as *s2p* file. On the other hand, by using DAS, the data is automatically transferred from PNA to the PC. Figure 4 indicates the differences between PNA and DAS data. The S_{11} initial values from frequency of zero to 0.5 GHz are almost equal according to the line graph shown in Figure 4.

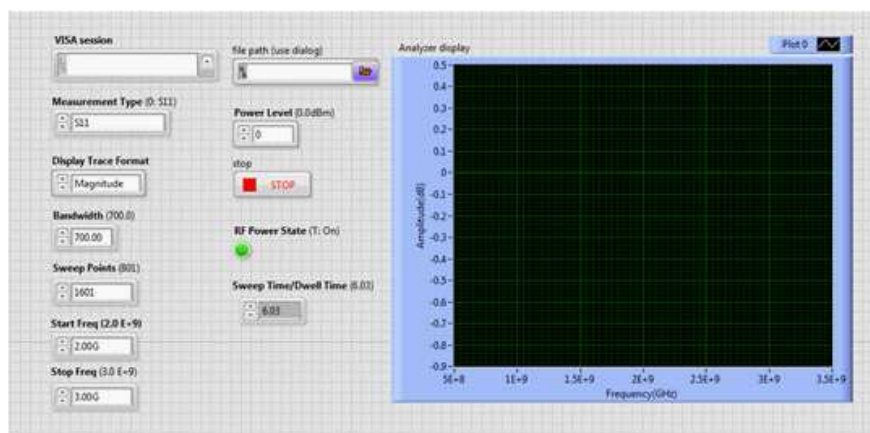


Figure 3: GUI (graphic user interface) of DAS.

The S_{11} magnitude at frequency of 0.5 GHz the PNA is 0.218359 dB and in DAS magnitude is 0.268300 dB. Both data has minor difference of 0.05 dB. The PNA magnitude is -0.011856 dB and DAS magnitude is 0.017873 dB with small difference of 0.006 dB at 1.1 GHz.

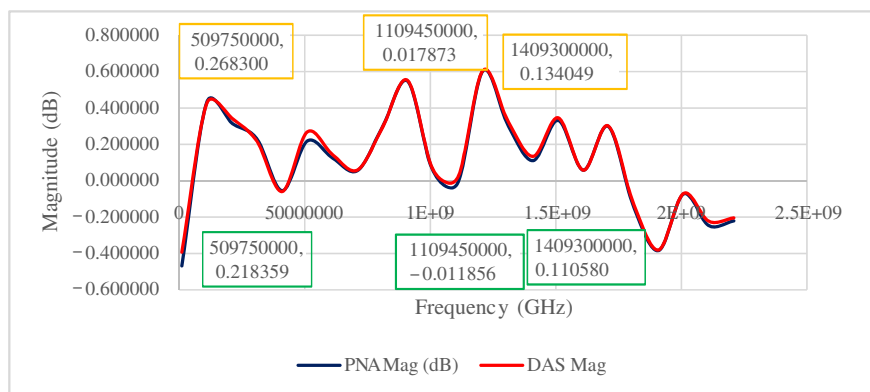


Figure 4: Comparison of PNA and DAS magnitudes in dB.

There is a small mismatch between PNA and DAS magnitudes around 0.02 dB at 1.41 GHz. In general, the overall magnitude results collected from the PNA and DAS are equal. This proves that the DAS satisfies the requirement to obtain real time data with minimum error. Figure 5 shows the phase data in degree. It is observed that there is very small variation between DAS and PNA results. All the data with very small difference can be eliminated after round off the decimal place. This graph also clearly shows that the phase data collected using DAS achieves the requirement by attaining almost equal results. This proves that the data acquisition system

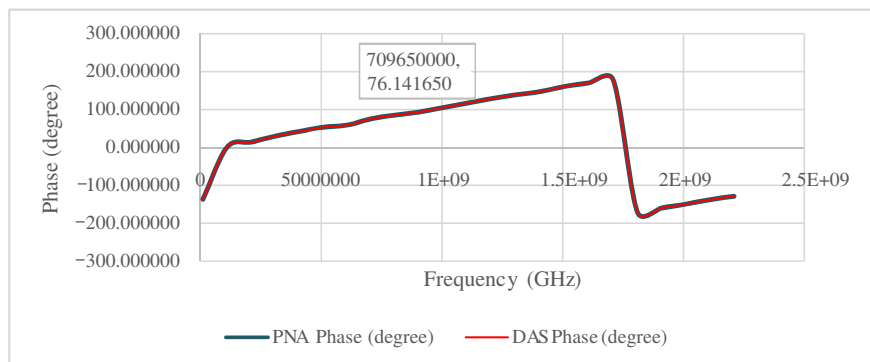


Figure 5: Comparison of PNA and DAS phase in degree.

Table 1: Comparison of measured S_{11} between without and with DAS.

Frequency (Hz)	Without DAS		With DAS	
	Magnitude (dB)	Phase (degree)	Magnitude (dB)	Phase (degree)
10000000	-0.467869	-136.450500	-0.392691	-136.505100
109950000	0.432964	0.774235	0.427213	0.634953
209900000	0.315940	14.332120	0.343037	13.643520
309850000	0.229078	30.035230	0.215615	29.792090
409800000	-0.054616	42.314820	-0.059438	42.060970
509750000	0.218359	53.683180	0.268300	53.363010
609700000	0.126100	59.233550	0.144890	58.931260
709650000	0.055836	76.379070	0.059058	76.141650
809600000	0.296493	85.646070	0.293478	85.445640
909550000	0.547233	94.204190	0.551720	94.053250

achieves the requirement and it is reliable and valid to be used for. This concludes that DAS can synchronize with the measurement data in the PNA.

4. CONCLUSION

This paper discusses a design of DAS for dynamic body-to-body radio communication channel using Labview software. The comparison of data acquisition between without and with the integrated software is analyzed. From the obtained results, it is shown that DAS satisfies the requirement to acquire real-time data with minimum error up to 0.02 dB for magnitude and almost 0 degree for phase of S_{11} parameter. As DAS will be employed for data collection in dynamic body-to-body radio channel, this software is capable of capturing rapid changes of S -parameter values in dynamic motions. Hence, this software is very potential to be used in the evaluation of channel fading of dynamic body-to-body radio propagation channel. Further work will be carried out to measure S_{21} -parameter for dynamic body-to-body radio communication channel using DAS.

REFERENCES

1. Hao, Y., "Antennas and propagation for body centric wireless communications," *2011 IEEE Int. Conf. on Microwave Technology & Computational Electromagnetics (ICMTCE)*, Beijing, China, May 22–25, 2011.
2. Ullah, S., H. Higgins, B. Braem, B. Latre, C. Blondia, I. Moerman, S. Saleem, Z. Rahman, and K. S. Kwak, "A comprehensive survey of wireless body area networks," *J. Med. Sys.*, Vol. 36, No. 3, 1065–1094, 2012.
3. Errico, R. D. and L. Ouvry, "A statistical model for on-body dynamic channels," *Int. Jof. Wireless Inf. Networks*, Vol. 17, 92–104, 2010.
4. Liu, L., D. Doncker, and C. Oestges, "Fading correlation measurement and modeling on the front side of a human body," *3rd European Conference on Antennas and Propagation (EuCAP) 2009*, 969–973, Berlin, Germany, Mar. 23–27, 2009.
5. Fort, A., C. Desset, J. Ryckaert, P. De Doncker, L. Van Biesen, and P. Wambacq, "Characterization of the ultra wideband body area propagation channel," *2005 IEEE Int. Conf. on Ultra-Wideband (ICU 2005)*, Sep. 5–8, 2005.
6. Rosini, R., R. D. Errico, and R. Verdona, "Body-to-body communications: A measurement-based channel at 2.45 GHz," *2012 IEEE 23rd Int. Symp. on Personal Indoor and Mobile Radio Communications (PIMRC)*, 1763–1768, Sydney, Australia, Sep. 9–12, 2012.

Beam Switching Antenna

W. L. Lim¹, F. H. Wee¹, F. Malek², K. Y. You³,
Y. S. Lee¹, H. A. Halim², and F. S. Abdullah²

¹School of Computer and Communication Engineering, Universiti Malaysia Perlis (UniMAP)
Pauh Putra Campus, Arau, Perlis 02600, Malaysia

²School of Electrical Systems Engineering, Universiti Malaysia Perlis (UniMAP)
Pauh Putra Campus, Arau, Perlis 02600, Malaysia

³Faculty of Electrical Engineering
Universiti Teknologi Malaysia, Skudai, Johor Bahru, Johor 81310, Malaysia

Abstract— In this paper is showing about Beam Switching Antenna that able to shift the antenna direction by using four microstrip antenna and aluminum. The antenna is using FR-4 and the saiz is 40 mm × 78 mm. By using aluminum it able increase the gain from 5.269 dB to 8.128 dB while the directivity is from 7.126 dBi to 11.09 dBi. With this antenna it able to control the direction of the radiation pattern up to four location.

1. INTRODUCTION

A beam-switching antenna consists of generating a multiplicity of juxtaposed beam (generated by an array) whose output may be switched to a receiver or a bank of receiver [1]. The addressed space is therefore served by a set of beam that may be switched on or off according to an algorithm that is able to sense the desired direction of transmission or reception beam switching antennas may, in some case [1]. Be cheaper than an equivalents phased array at millimeter wave communications, particularly when few beams are needed. It deploys fixed set of relatively narrow azimuthal beam [1].

A technique that able to switch the beam of the signal of an antenna with durable material that able make the signal stronger. The reason for switching the signal for the place that unwanted for signal is to reduce energy that did not used. It also able use as for security reason that for switch the location that only authorize people in the longing place of the area.

With using aluminum it able support four antenna in different direction and it also able to increase the gain by 64% and increase dielectric by 64.25%. The compounds of greatest importance are aluminum oxide, the sulfate, and the soluble sulfate with potassium (alum) [3]. The oxide, alumina, occurs naturally as ruby (Al_2O_3), sapphire, corundum, and emery, and is used in glassmaking and refractories. Synthetic ruby and sapphire are used in lasers for producing coherent light [3].

2. ANTENNA DESIGN

The Figure 1 is show the front view of a microstrip antenna that able to generate 2.45 GHz frequency with the gain of 5.269 dB and the directivity is 11.09 dBi. The saiz of the antenna is 60 × 80 mm. This antenna is using FR-4 material. FR-4 is a grade designation assigned to glass-reinforced epoxy laminate sheets, tubes, rods and printed circuit boards (PCB). FR-4 is a composite material composed of woven fiberglass that flame retardant, chemical resistance and water absorption [2].

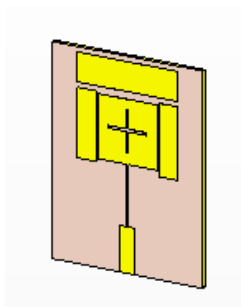


Figure 1: Front view of the anantenna.

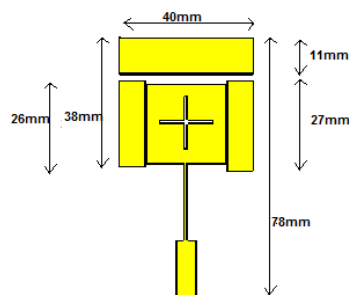


Figure 2: Dimension of the antenna.

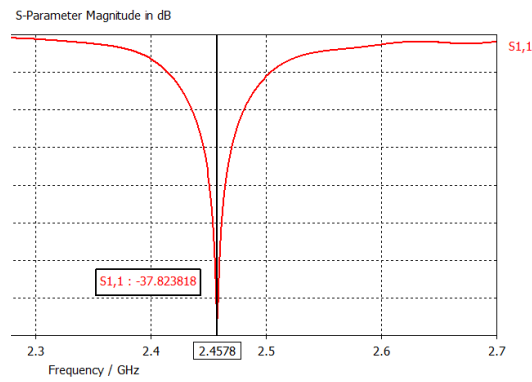


Figure 3: S -parameters.

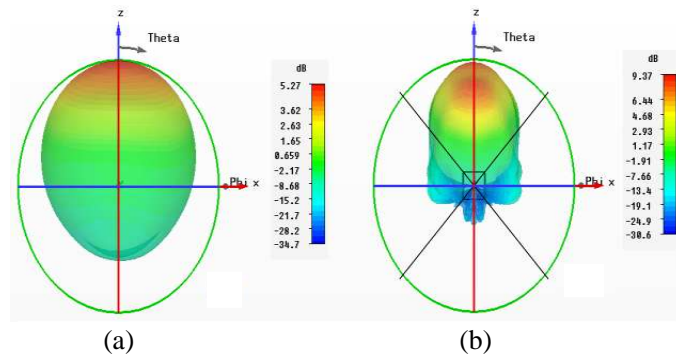


Figure 4: (a) Antenna without aluminium plate, (b) antenna with aluminium plate.

3. RESULT AND DISSCUSSION

The dimension in terms of width of the antenna is 40 mm while the length of the antenna is 78 mm and the height of the FR-4 material is 1.635 mm. The upper site of the antenna is 40 mm in width and 11 mm in height. The both site of the antenna is different saiz and on the right is a bit larger. On the left is 7.5 mm (Width) \times 26 mm (height) while on the right site is 7.5 mm (Width) \times 27 mm (height).

Figure 3 shows that the S -parameter magnitude of the antenna that have been simulate and it show that the frequency is at 2.4578 GHz and the $S_{1,1}$ is -37.823818 .

Figure 4 shows two different type of antenna that the different is with and without aluminum plate. From Figure 4(a) it shows that the antenna is without aluminum plate while Figure 4(b) is with aluminum plate and the two black line that across in the middle of the picture is the location of the aluminum.

The antenna on the right it show that the farfield is much higher than the left side and the radiation pattern also show antenna with aluminum plate is much sharp compare with the antenna on the left without aluminum plate this is because the aluminum play important role it not only act as the antenna holder and also make the antenna gain and dielectric stronger.

4. CONTROLLER PART

The HMC241QS16 & HMC241QS16E are general purpose low-cost non-reflective SP4T switches in 16-lead QSOP packages. Covering DC — 3.5 GHz, this switch offers high isolation and has a low insertion loss of 0.5 dB at 2 GHz. The switch offers a single positive bias and true TTL/CMOS compatibility [3]. A 2 : 4 decoder is integrated on the switch requiring only 2 control lines and a positive bias to select each path, replacing 8 control lines normally required by GaAs SP4T switches [3].

From Figure 5 shows that the IC model HMC241QS16 can be used to control all the four antennas. RF 1, 2, 3, and 4 are connect to the each of SMA connector that been solder to the

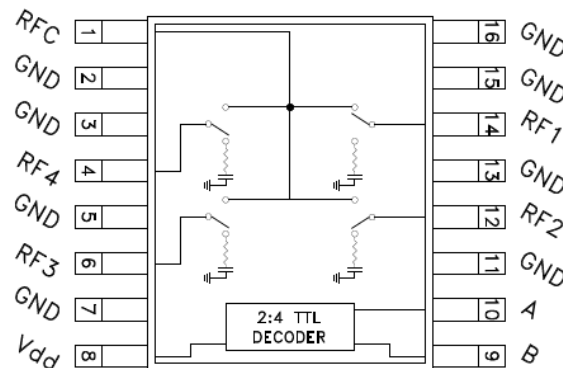


Figure 5: Function diagram.

Table 1: Truth table for HMC241QS16.

Control Input		Signal path State
A	B	RF com to:
Low	Low	RF 1
High	Low	RF 2
Low	High	RF 3
High	High	RF 4

patch antenna respectively. The FRC in pin 1 is the input signal that from the AP (Access Point) while Pin 9 and 10 are decoders that use to select which antenna that need to function [3].

From Table 1 it shows that the controller that used to control which direction of antenna that wanted. As can see from the Control input there have Input A (Pin 10) and Input B, (Pin 9) that able to control the direction of the signal of the antenna by using two switches it able to bring the signal that input from pin1 (RFC) and to Pin 14 (FR1), Pin 12 (FR2), Pin 6 (RF3) and Pin 4 (RF4) [3].

By using the switch is easy to control and can use several of electronic devices such as PLC, Microcontroller and much more to control the antenna direction.

5. CONCLUSION

This project can be implement in to various kind of place such as library, office, home and much more. With using 2.45 GHz frequency it not only suitable with Wi-Fi and also Bluetooth, video devices and much more device because 2.45 GHz in Industrial, Scientific and Medical (ISM) radio bands this is a free frequency. By changing different type of antenna it able to produce different frequency and by using same technic it able to use several of product such as for GSM used and military used.

ACKNOWLEDGMENT

The Author would like to thanks everone who is involved in completing this antenna especially to my supervisor Dr. Wee Fwee Hoon, my both co-supervisor Prof. Madya Dr. Fareq Malek and Dr. You Kok Yeow.

REFERENCES

1. Huang, K.-C. and D. J. Edwards, *Millimetre Wave Antennas for Gigabit Wireless Communications*, 199, John Wiley & Sons Ltd., 2008.
2. Khandpur, R. S., *Printed Circuit Boards: Design, Fabrication, Assembly and Testing*, 270, Tata McGraw-Hill Education, 2008.
3. <http://www.hittite.com/products/view.html/view/Hmc241qs16>.
4. <http://periodic.lanl.gov/13.shtml>.

A Wideband Metamaterial Absorber Based on Multilayer Rings and Lumped Resistors

Yujie Liu, Wei Tang, and Yuehe Ge

College of Information Science and Engineering, Huaqiao University, Xiamen, Fujian 361021, China

Abstract— A novel low-frequency wideband and polarization-insensitive metamaterial absorber is presented. It is composed of multiple dielectric slabs, lumped resistors, square-circular rings and a metal ground plane, with suitable air spacers sandwiched. An absorptive operating band, determined by absorption $A = 1 - |S_{11}|^2 - |S_{21}|^2 > 90\%$, is demonstrated in the frequency range of 1.96 GHz to 7.44 GHz numerically, up to a bandwidth of 116.6%. The wideband absorption design is based on the destructive interference of the reflection waves from the metamaterial and the magnetic resonance of the square-circular loops. The total thickness of the designed absorber is only $0.094\lambda_L$, where λ_L is the free-space wavelength at the lowest operating frequency.

1. INTRODUCTION

Metamaterials attracts much attention of researchers in the past decade. Various novel theories and applications based on metamaterials were proposed and studied. A metamaterial perfect absorber, proposed by David Smith [1–3], is able to provide a good absorption due to the simultaneous electric and magnetic resonances, however, with a narrower bandwidth. Wideband metamaterial absorbers have been studied using interference theory [4, 5] and implemented at a higher frequency band [5]. Low-profile planar absorbing materials have also been designed by using the left-handed transmission line theory [6, 7], achieving a reduction of 10 dB over a bandwidth of 50% at the center frequency of 2 GHz.

In this paper, a novel low-profile metamaterial absorber, composed of square-circular metal rings and lumped resistors, is proposed for wideband absorptive applications. The proposed structural model is original from the typically square and circular loops, which have strongly magnetic resonance. In addition, the result of the absorber is well explained with the interference theory, which shows that the metamaterial absorber can obtain wide absorptive bandwidth in a low frequency range. Simulated results show that this composite structure metamaterial absorber has a low-frequency wideband absorption in the range of 1.96 GHz to 7.44 GHz, almost 116.6% absorptive bandwidth. Another advantage of this design is that it provides a low profile, about 0.094 free-space wavelength at the lowest operating frequency.

2. ABSORBER CONFIGURATION AND DESIGN PRINCIPLE

The unit cell of the proposed metamaterial absorber is shown in Fig. 1. It consists of a PEC ground and three square-circular rings that have different sizes and are printed on three FR4 dielectric layers. The three FR4 dielectric layers have the same thickness, 2 mm, and their relative permittivity is 4.4. On each square-circular ring, four lumped resistors are employed to connect the square ring and the circular ring, in order to absorb the coupled energy of the magnetic resonance of the square-circular rings. As shown in Figs. 1(a) and (b), the unit cell is square, with side length $W = 32$ mm. The widths of square and circular rings in each layer are the same and denoted by d . The diameter of the circular loop is R_r . W_t and ss are the width and length of the rectangular resistors. The FR4 dielectric slabs are separated by the suitable thickness of air space.

For the analysis of such a periodic structure with an infinite size, the PMC and PEC boundaries are applied to the four sides of the unit cell [8]. The simulated model is shown in Fig. 1(c), where a waveport is applied to feed. Commercial software Ansys HFSS was used to carry out the simulations.

For the metamaterial absorber, the expression of the absorption is $A(\omega) = 1 - T(\omega) - R(\omega) = 1 - |S_{11}|^2 - |S_{21}|^2$, where $A(\omega)$ is the absorption. $|S_{11}|^2$ and $|S_{21}|^2$ are the reflection coefficient and transmission coefficient respectively that are the function of frequency ω .

For better understanding, the equivalent circuit of the metamaterial absorber is presented in the Fig. 2. The square-circular rings are equivalent to a parallel LC loop, and lumped resistors are connected in series to it. Dielectric layers and free space are replaced by the transmission line with different characteristic impedance. Through tuning the parameters of the metamaterial

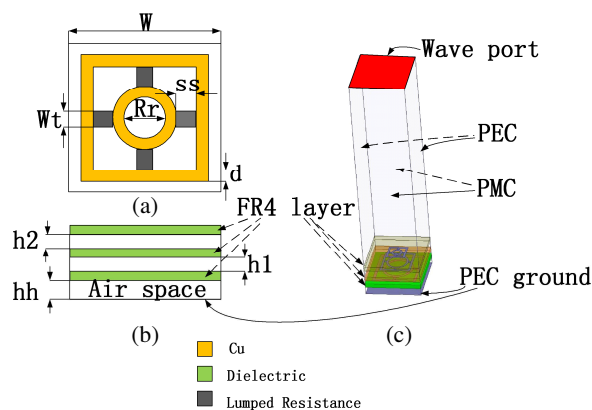


Figure 1: Schematic structure of the metamaterial absorber unit cell.

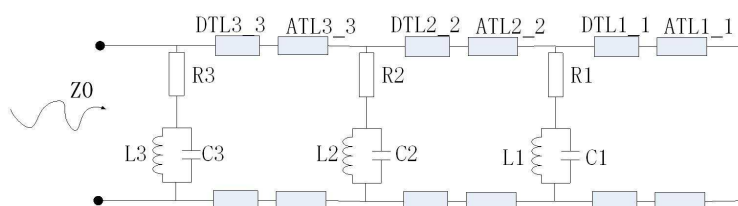


Figure 2: Equivalent circuit model of the proposed metamaterial absorber.

absorber, such as d , R_r , values of resistors, hh , $h1$, $h2$, etc., a good impedance matching over a wide bandwidth to the free space characteristic impedance Z_0 can be achieved, resulting in a wideband metamaterial absorber.

3. SIMULATED RESULTS

The proposed metamaterial absorber is investigated based on the interference theory [4, 5] and the magnetic resonance [1–3]. The model in Fig. 1(c) is used to find the expected reflection or absorption. Parameters d , R_r , values of resistors, hh , $h1$, $h2$ and the size of the unit cell were optimized. Table 1 shows the optimized dimensions of each square-circular rings on each FR4 layer. The height of the air space are $h2 = 3.4$ mm, $h1 = 1.6$ mm, and $hh = 3.5$ mm, as shown in Fig. 1(b).

Table 1: Dimensions of each square-circular rings on FR4 layers (unit: mm).

Location of layer	d	ss	R_r	W_t
Top layer	1.1	1.2	4.2	1.25
Middle layer	1.2	1.2	10.4	1.25
Bottom layer	1.5	2.2	14.8	1.6

In this work, only the reflection needs to be examined, and the absorption is calculated by the equation $A(\omega) = 1 - |S_{11}|^2$. As shown in the Fig. 3, the absorption within the frequency range of 1.96 GHz–7.44 GHz is over 90%, showing a wide bandwidth of up to 116%. The real part of normalized equivalent impedance, which is normalized to wave impedance of free space, 377Ω , is about one and the imaginary part maintains at around zero at the operating band, demonstrating that the absorber has a good impedance matching to the free space and its reflection is nearly zero.

The reflection coefficients for different incident angles are also investigated. Figs. 4(a) and (b) show the simulated results for TE and TM incident cases. It can be seen that a broadband $S_{11} < -10$ dB reflection is obtained at normal incidence for both TE and TM cases. With the increase of incident angles, the reflection remains unchanged at lower frequency, and has a little changing at the higher band. In summary, the proposed absorber is able to achieve polarization-insensitive performance and good absorption for wide-angle incidence, due to its symmetrical structure.

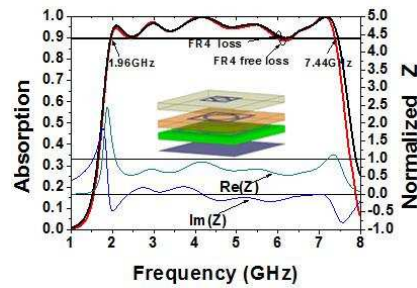


Figure 3: Simulated results of the absorption and the normalized impedance at 377Ω .

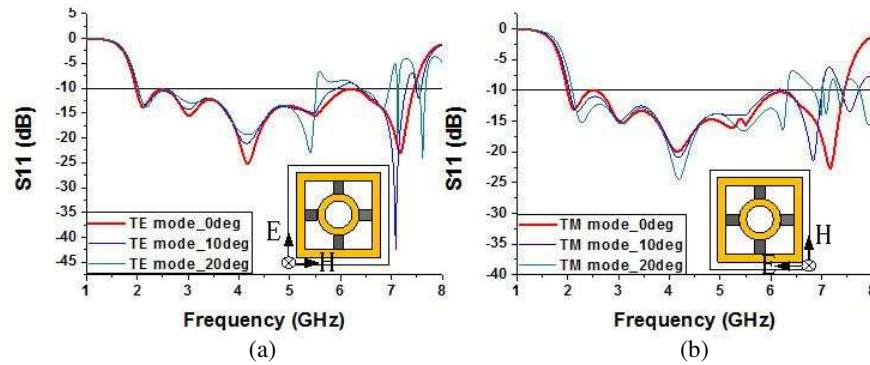


Figure 4: Reflection coefficients for incident angles 0° , 10° and 20° . (a) TE incidence. (b) TM incidence.

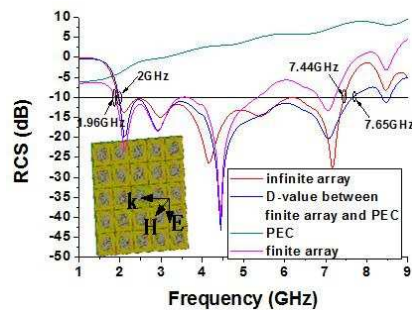


Figure 5: The RCS (Radar Cross-Section) reduction of the metamaterial absorber.

The unit cell of the proposed metamaterial absorber is simulated with the boundary conditions, which means that the absorber is a infinite array and hardly fabricated in reality. To investigate its RCS (Radar Cross-Section) reduction in practice, a model of 5×5 unit cells is applied and its structure is shown in the inset of Fig. 5. The RCS reduction of the model is the death value (D-value) between the finite array of the absorber and the PEC ground with the same dimension of the metamaterial finite array. As shown in Fig. 5, the agreement between RCS (< -10 dB) reductions of the finite and infinite array is excellent, validating the predicted performance of the proposed metamaterial absorber.

4. CONCLUSIONS

We propose a metamaterial absorber that has simultaneous magnetic responses and destructive interference, and has a good impedance matching to free space over a broad frequency band. By adding the lumped resistors, the employed square-circular rings produce a strong magnetic resonance loss. Simulations demonstrate that the proposed low-profile planar absorber has a good absorption ($S_{11} < -10$ dB) in the range of 1.96 GHz to 7.44 GHz, up to a bandwidth of about 116%. The simulated RCS reduction of a 5×5 finite array also validates the wideband absorption performance.

ACKNOWLEDGMENT

This work is supported by the Tongjiang Scholars Program, Fujian province, China, the Start-Up Program (11BS301) from Huaqiao University, China, Natural Science Foundation of Fujian Province (2012J01276), China, and Quanzhou Science and Technology Project (Z1424008), Quanzhou, Fujian province, China.

REFERENCES

1. Landy, N. I., S. Sajuyigbe, J. J. Mock, D. R. Smith, and W. J. Padilla, “A perfect metamaterial absorber,” *Physical Review Letters*, Vol. 100, 207402, 2008.
2. Alaei, R. and M. Farhat, “A perfect absorber made of a graphene micro-ribbon metamaterial,” *Optics Express*, Vol. 20, No. 27, 28017–28024, 2012.
3. Diem, M., T. Koschny, and C. M. Soukoulis, “Wide-angle perfect absorber/thermal emitter in the terahertz regime,” *Physical Review B*, Vol. 79, 033101, 2009.
4. Chen, H.-T., “Interference theory of metamaterial perfect absorbers,” *Optics Express*, Vol. 20, 7165–7172, 2012.
5. Sun, J. and L. Liu, “An extremely broad band metamaterial absorber based on destructive interference,” *Optics Express*, Vol. 19, No. 22, 21156–21162, 2011.
6. McVay, J., N. Engheta, and A. Hoorfar, “High impedance of the double-metamaterial surfaces using Hilbert-curve inclusions,” *IEEE Microwave and Wireless Components Letters*, Vol. 14, No. 3, 130–132, March 2004.
7. Wang, H, W. Tang, and Z. Shen, “On the design of radar absorbing materials using left-handed transmission line,” *IEEE MTT-S International Symposium*, 1475–1478, June 3–8, 2007.
8. Ge, Y., K. P. Esselle, and T. S. Bird, “A method to design dual-band, high-directivity EBG resonator antennas using single-resonant, single-layer partially reflective surface,” *Progress In Electromagnetic Research C*, Vol. 13, 245–257, 2010.

Self-reconstruction and Rectification of Non-diffracting Beams after Focusing

Lan Liu¹, Haitao Zhang¹, and Pengtie Wu²

¹Luohe Medical College, Luohe 462002, China

²Huaqiao University, Quanzhou 362021, China

Abstract— Based on Huygens-Fresnel diffraction integral, the expression of intensity distribution of the self-reconstruction beam is obtained and used to study the intensity evolution of self-reconstruction beams. It is shown that the intense central spot size of the self-reconstruction beam is larger than that of the non-diffracting beam before focusing. This property limits the application of the self-reconstruction beams.

1. INTRODUCTION

In 1998, the self-reconstruction of the non-diffracting beam in free space was fully demonstrated and explained by Bouchal et al. [1]. In 2002, Garces-Chavez et al utilized the self-reconstruction property of the beam in the application of manipulation [2]. Furthermore, the self-reconstruction of the non-diffracting beam in a nonlinear medium has also been examined [3, 4]. Recently, some researchers have further studied the self-reconstruction phenomenon of the non-diffracting beam [5–9]. In previous studies, the people seldom considered the variable properties of the parameters of reconstruction beam. In this paper, using Huygens-Fresnel diffraction integral, we discuss the self-reconstruction of focused non-diffracting beam generated by axicon. Especially, the effect of parameters of the reconstruction beams on the intensity evolution of self-reconstruction beams are considered. We numerically calculate the intensity distribution of the reconstruction beam. In this way, the beam can be used to micro-manipulate different size particles.

2. THEORETICAL FORMULATION

The electric field amplitude of a zero-order Bessel beam which illuminates on focal lens is given by

$$E_1(r_1) = A_0 J_0(k_r \cdot r_1), \quad (1)$$

where J_0 is the zero-order Bessel function of the first kind, k_r is the radial wave vector, and r_1 is the radial coordinate.

Using the generalized Huygens-Fresnel diffraction integral [10], the reconstructing field $E_2(r_2, \psi_2)$ at the position (r_2, L) is characterized by

$$E_2(r_2, \psi_2) = \left(-\frac{i}{\lambda B} \right) \exp(ikL) \iint_s E_1(r_1, \psi_1) \exp \left\{ \frac{ik}{2B} [Ar_1^2 + Dr_2^2 - 2r_1 r_2 \cos(\psi_1 - \psi_2)] \right\} r_1 dr_1 d\psi_1. \quad (2)$$

The electric field of reconstruction beam satisfy rotational symmetry. If the radius of the beam illuminating on focusing lens is b , by taking the integration of r and ψ , we have

$$E_2(r_2) = \frac{i}{\lambda \cdot B} \exp(i \cdot k \cdot L) \int_0^b E_1(r_1) \cdot 2\pi J_0 \left(\frac{k \cdot r_1 \cdot r_2}{B} \right) \cdot \exp \left[\frac{i \cdot k}{2B} [A \cdot (r_1)^2 + D \cdot (r_2)^2] \right] r_1 dr_1, \quad (3)$$

where k is the wave number which is related to λ by $k = 2\pi/\lambda$. The transfer matrix elements A , B , C , D following

$$\begin{pmatrix} A & B \\ C & D \end{pmatrix} = \begin{pmatrix} 1 & z \\ 0 & 1 \end{pmatrix} \cdot \begin{pmatrix} 1 & l \\ 0 & 1 \end{pmatrix} \begin{pmatrix} 1 & 0 \\ -\frac{1}{f} & 1 \end{pmatrix} = \begin{pmatrix} 1 - \frac{z+l}{f} & z+l \\ -\frac{1}{f} & 1 \end{pmatrix}. \quad (4)$$

On substituting from Eqs. (1) and (4) into (3), we obtain

$$E(r, z) = \frac{-i \cdot k}{(z+l)} A_0 \exp(i \cdot k \cdot z) \exp \left(\frac{ik}{2(z+l)} r^2 \right) \cdot \int_0^b J_0(k_r \cdot r_1) \cdot J_0 \left(\frac{k \cdot r_1 \cdot r}{z+l} \right) \cdot \exp \left[\frac{i \cdot k \cdot (r_1)^2}{2(z+l)} - \frac{i \cdot k}{2f} \cdot (r_1)^2 \right] r_1 dr_1. \quad (5)$$

And the intensity distribution of the reconstruction beams reads

$$I(r, z) = \left(\frac{k \cdot A_0}{z+l} \right)^2 \cdot \left[\int_0^b J_0(k_r \cdot r_1) \cdot J_0 \left(\frac{k \cdot r_1 \cdot r}{z+l} \right) \cdot \exp \left[\frac{i \cdot k \cdot (r_1)^2}{2(z+l)} - \frac{i \cdot k}{2f} \cdot (r_1)^2 \right] r_1 dr_1 \right]^2. \quad (6)$$

For correcting the transverse spatial frequency of the reconstructed beam restored to the original, a second lens is introduced to straighten the overlapping curved wave-fronts. The position z where the rectifying lens placed must be chosen in $z = f + f'$, and the foci of rectifying lens and the focusing lens satisfy $f = f'$. The rectifying transfer matrix elements A, B, C, D following:

$$\begin{pmatrix} A & B \\ C & D \end{pmatrix} = \begin{pmatrix} 1 & z \\ 0 & 1 \end{pmatrix} \begin{pmatrix} 1 & 0 \\ \frac{-1}{f'} & 1 \end{pmatrix} \begin{pmatrix} 1 & f+f' \\ 0 & 1 \end{pmatrix} \begin{pmatrix} 1 & 0 \\ \frac{-1}{f} & 1 \end{pmatrix} = \begin{pmatrix} \frac{-f'}{f} & \frac{f \cdot f' + f^2 - f \cdot z}{f'} \\ \frac{f'}{f^2} - \frac{1}{f} & \frac{-f}{f'} \end{pmatrix}. \quad (7)$$

Let $f = f'$, we obtain

$$\begin{pmatrix} A & B \\ C & D \end{pmatrix} = \begin{pmatrix} -1 & 2f - z \\ 0 & -1 \end{pmatrix}. \quad (8)$$

Substituting from Eqs. (1) and (8) into (3), the electric field of the rectifying beam can be derived

$$E(r, z) = \frac{ik \cdot A_0}{2f - z} \exp(i \cdot k \cdot z) \cdot \exp\left(-\frac{i \cdot k}{4f - 2z} \cdot r^2\right) \int_0^b J_0(k_r \cdot r_1) \cdot J_0 \left(\frac{k \cdot r_1 \cdot r}{2f - z} \right) \cdot \exp \left[\frac{i \cdot k}{4f - 2z} r_1^2 \right] r_1 dr_1. \quad (9)$$

The intensity distribution reads

$$I(r, z) = E(r, z) \cdot E(r, z)^* = \left(\frac{k \cdot A_0}{2f - z} \right)^2 \cdot \left[\int_0^b J_0(k_r \cdot r_1) \cdot J_0 \left(\frac{k \cdot r_1 \cdot r}{2f - z} \right) \cdot \exp \left[\frac{i \cdot k \cdot (r_1)^2}{4f - 2z} \right] r_1 dr_1 \right]^2, \quad (10)$$

where the asterisk $*$ represents the complex conjugation.

3. NUMERICAL CALCULATION RESULTS AND ANALYSES

The 3D intensity distribution and the intensity cross sections in different propagation distances are simulated, shown in Fig. 1 and Fig. 2 respectively.

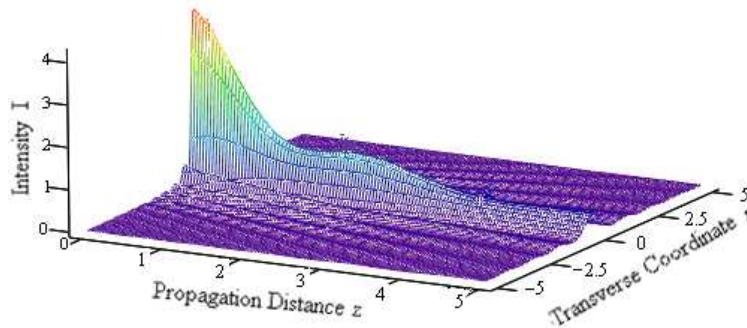


Figure 1: The 3D intensity distribution of reconstruction beam.

For the sake of convenience, the focal length f is normalized to $f = 3$. Fig. 1 shows that the intensity of the reconstruction beams attenuates quickly, the central spot size of the beams increasing with increasing propagation distance. The phenomenon can be seen easily in the Fig. 2. In Fig. 2, we note that the intense central spot size becomes larger. Comparing (a) with (c), the intensity of the beam reduces quickly. These results demonstrate the reconstruction beam is aberrational. It limits the application, so the reconstruction beam needs to be rectified.

Using the Eq. (10), the intensity distribution of rectifying beams is simulated, where the parameters $f = 3, f' = 3$. The results are compiled in Fig. 3 and Fig. 4.

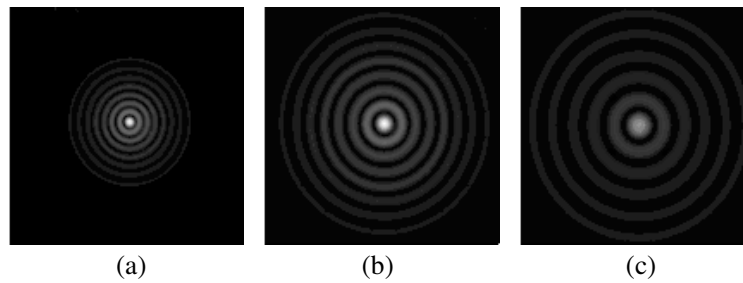


Figure 2: The reconstruction beam patterns at different points on z -axis. (a) $z = 1$; (b) $z = 3$; (c) $z = 5$.

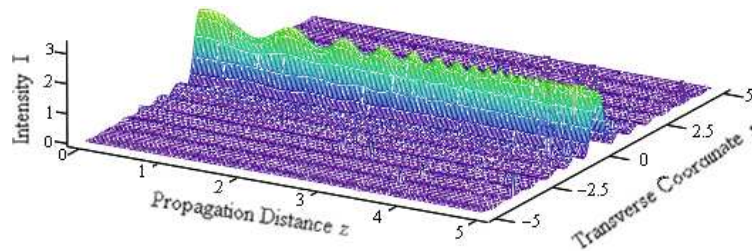


Figure 3: The 3D intensity distribution of rectified beam.

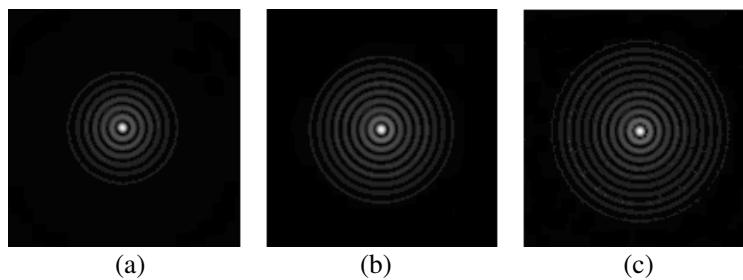


Figure 4: The rectified beam patterns at different points on z -axis behind the rectifying lens. (a) $z = 0$; (b) $z = 2$; (c) $z = 4$.

Figure 3 gives the 3D intensity distribution of rectified beam from which we can see that the intensity of the beam is almost invariable with increasing propagation distance. According to the Fig. 4, the intense central spot size, and the intensity of the rectified beam do not change any more with the propagation distance. Only the number of the bright rings increases. The rectified beam has the non-diffracting properties.

4. CONCLUSIONS

By using the generalized Huygens-Fresnel diffraction integral, the propagation properties of self-reconstruction beam are studied. It is shown that the non-diffracting beams can reconstruct its intensity profile after focusing. But the reconstruction beam occurs aberration upon propagation. A second lens is introduced to rectify the beam aberration and to get the original non-diffracting beam. Furthermore, we can generate different parameter non-diffracting beams by altering the propagation ratio of the foci of rectifying lens and focusing lens. The results obtained in this paper would be useful for application in micro-manipulation.

ACKNOWLEDGMENT

This research is supported by the National Natural Science Foundation of China (Grant No. 61178015) and the Natural Science Foundation Project of Fujian Province (Grant No. 2012J01278). We would like to thank Prof. Ke Wang for valuable discussion.

REFERENCES

1. Bouchal, Z., J. Wagner, and M. Chlup, "Self-reconstruction of a distorted nondiffracting beam," *Optics Communications*, Vol. 151, No. 4, 207–211, 1998.

2. Garcés-Chávez, V., D. McGloin, H. Melville, W. Sibbett, and K. Dholakia, “Simultaneous micromanipulation in multiple planes using a self-reconstructing light beam,” *Nature*, Vol. 419, No. 6903, 145–147, 2002.
3. Gadonas, R., V. Jarutis, R. Paškauskas, V. Smilgevičius, A. Stabinis, and V. Vaičaitis, “Self-action of Bessel beam in nonlinear medium,” *Optics Communications*, Vol. 196, No. 1, 309–316, 2001.
4. Butkus, R., R. Gadonas, J. Janušonis, A. Piskarskas, K. Regelskis, V. Smilgevičius, and A. Stabinis, “Nonlinear self-reconstruction of truncated Bessel beam,” *Optics Communications*, Vol. 206, No. 1, 201–209, 2002.
5. Vyas, S., Y. Kozawa, and S. Sato, “Self-healing of tightly focused scalar and vector Bessel-Gauss beams at the focal plane,” *JOSA A*, Vol. 28, No. 5, 837–843, 2011.
6. Zhu, X., A. Schülzgen, H. Wei, K. Kieu, and N. Peyghambarian, “White light Bessel-like beams generated by miniature all-fiber device,” *Optics Express*, Vol. 19, No. 12, 11365–11374, 2011.
7. Ersoy, T., B. Yalızay, and S. Akturk, “Self-reconstruction of diffraction-free and accelerating laser beams in scattering media,” *Journal of Quantitative Spectroscopy and Radiative Transfer*, Vol. 113, No. 18, 2470–2475, 2012.
8. Fahrbach, F. O., V. Gurchenkov, K. Alessandri, P. Nassoy, and A. Rohrbach, “Self-reconstructing sectioned Bessel beams offer submicron optical sectioning for large fields of view in light-sheet microscopy,” *Optics Express*, Vol. 21, No. 9, 11425–11440, 2013.
9. He, M., Z. Chen, S. Sun, and J. Pu, “Propagation properties and self-reconstruction of azimuthally polarized non-diffracting beams,” *Optics Communications*, Vol. 294, 36–42, 2013.
10. Lü, B., *Propagation and Control of High-power Lasers*, 23–24, National Defense Industrial Press, Beijing, 1999.

An Improved Method of Diagnosis of Failed Elements in Arrays Using Genetic Algorithm

Jing Miao, Bo Chen, and Wuqiong Luo

University of Electronic Science and Technology of China, China

Abstract— A cost function was used to compare the calculation pattern (associated to the chromosome encoded by GA) with the degraded pattern at the samples measured from the far field radiation pattern. Genetic algorithm was used to minimize the cost function to locate the failed elements. However, it was found that when using GA to diagnose the failed elements in an array, this method could not accurately distinguish symmetrical positions if the excitation of the arrays were symmetrical. In order to solve this ambiguity problem, an asymmetry factor was introduced in the mentioned diagnosis method to the excitation distribution (amplitude or phase) of the arrays artificially. This improved method was exploited to a linear array to validate the method. From the comparison between the symmetrical and asymmetrical excitation distributions of the arrays, it was showed that the improved method was applicable. And weight coefficients were introduced in the cost function in order to get better results.

1. INTRODUCTION

Diagnosis of the failed elements of an array was a problem of practical interest, especially in the large-scale antenna arrays [1]. Array antennas were working in the applications such as trace tracking, position locating, and communications and so on. The antenna, in such cases, had a lot of radiating elements, and the failure possibility of the elements increased due to the large number of radiators. These failed elements made the sidelobe level increased and caused unacceptable pattern distortion. With the failed elements been found in the array, the radiation pattern can be restored by changing their feeding distribution [2–5].

Artificial neural network (ANN) technique has been used for finding out the position of the fault element(s) in the array in [6], a neural network (MLP) is used to locate a maximum of three failed elements in a 16-element array, in [7], Also using the MLP ANN locate a maximum of two failed elements in a 6×6 microstrip patch antenna array. Nan Xu using the SVM (support vector machine) classifier for failure detection in a 4-element array [8]. A solution to locating the position of the fault element(s) in the array reported in [9] using genetic algorithms (GA). In that, using a cost function, the method compares the measured radiation pattern with that corresponding to the array with a given configuration of failed/un-failed elements. However, this method could not accurately distinguish symmetrical positions if the excitation of the array was symmetrical.

In order to solve this ambiguity problem, an asymmetry factor was introduced in the mentioned diagnosis method to the excitation distribution (amplitude or phase) of the arrays artificially. And weight coefficients were introduced in the cost function in order to get better results.

2. IMPROVED DIAGNOSIS METHOD

When there are failed elements in the antenna array, it would lead to changes in the far field pattern, particularly the side lobe level. And different numbers and the locations of the failed elements in the array will make different pattern distortion.

In this paper, each of the elements was assumed to have one of the two states, that were, states “On” and “Off”. In state “On”, the element worked properly, and in state “Off”, the element does not work at all [10]. As a theoretical study, the simulation result from HFSS was considered as the result obtained from the experiment.

Let us consider a linear array of N identical elements. The far field electrical field can be calculated with the following expression

$$E(\theta, \varphi) = f(\theta, \varphi) \cdot \sum_{n=1}^N I_n \cdot \exp(jnkd\mu) \quad (1)$$

where $f(\theta, \varphi)$ is the element pattern, I_n is the vector of the excitation of the N elements. $\mu = \sin \theta \cdot \cos \varphi$, The far field directivity of the array expressed in dB was:

$$F(\theta, \varphi) = 20 \cdot \log_{10} |E(\theta, \varphi)| \quad (2)$$

Encoding the configuration of I_n , we define the following cost function:

$$\xi = \sum_{i=1}^M \omega_k \cdot [\overline{F_{chr}}(\theta_i, \varphi_i) - \overline{F_M}(\theta_i, \varphi_i)] \quad (3)$$

M is the number of samples we selected. $F_M(\theta_i, \varphi_i)$ is measurement of the degraded pattern in M directions (θ_i, φ_i) , $F_{chr}(\theta_i, \varphi_i)$ is the amplitude pattern Calculated by (1) and (2) associated to the chromosome in the same direction. Where $\overline{F_{chr}}(\theta_i, \varphi_i)$ and $\overline{F_M}(\theta_i, \varphi_i)$ are the normalized pattern date of $F_{chr}(\theta_i, \varphi_i)$ and $F_M(\theta_i, \varphi_i)$. ω_k was the weight coefficient, we can get better results by change the weights. With the weight coefficient introduced can avoid a parameter change range too large overwhelmed the contributions of other parameters of the cost function. Genetic algorithm was used to minimize the cost function that compared the calculation pattern (associated to the chromosome encoded by GA) with the degraded pattern at the samples.

However, it was found that when using GA to diagnose the failed elements in an array, this method could not accurately distinguish symmetrical positions if the excitation of the array was symmetrical. Because the pattern calculated $F_{chr}(\theta_i, \varphi_i)$ associated to the chromosome is the same if the failed elements were at symmetrical positions when the excitation of the array was symmetrical.

In order to solve this ambiguity problem, an asymmetry factor was introduced in the mentioned diagnosis method to the excitation distribution (amplitude or phase) of the arrays artificially. This improved method was exploited to a linear array and validate the method. From the comparison between the symmetrical and asymmetrical excitation distributions of the above two arrays, it was

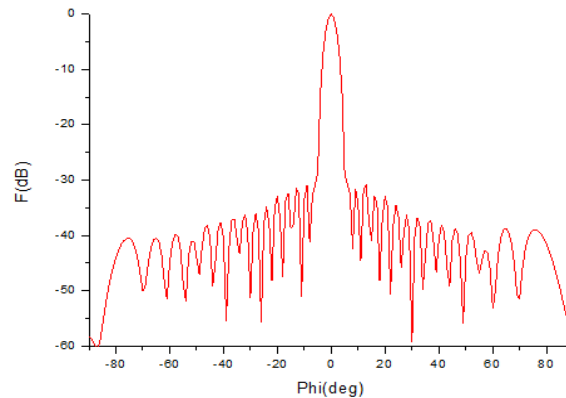


Figure 1: Linear Taylor pattern radiated by the 32 elements array of $\lambda/2$ -dipoles with no failures.

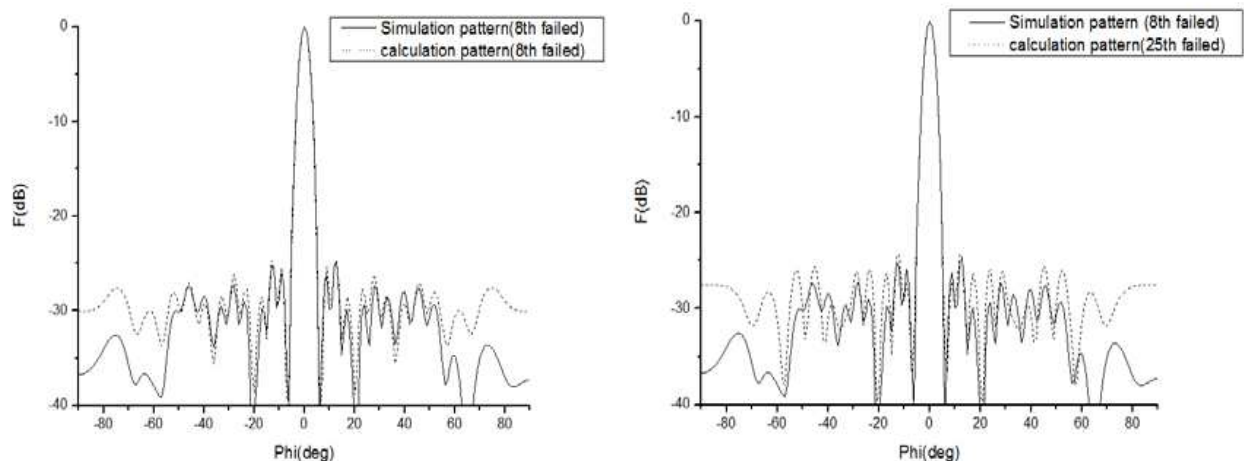


Figure 2: Simulation pattern and calculation pattern (8th was failed/25th was failed) when excitation amplitude was changed.

showed that the improved method was applicable.

3. ANALYSIS AND APPLICATION

We study a linear array composed of 32 center-fed cylindrical $\lambda/2$ -dipoles. The pattern, which is shown in Figure 1, has been emulated by a linear Taylor distribution with $SLL = -30$ dB and $d = \lambda/2$ using HFSS.

An asymmetry factor was introduced to the arrays by change excitation distribution (amplitude or phase) of a element artificially. For the selected array elements which need to be changed, change the element excitation closed to the center of the array will get further damage to the degraded pattern; however the effect was too small if change the element excitation in the edge of the array which was easily be overwhelmed by measurement error. So in this article, we select the 5th element as the one which need to be changed. And the method was verified by change the excitation amplitude and phase of the 5th element respectively.

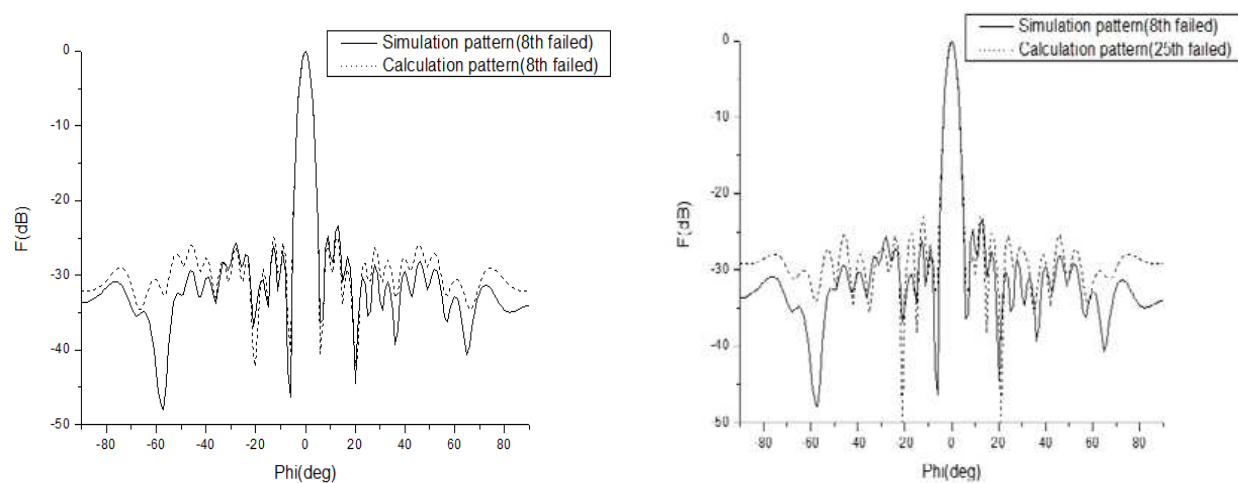


Figure 3: Simulation pattern and calculation pattern (8th was failed/25th was failed) when excitation phase was changed.

Table 1: Performance of genetic algorithm diagnosis of array failed elements when changed the excitation amplitude and phase of the 5th element respectively. Δ was the random measurement error.

25 pattern samples $\Delta = \pm 0.75$ dB				
Failed elements positions	Success rate (change the amplitude/change the phase) ω_k was introduced		Success rate (change the amplitude/change the phase) without ω_k	
	change the amplitude	change the phase	change the amplitude	change the phase
5	10/10	10/10	10/10	9/10
8	10/10	10/10	10/10	10/10
15	10/10	10/10	10/10	10/10
28	10/10	10/10	10/10	10/10
3, 10	10/10	10/10	9/10	8/10
5, 25	10/10	10/10	9/10	7/10
9, 31	10/10	10/10	8/10	8/10
4, 18	10/10	10/10	9/10	8/10
6, 10, 16	9/10	9/10	7/10	6/10
3, 8, 20	9/10	8/10	7/10	5/10
7, 9, 18	10/10	9/10	7/10	5/10
1, 5, 32	8/10	7/10	4/10	3/10
Total	116/120	113/120	101/120	93/120

1. Reduced 3 dB the amplitude of the excitation of the 5th element.
2. Reduced 22.5° the phase of the excitation of the 5th element.

The 8th elements were set failed in the HFSS models. Figure 2 showed the different between the simulation pattern and calculation pattern (8th was failed/25th was failed which was the symmetrical element of 8th element) when reduced 3 dB the amplitude of the excitation of the 5th element. And Figure 3 showed the different between the simulation pattern and calculation pattern (8th was failed/25th was failed which was the symmetrical element of 8th element) when reduced 22.5° the phase of the excitation of the 5th element.

From Figure 2 and Figure 3, by changing either the excitation amplitude or phase of 5th element will break the symmetry and solve the ambiguity problem when using Genetic Algorithm to diagnosis of failed elements in arrays.

In our study 4 random excitation distribution configurations were selected for each of the 3 conditions, they were, one element failed, two failed, and three failed. Each of the configurations was calculated ten times using GA. In our study, the test patterns were sampled in the region $\phi \in [-45, 45]$ and avoid the angle where the pattern amplitude is too small or difficult to measure. We raised the weight of samples at the main beam and side lobe, and decreased the weight of the samples with the increasing of the angle away from the main beam.

From Table 1, the performance of genetic algorithm diagnosis of array failed elements by changed the excitation amplitude and phase of the 5th element respectively were showed above. Diagnosis of failed elements in symmetrical array can be achieved. And by introducing weight coefficients into the cost function can get better results (even take random measurement error account).

4. CONCLUSION AND FUTURE WORK

An improved method of diagnosis of failed elements in symmetrical arrays using genetic algorithm through introducing asymmetry factor to the symmetric excitation arrays by change a certain element's excitation amplitude or phase. Failed elements can be found in symmetrical arrays. And weight coefficients were introduced in the cost function in order to get better results. Finally through a number of numerical examples shows the effectiveness of the method by simulation and calculation. The proposed method can be directly applicable to planar arrays. In the future the mutual coupling between radiating elements should be taken into account.

REFERENCES

1. Lord, J. A., G. G. Cook, and A. P. Anderson, "Reconstruction of the excitation of an array antenna from measured near-field intensity using phase retrieval," *Proc. Inst. Elect. Eng.*, Vol. 139, 392–396, 1992.
2. Peters, T. J., "A conjugate gradient-based algorithm to minimize the sidelobe level of planar arrays with element failures," *IEEE Trans. Antennas Propagat.*, Vol. 39, No. 10, 1497–1504, 1991.
3. Rodríguez, J. A. and F. Ares, "Optimization of the performance of arrays with failed elements using the simulated annealing technique," *Journal of Electromagnetic Waves and Applications*, Vol. 12, 1625–1637, 1998.
4. Yeo, B. and Y. Lu, "Array failure correction with a genetic algorithm," *IEEE Trans. Antennas Propagat.*, Vol. 47, 823–828, 1999.
5. Oliveri, G., M. Donelli, and A. Massa, "Linear array thinning exploiting almost difference sets," *IEEE Trans. Antennas Propag.*, Vol. 57, No. 12, 3800–3812, Dec. 2009.
6. Patnaik, A., B. Choudhury, P. Pradhan, R. K. Mishra, and C. Christodoulou, "An ANN application for fault finding in antenna arrays," *IEEE Trans. Antennas Propag.*, Vol. 55, No. 3, 775–777, 2007.
7. Mallahzadeh, A. R. and M. Taherzadeh, "Element failure diagnosis in a planar microstrip antenna array by the use of neural networks," *IEEE Trans. AEM2C*, 294–298, 2010.
8. Xu, N., C. G. Christodoulou, S. E. Barbin, and M. Martínez-Ramón, "Detecting failure of antenna array elements using machine learning optimization," *IEEE International Symposium on Antennas and Propagation*, 5753–5756, Jun. 2007.
9. Rodríguez, J. A., F. Ares, H. Palacios, and J. Vassal'lo, "Finding defective elements in planar arrays using genetic algorithms," *Progress In Electromagnetics Research*, Vol. 29, 25–37, 2000.
10. Bucci, O. M., A. Capozzoli, and G. D'Elia, "Diagnosis of array faults from far-field amplitude-only data," *IEEE Trans. Antennas Propag.*, Vol. 48, No. 5, 647–652, 2000.

Design of a C-band Coaxial Cavity Band Pass Filter

Xingxing Du, Pu Tang, and Bo Chen

University of Electronic Science and Technology of China, China

Abstract— In this paper, a coaxial cavity band pass filter was presented with the volume of $28\text{ mm} \times 15\text{ mm} \times 13\text{ mm}$ working at 4.88 GHz and the 3 dB bandwidth of 654.52 MHz. The classical comb lines structure in the coaxial cavity filter was un-applicable for small size. The dressing-line structure was introduced in the coaxial cavity. By adding the capacitance circular plate on the cavity resonant column, the resonant frequency was increased with the volume of the cavity reduced greatly, and requirement of small-size was satisfied. The designed filter was fabricated and measurement was conducted. From measurement, the insertion loss at the center frequency is less than 0.7 dB. The band rejection is greater than 49 dB at 1–2 GHz, and greater than 39 dB at 8 GHz–18 GHz. These showed that the designed filter met the requirements.

1. INTRODUCTION

With the rapid development of science and technology, waveguide filters, coaxial filter, strip-line filter and micro-strip filter and so on are widely used in recent years. However, when filters are asked to withstand high power capacity, low insertion loss, high rejection, narrow bandwidth, cavity filters are the best choice.

However, the biggest disadvantage of the cavity filter is that its size is much larger than the other filters available in microwave application. In order to adapt to the development needs of electronic system miniaturization and portability, to develop new kind and miniaturization of waveguide filters is a widespread concern subject in the industry. Coaxial cavity filter has a wide operating frequency range, high- Q value, good electromagnetic shielding, low loss, large power capacity and other characteristics, taking these factors and design requirements into consideration, this paper uses a coaxial cavity filter. Since the value of $\lambda/4$ at center frequency is approximately $L = \lambda/4 = c/(4\sqrt{\epsilon_r}) \approx 15.344\text{ mm}$, that is, the height of the required resonant rod is about 15.344 mm, this value can not meet the design requirements. Therefore, this designed filter uses loaded coaxial resonator cavity. Through using a form of stepped impedance to change the resonant rod structure, the designed filter further reduced the volume of the filter.

This paper is organized as follows: Section 2 presents the proposed resonator structure and describes the design principles of this structure. Section 3 presents the design of the filter. Section 4 presents and analyzes the obtained results of the proposed filter.

2. RESONATOR STRUCTURE

Coaxial resonator cavity [1] are generally divided into three types: $\lambda/2$ type, $\lambda/4$ type, capacitor-loading type. From the literature [1], by calculation and simulation, this paper derived the traditional capacitance-loaded coaxial resonator cavity does not meet the design requirements, therefore, based on the theory of predecessors, via adding stepped impedance to change the structure of the resonator rod, the single cavity model was successfully established. The structure diagram and equivalent circuit is shown in the following Figures 1(a) and 1(b) is equivalent to l_c segment, capacitance C_d is equivalent to discontinuity capacitance at the interface section l_c and section l_b , characteristic impedance Z_b of transmission line is equivalent to l_b segment, capacitance C_0 is equivalent to a discontinuity capacitance at the gap segment.

Resonance condition of the resonance circuit [2] is:

$$Y_L + Y_R + j\omega C_d = 0 \quad (1)$$

Here

$$Y_L = \frac{1}{Z_L} = \frac{-j}{\omega Z_c \tan \beta l_c} \quad (2)$$

$$Y_R = \frac{1}{Z_R} = \frac{-j}{Z_b} \cdot \frac{Z_b + \tan \beta l_b / \omega C_0}{Z_b \tan \beta l_b - 1 / \omega C_0} \quad (3)$$

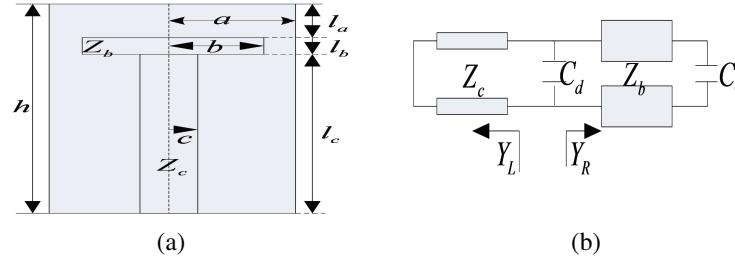


Figure 1: (a) The structure of resonator. (b) The equivalent circuit.

From [4], the impedance calculation formula of the rectangular cavity's resonance bar is

$$Z = \frac{60}{\sqrt{\varepsilon_r}} \ln \frac{1.0787R}{r} \quad (4)$$

In (4), r , R respectively represent the radius of the inner and outer conductors. From [2], the gap capacitance is calculated as

$$C_0 = \varepsilon_0 \frac{\pi b^2}{l_a} + 4\varepsilon_0 b \ln \frac{a-b}{l_a} \quad (5)$$

From [3], the discontinuity capacitor at the interface section l_c and section l_b is calculated as

$$C_d = 2\pi a C'_d \quad (6)$$

$$C'_d = \frac{\varepsilon_0}{100\pi} \left(\frac{\alpha^2 + 1}{\alpha} \ln \left(\frac{1 + \alpha}{1 - \alpha} \right) - 2 \ln \left(\frac{4\alpha}{1 - \alpha^2} \right) \right) + 1.11 (1 - \alpha) (\tau - 1) \times 10^{-15} \text{ (F/cm)} \quad (7)$$

In (7), $\alpha = \frac{a-b}{a-c}$, $\tau = \frac{a}{c}$.

Taking these principles and the volume requirements of this design into consideration, the design uses Chebyshev response. From [3], this paper calculated the cavity number is three.

The resonator cavity uses rectangular cavity, its length and width are 3 mm, the height is 8 mm.

According to the coaxial cavity theory, when the value of resonator impedance is 76Ω , the Q value of the resonator is the highest. In the engineering, generally we take $70\text{--}80 \Omega$. Taking into account the processing problems, this design takes 70Ω . Based on formula (4), the radius c is calculated as following:

$$c = \frac{1.0787b}{e^{\frac{70\sqrt{\varepsilon_r}}{60}}} \approx 1 \text{ mm} \quad (8)$$

To integrate cavity filter design requirements and simulation, we pre-set the initial of the parameters as following: $6 \text{ mm} \leq l_c \leq 7 \text{ mm}$, $0.3 \leq l_b \leq 0.8$, $2 \text{ mm} < b < 2.8 \text{ mm}$, by solving the transcendental Equation (1), the value of the parameters above were determined: $l_c = 7 \text{ mm}$, $l_b = 0.5 \text{ mm}$, $b = 2.56 \text{ mm}$, then substituted into the HFSS simulation and optimization, we get the optimal resolve.

3. DESIGN

3.1. Proposed Structure Model Establishment

Selected eigenmode solver in HFSS 15, through adjusting the height of the resonator rod in order to make the cavity resonate at the center frequency 4887.9 MHz, ultimately we obtained the optimizing value: $l_c = 6.91 \text{ mm}$, $l_b = 0.5 \text{ mm}$, $b = 2.53 \text{ mm}$, as is shown Fig. 2.

3.2. Coupling Coefficient Extraction

The coupling coefficient between two cavities is

$$k_{12} = k_{23} = \frac{BW}{\sqrt{g_1 g_2}} = \frac{BW}{\sqrt{g_2 g_3}} = 0.1 \quad (9)$$

Due to the volume of the filter is much smaller while the coupling coefficient is much bigger, therefore, we use this coupling structure which is in the form of coupling window plus a connecting rod, as is shown in Fig. 3. The change curve of the coupling coefficient versus the height of resonator rod plus line is shown in Fig. 4.

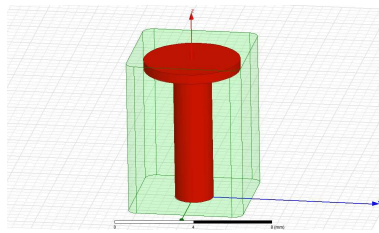


Figure 2: Proposed structure model.

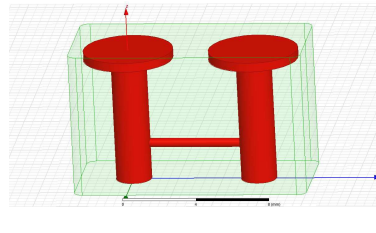


Figure 3: Coupling coefficient extraction between two cavities.

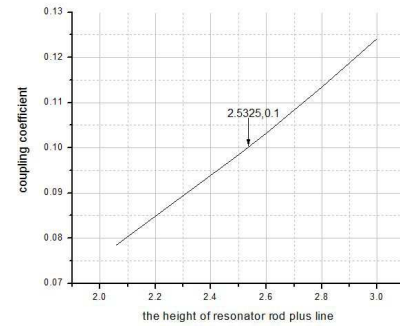


Figure 4: The coupling coefficient versus the height of resonance rod plus line.

4. RESULTS

The results S_{21} are shown in Fig. 5. and Fig. 6. As can be seen from the figure, the filter center frequency is 4887.9 MHz, 3 dB bandwidth is 688.8 MHz, band insertion loss is $L_0 = -0.5165$ dB, the band rejection is less than -50.2 dB at 1–2 GHz, and less than -44 dB at 8 GHz–18 GHz, the results show that it meet the design requirements, simultaneously verify the validity of the theory.

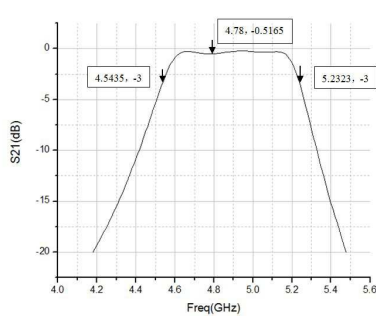


Figure 5: 4.18 GHz–5.48 GHz S_{21} image.

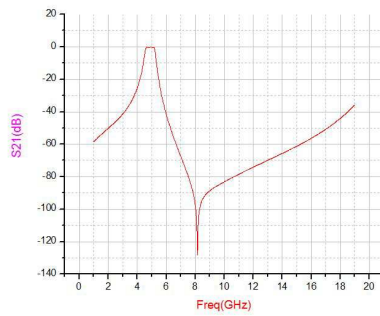


Figure 6: 1 GHz–19 GHz S_{21} image.



Figure 7: The physical cavity filter picture.



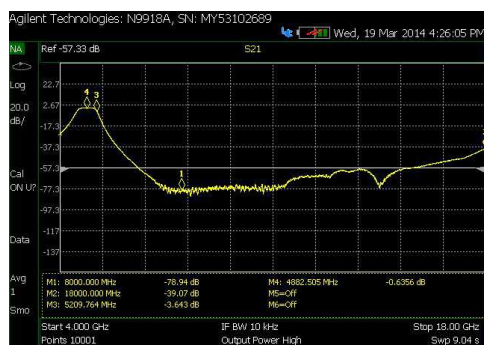
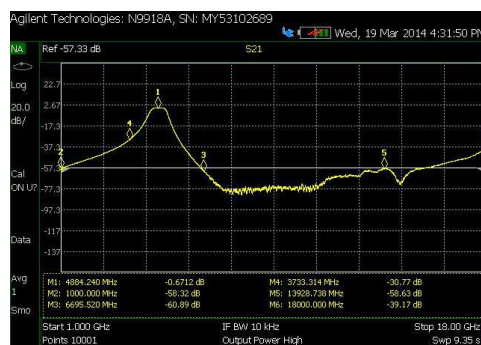
Figure 8: At 3.3 GHz–6.3 GHz S_{21} image.



Figure 9: 900 MHz–6.3 GHz S_{21} image.

Via processing and debugging, the physical is shown in Fig. 7. Using vector analyzer to measure the physical filter, the measured results S_{21} curve are shown in the following Fig. 8, Fig. 9, Fig. 10 and Fig. 11.

As is shown in figures above, the center frequency of the physical filter is 4882.505 MHz, the frequency deviation is $\Delta f = 5.4$ MHz, the bandwidth is 654.517 MHz, the insertion loss at the center frequency is less than 0.7 dB, the band rejection is greater than 49 dB at 1–2 GHz, and greater than

Figure 10: 4 GHz–18 GHz S_{21} image.Figure 11: 1 GHz–18 GHz S_{21} image.

39 dB at 8 GHz–18 GHz, the frequency deviation in the range of allowable error, these results meet the design requirements.

5. CONCLUSION

The design of a highly miniaturized cavity band pass filter is presented. By adding the capacitance circular plate on the cavity resonant column, significant size reduction of resonators was obtained. Using these miniature resonators in a compact designed cavity filter, good performance as well as considerable size reduction were achieved. Compared with the $\lambda/4$ coaxial cavity filter, the volume of this designed filter reduced 51.37%. Experimental results and simulation results are biased due to the following reasons: (1). In the filter assembly, the assembly of the resonator rod can not achieve the ideal simulation conditions, there will be a certain degree of bending and the height will be also some deviation; (2). The surface finish of the capacitance circular plate as well as the cavity outer wall on the cavity resonant column can not achieve the ideal simulation case in the manufacturing process, resulting in some projections or depressions. Overall, the experimental results agree with the simulation results.

REFERENCES

1. Zhao, K. and F. Xu, *Microwave Theory and Technology*, Higher Education Press, Beijing, 2006.
2. Liang, C., Y. Xie, and Z. Lei, "The calculation of a kind of loaded coaxial resonant frequency," *Xidian University Journal*, Vol. 20, No. 2, 56–65, 1993.
3. Gan, B. and W. Wu, *The Architecture and Design of Modern Microwave Filters*, Science Press, Beijing, 1973.
4. Xu, F., *Research and Application of LC and Coaxial Cavity Filter*, 41–45, University of Science and Technology of China, Chengdu, 2013.

Three-component Decomposition for Polarimetric SAR Images Based on Coherency Matrix

Yongjun Cai^{1,2}, Xiangkun Zhang², and Jingshan Jiang²

¹University of Chinese Academy of Sciences, China

²CAS Key Laboratory of Microwave Remote Sensing, National Space Science Center, CAS, China

Abstract— Original Freeman three-component decomposition was found useful in information extraction from a mix of area: city blocks, forest, ocean and land surfaces, etc.. However, it always suffers from some inconsistencies with real situation such as negative power and scattering mechanism ambiguity. It is probably because of the overestimate of volume scattering power. But intrinsically it is the inconsistency between the assumed models and the PolSAR. The deorientation method was initially found useful to alleviate this problem to some degree. However, because of the boundedness of deorientation, it is sometimes noneffective. Nonnegative eigenvalue decomposition (NNED) can absolutely solve the negative power problem. But the residual matrix except the volume scattering model is assumed equal to two. So in some sense it is under the volume scattering dominance assumption. Therefore, the decomposition should be separated into two individual parts. In this paper, for the pixels that volume scattering dominates, the NNED will be used. For the pixels that volume scattering doesn't dominate, we will start with the assumed models, and focus on developing a generalized model-based decomposition. Because for model-based scheme, we insist that one should radically start from the models and then a generalized three-component model-based decomposition is proposed, which consist of the surface, double bounce and volume scattering. Among it the generalized scattering mechanism proposed by Cloude is adopted, which provides a more accurate model for surface and dihedral scattering, and the dominant scattering component will be figured out according to the alpha angle parameter to be solved in the generalized model. Through this solution, the dominant scattering mechanism in one pixel will be preserved better. The performance of this approach is demonstrated and evaluated using the airborne AIRSAR and E-SAR data sets. The results show the advantages and improvements especially for alleviating the scattering mechanism ambiguity of oriented buildings from vegetation.

1. INTRODUCTION

Polarimetric target decomposition is found a reasonable and powerful way to analyze and interpret polarimetric SAR images, by decomposing polarimetric SAR data into several individual components representing different scattering mechanisms. There are two kinds of decompositions lying in the polarimetric decomposition theory, namely coherent and incoherent decomposition, which respectively deals with the Sinclair scattering matrix (single-look PolSAR data) and the coherency or covariance matrix (multilook PolSAR data). For many purposes and applications, a statistical averaging process for coherency matrix to reduce speckle or to compress data volume is necessary, which makes it impossible to decompose the Sinclair matrix. Therefore, the more widely used and studied decomposition technique now is the incoherent decomposition.

In Freeman decomposition, the volume model was always subtracted prior to other scattering mechanisms owing to the assumption that the HV component was only contributed by volume scattering. The nonnegative eigenvalue constraint was proved effective to limit the volume scattering power significantly. But it should be noted that the nonnegative eigenvalue method was intrinsically a coercive measure to avoid negative power, which takes the biggest one from all the values that ensure the residual matrix is still positive semi-definite, in other words, the rank of the residual coherency matrix is set equal to two. In some sense, it is based on the assumption that the volume scattering is always dominant, with the result that the surface or dihedral scattering component is partly replaced by volume scattering component, which is obviously not reasonable for all pixels. Consequently, the NNED will be employed to the pixels that volume scattering dominates. For the pixels that volume scattering doesn't dominate, we cannot use NNED anymore. Instead, we should undertake from the models themselves. Because for model-based techniques, models should be more fit with PolSAR data.

2. DEFICIENCIES DESCRIPTION AND ANALYSIS IN MODEL-BASED APPROACHES

Figure 1 shows the result of Freeman decomposition and its corresponding optical image. In Patch A are some urban buildings parallel to the radar line of sight, from which we can see that the buildings have been decomposed into red color displaying in RGB image. However, in Patch B are some buildings not parallel to radar line of sight, we can see the results display completely green color in RGB image, and that is to say, the true buildings are misinterpreted as vegetation.



Figure 1: The image on the left is from the Google Earth. The image on the right is the result of Freeman decomposition.

Yamaguchi added a helix scattering component to the original three component decomposition. Notably, the volume scattering model is also revised to better fit the real situation. By these steps, the power assigned to volume scattering is decreased, and the negative power problem and the scattering mechanism ambiguity are both spontaneously alleviated to some degree. However, because of its simplified selection criteria of volume scattering model involving the ratio of HH to VV power, the case of a dominant dihedral scattering with a small contribution from a uniformly oriented canopy may be regarded as the case that volume scattering dominates around the horizontal or vertical orientation. So we think that the selection criteria can only be applied to the pixels that volume scattering dominates. Because only under the condition that volume scattering is dominant can we utilize the total elements in coherency matrix to select a best fit volume scattering model. So in this paper, for the pixels that volume scattering dominates, the model proposed by Yamaguchi will be used for volume scattering, while for the pixels that surface or dihedral scattering dominates, the original model proposed by Freeman will be maintained.

Afterwards, the orientation angle compensation is also incorporated into model-based method, which is to minimize the last element, i.e., the cross-polarization HV component in coherency matrix. On one hand, the purpose is to decrease the value assigned to volume scattering, on other hand is to rotate the buildings or surfaces in the pixel to the direction orthogonal to the radar line of sight, i.e., the reflection symmetry condition. However, in some pixels the oriented buildings are still misinterpreted as vegetation, i.e., this idea will not work under some situations. Next we will talk about some causes.

First, let us start from the definition of deorientation,

$$R_{\theta} = \begin{pmatrix} 1 & 0 & 0 \\ 0 & \cos 2\theta & \sin 2\theta \\ 0 & -\sin 2\theta & \cos 2\theta \end{pmatrix}, \quad [T(\theta)] = R_{\theta}[T]R_{\theta}^{-1} \quad (1)$$

where θ can be solved from the following equation,

$$T'_{33}(\theta) = 0 \Rightarrow 2\theta = \frac{1}{2} \tan^{-1} \left(\frac{2\text{Re}(T_{23})}{T_{22} - T_{33}} \right) \quad (2)$$

it is clear that the deorientation angle 2θ ranges from $-\pi/4$ to $\pi/4$, but the orientation angle of the actual object usually ranges from $-\pi/2$ to $\pi/2$, so if the actual orientation angle is out of the deorientation angle, the deorientation is noneffective.

Secondly, the deorientation is a measure to fit the PolSAR data into the assumed surface and dihedral models by rotating the coherency matrix, however, if in one pixel there have buildings

or surfaces with different orientation angles, even though the deorientation is implemented, one cannot think that the buildings are readjusted to the direction orthogonal to radar line of sight as the models predict, under this condition the deorientation will also be noneffective.

3. PROPOSED DECOMPOSITION

3.1. Generalized Scattering Mechanism

The generalized scattering mechanism takes the normalized form of its corresponding Pauli-vector,

$$\underline{u} = \left[\cos \delta \quad \sin \delta \cos \omega e^{j\phi} \quad \sin \delta \sin \omega e^{j\varphi} \right]^T \quad (3)$$

The coherency matrix of generalized scattering mechanism can be described as follows,

$$[T_g] = \begin{pmatrix} \cos^2 \delta & \cos \delta \sin \delta \cos \omega e^{-j\phi} & \cos \delta \sin \delta \sin \omega e^{-j\varphi} \\ \cos \delta \sin \delta \cos \omega e^{j\phi} & \sin^2 \delta \cos^2 \omega & \sin^2 \delta \cos \omega \sin \omega e^{j(\phi-\varphi)} \\ \cos \delta \sin \delta \sin \omega e^{j\varphi} & \sin^2 \delta \cos \omega \sin \omega e^{j(\varphi-\phi)} & \sin^2 \delta \sin^2 \omega \end{pmatrix} \quad (4)$$

where δ , ω , ϕ , φ are unknown real angles, together with the power coefficient, there have a total of 5 free variables. It is clearly shown that generalized scattering mechanism takes the possible HV cross-polarization component contributed by surface or dihedral scattering into consideration.

3.2. Decomposition Framework

As mentioned above, for the pixels that volume scattering dominates, the general NNED will be used, while for the pixels that volume scattering is not dominant, we use the decomposition framework as follows,

$$\langle [T] \rangle = fT_g + f_s \begin{bmatrix} 1 & 0 & 0 \\ 0 & 0 & 0 \\ 0 & 0 & 0 \end{bmatrix} + f_d \begin{bmatrix} 0 & 0 & 0 \\ 0 & 1 & 0 \\ 0 & 0 & 0 \end{bmatrix} + f_v \begin{bmatrix} 0.5 & 0 & 0 \\ 0 & 0.25 & 0 \\ 0 & 0 & 0.25 \end{bmatrix} \quad (5)$$

in which we adopt the model proposed by Freeman for the volume scattering. Because we insist that the volume scattering is strongly depolarized and has the biggish entropy. It should be noted that this decomposition also takes the situation that there have buildings or surfaces with two different orientation angles into consideration.

Once the coefficients are solved, the alpha angle will be used to identify the dominant scattering mechanism in one pixel, when applied to the proposed decomposition, it is equivalent to the following expression,

$$k = \frac{T(1,1)}{T(2,2) + T(3,3)} = \frac{\cos^2 \delta}{\sin^2 \delta} \quad (6)$$

So, if $k \leq 1$, $P_s = f + f_s$, $P_d = f_d$, $P_v = f_v$, if $k \geq 1$, $P_d = f + f_d$, $P_s = f_s$, $P_v = f_v$.

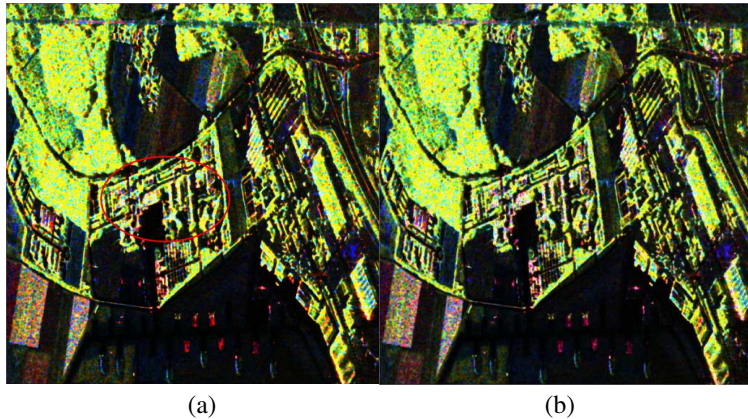


Figure 2: (a) General NNED. (b) The proposed.

4. EXPERIMENTS AND RESULTS

The E-SAR Oberpfaffenhofen polarimetric data are used to test the performance of this approach. The result of the proposed decomposition is shown in Figure 2. The general NNED are also carried out for comparison study.

Figure 2(a) shows the result of general NNED, Figure 2(b) shows the result of the proposed method. Let us see the area in the elliptic region, in which are some buildings in urban areas, from which we can clearly see that more pixels have been decomposed into dihedral scattering objects displaying in red color. This indicates that the true scattering mechanism has been preserved better by the proposed method such as surface dihedral scattering from the oriented buildings and the result is more consistent with the actual situation.

REFERENCES

1. Cloude, S. R. and E. Pottier, "A review of target decomposition theorems in radar polarimetry," *IEEE Trans. Geosci. Remote Sens.*, Vol. 34, No. 2, 498–518, 1996.
2. Freeman, A. and S. L. Durden, "A three-component scattering model for polarimetric SAR data," *IEEE Trans. Geosci. Remote Sens.*, Vol. 36, No. 3, 963–973, 1998.
3. Yamaguchi, Y., A. Sato, W. M. Boerner, R. Sato, and H. Yamada, "Four component scattering power decomposition with rotation of coherency matrix," *IEEE Trans. Geosci. Remote Sens.*, Vol. 49, No. 6, 2251–2258, 2011.
4. Van Zyl, J. J., M. Arii, and Y. Kim, "Model-based decomposition of polarimetric SAR covariance matrices constrained for nonnegative eigenvalues," *IEEE Trans. Geosci. Remote Sens.*, Vol. 49, No. 9, 3452–3459, 2011.
5. Cui, Y., Y. Yamaguchi, J. Yang, H. Kobayashi, S. E. Park, and S. G. ingh, "On complete model-based decomposition of polarimetric SAR coherency matrix data," *IEEE Trans. Geosci. Remote Sens.*, Vol. 52, No. 4, 1991–2001, 2014.
6. Chen, S. W., M. Ohki, M. Shimada, and M. Sato, "Deorientation effect investigation for model-based decomposition over oriented built-up areas," *IEEE Geosci. Remote Sens. Lett.*, Vol. 10, No. 2, 273–277, 2013.

An Improved Model-based Polarimetric Decomposition Preserving Dominant Scattering Characteristics

Yongjun Cai^{1,2}, Xiangkun Zhang², and Jingshan Jiang²

¹University of Chinese Academy of Sciences, China

²CAS Key Laboratory of Microwave Remote Sensing, National Space Science Center, CAS, China

Abstract— Original three-component polarimetric decomposition always suffers from some deficiencies such as negative power and scattering mechanism ambiguity. In fact, it is probably because of the inconsistency between the assumed models and PolSAR data. In this paper, we intend to solve the scattering mechanism ambiguity in original three-component decomposition, and later we will try to find out some solutions aiming at alleviating the negative power problem. Considering that the nonnegative eigenvalue decomposition (NNED) is only applicative for the pixels that volume scattering dominates (the details will be discussed in Section 1), an improved model-based scheme is proposed, in which the decomposition will be hierarchical. If volume scattering is dominant, a revised NNED is adopted, for which the volume scattering employs the model proposed by Yamaguchi, and if volume scattering is not dominant, a revised four-component decomposition is adopted, for which the volume scattering employs the model proposed by Freeman. The entropy and alpha parameter are employed to identify the dominant scattering mechanism. Through this revision, the decomposition will be more accurate and the dominant scattering mechanism in each pixel will be preserved better. To verify and demonstrate the performance and advantages of the proposed decomposition, the L-band airborne AIRSAR San Francisco data and E-SAR Oberpfaffenhofen polarimetric data are used. Comparison studies are also carried out to show the improvements by the proposed method especially for the oriented urban areas.

1. INTRODUCTION

In the original model-based three-component decomposition, the volume scattering is subtracted from the original data prior to surface or dihedral scattering, which not surprisingly results in the overestimation of volume scattering power as well as negative power in remainder scattering mechanisms. Owing to the overestimation of volume scattering power, research on model-based polarimetric decomposition has reached a climax in recent several years. The representatives are Yamaguchi decomposition with orientation angle compensation and NNED. However, deorientation cannot solve these problems fundamentally, because the double bounce or surface scattering objects will not always be rotated to the reflection symmetry condition as the original assumed models predict. So in order to extract the scattering objects better, we should develop and adopt more suitable and adaptive models. Details will be discussed in Section 2. NNED is a wonderful way to avoid negative powers completely. But it is under the assumption that the residual matrix has the rank of two, which cannot be applied to the strongly depolarized situation expect the volume scattering. In fact this defaults to the dominance of volume scattering. So in this paper, this will be used for the pixels that volume scattering dominates.

2. GENERALIZED SCATTERING MODELS

For model-based polarimetric decomposition techniques, we think we should firstly start from the models themselves. So we should develop more suitable models for the PolSAR data. In this paper, we consider a generalized scattering model for surface or double bounce scattering, which takes the condition that the oriented surface or dihedral objects can also contribute significant cross-polarization component. Details will be discussed below.

Assuming the measured coherency matrix to be,

$$[T] = \begin{pmatrix} T_{11} & T_{12} & T_{13} \\ T_{21} & T_{22} & T_{23} \\ T_{31} & T_{32} & T_{33} \end{pmatrix} \quad (1)$$

the coherency matrix after rotation by angel θ can be obtained by,

$$R_\theta = \begin{pmatrix} 1 & 0 & 0 \\ 0 & \cos 2\theta & \sin 2\theta \\ 0 & -\sin 2\theta & \cos 2\theta \end{pmatrix}, \quad [T(\theta)] = R_\theta [T] R_\theta^{-1} \quad (2)$$

2.1. Surface Scattering Model

The surface scattering component consists of a first-order Bragg scatterer in which the cross-polarization component is negligible. The scattering matrix has the form,

$$S = \begin{bmatrix} R_H & 0 \\ 0 & R_V \end{bmatrix} \quad (3)$$

in Freeman decomposition and Yamaguchi decomposition, the coherency matrix of surface scattering model is represented as follows,

$$[T_s] = \begin{pmatrix} 1 & \beta^* & 0 \\ \beta & |\beta|^2 & 0 \\ 0 & 0 & 0 \end{pmatrix} \quad (4)$$

where $\beta = (R_H - R_V)/(R_H + R_V)$, $|\beta| < 1$, β is unknown to be determined.

Because terrain slopes could rotate the polarization basis and induce significant cross-polarization component. In order to fit the actual environment, a generalized model for it should be adopted. According to (2), the generalized surface scattering model can be obtained by the multiplication of a unitary rotation matrix $R(\theta)$ as seen in (2),

$$[T_s(\theta)] = R(\theta) \begin{pmatrix} 1 & \beta^* & 0 \\ \beta & |\beta|^2 & 0 \\ 0 & 0 & 0 \end{pmatrix} R(\theta)^{-1} = \begin{pmatrix} 1 & \beta^* \cos 2\theta & -\beta^* \sin 2\theta \\ \beta \cos 2\theta & |\beta|^2 \cos^2 2\theta & -|\beta|^2 \sin 2\theta \cos 2\theta \\ -\beta \sin 2\theta & -|\beta|^2 \sin 2\theta \cos 2\theta & |\beta|^2 \sin^2 2\theta \end{pmatrix} \quad (5)$$

2.2. Double Bounce Scattering Model

The double bounce scattering component consists of a dihedral corner reflector, such as the reflection between the building block walls and the underlying surfaces such as roads. The scattering matrix can be written as follows,

$$S = \begin{bmatrix} e^{j2\gamma_H} R_H & 0 \\ 0 & e^{j2\gamma_V} R_V \end{bmatrix} \quad (6)$$

in Freeman decomposition and Yamaguchi decomposition, the coherency matrix is represented as follows,

$$[T_d] = \begin{pmatrix} |\alpha|^2 & \alpha & 0 \\ \alpha^* & 1 & 0 \\ 0 & 0 & 0 \end{pmatrix} \quad (7)$$

where $\alpha = (R_H + e^{j\phi} R_V)/(R_H - e^{j\phi} R_V)$, $|\alpha| < 1$ and $\phi = 2\gamma_V - 2\gamma_H$.

Obviously, this model also doesn't take the possible cross-polarization component induced by the oriented buildings into consideration. Let the induced orientation angle be θ , the double bounce scattering model can be obtained by the same way,

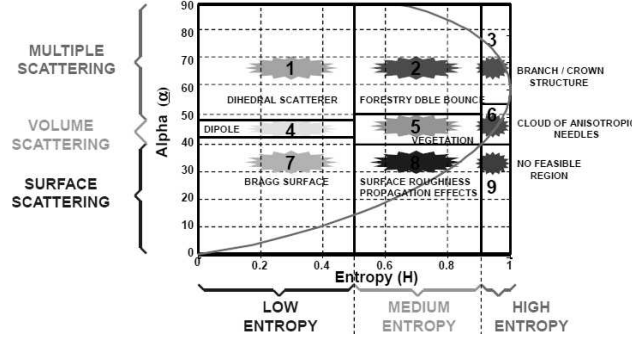
$$[T_d(\theta)] = R(\theta) \begin{pmatrix} |\alpha|^2 & \alpha & 0 \\ \alpha^* & 1 & 0 \\ 0 & 0 & 0 \end{pmatrix} R(\theta)^{-1} = \begin{pmatrix} |\alpha|^2 & \alpha \cos 2\theta & -\alpha \sin 2\theta \\ \alpha^* \cos 2\theta & \cos^2 2\theta & -\sin 2\theta \cos 2\theta \\ -\alpha^* \sin 2\theta & -\sin 2\theta \cos 2\theta & \sin^2 2\theta \end{pmatrix} \quad (8)$$

3. EXTRACTING DOMINANT SCATTERING MECHANISM

The entropy H and alpha parameters are firstly proposed by Cloude and Pottier, which are wonderful parameters to distinguish different scattering mechanisms, and based on which the H/α classification scheme was also proposed, the H/α space is given as Figure 1 shows.

The dominance of this space is given as follows,

- **Class Z1, 2 and 3:** Double bounce scattering,
- **Class Z4, 5 and 6:** Volume scattering,
- **Class Z7 and 8:** Surface scattering.


 Figure 1: Segmentation of the H/α space.

4. DECOMPOSITION FRAMEWORK

The proposed decomposition framework was divided into three individual parts according to the dominant scattering mechanism, so if one pixel belongs to Z7 and 8 in Figure 1, the decomposition will be written as follows,

$$\begin{aligned}
 \langle [T] \rangle &= f_s \langle [T_s(\theta)] \rangle + f_d \langle [T_d] \rangle + f_v \langle [T_v] \rangle + f_c \langle [T_c] \rangle \\
 &= f_s \begin{pmatrix} 1 & \beta^* \cos 2\theta & -\beta^* \sin 2\theta \\ \beta \cos 2\theta & |\beta|^2 \cos^2 2\theta & -|\beta|^2 \sin 2\theta \cos 2\theta \\ -\beta \sin 2\theta & -|\beta|^2 \sin 2\theta \cos 2\theta & |\beta|^2 \sin^2 2\theta \end{pmatrix} + f_d \begin{pmatrix} 0 & 0 & 0 \\ 0 & 1 & 0 \\ 0 & 0 & 0 \end{pmatrix} \\
 &\quad + \frac{f_v}{4} \begin{pmatrix} 2 & 0 & 0 \\ 0 & 1 & 0 \\ 0 & 0 & 1 \end{pmatrix} + \frac{f_c}{2} \begin{pmatrix} 0 & 0 & 0 \\ 0 & 1 & \pm j \\ 0 & \mp j & 1 \end{pmatrix} \quad (9)
 \end{aligned}$$

under this circumstance, the surface scattering is dominant, so the surface parameter should be solved explicitly.

While if one pixel belongs to Z1, 2 and 3, the decomposition is written as follows, similarly, the double bounce parameter should be solved explicitly,

$$\begin{aligned}
 \langle [T] \rangle &= f_d \langle [T_d(\theta)] \rangle + f_s \langle [T_s] \rangle + f_v \langle [T_v] \rangle + f_c \langle [T_c] \rangle \\
 &= f_d \begin{pmatrix} |\alpha|^2 & \alpha \cos 2\theta & -\alpha \sin 2\theta \\ \alpha^* \cos 2\theta & \cos^2 2\theta & -\sin 2\theta \cos 2\theta \\ -\alpha^* \sin 2\theta & -\sin 2\theta \cos 2\theta & \sin^2 2\theta \end{pmatrix} + f_s \begin{pmatrix} 1 & 0 & 0 \\ 0 & 0 & 0 \\ 0 & 0 & 0 \end{pmatrix} \\
 &\quad + \frac{f_v}{4} \begin{pmatrix} 2 & 0 & 0 \\ 0 & 1 & 0 \\ 0 & 0 & 1 \end{pmatrix} + \frac{f_c}{2} \begin{pmatrix} 0 & 0 & 0 \\ 0 & 1 & \pm j \\ 0 & \mp j & 1 \end{pmatrix} \quad (10)
 \end{aligned}$$

At last, if one pixel belongs to Z4, 5 and 6, that is the volume scattering dominant, general NNED with the volume scattering model proposed by Yamaguchi will be adopted instead. Because the volume scattering parameter should be solved explicitly.

It should be pointed out that because the unknown parameters we propose are unbalanced with the observations, consequently, the results of Equations (9) and (10) are both not unique. Therefore, for each solution, we then perform it to all pixels and then compare the numbers of negative powers by them, at last, we pick the solution that leaves the smallest relative amount of negative powers as the ultimate result. What's more, the models are scarcely possible to fit the data perfectly, so that the negative powers still inevitably exist in each of the results, so for the pixels with negative power, we use the Yamaguchi scheme instead this time. And later we will try to alleviate negative power problem by fitting data into models.

5. EXPERIMENTS AND RESULTS

The performance of the proposed approach is demonstrated using the AIRSAR San Francisco data sets. Figures 2(a), (b) show the decomposed results by the Yamaguchi scheme and the proposed. Figure 2(c), (d) show the close-ups of Patch B of Figures 2(a), (b), from the close-ups, we can clearly see the change in orientated buildings after the proposed decomposition is carried out. The more

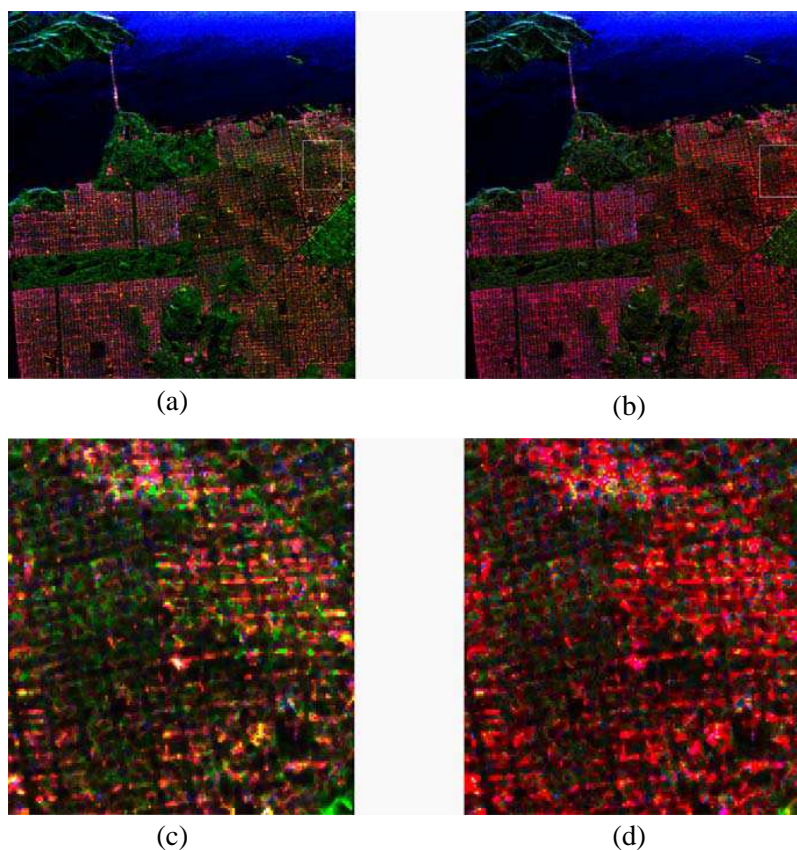


Figure 2: (a) Results of Yamaguchi decomposition and (b) the proposed; (c), (d) close-ups of patches in (a), (b).

pixels in urban areas in Yamaguchi decomposition have been decomposed into red color, which indicates the dihedral scattering mechanism from the building walls and the roads. This means that the buildings correctly turn into red color or to say the red color in urban areas is got enhanced although they are oriented in different directions. It shows that it is possible to discriminate the urban areas from forest areas, i.e., the ambiguity in original Freeman and Yamaguchi decomposition has been alleviated by the proposed decomposition.

REFERENCES

1. Cloude, S. R. and E. Pottier, "A review of target decomposition theorems in radar polarimetry," *IEEE Trans. Geosci. Remote Sens.*, Vol. 34, No. 2, 498–518, 1996.
2. Freeman, A. and S. L. Durden, "A three-component scattering model for polarimetric SAR data," *IEEE Trans. Geosci. Remote Sens.*, Vol. 36, No. 3, 963–973, 1998.
3. Yamaguchi, Y., A. Sato, W. M. Boerner, R. Sato, and H. Yamada, "Four component scattering power decomposition with rotation of coherency matrix," *IEEE Trans. Geosci. Remote Sens.*, Vol. 49, No. 6, 2251–2258, 2011.
4. Van Zyl, J. J., M. Arii, and Y. Kim, "Model-based decomposition of polarimetric SAR covariance matrices constrained for nonnegative eigenvalues," *IEEE Trans. Geosci. Remote Sens.*, Vol. 49, No. 9, 3452–3459, 2011.
5. Cui, Y., Y. Yamaguchi, J. Yang, H. Kobayashi, S. E. Park, and G. Singh, "On complete model-based decomposition of polarimetric SAR coherency matrix data," *IEEE Trans. Geosci. Remote Sens.*, No. 52, No. 4, 1991–2001, 2014.

A Method for Pose Estimation of Ship Target from SAR ROI Based on Ellipse Fitting

Xiaoqiang Zhang, Boli Xiong, Ganggang Dong, and Gangyao Kuang
National University of Defense Technology, China

Abstract— Pose estimation of target ROIs (region of interest) is an essential approach in Synthetic Aperture Radar (SAR) image interpretation. It brings high efficiency and fine accuracy in the process of target recognition and classification with accurate pose estimation. In this paper, firstly, the typical methods of target pose estimation are introduced, and the advantages and disadvantages of them are analyzed. Then, focusing on ship targets in SAR images, a novel method based on ellipse fitting is proposed to estimate the pose of the ship. According to the fact that the contour shape of ship target is generally similar to an ellipse in medium resolution SAR images, the principal axis of the fitted ellipse can be used to estimate the attitude angle of the ship. The ship target ROI is separated from the background and the contour of the target is extracted to fit an ellipse through a least squares ellipse fitting method. Although the contour of the ship target is generally coarse, the ellipse can be stably achieved by the complex real contour and a minority of singular points does not affect the final result significantly. At last, a number of experiments with ship target ROIs from TerraSAR-X SAR data are explored, and the mean error is less than 1.0° , which shows the robustness and validity of the proposed method in ship pose estimation with SAR images.

1. INTRODUCTION

Pose estimation of movable targets is very important for automatic target recognition (ATR) in SAR (Synthetic Aperture Radar) system. In template-based SAR ATR system, classification is applied by comparing the unknown targets SAR images with the SAR templates of known targets. Since the sensitivity of SAR images to the attitude angle of the targets, for each kind of the target, a series of SAR images in different attitude angles are contained in the templates. As a result, the template library is with massive data for supporting the classification, and it greatly increases the load of computation of template matching (classification). Therefore, the speed of template matching will be significantly accelerated and the efficiency of SAR ATR system will be much improved, if the attitude angle of unknown target is estimated in SAR image before classification and then the SAR image of unknown target is matched with the template of the known target with a certain attitude angle in the template library. While in model-based system for automatic target recognition, the library stores physical or theoretical models of samples, by processing which, images or feature vectors with any pose and under any arrangement can be estimated. The hypothesis of target's type, pose and so on is continually modified until it is matched well enough with the SAR image containing an unknown target or feature vectors extracted from the SAR image, through which the classification is explored. Similarly, if the pose of a target can be estimated by the SAR image accurately, feature vectors extracted from the model can be matched directly with that of the SAR image so that the efficiency of the SAR ATR system is improved.

Generally, pose estimation based on SAR image should meet two requirements. Firstly, it should be accurate, which is the most important and required by correct classification. Secondly it also should be robust against target deployment variation.

2. PREVIOUS METHODS

There are two classic methods for pose estimation of target, the leading edge method and the encapsulating box method [2]. The former usually focuses on the target of vehicle, whose contour includes a long straight line named the leading edge. In SAR images, however, it does not show the same effectiveness to the ship target, since the straightness and uniqueness of ship's long edge is not obvious enough. It is hard to choose the leading edge of the ship target properly and if the wrong choice is made, the estimation error will be great. The latter method ascertains the attitude angle through rotating the encapsulating rectangle of target. It usually lacks precision. Besides, plenty of other algorithms have been published on this topic. For example, Kefeng Ji [1], et al. used the linear regression strategy to find the line around which the scattering centers distribute. It is easy and fast, but still not accurate enough. Sometimes it is arbitrary and reluctant to fit a line to

a ship target in SAR images. The experimental results of the three methods above are analyzed in Section 4.

Most of pose estimation methods depend much on the quality of target extraction from SAR images. If the extraction is not good enough, this kind of method would become unstable. Unfortunately, noise and clutters of SAR images always bring great influence to the separation. In this paper, therefore, a new method for pose estimation, which is more robust and valid, is introduced.

3. A METHOD FOR POSE ESTIMATION OF SHIP TARGET BASED ON ELLIPSE FITTING

The principal axis of the fitted ellipse can be used to estimate the attitude angle of the ship. There is a priori knowledge that the contour shape of ship target is generally similar to an ellipse in medium resolution SAR images, so fitting an ellipse to a ship target is reasonable. The flow chart of the proposed method is shown in Fig. 1. The target is firstly separated from the background and the contour of the target is extracted for ellipse fitting. Then, an ellipse is fitted to the whole contour data. Finally the major axis of the ellipse indicates the direction of the ship target.

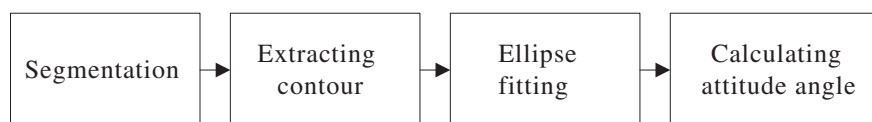


Figure 1: Flow chart of the proposed method.

3.1. Extraction of Contour Data

The 2-D OTSU segmentation algorithm is explored to deal with the ship target ROI (Fig. 2(a)). After the morphological image processing, the result is shown as Fig. 2(b), in which the connective region represents the ship target. Then the Canny operator is used to extract the contour of the connective region (Fig. 2(c)).

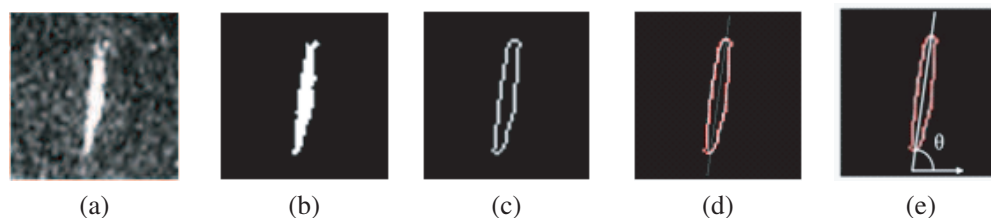


Figure 2: Schematic diagram of the proposed method. (a) Ship target clip. (b) Extracted target. (c) Extracted contour. (d) Fitted ellipse. (e) Attitude angle.

3.2. Ellipse Fitting

Ellipse fitting is the most important step in the method. The direct ellipse-specific fitting algorithm, proposed in Ref. [4], is used to fit an ellipse to the contour data. The precision of the ellipse fitting method is even stable and convinced enough for orbit fitting of the satellite [5]. A general conic can be represented by an implicit second order polynomial:

$$F(\mathbf{a}, \mathbf{x}) = \mathbf{a} \cdot \mathbf{x} = ax^2 + bxy + cy^2 + dx + ey + f = 0 \quad (1)$$

where $\mathbf{a} = [a \ b \ c \ d \ e \ f]^T$ and $\mathbf{x} = [x^2 \ xy \ y^2 \ x \ y \ 1]^T$. $F(\mathbf{a}; \mathbf{x}_i)$ is called the “algebraic distance” of a point (x, y) to the conic $F(\mathbf{a}; \mathbf{x}) = 0$. The fitted conic can be ascertained by minimizing the sum of squared algebraic distances of the curve to the N data points \mathbf{x}_i .

$$D(\mathbf{a}) = \sum_{i=1}^N F(\mathbf{x}_i)^2 \quad (2)$$

In order to force the the conic to be an ellipse and make the solution simple, Andrew imposes

the quadratic constraint $4ac - b^2 = 1$, which may be expressed in the matrix form $\mathbf{a}^T \mathbf{C} \mathbf{a} = 1$ as

$$\mathbf{a}^T \begin{pmatrix} 0 & 0 & 2 & 0 & 0 & 0 \\ 0 & -1 & 0 & 0 & 0 & 0 \\ 2 & 0 & 0 & 0 & 0 & 0 \\ 0 & 0 & 0 & 0 & 0 & 0 \\ 0 & 0 & 0 & 0 & 0 & 0 \\ 0 & 0 & 0 & 0 & 0 & 0 \end{pmatrix} \mathbf{a} = 1$$

where \mathbf{C} expresses the constraint. Since Bookstein [3] showed if a quadratic constraint is set on the parameters the minimization (2) can be solved by considering the eigenvalue system:

$$\mathbf{D}^T \mathbf{D} \mathbf{a} = \lambda \mathbf{C} \mathbf{a}$$

where $\mathbf{D} = [\mathbf{x}_1 \ \mathbf{x}_2 \ \dots \ \mathbf{x}_n]^T$, the constrained ellipse fitting problem may be rewritten as the system

$$\mathbf{D}^T \mathbf{D} \mathbf{a} = \lambda \mathbf{C} \mathbf{a} \quad (3)$$

$$\mathbf{a}^T \mathbf{C} \mathbf{a} = 1 \quad (4)$$

The Ref. [4] stated the one-to-one relationship between the eigenvalues and eigenvectors, the solutions of (3) subject to the constraint (4). Finally, it proved that (3) has exactly one positive eigenvalue $\lambda_i > 0$, giving the unique solution \mathbf{a}_i to (4). Therefore the problem can be solved and the ellipse can be ascertained by \mathbf{a}_i . Fig. 2(d) shows the fitted ellipse of the contour of Fig. 2(c).

3.3. Calculation of the Attitude Angle

The major axis is got from the fitted ellipse calculated in Subsection 3.2. The angle that the line of the major axis rotates counterclockwise to the positive direction of range is defined to be the attitude angle of the ship target, as θ in Fig. 2(e).

It should be noted that almost all of the existing methods for pose estimation based on SAR images cannot solve the problem of 180° uncertainty. Actually this problem does not cause large amount of computation. Therefore it is not discussed in this paper.

4. EXPERIMENTAL RESULTS

In order to verify the algorithm performance, 20 ship target clips extracted from the TerraSAR-X SAR images are used for experiments. This section presents some typical ones which illustrate the validness and robustness of the new method. The ROI clips, extracted contours and fitted ellipse are shown in Fig. 3. The experimental results, including the previous methods reviewed in Section 2 and the proposed method, are shown in Table 1. The performance of the proposed method is obviously better than the other and its mean error is 0.9° .

Sometimes the contours may not be ideal enough, e.g., Figs. 3(d), (e) and (f), in which some singular points, caused by noise and side lobe, make the shapes irregular. Under these circumstances, however, the proposed method, compared with other methods in Table 1, still maintain its accuracy. These experiments show that it is appropriate to introduce the priori knowledge of the high similarity between a ship contour and an ellipse. The influence, made by singular points,

Table 1: Experimental data.

	Real attitude angle	Leading edge method	Encapsulating box method	Linear regression method	The proposed method
Clip. 0	82.8°	88.1°	82°	82.7°	82.1°
Clip. 1	83.1°	86.5°	83°	83.3°	83.4°
Clip. 2	138.2°	125.6°	146°	135.2°	138.0°
Clip. 3	176.5°	179.6°	168°	158.2°	174.2°
Clip. 4	153.9°	140.3°	160°	146.9°	154.9°
Clip. 5	32.1°	38.7°	34°	38.7°	31.9°

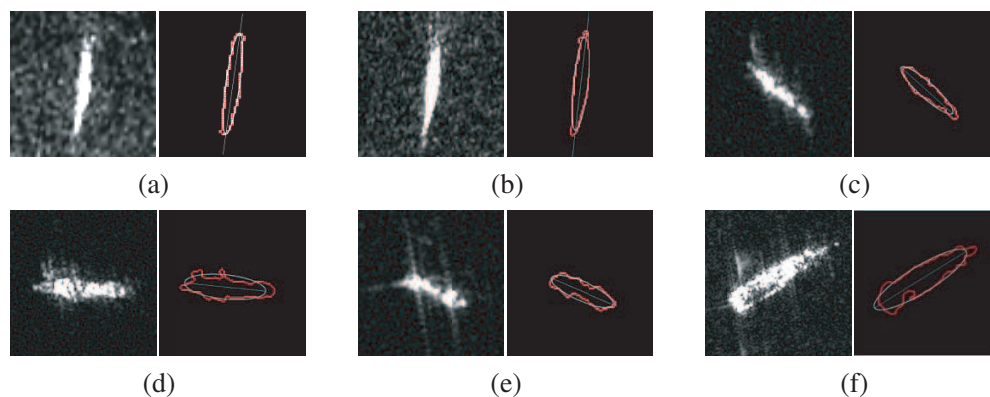


Figure 3: Pictures of some experiments. (a) Clip. 1. (b) Clip. 2. (c) Clip. 3. (d) Clip. 4. (e) Clip. 5. (f) Clip. 6.

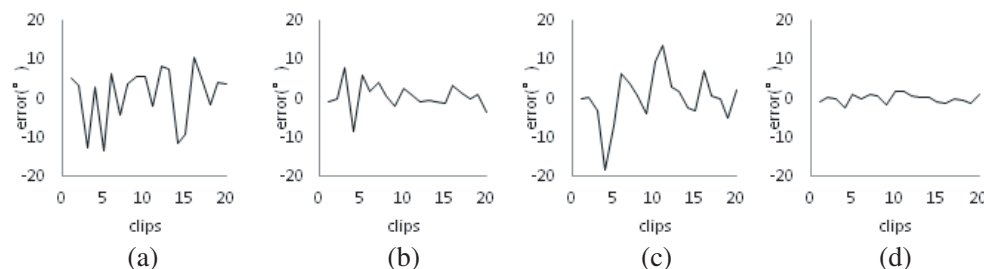


Figure 4: Error distribution of the four methods. (a) Leading edge method. (b) Encapsulating box method. (c) Linear regression method. (d) The proposed method.

to the result of the ellipse fitting algorithm is limited, since most points of the contour are in accord with the real shape of the ship target, which reflects the robustness of the method. All of the experimental results are presented in Fig. 4 in the form of diagram, which show the excellent performance of the proposed algorithm.

5. CONCLUSION

Nowadays SAR image interpretation is widely used in marine management and ocean survey and the pose estimation of ships plays an important role in this process. This paper focuses on the shape of ship target and presents a new method for pose estimation, fitting an ellipse to the ship contour through the least square fitting algorithm. Experiments with twenty SAR ship ROIs have proved its validity and robustness. Besides, it is no doubt that the method is timesaving, since the main computation is used in only once least square fitting.

There is still room for improvement in this method. It can be expected that if the contour data are filtered to eliminate the singular points, the fitted ellipse will be more similar to the ship target and the pose estimation will be more accurate. What's more, when the fitting similarity is high enough, we can even use the fitted ellipses, instead of the images, to extract geometric information and other features of the ship target, avoiding all kinds of interferences in SAR images. These will be studied in our further research in the future.

ACKNOWLEDGMENT

This work was supported by the National Natural Science Foundation of China under Grant No. 61201338.

REFERENCES

1. Ji, K., G. Kuang, and W. Yu, "A method of estimating target azimuth from sar image based on linear regression," *Modern Radar*, Vol. 26, No. 11, 26–29, Nov. 2004.
2. Zhou, L. and K. Ji, "A combined method for azimuth estimation of SAR target," *Computer Simulation*, Vol. 25, No. 8, 27–31, Aug. 2008.
3. Bookstein, F. L., "Fitting conic sections to scattered data," *Computer Graphics and Image Processing*, No. 9, 56–71, 1979.

4. Fitzgibbon, A., M. Pilu, and R. B. Fisher, “Direct least square fitting of ellipse,” *IEEE Transaction on Pattern Analysis and Machine Intelligence*, Vol. 21, No. 5, 476–480, 1999.
5. Xiong, B., J. M. Chen, et al., “Estimation of the repeat-pass ALOS PALSAR interferometric baseline through direct least square ellipse fitting,” *IEEE Transaction on Geoscience and Remote Sensing*, Vol. 50, 3610–3617, 2012.

Design of a Doherty Power Amplifier for Performance Enhancement

Yang Liu, Huaibao Xiao, and Guizhen Lu
Communication University of China, Beijing, China

Abstract— This work presents theory, design and simulation of an improved Power Amplifier (PA) based on the Doherty topology. It is theoretically shown that, using multiple iterations of source-pull and load-pull, a better main PA is accomplished. Taking into account that working conditions of the main and peak PAs affect the overall performance, the various performance indicators should be balanced. Optimal bias voltages are determined in the proposed DPA, providing higher efficiency both at full output power and at 6 dB back-off power, thus validating practical effects of the design and demonstrating a promising prospect to be used in the future wireless transmitter applications.

1. INTRODUCTION

Future wireless transmitters in the communication systems tend to be imposed more and more stringent constraints. To ensure that the communication transmitters could permit signal integrity upholding, base-station deployment operating cost reduction and an increase in battery life for mobile stations linearity and power efficiency are both crucial factors which must be considered in the design [1].

Improving the efficiency of the PA has been studied using efficiency enhancement techniques such as envelope elimination and restoration (EER), polar modulation, and envelope tracking (ET) [2–4]. These techniques could provide excellent efficiency performance using a complicated enveloped PA and/or switching PA, and high linearity performance can be achieved with the help of a digital predistortion technique.

Compared with technologies mentioned above, the Doherty Power Amplifier (DPA) stands out for its high efficiency, simple achievement, relatively low cost, small impact on the linearity system and other advantages. As well as its topology can be easily combined with the feed forward and predistortion techniques, the DPA has been widely studied and applied in the modern wireless communication systems.

2. DESIGN OF THE MAIN PA

The main PA is designed in this paper using an N-channel enhanced LDMOS tube MRF6S20010N of the Freescale Semiconductor with the center frequency of 2.14 GHz.

To guarantee a good performance the input and output matching sections are especially important in the design. So the optimum source impedance and load impedance should be found.

There is a platform which can provide templates of Load-Pull and Source-Pull simulations. By modifying the input signal power, scanning centers, scanning radius and sweep points, it is easy to get a team of equal efficiency circles and output power circles. Then we can obtain the optimum load impedance and source impedance according to the corresponding design requirements.

However, since source-pull and load-pull are divided into two separate steps to complete, it is probably that the source and load impedance end up not optimal. To solve this problem, the concept of multiple iterations is introduced into the design to achieve convergence solutions as follows [5].

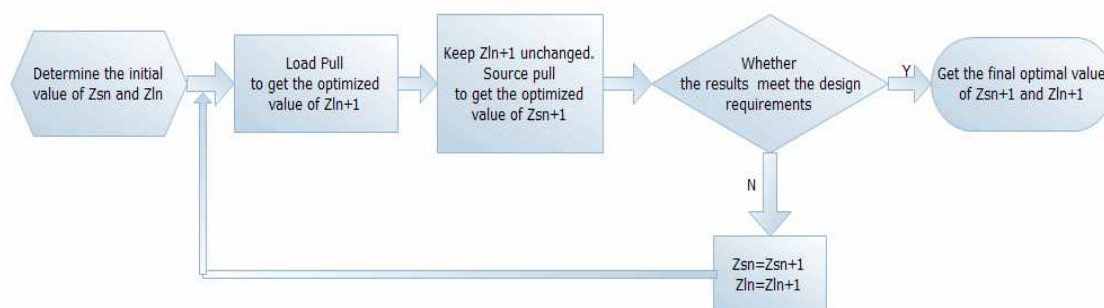


Figure 1: Flow chart of the multiple iterations using the source-pull and load-pull.

After several steps of multiple iterations, we get the optimum source impedance and load impedance. With the design of new matching circuits, an improved main PA is done. The new measured gain and power-added efficiency (PAE) are shown in Fig. 2, better than the results of single traction shown in the Fig. 3.

m1 indep(m1)=20.248 vs(P_gain_transducer,Spectrum[1])=18.248	m3 indep(m3)=37.863 vs(PAE,Spectrum[1])=36.146
m2 indep(m2)=41.703 vs(P_gain_transducer,Spectrum[1])=17.203	m4 indep(m4)=41.703 vs(PAE,Spectrum[1])=55.891

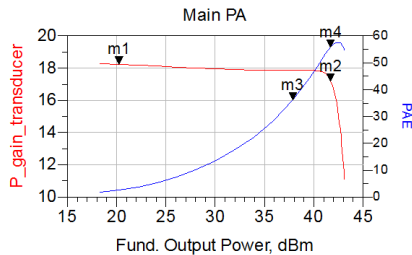


Figure 2: Simulation result after multiple iterations.

m1 indep(m1)=15.932 vs(P_gain_transducer,Spectrum[1])=15.932	m3 indep(m3)=38.001 plot_vs(PAE, Spectrum[1])=31.002
m2 indep(m2)=41.763 vs(P_gain_transducer,Spectrum[1])=14.763	m4 indep(m4)=41.763 plot_vs(PAE, Spectrum[1])=44.995

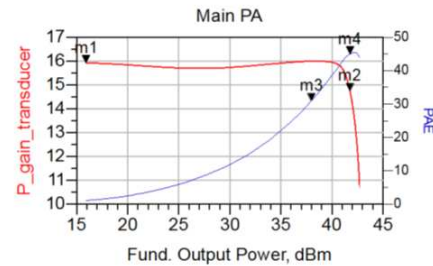


Figure 3: Simulation result before multiple iterations.

3. BASIC DESIGN OF THE WHOLE DPA

In this design, we use the inverted structure of Doherty mentioned in many literatures [6]. The compensation line after main PA is to enhance the drain resistance at small input power level to get earlier saturation and improve efficiency. The compensation line after peak PA is to transform small impedance into large impedance [7].

The transistors used for the main and peak PAs are identical in size and evenly driven. The main PA was biased in class AB condition and the peak PAs in class C. Using the Wilkinson power divider, we got the basic design.

4. FACTORS INFLUENCE ON THE PERFORMANCE OF THE DPA

In the DPA, efficiency and linearity are conflicting. In the area of low power levels, main PA works while peak PA is off, the overall linearity depends on the linearity of main PA. In the area of medium power levels, the participation of peak PA in Class C mode deteriorates the overall linearity. Only in the area of high power levels, the gain of main PA compresses while the gain of peak PA expands and then the effects just balances and makes improvement in the overall linearity. So based on the purposes of optimizing the DPA performance, the drain bias voltage of main PA and the gate bias voltage of peak PA are considered about that how to impact on the overall efficiency and linearity.

4.1. Drain Bias Voltage of Main PA

We know that main and peak PAs' drain bias voltages have a significant impact on the power back-off range and efficiency of the DPA. Based on the designed circuit above, sweeping and scanning the drain bias voltage of main PA from 25 V to 35 V by 2 V each step with other parameters unchanged, we can get the effect trends of gain and efficiency in Fig. 4, as well as the trends of linearity in Fig. 5.

As the simulation results shown above, since the drain bias voltage decreases, the main PA gets into saturation at a lower input power level, making efficiency at low power level greatly improved. But it is precisely because that the main PA unit gets into the saturated zone earlier, leading to the reduction of the gain and an overall deterioration of linearity at low power.

If we can properly reduce the drain bias voltage or dynamically adjust the drain bias voltage of the main PA unit according to the case of the input signal envelope, the efficiency of the PA will be greatly enhanced in a certain level of linearity.

4.2. Gate Bias Voltage of Peak PA

Gate bias voltage of the peak PA determines when it starts to work, so the gate bias voltage influences the linearity, gain, efficiency and other performance characteristics of the peak PA. The state of peak PA working in is mainly decided by the gate bias voltage. The lower gate bias voltage is, the "deeper" state of class C it works in.

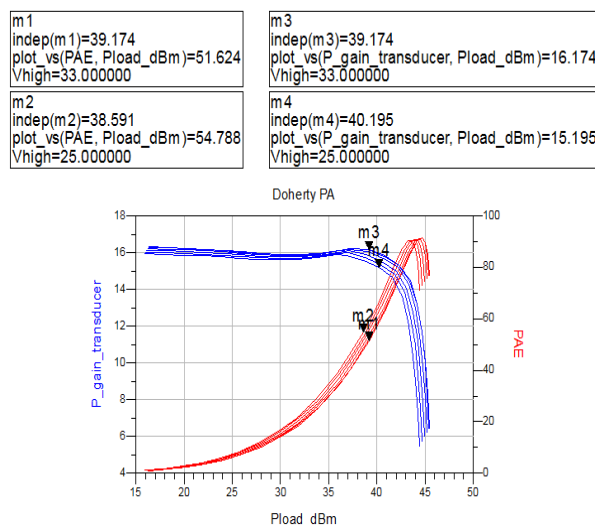


Figure 4: Trends of gain and efficiency.

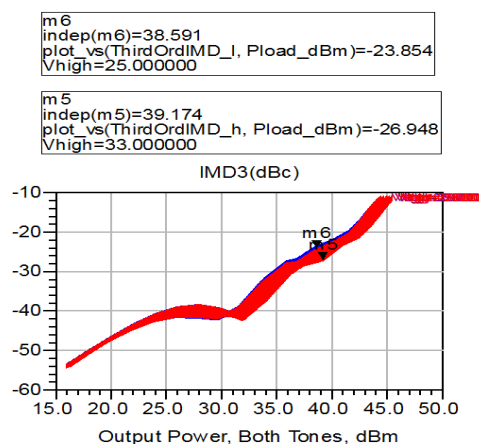


Figure 5: Trends of linearity.

The drain bias voltage of peak PA in this design ranges from 0.1 V to 2 V, stepping by 0.2 V. The scanning results of gate bias voltage of the peak PA are shown in Fig. 6 and Fig. 7.

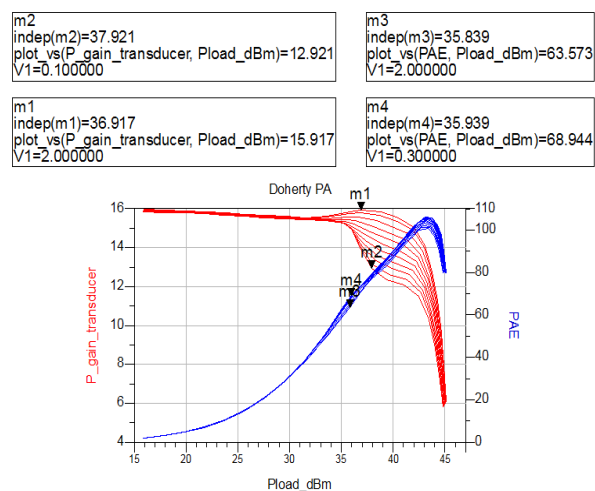


Figure 6: Trends of gain and efficiency.

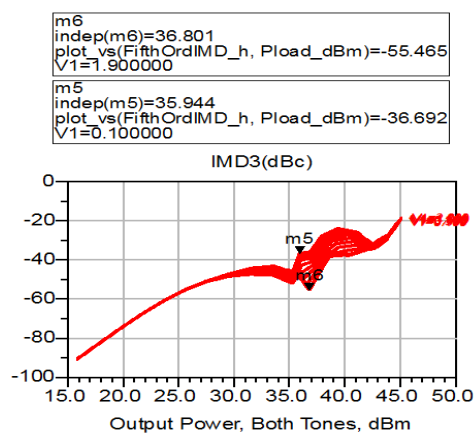


Figure 7: Trends of linearity.

According to the simulation results, the higher gate bias voltage is, the lower the starting point of peak PA. The inefficient operation state after its participation makes the total efficiency reduced. Therefore, the lower the gate bias voltage of peak PA is, the higher the efficiency can be while the worse the linearity will become.

5. IMPROVED DESIGN OF THE WHOLE DPA

Considering the impact of factors mentioned above on the overall performance of the DPA a balanced choice according to the actual needs of the various performance parameters is proposed. We make the main PA working in AB condition with a drain bias voltage of 28 V and the peak PA in a proper C condition with a gate bias voltage of 1.96 V. With other optimizations not described in detail, the final improved DPA is completed. The results are shown in the Fig. 8. Compared with the results shown in the Fig. 9 before improvement, the PAE at saturation point and 6 dB back point have greatly improved, while the gain and linearity still meet the design requirements without deterioration.

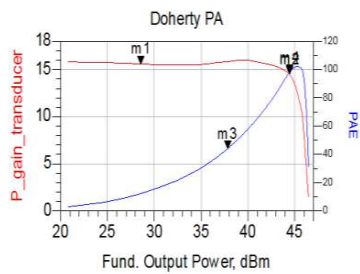
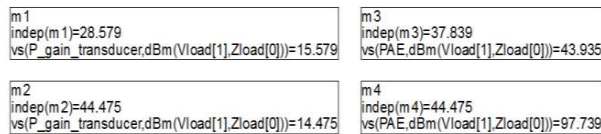


Figure 8: Results after improvement.

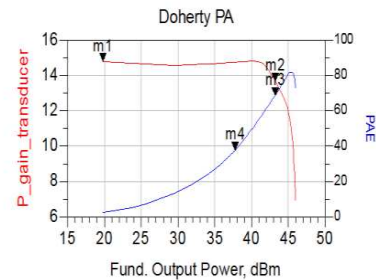
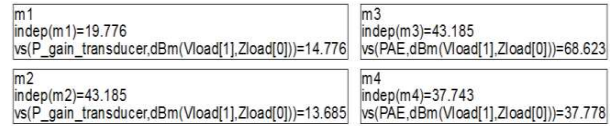


Figure 9: Results before improvement.

6. CONCLUSION

In this paper, an improved design of Doherty PA has been proposed. The design is based on the use of multiple iterations of source-pull and load-pull and a balanced consideration of the state of bias. The simulation results show that the proposed Doherty PA has a power-added efficiency (PAE) much higher than the traditional one with other performances not deteriorated.

REFERENCES

1. Gustafsson, D., C. M. Andersson, and C. Fager, "A novel wideband and reconfigurable high average efficiency power amplifier," *Microwave Symposium Digest (MTT)*, Vol. 17, 169–178, Department of Microtechnology and Nanoscience, Chalmers University of Technology, Kemivägen, 9, Göteborg SE-412 96, Sweden, 2007.
2. Raab, F. H., B. E. Sigmon, R. G. Myers, and R. M. Jackson, "L-band transmitter using Kahn EER technique," *IEEE Trans. Microw. Theory Tech.*, Vol. 46, No. 12, 2220–2225, Dec. 1998.
3. Chen, J.-H., P. Fedorenko, and J. S. Kenney, "A low voltage W-CDMA polar transmitter with digital envelope path gain compensation," *IEEE Microw. Wireless Compon. Lett.*, Vol. 16, No. 7, 428–430, Jul. 2006.
4. Kimball, D. F., J. Jeong, C. Hsia, P. Draxler, S. Lanfranco, W. Nagy, K. Linthicum, L. E. Larson, and P. M. Asbeck, "High-efficiency envelope tracking W-CDMA base-station amplifier using GaN HFETs," *IEEE Trans. Microw. Theory Tech.*, Vol. 54, No. 11, 3848–3856, Nov. 2006.
5. Liu, Y. and H. B. Xiao, "Design and simulation of an improved Doherty power amplifier," *IEEE Trans. Applied Mechanics and Materials*, Vol. 496–500, 1109–1112, 2014.
6. Yang, Y., J. Cha, B. Shin, and B. Kim, "A fully matched N-way Doherty amplifier with optimized linearity," *IEEE Trans. Microw. Theory Tech.*, Vol. 51, No. 3, 986–993, Mar. 2003.
7. Zhao, H. M., "Design on high-power amplifier module of communication," 2013.

Application of the Method of Fresnel Zone Analysis in Base Station Location Survey

Zhiyuan Song, Feng Gao, Kai He, and Wentao Zhu

China Mobile Group Design Institute Co., Ltd., Beijing 100080, China

Abstract— Along with the LTE mobile communication network rapid demand in China, it appears more trouble and difficulties in network plan and needs a faster and relative accurate scientific method to support the BS (base station) location survey with a view to the weakness transmissibility of the radio wave above 2GHz.

The BS location survey project is one of the important items in mobile communication network plan before construction; however there are less computation model methods and theoretical arithmetic based on measured data to be utilized. The conclusion of BS location survey projection is mainly depended on the experiences and subjective judgments of survey stuffs. In considering of objective factors of surroundings parameter collection, length of work time and etc. in location survey, the common methods including propagation model, ray tracing and etc. have such difficulties and incompetence to apply.

Huygens-Fresnel principle is one of most key point characters of radio wave. In the propagation of radio, every point on the surface of the wave is a secondary radiation wave of spherical wave. And space for a bit of radiation field is surrounded by the wave of each point on the arbitrary closed surface wave from the secondary waves in which the result of superposition of mutual interference. Take advantage of Huygens-Fresnel principle it has greater possibility to adapt the ability range of BS location survey tools and the requirement of work time with the rapid computation method of Fresnel Zone in BS location survey project. In this paper, it is reported that Fresnel Zone method for the mobile communication will be studied in-depth and the application and the propagation criterion selection of this method will be analyzed concretely.

1. INTRODUCTION

Mobile communication network, especially LTE, is being planned and built in a rapidly increasing speed in China. There are many methods including Okumura model COST231-Hata model, VolcanoMini model used in the network plan and simulation software. However, these software are almost suitable for the large computer servers and long-time simulation indoor. They need hundreds of data from streets, buildings, rivers, forest, towers and the relative position difference between them to input. The BS location survey project is one of important items in network plan. It has many different characters to evaluate the propagation environment from the network plan and simulation software, such as much shorter time to collect building parameters, small computer equipment as laptop or PAD.

The Fresnel Zone is an application product of the Huygens-Fresnel principle used in the mobile communication system. It has greater possibility to adapt the ability range of BS location survey tools and the requirement of work time in BS location survey project. In Sections 2 and 3, the operation method of Fresnel Zone is described concretely. In Section 4, the conclusion and suggestion are given.

2. FRESNEL ZONE THEORY

According to Huygens-Fresnel principle, in the process of radio transmission, each point on the surface of the wave is the wave source of a spherical wave of secondary radiation, called secondary wave source. And any point's radiation field in the space is surrounded by the wave of each point on the arbitrary closed surface wave from the secondary waves in which the result of superposition of mutual interference. Obviously, the closed surface on each point of the secondary waves reach the receiver system is different, which makes the receiver signal of the size of the field intensity change. It is shown as Fig. 1.

Furthermore, the definition of Fresnel Zone can be given visually in Fig. 2. Point Q is the wave source and point P is the receive point in the free space. The space region which is contained in the rotation ellipsoid, point Q and P as the focal point, is called Fresnel Zone.

In Fig. 2, S_1 is one point in the radio propagation space. And the plane including S_1 perpendicular to line QP , gets a circle C_1 in Fresnel Zone. The distance between point Q and P is d , the

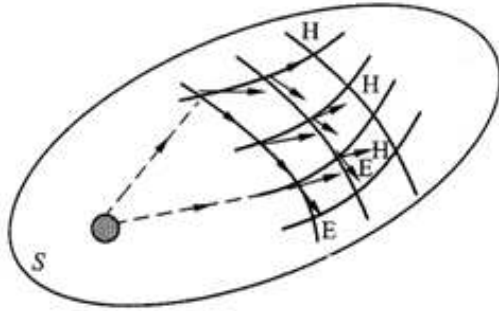


Figure 1: Secondary wave source of Huygens-Fresnel principle.

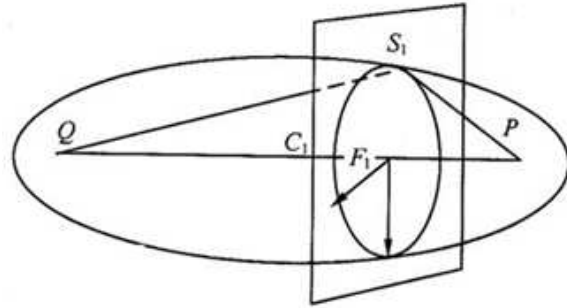


Figure 2: Fresnel zone.

distance between point Q and C_1 is d_1 , and the distance between point P and C_1 is d_2 . As the frequency of the radio is known, the radius of circle C_1 can be calculated by Eq. (1) as:

$$F_1 = \sqrt{\lambda d_1 d_2 / d} \quad (1)$$

In Fig. 2, the result of QS_1+S_1P-d , which could be named as T , is the distance different of the two different path of radio waves between transmitting antenna and receiving antenna. When T is odd times of $\lambda/2$, the two path of electromagnetic wave are on the same role and the electric field of the receiving point is strengthened. And when T is even times of $\lambda/2$, the two path of electromagnetic wave are on the contrary role and the electric field of the receiving point is offset. So we could obtain the division of Fresnel Zone.

$$\begin{aligned} T &= \lambda/2 \\ T &= 2 \times \lambda/2 \\ &\dots \\ T &= n \times \lambda/2 \end{aligned}$$

These formulas define the first Fresnel Zone, the second Fresnel Zone and the n th Fresnel Zone, respectively.

In free space, the radiation electromagnetic energy from the wave source point Q to point P is primarily spread by the first Fresnel Zone. As long as the first Fresnel Zone is not blocked, the free space propagation condition could be approximately obtained. So the blocks area between the transmitter and the receiver is asked to less than a certain ratio of the Fresnel Zone, which means the antenna can be raised to suitable height.

Including the first Fresnel Zone, the Minimum Fresnel Zone possesses important significance. The Minimum Fresnel Zone is in the first Fresnel Zone. And when the radio wave passes through the whole Minimum Fresnel Zone, the signal of different paths are added in the same phase at the receiving point, so the signal is strengthened.

$$F_0 = 0.577 \times \sqrt{\lambda d_1 d_2 / d} \quad (2)$$

It can be inferred that when the distance between the transmitting antenna and the receiving antenna is a fixed value, the shorter of the wave length, the smaller of the Fresnel radius of the main spread area, the more slender of the Fresnel ellipsoid area, and the Fresnel ellipsoid area degrades to be a straight line as one spread path of light.

3. APPLICATION OF THE METHOD OF FRESNEL ZONE

According to the theory of Fresnel Zone, a practical application method can be used in the BS location survey for the evaluation of the propagation environment. The BS location survey stuff can utilize the survey tools to obtain the block's area relative to the Fresnel Zone of the propagation environment of the survey building, and then can evaluate the kind, height, pitch angle of the antenna and that the planned scheme is feasible or not.

The application software can run on the Android system mobile phone and PAD. The key parameters of the application software include the Fresnel radius, the downtilt and the overlap area of the block and the Fresnel ellipsoid. Each parameter can be inferred from the normal survey tools, such as laser rangefinder, downtilt measuring instrument. These parameters would be introduced.

3.1. The Fresnel Radius

As the description in Section 2, the Fresnel radius F_1 can be deduced by Eq. (1) after the radio frequency, the distance between the transmitting point and the receiving point d , and. Before the BS location survey, the mobile network plan has already done. So the radio frequency is known. And the coverage radius which has been planned in the network plan could be regarded as d . Depended on the utilization of laser rangefinder, d_1 and d_2 can be obtained.

3.2. The Downtilt

The downtilt is the inclination of the antenna and the receiving point. It can be obtained by the downtilt measuring instrument.

3.3. The Overlap Area

The overlap area of the block and the Fresnel ellipsoid is the most difficult and important parameter in this software algorithm. There are nearly ten cases to consider.

Figure 3 shows the main relationship of Fresnel Zone and the block. A is middle point of the top side and C is the center of the Fresnel Circle. Then it is defined that angle α is the inclination of Q to A and α' is the inclination of Q to C , r is the radius of the Fresnel Circle. Then $H = QA \times \sin \alpha - \frac{\cos 3^\circ \times \sin 3^\circ}{\cos \alpha - \cos \alpha'}$, H is the relative height of A to C and h is $QA \times \sin \alpha$.

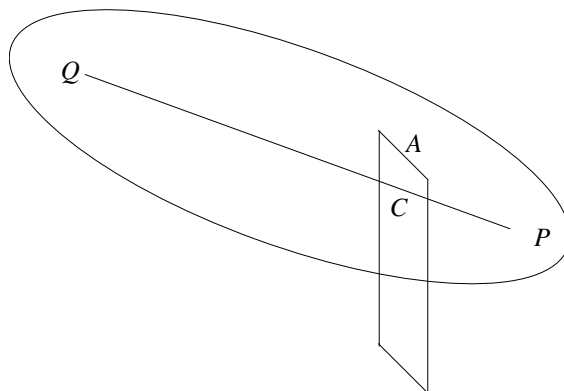


Figure 3: Judgment of the overlap area.

When C is out of the block:

- (1) $r < h$. It means that the Fresnel Circle and the block have no overlap area.
- (2) $r > h$. The overlap area can be computed by

$$\frac{2 \arccos \frac{h}{r} \cdot \pi r^2}{360} - \sin \left(\arccos \frac{h}{r} \right) \cdot r \cdot h \quad (3)$$

When C is in the block:

- (1) $r < h$. It means that the Fresnel Circle and the block have no overlap area.
- (2) $r > h$ and the vertical side is more than the value of r plus h and the horizontal side is more than the value of twice of r . It means that the Fresnel Circle and the block have no overlap area.
- (3) $r > h$ and the vertical side is more than the value of r plus h and the horizontal side is less than the value of twice of r . The overlap area is $(r + h) \cdot y$.

We had chosen a roof of dense urban building. Depend on distance meter and laptop, this method gives the result of different pitch angle of the antenna. When the pitch angle is 3 degree, the radio wave can bypass the block. When the pitch angle is 10 degree, the radio wave is blocked.

4. CONCLUSION AND SUGGESTION

The application of the method of Fresnel Zone provides a scientific way and a quick calculation model to evaluate the propagation environment compared to depending on the experiences and subjective judgments of survey stuffs in BS location survey, especially in the dense urban. However, how to simulate the accurate propagation way of radio in a sustainable time is still a difficulty problem. The work in this paper makes some helpful explore to solve the problem.

REFERENCES

1. Tian, B., T. Xu, and G. Re, *Wireless Communications*, Publishing house of Electronics Industry, 2008.
2. Fresnel Zone Calculation, Circuit Design, Inc., Weblink: <http://www.cdt21.com/>.

A Novel Mutual Coupling Matrix Monitoring Method in Two Dimensional Rectangle Antenna Array

Junhe Zhou¹, Jian Zhang¹, Hui Wang¹, Xuefeng Yin¹, Meisong Tong¹, and Jian Li²

¹Department of Electronics Science and Engineering
Tongji University, Shanghai 200092, China

²2012 Communication Technology Lab, Huawei Technologies, Shanghai, China

Abstract— In this paper, mutual coupling in two-dimensional rectangle antenna array is investigated. It is discovered that the mutual coupling matrix for such an antenna array can be decomposed into the product of a unitary matrix, a diagonal matrix and the Hermitian transpose of the unitary matrix. If the coupling between the non-adjacent elements is ignored, the unitary matrix will be the two dimensional discrete sine transform matrix and the diagonal matrix can be evaluated analytically. When the external excitation voltage of the array is set to be eigen vectors of the mutual coupling matrix, the resulting voltages on the array elements will also be the eigen vector of the mutual coupling matrix, except for a scaling factor. By analyzing the scaling factor, the coupling between the adjacent elements can be calculated.

1. INTRODUCTION

Mutual coupling is caused by the electro-magnetic interactions between the antenna elements inside the array. It will greatly impact the performance of the beamforming algorithms and the directional finding algorithms [1, 2].

It is generally accepted that the mutual coupling effect mainly exists between the closely arranged antenna elements. To monitor the coupling effect, one should inject independent excitation voltage vectors and measure the voltages on all of the antenna elements. Furthermore, a matrix inversion is necessary during the final calculation of the coupling coefficients. In [3], a calibration approach is proposed by using known sources from certain direction. This is, however, not practical for the real time monitoring of the mutual coupling matrix.

In this work, a novel method to characterize the mutual coupling matrix of the rectangle antenna array is proposed. The coupling matrix of the array can be decomposed into the product of the discrete sine transform matrix, a diagonal matrix and the transpose of the discrete sine transform matrix provided that only the coupling between the neighboring elements in the array is considered.

Based on this fact, the measuring of the mutual coupling between the neighboring elements can be accomplished by monitoring only one element within the array. It is accomplished as follows: the excitation voltage vector of the array is set to be the eigen vector of the coupling matrix, i.e., the row vector of the discrete sine transform matrix. It can be derived that the voltages on the antenna terminals will also be the row vector of the discrete sine transform matrix, albeit with a constant, which relates to the mutual coupling effect. By altering the voltage with respect to the row vectors of the discrete sine transform matrix and measuring the ratio of the excitation voltage over the load voltage on the monitoring antenna element, one is able to determine the mutual coupling coefficients.

2. MATHEMATICAL MODEL FOR THE MUTUAL COUPLING MATRIX IN A LINEAR ANTENNA ARRAY

The mutual coupling matrix for a linear antenna array can be formulated as

$$\mathbf{Z} = \begin{pmatrix} Z_1 & Z_2 & \cdots & 0 \\ Z_2 & Z_1 & \cdots & \vdots \\ \vdots & \vdots & \ddots & Z_2 \\ 0 & \cdots & Z_2 & Z_1 \end{pmatrix} \quad (1)$$

where Z_1 is the self impedance, Z_2 the mutual impedance resulting from coupling between neighboring elements, while all the coupling for non-neighboring elements is neglected.

\mathbf{Z} can be decomposed by [4]

$$\mathbf{Z} = \mathbf{Q}\mathbf{D}\mathbf{Q}^H \quad (2)$$

where \mathbf{Q} is the discrete sine transform (DST) matrix and \mathbf{Q}^H is its Hermitian transpose. Matrix \mathbf{Q} has the elements as [4]

$$Q_{mn} = \sqrt{\frac{2}{N}} \sin\left(\frac{\pi mn}{N+1}\right) \quad (3)$$

The diagonal elements of matrix \mathbf{D} can be formulated as [4]

$$D_{nn} = Z_1 + 2Z_2 \cos\left(\frac{n\pi}{N+1}\right) \quad (4)$$

The antenna voltage vector and the antenna current vector are related by [5]

$$\mathbf{U} = \mathbf{Z}\mathbf{I} \quad (5)$$

The external excitation voltage \mathbf{U}_E is applied to the antenna elements. However it is not directly proportionally related to the antenna voltage \mathbf{U} , the actual relationship is [5]

$$\mathbf{U} = \mathbf{U}_E - \mathbf{Z}_L\mathbf{I} \quad (6)$$

where \mathbf{Z}_L is the load impedance matrix, which is diagonal when the load impedances are the same for every antenna elements. Hence, we have [5]

$$\mathbf{U} = \mathbf{Z}(\mathbf{Z} + \mathbf{Z}_L)^{-1} \mathbf{U}_E \quad (7)$$

Combining with Eqs. (3)–(5), we have [5]

$$\mathbf{U} = \mathbf{Q}\mathbf{G}\mathbf{Q}^H \mathbf{U}_E \quad (8)$$

where \mathbf{G} is a diagonal matrix with the diagonal elements of [5]

$$G_{nn} = \frac{D_{nn}}{D_{nn} + Z_L} \quad (9)$$

Therefore, when the excitation voltage of the antenna elements are assumed to be the row vectors of matrix \mathbf{Q} , the real voltage that is applied to the antenna elements will also be the row vectors of matrix \mathbf{Q} , albeit with the factor of G_{nn} . By measuring the ratio of the real voltage and the excitation voltage on only one antenna element, the value of G_{nn} can be obtained. With two different values of G_{nn} , one is able to determine the final value of Z_1 and Z_2 .

3. EXTENSION OF THE CONCLUSION TO THE TWO-DIMENSIONAL RECTANGLE ANTENNA ARRAY

When the antenna array is extended from the one dimensional linear array to the two dimensional rectangle array, the matrix \mathbf{Z} can be formulated by

$$\mathbf{Z} = (\mathbf{Q} \otimes \mathbf{Q}) \mathbf{E} (\mathbf{Q} \otimes \mathbf{Q})^T \quad (10)$$

where \otimes denotes the Kronecker product. The matrix \mathbf{Q} is the same matrix as the one in the one dimensional array. The diagonal matrix \mathbf{E} has its diagonal elements as

$$E_{nN+m, nN+m} = Z_1 + 2Z_{2x} \cos\left(\frac{n\pi}{N+1}\right) + 2Z_{2y} \cos\left(\frac{m\pi}{N+1}\right) \quad (11)$$

There are three unknown variables in the formula, namely Z_1 , Z_{2x} and Z_{2y} , which are related to the self impedance and the mutual impedance between the two adjacent elements in the x and y directions. The impedances can also be obtained by measuring the ratio of the external excitation voltage over the real antenna element voltage while setting the excitation voltage vector to be the row vector of

$$\mathbf{Q} \otimes \mathbf{Q}$$

In such a configuration, measuring of only one elements' excitation voltage and real antenna voltage is adequate. By measuring the ratio three times and setting up the three linear equations, one is able to calculate Z_1 , Z_{2x} and Z_{2y} .

4. CONCLUSION

We have proposed a novel method to monitor the mutual coupling matrix in linear and rectangle antenna arrays. The method is based on the analysis of the mutual coupling without considering the non-adjacent coupling. The method is useful for the application in massive MIMO systems.

ACKNOWLEDGMENT

This work is supported in part by the Huawei Innovation Research Program, the Huawei company project (YB2013120038), the STCSM project (13510711000) and by the NSFC (61331009, 61201068).

REFERENCES

1. Ioannides, P. and C. A. Balanis, “Uniform circular and rectangular arrays for adaptive beam-forming applications,” *IEEE Antennas and Wireless Propagation Letters*, Vol. 4, 351–354, 2005.
2. *3D TDD: TD-SCDMA RFTRXU Subsystem Function Specification*, Aug. 1999.
3. Gupta, I. J., J. R. Baxter, S. W. Ellingson, H. Park, H. S. Oh, and M. G. Kyeong, “An experimental study of antenna array calibration,” *IEEE Trans. Antennas Propag.*, Vol. 51, No. 3, 664–667, Mar. 2003.
4. Kapon, E., J. Katz, and A. Yariv, “Supermode analysis of phase-locked arrays of semiconductor lasers,” *Opt. Lett.*, Vol. 9, 125–127, 1984.
5. Zhou, J., J. Zhang, H. Wang, X. Yin, M. Tong, and J. Li, “Simple impedance matrix characterization method for uniform circular antenna arrays,” *IEEE International Symposium on Antennas and Propagation*, 2014.

Multiband THz Metamaterial Absorber Based on Snowflake-type Resonators

Junchuan Zhuge, Di Bao, Xiaopeng Shen, and Tiejun Cui

State Key Laboratory of Millimeter Waves, Southeast University, Nanjing 210096, China

Abstract— Recently, the devices operating in the terahertz (THz) frequency band have aroused tremendous interests because of their gigantic potential applications in the areas such as security, public health, and biomedicine. In this work, ultrathin multiband THz metamaterial absorbers are proposed, and the design, simulation, and theoretical analysis of the absorbers are presented. First, a dualband absorber consisting of snowflake-type resonator array is designed, which is printed on a grounded polyimide dielectric spacer. Numerical simulations shows that the proposed structure has two perfect absorption peaks at 0.952 and 1.818 THz with absorption rates reaching 99.7% and 99.9%, respectively. By carefully designing the geometrical parameters and layout of the snowflake-type resonators, a quadband absorber with four perfect absorption peaks is implemented. The numerical simulation result shows that four different absorption peaks appear at 0.752, 0.950, 1.454, and 1.696 THz with the absorption rates of 98.8%, 97.8%, 92.1%, and 90%, respectively.

1. INTRODUCTION

Metamaterials, which are constitutive of artificial electromagnetic materials, have attracted considerable interests due to their ability to exhibit novel properties that may not be found in nature, including negative refractive index, cloaking and sound filtering [1–4].

The THz range is known as the terahertz gap because of its noticeable underutilization. However, with substantial advance of processing craft extending from the microwave band to the THz band, the research of THz metamaterials has achieved huge progress. In recent years, the idea of THz metamaterial absorbers has attracted wide interests among scientists [5–7]. In 2008, the first THz metamaterial absorber was designed and proposed with an experimental absorptivity of 70% at 1.3 terahertz by Hu Tao, etc. [8]. Afterwards, a triple-band THz metamaterial absorber was fabricated by Xiaopeng Shen, et al., which had three distinctive absorption peaks at 0.5, 1.03, and 1.71 THz with absorption rates of 96.4%, 96.3%, and 96.7%, respectively [9].

In this paper, we adopt a direct but efficient approach as is illustrated in [10] to achieve two kinds of multiband THz metamaterial absorbers based on snowflake-type resonators: a dualband THz absorber and a quadband THz absorber, both of which have perfect absorption rates in the designed frequency bands over wide angles of incident waves. These two kinds of designs are presented afterwards. In design A, two distinct absorption peaks appear at 0.952 and 1.818 THz with the absorption rates of 99.7% and 99.9%, respectively; in design B, four distinct absorption peaks appear at 0.752, 0.950, 1.454, and 1.696 THz with the absorption rates of 98.8%, 97.8%, 92.1%, and 90%, respectively. The current distributions on the surfaces of snowflake-type resonators in the peaks of absorption are also presented to gain a better insight into the physics behind the multiple absorption mechanism.

2. DESIGNS OF MULTIBAND ABSORBERS

2.1. Design of Dualband Absorber

The structure of the dualband absorber is shown in Fig. 1(a), which consists of three layers including a snowflake-type resonator array, a polyimide dielectric spacer and a metallic back layer. The upper aluminum snowflake-type resonator layer is responsible for the electric resonance when the THz electromagnetic wave illuminate on the surface. The back layer is also an aluminum sheet, hence the magnetic field is supposed to drive circulating currents between the upper layer and the back layer. The entire absorber is the periodic extension of the unit cell (Fig. 1(b)) in both X and Y directions.

By optimizing the geometry of the snowflake-type resonator and the thickness of the dielectric substrate, we can adjust the effective permittivity and permeability of the structure to realize the impedance matching between the structure and the free space, which means the minimum value of the reflection. The transmission is equal to zero due to the metal back layer. With the definition of the absorption $A = 1 - T - R = 1 - |S_{21}|^2 - |S_{11}|^2 = 1 - |S_{11}|^2$, we can easily draw a conclusion

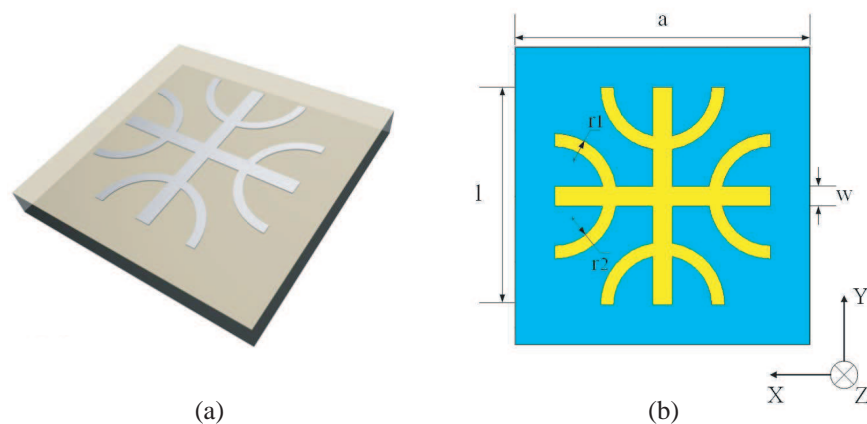


Figure 1: The structure of the dualband THz metamaterial absorber: (a) the perspective view of the unit cell, (b) the front view of the unit cell.

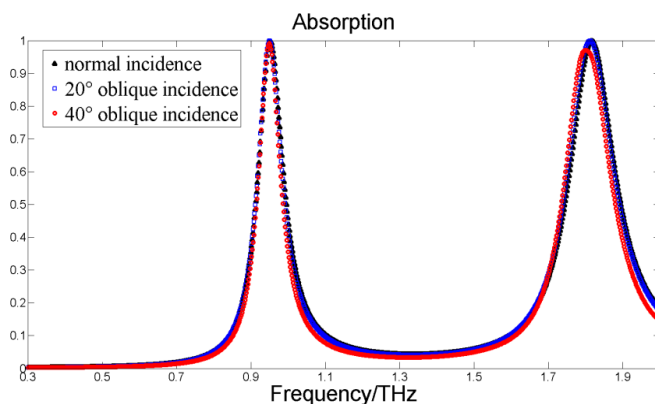


Figure 2: The simulated absorption spectra of the dualband absorber at various incident angles of THz waves.

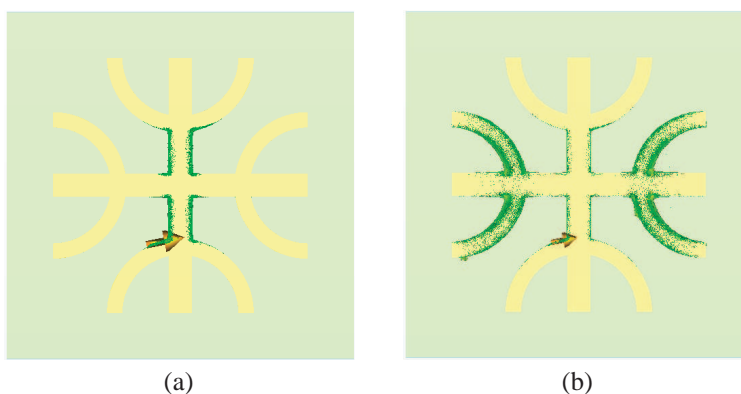


Figure 3: The current distributions on the surfaces of snowflake-type resonators: (a) at 0.952 THz, (b) at 1.818 THz..

that the maximum of the absorption rate could be achieved when the reflection rate meets the minimum value.

The final optimization geometry of the unit cell is given by: $a = 90 \mu\text{m}$, $l = 66 \mu\text{m}$, $w = 6 \mu\text{m}$, $r_1 = 19 \mu\text{m}$, and $r_2 = 15 \mu\text{m}$. The thickness of the polyimide dielectric spacer is only $10 \mu\text{m}$, whose relative permittivity is 3 and tangent loss is 0.03. The commercial software, CST Microwave Studio 2011, is used here for numerical simulations, which indicates that the proposed structure has two perfect absorption peaks at 0.952 THz and 1.818 THz with absorption rates reaching 99.7% and 99.9%, respectively, for the normal incidence THz wave, as is shown in Fig. 2. It is also shown that

the absorption rate can still maintained above 95% even when the incidence angle is increased to 40° .

In order to further investigate the absorption mechanism of the dualband absorber, the current distributions on the surfaces of snowflake-type resonators at 0.952 THz and 1.818 THz are presented in Fig. 3. It shows that at 0.952 THz, most of currents are distributed in the central cross structure while at 1.818 THz most of currents are distributed in the sideward semicircle structures, which implies that the central cross structure is responsible for the lower frequency absorption peak while the higher frequency absorption peak originates from the sideward semicircles.

3. DESIGN OF QUADBAND ABSORBER

Basing on the dualband absorber structure, we extend the unit cell in Fig. 1(a) to 2×2 of the snowflake elements, which is illustrated in Fig. 4(a). As presented in Fig. 4(b), the quadband absorber unit cell is composed of two sets of snowflake resonators with different geometrical parameters, which means we can achieve a quadband absorber by combining two different kinds of dualband absorber.

By carefully designing the geometrical parameters and layout of the snowflake-type resonators, four perfect absorption peaks are finally implemented as plotted in Fig. 5. The ultimate optimization geometry of the unit cell is given by: $a = 180 \mu\text{m}$, $l_1 = 80 \mu\text{m}$, $w_1 = 8 \mu\text{m}$, $l_2 = 64 \mu\text{m}$, $w_2 = 15 \mu\text{m}$, $r_{11} = 24 \mu\text{m}$, $r_{12} = 18 \mu\text{m}$, $r_{21} = 23 \mu\text{m}$, $r_{22} = 17 \mu\text{m}$. From the simulation result we acquire four excellent absorption peaks which appear at 0.752, 0.950, 1.454, and 1.696 THz with the absorption rates of 98.8%, 97.8%, 92.1%, and 90%, respectively, in the case of normal incidence. The wide angle performance is also investigated for the case of the quadband absorber which shows

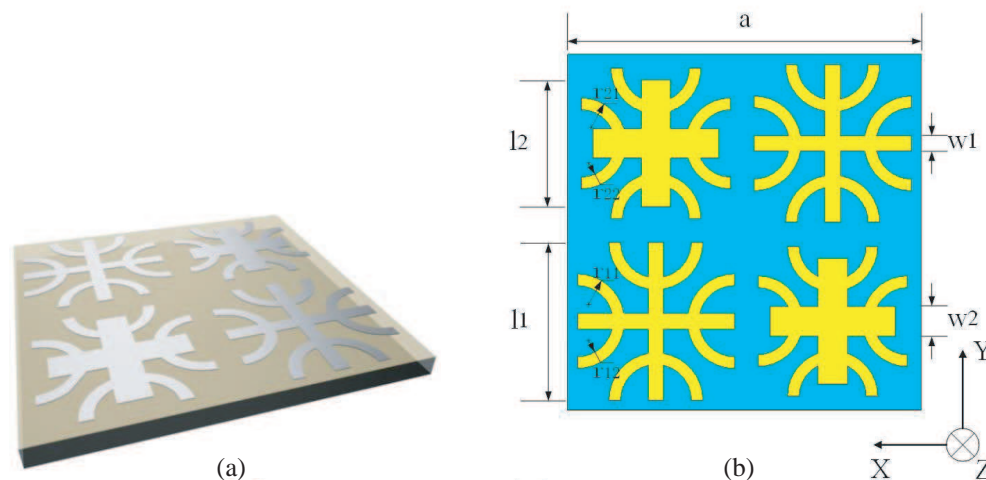


Figure 4: The structure of the quadband THz metamaterial absorber: (a) the perspective view of the unit cell, (b) the front view of the unit cell.

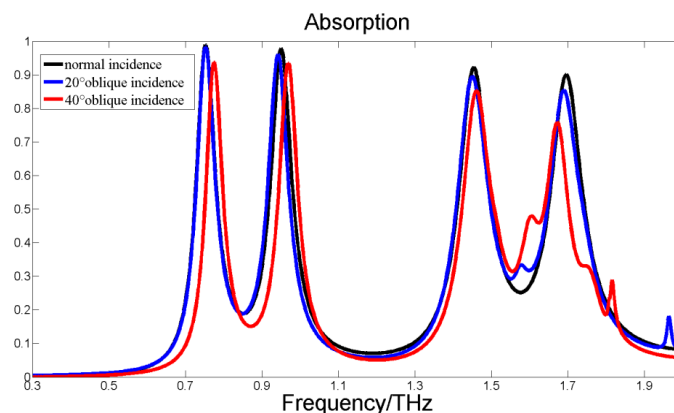


Figure 5: The simulated absorption spectra of the dualband absorber at various incident angles of THz waves.

that the structure still remain good absorptive performance even when the oblique incidence angle increase to 40° and the center frequencies of absorption peaks almost keep accord with the case of normal incidence.

Similar to the case of dualband absorber, only the particular part of the snowflake elements is resonant under each different absorption frequency. The current distributions on the surface of the structure at four resonant frequencies are omitted here.

4. CONCLUSION

In our paper, a series of ultrathin multiband THz metamaterial absorbers are proposed, in which the design, simulation and theoretical analysis of the absorbers are presented. The snowflake-type resonator is adopted to realize a dualband absorber and based on which a quadband absorber is subsequently achieved. Simulation results of both dualband and quadband absorbers are provided to verify our designs. And we've also drawn a conclusion that particular parts of the snowflake structures are responsible for each different absorption peaks by investigating the surface current distributions.

REFERENCES

1. Smith, D. R., J. B. Pendry, and M. C. K. Wiltshire, "Metamaterials and negative refractive index," *Science*, Vol. 305, No. 5685, 788–792, 2004.
2. Smith, D. R. and N. Kroll, "Negative refractive index in left-handed materials," *Physical Review Letters*, Vol. 85, No. 14, 2933, 2000.
3. Chen, H., B. I. Wu, B. Zhang, et al., "Electromagnetic wave interactions with a metamaterial cloak," *Physical Review Letters*, Vol. 99, No. 6, 063903, 2007.
4. Landy, N. and D. R. Smith, "A full-parameter unidirectional metamaterial cloak for microwaves," *Nature Materials*, Vol. 12, No. 1, 25–28, 2013.
5. Wen, Q. Y., H. W. Zhang, Y. S. Xie, et al., "Dual band terahertz metamaterial absorber: Design, fabrication, and characterization," *Applied Physics Letters*, Vol. 95, No. 24, 241111, 2009.
6. Tao, H., C. M. Bingham, A. C. Strikwerda, et al., "Highly flexible wide angle of incidence terahertz metamaterial absorber: Design, fabrication, and characterization," *Physical Review B: Condensed Matter and Materials Physics*, Vol. 78, No. 24, 241103R, 2008.
7. Landy, N. I., C. M. Bingham, T. Tyler, et al., "Design, theory, and measurement of a polarization-insensitive absorber for terahertz imaging," *Physical Review B*, Vol. 79, No. 12, 125104, 2009.
8. Tao, H., N. I. Landy, C. M. Bingham, et al., "A metamaterial absorber for the terahertz regime: Design, fabrication and characterization," *Optics Express*, Vol. 16, No. 10, 7181–7188, 2008.
9. Shen, X., Y. Yang, Y. Zang, et al., "Triple-band terahertz metamaterial absorber: Design, experiment, and physical interpretation," *Applied Physics Letters*, Vol. 101, No. 15, 154102, 2012.
10. Li, H., L. H. Yuan, B. Zhou, et al., "Ultrathin multiband gigahertz metamaterial absorbers," *Journal of Applied Physics*, Vol. 110, No. 1, 014909, 2011.

Analysis and Design of Multi-band Absorber with Periodic Three-dimensional Square Ring Units

Guorui Zhang, Yang Zhou, Nan Zhang, Peiheng Zhou, Haiyan Chen, and Longjiang Deng

State Key Laboratory of Electronic Thin Film and Integrated Devices

National Engineering Research Center of Electromagnetic Radiation Control Materials

University of Electronic Science and Technology of China, Chengdu 610054, China

Abstract— Multi-band electromagnetic (EM) wave absorbers have attracted considerable attention due to their wide practical applications such as antenna, stealth, and EM compatibility. In this paper, we present the simulation, implementation, and measurement of a unconventional multi-band metamaterial absorber, which appears as a cube and is composed of square ring resistive sheets with a metal plane laid at the bottom of the structure. The simulation and experiment results show that the proposed structure can eliminate the total reflection of planer structure and excite multi-resonant peaks at the same time. The proposed EM absorber could exhibits a promising and flexible method to control the propagation of the EM wave and to extend the absorption bandwidth greatly.

1. INTRODUCTION

Since N. I. Landy et al. proposed a perfect metamaterial absorber (MA) composed of electric resonators and cut wires, the researchers have shown extreme interest in the design of absorbers with nearly perfect absorption by means of using artificial electromagnetic metamaterials [1]. A great deal of efforts and works have been devoted to this field. But most of them focus on design an planer absorber exhibiting excellent performance with single-band or multi-band [2–4] and there is little information available in literatures about 3D multi-band absorbers [5, 6]. Especially, in the case of a absorber with a polyurethane foam substrate, the total reflect will occur at some frequencies for the reason that the thickness of the structure and the operating wavelength are equal.

Aiming at the above problems, the goal of this paper is thus to propose a novel multi-band metamaterial absorber, which appears as a cube and is composed of square ring resistive sheets with a metal plane laid at the bottom of the structure. By both numerical simulations and experimental measurements, the proposed structure eliminates the total reflection of planer structure quite well. Nearly perfect absorption can be achieved at resonant frequencies. The result demonstrated that the EM absorber could exhibits a promising and flexible method to control the propagation of the EM wave and to extend the absorption bandwidth greatly. Although the modeling and experiments are done in microwave frequencies, the absorber can be easily scaled to find applications at higher frequency regimes.

2. DESIGN AND SIMULATION

The proposed 3D multi-band metamaterial structure is shown in Fig. 1. Consider a uniform plane wave with \vec{E} along the positive direction of y axis normally incident on the cubic absorber.

The absorbance can be expressed as: $A = 1 - |S_{11}|^2 - |S_{21}|^2$, where $S_{11} = \frac{Z-1}{Z+1}$ is the reflectivity and $Z = \sqrt{\frac{\mu_r}{\epsilon_r}}$ is the characteristic impedance of the cube. In the expression of Z , ϵ_r and μ_r are the effective relative permittivity and permeability of the whole structure respectively.

Since the ground plane of the structure is metal the transmission coefficient S_{21} will be zero. Thus, the expression of A will become $A = 1 - |S_{11}|^2$. And the absorbance can be maximized by reducing the reflection from the structure.

In order to investigate the performance of the cube absorber in microwave region a full-wave electromagnetic simulation has been performed with a help of CST Studio Suite 2011. A unit cell boundary condition is set to calculate the reflective coefficient S_{11} . By parameters optimizing, the final geometric values of the cube are employed as $a_0 = 17$ mm, $a = 14$ mm, $w = 3.65$ mm, $R_{sq1} = 185\Omega$ and $R_{sq2} = 70\Omega$, respectively.

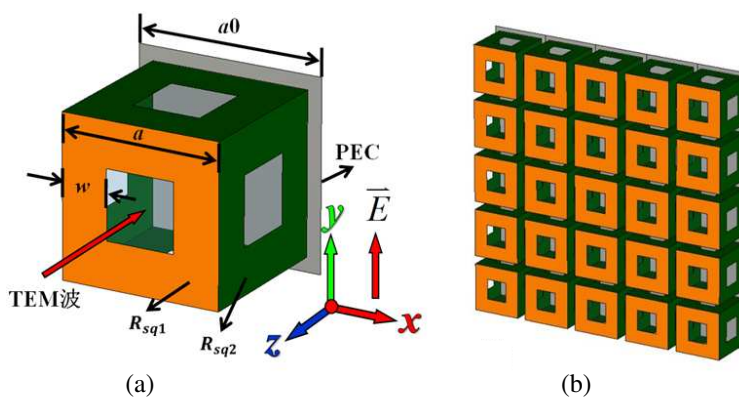


Figure 1: (a) One unit of the structure; (b) The 3D periodic array of the structure.

3. RESULTS AND ANALYSIS

According to the optimized model, the absorbance A is calculated by Microwave studio of CST Studio Suite 2011 and the result is shown in Fig. 2.

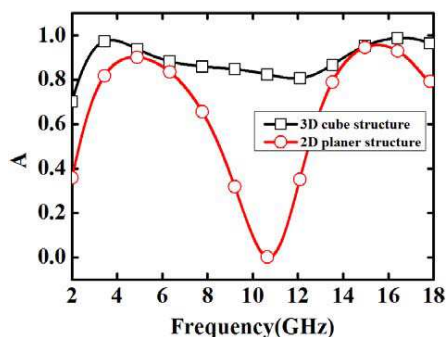


Figure 2: Result of simulation: A-1 is the absorbance of 3D cube structure and A-2 is the absorbance of corresponding planer having no lateral resistive sheets

In case of having no lateral resistive sheets of the cube, the structure will turn as a planar construction with a large thickness. When a uniform planar TEM wave irradiate on the surface of the structure, a total reflection, as shown in Fig. 2 will occur at 10.7 GHz for the reason that the thickness of the structure equals to half of the operating wavelength. However, if there are four resistive sheets printed on each side of the lateral surface, the total reflective peak at 10.7 GHz will be avoided since the interaction between these resistive sheets and the incident electromagnetic wave, as shown in Fig. 2. For 3D cube structure, the resonant peaks of planer structure at 4.8 GHz and 15.5 GHz shift to 3.7 GHz and 16.6 GHz. The absorbance is improved largely. The 90% absorbing bandwidth is from 2.7 GHz to 5.8 GHz and 14 GHz to 18 GHz. During almost the whole frequency range, from 2.5 GHz to 18 GHz, the absorbance is larger than 80%.

To gain a physical insight into the origin of the absorption peaks, electric field distribution in the absorbing structure at various resonant frequencies is obtained (see Fig. 3).

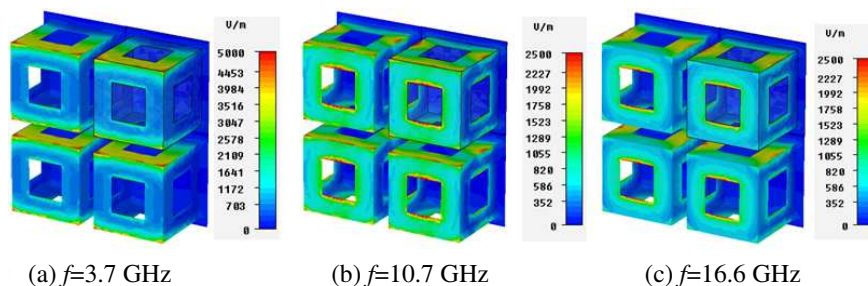


Figure 3: The electric field distribution of the proposed structure at different frequencies.

Benefiting from the loss of electric power by the square ring resistive sheets which are perpendicular to the metal plane, the total reflection of planer structure with thickness equaling to half of the operating wave length is eliminated quite well as shown in Fig. 3(b). In addition, due to the interreaction between the lateral square ring resistive sheets of the cube and the incident wave, the square ring resistive sheets near the top of the cube offers strong absorption for low frequency EM wave at 3.7 GHz while the ones near the bottom of the cube strongly absorb the high frequency EM waves at 16.6 GHz as shown in Figs. 3(a) and (c).

4. EXPERIMENTAL VERIFICATION

Based on the simulation setups, experiments have been also done to validate the absorption behavior of the proposed absorbing structures with a typical schematic photo shown in Fig. 4.

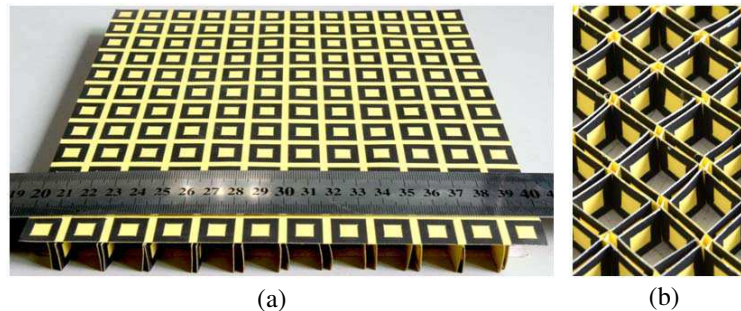


Figure 4: The fabricated absorbing structure with resistive square ring: (a) plan view and (b) partial enlarged view of the resistive sheets perpendicular to PEC.

The resistive sheet of the structure is produced by silk screen printing technology and the total dimension is 200 mm * 200 mm. Before test, the surface resistance of the resistive sheet is measured with a four-point resistivity test system and the results show that there is a reasonable resistance error (about $\pm 10\%$) between the simulation requirement and the practical printing.

Finally, the absorbance of the proposed absorber is measured. The result dovetailed quite well is shown in Fig. 5 compared with simulation. Two absorbing peaks are obtained at 3 GHz and 14 GHz, while the total reflective peak is restrained very well at 10.7 GHz.

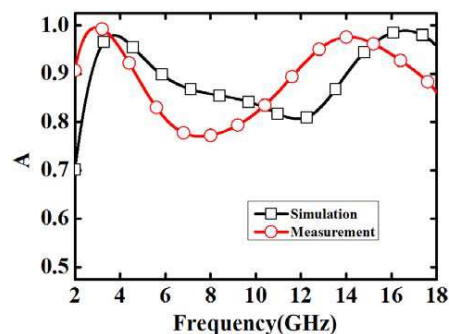


Figure 5: Absorbance comparison of the simulation and measurement.

5. CONCLUSIONS

In summary, a unconventional multi-band metamaterial 3D-cube absorber was proposed for multi-band microwave absorption in frequency range of 2–18 GHz. By the means of calculating the reflective coefficient and analyzing the distribution of the electric field, it is demonstrated that the cube absorber can eliminate the total reflect of the planer structure quite well. Meanwhile, the absorbing strength is largely improved compared with the planer absorber. This work provides a new solution to design multi-band absorbing structure without inducing the phenomenon of total reflect. Although the modeling and experiments are done in microwave frequencies, the absorber can be easily scaled to find applications at higher frequency regimes.

REFERENCES

1. Landy, N. I., S. Sajuyigbe, J. J. Mock, D. R. Smith, and W. J. Padilla, “Perfect metamaterial absorber,” *Physical Review Letters*, Vol. 100, No. 20, 207402, 2008.
2. Wang, B., T. Koschny, and C. M. Soukoulis, “Wide-angle and polarization-independent chiral metamaterial absorber,” *Physical Review B*, Vol. 80, No. 3, 33108, 2009.
3. Singh, P. K., K. A. Korolev, M. N. Afsar, and S. Sonkusale, “Single and dual band 77/95/110 GHz metamaterial absorbers on flexible polyimide substrate,” *Applied Physics Letters*, Vol. 99, No. 26, 264101, 2011.
4. Zhang, G. R., P. H. Zhou, H. B. Zhang, L. B. Zhang, J. L. Xie, and L. J. Deng, “Analysis and design of triple-band high-impedance surface absorber with periodic diversified impedance,” *Journal of Applied Physics*, Vol. 114, No. 16, 164103, 2013.
5. Li, W., T. Wu, W. Wang, J. Guan, and P. Zhai, “Integrating non-planar metamaterials with magnetic absorbing materials to yield ultra-broadband microwave hybrid absorbers,” *Applied Physics Letters*, Vol. 104, No. 2, 022903, 2014.
6. Fang, F., Y. Cheng, and H. Liao, “Numerical study on a three-dimensional broadband isotropic left-handed metamaterial based on closed rings,” *Physica Scripta*, Vol. 89, No. 2, 025501, 2014.

Electromagnetic Scattering Controlling for a Rectangular Groove with High Impedance Surfaces Loading

Dongjiao Guo, Haiyan Chen, Peiheng Zhou,
Xingxing Huang, Jianliang Xie, and Longjiang Deng

National Engineering Research Center of Electromagnetic Radiation Control Materials
State Key Laboratory of Electronic Thin Film and Integrated Devices
University of Electronic Science and Technology of China, Chengdu 610054, China

Abstract— In this paper, a possible solution for controlling electromagnetic scattering from a rectangular groove is presented based on high impedance surfaces (HIS) loaded on the two sides of the considering groove. The HIS is realized by loading the H-shape frequency selective surfaces on a grounded dielectric layer, which is optimized according to the relationship between the scale parameters and its dispersion diagrams. The use of HIS resulting in a significant scattering suppression for the groove over a wide angular range for transverse magnetic (TM) polarization, and the maximum reduction of RCS can reach 17 dB compared with the original structure. Moreover, the monostatic radar cross section (RCS) reduction with the proposed method is superior to other methods such as loading resistive sheets.

1. INTRODUCTION

As a basic requirement of modern fighter aircraft, improving the stealth properties is becoming an inevitable trend. However, there are many scattering sources on the aircraft, such as angular diffraction, cavity scattering and specular reflection, which can cause strong electromagnetic (EM) scattering and contribute to the radar cross section (RCS) [1]. With the development of low observable technology, the main scattering sources mentioned above are effectively controlled, and the scattering resulting from surface defects such as groove is becoming a prominent part in total scattering, especially in some polarization and incident angles. Therefore controlling the scattering caused by groove is becoming an important issue in the stealth technology [2–4].

With the increase of study interest in controlling groove scattering, various measures are proposed. Among the most practical and commonly used technique is filling the groove with materials to form a smooth contoured exterior surface [5, 6]. However, in most cases filling the groove with materials cannot be fully achieved. For example, in military vehicles, discontinuities occur inevitably at the interface between two different materials where two dissimilar parts of the vehicle meet, such as the interface between a radome and the vehicle skin. For these considerations, there are also other methods that can reduce the groove radiation without affecting the total area. One of the methods is introducing a step of proper height between the medium and groove, and then filling the step with a material to make impedance-matching thus the radiation is reduced [7]. Besides, according to the transmission line theory, the scattering can also be controlled by loading the resistive sheets around the groove [8]. However, the ways proposed in [7, 8] only considered the scattering suppression in a single incident angle.

In this paper, a method of loading high impedance surfaces (HIS) to suppress groove scattering is proposed. Different from the method of impedance-matching to control groove scattering, the method proposed here is based on surface-wave bandgap properties of HIS [9] to hinder the propagation of surface waves. The HIS is optimized according to dispersion diagrams with different scale parameters. Then the scattering problem of HIS loading in different incident angles at TM polarization (the electric field vector is parallel to the plane of incidence) is analyzed, and the monostatic RCS is also calculated by method of moments (MOM), and is compared with the case of loading resistive sheets. Furthermore, the E-field intensity in the groove channel is also analyzed to validate this method.

2. DESIGN OF HIS

The building block of our design consists of a metallic array of sub-wavelength sized capacitive loaded strip (CLS) inclusions and a metal ground plane, separated by a dielectric spacer of relative permittivity ϵ_r , is shown in Fig. 1. The CLS inclusion has been chosen among others due to its well established and easily adjustable electromagnetic specifications [10, 11]. The size of a unit cell

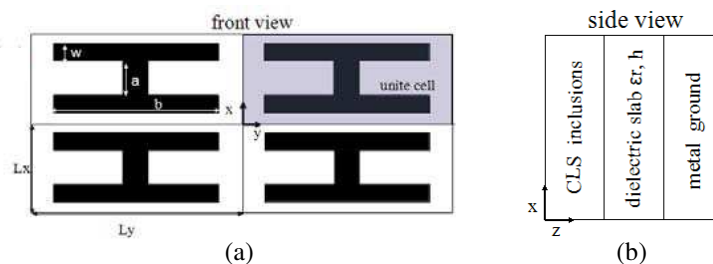


Figure 1: (a) Front view of the designed HIS. (b) Side view of the HIS.

is given by L_x and L_y . The dimension of a single CLS is determined by its vertical a and lateral b arm lengths, each being strips of width w .

An equivalent circuit model based on coupled microstrip line theory [12, 13] is used to design HIS. Through the optimization design, the structural parameters are taken as $L_x = 3.8$ mm, $L_y = 9$ mm, $w = 0.75$ mm, $a = 1.5$ mm, respectively, and the permittivity of the dielectric slab is taken as $\epsilon_r = 3.9$.

The dispersion diagram of surface waves propagating along the periodic HIS structure is calculated by the eigenmode solution [14]. The simulation is based on a unit cell and assumes that the model extends to infinity in the x, y -plane through the application of periodic boundary conditions. Fig. 2 shows the behavior of the dispersion diagram as a function of the dimension parameter b . As shown in Fig. 2, the cut-off frequency of TM waves decreases with the increasing of parameter b . According to Figs. 2(a) and (b), we can see that the HIS support TM modes $kL_x = 70^\circ$ and 85° when $b = 5$ mm and 6 mm at the frequency of 10 GHz, the kL_x can be defined in [9]. However, Figs. 2(c) and (d) show that there is no TM mode existing on the HIS structure in the cases of $b = 6.6$ mm and $b = 7$ mm in the frequency of 10 GHz, which meet the requirement of suppressing the propagation of TM surface waves. For the consideration of minimizing the size, we select the HIS of $b = 6.6$ mm to be loaded on the two sides of the groove.

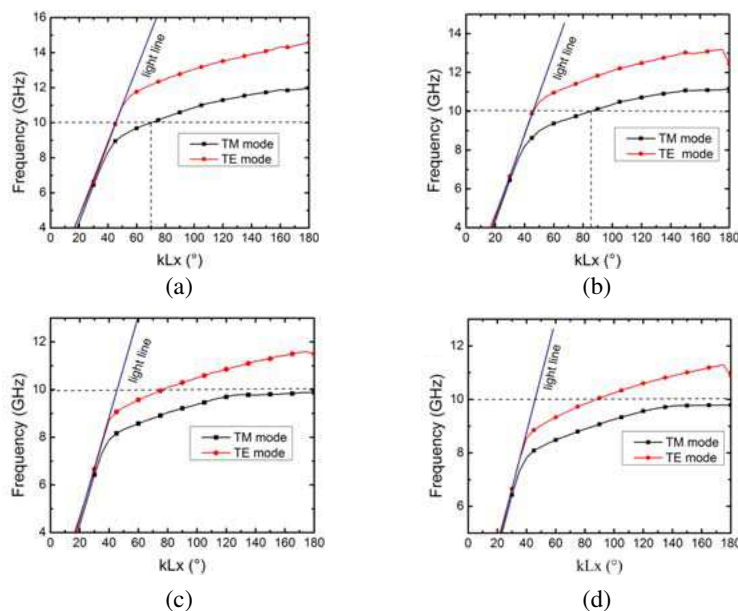


Figure 2: Dispersion diagrams of the HIS with different b . (a) $b = 5$ mm, (b) $b = 6$ mm, (c) $b = 6.6$ mm, (d) $b = 7$ mm.

3. RESULTS AND DISCUSSION

In this paper, the scattering properties of a rectangular groove in a finite perfect electric conductor (PEC) plate will be discussed, and its topology is shown in Fig. 3. Considered that strong EM radiation will be induced if the propagation direction of the incident waves is orthogonal to the edge of the plate, the groove is located at the diagonal position of the PEC plate.

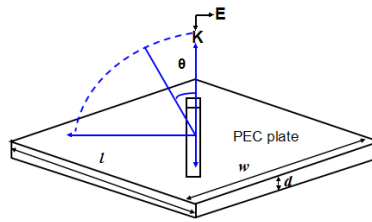


Figure 3: PEC plate with a rectangular groove. Parameters for the PEC plate are: $l = 130$ mm, $w = 30$ mm and $d = 6$ mm, parameters for the groove are: length $l' = 90$ mm, width $w' = 5$ mm and depth $d' = 5$ mm

Based on the MoM, the monostatic RCS of a rectangular groove in a finite PEC plate are computed, and the case of no groove PEC plate with similar size are also proposed for comparison, just as shown in Fig. 4. For small incident angles, the groove scattering is not apparent whether TE or TM polarizations, because the scattering is mainly caused by the specular reflection under this condition. For TE polarization, the existence of the groove has no obvious influence on the RCS with the increase of the incident angle, because the surface waves cannot exist on the PEC plate and the propagation through the groove is impossible. However, for TM polarization, the surface waves can emerge on the PEC plate and cause strong scattering when it go through the groove. The polarization-dependent phenomenon of the groove is consistent with the theory mentioned in [1]. Considering the polarization-dependent of the groove, only EM scattering properties of TM polarization is analyzed in the following discussion.

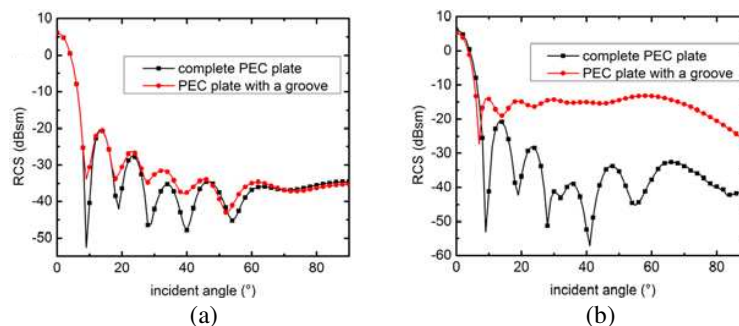


Figure 4: Monostatic RCS of groove in PEC plate compared with a complete PEC plate for various incident angles. (a) TE -polarization, (b) TM -polarization.

Then the scattering properties of the finite metal groove with loading the designed HIS is discussed. The loading operation is performed in two stages. Firstly, two discontinuity steps between PEC plate and groove are introduced on the two sides of the groove, just as shown in Fig. 5(a). The structure dimensions of the introduced steps are $l = 90$ mm, $a = 38$ mm, $d = 1.5$ mm. Nextly, the steps are filled with the designed HIS, just as shown in Fig. 5(b).

To identify the validity of HIS loading, it is necessary to compare the scattering results of the monostatic RCS with other conditions: the original structure and the case of filling the steps with resistive sheets proposed in [8]. As the Fig. 6 shows, in comparison with resistive sheets loading, the HIS loading can reduce the RCS over a wider angular range and the maximum reduction can reach 17 dB at the incident angle $\theta = 14^\circ$.

Furthermore, in order to check whether the HIS loading reduces EM penetration through the groove, we calculate the E -field intensity at the middle plane inside the groove channel (Fig. 7(a)). Fig. 7(b) shows the E -field intensity inside the groove channel with and without HIS loading at the maximum RCS reduction angle of $\theta = 14^\circ$, x and y represent the different positions in the calculated plane. As shown in Fig. 7, by HIS loading, the E -field intensity inside the groove channel is decreased nearly in all the positions, and the fields are significantly reduced at the front edge ($x = 2.5$ mm) of the groove, thus leading to a reduction of the EM radiation induced by the groove. The variation in E -field intensity is consistent with the simulation results of monostatic RCS.

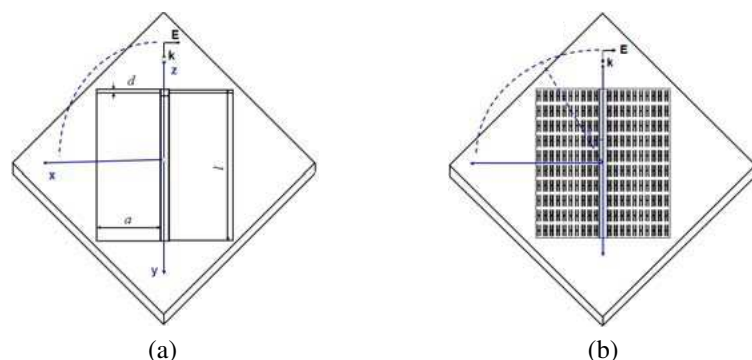


Figure 5: The HIS loading operation. (a) The introduced steps. (b) Filling the steps with designed HIS.

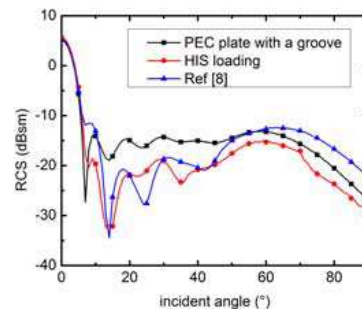


Figure 6: Scattering diagram from a rectangular groove with different loading.

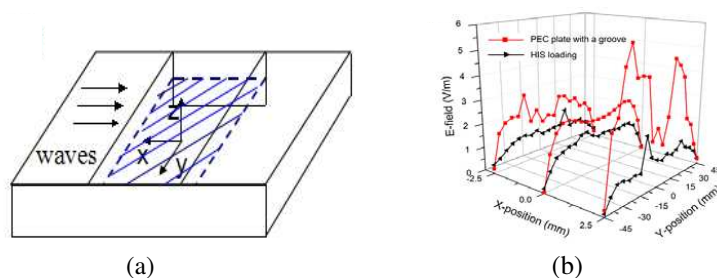


Figure 7: E -field in the rectangular groove channel. (a) The calculated plane in the groove channel. (b) E -field in the calculated plane.

4. CONCLUSION

This paper presents a method of HIS loading to control EM scattering of grooves while maintaining the overall see-through size. The method is based on the surface-wave bandgap properties of HIS to suppress the surface waves penetrating through the groove. The HIS is optimized according to the dispersion diagrams with different structure parameters. The monostatic RCS with different loading are tested numerically using the MOM method. It is observed that a significant RCS reduction of up to 17 dB can be achieved in comparison to the case of the unloaded groove. Furthermore, compared the resistive sheets loading, the RCS reduction can be derived over a wider incident angular range. Finally, the E -field intensity in the groove channel is also analyzed and validate the proposed HIS loading for reducing the monostatic RCS of the groove target.

ACKNOWLEDGMENT

This research was partially supported by the National Natural Science Foundation of China (Grant No. 51301031) and the fundamental research funds (Project No. ZYGX2013J029).

REFERENCES

1. Knott, E. F., J. Shaeffer, and M. Tuley, *Radar Cross Section*, SciTech Publishing, 2004.
2. Richardson, D., *Stealth Warplanes*, Zenith Imprint, 2001.
3. Simpson, G. R., "Electromagnetic scattering from a gap in a magneto-dielectric coating on an infinite ground plane," No. AFIT/DS/ENG/02-03, Air Force Inst. of Tech. Wright-Patterson AFB (Ohio) School of Engineering, 2002.
4. Senior, T. B. A. and J. L. Volakis, "Scattering by gaps and cracks," *IEEE Transactions on Antennas and Propagation* Vol. 37, No. 6, 744–750, 1989.
5. Barkeshli, K. and J. L. Volakis, "Scattering from narrow rectangular filled grooves," *IEEE Transactions on Antennas and Propagation*, Vol. 39, No. 6, 804–810, 1991.
6. Choi, W.-H., et al., "Monostatic RCS reduction by gap-fill with Epoxy/MWCNT in groove pattern," *Journal of Electromagnetic Engineering And Science*, Vol. 12, No. 1, 101–106, 2012.

7. Kohin-Nitschelm, M., “Reduction of scatter from material discontinuities,” U.S. Patent No. 5,570,092, Oct. 29, 1996.
8. Ramahi, O. M. and L. Li, “Analysis and reduction of electromagnetic field leakage through loaded apertures: A numerical study,” *Electromagnetics*, Vol. 25, Nos. 7–8, 679–693, 2005.
9. Abhari, R. and G. V. Eleftheriades, “Metallo-dielectric electromagnetic bandgap structures for suppression and isolation of the parallel-plate noise in high-speed circuits,” *IEEE Transactions on Microwave Theory and Techniques*, Vol. 51, No. 6, 1629–1639, 2003.
10. Ziolkowski, R. W., “Design, fabrication, and testing of double negative metamaterials,” *IEEE Transactions on Antennas and Propagation*, Vol. 51, No. 7, 1516–1529, 2003.
11. Donzelli, G., et al., “Metamaterial made of paired planar conductors: Particle resonances, phenomena and properties,” *Metamaterials*, Vol. 3, No. 1, 10–27, 2009.
12. Bahl, I. J., *Lumped Elements for RF and Microwave Circuits*, Artech House, 2003.
13. Hosseini, M. and M. Hakkak, “Characteristics estimation for Jerusalem cross-based artificial magnetic conductors,” *IEEE Antennas and Wireless Propagation Letters*, Vol. 7, 58–61, 2008.
14. Remski, R., “Analysis of photonic bandgap surfaces using Ansoft HFSS,” *Microwave J.*, Vol. 43, No. 9, 190–199, 2000.

A Novel Tri-band Patch Antenna Based on Complementary Triangle Split Ring Resonator Pair

J.-G. Liang¹, Z.-J. Song¹, L.-J. Yu², and X.-F. Zhang¹

¹Air and Missile Defense College, Air Force Engineering University, Xi'an 710051, China

²Center for Health Management and Policy, Shandong University, Jinan 250012, China

Abstract— A new resonant-type composite right/left-handed transmission line (CRLH TL) is proposed based on the combination of a complementary triangle split ring resonator pair (CTSRRP) etched on the ground plane and a series gap embedded in the conductor strip of a microstrip line. The CTSRRP, which is composed of two identical complementary triangle split ring resonators (CTSRR) with back-to-back splits, demonstrates negative permittivity. Besides, a center branch is added to the middle of each triangle split ring to divide it into two parts. In virtue of this, two current paths of different length are formed which primarily improve the multi-band characteristic of the transmission line (TL). The equivalent capacitor-inductor circuit model is put forward to analyze the TL. The S parameters are derived from electromagnetic full-wave simulation through simulation engine Ansoft HFSS13. Then the dispersion curve of the proposed structure is calculated based on S parameters to attest the left-handed characteristics. Two left-handed bands and two right-handed bands are observed from the dispersion curve. To demonstrate the applicability of the new type TL, a tri-band patch antenna of C band is designed and fabricated. Good agreement between simulated and measured return loss is obtained. Measured results present that three available bands centered at 4.45 GHz, 5.55 GHz and 7.35 GHz respectively are acquired. Peak gain of more than 7 dB and invariable radiation characteristics can be observed from the simulated radiation patterns. And the cross polarization in working bands is less than -15 dB with the minimal touching bottom of -55 dB.

1. INTRODUCTION

Left-handed metamaterials became a subject of intensive research when the first left-handed medium was fabricated and demonstrated with negative refractive index by Smith et al. [1]. Since then, metamaterial transmission lines have exhibited great value in the implementation of novel microwave components and antennas because of their unusual properties. In 2002, Caloz and Itoh [2] proposed a new method to realize metamaterials by using transmission line. Owing to the unavoidable parasitical right-handed effect, this metamaterial transmission line with composite right/left-handed (CRLH) behavior is also defined as the so-called composite right/left-handed transmission line (CRLH TL) with useful and unusual electromagnetic properties. In 2004, complementary split ring resonators (CSRRs) were proposed with negative permittivity [3] and were accompanied with a capacitive gap to obtain left-handed behavior by Falcone et al. [4], which was considered a breakthrough in this area and in turn opened a way to another crucial innovative orientation of metamaterial transmission line, namely the resonant-type CRLH TL.

In this paper, a new resonant-type CRLH TL based on a complementary triangle split ring resonator pair (CTSRRP) is proposed for a tri-band patch antenna. The CTSRRP is composed of two identical complementary triangle split ring resonators (CTSRRs) with back-to-back splits and a center branch is added to the middle of each triangle ring to divide the triangle split rings into two parts. The antenna which is easier to be fabricated because no grounded via is needed exhibits good performance in impedance width and radiation patterns.

2. ANALYSIS OF CTSRRP ELEMENT

As shown in Fig. 1, the CTSRRP is etched on the ground plane beneath two metal patches separated by a gap. The metal patches are depicted in grey in Fig. 1(a) and the CTSRRP is depicted in Fig. 1(b). The 1.5 mm-thick substrate with a dielectric constant $\epsilon_r = 2.65$ and a loss tangent $\tan \delta = 0.001$ is chosen for all simulation and antenna design. After optimization, the dimensions are: $L = 10$ mm, $L_p = 13$ mm, $W_p = 18$ mm, $g = 0.3$ mm, $g_1 = 0.4$ mm. And the width of the slot between the two patches is $g_2 = 0.2$ mm.

Figure 1(c) depicts the lumped-element equivalent circuit model of this resonant-type CRLH TL. Two smaller CTSRRs are formed because of the center branches added to the middle of the triangle rings. Corresponding to the two current paths engendered by the CTSRRs of different

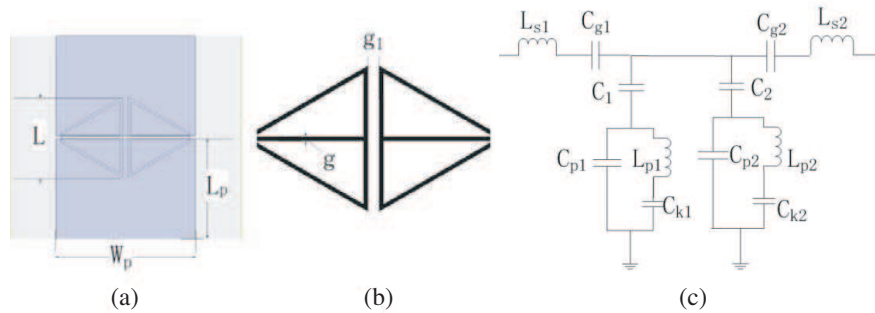


Figure 1: Topology of the proposed CRLH TL. (a) Top view. (b) Bottom view. (c) Equivalent circuit model.

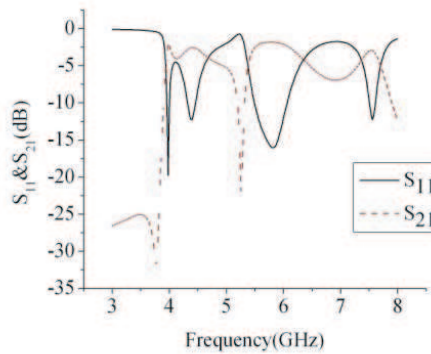


Figure 2: Frequency response of the CTSRRP-loaded CRLH TL.

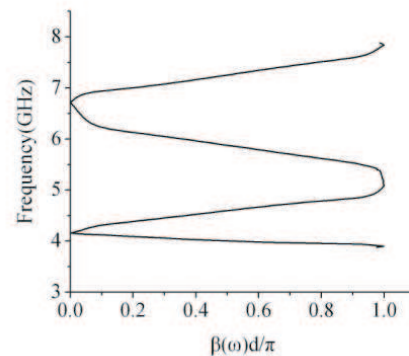


Figure 3: Dispersion curve of the CTSRRP-loaded CRLH TL.

size, there are two shunt resonant tanks formed by C_p , L_p and C_k modeling respectively the two CTSRRs of different size in the circuit model. The capacitances C_{g1} and C_{g2} model the series gap. The inductances L_{s1} and L_{s2} model the line inductance. C_1 and C_2 represent partially the line capacitance and partially the electrical coupling between the series gap and the CTSRRP. C_{k1} and C_{k2} are applied to model the resultant interaction between the two CTSRRs.

Figure 2 shows the frequency response of the CTSRRP-loaded CRLH TL obtained from electromagnetic full-wave simulation through simulation engine Ansoft HFSS13. As can be observed, the CRLH TL element performs nice characteristic of multi-band which foreshow its application in the following antenna.

The mathematical formula of dispersion curve is:

$$|\beta(\omega)d| = \left| \text{Re} \left[\arccos \left(\frac{1 - S_{11}S_{22} + S_{12}S_{21}}{2S_{21}} \right) \right] \right| \quad (1)$$

Here d denotes the dimension of one CRLH TL element.

According to (1), the dispersion curve of the proposed structure that is shown in Fig. 3 can be derived from the S parameters. It is obvious that one element of the CTSRRP-loaded CRLH TL has two left-handed bands and two right-handed bands in which the four resonant frequencies in Fig. 2 situate respectively. In general, the results in Fig. 2 and Fig. 3 give strong support to demonstrate the left-handed performance of the proposed structure.

3. APPLICATION IN ANTENNAS

To demonstrate the possibility of employing this new kind of artificial CRLH TL in the design of antennas, a tri-band patch antenna has been designed and fabricated. The topology of the antenna is shown in Fig. 4. It is the same with that in Fig. 1 except for the two segments of feeding line added to match with the 50Ω SMA connector. The geometrical parameters are $W_{s1} = 3$ mm, $L_{s1} = 7.8$ mm, $W_{s2} = 1.3$ mm and $L_{s2} = 8$ mm. Other dimensions are the same with those in Fig. 1.

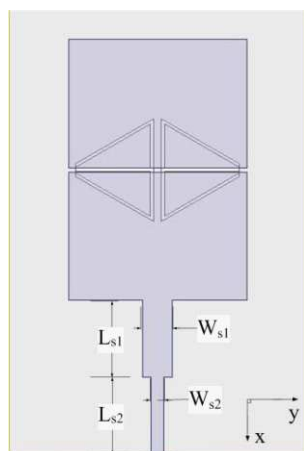
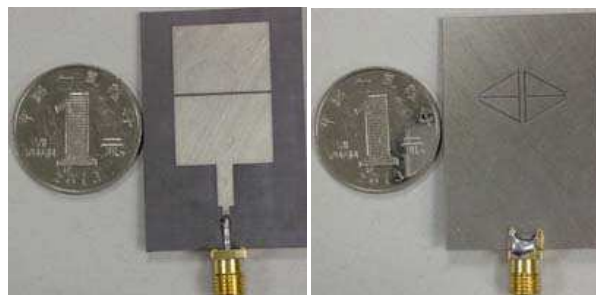


Figure 4: The topology of the designed antenna.



(a)

(b)

Figure 5: Photograph of fabricated antenna. (a) Top view. (b) Bottom view.

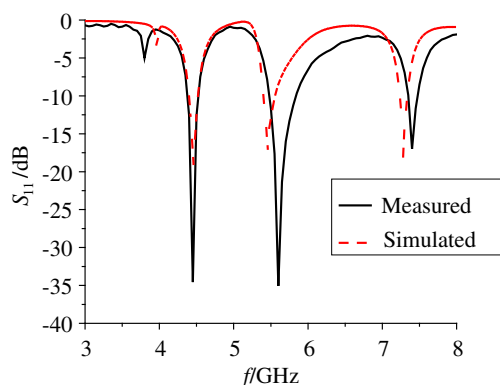


Figure 6: Simulated and measured return loss.

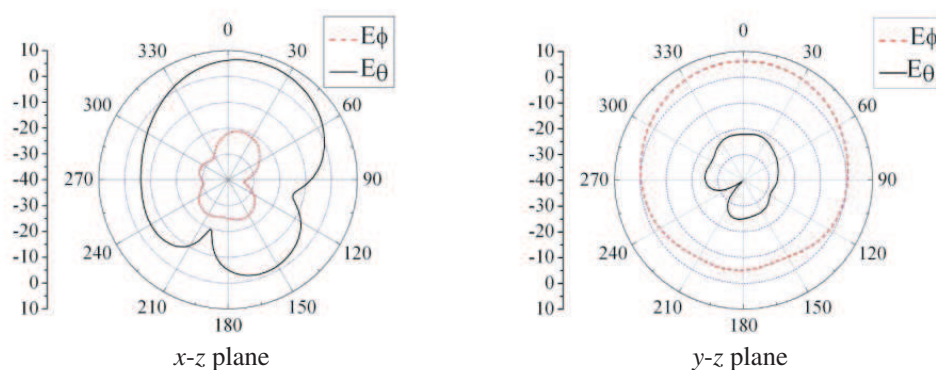


Figure 7: Radiation patterns at 4.45 GHz.

Figure 5 shows the photograph of fabricated antenna. Fig. 6 shows the simulated and measured return loss of the antenna. Good agreement between measured and simulated results is obtained except for a slight discrepancy in the higher bands. This discrepancy is partially attributable to the error of the dielectric constant of the utilized substrate and is partially induced by the tolerances of the dimensions that are inherent in the fabrication process. Almost the same results are obtained when regarding the tolerances in simulation. From the measured results, the three frequency bands are centered at 4.45 GHz, 5.55 GHz and 7.35 GHz with 10 dB impedance bandwidth of 130 MHz, 350 MHz and 110 MHz respectively. It is also observed that the first resonant point centered at 3.85 GHz can not work well. This is because the matching condition is not satisfied. It can be found that the first (centered at 3.85 GHz) and third (centered at 5.55 GHz) band belong to left-handed

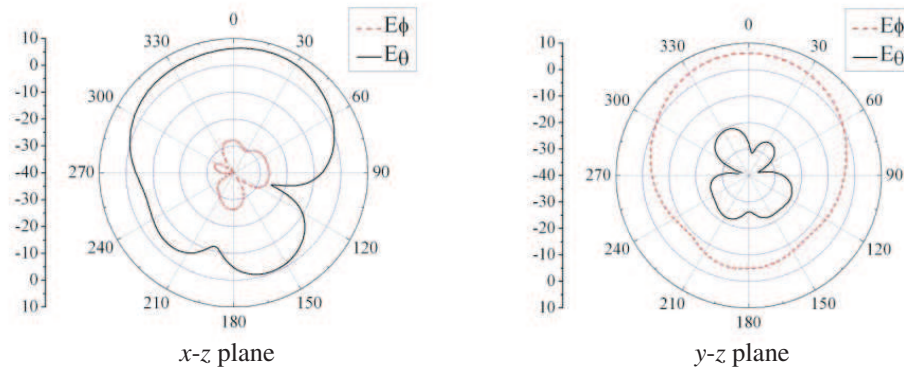


Figure 8: Radiation patterns at 5.55 GHz.

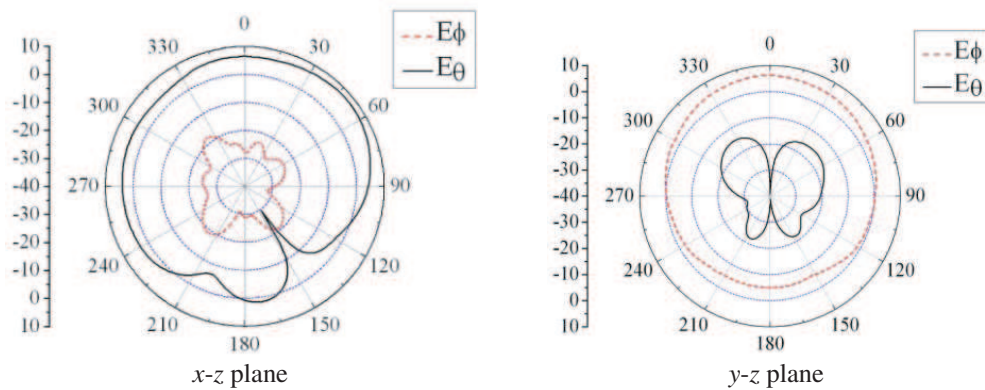


Figure 9: Radiation patterns at 7.35 GHz.

bands and the second (centered at 4.45 GHz) and fourth (centered at 7.35 GHz) band belong to right-handed bands when comparing Fig. 3 with Fig. 6 together.

Further simulated results have shown that all the three useful bands shift downwards when L increases but the third band shift very slightly. The increase in L is in the mechanism directly enhancing C_{p1} and C_{p2} and indirectly enhancing C_1 and C_2 . The increase of g_2 which brings on decrease of C_{g1} and C_{g2} will result in upwards shifting of the second and third bands. While changes in both g and g_1 make little influence.

The simulated radiation patterns for the center frequencies of the three useful bands are presented in Figs. 7~9. It can be observed that the antenna has a relatively invariable radiation patterns at different frequencies. The antenna radiates like the conventional patch antenna except for the comparatively big back lobe because of the existence of the CTSRRP on the ground. A peak gain of 6.8 dB to 7.9 dB is obtained for all the three center frequencies. The maximum cross polarization is less than -19 dB at x - z plane and -15 dB at y - z plane for all different center frequencies.

4. CONCLUSION

A new type of CRLH TL with performance of multi-band is proposed. Simulated and calculated results demonstrate that the new type TL has two left-handed bands and two right-handed bands. A novel tri-bands patch antenna of C band is proposed and fabricated based on the proposed TL. Measured and simulated results show that this antenna exhibits splendid impedance characteristic and radiation patterns and a peak gain of more than 7 dB is obtained.

ACKNOWLEDGMENT

This work is supported by the National Natural Science Foundation of China under Grant No. 61372034. Special thanks should also be delivered to the 206th study of China North Industries Group Corporation for the fabrication.

REFERENCES

1. Smith, D. R., W. J. Padilla, D. C. Vier, S. C. Nemat-Nasser, and S. Schultz, “Composite medium with simultaneously negative permeability and permittivity,” *Phys. Rev. Lett.*, Vol. 84, 4184–4187, 2000.
2. Caloz, C. and T. Itoh, “Application of the transmission line theory of left-handed (LH) materials to the realization of a microstrip LH transmission line,” *Proc. IEEE-AP-S USNC/URSI National Radio Science Meeting*, Vol. 2, 412–415, San Antonio, TX, Jun. 2002.
3. Falcone, F., T. Lopetegui, J. D. Baena, R. Marques, F. Martín, and M. Sorolla, “Effective negative-1 stop-band microstrip lines based on complementary split ring resonators,” *IEEE Microw. Wirel. Compon. Lett.*, Vol. 14, 280–282, 2004.
4. Falcone, F., T. Lopetegui, M. A. G. Laso, et al., “Babinet principle applied to the design of metasurfaces and metamaterials,” *Phys. Rev. Lett.*, Vol. 93, 197401, 2004.
5. Niu, J.-X., “Dual-band dual-mode patch antenna based on resonant-type metamaterial transmission line,” *Electronics Letters*, Vol. 46, No. 4, 266–268, 2010.
6. Xu, H.-X., G.-M. Wang, C.-X. Zhang, Z.-W. Yu, and X. Chen, “Composite right/left-handed transmission line based on complementary single-split ring resonator pair and compact power dividers application using fractal geometry,” *IET Microwaves, Antennas & Propagation*, Vol. 6, 1017–1025, 2011.
7. Liang, J.-G. and H.-X. Xu, “Harmonic suppressed bandpass filter using composite right/left handed transmission line,” *Journal of Zhejiang University — Science C*, Vol. 13, No. 7, 552–558, 2012.

Electromagnetic Force in the Complex Quaternion Space

Zi-Hua Weng

School of Physics and Mechanical & Electrical Engineering
Xiamen University, Xiamen 361005, China

Abstract— J. C. Maxwell applied simultaneously the vector terminology and the quaternion analysis to study the electromagnetic features. Nowadays the spaces of electromagnetic and gravitational fields can be chosen as the quaternion spaces, and the coordinates of quaternion spaces are able to be the complex numbers. The quaternion space of the electromagnetic field is independent to that of the gravitational field. These two quaternion spaces can combine together to become one octonion space. Contrarily the octonion space can be separated into two subspaces, the quaternion space and the S -quaternion space. In the quaternion space, it is able to deduce the field strength, field source, angular momentum, torque, force, and mass continuity equation etc. in the gravitational field. In the S -quaternion space, it is able to infer the field strength, field source, and current continuity equation etc. in the electromagnetic field. The results reveal that the quaternion space is suitable to depict the gravitational features, including the gravity and the mass continuity equation etc.. Meanwhile the S -quaternion space, it is suitable to describe the electromagnetic features, including the electromagnetic force and the current continuity equation etc..

1. INTRODUCTION

In the works about the electromagnetic theory, J. C. Maxwell mingled the quaternion analysis and vector terminology to depict the electromagnetic feature. Similarly the scholars begin to study the physics feature of gravitational field with the quaternion and octonion. A. Singh [1] applied the complex quaternion to deduce directly the Maxwell's equations in the classical electromagnetic theory. K. Morita [2] developed the study of the quaternion field theory. Similarly J. Edmonds [3] utilized the quaternion to depict the wave equation and gravitational theory in the curved space-time. F. A. Doria [4] adopted the quaternion to research the gravitational theory. A. S. Rawat etc. [5] discussed the gravitational field equation with the quaternion treatment. Moreover several of the scientists apply the octonion analysis to study the electromagnetic theory. V. L. Mironov etc. [6] described the electromagnetic equations and related features with the algebra of octonions. M. Gogberashvili [7] used the octonion to discuss the electromagnetic theory. O. P. S. Negi etc. [8] depicted the Maxwell's equations by means of the octonion.

The ordered couple of quaternions compose the octonion. On the contrary, the octonion is able to be separated into two parts, the quaternion and the S -quaternion (short for the second quaternion), and their coordinates can be chosen as the complex numbers. In the paper, it is able to find that the quaternion space is suitable to describe the gravitational features, while the S -quaternion space is proper to depict the electromagnetic features.

In the paper, the quaternion space and the S -quaternion space can be introduced into the field theory, in order to describe the physical feature of gravitational and electromagnetic fields. In the electromagnetic theory described with the complex quaternion, it is able to deduce directly the Maxwell's equations in the classical electromagnetic theory, without the help of the current continuity equation [9]. In this approach, substituting the S -quaternion for the quaternion, one can obtain the Maxwell's equations still. On the basis of this approach, the paper is able to deduce directly the force and the current continuity equation etc. further. Similarly the paper can apply the quaternion to research the gravitational theory, deducing directly the force, torque, energy, and the mass continuity equation etc..

2. FIELD EQUATIONS

In the quaternion space \mathbb{E}_g for the gravitational field, the basis vector is $\mathbb{E}_g = (\mathbf{i}_0, \mathbf{i}_1, \mathbf{i}_2, \mathbf{i}_3)$, the radius vector is $\mathbb{R}_g = ir_0\mathbf{i}_0 + \sum r_k\mathbf{i}_k \equiv ir_0 + \mathbf{r}$, and the velocity is $\mathbb{V}_g = iw_0\mathbf{i}_0 + \sum v_k\mathbf{i}_k \equiv iw_0 + \mathbf{v}$. The gravitational potential is $\mathbb{A}_g = ia_0\mathbf{i}_0 + \sum a_k\mathbf{i}_k \equiv ia_0 + \mathbf{a}$, the gravitational strength is $\mathbb{B}_g = h_0\mathbf{i}_0 + \sum h_k\mathbf{i}_k \equiv h_0 + \mathbf{h}$, and the gravitational source is $\mathbb{S}_g = is_0\mathbf{i}_0 + \sum s_k\mathbf{i}_k \equiv is_0 + \mathbf{s}$. In the S -quaternion space \mathbb{E}_e for the electromagnetic field, the basis vector is $\mathbb{E}_e = (\mathbf{I}_0, \mathbf{I}_1, \mathbf{I}_2, \mathbf{I}_3)$, the radius vector is $\mathbb{R}_e = iR_0\mathbf{I}_0 + \sum R_k\mathbf{I}_k \equiv i\mathbf{R}_0 + \mathbf{R}$, and the velocity is $\mathbb{V}_e = iV_0\mathbf{I}_0 + \sum V_k\mathbf{I}_k \equiv i\mathbf{V}_0 + \mathbf{V}$. The electromagnetic potential is $\mathbb{A}_e = iA_0\mathbf{I}_0 + \sum A_k\mathbf{I}_k \equiv i\mathbf{A}_0 + \mathbf{A}$, and the electromagnetic source is

$\mathbb{S}_e = iS_0\mathbf{I}_0 + \sum S_k\mathbf{I}_k \equiv i\mathbf{S}_0 + \mathbf{S}$. The electromagnetic strength is $\mathbb{B}_e = H_0\mathbf{I}_0 + \sum H_k\mathbf{I}_k \equiv \mathbf{H}_0 + \mathbf{H}$, with $\mathbf{H}_0 = H_0\mathbf{I}_0$. Herein $\mathbb{E}_e = \mathbb{E}_g \circ \mathbf{I}_0$. The symbol \circ denotes the octonion multiplication. $r_j, v_j, a_j, s_j, R_j, V_j, A_j, S_j, h_0$, and H_0 are all real. h_k and H_k are all complex numbers. i is the imaginary unit. $\mathbf{i}_0 = 1$. $j = 0, 1, 2, 3$. $k = 1, 2, 3$.

Two quaternion spaces, \mathbb{E}_g and \mathbb{E}_e , may compose one octonion space, $\mathbb{E} = \mathbb{E}_g + \mathbb{E}_e$. In the octonion space \mathbb{E} for the electromagnetic and gravitational fields, the octonion radius vector is $\mathbb{R} = \mathbb{R}_g + k_{eg}\mathbb{R}_e$, the octonion velocity is $\mathbb{V} = \mathbb{V}_g + k_{eg}\mathbb{V}_e$, with k_{eg} being the coefficient. The octonion field potential is $\mathbb{A} = \mathbb{A}_g + k_{eg}\mathbb{A}_e$, the octonion field strength is $\mathbb{B} = \mathbb{B}_g + k_{eg}\mathbb{B}_e$. From here on out, some physics quantities are extended to the octonion functions, according to the characteristics of octonion. Apparently \mathbb{V} and \mathbb{A} etc. are all octonion functions of \mathbb{R} .

The octonion field source \mathbb{S} of the electromagnetic and gravitational fields can be defined as,

$$\mu\mathbb{S} = -(i\mathbb{B}/v_0 + \square)^* \circ \mathbb{B} = \mu_g\mathbb{S}_g + k_{eg}\mu_e\mathbb{S}_e - (i\mathbb{B}/v_0)^* \circ \mathbb{B}, \tag{1}$$

where the field strength is $\mathbb{B} = \square \circ \mathbb{A}$. $\mathbb{B}_g = \square \circ \mathbb{A}_g$, $\mathbb{B}_e = \square \circ \mathbb{A}_e$. The quaternion operator is $\square = i\mathbf{i}_0\partial_0 + \sum \mathbf{i}_k\partial_k$. $\nabla = \sum \mathbf{i}_k\partial_k$, $\partial_j = \partial/\partial r_j$. μ, μ_g , and μ_e are coefficients. $\mu_g < 0$, and $\mu_e > 0$. $*$ denotes the conjugation of octonion. $v_0 = \partial r_0/\partial t$. v_0 is the speed of light, and t is the time. In the case for single one particle, a comparison with the classical field theory reveals that, $\mathbb{S}_g = m\mathbb{V}_g$, and $\mathbb{S}_e = q\mathbb{V}_e$. m is the mass density, while q is the density of electric charge.

The paper adopts the gauge condition, $h_0 = -\partial_0 a_0 + \nabla \cdot \mathbf{a} = 0$. And then the above can be written as $\mathbf{h} = i\mathbf{g}/v_0 + \mathbf{b}$, with $\mathbf{h} = \sum h_k\mathbf{i}_k$. One component of gravitational strength is the gravitational acceleration, $\mathbf{g}/v_0 = \partial_0\mathbf{a} + \nabla a_0$. The other is $\mathbf{b} = \nabla \times \mathbf{a}$, which is similar to the magnetic flux density. Similarly the paper adopts the gauge condition, $\mathbf{H}_0 = -\partial_0\mathbf{A}_0 + \nabla \cdot \mathbf{A} = 0$. While the electromagnetic strength can be written as $\mathbf{H} = i\mathbf{E}/v_0 + \mathbf{B}$, $\mathbf{H} = \sum H_k\mathbf{I}_k$. The electric field intensity is $\mathbf{E}/v_0 = \partial_0\mathbf{A} + \nabla \circ \mathbf{A}_0$, and the magnetic flux density is $\mathbf{B} = \nabla \times \mathbf{A}$.

Expanding of Eq. (1) is able to deduce the Maxwell's equations in the classical electromagnetic theory, and the Newton's law of universal gravitation in the classical gravitational theory when $\mathbf{b} = 0$ and $\mathbf{a} = 0$.

Table 1: The multiplication table of octonion.

	1	\mathbf{i}_1	\mathbf{i}_2	\mathbf{i}_3	\mathbf{I}_0	\mathbf{I}_1	\mathbf{I}_2	\mathbf{I}_3
1	1	\mathbf{i}_1	\mathbf{i}_2	\mathbf{i}_3	\mathbf{I}_0	\mathbf{I}_1	\mathbf{I}_2	\mathbf{I}_3
\mathbf{i}_1	\mathbf{i}_1	-1	\mathbf{i}_3	$-\mathbf{i}_2$	\mathbf{I}_1	$-\mathbf{I}_0$	$-\mathbf{I}_3$	\mathbf{I}_2
\mathbf{i}_2	\mathbf{i}_2	$-\mathbf{i}_3$	-1	\mathbf{i}_1	\mathbf{I}_2	\mathbf{I}_3	$-\mathbf{I}_0$	$-\mathbf{I}_1$
\mathbf{i}_3	\mathbf{i}_3	\mathbf{i}_2	$-\mathbf{i}_1$	-1	\mathbf{I}_3	$-\mathbf{I}_2$	\mathbf{I}_1	$-\mathbf{I}_0$
\mathbf{I}_0	\mathbf{I}_0	$-\mathbf{I}_1$	$-\mathbf{I}_2$	$-\mathbf{I}_3$	-1	\mathbf{i}_1	\mathbf{i}_2	\mathbf{i}_3
\mathbf{I}_1	\mathbf{I}_1	\mathbf{I}_0	$-\mathbf{I}_3$	\mathbf{I}_2	$-\mathbf{i}_1$	-1	$-\mathbf{i}_3$	\mathbf{i}_2
\mathbf{I}_2	\mathbf{I}_2	\mathbf{I}_3	\mathbf{I}_0	$-\mathbf{I}_1$	$-\mathbf{i}_2$	\mathbf{i}_3	-1	$-\mathbf{i}_1$
\mathbf{I}_3	\mathbf{I}_3	$-\mathbf{I}_2$	\mathbf{I}_1	\mathbf{I}_0	$-\mathbf{i}_3$	$-\mathbf{i}_2$	\mathbf{i}_1	-1

3. OCTONION FORCE

In the octonion space, the octonion linear momentum density \mathbb{P} is defined from the octonion field source \mathbb{S} , and can be written as follows,

$$\mathbb{P} = \mu\mathbb{S}/\mu_g, \tag{2}$$

where $\mathbb{P} = \mathbb{P}_g + k_{eg}\mathbb{P}_e$. $\mathbb{P}_g = \{\mu_g\mathbb{S}_g - (i\mathbb{B}/v_0)^* \circ \mathbb{B}\}/\mu_g$, and $\mathbb{P}_e = \mu_e\mathbb{S}_e/\mu_g$.

From the above, one can define the octonion angular momentum, $\mathbb{L} = (\mathbb{R} + k_{rx}\mathbb{X}) \times \mathbb{P}$, and the octonion torque density, $\mathbb{W} = -v_0(i\mathbb{B}/v_0 + \square) \circ \mathbb{L}$. Herein \mathbb{X} is the integral function of field potential \mathbb{A} , and \times denotes the conjugation of complex number, with k_{rx} being the coefficient. If we neglect the contribution of some tiny terms, the octonion torque density \mathbb{W} will be reduced to the term $(2\mathbb{P}v_0)$ approximately, when \mathbf{r} is one three-dimensional vector. And then the octonion force density \mathbb{N} can be defined as,

$$\mathbb{N}/2 = -v_0(i\mathbb{B}/v_0 + \square) \circ \mathbb{P}, \tag{3}$$

and the above can be expressed as,

$$\begin{aligned}\mathbb{N}/2 &= -v_0(i\mathbb{B}_g \circ \mathbb{P}_g/v_0 + ik_{eg}^2\mathbb{B}_e \circ \mathbb{P}_e/v_0 + \square \circ \mathbb{P}_g) \\ &= -k_{eg}v_0(i\mathbb{B}_g \circ \mathbb{P}_e/v_0 + i\mathbb{B}_e \circ \mathbb{P}_g/v_0 + \square \circ \mathbb{P}_e),\end{aligned}\quad (4)$$

where $\mathbb{N} = \mathbb{N}_g + k_{eg}\mathbb{N}_e$. $\mathbb{N}_g/2 = -v_0(i\mathbb{B}_g \circ \mathbb{P}_g/v_0 + ik_{eg}^2\mathbb{B}_e \circ \mathbb{P}_e/v_0 + \square \circ \mathbb{P}_g)$ situates on the quaternion space \mathbb{E}_g , including the inertial force, gravity, and electromagnetic force etc.. $\mathbb{N}_e/2 = -v_0(i\mathbb{B}_g \circ \mathbb{P}_e/v_0 + i\mathbb{B}_e \circ \mathbb{P}_g/v_0 + \square \circ \mathbb{P}_e)$ stays on the S -quaternion space \mathbb{E}_e , and is the interacting term between the gravitational and electromagnetic fields.

Table 2: The multiplication of the operator and octonion physics quantity.

definition	expression	meaning
$\nabla \cdot \mathbf{a}$	$-(\partial_1 a_1 + \partial_2 a_2 + \partial_3 a_3)$	
$\nabla \times \mathbf{a}$	$\mathbf{i}_1(\partial_2 a_3 - \partial_3 a_2) + \mathbf{i}_2(\partial_3 a_1 - \partial_1 a_3) + \mathbf{i}_3(\partial_1 a_2 - \partial_2 a_1)$	
∇a_0	$\mathbf{i}_1 \partial_1 a_0 + \mathbf{i}_2 \partial_2 a_0 + \mathbf{i}_3 \partial_3 a_0$	
$\partial_0 \mathbf{a}$	$\mathbf{i}_1 \partial_0 a_1 + \mathbf{i}_2 \partial_0 a_2 + \mathbf{i}_3 \partial_0 a_3$	
$\nabla \cdot \mathbf{A}$	$-(\partial_1 A_1 + \partial_2 A_2 + \partial_3 A_3)\mathbf{I}_0$	
$\nabla \times \mathbf{A}$	$-\mathbf{I}_1(\partial_2 A_3 - \partial_3 A_2) - \mathbf{I}_2(\partial_3 A_1 - \partial_1 A_3) - \mathbf{I}_3(\partial_1 A_2 - \partial_2 A_1)$	
$\nabla \circ \mathbf{A}_0$	$\mathbf{I}_1 \partial_1 A_0 + \mathbf{I}_2 \partial_2 A_0 + \mathbf{I}_3 \partial_3 A_0$	
$\partial_0 \mathbf{A}$	$\mathbf{I}_1 \partial_0 A_1 + \mathbf{I}_2 \partial_0 A_2 + \mathbf{I}_3 \partial_0 A_3$	

3.1. Gravitational and Electromagnetic Forces

In the quaternion space \mathbb{E}_g , the component \mathbb{N}_g of octonion force \mathbb{N} can be written as follows

$$\mathbb{N}_g = iN_{10}^i + N_{10} + i\mathbf{N}_1^i + \mathbf{N}_1, \quad (5)$$

where $\mathbb{P}_g = ip_0 + \mathbf{p}$. $\mathbf{p} = \sum p_k \mathbf{i}_k$. $\mathbb{P}_e = i\mathbf{P}_0 + \mathbf{P}$. $\mathbf{P} = \sum P_k \mathbf{I}_k$. $\mathbf{P}_0 = P_0 \mathbf{I}_0$. $\mathbf{N}_1 = \sum N_{1k} \mathbf{i}_k$, $\mathbf{N}_1^i = \sum N_{1k}^i \mathbf{i}_k$. P_j, p_j, N_{1j} , and N_{1j}^i are all real.

When there are the gravitational and electromagnetic fields, the above can be expressed as

$$N_{10}^i/2 = -\mathbf{b} \cdot \mathbf{p} - k_{eg}^2(\mathbf{B} \cdot \mathbf{P}), \quad (6)$$

$$N_{10}/2 = v_0 \partial_0 p_0 - v_0 \nabla \cdot \mathbf{p} + \mathbf{g} \cdot \mathbf{p}/v_0 + k_{eg}^2(\mathbf{E} \cdot \mathbf{P}/v_0), \quad (7)$$

$$\mathbf{N}_1^i/2 = -v_0 \partial_0 \mathbf{p} + p_0 \mathbf{g}/v_0 - v_0 \nabla p_0 - \mathbf{b} \times \mathbf{p} + k_{eg}^2(\mathbf{E} \circ \mathbf{P}_0/v_0 - \mathbf{B} \times \mathbf{P}), \quad (8)$$

$$\mathbf{N}_1/2 = -v_0 \nabla \times \mathbf{p} + \mathbf{g} \times \mathbf{p}/v_0 + p_0 \mathbf{b} + k_{eg}^2(\mathbf{E} \times \mathbf{P}/v_0 + \mathbf{B} \circ \mathbf{P}_0), \quad (9)$$

where N_{10} is the power density, including the term capable of translating into the Joule heat in the electromagnetic field. N_{10}^i contains the current helicity of electromagnetic field. \mathbf{N}_1 is the torque derivative. \mathbf{N}_1^i is the force density, including that of the inertial force, gravity, Lorentz force, and energy gradient etc.. $\nabla(\mathbb{B}^* \circ \mathbb{B}/\mu_g)$ is only dealt with the gradient of the norm of field strength, but is independent of the mass as well as the quantity of electric charge.

When $\mathbb{N}_g = 0$, the equation for force equilibrium is yielded from $\mathbf{N}_1^i = 0$. The mass continuity equation is derived from $N_{10} = 0$, and it will be reduced to that in the classical field theory when there is no field strength. The part current helicity of charged particle can be inferred from $N_{10}^i = 0$. While $\mathbf{N}_1 = 0$ can deduce the curl of torque component $\mathbf{p}v_0$. And this equation can infer the angular velocity of Larmor precession with respect to the orbital angular momentum of charged particle. The equation $\mathbf{N}_1^i = 0$ means that the gravitational acceleration \mathbf{g} is the counterpart of the linear acceleration, $v_0 \partial_0 \mathbf{v}$. The equation $\mathbf{N}_1 = 0$ states that the component \mathbf{b} is the counterpart of the velocity curl, $\nabla \times \mathbf{v}$, which is the double of the precessional angular velocity when the dimension of vector \mathbf{r} is 2.

Comparing with the force density in the classical field theory states that $k_{eg}^2 = \mu_g/\mu_e < 0$. The force density \mathbf{N}_1^i in the above requires that the gravitational field must situate on the quaternion space \mathbb{E}_g , while the electromagnetic field can only stay on the quaternion space \mathbb{E}_e , but not vice versa. The inertial force term ($-v_0 \partial_0 \mathbf{p}$) plays a crucial role in the space discrimination.

3.2. Interacting Force

In the S -quaternion space \mathbb{E}_e , the component \mathbb{N}_e of octonion force \mathbb{N} can be written as follows

$$\mathbb{N}_e = i\mathbf{N}_{20}^i + \mathbf{N}_{20} + i\mathbf{N}_2^i + \mathbf{N}_2, \quad (10)$$

where $\mathbf{N}_{20} = \Sigma N_{20}\mathbf{I}_0$, $\mathbf{N}_{20}^i = \Sigma N_{20}^i\mathbf{I}_0$, $\mathbf{N}_2 = \Sigma N_{2k}\mathbf{I}_k$, $\mathbf{N}_2^i = \Sigma N_{2k}^i\mathbf{I}_k$. N_{2j} and N_{2j}^i are all real.

When there are the gravitational and electromagnetic fields, the above can be expressed as

$$\mathbf{N}_{20}^i/2 = -\mathbf{b} \cdot \mathbf{P} - \mathbf{B} \cdot \mathbf{p}, \quad (11)$$

$$\mathbf{N}_{20}/2 = v_0\partial_0\mathbf{P}_0 - v_0\nabla \cdot \mathbf{P} + \mathbf{g} \cdot \mathbf{P}/v_0 + \mathbf{E} \cdot \mathbf{p}/v_0, \quad (12)$$

$$\mathbf{N}_2^i/2 = -v_0\partial_0\mathbf{P} - v_0\nabla \circ \mathbf{P}_0 + \mathbf{g} \circ \mathbf{P}_0/v_0 - \mathbf{b} \times \mathbf{P} + p_0\mathbf{E}/v_0 - \mathbf{B} \times \mathbf{p}, \quad (13)$$

$$\mathbf{N}_2/2 = -v_0\nabla \times \mathbf{P} + \mathbf{g} \times \mathbf{P}/v_0 + \mathbf{b} \circ \mathbf{P}_0 + \mathbf{E} \times \mathbf{p}/v_0 + p_0\mathbf{B}, \quad (14)$$

where \mathbf{N}_{20} covers the current continuity equation.

When $\mathbb{N}_e = 0$, the equilibrium equation of force-like is yielded from $\mathbf{N}_2^i = 0$. The current continuity equation is derived from $\mathbf{N}_{20} = 0$, and it will be reduced to that in the classical field theory when there is no field strength. Meanwhile $\mathbf{N}_{20}^i = 0$ deduces the helicity-like of the charged particle. $\mathbf{N}_2 = 0$ states that the strength components \mathbf{b} and \mathbf{B} will impact the curl of the torque component ($\mathbf{P}v_0$).

Table 3: Some definitions of the physics quantity in the gravitational and electromagnetic fields described with the complex quaternion/ S -quaternion spaces.

physics quantity	definition	note
radius vector	$\mathbb{R} = \mathbb{R}_g + k_{eg}\mathbb{R}_e$	$k_{eg}^2 = \mu_g/\mu_e < 0$
integral function	$\mathbb{X} = \mathbb{X}_g + k_{eg}\mathbb{X}_e$	
field potential	$\mathbb{A} = i\Box^\times \circ \mathbb{X}$	
field strength	$\mathbb{B} = \Box \circ \mathbb{A}$	gauge condition
field source	$\mu\mathbb{S} = -(i\mathbb{B}/v_0 + \Box)^* \circ \mathbb{B}$	field equations
linear momentum	$\mathbb{P} = \mu\mathbb{S}/\mu_g$	
angular momentum	$\mathbb{L} = (\mathbb{R} + k_{rx}\mathbb{X})^\times \circ \mathbb{P}$	$k_{rx} = 1/v_0$
octonion torque	$\mathbb{W} = -v_0(i\mathbb{B}/v_0 + \Box) \circ \mathbb{L}$	torque, work, energy
octonion force	$\mathbb{N} = -(i\mathbb{B}/v_0 + \Box) \circ \mathbb{W}$	power, force

4. CONCLUSIONS

The paper introduced the quaternion/ S -quaternion space into the field theory, to describe the physics features of gravitational and electromagnetic fields. The space extended from the electromagnetic field is independent of that from the gravitational field. Meanwhile the space of gravitational field and of electromagnetic field can be chosen as the quaternion space and S -quaternion space respectively. Furthermore the components of those two spaces and of relevant physics quantities may be complex numbers.

The above means that the vector analysis and quaternion analysis are suitable to describe the physics feature of gravitational and electromagnetic fields within two different confines. To a certain extent, the vector analysis may describe the vast majority of physics features of those two fields. Within a wider range, the quaternion analysis is able to depict more physics features of those two fields, including the force and continuity equation.

It should be noted that the paper discussed only some simple cases about the angular momentum, torque, force, and continuity equations etc. in the field theory described with the quaternion/ S -quaternion. However it clearly states that the complex quaternion and S -quaternion spaces are able to available describe the physics features of electromagnetic and gravitational fields. This will afford the theoretical basis for further analysis, and is helpful to research the property of the force and of continuity equations in the following researches.

ACKNOWLEDGMENT

This project was supported partially by the National Natural Science Foundation of China under grant number 60677039.

REFERENCES

1. Singh, A., “Quaternionic form of the electromagnetic-current equations with magnetic monopoles,” *Lettere al Nuovo Cimento*, Vol. 31, No. 5, 145–148, 1981.
2. Morita, K., “Quaternions, lorentz group and the dirac theory,” *Progress of Theoretical Physics*, Vol. 117, No. 3, 501–532, 2007.
3. Edmonds, J. D., “Quaternion wave equations in curved space-time,” *International Journal of Theoretical Physics*, Vol. 10, No. 2, 115–122, 1974.
4. Doria, F. A., “A Weyl-like equation for the gravitational field,” *Lettere al Nuovo Cimento*, Vol. 14, No. 13, 480–482, 1975.
5. Rawat, A. S. and O. P. S. Negi, “Quaternion gravi-electromagnetism,” *International Journal of Theoretical Physics*, Vol. 51, No. 3, 738–745, 2012.
6. Mironov, V. L. and S. V. Mironov, “Octonic representation of electromagnetic field equations,” *Journal of Mathematical Physics*, Vol. 50, No. 1, 012901, 10 pages, 2009.
7. Gogberashvili, M., “Octonionic electrodynamics,” *Journal of Physics A*, Vol. 39, No. 22, 7099–7104, 2006.
8. Chanyal, B. C., P. S. Bisht, and O. P. S. Negi, “Generalized octonion electrodynamics,” *International Journal of Theoretical Physics*, Vol. 49, No. 6, 1333–1343, 2010.
9. Honig, W. M., “Quaternionic electromagnetic wave equation and a dual charge-filled space,” *Lettere al Nuovo Cimento*, Vol. 19, No. 4, 137–140, 1977.

Computing Illuminated Area and Scattering for Double-bounce for SAR Manmade Target's Characteristic Modeling

Kai Yang, Kefeng Ji, and Huanxin Zou

College of Electronics Science and Engineering, National University of Defense Technology
Changsha, Hunan 410073, China

Abstract— We take the perfect electrical conductor (PEC) dihedral with large dimension for example to analyze its double-bounce illumination cases for SAR manmade target's characteristic modeling. The completeness of the illumination cases is proved by rigorous mathematical reasoning and the range of the transmit aspect angle corresponding to each integral case is offered. The total scattering field is derived. Experiment results validate the dihedral's double-bounce scattering effect for each illumination case.

1. INTRODUCTION

SAR targets' scattering modeling is of great importance in SAR image interpretation. It can be derived by a variety of approaches. Model using physical optics (PO) maintains high computational efficiency and excellent accuracy under certain conditions. Double-bounce scattering effect can be found in a variety of manmade targets in real world scenes, such as ship-to-sea, vehicle-to-ground, building-to-ground, etc. [1–3]. However, determining the illuminated area of the double-bounce, as the primary task of this model, is very difficult. Thus, a complete solution to determine the illuminated area easily and accurately is derived in this paper.

Under the assumption of high-frequency and far field, we take the PEC dihedral with large dimension for example to analyze its double-bounce's illumination cases and find that there existed six classes of different integral(s) domain along with the transmit angle varying. Then the completeness of the illumination cases is proved by rigorous mathematical reasoning and the range of the transmit aspect angle corresponding to each integral case is also offered. Dihedral's double-bounce scattering effect corresponding to each integral case is computed based on PO integral equation. And combining the results of the double-bounce scattering effect with the single-bounce scattering, total scattering field of the right-angle dihedral is derived. Experiments validate these conclusions. And the proposed method can be extended to other scatterers whose scattering are dominated by double-bounce scattering effect.

2. ILLUMINATION CASES CALCULATION AND DEMONSTRATION

Reference 4 gives PO integral

$$\vec{E} = \frac{-jk\eta}{4\pi} \int_S \hat{r} \times \left[\hat{r} \times \left(2\hat{n} \times \vec{H}_i \right) \right] e^{-jk\vec{r} \cdot (\hat{k}_t - \hat{r})} dS \quad (1)$$

where k is the wavenumber, $k = 2\pi f/c$, η is the impedance, and $\sqrt{j} \equiv -1$. \hat{r} is the receive direction, \hat{n} is the unit vector norm to the surface S , \vec{H}_i is the polarization of the incident magnetic field, \vec{r} is a vector from the origin to a point on the surface S , and \hat{k}_t is the transmit direction.

Taking one step further, we can get

$$\vec{E} = -\frac{jk\eta}{4\pi} \left\{ \hat{r} \times \left[\hat{r} \times \left(2\hat{n} \times \vec{H}_i \right) \right] \right\} \mathcal{I} \quad (2)$$

where $\mathcal{I} = \int_S e^{-jk\vec{r} \cdot (\hat{k}_t - \hat{r})} dS$. Using formula (2), reference 5 gives the bistatic scattering solution for a rectangular plate. Employing the same manner, we can derive the total scattering solution for a right-angle dihedral. And the main task is how to calculate \mathcal{I} for double-bounce.

2.1. Illumination Cases Analysis

Given the incident and scattered wave direction depicted in Figure 1, write them in Cartesian coordinates as

$$\hat{k}_t = -(\hat{x} \cos \phi_t \sin \theta_t + \hat{y} \sin \phi_t \sin \theta_t + \hat{z} \cos \theta_t) \quad (3)$$

$$\hat{r} = \hat{x} \cos \phi_r \sin \theta_r + \hat{y} \sin \phi_r \sin \theta_r + \hat{z} \cos \theta_r \quad (4)$$

The PEC right-angle dihedral is shown in Figure 2. Based on geometric optics (GO), we can get the single-bounce specular scattered wave direction, i.e., the double-bounce incident wave direction,

$$\hat{s}_{yz} = \hat{x} \cos \phi_t \sin \theta_t - \hat{y} \sin \phi_t \sin \theta_t - \hat{z} \cos \theta_t \quad (5)$$

$$\hat{s}_{xz} = -\hat{x} \cos \phi_t \sin \theta_t + \hat{y} \sin \phi_t \sin \theta_t - \hat{z} \cos \theta_t \quad (6)$$

where subscript denotes the plate reflected rays.

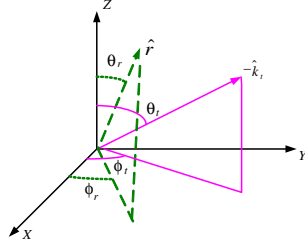


Figure 1: Bistatic spherical coordinate geometry.

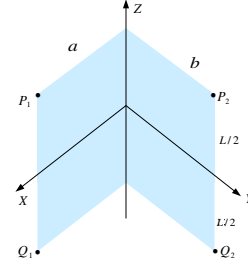


Figure 2: Right-angle dihedral.

From Figure 2, we get four corners coordinates: $P_1 = (a, 0, L/2)$, $Q_1 = (a, 0, -L/2)$, $P_2 = (0, b, L/2)$, $Q_2 = (0, b, -L/2)$. Based on space geometry, we can obtain the coordinates of the projections for four corners: $P'_1 = (0, a \tan \phi_t, L/2 - a \cot \theta_t / \cos \phi_t)$, $Q'_1 = (0, a \tan \phi_t, -L/2 - a \cot \theta_t / \cos \phi_t)$, $P'_2 = (b \cot \phi_t, 0, L/2 - b \cot \theta_t / \sin \phi_t)$, $Q'_2 = (b \cot \phi_t, 0, -L/2 - b \cot \theta_t / \sin \phi_t)$. Because of $0^\circ \leq \phi_t \leq 90^\circ$, we know that the projection points must be on the positive axis. If projection points, P'_1, Q'_1 , are both on the plate, they must satisfy

$$\tan \phi_t \leq b/a \quad (7)$$

Similarly for P'_2, Q'_2 , they must satisfy

$$\tan \phi_t \geq a/b \quad (8)$$

From formula (7) and (8), we can get

Conclusion 1: two set of projection points P'_1, Q'_1 and P'_2, Q'_2 , are no more than one set on the plate.

On the other hand,

$$|P'_1 - Q'_1| = |P'_2 - Q'_2| = L \quad (9)$$

We have

Conclusion 2: P'_1 and Q'_1 are no more than one point on the plate, as same for P'_2 and Q'_2 .

From Conclusion 1 and 2, we can easily acquire

Conclusion 3: P'_1, Q'_1, P'_2 and Q'_2 are no more than one projection point on the plate.

If all four points aren't on the plate, there are two cases. One is that all four points are up the plate. The sufficient and necessary conditions of this case are

$$-b \cot \theta_t > L \sin \phi_t, \quad -a \cot \theta_t > L \cos \phi_t \quad (10)$$

The other case is all four points are down the plate. And the sufficient and necessary conditions are

$$b \cot \theta_t > L \sin \phi_t, \quad a \cot \theta_t > L \cos \phi_t \quad (11)$$

2.2. Illuminated Area Determination

Now, we know there are at least six illumination cases. Further analysis shows that there only exist six cases. Next, we prove the completeness of the six illumination cases by rigorous mathematical reasoning now.

Case 1: when P'_1 is on the plate, the sufficient and necessary conditions are

$$0^\circ \leq \theta_t \leq 90^\circ, \quad \tan \phi_t \leq (b/a), \quad \cot \theta_t \leq (L/a) \cos \phi_t \quad (12)$$

Case 2: when P'_2 is on the plate, the sufficient and necessary conditions are

$$0^\circ \leq \theta_t \leq 90^\circ, \quad \tan \phi_t \geq (b/a), \quad \cot \theta_t \leq (L/b) \sin \phi_t \tag{13}$$

Case 3: when all four points are down the plate, the sufficient and necessary conditions are formula (11).

Case4: when Q'_1 is on the plate, the sufficient and necessary conditions are

$$90^\circ \leq \theta_t \leq 180^\circ, \quad \tan \phi_t \leq (b/a), \quad 0 \geq \cot \theta_t \geq -(L/a) \cos \phi_t \tag{14}$$

Case 5: when Q'_2 is on the plate, the sufficient and necessary conditions are

$$90^\circ \leq \theta_t \leq 180^\circ, \quad \tan \phi_t \geq (b/a), \quad 0 \geq \cot \theta_t \geq -(L/b) \sin \phi_t \tag{15}$$

Case 6: when all four points are up the plate, the sufficient and necessary conditions are formula (10).

All these illumination cases are shown in Figure 3 respectively.

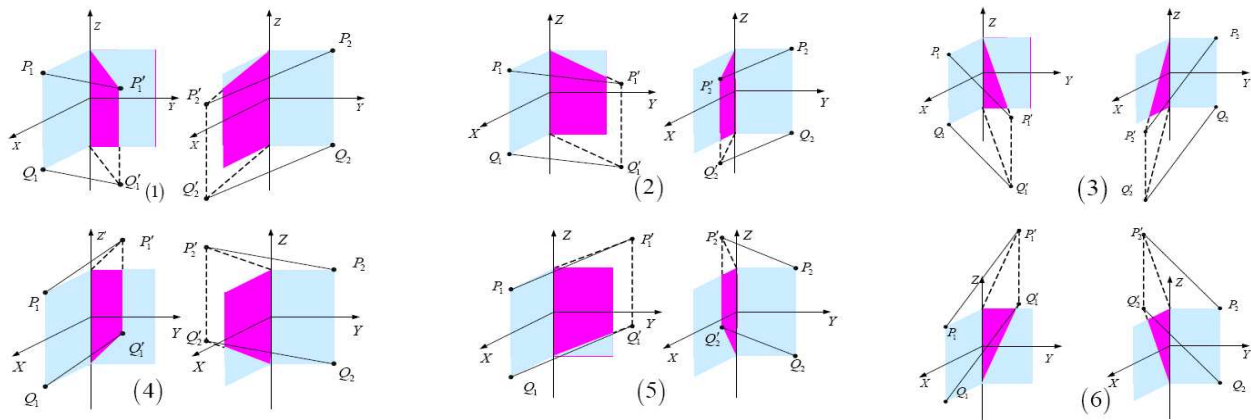


Figure 3: Illumination (illuminated area) of double-bounce for right-angle dihedral corresponding to illumination Cases 1–6.

Since Cases 4–6 are similar to Cases 1–3, now we just analyze the latter. The former can be done using the same manner. From Figure 3, we can see that there exist three cases for one plate of the dihedral, as shown in Figure 4. In the light of combination theory, there will be six cases existing.

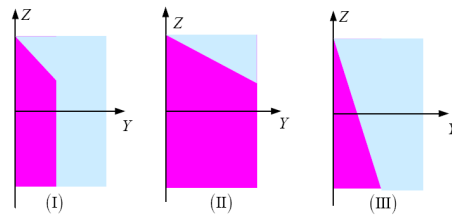


Figure 4: Illumination Cases (I)–(III) for one plate of the dihedral.

Now we analyze which case one plate is in when the other one (without loss of generality, we suppose it is yz plate) is in Case I. From Conclusion 1, we know that it is impossible for two plates both in Case I. The difference between the Cases II and III is the slope of the plate upper edge’s projection. The bigger is for Case II, and the smaller is for Case III. We know that the slope of the plate’s diagonal line is

$$k = -L/a \tag{16}$$

The slope of the projection line is

$$k' = -\cot \theta_t / \cos \phi_t \tag{17}$$

Since yz plate is in Case I, from formula (12), we know $k' \geq k$. Thus, this plate must be in Case II. Using the same analyzing manner, we have the following conclusions:

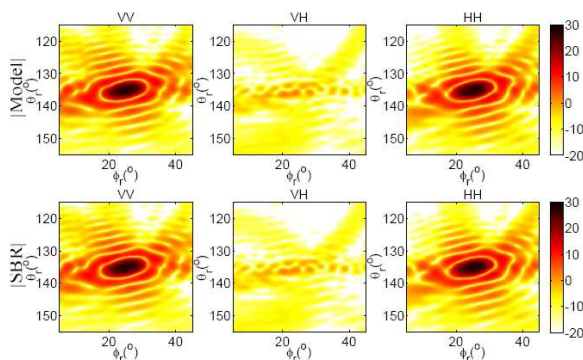
Conclusion 4: if one plate is in Case I, the other one must be in Case II.

Conclusion 5: if one plate is in Case II, the other one must be in Case I.

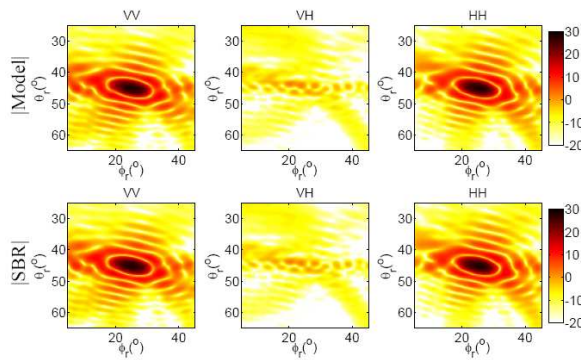
Conclusion 6: if one plate is in Case III, the other one also must be in Case III.

From Conclusions 4–6, we know that there just exist six illumination cases for right-angle dihedral for arbitrary transmit angles. The range of the transmit aspect angle corresponding to each illumination case are given in formula (10)–(15) respectively and illuminated area are shown in Figure 3.

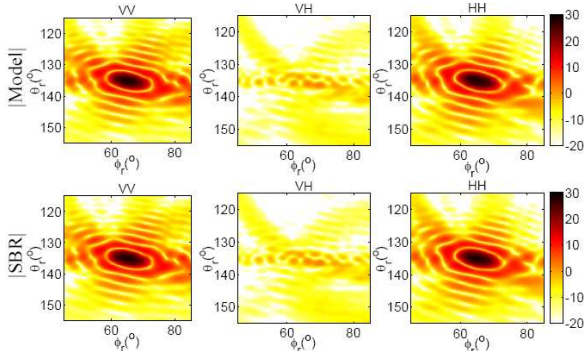
Case 1: Transmitter at $(\theta_t, \phi_t) = (45^\circ, 25^\circ)$



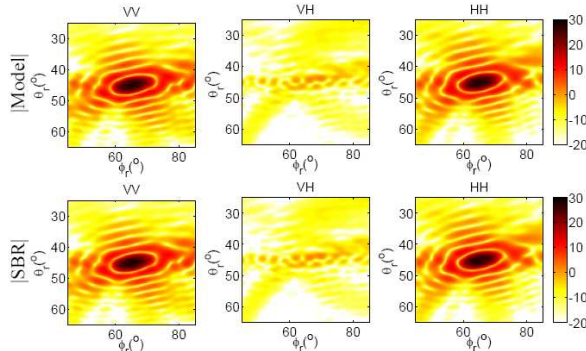
Case 4: Transmitter at $(\theta_t, \phi_t) = (135^\circ, 25^\circ)$



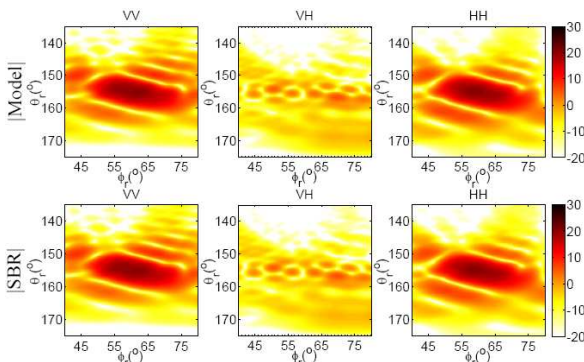
Case 2: Transmitter at $(\theta_t, \phi_t) = (45^\circ, 65^\circ)$



Case 5: Transmitter at $(\theta_t, \phi_t) = (135^\circ, 65^\circ)$



Case 3: Transmitter at $(\theta_t, \phi_t) = (25^\circ, 60^\circ)$



Case 6: Transmitter at $(\theta_t, \phi_t) = (155^\circ, 30^\circ)$

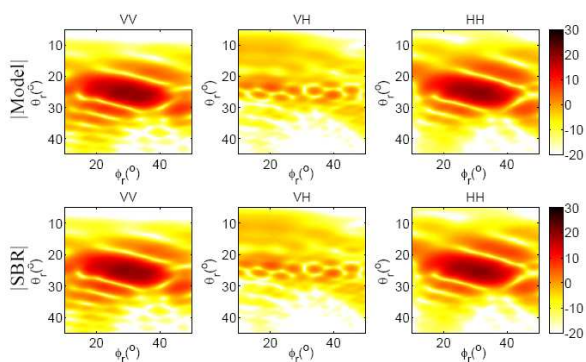


Figure 5: Comparison of bistatic dihedral polarization response for formula (19) and a shooting and bouncing rays prediction for six illumination cases.

3. SCATTERING FIELD CALCULATION

Section 2 analyzes illumination cases and gives the range of the transmit aspect angle corresponding to each illumination case. Thus, we can easily calculate \mathcal{I} = for each illumination cases,

$$\begin{aligned}\mathcal{I}_{xz}^{(1,2,3)} &= \frac{e^{j\frac{L}{2}\psi_z}}{j\psi_z} X \sin c\left(\frac{X}{2}\left(\psi_x + \frac{\cot\theta_t}{\cos\phi_t}\psi_z\right)\right) e^{-j\frac{X}{2}\left(\psi_x + \frac{\cot\theta_t}{\cos\phi_t}\psi_z\right)} - \frac{e^{-j\frac{L}{2}\psi_z}}{j\psi_z} X \sin c\left(\frac{X}{2}\psi_x\right) e^{-j\frac{X}{2}\psi_x} \\ \mathcal{I}_{yz}^{(1,2,3)} &= \frac{e^{j\frac{L}{2}\psi_z}}{j\psi_z} Y \sin c\left(\frac{Y}{2}\left(\psi_y + \frac{\cot\theta_t}{\sin\phi_t}\psi_z\right)\right) e^{-j\frac{Y}{2}\left(\psi_y + \frac{\cot\theta_t}{\sin\phi_t}\psi_z\right)} - \frac{e^{-j\frac{L}{2}\psi_z}}{j\psi_z} Y \sin c\left(\frac{Y}{2}\psi_y\right) e^{-j\frac{Y}{2}\psi_y} \\ \mathcal{I}_{xz}^{(4,5,6)} &= \frac{e^{j\frac{L}{2}\psi_z}}{j\psi_z} X \sin c\left(\frac{X}{2}\psi_x\right) e^{-j\frac{X}{2}\psi_x} - \frac{e^{-j\frac{L}{2}\psi_z}}{j\psi_z} X \sin c\left(\frac{X}{2}\left(\psi_x + \frac{\cot\theta_t}{\cos\phi_t}\psi_z\right)\right) e^{-j\frac{X}{2}\left(\psi_x + \frac{\cot\theta_t}{\cos\phi_t}\psi_z\right)} \\ \mathcal{I}_{yz}^{(4,5,6)} &= \frac{e^{j\frac{L}{2}\psi_z}}{j\psi_z} Y \sin c\left(\frac{Y}{2}\psi_y\right) e^{-j\frac{Y}{2}\psi_y} - \frac{e^{-j\frac{L}{2}\psi_z}}{j\psi_z} Y \sin c\left(\frac{Y}{2}\left(\psi_y + \frac{\cot\theta_t}{\sin\phi_t}\psi_z\right)\right) e^{-j\frac{Y}{2}\left(\psi_y + \frac{\cot\theta_t}{\sin\phi_t}\psi_z\right)}\end{aligned}\quad (18)$$

where superscripts 1, 2, 3 and 4, 5, 6 indicate illumination Cases 1–3 and 4–6, respectively. And the subscripts xz and yz indicate the plate reflected rays. $\psi_x = k(\cos\phi_t \sin\theta_t - \cos\phi_r \sin\theta_r)$, $\psi_y = k(\sin\phi_t \sin\theta_t - \sin\phi_r \sin\theta_r)$, $\psi_z = k(\cos\theta_t + \cos\theta_r)$. And $X = b \cot\phi_t$, $Y = b$ for Cases 1, 4, $X = a$, $Y = a \tan\phi_t$ for Cases 2, 5, $X = L \tan\theta_t \cos\phi_t$, $Y = L \tan\theta_t \sin\phi_t$ for Case 3, and $X = -L \tan\theta_t \cos\phi_t$, $Y = -L \tan\theta_t \sin\phi_t$ for Case 6. Combining \mathcal{I} with the result given by Reference 6, we obtain the bistatic 3D scattering solution for a right-angle dihedral,

$$\begin{aligned}\vec{E}_{total} &= \frac{jk}{2\pi} \left\{ E_\theta \hat{\theta}_r \left[L \sin c\left(\frac{L}{2}\mathcal{Z}\right) \sin\theta_r \left(a \sin c\left(\frac{a}{2}\mathcal{X}\right) e^{\frac{ia}{2}\mathcal{X}} \sin\phi_t + b \sin c\left(\frac{b}{2}\mathcal{Y}\right) e^{\frac{ib}{2}\mathcal{Y}} \cos\phi_t \right) \right. \right. \\ &\quad - \sin\theta_r (\mathcal{I}_{xz} \sin\phi_t + \mathcal{I}_{yz} \cos\phi_t) \left. \right] - E_\phi \hat{\phi}_r \left[(\sin\theta_t \cos\theta_r (\mathcal{I}_{xz} \cos\phi_r - \mathcal{I}_{yz} \sin\phi_r) + \right. \\ &\quad \left. \sin\theta_r \cos\theta_t (\mathcal{I}_{xz} \cos\phi_t - \mathcal{I}_{yz} \sin\phi_t) + L \sin c\left(\frac{L}{2}\mathcal{Z}\right) \left[a \sin c\left(\frac{a}{2}\mathcal{X}\right) e^{\frac{ia}{2}\mathcal{X}} (\cos\theta_r \cos\phi_r \sin\theta_t \right. \right. \\ &\quad \left. \left. - \sin\theta_r \cos\theta_t \cos\phi_t) + b \sin c\left(\frac{b}{2}\mathcal{Y}\right) e^{\frac{ib}{2}\mathcal{Y}} (-\cos\theta_r \sin\phi_r \sin\theta_t + \sin\theta_r \cos\theta_t \sin\phi_t) \right] \right. \\ &\quad \left. \left. + E_\phi \hat{\phi}_r \left[L \sin c\left(\frac{L}{2}\mathcal{Z}\right) \sin\theta_t \left(a \sin c\left(\frac{a}{2}\mathcal{X}\right) e^{\frac{ia}{2}\mathcal{X}} \sin\phi_r + b \sin c\left(\frac{b}{2}\mathcal{Y}\right) e^{\frac{ib}{2}\mathcal{Y}} \cos\phi_r \right) \right. \right. \right. \\ &\quad \left. \left. + \sin\theta_t (\mathcal{I}_{xz} \sin\phi_r + \mathcal{I}_{yz} \cos\phi_r) \right] \right\}\end{aligned}\quad (19)$$

where $\mathcal{X} = k(\cos\phi_t \sin\theta_t + \cos\phi_r \sin\theta_r)$, $\mathcal{Y} = k(\sin\phi_t \sin\theta_t + \sin\phi_r \sin\theta_r)$, $\mathcal{Z} = k(\cos\theta_t + \cos\theta_r)$.

4. EXPERIMENTS

Six sets of experiments corresponded to six different illumination cases are done. The dimensions of the dihedral are $L = 1$, $a = 0.5$, $b = 0.5$. And the results shown in Figure 5 have excellent agreement with the SBR predictions. For easy comparison, formula (19) is organized into co/cross-pol scattering. V indicates vertical polarization (θ -pol), H indicates horizontal polarization (ϕ -pol), and the first script indicates receive polarization while the second script indicates transmitter polarization (HV polarization is omitted since the response is zero).

5. CONCLUSION

We take PEC dihedral with large size dimension for example to compute illuminated area and scattering for double-bounce for SAR manmade target's characteristic modeling. From results, we can see that what we derive shows excellent agreement with the SBR predictions. These indicate that the six illumination cases we derived are right and also mean that our method computing the illuminated area of dihedral is valid. Using the same method, we can compute illuminated area and scattering for double-bounce for other scatterers whose scattering are dominated by double-bounce scattering effect.

ACKNOWLEDGMENT

This work is supported by the National Natural Science Foundation of China under Grant 61372163, 61331015 and 61240058.

REFERENCES

1. Shepilko, Y. V., "Scattering of H -polarized electromagnetic wave by grooved dihedral wedge co-axially coupled with dielectric covered metal slotted cylinder," *2013 XVIIth International*

Seminar/Workshop on Direct and Inverse Problem of Electromagnetic and Acoustic (DIPED), 49–54, Sept. 23–26, 2013.

2. Tang, K., X. Sun, H. Sun, and H. Q. Wang, “A geometrical-based simulator for target recognition in high-resolution SAR images,” *Geoscience and Remote Sensing Letters, IEEE*, Vol. 9, No. 5, 958–962, Sept. 2012.
3. Marble, J. A. and A. O. Hero, “See through the wall detection and classification of scattering primitives,” *Proc. SPIE, Radar Sensor Technology X*, R. N. Trebits and J. L. Kurtz, Eds., Vol. 6210, 2006.
4. Knott, E. F., J. F. Shaeffer, and M. T. Tuley, *Radar Cross Section*, 2nd Edition, Artech House Boston, 1993.
5. Jackson, J. A., “Three-dimensional feature models for synthesis aperture radar and experiments in feature extraction,” Ph.D. Dissertation, The Ohio State University, 2009.
6. Jackson, J. A., “Analytic physical optics solution for bistatic, 3D scattering from a dihedral corner reflector,” *IEEE Transactions on Antennas and Propagation*, Vol. 60, No. 3, 1486–1495, 2012.

Target Angular Scintillation Measurement of Wide-band Range Comparison Monopulse Radar in Anechoic Chamber

Yang Bai, Chao Ning, Ming Jin, Chao Gao, and Yanjie Cui

Science and Technology on Electromagnetic Scattering Laboratory, Beijing 100854, China

Abstract— The range comparison monopulse radar measures angles by comparing the range of the difference-channel signals with the range of the sum-channel signal. Practically, It has been generally accepted that what the radar measures is not the directions of the target, but angular glint errors. In order to realize this characteristic of radar target, a wide-band radar simulate system based on CATR (Compact Antenna Test Range) was used in this researching. By making use of high-frequency phase shift correcting algorithm, the effect of test errors caused by the difference-sum channels' non-equilibrium was weakened. With paying close attention to the complex dimension expend radar target, an algorithm including HRRP (high resolution range profile) method was used to extract and describe the nicety of angular scintillation. At last, the scintillation measurement results of double balls union and airplane model have been laid out.

1. INTRODUCTION

Angular scintillation, or angle glint, in the tracking loop of a radar missile seeker arises from warps in phase front of the scattered wave produced by interference between the individual centers of scattering on a complex target. Because the seeker attempts to orient itself at right angles to the phase front, these warps can produce a substantial displacement between the apparent radar center and the physical center of target. It will cause the angle test error that induces an inaccurate result. Because the glint is a type of connatural character of radar target, getting the angular scintillation to a nicety will accelerate the advancement of radar system and target identity research.

Generally, the methods of measuring angle glint can be distinguished into three classes: outdoor static testing, indoor static testing and dynamic testing. As an admitted fact, the targets scattering characters test result that obtained in CATR (Compact Antenna Test Range) Anechoic Chamber are exact. In order to realize this characteristic, a wide-band radar simulate system based on CATR was designed in this researching. The theory of Monopulse Radar Antenna angle testing and a new kind of calculating formula and angle glint analyze method based on HRRP (High Resolution Range Profile) have been expounded in the following disquisition. At last, a test result on angle glint of double-ball union and airplane model have been laid out.

2. THE METHOD OF ANGLE TEST BY MONOPULSE RADAR ANTENNA

2.1. Angle Test Elements

The range comparison monopulse radar measures angles by comparing the range of the difference-channel (Δ) signals with the range of the sum-channel (Σ) signal. Considering the solution in polar coordinate, the single (Σ - Δ) antenna pattern can be shown as Fig. 1, the pattern function is $F(\theta)$, the beam angle is θ_0 , the target angle is $\Delta\theta$, then the ranges of receiving singles A_1 and A_2 are,

$$\begin{cases} A_1 = kF(\Delta\theta - \theta_0) \\ A_2 = kF(\Delta\theta + \theta_0) \end{cases} \quad (1)$$

k is a const decided by radar equation. Because the $\Delta\theta$ is very small, the ranges of Σ signal and Δ signal are,

$$A_\Sigma = A_1 + A_2 = kF_\Sigma(\theta) \approx K \quad (2)$$

$$A_\Delta = A_1 - A_2 = kF_\Delta(\theta) \approx K\eta\varepsilon \quad (3)$$

where: $\eta = \frac{F'_\Delta(0)}{F'_\Sigma(0)}$ and $K = kF_\Sigma(0)$, the ε is the angle error which gained by ratio A_Δ and A_Σ .

2.2. Acquisition of the Angle Error

Commonly the acquirement of the angle test result is based on range comparison between the signals of difference-channel and sum-channel directly. If the input signal of the IQ receiver are

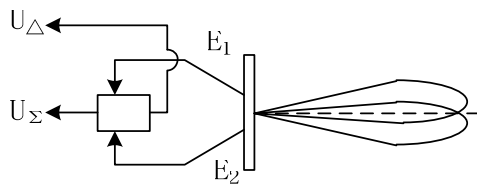


Figure 1: Monopulse radar antenna beam in one angular test plane.

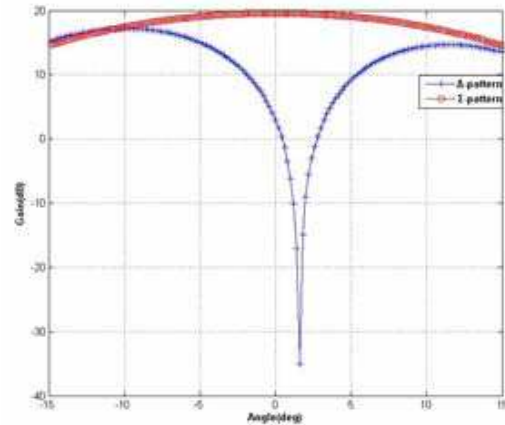


Figure 2: (Σ-Δ) antenna pattern with the differ-gain.

$S_{\Sigma}(t) = K \cos(\omega t + \varphi_0)$ and $S_{\Delta}(t) = K\eta\varepsilon \cos(\omega t + \varphi_0)$, the response by Σ and Δ can be described as,

$$\Sigma_I = K \cos \varphi_0, \quad \Sigma_Q = K \sin \varphi_0 \tag{4}$$

$$\Delta_I = K\eta\varepsilon \cos \varphi_0, \quad \Delta_Q = K\eta\varepsilon \sin \varphi_0 \tag{5}$$

According to the angle test elements, the angle error calculate expression is,

$$\varepsilon = \frac{\Delta}{\Sigma} \cos \varphi = \text{sgn}(\Sigma_I \Delta_I + \Sigma_Q \Delta_Q) \frac{|\Delta_I + j\Delta_Q|}{\eta |\Sigma_I + j\Sigma_Q|} \tag{6}$$

$\text{sgn}(\ast)$ is a function to get the sign of $\Sigma_I \Delta_I + \Sigma_Q \Delta_Q$ and describes the direction of the angle deflexion.

However, every independent receive channel couldn't be symmetric with another absolutely, these independence often represent as differ gain or differ phase. It will cause the (Σ-Δ) antenna pattern and angle testing curve to face a differ-error, as it shows in Fig. 2 and Fig. 3. When the differ gain and differ phase is subsistent in the same time, the 0° angle will leap on the angle testing curve. It is a serious balk that radar cannot estimate where is the 0° angle spot, see Fig. 4 the blue line with '+' in green circle. In order to avoid the 0° angle spot error, the angle error calculate expression has to be improved.

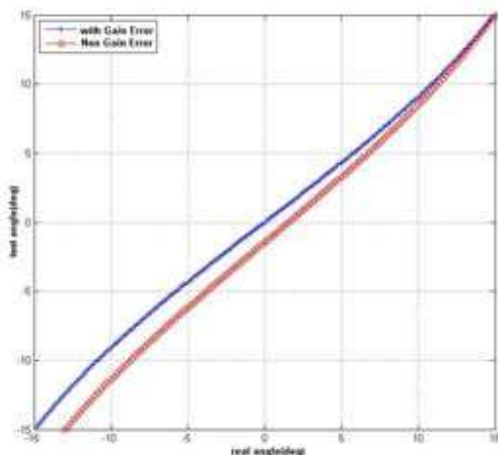


Figure 3: Angle testing curve with differ-phase.

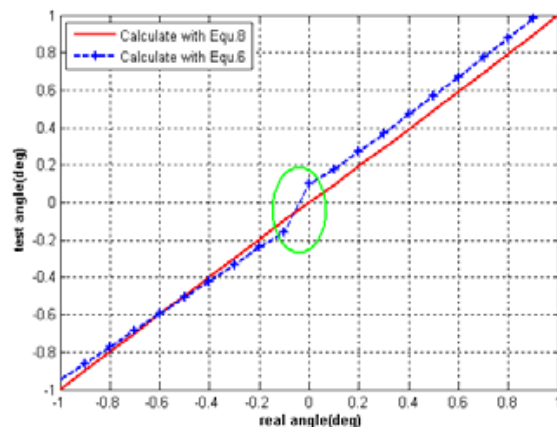


Figure 4: The angle testing curve with different angle error calculate expressions.

From Equation (6),

$$\Sigma_I \Delta_I + \Sigma_Q \Delta_Q = \frac{1}{4} |\Sigma| |\Delta| \cos(\varphi_\Delta - \varphi_\Sigma) = \frac{1}{4} |\Sigma| |\Delta| \cos(\varphi) \quad (7)$$

Improve the angle error calculate expression to following result from Equations (6) and (7),

$$\varepsilon = \frac{\Sigma_I \Delta_I + \Sigma_Q \Delta_Q}{\eta |\Sigma_I + j \Sigma_Q|} = \frac{A_\Delta}{\eta A_\Sigma} \cos \phi_\varphi \quad (8)$$

Calculating with the Equation (8), the $\cos \phi_\varphi$ will be always 0, so the angle error is 0 at the 0° angle spot, even if the channel is not symmetric. As it is shown by the red line in Fig. 4.

3. WIDE-BAND ANGULAR SCINTILLATION MEASUREMENT IN CATR ANECHOIC CHAMBER

3.1. Angle Glint Test in CATR Anechoic Chamber

As in Fig. 5, CATR in anechoic chamber is a common type of target scattering characters testing laboratory, which is made of reflecting antenna system that can take the spherical wave into plane wave to satisfy the far field test condition. As the above description, Angle Glint is a connatural identity of target which is not dependent with the range between radar and target in far field area, so the specialty of CATR is suitable for glint measurement. If the culmination of the reflecting face is spot O , the angle between center line of antenna beam and x axis is α , the points of intersection between center line of antenna beam and reflecting face is P_0 , P_1 , and P_2 . According as the geometry, angle glint $\tilde{\varepsilon} = \tilde{r}\varepsilon$, because the target's moving in the plant wave area (target area) will not cause the change of angle error test result.

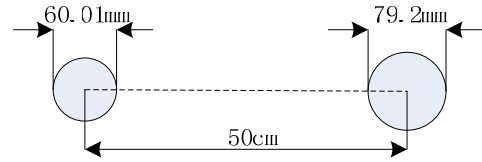
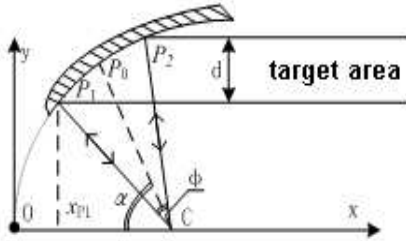


Figure 5: Configuration of CATR reflecting antenna system. Figure 6: The double balls union with looking down system.

From the angle glint calculation method, it is necessary to get \tilde{r} only with geometry. For spot P_0 ,

$$\begin{cases} y_{P_0} = (c + x_{P_0}) \sin(\alpha) \\ y_{P_0}^2 = 4cx_{P_0} \end{cases} \quad (9)$$

Then,

$$y_{P_0} = 2c \left(\frac{1 - \cos \alpha}{\sin \alpha} \right) = 2c \cdot \tan \left(\frac{\alpha}{2} \right) \quad (10)$$

So the angle glint calculation expression is,

$$\tilde{r} \approx |CP_0| = \sqrt{(x_{P_0} - c)^2 + y_{P_0}^2} = c \left(1 + \tan^2 \frac{\alpha}{2} \right) \quad (11)$$

Then,

$$\tilde{\varepsilon} \approx \varepsilon c \left(1 + \tan^2 \frac{\alpha}{2} \right) \quad (12)$$

3.2. Excellences of Dealing with HRRP

As the above dissertate, by using Equation (12) the angle error in different distance cells can be achieved, the refined measurement of angle glint of complex target is capable. Every radar target can be regarded as a series of scattering spot in wide-band system perfectly. When the test result is deal with HRRP, the main parts that rebound to increase the angular scintillation will be clearer than in narrow band system. To realize this particular can improve the research on mechanism about angle glint phenomenon and control technology of angular scintillation.

4. RESULTS AND DISCUSSIONS

In this section, the angle glint measurement results about double balls union and an airplane model have been laid out. When the test is actualizing, the range comparison monopulse radar system is working in Ka wave band and the frequency width is 500 MHz.

4.1. Double Balls Union

The double balls union is made of two aluminous balls with diameters 60.01 mm and 79.2 mm. In the experimentation, these balls was put in line and 50 cm away from each other, as Fig. 6. They were irradiated for 180° to get the angle glint in horizontal plane. The HRRP dealing result in angle changes is shown as Fig. 7. In this figure, it can be seen that both Δ -channel and Σ -channel are test the location distributing characters of the target, with Equation (8) and certain restrain arithmetic the angle glint in the distance cells where the double balls union is has been extracted. If the piece of the middle cells of angle glint is been take into rectangular coordinates, the traditional target angle glint will placed, and the comparison with theory calculate result in narrow band has been done in Fig. 8. There is the general identical movement between the test result and the calculate result, the differentia is resulted in noise of laboratory and the deference of frequency width.

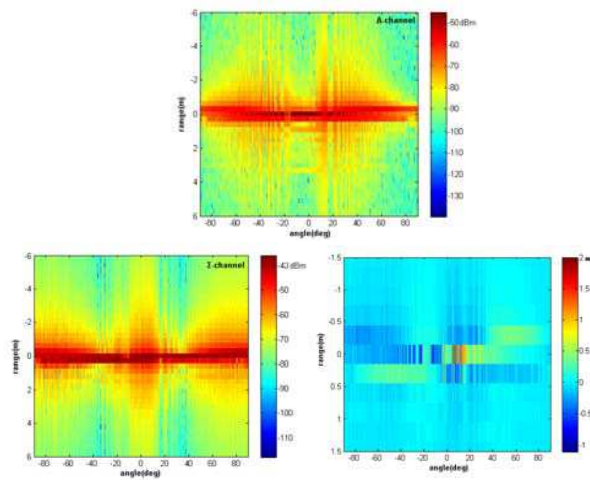


Figure 7: The test result of the double balls union, the HRRP with angle in Δ -channel (UP), the HRRP with angle in Σ -channel (Down-L), and the angle glint in different distance cells (Down-R).

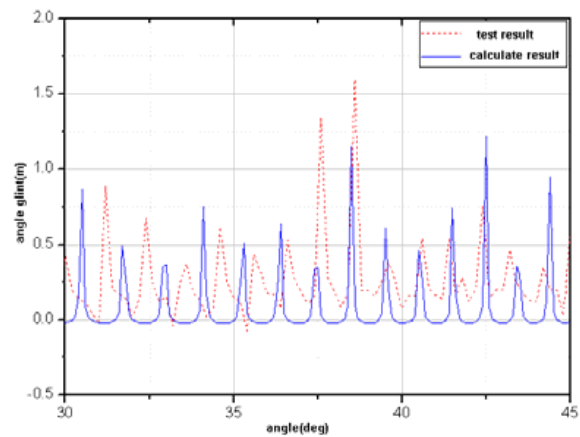


Figure 8: The angle glint curve of middle cell (red) and comparison with theory calculate result (blue) by double balls union test.

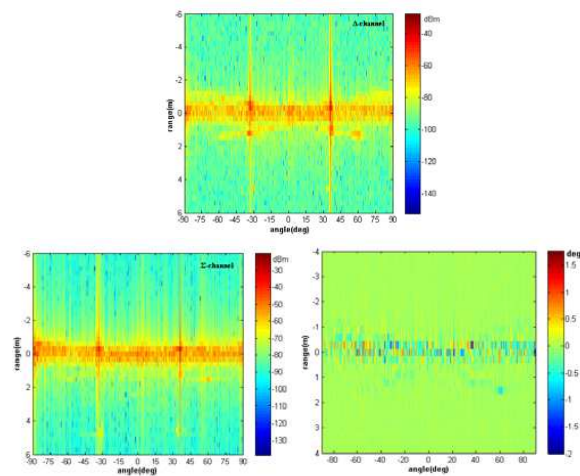


Figure 9: The test result of airplane model, the HRRP with angle in Δ -channel (UP), the HRRP with angle in Σ -channel (Down-L), and the angle glint in different distance cells (Down-R).

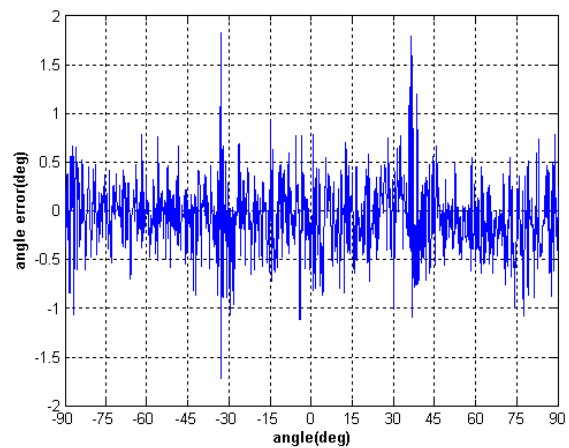


Figure 10: The angle error curve of middle cells by airplane model.

4.2. Airplane Model

In the same way, the angle glint measurement result of airplane model has been enumerated that are shown Fig. 9 and Fig. 10.

5. CONCLUSION

In this paper, author further discussed a type of new technique on target angular scintillation measurement, expatiated how to test target angle glint with wide-band range comparison monopulse radar in CATR anechoic chamber. A formulation about the excellences on dealing the angle error test result with HRRP has been given in the treatise also. At last, some measurement examples have been shown. Based on the comparison between the test result and the calculate result, it can be proved that the type of wide band test technique that this paper advanced is feasible.

REFERENCES

1. Ross, T. D., "Feature and extractor evaluation concepts for automatic target recognition (ATR)," WL-TR-95-1153, Oct. 1995.
2. Huang, P. K., H. C. Yin, and X. J. Xu, *Radar Target Characteristic*, Publishing House of Electronics Industry, Beijing, 2005.
3. Yin, H. C., P. K. Huang, and C. Wang, "Re-discussion about angular glint of the extended target," *Systems Engineering and Electronic*, Vol. 29, No. 4, 499–504, 2007.
4. Yin, H. C. and P. K. Huang, "Unification and comparison between two concepts of radar target angular glint," *IEEE Trans. on Aerospace and Electronic Systems*, Vol. 31, No. 2, 778–783, 1995.
5. Skolnik, M. I., *Radar Handbook*, 3rd Edition, The McGraw-Hill Companies Inc., 2008.
6. Kajenski, P. J., "Comparison of two theories of angle glint: Polarization consideration," *IEEE Trans. on Aerospace and Electronic Systems*, Vol. 42, No. 1, 206–210, 2006.
7. Ning, C., Y. B. Li, and X. Y. Zhang, "Glint measurement using monopulse radar in compact field," *Journal of Microwaves*, 2012.
8. Huang, B. K., Y. S. Jiang, and W. B. Wang, "Angular glint of some canonical target," *Systems Engineering and Electronic*, Vol. 25, No. 11, 1333–1335, 1340, 2003.
9. Liu, Y. L., S. B. Dong, G. Z. Mei, and H. Huang, "Effect and compensation of amplitude and phase inconsistency in MMW monopulse angle measurement," *Journal of Astronautic Metrology and Measurement*, Vol. 31, No. 1, 1–6, 2011.
10. Liang, S. L. and Z. Q. Hao, "A method of angle error extraction for monopulse radar," *Systems Engineering and Electronics*, Vol. 25, No. 1, 18–20, 2003.

Effective Implementation of the CFS-PML Using DSP Techniques for Truncating Dispersive Medium FDTD Domains

Naixing Feng¹, Yongqing Yue¹, Chunhui Zhu¹, and Qing Huo Liu²

¹Institute of Electromagnetics and Acoustics, Xiamen University, Xiamen, China

²Department of Electrical and Computer Engineering, Duke University, Durham, NC 27708, USA

Abstract— Efficient and unsplit-field finite-difference time-domain (FDTD) implementation of the complex frequency-shifted perfectly matched layer (CFS-PML), based on the digital signal processing (DSP) techniques and the material independence relations via applying the electric flux density (D) and the magnetic flux density (B), is proposed for truncating three dimensional FDTD computational domain entirely composed of dispersive material realized with a Drude model. The CFS-PML implementation is introduced based on the stretched coordinate PML (SC-PML) and the uniaxial anisotropic PML (UPML), respectively. The implementation of the proposed CFS-PML formulations is based on the SC-PML due to the fact that has advantage of simple implementation in the corners and the edges of the PML regions. Moreover, these proposed formulations are completely independent of the material properties of the FDTD computational domain and hence can be applied to truncate arbitrary media without any modification because of the D - B constitutive relations used in Maxwell's equations. Besides, the DSP techniques include the Bilinear Z -transform (BZT) method and the Matched Z -transform (MZT) method, respectively. However, from the point of view of the Courant-Friedrichs-Levy (CFL) condition, to the best of our knowledge, time step based on the BZT only needs to meet CFL condition, whereas time step based on the MZT method has to make it smaller for retaining stability and desirable accuracy. Consequently, the former one is introduced into the proposed formulations. A numerical example has been carried out in a three dimensional FDTD computational domain to validate the proposed formulations. It is clearly shown that the proposed formulations with CFS scheme are efficient in attenuating evanescent waves and reducing late-time reflections.

1. INTRODUCTION

One of the most widely methods in electromagnetic simulations, finite difference time domain (FDTD) method [1], has been used in various fields. Recently, the Z -transform method has been incorporated with FDTD scheme to model dispersive frequency dependent electromagnetic application [2]. This method takes the advantage of simplicity as it allows direct FDTD implementations of Maxwell's equations.

Meta-materials are specifically referred to as a class of artificial materials that have simultaneous negative electric permittivity and magnetic permeability [3] in a certain frequency band. These meta-materials have drawn considerable attention owing to their unusual electromagnetic properties [4]. To model open region double-negative (DNG) meta-material problems, absorbing boundary conditions (ABCs), such as perfectly matched layer (PML), are needed. New PML formulations have been successfully introduced for modeling DNG meta-material problems [6].

In this paper, an efficient DSP implementation of the CFS-PML is proposed based on stretched coordinate PML (SC-PML) and D - B formulations. In addition, these formulations are implemented using the electric flux density D and magnetic flux density B fields instead of the conventional E and H fields. This method has the advantage of making the PML completely independent of the material properties of the FDTD computational domain.

2. FORMULATIONS

In three-dimensional (3D) SC-PML regions, the frequency domain modified Maxwell's curl equations can be written in terms of D and B as:

$$j\omega\varepsilon_0 D(\omega) = \nabla_s \times H(\omega) \quad (1)$$

$$j\omega\mu_0 B(\omega) = -\nabla_s \times E(\omega) \quad (2)$$

where D and B are given by

$$D(\omega) = \varepsilon_r(\omega)E(\omega) \quad (3)$$

$$B(\omega) = \mu_r(\omega)H(\omega) \quad (4)$$

where $\varepsilon_r(\omega)$ and $\mu_r(\omega)$ are, respectively, the relative permittivity and permeability of the FDTD domain and the operator ∇_s is expressed as

$$\nabla_s = \hat{x}S_x^{-1}\partial_x + \hat{y}S_y^{-1}\partial_y + \hat{z}S_z^{-1}\partial_z \quad (5)$$

and S_η , ($\eta = x, y, z$) is the PML stretched coordinate variable given by [6].

$$S_\eta = 1 + \frac{\sigma_\eta}{j\omega\varepsilon_0\varepsilon_r(\omega)} \quad (6)$$

with the CFS scheme, S_η was defined as

$$S_\eta = \kappa_\eta + \frac{\sigma_\eta}{\alpha_\eta + j\omega\varepsilon_0\varepsilon_r(\omega)} \quad (7)$$

where σ_η and α_η are assumed to be positive real and κ_η is real and ≥ 1 . $\varepsilon_r(\omega)$ and $\mu_r(\omega)$ are, respectively, the DNG meta-material permittivity and permeability which are assumed to be identical and realized by the Drude-type DNG mode [4] as

$$\varepsilon_r(\omega) = \mu_r(\omega) = 1 + \frac{\omega_p^2}{-\omega^2 + j\omega\Gamma} \quad (8)$$

where ω_p and Γ are, respectively, the medium plasma frequency and loss factor.

Now the vector components of the curl operators of (1) and (2) are written out in three dimensions

$$j\omega\varepsilon_0 D_x(\omega) = S_y^{-1} \frac{\partial H_z(\omega)}{\partial y} - S_z^{-1} \frac{\partial H_y(\omega)}{\partial z} \quad (9)$$

$$j\omega\varepsilon_0 D_y(\omega) = S_z^{-1} \frac{\partial H_x(\omega)}{\partial z} - S_x^{-1} \frac{\partial H_z(\omega)}{\partial x} \quad (10)$$

$$j\omega\varepsilon_0 D_z(\omega) = S_x^{-1} \frac{\partial H_y(\omega)}{\partial x} - S_y^{-1} \frac{\partial H_x(\omega)}{\partial y} \quad (11)$$

$$j\omega\mu_0 B_x(\omega) = -S_y^{-1} \frac{\partial E_z(\omega)}{\partial y} + S_z^{-1} \frac{\partial E_y(\omega)}{\partial z} \quad (12)$$

$$j\omega\mu_0 B_y(\omega) = -S_z^{-1} \frac{\partial E_x(\omega)}{\partial z} + S_x^{-1} \frac{\partial E_z(\omega)}{\partial x} \quad (13)$$

$$j\omega\mu_0 B_z(\omega) = -S_x^{-1} \frac{\partial E_y(\omega)}{\partial x} + S_y^{-1} \frac{\partial E_x(\omega)}{\partial y} \quad (14)$$

It is clearly and easily observed that similar form can be found among (9)–(14).

First, let us consider the discretization of (14) taken as an example in the edges of SC-PML regions, which are overlaps of PML's faces that run parallel with the z direction Transforming (14) from the frequency to the Z -domain, Equation (14) can be written as

$$(1 - z^{-1})\mu_0 B_z / \Delta t = -\frac{1}{S_x(z)} \frac{\partial E_y}{\partial x} + \frac{1}{S_y(z)} \frac{\partial E_x}{\partial y} \quad (15)$$

where Δt is time step and $S_\eta(z)$, ($\eta = x, y, z$), can be obtained by applying the bilinear transform method [7] using relation $j\omega \rightarrow (2/\Delta t)(1 - z^{-1})/(1 + z^{-1})$

$$S_\eta(z) = w_\eta \frac{(1 + u_\eta z^{-1} + \theta_\eta z^{-2})}{(1 + v_\eta z^{-1} + \varphi_\eta z^{-2})} \quad (16)$$

where

$$w_\eta = \frac{\kappa_\eta [(\Delta t/2)^2(\alpha_\eta \Gamma + \varepsilon_0 \omega_p^2 + (\sigma_\eta \Gamma)/\kappa_\eta) + (\Delta t \alpha_\eta/2) + \varepsilon_0 + (\Delta t \varepsilon_0 \Gamma/2) + (\Delta t \sigma_\eta)/(2\kappa_\eta)]}{[(\Delta t/2)^2(\alpha_\eta \Gamma + \varepsilon_0 \omega_p^2) + (\Delta t \alpha_\eta/2) + \varepsilon_0 + (\Delta t \varepsilon_0 \Gamma/2)]}$$

$$u_\eta = \frac{[2(\Delta t/2)^2(\alpha_\eta \Gamma + \varepsilon_0 \omega_p^2 + (\sigma_\eta \Gamma)/\kappa_\eta) - 2\varepsilon_0]}{[(\Delta t/2)^2(\alpha_\eta \Gamma + \varepsilon_0 \omega_p^2 + (\sigma_\eta \Gamma)/\kappa_\eta) + (\Delta t \alpha_\eta/2) + \varepsilon_0 + (\Delta t \varepsilon_0 \Gamma/2) + (\Delta t \sigma_\eta)/(2\kappa_\eta)]}$$

$$v_\eta = \frac{[2(\Delta t/2)^2(\alpha_\eta \Gamma + \varepsilon_0 \omega_p^2) - 2\varepsilon_0]}{[(\Delta t/2)^2(\alpha_\eta \Gamma + \varepsilon_0 \omega_p^2) + (\Delta t \alpha_\eta/2) + \varepsilon_0 + (\Delta t \varepsilon_0 \Gamma/2)]}$$

$$\theta_\eta = \frac{[(\Delta t/2)^2(\alpha_\eta \Gamma + \varepsilon_0 \omega_p^2 + (\sigma_\eta \Gamma)/\kappa_\eta) - (\Delta t \alpha_\eta/2) + \varepsilon_0 - (\Delta t \varepsilon_0 \Gamma/2) - (\Delta t \sigma_\eta)/(2\kappa_\eta)]}{[(\Delta t/2)^2(\alpha_\eta \Gamma + \varepsilon_0 \omega_p^2 + (\sigma_\eta \Gamma)/\kappa_\eta) + (\Delta t \alpha_\eta/2) + \varepsilon_0 + (\Delta t \varepsilon_0 \Gamma/2) + (\Delta t \sigma_\eta)/(2\kappa_\eta)]}$$

$$\varphi_\eta = \frac{[(\Delta t/2)^2(\alpha_\eta \Gamma + \varepsilon_0 \omega_p^2) - (\Delta t \alpha_\eta/2) + \varepsilon_0 - (\Delta t \varepsilon_0 \Gamma/2)]}{[(\Delta t/2)^2(\alpha_\eta \Gamma + \varepsilon_0 \omega_p^2) + (\Delta t \alpha_\eta/2) + \varepsilon_0 + (\Delta t \varepsilon_0 \Gamma/2)]}$$

substituting (16) into (15), we obtain

$$(1 - z^{-1}) \mu_0 B_z / \Delta t = -\frac{1}{w_x} \frac{(1 + v_x z^{-1} + \varphi_x z^{-2})}{(1 + u_x z^{-1} + \theta_x z^{-2})} \frac{\partial E_y}{\partial x} + \frac{1}{w_y} \frac{(1 + v_y z^{-1} + \varphi_y z^{-2})}{(1 + u_y z^{-1} + \theta_y z^{-2})} \frac{\partial E_x}{\partial y} \quad (17)$$

Introducing the following auxiliary variables:

$$\phi_{zx} = \frac{1}{w_x} \frac{1}{(1 + u_x z^{-1} + \theta_x z^{-2})} \frac{\partial E_y}{\partial x} = -u_x z^{-1} \phi_{zx} - \theta_x z^{-2} \phi_{zx} + \frac{1}{w_x} \frac{\partial E_y}{\partial x} \quad (18)$$

$$\phi_{zy} = \frac{1}{w_y} \frac{1}{(1 + u_y z^{-1} + \theta_y z^{-2})} \frac{\partial E_x}{\partial y} = -u_y z^{-1} \phi_{zy} - \theta_y z^{-2} \phi_{zy} + \frac{1}{w_y} \frac{\partial E_x}{\partial y} \quad (19)$$

(18) and (19) can be written in simple FDTD form, respectively, as

$$\phi_{zx}^{n+1} = -u_x \phi_{zx}^n + Q_{zx}^n + \frac{1}{w_x} \frac{\partial E_y^{n+1/2}}{\partial x} \quad (20)$$

$$Q_{zx}^{n+1} = -\theta_x \phi_{zx}^n \quad (21)$$

$$\phi_{zy}^{n+1} = -u_y \phi_{zy}^n + Q_{zy}^n + \frac{1}{w_y} \frac{\partial E_x^{n+1/2}}{\partial y} \quad (22)$$

$$Q_{zy}^{n+1} = -\theta_y \phi_{zy}^n \quad (23)$$

where Q_{zx}^{n+1} and Q_{zy}^{n+1} are auxiliary variables. Substituting (20) and (22) into (17), we obtain

$$B_z^{n+1} = B_z^n + \frac{\Delta t}{\mu_0} [-(\phi_{zx}^{n+1} + v_x \phi_{zx}^n + m_{zx}^n) + (\phi_{zy}^{n+1} + v_y \phi_{zy}^n + m_{zy}^n)] \quad (24)$$

$$m_{zx}^{n+1} = \varphi_x \phi_{zx}^n \quad (25)$$

$$m_{zy}^{n+1} = \varphi_y \phi_{zy}^n \quad (26)$$

where m_{zx}^{n+1} and m_{zy}^{n+1} are auxiliary variables. Similar manipulations can be obtained for the FDTD implementations of (9)–(13).

3. NUMERICAL STUDY

To validate the proposed methods, a 3D numerical test was carried out for validating the proposed formulations. In this numerical example, a Gaussian pulse was excited at the center of $50\Delta x \times 50\Delta y \times 50\Delta z$ 3D domain composed of DNG meta-material realized by a Drude model [4] with the following parameters: $\omega_p = 2.665 \times 10^{11}$ rad/s and $\Gamma = 1 \times 10^8$ rad/s. Under these parameters, both $\varepsilon_r(\omega)$ and $\mu_r(\omega)$ are negative in the frequency range 0–42.5 GHz. The excited Gaussian pulse was given by $H_z = \sin(2\pi f_c t) \exp(-((t - T_0)/\tau)^2)$, where $f_c = 30$ GHz, $\tau = 26$ ps and $T_0 = 4\tau$. The computational domain was truncated by 10 cells thickness PML, as shown in Fig. 1. The

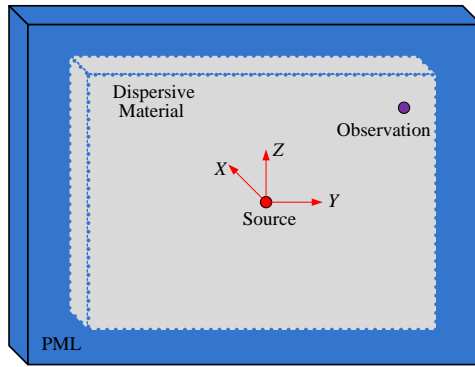


Figure 1: The FDTD grid geometry in this simulation.

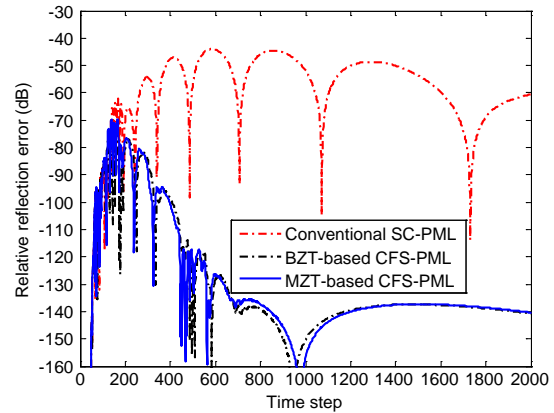


Figure 2: Relative reflection error versus time step.

observation point was chosen to be in the diagonal direction of the source and located one space cell from the PML corner region. The space cell size was taken as $\Delta x = \Delta y = \Delta z = 0.5$ mm. The time step size was chosen to satisfy the Courant-Friedrichs-Lewy (CFL) stability limit [1] for the 3D case.

The results are shown in Fig. 2. The maximum relative errors of the conventional SC-PML, the BZT-based CFS-PML, the MZT-based CFS-PML are -45 dB, -70 dB, and -70 dB, respectively. It can be concluded from Fig. 2 that the absorbing performance of the proposed BZT-based and MZT-based CFS-PMLs have 25 dB improvement in terms of the maximum relative reflection error as compared with the conventional SC-PML, and also holds better absorbing performance as compared with the conventional SC-PML in terms of reducing late-time reflections.

4. CONCLUSION

The CFS-PML formulations have been presented for truncating dispersive material FDTD computational domains. These formulations are independent of the material properties of the FDTD computational domains due to their features of the D - B constitutive relations. A numerical test carried out in a 3D FDTD computational domain shows that the proposed formulations provide better absorbing performance as compared with the conventional SC-PML without CFS scheme.

ACKNOWLEDGMENT

These works are partly supported by the Natural Science Foundation of China (NSFC) under Grant ZDYZ2012-1-03, 41390453 and 61301008, and partly supported by the Fundamental Research Funds for the Central Universities under Grant ZDYZ2012-1-03.

REFERENCES

1. Taflove, A. and S. C. Hangess, *Computational Electrodynamics: The Finite-difference Time-domain Method*, 2nd Edition, Artech House, 2000.
2. Li, J. X. and J. F. Dai, "Z-transform implementation of the CFS-PML for arbitrary media," *IEEE Microwave and Wireless Components Letters*, Vol. 16, No. 8, Aug. 2006.
3. Veselago, V. G., "The electrodynamics of substances with simultaneously negative values of ϵ and μ ," *Sov. Phys. Usp.*, Vol. 10, No. 4, 509–514, 1968.
4. Ziolkowski, R. W. and E. Heyman, "Wave propagation in media having negative permittivity and permeability," *Phys. Rev. E*, Vol. 64, 056625, 2001.
5. Berenger, J.-P., "A perfectly matched layer for the absorption of electromagnetic waves," *J. Comput. Phys.*, Vol. 114, 185–200, 1994.
6. Cummer, S. A., "Perfectly matched layer behavior in negative refractive index materials," *IEEE Antennas Wirel. Propag. Lett.*, Vol. 3, 172–175, 2004.
7. Proakis, J. G. and D. G. Manolakis, *Digital Signal Processing: Principles, Algorithms and Applications*, 3rd Edition, Prentice Hall International Editions, 1996.

Continuously Moving Target Simulator Design

Deping Zhang, Chao Wang, Chang Zhu, and Naichang Yuan

College of Electronic Science and Engineering, National University of Defense Technology, Changsha, China

Abstract— The delay time of echo generated by the moving target simulator is discrete, and the moving trace of simulated target is discontinuous. In order to solve this problem, firstly, the radar digital signal processor must adjust the range gate, and the range error will be limited within one range cell. Then the rest error cannot be removed but can be adjusted by phase pre-compensation in simulator. The idea is that let the phase of simulated target be equal to the one of the real target at sampling time. After the phase pre-compensation, a real continuously moving target will be generated and the problem will be solved. Then MATLAB simulation of the method is done for linear frequency modulation radar system. The simulated results can be used to validate the effectiveness of the method.

1. INTRODUCTION

At the present time, with the development of direct digital synthesizer (DDS) and digital signal processing (DSP) technique, the moving target simulator (MTS) can simulate a moving target with high Doppler frequency resolution and high amplitude resolution [1–5]. A MTS based on digital radio frequency memory (DRFM) and the impact of discrete delay time of the MTS on radar system coherency were separately analysed in [6]. The delay time of target generated by the MTS is discrete, so the range of simulated target is discrete and it is hard to simulate real moving target. In other words, the simulated target will jump towards the radar step by step. Its track is discontinuous, especially for high range resolution (HRR) radar. It is hard for us to find a method to solve the problem in previous references. So this paper will present a method to solve the problem.

2. COMPOSITION OF THE MOVING TARGET SIMULATION SYSTEM

Figure 1 shows the composition of the moving target simulation system. The radar and MTS share a common clock source. The radar transmitter is turned off and the receiver is turned on. Then the MTS generates the needed target according to the instructions of the radar. The DSP in the radar will adjust the range gate and the DSP in MTS will compensate the phase error. More details will be shown below.

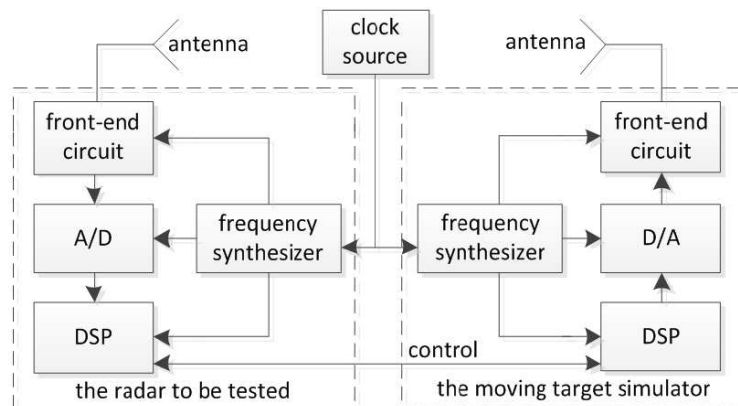


Figure 1: Composition of the moving target simulation system.

3. PROBLEM ANALYSIS

The pulses transmitted by the radar are

$$s_t = \text{rect}\left(\frac{t - nT_r}{\tau}\right) \sin(\Omega_{t0}t) \quad (1)$$

where $\Omega_{t_0} = 2\pi f_{t_0}$, f_{t_0} is carrier frequency, τ is pulse width, T_r is pulse repetition interval (PRI), n is integer. Consider a point target which is moving towards the radar at velocity v . Let R_0 refer to the range at time $t = 0$ (time reference), the pulses received by radar are

$$s_r = \text{rect}\left(\frac{ut - nT_r - t_0}{\tau}\right) \sin(u\Omega_{t_0}t - \phi_0) \quad (2)$$

where $u = 1 + 2v/c$, $t_0 = 2R_0/c$, $\phi_0 = \Omega_{t_0}t_0$. When the reflected pulses leading edge strikes the radar, the time is

$$t_{rn0} = \frac{-\tau/2 + nT_r + t_0}{u} \quad (3)$$

Now, the MTS should transmit signal s_r at time t_{rn0} . But the delay time of MTS is discrete, and t_{rn0} is continuous function of v . As a result, the delay time error is generated by MTS, and the simulated target will jump towards the radar. Consider a MTS with the delay time resolution T_{dl} . The delay time of MTS referring to t_{rn0} is

$$t_m = \text{fix}\left(\frac{t_{rn0}}{T_{dl}}\right) T_{dl} = mT_{dl}, \quad m = \text{fix}\left(\frac{t_{rn0}}{T_{dl}}\right) \quad (4)$$

where $\text{fix}(x)$ is MATLAB function. The delay time error is

$$\Delta t_{rn} = t_{rn0} - t_m \geq 0 \quad (5)$$

Now let us analyse the impact of delay time error on the radar. Suppose that the sampling interval of the radar is $T_s < T_{dl}$. The simulated target and the real target locate at different range gates and their phases are different at the sampling time, as illustrated in Fig. 2.

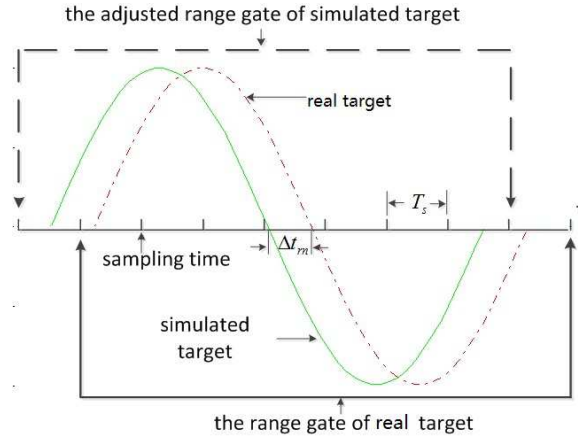


Figure 2: Illustrates the impact of delay time error on the radar.

4. METHOD TO SOLVE THE PROBLEM

We should firstly adjust the range gate. The number of range cell to be adjusted is

$$\Delta r_n = \text{fix}\left(\frac{t_{rn0}}{T_s}\right) - \text{fix}\left(\frac{t_m}{T_s}\right) \quad (6)$$

The adjusting process is shown in Fig. 2, and $\Delta r_n = 1$. After that, the simulated target and the real target will equivalently locate at the same range gate, as shown in Fig. 3. Then, the equivalent delay time error is given by

$$\Delta t_n = \left[t_{rn0} - \text{fix}\left(\frac{t_{rn0}}{T_s}\right) T_s \right] - \left[t_m - \text{fix}\left(\frac{t_m}{T_s}\right) T_s \right] = \Delta t_{rn} - \Delta r_n T_s \quad (7)$$

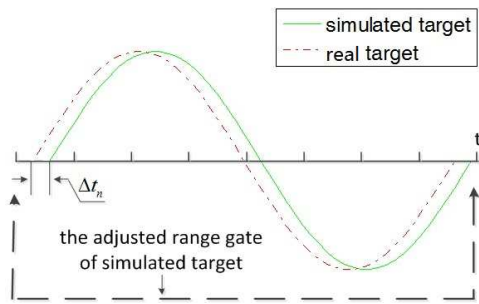


Figure 3: Equivalent result of range gate adjusting.

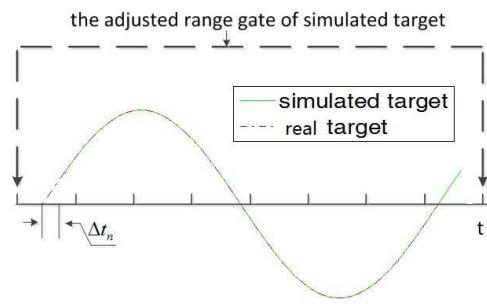


Figure 4: Simulated target after phase pre-compensation.

The error Δt_n cannot be removed due to the discrete delay time of MTS and their phases are different at sampling time. However, we can compensate the phase differences. The idea is that the MTS pre-adjusts the signal (2) and let the phase of the simulated target be equal to that of the real target at sampling time. In other words, their waveforms are the same at sampling time. That is why we do range gate adjusting firstly. In Fig. 4, the delay time error is Δt_n . But at any sampling time, their phases are equal and their waveforms are the same. So the radar digital signal processor will not treat them as distinct targets and they are the same for the radar. Then the simulated target would not jump towards the radar but continuously move towards the radar as real target. The adjusted signal transmitted by MTS is

$$s_{rm}(t) = \text{rect} \left[\frac{t - t_m - \tau/2}{\tau} \right] \sin[u\Omega_{t0}(t + \Delta t_n) - \phi_0] \quad (8)$$

5. APPLICATION TO LINEAR FREQUENCY MODULATION (LFM) RADAR

Consider a radar system using LFM waveforms. The pulse width is $\tau = 10 \mu\text{s}$, bandwidth is $B = 200 \text{ MHz}$, PRI is $T_r = 0.1 \text{ ms}$, the carrier frequency is $f_{t0} = 1.4 \text{ GHz}$ and the sampling frequency is $F_s = 800 \text{ MHz}$. Then a point target is moving towards the radar at velocity $v = 800 \text{ m/s}$ and its

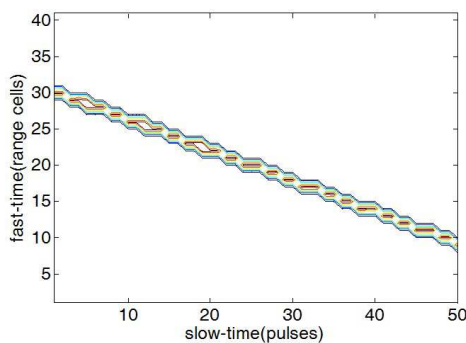


Figure 5: Trace of true moving target.

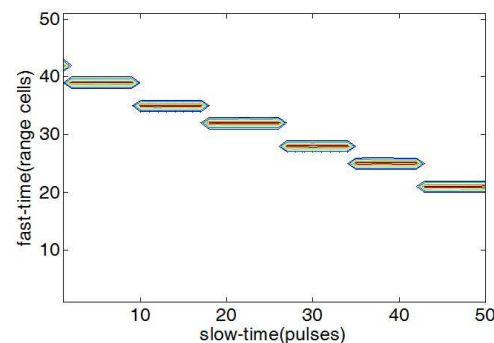


Figure 6: Trace of simulated moving target before adjusting.

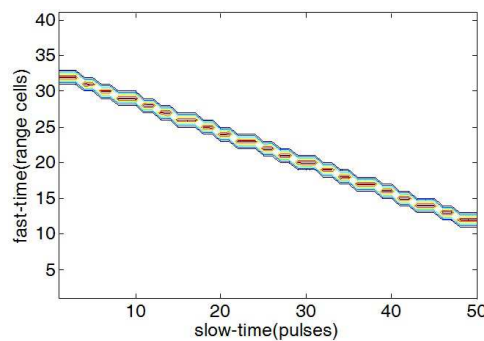


Figure 7: Trace of simulated moving target after adjusting.

initial range is $R_0 = 40$ km. After pulse compression, the trace of real target is shown in Fig. 5. Now consider a simulator with delay time resolution $T_{dt} = 1/225$ μ s. The trace of simulated target before adjusting is shown in Fig. 6. We can see that the trace is discontinuous, which implies that the simulated target is jumping towards the radar. After adjusting the range gate and adjusting the phase differences at sampling time, the trace of simulated target is nearly the same as the trace of real target, as shown in Fig. 7.

6. CONCLUSION

This paper treats the radar and MTS as a cooperation system to solve the problem. Firstly, the radar must adjust the range cell error, and then the MTS should pre-compensate the phase differences at sampling time. The equivalent effect on radar is that the simulated target will continuously move towards the radar. The MATLAB simulation results can validate the method. After solving the problem we can simulate real moving target by using MTS.

REFERENCES

1. Wang, X. and M. Pan, "Research on LFM signal linearity calibration in radar target simulator," *Chinese Journal of Scientific Instrument*, Vol. 32, No. 10, 2389–2392, 2011.
2. Zheng, Z. and J. Jiang, "Research on super close-in PD radars complex target echo synthesis," *Chinese Journal of Electronics*, Vol. 39, No. 3A, 43–46, 2011.
3. Bao, X., H. Fan, and J. Sha, "Design of simulator of target and jamming echo for frequency-agile pulse Doppler radar seeker," *Computer Measurement & Control*, Vol. 20, No. 2, 401–403, 2012.
4. Liu, Q., X. Li, and Y. Wan, "Modelling and simulation of short-distance MMW Doppler target simulator," *Journal of System Simulation*, Vol. 21, No. 16, 4954–4957, 2009.
5. Olivier, K., J. E. Cilliers, and M. Du Plessis, "Design and performance of wideband DRFM for radar test and evaluation," *Electronics Letters*, Vol. 47, No. 14, 824–825, 2011.
6. Zhou, G., "Coherency analysis of moving target simulator," *Chinese Journal of Modern Radar*, Vol. 27, No. 11, 33–44, 2005.

Accurate Statistical Modeling Method for Dynamic RCS

Ya-Qiang Zhuang, Chen-Xin Zhang, and Xiao-Kuan Zhang

Air and Missile Defense College, Air Force Engineering University, Xi'an 710051, China

Abstract— The dynamic RCS of an aircraft target varies dramatically with target geometry and motion information (position and velocity), the values fluctuate and have no pattern. So the fluctuation models are often adopted to describe the statistical nature of dynamic RCS. In this paper, we first introduce a simulation method of dynamic RCS for aircraft target. Secondly, a brief introduction of Chi2 distribution and Lognormal distribution model is given, and Gaussian Mixture distribution is proposed in order to describe the fluctuation more accurately. The parameter estimation method is discussed in detail to find the best fitting result. As an example, the dynamic RCS data of an aircraft target are analyzed with Chi2 distribution, Lognormal distribution model and Gaussian Mixture distribution. The fitting results show Gaussian Mixture distribution can provide a better approximation of the dynamic RCS than the other two distributions in accordance with error-of-fit and Kolmogorov-Smirnov fitting goodness test.

1. INTRODUCTION

RCS (Radar Cross Section) is an important parameter reflects target scattering ability for incident EM waves. It is often applied in the radar detection and target recognition field [1]. The dynamic RCS of aircraft in the movement has practical significance which can be acquired by field measurement and simulation method. Due to the high cost and uncertainty of field measurement, the latter is often adopted. The combinations of PO (Physical Optics) method with PTD (Physical Theory of Diffraction) [2, 3] are often used to evaluate the static RCS of the target in the simulation process.

RCS of aircraft depends on geometry and orientation whose values are often time-varying during its movement [4]. It has been advantageous to treat the target RCS as a statistic items for the dynamic RCS with random fluctuation. Statistical distributions are used for RCS characterization. Much work has been done over the years in statistical modeling of RCS, including conventional distribution such as Chi2 distribution, Rice distribution, Lognormal distribution and some new distributions such as Weibull distribution, NCGG (Non Central Gamma Gamma) distribution [5] and Two State Rayleigh-Chi distribution [6].

The EM calculation model of an aircraft is modeled and all-attitude static RCS database is calculated firstly in this paper. The dynamic RCS of spiral flying is calculated by linear interpolation based on static database. Then, the brief introduction of three distributions is given, and parameter estimation procedure of GM (Gaussian Mixture) distribution is provided. In addition, statistical characterization of dynamic RCS using three fluctuation models was investigated. The comparison results show that GM distribution can provide a better approximation of the dynamic RCS.

2. SIMULATION METHOD OF AIRCRAFT'S DYNAMIC RCS

2.1. Static RCS Calculation

In this section, the EM calculation model was modeled and the all-attitude static RCS database was calculated in FEKO as shown in Figure 1. The EM model was modeled by the size of scale target after multiplying its scale ration, and static RCS value was calculated by PO method at the steps of 1° under L band (165 MHz) for HH polarization. The target coordinate center is located at the geometrical center of the target. The attitude angle was defined as shown in Figure 1. The pitch angle is from X axis round to Z axis in the XOZ plane, and the azimuth angle is from X axis round to Y axis in the XOY plane.

2.2. Dynamic RCS Series

After the all-attitude static RCS database was calculated, the dynamic RCS series of the special flight path can be acquired by following procedures. Firstly, we predestined path the aircraft flies with and radar position as shown in Figure 2. Given the aircraft make a spiral flying with radius 40 km under speed 1.4 Ma at height 9 km level plane. From the flight path, the aspect angles of radar line of sight in radar coordinate system can be calculated easily. A coordinate transformation need to be done in order to acquired the aspect angles in target coordinate system. Then, the dynamic RCS can be acquired according to aspect angles using linear interpolation method. Plot of dynamic RCS for the aircraft in given flight path is provided in Figure 3.

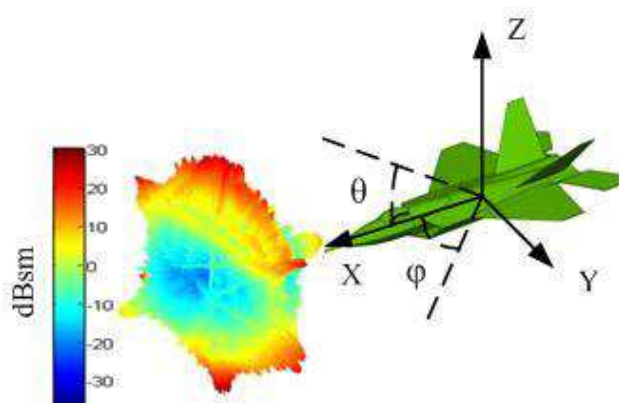


Figure 1: Aircraft EM model and all-attitude static RCS database.

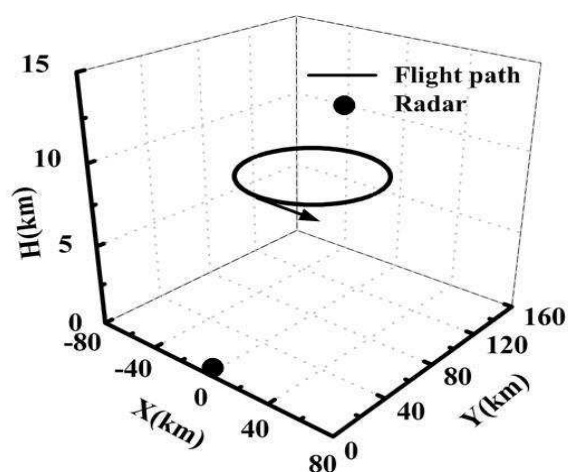


Figure 2: Aircraft flight path and radar position.

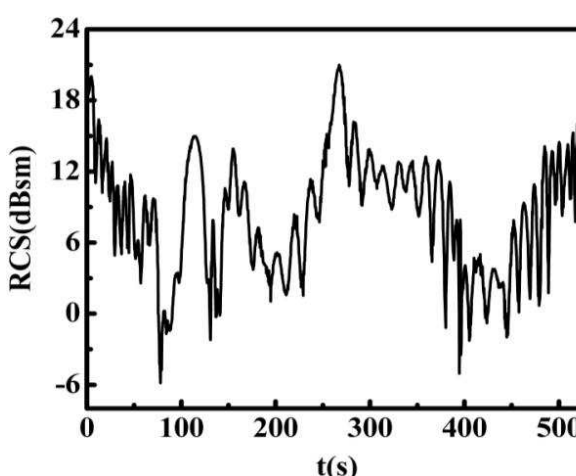


Figure 3: Dynamic RCS series.

3. TARGET FLUCTUATION MODELS

Among the existing RCS distribution models, Chi2 distribution and Lognormal distribution are worthwhile to promote. The parameter analysis has been discussed detailedly in [7, 8]. The statistical modeling method of dynamic RCS using Gaussian Mixture distribution is proposed.

3.1. Chi2 Distribution 1

This model was introduced by Swerling and assumes that the PDF (Probability Density Function) of the target RCS is a generalized Chi2 distribution is as Eq. (1)

$$p(\sigma) = \frac{k}{\Gamma(k)\bar{\sigma}} \left(\frac{k\sigma}{\bar{\sigma}}\right)^{k-1} \exp\left(-\frac{k\sigma}{\bar{\sigma}}\right), \quad \sigma > 0 \quad (1)$$

In Eq. (1), σ is RCS variable and $\bar{\sigma}$ is the mean of RCS value. k named double-degrees of freedom is equal to $\bar{\sigma}^2/\text{variance of } \sigma$. Parameter k can be positive integer or non-integer. So it's fitting to different distributions is very good. $\Gamma(k)$ is a gamma function with parameter k . The PDF (1) subsumes as a special case the Swerling I-IV and Marcum distribution, corresponding to $k = 1, 2, N, 2N$ and ∞ [9].

3.2. Lognormal Distribution

The fluctuation RCS of targets such as ships and missiles is often well modeled as a log-normal random variable. The PDF of Lognormal distribution can be written as Eq. (2)

$$p(\sigma) = \frac{1}{\sigma s \sqrt{2\pi}} \exp\left(-\frac{(\ln\sigma - \mu)^2}{2s^2}\right), \quad \sigma > 0 \quad (2)$$

In Eq. (2), σ is RCS variable. μ is the mean of σ and s is the standard deviation of σ . The normal and Lognormal distributions are closely related. If the RCS value σ is distributed log normally with parameters μ and s , then $\ln\sigma$ is distributed normally with mean μ and standard deviation s .

3.3. Gaussian Mixture Distribution

Gaussian Mixture distribution is a semi parametric density estimation method, and it combines the advantages of parameter estimation method and non-parametric estimation method [10]. Gaussian Mixture distribution has been used widely in the field of voice recognition, image processing, and microarray gene expression data and so on. The PDF of Gaussian Mixture distribution is as Eq. (3)

$$f(x, \Theta) = \sum_{i=1}^M \frac{a_i}{\sqrt{2\pi}s_i} \exp\left(-\frac{(x - \mu_i)^2}{2s_i}\right) \quad (3)$$

where $\Theta = (a_1, a_2, \dots, a_M; \mu_1, \mu_2, \dots, \mu_M; s_1, s_2, \dots, s_M)$, a_i is the weight of number i component, and it meets $\sum_{i=1}^M a_i = 1$. The variable μ_i and s_i are the mean and variance of number i component respectively. If the component number M is enough, the Gaussian Mixture distribution will approximate any continuous distribution with perfect accuracy.

The Expectation Maximization (EM) method is often adopted to estimate the parameter of Gaussian Mixture distribution. Given that

$$p(x|\Theta) = \sum_{i=1}^M a_i p_i(x|\theta_i) \quad (4)$$

In the Eq. (4), $\theta = (\mu, s)$, $p_i(x|\theta_i)$ is the number i Gaussian component with θ_i .

The iterative formula to calculate parameter by EM method is as Eq. (5):

$$\begin{cases} a_l^{new} = \frac{1}{N} \sum_{i=1}^N p(l|x_i, \Theta^g) \\ u_l^{new} = \frac{\sum_{i=1}^N x_i p(l|x_i, \Theta^g)}{\sum_{i=1}^N p(l|x_i, \Theta^g)} \\ s_l^{new} = \frac{\sum_{i=1}^N p(l|x_i, \Theta^g) (x_i - u_l^{new})^2}{\sum_{i=1}^N p(l|x_i, \Theta^g)} \end{cases} \quad (5)$$

In the Eq. (5), $p(l|x_i, \Theta^g) = \frac{a_l^g p_l(x_i|\theta_l^g)}{p(x_i|\Theta^g)} = \frac{a_l^g p_l(x_i|\theta_l^g)}{\sum_{j=1}^M a_j^g p_j(x_i|\theta_j^g)}$.

4. RESULTS

4.1. Fitting Results

The statistical modeling of dynamic RCS distribution and fitting method has been discussed for many years. We choose the Chi2 distribution, Lognormal distribution and two-order Gaussian Mixture distribution to fit the PDF (probability density function) and CDF (Cumulative Distribution Function) of dynamic RCS. The fitting parameters of Chi2 distribution and Lognormal distribution can be estimated by non-linear least squares algorithm. The distribution parameters of Gaussian Mixture distribution are estimated by EM method. The fitting results are shown in Figure 4.

4.2. Result Analysis

The errors-of-fit e_f is used to compare the fitting result which defined as Eq. (6)

$$e_f = \sum_i [p_e(\sigma_i) - p_m(\sigma_i)]^2 \quad (6)$$

In Eq. (6), $p_e(\sigma_i)$ is the RCS statistical distribution and $p_m(\sigma_i)$ is the fitting result of these distributions. The errors-of-fit are provided in Table 1.

The non-parametric fitting goodness test procedure is investigated to evaluate the probability model of the RCS sample data for three distributions applied above. The Kolmogorov-Smirnov test [11] statistically measures the absolute errors between an observed CDF of sample values and

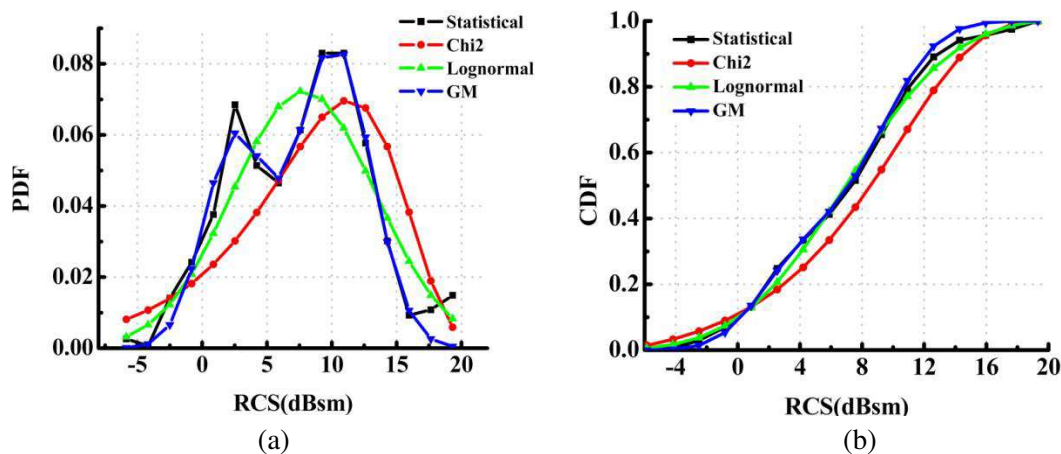


Figure 4: Fitting result of distribution of dynamic RCS. (a) PDF distribution. (b) CDF distribution.

Table 1: Errors-of-fit and K-S test results.

	Chi2	Lognormal	GM
errors-of-fit	0.43%	0.22%	0.05%
K-S test result	0.1232	0.0417	0.0377

a specified continuous distribution function. The test function is shown in Eq. (7), in which $F(x)$ is the statistical CDF of dynamic RCS data and $F'(x)$ is CDF of the fitting results. If the test result is too large, it can be determined that the distribution used is not applicable for the data. The results of K-S test are shown in Table 1.

$$D = \max |F(x) - F'(x)| \quad (7)$$

From the fitting curves, errors-of-fit and Kolmogorov-Smirnov test results, it can be concluded that Gaussian Mixture distribution and Lognormal distribution are better than Chi2 distribution for dynamic RCS of this target. In addition, the fitting result of Gaussian Mixture distribution is a quite better than Lognormal distribution form its extreme little errors-of-fit. Therefore, the dynamic RCS data can be modeled accurately by Gaussian Mixture distribution.

5. CONCLUSION

A new approach to obtain dynamic RCS quickly in the predestined path is proposed firstly in this paper. After time-varying attitude angles of radar line of sight in aircraft coordinate were calculated based on coordinate transformation, the dynamic data was obtained from all-attitude static RCS database using linear interpolation method. A statistical modeling method of dynamic RCS based on Gaussian Mixture distribution is investigated. The comparison on statistical characterization of dynamic RCS under typical paths using Ch2 distribution, Lognormal distribution and Gaussian Mixture distribution is analyzed. The fitting results show that Gaussian Mixture distribution is the best applicable among three distributions to describe the dynamic RCS. The research result of this paper can be applied in statistical characterization of aircraft's dynamic RCS, and can provide a reliable support for accurate simulation and examining of moving target's echo.

ACKNOWLEDGMENT

This work is supported by the National Natural Science Foundation of China (Grant No. 61372166).

REFERENCES

1. Mayer, D. P. and H. A. Mayer, *Radar Target Detection — Handbook of Theory and Practice*, Academic Press, New York, 1973.
2. Zhao, Y., X.-W. Shi, and L. Xu, "Modeling with NURBS surfaces used for calculation of RCS," *Progress In Electromagnetics Research*, Vol. 78, 49–59, 2008.
3. Wu, Y., L. Jiang, and W. C. Chew, "An efficient method for computing highly oscillatory physical optics integral," *Progress In Electromagnetics Research*, Vol. 127, 211–257, 2012.

4. Pierce, R. D., “RCS characterization using the alpha-stable distribution,” *1996 IEEE National Radar Conf.*, 154–159, Ann Arbor, Michigan, 1996.
5. De Maio, A., A. Farina, and G. Foglia, “New target fluctuation models and their experimental validation,” *2005 IEEE Radar Conf.*, 272–277, Arlington, USA, 2005.
6. Shnidman, D. A., “Expanded swerling target models,” *IEEE Transactions on Aerospace Electronic and Systems*, Vol. 39, No. 3, 1059–1069, 2003.
7. Shi, W. Q., X.-W. Shi, and L. Xu, “RCS characterization of stealth target using χ^2 distribution and lognormal distribution,” *Progress In Electromagnetics Research M*, Vol. 27, 1–10, 2012.
8. Shi, W. Q., X.-W. Shi, and L. Xu, “Radar cross section (RCS) statistical characterization using weibull distribution,” *Microwave and Optical Technology Letters*, Vol. 55, No. 6, 1355–1358, 2013.
9. Swerling, P., “Radar probability of detection for some additional fluctuating target cases,” *IEEE Transaction on Aerospace and Electronic Systems*, Vol. 33, No. 2, 698–709, 1997.
10. Bilmes, J., “A gentle tutorial of the EM algorithm and its application to parameter estimation for Gaussian mixture and hidden Markov models,” TR-97-021, 1–13, Department of Electrical Engineering and Computer Science. U. C. Berkeley, 1998.
11. Xie Z., J. P. Li, and Z. Chen, *Nonlinear Optimization Theory and Method*, Higher Education Press, Beijing, 2010 (in Chinese).

A Method for Predicting Far Field Radar Cross-section from Near Field Measurements on Cylindrical Scanning Mode

C. Gao^{1,2}, J. W. Chen^{1,2}, M. Jin², and Y. Bai²

¹Information Engineering School, Communication University of China, Beijing 100024, China

²Science and Technology on Electromagnetic Scattering Laboratory, Beijing 100854, China

Abstract— For studying the EM signatures of full-size target, it demands outdoor or indoor room large enough for measurement, but the construction of outdoor and indoor room which satisfy the far field conditional both lead to costly installation and require extraordinary elaborate technique, say nothing of carrying out the imaging and RCS diagnostic for stealth weapon in active service. This paper meets the demand of the development with the stealth and anti-stealth weapon, aims at the shortage of outdoor and indoor measuring of the far field electromagnetism feature, presents a research on 3-D near-field to far-field transformation algorithm, in which the far-field condition could not be satisfied on both vertical and horizontal plane for the target under test, and the target is illuminated by a spherical wave. A 3-D multi-scattering center model is built for the target and the near-field data is sampled by 3-D scan, using the extensions of spherical-wave function in cylindrical coordinates, the relationship between far-field and near-field scattering field is deduced under the condition that the antenna works at cylindrical-scan mode. The RCS and image pattern can be achieved by the 3-D IFFT algorithm and interpolation technique. The simulation results show that the algorithm is precise and effective.

1. INTRODUCTION

RCS measurement is necessary for designing stealth weapon system as well as for the research of the electromagnetic scattering properties of radar-illuminate target. The theory and algorithm of electromagnetic scattering computation can be verified by RCS measurement, moreover, it's difficult to compute electromagnetic scattering of complex and large objects, but the data can be obtained visually by RCS measurement.

However, due to the strong frequency-dependent scattering behavior of electromagnetic waves, it is often necessary to conduct the measurements using full-size structures rather than scale-models at high frequencies. Consequently, even moderately large components, as well as larger full-scale structures, have to be measured using outdoor radar measurement ranges. To reduce the cost and time consumed in outdoor range measurement, it is advantageous to develop a capability for characterizing representative structural components that are electrically large within a near distance. This always involves the near-field to far-field RCS measurements transformation methods which is mentioned in [1–5]. The near-field RCS measurement method based on plane scan mode has been presented in [6], while numerical simulation results proves the feasibility and superiority of the method.

But near field to far field transformation based on plane scanning mode is in the rectangular coordinate, in which the near field data grabbing is conducted on the wide plan scan stand, the near field testimony for the electro-magnificent dimension target requires high demand to the aperture and machining decision of the scan stand, however, many microwave anechoic or indoor testing yard could not reach the above criterion because of the confinement of the field. The more widely used near field scatter data collection mode is cylindrical-scan mode (the target rotates, and the radar antenna move along the vertical line to the ground), in order to control the test cost and improve the efficiency.

This paper presents a near field to far field transformation method based on cylindrical scan mode, which utilize the extensions of spherical-wave function in cylindrical coordinates, to deduce the relationship between far-field and near-field scattering field in cylindrical scan mode.

2. NEAR FIELD TO FAR FIELD TRANSFORMATION

The near field cylindrical scan illustration setup is shown in Fig. 1, in which the emit and receive antenna is placed along the vertical track (axis z), move linearly in a fixed step, and the target rotates under the control of the rotate platform in a linearly equal angle interval, antenna measures and records the scatter field data of the target, including the amplitude and phase, on every wave

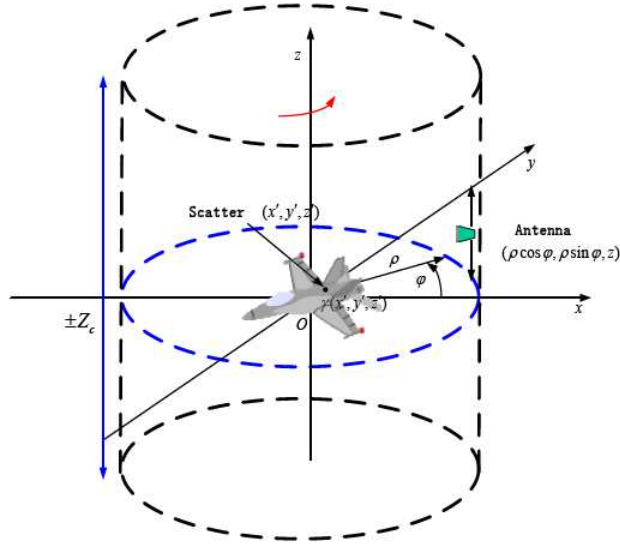


Figure 1: Cylindrical scan mode illustration.

frequency according to the fixed starting frequency and band width, then move to the next record point to repeat.

The time-harmonic weight of the electro-magnetic wave is $e^{-j\omega t}$, the scattering field signal of the target backscatter could be written as:

$$u(k, \varphi, z) = \frac{1}{(4\pi)^2} \iiint \gamma(x', y', z') \left[\frac{e^{-j2kR}}{R^2} \right] dx' dy' dz' \quad (1)$$

where,

$$R = \sqrt{(x' - \rho \cos \varphi)^2 + (y' - \rho \sin \varphi)^2 + (z' - z)^2} \quad (2)$$

The square brackets in Equation (1) is double-distance spherical factor e^{-j2kR}/R^2 , as to the three-dimensional scatter target, the near field illumination is spherical illumination, as to set up the relation between the near field scatter and far field scatter, the double-distance spherical wave factor needs to be transformed into the single-distance spherical factor e^{-j2kR}/R .

According to the character of the Fourier Transform, the realization of the transformation between the double-distance spherical wave factor and the single-distance spherical factor is very convenient when assuming wideband measurements, it just needs to conduct 2 Fourier transform in the frequency domain and distance domain, as follows:

$$U(k, y, z) = \frac{1}{\pi} \int R \left[\int u(k, y, z) e^{-j2kR} dk \right] e^{j2kR} dR \quad (3)$$

The Equation (3) equals to add-up the echo data $u(k, \varphi, z)$ in the distance domain, in which the add-up factor is R , the detailed process is shown in following diagram:

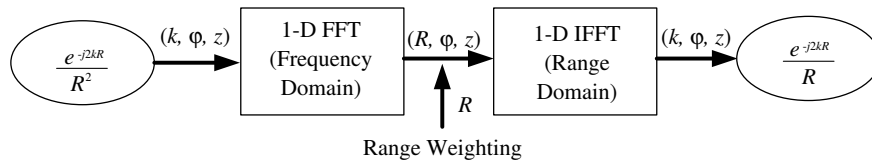


Figure 2: The distance domain add-up process.

Then the Equation (1) transforms into

$$U(k, \varphi, z) = \frac{1}{4\pi} \iiint \gamma(r') \left[\frac{e^{-j2k|\mathbf{r}-\mathbf{r}'|}}{4\pi |r-r'|} \right] dr^3 \quad (4)$$

The square brackets in the above equation are spherical wave factor, also called as the free space Green Function, which has the form:

$$\psi = \frac{e^{-j2k|\mathbf{r}-\mathbf{r}'|}}{4\pi|\mathbf{r}-\mathbf{r}'|} \quad (5)$$

Express ψ with the basic wave function in rectangular coordinate

$$\psi = \iiint_{\kappa_x \kappa_y \kappa_z} A(\kappa_x, \kappa_y, \kappa_z) e^{-j\boldsymbol{\kappa} \cdot \mathbf{r}} d\kappa_x d\kappa_y d\kappa_z \quad (6)$$

In the infinitely large uniform space, the point source field located at the source point \mathbf{r}' satisfies the scalar Hermhoz Equation

$$\nabla^2 \psi + k^2 \psi = \delta(\mathbf{r} - \mathbf{r}') \quad (7)$$

Conduct the plane wave extension of the Green function under the 3-dimensional rectangular coordinate, the Equation (4) changes its form into:

$$\psi = \frac{j}{8\pi^2} \iiint_{k_y k_z} \frac{e^{-j[k_x|x-x'|+k_y(y-y')+k_z(z-z')]} k_x}{k_x} dk_y dk_z$$

In which

$$\begin{cases} k_y = \kappa_y \\ k_z = \kappa_z \\ k_x = \sqrt{k^2 - k_y^2 - k_z^2} \end{cases} \quad (8)$$

Calculated from the above equation, $k_x^2 + k_y^2 + k_z^2 = k^2$, the factor $k_x(x-x') + k_y(y-y') + k_z(z-z')$ in the Equation (7) denote the plane wave's phase factor, and $j/8\pi^2 k_x$ represents the plane wave amplitude. The integration transform could be utilized to simplify the 3-D integration with 2-D integration, and deduce the spherical factor extension under cylindrical coordinate.

In cylindrical coordinate, the wavenumber and coordinate have the form:

$$\begin{cases} k_x = k_\rho \cos \varphi \\ k_y = k_\rho \sin \varphi \\ x - x' = \rho \cos \varphi' \\ y - y' = \rho \sin \varphi' \\ k_\rho^2 + k_z^2 = k^2 \end{cases} \quad (9)$$

Using the above relation, the Equation (7) transforms into

$$\begin{aligned} \psi &= \frac{j}{8\pi^2} \int_0^\infty \frac{e^{-j\sqrt{k^2 - k_\rho^2}(z-z')}}{\sqrt{k^2 - k_\rho^2}} k_\rho dk_\rho \int_{-\pi}^\pi e^{-jk_\rho \rho \cos(\varphi - \varphi')} d\varphi \\ J_0(x) &= \frac{1}{2\pi} \int_{-\pi}^\pi e^{-jx \cos(\varphi - \varphi')} d\varphi \end{aligned} \quad (10)$$

Subscribe into Equation (5), and one gets

$$\psi = \frac{j}{4\pi} \int_0^\infty \frac{J_0(k_\rho \rho) e^{-j\sqrt{k^2 - k_\rho^2}(z-z')}}{\sqrt{k^2 - k_\rho^2}} k_\rho dk_\rho \quad (11)$$

Using the relation between the Brussels Function and Hanker Function, the above equation can be expressed as

$$\psi = \frac{j}{8\pi} \int_0^\infty \frac{H_0^2(k_\rho \rho) e^{-j\sqrt{k^2 - k_\rho^2}(z-z')}}{\sqrt{k^2 - k_\rho^2}} k_\rho dk_\rho \quad (12)$$

Subscribe the Equation (12) into Equation (3)

$$U(k, \varphi, z) = \int \rho(r') \frac{j}{8\pi} \int_0^\infty \frac{H_0^2(k_\rho \rho) e^{-j\sqrt{k^2 - k_\rho^2}(z-z')}}{\sqrt{k^2 - k_\rho^2}} k_\rho dk_\rho dr^3 \quad (13)$$

Using the Hanker Function's Add-up theorem

$$H_0^2(k_\rho \rho) = \sum_{n=0}^{\infty} H_n^2(k_\rho \rho) e^{jn\varphi} J_n(k\rho') \quad (14)$$

Subscribe the Equation (14) into Equation (13)

$$U(k, \varphi, z) = \sum_{n=0}^{\infty} H_n^2(k_\rho \rho) e^{jn\varphi} J_n(k\rho') \frac{j}{8\pi} \int_0^\infty \frac{e^{-j\sqrt{k^2 - k_\rho^2}(z-z')}}{\sqrt{k^2 - k_\rho^2}} k_\rho dk_\rho \quad (15)$$

Transform the Equation (15)'s Integration order and add up, one gets

$$U'(k, \varphi, z) = \sum_{n=0}^{\infty} H_n^2(k_\rho \rho) e^{jn\varphi} e^{j\sqrt{k^2 - k_\rho^2}z} \int_0^\infty \frac{j}{8\pi} J_n(k\rho') \frac{e^{-j\sqrt{k^2 - k_\rho^2}z'}}{\sqrt{k^2 - k_\rho^2}} k_\rho dk_\rho \quad (16)$$

Set $S_0 = \int_0^\infty \frac{j}{8\pi} J_n(k\rho') \frac{e^{-j\sqrt{k^2 - k_\rho^2}z'}}{\sqrt{k^2 - k_\rho^2}} k_\rho dk_\rho$, and connect with Equation (9), and the Equation (16) is simplified as

$$U(k, \varphi, z) = \sum_{n=0}^{\infty} H_n^2(k_\rho \rho) e^{jn\varphi} e^{jk_z z} S_0 \quad (17)$$

Conduct 2D Fourier Transform to Equation (17)

$$\int_{-\infty}^{\infty} e^{-jk_z z} dz \int_0^{2\pi} U'(k, z, \varphi) e^{-jn\varphi} d\varphi = \sum_{n=0}^{\infty} H_n^2(k_\rho \rho) S_0 \quad (18)$$

Tidy up Equation (18) and one gets

$$S_0 = \sum_{n=0}^{\infty} \frac{\int_{-\infty}^{\infty} e^{-jk_z z} dz \int_0^{2\pi} U'(k, z, \varphi) e^{-jn\varphi} d\varphi}{H_n^2(k_\rho \rho)} \quad (19)$$

When the distance between antenna and target satisfy the far field condition, and the following calculation approximation stands

$$|r - r'| \cong r - r \cdot r' \quad (20)$$

And

$$\frac{e^{-j2k|r-r'|}}{4\pi|r-r'|} = \frac{e^{-j2kr}}{4\pi\rho} e^{j2kr \cdot r'} \quad (21)$$

At the same time, the Hanker Function large volume approximation is

$$H_n^{(2)}(k_\rho \rho) \underset{k_\rho \rho \rightarrow \infty}{=} \sqrt{\frac{2}{\pi k_\rho \rho}} e^{-j(k_\rho \rho - \frac{2n+1}{4}\pi)} \quad (22)$$

Subscribe the Equations (19), (21), (22) into Equation (17), the transform relation between near field and far field scattering under cylinder scan mode after tidy-up

$$S_{FF}(k, \varphi, k_z) = \sqrt{\frac{\rho}{\pi k_\rho}} e^{-j\rho(k_\rho - k)} e^{j\frac{2n+1}{4}} \sum_{n=0}^N \frac{e^{jn\varphi}}{H_n^2(k_\rho \rho)} \int_{-\infty}^{\infty} e^{-jk_z z} dz \int_0^{2\pi} U'(k, z, \varphi) e^{-jn\varphi} d\varphi \quad (23)$$

The above equation is the near-far field transform relation under scan-frequency system, and it could be applied into the spot-frequency system, which needs only substitute $U(k, z, \varphi)$ with $u(k, z, \varphi)$, where the H_n^2 is the second sort n order Hanker Function, truncated at the $kD + 10$ order, where D is the minimum diameter of the cylinder surrounding target which have the same concentric point with the survey circular. The $S_{FF}(k, \varphi, k_z)$ in Equation (23) is the 3-dimension wave number data of the target. Utilizing the 3D-IFFT imaging arithmetic under rectangular coordinate, conducting the 3D reverse Fourier transform to the Equation (23), one could get the far field image of the target. However, before conducting the 3D reverse Fourier transform, the extrapolated far field $S_{FF}(k, \varphi, k_z)$ needs to be interposed according to the relation $(k, \varphi, k_z) \rightarrow (k_x, k_y, k_z)$, in order to finish the reestablishment of the target image. Meanwhile, interpose the $S_{FF}(k, \varphi, k_z)$ according to the mapping relation of Equation (9), the far-field RCS is related to the far-field pattern via

$$\sigma(k, \phi) = 4\pi |S_{FF}(k, \phi)|^2 \tag{24}$$

3. SIMULATION EXAMPLES

In order to testify our transformation method, numerical simulation is conducted to observe the actual imaging performance. In the numerical scene, the point target's position and RCS amplitude is shown in Fig. 3. The simulation measurement parameters are: central frequency f_0 is 4 GHz, the scan band width B is 4 GHz, he frequency points number is 301, the cylinder scan radius is 5 m, the moving scale along axis z is ± 3 m, the scan step is 2 cm, the scan azimuth angle is $-180^\circ \sim 180^\circ$, the angle interval is 0.5° . The RCS variation relation with azimuth angle, pitch angle and frequency is shown in Figs. 4~6.

Through calculation, the average square error of the near field extrapolation data and far field data in azimuth angle, pitch angle and frequency domain are 0.1608 dB (5° smooth window), 0.3046 dB (1° smooth window), 0.4101 dB. The 3-dimensional rebuild image is shown in Fig. 7. From the imaging results, one can find that the scattering center position in 3D image is identical

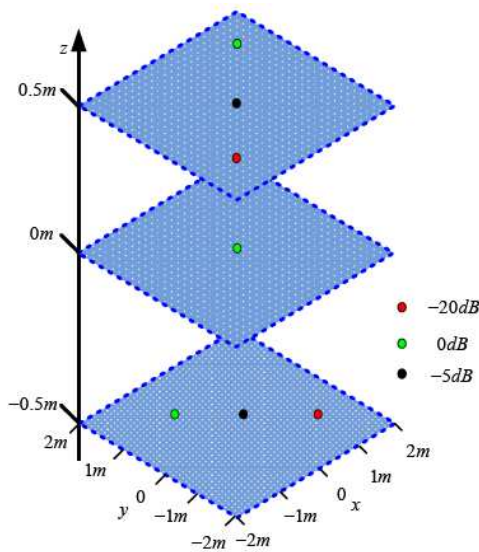


Figure 3: Scatters distribution map.

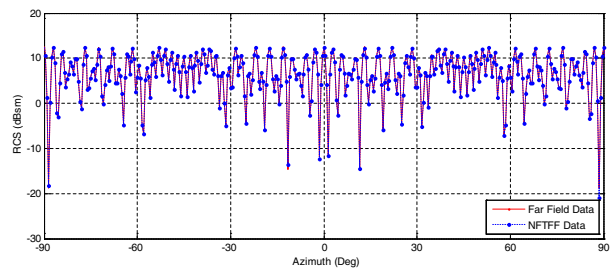


Figure 4: RCS variation with the azimuth.

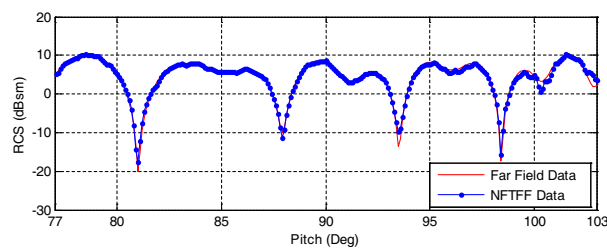


Figure 5: RCS variation with the pitch angle.

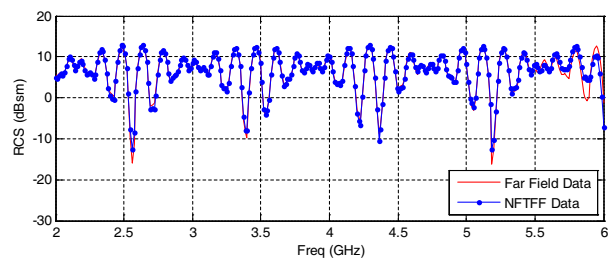


Figure 6: RCS variation with frequency.

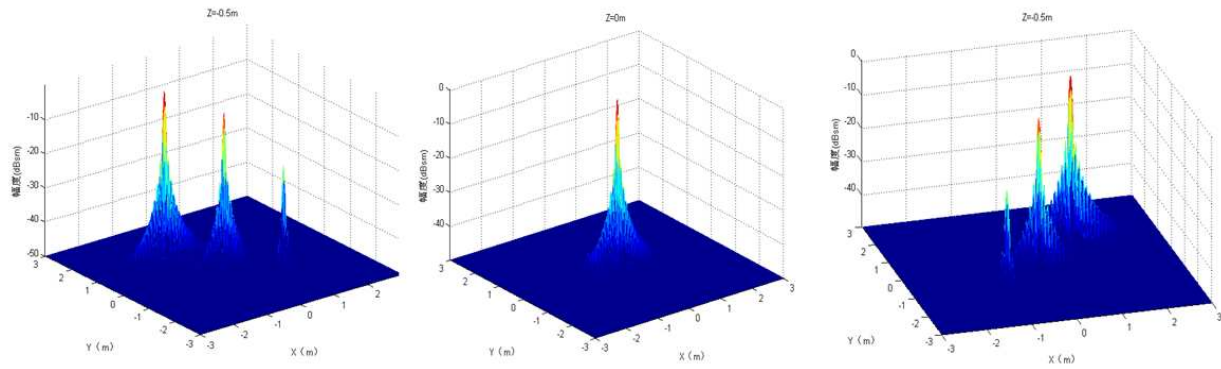


Figure 7: Point scatters 3D rebuild image.

with actual situation. And the largest position error is only 1 cm; the largest amplitude error of the scattering center is below 0.3 dB.

4. CONCLUSIONS

This article studied near field to far field transformation based on cylindrical scan mode. This arithmetic first transformed the double-distance spherical wave factor in echo data into the single-distance spherical wave factor, and utilize the 3D rectangular coordinate extension theorem of the spherical electro-magnetic wave into plan wave, established the relationship between near field backscatter and far field backscatter field, finally obtained the far field RCS character by 3D IFFT and 2D interpose and target's image. The numerical simulation result testified the validity and effectiveness of the above transformation arithmetic.

REFERENCES

1. Watkins, J. R., "Utilizing near-field measurements to characterize far-field radar signatures," Master Thesis, 2004.
2. Cady, E. M., "A study of near field data transformed to the far field for a canonical PEC scatter," Master Thesis, 2006.
3. LaHaie, I. J., "Overview of an image-based technique for predicting far field radar cross-section from near field measurements," *IEEE Ant. Prop. Mag.*, Vol. 45, No. 6, 159–169, 2003.
4. LaHaie, I. J., et al., "An improved version of the circular near field-to-far field transformation (CNFFFT)," *Proc. AMTA '05*, 196–201, 2005.
5. Norton, S. J. and M. Linzer, "Ultrasonic reflectivity imaging in three dimensions exact inverse scattering solutions for plane, cylindrical and spherical apertures," *IEEE Transactions on Biomedical Engineering*, 202–220, 1981.
6. Gao, C., Z. H. Xiao, and C. Ning, "Near-field three dimensional imaging and RCS extrapolation," *Antenna Journal B*, Vol. 2, 249–262, 2010.
7. Fischer, B. E., et al., "On the use of wavenumber migration for linear SAR image formation and near-field to far-field RCS transformation," *Proc. of 23rd Annual Meeting of the Antenna Measurement Techniques Association (AMTA '01)*, 117–122, Denver, CO, 2001.
8. LeBaron, E. I. and K. R. Aberegg, "Application of an image-based near field-to-far field transformation to measured data," *Proc. of the 19th Annual Meeting of the Antenna Measurement Techniques Association (AMTA '97)*, 340–345, Boston, MA, 1997.
9. Lopez-Sanchez, J. M. and J. Fortuny-Guasch, "3-D Radar imaging using range migration techniques," *IEEE Trans. Antennas Propagat.*, Vol. 48, 728–737, May 2000.
10. Hansen, J. E., *Spherical Near-field Antenna Measurements*, Peter Peregrinus Ltd., Stevenage, U.K., 1988
11. Fortuny-Guasch, J. and J. M. Lopez-Sanchez, "Extension of the 3-D range migration algorithm to cylindrical and spherical scanning geometries," *IEEE Trans.*, Vol. 49, No. 10, Oct. 2001.

Relationships between Surface Wave Attenuation and the Reflection Properties of Thin Surface Wave Absorbing Layer

Hai-Yan Chen, Li-Juan Lu, Dong-Jiao Guo, Hai-Peng Lu,
Pei-Heng Zhou, Jian-Liang Xie, and Long-Jiang Deng

State Key Laboratory of Electronic Thin Films and Integrated Device
National Engineering Research Center of Electromagnetic Radiation Control Materials
University of Electronic Science and Technology of China, Chengdu 610054, China

Abstract— Compared and analyzed the surface impedance defined by the basic definition of surface wave and by the reflection coefficient of thin radar absorbing material (RAM) layers backed with a perfect electric conductor (PEC) plate, the relationships between its surface wave attenuation property and its reflection characteristics can be founded. Equivalent surface impedance for a perfect electrical conductor (PEC) plate coated by a thin layer of RAM can be easily obtained based on the reflection coefficient for an infinite plate coated with same thin RAM layers, which can be regarded as a function for computing the attenuation of surface wave in this RAM layers. In this paper, two kinds of reality RAM for single layer coating and two layers coating will be considered for verifying this approach respectively. For two layers coating, the mono-static radar cross section (RCS) reduction properties of a slab coated with this RAM are discussed for evaluating the attenuation of surface wave because the equivalent medium theory is not appropriated under this condition. The proposed approach is effective and advantageous especially for thin multi-layers RAM coating.

1. INTRODUCTION

In recent years, with the development of low observable technology, much interest has been shown in reducing the non-specular scattering caused by surface wave. Surface wave becomes one of the most important issues in RCS design since the main scattering sources such as specular reflections are effectively eliminated [1]. The control of surface wave has been utilized as the motivation for exploring new RAM as well as the shaping of edges and other electromagnetic discontinuities. Surface wave radiates energy at discontinuities such as edges of the target [2]. By reciprocity, surface wave will be excited by plane electromagnetic (EM) wave incident upon such a discontinuity [3]. Properties of surface wave in absorbing layers are widely investigated, such as the works done by Ufimtsev [4, 5], Paknys [6], and Neve [7]. In these literatures, fundamental characteristics of surface wave including attenuation and propagation constants, electric and magnetic losses, phase and energy velocities, etc., are analyzed. These works start with the definition of surface wave, but ignore the properties of surface wave in multi-layers RAM coating. The equivalent medium theory is not appropriated for computing the surface wave properties under this condition of multi-layers RAM coating. Thus, it is necessary to study another approach for evaluating the surface wave properties especially for the case of multi-layers RAM coating.

Based on the Collin's guided wave analysis method of dielectric plate [8], equivalent surface impedance of thin coating layers over which surface wave propagates is defined to predict the performances of surface wave attenuation. Reflection coefficient of an impedance-coated surface can be measured expediently at plane EM wave incidence from normal to near grazing incidence. Then, attenuation properties of surface wave in thin RAM at oblique incidence can be obtained. Relationships between the surface wave properties and the reflection characteristic of a grounded dielectric slab covered a doubly periodic array of metal patches was analyzed [9], but this problem is still needed further research.

In this paper, the relationships between its surface wave attenuation property and its reflection characteristics will be founded by compared surface impedance defined by the basic definition of surface wave and the reflection coefficient at plane EM wave incidence respectively. Single layer RAM coating and two layers RAM coating are considered respectively for analyzing this conclusion. For single layers RAM coating, an actual magnetic material is considered. For two layers RAM coating, two kinds of actual RAMs will be considered, in one of the materials exist only electric loss, in another exist simultaneously electric loss and magnetic loss, and their relative permittivity and relative permeability are obtained from measured data. Based on these intrinsic parameters, reflection properties of the entire coating layers can be computed for various combinations of coating

thicknesses and coating orders according to the transmission line theory. For thin RAM layers, this planar coated structure is equivalent to an impedance-coated surface, and its surface impedance can be obtained based on computed reflection coefficient. The properties of surface wave in RAM layers have certain correspondence to its contributions to mono-static RCS reduction. According to this conclusion proposed in Ref. [10], the mono-static RCS reduction of a slab coated with corresponding thin RAM layers are calculated to validate the analysis of surface wave attenuation property in thin RAM layers based on their electromagnetic reflection characteristics.

In the following discussion, unless otherwise indicated, the analysis is limited to the attenuation and propagation property of TM surface wave in thin RAM layers, since the analysis of transverse-electric (TE) surface wave is similar.

2. DESIGN

2.1. The Attenuation of Surface Wave

We consider the two-dimensional (2-D) TM surface wave in thin homogeneous RAM layer backed up by a perfect conducting plane. Schematic of the problem is illustrated in Figure 1. In this figure, region 1 is free space; region 2 is a thin RAM layer with equivalent relative permittivity ε and equivalent relative permeability μ . The layer thickness is denoted by d . the wave number in free-space is denoted as $k_0 = \omega\sqrt{\varepsilon_0\mu_0} = 2\pi/\lambda_0$, where ε_0, μ_0 is the permittivity and the permeability of free space respectively, ω is the angular frequency of harmonic oscillation and λ_0 is the free-space wavelength. The time dependence $\exp(-j\omega t)$ is assumed and suppressed below.

Based on Ref. [11], the surface wave attenuation can be obtained,

$$\beta'' = -k_0 \text{Im} \left(\sqrt{1 - \left(\frac{\eta_s^s}{Z_0} \right)^2} \right) \text{ (Np/m)}. \quad (1)$$

where

$$\eta_s^s = \frac{E_{\text{tan}}}{H_{\text{tan}}} = -Z_0 \frac{k_1}{k_0} \quad (2)$$

2.2. Reflection at the Interface of Free Space and the Thin RAM Layer Backed by Ground Plane

In the case of TM polarization, the electric field vector is parallel to the plane of incidence as shown in Figure 2. The wave is incident at an angle θ_i with respect to the surface normal \hat{n} and reflected at an angle θ_r . Region 1 is free space with parameters (ε_0, μ_0) and region 2 is the thin RAM layer with parameters (ε, μ) .

Base on the Maxwell's equation, we obtain

$$\eta_s^r = -\frac{E_x^{\text{inc}} + E_x^{\text{ref}}}{H_x^{\text{inc}} + H_x^{\text{ref}}} = -\frac{\cos\theta_i Z_0(1 - \Gamma)}{1 + \Gamma} \quad (3)$$

where η_s^r represents the surface impedance based on the reflection coefficient. Eq. (2) is consistent with the Eq. (9.20) in Page 426 of Ref. [12].

η_s^s can be equivalent with η_s^r under the certain conditions, which is the main target in this paper.

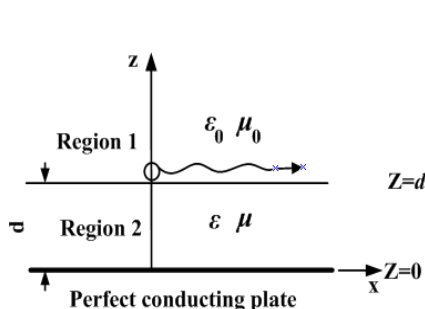


Figure 1: Model for surface wave analyzing.

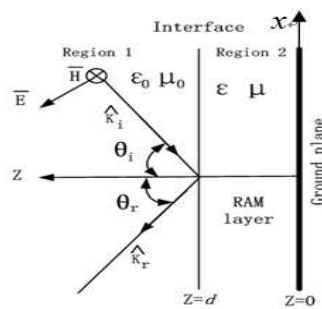


Figure 2: Plane wave incidence on a plane boundary.

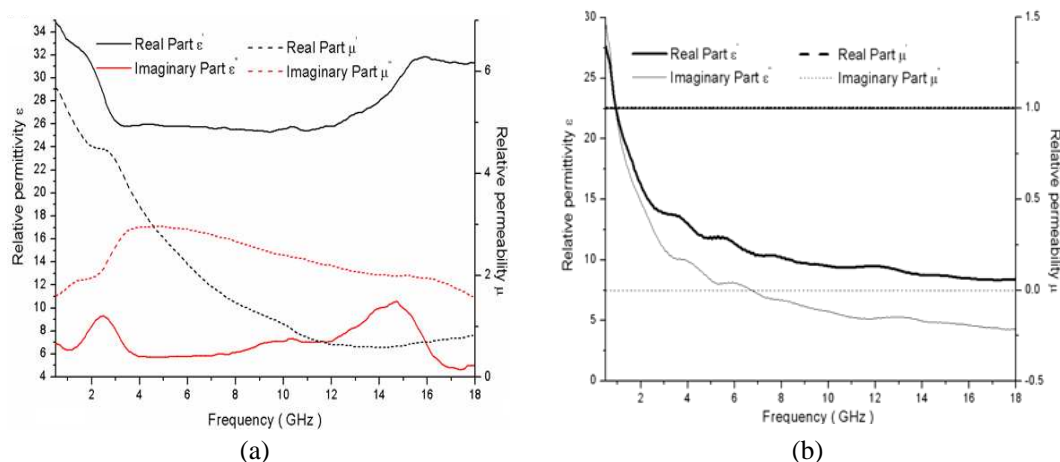


Figure 3: The relative permittivity and relative permeability dispersion characteristics. two actual absorbing materials: (a) RAM A, and (b) RAM B.

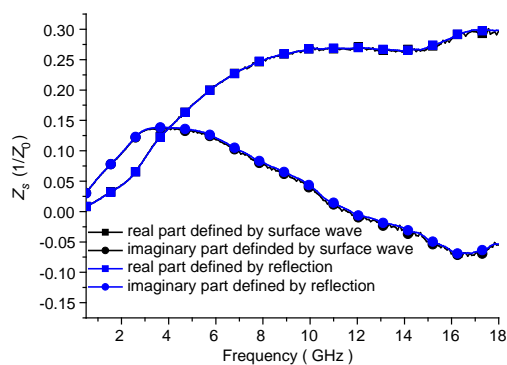


Figure 4: Surface impedance defined by surface wave characteristic and by the reflection coefficient of RAM A backed with a perfect electric conductor (PEC) plate, and its thickness is 0.5 mm.

3. RESULTS AND ANALYSIS

3.1. Single Layer RAM Coating

In this paper, two kinds of RAMs for single layer coating and two layers coating will be considered, RAM A is obtained on the basis of polymer composites filled with carbonyl iron and Co_2Z ferrite [13], but RAM B is obtained on the basis of Carbon black in polyethylene, which the relative permittivity ϵ and relative permeability μ shown in Figure 3 are gained from measured results. For single layer RAM coating, only RAM A is considered, and its thickness is 0.5 mm.

Based on the transmission line theory, the reflection loss determined in coating layer of RAM A with the thickness of 0.5 mm can be obtained for TM polarization, and the surface impedance defined by surface wave characteristic can be obtained based on the Formula (2), and the surface impedance defined by reflection coefficient at 30° of incidence angle is also proposed for comparison, just as shown in Figure 4. We can observe that the surface impedance defined by surface wave characteristic is exactly identical to that defined by reflection coefficient. That is to say, the evaluation of surface wave attenuation property in thin RAM layers based on their electromagnetic reflection characteristics is good enough.

3.2. Two Layers RAM Coating

Considered the propagation properties of surface wave, the equivalent medium theory is not appropriated for thin multi-layers RAM coating. Therefore, the evaluation of surface wave properties of thin multi-layers RAM coating is very difficult. In this paper, based on the relationships between the properties of surface wave in coated RAM layers and mono-static RCS reduction performances of the coated slab [10, 15], its surface wave characteristics can be easily obtained.

Double layers coating order is kept and as follow, the bottom layer is RAM A with the thickness of 0.5 mm, and the top layer is RAM B with the thickness of 1.0 mm. To this case, the surface

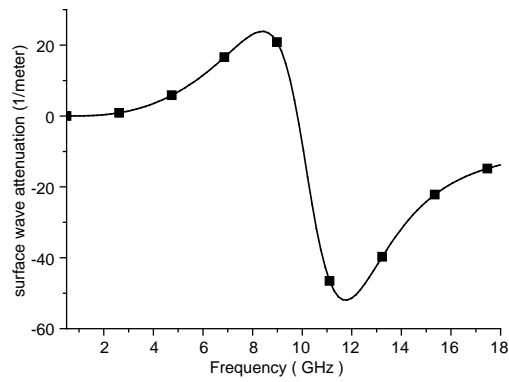


Figure 5: The surface wave attenuation defined by reflection coefficient.

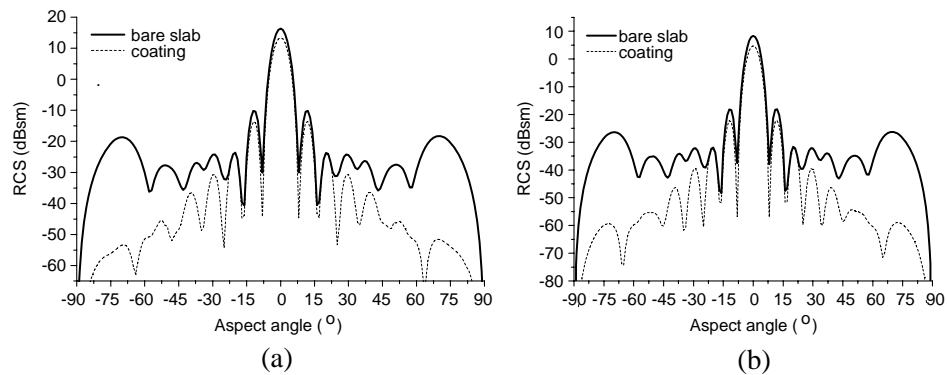


Figure 6: Mono-static RCS with TM polarization for different frequency ((a) 4 GHz, (b) 10 GHz).

impedance based on the reflection coefficient can be obtained according to the Eq. (3). Supposed that the η_s^s can be equivalent with η_s^r , the surface attenuation of this structure can be obtained based on the Eq. (1), just as shown in Figure 5. In the following, the surface attenuation defined by reflection coefficient will be certified based on the relationships in between the travelling wave attenuation and the radar cross section reduction.

In this paper, a slab will be considered to lie in the xy -plane with a plane wave incident at an angle θ_i with respect to the z -axis, as shown in Figure 2. The flat plate (aluminum slab) of size $a \times b = 5\lambda \times 5\lambda$ (λ is the wavelength in free space) and thickness equal to 0 mm, has RAM coatings on the upper surface. Based on the definition of the RCS of surface traveling wave [15], the main-lobe of surface traveling wave is located at 75° .

Figure 6 shows the mono-static RCS with TM polarization at 4 and 10 GHz. Tapered R-card [16–18] was loaded to the edges of the considered metal slab to reduce its edge scatter. The mono-static RCS of uncoated slab is also provided for RCS reduction analysis. The differences between mono-static RCS for coated and uncoated cases are shown by RCS reduction values. Based the RCS reduction at the observe angle of 75° , the surface wave attenuation can be computed, 3.82 Np/m and 9.82 Np/m for 4 GHz and 10 GHz respectively. Compared these results with Figure 5, good agreement is observed.

4. CONCLUSION

The surface wave attenuation property can be obtained based on the reflection coefficient of thin RAM layers backed with PEC ground plate. This approach is effective and advantageous especially for thin multi-layers RAM coating. The case of double layers RAM coating is analyzed in this paper, and the results verify this analysis effectively. In general, the thickness of surface wave absorbing materials layers should be much thinner than the effective wavelength, and its refractive index is large relative to free space, which is a prerequisite to using this approach. In conclusion, we verified that the surface impedance Z_s with near constant for all angles of incidence defined by reflection coefficient of plane wave incidence on it is practically identical to that defined by surface wave properties.

ACKNOWLEDGMENT

This research was partially supported by the National Natural Science Foundation of China (Grant No. 51025208, and Grant No. 51301031) and the fundamental research funds (Project No. ZYGX20-13J029).

REFERENCES

1. Smith, F. C., "Edge coatings that reduce monostatic RCS," *IEE Proc. — Radar Sonar Navig.*, Vol. 149, No. 6, 310–314, Dec. 2002.
2. Chen, H. Y., L. J. Deng, and P. H. Zhou, "Suppression of surface wave from finite conducting surfaces with impedance loading at margins," *Journal of Electromagnetic waves and Applications*, Vol. 24, Nos. 14–15, 1977–1989, 2010.
3. Monteith, D. H. and R. G. Olsen, "Radiation due to a convex curvature discontinuity of a dielectric-coated perfect conductor," *IEEE Trans. Antennas and Propagation*, Vol. 46, No. 8, 1220–1228, Aug. 1998.
4. Ufimtsev, P. Y., R. T. Ling, and J. D. Scholler, "Transformation of surface waves in homogeneous absorbing layers," *IEEE Trans. Antennas and Propagation*, Vol. 48, No. 2, 214–222, Feb. 2000.
5. Ufimtsev, P. Y. and R. T. Ling, "New results for the properties of TE surface waves in absorbing layers," *IEEE Trans. Antennas and Propagation*, Vol. 49, No. 10, 1445–1452, Oct. 2001.
6. Paknys, R. and D. R. Jackson, "The relation between creeping waves, leaky waves, and surface waves," *IEEE Trans. Antennas and Propagation*, Vol. 53, No. 3, 898–907, Mar. 2005.
7. Neve, M. J. and R. Paknys, "A technique for approximating the location of surface- and leaky-wave poles for a lossy dielectric slab," *IEEE Trans. Antennas and Propagation*, Vol. 54, No. 1, 115–120, Jan. 2006.
8. Collin, R. E., *Field Theory of Guided Waves*, McGraw-Hill, New York, 1960.
9. Terracher, F. and G. Berginc, "A numerical study of TM-type surface waves on a grounded dielectric slab covered by a doubly periodic array of metallic patches," *Progress In Electromagnetics Research*, Vol. 43, 75–100, 2003.
10. Chen, H. Y., P. H. Zhou, L. Chen, and L. J. Deng, "Study on the properties of surface waves in coated RAM layers and mono-static RCS performances of the coated slab," *Progress In Electromagnetics Research M*, Vol. 11, 123–135, 2010.
11. Xu, C. L., J. K. Yan, and D. M. Xu, "Performance prediction of surface wave absorbers," *1997 Asia-Pacific Microwave Conference Proceedings, APMC'97*, Vol. 2, 605–607, 1997, Doi: 10.1109/APMC.1997.654614.
12. Van Bladel, J. G., *Electromagnetic Fields*, 2nd Edition, 426, Wiley-Inter Science, A John Wiley & Sons, Inc., Publication, 2007.
13. Chen, H. Y., H. B. Zhang, and L. J. Deng, "Design of an ultra-thin magnetic-type radar absorber embedded with FSS," *IEEE Antenna and Wireless Propagation Letters*, Vol. 9, 899–901, 2010.
14. Lam, J., "Surface-wave reflection and refraction at an impedance discontinuity," *J. Appl. Phys.*, Vol. 66, No. 8, 3437–3444, Oct. 15, 1989.
15. Ross, R. A., "Radar cross section of rectangular flat plates as a function of aspect angle," *IEEE Trans. Antennas and Propagation*, Vol. 14, No. 3, 329–335, May 1966.
16. Chen, H. Y., L. J. Deng, P. H. Zhou, and J. L. Xie, "Tapered impedance loading for suppression of edge scattering," *IET Microwaves Antennas & Propagation*, Vol. 5, No. 14, 1744–1749, 2011.
17. Chen, H. Y., J. L. Xie, Z. W. Zhu, and L. J. Deng, "Method of tapered resistive sheet loading for controlling edge scattering," *Microwave and Optical Technology Letters*, Vol. 55, No. 9, 1992–1996, 2013.
18. Chen, H. Y., Z. W. Zhu, L. J. Lu, et al., "Design and implementation of tapered resistive sheets to control edge scattering," *Journal of Applied Physics*, Accepted, 2014.

The RF Immunity Characteristics Analysis of SSD Performance due to Wireless Communications Emission in Proximity

Han-Nien Lin¹, Po-Yan Wang¹, Hung-Yun Tsai¹, and Yung-Chi Tang²

¹Department of Communications Engineering, Feng-Chia University
No. 100 Wen-Hua Rd., Taichung 40724, Taiwan, R.O.C.

²Section of EMC, Bureau of Standards, Metrology and Inspection, M.O.E.A
No. 4, Sec. 1, Jinan Rd., Zhongzheng Dist., Taipei City 100, Taiwan, R.O.C.

Abstract— To facilitate the high speed data access/storage with vibrating and swaying proof, the Solid State Drive (SSD) is now commonly integrated with mobile or portable device like Ultrabook with its compact size. Besides RFI noise generated from such high speed digital device is observed imposing an inferior impact on RF wireless communications performance, it is also possible that the SSD storage module might be failed for data accessing caused by high level RF transmitted power from various transmitters of wireless communications systems. In addition, when WiFi tethering is used for cloud applications with the 3G/4G WWAN network through smart phone, the transmitted RF power from mobile phone might also affect the data access/storage of SSD memory. Because when we use WWAN network for Internet surfing, we would usually place the mobile phones by side of ultrabook/notebook computer with built-in SSD and thus the high level output signal from nearby mobile phone might cause memory mapping error of SSD. To analyze the EM immunity characteristics of SSD and related memory module, we will categorize the coupling mechanism of RF power between SSD and RF transmitter into antenna coupling, circuitry coupling, and cavity resonance coupling. With the help of dedicated near-field RF signal generator and stripline [1] for closely located digital modules like SSD and flash memory in this study, we can identify the location and root cause of data accessing and storing degradation to benefit the manufacturers for proper SSD integration with mobile or portable device with compact design form limitation. We also evaluated the pass/fail EM immunity characteristics for SSD storage module, and hope to apply the IEC 63132 [2] series IC-EMS measurement techniques on the component level to help solving the problem and further improve the integrating design to meet the EMC/performance requirement in the future study.

1. INTRODUCTION

Cloud computation and always-connected Internet service attracts the most industrial attention for the past few years. Therefore, the Solid State Drive (SSD) and flash memory is now commonly integrated with mobile or portable device with its inherent vibrating and swaying proof characteristic. Owing to its compact size and fast processing speed, the Solid State Drive (SSD) is also commonly found installed in Ultrabook and similar devices. Besides such high speed digital module has malignant impact on RF receiving performance of wireless communications, the digital components or modules might also suffer functional degradation due to near field electromagnetic interference. For instance, when WiFi tethering is used for cloud applications with the 3G/4G WWAN network through smart phone, the transmitted RF power from mobile phone might also affect the data access/storage of SSD memory. Because when we use WWAN network for Internet surfing, we would usually place the mobile phones by side of ultrabook/notebook computer with built-in SSD and thus the high level output signal from nearby mobile phone might cause memory mapping error of SSD. The scenario of WiFi tethering with mobile phone placed aside of SSD is illustrated in Figure 1, which explains the RF output signal of mobile phone might cause the bit error of SSD memory access.

2. RF TRANSMITTED POWER COUPLING MECHANISM FOR EM IMMUNITY ANALYSIS

To quantify the RF power impact on SSD functionality from transmitters of various wireless communication systems via embedded or integrated antennas as shown below in Figure 2, we conduct the 1000 times test for data bit read/write/erase operation to validate the SSD module.

From the analysis of above illustration, it indicates the major RF coupling being circuitry coupling and direct antenna coupling. The circuitry coupling means that the SSD suffers noise coupling from the mini-coaxial cable connecting WLAN/WWAN antennas and WLAN/WWAN



Figure 1: Scenario of WiFi tethering with mobile phone placed aside of SSD.

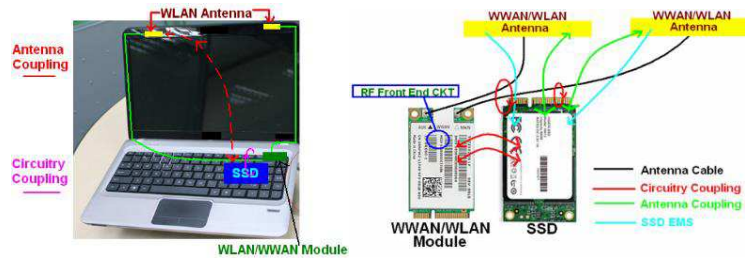


Figure 2: SSD module suffers WLAN/WWAN antennas and cable coupling.

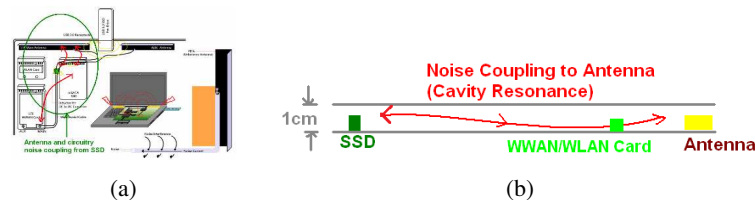


Figure 3: (a) Detailed coupling mechanism between WLAN/WWAN antenna and SSD module. (b) Cavity resonance coupling between WLAN antenna and SSD module.

module. If the antennas are further moved down to ultrabook computer base due to the shrinking lid form limitation design, the SSD will even suffer direct RF power coupling from those transmitting antennas which is categorized as “Antenna Coupling”. The possible coupling mechanism between WLAN/WWAN and SSD module is detailed in Figure 3(a).

We also found out that even the SSD is moved away from the transmitting antenna, as shown below in Figure 3(b), high level transmitted RF power might still couple to the SSD module and cause functional failure. Since the chassis of Ultrabook is normally made of Al-Mg alloy and forms a cavity structure, we therefore call such phenomenon as “cavity resonance” coupling. From the possible coupling mechanism mentioned above, it could provide designers the solution for RFI problems by modifying the components placement layout for better isolation between SSD and transmitted antennas to enhance the EM immunity capability.

3. IMMUNITY CHARACTERISTICS REQUIREMENT FOR SSD INTEGRATED WITH RF RADIATORS

Before SSD is integrated or installed into Ultrabook or similar portable device, the SSD manufacturers should take the following issues into consideration.

- 1) The SSD should remain its normal operation when the antennas of wireless communications transmits and radiates RF power. Because the near field magnetic field from antennas might cause strong coupling to SSD, and therefore it is necessary to conduct SSD EMS test with dedicated portable generator.
- 2) The SSD should remain its normal operation when the antennas of wireless communications transmits and radiates RF power, which the RF current from main PCB or mini-coaxial cable might also couple the magnetic flux to SSD. Therefore it is necessary to conduct SSD EMS test with stripline fixture.

3) With more and more programming and erasing activities for SSD accessing/storage, the “wearing” effect decreases the isolation property of dielectric and changes its tunneling effectiveness as shown in Figure 4. The effect will ultimately result in the following consequences.

- a) Incorrect reading from the NAND cell after relatively short retention times.
- b) Program/erase failure.

Therefore, it is required for SSD EMS test that should also pass the test and remain functional operation after 1000 times Read/Write activities.

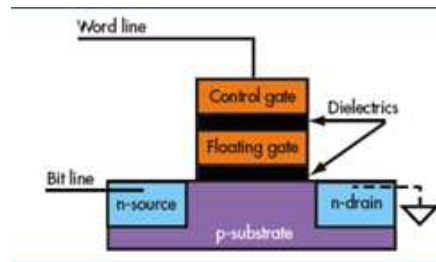


Figure 4: Isolation property of dielectric and tunneling effectiveness of NAND cell.

4. IMMUNITY TEST PROCEDURES AND MEASUREMENT SETUP

To help the SSD manufacturers identify the level of SSD’s RF immunity from high level nearby radiators, we propose the RF testing procedure for SSD immunity diagnosis.

- 1) Use the self-developed dedicated SG module (for GSM/WCDMA) to impose RF power on SSD module for electromagnetic susceptibility test as shown in Figure 5(a). The portable SG device for this EMS test is used to simulate whether the SSD is in normal operation or not when nearby WWAN antennas radiate the RF power.
- 2) Put the SSD on stripline to observe whether the SSD is abnormal or not when RF power is injected into the terminated stripline as shown in Figure 5(b). The stripline is used to simulate the RF current flow either from main PCB or from mini-coaxial cable in ultrabook/notebook PC. During the test SSD is placed on top of the stripline which is transmitting signal and couples the magnetic flux to SSD to observe whether the SSD operation is abnormal or not.
- 3) Use WWAN (like GSM/WCDMA) transmitting antennas built in PNS (Platform Noise Scanner) to execute SSD EMS test. This test case simulates the condition for mobile phone being placed beside the SSD module, as shown below in Figure 6(a).



Figure 5: (a) Portable SG device for SSD EMS test. (b) Configuration of Stripline for SSD EMS test.



Figure 6: (a) Test condition for mobile phone placed beside the SSD. (b) The PNS setup for EMS test using mobile phone simulator.

We place the SSD under the GSM/WCDMA transmitting antenna and observe if the SSD operates abnormally or not. It should be noted that E_x, E_y, H_x, H_y of horizontal components be taken into account, where E and H denotes the electric field and magnetic field respectively. The PNS test setup is illustrated in Figure 6(b).

- 4) Finally, we will evaluate SSD endurance under EMS Test. After 1000 times Read/Write operation, the SSD should also pass the EMS test of step 1 and 2 in order to ensure sufficient life time of SSD.

The EMS test plan and procedure described above is totally based on the actual applications, and it can provide manufacturers an efficient diagnosis to solve the EMS problems and improve the quality of product. On the other hand, if the SSD fails some of the SSD near field EMC test criteria described above, then the ultrabook/notebook PC manufacturers will refuse to utilize such SSD from system crashing.

5. ESTIMATION OF IMMUNITY LEVEL AND CORRESPONDING FREQUENCY RANGE FOR SSD EMS TEST

The power level and frequency range for immunity test against transmitters of WWAN system depends on communication band the rated transmitting power. The maximum Tx power level for EMS test in each band is estimated first as shown below in Table 1, and then the test is executed to validate the proper function.

Table 1: Maximum Tx power level for EMS test.

Band	Radio	TX Frequency	Max TX power level
	Channels	Range MHz	Note: With GSM(1/8 pulse ratio) And with GPRS(pulse ratio 2/8)
GSM850	128. 190.251	824-849	2.0 W(33 dBm)
GSM900	975.38.124	880-915	2.0 W(33 dBm)
GSM1800	512.699.885	1710-1785	1 W(30 dBm)
GSM1900	512.661.810	1850-1910	1 W(30 dBm)

Table 2: SSD near field EMS test by SG module.

Idle			
Band	Tx Frequency	Max Tx Power Level	Pass(P) or Fail (F)
GSM850	824.2MHz	32dBm	P
GSM900	880.2MHz	32dBm	P
GSM1800	1710.2MHz	29dBm	P
GSM1900	1850.2MHz	29dBm	P
WCDMA850	826.4MHz	23dBm	P
WCDMA1900	1852.4MHz	23dBm	P
WCDMA2100	1922.4MHz	23dBm	P
Read/Write			
Band	Tx Frequency	Max Tx Power Level	Pass(P) or Fail (F)
GSM850	824.2MHz	32dBm	P
GSM900	880.2MHz	32dBm	P
GSM1800	1710.2MHz	29dBm	P
GSM1900	1850.2MHz	29dBm	P
WCDMA850	826.4MHz	23dBm	P
WCDMA1900	1852.4MHz	23dBm	P
WCDMA2100	1922.4MHz	23dBm	P
Comments for test result: Passed			

Table 3: SSD near field EMS test by stripline.

Idle			
Band	Tx Frequency	Max Tx Power Level	Pass(P) or Fail (F)
GSM850	824.2MHz	32dBm	P
GSM900	880.2MHz	32dBm	P
GSM1800	1710.2MHz	29dBm	P
GSM1900	1850.2MHz	29dBm	P
WCDMA850	826.4MHz	23dBm	P
WCDMA1900	1852.4MHz	23dBm	P
WCDMA2100	1922.4MHz	23dBm	P
Read/Write			
Band	Tx Frequency	Max Tx Power Level	Pass(P) or Fail (F)
GSM850	824.2MHz	32dBm	P
GSM900	880.2MHz	32dBm	P
GSM1800	1710.2MHz	29dBm	P
GSM1900	1850.2MHz	29dBm	P
WCDMA850	826.4MHz	23dBm	P
WCDMA1900	1852.4MHz	23dBm	P
WCDMA2100	1922.4MHz	23dBm	P
Comments for test result: Passed			

6. TEST RESULTS

After performed the EMS tests mentioned earlier for sample SSD module for various operating modes, the results are summarized as following.

7. CONCLUSION

The SSD EMS test against RF power from WWAN transmitters is conducted to evaluate the immunity level and shielding effectiveness needed for SSD integrated with nearby RF transmitting module. For the Ultrabook and notebook PC manufacturers, they can benefit the SSD failure analysis against WWAN/WLAN systems and further utilize the isolation techniques from this study. As to the SSD related manufacturers, they can also benefit from this study about failure mode from EM susceptible test to identify their SSD design weakness for future improvement.

ACKNOWLEDGMENT

The authors would like to thank TRC (Training and Research Company) Taiwan for technical support, measurement assistance and test fixture for this study. We would also like to sincerely express appreciation to BSMI (Bureau of Standards, Metrology and Inspection) and NSC (National Science Council) for their financial grants support to this study. The original research work presented in this paper was made possible in part by the BSMI under Contract grant from BSMI Taiwan.

REFERENCES

1. Helttula, J., "Display and touch module electromagnetic verification specification," 6–15, Nokia SD NWP Product Quality, Feb. 2012.
2. IEC 62132-8, "Integrated circuits — Measurement of electromagnetic immunity 150 kHz to 3 GHz — Part 8: Measurement of radiated immunity — IC stripline method," 2012.
3. Lin, H.-N., C.-H. Lin, T.-J. Cheng, and M.-C. Liao, "Antenna effect analysis of laptop platform noise on WLAN performance," *PIERS Proceedings*, 585–590, Beijing, China, March 23–27, 2009.
4. Lin, H.-N., C.-H. Lin, M. C. Chang, and Y.-Y. Shih, "Analysis of platform noise effect on WWAN performance," *2010APEMC*, 12–16, TH-PM-A1-2: SS-13, Apr. 2009.
5. Lin, H.-N., J.-L. Chang, and C.-W. Kuo, "Radiated EMI coupling analysis between high-speed modules and receiving antennas of mobile devices," *2012 Asia-Pacific Symposium Electromagnetic Compatibility*, WE-AM-MS-1, May 2012.

A Simple High-resolution Imaging System Made of Metamaterials

Shuo Ge and Wei Xiang Jiang

State Key Laboratory of Millimeter Waves, Southeast University, Nanjing 210096, China

Abstract— High resolution imaging or super resolution imaging is always a hot topic in the field of artificial metamaterials. Since the conventional optical imaging lenses suffer from the so-called diffraction limit, the resolution is limited to half a wavelength. In order to break this restriction, many metamaterial-based superlenses and hyperlenses have been proposed and investigated. In this work, we present a simple high-resolution imaging system, which is composed of a magnifying lens and a planar focusing lens. The all-dielectric metamaterial magnifying lens is a modified hemispherical solid immersion lens (SIL) with impedance-matching layer, which is made of gradient-index materials. The high permittivity materials in the core of the magnifying lens can magnify evanescent waves that carry subwavelength imaging information. The magnified waves will propagate smoothly to the free space by the matching layer outside the core region. The planar focusing lens will gather the imaging information and produce the image. Therefore, the image formed by the focusing lens contains the magnified subwavelength-imaging information. The planar focusing lens is designed by geometry optics and cylindrically symmetrical. In the simulation, two point sources with a distance of less than half a wavelength are embedded in the core of the magnifying lens. Thus, the two point sources are imaged at the focus of the planar focusing lens with enlarged distance. Both of the magnifying lens and planar focusing lens are made of isotropic dielectric metamaterials, hence, such a simple high-resolution imaging system works efficiently in a broad band.

1. INTRODUCTION

To break Abbe's "diffraction limit" [1], a lot of theoretical and experimental works have been reported in recent decade [2–8]. In 2000, J. B. Pendry proposed a theory about "perfect lens" composed of negative permittivity and negative permeability, which can amplify the evanescent waves and realize the perfect imaging [2]. After that, metamaterial-based superlens [3, 4] and hyperlens [5–8] have been proposed and investigated to achieve the subwavelength imaging. Recently a dielectric metamaterial magnifier was proposed, it is capable of creating a virtual color image with far-field subwavelength information [9]. The magnifier is a gradient refractive index lens that can magnify the imaging target and enhance the resolution. The corresponding device was verified experimentally soon after that, which is also a modified immersion lens [10].

In this work, we propose and design a planar focusing lens, together with the modified immersion lens to form a simple imaging system in microwave band. The simple imaging system can magnify electromagnetic information of the object, and focus the image in the focusing plane. Both the magnifying lens and planar focusing lens are made of inhomogeneous isotropic dielectrics which is easier to implement. The simulation result shows that these two lenses can produce a magnified image in front of the planar focusing lens. It was verified that the simple high-resolution imaging system have excellent super-resolution performance in simulation from 12 to 16 GHz.

2. THEORETICAL ANALYSIS

The main component of our high-resolution imaging system is the magnifying lens. Because of the symmetry of lens structure, we construct a half spherical magnifying lens. The design of magnifying lens follows the coordinate transformation shown in Figures 1(a) and 1(b). The real and virtual spaces are denoted with (x, y, z) and (x', y', z') respectively. In order to construct the magnifying lens a two-fold transformation needs to be implemented. First, the region I' in the virtual space is compressed into region I in real space. Second, the annular region II' in the virtual space is stretched into region II in the real space.

When compressing region I' into region I , the transformation formula is

$$r = \frac{L}{R-t} r', \quad \phi = \phi' \quad (1)$$

To stretch the annular region II' into region II , the following transformation can be used

$$r = \frac{R-L}{t} (r' - R) + R, \quad \phi = \phi' \quad (2)$$

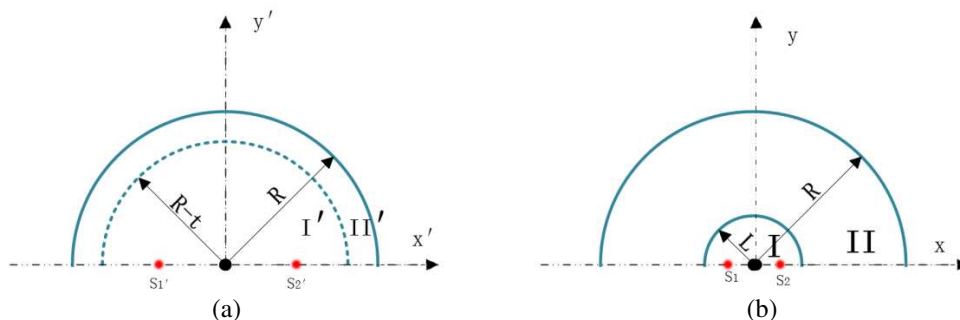


Figure 1: The schematic illustration of coordinate transformation for the design of magnifying lens. (b) The far-field patterns of two sources (s_1 and s_2) in the real space (a) is equivalent to two sources (s_1' and s_2') in the virtual space.

After some approximate treatment, the simplified refractive index of magnifying lens is

$$n(r) = \begin{cases} \frac{R}{L} & r \leq L \\ \frac{R}{r} & L < r \leq R \end{cases} \quad (3)$$

The planar focusing lens is composed of two parts, the core (Part A in Figure 2) and the matching layer (Part B in Figure 2). Two pieces of thin layer can achieve the impedance matching between the core and the free space. Both of the refractive index distributions of two parts are illustrated in Figure 2. The refractive index distribution of the magnifying lens is also shown in Figure 2, which is governed by Equation (3). The core of the magnifying lens is composed of high permittivity materials. The refractive index of the annular region outside the core decrease gradually from the center to the periphery. The distance between two point sources S_1 and S_2 are magnified by the magnifying lens, then the planar focusing lens will focus the imaging information and produce the magnified image. The magnification factor of our simple high-resolution imaging system can be adjusted according to specific case. In this work, we set the magnification factor as four to demonstrate the amplification characteristic of high-resolution imaging system.

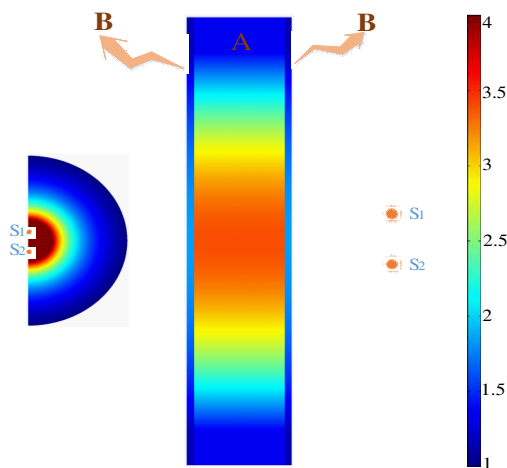


Figure 2: The refractive index distribution of magnifying lens and planar focusing lens. The distance of two point source S_1 and S_2 will be magnified in the imaging plane.

3. NUMERICAL DEMONSTRATION OF HIGH RESOLUTION IMAGING

To verify the performance of the designed high-resolution imaging system, numerical simulations are made by using commercial package, COMSOL Multiphysics. The simulation results are illustrated in Figure 3. We set the distance of the sources as 7 mm and free space wavelength $\lambda_0 = 21.4$ mm. It can be seen from the data that the distance of sources is smaller than the half-wavelength. It is obvious that two sources cannot be separated in the far-field image plane. Figure 3(a) shows the

simulation result without the solid immersion lens. The size of Part A in the planar focusing lens is 78 mm * 450 mm, Part B is set to be 6 mm * 450 mm. The planar focusing lens is designed using the theory of geometry optics [1]. By phase compensation the lens can gather the information and then reproduce them in the imaging plane, which is represented by the red dotted line in Figure 3(a).

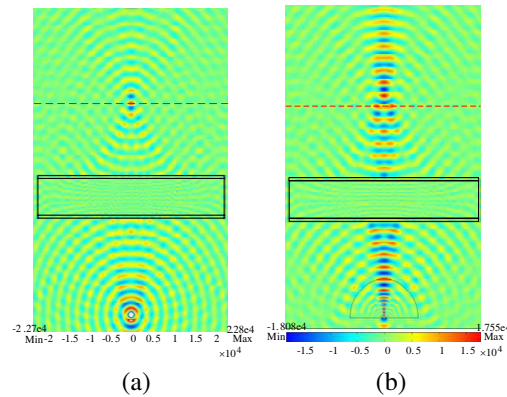


Figure 3: The electric field distribution (a) without and (b) with magnifying lens.

In Figure 3(b), the electric-field distribution of two sources with the magnifying lens is illustrated. We set $R = 80$ mm, $L = 20$ mm and the free space wavelength $\lambda_0 = 21.4$ mm. The parameters of the planar focusing lens are the same as the above. By observing the electric field distribution, two sources are clearly separated comparing with Figure 3(a).

In order to further illustrate the effect of our simple high-resolution imaging system, we analyze the magnitude distributions of the electric fields. In Figure 4(a), two sources are clearly focused on the red dotted line. To validate the broadband feature of our system, we make the similar simulations at the wavelength of 25 mm, 21.4 mm and 18.75 mm. Then the magnitudes of electric

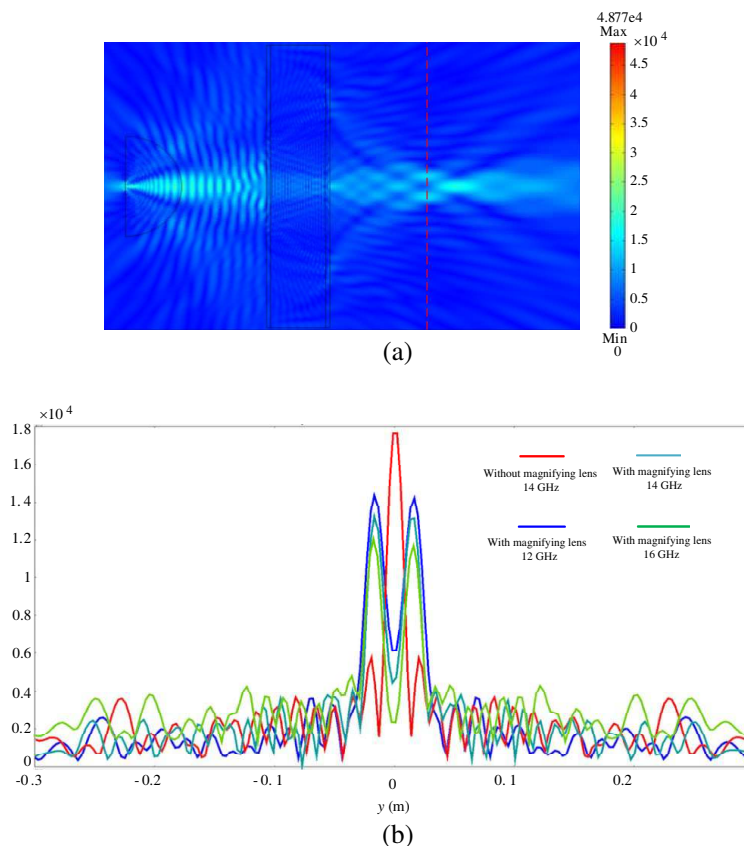


Figure 4: (a) Distribution of the magnitude of electric field; (b) The magnitude of electric fields along the red dotted line under four different cases.

field on the red dotted line are shown in Figure 4(b). The red line in Figure 4(b) is the simulation result without the magnifying lens. Only one peak represents that two sources cannot be separated. The lines of other three colors are the simulation results at the wavelength of 25 mm, 21.4 mm and 18.75 mm with the magnifying lens, respectively. All of them have two peaks and the distance between them is about four times long of the real distance between the two sources. It means that our simple high-resolution imaging system has excellent super-resolution performance from 12 to 16 GHz.

4. CONCLUSION

In this paper, we propose a high-resolution imaging system in two dimensions. The simulation result demonstrates that imaging system can work well in a broadband. We will investigate the high-resolution imaging system in three dimensions in near future.

REFERENCES

1. Born, M. and E. Wolf, *Principles of Optics*, Cambridge University Press, Cambridge, 1999.
2. Pendry, J. B., “Negative refraction makes a perfect lens,” *Phys. Rev. Lett.*, Vol. 85, 3966–3969, 2000.
3. Fang, N., H. Lee, C. Sun, and X. Zhang, “Sub-diffraction-limited optical imaging with a silver superlens,” *Science*, Vol. 308, 534–537, 2005.
4. Taubner, T., D. Korobkin, Y. Urzhumov, G. Shvets, and R. Hillenbrand, “Near-field microscopy through a SiC superlens,” *Science*, Vol. 313, 1597, 2006.
5. Jacob, Z., L. V. Alekseyev, and E. Narimanov, “Optical hyperlens: Far-field imaging beyond the diffraction limit,” *Opt. Express*, Vol. 14, 8247–8256, 2006.
6. Salandrino, A. and N. Engheta, “Far-field subdiffraction optical microscopy using metamaterial crystals: Theory and simulations,” *Phys. Rev. E*, Vol. 74, 075103, 2006.
7. Liu, Z., H. Lee, Y. Xiong, C. Sun, and X. Zhang, “Far-field optical hyperlens magnifying sub-diffraction-limited objects,” *Science*, Vol. 315, 1686, 2007.
8. Smolyaninov, I. I., Y. J. Hung, and C. C. Davis, “Magnifying superlens in the visible frequency range,” *Science*, Vol. 315, 1699–1701, 2007.
9. Zhang, B. L. and G. Barbastathis, “Dielectric metamaterial magnifier creating a virtual color image with far-field subwavelength information,” *Opt. Express*, Vol. 18, 11216, 2010.
10. Jiang, W. X., C. W. Qiu, T. C. Han, et al., “Broadband all-dielectric magnifying lens for far-field high-resolution imaging,” *Advanced Materials*, Vol. 25, No. 48, 6963–6968, 2013.

A Metasurface for RCS Reduction in X Band

Di Sha Dong, Qiang Cheng, Jie Chen, Jie Zhao, and Li Hua Gao

State Key Laboratory of Millimeter Waves, Southeast University, Nanjing 210096, China

Abstract— In this paper, we will introduce an ultrathin metasurface, which is based on destructive interference between the incident and reflected waves and therefore leads to dramatic decrease of backward RCS. The main lobe and some of the side lobes of the scattering pattern of the targets could be suppressed significantly. When the phase shifts of metallic patches of the metasurface are randomly distributed, the reflected energy from the random metasurface will be scattered in various directions, resulting in the RCS reduction. By comparing the scattering pattern of the designed metasurface and a pure metallic plate with the same dimensions, the backward RCS can be reduced by more than 10 dB within the whole X band.

1. INTRODUCTION

With many novel detection systems and precision-guided weapons developed, stealth technologies based on metamaterials [1–15] have attracted much attention in the military field. As radar is the mainstream technology for target detection, RCS reduction [16–19] plays an important role for military targets to survive.

In this paper, we have proposed an ultrathin metasurface [20] based on destructive interference between the incident and reflected waves to reduce the RCS of targets. By tuning the structural parameters of the composing elements, a phase range of 0° – 360° can be realized. Through particular arrangement of these basic elements, the whole metasurface can reflect the incident waves in different directions, resulting in RCS reduction. Simulation results have shown that the backward RCS of this metasurface is reduced by over 10 dB in comparison to a pure metallic plate.

2. DESIGN AND SIMULATION

In our design, a single-layer metasurface, which is more compact in size, is designed to realize the backward RCS reduction instead of multilayer structures. And a multi-resonance structure has been chosen as the basic unit as shown in Fig. 1, which is composed by an inner quadrature ring and an outer ring with several branches on a grounded substrate. This structure can create two adjacent resonant frequency bands so as to broaden the frequency band of the basic unit, which can also be used as the unit of reflect-array antennas. In addition, the two-ring combination can also increase the total phase shift range by introducing a second resonant band.

F4B ($\varepsilon = 2.65$) is chosen as the substrate of the metasurface, and the thickness is 4 mm. The line width d is 0.35 mm, and the gap width g is 0.3 mm. The unit period b is 10 mm. The reflected phase varies with the change of the branch length. We have plotted the reflected phase curves with the branch length changing from 0.2 mm to 2.4 mm at 8 GHz, 9 GHz, 10 GHz, 11 GHz and 12 GHz in Fig. 2. The linearity of the reflected phase curves can meet the final design requirements as in Fig. 2.

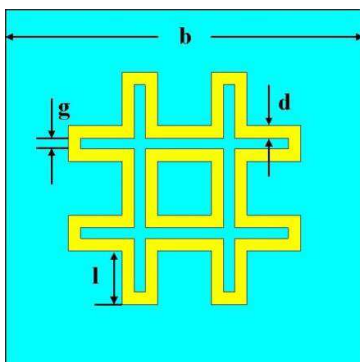


Figure 1: The front view of the basic unit.

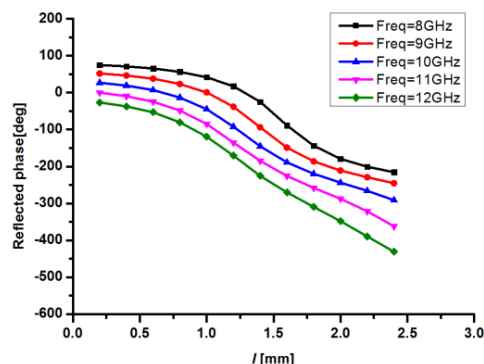


Figure 2: Reflected phase curves versus length of different frequencies.

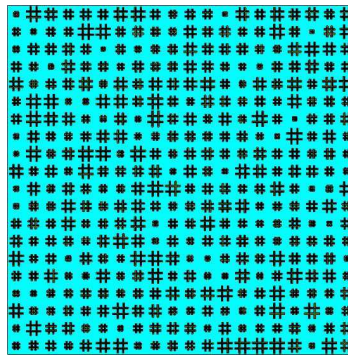


Figure 3: The final design of the metasurface for backward RCS reduction.

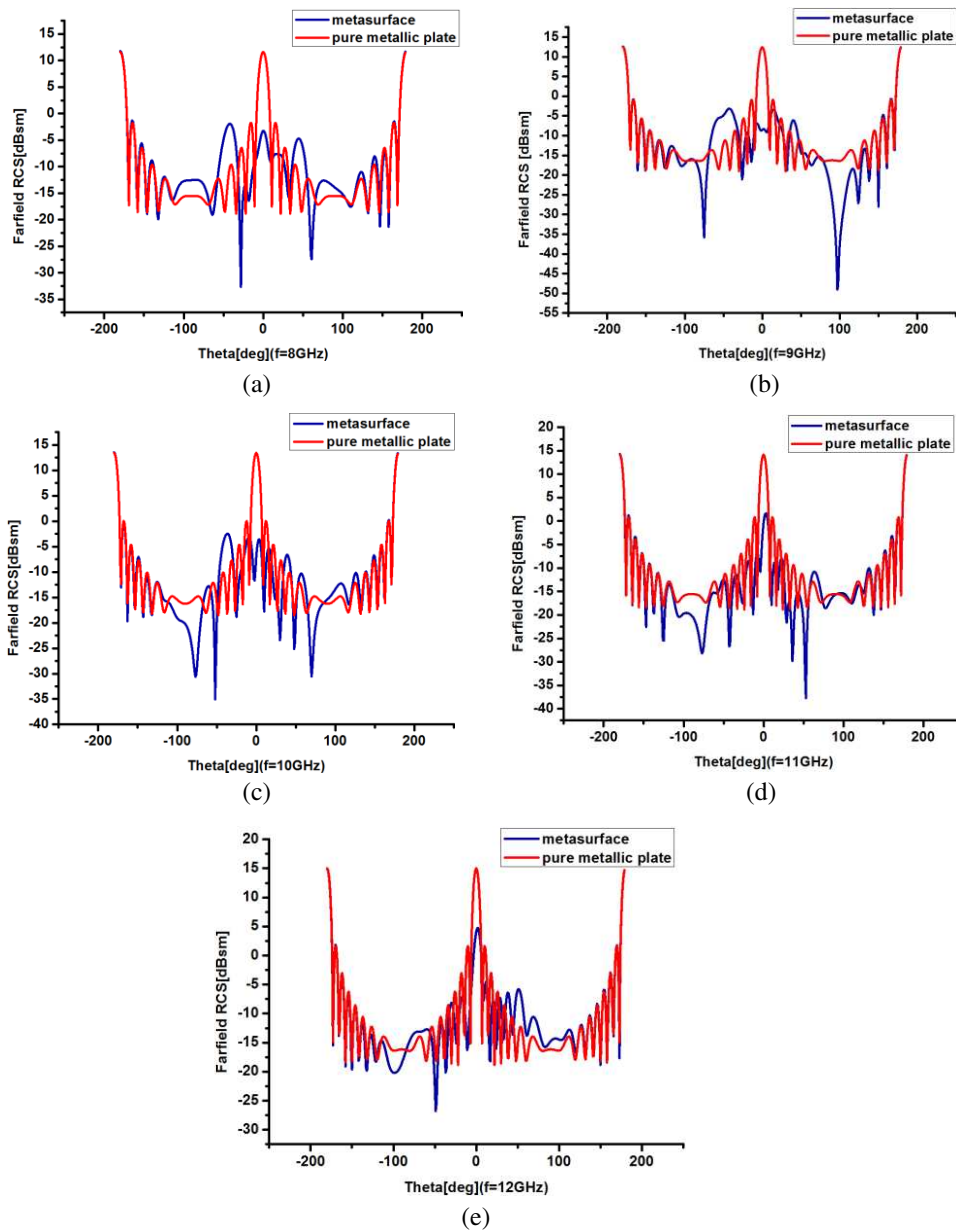


Figure 4: Comparison between the backward RCS of the metasurface and that of the pure metallic plate at (a) 8 GHz, (b) 9 GHz, (c) 10 GHz, (d) 11 GHz, (e) 12 GHz under normal incident waves.

The final metasurface is a 20×20 array as shown in Fig. 3. For waves incident normally, the reflected energy from the single layer metasurface will be scattered in various directions since the phase shifts of metallic patches are designed to be randomly distributed. And it can be concluded that the phase has a linear relationship with the length l from Fig. 2. In our design, we have randomly produced a 20×20 phase matrix ranging from 0 to 360 degrees first. Then the corresponding dimensions for the phases can be obtained from Fig. 2. With all these parameters confirmed, we construct the model through the electromagnetic simulation tool CST and compare the RCS of the metasurface and that of a pure metallic plate in X band, as shown in Fig. 4.

Also we have plotted the backward RCS reduction in Fig. 5 based on the simulation results. From Fig. 5, we can conclude that when covered by the designed metasurface, the RCS of targets can be reduced by at least 10 dB in the whole X band. And it can even reach above 20 dB at some frequencies, which proves the correctness of our design.

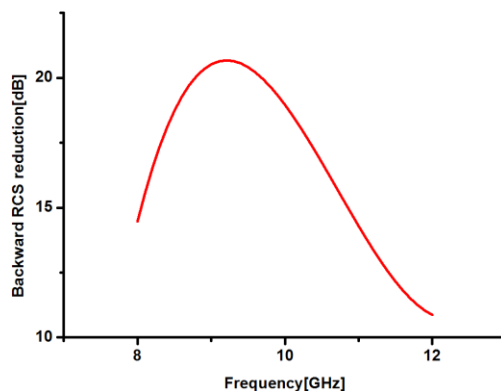


Figure 5: Backward RCS reduction in X band under normal incident waves.

REFERENCES

- Schurig, D., J. J. Mock, B. J. Justice, et al., "Metamaterial electromagnetic cloak at microwave frequencies," *Science*, Vol. 314, No. 5801, 977–980, 2006.
- Cai, W., U. K. Chettiar, A. V. Kildishev, et al., "Optical cloaking with metamaterials," *Nature Photonics*, Vol. 1, No. 4, 224–227, 2007.
- Valentine, J., J. Li, T. Zentgraf, et al., "An optical cloak made of dielectrics," *Nature Materials*, Vol. 8, No. 7, 568–571, 2009.
- Milton, G. W., M. Briane, and J. R. Willis, "On cloaking for elasticity and physical equations with a transformation invariant form," *New Journal of Physics*, Vol. 8, No. 10, 248, 2006.
- Landy, N. I., S. Sajuyigbe, J. J. Mock, et al., "Perfect metamaterial absorber," *Physical Review Letters*, Vol. 100, No. 20, 207402, 2008.
- Hao, J., L. Zhou, and M. Qiu, "Nearly total absorption of light and heat generation by plasmonic metamaterials," *Physical Review B*, Vol. 83, No. 16, 165107, 2011.
- Cheng, Q., T. J. Cui, W. X. Jiang, et al., "An omnidirectional electromagnetic absorber made of metamaterials," *New Journal of Physics*, Vol. 12, No. 6, 063006, 2010.
- Hao, J., Y. Yuan, L. Ran, et al., "Manipulating electromagnetic wave polarizations by anisotropic metamaterials," *Physical Review Letters*, Vol. 99, No. 6, 063908, 2007.
- Menzel, C., C. Helgert, C. Rockstuhl, et al., "Asymmetric transmission of linearly polarized light at optical metamaterials," *Physical Review Letters*, Vol. 104, No. 25, 253902, 2010.
- Yu, A., F. Yang, and A. Z. Elsherbeni, "A dual band circularly polarized ring antenna based on composite right and left handed metamaterials," *Progress In Electromagnetics Research*, Vol. 78, 73–81, 2008.
- Qureshi, F., M. A. Antoniadis, and G. V. Eleftheriades, "A compact and low-profile metamaterial ring antenna with vertical polarization," *IEEE Antennas and Wireless Propagation Letters*, Vol. 4, 333–336, 2005.
- Papasimakis, N., Y. H. Fu, V. A. Fedotov, et al., "Metamaterial with polarization and direction insensitive resonant transmission response mimicking electromagnetically induced transparency," *Applied Physics Letters*, Vol. 94, No. 21, 211902, 2009.

13. Ma, Y., Q. Chen, J. Grant, et al., “A terahertz polarization insensitive dual band metamaterial absorber,” *Optics Letters*, Vol. 36, No. 6, 945–947, 2011.
14. Huang, L. and H. Chen, “Multi-band and polarization insensitive metamaterial absorber,” *Progress In Electromagnetics Research*, Vol. 113, 103–110, 2011.
15. Chen, H., C. T. Chan, and P. Sheng, “Transformation optics and metamaterials,” *Nature Materials*, Vol. 9, No. 5, 387–396, 2010.
16. Rius, J. M., M. Ferrando, and L. Jofre, “High-frequency RCS of complex radar targets in real-time,” *IEEE Transactions on Antennas and Propagation*, Vol. 41, No. 9, 1308–1319, 1993.
17. Mosallaei, H. and Y. Rahmat-Samii, “RCS reduction of canonical targets using genetic algorithm synthesized RAM,” *IEEE Transactions on Antennas and Propagation*, Vol. 48, No. 10, 1594–1606, 2000.
18. Edalati, A., K. W. Sarabandi, and A. Wide, “Polarization independent RCS reduction using non-absorptive miniaturized-element frequency selective surfaces,” 2013.
19. De Cos, M. E., Y. Alvarez, and F. Las-Heras, “On the influence of coupling amc resonances for RCS reduction in the SHF band,” *Progress In Electromagnetics Research*, 117, 2011.
20. Zhao, Y. and A. Alù, “Manipulating light polarization with ultrathin plasmonic metasurfaces,” *Physical Review B*, Vol. 84, No. 20, 205428, 2011.

Polarization Conversion and Splitting by Using Thin Reflective Anisotropic Metasurface

Gui Zhen Wang, Hui Feng Ma, and Gu Sheng Kong

State Key Laboratory of Millimeter Waves, School of Information Science and Engineering
Southeast University, Nanjing 210096, China

Abstract— A kind of bi-reflective anisotropic metasurface has been proposed, which can manipulate the polarization states of the electromagnetic waves independently. The bi-reflective anisotropic metasurfaces are made up of two mutually perpendicular I-shaped structures, which have capacities to control the vertical and horizontal polarizations by using each of I-shaped structures, respectively. Two typical devices of such reflective anisotropic metasurfaces have been proposed: polarization converters and polarization beam splitters. Polarization converters are designed by using homogenous anisotropic metasurfaces with thickness of $\lambda_0/10$, which can transform a linearly polarized incident wave into a circularly polarized wave in a broad frequency band. Polarization beam splitters are designed by using gradient anisotropic metasurfaces with thickness of $\lambda_0/15$, which can manipulate the vertical and horizontal polarizations to different directions independently. The full-wave simulated results of polarization converters and polarization beam splitters are calculated by using of CST, and good polarization conversion and splitting are clearly observed, which verify the capacities of such reflective anisotropic metasurfaces to manipulate the polarization states of electromagnetic waves.

1. INTRODUCTION

Reflective metasurface made up of an array of subwavelength structures has been attracted more and more attentions in recent years, which has a lot of potential applications such as mantle cloaking [1], controllable surface [2], absorbers [3] and so on [4]. The most of reflective metasurfaces are isotropic with the same responses for both TE-polarized and TM-polarized waves, which limits the ability to control the different polarizations of the electromagnetic waves. However, the anisotropic reflective metasurface provides a method to manipulate the TE-polarized and TM-polarized waves independently, which has much stronger ability to control electromagnetic waves.

Polarization converter is one of applications for anisotropic reflective metasurface to modulate the polarization states of electromagnetic waves [6]. However, the most of existing reflective polarization converters are narrow band. Many efforts have been made to expand the bandwidth by using multilayered structures [7, 8], but thicknesses of the structures are increased obviously.

Polarization beam splitter (PBS), which can separate two orthogonally polarized reflected waves two different directions, is another application for anisotropic reflective metasurface in both microwave and optical regions. Gradient periodic array placed on a top of grounded printed circuit board (PCB) are required for designing such reflective PBS. The isotropic metasurfaces are usually used to realize reflectarray antenna [9, 10], and the anisotropic metasurfaces are usually used to control the reflection of different polarizations [11, 12].

In this paper, we propose an anisotropic reflective metasurface to manipulate the different polarizations of the electromagnetic waves independently. The metasurface is made up of two mutually perpendicular I-shaped structures placed on a grounded PCB, which has capacity to control the vertical and horizontal polarizations by using each of I-shaped structures, respectively. Two above mentioned devices have been designed by such reflective anisotropic metasurfaces in the paper: polarization converter and polarization beam splitter. Polarization converter can transform a linearly polarized incident wave into a circularly wave in a broadband, which is designed by homogenous anisotropic metasurface. Polarization beam splitter can separate the vertical and horizontal polarizations to different directions independently, which is designed by gradient anisotropic metasurfaces. The full-wave simulations are calculated by using CST, and good polarization conversion and splitting are clearly observed from the simulation results, which demonstrate that these reflective anisotropic metasurfaces have good ability to control orthogonally polarized electromagnetic waves independently.

2. DESIGN AND SIMULATION

We start from the unit cell shown in Fig. 1(a), which is composed of two mutually perpendicular I-shaped structures fabricated on grounded printed circuit board (PCB) of F4B, whose relative

permittivity is 2.65 and loss tangent is 0.001. Figs. 1(b) and (c) are the electric-field distributions of unit cell at 10 GHz, which show that the x directional I-shaped structure is only excited by x -polarized waves as shown in Fig. 1(b) and the y directional I-shaped structure is only excited by y -polarized waves as shown in Fig. 1(c). Hence the responses of horizontal (x) and vertical (y) polarizations can be controlled independently by each of I-shaped structures.

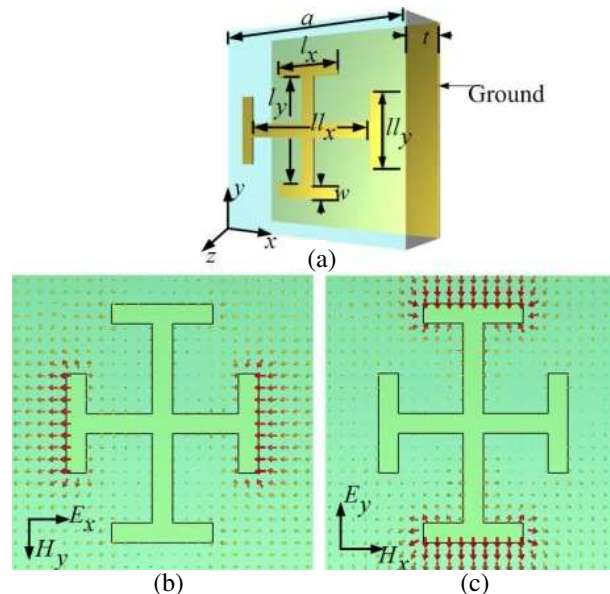


Figure 1: Unit cell of metasurface and its electric-field responses. (a) The structure of the unit cell. (b) Electric-field distributions under x -polarized waves. (c) Electric-field distributions under y -polarized waves.

The first device realized by reflective metasurface is polarization converter, which is made up of homogenous periodic units as shown in Fig. 1(a). The linearly polarized incident waves can be converted into circularly polarized waves in a broadband after reflected by the metasurface. The dimensions of unit cell are $a = 6$ mm, $w = 0.4$ mm, $l_x = l_y = 2$ mm, $l_x' = 4.4$ mm and $t = 3$ mm. We assume that the linearly polarized incident waves propagate along $-z$ direction, which are reflected by metasurface as shown in Fig. 1(a). The magnitudes and phases of S_{11} -parameter for both x - and y -polarized incident waves are demonstrated in Fig. 2. The simulated results show that the magnitudes of S_{11} -parameter for both x - and y -polarized waves are nearly 0 dB with total reflection as shown in Fig. 2(a), while the phase difference between x - and y -polarized reflected waves is -90° or 270° from 9.5 GHz to 10.7 GHz as shown in Fig. 2(b). We define a new local coordinate system of uvw , and the angle between the u axis and x axis is $\varphi = 45^\circ$ as shown in Fig. 3(a). In order to transform a linear-polarized incident waves to a circular-polarized reflected waves, the linear-polarized waves are illuminated to the metasurface along the $-z$ axis with u polarization. Hence total electric field of E can be decomposed to $E_x = E \cos \varphi$ and $E_y = E \sin \varphi$ with $|E_x| = |E_y|$ for $\varphi = 45^\circ$. From the simulation results shown in Fig. 2, we can obtain that the magnitudes of reflected electric-field vectors of E_{rx} and E_{ry} are equal, i.e., $|E_{rx}| = |E_{ry}|$, while phase difference between E_{rx} and E_{ry} is $\arg(E_{ry}) - \arg(E_{rx}) = 270^\circ$ or -90° from 9.5 GHz to 10.7 GHz, which imply that such linear-polarized incident waves can be transformed into circular-polarized reflection waves in a broad frequency band from 9.5 GHz to 10.7 GHz. We define the S_{uu} and S_{uv} are the reflection coefficients of u -polarized and v -polarized reflection waves compared to the u -polarized incident waves, and the full-wave simulated results magnitudes and phase differences of S_{uu} and S_{uv} are shown in Figs. 3(a) and 3(b), respectively. The results show that the magnitudes of S_{uu} and S_{uv} are nearly equal from 9.5 GHz to 10.7 GHz, i.e., $|S_{uu}| = |S_{uv}|$, while the phase difference between the S_{uu} and S_{uv} is -90° shown in Fig. 3(b), which imply that the circular-polarized reflected waves are achieved.

The second device realized by metasurface is polarization beam splitter (PBS), which is made up of inhomogeneous gradient unit cells. The metasurface is designed gradually changed along the x direction with a phase discontinuity of $\phi(x)$, which can make the reflection waves deflected with

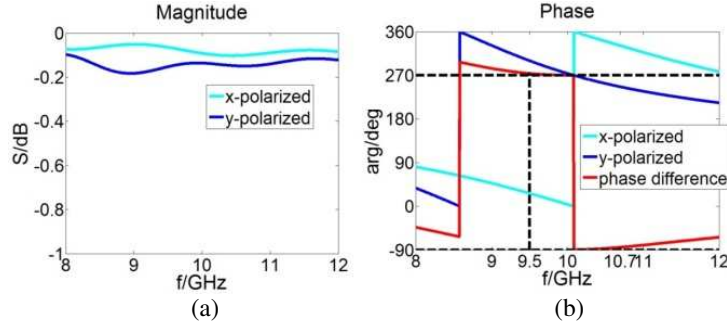


Figure 2: The simulated results of S_{11} parameters for x - and y -polarized waves. (a) Magnitudes. (b) Phases and phase difference.

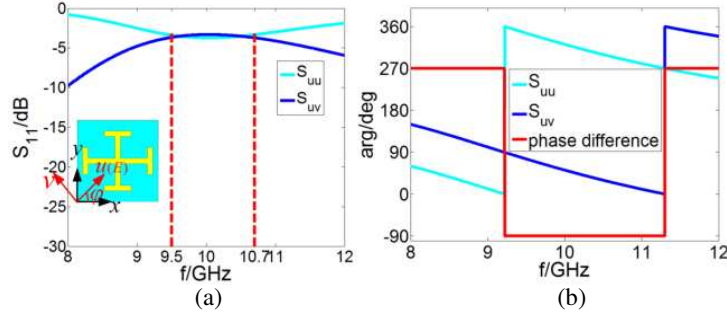


Figure 3: The simulated magnitudes and phase differences of S_{uu} and S_{uv} , in which S_{uu} and S_{uv} are the reflection coefficients of u -polarized and v -polarized reflection waves compared to the u -polarized incident waves. (a) Magnitudes. (b) Phases and phase difference between S_{uu} and S_{uv} .

an angle of θ as shown in Fig. 4(a). The relationship between $\phi(x)$ and θ can be defined as:

$$\phi(x) = \phi(x_0) - k \cdot x \cdot \sin \theta \quad (1)$$

where k is the wave number in free space, and $\phi(x_0)$ is the phase at location of $x = x_0$, which can be a constant.

In order to realize the required phase discontinue in Eq. (1) by using metasurface, we first investigate the phase responses of S_{11} -parameter of the unit cell by changing its dimensions as shown in Fig. 4(b). From the simulation results, 360° phase shift for y -polarized reflected waves can be obtained by changing the l_y from 2 mm to 5.1 mm, while the phases of x -polarized reflected waves will not be affected by changing the l_y . Similarly, 360° phase shift for x -polarized reflected waves also can be obtained by changing the l_x from 2 mm to 5.1 mm, while the phases of y -polarized reflected waves will not be affected by changing the l_x . Hence, the l_x and l_y can be adjusted to obtain different reflected phases of x -polarized and y -polarized waves independently, which imply that the deflection of x -polarized and y -polarized reflected waves can be controlled independently. We remark that the meta-structures are fabricated on the grounded PCB of F4B, whose thickness is 2 mm.

Based on above discussions, we designed a PBS, which can deflect x -polarized and y -polarized reflected waves to the different directions of θ_x and θ_y in xz plane, respectively. According the Eq. (1), the $\phi_x(x)$ and $\phi_y(x)$ should be designed independently to control the x - and y -polarized waves:

$$\phi_x(x) = \phi_x(x_0) - k_0 \cdot x \cdot \sin \theta_x, \quad (2)$$

$$\phi_y(x) = \phi_y(x_0) - k_0 \cdot x \cdot \sin \theta_y. \quad (3)$$

In which θ_x and θ_y are deflection angles for x - and y -polarized waves, respectively. We define that θ_x (or θ_y) is positive (or negative) for reflected beam deflected clockwise (or anticlockwise) to z axis in xz plane, respectively. The and of the designed PBS are demonstrated in Figs. 5(a) and 5(b), respectively, in which $\phi_x(x_0) = \phi_y(x_0) = 0$ and $\theta_y = -\theta_x = 30^\circ$. From the simulation results shown in Fig. 4(b), the dimensions of the unit cells can be obtained to satisfy the Eqs. (2) and (3), and one period of the designed gradient anisotropic metasurface is demonstrated in Fig. 5(c), in which $l_x(l_y)$

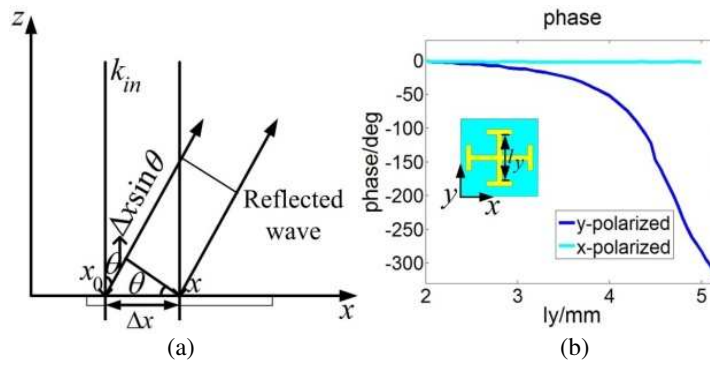


Figure 4: (a) The sketch of incident plane waves and reflected waves deflected by reflective metasurface. (b) The reflective phase responses of unit cell for both x - and y -polarized waves by varying the length of l_y at 10 GHz.

are decreased (increased) gradually from left to right. The red dots shown in Figs. 5(a) and 5(b) are the decreased phase realized by using actual unit cell, which show good agreements with the calculations. A further full-wave simulation has been made by using CST to show the performance of our designed PBS. A plane wave illuminates to the metasurface along $-z$ direction with normal incidence, whose electric-field vector is polarized with an angle of $\varphi = 45^\circ$ to the x axis as shown in Fig. 5(c). Hence both x - and y -polarized electric vectors can be achieved by decomposing the total electric vector. The simulation results of near electric field distributions in Figs. 5(d) and 5(e) show that the reflected waves are clearly separated to two different directions: x -polarized (horizontal polarized) wave is deflected to -30° and y -polarized (vertical polarized) wave is deflected to 30° , which have good agreements with the theoretical expectation.

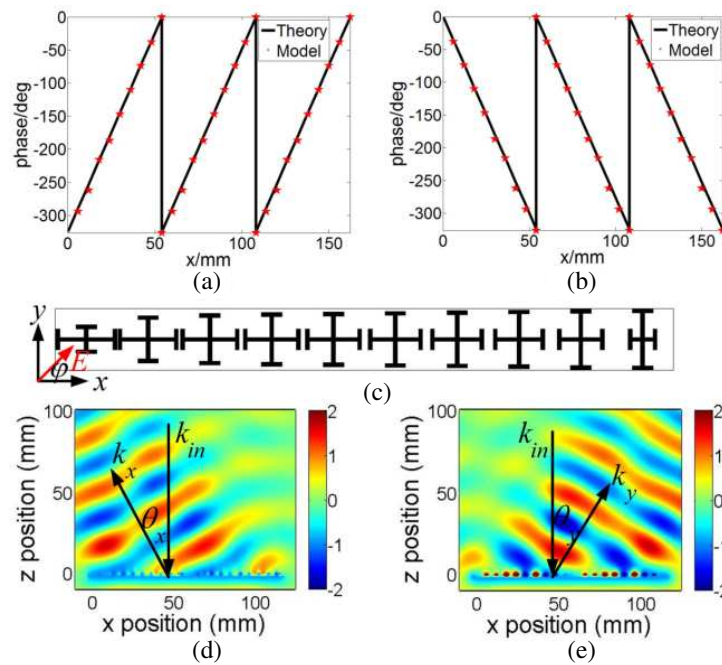


Figure 5: The phase shifts generated by one period of metasurface along x direction (a) for x -polarized waves and (b) for y -polarized waves. (c) One period of designed metasurface. (d) The near electric-field distribution of x -polarized reflected waves at 10 GHz. (e) The near electric-field distribution of y -polarized reflected waves at 10 GHz.

3. CONCLUSIONS

In this work, we proposed a kind of reflective anisotropic metasurface, which can manipulate the vertically and horizontally polarized waves independently. Two functional devices have been proposed based on such metasurfaces: broadband polarization converter and polarization beam split-

ter. Polarization converter is made up of homogeneous anisotropic metasurface with thickness of $\lambda/10$, which can transform linear polarized incident waves to circular polarized waves in a broad frequency band from 9.5 GHz to 10.7 GHz. Polarization beam splitters are made up of gradient anisotropic metasurface with thickness of $\lambda/15$, which can deflect horizontally and vertically polarized reflected waves to different directions with angle of $\theta_x = -30^\circ$ and $\theta_y = 30^\circ$. The metasurfaces are designed and simulated, which show good performances of broadband polarization conversion and polarization beam splitting.

REFERENCES

1. Alù, A., “Mantle cloak: invisibility induced by a surface,” *Physical Review B*, Vol. 80, No. 24, 245115, 2009.
2. Holloway, C. L., M. A. Mohamed, E. F. Kuester, et al., “Reflection and transmission properties of a metafilm: With an application to a controllable surface composed of resonant particles,” *IEEE Transactions on Electromagnetic Compatibility*, Vol. 47, No. 4, 853–865, 2005.
3. Feng, Q., M. Pu, C. Hu, et al., “Engineering the dispersion of metamaterial surface for broadband infrared absorption,” *Optics Letters*, Vol. 37, No. 11, 2133–2135, 2012.
4. Holloway, C. L., E. F. Kuester, J. A. Gordon, et al., “An overview of the theory and applications of metasurfaces: The two-dimensional equivalents of metamaterials,” *IEEE Antennas and Propagation Magazine*, Vol. 54, No. 2, 10–35, 2012.
5. Zhao, Y. and A. Alù, “Manipulating light polarization with ultrathin plasmonic metasurfaces,” *Physical Review B*, Vol. 84, No. 20, 205428, 2011.
6. Hao, J., Y. Yuan, L. Ran, et al., “Manipulating electromagnetic wave polarizations by anisotropic metamaterials,” *Physical Review Letters*, Vol. 99, No. 6, 063908, 2007.
7. Wei, Z., Y. Cao, Y. Fan, et al., “Broadband polarization transformation via enhanced asymmetric transmission through arrays of twisted complementary split-ring resonators,” *Applied Physics Letters*, Vol. 99, No. 22, 221907, 2011.
8. Gansel, J. K., M. Thiel, M. S. Rill, et al., “Gold helix photonic metamaterial as broadband circular polarizer,” *Science*, Vol. 325, No. 5947, 1513–1515, 2009.
9. Li, H., B. Z. Wang, and W. Shao, “Novel broadband reflectarray antenna with compound-cross-loop elements for millimeter-wave application,” *Journal of Electromagnetic Waves and Applications*, Vol. 21, No. 10, 1333–1340, 2007.
10. Li, H., B. Z. Wang, and P. Du, “Novel broadband reflectarray antenna with windmill-shaped elements for millimeter-wave application,” *International Journal of Infrared and Millimeter Waves*, Vol. 28, No. 5, 339–344, 2007.
11. Farmahini-Farahani, M. and H. Mosallaei, “Birefringent reflectarray metasurface for beam engineering in infrared,” *Optics Letters*, Vol. 38, No. 4, 462–464, 2013.
12. Pfeiffer, C. and A. Grbic, “Millimeter-wave transmitarrays for wavefront and polarization control,” 2013.

Variable Gravitational Mass in the Electromagnetic Field Described with the Complex Quaternion

Zi-Hua Weng

School of Physics and Mechanical & Electrical Engineering
Xiamen University, Xiamen 361005, China

Abstract— J. C. Maxwell represented the physical feature of electromagnetic field with the vector terminology and the quaternion analysis. The method inspires other scholars to apply the complex quaternion depicting the classical field theory. The complex quaternion is able to deduce the field equations and force in the electromagnetic and gravitational fields, and predict some inferences. One of them is that the gravitational mass is variable. The gravitational mass will fluctuate with the alteration of the electromagnetic and gravitational strengths. Further the gradient of the variable part of the gravitational mass may form the gradient force. The gradient force can be used to capture the charged/neutral particles, and even the dark matter particles. And it is capable of explaining the bidirectional jets phenomenon of the accretion disc surrounding certain objects. The results reveal that the feature of the gravitational mass is different to that of the inertial mass. Strictly speaking, only in the case there is neither the electromagnetic strength nor the gravitational strength, the gravitational mass may equal to the inertial mass accurately. Therefore it is necessary to further validate the Eötvös experiment under the uniform and strong electromagnetic strength.

1. INTRODUCTION

In 1843 W. R. Hamilton invented the quaternion. Later J. T. Graves and A. Cayley introduced independently the octonion. In the twentieth century the scholars began to apply the complex quaternion/octonion to depict the electromagnetic theory [1], and even the gravitational theory [2]. In the twenty-first century the researches on these field theories have been inheriting and further developing. In the field theory described with the complex octonion, it is able to deduce directly the Maxwell's equations [3] and the force equilibrium equation, and refine further the inference that the gravitational mass varies with the fluctuation of field strength [4]. Moreover the energy gradient associated with the variable gravitational mass will impact the movement of the particle. The deduction can be applied to capture the low-speed neutral particle.

The field theory described with the complex octonion believes that the comparative strong gravitational and electromagnetic strength will evidently result in the fluctuation of gravitational mass. In the gravitational field, the gravitational acceleration will decrease the gravitational mass. In the electromagnetic field, the electric intensity increases the gravitational mass, while the magnetic flux density decreases that. It is similar to the mass difference amongst some particles in the strong nuclear field, including the proton/neutron, and the charged/neutral pi meson etc..

The gradient of the norm of field strength is one component of force, and may be called as the 'gradient force' for the moment. The gradient force will result in the accretion disc surrounding certain objects to emit jet bidirectionally [5]. For the magnetic flux density, the gradient force is attractive. For the electric intensity, the gradient force is repulsive. In the gravitational and electromagnetic fields, when the gradient force is attractive, the particle will be in repeating motion within one local region, which is similar to the repeating motion of the quark particle with the asymptotic freedom. When the gradient force is repulsive, the particle will be in repeating motion within one local region, which is located in between two face-and-face and collinear gradient forces. And it is similar to the repeating motion of charged particle in the magnetic mirror effect.

Up to now each Eötvös experiment [6] has only been validated in the weak gravitational field, but has never been tested in the strong gravitational field. Further the Eötvös experiment has never been tested in the electromagnetic field, and the high-speed situation. So the scholars never stop doubting the validity of Eötvös experiment. In the force equilibrium equation, the force includes the inertial force, gravity, energy gradient, and Lorentz force etc.. As long as the energy distribution is no uniform, the energy gradient, as one part of force, will impact the equilibrium relation of the inertial force and the gravity. Therefore it is necessary to further validate the Eötvös experiment under an electromagnetic environment.

2. FIELD EQUATIONS

In the quaternion space \mathbb{E}_g for the gravitational field, the basis vector is $\mathbb{E}_g = (\dot{\mathbf{i}}_0, \dot{\mathbf{i}}_1, \dot{\mathbf{i}}_2, \dot{\mathbf{i}}_3)$, the radius vector is $\mathbb{R}_g = i r_0 \dot{\mathbf{i}}_0 + \Sigma r_k \dot{\mathbf{i}}_k$, and the velocity is $\mathbb{V}_g = i v_0 \dot{\mathbf{i}}_0 + \Sigma v_k \dot{\mathbf{i}}_k$. The gravitational potential is $\mathbb{A}_g = i a_0 \dot{\mathbf{i}}_0 + \Sigma a_k \dot{\mathbf{i}}_k$, the gravitational strength is $\mathbb{B}_g = h_0 \dot{\mathbf{i}}_0 + \Sigma h_k \dot{\mathbf{i}}_k$, and the gravitational source is $\mathbb{S}_g = i s_0 \dot{\mathbf{i}}_0 + \Sigma s_k \dot{\mathbf{i}}_k$. In the S -quaternion space \mathbb{E}_e (short for the second quaternion space) for the electromagnetic field [7], the basis vector is $\mathbb{E}_e = (\mathbf{I}_0, \mathbf{I}_1, \mathbf{I}_2, \mathbf{I}_3)$, the radius vector is $\mathbb{R}_e = i R_0 \mathbf{I}_0 + \Sigma R_k \mathbf{I}_k$, and the velocity is $\mathbb{V}_e = i V_0 \mathbf{I}_0 + \Sigma V_k \mathbf{I}_k$. The electromagnetic potential is $\mathbb{A}_e = i A_0 \mathbf{I}_0 + \Sigma A_k \mathbf{I}_k$, the electromagnetic strength is $\mathbb{B}_e = H_0 \mathbf{I}_0 + \Sigma H_k \mathbf{I}_k$, and the electromagnetic source is $\mathbb{S}_e = i S_0 \mathbf{I}_0 + \Sigma S_k \mathbf{I}_k$. Herein $\mathbb{E}_e = \mathbb{E}_g \circ \mathbf{I}_0$. The symbol \circ denotes the octonion multiplication. $r_j, v_j, a_j, s_j, R_j, V_j, A_j, S_j, h_0$, and H_0 are all real. h_k and H_k are all complex numbers. i is the imaginary unit. $\dot{\mathbf{i}}_0 = 1, \dot{\mathbf{i}}_k^2 = -1, \dot{\mathbf{I}}_j^2 = -1$. $j = 0, 1, 2, 3$. $k = 1, 2, 3$.

Two quaternion spaces, \mathbb{E}_g and \mathbb{E}_e , may combine together to become one octonion space, $\mathbb{E} = \mathbb{E}_g + \mathbb{E}_e$. In the octonion space \mathbb{E} for the electromagnetic and gravitational fields, the octonion radius vector is $\mathbb{R} = \mathbb{R}_g + k_{eg} \mathbb{R}_e$, the octonion velocity is $\mathbb{V} = \mathbb{V}_g + k_{eg} \mathbb{V}_e$, with k_{eg} being the coefficient. The octonion field potential is $\mathbb{A} = \mathbb{A}_g + k_{eg} \mathbb{A}_e$, the octonion field strength is $\mathbb{B} = \mathbb{B}_g + k_{eg} \mathbb{B}_e$. Apparently \mathbb{V} and \mathbb{A} etc. are all octonion functions of \mathbb{R} .

The octonion definition of field strength is,

$$\mathbb{B} = \square \circ \mathbb{A}$$

where $\mathbb{B}_g = \square \circ \mathbb{A}_g, \mathbb{B}_e = \square \circ \mathbb{A}_e$. The quaternion operator is $\square = i \dot{\mathbf{i}}_0 \partial_0 + \Sigma i \dot{\mathbf{i}}_k \partial_k$. $\nabla = \Sigma \dot{\mathbf{i}}_k \partial_k$, $\partial_j = \partial / \partial r_j$. $v_0 = \partial r_0 / \partial t$. v_0 is the speed of light, and t is the time.

In the quaternion space \mathbb{E}_g , the gauge condition is, $h_0 = -\partial_0 a_0 + \nabla \cdot \mathbf{a} = 0$. And then the \mathbb{B}_g is reduced to $\mathbf{h} = \mathbf{ig}/v_0 + \mathbf{b}$. The gravitational acceleration is, $\mathbf{g}/v_0 = \partial_0 \mathbf{a} + \nabla a_0$, while the other component of gravitational strength is $\mathbf{b} = \nabla \times \mathbf{a}$, which is similar to the magnetic flux density. In the S -quaternion space \mathbb{E}_e , the gauge condition is, $\mathbf{H}_0 = -\partial_0 \mathbf{A}_0 + \nabla \cdot \mathbf{A} = 0$. Therefore the \mathbb{B}_e is reduced to $\mathbf{H} = \mathbf{iE}/v_0 + \mathbf{B}$. The electric field intensity is $\mathbf{E}/v_0 = \partial_0 \mathbf{A} + \nabla \circ \mathbf{A}_0$, while the magnetic flux density is $\mathbf{B} = \nabla \times \mathbf{A}$. Herein $\mathbf{a} = \Sigma a_k \dot{\mathbf{i}}_k, \mathbf{h} = \Sigma h_k \dot{\mathbf{i}}_k$. $\mathbf{A}_0 = A_0 \mathbf{I}_0, \mathbf{A} = \Sigma A_k \mathbf{I}_k$. $\mathbf{H}_0 = H_0 \mathbf{I}_0, \mathbf{H} = \Sigma H_k \mathbf{I}_k$.

The octonion field source \mathbb{S} of the electromagnetic and gravitational fields can be defined as,

$$\mu \mathbb{S} = -(i \mathbb{B}/v_0 + \square)^* \circ \mathbb{B} = \mu_g \mathbb{S}_g + k_{eg} \mu_e \mathbb{S}_e - (i \mathbb{B}/v_0)^* \circ \mathbb{B}, \quad (1)$$

where μ, μ_g , and μ_e are coefficients. $\mu_g < 0$, and $\mu_e > 0$. $*$ denotes the conjugation of octonion. In the case for single one particle, a comparison with the classical field theory reveals that, $\mathbb{S}_g = m \mathbb{V}_g$, and $\mathbb{S}_e = q \mathbb{V}_e$. m is the mass density, while q is the density of electric charge. For the charged particle, there is $\mathbb{V}_e = \mathbb{V}_g \circ \mathbf{I}(I_j)$. The unit $\mathbf{I}(I_j)$ is one function of \mathbf{I}_j , with $\mathbf{I}(I_j)^* \circ \mathbf{I}(I_j) = 1$.

Expanding of Eq. (1) is capable of deducing the Maxwell's equations in the classical electromagnetic theory, and the Newton's law of universal gravitation in the classical gravitational theory when $\mathbf{b} = 0$ and $\mathbf{a} = 0$.

Table 1: The multiplication of the operator and octonion physics quantity.

definition	expression	meaning
$\nabla \cdot \mathbf{a}$	$-(\partial_1 a_1 + \partial_2 a_2 + \partial_3 a_3)$	
$\nabla \times \mathbf{a}$	$\dot{\mathbf{i}}_1(\partial_2 a_3 - \partial_3 a_2) + \dot{\mathbf{i}}_2(\partial_3 a_1 - \partial_1 a_3) + \dot{\mathbf{i}}_3(\partial_1 a_2 - \partial_2 a_1)$	
∇a_0	$\dot{\mathbf{i}}_1 \partial_1 a_0 + \dot{\mathbf{i}}_2 \partial_2 a_0 + \dot{\mathbf{i}}_3 \partial_3 a_0$	
$\partial_0 \mathbf{a}$	$\dot{\mathbf{i}}_1 \partial_0 a_1 + \dot{\mathbf{i}}_2 \partial_0 a_2 + \dot{\mathbf{i}}_3 \partial_0 a_3$	
$\nabla \cdot \mathbf{A}$	$-(\partial_1 A_1 + \partial_2 A_2 + \partial_3 A_3) \mathbf{I}_0$	
$\nabla \times \mathbf{A}$	$-\mathbf{I}_1(\partial_2 A_3 - \partial_3 A_2) - \mathbf{I}_2(\partial_3 A_1 - \partial_1 A_3) - \mathbf{I}_3(\partial_1 A_2 - \partial_2 A_1)$	
$\nabla \circ \mathbf{A}_0$	$\mathbf{I}_1 \partial_1 A_0 + \mathbf{I}_2 \partial_2 A_0 + \mathbf{I}_3 \partial_3 A_0$	
$\partial_0 \mathbf{A}$	$\mathbf{I}_1 \partial_0 A_1 + \mathbf{I}_2 \partial_0 A_2 + \mathbf{I}_3 \partial_0 A_3$	

3. OCTONION FORCE

In the octonion space, the octonion linear momentum density \mathbb{P} is defined from the octonion field source \mathbb{S} , and can be written as follows,

$$\mathbb{P} = \mu \mathbb{S} / \mu_g,$$

where $\mathbb{P} = \mathbb{P}_g + k_{eg}\mathbb{P}_e$. $\mathbb{P}_g = \{\mu_g\mathbb{S}_g - (i\mathbb{B}/v_0)^* \circ \mathbb{B}\}/\mu_g$, and $\mathbb{P}_e = \mu_e\mathbb{S}_e/\mu_g$.

From the above, one can define the octonion angular momentum, $\mathbb{L} = (\mathbb{R} + k_{rx}\mathbb{X})^\times \circ \mathbb{P}$, the octonion torque \mathbb{W} , and octonion force \mathbb{N} in the Table 2. Herein \mathbb{X} is the integral function of field potential \mathbb{A} , and \times denotes the conjugation of complex number, with k_{rx} being the coefficient.

If it is able to neglect the contribution of some tiny terms, the octonion torque will be reduced to, $\mathbb{W} \approx (2\mathbb{P}v_0)$, when $(\Sigma r_k \dot{\mathbf{i}}_k)$ is one three-dimensional vector. And then the octonion force is written as follows,

$$\begin{aligned} \mathbb{N}/2 &= -v_0(i\mathbb{B}_g \circ \mathbb{P}_g/v_0 + ik_{eg}^2\mathbb{B}_e \circ \mathbb{P}_e/v_0 + \square \circ \mathbb{P}_g) \\ &\quad -k_{eg}v_0(i\mathbb{B}_g \circ \mathbb{P}_e/v_0 + i\mathbb{B}_e \circ \mathbb{P}_g/v_0 + \square \circ \mathbb{P}_e), \end{aligned}$$

where $\mathbb{N}_g/2 = -v_0(i\mathbb{B}_g \circ \mathbb{P}_g/v_0 + ik_{eg}^2\mathbb{B}_e \circ \mathbb{P}_e/v_0 + \square \circ \mathbb{P}_g)$ stays on the quaternion space \mathbb{E}_g , including the inertial force, gravity, and Lorentz force etc.. $\mathbb{N}_e/2 = -v_0(i\mathbb{B}_g \circ \mathbb{P}_e/v_0 + i\mathbb{B}_e \circ \mathbb{P}_g/v_0 + \square \circ \mathbb{P}_e)$ situates on the S -quaternion space \mathbb{E}_e , and is the interacting term between the gravitational field and electromagnetic field, including the current continuity equation etc..

In the quaternion space \mathbb{E}_g , when there are the gravitational and electromagnetic fields, the force term \mathbb{N}_g can be expressed as

$$N_{10}^i/2 = -\mathbf{b} \cdot \mathbf{p} - k_{eg}^2(\mathbf{B} \cdot \mathbf{P}), \quad (2)$$

$$N_{10}/2 = v_0\partial_0 p_0 - v_0\nabla \cdot \mathbf{p} + \mathbf{g} \cdot \mathbf{p}/v_0 + k_{eg}^2(\mathbf{E} \cdot \mathbf{P}/v_0), \quad (3)$$

$$\mathbf{N}_1^i/2 = -v_0\partial_0 \mathbf{p} + p_0\mathbf{g}/v_0 - v_0\nabla p_0 - \mathbf{b} \times \mathbf{p} + k_{eg}^2(\mathbf{E} \circ \mathbf{P}_0/v_0 - \mathbf{B} \times \mathbf{P}), \quad (4)$$

$$\mathbf{N}_1/2 = -v_0\nabla \times \mathbf{p} + \mathbf{g} \times \mathbf{p}/v_0 + p_0\mathbf{b} + k_{eg}^2(\mathbf{E} \times \mathbf{P}/v_0 + \mathbf{B} \circ \mathbf{P}_0), \quad (5)$$

where $\mathbb{N}_g = iN_{10}^i + N_{10} + i\mathbf{N}_1^i + \mathbf{N}_1$. $\mathbb{P}_g = ip_0 + \mathbf{p}$. $\mathbf{p} = \Sigma p_k \dot{\mathbf{i}}_k$. $\mathbb{P}_e = i\mathbf{P}_0 + \mathbf{P}$. $\mathbf{P} = \Sigma P_k \mathbf{I}_k$. $\mathbf{P}_0 = P_0 \mathbf{I}_0$. $\mathbf{N}_1 = \Sigma N_{1k} \dot{\mathbf{i}}_k$, $\mathbf{N}_1^i = \Sigma N_{1k}^i \dot{\mathbf{i}}_k$. P_j , p_j , N_{1j} , and N_{1j}^i are all real.

When $\mathbb{N}_g = 0$, the equation for force equilibrium is yielded from $\mathbf{N}_1^i = 0$. The mass continuity equation is derived from $N_{10} = 0$, and it will be reduced to that in the classical field theory when there is no field strength. The strength components \mathbf{b} and \mathbf{B} will impact the current helicity of charged particle according to $N_{10}^i = 0$. While $\mathbf{N}_1 = 0$ can deduce the curl of toque component $\mathbf{p}v_0$. And it is capable to infer the angular velocity of Larmor precession with respect to the orbital angular momentum of charged particle. The equation $\mathbf{N}_1^i = 0$ means that the gravitational acceleration \mathbf{g} is the counterpart of the linear acceleration, $v_0\partial_0 \mathbf{v}$. The equation $\mathbf{N}_1 = 0$ states that the component \mathbf{b} is the counterpart of the velocity curl, $\nabla \times \mathbf{v}$, which is the double of the precessional angular velocity when the dimension of vector \mathbf{r} is 2.

The force \mathbf{N}_1^i consists of the inertial force, gravity, Lorentz force, and proper energy gradient etc.. Comparing with the force density in the classical field theory states that $k_{eg}^2 = \mu_g/\mu_e < 0$ and $k_{rx} = 1/v_0$. The inertial force $(-v_0\partial_0 \mathbf{p})$ claims that the gravitational field must situate on the quaternion space \mathbb{E}_g , while the electromagnetic field has to stay on the quaternion space \mathbb{E}_e , but not vice versa.

4. VARIABLE GRAVITATIONAL MASS

In the electromagnetic and gravitational fields, the inertial mass density is m , and the gravitational mass density is $m_g = m + m'$, with m' being $\{-\mathbb{B}^* \circ \mathbb{B}/(\mu_g v_0^2)\}$. Obviously the m_g will fluctuate with the alteration of the electromagnetic strength \mathbb{B}_e and of gravitational strength \mathbb{B}_g . According to Eq.(4), the variation of gravitational mass density is,

$$m' = -(\mathbf{b}^* \cdot \mathbf{b} - \mathbf{g}^* \cdot \mathbf{g}/v_0^2)/(\mu_g v_0^2) - (\mathbf{B}^* \cdot \mathbf{B} - \mathbf{E}^* \cdot \mathbf{E}/v_0^2)/(\mu_e v_0^2). \quad (6)$$

Comparative strong field strength will impact the fluctuation of gravitational mass. Apparently the magnetic flux density \mathbf{B} or the gravitational acceleration \mathbf{g} will cause the decrease of gravitational mass. While the electric field intensity \mathbf{E} or the gravitational strength component \mathbf{b} will result in the increase of gravitational mass.

On the basis of the existing Eötvös experiments, the application of comparative strong electromagnetic strength will impact the ratio of these two masses to a certain extent. This test scheme can be considered as one direct validation experiment for the variable gravitational mass. One of inferences about the variable gravitational mass is the gradient force, which can be regarded as the indirect evidence for the variable gravitational mass.

According to Eq. (4), when $\nabla m = 0$, the gradient force can be written as,

$$\mathbf{N}_B/2 = -v_0 \nabla p_0 = -v_0^2 \nabla(m + m') = \nabla(\mathbb{B}^* \circ \mathbb{B}/\mu_g) . \quad (7)$$

In the electromagnetic and gravitational fields, the gradient force is in a directly proportional to the gradient of the norm of field strength. And the gradient force is independent to not only the mass and electric charge of the test particle, but also the direction of field strength. Either the steep gradient of field strength or the strong field strength can result in the prominent gradient force. It can be used to impel the bulk flow of the plasma, and drive/capture the particles of the normal matter and even of the dark matter.

In the electromagnetic and gravitational fields, four components of field strength are capable of impacting the gradient force.

(1) For the magnetic flux density \mathbf{B} or the gravitational acceleration \mathbf{g} , the gradient force has the attraction effect. And it will arouse the repeating motion of the particle within one local region, which is similar to the reciprocating motion of the small object fixed on the end of the spring.

(2) For the electric field intensity \mathbf{E} or the gravitational strength component \mathbf{b} , the gradient force has the repulsion effect. Also it will cause repeating motion of the particle within one local region, which is similar to the repeating motion of charged particle in the magnetic mirror effect.

Specially the distribution of the gravitational strength component \mathbf{b} is similar to that of the magnetic flux density \mathbf{B} . Because of the closing feature of \mathbf{b} force-line, the magnitude of \mathbf{b} within the central region of galaxy will increase drastically. According to the above analysis, the galaxy center may emit the jet and counter-jet along the precessional axis associated with \mathbf{b} . When the axis of total angular velocity keeps still, the precessional axis will circle around the axis of total angular velocity. Such as the Cygnus X-1, Messier 87, SS433, and neutron star etc..

Table 2: Some definitions of the physics quantity in the gravitational and electromagnetic fields described with the complex quaternion/octonion spaces.

physics quantity	definition	note
radius vector	$\mathbb{R} = \mathbb{R}_g + k_{eg}\mathbb{R}_e$	$k_{eg}^2 = \mu_g/\mu_e < 0$
integral function	$\mathbb{X} = \mathbb{X}_g + k_{eg}\mathbb{X}_e$	
field potential	$\mathbb{A} = i\Box^\times \circ \mathbb{X}$	
field strength	$\mathbb{B} = \Box \circ \mathbb{A}$	gauge condition
field source	$\mu\mathbb{S} = -(i\mathbb{B}/v_0 + \Box)^* \circ \mathbb{B}$	field equations
linear momentum	$\mathbb{P} = \mu\mathbb{S}/\mu_g$	
angular momentum	$\mathbb{L} = (\mathbb{R} + k_{rx}\mathbb{X})^\times \circ \mathbb{P}$	$k_{rx} = 1/v_0$
octonion torque	$\mathbb{W} = -v_0(i\mathbb{B}/v_0 + \Box) \circ \mathbb{L}$	torque, work, energy
octonion force	$\mathbb{N} = -(i\mathbb{B}/v_0 + \Box) \circ \mathbb{W}$	power, force

5. CONCLUSIONS

For a long time, the scholars never stop doubting the validity of Eötvös experiment. Up to now each Eötvös experiment has only been validated in the weak gravitational field. And it has never been tested in the strong gravitational field, or in the strong electromagnetic field, or in the high-speed situation. Apparently the Eötvös experiment should consider more influence factors, including the uniform and comparative strong electromagnetic strength etc..

The application of the complex quaternion approach can depict the classical electromagnetic and gravitational theories. Further it is able to predict some inferences, including the variable gravitational mass, gradient force, and repeating motion within one local region etc.. In the description method of complex quaternion, the variation of gravitational mass is related with both of the electromagnetic strength and the gravitational strength. And that the gradient of the norm of electromagnetic strength and of gravitational strength yield the gradient force. The force is independent to not only the direction of field strength, but also the mass or electric charge of the test particle. The gradient force can drive/capture several kinds of particles, and confine the motion of test particles within the local region. And it is capable of explaining the jet phenomenon of accretion disc surrounding certain objects along the precessional axis.

The paper discussed the variability of gravitational mass in the electromagnetic and gravitational fields, and some simple applications of gradient force. And it expatiated on distinctly some major influence factors to alter the gravitational mass, and the application range of the variable gravitational mass etc.. It set the foundation for the further research about the gravitational mass. In the following study, we plan, (1) to validate the Eötvös experiment within some comparative strong uniform magnetic fields; (2) to observe the repeating motion of the escaping particles near the ends of magnetic mirror, based on the existing experiments of magnetic mirror; (3) to apply the gradient force to capture particles of the normal matter, and even of the dark matter.

ACKNOWLEDGMENT

This project was supported partially by the National Natural Science Foundation of China under grant number 60677039.

REFERENCES

1. Honig, W. M., “Quaternionic electromagnetic wave equation and a dual charge-filled space,” *Lettere al Nuovo Cimento*, Vol. 19, No. 4, 137–140, 1977.
2. Doria, F. A., “A Weyl-like equation for the gravitational field,” *Lettere al Nuovo Cimento*, Vol. 14, No. 13, 480–482, 1975.
3. Mironov, V. L. and S. V. Mironov, “Octonic representation of electromagnetic field equations,” *Journal of Mathematical Physics*, Vol. 50, No. 1, 012901, 10 pages, 2009.
4. Weng, Z.-H. and Y. Weng, “Variation of gravitational mass in electromagnetic field,” *PIERS Proceedings*, 105–107, Beijing, China, March 23–27, 2009.
5. Goodall, P. T., K. M. Blundell, and S. J. Bell Burnell, “Probing the history of SS 433’s jet kinematics via decade-resolution radio observations of W 50,” *Monthly Notices of the Royal Astronomical Society*, Vol. 414, No. 4, 2828–2837, 2011.
6. Braginsky, V. B., “Experiments with probe masses,” *Proceedings of the National Academy of Sciences of the United States of America*, Vol. 104, No. 10, 3677–3680, 2007.
7. Weng, Z.-H., “Transformations of field equations in octonion spaces,” *PIERS Proceedings*, 1367–1371, Moscow, Russia, August 19–23, 2012.

Study on Barium Strontium Titanium (BST)-based Metamaterial

J. Yuan, G. Yin, G.-B. Yin, and Y.-G. Ma

Centre for Optical and Electromagnetic Research, Zhejiang University, Hangzhou 310058, China

Abstract— In this paper, the barium strontium titanium (BST) is employed to form the moderm layer in the metamaterial. We demonstrate an active metamaterial device capable of efficient real-time control and manipulation of microwave radiation. It is demonstrated that both the resonance frequency and bandwidth of the metamaterial can be tuned by varying the external electric voltage. Additionally, BST-based metamaterial with different geometries are explored.

1. INTRODUCTION

Well-structured artificial electromagnetic material, known as metamaterial, has realized many unique phenomena which natural materials cannot be. In recent years, reconfigurable metamaterial has some exciting properties in scientific areas, including sensors, cloaks, and switches in optical communication [1–3]. Through the modulation of voltage, magnetic field, etc. [4–7], artificial electromagnetic materials add some new properties into materials. And makes them have more extensive applications [8].

A great deal of work in metamaterial has used microwave radiation, this is because the microwave is widely used in communication as well as the ease of fabrication of sub-wavelength structures at these frequencies. Here, we demonstrate that the metamaterial with capacitor structure conclude BST film could achieve good effect of modulation in microwave frequency. Because the BST film has a high dielectric constant in the microwave and could be modulated by the external electric voltage [9]. This paper introduces a new method of modulating structure resonance frequency by voltage. The equivalent capacitance of the structure can be dramatically tuned, and the resonance frequency shifts subsequently.

2. LAALO₃-BASED METAMATERIAL

Figure 1(a) shows the LaAlO₃-based metamaterial unit, the substrate is made by LaAlO₃ which permittivity is 25, the top electrode is made by gold and the BST films is between them. The surface impedance can be characterized as a capacitor. The equivalent circuit model is shown in Figure 1(b).

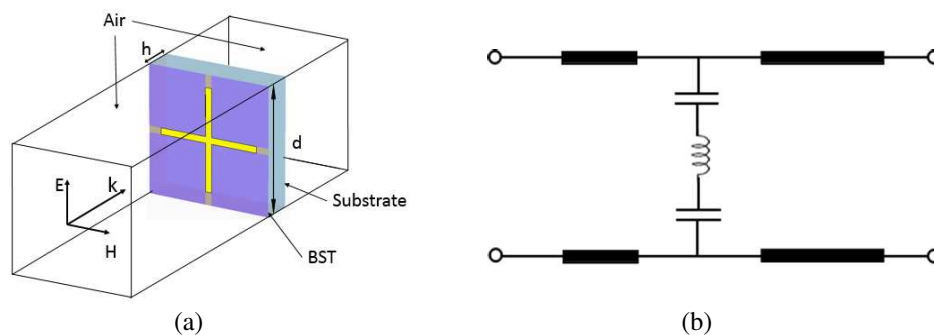


Figure 1: (a) Schematic of the unit, the parameter: d is 3.5 mm, h is 251 μm (includes the thickness of BST film is 1 μm), and (b) equivalent circuit model.

2.1. Analytical Modeling

The reflectance R for LaAlO₃-BASED metamaterial with square patches is obtained by [10]

$$R = \frac{Z_s - \eta_0}{Z_s + \eta_0} \quad (1)$$

where $\eta_0 (= 377\Omega)$ is the intrinsic impedance of free-space, and Z_s is the total surface impedance. Here we set the periodic constant $d = 3.5$ mm, the length of the cross b is 3 mm. the thickness of electrode both on the top and bottom is 200 nm, with the BST film between them. And the width

of the electrode is $120\ \mu\text{m}$. The thickness h of the substrate which was made by LaAlO_3 is about $0.25\ \text{mm}$. We set the length of the bottom electrode $n = 300\ \mu\text{m}$ in order to keep the overlapping part between the electrodes is $50\ \mu\text{m}$.

We get the variation range of dielectric constant is 74.6% from 0 to $1500\ \text{V/mm}$ of the biased voltage [9]. Therefore, we will know the reflectivity under different dielectric constant due to applied voltage.

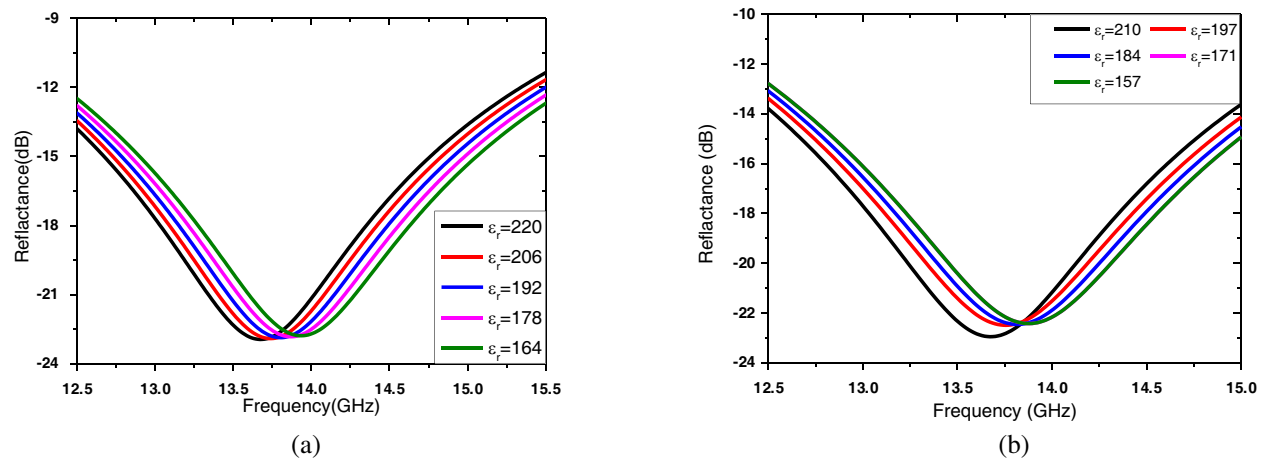


Figure 2: (a) Reflectance of the structure made by Au, relative dielectric constant are 220, 206, 192, 178, 164 and (b) Reflectance of the structure made by Pt, relative dielectric constant are 210, 197, 184, 171, 157 [11].

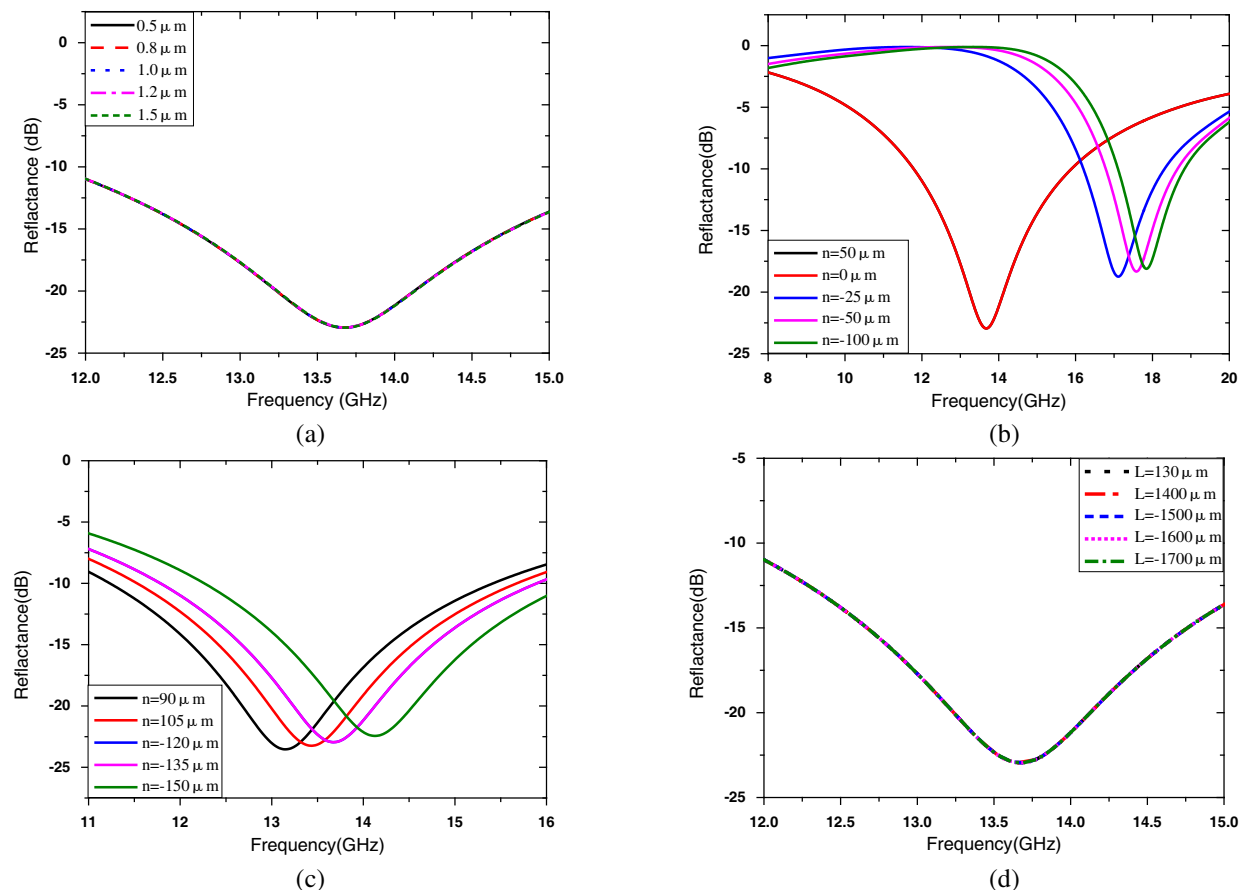


Figure 3: Parametric study of BST-based metamaterial with (a) thickness of BST film; (b) coincidence length between top and bottom electrode; (c) width of electrode; (d) length of the cross.

2.2. Study of Geometries

The thickness of BST film, the width of the electrode, the length of the bottom electrode and the cross may has an impact on the resonance frequency of the structure.

Figure 2(a) shows that the thickness of BST film has no effect on the resonance frequency with the permittivity of the BST film is 220. But this situation is based on that the stability of the permittivity of the BST film. And the thickness of the BST film will affect the permittivity if the voltage stay the same. So, if we want to keep the resonance frequency do not shift during the growing of the BST film, we must increase the voltage the same magnification of with the thickness. Figure 2(b) shows the influence of the top and bottom electrode's coincidence length on the resonance frequency. The black line means the coincidence length is $50\ \mu\text{m}$, and the green line means the horizontal distance between the top and bottom electrode is $100\ \mu\text{m}$, where we signed $-100\ \mu\text{m}$. We could easily get the coincidence length has an impact on the resonance frequency when it is negative. But has no effect when it becomes positive (black line and red line coincide in Figure 2(b)). From Figure 2(c), we could clearly see that the width of the electrode has huge impact on the resonance frequency. And Figure 2(d) show the length of the cross has no impact on it.

2.3. Different Geometric Shape

Other interesting geometric shape is studied here (see Figure 4(a)), and its reflection is plotted in Figure 4(b). The modulation bandwidth is 0.3 GHz, it is similar to the original structure. This indicate the modulation ability are more dependent on the special properties of BST materials under applied voltage.

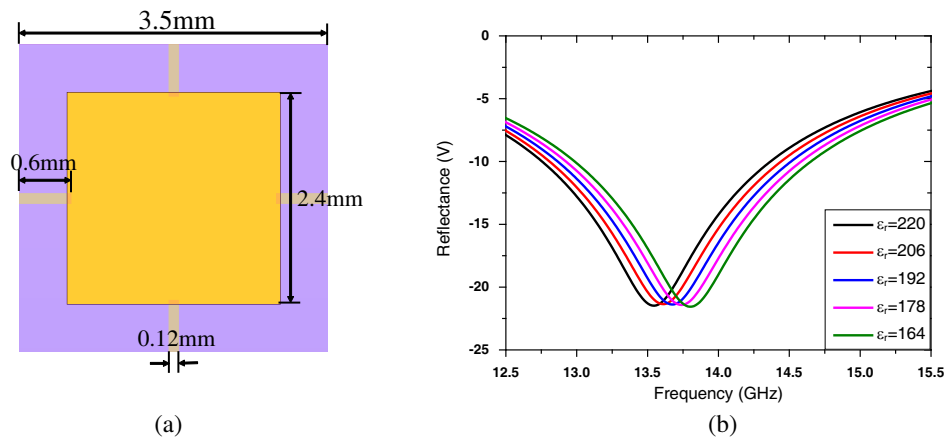


Figure 4: Parametric study of BST-based metamaterial with (a) thickness of BST film; (b) coincidence length between top and bottom electrode; (c) width of electrode; (d) length of the cross.

3. CONCLUSION

In this work, the structure which could be adjusted by applied voltage has been proposed and demonstrated. The parameter of the structure has been fully studied and compared. At last, the comparison of the tuning results of different structures confirm the tuning properties was mainly from the material itself.

ACKNOWLEDGMENT

This work is partially supported by the National High Technology Research and Development Program (863) of China (No. 2012AA030402)

REFERENCES

1. Nan, T. X., Y. Hui, M. Rinaldi, and N. X. Sun, "Self-biased 215 MHz magnetoelectric NEMS resonator for ultra-sensitive DC magnetic field detection," *Scientific Reports*, Vol. 3, No. 1985, 1–6, 2013.
2. Kort-Kamp, W. J. M., F. S. S. Rosa, F. A. Pinheiro, and C. Farina, "Tuning plasmonic cloaks with an external magnetic field," *Physical Review Letters*, Vol. 111, No. 21, 1–5, 2013.

3. Temnov, V. V., G. Armelles, U. Woggon, D. Guzatov, A. Cebollada, A. Garcia-Martin, J.-M. Garcia-Martin, T. Thomay, A. Leitenstorfer, and R. Bratschitsch, “Active magneto-plasmonics in hybrid metal-ferromagnet structures,” *Nature Photonics*, Vol. 4, No. 2, 103–106, 2010.
4. Chen, H. T., W. J. Padilla, J. M. O. Zide, A. C. Gossard, A. J. Taylor, and R. D. Averitt, “Active terahertz metamaterial devices,” *Nature*, Vol. 444, No. 7119, 597–600, 2006.
5. Gil, M., C. Damm, A. Giere, M. Sazegar, J. Bonache, R. Jakoby, and F. Martín, “Electrically tunable split-ring resonators at microwave frequencies based on barium-strontium-titanate thick films,” *Electronics Letters*, Vol. 45, No. 8, 417–418, 2009.
6. Belotelov, V. I., L. E. Kreilkamp, I. A. Akimov, A. N. Kalish, D. A. Bykov, S. Kasture, V. J. Yallapragada, A. V. Gopal, A. M. Grishin, S. I. Khartsev, M. Nur-E-Alam, M. Vasiliev, L. L. Doskolovich, D. R. Yakovlev, K. Alameh, A. K. Zvezdin, and M. Bayer, “Plasmon-mediated magneto-optical transparency,” *Nature Communications*, Vol. 4, No. 2128, 1–7, 2013.
7. Kreilkamp, L. E., V. I. Belotelov, J. Y. Chin, S. Neutzner, D. Dregely, T. Wehlius, I. A. Akimov, M. Bayer, B. Stritzker, and H. Giesse, “Waveguide-plasmon polaritons enhance transverse magneto-optical Kerr effect” *Physical Review X*, Vol. 3, No. 4, 041019-1-7, 2013.
8. Zamani, M. and M. Ghanaatshoar, “Adjustable magneto-optical isolators with flat-top responses,” *Optics Express*, Vol. 20, No. 22, 24524–24535, 2012.
9. Liang, R. H., X. L. Dong, Y. Chen, F. Cao, and Y. L. Wang. “Mechanism of nonlinear dielectric constant of BaTiO₃-based ceramics under high DC electric field,” *Acta Physica Sinica*, Vol. 54, No. 10, 4914-4919, 2005.
10. Wang, X.-C., W.-Y. Li, W.-S. Zhao, J. Hu, Y.-Y. Xu, and Q.-S. Huang, “Comparative study on graphene-based artificial magnetic conductor (AMC),” *PIERS Proceeding*, Stockholm, Sweden, Aug. 12–15, 2013.
11. Sheng, S., X.-Y. Zhang, P. Wang, and C. K. Ong, “Effect of bottom electrodes on dielectric properties of high frequency Ba_{0.5}Sr_{0.5}TiO₃ parallel plate varactor,” *Thin Solid Films*, Vol. 518, No. 10, 2846–2866, 2010.

The Roles of Different NiO Compact Blocking Layers in P-type Sensitized Solar Cells

Huan Wang, Xianwei Zeng, Wenjun Zhang, and Wei Chen

Michael Grätzel Centre for Mesoscopic Solar Cells, Wuhan National Laboratory for Optoelectronics
Huazhong University of Science and Technology, Wuhan 430074, China

Abstract— Compact blocking layers made of wide band gap semiconductors, such as TiO_2 , ZnO , are widely used to suppress recombination at the conductive FTO substrate/electrolyte interface in dye or quantum dot sensitized solar cells, especially in the solid-state devices. Though sharing similar mechanism, blocking layers in p-type sensitized solar cells are rarely studied. Our recent works have demonstrated that the compact NiO films dependent upon the preparation ways play important roles in both p-type dye and quantum dots sensitized solar cells. In p-type dye sensitized NiO solar cell, the compact NiO layer prepared by spin-coating of a sol-gel film, can prevent the recombination at the FTO glass/electrolyte interface and retard the whole cell's recombination kinetics. Therefore, the fill factor and photovoltage can be increased, leading to a 40.77% improved performance of p-type solar cell. In p-type organometal halide perovskite sensitized mesoporous NiO solar cell, it is found that only the spray pyrolysis deposited NiO dense film is effective for selective hole gathering, rather not the sol-gel deposited NiO dense film. The difference may be ascribed to their coverage status on the rough FTO glasses. The existence of such a NiO block layer not only effects on the cell performance but also determines the current flow direction in the p-type perovskite sensitized NiO solar cell.

1. INTRODUCTION

Most of the reported dye or quantum dots sensitized solar cells are based on n-type mesoporous semiconductors like nanocrystalline TiO_2 , which we can call n-type sensitized solar cells. Their efficiency record moves very slowly in recent years [1, 2]. Efforts to make efficient p-type sensitized solar cells as the important supplementary to conventional n-type sensitized solar cells have attracted growing interests, because it provides a possible solution to break through the efficiency bottleneck by combining them to build pn tandem cell [3–5]. To suppress interfacial recombination is important for high efficiency p-type solar cell. One approach is to build an electron barrier at the conductive FTO substrate/electrolyte interface [6]. The cell configuration for such p-type sensitized solar cells is illustrated in Figure 1. NiO thin film is used as blocking layer because of its wide band gap, suitable valance band position and chemical stability [7].

In this paper, we report two methods to prepare compact NiO thin films as the compact blocking layers. One was made by spin-coating (SC) and the other was accomplished by spray pyrolysis (SP). There is a big morphology difference between the two kind NiO films. It's found that the SC deposited NiO blocking layer plays a critical role in p-type dye sensitized solar cell on enhancing open-circuit voltage (V_{oc}) and short-circuit current density (J_{sc}); while the SP deposited NiO blocking layer plays a critical role on determining the current flow direction of p-type perovskite sensitized NiO solar cell.

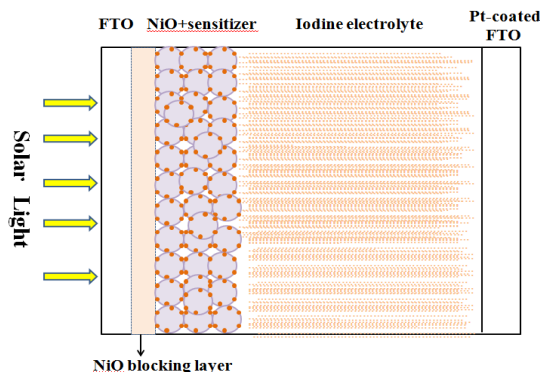


Figure 1: Schematic diagram of the DSSC with a NiO blocking layer.

2. EXPERIMENTAL SECTION

Compact NiO thin film preparation.

Compact film 1 made by spin-coating: 0.5 M Nickel acetate tetrahydrate in 2-methoxyethanol was used as the so-gel precursor for deposition, which was subsequently deposited on cleaned FTO glass by spin coating at the speed of 2000 rpm for 30 seconds. Finally, the film was sintered at 550°C for 3 h [8].

Compact film 2 prepared by spray pyrolysis: 0.04 M nickel acetylacetonate in acetonitrile was spray pyrolysed on FTO glass at 500°C by using an air nozzle. After that, the film was further sintered at 500°C for 30 minutes [6].

3. RESULTS AND DISCUSSION

As the SEM image in Figure 2 clearly shown, the morphology of SC deposited NiO compact film is different from SP deposited NiO compact film. For the SP deposited film, an ultrathin layer of NiO fully covers the turreted FTO microcrystals without changing the FTO surface roughness (Figures 2(a)–(c)). In contrast, the SC deposited film (Figure 2(d)) leads to a flat the NiO capture surface, concaves between the turreted FTO microcrystals have been filled by sol-gel NiO. However, such kind compact layer has a lot of sub-micron pin-holes inside due to volume shrinking during evaporation and sintering procedures.

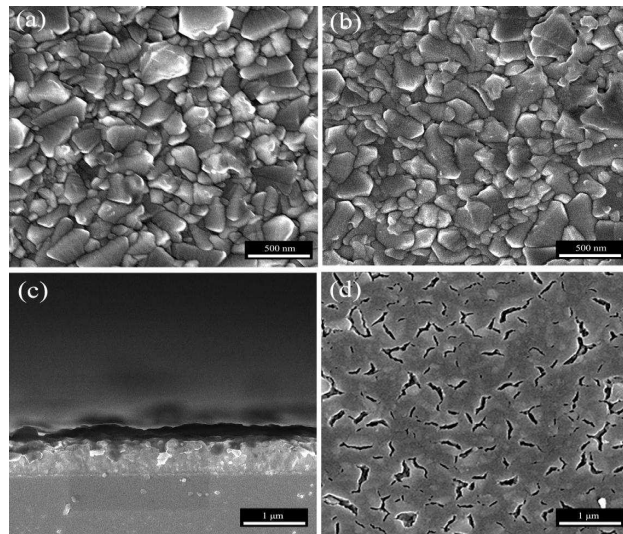


Figure 2: SEM images of (a) bare FTO substrate; (b) NiO film made by SP on FTO surface substrate and (c) its cross cross-section view; (d) NiO film made by SC on FTO substrate.

Figure 3(a) clearly depicts the performance difference between the p-type “P1 dye” sensitized NiO solar cells with and without SC deposited NiO blocking layer. By introducing such a blocking layer, the solar cell’s V_{oc} , J_{sc} and fill factor (FF) are all improved, which in total results in a 40.77% higher solar conversion efficiency in comparison to the solar cell without blocking layer as clearly shown in Table 1. The inherent reason for such improvements should be ascribed to the recombination suppression at the FTO glass/electrolyte interface. The transient photovoltage decay curves in Figure 3(b) strongly support this point. The lifetimes, quoted as the time taken to reach 1/e of the initial photovoltage, are 8.9 ms and 2.9 ms respectively for the solar cells with and without the blocking layer. The results suggest that the whole solar cell’s recombination kinetics is significantly retarded by the FTO surface passivation, which highlights the importance of such blocking layer.

Figure 4 compares the CH₃NH₃PbI₃ perovskite sensitized mesoporous NiO solar cells with and without the SP coated compact NiO blocking layer. We previously found that the SC coated blocking layer cannot work in the perovskite sensitized solar cell system, which might be due to the pin-holes, leading to short circuit contacts between perovskite and FTO. In such a case, the solar cell works as a n-type cell, just like the J-V curve of the solar cell without compact NiO blocking layer (Figure 4(a)). The current flow direction is the same as that of the conventional n-type dye or quantum dots sensitized TiO₂ solar cells. What the FTO substrate gathers is the photon-induced

Table 1: Performance of NiO DSSC with and without blocking layer.

	V_{oc} (mv)	J_{sc} (mA/cm ²)	FF	η
NiO blocking layer	81.54	4.16	32.36	0.107
Without blocking layer	65.37	3.82	31.24	0.076

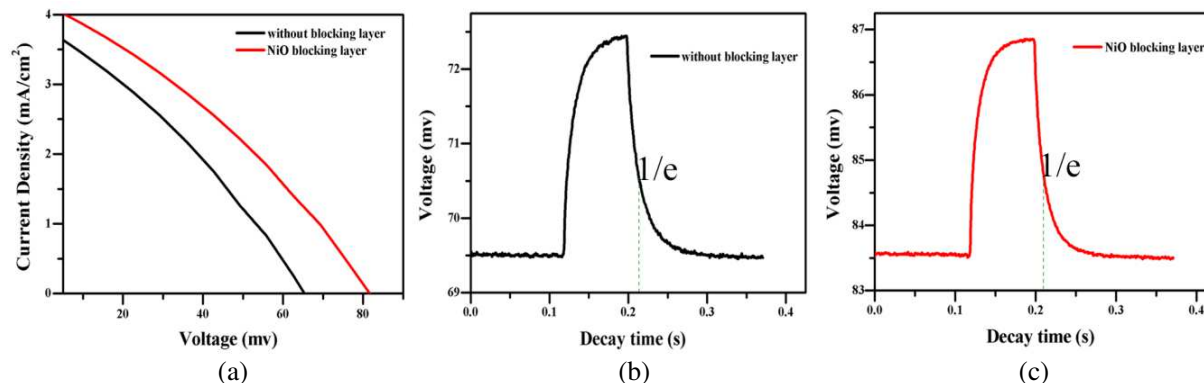


Figure 3: (a) J-V curve of NiO DSSC with and without blocking layer; (b) and (c) open-circuit voltage decay curves of DSSC fabricated with and without blocking layer.

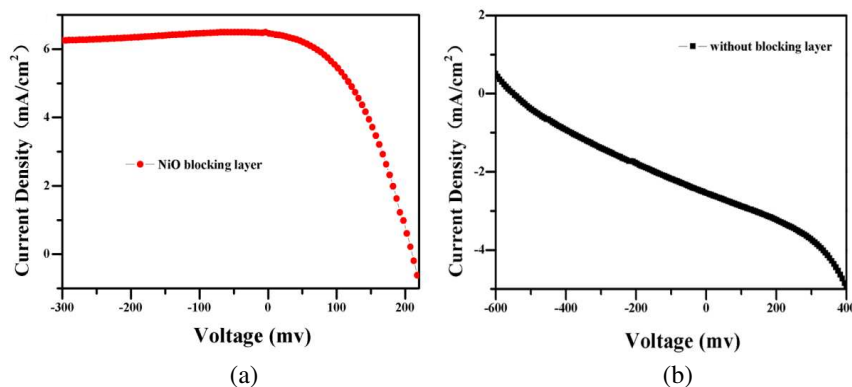


Figure 4: J-V curves of the perovskite sensitized NiO solar cells with (a) and (b) without a SP coated NiO blocking layer.

electrons transfer through the perovskites not the holes transfer from the mesoporous NiO network. If a SP coated NiO blocking layer is added, the current flow will be p-type like, namely, the front FTO glass will collect the photoinjected holes. This comparison strongly highlights the important role of the SP coated blocking layer in determining the current flow direction in perovskite sensitized NiO solar cell. The morphology of the NiO compact layer is very important for the blocking effect.

4. CONCLUSIONS

Compact nickel oxide thin films on FTO glass have been successfully fabricated by spray pyrolysis and spin coating methods. SEM characterization shows that the morphologies are different between SP and SC coated compact films. Compact NiO blocking layers are essential for p-type dye or perovskite sensitized solar cells. Not only do they play the roles as electron barriers but also boost the cell performance.

ACKNOWLEDGMENT

The authors would like to express sincere thanks for the financial supports by the National Natural Science Foundation (21103058, 21173091, 20903030), 973 Program of China (2011CBA00703) and Basic Scientific Research Funds for Central Colleges (2012YQ027, 2013TS040). We also thank Analytical and Testing Center of Huazhong University Science & Technology for the sample measurements.

REFERENCES

1. O'regan, B. and M. Grätzel, *Nature*, Vol. 353, 737–740, 1991.
2. Yella, A., H. W. Lee, H. N. Tsao, C. Yi, A. K. Chandiran, M. K. Nazeeruddin, E. W. G. Diau, C. Y. Yeh, S. M. Zakeeruddin, and M. Grätzel, *Sicence*, Vol. 334, 629–634, 2011.
3. He, J., H. Lindstrom, A. Hagfeldt, and S.-E. Lindquist, *J. Phys. Chem. B*, Vol. 103, 8940–8943, 1999.
4. Xiong, D., Z. Xu, X. Zeng, W. Zhang, W. Chen, X. Xu, M. Wang, and Y.-B. Cheng, *J. Mater. Chem.*, Vol. 22, 24760–24768, 2012.
5. Xu, Z., D. Xiong, H. Wang, W. Zhang, X. Zeng, L. Ming, W. Chen, X. Xu, J. Cui, M. Wang, S. Powar, U. Bach, and Y.-B Cheng, *J. Mater. Chem. A*, Vol. 2, 2968–2976, 2014.
6. Chan, X. H., J. R. Jennings, M. A. Hossain, K. K. Z. Yu, and Q. Wang, *J. Electrochem. Soc.*, Vol. 158, H733–H740, 2011.
7. Kunz, A. B., *J. Phys. C*, Vol. 14, L455–L460, 1981.
8. Boutwell, R. C., M. Wei, A. Scheurer, J. W. Mares, and W. V. Schoenfeld, *Thin Solid Films*, Vol. 520, 4302–4304, 2012.

Efficient Wide-band Analysis of GPR Antenna Around a Platform Using the Best Uniform Rational Approximation Technique

Ji Ma, Guangyou Fang, and Yicai Ji

Key Laboratory of Electromagnetic Radiation and Sensing Technology
Chinese Academy of Sciences, Beijing 100190, China

(Invited Paper)

Abstract— Evaluating wide-band performance of ground-penetrating radar (GPR) antennas is a challenging task due to the complex electromagnetic coupling effects between the GPR antennas and the platform. Typically, the efficiency of conventional methods utilized to deal with the problem is quite low. However, there are various frequency sweeping techniques which can achieve fast analysis of antennas over a broadband. Accordingly, this paper describes an efficient hybrid scheme, based upon the electric field integral equation (EFIE), for modeling a GPR antenna which is mounted on an electrically large platform.

In this paper, an antenna with two half-elliptical-shape arms, which is an improvement of bowtie antennas, is presented with resistances loaded in the terminal. A shallow rectangular conducting backed cavity is attached to the antenna. On the other hand, the best uniform rational approximation technique is applied to analyze the wide-band property of the antenna since it can avoid repeatedly solving the integral equation at each single frequency point. The main scheme of the frequency sweeping method is as follows: 1) determining the Chebyshev nodes within a given frequency range; 2) computing the equivalent surface currents of antennas at the frequency points corresponding to those Chebyshev nodes; 3) calculating the wide-band response of surface currents according to the Chebyshev series. Finally, the Maehly approximation is utilized to improve the accuracy by matching the Chebyshev series to a rational function.

In the hybrid scheme, the adaptive integral method (AIM) is applied to accelerate matrix-vector products as the IE algorithm and the impedance matrix is stored in a sparse form to facilitate analysis of large antenna-platform system. It is easy to combine the best uniform rational approximation technique with AIM but also other IE methods which are suited for modeling radiation of antennas. This hybrid method greatly extends the range of conventional numerical modeling for GPR antenna system. Furthermore, the efficiency and capability of the presented algorithm can be validated by the designed GPR antenna.

1. INTRODUCTION

As an effective instrument, ground penetrating radar (GPR) has been widely used in the geophysical research field based on a nondestructive testing (NDT) technique. It is well known that the antenna system is one of the most critical parts in the GPR equipment. To design a GPR antenna, there are several aspects which should be taken into account, such as structure, bandwidth, polarization, gain. In this paper, a half-ellipse antenna (HEA) is employed as a result of its simple structure and linear-phase characteristic in the operating frequency band. Furthermore, the radiation properties can be improved by attaching a conducting rectangular reflector above the HEA and adding loaded resistors between the antenna and the reflector.

In general, the GPR antenna is usually mounted on a platform for the convenience of motion. One of the most popular methods for antenna analysis is the frequency domain integral equation solved using method of moments (MoM) [1]. However, if MoM is utilized to analyze the antenna-platform system, the number N of unknowns resulting from MoM will be so large that excessive computer memory and long solution time are required. To facilitate the analysis of large problems, some fast numerical techniques have been proposed to reduce the memory storage and the computation complexity, such as fast multipole method (FMM) [2], multilevel fast multipole algorithm (MLFMA) [3], precorrected fast Fourier transform (p-FFT) [4], sparse-matrix/canonical-grid (SM/CG) [5] and adaptive integral method (AIM) [6]. All of these approaches reach the computational complexity and the memory requirements to $O(N^{1.5}\log(N))$ and $O(N^{1.5})$, which is less than $O(N^2)$ for the conventional MoM.

Since the GPR antenna works over a broadband, the frequency response of the antenna is concerned mostly. With the fast algorithm, it is still time-consuming due to the repeated solution of matrix equation at each frequency point. Over the past few years, there were some efforts to achieve

fast frequency sweep, such as impedance matrix interpolation [7], asymptotic waveform evaluation (AWE) [8], model-based parameter estimation (MBPE) [9] and the best uniform approximation technique [10]. Among these methods, the best uniform rational approximation technique is excellent for simplicity and accuracy. To begin with, it implements the Chebyshev approximation at certain selected frequencies within the considered wideband, that is, the Chebyshev nodes. Then, the Maehly rational approximation is adopted to improve the numerical results. Compared with other approximate solutions, the best uniform rational approximation can be incorporated into the existing computer codes.

In this paper, AIM is combined with the best uniform rational approximation technique to analyze the antenna-platform system over a wide frequency band. To achieve the analysis fast, AIM is employed to store all the full matrices in a sparse form and accelerate matrix-vector products. Furthermore, the best uniform rational approximation is applied to implement fast frequency sweeping by avoiding repeatedly solving integral equation at each frequency point. Finally, numerical results show that the HEA has a good radiation property and the proposed hybrid method is valid and efficient.

2. METHOD DESCRIPTION

2.1. Adaptive Integral Method (AIM)

To analyze the antenna above the platform with integral equation approach, AIM is employed to reduce the matrix storage and to accelerate the matrix-vector multiplications.

The procedures of AIM can be summarized as follows:

- 1) enclose the antenna and platform in a cube and partition the cube uniformly into Cartesian cells;
- 2) establish auxiliary basis functions and calculate the translation coefficient;

The RWG basis function [11] $\mathbf{f}_n(\mathbf{r})$ and its convergence $\nabla \cdot \mathbf{f}_n(\mathbf{r})$ can be approximated as linear combinations of Dirac delta functions:

$$\begin{aligned} \psi_{\alpha,n}(\mathbf{r}) &\cong \sum_{u=1}^{(p+1)^3} \Lambda_{\alpha,nu} \delta(\mathbf{r} - \mathbf{r}_{nu}) \quad \alpha = x, y, z, d \\ \psi_{\alpha,n}(\mathbf{r}) &\in \{\mathbf{f}_{x,n}(\mathbf{r}), \mathbf{f}_{y,n}(\mathbf{r}), \mathbf{f}_{z,n}(\mathbf{r}), \nabla \cdot \mathbf{f}_n(\mathbf{r})\} \end{aligned} \quad (1)$$

where $\Lambda_{\alpha nu}$ are the translation coefficients for the x , y , z components and the divergence of basis function, $\mathbf{r}_{nu} = (x_{nu}, y_{nu}, z_{nu})$ is the coordinate of the grid, and p is the order of the translation. Therefore, the translation coefficient can be obtained via matching the multipole moments to basis functions.

- 3) By using the near-zone threshold d_{near} , the impedance matrix can be divided into near-zone group and far-zone group, which can be expressed as follows,

$$\mathbf{Z} = \mathbf{Z}_{near} + \mathbf{Z}_{far} \quad (2)$$

The element of near-zone interaction matrix \mathbf{Z}_{near} can be calculated by the conventional MoM, and the element of far-zone interaction matrix \mathbf{Z}_{far} can be calculated as follows:

$$\mathbf{Z}_{far} = \mathbf{\Lambda} \mathbf{G} \mathbf{\Lambda}^T - \tilde{\mathbf{Z}} \quad (3)$$

where $\mathbf{\Lambda}$ denote the translation coefficients; \mathbf{G} is the Green's function matrix; and $\tilde{\mathbf{Z}}$ the inaccurate contributions from the near-zone grid sources which should be removed.

- 4) Since \mathbf{G} is a Toeplitz matrix, this fact can make use of FFT to accelerate the matrix-vector multiplication as follows,

$$\begin{aligned} \mathbf{Z} \mathbf{I} &= (\mathbf{Z}_{near} + \mathbf{Z}_{far}) \mathbf{I} \\ &= (\mathbf{Z}_{near} - \tilde{\mathbf{Z}}) \mathbf{I} + \mathbf{\Lambda} \text{IFFT} \{ \text{FFT}(\mathbf{G}) \text{FFT}(\mathbf{\Lambda}^T \mathbf{I}) \} \end{aligned} \quad (4)$$

Due to that \mathbf{Z}_{near} , $\mathbf{\Lambda}$ and \mathbf{G} are all sparse matrices, the memory requirements can be reduced drastically.

2.2. The Best Uniform Rational Approximation Technique

When the frequency response of the antenna is of interest, the matrix equation can be written as follows,

$$\mathbf{Z}(k) \mathbf{I}(k) = \mathbf{V}(k) \quad (5)$$

where $\mathbf{Z}(k)$, $\mathbf{I}(k)$ and $\mathbf{V}(k)$ are the impedance matrix, unknown coefficients, and excitation vector, respectively. And all of them are frequency dependent. It can be seen that Equation (5) must be solved repeatedly for different frequency points within the interest band, which must be very time-consuming.

To alleviate this problem, the best uniform rational approximation technique is introduced as follows:

1) For a given frequency band $f \in [f_a, f_b]$ and the wave-number $k \in [k_a, k_b]$, the coordinate transform is expressed as:

$$\tilde{k} = \frac{2k - (k_a + k_b)}{k_b - k_a} \quad \tilde{k} \in [-1, 1] \quad (6)$$

2) The Chebyshev nodes within the band $[k_a, k_b]$ can be obtained as follows,

$$k_i = \frac{\tilde{k}_i (k_b - k_a) + (k_a + k_b)}{2} \quad (7)$$

$$\text{where } \tilde{k}_i = \cos\left(\frac{i - 0.5}{n} \pi\right), \quad i = 1, 2, \dots, n \quad (8)$$

3) Based on the Chebyshev approximation theory, the unknowns coefficients vector $\mathbf{I}(k)$ can be expressed as,

$$\mathbf{I}(k) = \mathbf{I}\left(\frac{\tilde{k}(k_b - k_a) + (k_a + k_b)}{2}\right) \approx \sum_{l=1}^n c_l T_l(\tilde{k}) - \frac{c_1}{2} \quad (9)$$

where c_l is the coefficient and given by

$$c_l = \frac{2}{n} \sum_{i=1}^n \mathbf{I}(k_i) T_l(\tilde{k}_i) \quad (10)$$

Furthermore, $T_l(x) (l = 1, 2, \dots, n)$ is l th order of the Chebyshev polynomial, and the recursion formula about $T_l(x)$ is concluded below,

$$\begin{cases} T_0(x) = 1 \\ T_1(x) = x \\ \dots \\ T_{l+1}(x) = 2xT_l(x) - T_{l-1}(x) \end{cases} \quad (11)$$

4) The Maehly approximation is applied to improve the accuracy of the numerical solution by matching the Chebyshev series to a rational function as follows,

$$\mathbf{I}(k) \approx R_{LM}(\tilde{k}) = \frac{P_L(\tilde{k})}{Q_M(\tilde{k})} = \frac{a_0 T_0(\tilde{k}) + a_1 T_1(\tilde{k}) + \dots + a_L T_L(\tilde{k})}{b_0 T_0(\tilde{k}) + b_1 T_1(\tilde{k}) + \dots + b_M T_M(\tilde{k})} \quad (12)$$

In generally, b_0 is set to be 1. Substitute (12) into (9) and use the identity

$$T_p(x)T_q(x) = \frac{1}{2}(T_{p+q} + T_{|p-q|}(x)) \quad (13)$$

the unknown coefficients a_i ($i=0,1,\dots,L$) and b_j ($j=1,2,\dots,M$) can be obtained as:

$$\begin{cases} a_0 = \frac{1}{2}b_0c_0 + \frac{1}{2}\sum_{j=1}^M b_jc_j \\ a_i = c_i + \frac{1}{4}b_0c_0 + \frac{1}{2}\sum_{j=1}^M b_j(c_{j+i} + c_{|j-i|}) \\ i = 1, 2, \dots, L \end{cases} \quad (14a)$$

$$\begin{bmatrix} c_{L+2} + c_L & c_{L+3} + c_{L-1} & \cdots & c_{L+M+1} + c_{L-M+1} \\ c_{L+3} + c_{L+1} & c_{L+4} + c_L & \cdots & c_{L+M+2} + c_{L-M+2} \\ \vdots & \vdots & \vdots & \vdots \\ c_{L+M+1} + c_{L+M-1} & c_{L+M+2} + c_{L+M-2} & \cdots & c_{L+2M} + c_L \end{bmatrix} \begin{bmatrix} b_1 \\ b_2 \\ \vdots \\ b_M \end{bmatrix} = -2 \begin{bmatrix} c_{L+1} \\ c_{L+2} \\ \vdots \\ c_{L+M} \end{bmatrix} \quad (14b)$$

Once the coefficients of the rational function are calculated, the induced current distribution can be obtained at any frequency within the whole frequency band.

3. HALF-ELLIPSE ANTENNA AND NUMERICAL ANALYSIS

3.1. Half-Ellipse Antenna

The geometry of the half-ellipse antenna is shown in Fig. 1. The half-ellipse antenna was mounted at the open side of the cavity. The length and the width of the cavity are 300 mm and 180 mm, respectively. Furthermore, two 100- Ω resistors were used to connect each end of the antenna to the cavity. The dimensions of the antenna are as follows: $2L = 270$ mm, $W = 120$ mm, and $h = 20$ mm, where $2L$ is the length of the antenna, W is the antenna width, and h is the height of the cavity. As seen in Fig. 2, the GPR antenna was located above the top of the conducting platform, whose size is 800 mm \times 600 mm \times 260 mm.

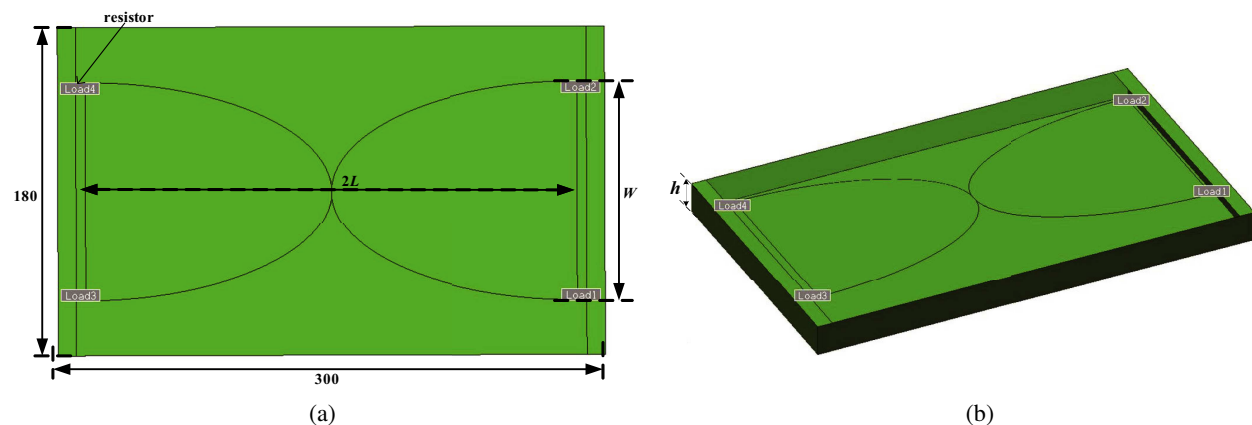


Figure 1: Geometry of the half-ellipse antenna. (a) 2-D view. (b) 3-D view.

3.2. Numerical Analysis

In this section, numerical results will be presented to show the accuracy and efficiency of AIM in conjunction with the best uniform rational approximation ($L = M = 4$) for solving the wideband problem of the half-ellipse antenna on the platform. All the computation is performed on a PC with Intel Core i5-2400 CPU 3.10 GHz and 2.0G RAM. Furthermore, all the variables used in the program code are double precision.

In the simulation, the frequency response of the half-ellipse antenna over 0.1 to 1 GHz is analyzed and the interval is 9 MHz. The whole structure is modeled by triangular meshes. And there are 1546 basis functions on the surface of antenna while 8342 basis functions are on the surface of platform. Firstly, the conventional MoM is employed to calculate the normalized radiation pattern of the half-ellipse antenna, as shown in Fig. 3. It can be seen that the antenna has a smooth main lobe and good directivity. Furthermore, the higher the frequency, the smaller the backward radiation. Fig. 4 shows the input impedance of the antenna mounted on the platform over the frequency band. The

results computed by the direct AIM agree very well with that obtained by AIM combined with the Maehly approximation technique, which shows the proposed algorithm is valid. On the other hand, it is indicated that the real part of HEA's impedance is around $100\text{-}\Omega$ from 100 MHz to 750 MHz. Table 1 shows some computational characteristics of the two methods. The presented algorithm can reduce the solution time drastically without significant memory increase. Therefore, it is an efficient approach to solve the wideband problem of antennas on a large conducting platform.

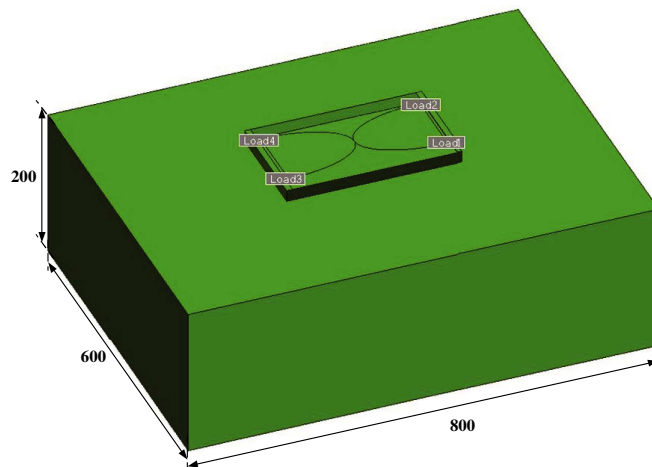


Figure 2: HEA on the top of the platform.

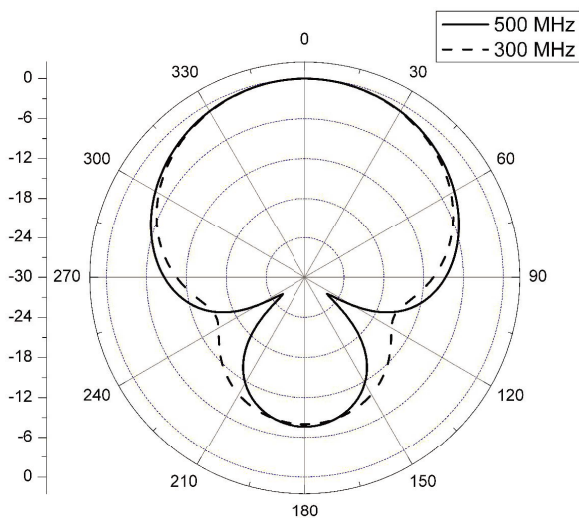


Figure 3: Normalized radiation pattern of the HEA.

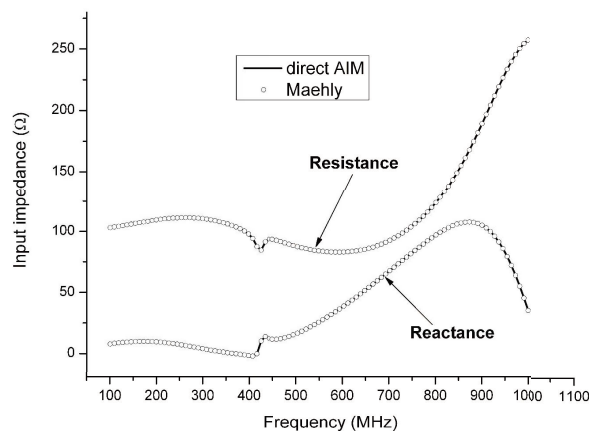


Figure 4: Frequency response of input impedance.

Table 1: Computational characteristics of the two methods for Fig. 4.

Method	Memory (MB)	Total CPU time (h)
Direct AIM	142	35.2
Maehly	147	4.5

4. CONCLUSION

AIM in conjunction with the best uniform rational approximation technique has been presented to achieve fast frequency sweep analysis of a half-ellipse antenna mounted on a conducting platform. Numerical results show that the HEA has a smooth main lobe, good directivity, and small backward

radiation. The real part of HEA's impedance is around $100\text{-}\Omega$ from 100 MHz to 750 MHz. On the other hand, the proposed algorithm in this paper can offer saving in terms of CPU time without significant memory increase than the conventional one.

ACKNOWLEDGMENT

This project was supported by China Postdoctoral Science Foundation. (Grant No. 2014M550839).

REFERENCES

1. Harrington, R. F., *Field Computation by Moment Methods*, MacMillan, New York, 1968.
2. Coifman, R., V. Rokhlin, and S. Wandzura, "The fast multipole method for the wave equation: A pedestrian prescription," *IEEE Antennas Propag. Mag.*, Vol. 35, No. 3, 7–12, Jun. 1993.
3. Song, J. M., C. C. Lu, and W. C. Chew, "Multilevel fast multipole algorithm for electromagnetic scattering by large complex objects," *IEEE Trans. Antennas Propag.*, Vol. 45, No. 10, 1488–1493, Oct. 1997.
4. Phillips, J. R. and J. K. White, "A precorrected-FFT method for electrostatic analysis of complicated 3-D structures," *IEEE Trans. Computer-Aided Design Integr. Circuits Syst.*, Vol. 16, No. 10, 1059–1072, Oct. 1997.
5. Li, S. Q., Y. Yu, C. H. Chan, K. F. Chan, and L. Tsang, "A sparse-matrix/canonical grid method for analyzing densely packed interconnects," *IEEE Trans. Microwave Theory Tech.*, Vol. 49, No. 7, 1221–1228, Jul. 2001.
6. Bleszynski, E., M. Bleszynski, and T. Jaroszewicz, "AIM: Adaptive integral method for solving large-scale electromagnetic scattering and radiation problems," *Radio Sci.*, Vol. 31, No. 5, 1225–1251, 1996.
7. Fan, Z. H., Z. W. Liu, D. Z. Ding, and R. S. Chen, "Preconditioning matrix interpolation technique for fast analysis of scattering over broad frequency band," *IEEE Trans. Antennas Propag.*, Vol. 58, No. 7, 2484–2487, Jul. 2010.
8. Ma, J., S. X. Gong, X. Wang, Y. Liu, and Y. X. Xu, "Efficient wide-band analysis of antennas around a conducting platform using MoM-PO hybrid method and asymptotic waveform evaluation technique," *IEEE Trans. Antennas Propag.*, Vol. 60, No. 12, 6048–6052, Dec. 2012.
9. Wang, X. D. and D. H. Werner, "Improved model-based parameter estimation approach for accelerated periodic method of moments solutions with application to analysis of convoluted frequency selected surfaces and metamaterials," *IEEE Trans. Antennas Propag.*, Vol. 58, No. 1, 122–131, Jan. 2010.
10. Chen, M. S., X. L. Wu, W. Sha, and Z. X. Huang, "Fast and accurate radar cross section computation over a broad frequency band using the best uniform rational approximation," *IET Microw. Antennas Propag.*, Vol. 2, No. 2, 200–204, Mar. 2008.
11. Rao, S. M., D. R. Wilton, and A. W. Glisson, "Electromagnetic scattering by surfaces of arbitrary shape," *IEEE Trans. Antennas Propag.*, Vol. 30, No. 3, 409–418, Mar. 1982.

Electromagnetic Characterization of Tunable Bandpass Filters with a PET-controlled Perturber

G. C. Wan, J. X. Hong, Z. G. Zhou, X. W. Zhang, and M. S. Tong

Department of Electronic Science and Technology

Tongji University, Shanghai, China

(Invited Paper)

Abstract— Electromagnetic (EM) analysis is performed for a tunable bandpass filter with a magnetodielectric perturber controlled by an elastic piezoelectric transducer. The structure includes a perturber as a superstrate which consists of thin ferrite film with a high permeability and Rogers dielectric material with a high permittivity in a sandwich style. The structure is of multiscale feature because the thickness of the thin film is very small but cannot be ignored. The problem can be solved by surface integral equations (SIEs) in the integral equation approach, but the conditioning of system matrix may not be good. We use volume-surface integral equations to formulate the problem in this work and the disadvantage of pure SIEs can be overcome. A numerical example is presented to illustrate the approach.

1. INTRODUCTION

Tunable bandpass filters (BPFs) are vital microwave components and they have been widely used in communication systems. The design of tunable BPFs is challenging because they require a low loss and compact size. Recently, the tunable BPF with a magnetodielectric perturber controlled by an elastic piezoelectric transducer (PET) was developed and it looks very promising [1]. Such a tunable BPF uses a perturber as a superstrate touching on the microstrip and its position can be controlled by a PET. The perturber is made of a high-permeability ferrite film and a high-permittivity dielectric Rogers material in a sandwich style. The resonant frequency of the BPF can be tuned by applying different bias DC voltages to the PET or by using different layers of magnetodielectric sandwich. The tunable BPF can be easily fabricated with a compact size and low loss and its resonant frequency could be adjusted in a wide range.

Characterizing the tunability of the BPF relies on the electromagnetic modeling and analysis although a costly experimental method can be used. The structure is of multiscale characteristic because some dimensions are very small compared with others in geometry. Although the thickness of microstrip and ground may be ignored to simplify the analysis, the small thickness of high-permeability ferrite film cannot be ignored due to its significant influence and should be accounted for carefully [2]. The structure can be modelled by surface integral equations (SIEs) when all materials are assumed to be homogeneous [3], but the SIEs may not generate well-conditioned system matrices, especially for multiscale structures. Also, the SIEs need to use appropriate basis functions to represent the electric and magnetic current densities, respectively, in the method of moments (MoM) solution [4] and the choice of the basis functions or testing schemes could strongly affect the accuracy of solutions [5]. In this work, we use volume integral equations (VIEs) to describe the dielectric substrate and magnetodielectric perturber, and form volume-surface integral equations (VSIEs) after combining with the SIE governing the conducting microstrip and ground. The VIEs or VSIEs are usually more well-conditioned because they include the second-kind of integral equations [8]. We present a numerical example to demonstrate the analysis of the BPF and its effectiveness has been verified.

2. GOVERNING INTEGRAL EQUATIONS

The BPF structure includes both conducting microstrip and ground, dielectric substrate and Rogers material, and magnetic ferrite film. We assume that the microstrip and ground are perfectly electric conductors (PECs) with a negligible thickness and their EM feature can be described by the electric field integral equation (EFIE) when disregarding the coupling with other parts [3]

$$-\hat{n} \times \mathbf{E}^{ex}(\mathbf{r}) = \hat{n} \times i\omega\mu_0 \int_S \overline{\mathbf{G}}(\mathbf{r}, \mathbf{r}') \cdot \mathbf{J}_S(\mathbf{r}') dS', \quad \mathbf{r} \in S \quad (1)$$

where $\mathbf{J}_S(\mathbf{r}')$ is the electric current density induced on the conductor surface S whose unit normal vector is \hat{n} and $\mathbf{E}^{ex}(\mathbf{r})$ represents a delta-gap excitation at an appropriate position in a port. Also, $\overline{\mathbf{G}}(\mathbf{r}, \mathbf{r}')$ is the dyadic Green's function defined by

$$\overline{\mathbf{G}}(\mathbf{r}, \mathbf{r}') = \left(\overline{\mathbf{I}} + \frac{\nabla \nabla}{k_0^2} \right) g(\mathbf{r}, \mathbf{r}') \quad (2)$$

where $\overline{\mathbf{I}}$ is the identity dyad, k_0 is the wavenumber of the free space with a permittivity ϵ_0 and a permeability μ_0 , and $g(\mathbf{r}, \mathbf{r}') = e^{ik_0 R}/(4\pi R)$ is the scalar Green's function with $R = |\mathbf{r} - \mathbf{r}'|$ being the distance between an observation point \mathbf{r} and a source point \mathbf{r}' . For homogeneous penetrable materials with a relative permittivity ϵ_r and a relative permeability μ_r , we can use the VIEs to catch up with the EM characteristic when disregarding the coupling with the conductors [3]

$$\mathbf{E}(\mathbf{r}) = \mathbf{E}^{ex}(\mathbf{r}) + i\omega\mu_0 \int_V \overline{\mathbf{G}}(\mathbf{r}, \mathbf{r}') \cdot \mathbf{J}_V(\mathbf{r}') d\mathbf{r}' - \nabla \times \int_V \overline{\mathbf{G}}(\mathbf{r}, \mathbf{r}') \cdot \mathbf{M}_V(\mathbf{r}') d\mathbf{r}', \quad \mathbf{r} \in V \quad (3)$$

$$\mathbf{H}(\mathbf{r}) = \mathbf{H}^{ex}(\mathbf{r}) + i\omega\epsilon_0 \int_V \overline{\mathbf{G}}(\mathbf{r}, \mathbf{r}') \cdot \mathbf{M}_V(\mathbf{r}') d\mathbf{r}' + \nabla \times \int_V \overline{\mathbf{G}}(\mathbf{r}, \mathbf{r}') \cdot \mathbf{J}_V(\mathbf{r}') d\mathbf{r}', \quad \mathbf{r} \in V \quad (4)$$

where $\mathbf{E}^{ex}(\mathbf{r}) = \mathbf{H}^{ex}(\mathbf{r}) = 0$ inside the materials and

$$\mathbf{J}_V(\mathbf{r}') = i\omega\epsilon_0(1 - \epsilon_r)\mathbf{E}(\mathbf{r}') \quad (5)$$

$$\mathbf{M}_V(\mathbf{r}') = i\omega\mu_0(1 - \mu_r)\mathbf{H}(\mathbf{r}') \quad (6)$$

are the volumetric electric and magnetic current densities inside the materials, respectively. When considering the coupling of fields produced by the current density on the conductors and the volume current densities inside the materials, we can form the following VSIEs

$$0 = \hat{n} \times \left[\mathbf{E}^{ex}(\mathbf{r}) + i\omega\mu_0 \int_S \overline{\mathbf{G}}(\mathbf{r}, \mathbf{r}') \cdot \mathbf{J}_S(\mathbf{r}') dS' + i\omega\mu_0 \int_V \overline{\mathbf{G}}(\mathbf{r}, \mathbf{r}') \cdot \mathbf{J}_V(\mathbf{r}') d\mathbf{r}' - \nabla \times \int_V \overline{\mathbf{G}}(\mathbf{r}, \mathbf{r}') \cdot \mathbf{M}_V(\mathbf{r}') d\mathbf{r}' \right], \quad \mathbf{r} \in S \quad (7)$$

$$\mathbf{E}(\mathbf{r}) = i\omega\mu_0 \int_S \overline{\mathbf{G}}(\mathbf{r}, \mathbf{r}') \cdot \mathbf{J}_S(\mathbf{r}') dS' + i\omega\mu_0 \int_V \overline{\mathbf{G}}(\mathbf{r}, \mathbf{r}') \cdot \mathbf{J}_V(\mathbf{r}') d\mathbf{r}' - \nabla \times \int_V \overline{\mathbf{G}}(\mathbf{r}, \mathbf{r}') \cdot \mathbf{M}_V(\mathbf{r}') d\mathbf{r}', \quad \mathbf{r} \in V \quad (8)$$

$$\mathbf{H}(\mathbf{r}) = -\frac{1}{2}\hat{n} \times \mathbf{J}_S(\mathbf{r}') + \int_S \nabla g(\mathbf{r}, \mathbf{r}') \times \mathbf{J}_S(\mathbf{r}') + i\omega\epsilon_0 \int_V \overline{\mathbf{G}}(\mathbf{r}, \mathbf{r}') \cdot \mathbf{M}_V(\mathbf{r}') d\mathbf{r}' dS' + \nabla \times \int_V \overline{\mathbf{G}}(\mathbf{r}, \mathbf{r}') \cdot \mathbf{J}_V(\mathbf{r}') d\mathbf{r}', \quad \mathbf{r} \in V \quad (9)$$

from which the unknown current densities can be solved and the frequency characteristic of the structure can then be found.

3. METHOD OF MOMENTS (MOM) SOLUTION

The above VSIEs can be solved by the MoM in which the surface current density on the conductors is expanded by the Rao-Wilton-Glisson (RWG) basis function [6] while the electric flux density and magnetic flux density inside the materials are represented with the Schaubert-Wilton-Glisson (SWG) basis function [7], i.e.,

$$\mathbf{J}_S(\mathbf{r}') = \sum_{n=1}^{N_c} J_n \mathbf{e}_n(\mathbf{r}') \quad (10)$$

$$\mathbf{D}(\mathbf{r}') = \sum_{n=1}^{N_a} D_n \mathbf{f}_n(\mathbf{r}') \quad (11)$$

$$\mathbf{B}(\mathbf{r}') = \sum_{n=1}^{N_a} B_n \mathbf{f}_n(\mathbf{r}') \quad (12)$$

where $\mathbf{e}_n(\mathbf{r}')$ is the RWG basis function and N_c is the number of RWG triangle pairs while $\mathbf{f}_n(\mathbf{r}')$ is the SWG basis function and N_d is the number of SWG tetrahedron pairs. Also, J_n , D_n , and B_n are the expansion coefficients for the current densities, respectively. The flux densities are related to the current densities inside the materials through $\mathbf{D}(\mathbf{r}') = \epsilon_0\epsilon_r\mathbf{E}(\mathbf{r}')$ and $\mathbf{B}(\mathbf{r}') = \mu_0\mu_r\mathbf{H}(\mathbf{r}')$, respectively, i.e.,

$$\mathbf{J}_V(\mathbf{r}') = i\omega\kappa_\epsilon\mathbf{D}(\mathbf{r}') \quad (13)$$

$$\mathbf{M}_V(\mathbf{r}') = i\omega\kappa_\mu\mathbf{B}(\mathbf{r}') \quad (14)$$

where $\kappa_\epsilon = \frac{1}{\epsilon_r} - 1$ and $\kappa_\mu = \frac{1}{\mu_r} - 1$ are the contrast ratio of permittivity and permeability, respectively. The above VSIEs can be transformed into a matrix equation by using the RWG and SWG basis functions as testing functions to test corresponding equations, respectively. By doing so, we can obtain the following matrix equation

$$-\left\langle \mathbf{e}_m(\mathbf{r}), \frac{\mathbf{E}^{ex}(\mathbf{r})}{i\omega\mu_0} \right\rangle = \sum_{n=1}^{N_c} J_n \langle \mathbf{e}_m(\mathbf{r}), \overline{\mathbf{G}}(\mathbf{r}, \mathbf{r}'), \mathbf{e}_n(\mathbf{r}') \rangle + \sum_{n=1}^{N_d} D_n \langle \mathbf{e}_m(\mathbf{r}), \overline{\mathbf{G}}_0(\mathbf{r}, \mathbf{r}'), \mathbf{f}_n(\mathbf{r}') \rangle, \quad m = 1, 2, \dots, N_c \quad (15)$$

$$D_m \left\langle \mathbf{f}_m(\mathbf{r}), \frac{\mathbf{f}_m(\mathbf{r})}{i\omega\mu_0\epsilon(\mathbf{r})} \right\rangle = \sum_{n=1}^{N_c} J_n \langle \mathbf{f}_m(\mathbf{r}), \overline{\mathbf{G}}(\mathbf{r}, \mathbf{r}'), \mathbf{e}_n(\mathbf{r}') \rangle + \sum_{n=1}^{N_d} D_n \langle \mathbf{f}_m(\mathbf{r}), \overline{\mathbf{G}}_0(\mathbf{r}, \mathbf{r}'), \mathbf{f}_n(\mathbf{r}') \rangle, \quad m = 1, 2, \dots, N_d \quad (16)$$

$$D_m \left\langle \mathbf{f}_m(\mathbf{r}), \frac{\mathbf{f}_m(\mathbf{r})}{i\omega\mu_0\epsilon(\mathbf{r})} \right\rangle = \sum_{n=1}^{N_c} J_n \langle \mathbf{f}_m(\mathbf{r}), \overline{\mathbf{G}}(\mathbf{r}, \mathbf{r}'), \mathbf{e}_n(\mathbf{r}') \rangle + \sum_{n=1}^{N_d} D_n \langle \mathbf{f}_m(\mathbf{r}), \overline{\mathbf{G}}_0(\mathbf{r}, \mathbf{r}'), \mathbf{f}_n(\mathbf{r}') \rangle, \quad m = 1, 2, \dots, N_d \quad (17)$$

where $\overline{\mathbf{G}}_0(\mathbf{r}, \mathbf{r}') = -i\omega\kappa(\mathbf{r}')\overline{\mathbf{G}}(\mathbf{r}, \mathbf{r}')$. The above matrix equation can be solved with a matrix solver so that the unknown current density and flux density can be found.

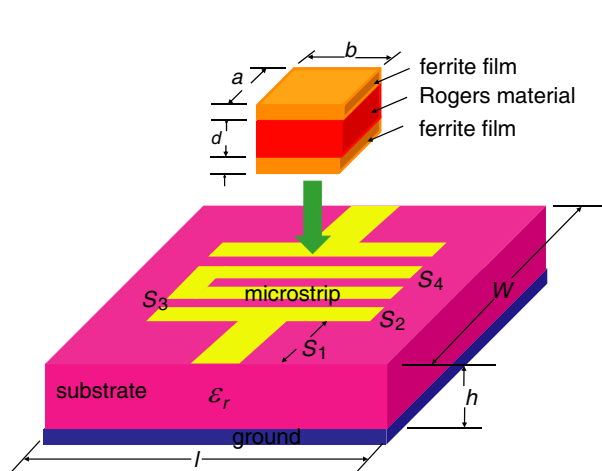


Figure 1: Geometry of a tunable BPF with a magnetodielectric perturber consisting of ferrite film and Rogers material in a sandwich style.

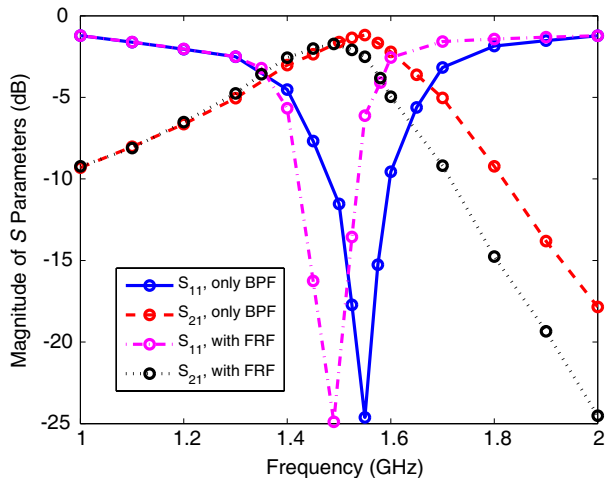


Figure 2: S parameters of a tunable BPF with a magnetodielectric perturber consisting of ferrite film and Rogers material in a sandwich style.

4. NUMERICAL EXAMPLE

We present a numerical example to demonstrate the approach. A tunable BPF as shown in Figure 1 is considered and the geometry is defined by $l = 22.0$, $w = 20.26$, $h = 1.28$, $s_1 = 9.0$, $s_2 = 0.23$, $s_3 = 0.07$, $s_4 = 1.2$, $d = 0.254$, $t = 0.01$, $a = 20$, and $b = 10$, all in millimeter (mm). The substrate and Rogers material of the perturber have a relative permittivity $\epsilon_r = 10.2$ and a relative permeability $\mu_r = 1.0$ while the relative permittivity and permeability of the ferrite film are $\epsilon_r = 13.0$ and $\mu_r = 10.0$, respectively. Figure 2 shows the solutions of S parameters (magnitude) for the structure with or without the perturber and the results are close to the experimental results as shown in [1].

5. CONCLUSION

In this work, we address the EM analysis for a tunable BPF structure which includes a PET-controlled perturber with a high-permittivity Rogers material and high-permeability thin ferrite film in a sandwich style. Although the problem can be solved by pure SIEs with an assumption of homogeneous penetrable materials, we use the VSIE to solve it instead. Compared the SIEs, the VSIEs can usually result in a well-conditioned system matrix with the regular basis functions and testing scheme. A typical numerical example has been presented to demonstrate the effectiveness of the approach.

ACKNOWLEDGMENT

This work was supported by the Program of Pujiang Talents, Shanghai, China, with the Project No. 12PJ1408600.

REFERENCES

1. Yang, G.-M., O. Obi, G. Wen, and N. X. Sun, "Design of tunable bandpass filters with ferrite sandwich materials by using a piezoelectric transducer," *IEEE Trans. Magn.*, Vol. 47, No. 10, 3732–3735, Oct. 2011.
2. Yang, G.-M., X. Xing, A. Daigle, M. Liu, O. Obi, J. W. Wang, K. Naishadham, and N. X. Sun, "Electronically tunable miniaturized antennas on magnetoelectric substrates with enhanced performance," *IEEE Trans. Magn.*, Vol. 44, No. 11, 3091–3094, Nov. 2008.
3. Chew, W. C., M. S. Tong, and B. Hu, *Integral Equation Methods for Electromagnetic and Elastic Waves*, Morgan & Claypool, San Rafael, CA, 2008.
4. Harrington, R. F., *Field Computation by Moment Methods*, Macmillan, New York, 1968.
5. Tong, M. S., "Efficient electromagnetic analysis for interconnect and packaging structures using dual basis function in the method of moments," *IEEE Trans. Compon., Packag., Manuf. Technol.*, Vol. 1, No. 7, 1089–1097, Jul. 2011.
6. Rao, S. M., D. R. Wilton, and A. W. Glisson, "Electromagnetic scattering by surfaces of arbitrary shape," *IEEE Trans. Antennas Propagat.*, Vol. 30, 409–418, 1982.
7. Schaubert, D. H., D. R. Wilton, and A. W. Glisson, "A tetrahedral modeling method for electromagnetic scattering by arbitrary shaped inhomogeneous dielectric bodies," *IEEE Trans. Antennas Propagat.*, Vol. 32, No. 1, 77–85, 1984.
8. Usner, B. C., K. Sertel, M. A. Carr, and J. L. Volakis, "Generalized volume-surface integral equation for modeling inhomogeneities within high contrast composite structures," *IEEE Trans. Antennas Propagat.*, Vol. 54, No. 1, 68–75, Jan. 2006.

A Combined Method for Computing Installed Radiation Patterns of Antennas on Large Conducting Platforms

H. Zhao*, S. Gao, B.-F. Wang, and W.-J. Zhao

Institute of High Performance Computing, 1 Fusionopolis Way, 138632, Singapore

(Invited Paper)

Abstract— The installed radiation patterns of antennas on large platforms are of great interest when installing antennas. The computation of installed radiation patterns is challenging due to the large size of the platform. To reduce the effort of modeling the large platform, this work adopts the hybridization of the method of moments (MoM) and physical optics (PO) method. The multi-level fast multipole method is used to accelerate the solution of matrix equations, so that a large MoM region can be used to improve the accuracy of modeling the antenna and its surrounding structures. Another challenge of modeling antennas on large platforms comes from the complexity of the antennas. Furthermore, when an antenna is outsourced, detailed design information may be unavailable to those who install the antenna, which hinders direct modeling of antennas on large platforms. In this case, equivalent models of antennas are derived based on their uninstalled far field radiation patterns. Using the equivalent models, installed radiation patterns of antennas can be computed without knowing their detailed design information. By combining the hybrid method with the equivalent model, the installed radiation patterns are computed efficiently.

1. INTRODUCTION

Nowadays, there are many antennas installed on large platforms such as aircrafts, ships, missiles, etc.. A large platform may significantly affect the performance of antennas and it is highly desirable to know the antennas' performance on the large platform. Since these platforms are usually bulky, it is expensive to fabricate them. Meanwhile, it is difficult to find a large measurement site which is able to accommodate large platforms. Furthermore, it is tedious to move and rotate a large platform during measurement. Due to the aforementioned difficulties, scaled models are usually used in practical measurements. On the other hand, simulation provides a cost-effective and convenient option to evaluate the performance of antennas on large platforms. Therefore, simulation of antennas on large platform attracted much interests in the past decades.

In order to satisfy tight specifications, the design of an antenna may be complex. In the meanwhile, as the frequency of operation rises, the electrical size of the platform increases. The complexity of the antenna design and the large electrical size of the platform make it challenging to simulate antennas on large platforms. The challenges come from the following aspects. First of all, it is usually time consuming to model electrically large structures, unless certain approximation is introduced. Second, in practice, the antenna may have tiny features requiring fine meshes. This leads to a mixed-scale structure, whose numerical modeling usually results in an ill-conditioned matrix. Third, there are cases where the antenna design details are unavailable. This happens when the antenna is provided by external manufacture. Last but not least, because antennas in various frequency bands coexist on a platform, wide-band simulation is needed when interference between antennas is computed.

For fast modeling of electrically large platforms, it is desirable to use hybrid low frequency-high frequency methods, where the effect of large platform is taken into account by high frequency methods such as physical optics (PO) method [1, 2]. In order to deal with the challenge of modeling multi-scale structures, various domain decomposition methods were developed [3–8]. These methods divide small-scale and large-scale structures into sub-domains and model every sub-domain separately. Different schemes were proposed to account for the coupling between sub-domains, and more details about these coupling schemes are available in [3–8]. Although domain decomposition methods facilitate the modeling of multi-scale structures, they require the detailed design information of antennas. In [9], the fast multipole technique was used to model antennas without their design details. In the meanwhile, the equivalent sources can be used to represent complex

*Corresponding author: H. Zhao (huapengzhao@ieee.org).

radiators [10–13]. In [11], wide-band analysis was accelerated by an adaptive frequency sampling technique, which could also be used for wide-band simulation of antennas on large platforms.

Despite the aforementioned progresses, it is still challenging to analyze antennas on large platforms without antennas' design information. First, although equivalent sources are effective to represent antennas, it usually takes long time to derive these equivalent sources. Second, most existing hybrid low frequency-high frequency methods use a small low frequency region, which causes inaccuracy when the surrounding environment of the antenna is complex.

To achieve fast and accurate computation of antennas' installed radiation patterns, this work combines physics-inspired equivalent model of antennas with a recently proposed hybrid multilevel fast multipole method (MLFMM)-PO method. In the physics-inspired equivalent model, it is assumed that the type of the antenna is known and the radiation mechanism of the antenna is utilized to simplify its equivalent model, which reduces the effort of constructing equivalent model. Furthermore, different from existing hybrid methods, the new hybrid method relies on the efficiency of MLFMM and uses a large MLFMM region to accurately model the antenna and its surrounding environment. In the meanwhile, for efficiency consideration and based on locality principle, only a small region near the antenna is used to compute the incident magnetic field in PO region.

2. DESCRIPTION OF THE METHOD

In order to model the antenna without its design details, an equivalent model is constructed based on the antenna's radiation pattern. A popular equivalent model is the equivalent dipole model [12, 13]. In the work of [12, 13], a number of small dipole antennas are placed on the Huygens' surface enclosing the antenna. Because the number of dipole antennas is large, it may take long time to optimize the dipole antennas. In practice, it is reasonable to assume that the type of the antenna is known, because such information can be provided by the vendor. In this case, one may utilize the antenna's radiation mechanism to simplify the equivalent model. For example, [15] presented a physics-inspired equivalent model for microstrip antenna. Based on the radiation mechanism of the microstrip antenna, only four equivalent dipole antennas with three optimization parameters are required and excellent accuracy is obtained [15]. Furthermore, a simple equivalent model of the slotted waveguide antenna was proposed in [16]. In both [15, 16], the antenna's radiation mechanisms are taken into consideration when constructing the equivalent model, and thus the effort of optimizing the equivalent model is reduced.

Once the equivalent model is obtained, it is used together with the hybrid method to compute the installed radiation pattern. In most existing hybrid integral equation method (IEM)-PO methods, only two regions exist, namely IEM region and PO region. In this case, the IEM region is usually chosen to be small. Otherwise, it will be very time consuming to calculate the incident magnetic field in the PO region. Recently, Zhao et al. proposed a three-region hybrid method, where the IEM region is further divided into coupled and decoupled IEM regions [14]. Here, the method of [14] is further accelerated by MLFMM and the hybrid method is named as hybrid MLFMM-PO. Figure 1 illustrates the region division in the hybrid MLFMM-PO. It is seen that the whole computational domain is divided into three regions, two of which are around the antenna to be analyzed. Note that the equivalent model of the antenna is also included in the coupled MLFMM region. The terms 'coupled' and 'decoupled' are used to indicate whether the MLFMM region is coupled with PO region. Here, it is assumed that the energy reflected from PO region to MLFMM regions is negligible. In this case, one only needs to consider the first-order coupling from the coupled MLFMM region to PO region. Furthermore, the surface of the large platform and the equivalent model is assumed to be perfect electric conductor. The MLFMM regions are then modeled by the

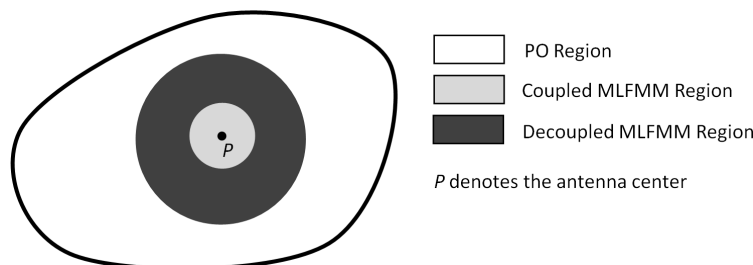


Figure 1: Region division of hybrid MLFMM-PO.

following well-known electric field integral equation

$$-\frac{j}{\omega\mu}\hat{t}(\vec{r})\cdot\vec{E}^i(\vec{r})=\hat{t}(\vec{r})\cdot\iint_S\left(1+\frac{1}{k^2}\nabla\nabla\right)\vec{J}(\vec{r}')G(\vec{r},\vec{r}')d\vec{r}', \quad (1)$$

where S denotes the surface of MLFMM regions. \vec{E}^i is the incident electric field on S . For equivalent model using small dipole antennas, the incident electric field is only non-zero at the dipole antenna feeding port. If equivalent model with current source is used, the incident electric field is the radiated field of the current source. By solving Equation (1) with MLFMM, the induced current on S is obtained. The induced current in the coupled MLFMM region and the current source of the equivalent model (if any) are used to compute the incident magnetic field in the PO region. Namely,

$$\vec{H}^i(\vec{r})=\nabla\times\iint_{S_c}\vec{J}(\vec{r}')G(\vec{r},\vec{r}')d\vec{r}'+\nabla\times\iint_{S_0}\vec{J}_0(\vec{r}')G(\vec{r},\vec{r}')d\vec{r}'. \quad (2)$$

In (2), S_c denotes the surface of the coupled MLFMM region, J_0 is the current source of the equivalent model, and S_0 is the surface where J_0 exists. With \vec{H}^i , the PO current is simply $\vec{J}_{PO}(\vec{r})=2\hat{n}(\vec{r})\times\vec{H}^i(\vec{r})$. Finally, the installed radiation pattern is computed using \vec{J} on S , \vec{J}_0 on S_0 (for equivalent model with current source), and \vec{J}_{PO} in PO region.

3. NUMERICAL RESULTS

This section presents simulation results to illustrate the capability of the proposed method. Code validation is first conducted using four dipole antennas above a $20\lambda\times 20\lambda$ square conducting plane. A microstrip antenna is then modeled using its equivalent model, and the hybrid MLFMM-PO is used to compute its radiation pattern on the $20\lambda\times 20\lambda$ rectangular conducting plane.

Figure 2 presents the far field radiation pattern of an array consisting of four quarter-wavelength dipole antennas. The results from hybrid MLFMM-PO agree well with those of MLFMM, except these angles in the shadowed region. The discrepancies in the shadowed region is due to the ignored edge diffraction, which can be fixed using the uniform theory of diffraction [14]. For this example, in-house developed codes are used for both methods. The CPU time required by MLFMM and hybrid MLFMM-PO is 3,611 and 233 seconds, respectively. The memory costs are 600.3 and 53.2 MB for MLFMM and hybrid MLFMM-PO, respectively.

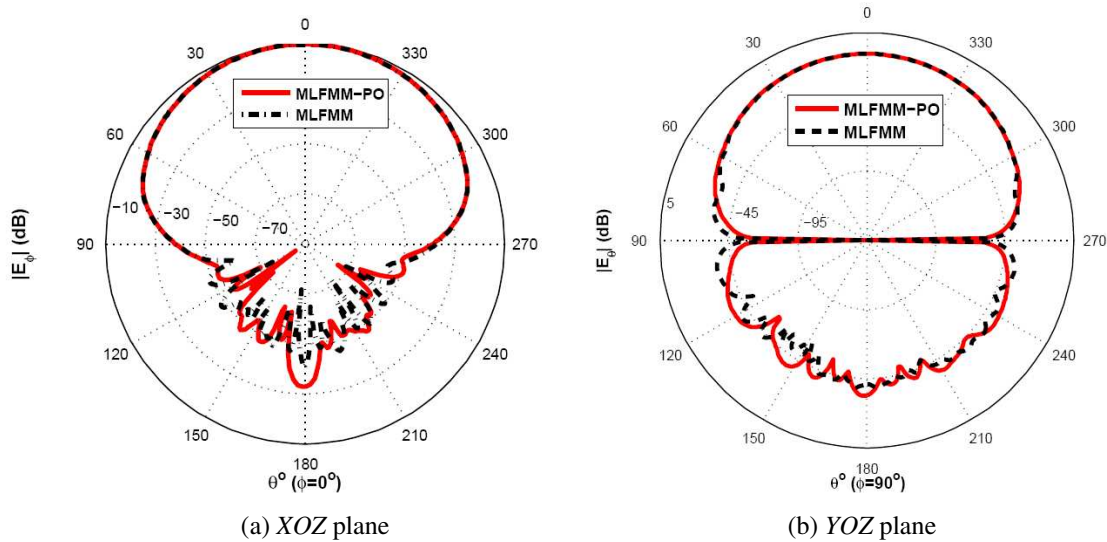


Figure 2: Radiation pattern of four dipole antennas above a $20\lambda\times 20\lambda$ square conducting plane.

Figure 3 shows the normalized radiation pattern of the microstrip antenna above the $20\lambda\times 20\lambda$ square conducting plane. Results from the proposed combined method are validated by those from FEKO [17]. Again, except for angles in the shadowed region, the proposed combined method agree well with FEKO. Note that the equivalent model of the microstrip antenna is obtained using the phaseless normalized radiation pattern of the microstrip antenna, which is usually available in the

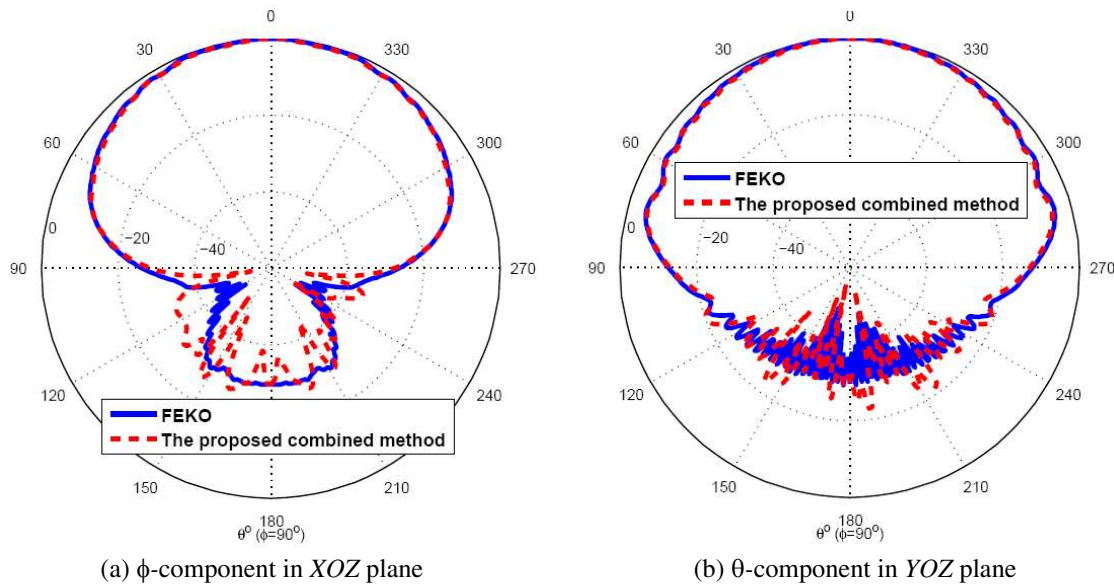


Figure 3: Normalized radiation pattern of a microstrip antenna above a $20\lambda \times 20\lambda$ square conducting plane.

data sheet of the antennas. The CPU time and memory cost are summarized in Table 1. It is seen that the CPU time of the proposed method is close to that of FEKO, while the proposed method requires twenty times less memory. Because FEKO requires detailed design of the antenna, it is difficult to make fair comparison between the proposed method and FEKO. Meanwhile, different code implementations make it more difficult to conduct efficiency comparison. However, considering FEKO incorporates state-of-the-art techniques, the proposed method can be considered as efficient. Therefore, the proposed method renders efficient prediction of an antenna's installed radiation pattern, without knowing its design details.

Table 1: Summary of CPU time and memory costs.

Method	CPU time (Minutes)	Memory cost (GB)
FEKO	11	2.61
The proposed combined method	16	0.11

4. CONCLUSION

This paper presented a combined method for efficient prediction of antennas' installed radiation patterns without knowing antennas' design details. Numerical results have shown the validity and efficiency of the proposed method. Except for these angles in shadowed region, excellent agreement has been observed between the proposed method and its alternatives. The proposed method requires no detailed design information of the antenna, and it is very useful when the antenna design is not provided by the its vendor. Work is undergoing to improve the accuracy in shadowed region by including the diffraction effect.

ACKNOWLEDGMENT

This work is supported by the A*STAR Aerospace Program (Grant No. 112 155 0613). The first author would like to express his gratitude to Professor Jun Hu from the University of Electronic Science and Technology of China, Chengdu, P. R. China, for his great help on the development of MLFMM code.

REFERENCES

1. Jakobus, U. and F. M. Landstorfer, "Improvement of the PO-MoM hybrid method by accounting for effects of perfectly conducting wedges," *IEEE Trans. Antennas Propag.*, Vol. 43, No. 10, 1123–1129, Oct. 1995.

2. Giovampaola, C. D., et al., “A hybrid PO/generalized-scattering-matrix approach for estimating the reflector induced mismatch,” *IEEE Trans. Antennas Propag.*, Vol. 60, No. 9, 4316–4325, Sep. 2012.
3. Barka, A. and P. Caudrillier, “Domain decomposition method based on generalized scattering matrix for installed performance of antennas on aircraft,” *IEEE Trans. Antennas Propag.*, Vol. 55, No. 6, 1833–1842, Jun. 2007.
4. Barka, A., “Integration of antennas onboard vehicles and diffraction by large and complex structures with multiple-domain-multiple-methods techniques,” *Proc. IEEE*, Vol. 101, No. 2, 280–297, Feb. 2013.
5. Wang, X., et al., “Multisolver domain decomposition method for modeling EMC effects of multiple antennas on a large air platform,” *IEEE Trans. Electromagn. Compat.*, Vol. 54, No. 2, 375–388, Apr. 2012.
6. Peng, Z., K.-H. Lim, and J.-F. Lee, “Nonconformal domain decomposition methods for solving large multiscale electromagnetic scattering problems,” *Proc. IEEE*, Vol. 101, No. 2, 298–319, Feb. 2013.
7. Li, M.-K. and W. C. Chew, “Multiscale simulation of complex structures using equivalence principle algorithm with high-order field point sampling scheme,” *IEEE Trans. Antennas Propag.*, Vol. 56, No. 8, 2389–2397, Aug. 2008.
8. Chen, J., et al., “Efficient implicit-explicit time stepping scheme with domain decomposition for multiscale modeling of layered structures,” *IEEE Transactions on Components Packaging and Manufacturing Technology*, Vol. 1, No. 9, 1438–1446, Sep. 2011.
9. Bartoli, N., et al., “A far-near field transformation using the fast multipole techniques,” *IEEE Trans. Antennas Propag.*, Vol. 52, No. 12, 3329–3336, Dec. 2004.
10. Regue, J.-R., et al., “A genetic algorithm based method for source identification and far-field radiated emissions prediction from near-field measurements for PCB characterization,” *IEEE Trans. Electromagn. Compat.*, Vol. 43, No. 4, 520–530, Nov. 2001.
11. Li, P., et al., “A wide band equivalent source reconstruction method exploiting the Storer-Bulirsch algorithm with the adaptive frequency sampling,” *IEEE Trans. Antennas Propag.*, Vol. 61, No. 10, 5338–5343, Oct. 2013.
12. Mikki, S. M. and A. A. Kishk, “Theory and applications of infinitesimal dipole models for computational electromagnetics,” *IEEE Trans. Antennas Propag.*, Vol. 55, No. 5, 1325–1337, May 2007.
13. Mikki, S. M. and Y. M. Antar, “Near-field analysis of electromagnetic interactions in antenna arrays through equivalent dipole models,” *IEEE Trans. Antennas Propag.*, Vol. 60, No. 3, 1381–1389, Mar. 2012.
14. Zhao, W.-J., J. L. W. Li, and L. Hu, “Efficient current-based hybrid analysis of wire antennas mounted on a large realistic aircraft,” *IEEE Trans. Antennas Propag.*, Vol. 58, No. 8, 2666–2672, Aug. 2010.
15. Gao, S., et al., “Predicting installed radiation pattern of patch antennas using equivalent model method,” *IEEE Antennas and Propagation Magazine*, 2014.
16. Gao, S., et al., “Analysis of slotted waveguide antennas on large platforms using an equivalent model,” To be Presented in the *31st URSI General Assembly and Scientific Symposium*, Beijing, China, Aug. 16–23, 2014.
17. <http://www.feko.info/>.

Multi-scale Electromagnetic Modeling by Integral Equation Domain Decomposition Method with Hybrid Basis Functions

Ran Zhao, Mi Tian, Jun Hu, and Zai Ping Nie

School of Electronic Engineering, University of Electronic Science and Technology of China
Chengdu 611731, China

Abstract— In this paper, a novel electromagnetic (EM) modeling method by integral equation domain decomposition method with hybrid basis functions is developed for the solution of multi-scale problems. Based on the integral equation domain decomposition method, the original multi-scale object were decomposed into several closed sub-domains and transmission condition is enforced on the touching faces to maintain the continuity of current across the interfaces. The higher order hierarchical vector basis functions and low order Rao-Wilton-Glisson (RWG) basis functions are used in different sub-domains to reduce remarkably the number of unknowns. Because the domain decomposition method provides an effective preconditioner, the convergence history will be much better than traditional method of moments (MoM). And because of the non-conformal property of the domain decomposition method, each sub-domain can be meshed independently, which enables the mesh generation be much easier than the traditional method, especially for complex multi-scale objects. Finally, some numerical results are given to validate the ability of the present method.

1. INTRODUCTION

Method of Moments (MOM) based on integral equation (IE) is one of the most well-known method for electromagnetic scattering, radiation problem. Compare to the differential equation method, finite element method (FEM) and finite difference method (FDM), the unknowns of the integral equation method is only distributed on the surface of perfect electric conductor (PEC), the number of unknowns is much less than them. And because the Green's function satisfy the radiation condition automatically, the absorption boundary condition (ABC) is not required. However, application of the MoM usually leads to a dense matrix equation. At the same time, MoM discretized with low order basis as Rao-Wilton-Glisson (RWG) basis functions or roof-top basis functions [1] often leads to a great deal of unknowns, it is difficult to solve the electrically large problems. This is because both the memory requirement and computational complexity of matrix vector multiplication is $O(N^2)$ where the N is the number of unknowns. To overcome this difficulty, two categories have been developed. One of the categories is develop the fast algorithm to accelerate the matrix-vector multiplication in iterative methods, in order to reduce the computational complexity and memory requirement, such as well-known multilevel fast multipole algorithm (MLFMA) [2] with the complexity of $O(N \log(N))$, adaptive integral method (AIM) [3], IE-FFT [4]. Another category is to discretize the IE with higher order basis functions to reduce the dimension of the matrix. The higher order basis function can be also categorized as two kinds, the interpolatory type and hierarchical type [5–7]. By using the orthogonal Legendre polynomials and modified Legendre polynomials combined with the scaling factor in the hierarchical vector basis function, a well-conditioned matrix is obtained in [6].

However, the simulation of multi-scale problems with IE method in the real world will lead to an ill-conditioned dense matrix equation. When the iterative solvers are used to deal with the matrix equation, the solvers always converge very slowly or even do not converge at all. When the high order hierarchical vector basis function were used, the convergence will be even worse. Recently, a novel non-conformal, non-overlapping integral equation domain decomposition method (IE-DDM) has been developed by Peng et al. [8, 9]. It divides the original domain into many smaller sub-domains and provides a very effective preconditioner for the multi-scale ill-conditioned dense matrix. Because the non-conformal property of the IE-DDM, each sub-domain can be meshed independently.

In these paper, a non-conformal non-overlapping integral equation domain decomposition method (IE-DDM) with hybrid basis functions is presented to simulate the EM scattering of multi-scale objects. The high order hierarchical vector basis functions and low order RWG basis functions can be chosen in different sub-domains based on its local physical and geometrical property.

2. HYBRID BASIS FUNCTIONS

2.1. High Order Hierarchical Basis Function

As shown in Fig. 1(a), the surface current defined on the higher order hierarchical vector basis function (HOHV) based on the quadrilateral which were proposed in [6] can be expressed in the following:

$$\mathbf{f}_{HO} = J_{su}\hat{a}_u + J_{sv}\hat{a}_v \quad (1)$$

where \hat{a}_u and \hat{a}_v are the covariant unit vectors with $\hat{a}_u = \partial\vec{r}/\partial u$ and $\hat{a}_v = \partial\vec{r}/\partial v$. $\vec{r}(u, v)$ is local coordinate the position vector corresponding to $\vec{r}(x, y, z)$ on each patch with $-1 \leq u, v \leq 1$. The u -directed current can be expanded as:

$$J_{su} = \frac{1}{\eta_S(u, v)} \sum_{m=0}^{M_u} \sum_{n=0}^{N_v} b_{mn}^u \tilde{C}_m P_m(u) C_n P_n(v) \quad (2)$$

where b_{mn}^u are the unknown coefficients, $\eta_S(u, v)$ is the Jacobian factor, which is defined as $\eta_S(u, v) = |\hat{a}_u \times \hat{a}_v|$ and M_u, N_v are the basis order along the current flow direction and transverse direction. The v -directed current can be also obtained just need to interchange the u and v in (2). $P_m(u)$ and $P_n(v)$ are the Legendre polynomials, $\tilde{P}_m(u)$ and $\tilde{P}_n(v)$ are the modified Legendre polynomials, which can be defined as:

$$\tilde{P}_m(u) = \begin{cases} 1 - u, & m = 0 \\ 1 + u, & m = 1 \\ P_m(u) - P_{m-2}(u), & m \geq 2 \end{cases} \quad (3)$$

\tilde{C}_m, C_n are the scaling factor, defined as:

$$\tilde{C}_m = \begin{cases} \frac{\sqrt{3}}{4}, & m = 0, 1 \\ \frac{1}{2} \sqrt{\frac{(2m-3)(2m+1)}{(2m-1)}}, & m \geq 2 \end{cases} \quad (4)$$

$$C_n = \sqrt{n + \frac{1}{2}} \quad (5)$$

Obviously, (2) will be degenerated to the well-known roof-top basis function, when the order of the function equals to one. Only this order's basis function has the nonzero value across the edge of the adjacent patches.

2.2. RWG Basis Function

As shown in Fig. 1(b), the well-known RWG basis function based on triangular can be expressed as following:

$$\mathbf{f}_{RWG} = \begin{cases} l_m \boldsymbol{\rho}_m^+ / 2A_m^+, & r \in T_m^+ \\ l_m \boldsymbol{\rho}_m^- / 2A_m^-, & r \in T_m^- \\ 0, & \text{others} \end{cases} \quad (6)$$

where T_m^+ and T_m^- are the adjacent triangles that support the m th RWG basis function, l_m is the length of common edge, A_m^+ and A_m^- are the areas of the triangles T_m^+ and T_m^- , respectively. $\boldsymbol{\rho}_m^+$ and $\boldsymbol{\rho}_m^-$ are a vector pointing from a free vertex of triangle T_m^+ to a point \mathbf{r} in to it, and a vector pointing from a point \mathbf{r} in T_m^- to its free vertex, respectively.

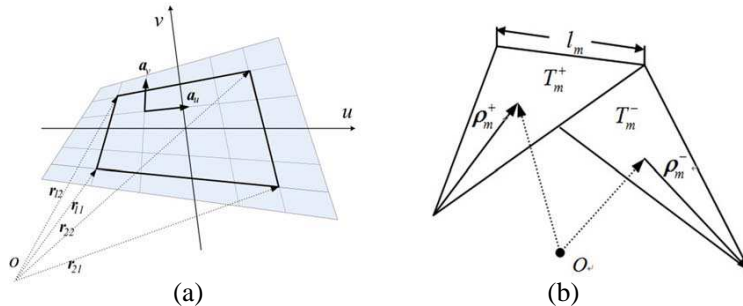


Figure 1: (a) The high order hierarchical basis function defined on the quadrilateral. (b) The RWG basis function associated with the m -th edge.

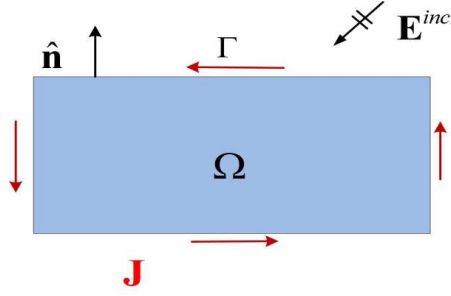


Figure 2: EM scattering from a PEC object.

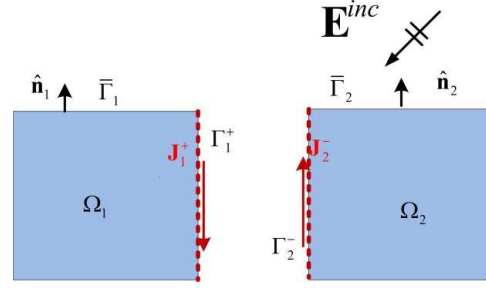


Figure 3: The notation of the decomposition of the original PEC object.

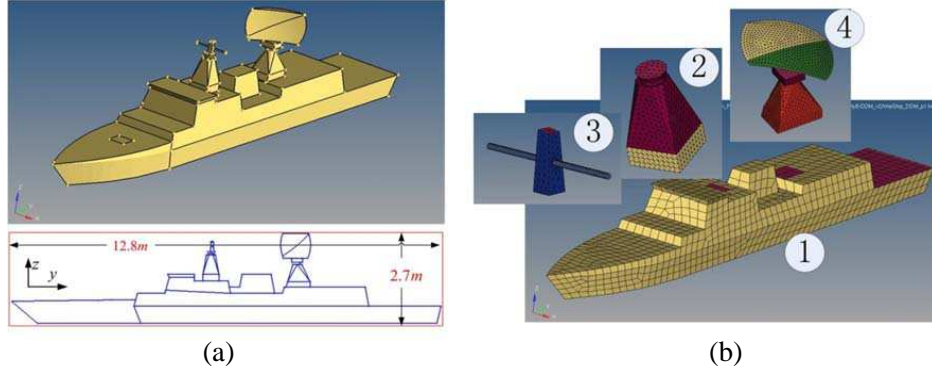


Figure 4: (a) The Geometry and dimension of the simplified ship. (b) Domain partition by using IE-DDM with hybrid basis functions to solve the EM scattering of the simplified ship.

3. FORMULATION

Considering the electromagnetic scattering of a PEC object Ω , as shown in Fig. 3. It can be decomposed into two non-overlapping objects Ω_1 and Ω_2 , as shown in Fig. 4. The HOHV basis functions \mathbf{f}_{HO} based on quadrilateral are used to discrete the current on the surface of Ω_1 , the RWG basis functions \mathbf{f}_{RWG} are used to discrete the current on on the surface of Ω_2 . The system matrix equations can be written as:

$$[\mathbf{M}] \mathbf{x} = [\mathbf{b}] + [\mathbf{N}] \mathbf{x} \quad (7)$$

where

$$[\mathbf{M}] = \begin{bmatrix} \mathbf{A}_{\bar{\Gamma}_1 \bar{\Gamma}_1} & \mathbf{A}_{\bar{\Gamma}_1 \Gamma_1^+} & & \\ \mathbf{A}_{\Gamma_1^+ \bar{\Gamma}_1} & \mathbf{A}_{\Gamma_1^+ \Gamma_1^+} & & \\ & & \mathbf{A}_{\bar{\Gamma}_2 \bar{\Gamma}_2} & \mathbf{A}_{\bar{\Gamma}_2 \bar{\Gamma}_2} \\ & & \mathbf{A}_{\bar{\Gamma}_2 \Gamma_2^-} & \mathbf{A}_{\bar{\Gamma}_2 \Gamma_2^-} \end{bmatrix} \quad (8)$$

The matrix bocks $\mathbf{A}_{\bar{\Gamma}_j \bar{\Gamma}_j}$, $\mathbf{A}_{\bar{\Gamma}_j \Gamma_j^+}$, $\mathbf{A}_{\Gamma_j^+ \bar{\Gamma}_j}$, $\mathbf{A}_{\Gamma_j^+ \Gamma_j^+}$, stand for the self-coupling of each sub-domain Ω_j , $j = 1, 2$ itself.

$$[\mathbf{N}] = \begin{bmatrix} & & \mathbf{C}_{\bar{\Gamma}_1 \Gamma_2^-} & \mathbf{C}_{\bar{\Gamma}_1 \bar{\Gamma}_2} \\ \mathbf{B}_{\Gamma_1^+ \bar{\Gamma}_1} & \mathbf{B}_{\Gamma_1^+ \Gamma_1^+} & \mathbf{D}_{\Gamma_1^+ \Gamma_2^-} & \\ & \mathbf{D}_{\bar{\Gamma}_2 \Gamma_1^+} & \mathbf{B}_{\bar{\Gamma}_2 \bar{\Gamma}_2} & \mathbf{B}_{\bar{\Gamma}_2 \bar{\Gamma}_2} \\ \mathbf{C}_{\bar{\Gamma}_2 \bar{\Gamma}_1} & \mathbf{C}_{\bar{\Gamma}_2 \Gamma_1^+} & & \end{bmatrix} \quad (9)$$

$$\mathbf{b} = [\mathbf{b}_{\bar{\Gamma}_1}, \mathbf{b}_{\Gamma_1^+}, \mathbf{b}_{\bar{\Gamma}_2}, \mathbf{b}_{\Gamma_2^-}]^T \quad (10)$$

$$\mathbf{x} = [\mathbf{J}_{\bar{\Gamma}_1}, \mathbf{J}_{\Gamma_1^+}, \mathbf{J}_{\bar{\Gamma}_2}, \mathbf{J}_{\Gamma_2^-}]^T \quad (11)$$

The matrix blocks $\mathbf{C}_{\bar{\Gamma}_1 \Gamma_2^-}$, $\mathbf{C}_{\bar{\Gamma}_1 \bar{\Gamma}_2}$, $\mathbf{C}_{\bar{\Gamma}_2 \bar{\Gamma}_1}$, $\mathbf{C}_{\bar{\Gamma}_2 \Gamma_1^+}$ stand for coupling among each sub-domain, and the $\mathbf{D}_{\Gamma_1^+ \Gamma_2^-}$, $\mathbf{D}_{\bar{\Gamma}_2 \Gamma_1^+}$ are the cement matrixes that enforcing the transmission condition. To realize a

fast solution of Equation (7), a preconditioner is necessary. Here, the inverse of matrix \mathbf{M} is used as the preconditioner, as follows,

$$\mathbf{M}^{-1} [\mathbf{M} - \mathbf{N}] \mathbf{x} = \mathbf{M}^{-1} \mathbf{b} \quad (12)$$

Because it is difficult to calculate the inverse of the matrix \mathbf{M} , directly, especially for the electrically large problem, the inner-outer iteration based on the Krylov subspace method can be used to solve the equation.

4. NUMERICAL RESULT

In the numerical example, the EM scattering from a simplified PEC ship model is investigated. The incident plane wave illuminate the model along the negative of the z axis, at 0.6 GHz. The dimension and geometry of the ship is shown in Fig. 4(a). This ship is decomposed into 4 closed sub-regions, the domain partition of this ship and the mesh of the IE-DDM with hybrid basis functions are shown in the Fig. 4(b). The second order HOHV basis functions are used in the first sub-region, the RWG basis functions are used in the other sub-regions. Traditional higher order MoM can also be used to solve this problem, but because of the multi-scale property of the geometry, it will lead to an ill-conditioned matrix. The maximum and minimum size of HOHV basis functions are 0.5λ , 0.01λ , if the mesh size less than 0.1λ the first order are used and the others use the second order. The bistatic RCS for H - H polarization of the IE-DDM with hybrid basis functions compare with traditional MoM discretized with RWG basis functions are shown in the Fig. 5. Obviously, the result of the IE-DDM with hybrid basis functions agrees with the result of the MoM discretized with RWG basis functions. The computational statistics of these three methods are shown in the Table 1. The GMRES [10] method is used both in the inner and outer iteration, the convergence tolerance of outer iteration is 0.01, and the convergence tolerance of inner iteration is 0.001.

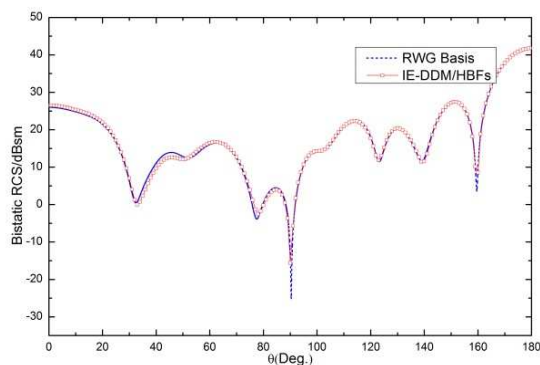


Figure 5: The result of the ship of IE-DDM with hybrid basis functions compare with the result of MoM discretized with RWG basis functions.

Table 1: Computational statistics of the ship.

Method	Unknowns	Mem. (GB)	Time Filling/Iteration (hh:mm)	Iter. Num.
MoM-RWG	89,739	60	121:00	86
HO-MoM	25,034	4.7	03:00 / 01:07	2420
IEDDM/HBFs	21,421	3.5	02:45 / 00:08	9

5. CONCLUSION

The integral equation domain decomposition method with hybrid basis functions is developed to solve time harmonic multi-scale EM scattering problems. By using this method, the HOHV basis and RWG basis can be chosen in different sub-regions and several multi-scale problems can be solved, successfully.

ACKNOWLEDGMENT

This work is supported partly by NSFC under Grant 61271033.

REFERENCES

1. Rao, S. M., D. R. Wilton, and A. W. Glisson, "Electromagnetic scattering by surfaces of arbitrary shape," *IEEE Trans. Antennas Propagat.*, Vol. 30, No. 5, 409–418, 1982.
2. Song, J. M., C. C. Lu, and W. C. Chew, "Multilevel fast multipole algorithm for electromagnetic scattering by large complex objects," *IEEE Trans. Antennas Propagat.*, Vol. 45, No. 10, 1488–1493, 1997.
3. Ling, F., C.-F. Wang, and J.-M. Jin, "Efficient algorithm for analyzing large-scale microstrip structures using adaptive integral method combined with discrete complex-image method," *IEEE Trans. Microwave Theory Tech.*, Vol. 48, No. 5, 832–839, 2000.
4. Seo, S. M. and J.-F. Lee, "A fast IE-FFT algorithm for solving PEC scattering problems," *IEEE Trans. Magn.*, Vol. 41, No. 5, 1476–1479, 2004.
5. Graglia, R. D., D. R. Wilton, and A. F. Peterson, "Higher order interpolatory vector bases for computational electromagnetics," *IEEE Trans. Antennas Propagat.*, Vol. 45, No. 3, 329–342, 1997.
6. Jorgensen, E., J. L. Volakis, P. Meincke, and O. Breinbjerg, "Higher order hierarchical Legendre basis functions for electromagnetic modeling," *IEEE Trans. Antennas Propagat.*, Vol. 52, No. 11, 2985–2995, 2004.
7. Nie, Z., W. Ma, Y. Ren, Y. Zhao, J. Hu, and Z. Zhao, "Wideband electromagnetic scattering analysis using MLFMA with higher order hierarchical vector basis functions," *IEEE Trans. Antennas Propagat.*, Vol. 57, No. 10, 3169–3178, 2009.
8. Peng, Z., X.-C. Wang, and J.-F. Lee, "Integral equation based domain de-composition method for solving electromagnetic wave scattering from non-penetrable objects," *IEEE Trans. Antennas Propagat.*, Vol. 59, No. 9, 3328–3338, 2011.
9. Peng, Z., K.-H. Lim, and J.-F. Lee, "Computations of electromagnetic wave scattering from penetrable composite targets using a surface integral equation method with multiple traces," *IEEE Trans. Antennas Propagat.*, Vol. 61, No. 1, 256–270, 2013.
10. Saad, Y. and M. H. Schultz, "GMRES: A generalized minimal residual algorithm for solving nonsymmetric linear systems," *SIAM J. Sci. Stat. Comput.*, Vol. 7, No. 3, 1986.

Performance Enhancement of RMPA Using ESRR Metamaterial at THz

Parul Dawar¹ and Asok De²

¹Department of ECE, Guru Tegh Bahadur Institute of Technology
G-8 Area, Rajouri Garden, New Delhi-110064, India

²National Institute of Technology, Patna, Bihar-800005, India

Abstract— Left handed materials which have both negative permittivity and permeability, have been the area of potential research over a decade. This paper elucidates antenna parameter optimization using Double Negative Group (DNG) Electric SRR, having 19.13 THz as resonant frequency forming metamaterial array embedded in antenna substrate at high frequency (THz). Ansoft HFSS has been used to design and analyse the RMPA (Rectangular Microstrip Patch Antenna) with design frequency 22.5 THz and operating range of 20 THz to 25 THz having FR4 ($\epsilon_r = 4.4$) as substrate material. Nicolson Ross Wier (NRW) method has been used to retrieve the material parameters from transmission and reflection coefficient. Upon incorporation, remarkable enhancement in parameters is observed whereby bandwidth increases by factor of 3.75, directivity increases by 5% and front to back lobe ratio improves by 31% with ESRR metamaterial.

1. INTRODUCTION

The past few years have been very eventful with respect to the evolution of the concept and implementation of ‘left-handed materials (LHMs)’. ‘Metamaterials’ (MTMs) are engineered to modify the bulk permeability and/or permittivity of the medium [1]. It is realized by placing periodically, structures that alter the material parameters, with elements of size less than the wavelength of the incoming electromagnetic wave. It results in “meta” i.e., “altered” behaviour or behaviour unattainable by natural materials. Slight changes to a repeated unit cell can be used to tune the effective bulk material properties of a MTM, replacing the need to discover suitable materials for an application with the ability to design a structure for the desired effect. Examples of MTMs are single negative materials (SNG) like ϵ negative (ENG) which have effective negative permittivity and μ negative (MNG) which have effective negative permeability, and double negative materials (DNG).

It is worth recalling that negative values of permittivity are inherently bandlimited phenomena and such a condition can hold only at a certain frequency (accompanied with imaginary part of permittivity). Frequency for which real part of permittivity hits value ‘ -2 ’ and infinity condition goes named as Frohlich frequency [2]. Particle shape has effect on the value of negative permittivity corresponding to Frohlich resonance. The geometry of negative permittivity particle has a strong effect on its surface plasmonic properties.

A fresh approach to microwave and optical devices presented itself with the interesting breakthrough in the area of MTMs at high frequencies. The need of hour is to optimize the antenna parameters (gain, bandwidth, directivity) without altering its dimensions, i.e., external control over antenna parameters using MTM. The software tool HFSS is used because it is a high performance full wave electromagnetic (EM) field simulator [3].

This paper abridges the design of RMPA with resonant frequency 22.5 THz and operating frequency range of 20 THz to 25 THz having FR4 ($\epsilon_r = 4.4$) as substrate material in Section 2. Section 3 describes proposed DNG MTM Electric SRR having negative refraction in the designed RMPA range. Section 4 elucidates upon their application in antenna parameter optimization by embedding their array in the middle of the antenna substrate and just below the microstrip rectangular patch. Section 5 concludes the paper.

2. RMPA DESIGN

2.1. Design

RMPA, i.e., Rectangular Microstrip Patch Antenna, as the name implies consists of a rectangular patch over a microstrip substrate. Its major disadvantage is relatively low-impedance bandwidth which limits the field of application of these antennas. Bandwidth of RMPA can be improved by several methods available in literature, e.g., use of thick substrates, addition of parasitic patches.

The implication of such methods will not just increase the complexity of system, but will have adverse effect on gain of the antenna. Also, such methods involve changes in the parameters of the designed antenna. This calls for a novel technique to increase the bandwidth of antenna without altering its parameters and without much effecting the antenna's radiation properties. Henceforth, metamaterial based antennas have been introduced [4].

Transmission Line model represents RMPA as two slots of width, w , and height, h , separated by transmission line of length, l . Thus, it is a non homogeneous structure made up of two dielectrics, i.e., substrate and air. This shows that substrate and air will have different phase velocity and the dominant mode of propagation will be quasi-TEM. Therefore effective permittivity, ϵ_{eff} , comes into consideration. There is fringing effect at the edges of patch, due to which the patch appears to be longer. So, L_{eff} , i.e., effective length is defined which is obtained by adding $2\Delta l$ (additional length Δl due to fringing on each end) to the length obtained by using mathematical design equations [5]. Ground plane has length, l_g , and width, w_g . The tangential components of electric field are in phase. Therefore, maximum radiated field is normal to the surface of the structure. However, normal components of the electric field at the two edges along the width out of phase. Hence, no radiation in broadside direction.

Microstrip feed using quarter wave transformer has been used for feeding the antenna as calculated from Equation (7). The input impedance is taken at the base of microstrip feedline and is referred to 50Ω . i.e., Z_o .

$$Z_{qw} = \sqrt{Z_{rmpa} * Z_o} \quad (1)$$

where the W_{qw} and L_{qw} represent the width and length of the quarter wave transformer as calculated from Z_{qw} , i.e., impedance of quarter wave transformer using txline software by AWR. The operating frequency range of the RMPA, shown in Figure 1, designed for Electric SRR MTM is from 20 THz to 25 THz with centre frequency 22.5 THz with FR4 ($\epsilon_r = 4.4$) as substrate. Constructional details are shown in Table 1.

Frequency range	20–25 THz
Center frequency	22.5 THz
ϵ_r	4.44
ϵ_{eff}	3.78
h	0.5 μm
w	4.06 μm
L_{eff}	3.43 μm
ΔL	0.22 μm
L	2.98 μm
L_g	15 μm
W_g	15 μm
L_{qw}	1.88 μm
W_{qw}	0.15 μm
L_{zo}	1.76 μm
W_{zo}	0.98 μm

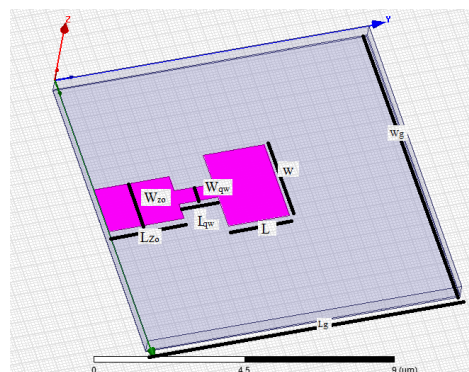


Table 1: Design parameters of RMPA for ESRR MTM. Figure 1: Rectangular microstrip patch antenna.

2.2. Simulation Results

RMPA has been simulated in HFSS. Figure 2 shows the simulation results where S_{11} is return loss or reflection coefficient.

Simulation results have been shown in Table 2.

It can be seen that S_{11} is crossing 10 dB line and VSWR is less than 2. Bandwidth is 0.326 THz, which is range of frequencies with VSWR < 2.

3. PROPOSED MTM

In 1968, Russian scientist Veselago [6] postulated a negative material and theoretically proved the phenomenon that a uniform plane-wave followed the left hand rule in a medium with negative permittivity (ϵ) and negative permeability (μ). The first work in this direction was by Pendry. He created a medium consisting of thin wires arranged in a periodic array [7]. These wires acted as a plasma medium, whereby ϵ varies with frequency, Pendry next achieved a negative μ with a periodic array of metallic loops called Split Ring Resonators [8]. In a medium composed of these rings the permeability, μ , varied with frequency, and could become negative. In 1999, Smith

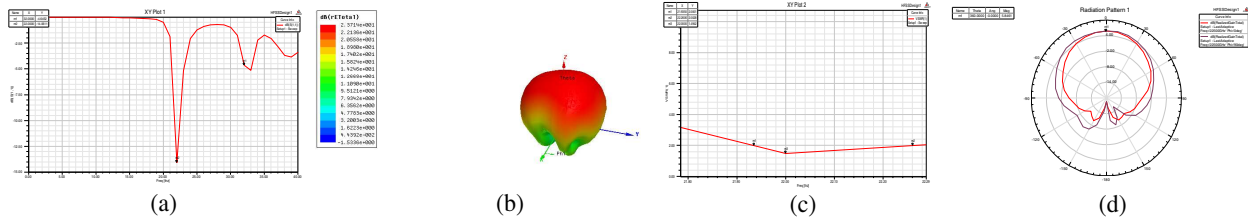


Figure 2: (a) Return loss, (b) 3D polar plot, (c) VSWR, (d) radiation pattern in E and H plane of RMPA.

combined the rod and ring materials to finally produce a material with simultaneously negative ε and μ , a left-handed material [9]. The wire strips affect the ε and the split-ring resonators (SRRs) alter the μ of the medium thus giving a frequency dependent negative material with both the parameters negative. The wire medium and the SRRs have certain frequency dependence. The rod gives negative permittivity, ε , and ring material creates a negative permeability, μ , this combined rod and ring material gives negative index of refraction.

Electric SRR metamaterial has been proposed behaving as DNG, i.e., Double Negative Group. Such materials have negative permittivity and negative permeability in the same frequency region. Thus having negative refraction in the same [10, 11] region. The parameter retrieval, i.e., parameter extraction using S parameters [12] has been followed using NRW approach to observe the negative refraction region of MTM. The constructional details along with the curve showing negative refraction are as under.

3.1. Constructional Details

It is constructionally very simple, and has been designed as per Figure 3(a) with design parameters specified in Figure 3(b). It forms the LC resonant structure by having capacitance due to the dielectric gaps and inductance due to the conducting loops [13]. Each unit cell is designed on a $0.5 \mu\text{m}$ thick FR4 substrate with length $a = 1.3 \mu\text{m}$. The thickness of the metal strip is $0.035 \mu\text{m}$ and is made up of gold.

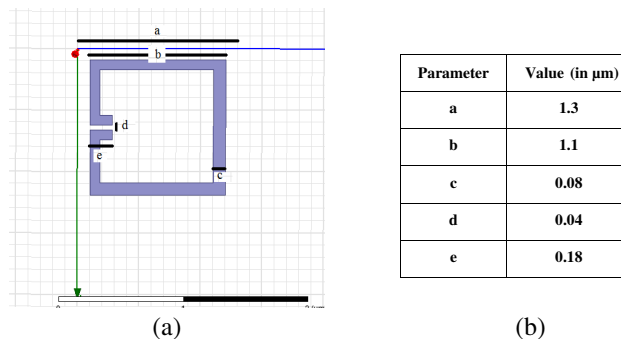


Figure 3: Electric SRR shaped MTM, (a) unit cell designed in HFSS, (b) constructional details.

3.2. Simulation Results

Ansoft HFSS has been used to simulate the unit cell designed in Figure 3(a) by assigning the boundaries (E field and H field) and lumped ports (1 and 2). Nicolson Ross Wier method has been used to calculate the material properties from transmission and reflection coefficients. It can be observed as in Figure 4(a) that region of negative refraction extends from 19.12 THz.

4. MATHEMATICAL PROOF

Proposed MTM has magnetic properties because of internal inductances and capacitances. It can be simplified in terms of combinations of C and L . Using transmission line theory (quasi-static regime), we can draw its equivalent circuit as in Figures 5(a), (b).

The L is the inductance per unit length of the loop and C_1 and C_2 are the capacitances of the gap.

The expressions for L and C are given by Equations (2) and (3) as below [11]:

$$L_s = \frac{2\mu_0 b}{\pi} \left[\sinh^{-1} \left(\frac{b}{c/2} \right) - 1 \right] \quad (2)$$

where $\mu = \mu_0$ is the vacuum permeability and parameter values can be referred to Figure 4(b).

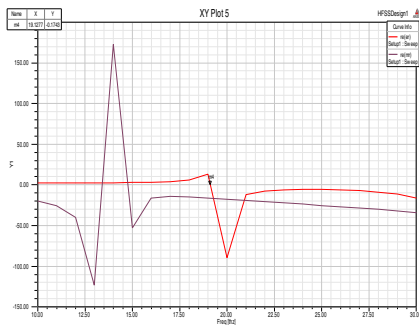


Figure 4: Resonance at 19.12 THz.

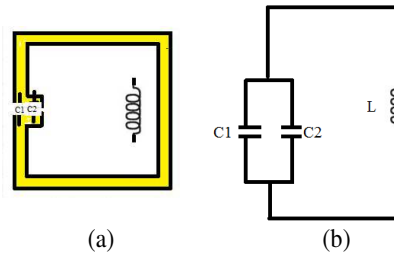


Figure 5: (a), (b) Equivalent LC circuit of ESRR.

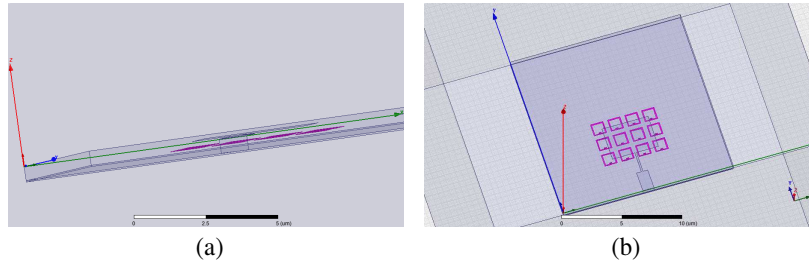
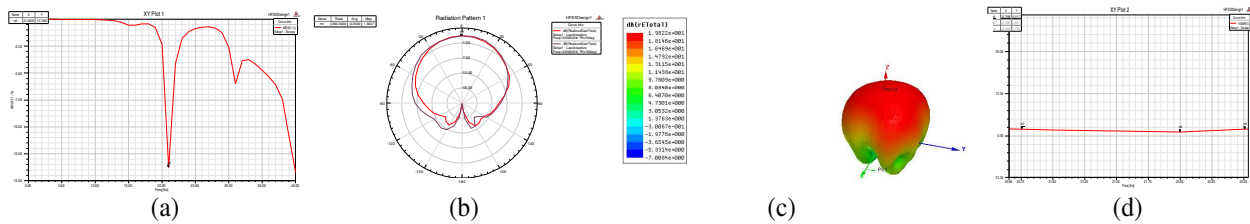


Figure 6: Embedding ESRR MTM array inside RMPA substrate, (a) side view, (b) top view.


 Figure 7: (a) Return loss, (b) E and H radiation pattern, (c) 3D polar plot, (d) VSWR.

Therefore, L_m is 2.037×10^{-12} H.

$$C = \frac{\varepsilon A}{d} \quad (3)$$

where C is the expression for calculating parallel plate capacitance with C_1 as capacitance between the ring and C_2 as capacitance in the electric gap of the ring.

Therefore, C_1 is 0.0062×10^{-15} F and C_2 is 0.014×10^{-15} F.

Neglecting high frequency losses, magnetic resonance frequency is given by Equation (4)

$$\omega_m = \sqrt{\frac{1}{L \cdot (C_1 + C_2)}} \quad (4)$$

Thus, magnetic resonance frequency is found out to be 24.8 THz. However, using simulational study of MTM in Ansoft HFSS, magnetic resonance frequency has been found out to be 19.12 THz. Thus, net error between simulational and analytical study of Electric SRR is around 23%.

5. ANTENNA PARAMETER OPTIMIZATION

5.1. Design

Antenna is characterized by different parameters, e.g., gain, bandwidth, VSWR, 3 dB beamwidth in E , H plane, return loss. These parameters have been obtained for RMPA as in Table 2 using HFSS. Parameter optimization is done by embedding the proposed Electric SRR metamaterial in middle of substrate in array of 3×4 elements spaced at $0.4 \mu\text{m}$ from each other and center of the array coincides with the center of the antenna substrate just below the patch as shown in Figure 6.

5.2. Simulation

Simulation results for MTM array inside RMPA substrate are shown in Figure 7.

Table 3 gives the obtained simulated values of parameters and comparison of ESRR MTM array RMPA with RMPA without MTM.

Table 2: Simulation results of RMPA at 22.5 THz.

Parameters	RMPA
S_{11} (dB)	-14.06
VSWR	1.49
Bandwidth (THz)	0.326
H plane gain in dB	5.86
E plane gain in dB	5.86
Peak directivity (dB)	4
Front to back lobe ratio	121

Table 3: Simulation and comparison results of ESRR MTM array embedded in RMPA substrate.

Antenna/ Parameters	RMPA	RMPA with MTM	Improvement (approx)
S_{11} (dB)	-14.06	-13.75	-2%
VSWR	1.49	1.2	24%
Bandwidth (THz)	0.33	1.24	3.75 times increase
H plane gain in dB	5.86	1.92	1/3rd
E plane gain in dB	5.86	1.92	1/3rd
Peak directivity (dB)	4	4.21	5%
Front to back lobe ratio	121	158.95	31%

6. CONCLUSION

Upon designing and analysing proposed MTM inside RMPA substrate we obtain results as in Table 3. It can be seen that bandwidth is almost three times with proposed Electric SRR MTM, directivity has been enhanced by 5%. Thereby, improving Front to back lobe ratio by 31%. However, gain (S_{21}) is reduced by 33%. Trade off lies in improvement of above antenna parameters over gain and return loss.

REFERENCES

- Ziolkowski, R. W., "Design, fabrication and testing of double negative metamaterials," *IEEE Transactions on Antenna and Propagation*, Vol. 51, No. 7, 1516–1529, 2003.
- Sihnola, A., "Character of surface plasmons in layered spherical structures," *Progress In Electromagnetics Research*, Vol. 62, 317–331, 2006.
- www.docstoc.com/docs/127876758/High-Frequency-Structure-Simulator-HFSS-Tutorial.
- Asok De, P. D., "Bandwidth enhancement of RMPA using 2 segment labyrinth metamaterial at THz," *Materials Sciences and Applications*, Vol. 4, No. 10, 579–588, 2013.
- Balanis, C. A., *Antenna Theory*, John Wiley & Sons Inc, 1999.
- Veselago, V. G., "The electrodynamics of substances with simultaneously negative values of ϵ and μ ," *Soviet Physics-Uspekh*, Vol. 10, No. 4, 509–514, Jan.–Feb. 1968.
- Pendry, J. B., A. J. Holden, W. J. Stewart, and I. Youngs, "Extremely low frequency plasmons in metallic micro structures," *Phys. Rev. Lett.*, Vol. 76, 4773–4776, 1996.
- Pendry, J. B., A. J. Holden, D. J. Robbins, and W. J. Stewart, "Magnetism from conductors and enhanced nonlinear phenomena," *IEEE Trans. Microwave Theory Tech.*, Vol. 47, 2075–2084, Nov. 1999.
- Smith, D. R., Willie J. Padilla, D. C. Vier, S. C. Nemat-Nasser, and S. Schultz, "Composite medium with simultaneously negative permeability and permittivity," *Physical Review Letters*, Vol. 84, No. 18, 4184–4187, May 2000.
- Derek Abbott, W. W., "Metamaterials in the Terahertz regime," *IEEE Photonics Journal*, Vol. 1, No. 2, 99–118, Aug. 2009.
- Benosman, H. and N. B. Hacene, "Design and simulation of double "S" shaped metamaterial," *IJCSI International Journal of Computer Science Issues*, Vol. 9, No. 2, No 1, 534–537, 1694–0814, ISSN, Mar. 2012.
- Ionescu, D. and M. Kovaci, "About the negative permittivity of some metamaterial composites — Simulational study," *IEEE 17th International Symposium for Design and Technology in Electronic Packaging (SIITME)*, 197–200, 2011.
- Li, J. N., W. Withayachumnankul, S. Chang, and D. Abbott, "Practical method for determining inductance and capacitance of metamaterial resonators," *Electronics Letters*, Vol. 48, No. 4, 225–226, 2012.

Supercontinuum Generation in Elliptical Silicon Nanowire Embedded Spiral Photonic Crystal Fiber

Abdosllam M. Abobaker¹, E. Gunasundari², K. Senthilnathan²,
S. Sivabalan³, K. Nakkeeran⁴, and P. Ramesh Babu²

¹Department of Communications Engineering, College of Electronic Technology, Bani Walid, Libya

²Photonics, Nuclear and Medical Physics Division

School of Advanced Sciences, VIT University, Vellore 632 014, India

³School of Electrical Engineering, VIT University, Vellore 632 014, India

⁴School of Engineering, University of Aberdeen, Aberdeen AB24 3UE, UK

Abstract— In this paper, we design an elliptical core silicon nanowire embedded spiral photonic crystal fiber (SN-SPCF) using fully vectorial finite element method. Further, we analyze the various optical properties, namely, waveguide dispersion, birefringence and effective nonlinearity by varying the ellipticity for a wide range of wavelengths from 0.450 μm to 2.050 μm . The proposed structure exhibits a high birefringence of 0.74143 for a small ellipticity of 0.3 at a longer wavelength of 2.05 μm . Besides, we investigate the evolution of supercontinuum generation both in spectral and temporal domains as a function of ellipticity at 1.550 μm wavelength for an input pulse of width 100 fs and peak power of 50 W in a fiber of 2 mm length. The numerical results corroborate that the proposed SN-SPCF provides a wider bandwidth of supercontinuum (600 to 2600 nm) and the findings of this work may be useful in ultrahigh-resolution optical coherence tomography.

1. INTRODUCTION

In recent times, supercontinuum (SC) generation in photonic crystal fibers (PCF) has attracted considerable attention because of its wide applications in the fields of the optical communications, optical coherence tomography (OCT), optical metrology, time resolved absorption and spectroscopy [1–3]. Photonic crystal fibers are ideal media for SC as the desired dispersion can be achieved to help generate supercontinuum for a specific wavelength. By this way, it is possible to convert a light of fixed wavelength into both longer and shorter wavelengths around the operating wavelength. The basic requirements for the generation of broadband continuum are anomalous group velocity dispersion (GVD) with a small third order dispersion (TOD) and a high nonlinearity at the operating wavelength [4].

Recently, the generation of SC in photonic nanowires (PhNs) has received significant interest because of their unique properties and wide range of applications [5]. The dielectric waveguides with a nanocore diameter exhibit a remarkably strong field confinement, enhanced light-matter interactions and strong control over linear and nonlinear optical properties. When a nanowire made of silicon is embedded into a photonic crystal fiber, the resulting structure is referred to as a silicon nanowire embedded photonic crystal fiber (SN-PCF) wherein the core diameter is lesser than the operating wavelength [6, 7]. This SN-PCF provides the enhanced linear and nonlinear optical properties and hence, it has attracted considerable interest in the recent past. Thus, with this special nanowire, it is possible to generate supercontinuum within a short length of fiber with less input power.

The motivation for choosing a novel biomimetic spiral structure PCF stems from a myriad of possible applications in nonlinear optics, especially, in SCG and pulse compression with the properties of high nonlinearity assisted by tunable dispersion [8]. The main advantages of the spiral PCF are the improved field confinement and the less air filling fraction in comparison to conventional PCF. Here, we report the supercontinuum of bandwidth wider than 1500 nm with less input peak power (50 W) using a short piece (2 mm) of SN-PCF.

In this work, we design a silicon nanowire embedded spiral photonic crystal fiber (SN-SPCF) with elliptical nanocore for generating supercontinuum with the requirements mentioned above. The paper is laid out as follows. In Section 2, we present the design analysis of the proposed structure. In Section 3, we study the optical properties of the fundamental mode, namely, the group velocity dispersion (GVD), third order dispersion (TOD), birefringence and effective nonlinearity by varying the ellipticity of SN-SPCF. Further, we investigate the evolution of SC in both spectral and temporal domains at 1.550 μm wavelength in Section 4. Finally, we summarize the findings in Section 5.

2. DESIGN OF THE PROPOSED SN-SPCF

The schematic cross section of the proposed SN-SPCF is as shown in Fig. 1(a). It is composed of circular air holes in the cladding arranged in a spiral array and an elliptical defected core, with \mathbf{a} and \mathbf{b} being the major and the minor axes diameters, respectively. Generally hybrid waveguides have been fabricated by means of the pressure-cell filling technique, splice-filling technique and direct fiber drawing technique [9]. In the proposed structure, the outer cladding air hole distribution is composed of 9 spiral arms each containing 5 air holes. In each spiral arm, the first air hole is at a distance of $r_0 = 1.2 \mu\text{m}$ from the center and each successive air holes are placed at an angular displacement of θ . The distance of the n th air hole of that spiral arm is $r_n = r_{n-1} + (0.8 \times d_h)$ with an angular displacement of $\theta_n = 360^\circ / (n \times N)$ from the previous hole of the spiral arm. Here, N is the total number of spiral arms and $d_h (= 600 \text{ nm})$ is the diameter of the air hole in each arm.

We study the optical properties of the fundamental mode by increasing the ellipticity (\mathbf{b}/\mathbf{a}) value by keeping \mathbf{a} constant and by varying \mathbf{b} as a function of the wavelength from $0.450 \mu\text{m}$ to $2.050 \mu\text{m}$. We fix the major core diameter as $\mathbf{a} = 550 \text{ nm}$ and slightly increase the ellipticity (\mathbf{b}/\mathbf{a}) from 0.3 to 0.7 in steps of 0.1. At this juncture, we point out that this range of ellipticity (\mathbf{b}/\mathbf{a}) results in a dimension comparable to that of the diameter of the nanowire, i.e., less than $1 \mu\text{m}$ [10]. In the simulation, we fix the diameter of the air-holes in the cladding to be higher than the major core diameter \mathbf{a} to meet with the requirements of SC generation. The electric field distribution of the x -polarized fundamental mode for SN-SPCF with the parameter of \mathbf{b}/\mathbf{a} being 0.5 at $1.55 \mu\text{m}$ wavelength is as shown in Fig. 1(b).

3. LINEAR PROPERTIES

In this section, we delineate the important linear effects, namely, second and third order dispersions and birefringence. It is known that the dispersion does depend on both operating wavelength and the nanocore diameter. The core diameter dependent GVD and TOD of the x -polarized mode have

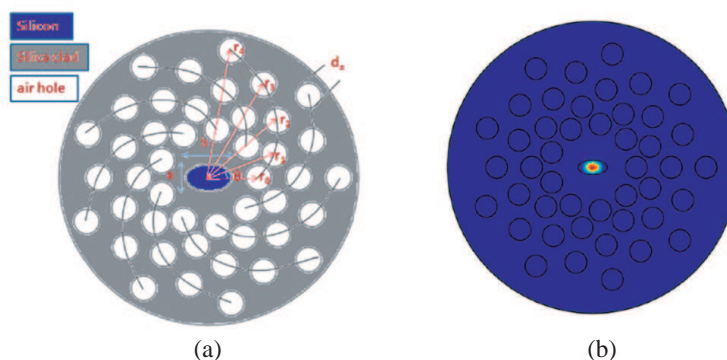


Figure 1: (a) Geometrical structure and (b) mode field distribution of the proposed SN-SPCF with an ellipticity of 0.7.

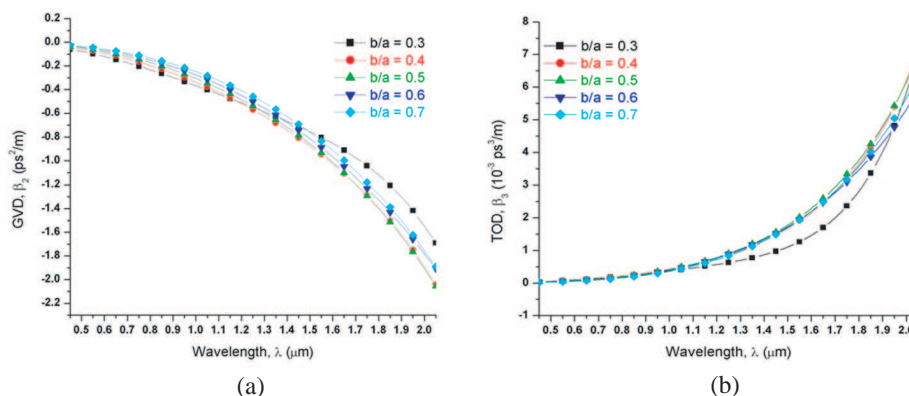


Figure 2: (a) Group velocity dispersion and (b) third order dispersion of the proposed SN-SPCF for various ellipticity.

been determined from the second and third derivatives of the computed n_{eff} . The variations of GVD and TOD of the x -polarized mode over the entire wavelength for various ellipticity are as shown in Figs. 2(a) and (b).

From Fig. 2(a), it is clear that the SN-SPCF exhibits anomalous GVD for all ellipticity at a chosen wavelength as the field distribution inside the elliptical nanocore increases gradually towards the cladding region. Upon increasing the wavelength, the GVD value increases on the negative side as a result of less confinement within the core and the same trend is observed for all ellipticity values. We achieve a less anomalous GVD of $-0.0265 \text{ ps}^2/\text{m}$ for an ellipticity of 0.7 at $0.450 \mu\text{m}$ wavelength. We find almost a flattened TOD up to $1.050 \mu\text{m}$ wavelength for all ellipticity values. It is noticed that for further increase in wavelength, the TOD increases slowly. We report a less value of TOD as $0.018 \times 10^{-3} \text{ ps}^3/\text{m}$ at $0.450 \mu\text{m}$ wavelength for 0.7 ellipticity. Next, we turn to compute the birefringence for the proposed fiber. The SN-SPCF exhibits a high birefringence of 0.4017 for 0.3 ellipticity at $1.55 \mu\text{m}$ wavelength, which is two to three orders of magnitude higher than that of the elliptical PCF (1.94×10^{-2}) and conventional elliptical-hole PCF (4.91×10^{-3}) at $1.55 \mu\text{m}$ [11, 12].

4. NONLINEAR PROPERTY

Due to the small core diameter and high nonlinear index coefficient of silicon ($4 \times 10^{-18} \text{ m}^2/\text{W}$), the SN-SPCF exhibits tight light confinement compared to that of the conventional PCF. The variations of the effective nonlinearity (γ^V) against wavelength of the fundamental mode for various ellipticity values are depicted in Fig. 3. The small core ellipticity exhibits tight mode confinement and very high nonlinearity ($1908 \text{ W}^{-1}\text{m}^{-1}$) at $0.450 \mu\text{m}$ wavelength compared to other ellipticity fibers.

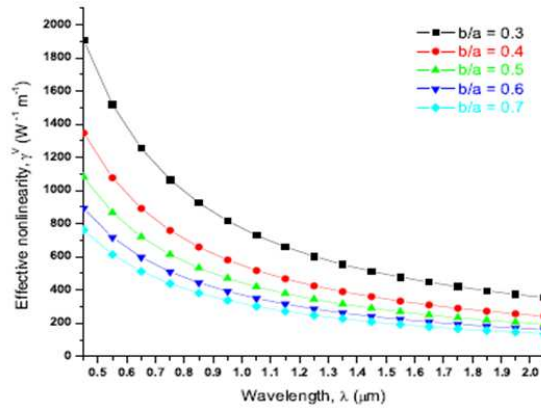


Figure 3: Variation of effective nonlinearity of the SN-SPCF for different ellipticity.

5. SIMULATION OF SUPERCONTINUUM GENERATION

To investigate the generation of SC in SN-SPCF, we employ the modified nonlinear Schrödinger equation in which the loss ($\alpha \approx 0$ and $\alpha^f \approx 0$), higher order dispersion (β_2 and β_3), nonlinear response function ($R(T - \tau)$) and γ^V can be expressed in time domain as follows [13],

$$\frac{\partial A}{\partial z} = -\frac{1}{2} (\alpha + \alpha^f) A - \frac{i}{2} \beta_2 \frac{\partial^2 A}{\partial T^2} + \frac{\beta_3}{6} \frac{\partial^3 A}{\partial T^3} + i\gamma^V \left[1 + \frac{\omega}{\omega_0} \right] A \int_{-\infty}^{\infty} [R(T - \tau) |A|^2] d\tau \quad (1)$$

where, $A(z, T)$ is the field envelope. $R(t)$ is defined by [13], $R(t) = (1 - f_R)\delta(t) + f_R h_R(t)$, with fractional Raman contribution $f_R = 0.043$. The delayed Raman response $h_R(t)$ of silicon is expressed as: $h_R(t) = \Omega_R^2 \tau_1 \exp(-\frac{t}{\tau_2}) \sin(\frac{t}{\tau_1})$, where $\tau_1 = 10 \text{ fs}$ and $\tau_2 = 3 \text{ ps}$ correspond to the Raman shift and Raman gain spectrum, respectively. The pulse propagation in SN-SPCF is solved by symmetrized split-step Fourier method [14].

We consider the input soliton order, N , having an envelope field expression given by [15]: $A(0, t) = N\sqrt{P_0} \text{sech}[\frac{t}{T_0}]$, where P_0 is the peak power and T_0 is the input soliton duration defined as $T_{FWHM}/1.763$. The soliton order of the input pulse $N [= \sqrt{\frac{T_0^2 P_0 \gamma}{\beta_2}}]$ is determined by both pulse and fiber parameters.

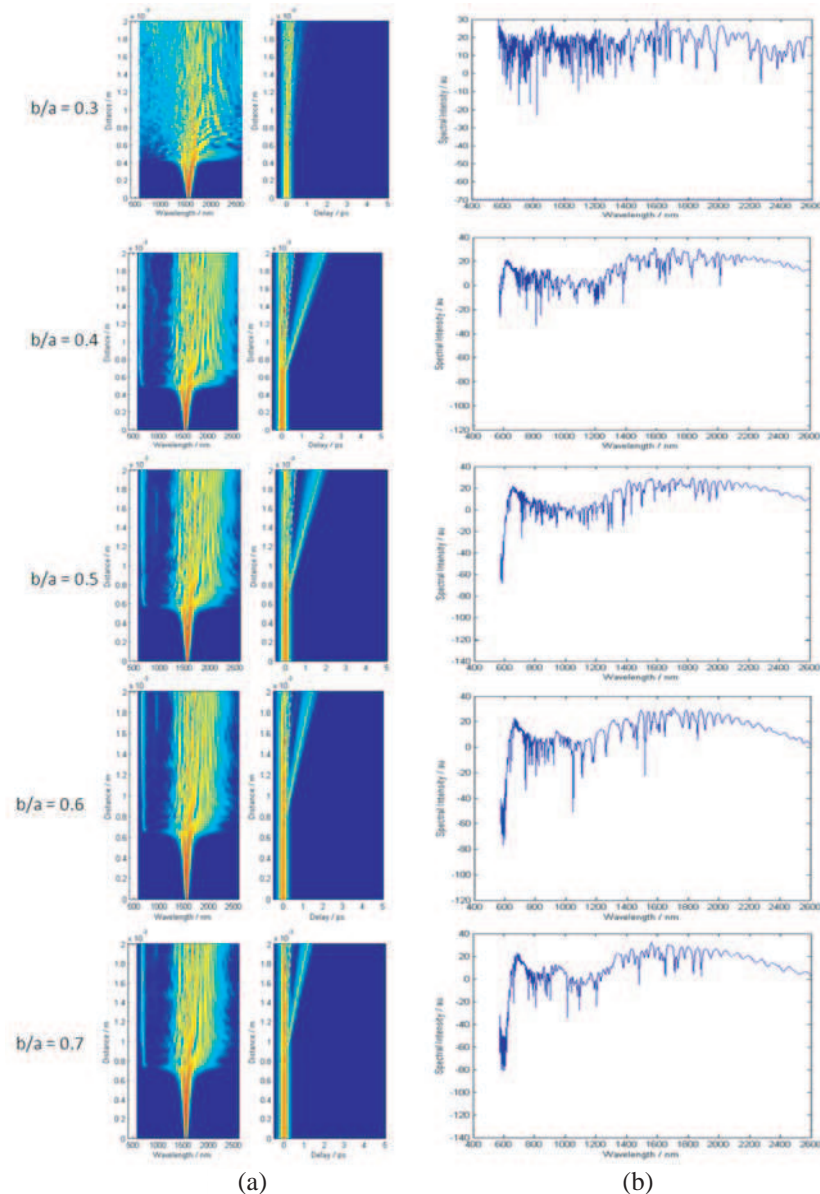


Figure 4: (a) Spectral, temporal evolution and (b) spectral intensity of supercontinuum pulse for 50 W power of different ellipticity at 1.550 μm wavelength.

We consider the propagation of a hyperbolic secant pulse of width 100 fs with a peak power of 50 W in a short piece of fiber (2 mm). Figs. 4(a) and (b) represent the evolution of the waveforms and their spectral components at 1.550 μm wavelength. As can be seen in Fig. 4, a relatively wider SC spectrum (600 to 2600 nm) is observed due to the combined action of self-phase modulation, Raman effect and soliton fission.

6. CONCLUSION

In this paper, we have proposed an elliptical silicon nanowire embedded spiral photonic crystal fiber and studied the optical properties using a fully-vectorial finite element method. We have numerically investigated the supercontinuum generation using a short piece (2 mm) of SN-SPCF at an operating wavelength of 1.55 μm with a less input power of 50 W for the input pulse of 100 fs. Further, we have been able to achieve a wider bandwidth of 2000 nm. We are of the opinion that the proposed SN-SPCF would turn out to be a right candidate for the precise measurement of optical frequencies, high resolution noninvasive medical imaging (optical coherence tomography), atomic spectroscopy and telecommunication wavelength division multiplexing.

ACKNOWLEDGMENT

KSN wishes to thank CSIR [No. 03(1264)/12/EMR-II] and DST [No. SR/FTP/PS-66/2009], Government of India, for the financial support through the sponsored projects. SS wishes to thank DST [No. SR/S2/LOP-0014/2012], Government of India, for the financial support through the sponsored project.

REFERENCES

1. Dudley, J. M., G. Genty, and S. Coen, "Supercontinuum generation in photonic crystal fiber," *Rev. Mod. Phys.*, Vol. 78, No. 4, 1135–1184, 2006.
2. Holzwarth, R., T. Udem, T. W. Hansch, J. C. Knight, W. J. Wadsworth, and P. St. J. Russell, "Optical frequency synthesizer for precision spectroscopy," *Phys. Rev. Lett.*, Vol. 85, No. 11, 2264–2267, 2000.
3. Smirnov, S., J. D. Ania-Castanon, T. J. Ellingham, S. M. Kobtsev, S. Kukarin, and S. K. Turitsyn, "Optical spectral broadening and supercontinuum generation in telecom applications," *Opt. Fiber Technol.*, Vol. 12, No. 2, 122–147, 2006.
4. Liao, M., X. Yan, G. Qin, C. Chaudhari, T. Suzuki, and Y. Ohishi, "A highly non-linear tellurite microstructure fiber with multi-ring holes for supercontinuum generation," *Opt. Express*, Vol. 17, No. 18, 15481–15490, 2009.
5. Tong, L., J. Lou, and E. Mazur, "Single-mode guiding properties of sub-wavelength diameter silica and silicon wire waveguides," *Opt. Express*, Vol. 12, No. 6, 1025–1035, 2004.
6. Biancalana, F., T. X. Tran, S. Stark, M. A. Schmidt, and P. St. J. Russell, "Emergence of geometrical optical nonlinearities in photonic crystal fiber nanowires," *Phys. Rev. Lett.*, Vol. 105, No. 9, 093904–093907, 2010.
7. Gunasundari, E., K. Senthilnathan, S. Sivabalan, M. Abdosllam Abobaker, K. Nakkeeran, and P. Ramesh Babu, "Waveguiding properties of silicon nanowire embedded photonic crystal fiber," *Opt. Materials*, Vol. 36, No. 5, 958–964, 2014.
8. Agrawal, A., N. Kejalakshmy, J. Chen, B. M. A. Rahman, and K. T. V. Grattan, "Soft glass equiangular spiral photonic crystal fiber for supercontinuum generation," *IEEE Photon. Technol. Lett.*, Vol. 21, No. 22, 1722–1724, 2009.
9. Tyagi, H. K., M. A. Schmidt, L. Prill Sempere, and P. S. Russell, "Optical properties of photonic crystal fiber with integral micron-sized Ge wire," *Opt. Express*, Vol. 16, No. 22, 17227–17236, 2008.
10. Salem, A. B., R. Cherif, and M. Zghal, "Rigorous optical modelling of elliptical photonic nanowires," *J. Lightw. Technol.*, Vol. 30, No. 13, 2176–2180, 2012.
11. Lehtonen, M, G. Genty, and H. Ludvigsen, "Supercontinuum generation in a highly birefringent microstructured fiber," *Appl. Phy. Lett.*, Vol. 82, No. 14, 2197–2199, 2003.
12. Yang, Y., G. Kai, Z. Wang, Y. Lu, C. Zhang, T. Sun, Y. Li, L. Jin, J. Liu, Y. Liu, S. Yuan, and X. Dong, "Highly birefringent elliptical-hole photonic crystal fiber with two big circular air holes adjacent to the core," *IEEE Photonics Tech. Lett.*, Vol. 18, No. 24, 2638–2640, 2006.
13. Yin, L., Q. Lin, and G. P. Agrawal, "Soliton fission and supercontinuum generation in silicon waveguides," *Opt. Lett.*, Vol. 32, No. 4, 391–393, 2007.
14. Dudley, J. M. and J. R. Taylor, *Supercontinuum Generation in Optical Fibers*, Cambridge University Press, 2010.
15. Agrawal, G. P., *Nonlinear Fiber Optics*, Academic Press, 2007.

Observation and Phenomenological Interpretation of Shifts in Electrical Resonance of Square Shaped Planar THz Split Ring Resonators

Rahul Kumar¹, Ankit Arora¹, Shaumik Ray², Bala Pesala²,
Enakshi Bhattacharya¹, and Ananth Krishnan¹

¹Department of Electrical Engineering
Indian Institute of Technology Madras, Chennai 600036, India

²CEERI, CSIR Campus, Chennai 600113, India

Abstract— The electrical resonance in Square shaped planar THz Split Ring Resonators (*SqSRR*) is observed at all polarizations of the incident wave. This resonance has been conventionally attributed to dipole oscillations in the arms parallel to the incident E -field (vertical arm), while neglecting the effect of arm perpendicular to the incident E -field (horizontal arm) that has been described in the past as the cut-wire approximation. In order to study the effect of horizontal arm on electrical resonance, several geometrical modifications of *SqSRR* consisting of identical vertical arms with varying horizontal arm lengths, were designed, fabricated and characterized at frequencies from 0.1 to 0.3 THz, at normal incidence. Contrary to the cut wire approximation, significant shift in electrical resonance frequency was observed with varying horizontal arm lengths of *SqSRR*. The presented experimental results and analysis based on the surface current profile in these structures, indicate the necessity to include the effect of horizontal arm in design of *SqSRR*. The shifts in plasma frequency with variation in horizontal arm length is explained as dilution of the effective electron density of the vertical arm. Simple modification in existing models for plasma frequency and electrical resonance frequency is proposed to consider the effect of horizontal arm lengths. Experimental and simulated results were found to be in good agreement with the proposed model.

1. INTRODUCTION

The first experimental demonstration of negative index material was achieved at microwave frequency by using periodic arrangement of circular Split Ring Resonator (*SRR*) structures (for negative effective relative permeability (μ_r)) and thin metallic wires (for negative effective relative permittivity (ϵ_r)) in alternating layers [1]. Since the first experimental demonstration, several efforts have been made to increase the operating frequency of *SRR* by reduction of size or by modification of shapes of *SRR* or both [2–5]. Among these structures, square shaped *SRR* (*SqSRR*) is one of the popular geometries because of the ease in micro and nanoscale fabrication of Cartesian structures [2–5]. However, apart from the magnetic resonance, *SqSRR* also exhibit an electrical resonance in all the orientations [3, 6]. This resonance is attributed to oscillatory current in the vertical arm and generally referred to as the cut-wire approximation of *SqSRR* [3, 6]. To the best of our knowledge, thus far, in the cut-wire approximation, the effect of horizontal arms has always been neglected. In this work, we have designed, fabricated and characterized several modifications of planar *SqSRR* to experimentally investigate the effect of horizontal arm length on electrical resonance for frequencies from 0.1 to 0.3 THz at normal incidence. We show that, though in electrical resonance the vertical arms play dominant role, effect of horizontal arm length can not be neglected. We have also provided a simple modification factor in the analytical expression of the plasma frequency ($f_p = \omega_p/2\pi$) given in [7] and electrical resonance frequency (f_0) given in [8] to explain the blue shift in electrical resonance with decrease in horizontal arm length. The modified analytical models were found to be in good agreement with experimental and simulated frequency of minimal transmission f_m . These results provide a better insight into the electrical resonance and will be helpful in designing *SqSRR* based filters in THz frequencies (0.1 to 10 THz) [9] for applications like sensing, security systems, imaging, explosive detection [10–12], etc..

2. METHODOLOGY

The geometrical parameters of *SqSRR* exhibiting resonances in THz region were determined by commercial full wave Maxwell's equation solver [13]. The top view of the unit cell along with optimized geometrical parameters of *SqSRR* suitable for the experimental setup is shown in Fig. 1(a).

The boundary conditions of unit cell used in simulation to maintain the incident polarization (shown by red arrows in Fig. 1(a)) are same as mentioned in [14]. The refractive index of glass substrate at frequencies ranging from 0.1 THz to 0.3 THz was taken as 2.45 [15]. *SqSRR* was defined using 120 nm thick gold layer with a conductivity of 58×10^6 S/m [16].

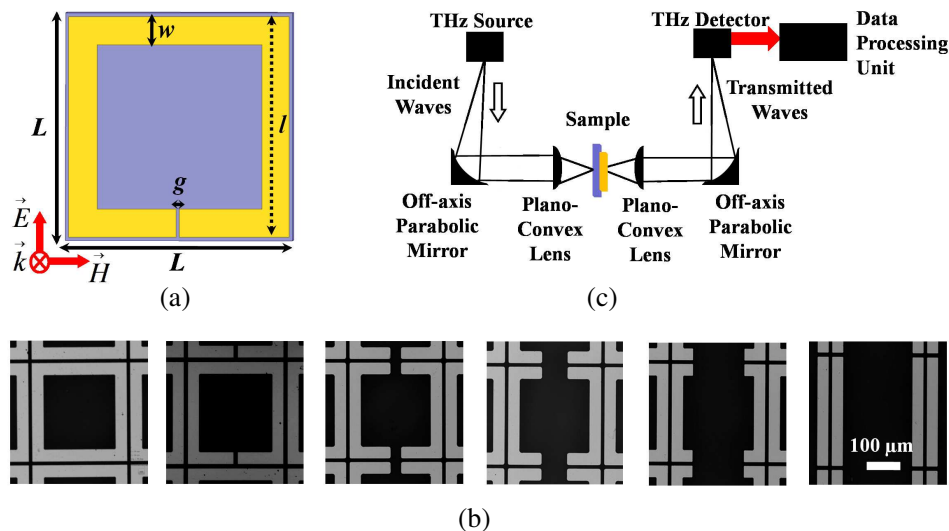


Figure 1: (a) Top view of unit cell along with incident wave polarization (shown in red arrows). Geometrical parameters are: unit cell length $L = 288 \mu\text{m}$, metal arm length $l = 280 \mu\text{m}$, arm width $w = 36 \mu\text{m}$, slit width $g = 8 \mu\text{m}$, metal thickness $t = 120 \text{ nm}$, substrate thickness $t_{sub} = 180 \mu\text{m}$. (b) Micro graphs of some of the fabricated structures. Common scale is shown in the last micro graph. (c) Schematic of the characterization setup.

Structures corresponding to optimized geometrical dimensions were fabricated on $\approx 18 \text{ mm} \times 18 \text{ mm} \times 180 \mu\text{m}$ glass substrate. A 20 nm thick Cr layer for adhesion followed by a 120 nm thick Au layer was deposited using electron beam evaporation at 100°C . The deposited Cr/Au layers were patterned using UV photolithography technique followed by wet etching to obtain the final structures. The top views of some of the fabricated structures are shown in Fig. 1(b).

A Continuous-Wave THz transmitter/receiver arrangement (Toptica Photonics AG) was used to obtain transmission characteristics of fabricated structures. The schematic of the characterization setup is shown in Fig. 1(c). The obtained photocurrents were normalized w.r.t. the photocurrents of a bare glass wafer of same thickness.

3. RESULTS AND DISCUSSION

Experimental transmission characteristics of Closed Ring (CR) and *SqSRR* from 0.1 THz to 0.3 THz shows a single dip in transmission occurring at ≈ 0.162 THz and ≈ 0.164 THz respectively, as shown in Fig. 2(a). In order to establish the exact mechanism of resonance, the instantaneous surface current density of CR and *SqSRR* were calculated at f_m (shown in Fig. 2(b)). It can be seen that, the surface current density in vertical arms are oscillatory in nature, going from bottom to top as shown (or bottom to top depending on the phase of incident E -field, not shown in Figure). In literature, this current has been attributed to dipole oscillation of electrons of vertical arm, in presence of incident E -field. The corresponding resonance is termed as the electrical resonance, as this resonance is due to coupling of incident E -field with structures under study. In earlier reports, only vertical arms were considered to be participating in electrical resonance, therefore the electrical response of CR and *SqSRR* were approximated to be equivalent to a cut-wire geometry as shown in Fig. 2(c). But, on meticulously analyzing the instantaneous surface current densities of CR and *SqSRR* (shown in Fig. 2(b)), the electrons seem to be moving into horizontal arm from the bottom extrema of vertical arms and out of horizontal arm at top extrema of vertical arms. The possible reason for this current can be the movement of electrons in horizontal arms in response of the creation of a potential gradient along horizontal arms due to momentary charge accumulation in the vertical arms at the top and bottom (as shown in Fig. 2(d)). This movement of electrons reduces the net concentration of charges accumulated in vertical arms.

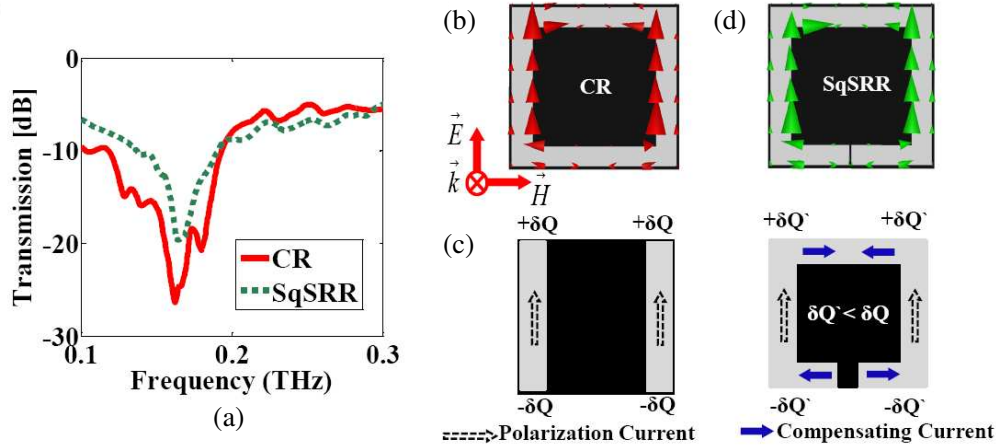


Figure 2: (a) Experimental transmission characteristics of *CR* and *SqSRR*. (b) Instantaneous surface current profile of *CR* and *SqSRR* at frequency of minimum transmission f_m . Polarization of incident EM waves is given in red color arrows. (c) Conventional Cut-wire approximation. (d) Modified model after taking horizontal arm into consideration. Accumulated charges at tip of vertical arm will be diluted be due to presence of surface current in horizontal arm.

The simulated transmission characteristics of *SqSRR* with decreasing horizontal arm length, shown in Fig. 3(a), shows the significant blue shift in resonance frequency, i.e., moving from closed ring to vertical stripes. To understand the physical phenomenon behind this blue shift, we started with the plasma frequency expression (ω_p) for periodic structures of thin wires given in [7] by Eq. (1).

$$\omega_p^2 = \frac{n_{eff} e^2}{\epsilon_0 m_{eff}} \quad (1)$$

where n_{eff} is effective electron density in a unit cell, e is charge of electron, m_{eff} is effective mass of electron and ϵ_0 is permittivity of free space. In case of *SqSRR*, if the effect of the horizontal arms are neglected, the effective electron density n_{eff} can be given as,

$$n_{eff} = 2 \times n \frac{lw}{L^2} \quad (2)$$

where n is electron density in bulk medium, l is length, w is width and L is lattice constant (refer to Fig. 1(a)). The factor of 2 comes in the equation due to the presence of 2 vertical arms that are symmetric about the vertical axis. In this study, all *SqSRR* structures considered were symmetric about vertical axis and asymmetric modifications even though possible are not considered for simplicity. If the effect of horizontal arms are considered, n_{eff} will decrease due to flow of accumulated charges from vertical arms into the horizontal arms. In Eq. (1), m_{eff} is assumed to be constant for all the variation of horizontal arms, as in all cases, the surface current densities in vertical arms are of the same order. Due to the vertical symmetry, let us consider only the left half of the unit cell. Now, assuming uniform distribution of electrons over the entire length of metal in the left half of the unit cell (as electron will quickly redistribute along horizontal arm to nullify potential gradient), the effective metal length on left half of unit cell can be rewritten as
Effective Metal Length = Vertical Arm length + Top Horizontal Arm Extension + Bottom Horizontal Arm Extension

$$\begin{aligned} \text{Each horizontal arm extension} &= \frac{l}{2} - w - \frac{g}{2} \\ \text{Effective Metal Length} &= 2l - 2w - g \end{aligned}$$

Now, the effective electron density will be reduced and let it be denoted by ($n_{eff_{modified}}$).

$$n_{eff_{modified}} = n_{eff} \times \frac{l}{(2l - 2w - g)} \quad (3)$$

where g is gap width. In case of vertical stripes (cut-wire), the above modification will reduce to Eq. (2). On substituting Eq. (3) in Eq. (1) and representing it in terms of cut-wire plasma frequency we get,

$$\omega_{p_{modified}}^2 = \omega_{cutwire}^2 \frac{l}{(2l - 2w - g)} \quad (4)$$

where,

$$\omega_{cutwire}^2 = \frac{n_{eff} e^2}{\epsilon_0 m_{eff}}. \quad (5)$$

Also due to finite length of vertical arm, ϵ_r is negative between f_0 and f_p [8]. This lower cut-off frequency (f_0) has been empirically derived in [8] as,

$$f_0 = [c_{light}/\sqrt{2\pi}l] \times [a_0 \ln(l/\Delta) + a_1]^{-1/2} \quad (6)$$

where c_{light} is speed of light in vacuum, Δ is separation between vertical arm of adjacent unit cells, a_0 and a_1 are fitting parameters. Since, we have assumed uniform distribution of electrons over the entire length of metal, l in the above expression can be modified as,

$$f_{0_{modified}} = [c_{light}/\sqrt{2\pi}(2l - 2w - g)] \times [a_0 \ln((2l - 2w - g)/\Delta) + a_1]^{-1/2} \quad (7)$$

In order to experimentally validate the effect of horizontal arm length, several *SqSRR* structures with varying horizontal arm length were fabricated and characterized. Variation of modified plasma frequency ($f_{p_{modified}} = \omega_{p_{modified}}/2\pi$), modified resonant frequency ($f_{0_{modified}}$), f_m after normalizing w.r.t. their cut-wire response as function of horizontal length are plotted in Fig. 3(b). It can be seen that they are in good agreement. Mismatch between experimental and simulated results is attributed to the difference in material constants and fabrication tolerances.

Same concept can be extended to explain the origin of negative epsilon in case of EEMR [17]. Due to asymmetry along the direction of external E -field, at EEMR the charge gradient in one arm dominates over other, thus giving raise to circulating current. This circulating current leads to the distribution of effective electrons over the complete circumference of *SqSRR*, resulting in substantial reduction of plasma frequency.

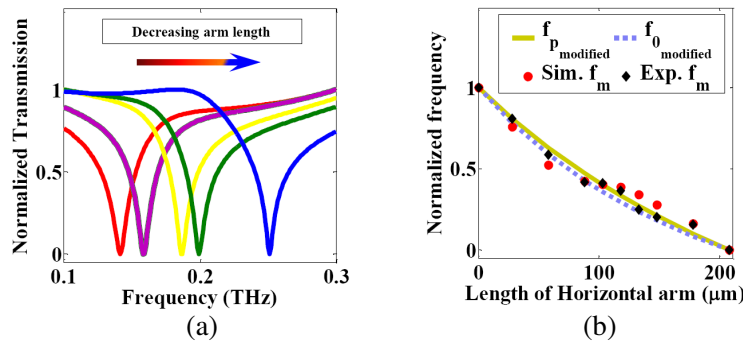


Figure 3: (a) Simulation showing blue shift in normalized transmission spectra with decrease in length of horizontal arm. Red color and Blue color transmission spectra corresponds to *CR* and vertical strips respectively. (b) Normalized modified plasma frequency ($f_{p_{modified}}$), electrical resonance frequency ($f_{0_{modified}}$) and the corresponding transmission (f_m) versus length of horizontal arm. These frequencies are normalized w.r.t. the corresponding cut-wire response.

4. CONCLUSION

We have investigated the effect of horizontal arm length on electrical resonance. We showed that, contrary to conventional cut-wire approximation, the horizontal arm plays a significant role in determining the electrical resonance by providing path for flowing of momentarily accumulated charges at ends of the vertical arm into horizontal arm. We modelled this effect, assuming uniform distribution of electrons over the entire length of metal and found it to be in good agreement with simulated and experimental results. These results will be helpful in better designing of *SqSRR* for various applications like filters, sensors, etc. in THz frequencies.

ACKNOWLEDGMENT

Author would like to acknowledge NPMASS for providing HFSS license and CNNP for providing fabrication facilities.

REFERENCES

1. Smith, D. R., W. J. Padilla, D. C. Vier, S. C. Nemat-Nasser, and S. Schultz, “Composite medium with simultaneously negative permeability and permittivity,” *Physical Review Letters*, Vol. 84, No. 18, 4184, 2000.
2. Dolling, G., M. Wegener, C. M. Soukoulis, and S. Linden, “Negative-index metamaterial at 780 nm wavelength,” *Optics Letters*, Vol. 32, No. 1, 53–55, 2007.
3. Linden, S., C. Enkrich, M. Wegener, J. Zhou, T. Koschny, and C. M. Soukoulis, “Magnetic response of metamaterials at 100 terahertz,” *Science*, Vol. 306, No. 5700, 1351–1353, 2004.
4. Kafesaki, M., I. Tsiapa, N. Katsarakis, T. Koschny, C. M. Soukoulis, and E. N. Economou, “Left-handed metamaterials: The fishnet structure and its variations,” *Physical Review B*, Vol. 75, No. 23, 235114, 2007.
5. Shalaev, V. M., “Optical negative-index metamaterials,” *Nature Photonics*, Vol. 1, No. 1, 41–48, 2007.
6. Koschny, T., M. Kafesaki, E. N. Economou, and C. M. Soukoulis, “Effective medium theory of left-handed materials,” *Physical Review Letters*, Vol. 93, No. 10, 107402, 2004.
7. Pendry, J. B., A. J. Holden, W. J. Stewart, and I. Youngs, “Extremely low frequency plasmons in metallic mesostructures,” *Physical Review Letters*, Vol. 76, No. 25, 4773, 1996.
8. Koschny, Th, P. Marko, D. R. Smith, and C. M. Soukoulis, “Resonant and antiresonant frequency dependence of the effective parameters of metamaterials,” *Physical Review E*, Vol. 68, No. 6, 065602, 2003.
9. Ferguson, B. and X.-C. Zhang, “Materials for terahertz science and technology,” *Nature Materials*, Vol. 1, No. 1, 26–33, 2002.
10. Yen, T.-J., W. J. Padilla, N. Fang, D. C. Vier, D. R. Smith, J. B. Pendry, D. N. Basov, and X. Zhang, “Terahertz magnetic response from artificial materials,” *Science*, Vol. 303, No. 5663, 1494–1496, 2004.
11. Fitzgerald, A. J., E. Berry, N. N. Zinovev, G. C. Walker, M. A. Smith, and J. M. Chamberlain, “An introduction to medical imaging with coherent terahertz frequency radiation,” *Physics in Medicine and Biology*, Vol. 47, No. 7, R67, 2002.
12. Federici, J. F., B. Schulkin, F. Huang, D. Gary, R. Barat, F. Oliveira, and D. Zimdars, “THz imaging and sensing for security application sexplosives, weapons and drugs,” *Semiconductor Science and Technology*, Vol. 20, No. 7, S266, 2005.
13. High Frequency Structural Simulator (HFSS).
14. Yasar-Orten, P., E. Ekmekci, and G. Turhan-Sayan, “Equivalent circuit models for split-ring resonator arrays,” *PIERS Proceedings*, 534–537, Cambridge USA, July 5–8, 2010.
15. Naftaly, M. and R. E. Miles, “Terahertz time-domain spectroscopy for material characterization,” *Proceedings-IEEE*, Vol. 95, No. 8, 1658, 2007.
16. HFSS material data base.
17. Katsarakis, N., T. Koschny, M. Kafesaki, E. N. Economou, and C. M. Soukoulis, “Electric coupling to the magnetic resonance of split ring resonators,” *Applied Physics Letters*, Vol. 84, No. 15, 2943–2945, 2004.

Photonic Crystal Slabs for Biosensing

S. Jahns, F. von Oertzen, T. Karrock, Y. Nazirizadeh, and M. Gerken

Institute of Electrical and Information Engineering, Christian-Albrechts-Universität zu Kiel, Germany

Abstract— We investigated the functionalization of photonic crystal slabs with aptamers for the label-free detection of biomolecules. Photonic crystal slabs are slab waveguides with a periodic nanostructure that supports quasi guided modes coupling to far field radiation. Measurements were performed with light at normal incidence to the photonic crystal slab. The influence of the nanostructure duty cycle as well as the high index layer thickness is investigated for the surface and the bulk sensitivity. Nanoimprint lithography with subsequent deposition of a high index layer and biofunctionlization is presented as one approach for fabricating photonic crystal slab biosensors. In comparison photonic crystal slabs fabricated by injection-molding are considered. Oblique angle layer deposition is introduced as a means to achieve structured high index layers. Results obtained with wavelength dependent measurements are compared to simple intensity measurements in a particular wavelength range. Both methods are applicable for label-free detection. In a spectrometer-free setup we measured the binding kinetics of a 250 nM solution of the protein thrombin to the photonic crystal surface functionalized with aptamers.

1. INTRODUCTION

Label-free and compact biosensors get more and more in focus for point-of-care applications. Typically, they consist of a selective biological recognition component (receptor) connected directly with the transducer [1, 2]. The transducer transforms the binding kinetics into a detectable signal. Depending on the type of transducer the signal can be detected by, e.g., an electrochemical, colorimetric, or optical read-out system [3–5]. Using photonic crystal slabs (PCS) as the base platform for biosensors a label-free, sensitive, compact and cost-efficient system may be realized [6–8]. PCS are waveguides with a periodic nanostructure in a high refractive index material. Due to the nanostructure quasi guided modes form and may couple to far-field radiation. These modes can be excited in transmission as well as in reflection measurements and are the origin of guided mode resonances (GMR) in the optical spectrum. The quasi guided modes in the high-index layer have an evanescent fraction propagating above the PCS surface. This evanescent fraction interacts with the sample volume close to the PCS surface and produces a shift in the spectrum of the GMR caused by a refractive index change due to a mass change on the surface. By functionalizing the surface with, e.g., aptamers the protein binding kinetics results in a wavelength shift of the GMR, which may be tracked in real time with an optical read-out system [11–13]. Especially the sensitivity of the PCS to mass changes on its surface is an important factor in realizing sensitive protein detection in the pM range. Thus, in the design of PCS for protein binding the sensitivity to small refractive index changes in a thin layer above the surface needs to be optimized. This “surface sensitivity” requires a different optimal structure compared to the bulk sensitivity. Therefore, we investigated the influence of the duty cycle of the nanostructure as well as the influence of the high refractive index layer thickness. Additionally, a new approach to optimize the surface sensitivity is given by structuring the high refractive index layer using oblique angle deposition. Finally, we demonstrate label-free detection of 250 nM thrombin with our sensor using first a spectrometer based and then a compact camera based measuring setup.

2. FABRICATION OF PHOTONIC CRYSTAL SLABS

We realized photonic crystal slabs via UV nanoimprint lithography. First, the nanostructure is transferred from a glass master into a stamp consisting of polydimethylsiloxane (PDMS). Sylgard 184 and Curing Agent (*DOW Corning*) were mixed in a ratio of 8 : 1 for 15 minutes in a mixing tube (*IKA*). Then the PDMS is poured over the glass master placed within a teflon adapter. This is followed by a 15-minute evacuation inside a vacuum chamber to remove all bubbles from the PDMS. Afterwards, the PDMS is hardened in an oven at 130°C for 20 minutes. When the PDMS is hardened, it is cut out of the adapter and is pulled off the glass master. The glass master and thus the fabricated PCS have a period $\Lambda = 400$ nm, a structure depth $t = 150$ nm, and a duty cycle of 40 : 60.

For sample fabrication 25×25 mm² glass substrates with a thickness of 1 mm were cleaned with acetone and isopropanol for 15 minutes each in an ultrasonic bath and then were dehydrated on

a hotplate at 160°C for 10 minutes. After dehydration the glass substrates are cooled down for 2 minutes before 150 μl of Amoprime (*AMO GmbH*) are spin coated for 30 seconds at 3000 rpm onto the substrates to generate a 200-nm adhesive layer. Thereafter, the substrates were baked on a hotplate for 2 minutes at 115°C and cooled down for another 2 minutes. Now 150 μl of the photoresist Amonil (*AMO GmbH*) are spin coated with the same parameters as used before. To transfer the nanostructure into the photoresist the PDMS stamp is pressed carefully into the resist and the resist is hardened for 1 minute with a UV halogen lamp with the stamp on top. After that the PDMS stamp was pulled off the resist layer and the high refractive index layer of silicon monoxide (SiO_x) was deposited by thermal evaporation. By positioning the substrates at different oblique angles we achieved angle-dependent deposition layers [10].

Another way to fabricate PCS is to use injection molding for nanostructured nickel mold replication and sputtering for the high refractive index layer. As described in detail in [9] a process has been demonstrated, in which the nanostructured nickel mold master was assembled to an adapter and positioned into a two-part injection-molding tool. 245°C hot PMMA was injected into a down to 0.4 mbar evacuated and 135°C warm injection molding tool. After cooling down to 45°C the molding tool was opened and the nanostructured PMMA was baked once again avoiding unwanted polarization rotation caused possibly by residual mechanical stress inside the material. In the last fabrication step the nanostructured PMMA was deposited with tantalum pentoxide (Ta_2O_5) via reactive sputtering.

3. DESIGN OPTIMIZATION

3.1. Duty Cycle and Layer Thickness

Sensitivity measurements were performed by evaluating transmission spectra. The PCS was placed on a microscope plate between two crossed polarization filters as described in [9]. The halogen lamp of the microscope was used as excitation source. In this measurement configuration only light interacting with the quasi-guided modes is transferred to the objective of the microscope, which is coupled to a spectrometer. The surface of the PCS was covered sequentially with two liquids with two different refractive indices to determine the bulk sensitivity. Changing the refractive index (Δn) from $n = 1.33$ (water) to $n = 1.38$ (glycerol-water-solution) above the PCS surface results in a shift ($\Delta\lambda$) of the guided mode resonance (GMR) detectable with a spectrometer. To calculate the bulk sensitivity $\Delta n/\Delta\lambda$ the shift of the resonance with the highest intensity was tracked.

For determining the surface sensitivity we first measured the GMR with water as the surrounding medium. Then we evaporated a 25 nm thick lithium fluoride (LiF) layer with a refractive index of $n = 1.39$ on top of the fabricated PCS and repeated the measurement. The surface sensitivity was then calculated by comparing both resonance wavelengths and dividing the resonance shift by the refractive index difference of water and LiF.

With these characterization methods and using the PCS fabricated with the injection-mold process we investigated the influence of the duty cycle and the layer thickness on the bulk as well as on the surface sensitivity. The bulk sensitivities range from 31.5 nm/RIU (RIU = refractive index unit) for a duty cycle of 0.2 and a high-index layer thickness of 301 nm to 138 nm/RIU for a duty cycle of 0.7 and a high-index layer thickness of 99 nm. This is a 4.38 fold enhancement. As Figure 1 shows, a high refractive index layer thickness of 99 nm causes a maximum for both sensitivities. But comparing the results of the duty cycle the maximum of the surface sensitivity is obtained for a duty cycle of 0.5 whereas a duty cycle of 0.7 causes a maximum for the bulk sensitivity. As shown by Nazirizadeh et al. [8], the mode is pulled up to the analyte area until it passes a state, where it has a maximum interaction area with the surface of the nanostructure. This may explain the differing behavior of the surface sensitivity.

3.2. Oblique Angle Deposition

Another approach to enhance the surface sensitivity is to structure the high refractive index layer additionally by oblique angle deposition. Here, we used first the finite difference time domain (FDTD) to simulate the behavior of the surface and bulk sensitivities corresponding to various deposition angles. In the simulations the sensitivities are calculated for the cases described in the last section. In Figure 2 the bulk (a) and the surface (b) sensitivities are plotted as a function of the high-index layer thickness and the deposition angle. The maximum of 93 nm/RIU for the bulk sensitivity at a deposition angle of 0° is obtained for a layer thickness of 125 nm. Changing the deposition angle to be 10° causes an improvement of 7% for the bulk sensitivity keeping the layer thickness constant. In contrast, for the surface sensitivity the maximum value of 58 nm/RIU for a

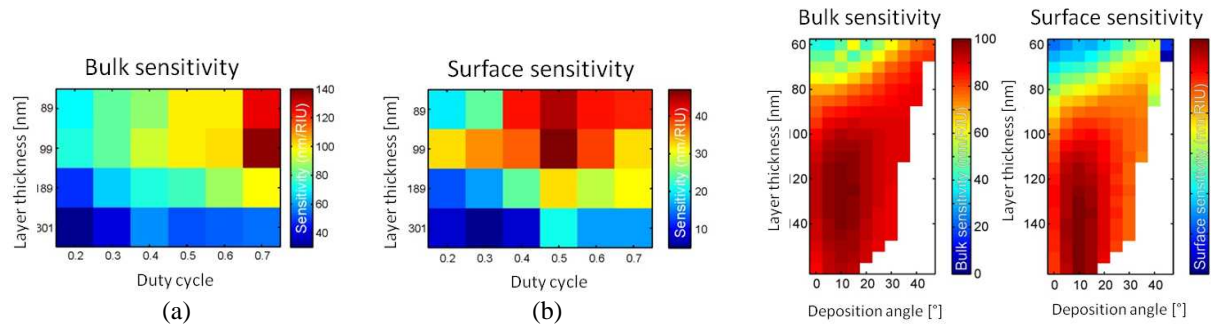


Figure 1: Results of (a) bulk and (b) surface sensitivity measurements as a function of duty cycle and layer thickness.

Figure 2: Simulation results of (a) bulk and (b) surface sensitivity as a function of layer thickness and deposition angle.

layer thickness of 135 nm and a deposition angle of 10° . This corresponds to a 16% enhancement compared to the normal incidence deposition. For the bulk sensitivity the simulated results were confirmed with experimental results as shown in [10].

4. PHOTONIC CRYSTALS AS BIOSENSORS

4.1. Protein Detection with Spectrometer

First, we functionalized the surface of PCS fabricated via nanoimprint lithography with thrombin binding aptamers [10]. We tested the PCS sensor within a fluid cell by evaluating the resonance wavelength shift during thrombin binding with a spectrometer setup. We use the same spectrometer setup as described in chapter III. A. For Figure 3 the peak wavelength of the GMR was tracked over time. To generate a baseline a neutral tris-HCl-buffer (pH 7.4) is filled inside the fluid cell. After 10 minutes the pure buffer is replaced by a 250 nM thrombin-buffer solution. Due to thrombin association to the surface of the PCS the wavelength increases until all aptamers are saturated with thrombin. Washing again with pure buffer the unbound thrombin is washed away and the wavelength decreases a bit. Regeneration of the sensor was achieved by replacing the pure buffer with slightly acid buffer. This caused a different folding of the aptamers and therefore a dissociation of the bound thrombin. As shown we can repeat this measuring sequence with nearly the same results. The association, dissociation, and regeneration kinetics of 250 nM thrombin are clearly visible in the wavelength shift of the GMR.

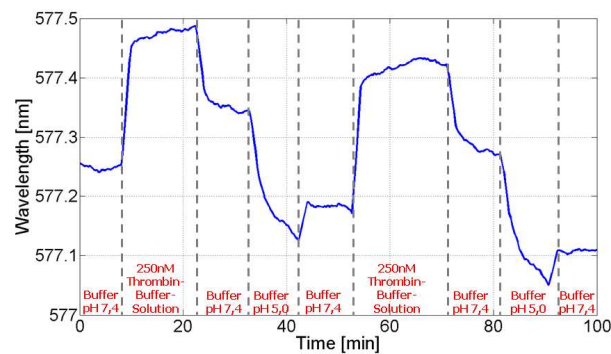


Figure 3: Resonance wavelength shift resulting from association, dissociation and regeneration kinetics of 250 nM thrombin solution.

4.2. Protein Detection without Spectrometer

Next we investigated a measurement configuration without a spectrometer. This spectrometer-free setup is particularly promising for parallel detection of many functionalized spots with a camera. The wavelength shift is transformed into an intensity change using a colored light emitting diode (LED) as excitation source and again crossed polarization filters. The resulting intensity change may be observed with a simple CMOS sensor of a camera [12] or a photodiode [13].

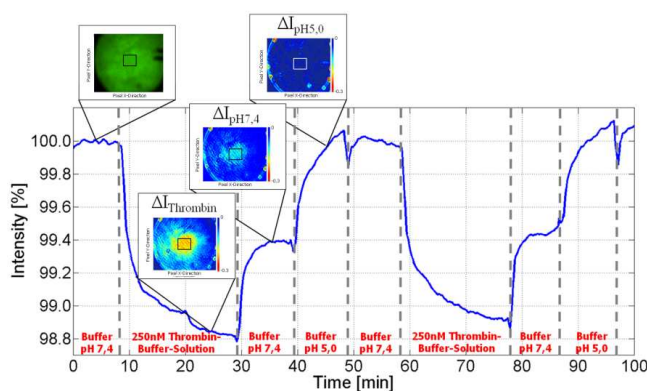


Figure 4: Association, dissociation and regeneration kinetics of 250 nM thrombin solution observed without spectrometer.

Initially, the thrombin detection was repeated with the same measuring sequence mentioned before using the camera setup. Figure 4 shows the intensity values corresponding also to the association, dissociation and regeneration kinetics. The wavelength increase results in an intensity reduction and the wavelength decrease in an intensity increase.

5. CONCLUSION

We investigated different design possibilities to improve the sensitivity of a PCS biosensor. By varying the duty cycle and the layer thickness of the PCS we identified a duty cycle of 0.5 and a layer thickness of 99 nm as optimal values for a high surface sensitivity. Depositing the high-index layer with the substrates tilted to 10° improves the surface sensitivity additionally. Furthermore, a label-free detection of 250 nM thrombin was demonstrated with a spectrometer setup as well as with a compact and spectrometer-free camera setup. Particularly the camera-based configuration has a high miniaturization potential paving the way towards smartphone biosensing. This approach is promising for mobile biosensors applicable, for example, for home diagnostics.

ACKNOWLEDGMENT

The authors acknowledge support by the German Federal Ministry of Education and Research (BMBF) within the project BioCard (0316145B).

REFERENCES

- Scheller, F., et al., *Cur. Opt. Biotechnol.*, Vol. 12, 35–40, 2001.
- Qureshi, A., et al., *Sens. Actuat. B*, 62–76, 171–172, 2012.
- Wang, Y., et al., *Chem. Commun.*, Vol. 22, 2520–2522, 2008.
- Jung, L., et al., *Sens. Actuat. B*, Vol. 129, 372–379, 2008.
- Lifson, M. A., et al., *Anal. Chem.*, Vol. 86, 1016–1022, 2014.
- Magnusson, R., et al., *Sensors*, Vol. 11, 1476–1488, 2011.
- Han, J., et al., *Anal. Chem.*, Vol. 85, 3104–3109, 2013.
- Threm, D., et al., *Journal of Biophotonics*, Vol. 5, Nos. 8–9, 601–616, 2012.
- Nazirizadeh, Y., et al., *Opt. Mater. Express*, Vol. 3, 556–565, 2013.
- Nazirizadeh, Y., et al., *Opt. Express*, Vol. 21, 18661–18670, 2013.
- Lin, S.-F., et al., *Sensors*, Vol. 11, No. 9, 8953–8965, 2011.
- Jahns, S., et al., *Proc. IEEE Sensors*, Baltimore, USA, 2013.
- Nazirizadeh, Y., et al., *Opt. Express*, Vol. 18, 19120–19128, 2010.

Polymer-based Two Dimensional Photonic Crystal for Biosensing Application

Tatsuro Endo

Department of Applied Chemistry, Osaka Prefecture University, Osaka, Japan

Abstract— We experimentally demonstrate an ultra-sensitive and polymer-based two-dimensional photonic crystal (2D-PhC) cavity optical sensor. The device was fabricated with polymer on silicon substrate by using electron beam lithography (EBL) and operated near its resonance at 532 nm. Using 2D-PhC cavity optical sensor, reflection intensity was 60 times higher than without cavity. In addition, coating the sensor surface using layer-by-layer (LbL) assembly methodology by deposition of cationic (poly(sodium 4-styrenesulfonate)) and anionic (poly(allylamine hydrochloride)) layers for produces a different reflection intensity change. By deposition of LbL layers using 2D-PhC cavity optical sensor, reflection intensity was decreased systematically and high sensitively (at least 1 layer (thickness: 2 nm [1])). Furthermore, using this optical sensor, high sensitive detection of DNA hybridization could be achieved.

1. INTRODUCTION

PhCs are an attractive sensing platform because PhC provide strong light confinement which depend on the size and periodicity. In addition, optical response of PhCs are sensitive to surrounding refractive index changes. Hence, using PhCs, we have been developed polymer-based high sensitive biosensors that utilize the detection of surrounding refractive index change by the antigen-antibody reaction [2]. However, to develop the more sensitive PhC-based label-free biosensor, investigation on the PhC design is significant challenge.

PhCs can be designed to localize the electric field in the low refractive index region (e.g., air gap), which makes the sensors extremely sensitive to a small refractive index change. By introducing a point cavity into a PhC, defect states can be pulled down from the air band or up from the substrate band [3]. The corresponding optical spectrum shows narrow reflection peaks inside the photonic band gap (PBG), whose precise position is determined by the refractive index of the gap (Fig. 1). Thus, the presence of molecules inside the gaps can be detected by monitoring a large reflection intensity change. In this study, we designed a 2D-PhC cavity optical sensor that is capable of monitoring of surrounding refractive index change on the gap walls.

Based on these back grounds, we tried to design and fabricate the polymer-based two-dimensional photonic crystal (2D-PhC) cavity optical sensor for biosensing applications. By using polymers for fabrication of 2D-PhC, biosensor will be realized by using more simplified fabrication techniques such as a nanoimprint lithography (NIL). In addition, based on the optical characteristics of polymers, PBG will be formed in the visible region. As a result, using this polymer-based 2D-PhC for biosensing application, sensor system can be established using cost effective optical set up.

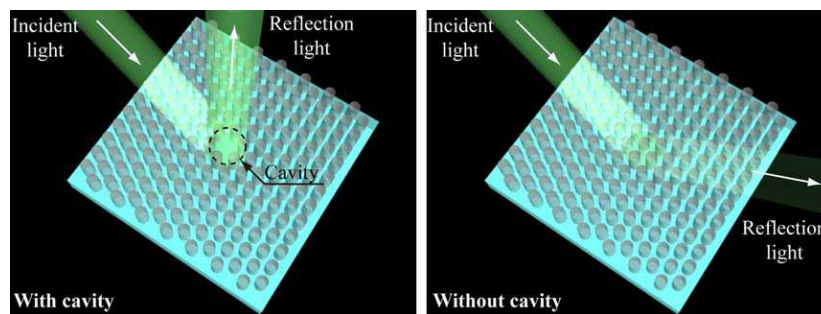


Figure 1: Schematic illustration of 2D-PhC cavity optical sensor. By introducing a point cavity into a PhC, reflection light will be drastically changed by the surrounding refractive index change.

2. EXPERIMENTS AND RESULTS

For the fabrication of the polymer-based 2D-PhC cavity optical sensor, negative tone electron beam resist (NEB22) was coated (thickness: 400 nm) onto the silicon substrate. The triangular

configured pillar array 2D-PhC cavity patterns (pillar diameter: 168 nm, pitch: 112 nm) were prepared on the electron beam resist-coated silicon substrate using EBL (Fig. 2). To investigate the sensing performance using EBL patterned 2D-PhC cavity, a LbL assembly methodology for deposition of cationic and anionic layers by electrostatic interaction for changing of the surrounding refractive index (Fig. 3), and the reflection intensity change by the irradiation of green laser (532 nm, 1 mW) was employed.

The 2D-PhC cavity was applied to evaluate the sensitivity, higher reflection intensity than similar design without cavity could be observed (Fig. 4). Using the 2D-PhC cavity, detection of LbL layers and the detectable number of layers was investigated. By deposition of LbL layers, reflection peak intensity was drastically decreased (Fig. 5). Result from the comparison of sensing performance using 2D-PhC which has reflection peak wavelength according to the Bragg reflection by calculating the changing ratio defined by reflection intensity (after deposition)/reflection intensity (bare 2D-PhC), 2D-PhC cavity could detect the extremely low number of LbL layer systematically.

In addition, 2D-PhC cavity was applied to detect the DNA hybridization. The probe DNA for tumor necrosis factor (TNF- α) was immobilized onto the 2D-PhC cavity surface. And the reflection intensity change due to the DNA hybridization-based refractive index change was monitored. As a result, the refractive index change with target DNA concentration could also be observed. From these results, this sensor has great potential for high sensitive detection of target molecules in visible region.

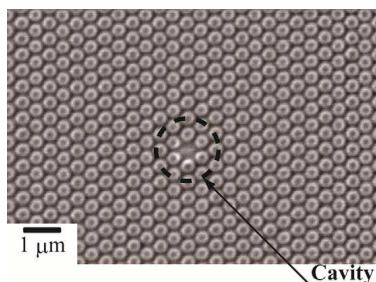


Figure 2: Scanning electron microscopy image of 2D-PhC cavity optical sensor.

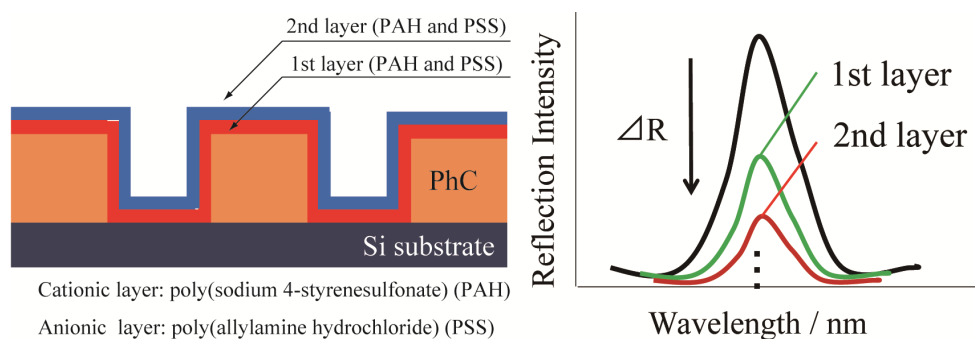


Figure 3: Schematic illustration of sensing performance evaluation using LbL assembly methodology.

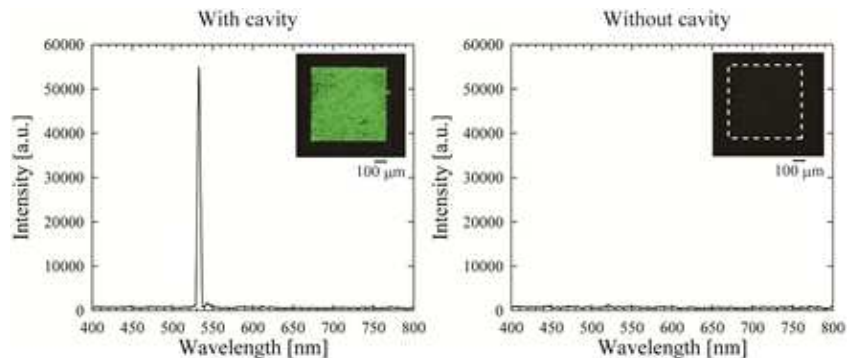


Figure 4: Reflection spectra and photograph of 2D-PhC cavity and without cavity.

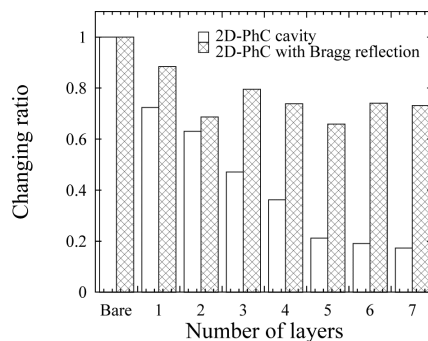


Figure 5: Reflection peak intensity change with number of LbL layers.

3. CONCLUSION

In this study, we succeeded to design and fabricate the polymer-based 2D-PhC cavity sensor for biosensing application. Using this sensor, high-sensitive detection of LbL layer deposition and DNA hybridization. From these results, this sensor has a great potentials for detection of biomolecular interactions such as an antigen-antibody for future medical diagnostics.

REFERENCES

1. Ray, K., R. Badugu, and J. R. Lakowicz, "Polyelectrolyte layer-by-layer assembly to control the distance between fluorphores and plasmonic nanostructures," *Chemistry of Materials*, Vol. 19, 5902–5909, 2007.
2. Endo, T., M. Sato, H. Kajita, N. Okuda, S. Tanaka, and H. Hisamoto, "Printed two-dimensional photonic crystals for single-step label-free biosensing of insulin under wet conditions," *Lab on a Chip*, Vol. 12, 1995–1999, 2012.
3. Bardosonova, M., M. E. Pemble, I. M. Povey, R. H. Tredgold, and D. E. Whitehead, "Enhanced bragg reflections from size-matched heterostructure photonic crystal thin films prepared by the langmuir-blodgett method," *Applied Physics Letters*, Vol. 89, 093116, 2006.

PEDOT:PSS/planar-Si Hybrid Solar Cells with 12.70% Efficiency

Yuanfan Zhao¹, Dan Xie¹, Jianlong Xu¹, Tingting Feng¹, Xiaowen Zhang¹,
Tianling Ren¹, Miao Zhu², and Hongwei Zhu²

¹Tsinghua National Laboratory for Information Science and Technology (TNList)

Institute of Microelectronics, Tsinghua University, Beijing 100084, China

²State Key Laboratory of New Ceramics and Fine Processing

Key Laboratory of Materials Processing Technology of MOE

School of Materials Science and Engineering, Tsinghua University, China

Abstract— In the paper, we demonstrate efficient hybrid solar cells based on the Poly(3,4-ethylenedioxythiophene):poly(styrene sulfonic acid) (PEDOT:PSS) and planar Silicon with a hydrogen-terminated Si (H-Si) surface. PEDOT:PSS/planar Si hybrid solar cells show high power conversion efficiency (PCE) of 8.27 ~ 12.70%. The cell with the PCE of 12.70% presents short circuit current density (J_{SC}), open circuit voltage (V_{OC}) and fill factor (FF) of 20.92 mA/cm², 0.63 V and 70.26%, respectively. The better contact of PEDOT:PSS film with the Si substrate is contributed to the formation of effective PEDOT:PSS/Si heterojunction, resulting in the enhanced photovoltaic performances.

1. INTRODUCTION

Although conventional crystalline silicon solar cells have achieved much higher power conversion efficiency (PCE) [1], they suffer from expensive fabrication costs due to their high temperature steps, material scarcity as well as complicated equipments [2]. Therefore, some alternative solar cells based on new device structures and materials have been designed and reported. Among them, the conductive polymer Poly(3,4-ethylenedioxythiophene):Poly(styrene sulfonic acid) (PEDOT:PSS) has attracted great interests owing to its high transparency, excellent conductivity and mechanical flexibility which is a promising candidate for further solar cell materials [3].

In the PEDOT:PSS/planar Si hybrid solar cells, the PEDOT:PSS works as a hole collecting layer and form a heterojunction with Si to induce a built-in electric field where the photo-generated carriers are separated to generate photocurrent [4]. Generally, in the process of solar cells preparation, a diluted HF solution treatment is needed to remove the native oxide layer on Si substrates to obtain clean silicon surface. After the HF solution treatment, H-Si bonds terminated surfaces are formed [5]. According to the reports [6, 7], however, almost all the PEDOT:PSS/planar Si cells with a H-Si interface achieve lower PCE probably due to difficulty of PEDOT:PSS film formation on the Si surface. In order to overcome it, the diluted HF treated Si substrates are exposed in air for some hours to form an ultrathin SiO₂ layer, which brings in a favorable contact between PEDOT:PSS and planar Si resulting in good interface for photo-excited carrier separation [8, 9]. However, the oxide layer between PEDOT:PSS film and Si substrate will degrade its performance due to the higher series resistance (R_S) [7].

Recently, Liu et al. have reported that some surfactants such as Triton X-100, etc. are added into the PEDOT:PSS solution [10, 11] to enhance its wettability and make PEDOT:PSS well contact with the hydrophobic H-Si surface [12] leading to better diode characteristics. Other ways such as modifying PEDOT:PSS solutions with other polymers could improve the built-in potential as well as suppress photo-generated carrier recombination [10, 12] or increase the hole mobility of the PEDOT:PSS films [11]. However, any polymer additives added into PEDOT:PSS solutions will change its perfect inherent electrical properties, thus it is necessary to further investigate the PEDOT:PSS/planar Si solar cells to improve the solar cell properties including alternative cell structure or the process optimization.

In our work, we designed a new solar cell structure with pristine PEDOT:PSS solutions being deposited on the planar crystalline Si that achieves high PCE of 8.27 ~ 12.70%. In our PEDOT:PSS/planar Si hybrid solar cells, junction region between PEDOT:PSS and planar Si is defined, which is surrounded by the SiO₂ insulating region. The hydrophilic insulating region can make sure better contact between PEDOT:PSS and planar Si in junction region, which is contributed to the formation of the PEDOT:PSS/Si heterojunction. The preparation processes are discussed and the results are investigated.

2. EXPERIMENT

The PEDOT:PSS/planar Si hybrid solar cells were fabricated using single crystal n-type Si (100) wafers with a resistivity of $2 \sim 3 \Omega \cdot \text{cm}$ and the thickness of about $550 \mu\text{m}$ (Figure 1(a)).

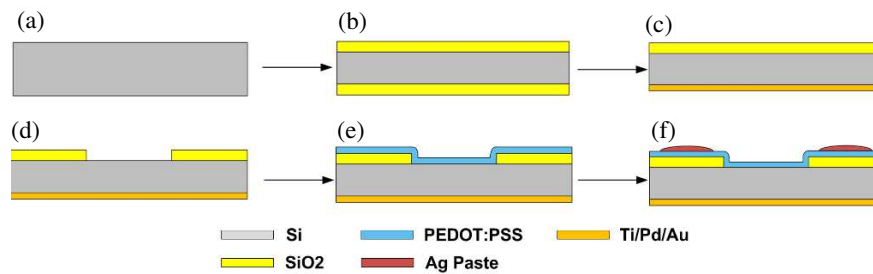


Figure 1: Illustration of the PEDOT:PSS/Si hybrid solar cell preparing processes. (a) The start silicon wafer. (b) A 300 nm-thick SiO₂ layer was thermally grown on the silicon surface and then the backside was etched by HF solution. (c) Ti/Pd/Au layers of 5/10/30 nm was deposited backside as bottom electrodes. (d) The $3 \times 3 \text{ mm}^2$ junction area was patterned by lithography and the SiO₂ layer was then etched until Si surface by RIE. (e) The PEDOT:PSS solutions was spin-coated on Si substrate. (f) Silver paste was applied onto the PEDOT:PSS film as top electrodes.

A 300 nm-thick SiO₂ layer was thermally grown on the silicon surface as the insulating layer (Figure 1(b)). Ti/Pd/Au layers of 5/10/30 nm were deposited backside by electron beam evaporation as bottom electrodes (Figure 1(c)). The $3 \times 3 \text{ mm}^2$ junction area was patterned by lithography and the SiO₂ layer was then etched until Si surface by reactive ion etching (RIE) (Figure 1(d)). After that, the wafer were cut into small pieces as the cell substrates. The substrates were dipped in diluted HF solution for 10 s to remove the native oxide layer of junction region immediately after being ultrasonically cleaned in acetone, ethanol and deionized (DI) water. The PEDOT:PSS (Clevios, PH1000, 20 wt.%) solutions mixed with Dimethyl Sulfoxide (DMSO, 5 wt.%) were then spin-coated onto the Si substrates (Figure 1(e)), followed by a thermal annealing process at 140° for 10 min. Finally, silver paste was applied onto the PEDOT:PSS film as top electrode. Figure 1(f) shows the structural schematic of the finished PEDOT:PSS/Si hybrid solar cell.

3. RESULTS

The top-view SEM image of PEDOT:PSS film is shown in Figure 2(a). It can be seen that the spin-coated PEDOT:PSS film is uniform and almost no defect exists in it. Figure 2(b) presents the cross-sectional SEM image of the PEDOT:PSS/planar Si solar cell. It exhibits a clear and good interface between PEDOT:PSS film and Si substrate and demonstrates the thickness of PEDOT:PSS film is about 56 nm.

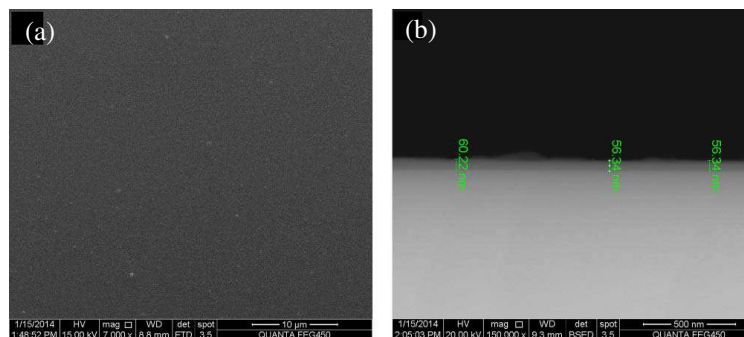


Figure 2: (a) Top-view SEM image of the PEDOT:PSS film. (b) Cross-sectional SEM image of the solar cell.

In our experiments, 16 solar cells were fabricated and a PCE distribution of $8.27 \sim 12.70\%$ with an average PCE of 9.94% was achieved. The highest PCE of 12.70% exhibited J_{SC} , V_{OC} and FF of 20.92 mA/cm^2 , 0.63 V and 70.26% , respectively. Figure 3(a) shows the Current density-Voltage (J - V) characteristics of five representing solar cells under illumination of AM1.5G, 73 mW/cm^2

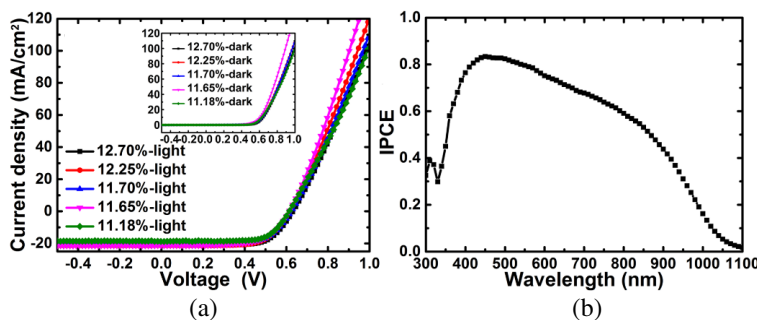


Figure 3: (a) The current density-voltage ($J-V$) characteristics of five representing solar cells under illumination of AM 1.5G, 73 mW/cm² simulated sunlight. The inset shows the corresponding $J-V$ curves of such five solar cells in dark. (b) The IPCE spectrum of the one typical solar cells.

simulated sunlight calibrated by a standard cell unit, and Table 1 shows their photovoltaic parameters of J_{SC} , V_{OC} , FF , PCE, R_S and shunt resistance (R_{SH}). Standard diode characteristics can be found in both dark and light $J-V$ curves. The cells also has a lower R_S , a large R_{SH} and a higher V_{OC} , FF which together account for the high PCE. Figure 3(b) presents the monochromatic incident photon-to-electron conversion efficiency (IPCE) characteristics of one typical sample. It indicates that the cells could absorb the photons whose wavelength is less than 1100 nm and the visible light (350 ~ 770 nm) can be absorbed strongly with an average IPCE of 73.46% consistent with the high J_{SC} .

Table 1: Summary of the photoelectric parameters of the typical solar cells.

No.	V_{OC} (mV)	J_{SC} (mA/cm ²)	FF (%)	R_S ($\Omega\cdot\text{cm}^2$)	R_{SH} ($\Omega\cdot\text{cm}^2$)	PCE (%)
1	630.68	20.92	70.26	3.86	2.36E5	12.70
2	615.62	21.30	68.17	3.68	2.53E5	12.25
3	623.14	20.23	67.78	3.65	1.26E3	11.70
4	608.09	21.29	65.67	2.80	4.76E3	11.65
5	608.08	18.40	72.92	4.40	2.87E4	11.18

4. DISCUSSION

During our experiments, it is found that the PEDOT:PSS aqueous solutions can't form good films on the hydrophobic H-Si surface, which is the main reason for the poor performances of the PEDOT:PSS/planar Si structure solar cells with H-Si surface. However, our designed cell structure with effective junction region and SiO₂ insulating region could solve this problem. The SiO₂ insulating region surrounding the junction area is hydrophilic [13] which lowers the PEDOT:PSS solutions surface tension and makes it spread onto the junction region with a very small contact angle, resulting in uniform and high quality PEDOT:PSS film on the silicon surface. In this way, PEDOT:PSS forms a direct contact with H-Si surface which can be proved in Figure 2(b), resulting in effective PEDOT:PSS/Si heterojunction and better photovoltaic performances.

5. CONCLUSION

In summary, the PEDOT:PSS/planar Si hybrid solar cells with high PCE value of 8.27 ~ 12.70% have been fabricated and investigated. The solar cell with a PCE value of 12.70% exhibited J_{SC} , V_{OC} and FF of 20.92 mA/cm², 0.63 V and 70%, respectively. The device design of junction region and SiO₂ insulating region can make sure the better contact between PEDOT:PSS film and planar Si, which is contributed to the formation of the PEDOT:PSS/Si heterojunction. Therefore, R_S is lower and R_{SH} is much higher, as well as the enhanced photovoltaic performances are obtained.

REFERENCES

1. Zhao, J., A. Wang, and M. A. Green, "19.8% efficient 'honeycomb' textured multi-crystalline and 24.4% monocrystalline silicon solar cells," *Appl. Phys. Lett.*, Vol. 73, 1991–1993, Jul. 30, 1998.

2. Chen, T.-G., B.-Y. Huang, E.-C. Chen, P. Yu, and H.-F. Meng, “Micro-textured conductive polymer/silicon heterojunction photovoltaic devices with high efficiency,” *Appl. Phys. Lett.*, Vol. 101, 033301, Jul. 16, 2012.
3. Kirchmeyer, S. and K. Reuter, “Scientific importance, properties and growing applications of poly(3,4-ethylenedioxythiophene),” *J. Mater. Chem.*, Vol. 15, 2077–2088, Jan. 28, 2005.
4. Zhang, Y., F. Zu, S.-T. Lee, L. Liao, N. Zhao, and B. Sun, “Heterojunction with organic thin layers on silicon for record efficiency hybrid solar cells,” *Adv. Energy Mater.*, Vol. 4, 1300923, Jan. 28, 2014.
5. Grundner, M. and H. Jacob, “Investigations on hydrophilic and hydrophobic silicon (100) wafer surfaces by X-ray photoelectron and high-resolution electron energy loss spectroscopy,” *Appl. Phys. A*, Vol. 39, 73–82, Sep. 12, 1985.
6. He, L., C. Jiang, H. Wang, D. Lai, and R. He, “High efficiency planar Si/organic heterojunction hybrid solar cells,” *Appl. Phys. Lett.*, Vol. 100, 073503, Feb. 13, 2012.
7. He, L., C. Jiang, H. Wang, H. Lei, D. Lai, and R. He, “11.3% efficient planar Si-PEDOT:PSS hybrid solar cell with a thin interfacial oxide,” *38th IEEE Photovoltaic Specialists Conference (PVSC)*, 002785–002787, 2012.
8. Liu, Q., M. Ono, Z. Tang, R. Ishikawa, K. Ueno, and H. Shirai, “Highly efficient crystalline silicon/Zonylfluorosurfactant-treated organic heterojunction solar cells,” *Appl. Phys. Lett.*, Vol. 100, 183901, May 1, 2012.
9. Shen, X., Y. Zhu, T. Song, S.-T. Lee, and B. Sun, “Hole electrical transporting properties in organic-Si Schottky solar cell,” *Appl. Phys. Lett.*, Vol. 103, 013504, Jul. 2, 2013.
10. Zhu, Y., T. Song, F. Zhang, S.-T. Lee, and B. Sun, “Efficient organic-inorganic hybrid Schottky solar cell: The role of built-in potential,” *Appl. Phys. Lett.*, Vol. 102, 113504, Mar. 19, 2013.
11. Liu, Q., T. Imamura, T. Hiata, I. Khatri, Z. Tang, R. Ishikawa, K. Ueno, and H. Shirai, “Optical anisotropy in solvent-modified poly(3,4-ethylenedioxythiophene):poly(styrenesulfonic acid) and its effect on the photovoltaic performance of crystalline silicon/organic heterojunction solar cells,” *Appl. Phys. Lett.*, Vol. 102, 243902, Jun. 17, 2013.
12. Khatri, I., Z. Tang, Q. Liu, R. Ishikawa, K. Ueno, and H. Shirai, “Green-tea modified multiwalled carbon nanotubes for efficient poly(3,4-ethylenedioxythiophene):poly(stylenesulfonate)/n-silicon hybrid solar cell,” *Appl. Phys. Lett.*, Vol. 102, 063508, Feb. 14, 2013.
13. Williams, R. and A. M. Goodman, “Wetting of thin layers of SiO₂ by water,” *Appl. Phys. Lett.*, Vol. 25, 531–532, Aug. 14, 1974.

Tailoring Specific Heat and Density in the Design of Thermal Transformation Media

Yu-Lin Tsai and Tungyang Chen

Department of Civil Engineering, National Cheng Kung University, Tainan 70101, Taiwan

Abstract— The transformation optics or acoustics in the design of metamaterials has been successfully applied to a number of physical phenomena. This novel method provides simple routes to attain certain significant effects such as invisibility cloaks, concentrators, and others. Given a mapping between two geometric configurations, the material properties of the transformed domain can be accordingly determined. They are in general anisotropic, position varying and sometimes of extreme values at certain points. This in fact restricts the practicality of real fabrication. Here we are concerned with the transient behavior of heat conduction. An inverse algorithm is presented here in the design of transformed medium based on the invariance of governing equation between physical and virtual configurations. We will demonstrate that the thermal capacity (thermal conductivity and heat capacity) can be tailored in specific forms, spatially uniform, linear or quadratic functions of positions, so that the design can be materialized more easily. Numerical illustrations are also presented for 2D and 3D thermal cloak for transient thermal conduction.

1. INTRODUCTION

In recent years, many significant achievements of invisibility cloaking have been motivated thanks to pioneering theoretical works [1, 2]. Recent advances in the field of metamaterials have extended beyond the manipulation of electromagnetic waves. A variety of cloaks working for different physical fields such as acoustic waves [3–6], and thermal dynamics [7]. The concept of the transformation method is based on the form invariance of the governing equation. Given a mapping between two configurations, the material properties of the transformed domain can be accordingly determined. However, most cloak realizations usually require extreme constitutive parameters (inhomogeneous, anisotropic, or even singular). In other words, this restricts the practicality of real fabrication. For feasible, several investigations have been demonstrated by using reduced cloak [8–10]. Another strategy for geometry transformations is quasi-conformal map [11–13]. It results in isotropic material parameters but requires a cloaking many times larger than the object to be hidden. Here we show a specific transformation can tailor the thermal capacity in specific form, spatially uniform, linear or quadratic functions of positions, so that the design can be materialized more easily.

A direct approach to analytically determined the material parameters of transformation shell ensures that the field exterior to shell will be the same as the original medium, as the governing equations remains unchanged and the continuous conditions are exactly fulfilled along the boundary [14]. In this paper, for transient thermal conductions, we propose a way to get the transformation function in an inverse manner when the thermal capacity is given, and then using the transformation function to get relative thermal conductivities.

2. TRANSFORMATION MEDIA FOR HEAT FLUX

The governing equation of heat flux without local source is given by $\nabla \cdot (\kappa \nabla T) = \rho C \partial T / \partial t$, where C is the specific heat, ρ is the material density and κ is the thermal conductivity. To demonstrate our algorithm, we use the cylindrical coordinates and write the components of κ as the relative conductivity with background media. For a time harmonic heat flux, the governing equation can be expressed as

$$\begin{aligned} & \kappa_{rr} \frac{\partial^2 T}{\partial r^2} + \frac{\kappa_{\theta\theta}}{r^2} \frac{\partial^2 T}{\partial \theta^2} + \kappa_{zz} \frac{\partial^2 T}{\partial z^2} + \frac{2\kappa_{r\theta}}{r} \frac{\partial^2 T}{\partial r \partial \theta} + \frac{2\kappa_{\theta z}}{r} \frac{\partial^2 T}{\partial \theta \partial z} + 2\kappa_{rz} \frac{\partial^2 T}{\partial r \partial z} + \left(\frac{\kappa_{rr}}{r} + \frac{\partial \kappa_{rr}}{\partial r} + \frac{1}{r} \frac{\partial \kappa_{r\theta}}{\partial \theta} + \frac{\partial \kappa_{rz}}{\partial z} \right) \frac{\partial T}{\partial r} \\ & + \left(\frac{1}{r} \frac{\partial \kappa_{r\theta}}{\partial r} + \frac{1}{r^2} \frac{\partial \kappa_{\theta\theta}}{\partial \theta} + \frac{1}{r} \frac{\partial \kappa_{\theta z}}{\partial z} \right) \frac{\partial T}{\partial \theta} + \left(\frac{\kappa_{rz}}{r} + \frac{\partial \kappa_{rz}}{\partial r} + \frac{1}{r} \frac{\partial \kappa_{\theta z}}{\partial \theta} + \frac{\partial \kappa_{zz}}{\partial z} \right) \frac{\partial T}{\partial z} = -\rho C i \omega T. \end{aligned} \quad (1)$$

Using the transformation media, an obstacle in the physical space can be formed as a different shape in the virtual space, in other words, transformation media makes an illusion. That is, to achieve any desired virtual reshaping effect provided an appropriate transformation can be found

between the virtual space and the physical space. Here, we consider a coordinate transformation that maps the physical space \mathbf{x} onto the virtual space \mathbf{x}'

$$r' = f(r, \theta, z), \quad \theta' = \theta, \quad z' = z. \quad (2)$$

Upon the transformation (2) and chain rule, the heat conduction Equation (1) can be transformed into virtual space as

$$\begin{aligned} & \left[\kappa_{rr} \left(\frac{\partial f}{\partial r} \right)^2 + \frac{\kappa_{\theta\theta}}{r^2} \left(\frac{\partial f}{\partial \theta} \right)^2 + \kappa_{zz} \left(\frac{\partial f}{\partial z} \right)^2 + \frac{2\kappa_{r\theta}}{r} \frac{\partial f}{\partial r} \frac{\partial f}{\partial \theta} + \frac{2\kappa_{\theta z}}{r} \frac{\partial f}{\partial \theta} \frac{\partial f}{\partial z} + 2\kappa_{rz} \frac{\partial f}{\partial r} \frac{\partial f}{\partial z} \right] \frac{\partial^2 T}{\partial r'^2} \\ & + \frac{\kappa_{\theta\theta}}{r^2} \frac{\partial^2 T}{\partial \theta'^2} + \kappa_{zz} \frac{\partial^2 T}{\partial z'^2} + \left(\frac{2\kappa_{\theta\theta}}{r^2} \frac{\partial f}{\partial \theta} + \frac{2\kappa_{r\theta}}{r} \frac{\partial f}{\partial r} + \frac{2\kappa_{\theta z}}{r} \frac{\partial f}{\partial z} \right) \frac{\partial^2 T}{\partial r' \partial \theta'} + \frac{2\kappa_{\theta z}}{r} \frac{\partial^2 T}{\partial \theta' \partial z'} \\ & + \left(2\kappa_{zz} \frac{\partial f}{\partial z} + \frac{2\kappa_{\theta z}}{r} \frac{\partial f}{\partial \theta} + 2\kappa_{rz} \frac{\partial f}{\partial r} \right) \frac{\partial^2 T}{\partial r' \partial z'} + \left[\kappa_{rr} \frac{\partial^2 f}{\partial r^2} + \frac{\kappa_{\theta\theta}}{r^2} \frac{\partial^2 f}{\partial \theta^2} + \kappa_{zz} \frac{\partial^2 f}{\partial z^2} + \frac{2\kappa_{r\theta}}{r} \frac{\partial^2 f}{\partial r \partial \theta} + \frac{2\kappa_{\theta z}}{r} \frac{\partial^2 f}{\partial \theta \partial z} \right. \\ & + 2\kappa_{rz} \frac{\partial^2 f}{\partial r \partial z} + \left(\frac{\kappa_{rr}}{r} + \frac{\partial \kappa_{rr}}{\partial r} + \frac{1}{r} \frac{\partial \kappa_{r\theta}}{\partial \theta} + \frac{\partial \kappa_{rz}}{\partial z} \right) \frac{\partial f}{\partial r} + \left(\frac{1}{r} \frac{\partial \kappa_{r\theta}}{\partial r} + \frac{1}{r^2} \frac{\partial \kappa_{\theta\theta}}{\partial \theta} + \frac{1}{r} \frac{\partial \kappa_{\theta z}}{\partial z} \right) \frac{\partial f}{\partial \theta} \\ & + \left(\frac{\kappa_{rz}}{r} + \frac{\partial \kappa_{rz}}{\partial r} + \frac{1}{r} \frac{\partial \kappa_{\theta z}}{\partial \theta} + \frac{\partial \kappa_{zz}}{\partial z} \right) \frac{\partial f}{\partial z} \left. \right] \frac{\partial T}{\partial r'} + \left(\frac{1}{r} \frac{\partial \kappa_{r\theta}}{\partial r} + \frac{1}{r^2} \frac{\partial \kappa_{\theta\theta}}{\partial \theta} + \frac{1}{r} \frac{\partial \kappa_{\theta z}}{\partial z} \right) \frac{\partial T}{\partial \theta'} \\ & + \left(\frac{\kappa_{rz}}{r} + \frac{\partial \kappa_{rz}}{\partial r} + \frac{1}{r} \frac{\partial \kappa_{\theta z}}{\partial \theta} + \frac{\partial \kappa_{zz}}{\partial z} \right) \frac{\partial T}{\partial z'} + i\rho C\omega T = 0. \end{aligned} \quad (3)$$

To let the heat flux in the transformation device be effectively equivalent to the background material in virtual space. The governing equation of heat flux in background material can be written as

$$\frac{\partial^2 T'}{\partial r'^2} + \frac{1}{r'^2} \frac{\partial^2 T'}{\partial \theta'^2} + \frac{\partial^2 T'}{\partial z'^2} + \frac{1}{r'} \frac{\partial T'}{\partial r'} = -i\omega T'. \quad (4)$$

When the transformation media is effectively equivalent to that of the same domain filling with the background homogeneous material, it means that $T(r', \theta', z')$ equals to $T'(r', \theta', z')$ and then (3) should be identical with (4). According to equate the coefficients in each term, we obtain the thermal capacity which are expressed by transformation function as

$$\begin{aligned} \kappa_{rr} &= A^* \left(\frac{f + \frac{(\partial f / \partial \theta)^2}{f} + f \left(\frac{\partial f}{\partial z} \right)^2}{r \partial f / \partial r} \right), \quad \kappa_{r\theta} = -\frac{A^*}{f} \frac{\partial f}{\partial \theta}, \quad \kappa_{rz} = -\frac{A^*}{r} \frac{\partial f}{\partial z}, \\ \kappa_{\theta\theta} &= \frac{A^* r}{f} \frac{\partial f}{\partial r}, \quad \kappa_{\theta z} = 0, \quad \kappa_{zz} = \rho C = \frac{A^*}{r} \frac{\partial f}{\partial r}, \end{aligned} \quad (5)$$

where A^* is a constant which is determined by the boundary conditions. According to the continuous conditions, we demand the temperature and normal heat flux along the outer boundary must be the same for the two configurations (physical space Ω and virtual space Ω'), that are $T|_{\partial\Omega} = T|_{\partial\Omega'}$ and $\kappa \partial T / \partial n|_{\partial\Omega} = \kappa' \partial T' / \partial n'|_{\partial\Omega'}$. Therefore, the undetermined coefficient A^* is obtained as 1. In this paper, we consider the geometry of the transformation media as a cylinder, so the transformation relation in (2) would be simplified as $r' = f(r)$, $\theta' = \theta$, $z' = z$. And then, the material parameters of the transformation media are

$$\kappa_{rr} = \frac{f}{r \partial f / \partial r}, \quad \kappa_{\theta\theta} = \frac{r \partial f / \partial r}{f}, \quad \kappa_{zz} = \frac{f \partial f}{r \partial r}, \quad \kappa_{r\theta} = \kappa_{rz} = \kappa_{\theta z} = 0 \quad \text{and} \quad \rho C = \frac{f \partial f / \partial r}{r}. \quad (6)$$

3. TAILOR A SPECIFIC THERMAL CAPACITY

From (6), we can tailor the thermal capacity in specific forms, uniform, linear or quadratic functions of positions, etc., by appropriate transformation function. Let thermal capacity be an arbitrary function of positions, $G(r)$, then we suppose the capacity as

$$\rho C = \frac{f \partial f / \partial r}{r} = G(r). \quad (7)$$

First, we consider a uniform thermal capacity. To proceed, we suppose the capacity as α . By integration, the transformation function between to configurations is formed as $f(r) = \sqrt{\alpha r^2 + \xi}$. Since the outer boundary remains unchanged, $f(a) = 0$, and inner boundary shrinks into a point in the virtual space, $f(b) = b$, where a and b are the radii of the inner and outer boundary, then the coefficients α and ξ are obtained as $\alpha = b^2/(b^2 - a^2)$ and $\xi = -a^2b^2/(b^2 - a^2)$. Therefore, the thermal conductivities of the transformation media in (6) become

$$\kappa_{rr} = \frac{r^2 - a^2}{r^2}, \quad \kappa_{\theta\theta} = \frac{r^2}{r^2 - a^2}, \quad \kappa_{zz} = \frac{b^2}{b^2 - a^2}, \quad \kappa_{r\theta} = \kappa_{rz} = \kappa_{\theta z} = 0 \quad \text{and} \quad \rho C = \frac{b^2}{b^2 - a^2}. \quad (8)$$

Corresponding the finite element simulations, uniform hot and cold side temperature boundary conditions of 373 K and 273 K, respectively, were applied to the structure shown in Fig. 1(a). To demonstrate the validity of the cloak design, we consider the inner radius as $a = 0.2$ m and the outer radius as $b = 0.5$ m. Fig. 1(b) depicts the snap-shot of our cloak at various times t . In our simulation, the conductivity of background media is 400 W/m-K. The contours of temperature display curved line in cylindrical cloak medium. After passing through the cloak, the potential fields outside of the cloaking region remain undisturbed and the fluxes return to their original trajectories without changing direction and magnitude. However, in the long-time limit or static, as shown in Fig. 1(b) ($t = 120$ min), the to-be-protected inner region does eventually heat up.

The thermal capacity also can be a linear function of positions, for example, we alter the arbitrary function $G(r)$ of (7) as $G(r) = \zeta r$. Similar as the processing of uniform capacity, the transformation function is obtained as $f = (b^2(r^3 - a^3)/(b^3 - a^3))^{1/2}$ by the geometry boundary conditions. At last,

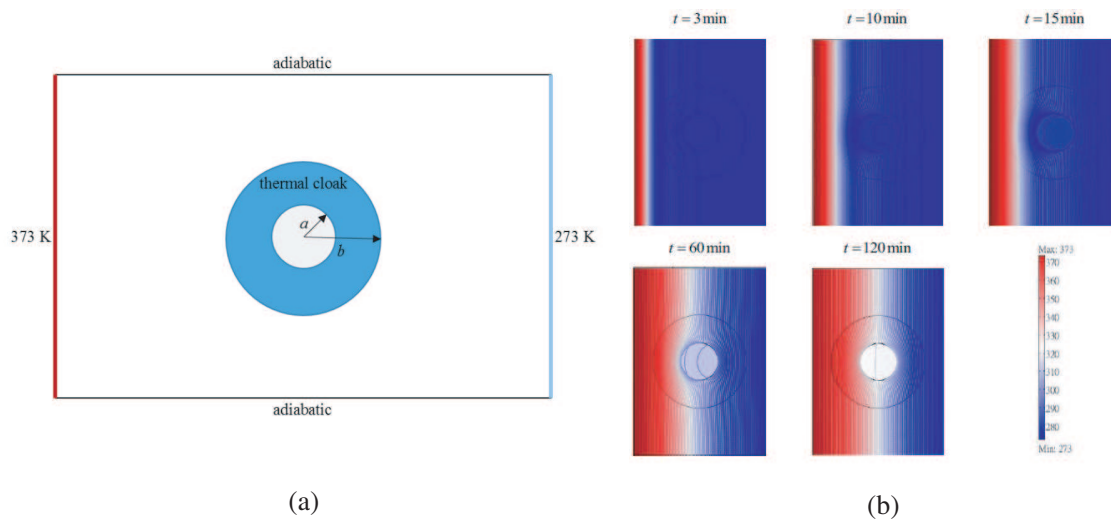


Figure 1: (a) Illustration of the 2D cylindrical cloaking numerical simulation. The to-be-protected region ($r < a$) is coated by a cloaking device. (b) Snapshots of the transient thermal conduction for each time. The contours of temperature are bent in the cloaking region.

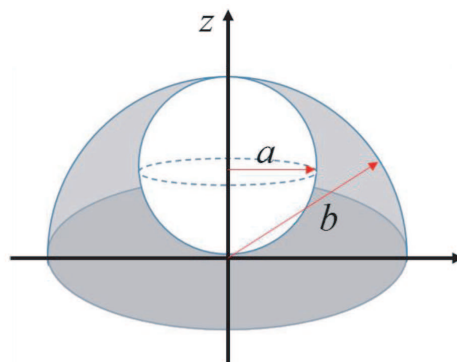


Figure 2: A schematic of the 3D cloaking device. There is a ball-region with radius a embedded in the half-sphere with radius b .

we design a 3D thermal cloaking device with a uniform thermal capacity for each layer. Fig. 2 illustrates that a sphere with radius a is embedded in a half-sphere with radius b . According to the outer boundary remains unchanged and the inner boundary shrinks into zero, the coefficient α and ξ are determined as $(b^2 - z^2)/(b^2 - 2az)$ and $(b^2 - a^2)(z^2 - 2az)/(b^2 - 2az)$, respectively. Then the transformation for this 3D thermal cloak is obtained as $f(r, z) = \sqrt{(b^2 - z^2)(r^2 + z^2 - 2az)/(b^2 - 2az)}$.

4. CONCLUSION

In this paper, we propose a way to obtain a specific heat conductivity and capacity for a transient thermal flux. In manufacture, although some investigations have proposed multilayer structures to approach the anisotropic and inhomogeneous material parameters, the fabrication is still difficult because the capacity tends to infinite at inner boundary. When the capacity is a constant, the fabrication becomes much easier. We also demonstrate a 3D cloaking device with a specific capacity varied by z direction. For fabrication, it can be built by 3D printing technology.

ACKNOWLEDGMENT

The financial support from the National Science Council of Taiwan under the grant NSC 99-2221-E-006-070-MY3 is acknowledged.

REFERENCES

1. Pendry, J. B., D. Schurig, and D. R. Smith, "Controlling electromagnetic fields," *Science*, Vol. 312, 1780, 2006.
2. Leonhardt, U., "Optical conformal mapping," *Science*, Vol. 312, 1777, 2006.
3. Cummer, S. A. and D. Schurig, "One path to acoustic cloaking," *New Journal of Physics*, Vol. 9, 45, 2007.
4. Chen, H. and C. T. Chan, "Acoustic cloaking and transformation acoustics," *Journal of Physics D: Applied Physics*, Vol. 43, 113001, 2010.
5. Torrent, D. and J. Sanchez-Dehesa, "Acoustic metamaterials for new two dimensional sonic devices," *New Journal of Physics*, Vol. 9, 323, 2007.
6. Chen, H. and C. T. Chan, "Acoustic cloaking in three dimensions using acoustic metamaterials," *Applied Physics Letter*, Vol. 91, 183518, 2007.
7. Schittny, R., M. Kadic, S. Guenneau, and M. Wegener, "Experiments on transformation thermodynamics: Molding the flow of Heat," *Physical Review Letter*, Vol. 110, 195901, 2013.
8. Cai, L. W. and J. Sanchez-Dehesa, "Analysis of Cummer-Schurig acoustic cloaking," *New Journal of Physics*, Vol. 9, 450, 2007.
9. Huang, Y., Y. Feng, and T. Jiang, "Electromagnetic cloaking by layered structure of homogeneous isotropic materials," *Optics Express*, Vol. 15, 11133, 2007.
10. Yan, M., Z. Ruan, and M. Qiu, "Scattering characteristics of simplified cylindrical invisibility cloaks," *Optics Express*, Vol. 15, 17772, 2007.
11. Ergin, T., N. Stenger, P. Brenner, J. B. Pendry, and M. Wegener, "Three-dimensional invisibility cloak at optical wavelengths," *Science*, Vol. 328, 337, 2010.
12. Li, J. and J. B. Pendry, "Hiding under the carpet: A new strategy for cloaking," *Physical Review Letter*, Vol. 101, 203901, 2008.
13. Valentine, J., J. Li, T. Zentgraf, G. Bartal, and X. Zhang, "An optical cloak made of dielectrics," *Nature Material*, Vol. 8, 568, 2009.
14. Chen, T. and Y. L. Tsai, "A derivation for the acoustic material parameters in transformation domains," *Journal of Sound and Vibration*, Vol. 332, 766, 2013.

Near-field Optical Storage System with a Real Artificial Negative Index Film

Taikei Suyama¹, Xiaowei Ji², Akira Matsushima², and Yaoju Zhang³

¹Department of Electrical and Computer Engineering
Akashi National College of Technology, Akashi, Japan

²Graduate School of Science and Technology, Kumamoto University, Kumamoto, Japan

³Department of Physics and Electronic Information, Wenzhou University, Wenzhou, China

Abstract— We develop the concept of the near-field optical storage using a NIF and propose a new near-field solid immersion lens (SIL) optical recording system. Our method is based on the surface plasmas (SP) excited by a NIF-polymer composite nano-layer which is attached on the plane surface of the SIL. An experimentally-fabricated negative index material comprising silver nanorods is chosen as the NIF and the refractive indices mismatching effect is considered in our simulations. The proposed system may be much more close to an actual near-field optical recording system.

1. INTRODUCTION

We propose a new method of enhancing the intensity of spot and improving the air-gap width of a near-field optical storage system with a real artificial negative index film (NIF). This method is based on surface plasmas excited by NIF combined with a polymer film. In 2004, Liu and He has proposed a near-field SIL optical storage system by utilizing a negative index material [1]. In this paper, we have developed the concept of the near-field optical storage using a NIF introduced by Liu and He and propose a new near-field solid immersion lens (SIL) optical recording system. Our method is based on the surface plasmas (SP) excited by a NIF-polymer composite nano-layer which is attached on the plane surface of the SIL. An experimentally-fabricated negative index material comprising silver nanorods [2, 3] is chosen as the NIF and the refractive indices mismatching effect is considered in our simulations. The proposed system may be much more close to an actual near-field optical recording system. Numerical results based on the simple vector diffraction theory showing that the present system is able reduce energy loss remarkably and substantially increase the gap's width of the near-field optical storage system with a SIL.

2. VECTOR DIFFRACTION THEORY

Figure 1 shows the schematic diagram of the focusing system in near-field optical storage used in our studies. An aplanatic solid immersion lens [4] is placed in the focal region of the objective and the focus is in the bottom surface of the SIL. The SIL is attached a layer of the negative-index nano-film and then a polymer nano-film is attached on the lower surface of the NIF. This structure is different from that in Ref. [1]. First of all, it is a 3D structure with an aplanatic SIL which can lower the limitation to the objective. Secondly, the NIF is an experimentally-fabricated negative

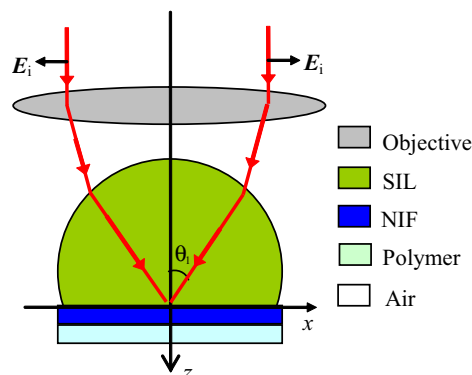


Figure 1: Schematic diagram of the focusing system in the near-field optical storage with an aplanatic solid immersion lens.

index material and is not an ideal material. The NIF's thickness is in nanometer scale to excite SP and is no any large. Thirdly, a layer of thin polymer film is used to further enhance the SP effect of the nano-NIF, which can be also considered a protecting layer of the NIF. Finally, the system is illuminated by a radially-polarized beam to achieve a small spot. According to the vector diffraction theory presented by Richards and Wolf [5], the electric field distribution near the focus of the lens can be expressed, in the cylindrical coordinates, as [6, 7]

$$\begin{aligned} E_\rho(\rho, z) &= i \int_0^{\theta_{1\max}} t_{sys}^p \cos \theta_4 \sqrt{\cos \theta} \sin \theta_1 l_0(\theta) J_1(k_1 \rho \sin \theta_1) \exp[ik_3(z-d-h) \cos \theta_4] d\theta_1 \\ E_z(\rho, z) &= - \int_0^{\theta_{1\max}} t_{sys}^p \sin \theta_4 \sqrt{\cos \theta} \sin \theta_1 l_0(\theta) J_0(k_1 \rho \sin \theta_1) \exp[ik_3(z-d-h) \cos \theta_4] d\theta_1 \end{aligned} \quad (1)$$

where $\theta_{1\max} = \arcsin(n_1 \text{NA}_{\text{obj}})$ is the convergence angle related to the numerical aperture (NA_{obj}) of the objective. $k_i = 2\pi n_i / \lambda$ is the wavenumber in the dielectric i and n_i ($i = 1, 2, 3, 4$) is the refractive index of the SIL, NIF, polymer, and air, respectively. According to the condition of the aplanatic SIL and Snell's law, we have $\theta = \arcsin(\sin \theta_1 / n_1)$ and $\theta_4 = \arcsin(n_1 \sin \theta_1 / n_4)$. d and h is the thickness of the NIF and polymer films, respectively. J_n is the n th-order Bessel function of the first kind. t_{sys}^p is the effective transmittance complex amplitude coefficient of the system, which can be obtained by using the transfer-matrix method [8]. $l_0(\theta)$ is the relative amplitude of the electric field in front of a pupil. For a radially-polarized beam, $l_0(\theta)$ can be expressed as

$$l_0(\theta) = \frac{\beta_0 \sin \theta}{\text{NA}_{\text{obj}}} \exp \left[- \left(\frac{\beta_0 \sin \theta}{\text{NA}_{\text{obj}}} \right)^2 \right]. \quad (2)$$

Here β_0 is the size parameter of the incident beam determined by the ratio of the pupil radius to the incident beam waist in front of the objective.

3. NUMERICAL RESULTS

In numerical calculations we use following parameters. The wavelength of the incident laser is $\lambda = 532$ nm. The glass of $n_1 = 2.2$ and the polymethyl methacrylate (PMMA) of $n_3 = 1.6$ are chosen as the materials of the SIL and polymer films, respectively. The numerical aperture of the objective is $\text{NA}_{\text{obj}} = 0.45$ and the size parameter of beam is $\beta_0 = 1.2$ for the focusing system shown in Fig. 1. The NIF's refractive index is chosen to be the experimental values presented by Jen et al. [2]: $n_2 = -0.705 + i1.091$ for the TM wave. This NIF material has been fabricated by depositing thin films comprising parallel, tilted silver nanorods on the fused silica substrate and it has the negative refraction effect at visible light frequency band for all angles [2].

3.1. SP Excitation

It is seen from Eq. (1) that the transmission field distribution of the system shown in Fig. 1 is related to the system's effective Fresnel coefficient t_{sys}^p . To strengthen the intensity of the transmission field, we apply the SP effect of the NIF-polymer composite layer. The thickness of the NIF-polymer

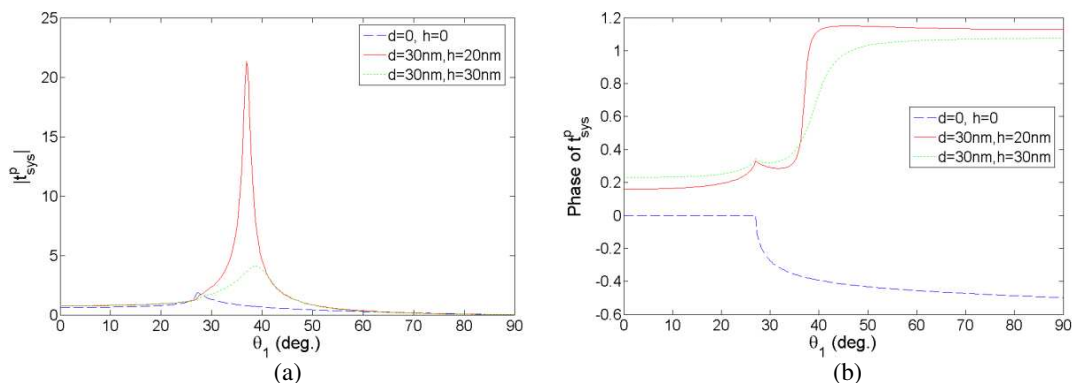


Figure 2: The transmission curves of the SIL/NIF/PMMA/air four-layer structures of (a) amplitude and (b) phase.

composite layer should be chosen in nanoscale, generally tens of nanometers. Fig. 2 shows that the transmission curves of two SIL/NIF/PMMA/air four-layer structures. As comparison, the transmission curve of a bare SIL system ($d = h = 0$) is also compiled together.

In the transmission curves of t_{sys}^p with a NIF-PMMA composite layer, the transmission maximum is the SP excitation position, meaning that the energy of the incident light transfer into the SP energy at this incident angle (the incident angle θ_1 inside the SIL corresponding to the in-plane wavevector $k_1 \sin \theta_1$). At this maximum position, the in-plane wavevector of the incident light is equal to that of the excited SP ($k_{sp} = k_1 \sin \theta_{sp}$, where θ_{sp} is called the SP's characteristic angle). From Fig. 2(a) it is found the transmission intensity of the two four-layer structures near the condition that the SP is excited is much larger than that of a bare SIL, for examples, $|t_{sys}^p| = 21.35$ when $d = 30$ nm and $h = 20$ nm, $|t_{sys}^p| = 4.09$ when $d = 30$ nm and $h = 30$ nm, but $|t_{sys}^p| = 1.89$ when $d = h = 0$. When SP wave passing through these dielectric structures, its phase can be differentially changed (see Fig. 2(b)). Figs. 3(a) and (b) display the dependence of the SP's magnitude on the PMMA's thickness h and on the NIF's thickness d , respectively. It is seen from Fig. 3 that when the PMMA's thickness is in the range of about $10 \text{ nm} < h < 22 \text{ nm}$ and the NIF's thickness is in the range of about $25 \text{ nm} < d < 35 \text{ nm}$, the NIF-PMMA composite layer can excite strong SP, therefore, one should choose the values of h and d within above these ranges to utilize the SP effect as adequately as possible.

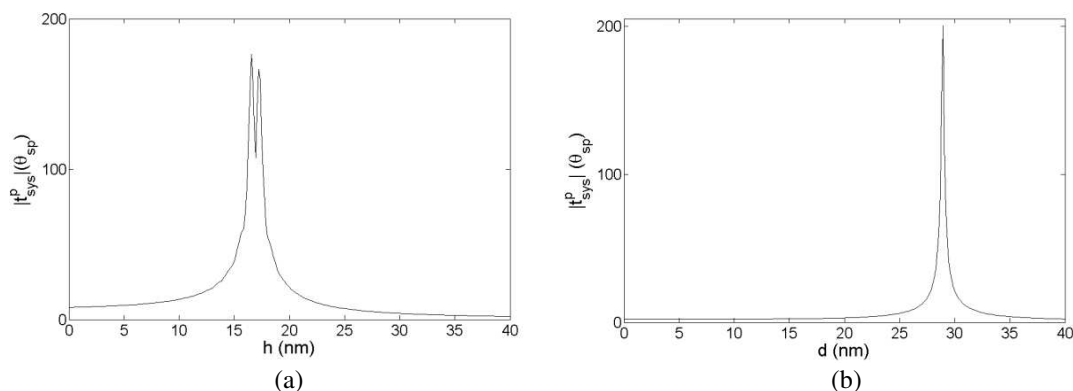


Figure 3: The SP's magnitude versus (a) h when $d = 30$ nm and versus (b) d when $h = 20$ nm.

3.2. Focused Field Distribution with a SIL-PMMA Composite Layer

Figure 4 shows the intensity distributions, in the plane of $z_c = d + h$, of the focusing system in Fig. 1. All of intensities in Fig. 4(a) are normalized to the center intensity of spot without the NIF-PMMA composite layer. Each intensity in Fig. 4(b) is normalized to its corresponding intensity in the interface of $z = d + h$. It is obvious that the intensity of spot with a composite layer is much larger than that without a composite layer in Fig. 4(a).

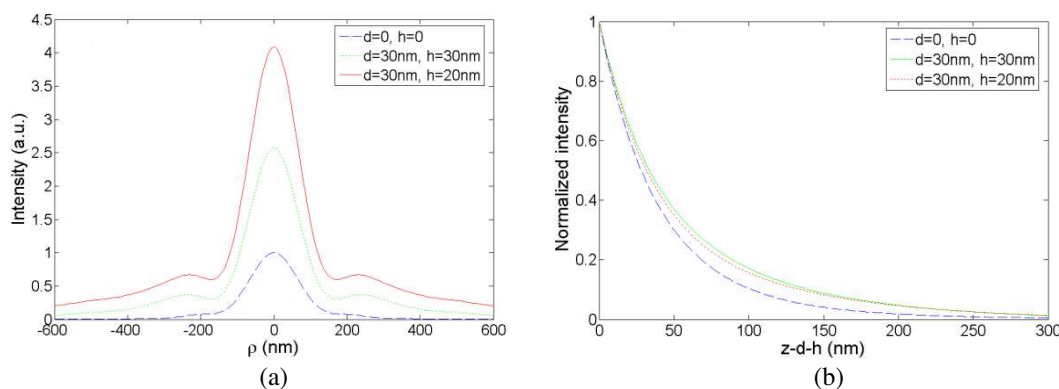


Figure 4: The intensity distributions in the transverse direction (a) in the plane of $z = d + h$ and (b) along the optical axis for the focusing system with different four-layer structures.

4. CONCLUSION

A new near-field focusing system has been proposed by attaching a NIF-polymer composite layer to a SIL. Strong surface plasmas effect excited by a real NIF combining a polymer film is used to enhance the transmission of light from the near-field optical storage system with a SIL. This is achieved by recognizing that recently fabricated films comprising of metal nanorods do have the negative refraction effect at visible light frequency band for all angles [2, 3]. The 3-D field distribution of a near-field optical storage system is calculated by using the vector diffraction theory. Numerical results show that the intensity of spot and air-gap width with the properly designed SIL-attaching-NIF-PMMA-composite-layer, are much larger than those of a conventional near-field optical recording system with a bare SIL, whereas the size of spot is almost unchanged. The present method can readily be extended from the optical storage to the fields of nanolithography and microscopy.

REFERENCES

1. Liu, L. and S. He, “Near-field optical storage system using a solid immersion lens with a left-handed material slab,” *Opt. Express*, Vol. 12, 4835–4840, 2004.
2. Jen, Y. J., A. Lakhtakia, C. W. Yu, and C. T. Lin, “Vapor-deposited thin films with negative real refractive index in the visible regime,” *Opt. Express*, Vol. 17, 7784–7789, 2009.
3. Yao, J., Z. Liu, Y. Liu, Y. Wang, C. Sun, G. Bartal, A. M. Stacy, and X. Zhang, “Optical negative refraction in bulk metamaterials of nanowires,” *Science*, Vol. 321, 930, 2008.
4. Terris, B. D., H. J. Mamin, and D. Rugar, “Near-field optical data storage using a solid immersion lens,” *Appl. Phys. Lett.*, Vol. 65, 388–390, 1994.
5. Richards, B. and E. Wolf, “Electromagnetic diffraction in optical systems. II. Structure of the image field in an aplanatic system,” *Proc. Roy. Soc. A*, Vol. 253, 358–379, 1959.
6. Zhang, Y. and J. Bai, “Improving the recording ability of a near-field optical storage system by higher-order radially polarized beams,” *Opt. Express*, Vol. 17, 3698–3706, 2009.
7. Helseth, L. E., “Roles of polarization, phase and amplitude in solid immersion lens systems,” *Opt. Commun.*, Vol. 191, 161–172, 2001.
8. Born, M. and E. Wolf, *Principles of Optics*, 7th Edition, Cambridge University Press, 1999.

Polarization-independent Metamaterial with Unnaturally High Refractive Index in the Terahertz Region

Zhengxian Liu and Shumin Xiao

Department of Material Science and Engineering Shenzhen Graduate School
Harbin Institute of Technology, Shenzhen 518055, China

Abstract— Refractive index is the most important property of material in optics and most naturally existing transparent materials possess small positive indices of refraction. With the progress of metamaterials, we can manipulate the electromagnetic properties of materials. Metamaterials promise unexpected physical phenomena through creating artificial “atoms” with an array of period metallic structure. However most researches are focusing on the negative refractive index materials at present, on the contrary the opposite side of high refractive index materials attracts far less attention. Previous approaches using metamaterials were not successful in realizing broadband isotropy high refractive indices. Here we design a broadband, isotropy three-dimensional metamaterial with extremely high index of refraction in terahertz region which composed of strongly coupled unit cells. We increase the effective permittivity through strong capacitive coupling and decrease the diamagnetic response with a thin metallic structure in the unit cell. A peak refractive index of 67.9 at 2.14 THz is observed under TE mode and a peak refractive index of 66.9 at 2.16 THz under TM mode. Both of polarizations maintain low loss with figure of merit go to as high as 2.12 and 2.48 separately. Moreover, the refractive index does not fall sharply at higher frequencies, and shows an extremely broadband behavior with a full-width at half-maximum (FWHM) of more than 2 THz.

1. INTRODUCTION

Metamaterial is a kind of artificial material composed of dense arrays of sub-wavelength strongly coupled unit cells. Plenty of unexpected electromagnetic phenomena have been realized by specially designed metamaterials [1], including controlling refractive-index [2–4], which is the most important property of material in optics. However, most of the previous researches on metamaterials in the terahertz region was focused on the negative refractive index materials [5]. High refractive index metamaterial was experimentally investigated only recently [6–11]. Expanding the refractive index into a high positive regime will complete the spectrum of achievable refractive index and provide more design flexibility for transformation optics [12–14].

The universality and scalability of the metamaterial design enables their deployment across the electromagnetic spectrum. Especially attractive are the metamaterials designed to operate in the terahertz (THz) region of the optical spectrum. Because of its special properties, the terahertz can be widely applied to medical imaging, communication, sensing and national defense [15]. However, previous approaches using metamaterials were not successful in realizing polarization-independent broadband high refractive index. The proposed metamaterials exhibit polarization dependency because of the structural anisotropy of the unit cell. In this letter, we design a broadband, isotropy three-dimensional metamaterial with extremely high index of refraction in terahertz region.

According to the Maxwellian macroscopic description, the effective permittivity of a metamaterial can be expressed as $\varepsilon = 1 + (P/\varepsilon_0 E)$ and the effective permeability can be defined by $\mu = 1 + (M/H)$, where E , H , P , and M represent the electric field, magnetizing field, polarization, and magnetization, respectively, and the refractive index of materials is determined by effective permeability and effective permittivity. In order to achieve high effective refractive index, it is required to implement a large capacitance unit cell structure to maximize the effective permittivity. Here we design a two-layer high refractive index metamaterial. The upper layer is made of a strongly coupled, thin ‘I’-shaped metallic patch. Then an alike structure which is rotate by 90 degrees around the propagation axis of the incident terahertz wave act as the under layer. The upper and under layer form a symmetrical structure together.

As a demonstration of the properties of the high refractive index metamaterial, the electromagnetic response of the structure is simulated using the finite-elements method COMSOL Multiphysics simulation package. The thin ‘I’-shaped metallic patch is considered to be embedded symmetrically in the dielectric substrate and illuminated with a plane wave at normal incidence.

The basic building block (two-layer unit cell) of the proposed high-refractive-index terahertz metamaterial is shown in Figure 2(a), together with the polarization of an incident TE terahertz

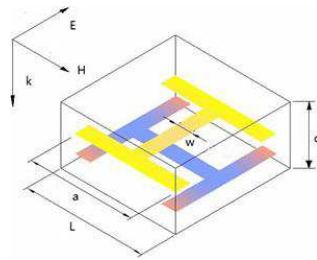


Figure 1: Schematic view of unit cell structure of the high-index metamaterial.

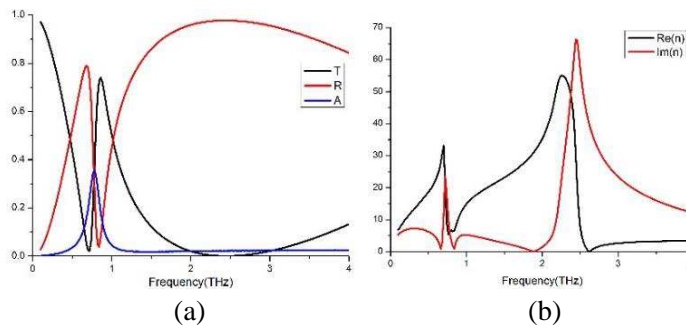


Figure 2: (a) Simulated transmission (T) and reflection (R) and absorption (A) spectra of the structure. (b) Numerically extracted values of complex refractive index (n) obtained from the S -parameter retrieval method.

wave. The substrate was implemented with polyimide ($n_{poly} = 1.8 + 0.04i$), and the metals used to construct the metamaterials were gold. The complex dielectric constant of gold for the frequency range of interest can be fitted using the Drude model with a plasma frequency of $\omega_p = 1.37 \times 10^{16} \text{ s}^{-1}$ and collision frequency of $\gamma = 4.07 \times 10^{13} \text{ s}^{-1}$. The geometric parameters used for simulation of the metamaterial are: $L = 40 \mu\text{m}$, $a = 39 \mu\text{m}$, $w = 3 \mu\text{m}$, $d = 1 \mu\text{m}$. The thickness of both metallic patch is 100 nm. The gap width between the metallic patches is defined as $g = L - a$. It's worth noting that both metallic structure are the same size.

As can be seen from Figure 2(a), there are two reflectivity peaks in the interval of 0.1–4 THz, corresponds to two peaks index of refraction of $n = 33.1$ at 0.7 THz and $n = 55.1$ at 2.26 THz are observed in Figure 2(b). Each layer of metallic structure provide a refraction peak, respective. But each peak are caused by different mechanism. The electric field was strongly concentrated in the gap along the long side between each 'I'-shaped metallic structure in the upper layer at a incident frequency of 0.65 THz and a different electric field distribution along the short side produced by the under layer at a higher incident frequency of 2.26 THz. Meanwhile both of the magnetic field penetrated deeply into the unit cell because of the negligible metallic volume fraction. The saturated of electric field and magnetic field of both layer are shown in Figures 3(a), (b), (c), (d), respective. So it is apparent that the upper layer and under layer produce a lower peak of refractive at a lower frequency and he under layer produce a higher peak of refractive at a higher frequency. Actually we can find that when the incident wave is polarized along the central beam (defined as a TE wave) at 0.65 THz, there is a larger capacitance of the upper layer comparing with the case of the under layer illuminated with a wave at 2.25 THz. However the capacitance of the under layer illuminated with a wave at 0.65 THz is far less than the case of the upper layer with a wave at 2.25 THz. In a broad sense, the peak of refraction is influenced by both of the two layers.

After the possibility of realizing a dualband high refractive index for double-layer metamaterial, further insights can be acquired with an investigation into three-dimensional high refractive index metamaterials. In order to investigate the bulk properties, a high refractive index metamaterials containing up to four layers were tested. Figure 4(a) shows the simulated transmission/reflection plotted as a function of frequency; and the simulation complex refractive index are plotted in Figure 4(b). As can be seen in the picture, there are still two high refractive index peaks for the three-dimensional metamaterial. The index of refraction of 24.9 and 67.9 are obtained at a frequency of 0.48 THz and 2.14 THz, respectively. Meanwhile, the refractive index does not fall sharply at higher frequencies, and shows an extremely broadband high refractive index with a

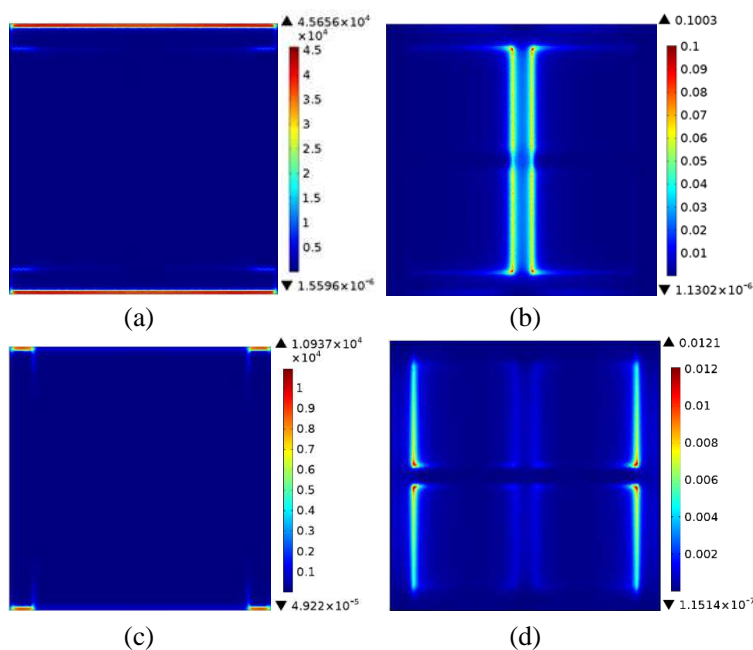


Figure 3: Saturated (a) electric and (b) magnetic field of upper layer at 0.65 THz, (c) electric and (d) magnetic field of under layer at 2.25 THz for a double-layer metamaterial, respectively.

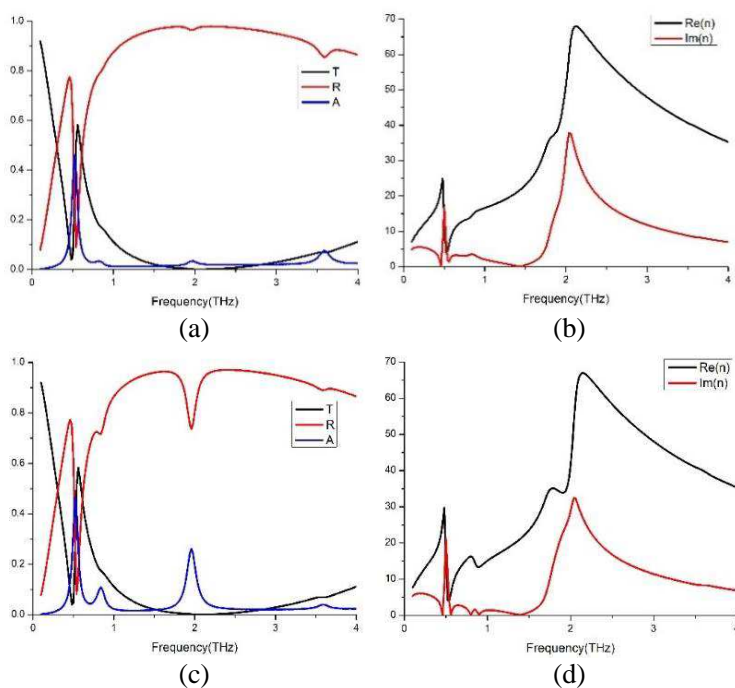


Figure 4: Simulated transmission (T) and reflection (R) and absorption (A) spectra of the structure for (a) TE polarization and (c) TM polarization, respectively; numerically extracted values of complex refractive index (n) obtained from the S -parameter retrieval method for (b) TE polarization and (d) TM polarization.

full-width at half-maximum (FWHM) of more than 2.24 THz. The four-layer metamaterials leads to different mechanism in the refractive spectra compared to double-layer metamaterials [16, 17] because of the coupling between layers. Considering the effective wavelength of a terahertz wave inside the metamaterial, the thickness ($d = 2 \mu\text{m}$) in the direction of propagation is much smaller than the effective wavelength, which justifies the application of homogenization theory, so the four-layer metamaterial can be considered as a Fabry-Pérot etalon. So the four-layer metamaterials maintain low loss with figure of merit go to as high as 2.12.

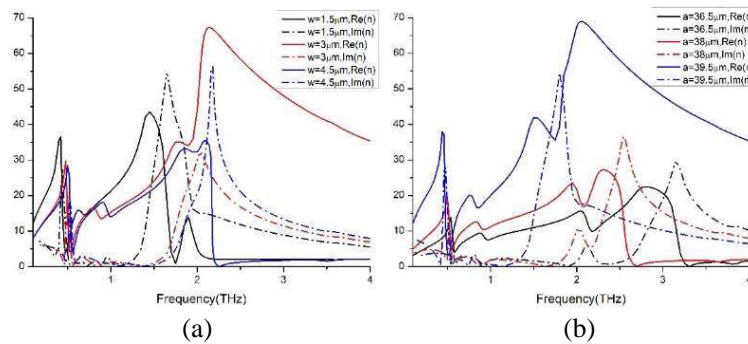


Figure 5: Geometrical parameter-dependent effective refractive index. (a) Effective refractive index plotted as a function of central beam width w . (b) Effective refractive index plotted as a function of gap width g .

As the proposed high-index metamaterial is a symmetrical structure, we can easily predict that the metamaterial has an isotropous refractive index. Figures 4(a), (c) show the simulated transmission (T) and reflection (R) and absorption (A) spectra of the structure for TE polarization and TM polarization, respectively. Figures 4(b), (d) show numerically extracted values of complex refractive index (n) obtained from the S -parameter retrieval method for TE polarization and TM polarization, respectively. It is noted that there are still two refractive peaks in the interval of 0.1–4 THz. They are $n = 39.6$ at 0.48 THz and $n = 66.9$ at 2.16 THz respectively. And it also keeps the feature of broadband, and the figure of merit maintains 2.48. There are still some differences when the incident wave changes from TE wave into TM wave. This is mainly caused by the different spatial locations between them.

The value of the refractive index is a sensitive function of the gap width (g) and the central beam width (w) for the proposed high-index metamaterials. In order to verify this two geometrical size dependency, the effective refractive index are numerically estimated for samples having different geometrical parameters. The dependency of refractive on the central beam width (w) is plotted in Figure 5(a). For this simulation, the parameter of the structure is $L = 40 \mu\text{m}$, $d = 2 \mu\text{m}$, $a = 39 \mu\text{m}$. In the plot, we can find that when the central beam width is too narrow, the current loops decrease, leading to a decrease of the refractive index. However, when the central beam width (w) is too board, there is a great of diamagnetic effect in the structure which also resulting the refractive index decreases. It is also worthwhile to note that, the central beam width control can also be used to tune the electric resonance frequency of the metamaterial, which is caused by the change in the inductance of the metallic patch. Figure 5(b) shows the numerically estimated index of refraction as a function of the gap width. As the gap width decreases, there is a great increase of the capacitive due to coupling between unit cells. As a result, the index of refraction is drastically increased. Therefore, an even higher index of refraction can be achieve by further reducing the gap width (g). As the gap closes, this increase is expected to continue until the gap width approaches the Thomas–Fermi length scale [18] or the quantum tunneling scale of electrons. Moreover, the effective refractive index is proportional to the substrate index; thus, the introduction of a higher-index substrate will lead to greater amplification of the refractive index and an unprecedentedly large effective refractive index.

In summary, we have designed a dualband polarization-independent broadband metamaterial with high refractive index in the terahertz region. The obtained dependence of the effective refractive index on the geometric parameters provides us with a general recipe for designing such metamaterials. Moreover, we can predict that a high-performance high-index metamaterials can also be realized to even higher frequency ranges, such as mid-infrared frequencies via rational design.

REFERENCES

1. Schurig, D., J. J. Mock, B. J. Justice, et al., “Metamaterial electromagnetic cloak at microwave frequencies,” *Science*, Vol. 314, No. 5801, 977–980, 2006.
2. Smith, D. R. and N. Kröll, “Negative refractive index in left-handed materials,” *Physical Review Letters*, Vol. 85, No. 14, 2933, 2000.
3. Shalaev, V. M., “Optical negative-index metamaterials,” *Nature Photonics*, Vol. 1, No. 1, 41–48, 2007.

4. Wei, X., H. Shi, X. Dong, et al., “A high refractive index metamaterial at visible frequencies formed by stacked cut-wire plasmonic structures,” *Applied Physics Letters*, Vol. 97, No. 1, 011904, 2010.
5. Xiao, S., V. P. Drachev, A. V. Kildishev, et al., “Loss-free and active optical negative-index metamaterials,” *Nature*, Vol. 466, No. 7307, 735–738, 2010.
6. Shen, J. T., P. B. Catrysse, and S. Fan, “Mechanism for designing metallic metamaterials with a high index of refraction,” *Physical Review Letters*, Vol. 94, No. 19, 197401, 2005.
7. Shin, J., J. T. Shen, and S. Fan, “Three-dimensional metamaterials with an ultra-high effective refractive index over broad bandwidth,” *Physical Review Letters*, Vol. 102, 093903, 2009.
8. Pimenov, A. and A. Loidl, “Experimental demonstration of artificial dielectrics with a high index of refraction,” *Physical Review B*, Vol. 74, No. 19, 193102, 2006.
9. Choi, M., S. H. Lee, Y. Kim, et al., “A terahertz metamaterial with unnaturally high refractive index,” *Nature*, Vol. 470, No. 7334, 369–373, 2011.
10. Mina, B., “Ultrafast refractive index control of THz graphene metamaterials,” *2013 38th International Conference on Infrared, Millimeter, and Terahertz Waves (IRMMW-THz)*, 1–2, 2013.
11. Kim, Y., M. Choi, S. H. Lee, et al., “Two-dimensionally isotropic high index metamaterials,” *2011 Conference on Lasers and Electro-Optics (CLEO)*, 1–2, 2011.
12. Pendry, J. B., D. Schurig, and D. R. Smith, “Controlling electromagnetic fields,” *Science*, Vol. 312, No. 5781, 1780–1782, 2006.
13. Liu, R., C. Ji, J. J. Mock, et al., “Broadband ground-plane cloak,” *Science*, Vol. 323, No. 5912, 366–369, 2009.
14. Gabrielli, L. H., J. Cardenas, C. B. Poitras, et al., “Silicon nanostructure cloak operating at optical frequencies,” *Nature Photonics*, Vol. 3, No. 8, 461–463, 2009.
15. Li, J., C. M. Shah, W. Withayachumnankul, et al., “Mechanically tunable terahertz metamaterials,” *Applied Physics Letters*, Vol. 102, No. 12, 121101, 2013.
16. Liu, N. and H. Giessen, “Three-dimensional optical metamaterials as model systems for longitudinal and transverse magnetic coupling,” *Optics Express*, Vol. 16, No. 26, 21233–21238, 2008.
17. Papasimakis, N., V. A. Fedotov, S. L. Prosvirnin, et al., “Metamaterial analog of electromagnetically induced transparency,” *Physical Review Letters*, Vol. 101, 253903, 2008.
18. Seo, M. A., H. R. Park, S. M. Koo, et al., “Terahertz field enhancement by a metallic nano slit operating beyond the skin-depth limit,” *Nature Photonics*, Vol. 3, No. 3, 152–156, 2009.

Photon Hopping and Nanowire Based Hybrid Plasmonic Ring-resonator

Zhiyuan Gu¹, Shumin Xiao², Shuai Liu¹, Shang Sun², Kaiyang Wang¹, and Qinghai Song^{1,3}

¹Department of Electrical and Information Engineering
Harbin Institute of Technology, Shenzhen, Guangdong 518055, China

²Department of Materials Science and Engineering
Harbin Institute of Technology, Shenzhen, Guangdong 518055, China

³National Key Laboratory on Tunable Laser Technology
Harbin Institute of Technology, Harbin 158001, China

Abstract— Here we demonstrate the transmission of waves through a gap in hybrid plasmonic waveguide, which is termed as “photon hopping”. Based on the photon hopping, we explore the possibility to achieve high Q resonator by nano-manipulating the nanowire to a pseudo-ring. Our numerical results show that the Q factors, effective mode volumes, and Purcell factors of nanowire based ring-resonator are very close to a perfect hybrid plasmonic ring resonator, expanding the potential applications of nanowires to nano-cavity quantum electrodynamics (QED) and nanolasers.

1. INTRODUCTION

Manipulation of light in subwavelength and nanoscale structures is of central importance for the researches on miniaturizations of coherent light sources and highly integrated photonic network [1]. A number of nanostructures such as nanoparticles [2] and antennas [3] have been successfully developed to control the light confinement and emission in nanoscale. Nanowires are prominent examples due to their intrinsic advantages, e.g., dislocation free single crystalline, cost-effective synthesis, high index of refraction, and broad range of materials [4–6]. In past decade, coherent light sources with tiny effective mode areas have been successfully detected from different nanocavities, including ZnS [7], CdS [8], GaN [9], and GaSb [10] nanowires. However, the performances of such devices face severe challenge when their sizes are further reduced to nanoscale. This is caused by two main limitations. The mode volumes are usually comparable to nanowire dimensions [11]. And the light confinements are very poor due to their extremely low end-facet reflections [12, 13].

Owing to the better confinement of surface plasmon polaritons (SPP) [14], the combination of semiconductor nanowire and plasmonic waveguide has been utilized to reduce the effective mode volume (V_{eff}) [15]. However, the light confinement is still an awesome task for the nanowire based plasmonic devices. Here we demonstrate the photon hopping phenomenon in hybrid plasmonic waveguide and explore its applications in high- Q nanocavities.

2. RESULTS

As depicted in Fig. 1(a), the hybrid waveguide consists of a dielectric nanowire separated from a silver layer by a nanoscale insulating layer with lower refractive index. Here we set $d = 100$ nm, $h = 5$ nm, $\varepsilon_c = 5.76$ (for CdSe or GaN), and $\varepsilon_d = 1.96$ (for MgF₂). The permittivity of silver is defined with a Drude model. And the material dispersion and loss of dielectric structures are neglected.

The calculated n_{eff} for the hybrid plasmonic mode at 530 nm is only about 1.7, which is not too much higher than the surrounding medium. From the Fresnel law, we can find that the reflectance is only $\sim 9\%$ in a wide frequency range, consistent with the small n_{eff} . For the conventional Fabry-Perot like nanowire cavities, their quality (Q) factors can be estimated with the equation $Q = -Lk_a / \ln|r_1r_2|$, where L , k_a , r_1 , and r_2 are the nanowire length, propagation constant, and reflection coefficients at two end facets. Following the results in Fig. 1(b), the Q factor of a hybrid plasmonic waveguide with $L = 1$ μ m is only around 7.5, which prevents short nanowires from lasing and restricts the lower limit of nanowire dimensions.

As the reflection and propagation loss are both low in the hybrid plasmonic waveguide [16–18], most of the waves shall transmit refractively at the end facet. The opened squares in Fig. 1(b) show the calculated transmission spectrum at interface S_1 , where almost 40%–50% of energy can be detected outside the hybrid plasmonic waveguide.

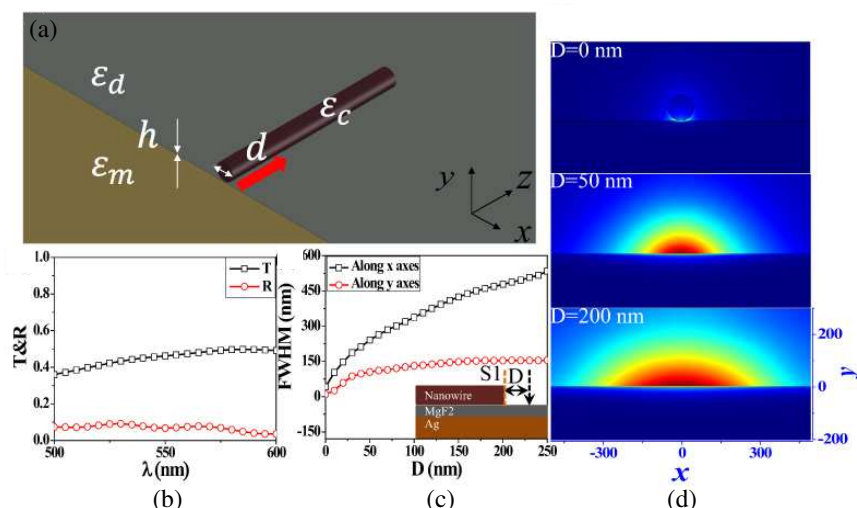


Figure 1: (a) The schematic picture of the hybrid plasmonic waveguide. A semi-infinite long nanowire is placed on a metal substrate insulated by a thin low-index dielectric layer. The end-facet is marked as $S1$. The silver is modeled by Drude model and the permittivity of CdS and MgF_2 are set as $\epsilon_c = 5.76$ and $\epsilon_d = 1.96$. (b) The transmission (T , open squares) and reflection (R , open circles) of the waveguide at interface $S1$. Here $d = 100$ nm and $h = 5$ nm. (c) The evolutions of FWHM of the output beam in horizontal direction (open squares) and vertical direction (open circles). (d) The field pattern of propagating mode at the plane with distance $D = 0, 50$, and 200 nm from the interface $S1$.

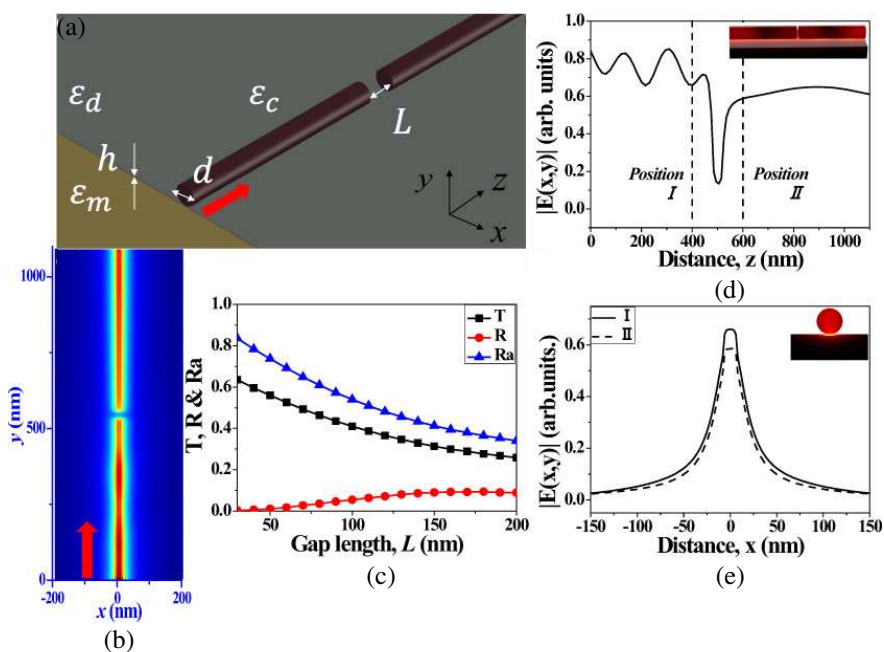


Figure 2: (a) The Schematic picture of two nanowire based hybrid plasmonic waveguide. The separation distance between two nanowires is L . (b) the electric density distribution in MgF_2 insulating layer. Efficient photon hopping can be directly observed. (c) The transmittance (T , black squares), reflectance (R , red dots), and ratio (blue triangles) as a function of L . (d) the electric field along the z -axis. (e) The electric field along x -axis at position I (solid line) and II (dashed line) marked in (d). The insets are the corresponding field patterns.

To explore the possibility of nanoscale light collection, we have studied the field distributions of the transmitted light. With the increasing of distance from end-facet $S1$ (D), we can see that the full width half maximum (FWHM) of the output beam increases gradually from 40 nm at $D = 0$ nm to about 530 nm at $D = 250$ nm in the plane. This divergence is caused by the diffraction of waves

from the small aperture, similar to the emission from conventional waveguide. The field distribution in the vertical direction is quite different. While the FWHM also increases at the beginning, it turns to be saturate at $D > 30$ nm. From the field distributions in Fig. 1(d), we thus know that the electromagnetic waves transit from hybrid plasmonic mode to regular SPP along the Silver-MgF₂ interface when they leave the hybrid waveguide.

To fully explore the applications of nanowire, we place a nanowire behind the first one. The schematic picture is depicted in Fig. 2(a). Fig. 2(b) shows the electric density distribution of hybrid plasmonic mode at $\lambda = 550$ nm at the Ag-MgF₂ interface. While a gap appears, we can see that the waves mostly transmit into the second nanowire. It is worth to note that the low transmittance doesn't mean the high loss caused by the gap. There is still reflection caused by the interfaces at the gap. The calculated values are shown as red dots in Fig. 2(c). The blue triangles represent the ratio $[Ra = (T + R)/T_{WO}]$, where T_{WO} is the transmittance in single nanowire with the same overall length without gap. We can see that ratio can be larger than 40% when the separation distance $L < 150$ nm, clearly demonstrating the high collecting efficiency of the second waveguide. In principle, the high transmittance is not surprising. Similar to the previous study on the propagation of SPP across narrow grooves in silver film [19], the transmitted waves experience a transition from hybrid plasmonic to regular SPP and a transition back to hybrid plasmonic. Fig. 2(d) shows the field distribution along the z -axis. The reduction of $|E(x, y)|$ at the gap is consistent with the transition processes. Meanwhile, the field distributions before and behind the gap [see Figs. 2(b) and 2(e)] are almost the same, indicating that the transmitted waves follows the same hybrid plasmonic mode as the incident one. Below, we term this process as “photon hopping”.

Placing two nanowires end by end is of course possible in nano-manipulation [11]. However, it is extremely difficult to arrange their axes in a single line experimentally as Fig. 2. To explore the light collection for real applications, we have numerically studied the dependences of transmittance on the transverse shift along x -axis (see Fig. 3(a)). The results are summarized in Fig. 3(c). With the increasing of w , the transmittance decreases slowly. When $w = 100$ nm and $d = 50$ nm, the transmittance is still around 32%. Taking account the reflection, the ratio Ra is almost 42.5%, which means that almost half energy can be collected by placing two nanowires end by end with slight overlap. The high transmission at large w is consistent with the horizontal divergence of regular SPP in Fig. 1(c). Similarly, the transmittance T and ratio Ra are also quite robust to the tilt of the second wire. When the tilt angle $\theta \leq 40$ degree, the transmittance is higher than 39.5% and the ratio Ra is larger than 49.5%. The examples of field patterns in MgF₂ layer are plotted in Figs. 3(b) and 3(e).

Based on this effect of “photo hopping”, we can propose a new scheme to achieve the high

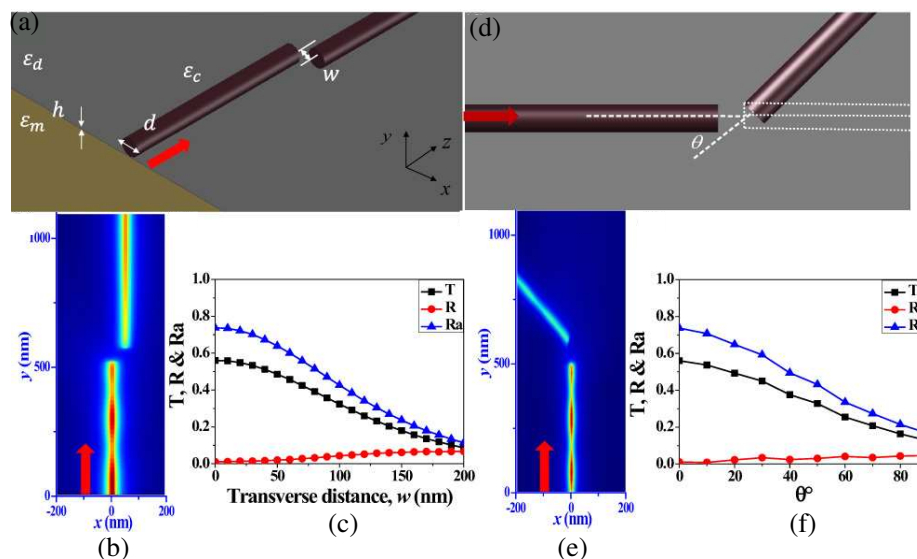


Figure 3: The robustness of the light collection by the second nanowire. (a) and (c) depict the transverse shift and tilt angle. (c) and (f) are the dependence of T , R , and Ra on w and θ , respectively. (b) and (e) show the example electric density distributions with $w = 50$ nm and $\theta = 50$ degree.

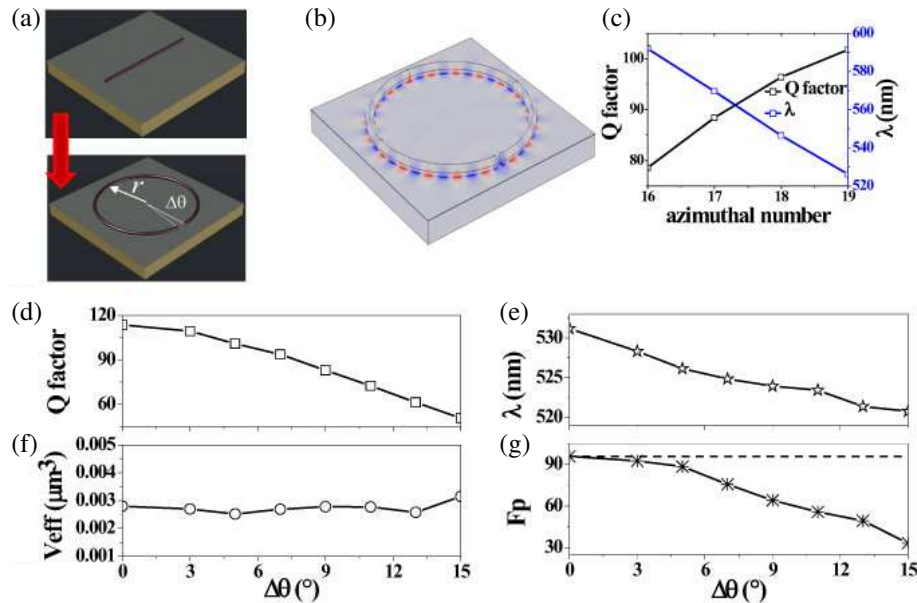


Figure 4: (a) Schematic of hybrid plasmonic ring-resonator. The size parameters of ring resonator and nanowire are $r = 1000$ nm and $d = 100$ nm, respectively. And the separation between two end-facets is determined by $\Delta\theta$. (b) The field pattern of resonance at $\lambda = 527$ nm. Here $\Delta\theta = 5^\circ$ and the Azimuthal number m is 19. (c) The Q factor and resonant wavelength of different resonances. (d)–(g) are the Q factor, resonant wavelength, effective mode volume, and Purcell effect of the mode with $m = 19$ as a function of $\Delta\theta$.

Q factor. As depicted in Fig. 4(a), a nanowire can be tailored to a ring resonator via nanomanipulation [11]. Fig. 4(b) shows an example of the resonance in the nanowire-based ring-resonator. While the gap introduces some additional loss, the calculated Q factor is still about 100, which is more than an order of magnitude higher than the Fabry-Perot cavity [17]. One may argue that the Q factor of this ring resonator is not as good as regular ring resonator with similar size [20]. Here we will emphasize again the significant advantages of hybrid plasmonic device, the extremely small mode volume (V_{eff}) and larger Purcell factor (F_p). For the mode in Fig. 4(b), the calculated V_{eff} is about $3 \times 10^{-3} \mu\text{m}^3$. Then the corresponding Purcell factor ($F_p = 3Q(\lambda/n)^3/4\pi^2V_{eff}$) can be as high as 90. Both V_{eff} and F_p are orders of magnitude higher than regular dielectric cavity [20, 21], indicating the potential applications in nanosensors and nano-cavity quantum electrodynamics.

The resonance in Fig. 4(b) is not a special mode that generate high Q factor like the modes around avoided resonance crossing [22]. This calculated WG-like modes with different Azimuthal number in Fig. 4(c) shows that the high Q resonance is quite general in the nanowire based ring-resonator. Similar to Fig. 2, the high Q factor is also robust to the changes on separation gap. Figs. 4(d)–(g) show the dependences of quality factor, resonant wavelength, effective mode volume, and Purcell factor on the size of separation distance $\Delta\theta$. With the increase of $\Delta\theta$ (size of air gap), the resonant wavelength shifts to blue side in Fig. 4(e). According to Figs. 2 and 3, the collection ratio of the nanowire also decreases, generating a reduction in Q factor in Fig. 4(d). When $\Delta\theta$ is smaller than 5 degree, which corresponds to a gap size $\Delta\theta \times R$ about 87 nm, the reduction is very slow and the Q factor is very close to that of a perfect ring resonator with $\Delta\theta = 0$. The reduction increases at larger $\Delta\theta$. But the Q factor at $\Delta\theta = 13$ degree (gap size ~ 226 nm) is still around half of the value of perfect ring.

It is important to note that perfect hybrid plasmonic ring-resonator has been thoroughly studied before. In previous studies, the transverse cross-sections are usually the rectangles [23, 24], which is supposed to be fabricated with top-down etching. However, the nanoscale devices are extremely difficult to be fabricated even with E-beam lithography. And the etching faces sever challenge in wide bandgap materials such as GaN, where the surface roughness is too large to kill the light confinement [25].

In Summary, we have studied the photon hopping effect between two nanowires. Based on the high collection ratio at the nanoscale, we proposed a new design to achieve high Q , small V_{eff} , and large F_p simultaneously by tailoring the well-known semiconductor nanowire to a ring-like

resonator. As both the synthesis of nanowire and the nanoscale manipulation have been widely explored, our findings will significantly expanding the applications of nanowires in active devices such as nanolasers and passive devices such as nano-waveguide and nano-network.

ACKNOWLEDGMENT

This work is supported by NSFC11204055, SFC61222507, NSFC11374078, NCET-11-0809, KQCX2012080709143322, and KQCX20130627094615410.

REFERENCES

1. Shacham, A., K. Bergmann, and L. P. Coloni, *IEEE Trans. Comput.*, Vol. 57, 1246, 2008.
2. Michalet, X., et al., *Science*, Vol. 307, 538, 2005.
3. Novotny, L., *Nature*, Vol. 455, 887, 2008.
4. Yan, R. X., D. Gargas, and P. D. Yang, *Nature Photon.*, Vol. 3, 569, 2009.
5. Xia, Y., et al., *Adv. Mater.*, Vol. 15, 353, 2003.
6. Huang, M. H., et al., *Science*, Vol. 292, 1897, 2001.
7. Zapien, J. A., et al., *Appl. Phys. Lett.*, Vol. 84, 1189, 2004.
8. Duan, X., Y. Huang, R. Agarwal, and C. M. Lieber, *Nature*, Vol. 421, 241, 2003.
9. Johnson, J. C., et al., *Nature Mater.*, Vol. 1, 106, 2002.
10. Chin, A. H., et al., *Appl. Phys. Lett.*, Vol. 88, 163115, 2006.
11. Pauzauskie, P. J., D. J. Sirbully, and P. D. Yang, *Phys. Rev. Lett.*, Vol. 96, 143903, 2006.
12. Qian, F., et al., *Nature Mater.*, Vol. 7, 701, 2008.
13. Li, Y., F. Qian, J. Xiang, and C. M. Lieber, *Mater. Today*, Vol. 9, 18, 2006.
14. Barnes, W. L., A. Dereus, and W. Ebbesen, *Nature*, Vol. 424, 824, 2003.
15. Ditlbacher, H., et al., *Phys. Rev. Lett.*, Vol. 95, 257403, 2005.
16. Oulton, R. F., V. J. Sorger, D. A. Genov, D. F. P. Pile, and X. Zhang, *Nature Photon.*, Vol. 2, 496, 2008.
17. Oulton, R. F., et al., *Nature*, Vol. 461, 629, 2009.
18. Yu, Y.-J., et al., *Science*, Vol. 337, 450, 2012.
19. Seidel, J., S. Grafstrom, L. Eng, and L. Bischoff, *Appl. Phys. Lett.*, Vol. 82, 1368, 2003.
20. Song, Q. H., H. Cao, S. T. Ho, and G. S. Solomon, *Appl. Phys. Lett.*, Vol. 94, 061109, 2009.
21. Song, Q. H. and H. Cao, *Phys. Rev. Lett.*, Vol. 105, 053902, 2010.
22. Song, Q. H., Z. Y. Gu, S. Liu, and S. M. Xiao, *Sci Rep.*, Vol. 4, 4858, 2014.
23. Xiao, Y.-F., et al., *J. Phys. B: Atomic, Molecular and Optical Physics*, Vol. 43, 035402, 2010.
24. Chen, Y., C. Zou, Y. Hu, and Q. Gong, *Phys. Rev. A*, Vol. 87, 023824, 2013.
25. Zhang, Y., et al., *Phys. Status. Solidi.*, Vol. 247, 1713, 2010.

Cortical Functional Connectivity Revealed by Optical Brain Imaging

Jun Li and Lina Qiu

Centre for Optical and Electromagnetic Research
South China Normal University, Guangzhou 510006, China

Abstract— Optical brain imaging is emerging as a novel technique for non-invasively investigating functioning brain. It uses near-infrared light to probe human cortex through intact scalp and skull, providing cerebral hemodynamic information closely associated with neuronal activity. In addition to investigating various task-related cortical activations, very recently optical brain imaging has been demonstrated to be able to assess resting state functional connectivity (RSFC) by recording and cross-correlating the cortical spontaneous fluctuations. In this work, we performed two experiments by using an optical brain imaging system to reveal cortical RSFC. In Experiment I, the cortical areas measured included bilateral temporal and adjacent inferior frontal cortices. In experiment II, we measured the prefrontal cortex. The data from Experiment I show that there are significant differences in the network between children and adults, implying the developmental differences in the language network. The data from Experiment II show significant differences between males and females in prefrontal RSFC, which may be associated with the underlying physiological basis for sex-related differences in cognitive control and emotional regulation in humans.

1. INTRODUCTION

A large amount of studies over the past twenty years have demonstrated that optical brain imaging is a useful technique for imaging functioning brain [1–5]. Due to its low cost, portability, as well as noninvasive measure on the concentration variations of hemoglobin, optical brain imaging has been increasingly used for studying healthy brain [5–7] and a variety of psychiatric disorders [8–10].

Resting state functional connectivity (RSFC) studies with functional magnetic resonance imaging (fMRI) showed that low frequency (< 0.1 HZ) fluctuations of spontaneous neural activity are temporally correlated between functional relevant regions during the resting state [11, 12]. Recent studies have also demonstrated optical brain imaging has the ability to reveal RSFC by recording cerebral spontaneous hemodynamic signals [13–16].

Very recently, optical brain imaging has been applied to quantitatively evaluating intra- and/or inter-hemispheric correlations across functional regions during resting state, such as prefrontal, sensorimotor, and visual cortices [14]. These correlations could provide useful information about cortical networks, such as network range and connectivity strength.

In this work, we performed two experiments by using a continuous-wave optical brain imaging system to identify RSFC for healthy children and adults. In Experiment I, the cortical areas measured included bilateral temporal and adjacent inferior frontal cortices. These regions are human language areas responsible for language generation and comprehension. In Experiment II we measured prefrontal cortex, the high functional area in human responsible for cognition, memory, and emotion, et al.. From Experiment I, we found significant differences in network connectivity and range between adults and children, which may reflect developmental differences in language network. Data from Experiment II showed significant differences between adult males and females in RSFC, which may shed light on the underlying physiological basis for sex-related differences in cognitive control and emotional regulation.

2. METHODS

2.1. Subjects

Experiment I was to investigate RSFC for language areas, in which twenty-two healthy subjects (11 adults and 11 children) were involved. In the adult group, there were eight males with an average age of 23.4 (± 0.9) years old. The children group consisted of eight boys with an average age of 9.0 (± 1.5) years old. Experiment II was to detect RSFC for prefrontal cortex, in which twenty-two adult healthy subjects (11 males) were included, with an average age of 23.6 (± 0.9) years old. All subjects were right handed. Before experiments, subjects were informed about the measuring procedure and written consent was obtained from adults and parents of the children. The study protocol was approved by the University's Ethical Review Board.

2.2. Experimental Setup and Experimental Protocol

Measurements were conducted with a commercial continuous-wave optical brain imaging system (FOIRE-3000, Shimadzu Corporation, Kyoto, Japan) working at three different wavelengths (780 nm, 805 nm and 830 nm). In all measurements, 8-min spontaneous cortical fluctuations were recorded. During measurements, the subject was sitting quietly on a comfortable chair in a dim room with his/her eyes closed.

The locations of the optical sensors were positioned based on the international 10/20 EEG system [17]. In Experiment I, 44 channels (22 for each hemisphere) were used to cover bilateral temporal and inferior frontal cortices, which is schematically shown in Fig. 1(a). In Experiment II, 42 channels were used to cover prefrontal cortex, as schematically shown in Fig. 1(b).

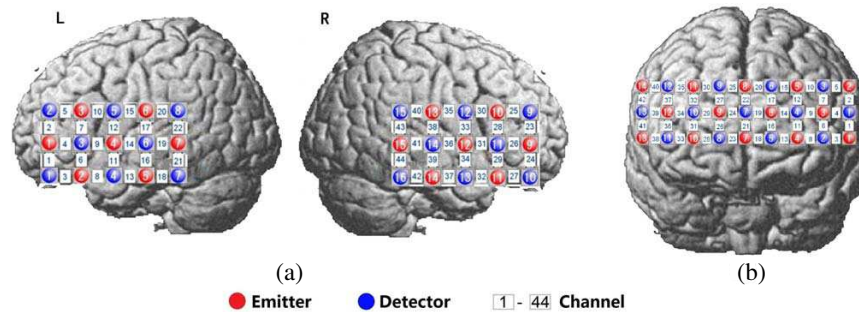


Figure 1: Experimental schematics. (a) Schematic representation of the brain showing the location of each measurement channel over bilateral temporal and inferior frontal cortices. (b) Schematic representation of the brain showing the location of each measurement channel over the prefrontal cortex.

2.3. Data Analysis

As the first step of data processing, a band pass filter (0.009–0.08 Hz) was applied to the optical data (time series of HBO, HB and HBT) [14] to reduce systemic oscillations (such as that due to cardiac cycles ~ 1 Hz, respirations ~ 0.2 Hz and blood pressure fluctuations ~ 0.1 Hz). To further remove the remaining global component which is not specific to local cortex, an ICA based algorithm [16] is used for processing data from Experiment I. While for Experiment II, a conventional regression algorithm is used [18]. The conventional regression algorithm is based on an assumption that the overall mean value for all local intrinsic signals is zero. This may be applied to the case where signals come from many functionally independent regions. Obviously, it does not hold when all signals come from functionally closely related regions such as language areas. The Pearson correlation coefficients are used for the correlation analysis. To map the correlations, a ‘seed-based’ approach [14] is used in which the correlations between the seed channel and all other channels are projected on the measured areas. This correlation map shows the connectivity (or synchronization) pattern of cortical spontaneous activity.

3. RESULTS

3.1. The Results for Experiment I

The connectivity (or correlation) matrices for left and right language areas are shown in Fig. 2. Each pixel value corresponds to a group average correlation value for oxygenated hemoglobin (HBO) in the 44×44 correlation matrix. From Fig. 2, one can see the adult group is stronger than the children group on both intra-hemispheric (e.g., L-L, R-R) and inter-hemispheric (e.g., L-R) correlations. Since language processing is left lateralized, relying mainly on left hemispheric networks, a seed (channel) for generating a correlation map was selected on left hemisphere. Fig. 3 gives HBO correlation maps for the adult [Fig. 3(a)] and the children [Fig. 3(b)] group. The correlation map shows correlations on the measured area between the seed and all the other channels. In comparison, within each hemisphere, the adult group shows stronger correlation and larger correlation range. Between hemispheres, the inter-hemispheric correlation is stronger for the adult group than the children group. These findings are in line with the fact that language network is developed better for adults than children who are still developing.

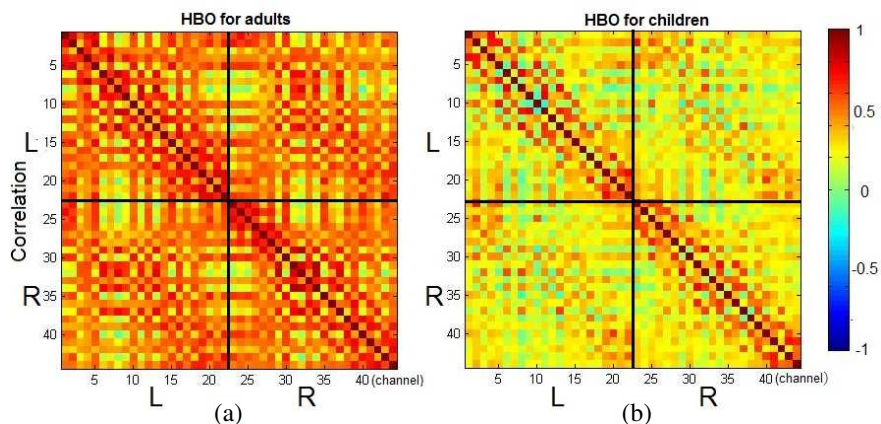


Figure 2: Group average connectivity matrices showing HBO correlations between all channels, (a) is for the adult group, and (b) for the children group.

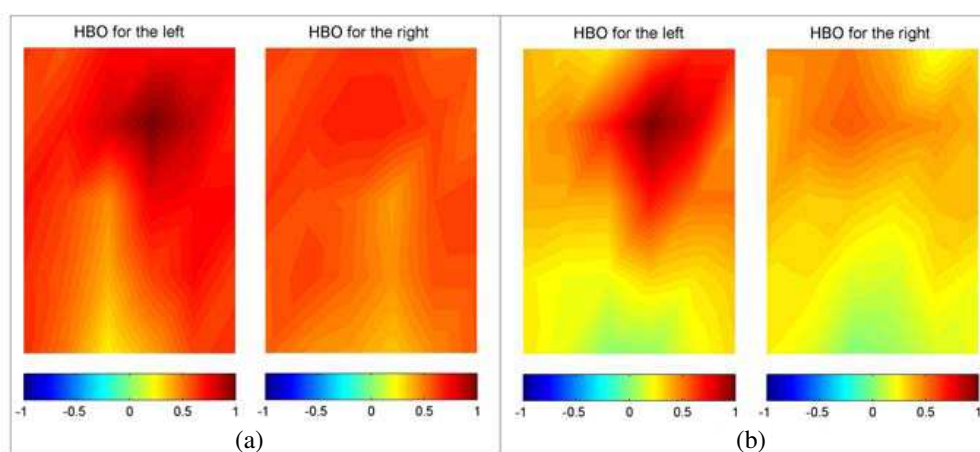


Figure 3: HBO connectivity maps showing correlations between the seed (channels 19) and all other channels, (a) is for the adult group, and (b) for the children group. The seed is located on the left hemisphere and can be visually recognized by the maximal color value in each map.

3.2. The Experiment of Prefrontal Cortex

Figure 4 illustrates prefrontal connectivity matrices for males [Fig. 4(a)] and females [Fig. 4(b)]. One can see that the male group has stronger connectivity in the anterior prefrontal cortex (BA 10) than the female group, which is revealed by the significant difference in the correlation values around the center of the figure. This finding can be also seen from the connectivity maps (Fig. 5), generated by choosing a seed (channel 19) in BA 10. Both network range and connectivity strength for males are significantly larger than females. It should be noted this finding does not depend on the selection of the seed.

4. DISCUSSION

In this work, using optical brain imaging, we examined the resting state spatial and temporal correlations over language (bilateral temporal and adjacent inferior frontal) and prefrontal cortices on healthy children and adult subjects. In the experiment on language region, our result has shown that the local correlation range and strength in left hemisphere are larger for adults than children, which is consistent with the previous fMRI study [19]. This may reflect the differences between adults and children on language skills, provided that language skills, such as skills on language production and comprehension, are associated with the strength of the language network connectivity. For the prefrontal measurement, the male group has shown significantly larger network range and stronger connectivity strength than the female group. The significant differences between males and females in the prefrontal RSFC may shed light on the underlying physiological basis for sex-related differences in cognitive control and emotional regulation, and may also provide insight into sex-related differences in the prevalence of some neurological diseases.

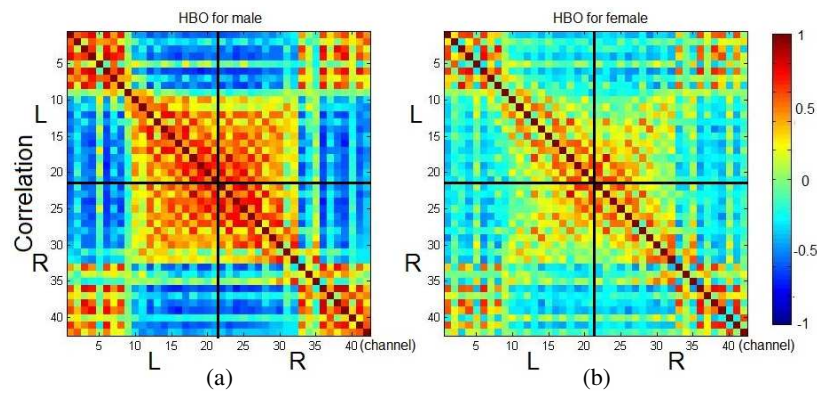


Figure 4: Group average connectivity matrices showing HBO correlations between all channels, (a) is for the male group, and (b) for the female group.

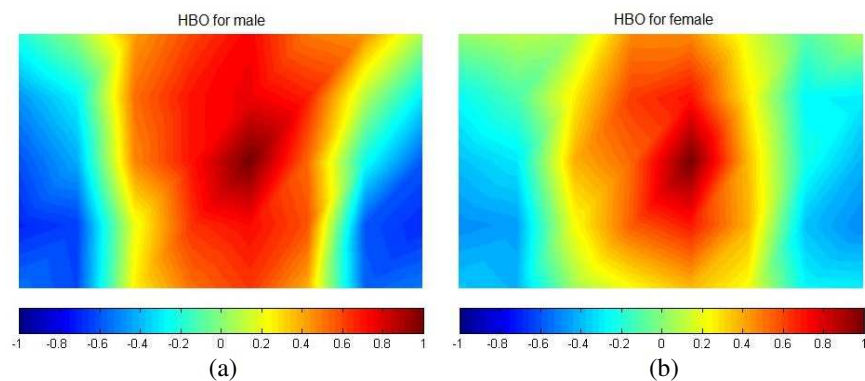


Figure 5: The connectivity map for (a) the males and (b) the females, the seed is Ch 19 in BA 10.

5. CONCLUSION

Optical brain imaging can be used to non-invasively assess resting state functional connectivity in language and prefrontal cortices. Our data show the developmental difference in the language network and sex-related differences in prefrontal network can be revealed by optical brain imaging. This suggests that optical brain imaging is of potential applications for diagnosing neurological diseases relevant to language network development and cognitive function degeneration and defect.

ACKNOWLEDGMENT

This work was supported by Guangdong (China) Innovative Research Team Program (No. 201001D-0104799318).

REFERENCES

1. Jobsis, F. F., "Noninvasive, infrared monitoring of cerebral and myocardial oxygen sufficiency and circulatory parameters," *Science*, Vol. 198, No. 4323, 1264–1267, 1977.
2. Chance, B., Z. Zhuang, C. Unah, and L. Lipton, "Cognition-activated low-frequency modulation of light absorption in human brain," *Proceedings of the National Academy of Sciences*, Vol. 90, No. 8, 3770–3774, 1993.
3. Villringer, A. and B. Chance, "Non-invasive optical spectroscopy and imaging of human brain function," *Trends in Neurosciences*, Vol. 20, No.10, 435–442, 1997.
4. Hillman, E. M. C., "Optical brain imaging in vivo: Techniques and applications from animal to man," *Journal of Biomedical Optics*, Vol. 12, No. 5, 051402, 2007.
5. Quaresima, V., S. Bisconti, and M. Ferrari, "A brief review on the use of functional near-infrared spectroscopy (fNIRS) for language imaging studies in human newborns and adults," *Brain and Language*, Vol. 121, No. 2, 79–89, 2012.
6. Hoshi, Y., "Functional near-infrared optical imaging: Utility and limitations in human brain mapping," *Psychophysiology*, Vol. 40, No. 4, 511–520, 2003.

7. Funane, T., M. Kiguchi, H. Atsumori, et al., “Synchronous activity of two people’s prefrontal cortices during a cooperative task measured by simultaneous near-infrared spectroscopy,” *Journal of Biomedical Optics*, Vol. 16, No. 7, 077011, 2011.
8. Ehlis, A. C., S. Schneider, T. Dresler, et al., “Application of functional near-infrared spectroscopy in psychiatry,” *Neuroimage*, Vol. 85, 478–488, 2014.
9. Fallgatter, A. J., M. Roesler, L. Sitzmann, et al., “Loss of functional hemispheric asymmetry in Alzheimer’s dementia assessed with near-infrared spectroscopy,” *Cognitive Brain Research*, Vol. 6, No. 1, 67–72, 1997.
10. Kita, Y., A. Gunji, Y. Inoue, et al., “Self-face recognition in children with autism spectrum disorders: a near-infrared spectroscopy study,” *Brain and Development*, Vol. 33, No. 6, 494–503, 2011.
11. Biswal, B., F. Zerrin Yetkin, V. M. Haughton, et al., “Functional connectivity in the motor cortex of resting human brain using echo-planar MRI,” *Magnetic Resonance in Medicine*, Vol. 34, No. 4, 537–541, 1995.
12. Xiang, H. D., H. M. Fonteijn, D. G. Norris, et al., “Topographical functional connectivity pattern in the perisylvian language networks,” *Cerebral Cortex*, Vol. 20, No. 3, 549–560, 2010.
13. Biswal, B. B., Y. F. Zang, Y. J. Zhang, et al., “Detecting resting-state functional connectivity in the language system using functional near-infrared spectroscopy,” *Journal of Biomedical Optics*, Vol. 15, No. 4, 047003, 2010.
14. Mesquita, R. C., M. A. Franceschini, D. A. Boas, “Resting state functional connectivity of the whole head with near-infrared spectroscopy,” *Biomedical Optics Express*, Vol. 1, No. 1, 324–336, 2010.
15. Lu, C. M., Y. J. Zhang, B. B. Biswal, et al., “Use of fNIRS to assess resting state functional connectivity,” *Journal of Neuroscience Methods*, Vol. 186, No. 2, 242–249, 2010.
16. Li, J., L. N. Qiu, “Temporal correlation of spontaneous hemodynamic activity in language areas measured with functional near-infrared spectroscopy,” *Biomedical Optics Express*, Vol. 5, No. 2, 587–595, 2014.
17. Okamoto, M., H. Dan, K. Sakamoto, et al., “Three-dimensional probabilistic anatomical cranio-cerebral correlation via the international 10–20 system oriented for transcranial functional brain mapping,” *Neuroimage*, Vol. 21, No. 1, 199–111, 2004.
18. Murphy, K., R. M. Birn, D. A. Handwerker, et al., “The impact of global signal regression on resting state correlations: Are anti-correlated networks introduced?” *Neuroimage*, Vol. 44, No. 3, 893–905, 2009.
19. Friederici, A. D., J. Brauer, G. Lohmann, “Maturation of the language network: from inter-to intra-hemispheric connectivities,” *PLoS One*, Vol. 6, No. 6, e20726, 2011.

Studies of Oxygen and Oxygen Exchange in Fruits Using Gas in Scattering Media Absorption Spectroscopy

Jing Huang¹, Hao Zhang¹, Tianqi Li¹, Guangyu Zhao¹,
Sune Svanberg^{1,2}, and Katarina Svanberg^{1,2}

¹Center for Optics and Electromagnetic Research
South China Normal University, University City Campus, Guangzhou 51006, China
²Lund Laser Center, Lund University, Lund SE-221 00, Sweden

Abstract— The concentration of the biologically active molecular oxygen gas is of crucial importance for fruits, not only in the maturation and ripening processes, but also in the metabolic respiration. We have studied oxygen content and oxygen exchange in fruits non-invasively by using Gas in Scattering Media Absorption Spectroscopy (GASMAS). By studying how the GASMAS oxygen signal changes during the ripening process of different kinds of tropical fruits—nectarine (NE), mango (MG), papaya (PA), and guava (GU), the state of ripeness of fruits can be assessed. Oxygen diffusion measurements on peeled and unpeeled apples are also performed, and the results show that the skin strongly influences the gas exchange with the environment.

1. INTRODUCTION

From a marketing point of view, it is very important to discriminate between mature and immature fruits. Generally, fruits undergo three main maturity stages, maturation, ripening and senescence. After the fruit reaches maturation, a series of dramatic physiological and biochemical changes occur in the fruits influencing color, flavor, texture and hardness. The concentration of the biologically active molecular oxygen gas is of crucial importance for fruits in the maturation and ripening processes. In metabolic respiration, oxygen is consumed to break down organic compounds of the fruits to release the energy necessary to maintain the life activity. Carbon dioxide is produced in the process. By increasing the carbon dioxide and decreasing the oxygen concentrations in the surrounding, a prolonged fruit shelf-life will result. However, anaerobic respiration happens when the oxygen is below a limit. Thus, the fruits need an optimal surrounding gas concentration in storage. The skin of the fruits is of critical importance in regulating the gas diffusion in fruits.

We have studied oxygen and oxygen exchange in fruits non-invasively by using Gas in Scattering Media Absorption Spectroscopy (GASMAS) [1]. This technique employs a narrow-band tunable diode laser to measure gases in pores and cavities in solid-state matrices. GASMAS relies on the fact that free gases typically have 10,000 times narrower absorption features than the surrounding tissue. The GASMAS imprint is quite small — thus wavelength modulation spectroscopy (WMS) is used for high sensitivity detection. We have studied how the GASMAS oxygen signal changes during the ripening process of different kinds of tropical fruits—nectarine (NE), mango (MG), papaya (PA), and guava (GU). Combining with measurements of reflectance and fluorescence, we show that optical techniques are very powerful in evaluating the state of ripeness of fruits [2]. To study the role of the skin in regulating gas transport in fruits, oxygen diffusion measurements on peeled and unpeeled apples are performed. As illustrated in the present paper, the skin strongly influences the gas exchange with the environment.

2. MATERIALS AND SET-UP

For ripening experiment, four kinds of tropical and climacteric fruits; nectarine (NE), mango (MG), papaya (PA) and guava (GU) are selected for the measurements. The fruits were bought in a local market in South China, and visually immature samples were chosen. Each type of fruit is represented by a group of six fruits from the same batch. Each fruit is marked with a prefix and a number (e.g., NE1, NE2 etc.) written on a small piece of paper which is attached to the fruit far away from the measurement site, in order to avoid interaction with the skin surface to be investigated. The six fruits of the same kind are divided into two groups, among which one group (such as, NE1, NE2 and NE3) is placed in an ambient temperature of 20°C, and another group (such as, NE4, NE5 and NE6) is placed in a temperature of 30°C. The injection of light and the detection are made at positions on the equator of the fruits separated by 5 cm.

For the oxygen exchange case, five climacteric Fuji apples were acquired from the same batch at the same local fruit shop and one was bought in a different place. Each apple is studied regarding

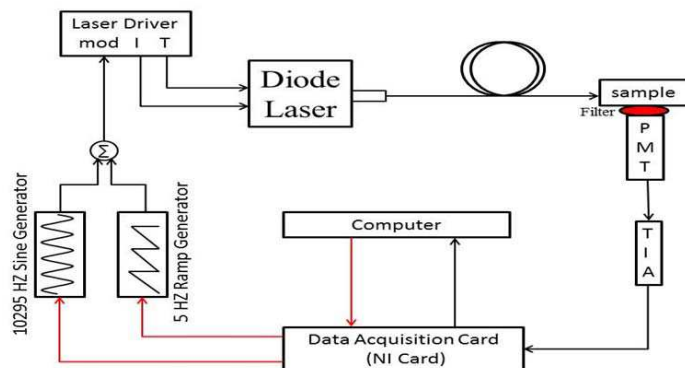


Figure 1: Schematic layout of the GASMAS set-up used for the $2f$ WMS signal recording for oxygen.

gas exchange, first unpeeled, and the following day in a peeled state. Thus, each apple experiences two different experiments in two consecutive days. Before the measurements, the samples are placed in a sealed plastic bag filled with pure oxygen gas overnight. Each peeled and non-peeled apple is placed in the same transparent and sealed plastic bag in the two consecutive days, and the bag is marked with different prefixes and numbers (e.g., Apple_1, Apple_2 etc.) matched to the samples for identification.

A distributed feed-back diode laser (LD-0760-0100, Toptica) with a nominal output power of 1.5 mW, is used as the light source to generate the probing light. A laser temperature controller (TED200C, Thorlabs) and a laser current controller (LCD201C, Thorlabs) are used to control the drive temperature and current of the DFB diode laser. The diode laser is scanned across an O_2 absorption line at 760.445 nm (vacuum wavelength) by sweeping the operating current of the laser by using a 5 Hz saw tooth ramp. In order to achieve sensitive wavelength modulation spectroscopy (WMS) by using lock-in amplification techniques, the diode laser injection current is also modulated by a sinusoidal wave at 10295 Hz. An optical fiber with 600 μm core diameter (727-733-2447, Ocean Optics) is used to guide the light to the sample under our study. A photomultiplier tube with 10 cm cathode diameter (H10722-01, Hamamatsu) is used to detect the diffusely emerging light which contains a weak absorption signal due to the oxygen inside the sample. Ambient light is suppressed not only by the combination of a coloured glass long-pass filter (RG715, Edmund), and the photomultiplier tube quantum efficiency falloff in the near IR region, but also with several black shields to suppress the ambient light even further. For the fruit ripening case, the coloured glass filter was not used. The signal from the photomultiplier tube is amplified by a trans-impedance amplifier (DLPCA-200, Femto) to yield a voltage signal. Then the voltage signal is fed to the same DAQ card (PCI-6120, NI) which is also used to generate the modulation signal for the DFB diode laser. The data from the DAQ card are stored in a computer. The lock-in detection and signal processing procedure of the $2f$ WMS signal are digitally performed with MATLAB. A detailed description of the signal processing is given in [3].

3. RESULTS AND DISCUSSION

Since the optical path length that light travels through the fruits is unknown due to strong scattering, the Beer-Lambert law is not applicable in determining the exact oxygen concentration. Instead, L_{eq} , the equivalent mean path length in normal 21% oxygen air, resulting in the same fractional imprint on the received light intensity, is used to express the gas content. L_{eq} is proportional to the normalized WMS signal (i.e., the $2f$ WMS signal amplitude divided by the light intensity received by the detector). Thus, it is convenient to use L_{eq} to estimate the changes of oxygen contents in fruits maturing and the oxygen content in the process of gas exchange.

3.1. Fruit Ripening

From Fig. 2, it can be seen that the value of L_{eq} decreases gradually to a minimum value from a high value, and then rises to a secondary peak. Finally, it decreases to a quite low value. During this period, the fruits experience a series of physiological and biochemical changes. Changes in L_{eq} are the results of changes in oxygen concentration or in the path length through the gas, or

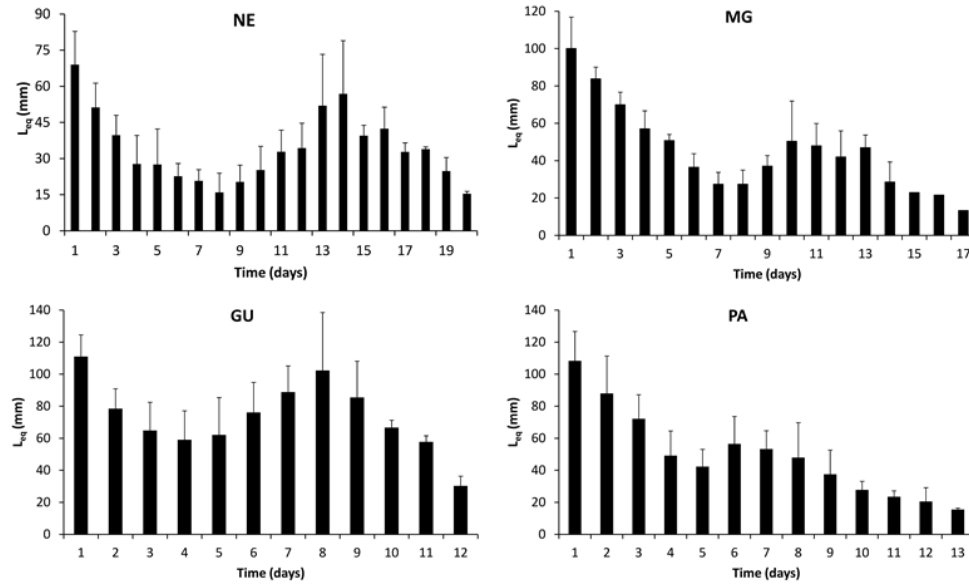


Figure 2: The measured time evolution of the oxygen signal for nectarine, mango, guava and papaya [2].

both. For climacteric fruits, the respiratory rate increases to a peak value with fruit maturation, and then returns to or even goes below the point before the event [4, 5]. The initial reduction of L_{eq} could be attributed to the changes of respiratory rate during fruit ripening. After reaching the climacteric point, the climacteric fruits are more susceptible to fungal invasion and begin to degrade, ultimately leading to cell death. So, in Fig. 2 the L_{eq} rises to a secondary peak and then decreases to a very low value after the climacteric point. The characteristic temporal variation of L_{eq} is useful for assessment of maturity, and the likely day of ripeness can be inferred, as coupled to the occurrence of the initial minimum in the GASMAS signal. The days of estimated ripeness are shown in Table 1, with errors bars considering the standard deviations.

Table 1: The indicated days of ripening for four kinds of fruits as assessed from the minimum of the GASMAS signal.

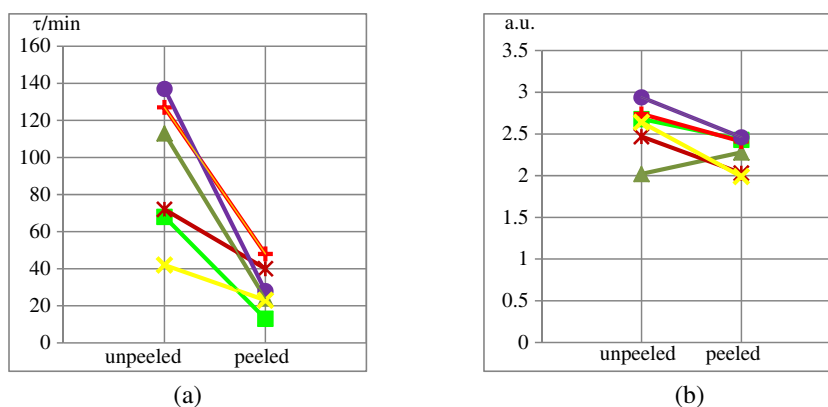
Type	Nectarine (NE)	Mango (MG)	Guava (GU)	Papaya (PA)
Day of ripening	8 ± 1	8 ± 1	4 ± 1	5 ± 1

4. GAS EXCHANGE

After taking the apple out from a pure oxygen environment and putting it into the GASMAS system, by fitting an exponential function to the experimental data with a Matlab program, the initial L_{eq} for apple out of the oxygen filled bag, the final equilibrium L_{eq} and the time-constant (τ) are all evaluated. τ is the time the signal takes to change its initial value by a factor of $1/e$ in relation to the final equilibrium value.

By analyzing τ for unpeeled and peeled apples (i.e., Fig. 3(a)), it can be seen that the time-constant τ for unpeeled ones are larger than for the peeled ones, which means that the unpeeled ones exchange gas slower than the peeled ones. It agrees with the assumption that the major site of resistance to gas exchange in fruits is probably the skin [6] and agrees with the results of [7]. As can be seen in Fig. 3(b), the ratios of the initial L_{eq} and the final equilibrium L_{eq} for the six apples are just slightly different, it seems that either with skin or without skin, the fruits experience gas exchange of the same magnitude, although of different rates.

As shown in Fig. 4, after the apples exchange gas and get to the equilibrium state, the final equilibrium L_{eq} values for unpeeled apples are smaller than the peeled ones. The apple skin seems to keep apples in a lower oxygen condition with than without the peel, while the apples experience gas exchange slower with than without the skin. An active role by the skin in regulating oxygen content was earlier suggested in a test on a single apple [7]. More efforts should be put into these

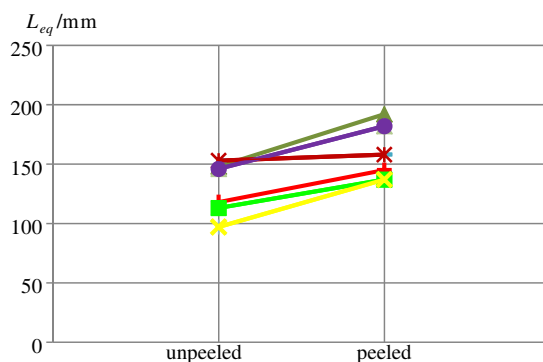


Left: unpeeled and right: peeled.

Six apples were measured, Apple_1 \blacksquare , Apple_2 \blacktriangle , Apple_3 \times , Apple_4 $+$, Apple_5 \bullet , Apple_6 \times .

Figure 3: (a) Time-constant τ for gas exchange for the same apple with different treatment. (b) Ratio of initial L_{eq} for apple out of the oxygen filled bag and the final equilibrium L_{eq} .

aspects, where eliminating the large data spread due to interference fringe problems in the present study, would be a priority.



Six apples were measured, Apple_1 \blacksquare , Apple_2 \blacktriangle , Apple_3 \times , Apple_4 $+$, Apple_5 \bullet , Apple_6 \times .

Figure 4: The final equilibrium L_{eq} for apples after experiencing gas exchange.

5. CONCLUSION

As illustrated in this paper, optical techniques are very powerful in evaluating the state of ripeness of fruits. Further, the skin was found to strongly influence the gas exchange with the environment. In contrast to other techniques, our technique has the advantages of measuring the gas content inside the sample non-intrusively, in situ and in real-time. It suggests the prospect of developing the GASMAS technique into a valuable and portable tool for gas studies in fruits and foods.

ACKNOWLEDGMENT

The authors are grateful for the support from Prof. Sailing He. This work was financially supported by the Guangdong Innovative Research Team Program (Grant 201001D0104799318).

REFERENCES

1. Svanberg, S., "Gas in scattering media absorption spectroscopy — From basic studies to biomedical applications," *Laser Photonics Rev.*, Vol. 7, 779–796, 2013.
2. Zhang, H., J. Huang, T. Q. Li, X. X. Wu, S. Svanberg, and K. Svanberg, "Studies of tropical fruit ripening using three different spectroscopic techniques," 2014, in Press.
3. Svensson, T., M. Andersson, L. Rippe, S. Svanberg, S. Andersson-Engels, J. Johansson, and S. Folestad, "VCSEL-based oxygen spectroscopy for structural analysis of pharmaceutical solids," *Applied Physics B*, Vol. 90, 345–354, 2008.

4. Bashir, H. A. and A. A. Abu-Goukh, “Compositional changes during guava fruit ripening,” *Food Chemistry*, Vol. 80, 557–563, 2003.
5. Zaharah, S. S., et al., “Role of brassinosteroids, ethylene, abscisic acid, and indole-3-acetic acid in mango fruit ripening,” *Journal of Plant Growth Regulation*, Vol. 31, 363–372, 2012.
6. Cameron, A. C., P. C. Talasila, and D. W. Joles, “Predicting film permeability needs for modified-atmosphere packaging of lightly processed fruits and vegetables,” *Hortic Sci.*, Vol. 30, 25–34, 1995.
7. Persson, L., H. Gao, M. Sjöholm, and S. Svanberg, “Diode laser absorption spectroscopy for studies of gas exchange in fruits,” *Optics and Lasers in Engineering*, Vol. 44, 687–698, 2006.

Influence of an Intense Electromagnetic Wave on Magnetoconductivity and Hall Coefficient in Compositional Semiconductor Superlattices: Optical Phonon Interaction

B. D. Hoi^{1,2}, H. V. Ngoc¹, and N. Q. Bau¹

¹Department of Physics, College of Natural Science, Vietnam National University, Hanoi, Vietnam

²Department of Physics, National University of Civil Engineering, Hanoi, Vietnam

Abstract— We theoretically study the influence of an intense electromagnetic wave (EMW) on the Hall effect in compositional semiconductor superlattices (CSSLs) with a periodical superlattice potential in the z direction, subjected to a crossed dc electric field $\vec{E}_1 = (E_1, 0, 0)$ and magnetic field $\vec{B} = (0, 0, B)$. By considering the electron-optical phonon interaction at high temperature, we obtain analytical expressions for the magnetoconductivity (MC) and the Hall coefficient (HC) with a dependence on external fields, the temperature of the system, and characteristic parameters of the CSSL. These expressions are fairly different in comparison to those obtained for bulk semiconductors. The influence of the EMW is interpreted by using the dependencies of the MC and the HC on the amplitude and the frequency of the EMW. The analytical results are computationally evaluated for GaAs/AlGaAs CSSL. The optically detected magnetophonon resonance conditions are obtained. The HC reaches saturation when the magnetic field or the EMW frequency increases.

1. INTRODUCTION

The propagation of an electromagnetic wave (EMW) in materials leads to some interesting effects that can be applied experimentally to determine materials information. For example, the cyclotron effect, magneto-phonon-photon resonance, optically detected electron-phonon resonance, and so on. The Hall effect in bulk semiconductors under the influence of EMWs has been studied in much details [1–5]. In Refs. [1, 2] the odd magnetoresistance was calculated when the nonlinear semiconductors are subjected to a magnetic field and an EMW with low frequency, the nonlinearity is resulted from the nonparabolicity of distribution functions of carriers. In Refs. [3, 4], the magnetoresistance was derived in the presence of a strong EMW for two cases: the magnetic field vector and the electric field vector of the EMW are perpendicular [3], and are parallel [4]. The existence of the odd magnetoresistance was explained by the influence of the strong EMW on the probability of collision, i.e., the collision integral depends on the amplitude and frequency of the EMW. This problem was also studied in the presence of both low and high frequency EMWs [5]. Throughout these problems, the quantum kinetic equation method have been seen as a powerful tool. In low-dimensional semiconductor systems, the carrier confinement leads to unusual behaviors in comparison with bulk semiconductors under external stimuli. So, in recent works, we have used this method to study the influence of an intense EMW on the Hall effect in rectangular and parabolic quantum wells [6, 7], in doped semiconductor superlattices [8].

In this work, by using the quantum kinetic equation method we study the Hall effect in a compositional semiconductor superlattice (CSSL) subjected to a crossed dc electric field and magnetic field in the presence of an EMW. We only consider the case of high temperature when the electron-optical phonon interaction is assumed to be dominant and electron gas is nondegenerate. We derive analytical expressions for the conductivity tensor and the Hall coefficient (HC) taking account of arbitrary transitions between the energy levels. The analytical result is numerically evaluated and graphed for the GaAs/AlGaAs CSSL.

2. MODEL OF THE PROBLEM AND ANALYTICAL RESULTS

In this model, we consider a compositional semiconductor superlattice composed of N_0 layers of the semiconductor I (the layer thickness is d_I) and N_0 layers of the semiconductor II (the layer thickness is d_{II}) arranged alternatively along the z -direction. The energy-gap difference between these two materials is U . If a static magnetic field \vec{B} is applied in the z -direction and a dc electric field \vec{E}_1 is applied in the x -direction, then the one-electron normalized eigenfunctions and

eigenvalues in the Landau gauge for the vector potential $\vec{A} = (0, Bx, 0)$ are, respectively, given by [9, ?]

$$|\xi\rangle \equiv |N, n, k_y, k_z\rangle = \frac{1}{\sqrt{L_y}} \exp(ik_y y) \phi_N(x - x_0) \otimes |n, k_z\rangle, \quad (1)$$

$$\varepsilon_\xi(\vec{k}_y) \equiv \varepsilon_{N, n, k_z}(\vec{k}_y) = \left(N + \frac{1}{2}\right) \hbar\omega_c + \varepsilon_{n, k_z} - \hbar v_d k_y + \frac{1}{2} v_d^2, \quad N, n = 0, 1, 2, \dots, \quad (2)$$

where N is the Landau level index and n denotes level quantization in the z -direction; k_y (k_z) and L_y are the wave vector and normalization length in the y (z)-direction, respectively; $v_d = E_1/B$ being the drift velocity and $\omega_c = eB/m_e$ is the cyclotron frequency in which e is the charge of a conduction electron and m_e is its effective mass. Also, $\phi_N(x)$ represents harmonic oscillator wave functions, centered at $x_0 = -\ell_B^2(k_y - m_e v_d/\hbar)$ where $\ell_B = (\hbar/(m_e \omega_c))^{1/2}$ is the radius of the Landau orbit in the x - y plane; $|n, k_z\rangle$ is the wave function in the z -direction. Moreover, in the tight-binding approximation we have [9, 11]

$$\varepsilon_{n, k_z} = \varepsilon_n - t_n \cos(k_z d), \quad (3)$$

where $d = d_I + d_{II}$ is the superlattice period, $\varepsilon_n = \hbar^2 \pi^2 (n+1)^2 / (2m_e d_I^2)$, t_n is the half-width of the n th mini-band given by [12, 13]

$$t_n = -4(-1)^n \frac{d_I}{d - d_I} \varepsilon_n \frac{\exp(-2\sqrt{2m_e(d - d_I)^2 U/\hbar^2})}{\sqrt{2m_e(d - d_I)^2 U/\hbar^2}}. \quad (4)$$

If the specimen is subjected to an intense EMW with the electric field vector $\vec{E} = (0, E_0 \sin \omega t, 0)$ (E_0 and ω are the amplitude and frequency, respectively), the Hamiltonian of the electron-phonon system, in the second quantization representation, can be written similarly to the one obtained in Refs. [6–8]. From this Hamiltonian, the Hall conductivity and the HC are derived in the single (constant) relaxation time approximation. In this calculation, we also consider only the electron-optical phonon interaction at high temperature, so the electrons system is nondegenerate and obeys the Boltzmann distribution function. After some manipulation, we obtain the expression for the conductivity tensor as

$$\sigma_{im} = \frac{e^2 \tau}{\hbar(1 + \omega_c^2 \tau^2)} (\delta_{ij} - \omega_c \tau \epsilon_{ijk} h_k + \omega_c^2 \tau^2 h_i h_j) \{a \delta_{jm} + b \delta_{jl} (\delta_{lm} - \omega_c \tau \epsilon_{lmp} h_p + \omega_c^2 \tau^2 h_l h_m)\}, \quad (5)$$

where δ_{ij} is the Kronecker delta; ϵ_{ijk} being the antisymmetric Levi-Civita tensor; the Latin symbols i, j, k, l, m, p stand for the components x, y, z of the Cartesian coordinates;

$$a = -\frac{\hbar \beta v_d L_y I}{2\pi m_e} \sum_{N, n} e^{\beta(\varepsilon_F - \varepsilon_{N, n})} \quad (6)$$

with ε_F is the Fermi level; and

$$b = \frac{\beta A N_0 L_y I}{8\pi^2 m_e^2} \frac{\tau}{1 + \omega_c^2 \tau^2} \sum_{N, N'} \sum_{n, n'} I(n, n') (b_1 + b_2 + b_3 + b_4 + b_5 + b_6 + b_7 + b_8), \quad (7)$$

$$b_1 = \frac{1}{M} \frac{eB\bar{\ell}}{\hbar} e^{\beta(\varepsilon_F - \varepsilon_{N, n})} \left[\frac{(N+M)!}{N!} \right]^2 \delta(X_1),$$

$$b_2 = -\frac{\theta}{2} \left(\frac{eB\bar{\ell}}{\hbar} \right)^2 b_1,$$

$$b_3 = \frac{\theta}{4M} \left(\frac{eB\bar{\ell}}{\hbar} \right)^3 e^{\beta(\varepsilon_F - \varepsilon_{N, n})} \left[\frac{(N+M)!}{N!} \right]^2 \delta(X_2),$$

$$b_4 = \frac{\theta}{4M} \left(\frac{eB\bar{\ell}}{\hbar} \right)^3 e^{\beta(\varepsilon_F - \varepsilon_{N, n})} \left[\frac{(N+M)!}{N!} \right]^2 \delta(X_3),$$

$$\begin{aligned}
b_5 &= \frac{1}{M} \frac{eB\bar{\ell}}{\hbar} e^{\beta(\varepsilon_F - \varepsilon_{N,n})} \left[\frac{N!}{(N+M)!} \right]^2 \delta(X_4), \\
b_6 &= -\frac{\theta}{2} \left(\frac{eB\bar{\ell}}{\hbar} \right)^2 b_5, \\
b_7 &= \frac{\theta}{4M} \left(\frac{eB\bar{\ell}}{\hbar} \right)^3 e^{\beta(\varepsilon_F - \varepsilon_{N,n})} \left[\frac{N!}{(N+M)!} \right]^2 \delta(X_5), \\
b_8 &= \frac{\theta}{4M} \left(\frac{eB\bar{\ell}}{\hbar} \right)^3 e^{\beta(\varepsilon_F - \varepsilon_{N,n})} \left[\frac{N!}{(N+M)!} \right]^2 \delta(X_6), \quad M = |N - N'| = 1, 2, 3, \dots, \\
X_1 &= (N' - N)\hbar\omega_c + \varepsilon_{n',\pi/d} - \varepsilon_{n,0} - eE_1\bar{\ell} - \hbar\omega_0, \quad X_2 = X_1 + \hbar\Omega, \quad X_3 = X_1 - \hbar\Omega, \\
X_4 &= (N - N')\hbar\omega_c + \varepsilon_{n',\pi/d} - \varepsilon_{n,0} + eE_1\bar{\ell} + \hbar\omega_0, \quad X_5 = X_4 + \hbar\Omega, \quad X_6 = X_4 - \hbar\Omega,
\end{aligned}$$

where ω_0 is the frequency of the longitudinal optical phonons, $\beta = 1/(k_B T)$ with k_B being Boltzmann constant, $\theta = e^2 E_0^2 / (m_e^2 \Omega^4)$, $A = 2\pi e^2 \hbar \omega_0 (\chi_\infty^{-1} - \chi_0^{-1}) / \epsilon_0$, $\bar{\ell} = (\sqrt{N+1/2} + \sqrt{N+1+1/2}) \ell_B / 2$, $I = a_1 (\alpha\beta)^{-1} [\exp(\alpha\beta a_1) + \exp(-\alpha\beta a_1)] - (\alpha\beta)^{-2} [\exp(\alpha\beta a_1) - \exp(-\alpha\beta a_1)]$, $a_1 = L_x / 2\ell_B^2$, $\alpha = \hbar v_d$, $\varepsilon_{N,n} = (N+1/2)\hbar\omega_c + \varepsilon_{n,0} + m_e v_d^2 / 2$, and

$$I(n, n') = \int_{-\infty}^{\infty} |I_{n,n'}(0, \pi/d, q_z)|^2 dq_z, \quad (8)$$

$$I_{n,n'}(k_z, k'_z, q_z) = \frac{1}{2} \frac{\sin\{[q_z \pm (k_{n'} \pm k_n)]d_I/2\}}{[q_z \pm (k_{n'} \pm k_n)]d_I/2} \exp\{i[q_z \pm (k_{n'} \pm k_n)]d_I/2\}, \quad (9)$$

where $k_n = (2m_e \varepsilon_{n,k_z} / \hbar^2)^{1/2}$.

The divergence of the delta functions is avoided by replacing them by the Lorentzians as [14]

$$\delta(X) = \frac{1}{\pi} \left[\frac{\Gamma}{X^2 + \Gamma^2} \right], \quad (10)$$

where Γ is the damping factor associated with the momentum relaxation time τ by $\Gamma \approx \hbar/\tau$. The HC is given by the formula [15]

$$R_H = \frac{\rho_{yx}}{B} = -\frac{1}{B} \frac{\sigma_{yx}}{\sigma_{yx}^2 + \sigma_{xx}^2}, \quad (11)$$

where σ_{yx} and σ_{xx} are given by Eq. (5).

Equations (5) and (11) show the complicated dependencies of the conductivity tensor and the HC on the external fields, including the EMW. It is obtained for arbitrary values of the indices N , n , N' and n' . In the next section, we will give a deeper insight into these results by carrying out a numerical evaluation and a graphic consideration by the computational method.

3. NUMERICAL RESULTS AND DISCUSSION

In this section, we present detailed numerical calculations of the conductivity and the HC for the GaAs/AlGaAs CSSL with the parameters [16]: $\varepsilon_F = 50$ meV, $\chi_\infty = 10.9$, $\chi_0 = 12.9$, $\hbar\omega_0 = 36.25$ meV (optical phonon frequency), and $m_e = 0.067 \times m_0$ (m_0 is the mass of a free electron). For the sake of simplicity, we also choose $N = 0$, $N' = 1$, $n = 0$, $n' = 0 \div 1$, $\tau = 10^{-12}$ s, and $L_x = L_y = 100$ nm.

In Figure 1, the solid curve describes the dependence of the magnetoconductivity on the cyclotron energy in the case of absence of the EMW. We can see that this curve has three maximum peaks and the values of conductivity at the peaks are very much larger than they are at others. Physically, the existence of the peaks can be explained in details as follows by using the computational method to determine their positions. All the peaks correspond to the conditions

$$(N' - N)\hbar\omega_c = \hbar\omega_0 + eE_1\bar{\ell} \pm \Delta_{n,n'}, \quad \Delta_{n,n'} = \varepsilon_{n',\pi/d} - \varepsilon_{n,0}. \quad (12)$$

This condition is generally called the intersubband magnetophonon resonance (MPR) condition under the influence of an dc EF (all the peaks now may be called resonant peaks). However, the

values of the term $eE_1\bar{\ell}$ are very small in comparison to the optical phonon energy and can be neglected. For instance, if we take $B = 20$ T (approximately $\hbar\omega_c = 34.59$ meV), then $eE_1\bar{\ell} = 0.0277$ meV.

The dashed curve in Figure 1 shows the dependence of on the cyclotron energy in the presence of a strong EMW. It is seen that besides the main resonant peaks as in the case of absence of the EMW, the subordinate peaks appear. The appearance of the subordinate peaks is due to the contribution of a photon absorption/emission processes that satisfy the conditions $\hbar\omega_c = \hbar\omega_0 \pm \Delta_{0,1} \pm \hbar\Omega$. It is also seen that the main peaks are much higher than the subordinate peaks. This means that the possibility of processes without photon is much larger than it is for the processes with one photon absorption/emission. The above conditions with the presence of the EMW are actually the optically detected MPR conditions.

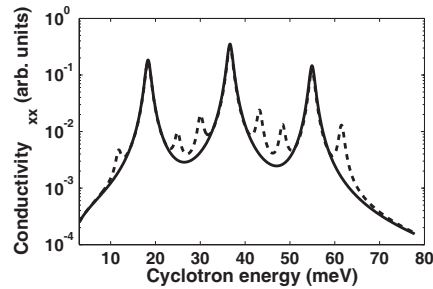


Figure 1: The magnetoconductivity (arb. units) as functions of the cyclotron energy for two cases: absence (solid line) and presence (dashed line) of the EMW. Here, $E_1 = 5 \times 10^3$ V · m⁻¹, $E_0 = 10^5$ V · m⁻¹, $d = 35$ nm, and $T = 270$ K.

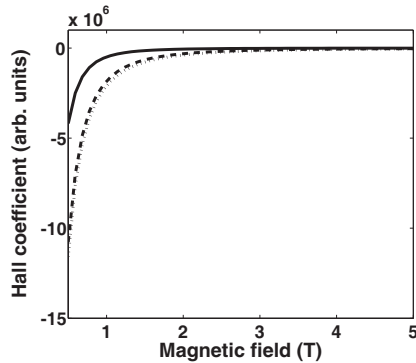


Figure 2: Hall coefficients (arb. units) as functions of the magnetic field at the EMW frequency of 10^{12} Hz (solid line), 4×10^{12} Hz (dashed line), and 7×10^{12} Hz (dotted line). Here, $d = 35$ nm, $E_1 = 5 \times 10^3$ V · m⁻¹, $E_0 = 10^5$ V · m⁻¹, and $T = 270$ K.

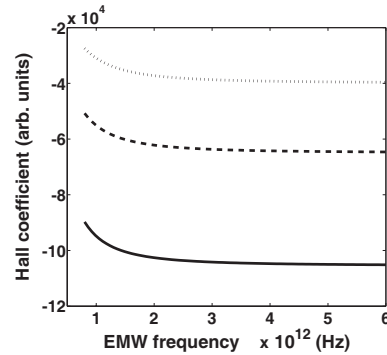


Figure 3: Hall coefficients (arb. units) as functions of the EMW frequency at the CSSL period of 35 nm (solid line), 36 nm (dashed line), and 37 nm (dotted line). Here, $B = 4.2$ T, $E_1 = 5 \times 10^3$ V · m⁻¹, $E_0 = 10^5$ V · m⁻¹, and $T = 270$ K.

In Figure 2 and Figure 3, we show the dependence of the HC on the magnetic field and on the EMW frequency, respectively, at different values of the temperature T ; the necessary parameters involved in the computation are the same as those in Figure 1. As the magnetic field increases, the HC increases. When the magnetic field is increased further, the HC reaches saturation at high magnetic fields. This behavior is similar to the case of low temperature in two-dimensional electron systems have been observed before for both the in-plane and perpendicular magnetic fields (see Ref. [17] and references therein). The HC can be seen to decrease slowly with increasing EMW frequency for the region of small values ($\Omega < 2 \times 10^{12}$ Hz) and reaches saturation as the EMW frequency continues to increase. Moreover, the HC depends strongly on the CSSL period at the chosen values of the other parameters as we can see that the value of the HC raises remarkably when the period increases slightly.

4. CONCLUSION

We have studied the influence of laser radiation on the Hall effect in CSSLs subjected to crossed dc electric and magnetic fields. The electron-optical phonon interaction is taken into account at high temperature, and the electron gas is nondegenerate. We obtain the expressions for the conductivity as well and the HC. The influence of the EMW is interpreted by using the dependencies of the Hall conductivity and the HC on the amplitude E_0 and the frequency Ω of the EMW and by using the dependencies on the magnetic B and the dc electric field E_1 as in the ordinary Hall effect. The most important thing is the appearance of the maximum peaks satisfying the MPR condition optically detected MPR condition. The HC reaches saturation as the magnetic field or the EMW frequency increases. These behaviors are similar to the case of the in-plane magnetic field. Moreover, the HC in this work is always negative while it has both negative and positive values in the case of in-plane magnetic field

REFERENCES

1. Epshtein, E. M., “Odd magnetophotoresistance effect in semiconductors,” *Sov. Phys. Semicond.* [*Fiz. Tekh. Poluprovodn.*], Vol. 10, 1414–1415, 1976 (in Russian).
2. Epshtein, E. M., “Odd magnetoresistance of nonlinear conductors in time-dependent electric fields,” *Sov. J. Theor. Phys. Lett.*, Vol. 2, No. 5, 234–237, 1976 (in Russian).
3. Malevich, V. L. and E. M. Epshtein, “Photostimulated odd magnetoresistance in semiconductors,” *Sov. Phys. Solid State* [*Fiz. Tverd. Tela*], Vol. 18, 1286–1289, 1976 (in Russian).
4. Pankratov, A. A. and E. M. Epshtein, “Kinetic theory of longitudinal Hall effect in high-frequency electric field,” *Sov. Phys. Semicond.* [*Fiz. Tekh. Poluprovodn.*], Vol. 16, No. 9, 1689–1691, 1982 (in Russian).
5. Shmelev, G. M., G. I. Tsurkan, and N. H. Shon, “The magnetoresistance and the cyclotron resonance in semiconductors in the presence of strong electromagnetic wave,” *Sov. Phys. Semicond.* [*Fiz. Tekh. Poluprovodn.*], Vol. 15, No. 1, 156–161, 1981 (in Russian).
6. Bau, N. Q. and B. D. Hoi, *Int. J. Mod. Phys. B*, Vol. 28, 1450001, 14 pages, 2014.
7. Bau, N. Q. and B. D. Hoi, “Influence of a strong electromagnetic wave (laser radiation) on the Hall effect in quantum wells with a parabolic potential,” *J. Korean Phys. Soc.*, Vol. 60, 59–64, 2012.
8. Bau, N. Q., N. V. Nghia, N. V. Hieu, and B. D. Hoi, “Influence of a strong electromagnetic wave (laser radiation) on the hall coefficient in doped semiconductor superlattices with an in-plane magnetic field,” *PIERS Proceedings*, 416–421, Taipei, March 25–28, 2013.
9. Mitra, B. and K. P. Ghatak, “Effect of crossed electric and quantizing magnetic fields on the Einstein relation in semiconductor superlattices,” *Phys. Stat. Sol. (b)*, Vol. 164, K13–K18, 1991.
10. Vasilopoulos, P., M. Charbonneau, and C. M. Van Vliet, “Linear and nonlinear electrical conduction in quasi-two-dimensional quantum wells,” *Phys. Rev. B*, Vol. 35, No. 3, 1334–1344, 1987.
11. Ploog, K. and G. H. Dohler, “Compositional and doping superlattices in III-V semiconductors,” *Adv. Phys.*, Vol. 32, No. 3, 285–359, 1983.
12. Esaki, L. and R. Tsu, “Superlattice and negative differential conductivity in semiconductors,” *IBM. J. Res. Develop.*, Vol. 14, 61–65, 1970.
13. Silin, A. P., “Semiconductor superlattices,” *Sov. Phys. Usp.*, Vol. 28, 972, 1985.
14. Chaubey, M. P. and C. M. V. Vliet, “Transverse magnetoconductivity of quasi-two-dimensional semiconductor layers in the presence of phonon scattering,” *Phys. Rev. B*, Vol. 33, 5617–5622, 1986.
15. Charbonneau, M., K. M. Van Vliet, and P. Vasilopoulos, “Linear response theory revisited III: One-body response formulas and generalized Boltzmann equations,” *J. Math. Phys.*, Vol. 23, 318–336, 1982.
16. Lee, S. C., “Optically detected magnetophonon resonances in quantum wells,” *J. Korean Phys. Soc.* Vol. 51, No. 6, 1979–1986, 2007.
17. Hwang, E. H. and S. Das Sarma, “Hall coefficient and magnetoresistance of two-dimensional spin-polarized electron systems,” *Phys. Rev. B*, Vol. 73, No. 12, 121309(R), 2006.

Calculating the Current Density of the Radio Electrical Effect in Parabolic Quantum Wells

B. D. Hung, N. D. Nam, and D. Q. Vuong

Department of Physics, College of Natural Sciences, Hanoi National University
No. 334, Nguyen Trai Str., Thanh Xuan Dist., Hanoi, Vietnam

Abstract— We study the current density of charge carriers of the radio electrical effect in parabolic quantum wells (PQW) subjected to a dc electric field \vec{E}_0 and in a linearly polarized electromagnetic wave (EMW) ($\vec{E}(t) = \vec{E}(e^{-i\omega t} + e^{i\omega t})$, $\vec{H}(t) = [\vec{n}, \vec{E}(t)]$), ($\hbar\omega \ll \bar{\varepsilon}$; $\bar{\varepsilon}$ is an average carrier energy, in this paper), in the presence of a laser radiation $\vec{F}(t) = \vec{F} \sin \Omega t$; $\Omega\tau \gg 1$ (τ is the characteristic relaxation time). By using the quantum kinetic equation method for electrons interacting with acoustic phonon at low temperatures, we obtain the expressions for the drag of the charge carriers in case the electron gas is completely degenerate. The dependence of the current density on the intensity F and the frequency Ω of the laser radiation, the frequency ω of the linearly polarized EMW, the frequency ω_0 of the parabolic potential are obtained. The analytic expressions are numerically evaluated and plotted for a specific quantum wells, GaAs/AlGaAs, to show clearly the dependence of the current density of charge carriers on the radioelectrical effect on above parameters. The results of current density calculation in this case are compared with bulk semiconductors to show the dissimilarity.

1. INTRODUCTION

It is well-known that the confinement of electrons in low-dimensional systems makes their optical and electrical properties considerably different in comparison to bulk materials [1–4]. Thus, there has been considerable interest in the behavior of low-dimensional systems, in particular two-dimensional systems, such as semiconductor superlattices, doped superlattices and quantum wells. In recent years, many papers have dealt with problems related to the incidence of EMW in low-dimensional semiconductor systems. For example, the linear absorption of a weak EMW caused by confined electrons in low dimensional systems has been investigated by using Kubo-Mori method [5, 6]; calculations of the nonlinear absorption coefficients of a strong EMW by using the quantum kinetic equation for electrons [7, 8] have also been reported; or the study of influence of a weak EMW on low-dimensional systems in the presence of a strong EMW has been researched [9–11]. However, research into influence of two EMW in PQW is still open.

The radioelectrical effect (RE) which is explained by the momentum transfer from photons to the electron, can be understood quasi-classically as being the result of the action of the Lorentz force on charge carriers moving in the ac electric and magnetic fields of the wave [12, 13]. The RE in semiconductors [14–16] have also been investigated and resulted from using the quantum kinetic equation for electrons system. In the past few years, the RE in semiconductor superlattices has been examined under the action of strong electric fields [17, 18] and of an elliptically polarized EMW [19]. The difference between the RE in bulk semiconductors and low-dimensional systems lies in a nonlinear dependence of the current density of charge carriers (CDCC) on EMW [19–23].

In this work, we investigated the CDCC in a PQW under the action of a linearly polarized EMW field $\vec{E}(t) = \vec{E}(e^{-i\omega t} + e^{i\omega t})$ and in the presence of a laser radiation field $\vec{F}(t) = \vec{F} \sin \Omega t$. We consider the case in which the electron-acoustic phonon interaction at low temperatures is assumed to be dominant and electron gas to be completely degenerate. Numerical calculations are carried out with a specific GaAs/GaAsAl quantum wells. The comparison of the result of quantum wells to bulk semiconductors shows that difference.

2. CALCULATING THE CURRENT DENSITY OF THE RADIO ELECTRICAL EFFECT IN PQW

2.1. Quantum Kinetic Equation for Electrons in PQW

We examine the motion of an electron in PQW confined to the parabolic potential $V(z) = m\omega_0^2 z^2/2$ and that its energy spectrum is quantized into discrete levels. We assume that the quantization direction is the z direction. In this work, we consider the system (the CDCC and scatterers), which is placed in a linearly polarized EMW field ($\vec{E}(t) = \vec{E}(e^{-i\omega t} + e^{i\omega t})$, $\vec{H}(t) = [\vec{n}, \vec{E}(t)]$), ($\hbar\omega \ll \bar{\varepsilon}$; $\bar{\varepsilon}$

is an average carrier energy), in a dc electric field \vec{E}_0 and in the presence of a laser radiation field $\vec{F}(t) = \vec{F} \sin \Omega t$.

The Hamiltonian of the electron-acoustic phonon system in the PQW in the second quantization representation can be written as:

$$H = \sum_{N, \vec{p}_\perp} \varepsilon_N \left(\vec{p}_\perp - \frac{e}{\hbar c} \vec{A}(t) \right) \cdot a_{N, \vec{p}_\perp}^+ a_{N, \vec{p}_\perp} + \sum_{\vec{q}} \hbar \omega_{\vec{q}} b_{\vec{q}}^+ b_{\vec{q}} + \sum_{\substack{N, N' \\ \vec{p}_\perp, \vec{q}}} D_{N, N'}(\vec{q}) \cdot a_{N', \vec{p}_\perp + \vec{q}}^+ a_{N, \vec{p}_\perp} \left(b_{\vec{q}} + b_{-\vec{q}}^+ \right) \quad (1)$$

where N denotes the quantization of the energy spectrum in the z direction ($N = 1, 2, \dots$), $|N, \vec{p}_\perp\rangle$ and $|N', \vec{p}_\perp + \vec{q}\rangle$ are electron states before and after scattering, a_{N, \vec{p}_\perp}^+ and a_{N, \vec{p}_\perp} ($b_{\vec{q}}^+$ and $b_{\vec{q}}$) are the creation and annihilation operators of electron (phonon); $\omega_{\vec{q}}$ is the frequency of a phonon with the wave vector $\vec{q} = (\vec{q}_\perp, q_z)$; $\vec{A}(t)$ is the vector potential of laser field; $D_{N, N'}(\vec{q}) = C_{\vec{q}} I_{N, N'}(q_z)$, where $I_{N, N'}(q_z)$ is the electron form factor in the PQW, $C_{\vec{q}}$ is the electron-acoustic phonon interaction constant: $|C_{\vec{q}}|^2 = \frac{\xi^2 q}{2\rho v_S V} = C_0 q$, here V , ρ , v_S and ξ are the volume, the density, the acoustic velocity and the deformation potential constant, respectively.

The electron energy takes the simple:

$$\varepsilon_N(\vec{p}_\perp) = \hbar \omega_p \left(N + \frac{1}{2} \right) + \frac{\hbar^2 \vec{p}_\perp^2}{2m} \quad (N = 0, 1, 2, \dots) \quad (2)$$

with $\omega_p^2 = \omega_0^2 + \omega_H^2$ and $\omega_H = eH/mc$ as the confinement and the cyclotron frequencies. The quantum kinetic equation for electrons in the constant scattering time (τ) approximation takes the form [17–19]

$$\frac{\partial f_{N, \vec{p}_\perp}(t)}{\partial t} - \left(e\vec{E}(t) + e\vec{E}_0 + \omega_H [\vec{p}_\perp, \vec{h}] \right) \frac{\partial f_{N, \vec{p}_\perp}(t)}{\partial \vec{p}_\perp} + \frac{\vec{p}_\perp}{m} \frac{\partial f_{N, \vec{p}_\perp}(t)}{\partial \vec{r}} = - \frac{f_{N, \vec{p}_\perp}(t) - f_0(\varepsilon_{N, \vec{p}_\perp})}{\tau} \quad (3)$$

where $\vec{h} = \frac{\vec{H}(t)}{H(t)}$ is the unit vector in the direction of magnetic field; $f_0(\varepsilon_{N, \vec{p}_\perp})$ is the equilibrium electron distribution function (Fermi-Dirac distribution); $f_{N, \vec{p}_\perp}(t)$ is an unknown electron distribution function perturbed due to the external fields.

In order to find $f_{N, \vec{p}_\perp}(t) = \langle a_{N, \vec{p}_\perp}^+ a_{N, \vec{p}_\perp} \rangle_t$, we use the general quantum equation for the particle number operator or the electron distribution function

$$i\hbar \frac{\partial}{\partial t} f_{N, \vec{p}_\perp}(t) = \left\langle \left[a_{N, \vec{p}_\perp}^+ a_{N, \vec{p}_\perp}, H \right] \right\rangle_t \quad (4)$$

From Eqs. (3) and (4), using the Hamiltonian in Eq. (1), we obtain the quantum kinetic equation for electrons in PQW

$$\begin{aligned} & - \left(e\vec{E}(t) + e\vec{E}_0 + \omega_H [\vec{p}_\perp, \vec{h}(t)] \right) \frac{\partial f_{N, \vec{p}_\perp}(t)}{\partial \vec{p}_\perp} \\ & = - \frac{f_{N, \vec{p}_\perp}(t) - f_0(\varepsilon_{N, \vec{p}_\perp})}{\tau} + \frac{2\pi}{\hbar} \sum_{N', \vec{q}} |D_{N, N'}(\vec{q})|^2 \sum_{l=-\infty}^{+\infty} J_l^2(\vec{a}\vec{q}_\perp) \\ & \quad \times \left\{ [f_{N', \vec{p}_\perp + \vec{q}}(t) \cdot (N_{\vec{q}} + 1) - f_{N, \vec{p}_\perp}(t) \cdot N_{\vec{q}}] \times \delta(\varepsilon_{N', \vec{p}_\perp + \vec{q}} - \varepsilon_{N, \vec{p}_\perp} - \hbar\omega_{\vec{q}} - l\hbar\Omega) \right. \\ & \quad \left. + [f_{N', \vec{p}_\perp - \vec{q}}(t) \cdot N_{\vec{q}} - f_{N, \vec{p}_\perp}(t) \cdot (N_{\vec{q}} + 1)] \times \delta(\varepsilon_{N', \vec{p}_\perp - \vec{q}} - \varepsilon_{N, \vec{p}_\perp} + \hbar\omega_{\vec{q}} - l\hbar\Omega) \right\} \quad (5) \end{aligned}$$

where $J_l(x)$ is the Bessel function of argument x ; $\vec{a} = \frac{e\vec{F}}{m\Omega^2}$; $N_{\vec{q}} + 1 \approx N_{\vec{q}} = \frac{1}{\exp\{\beta\hbar\omega_{S\vec{q}_\perp}\} - 1}$ is the time-independent component of distribution function of phonons, here $\beta = \frac{1}{k_B T}$.

2.2. Calculating the CDCC of the RE in PQW

For simplicity, we limit the problem to the case of $l = 0, \pm 1$. We multiply both sides of Eq. (5) by $(-e/m)\vec{p}_\perp \cdot \delta(\varepsilon - \varepsilon_{N, \vec{p}_\perp})$ and carry out the summation over N and \vec{p}_\perp . We obtain

$$\frac{\vec{R}_0(\varepsilon)}{\tau} = \vec{Q}_0(\varepsilon) + \vec{S}_0(\varepsilon) + \omega_H \left[\vec{R}(\varepsilon) + \vec{R}^*(\varepsilon), \vec{h} \right] \quad (6)$$

The total current density is given by

$$\vec{j}_{tot} = \vec{j}_0 + \vec{j}_1(t) = \int_0^\infty \left\{ \vec{R}_0(\varepsilon) + \left[\vec{R}(\varepsilon) \cdot e^{-i\omega t} + \vec{R}^*(\varepsilon) \cdot e^{i\omega t} \right] \right\} d\varepsilon \quad (7)$$

In the case, $\omega_{\vec{q}} \ll \Omega$ ($\omega_{\vec{q}}$ is the frequency of acoustic phonons), so we let it pass. After some mathematical manipulation Eq. (7), we obtain the expression for the CDCC of the RE in PQW for the case electron-acoustic phonon scattering:

$$j_i = (j_0)_i + (j_1)_i = \tau(\varepsilon_F) \delta_{ik} \cdot \delta_{kn} \left(a_0 - \frac{e}{m} \tau(\varepsilon_F) b_0 \right) \frac{E_{0n}}{2} + \frac{\omega_p \tau^2(\varepsilon_F)}{1 + \omega^2 \tau^2(\varepsilon_F)} \varepsilon_{ikl} h_l \delta_{kn} \left(a_0 - \frac{e}{2m} \tau(\varepsilon_F) b_0 \right) \frac{E_n}{2} + \frac{\tau(\varepsilon_F)}{1 + \omega^2 \tau^2(\varepsilon_F)} \delta_{ik} \delta_{km} \left(a_0 - \frac{e}{2m} \frac{1 - \omega^2 \tau^2(\varepsilon_F)}{1 + \omega^2 \tau^2(\varepsilon_F)} \tau(\varepsilon_F) b_0 \right) \frac{E_m}{2} \quad (8)$$

where δ_{ik} is the Kronecker delta; ε_{ikl} being the antisymmetrical Levi-Civita tensor, and

$$\begin{aligned} a_0 &= \frac{e^2 L_x}{\pi} \sum_N a_N = \frac{e^2 L_x}{\pi} \sum_N \sqrt{\frac{2}{m \hbar^2} \left(\varepsilon_F - \hbar \omega_p \left(N + \frac{1}{2} \right) \right)}; \\ b_0 &= \frac{8\pi e \cdot C_0 L_x}{(2\pi \hbar)^3} (b_1 + b_2 + b_3 - b_4 - b_5 - b_6); \\ b_1 &= - \sum_{N, N'} \frac{I_{N, N'}}{\sqrt{\Delta_1}} \left\{ \frac{(q_1^+)^3}{e^{\hbar \beta v_s(q_1^+)} - 1} \times \left[1 - \frac{e^2 F^2 (q_1^+)^2}{4m^2 \Omega^4} \right] + \frac{(q_1^-)^3}{e^{\hbar \beta v_s(q_1^-)} - 1} \times \left[1 - \frac{e^2 F^2 (q_1^-)^2}{4m^2 \Omega^4} \right] \right\} \\ b_2 &= - \sum_{N, N'} \frac{I_{N, N'}}{\sqrt{\Delta_2}} \frac{e^2 F^2}{8m^2 \Omega^4} \left\{ \frac{(q_2^+)^5}{e^{\hbar \beta v_s(q_2^+)} - 1} + \frac{(q_2^-)^5}{e^{\hbar \beta v_s(q_2^-)} - 1} \right\} \\ b_3 &= b_2(\Delta_2 \rightarrow \Delta_3); \quad b_4 = b_1(q_1 \rightarrow q_4); \quad b_5 = b_2(q_2 \rightarrow q_5); \quad b_6 = b_3(q_2 \rightarrow q_6); \\ \sqrt{\Delta_1} &= \hbar^2 a'_N; \quad q_1^\pm = -m(a_N \mp a'_N); \quad \sqrt{\Delta_2} = \hbar^2 \sqrt{a_N'^2 - \frac{2\Omega}{m\hbar}}; \quad q_2^\pm = -ma_N \pm \frac{m}{\hbar^2} \sqrt{\Delta_2}; \\ \sqrt{\Delta_3} &= \hbar^2 \sqrt{a_N'^2 + \frac{2\Omega}{m\hbar}}; \quad q_4^\pm = m(a_N \pm a'_N); \quad q_5^\pm = ma_N \pm \frac{m}{\hbar^2} \sqrt{\Delta_2}; \quad q_6^\pm = ma_N \pm \frac{m}{\hbar^2} \sqrt{\Delta_3} \end{aligned}$$

with ε_F is the Fermi level; L_x is the normalization length in the x -direction.

Choose the axis Oz along \vec{n} , $\vec{Ox} \uparrow \vec{E}$, and $\vec{Oy} \uparrow \vec{H}$, from Eq. (8), we find the CDCC components

$$j_x = \tau(\varepsilon_F) \left(a_0 - \frac{e}{m} \tau(\varepsilon_F) b_0 \right) \frac{E_{0x}}{2} + \frac{\tau(\varepsilon_F)}{1 + \omega^2 \tau^2(\varepsilon_F)} \left(a_0 - \frac{e}{2m} \frac{1 - \omega^2 \tau^2(\varepsilon_F)}{1 + \omega^2 \tau^2(\varepsilon_F)} \tau(\varepsilon_F) b_0 \right) \frac{E_x}{2} \quad (9)$$

$$j_y = \tau(\varepsilon_F) \left(a_0 - \frac{e}{m} \tau(\varepsilon_F) b_0 \right) \frac{E_{0y}}{2} \quad (10)$$

$$j_z = \tau(\varepsilon_F) \left(a_0 - \frac{e}{m} \tau(\varepsilon_F) b_0 \right) \frac{E_{0z}}{2} + \frac{\omega_p \tau^2(\varepsilon_F)}{1 + \omega^2 \tau^2(\varepsilon_F)} \left(a_0 - \frac{e}{2m} \tau(\varepsilon_F) b_0 \right) \frac{h_y E_x}{2} \quad (11)$$

Equations (9), (10) and (11) show the dependence of the CDCC of the RE in PQW on the intensity F and the frequency Ω of the laser radiation, the frequency ω of the linearly polarized EMW field, the frequency ω_0 of the parabolic potential. As one can see, the above equations clearly show the dependence of the CDCC on the quantum number N, N' of the electron's state which is confined by the parabolic potential $V(z) = m\omega_0^2 z^2/2$. This is different from that in the normal bulk semiconductors [13–16, 22].

3. NUMERICAL RESULTS AND DISCUSSION

In this section, the CDCC of the RE is numerically calculated for the specific case of GaAs/GaAsAl PQW. The parameters used in the calculations are as follows [7, 8]: $\varepsilon_F = 30$ meV; $\xi = 13.5$ eV;

$\rho = 5.32 \text{ g} \cdot \text{cm}^{-3}$, $v_S = 5378 \text{ m} \cdot \text{s}^{-1}$, $m = 0.0665 m_0$ (m_0 is the mass of free electron); $L_x = 10^{-9} \text{ m}$, and we choose $\tau \sim 10^{-12} \text{ s}^{-1}$;

In Fig. 1 and Fig. 2, we show the dependence of the CDCC's components $\langle j_x \rangle$ and $\langle j_z \rangle$ on the frequency Ω of the laser radiation at different values of the confinement frequency ω_0 . In Fig. 2, we can see that the values of the component $\langle j_z \rangle$ are much larger than $\langle j_x \rangle$. That is due to the quantization on Oz axis of electrons. Moreover, we can describe the behavior of the CDCC in Fig. 1 and Fig. 2 as follows: each curve has one maximum (peak) and one minimum. We know that in PQW, state of the electron is quantized into discrete levels by quantum number N . So when the energy of a photon of laser wave is equal to the difference of two electron energy levels: $\varepsilon_{N', \vec{p}_\perp - \vec{q}_\perp} - \varepsilon_{N, \vec{p}_\perp} \pm \hbar\Omega$, resonance peak will appear.

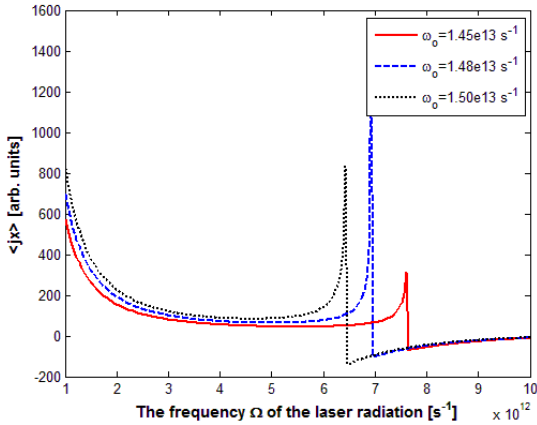


Figure 1: The dependence of $\langle j_x \rangle$ on Ω at $\omega = 5 \times 10^{12} \text{ (s}^{-1}\text{)}$, $T = 2 \text{ K}$, $E_{0x} = 10^5 \text{ V/m}$ and $F = 10^6 \text{ V/m}$.

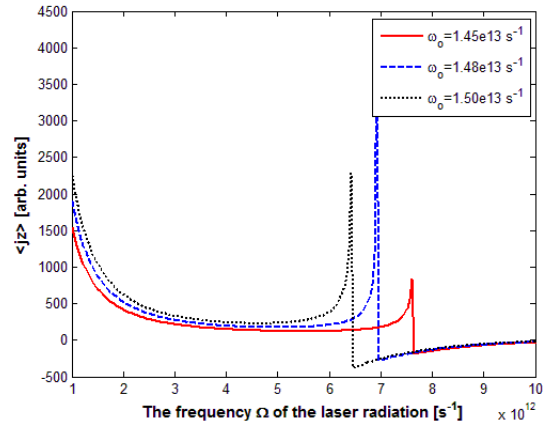


Figure 2: The dependence of $\langle j_z \rangle$ on Ω at $\omega = 5 \times 10^{12} \text{ (s}^{-1}\text{)}$, $T = 2 \text{ K}$, $E_{0x} = 10^5 \text{ V/m}$ and $F = 10^6 \text{ V/m}$.

The dependence of the CDCC component $\langle j_x \rangle$ on the frequency ω of EMW is described by Fig. 3. In Fig. 3, we can see that $\langle j_x \rangle$ depends strongly and nonlinear on ω . When the frequency ω changes, the curves of $\langle j_x \rangle$ have a maximum value (or a minimum value). All those values correspond to the resonant condition $\hbar\omega_p = \hbar\omega$ or $\hbar\sqrt{\omega_0^2 + \omega_H^2} = \hbar\omega$. Besides, Fig. 3 shows that if the frequency Ω of laser radiation slowly changes, $\langle j_x \rangle$ will quickly change.

In Fig. 4, we show the dependence of the CDCC component $\langle j_z \rangle$ on the frequency ω of EMW. From the figure we can see that the curves can begin at the negative branch or at the positive branch, which depends on the value of the frequency Ω . When the frequency ω of EMW increases,

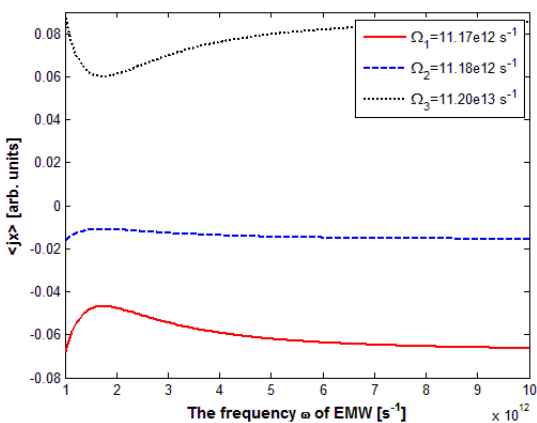


Figure 3: The dependence of $\langle j_x \rangle$ on ω at $\omega_0 = 1.5 \times 10^{13} \text{ (s}^{-1}\text{)}$, $T = 2 \text{ K}$, $E_{0x} = 10^5 \text{ V/m}$ and $F = 10^6 \text{ V/m}$.

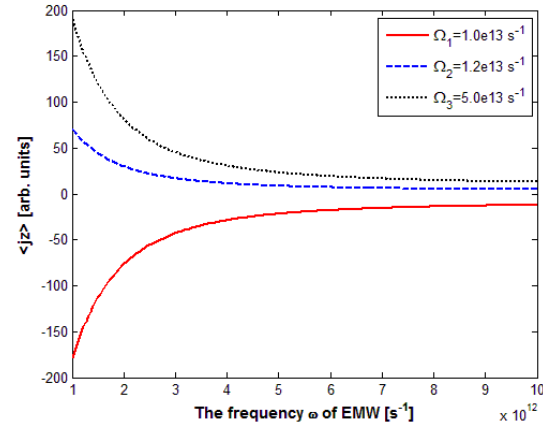


Figure 4: The dependence of $\langle j_z \rangle$ on ω at $\omega_0 = 1.5 \times 10^{13} \text{ (s}^{-1}\text{)}$, $T = 2 \text{ K}$, $E_{0x} = 10^5 \text{ V/m}$ and $F = 10^6 \text{ V/m}$.

the values of $\langle j_z \rangle$ on these curves are decreasing to zero.

4. CONCLUSIONS

In this paper, we have investigated the CDCC of the RE in PQW subjected to a dc electric field, a linearly polarized EMW field and in the presence of a laser field. The electron — acoustic phonon interaction is taken into account at low temperature and electron gas is completely degenerate. We obtain the expressions for the CDCC of the RE in PQW. We interpret the dependences of the CDCC of the RE on the frequency Ω of the laser radiation field, on the frequency ω of the linearly polarized EMW field, on the frequency ω_0 of the parabolic potential. The analytical results are numerically evaluated and plotted for specific quantum well, GaAs/AlGaAs, to confirm clearly once again that the the CDCC of the RE strongly depends on the above elements. The comparison of the result of quantum well to bulk semiconductors shows that difference.

ACKNOWLEDGMENT

This research is completed with financial support from Vietnam NAFOSTED.

REFERENCES

1. Shmelev, G. M., L. A. Chaikovskii, and N. Q. Bau, “HF conduction in semiconductors superlattices,” *Sov. Phys. Semicond.*, Vol. 12, 1932, 1978.
2. Bau, N. Q., D. M. Hung, and L. T. Hung, “The influences of confined phonons on the nonlinear absorption coefficient of a strong electromagnetic wave by confined electrons in doping superlattices,” *Progress In Electromagnetics Research Letters*, Vol. 15, 175–185, 2010.
3. Bau, N. Q. and D. M. Hung, “Calculation of the nonlinear absorption coefficient of a strong electromagnetic wave by confined electrons in doping superlattices,” *Progress In Electromagnetics Research B*, Vol. 25, 39–52, 2010.
4. Bau, N. Q., D. M. Hung, and N. B. Ngoc, “The nonlinear absorption coefficient of a strong electromagnetic wave caused by confined electrons in quantum wells,” *J. Korean Phys. Soc.*, Vol. 54, 765, 2009.
5. Bau, N. Q. and T. C. Phong, “Calculations of the absorption coefficient of a weak electromagnetic wave by free carriers in quantum wells by the Kubo-Mori method,” *J. Japan. Phys. Soc.*, Vol. 67, 3875, 1998.
6. Bau, N. Q., N. V. Nhan, and T. C. Phong, “Calculations of the absorption coefficient of a weak electromagnetic wave by free carriers in doped superlattices by using the Kubo-Mori method,” *J. Korean Phys. Soc.*, Vol. 41, 149, 2002.
7. Bau, N. Q. and H. D. Trien, “The nonlinear absorption coefficient of strong electromagnetic waves caused by electrons confined in quantum wires,” *J. Korean Phys. Soc.*, Vol. 56, No. 1, 120, 2010.
8. Bau, N. Q. and H. D. Trien, “The nonlinear absorption of a strong electromagnetic wave in low-dimensional systems,” *Wave Propagation*, Chap. 22, 461, Intech, Croatia, 2011.
9. Nhan, N. V., N. T. T. Nhan, N. van Nghia, S. T. L. Anh, and N. Q. Bau, “Ability to increase a weak electromagnetic wave by confined electrons in quantum wells in the presence of laser radiation modulated by amplitude,” *PIERS Proceedings*, 1054–1059, Kuala Lumpur, Malaysia, Mar. 27–30, 2012.
10. Nhan, N. T. T. and N. V. Nhan, “Calculation absorption coefficient of a weak electromagnetic wave by confined electrons in cylindrical quantum wires in the presence of laser radiation by using the quantum kinetic equation,” *Progress In Electromagnetics Research M*, Vol. 34, 47–54, 2014.
11. Konchenkov, V. I., S. V. Kryuchkov, T. A. Nosaeva, and D. V. Zav’yalov, “Mutual rectification of alternating currents in graphene in the field of two electromagnetic waves,” *Physics of Wave Phenomena*, Vol. 21, No. 1, 56, 2013.
12. Bass, F. G., A. A. Bulgakov, and A. P. Tetervov, *High-frequency Properties of Semiconductors with Superlattices*, Nauka, Moscow, 1989.
13. Seeger, K., *Semiconductor Physics*, Springer-Verlag, Wien, New York, 1973.
14. Malevich, V. L. and É. M. Épshtein, “Photostimulated kinetic effects in semiconductors,” *Izv. Vyssh. Uch. Zaved. Fiz.*, Vol. 2, 121, 1976.
15. Malevich, V. L., “High-frequency conductivity of semiconductors in a laser radiation field,” *Izv. Vyssh. Uch. Zaved. Radio Fizika*, Vol. 20, 151, 1977.

16. Shmelev, G. M., G. I. Tsurkan, and É. M. Épshtein, “Photostimulated radioelectrical transverse effect in semiconductors,” *Physica Status Solidi B*, Vol. 109, 53, 1982.
17. Zav’yalov, D. V., S. V. Kryuchkov, and E. S. Sivashova, “Electron-photon drag in a superlattice under the action of a strong electric field,” *Tech. Phys. Lett.*, Vol. 32, 143, 2006.
18. Zav’yalov, D. V., S. V. Kryuchkov, and E. I. Kukhar, “Electron photon drag effect in a semiconductor superlattice subjected to a high electric field,” *Semiconductors*, Vol. 41, 704, 2007.
19. Kryuchkov, S. V., E. I. Kukhar, and E. S. Sivashova, “Radioelectric effect in a superlattice under the action of an elliptically polarized electromagnetic wave,” *Physics of the Solid State*, Vol. 50, 1150, 2008.
20. Milovzorov, D. E., “Photostimulated resonant tunneling of electrons in two-level quantum wells,” *Technical Physics Letters*, Vol. 22, 896, 1996.
21. Zav’yalov, D. V., S. V. Kryuchkov, and N. E. Meshcheryakova, “The influence of a nonlinear electromagnetic wave on electric current density in a surface superlattice in a strong electric field,” *Semiconductors*, Vol. 39, No. 2, 198, 2005.
22. Zav’yalov, D. V., S. V. Kryuchkov, and E. I. Kukhar, “Effect of transverse entrainment of charge carriers by the field of two electromagnetic waves in a semiconductor,” *Physics of the Solid State*, Vol. 54, No. 9, 1853, 2012.
23. Hung, B. D., N. V. Nhan, L. V. Tung, and N. Q. Bau, “Photostimulated quantum effects in quantum wells with a parabolic potential,” *Proc. Natl. Conf. Theor. Phys.*, Vol. 37, 168, 2012.

Incorporation of Cascaded Metallic Gratings into Thin Film Solar Cells for Broadband Plasmonic Light Trapping

Long Wen, Fuhe Sun, and Qin Chen

Key Laboratory of Nanodevices and Applications-CAS
Collaborative Innovation Center of Suzhou Nano Science and Technology
Suzhou Institute of Nano-Tech and Nano-Bionics, Chinese Academy of Sciences (CAS)
Suzhou 215123, China

(Invited Paper)

Abstract— Plasmonic nanostructures have been regarded as a promising light trapping strategy towards boosting solar cell efficiency recently. However, the absorption enhancement stemming from surface plasmon excitations always suffers from an inherent limitation of narrow bandwidths, which may hamper the complete utilization of the solar radiation in a broadband spectrum for solar cells. In this paper, we theoretically show that by cascading metal gratings with different sizes atop the amorphous Silicon thin film solar cells (TFSCs), the enhanced light absorption band of the ultrathin active layer is extended due to the excitation of multiple localized surface plasmon resonances (LSPRs). For one-dimensional (1D) cascaded grating structure, the metallic gratings with different widths act as discrete nanoantennas which independently and efficiently collect the incoming photons at the LSPR wavelengths, leads to an enhancement of 60% in photocurrent for the *TM*-polarized incident illumination. Furthermore, it appears that both the coupling of plasmonic/photonic modes and their inter-coupling effects contribute to the light trapping in the 2D cascaded grating structures, which leads to an enhancement of 66.5% in the photocurrent over the bare TFSCs.

1. INTRODUCTION

In the past few years, the field of plasmonics has emerged as a rapidly expanding new area in photonics, with researchers exploring its potential applications in photovoltaics, biochemical sensing and optical computing [1–4]. Surface plasmon effects stemming from the collective oscillations of electromagnetic waves and free electrons at metal/dielectric interfaces, provide an effective method to manipulate and concentrate light into the nanoscale. The localized surface plasmons resonance (LSPR) excited in metal nanostructures and surface plasmon polaritons (SPPs) propagating at the metal/semiconductor interface are found to greatly enhance the absorption of semiconductors [2–5]. Beside the benefits of near-field light concentration, plasmonic nanostructures can serve as scattering objects [2, 5, 6] or photonic mode couplers [7, 8] to trap light more efficiently into the photoactive semiconductor with a elongated light path length. These unique optical properties associated with plasmonic structures render them promising light trapping elements for the next generation thin-film solar cells (TFSCs).

Previous studies have shown that the performance of the TFSCs can be improved considerably by incorporating randomly distributed metal nanoparticles [5, 6] or nanopatterned metal layers [7–9] on the front or rear side of the cells. Although the former structures are fabricated using relatively cheap self-assemble technologies, they suffer from limited spatial control of sharps or positions of the metallic nanoparticles, which may result in high level of parasitic losses in the metal. In contrast, the latter enables precisely patterning the metal elements and therefore engineering the plasmonic resonances. Nevertheless, such a single layer metallic patterns suffers inherently narrow bandwidths of surface plasmon excitations, which does not meet the requirement for broadband absorption enhancement. With the aim of extending the plasmonic light trapping over a broadband spectrum, researchers have proposed the dual plasmonic structures containing metallic patterns on both front and rear side of the active layer [10, 11]. However, the increased complexity in fabrication as well as the sensitivity to the lateral offset between the front and back metal elements makes this approach less attractive. In this paper, we present that by cascading metallic gratings with different sizes atop the TFSCs, the absorption in the ultrathin absorber is enhanced in an extended spectral band due to the excitation of multiple LSPRs. It was found that our proof-of-concept amorphous silicon (a-Si) TFSC containing one-dimensional (1D) cascaded gratings enables an enhancement of 60% in photocurrent over the reference cell under the *TM*-polarized incident illumination. When

incorporating with 2D cascaded gratings, the coexistence and coupling of cascaded LSPRs and photonic modes were identified as gain mechanisms of light absorption in TFSCs.

As the LSPR behavior is exquisitely sensitive to the geometrical parameters of metallic nanostructures [7, 12], we adopt it as a platform in present work to construct our cascaded plasmonic light trapping TFSCs. As shown in Figure 1(a), we began with a simple front grating TFSCs consisting of a periodic array of 1D Ag gratings on a silica-coated 50 nm thick a-Si film followed by a 300 nm thick Ag as a reflective mirror. We will refer to this single-sized grating structure as non-cascaded TFSC in the following. Normally incident sunlight with *TM* polarizations is considered for the purpose of excitation of LSPR. From Figure 1(a) (bottom), the strong localized feature observed in the normalized magnetic field gives a direct evidence of the excitation of LSPR in the non-cascaded TFSCs. The calculated absorption spectra in the active layer are plotted in Figure 1(b). It is found that the reference TFSC in absence of gratings exhibits poor absorption ability, especially in the longer wavelengths. The non-cascaded TFSC have higher absorption in most wavelengths as compared with the reference cell. At wavelengths near LSPR, we observe a narrow peak exhibiting high enhancements up to 8 for the non-cascaded TFSCs. However, the absorption quickly decreases to 50% at a wavelength of 25 nm away from the peak because of the strong resonant nature of LSPR.

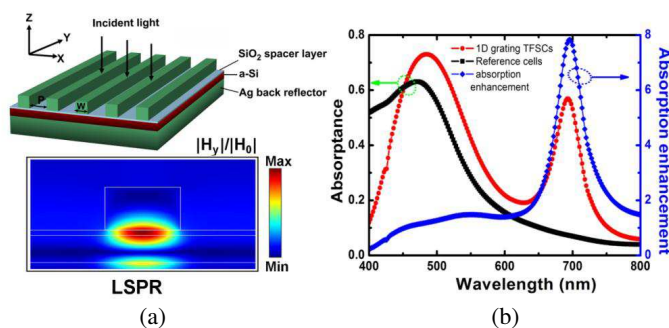


Figure 1: (a) Schematic of the 1D non-cascaded TFSC (top) and the LSPR H -field intensity distribution in the XZ plane for a non-cascaded TFSC with the grating width of 120 nm and period of 360 nm (bottom). (b) The absorption spectra of the non-cascaded TFSC and the reference TFSC. The absorption enhancement from the non-cascaded TFSC is also given.

Figure 2(a) shows the contour plots of the calculated light absorption in a-Si layer of the non-cascaded TFSCs as a function of the incident wavelength and the grating width. Two strong absorption bands can be distinguished. The first band around 400–500 nm for the grating widths smaller than 60 nm can be attributed to the longitudinal Fabry-Perot (FP) cavity modes supported by the air/a-Si/Ag cavity. As it is inherent to the flat stacks, this band does not significantly enhance the absorption over the reference TFSCs. With the increasing grating width, the resonance wavelength of the cavity mode has a red-shift owing to the coupling with the transverse propagation SPP modes. The second strong absorption band represents the LSPR excitation extends its resonance wavelengths through 350 nm to 780 nm and overlaps with the first absorption band at the wavelengths around 470 nm leading to the strongest absorption. With the strong light localization, the LSPR band gives rise to absorption enhancement factors up to 3.6 and 8 for gratings with widths of 80 and 120 nm at their resonant wavelengths. Figure 2(b) shows the a-Si absorption of the non-cascaded TFSCs at the different reciprocal lattice constants, $G = 2\pi/P$ with a fixed grating width of 100 nm. It is found that the position of the LSPR band is insensitive with the grating periods but its amplitude decrease slightly towards larger periods. Nevertheless, even for gratings with a large period of 900 nm, the LSPR induced absorption enhancement still maintains a high value of 3.2. Finally, several other trivial features observed in Figures 2(a), (b) are marked by white circles, black and red dashed lines, which represent respectively the excitation of Wood's anomalies and the bound SPPs at the Ag/SiO₂ and Ag/Air interfaces.

The broadband excitation of LSPRs by simply manipulating the widths of grating provides a large free degree in designing of the cascaded grating systems. Keeping the LSPRs in the weak absorption band of the a-Si, four gratings with the widths $W = 60, 80, 100,$ and 120 nm are chosen to construct the 1D cascaded TFSCs. As shown in Figure 2(d), the multi-sized gratings serve as four discrete LSPR resonators patterned side by side with a lateral spacing of 120 nm. Figure 2(c)

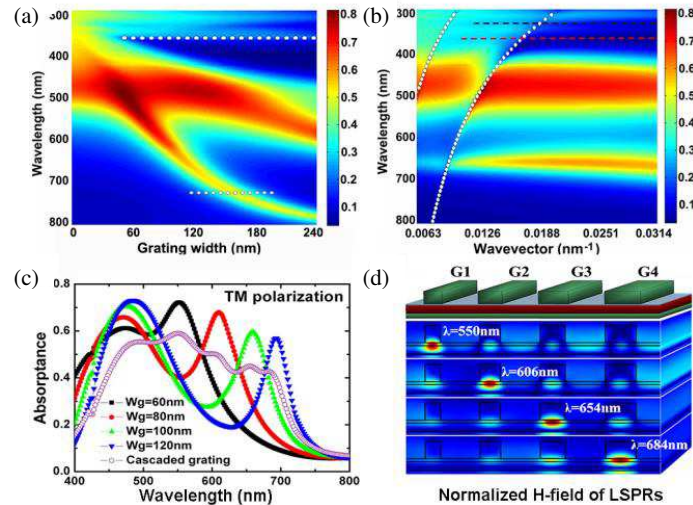


Figure 2: Contour plots of the a-Si absorption spectra as a function of (b) the grating width ($P = 360$ nm) and (c) the reciprocal lattice vector of the 1D gratings ($W = 100$ nm). (c) a-Si absorption spectra of the cascaded and non-cascaded TFSCs under TM -polarized illumination. (d) Schematic of 1D cascaded TFSC and the H -field profiles of the cascaded TFSCs at four LSPR wavelengths.

shows the absorption of a-Si in the cascaded and non-cascaded ($P = 240$ nm) TFSCs with different grating widths ($W = 60, 80, 100, 120$ nm). In consistent with the LSPR induced absorption peaks observed in the regular non-cascaded cells, four resonance peaks can be distinguished from the absorption spectrum of the cascaded TFSCs. Compared to the non-cascaded structures, the cascaded TFSCs significantly broaden the absorption band because of the simultaneous excitations of multiple LSPRs. As confirmed by the normalized H -field patterns shown in Figure 3(c), G1, G2, G3, and G4 act as four independent resonators with their resonances localized in specific positions. Considering the AM1.5G spectrum, we calculated the integrated photocurrent enhancement for the cascaded TFSCs over the reference structure. It is found that the cascaded structure gives rise to an enhancement of 60% in photocurrent for the TM -polarized illumination. As the enhancement mainly attribute to the simultaneous excitations of multiple LSPRs, broadband angle-insensitive enhancement can be expected in the cascaded TFSCs. Figure 3(a) shows the absorptance of the 1D cascaded TFSC under normal and oblique light incidence (30 degree). For the two different incident angles, we observed almost identical absorption spectra. Figure 3(b) presents the photocurrent enhancement as a function of the incident angle for TM polarizations. At an angles around 15° , the maximum enhancement of ~ 1.68 is observed. It can be seen that the cascaded design exhibits photocurrent enhancement for angles up to 60° , confirming that the cascaded TFSC allows for broadband angle-independent light absorption.

Until now, we have mainly focused on the 1D cascaded grating configurations under the TM -polarized illumination. However, to account for the randomly polarized nature of sunlight, both the polarizations need to be considered. At TE -polarized illumination, a significant part of incoming light is directly blocked by the front metallic gratings, resulting in a significantly suppressed absorption in the 1D cascaded TFSC referred in Figures 3, 4. In the following, we will extend

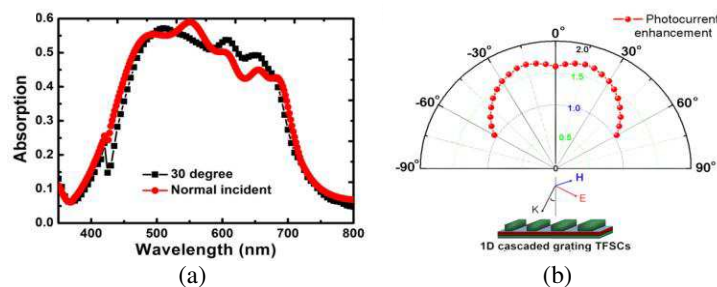


Figure 3: (a) Absorption spectra of 1D cascaded TFSCs under normal and oblique light incidence. (b) Photocurrent enhancement as a function of the angle of incidence for TM polarization.

our considerations into the 2D grating patterned TFSCs, in which an array of Ag nanocubes arranged into a rectangle lattice was employed to achieve the polarization insensitive performance. By breaking the continuity of 1D grating and shrinking its length (W_y) in the direction parallel to grating groove, the physical mechanisms involved in geometric transformation from 1D to 2D grating structures can be distinguished in a straightforward and intuitive manner. The schematic of 2D non-cascaded TFSC is shown in Figure 4(a), the grating width in the x -direction is fixed to 80 nm, the grating periods in the x and y -direction are fixed to 360 nm, and the thickness of SiO₂ spacer layer is charged to 20 nm for the sake of more efficiently excite of LSPR for 2D coupler. As shown in Figure 4(b), the absorption spectra of TFSCs under TM -polarized illumination hold their general profiles with gradually and mildly decreasing in absorption as 1D gratings change to 2D cuboids. Besides to the aforementioned cavity mode and LSPR (marked as peak A and B), two new weak peaks (marked as C_1 and C_2) emerged for the smaller W_y values, which are attributed to the fundamental TE waveguide mode resonances excited by the G [10] and G [11] grating diffractions.

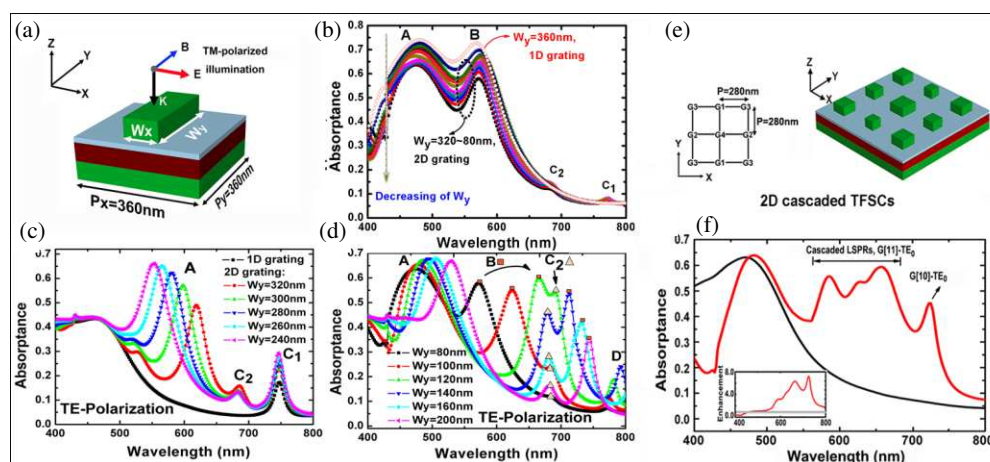


Figure 4: (a) Schematic of 2D non-cascaded TFSC. (b)–(d) Calculated a-Si absorption spectra of 2D non-cascaded TFSCs with different W_y : (b) Results for TM -polarized illumination; (c), (d) Results for TE -polarized illumination. (e) Schematic of 2D cascaded TFSC. (f) Absorption spectra and enhancement in absorption of the 2D cascaded grating TFSC.

Under TE -polarized illumination, it is found that the shrinking of W_y leads to a more complex evolution of the absorption spectra as the LSPRs shift their resonance positions and opt to couple with the photonic modes. In order to make a clear illustration, the absorption spectra is divided into two length regions ($W_y = 360$ – 240 nm and $W_y = 200$ – 80 nm) corresponding to Figures 4(c), (d). As depicted in the Figure 2(a), we have observed that the position of LSPR for the grating width of 240 nm is close to the red end of the spectrum. Consequently, for W_y larger than 240 nm, no LSPR related absorption peak was observed in Figure 4(c). For W_y larger than 240 nm, C_1 and C_2 peaks referred as two grating coupled waveguide modes have higher absorption as compared with the peaks under TM illumination owing to the elongated confinement of the modal fields beneath the gratings along the y direction. In addition, a sharp and pronounced peak A emerges even for a very small slit width in the y direction. The increase of W_y leads to a significant red-shift of the peak A, which may imply a different origin from the peak A for TM illumination (longitudinal FP cavity mode). For W_y smaller than 200 nm, the LSPR peaks can be observed in the absorption spectra (Figure 4(d)). In consistent with the results of 1D structures, the LSPR peak wavelengths decrease with the W_y . We noticed that C_1 peak is absent in this figure (except for $W_y = 80$ nm). It appears that the shrinking of W_y leads to a slight red-shift and a decrease of the modal confinement of the waveguide resonance. Thus, one may expect that the peak C_1 is swamped by other peaks. Interestingly, when the LSPR and C_2 peaks approach, their resonances are significantly enhanced due to the formation of a waveguide-plasmon-polariton [7]. The strong coupling between the LSPR and the waveguide modes also can be confirmed by the shifted C_2 resonance for $W_y = 120$ nm, where the absorption enhancement of C_2 resonance peak is 9.5, much higher than the pure waveguide mode. The newly emerged peak D red shifts its resonance with the increasing W_y , which we attribute to the longitudinal FP cavity mode supported by grating patterned slabs. According to the effective medium theory, the significantly divergence between

peak D and the aforementioned peak A can be understood by regarding the strong anisotropic refractive index of gratings under the TE and TM -polarized incidence.

To achieve the cascading LSPR enhancement, four 2D LSPR resonators with different grating widths of 80, 100, 110, 120 nm are incorporated in the cascaded TFSCs, as depicted in Figure 4(e). The 2D cuboids are arranged squarely with a period of 280 nm. For this period, both first grating order and the diagonal order coupled waveguide modes interact efficiently with the LSPRs. Figure 4(b) shows the absorption spectra and the enhancement of the proposed 2D cascaded TFSCs. Multiple absorption peaks related to LSPRs cascading and waveguide modes coupling can clearly be identified in the absorption spectra of the cells. It is very remarkable that a broadband enhancement can be achieved for the spectral range of 550–750 nm as shown in the inset of Figure 4(f). By integrating the AM1.5G solar spectral photocurrent in the case of a non-polarized illumination, we found that the 2D cascaded TFSCs gives rise to a 66.5% increase in the photocurrent over the reference structure.

In conclusion, we proposed a cascaded design based on integrating multi-sized plasmonic resonators for enhancing the optical absorption in ultra-thin TFSCs, beyond the limit of regular non-cascaded structures. We numerically demonstrated that the cascaded TFSC enable the excitations of multiple LSPRs in a broad wavelength region due to the presence of multi-sized front gratings. In addition, the coexistence and coupling of cascaded LSPRs and photonic modes further contributes to the optical absorption enhancement leading to an enhancement of 66.5% in the photocurrent in the 2D cascaded TFSC.

ACKNOWLEDGMENT

This work was supported by the grants from the National Natural Science Foundation of China (Grant Nos. 11274344), the Hundred Talents Program of Chinese Academy of Sciences, the Scientific Research Foundation for the Returned Overseas Chinese Scholars, State Education Ministry.

REFERENCES

- Schuller, J. A., E. S. Barnard, W. Cai, Y. C. Jun, J. S. White, and M. Brongersma, "Plasmonics for extreme light concentration and manipulation," *Nat. Mater.*, Vol. 9, 193–204, 2010.
- Atwater, H. A. and A. Polman, "Plasmonics for improved photovoltaic devices," *Nat. Mater.*, Vol. 9, 205–213, 2010.
- Feng, J., V. S. Siu, A. Roelke, V. Mehta, S. Y. Rhiu, G. T. Palmore, and D. Pacifici, "Nanoscale plasmonic interferometers for multispectral, high-throughput biochemical sensing," *Nano Lett.*, Vol. 8, 602–9, 2012.
- Lu, C., X. Hu, H. Yang, and Q. Gong, "Integrated all-optical logic discriminators based on plasmonic bandgap engineering," *Sci. Rep.*, Vol. 3, 2778–7, 2013.
- Spinelli, P., V. E. Ferry, J. Van de Groep, M. Van Lare, M. A. Verschuuren, R. E. I. Schropp, H. A. Atwater, and A. Polman, "Plasmonic light trapping in thin-film Si solar cells," *J. Opt.*, Vol. 14, 024002, 2012.
- Pillai, S., K. R. Catchpole, T. Trupke, and M. A. Green, "Surface plasmon enhanced silicon solar cells," *J. Appl. Phys.*, Vol. 101, 093105, 2007.
- Pala, R. A., J. White, E. Barnard, J. Liu, and M. L. Brongersma, "Design of plasmonic thin-film solar cells with broadband absorption enhancements," *Adv. Mater.*, Vol. 21, 3504–3509, 2009.
- Pala, R. A., J. S. Q. Liu, E. S. Barnard, D. Askarov, E. C. Garnett, S. Fan, and M. L. Brongersma, "Optimization of non-periodic plasmonic light-trapping layers for thin-film solar cells," *Nat. Mater.*, Vol. 4, 2095, 2013.
- Ferry, V. E., M. A. Verschuuren, H. B. T. Li, E. Verhagen, R. J. Walters, R. E. I. Schropp, H. A. Atwater, and A. Polman, "Light trapping in ultrathin plasmonic solar cells," *Opt. Express*, Vol. 18, A237–A245, 2010.
- Sefunc, M. A., A. K. Okyay, and H. V. Demir, "Volumetric plasmonic resonator architecture for thin-film solar cells," *Appl. Phys. Lett.*, Vol. 98, 093117, 2011.
- Shen, H. and B. Maes, "Combined plasmonic gratings in organic solar cells," *Opt. Express*, Vol. 19, A1202–A1210, 2011.
- Munday, J. N. and H. A. Atwater, "Large integrated absorption enhancement in plasmonic solar cells by combining metallic gratings and antireflection coatings," *Nano Lett.*, Vol. 11, 2195–2201, 2011.

A MZI Based Integrated Optical Accelerometer

Wei Hu^{1,3}, Guang Qian^{1,3,4}, Ruo-Zhou Li^{2,3,4},
Feng-Hua Wan^{1,3}, Jie Tang^{1,3}, and Tong Zhang^{1,2,3,4}

¹School of Instrument Science and Engineering, Southeast University, Nanjing 210096, China

²School of Electronic Science and Engineering, Southeast University, China

³Key Laboratory of Micro-Inertial Instrument and Advanced Navigation Technology
Ministry of Education, Nanjing 210096, China

⁴Suzhou Key Laboratory of Metal Nano-Optoelectronic Technology
Suzhou Research Institute of Southeast University, Suzhou 215123, China

Abstract— We demonstrate an optical accelerometer based on geometrically asymmetric Mach-Zehnder interferometer which is proposed to be fabricated on a flexible substrate. The asymmetric MZI based device made by polymer waveguides and substrate to realize the elastic property with a double arms cantilever beam. The relation between the structure parameters and the sensitivity are analyzed. A prototype is fabricated and a detecting experiment scheme designed for this flexible optical accelerometer is proposed. Due to simplicity of the structure, the sensor is suitable for mass production.

1. INTRODUCTION

Accelerometers are the important inertial measurement devices which are widely adopted in guidance system, automation control system, vibration sensing, and impact detection. Various physical principles such as, capacitive [1], piezoelectric [2], piezoresistive [3], magneto-resistive, and optical effects [4, 6], have been utilized to design different types of accelerometers so far. Compared with accelerometers based on electromagnetic principles, the ones utilizing optical effects show several significant advantages. For example, they are immune to electromagnetic interference, electrically insulated, more sensitive, corrosion-resistant, and reliable in inflammable or explosive conditions. Conventional optical accelerometers realized by using fibers or other separated optical components as signal carrier units are of large size [7]. With the development of integrated optical technique, researches of accelerometers based on MOEMS (Micro-Opto-Electro-Mechanical-Systems) have attracted a lot of attention in past few years, as they have lower manufacturing cost, higher integration, lighter weight, and smaller size.

In this paper, we demonstrate an optical accelerometer based on geometrically asymmetric Mach-Zehnder interferometer which is proposed to be fabricated on a flexible substrate as shown in Fig. 1. The asymmetric MZI based device made by polymer waveguides and substrate to realize the elastic property with a double arms cantilever beam. When the acceleration to be measured exerts a force on the flexible beam, the long arm waveguide of the MZI experiences a strain which causes optic transmission phase to change due to strain-optic effect and the physical elongation of the waveguide. The device meters the acceleration through measuring the interference optic intensity of the light beams in the two arms. The relation between the structure parameters and the sensitivity are analyzed. We have fabricated a prototype utilizing a flexible substrate fabrication

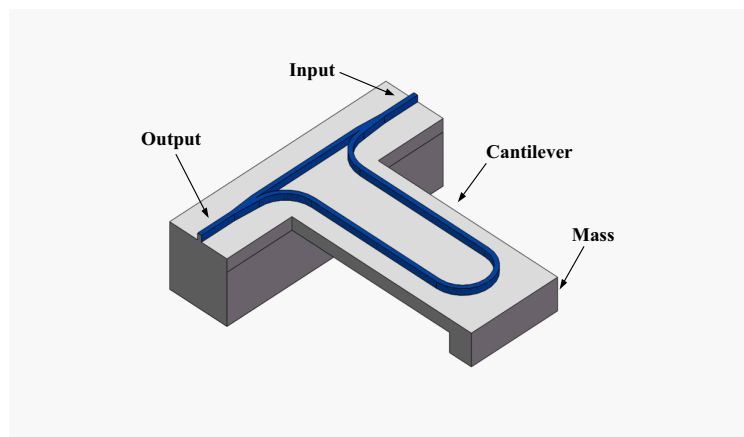


Figure 1: Schematic diagram of the proposed MZI based accelerometer fabricated on a flexible substrate.

scheme in our previous work [8]. Due to simplicity of the structure, the sensor is suitable for mass production.

2. THEORY OF THE MZI BASED ACCELEROMETER

Figure 2 shows the schematic picture for the structure of the proposed polymer MZI based accelerometer. The layout design for the device is shown in Fig. 2. The structure consists of two identical Y branches and two asymmetric arms. The length of the reference arm is $L_1 = 4R$, the bending radius is R , and the total length of the measuring arm is $L = 2\pi R + 2L_2 = VL_1$ where L_2 is the length of the straight waveguide in the measuring arm, and V is a numerical value larger than 1. Several S-bend waveguides are used in Y branches, their bend angles Φ are designed to be 1.1° . For the purpose of studying the sensing characteristics of this accelerometer, it's necessary to deduce the Phase-Intensity relationship accurately.

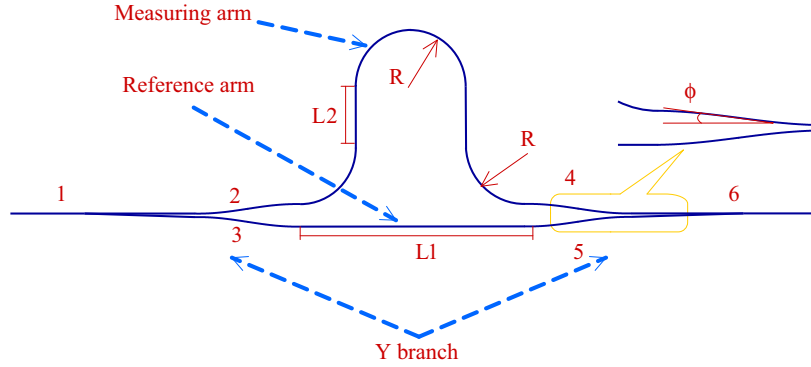


Figure 2: Schematic picture of the proposed MZI structure.

As is depicted in Fig. 2, light launched into the circuit at port 1, is split into the measuring and reference arms through the Y branch, and comes out from the port 6. The Y branch is geometrically symmetric so that we can ensure the half-half power split at port 2 and 3. The complex electric fields at different ports can be deduced as follows,

$$E_2 = E_3 = \frac{E_1}{\sqrt{2}} \quad (1)$$

$$E_4 = \exp(-\alpha VL_1 + i\varphi_{42}) E_2 \quad (2)$$

$$E_5 = \exp(-\alpha L_1 + i\varphi_{53}) E_3 \quad (3)$$

$$E_6 = \frac{E_4}{\sqrt{2}} + \frac{E_5}{\sqrt{2}} \quad (4)$$

where $\varphi_{42} = \beta VL_1 + \Delta\varphi_{42}$, and $\varphi_{53} = \beta L_1$ corresponding to the phase transfer operators through the measuring and reference arms respectively, $\Delta\varphi_{42}$ is the phase shift induced by the acceleration, and 2α is the propagation loss, $\beta = 2\pi n/\lambda$ is the mode propagation constant, n is the mode effective index, λ is the light wavelength in the vacuum. So the intensity of output signal can be written as

$$I_6 = \frac{I_1}{4} g_2 \{g_1 + g_3 \cos[\beta(V-1)L_1 + \Delta\varphi_{42}]\} \quad (5)$$

where $g_1 = 1 + \exp[-2\alpha(V-1)L_1]$, $g_2 = \exp(-2\alpha L_1)$, $g_3 = 2 \exp[-\alpha(V-1)L_1]$. Thus, from the above expression, we can say that the output intensity will vary along with the variation of $\Delta\varphi_{42}$ caused by the force exerted on the flexible cantilever.

The sensitivity of the accelerometer is deduced as follows [10],

$$S = \frac{\partial(I_6)}{\partial(a)} = \frac{\partial(I_6)}{\partial(\Delta\varphi_{42})} \times \frac{\partial(\Delta\varphi_{42})}{\partial(a)} \quad (6)$$

$$\frac{\Delta\varphi_{42}}{\varphi_{42}} = \frac{\Delta n}{n} + \frac{\Delta L}{L} \quad (7)$$

In the above equation, $\Delta n/n$ is the phase variation due to the strain-optic effect, while $\Delta L/L$ stands for the change induced by the mechanical deformation. The force exerted on the mass is

$F = ma$, provided that, the acceleration is a . Then, the strain of the cantilever can be described as [9, 10],

$$\varepsilon(x) = \frac{6F(L_a - x)}{Ebt^2} \quad (8)$$

where ε is the strain experienced by the measuring arm, x is the position of the beam with respect to the fixed end. E is the Young's modulus of the substrate, and b , L_a and t are the width, length, and thickness of the device, respectively. We give $\Delta L = 2 \int_0^{2R+L_2} \varepsilon(x) dx$ [10] and assume the value of $\Delta n(x)/n$ is $-0.11\varepsilon(x)$ [9, 10]. We can get that the shift in the transmission phase is given by

$$\Delta\varphi_{42} = ag_4 [L_a(2R + L_2) - 0.5 \times (2R + L_2)^2] \quad (9)$$

where $g_4 = 21.36 \text{ nm}/Ebt^2\lambda$, c is the speed of light in the vacuum, f is the frequency of the light signal. From (5), (6) and (9), the output intensity and sensitivity become

$$I_6 = \frac{I_1}{4} g_2 \left\{ g_1 + g_3 \cos \left[\beta(V - 1)L_1 + ag_4 L_a (2R + L_2) - ag_4 0.5 \times (2R + L_2)^2 \right] \right\} \quad (10)$$

$$S = \frac{\partial(I_6)}{\partial(a)} = \frac{\partial(I_6)}{\partial(\Delta\varphi_{42})} \times \frac{21.36nfm}{Ebt^2c} \left[L_a (2R + L_2) - 0.5 \times (2R + L_2)^2 \right] \quad (11)$$

The two expressions indicate that the sensitivity is proportional to the length of beam L_a , inversely proportional to b , t^2 and E . So the sensitivity can be tailored based upon the geometrical parameters and Young's modulus of the cantilever. We set the parameters of the accelerometer as follows. The light wavelength in the vacuum λ , the mode effective refractive index n , the amplitude coefficient of the waveguides α , radius of the bend waveguides and the length of the straight waveguide in the measuring arm R and L_2 are 1550 nm, 1.4533, 0.1, 0.25 cm, and 0.5 cm respectively. The Young's modulus E , mass of the proof mass m , and the size of the beam b , t are $0.087 \text{ N}/\mu\text{m}^2$, 15 g, 1.5 cm, and 0.05 cm respectively. Based upon these parameters, the relation between intensity and acceleration are shown in Fig. 3. It also indicates that the sensitivity and dynamic range can be easily tailored by applying different L_a .

3. FABRICATION AND EXPERIMENTAL DESIGN

In order to achieve flexible polymer substrate of our device, a special lift-off process is applied as described in our previous publication [8]. The post-off process in this work is based on the water-solubility of the polyvinyl alcohol (PVA). The schematic outline of the fabrication procedure is illustrated in Fig. 4. As a first step, we spin coated a layer of PVA, which can firmly adhere to both Si wafer and flexible polymer substrate, on a Si wafer. Then, the flexible polymer substrate

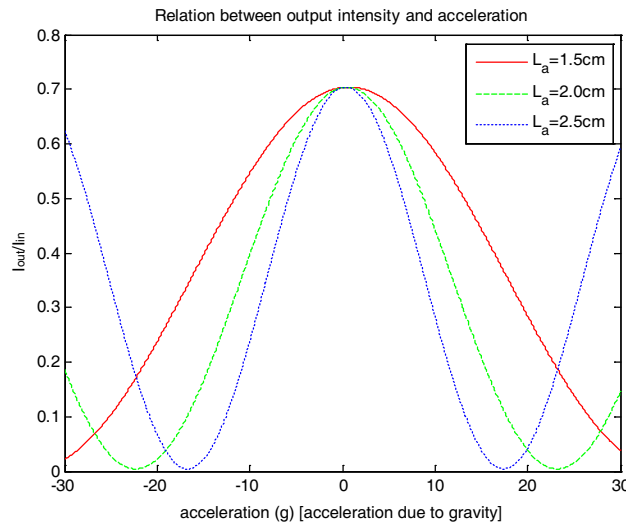


Figure 3: The relation between the acceleration and the output intensity with different values of length (L_a) of the beam.

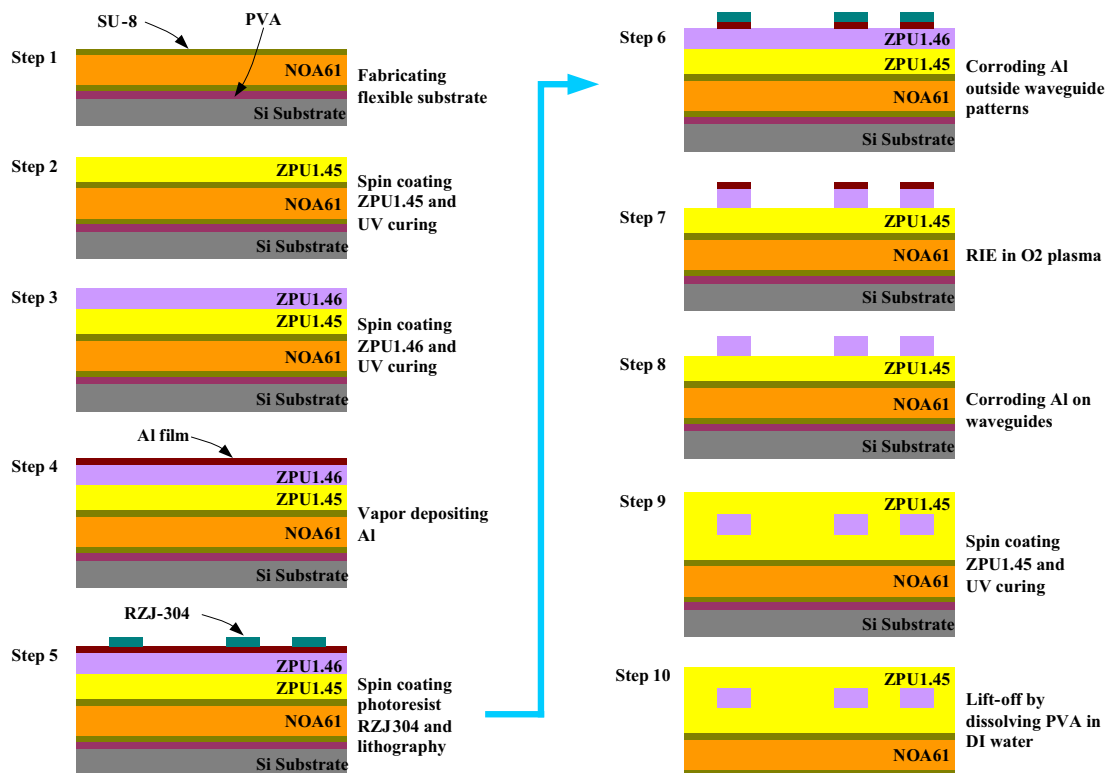
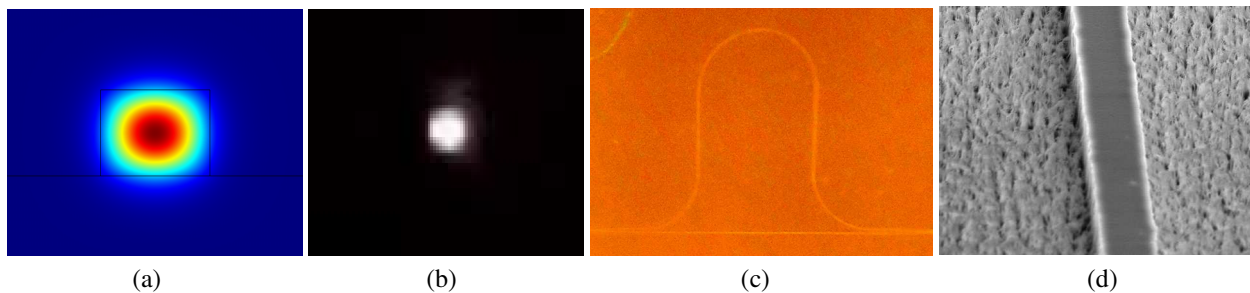


Figure 4: Fabrication procedure for the MZI based accelerometer.

Figure 5: (a) The simulated intensity distribution of HE_{11} mode at 1550 nm. (b) Light spot captured by an infrared camera. (c) a photograph of a practical device. (d) The SEM image of a waveguide.

was fabricated on the PVA layer in the structure of two SU-8 layers sandwiching a layer of NOA61, thus tunable Young's modulus can be achieved through changing the thickness of SU-8 and NOA61.

The device was designed and characterized for 1550 nm. After the flexible substrate was achieved, a $20\ \mu\text{m}$ thick layer of ZPU1.45 with refractive index of 1.45 was spin-coated on the substrate as the lower cladding. Then the membrane was cured in a UV chamber for 2 minutes, followed by a hard bake process for 30 minutes at 160°C . After that, we spin coated a $5\ \mu\text{m}$ film of another ZPU material (ZPU1.46) with refractive index of 1.46 as the core layer and cured it in UV chamber for 2 minutes too. A film of Al of $100\ \text{nm}$ – $300\ \text{nm}$ is coated on it as the barrier layer by vapor deposition so that we can protect the wanted waveguides from being etched in the following RIE process. The MZI structures were then patterned on the layer by conventional photolithography using RZJ-304 photoresist. The photoresist pattern was then transferred to the core layer by corroding Al layer outside the waveguide patterns in the phosphoric acid solution and a reactive ion etching (RIE) in O_2 plasma in sequence. Then we corrode the Al on the waveguides. The cross dimension of the stripe waveguide is $7\ \mu\text{m} \times 5\ \mu\text{m}$ so that it only supports fundamental mode as shown in Figs. 5(a) and (b). Again, we spin coated and cured a film of ZPU1.45 as the upper cladding layer. The flexible device can be separated from the Si wafer by dissolving it in deionized water. A photograph of the final device and a Scanning Electron Microscope (SEM) image of a waveguide is shown in Figs. 5(c) and (d) respectively.

For the accelerometer experiment, we fix the end with input and output ports of the flexible device on the optic measuring platform, and a proof mass with moderate iron powder is attached at the other end. Both the input and output ports are pigtailed to single-mode optical fibers which are connected to a laser ($\lambda = 1550\text{ nm}$) and an optical detector respectively. A micro electromagnet controlled by a tunable voltage source is put under the proof mass. Thus, we can effectively exert different force on the proof mass through adjusting the control voltage, that is, the equivalent acceleration can be controlled easily according to Newton's Second Law of Motion. Through detecting the signal of the optical detector on the condition of different acceleration, we can obtain the sensitivity characteristic of the device.

4. CONCLUSION

An MZI based optical accelerometer fabricated by flexible waveguide technique has been investigated. The relation between the output optical intensity and acceleration is deduced theoretically. The result shows that the sensitivity and dynamic range can be tuned by applying different dimension parameters. Meantime, the fabrication of the flexible device is exhibited and a viable test scheme is proposed. Owing to simplicity of the structure and fabrication process, such optical accelerometer is suitable for mass production in the future.

ACKNOWLEDGMENT

This work is supported by NSFC under grant number 61307066, Doctoral Fund of Ministry of Education of China under grant number 20110092110016 and 20130092120024, Natural Science Foundation of Jiangsu Province under grant number BK20130630, the National Basic Research Program of China (973 Program) under grant number 2011CB302004 and the Foundation of Key Laboratory of Micro-Inertial Instrument and Advanced Navigation Technology, Ministry of Education, China under grant number 201204.

REFERENCES

1. Chau, K. L., S. R. Lewis, Y. Zhao, R. T. Howe, S. F. Bart, and R. G. Marcheselli, "An integrated force-balanced capacitive accelerometer for low-G applications," *Sensors and Actuators A: Physical*, Vol. 54, No. 1, 472–476, 1996.
2. Nemirovsky, Y., A. Nemirovsky, P. Mural, and N. Setter, "Design of novel thin-film piezoelectric accelerometer," *Sensors and Actuators A: Physical*, Vol. 56, No. 3, 239–249, 1996.
3. Huang, S., X. Li, Z. Song, Y. Wang, H. Yang, L. Che, and J. Jiao, "A high-performance micromachined piezoresistive accelerometer with axially stressed tiny beams," *Journal of Micromechanics and Microengineering*, Vol. 15, No. 5, 993, 2005.
4. Tang, D., D. Zhao, Y. Wang, X. Zhang, Z. Liang, and F. Guo, "A MOEMS accelerometer based on photoelastic effect," *Optik-International Journal for Light and Electron Optics*, Vol. 122, No. 7, 635–638, 2011.
5. Morikawa, S. R. K., A. S. Ribeiro, R. D. Regazzi, L. C. G. Valente, and A. M. B. Braga, "Triaxial bragg grating accelerometer," *15th IEEE Optical Fiber Sensors Conference Technical Digest, 2002, OFS 2002*, 95–98, May 2002.
6. Berkoff, T. A. and A. D. Kersey, "Experimental demonstration of a fiber Bragg grating accelerometer," *IEEE Photonics Technology Letters*, Vol. 8, No. 12, 1677–1679, 1996.
7. Kim, D. H. and M. Q. Feng, "Real-time structural health monitoring using a novel fiber-optic accelerometer system," *IEEE Sensors Journal*, Vol. 7, No. 4, 536–543, 2007.
8. Li, R. Z., T. Zhang, Y. Yu, Y. J. Jiang, X. Y. Zhang, and L. D. Wang, "Flexible multilayer substrate based optical waveguides: Applications to optical sensing," *Sensors and Actuators A: Physical*, 2014.
9. Bholia, B. and W. H. Steier, "A novel optical microring resonator accelerometer," *IEEE Sensors Journal*, Vol. 7, No. 12, 1759–1766, 2007.
10. Zhang, T., B. B. Qu, X. J. Xue, J. L. Zhang, P. Q. Wu, and X. Y. Zhang, "Simulation of an optical accelerometer based on integrated optical ring resonator," *2010 International Conference on Networking, Sensing and Control (ICNSC)*, 675–678, 2010.

Graphene Photodetector Based on Metamaterial Perfect Absorber

Shichao Song¹, Long Wen¹, and Qin Chen^{1,2}

¹Key Lab of Nanodevices and Applications-CAS
Collaborative Innovation Center of Suzhou Nano Science and Technology
Suzhou Institute of Nano-Tech and Nano-Bionics, Chinese Academy of Sciences (CAS)
Suzhou 215123, China

²Peking University Shenzhen SOC Key Laboratory, PKU-HKUST Shenzhen-Hong Kong Institute
Hi-Tech Industrial Park South, Shenzhen 518057, China

Abstract— A graphene-metamaterial composite photodetectors with graphene embedded in metamaterial perfect absorbers (MPAs) is proposed and their light absorption properties are numerically investigated. Absorption above 40% in graphene monolayer is obtained due to the strongly localized electromagnetic resonance and the suppression of reflection and transmission loss in MPAs. The working frequency of the graphene photodetector can be tunable and determined by MPAs due to the ultrabroad absorption band of graphene. The novel idea of using MPAs to enhance the interaction between light and graphene could be also adopted in other graphene optoelectronic devices.

1. INTRODUCTION

Graphene is an attractive material for optoelectronic devices such as transparent conductive electrode, polarization controller, modulator, photodetector, due to its ultra-broadband absorption, unusually high electron mobility, atomic layer thickness, and unique mechanical flexibility [1]. With a thickness of only 0.335 nm, monolayer graphene exhibits remarkable optical absorption nearly 2.3% in a wide frequency range from ultraviolet to infrared [2]. However, monolayer or few layer graphene has very weak light absorption due to the sub-1 nm-scale thickness, resulting in very low photoresponsivity, especially in graphene photodetectors. An ultrafast transistor-based photodetector with a bandwidth of 40 GHz was demonstrated but the photoresponse was only 0.5 mA W^{-1} [3]. Konstantatos et al. constructed a graphene-colloidal quantum dots composited nanostructure with a responsivity of $\sim 10^7 \text{ AW}^{-1}$, but it is a responsivity of composited nanostructure rather than simple graphene response [4]. Various methods have been presented to improve the photoresponse by enhancing the interaction between graphene and light. Furchi et al. demonstrated a graphene photodetector based on a dielectric planar microcavity with a photoresponse of 21 mA W^{-1} . Absorption as high as 60% was obtained but the device was quite complex due to the large number of dielectric layers in the distributed Bragg reflectors [5]. Instead, Engel et al. used metallic mirrors to form a simple microcavity but the surface reflection and the metal attenuation reduced the photoresponse [6]. Alternatively, Zhang et al. has proposed a novel idea to greatly enhance the photoresponsivity of the graphene photodetector by engineering the lifetime of the photo-excited carriers, where the graphene was patterned into quantum dot-like structures [7]. On the other hand, perfect absorption at terahertz frequency was achieved in graphene by patterning into nanodisk array and forming a metamaterial perfect absorber (MPA) [8]. In this case, doped graphene, like the noble metals in the visible and near infrared regime, supports surface plasmon resonances (SPRs). It therefore acts as surface impedance matching layer in a MPA. But for infrared and visible range, the electron density in doped graphene is not high enough to support SPRs. Meanwhile, metallic MPAs have been widely investigated and demonstrated promising applications in biosensor [9], microbolometers [10], solar cells [11, 12], etc. Usually, it consists of a structured metallic surface and a metallic ground plane intermediated by a dielectric layer [9, 13, 14]. Matching the surface impedance by optimizing the periodic subwavelength structures in the top metal film, a near-zero reflection can be achieved. The metallic ground plane acts as a perfect reflector. As a result, near-unity absorption of the whole structure is obtained at the electromagnetic resonance.

In this letter, a pair of novel graphene-material composite structures for high-efficiency photodetection is proposed, where each graphene monolayer is embedded in a MPA. The configuration of a graphene MPA naturally coincides with a transistor, where the metallic impedance matching layer and the ground plane can be used as electrodes and gate, respectively. Compared to the previous devices, it provides both high light absorption in graphene and simple device structures. Finite difference time domain (FDTD) method is used to simulate the light transmission behaviour. The

electromagnetic properties of the sandwich structure are optimized to perfectly meet the impedance match condition. As a result of the high reflection back mirror and the impedance matching, a nearly unit absorption could be achieved on resonance, in which 40% incident light is absorbed in graphene, 17 times enhancement compared to graphene intrinsic absorption. Tunable absorption spectra are also demonstrated.

Schematic of a pair of graphene photodetectors with graphene embedded in MPAs are shown in Fig. 1. One dimensional (1D) metal gratings (Fig. 1(a)) or a continuous metal film with square hole arrays (Fig. 1(b)) is separated from a continuous metal film by a layer of Al_2O_3 . Graphene is just at the bottom of the metal gratings. FDTD simulations of a unit cell were performed with periodic boundary conditions in the x direction or xy plane and perfect matching layers in the z direction. Non-uniform meshes were used in the FDTD simulation, where the minimum mesh sizes at the interfaces are 5 nm and 0.1 nm in horizontal and vertical directions, respectively. The incident light is assumed to be transverse magnetic (TM) polarized (the magnetic field parallel to the grating) and normal to the structure surface. The refractive index of Al_2O_3 is 1.7. Gold is used as the metal material with dielectric constant from the data of Johnson and Christ [15]. The dielectric constant of graphene is $1 + 4\pi i\sigma/\omega t$, where σ is the conductivity, ω is the angular frequency and t is the thickness of graphene (0.5 nm in the simulation) [16]. The conductivity from both interband and intraband contributions for graphene are calculated using the Kubo formula [17, 18]

$$\sigma_{inter}(\omega) = \frac{\pi e^2}{4h} \left(\tanh \frac{\hbar\omega + 2\mu}{4k_bT} + \tanh \frac{\hbar\omega - 2\mu}{4k_bT} \right) + i \left(\frac{1}{\hbar\omega} \frac{2e^2}{h} \mu - \frac{e^2}{2h} \log \left| \frac{\hbar\omega + 2\mu}{\hbar\omega - 2\mu} \right| \right) \quad (1)$$

$$\sigma_{intra}(\omega) = i \frac{2e^2}{h} \frac{2k_bT}{\hbar(\omega + i\tau^{-1})} \log \left(2 \cosh \left(\frac{\mu}{2k_bT} \right) \right) \quad (2)$$

$$\sigma(\omega) = \sigma_{inter}(\omega) + \sigma_{intra}(\omega) \quad (3)$$

where σ_{intra} , σ_{inter} are the intraband and interband contribution to conductivity, respectively. h and \hbar are Planck and reduced Planck constant. ω is the angular frequency, μ is the chemical potential of graphene, which can be set to 0 eV via the applied voltage. k_b is Boltzmann constant, T is the thermodynamic temperature (300 K). e is the charge of electron, τ is the average scattering lifetime of free electrons.

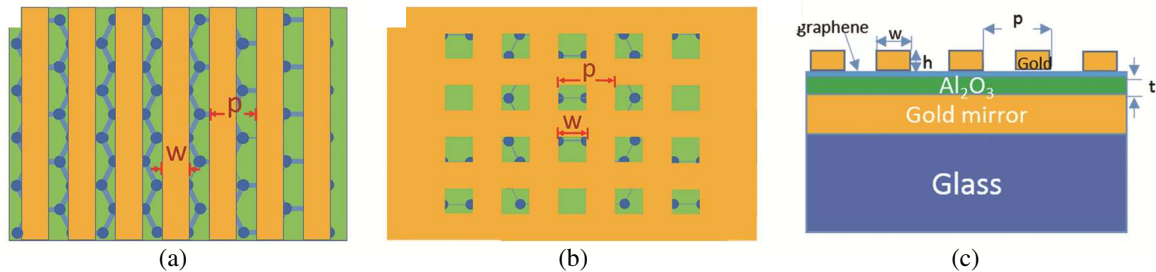


Figure 1: Schematic of a pair of graphene photodetectors with graphene embedded in MPAs. (a) Top view of a graphene photodetector. The metallic matching layer is the gold gratings. (b) Top view of metallic hole array assembled graphene photodetector. The metallic matching layer is the gold film with square hole arrays. (c) The section cross view of the first MPA structure (a).

Figure 2(a) shows the calculated absorption spectra of a whole MPA and the contribution from graphene. It can be seen that the light is nearly completely absorbed at the resonant wavelength, among which 40.1% absorption occurs in graphene. The effective permeability ($\mu' + i\mu''$) of the MPA were also calculated [19]. As presented in Fig. 2(b), μ' cross zero at $1.065 \mu\text{m}$, which results in the impedance matching at this wavelength. Meanwhile, μ'' has a positive resonance at the corresponding wavelength. Thus, the complete absorption is mainly attributed to the occurrence of the magnetic absorption resonance. With this effect, the light absorption is enhanced by over 17 times that of an intrinsic graphene monolayer. The proposed graphene MPA photodetector can be regarded as a combination of a plasmonic photodetector and a microcavity photodetector, where both SPR near field enhancement and light path recycling contribute to the light absorption. Furthermore, the perfect impedance match at the patterned metal structure eliminates the reflection loss. The plasmonic near field enhancement can be seen from Fig. 2(e), where hot spots exist beneath the

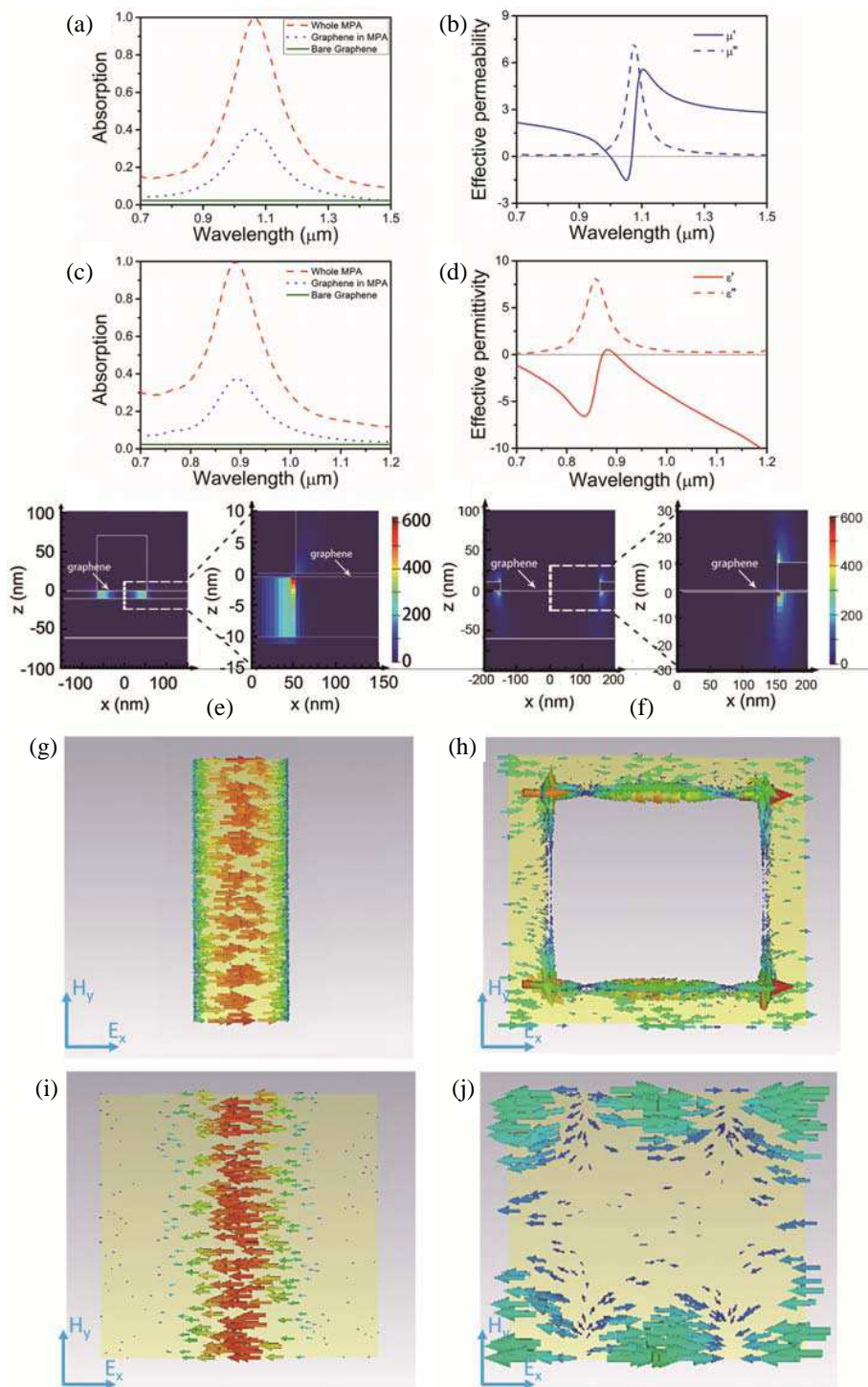


Figure 2: (a) Absorption spectrum of a graphene monolayer in MPA with the TM polarized normal incident light, with $p = 300$ nm, $w = 110$ nm, $h = 70$ nm, and $t = 10$ nm. The absorption spectra of the whole MPA and a bare graphene monolayer are shown for comparison. Graphene locates at the bottom of the gratings. (b) Absorption spectrum of a graphene monolayer in MPA (shown in the Fig. 1(b), which $p = 400$ nm, $w = 310$ nm, $h = 10$ nm, and $t = 60$ nm). (c), (d) The effective permittivity and permeability are also calculated. The distribution of $|E_z|^2$ at the resonant wavelength of (e) $1.065 \mu\text{m}$ and (f) $0.896 \mu\text{m}$ in a unit cell. The zoom-in electric field distribution around the edge of the nanostructure is also presented. The semi-transparent schematics of the induced surface currents of the MPA at each resonant wavelength with different metallic surfaces. (g) and (h) are the top view of induced surface currents of nanostructures, (i) and (j) are the induced surface currents of the metallic mirrors, respectively.

grating corners with more than 600 times enhancement of $|E_z|^2$. The excellent light trapping allows a strong interaction between graphene and light. MPA consisting of two-dimensional metallic hole array as shown in Fig. 1(b) were also investigated for the metamaterial-graphene photodetector. As shown in Fig. 2(c), the light has almost been completely absorbed at the resonant wavelength, where 37.3% absorption contribution is from graphene. The effective permittivity ($\epsilon' + i\epsilon''$) of the MPA are presented in the Fig. 2(d). ϵ' cross zero at 0.896 μm . Moreover, the imaginary part has a positive value, contributing to the light absorption. So the light absorption in graphene can be significantly enhanced by electromagnetic resonance at the resonant wavelength. The strong plasmonic near field enhancement can be seen from Fig. 2(f), where hot spots exist at the edge of the nanostructures. Owing to enhancement of $|E_z|^2$, the absorption of graphene has been largely enhanced. The schematic figures of calculated surface current of these two MPAs at each resonant wavelength are shown in Figs. 2(g)–(j), respectively. In Figs. 2(g) and (i), the induced surface currents at two metal/dielectric interfaces flow in opposite directions, generating a magnetic field opposite to the external field. This also confirms that the absorption of this MPA structure (gratings) at the resonant wavelength is donated by the magnetic resonance. While the current distribution in the hole array nanostructures are different as shown in Fig. 2(h). In each metal-dielectric interface, the surface current has opposite flow directions at different regions, for example, in Fig. 2(j), the surface currents at four corners flow from right to left while those at the top and bottom edges flow from left to right. The sum of surface current is very small resulting the suppression of the magnetic resonance. On the contrary, the dipole-like current distributions between the two corners along the direction of the excitation electric field show an electric resonance. Therefore, by constructing different subwavelength structures, we can manipulate the spectral response of the MPA based on both electric and magnetic resonances and optimize the graphene-metamaterial photodetectors.

Since the absorption enhancement results from the strong light localization in MPA and its interaction with graphene, it is necessary to investigate the effect of various structure parameters. The positions of graphene in the MPA are proved to be at the bottom of the gold gratings, contributing to the largest enhancement. Moreover, the period has little effect on the resonant wavelength and absorption, while the duty ratio of the nanostructures has a great influence on them [20]. Shown in Fig. 3(a), six graphene embedded MPAs with a same period are shown, where the absorption wavelengths are linearly tuned by the widths or fill factor of the gold gratings. The maximum light absorbance of 40.1%, approximately 17.4 times of the instinct graphene absorption, is observed at $w = 100 \text{ nm}$, where the near-field enhancement approaches a maximum at the edge of the gratings. Several graphene embedded hole array MPAs with a same period are also shown in Fig. 3(b), where the absorption wavelengths are monotonously changed by the duty ratio or the side length of the hole. Moreover, over 35% absorption of graphene can be achieved in these MPAs with the near-field enhancement.

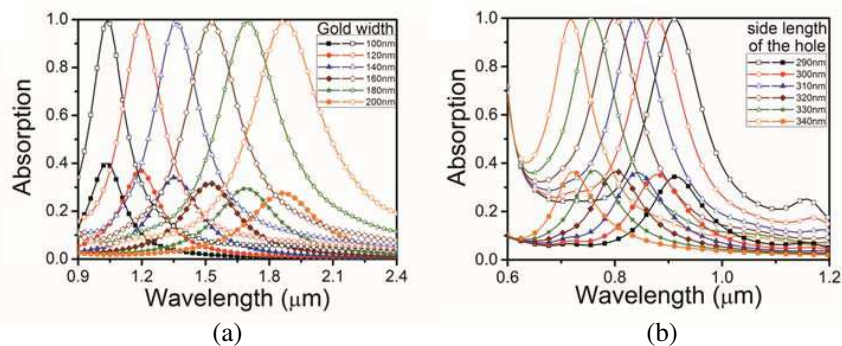


Figure 3: The absorption spectra in various MPAs. Graphene is at the bottom of the gold nanostructures. (a) Whole structure (open scatters) and graphene (solid scatters) absorption spectra for $w = 100\text{--}200 \text{ nm}$. $p = 300 \text{ nm}$, $h = 70 \text{ nm}$, $t = 10 \text{ nm}$. (b) Whole structure (open scatters) and graphene (solid scatters) absorption spectra for $w = 290\text{--}340 \text{ nm}$. $p = 400 \text{ nm}$, $h = 10 \text{ nm}$, $t = 60 \text{ nm}$.

2. CONCLUSIONS

A novel graphene-metamaterial composite structure with graphene monolayer embedded in a MPA is proposed and its light absorption property is numerically investigated. Over 40% absorption in graphene is achieved, which is over 17 times that of a bare monolayer graphene. Owing to

the strongly localized electromagnetic resonance and the suppression of reflection and transmission loss in MPAs, the absorption can be significantly enhanced. Benefiting from graphene's ultra-wideband optical absorption and high electron mobility, we can obtain a photodetector with high speed, broad band and high photoelectric conversion efficiency. This novel idea using MPAs to enhance the interaction between light and graphene not only presents a new solution to graphene photodetectors, but also could be adopted in other graphene optoelectronic devices.

ACKNOWLEDGMENT

This work is supported by the General Program of the National Natural Science Foundation of China (No. 11274344), the Hundred Talents Program of Chinese Academy of Sciences and the Fundamental Research Project of Shenzhen Science and Technology Foundation (No. JC201105180781A).

REFERENCES

1. Mueller, T., F. N. A. Xia, and P. Avouris, *Nat. Photonics*, Vol. 4, No. 5, 297–301, 2010.
2. Nair, R. R., P. Blake, A. N. Grigorenko, K. S. Novoselov, T. J. Booth, T. Stauber, N. M. R. Peres, and A. K. Geim, *Science*, Vol. 320, No. 5881, 1308–1308, 2008.
3. Xia, F. N., T. Mueller, Y. M. Lin, A. Valdes-Garcia, and P. Avouris, *Nat. Nanotechnol.*, Vol. 4, No. 12, 839–843, 2009.
4. Konstantatos, G., M. Badioli, L. Gaudreau, J. Osmond, M. Bernechea, F. P. G. de Arquer, F. Gatti, and F. H. L. Koppens, *Nat. Nanotechnol.*, Vol. 7, No. 6, 363–368, 2012.
5. Furchi, M., A. Urich, A. Pospischil, G. Lilley, K. Unterrainer, H. Detz, P. Klang, A. M. Andrews, W. Schrenk, G. Strasser, and T. Mueller, *Nano. Lett.*, Vol. 12, No. 6, 2773–2777, 2012.
6. Engel, M., M. Steiner, A. Lombardo, A. C. Ferrari, H. V. Löhneysen, P. Avouris, and R. Krupke, *Nat. Commun.*, Vol. 3, 906, 2012.
7. Zhang, B. Y., T. Liu, B. Meng, X. Li, G. Liang, X. Hu, and Q. J. Wang, *Nat. Commun.*, Vol. 4, 1811, 2013.
8. Thongrattanasiri, S., F. H. L. Koppens, and F. J. G. de Abajo, *Phys. Rev. Lett.*, Vol. 108, No. 4, 047401, 2012.
9. Liu, N., M. Mesch, T. Weiss, M. Hentschel, and H. Giessen, *Nano. Lett.*, Vol. 10, No. 7, 2342–2348, 2010.
10. Maier, T. and H. Bruckl, *Opt. Lett.*, Vol. 34, No. 19, 3012–3014, 2009.
11. Choi, H., F. Borondics, D. A. Siegel, S. Y. Zhou, M. C. Martin, A. Lanzara, and R. A. Kaindl, *Appl. Phys. Lett.*, Vol. 94, 172102, 2009.
12. Wen, L., F. H. Sun, and Q. Chen, *Appl. Phys. Lett.*, Vol. 104, No. 15, 151106, 2014.
13. Landy, N. I., S. Sajuyigbe, J. J. Mock, D. R. Smith, and W. J. Padilla, *Phys. Rev. Lett.*, Vol. 100, No. 20, 207402, 2008.
14. Chen, Q., F. Sun, and S. Song, *Opt. Express*, Vol. 21, No. 13, 15896–15903, 2013.
15. Johnson, P. B. and R. W. Christy, *Phys. Rev. B*, Vol. 6, No. 12, 4370–4379, 1972.
16. Koppens, F. H. L., D. E. Chang, and F. J. G. de Abajo, *Nano. Lett.*, Vol. 11, No. 8, 3370–3377, 2011.
17. Gusynin, V. P., S. G. Sharapov, and J. P. Carbotte, *Phys. Rev. B*, Vol. 75, 165407, 2007.
18. Mak, K. F., M. Y. Sfeir, Y. Wu, C. H. Lui, J. A. Misewich, and T. F. Heinz, *Phys. Rev. Lett.*, Vol. 101, 196405, 2008.
19. Smith, D. R., S. Schultz, P. Markos, and C. M. Soukoulis, *Phys. Rev. B*, Vol. 65, No. 19, 195104, 2002.
20. Song, S. C., Q. Chen, L. Jin, and F. H. Sun, *Nanoscale*, Vol. 5, No. 20, 9615–9619, 2013.

Improved Calibration Method for Raman Distributed Temperature Sensor

K. Oishi, T. Umeno, N. Takeuchi, and S. Adachi
Yokogawa Electric Corporation, Japan

Abstract— We propose an improved calibration technique that simultaneously and simply determines an accurate Raman shift wave number and the differential loss of the sensing fiber in order to take highly accurate temperature measurements over a wide range of temperatures.

1. INTRODUCTION

The Raman Distributed Temperature Sensor (DTS) has recently been successfully adopted in the oil & gas fields, site safety, assets monitoring, and facilities maintenance [1]. According to the DTS principle, local temperature T_s can be determined by knowing the temperature T_0 in the temperature reference fiber, the ratios of the anti-Stokes and Stokes intensities, and the Raman shift wave number of the sensing fiber. However, the optical device characteristics such as the light source (wavelength), optical filter, photodiode, reference thermometer (uncertainty), optical switch, optical connector, splice, and sensing fiber under actual conditions may affect the temperature measurement accuracy. We already reported on a novel calibration technique to determine the accurate Raman shift wave number of the sensing fiber (fiber having the differential characteristics from a built-in fiber) to perform highly accurate temperature measurements over a wide range of temperatures although the conventional linear approximation method is only effective over a small temperature range [2]. However, the differential loss (attenuation difference at the Stokes and anti-Stokes wavelengths) needs to be corrected beforehand.

We propose an improved calibration method in this paper that automatically, simultaneously and simply calculates the calibration parameters such as the Raman shift wave number and the differential loss of the sensing fiber.

2. PRINCIPLE [3]

Raman scattering occurs due to the interaction between the light and optical phonons present in a continuum medium. In such an interaction, the medium can lose energy (anti-Stokes) or acquire energy (Stokes) by means of scattering. The molecular vibrational states — the phonons — obey the Bose-Einstein statistics distribution, which is a function of the temperature. The Stokes and anti-Stokes intensities (I_{st} , I_{as}) are given by Equation (1)

$$I_{st} \propto (\nu_0 - \Delta\nu)^4 (1 + n(\Delta\nu, T)) \quad I_{as} \propto (\nu_0 + \Delta\nu)^4 n(\Delta\nu, T), \quad (1)$$

where ν_0 is the wave number of incident light, $\Delta\nu$ is the Raman shift wave number, and n is the number of photons as expressed by Equation (2)

$$n(\Delta\nu, T) = \frac{1}{\exp(hc\Delta\nu/kT) - 1}, \quad (2)$$

where h is the Plank's constant, k is the Boltzmann's constant, and c is the speed of light. The Raman shift wave number is determined by the molecular structure of the medium. The Raman spectrum has a peak at around 400–500 cm^{-1} in the silica optical fiber. The ratio of the anti-Stokes to Stokes intensities can be expressed as

$$R(T) = I_{as}/I_{st} = \frac{(\nu_0 + \Delta\nu)^4}{(\nu_0 - \Delta\nu)^4} \exp\left(-\frac{hc\Delta\nu}{kT}\right) \quad (3)$$

Using the temperature in the built-in fiber (for temperature reference) T_0 ,

$$R(T)/R(T_0) = \exp\left(-\frac{hc\Delta\nu}{kT}\right) / \exp\left(-\frac{hc\Delta\nu}{kT_0}\right). \quad (4)$$

Equation (5) is obtained by taking the logarithm of both sides

$$T = \frac{hc\Delta\nu}{k} \left[\frac{1}{-\ln R(T) + \ln R(T_0) + \frac{hc\Delta\nu}{k} \frac{1}{T_0}} \right]. \quad (5)$$

Local temperature T_s can be determined by priorly knowing T_0 , $R(T_0)$, $R(T)$, and $\Delta\nu$. We assume here that the differential loss (attenuation difference at the Stokes and anti-Stokes wavelengths) is corrected beforehand and the sensing fiber has the same characteristics as the built-in fiber. Moreover, we assume that the optical connector does not experience differential loss.

3. HIGHLY ACCURATE MEASUREMENT USING HIGHLY ACCURATE $\Delta\nu$ [2]

Let us connect the sensing fiber (fiber having differential characteristics from built-in fiber) to the interrogator (Figure 1). The measured temperature T'_s at the point of scattering can be calculated by measuring $R_r(T_0)$ and $R(T_s)$. Here, T_s is the true temperature and the Raman shift wave number of the sensing fiber is set to the same value as the built-in fiber. $R_r(T_0)$ and $R(T_s)$ are the ratios of the anti-Stokes to Stokes intensities of the built-in fiber and the measured position.

$$T'_s = \frac{hc\Delta\nu_r}{k} \left[\frac{1}{-\ln R(T_s) + \ln R_r(T_0) + \frac{hc\Delta\nu_r}{k} \frac{1}{T_0}} \right]. \quad (6)$$

The actually measured $R(T_s)$ can be expressed by using Equation (7)

$$R(T_s) = \Delta L_{conn} \frac{(\nu_0 + \Delta\nu_s)^4}{(\nu_0 - \Delta\nu_s)^4} \exp\left(-\frac{hc\Delta\nu_s}{kT_s}\right), \quad (7)$$

where ΔL_{conn} is the differential loss of the connector and $\Delta\nu_s$ is the Raman shift wave number of the sensing fiber. Then $R_r(T_0)$ is given by using Equation (8)

$$R_r(T_0) = \frac{(\nu_0 + \Delta\nu_r)^4}{(\nu_0 - \Delta\nu_r)^4} \exp\left(-\frac{hc\Delta\nu_r}{kT_0}\right), \quad (8)$$

where $\Delta\nu_r$ is the Raman shift wave number and T_0 is the absolute temperature of the built-in fiber.

When the temperature is measured at the scattering position, it is calculated by using Equation (6) and the true temperatures are set to T'_1 and T_1 . Then, for another temperature measurement, the temperature calculated by using Equation (6) and the true temperature are set to T'_2 and T_2 as well. Next, a highly accurate Raman shift wave number of the sensing fiber can be determined by using Equation (9)

$$\Delta\nu_s = \Delta\nu_r \frac{T'_1 - T'_2}{T'_1 T'_2} \frac{T_1 \cdot T_2}{T_1 - T_2}. \quad (9)$$

Then, the highly accurate temperature can be determined using Equation (10)

$$T_s = \Delta\nu_s \frac{1}{\frac{\Delta\nu_r}{T'_s} - \frac{\Delta\nu_r}{T'_1} + \frac{\Delta\nu_s}{T_1}}. \quad (10)$$

On the basis of the above examination, we evaluated the temperature measurement accuracy using a highly accurate $\Delta\nu_s$. First, we determined the highly accurate Raman shift wave number $\Delta\nu_s$ of the sensing fiber by using Equation (9) at 80°C (T_1) and 300°C (T_2). The measured temperature difference between the DTS and the reference thermometer was within $\pm 0.2^\circ\text{C}$ in the wide temperature range from 80–300°C (Figure 2).

4. IMPROVED CALIBRATION METHOD

As mentioned above, a highly accurate $\Delta\nu_s$ is very important for taking highly accurate temperature measurements. However, we assume that the differential loss (attenuation difference at the Stokes and anti-Stokes wavelength) is corrected beforehand. There are several methods for determining the differential loss of the sensing fiber. 1) Differential loss $\Delta\alpha_s$ (dB/km) can be determined by calculating the temperature so that it matches the temperature at two different positions where

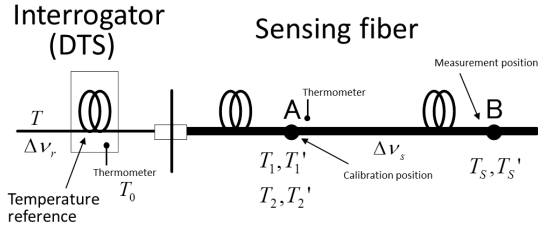
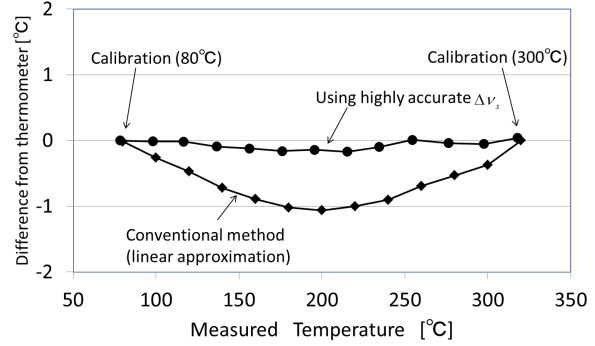


Figure 1: Measurement set-up.

Figure 2: Evaluated results using highly accurate $\Delta\nu_s$.

the temperatures are set to the same level. Since the calculated temperature has various parameters and there is a complicated relation between all of them, the temperatures from two positions need to be the same. 2) At a position in the near end where the differential loss is neglected, the highly accurate $\Delta\nu_s$ can be determined by using the above mentioned method. After that, the differential loss can be determined by calculating the temperature at the far end so that it is the same as the true temperature. However, every method has a complicated step, and needs much more time and labor to complete it.

We propose an improved method here for simultaneously and simply determining a highly accurate $\Delta\nu_s$ and $\Delta\alpha_s$ using the temperatures at three positions.

In the measurement setup shown in Figure 1, Equation (6) is rewritten as Equation (10) by taking the differential loss into consideration.

$$T'_n = \frac{hc\Delta\nu_r}{k} \left[\frac{1}{-\ln R(T_n, L) - \ln \left(10^{\frac{\Delta\alpha_s L}{5}} \right) + \ln R_r(T_0) + \frac{hc\Delta\nu_r}{k} \frac{1}{T_0}} \right], \quad (11)$$

where $\Delta\alpha_s$ (dB/km) is the differential loss of the sensing fiber and L (km) is the distance from the interrogator to the measured position. The distance of the three measured positions are L_1 , L_2 , and L_3 and the true temperatures at the three positions are T_1 , T_2 , and T_3 . Using Equations (9) and (11), $\Delta\nu_s$ and $\Delta\alpha_s$ are calculated as

$$\begin{aligned} \Delta\nu_s &= \Delta\nu_r \frac{T'_1 - T'_2}{T'_1 T'_2} \frac{T_1 T_2}{T_1 - T_2} \\ &= \frac{T_1 T_2}{T_2 - T_1} \frac{k}{hc} \ln \frac{R(T_2, L_2)}{R(T_1, L_1)} 10^{\frac{\Delta\alpha_s (L_2 - L_1)}{5}} = \frac{T_1 T_3}{T_3 - T_1} \frac{k}{hc} \ln \frac{R(T_3, L_3)}{R(T_1, L_1)} 10^{\frac{\Delta\alpha_s (L_3 - L_1)}{5}} \end{aligned} \quad (12)$$

and

$$\Delta\alpha_s = \frac{5 \left(\ln \frac{R(T_1, L_1)}{R(T_3, L_3)} - \frac{T_1 - T_3}{T_3} \frac{T_2}{T_2 - T_1} \ln \frac{R(T_2, L_2)}{R(T_1, L_1)} \right)}{\ln(10) \left((L_3 - L_1) + \left(\frac{T_1 - T_3}{T_3} \right) \left(\frac{T_2}{T_2 - T_1} \right) (L_2 - L_1) \right)} \quad (13)$$

5. EXPERIMENT

We evaluated two cases based on the above study.

The temperature measurement was conducted on the installed and turned up in the oil well (Figure 3(a)). The initial values used in Equation (11) are $\Delta\nu_s = \Delta\nu_r = 386 \text{ cm}^{-1}$, $\Delta\alpha_s = 0.28 \text{ dB/km}$. Using Equations (10), (12) and (13) for three temperatures at three positions, $\Delta\nu_s = 379 \text{ cm}^{-1}$ and $\Delta\alpha_s = 0.18 \text{ dB/km}$ were found to be highly accurate. The temperature distribution agreed well with the actual temperature.

Figure 3(b) shows a calibration example using two positions and three temperatures. The initial values used in Equation (11) were $\Delta\nu_s = \Delta\nu_r = 392 \text{ cm}^{-1}$, $\Delta\alpha_s = 0.30 \text{ dB/km}$. $\Delta\nu_s = 394 \text{ cm}^{-1}$ and $\Delta\alpha_s = 0.21 \text{ dB/km}$ were calculated using Equations (10), (12) and (13) for three temperatures at two positions. Figure 3(b) indicates there is a good agreement in both the high and low temperature ranges after calibration.

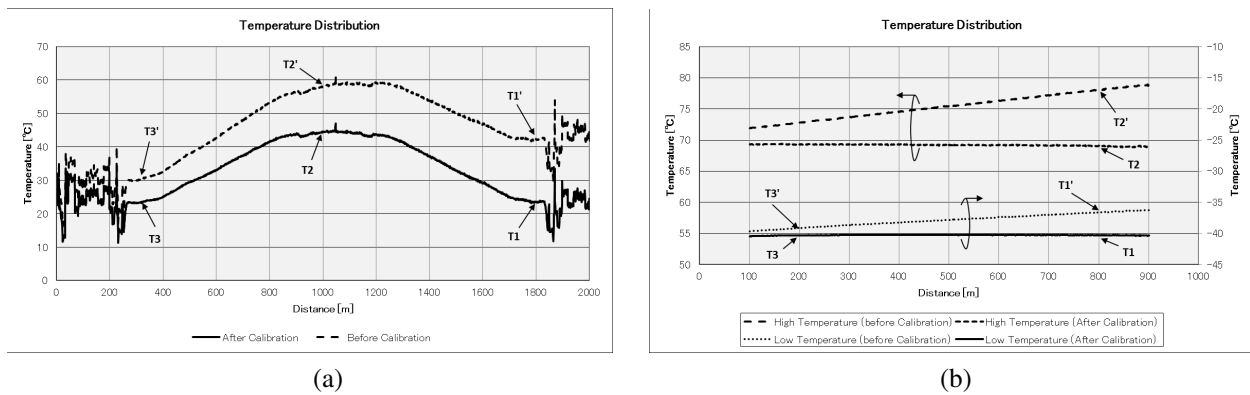


Figure 3: (a) For three positions and three temperatures and (b) two positions and three temperatures for calibration.

6. CONCLUSION

We proposed an improved calibration method that automatically simultaneously and simply calculates the calibration parameters such as the Raman shift wave number and the differential loss of the sensing fiber. The demonstrated results agreed well using the proposed method.

REFERENCES

1. Hartog, A. H., "Raman sensors and their applications," *Proc. 22nd International Conf. on Optical Fiber Sensors, SPIE*, 8421, 2012.
2. Fukuzawa, T., H. Shida, K. Oishi, N. Takeuchi, and S. Adachi, "Performance improvements of raman distributed temperature sensor," *Photonic Sensors*, Vol. 3, No. 4, 314–319, 2013.
3. Dakin, J. P., D. J. Pratt, G. W. Bibby, and J. N. Ross, "Distributed optical fiber raman temperature sensor using a semiconductor light source and detector," *Electron. Lett.*, Vol. 21, 569–570, 1985.

Structural Health Monitoring Based on Strain Distributions Measured by Fiber-optic Sensors

Hideaki Murayama¹, Daichi Wada¹, and Hirotaka Igawa²

¹School of Engineering, The University of Tokyo
7-3-1 Hongo, Bunkyo-ku, Tokyo 113-8656, Japan

²Japan Aerospace Exploration Agency
6-13-1 Ohsawa, Mitaka, Tokyo 181-0015, Japan

Abstract— We have developed a fiber-optic sensing technique that provides strain distributions along a sensing fiber with a high spatial resolution. Using long-length fiber Bragg gratings (FBGs), strain profile along FBGs is obtained based on optical frequency domain reflectometry. We demonstrate an experimental example of the technique and show its applicability for the purpose of structural health monitoring. We also demonstrate a simulation-based design process which has been developed in order to allow numerical discussion about the applicability and the capability of the sensing technique.

1. INTRODUCTION

The purpose of structural health monitoring (SHM) is to lead a structure such as aerospace, ship, and civil and mechanical engineering infrastructure, to be safer at the lower cost. SHM systems conduct assessment of structural integrity during manufacturing and/or in-service operation, which results in optimal operation, effective maintenance and longer service life [1].

Optical fiber distributed sensing techniques demonstrate the promising capability for the purpose of SHM [2]. By installing sensing fibers to target structures, one can obtain abundant structural parameters with high efficiency based on which the assessment of structural integrity is performed. In a previous study, the overall structural response is successfully monitored using Brillouin optical time domain reflectometry [3]. When it comes to the detection and identification of structural damages, however, it is concluded that high spatial resolution is required for the distributed sensing techniques in order to observe abrupt strain distribution variations induced by the damages.

We have developed a distributed sensing technique with high spatial resolution based on optical frequency domain reflectometry (OFDR) [4–6]. We use a long-length fiber Bragg grating (FBG) with a length of 10 cm and interrogate its spectra at an arbitrary location with a spatial interval of less than 1 mm. The sensing range can be expanded by sequentially inscribing the long-length FBGs with a minimum gap between each.

In order to measure the strain distribution which leads to identification of structural damages of interest, various factors have to be considered in advance of the sensor installation such as sensing locations, installation method (for example, bonding or embedding) and tuning parameters for signal processing. The expected strain distribution after damage might also need to be considered a priori so that one can discuss whether the capability of the sensing technique meets the demands for damage identification. In this paper, we introduce a simulation-based design process which models measurement environment and provides expected measurement results, as a result allows theoretical discussion of the sensing feasibility.

2. OFDR

Figure 1 shows the configuration of the OFDR system. The tunable laser source sweeps the wavenumber and inserts the lights into Interferometer 1 and 2. Interferometer 1 provides clock signal based on which the interfered signal of M3 and the FBG is sampled at D2 with a constant interval of wavenumber. We use low reflectivity FBGs in this work. In this case, the following approximate description of the signal at D2, D_2 , is sufficient expressed as

$$D_2 = \sum_i R_i(k) \cos(2n_{eff}L_i k), \quad (1)$$

where k is the wavenumber, n_{eff} is the effective refractive index of the fiber core, R_i represents the spectrum reflected at the location where the distance L_i is away from the mirror M3 [7]. A Bragg spectrum at a certain location, R_i , has an accompanying wave whose frequency is proportionate to

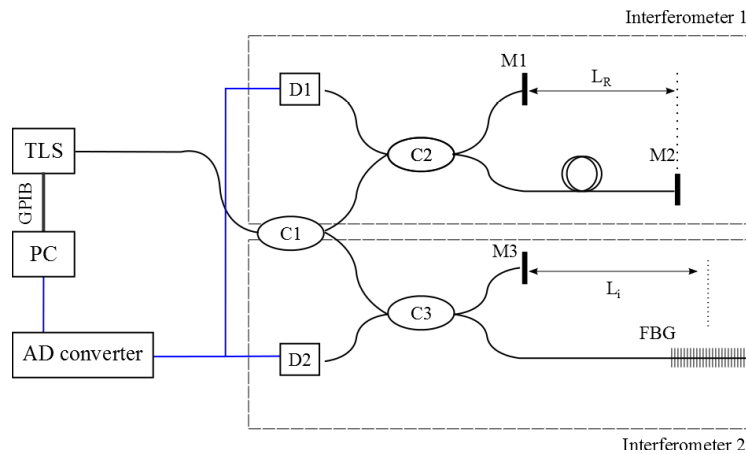


Figure 1: Configuration of OFDR. TLS: tunable laser source, D: photo detector, C: optical 3 dB coupler, M: optical mirror.

the location of the reflection. Therefore, we can demodulate Bragg spectra at arbitrary locations by applying short time Fourier transform (STFT) to D_2 .

3. SIMULATION-BASED DESIGN PROCESS

In structural monitoring process, there are various steps which connect the structural parameters of interest (for example, deformation) and the output of the sensing system as depicted in Fig. 2. Deformation yields strains in sensing elements, an FBG in this case. The strains affect the optical response of the FBG. The FBG signal is interfered and detected at a photo detector. Finally, the interfered signal is demodulated into the form of strain through signal processing. A series of numerical simulation model concatenates these steps in the simulation-based design process as seen in Fig. 2.

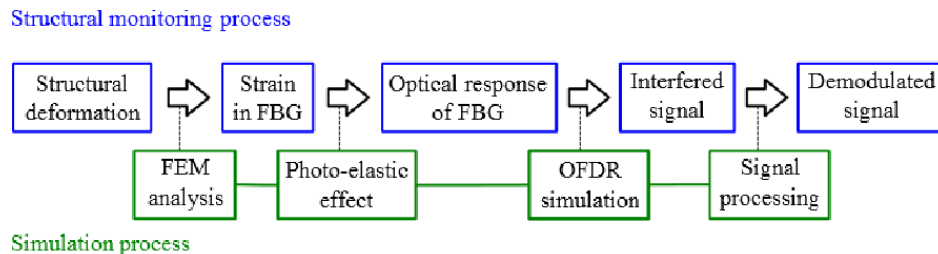


Figure 2: Flow of the structural monitoring process and the simulation-based design process.

We take an example of a tensile loading of an aluminum coupon with holes. The geometry of the coupon is depicted in Fig. 3. The coupon is loaded in longitudinal direction. 7 cm FBG is bonded, and the 5 cm portion of the FBG is in interest.

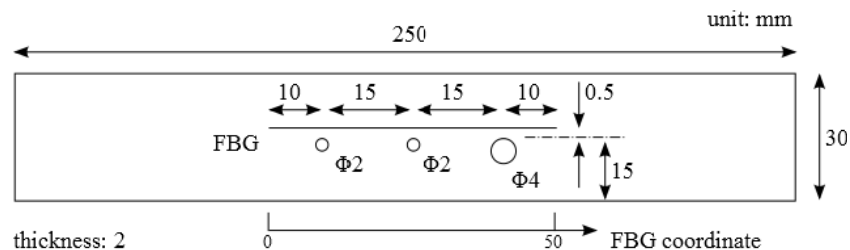


Figure 3: Schematic of the aluminum coupon with three holes.

Firstly, we conduct finite element method (FEM) analysis to calculate strains/stresses which are applied to the FBG as depicted in Fig. 4. Then, we calculate the optical response of the FBG

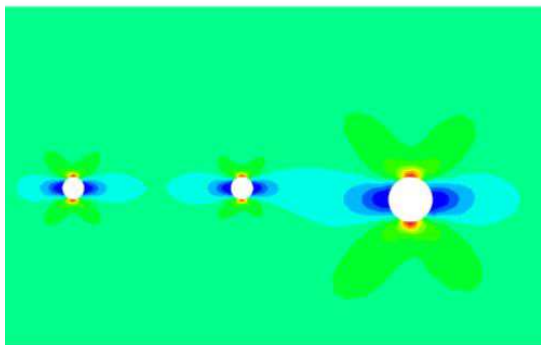


Figure 4: Longitudinal strain distribution around the holes calculated by FEM.

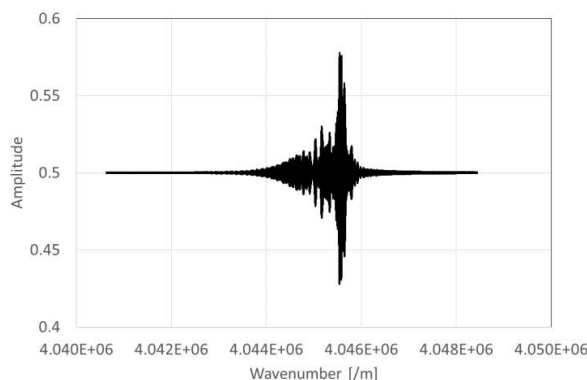


Figure 5: Calculated interfered signal of the loaded coupon with the holes using numerical simulation model of the OFDR system.

based on the equation of the photo-elastic effect which is expressed as

$$\begin{cases} \Delta\lambda_{Bx} = -\frac{n_{eff}^3 \Lambda}{E} \{ (P_{11} - 2\nu P_{12}) \sigma_x + [(1 - \nu) P_{12} - \nu P_{11}] (\sigma_y + \sigma_z) \} + \frac{2n_{eff} \Lambda}{E} [\sigma_z - \nu (\sigma_x + \sigma_y)] \\ \Delta\lambda_{By} = -\frac{n_{eff}^3 \Lambda}{E} \{ (P_{11} - 2\nu P_{12}) \sigma_y + [(1 - \nu) P_{12} - \nu P_{11}] (\sigma_x + \sigma_z) \} + \frac{2n_{eff} \Lambda}{E} [\sigma_z - \nu (\sigma_x + \sigma_y)] \end{cases}, \quad (2)$$

where $\Delta\lambda_B$ expresses the Bragg wavelength shift, L the grating pitch, E Young's modulus and ν the Poisson's ratio of the optical fiber, P the Pockels coefficient and σ the stress. x and y represents the orthogonal axes in the fiber cross-section plane and z represents the longitudinal axis.

The interfered signal at the photo detector in the OFDR system is calculated using the optical response of the FBG obtained previously and the numerical simulation model of the OFDR as shown in Fig. 5 [8, 9]. Finally, STFT is applied to the interfered signal and demodulated signal is obtained in the form of spectrogram as seen in Fig. 6. By extracting the distribution of the Bragg wavelength shifts, one can calculate strain distributions. Fig. 7 shows the strain distributions obtained from the simulation process and an experiment, and the strain distribution calculated by FEM. Longitudinal load of 300 kgf is applied. It can be seen that the simulation process successfully predicts the measurement results.

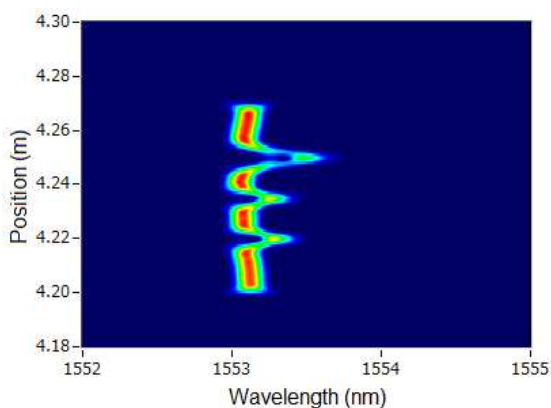


Figure 6: Calculated spectrogram. 7 cm FBG is located at from 4.20 m to 4.27 m.

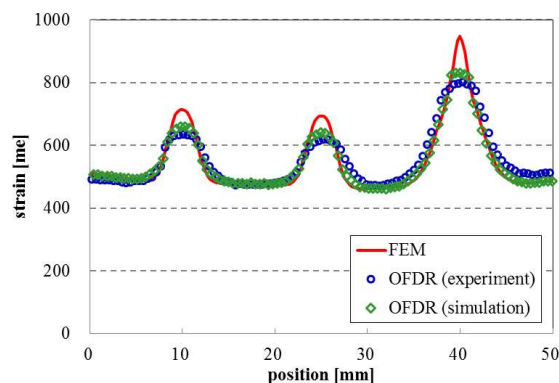


Figure 7: Strain distribution of the coupon with three holes.

4. CONCLUSION

This paper showed that the simulation-based design process successfully predicted the measurement results. Individual simulation steps can calibrate effects of individual steps of structural monitoring process on the output of the OFDR measurement. Therefore, this process can contribute to various discussions regarding SHM such as the optimal sensor location, installation method, tuning parameters for signal processing, noise effect and interpretation of unpredicted signals.

REFERENCES

1. Balageas, D., C. P. Fritzen, and A. Gumes, *Structural Health Monitoring*, 15–18, ISTE, London, UK, 2006.
2. Bao, X. and L. Chen, “Recent progress in distributed fiber optic sensors,” *Sensors*, Vol. 12, 8601–8639, 2012.
3. Murayama, H., K. Kageyama, H. Naruse, A. Shimada, and K. Uzawa, “Application of fiber-optic distributed sensors to health monitoring for full-scale composite structures,” *J. Intell. Mater. Syst. Struct.*, Vol. 14, 3–13, 2001.
4. Igawa, H., K. Ohta, T. Kasai, I. Yamaguchi, H. Murayama, and K. Kageyama, “Distributed measurements with a long gauge FBG sensor using optical frequency domain reflectometry (1st report, system investigation using optical simulation model),” *J. Solid Mech. Mater. Eng.*, Vol. 2, 1–11, 2008.
5. Igawa, H., H. Murayama, T. Nakamura, I. Yamaguchi, K. Kageyama, K. Uzawa, D. Wada, I. Ohsawa, M. Kanai, and K. Omichi, “Measurement of distributed strain and load identification using 1500 mm gauge length FBG and optical frequency domain reflectometry,” *Proc. of SPIE*, Vol. 7503, 750351, 2009.
6. Murayama, H., D. Wada, and H. Igawa, “Structural health monitoring by using fiber-optic distributed strain sensors with high spatial resolution,” *Photonic Sensors*, Vol. 3, 355–376, 2013.
7. Childers, B. A., M. E. Froggatt, S. G. Allison, T. C. Sr. Moore, D. A. Hare, C. F. Batten, and D. C. Jegley, “Use of 3000 Bragg grating strain sensors distributed on four eight-meter optical fibers during static load tests of a composite structure,” *Proc. of SPIE*, Vol. 4332, 133–142, 2001.
8. Murayama, H., K. Kageyama, K. Uzawa, K. Ohara, and H. Igawa, “Strain monitoring of a single lap joint with embedded fiber-optic distributed sensors,” *Struct. Health Monit.*, Vol. 11, 325–344, 2012.
9. Wada, D. and H. Murayama, “Analytical investigation of response of birefringent fiber Bragg grating sensors in distributed monitoring system based on optical frequency domain reflectometry,” *Optics and Lasers in Engineering*, Vol. 52, 99–105, 2014.

Distributed Measurement of Intense Magnetic Fields by Means of Optical Fibers

L. Palmieri¹ and A. Galtarossa^{1,2}

¹Department of Information Engineering, University of Padova, Padova, Italy

²IIUSE, Southeast University, Nanjing, China

Abstract— A novel class of distributed fiber optic sensors for the measurement of intense magnetic fields has been recently introduced. The sensors are based on Faraday rotation of polarization and on the distributed polarization measurement of the Rayleigh backscattered light. This paper reviews the current results showing how the technique can be used to map both intensity and direction of strong magnetic field in the area spanned by the optical fiber, with spatial resolution in the order of centimeters.

1. INTRODUCTION

Optical fiber sensors (OFS) are finding wide and successful applications in the monitoring of several structures as diverse as civil buildings, natural sites, energy plants and mechanical components [1]. OFSs offer two main advantages over electro-mechanical sensors; namely, they enable distributed, or quasi-distributed, monitoring and they are intrinsically immune to electromagnetic interference. In particular, the possibility of implementing distributed sensors is an unique feature of OFSs, unparalleled by any other technology, and already successfully exploited in the monitoring of temperature, strain and vibration [1].

The measurement of magnetic fields, based on Faraday rotation of polarization, has been one of the earliest application of OFS [2, 3]. Nonetheless, all magnetic-field OFS developed so far are point sensors, being able to measure the magnetic field only at a specific location. Recently, however, a new distributed optical fiber sensors (DOFS) able to measure the spatial variation of magnetic field along the fiber has been introduced [4–7]. This novel sensor is based on the measurement of the state of polarization (SOP) of the light backscattered by the fiber, as a function of the scattering position, and on the variation of such SOP as a consequence of Faraday rotation. For the sake of completeness, we remark that an early attempt to perform a similar distributed measurement was made by Ross in 1981 [8]. In that case, however, the system was able only to locate the point along the fiber where the magnetic field was varying. More recently, other approaches have been proposed, but the retrieved information about Faraday rotation is not complete [9, 10]. Differently, in the new technique described here the variation of the magnetic field over the whole length of the fiber is completely determined. Tests have been performed using standard telecom fibers, over lengths ranging from few tens of meters to about hundred meters. The reported limit of detection is 100 mT, with a spatial resolution of few centimeters. The measurement uncertainty is about 7%. This paper reviews the main results achieved so far.

2. MEASUREMENT PRINCIPLE

In a non-ideal single-mode optical fiber the polarization of light is not preserved during propagation, but it is changed by almost any kind of perturbation acting along the fiber [11]. Therefore, if we were able to measure that polarization along the fiber, we could retrieve information about those perturbations, and hence about the environment surrounding the fiber. Of course, a direct measurement of the light propagating in the fiber is not practicable, especially over lengths of several tens of meters and beyond. Nonetheless, we can measure the polarization of the Rayleigh backscattered light, and try to infer local information along the fiber. This is the basic idea behind polarization distributed measurements as originally proposed by Rogers [12].

This principle can be used also to measure the magnetic field acting along the fiber through Faraday rotation; there are however two main difficulties. Actually, the backscattered SOP does not directly provide information on the local Faraday rotation, but rather it is the accumulated effect of forward propagation up to a specific point in the fiber, Rayleigh scattering and subsequent back-propagation to the fiber input. Furthermore, the SOP in an optical fiber is not affected only by magnetic field, but also by other perturbations like bending, twist, anisotropy, geometrical asymmetries, etc., which are well known to impair the effectiveness of standard magnetic field

OFS [3]. Therefore, the variation of the backscattered SOP as a function of the scattering position is quite a complex cumulative vectorial function of all perturbations acting along the fiber, where the local information about Faraday rotation is not directly accessible. This difficulty has been however recently overcome by means of an accurate theoretical model, which has enabled the solution of the inverse scattering problem [4].

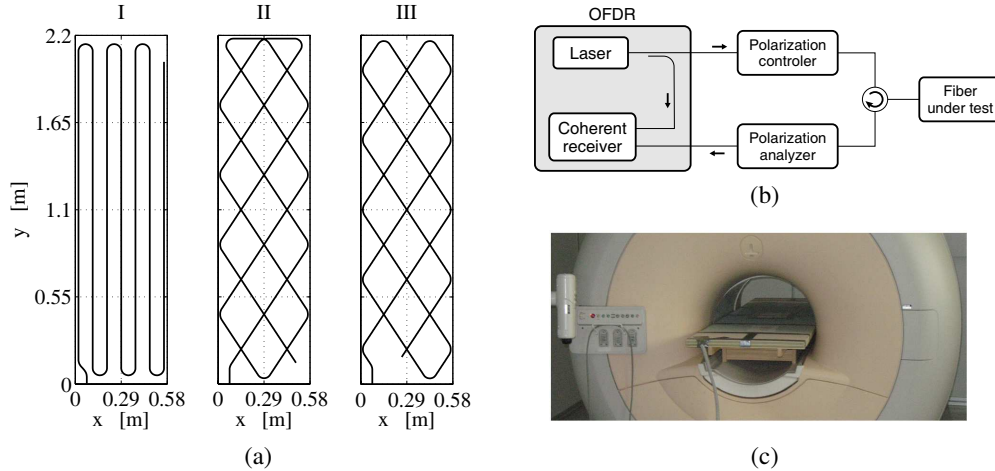


Figure 1: (a) Paths of the three fibers in sensor A. (b) Schematic of the POFDR setup. (c) Picture of sensor arrangement.

A detailed mathematical description of the measurement procedure would be out of scope, therefore here we report only the main steps of the analysis needed to retrieve the local information; the interested reader may find the complete treatment in the literature [4]. The first step is to measure the 3-dimensional unit Stokes vector, $\mathbf{s}_B(z)$, of the backscattered light as a function of the scattering position, z , for at least 2 different input SOPs. This task can be accomplished by using any polarization sensitive reflectometer, either in the time domain (POTDR), or in the frequency domain (POFDR) [13]. Once the SOPs have been measured, we have to calculate the vector $\boldsymbol{\beta}_B(z)$ such that $d\mathbf{s}_B/dz = \boldsymbol{\beta}_B \times \mathbf{s}_B$. This operation can be solved with the so called Mueller matrix method developed in the framework of polarization mode dispersion measurements [14]. Afterwards, the vector $\boldsymbol{\beta}_B(z)$ is used to numerically solve the differential equation $d\mathbf{B}/dz = (\boldsymbol{\beta}_B/2) \times \mathbf{B}$ with $\mathbf{B}(0) = \mathbf{I}$, where it can be shown that $\mathbf{B}(z)$ is the 3×3 Mueller matrix representing (in a proper reference frame) the backward propagation from the scattering point to the fiber input [4]. Finally, we calculate the vector

$$\boldsymbol{\beta}(z) = (\beta_1(z), \beta_2(z), \eta(z))^T = \frac{1}{2} \mathbf{B}^T(z) \boldsymbol{\beta}_B(z), \quad (1)$$

where T means transposition, and the first two components, β_1 and β_2 , summarize the local effects of all perturbations except Faraday rotation, which affects only the third component $\eta(z)$. This net separation enables the distributed measurement of magnetic field along the fiber, and it is due to the non-reciprocal nature of Faraday rotation, which makes it intimately different from all other sources of perturbation [15]. More specifically, the third component of $\boldsymbol{\beta}(z)$ can be expressed as

$$\eta(z) = 2V B(z) \cos \psi(z), \quad (2)$$

where $B(z)$ is the amplitude of the magnetic induction, $\psi(z)$ is the angle subtended by the magnetic induction and the direction of forward propagation of light, and V is the Verdet constant, which for silica fibers is about $1.43/\lambda_{\mu\text{m}}^2$ (rad/T)/m, so at 1550 nm we have $V \simeq 0.60$ (rad/T)/m [16].

Exploiting the above method and the relationship (2) it is then possible to measure the component of the magnetic field parallel to the fiber axis as a function of the position along the fiber. As shown below, exploiting a proper fiber layout it is also possible to measure more than 1 spatial component of the magnetic field, enabling the making 2- or 3-dimensional vectorial maps. Note, however, that owing to the small value of the Verdet constant and to the distributed nature of the sensor, the proposed sensor is most suited to high intensity fields.

3. 2D VECTORIAL MAPPING OF MAGNETIC FIELD

A first example of application is a sensor, hereinafter “sensor A”, to make 2-dimensional vectorial maps of the magnetic field in the area spanned by the fiber. The idea is to deploy the fiber on a mesh so that at each crossing the magnetic field is measured along two directions, enabling the 2-dimensional vectorial mapping [5]. Specifically, 3 standard G.652 fibers have been deployed on wooden boards along the paths shown in Fig. 1(a); the boards were then stacked to form the sought fiber mesh. We used three separate fibers because the range of the measurement setup is limited to 30 m.

The polarization of the backscattered light, $\mathbf{s}_B(z)$, has been measured with a polarization sensitive OFDR, schematically represented in Fig. 1(b). The polarization controller in the forward path allows to change in the input SOP, whereas the polarization analyzer in the backward path allows to calculate $\mathbf{s}_B(z)$. Measurements were performed in a bandwidth of about 40 nm around 1550 nm. Note that while this bandwidth can nominally enable a sub-millimeter spatial resolution, when it comes to SOP measurements further SNR enhancement is required, which is achieved by proper spatial filtering. As a result, the spatial resolution is increased to about 2 cm. Owing to the small value of the Verdet constant in silica, the sensor has been tested exploiting the high magnetic field of a magnetic resonance imaging (MRI) scanner for medical application, which achieved 1.5 T in the imaging area (see Fig. 1(c)).

Figure 2(a) shows the three components of the vector $\beta(z)$ defined in (1) and measured along the fiber of path I (see Fig. 1(a)). The difference between the first two components and the third one is evident. While $\beta_1(z)$ and $\beta_2(z)$ are related to the reciprocal effects, such as anisotropy, bending, twist, etc., and hence vary randomly as a function of z , the third component $\eta(z)$ is affected only to Faraday rotation, and therefore it has markedly ordered behavior. Specifically, up to about 7 m in the fiber η is almost zero, meaning that the Faraday rotation is negligible as it should be, since this is the portion of the fiber that lays outside the MRI and links the sensor to the POFDR. Beyond that distance, the fiber enters the MRI and the effects of the magnetic field become clear. The periodic changes in sign of $\eta(z)$ are actually related to the periodic changes in direction of the fiber with respect to the magnetic field, which make the factor $\cos\psi(z)$ in (2) change its sign accordingly. The value of the magnetic field component along the fiber axis can then be readily calculated exploiting (2), and the results for each of the three fibers are in good agreement with the nominal peak value of 1.5 T. By merging the measurements taken on each fiber separately it is then possible to build the 2-dimensional vector map shown in Fig. 2(b). Each arrow indicates modulus and direction of the magnetic field component parallel to the sensor plane, evaluated at each of the more than 100 crossing points of the fiber mesh.

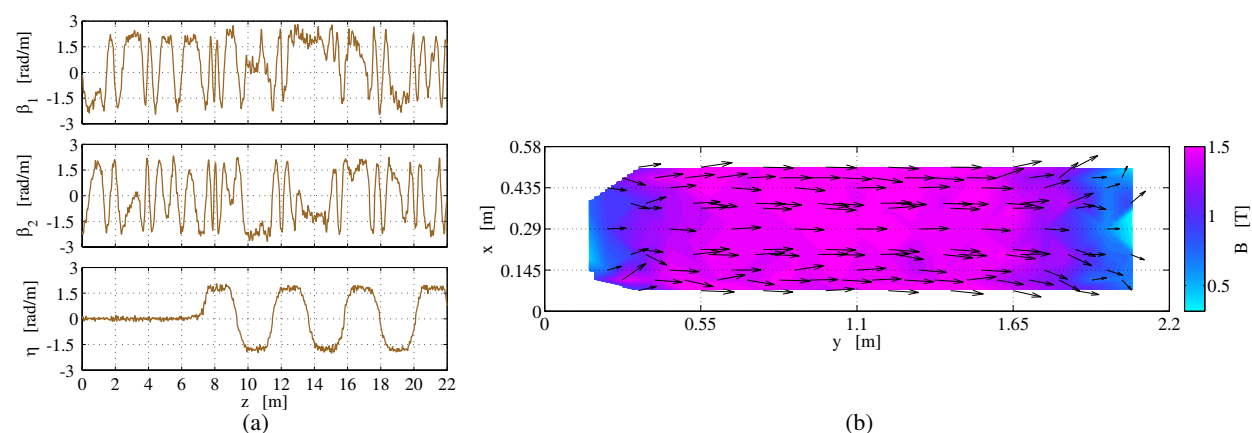


Figure 2: (a) Components of $\beta(z)$ measured along fiber path I of sensor A. (b) 2D vectorial map of magnetic field in the MRI scanner.

Along the board axis, at $x = 0.29$ m, the fibers create nine crossing where the magnetic field can be measured along three different directions. These points offer the opportunity to estimate the uncertainty of the magnetic field measure, which is about 7%. Furthermore, the limit of detection of the sensor is around 100 mT, as evaluated from the fiber sections not exposed to the magnetic field. We remark, however, that these measurements have been performed by using standard G.652 telecommunication fibers.

4. 3D VECTORIAL MEASUREMENT OF MAGNETIC FIELD

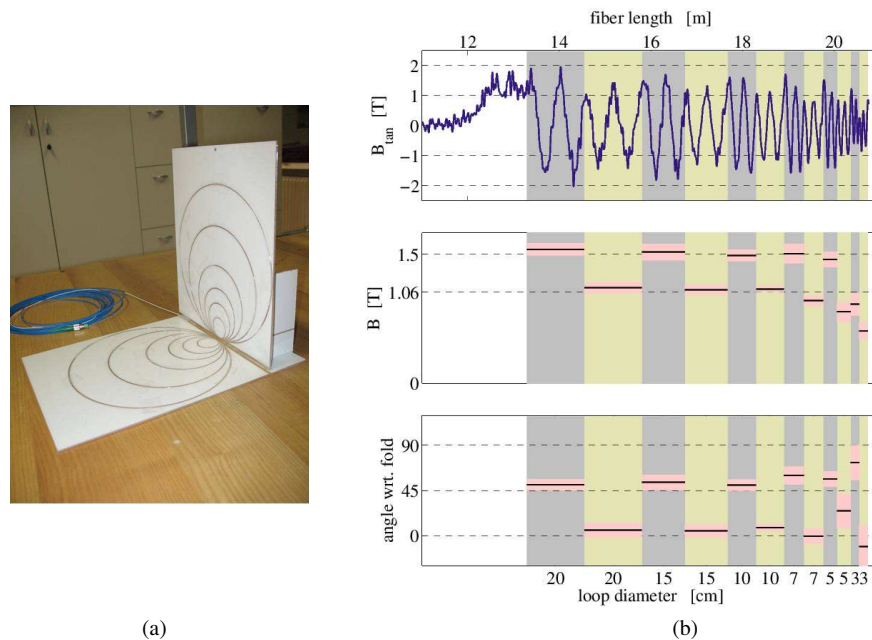


Figure 3: (a) Layout of the 3D magnetic field sensor B. (b) Measurements taken on the sensor when oriented at 45° with respect to the magnetic field.

The principle exposed in the previous section can be generalized to perform 3-dimensional vectorial measurements, provided that the fiber is arranged so to span the 3 dimensions. As a proof of concept, we have implemented the sensor “B” shown in Fig. 3(a), where the basic idea is to have the fiber wound on loops on two orthogonal plates [7]. We assume that the magnetic field is constant in the volume of the sensor; this sets the spatial resolution of the sensor. We also use the “fold axis”, i.e., the axis along which the loop plates are in contact, as a reference. All loops are, by construction, tangent to the fold axis.

Let consider first the effect of a single loop. Since the magnetic field is constant, the angle $\psi(z)$ in (2) varies sinusoidally along the fiber of the loop. Therefore, we can express the Faraday rotation along the fiber loop as

$$\eta(z) = 2VB_{\text{plane}} \cos(2\pi z/L_{\text{loop}} + \phi_0), \quad (3)$$

where B_{plane} is the intensity of the magnetic induction component projected on to the loop plane and L_{loop} is the loop length. If we set $z = 0$ at the point where the loop is tangent to the fold axis, we can say that ϕ_0 is the angle subtended by the magnetic field projection on the loop plane and the fold axis. So if these two are, for example, anti-parallel, then $\phi_0 = \pi$.

According to the above model, by performing a Fourier analysis of the measured Faraday rotation $\eta(z)$ and considering only the signal at the known spatial frequency given by the loop length, we can extract the intensity B_{plane} of the magnetic induction projection on the loop plane and its orientation ϕ_0 with respect to the fold axis. Finally, repeating the measurement on an orthogonal plane we have a complete 3-dimensional measurement of the magnetic induction.

The sensor we implemented had several circular paths with diameters of 3, 5, 7, 10, 15 and 20 cm. This was done to determine the best achievable spatial resolution and, at the same time, to prove that many of these sensors can be concatenated. Each path hosts two loops of fiber; the fiber enters the sensor along the fold axis, and goes twice along each loop, starting from the larger ones, and alternating horizontal and vertical planes. The results of the measurement performed in the same MRI scanner of Fig. 1(c) are shown in Fig. 3(b). The sensor was oriented in such a way that the magnetic induction was parallel to the horizontal plane, and at 45° with respect to the vertical one and to the fold axis. The top graph shows $\eta(z)/(2V)$, which is the intensity of the magnetic induction component tangent to the fiber at each point z . Gray (yellow) background refers to fiber sections on the horizontal (vertical) planes. We clearly see the oscillation described by (3), and a closer look reveals also the change of amplitude and phase between vertical and horizontal planes. Despite the raw data is noisy, the Fourier analysis extracts B_{plane} and ϕ_0 quite accurately.

These are shown in the middle and lower graphs, respectively, where the solid black line indicate the calculated values and the pink band their uncertainties. While at lower loop diameters the measurement is not accurate due to the limited spatial resolution of the POFDR, for diameters of 10 cm or above results are in good agreement with the nominal ones, marked by the dashed lines.

5. CONCLUSION

In this paper we have reviewed the recent achievements on distributed measurements of intense magnetic fields. This new class of distributed sensors is based on polarization reflectometry and on a novel data analysis algorithm, that allows to single Faraday rotation out of the random variations of the backscattered polarization. Two different sensors have been described. The first one enables the 2-dimensional vectorial mapping of the magnetic field with a spatial resolution in the order of few centimeters; as an example, the field of an MRI scanner for medical applications has been successfully mapped. The second sensors enables the 3-dimensional vectorial measurement of magnetic field at specific position, with resolution in the order of 10 cm. Owing to its distributed nature, this sensor can be easily concatenated to have a multi-point sensor. Despite limited to strong magnetic field due to the small Verdet constant of silica fibers, this new class of distributed magnetic field optical fiber sensors paves the way to unprecedented applications, such as distributed current measurements.

REFERENCES

1. Grattam, K. T. V. and B. T. Maggitt, *Optical Fiber Sensor Technology*, Kluwer Academic Publishers, Dordrecht, 2000.
2. Rashleigh, S. C., "Magnetic-field sensing with a single-mode fiber," *Opt. Lett.*, Vol. 6, No. 1, 19–21, 1981.
3. Annovazzi-Lodi, V., S. Donati, and S. Merlo, "Coiled-fiber sensor for vectorial measurement of magnetic field," *J. Lightw. Technol.*, Vol. 10, No. 12, 2006–2010, 1992.
4. Palmieri, L. and A. Galtarossa, "Distributed polarization-sensitive reflectometry in nonreciprocal single-mode optical fibers," *J. Lightwave Technol.*, Vol. 29, No. 21, 3178–3184, 2011.
5. Palmieri, L. and A. Galtarossa, "Distributed fiber optic sensor for mapping of intense magnetic fields based on polarization sensitive reflectometry," *Proc. SPIE*, Vol. 8351, 2012.
6. Palmieri, L., "Distributed polarimetric measurements for optical fiber sensing," *Optical Fiber Technology*, Vol. 19, No. 6, Part B, 720–728, 2013.
7. Palmieri, L., E. Autizi, and A. Galtarossa, "A novel quasi-distributed fiber optic sensor for 3D vector measurement of static magnetic fields," *Proc. SPIE*, Vol. 8794, 2013.
8. Ross, J. N., "Measurement of magnetic field by polarisation optical time-domain reflectometry," *Electron. Lett.*, Vol. 17, No. 17, 596–597, 1981.
9. Wuilpart, M., C. Caucheteur, A. Goussarov, M. Aerssens, V. Massaut, and P. Mégret, "Measurement of magnetic field using Rayleigh backscattering in optical fibres," *ANIMMA 2011*, 1–6, 2011.
10. Aerssens, M., A. Gusarov, P. Moreau, P. Malard, V. Massaut, P. Mégret, and M. Wuilpart, "Development of a Jones vector based model for the measurement of a plasma current in a thermonuclear fusion reactor with a POTDR setup," *Proc. SPIE*, Vol. 8439, 2012.
11. Rashleigh, S., "Origins and control of polarization effects in single-mode fibers," *Journal of Lightwave Technology*, Vol. 1, 312–331, 1983.
12. Rogers, A. J., "Polarization-optical time domain reflectometry: A technique for the measurement of field distributions," *Appl. Opt.*, Vol. 20, 1060–1074, 1981.
13. Palmieri, L. and L. Schenato, "Distributed optical fiber sensing based on Rayleigh scattering," *The Open Optics Journal*, Vol. 7, Special Issue 1, 104–127, 2013.
14. Jopson, R., L. Nelson, and H. Kogelnik, "Measurement of second-order polarization-mode dispersion vectors in optical fibers," *IEEE Photon. Technol. Lett.*, Vol. 11, No. 9, 1153–1155, 1999.
15. Someda, C. G., *Electromagnetic Waves*, CRC/Taylor & Francis, Boca Raton, FL, 2006.
16. Noda, J., T. Hosaka, Y. Sasaki, and R. Ulrich, "Dispersion of verdet constant in stress-birefringent silica fibre," *Electron. Lett.*, Vol. 20, No. 22, 906–908, 1984.

Supercontinuum Generation at 1.55 μm in a Silicon Nanowire Embedded Photonic Crystal Fiber

E. Gunasundari¹, Abdosllam M. Abobaker², K. Senthilnathan¹,
S. Sivabalan³, K. Nakkeeran⁴, and P. Ramesh Babu¹

¹Photonics, Nuclear and Medical Physics Division, School of Advanced Sciences
VIT University, Vellore 632 014, India

²Department of Communications Engineering, College of Electronic Technology, Bani Walid, Libya

³School of Electrical Engineering, VIT University, Vellore 632 014, India

⁴School of Engineering, University of Aberdeen, Aberdeen AB24 3UE, UK

Abstract— In this paper, we design an elliptical silicon nanowire embedded photonic crystal fiber (SN-PCF) using fully vectorial finite element method. Further, we analyze the various optical properties, namely, waveguide dispersion, birefringence, fractional power inside the core and effective nonlinearity by varying the ellipticity for a wide range of wavelengths from 0.8 to 1.8 μm . The proposed structure exhibits a high birefringence of 0.4815 for a small ellipticity of 0.3 at a longer wavelength of 1.8 μm . Besides, we investigate the evolution of supercontinuum at 1.55 μm wavelength for an input pulse width of 25 fs by varying the peak power of the input pulse as well as length of the SN-PCF. The numerical results corroborate that the proposed SN-PCF provides a wider supercontinuum bandwidth for a high input power within a few mm length (2 mm) of fiber. The findings of this work may be useful in ultrahigh-resolution optical coherence tomography and optical communication systems.

1. INTRODUCTION

The supercontinuum generation in photonic crystal fibers (PCFs) has been a topic of intense research ever since it was reported by Ranka et al. [1]. To generate the supercontinuum (SC), the medium should at least exhibit a flat low anomalous dispersion with a small third order dispersion or zero dispersion [2]. It is obvious that the PCFs operating near a zero dispersion wavelength (ZDW) with higher nonlinearity do not demand large input power for generating the SC. In addition, these desired conditions help smoothen the power spectra of SC [3]. Therefore, highly nonlinear dispersion flattened PCF turns out to be the right candidate for generating SC. Nowadays, the generation of SC in photonic nanowire (PN) have been attracted significant interest with their sub-wavelength diameter due to their unique properties. Such a dielectric waveguides with a nanocore diameter can achieve a tight mode confinement and a strong normal and anomalous waveguide dispersions are combined to allow high nonlinear interactions with the aid of an efficiently designed photonic crystal fiber geometry. Such a photonic device known as photonic crystal fiber nanowire (PCF-NW) has been proposed very recently [4, 5]. These small core PCF structures can be a good candidate for nonlinear applications such as soliton — effect pulse compression and SC generation using very low input power within a short length of fiber [6–9].

In this work, we design a silicon nanowire embedded PCF (SN-PCF) consisting of an elliptical core with equivalent nanowire diameter and a triangular arrangement of air-holes in the cladding and investigate the SC by varying the input peak power and length of the proposed fiber. The paper is laid out as follows. In Section 2, we present the design analysis of the proposed structure. In Section 3, we study the optical properties of the fundamental mode, namely, the group velocity dispersion (GVD), third order dispersion (TOD), birefringence and effective nonlinearity by varying the ellipticity of SN-PCF. Further, we investigate the nonlinear pulse propagation in the anomalous dispersion regime and analyze the evolution of SC at 1.55 μm wavelength with various input powers and various length of SN-PCFs in Section 4. Finally, we summarize the findings in Section 5.

2. DESIGN OF THE PROPOSED SN-PCF

The schematic cross section and mode field distribution of the proposed SN-PCF are as shown in Figs. 1(a) and (b). In the proposed structure, a and b are chosen to be the major and the minor diameters of the elliptical nanocore and the air-hole distribution in the cladding region is composed of 5 rings. In this design, we choose the ellipticity (b/a) value in terms of core diameter (d_c) which is less than 1 μm [10]. The distance between two consecutive air holes (pitch, Λ) is kept at 2 μm and diameter of the air hole (d_h) is 0.7 μm . In this work, we study the optical properties of the

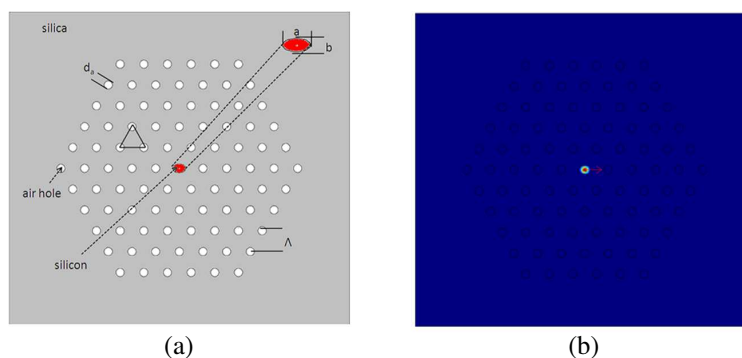


Figure 1: (a) Geometrical structure and (b) mode field distribution of the proposed SN-PCF with an ellipticity of 0.7.

fundamental mode by increasing the ellipticity values for a range of optical wavelengths from 0.8 to 1.8 μm by keeping a constant value of major core diameter ($a = 550 \text{ nm}$).

3. WAVEGUIDE DISPERSION

The dispersion is a well known linear effect that depends on the operating wavelength and the nanocore diameter. The diameter dependent GVD and TOD of the x -polarized mode are determined from the effective index of the fundamental mode obtained by finite element method. Fig. 2(a) shows that there is an anomalous GVD for all ellipticity values due to the gradual increase of the field distribution towards the cladding region. When increasing the wavelength, the GVD value increases on the negative side as a result of less confinement within the core and the same trend is observed for all ellipticity values. We achieve a less anomalous GVD of $-0.133 \text{ ps}^2/\text{m}$ for an ellipticity of 0.7 at 0.8 μm wavelength. The variations of TOD with different ellipticity values are shown in Fig. 2(b). Further, we find an almost flattened TOD for all ellipticities up to 1.05 μm wavelength. After increasing the wavelength, we notice that the TOD increases slowly. The proposed fiber exhibits a less TOD ($0.1572 \times 10^{-3} \text{ ps}^3/\text{m}$) for $b/a = 0.7$ at 0.8 μm wavelength. We achieve a very high birefringence (0.4017) for a smaller ellipticity ($b/a = 0.3$) and lower birefringence (0.0519) for a larger ellipticity ($b/a = 0.7$) at 1.55 μm wavelength as shown in Fig. 3(a). In addition, we notice that the power distribution inside the core decreases rapidly by increasing the ellipticity from 0.3 to 0.7 as is seen in Fig. 3(b). The confinement factor is very high at shorter wavelength (0.8 μm) owing to the tight field confinement within the core. However, at longer wavelength (1.8 μm), the fractional power inside the core is relatively less for a smaller ellipticity of 0.3 due to the large amount of power spreading outside the elliptical nanocore.

4. EFFECTIVE NONLINEARITY

Due to the small core diameter dimensions and the high-index contrast between core and cladding, the air-silicon nanowire exhibits tight mode confinement. Generally, for sub-wavelength nanowire structure, the γ^V value is computed using vectorially-based nonlinear Schrödinger equation (VNSE)

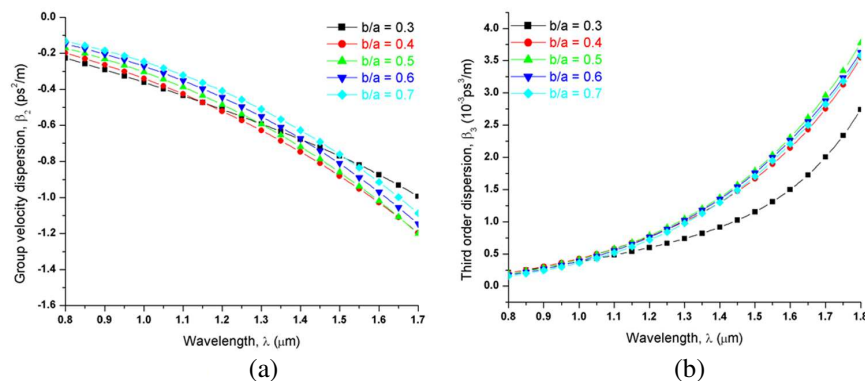


Figure 2: (a) Group velocity dispersion and (b) third order dispersion of the proposed SN-PCF for various ellipticity.

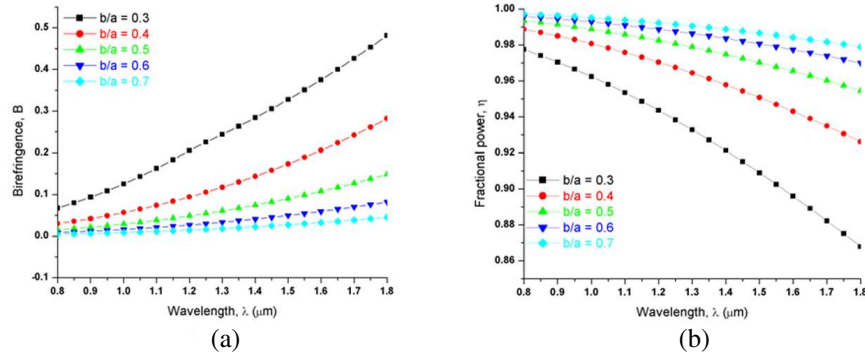


Figure 3: Variations of (a) birefringence and (b) fractional power of the proposed SN-PCF for various ellipticity.

[11],

$$\gamma^V = k_0 \left(\frac{\epsilon_0}{\mu_0} \right) \frac{\int n_0^2(x, y) n_2(x, y) |e_m|^4 dA}{\left| \int (e_m \times h_m^*) \cdot \hat{z} dA \right|^2}, \quad (1)$$

where k_0 , ϵ_0 , μ_0 and n_0 are the free space wavenumber, free-space dielectric constant, free space permeability and refractive index of silicon, respectively. Here n_2 is the nonlinear index coefficient ($4.5 \times 10^{-18} \text{ m}^2/\text{W}$) of silicon whose value is two orders greater than that of silica. The nonlinearity variation of the fundamental mode for different ellipticity values as a function of wavelength is shown in Fig. 4. The small core ellipticity (0.3) exhibits tight mode confinement and very high nonlinearity ($991 \text{ W}^{-1}\text{m}^{-1}$) at $0.8 \mu\text{m}$ wavelength when compared to other ellipticity values of SN-PCF.

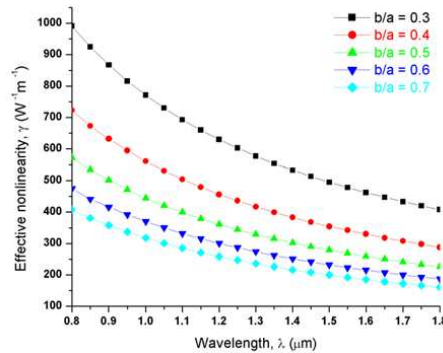


Figure 4: Variation of effective nonlinearity of the SN-PCF for different ellipticity.

5. SIMULATION OF SUPERCONTINUUM GENERATION

The SC generation in the SN-PCF is demonstrated by the generalized nonlinear Schrödinger equation (NLS) with the effects of two-photon absorption and free-carrier absorption as follows [12],

$$\frac{\partial A}{\partial z} = -\frac{1}{2} (\alpha + \alpha^f) A - \frac{i}{2} \beta_2 \frac{\partial^2 A}{\partial T^2} + \frac{\beta_3}{6} \frac{\partial^3 A}{\partial T^3} + i\gamma^V \left[1 + \frac{\omega}{\omega_0} \right] A \int_{-\infty}^{\infty} [R(T - \tau) |A|^2] d\tau \quad (2)$$

where, $A(z, T)$, α , α^f , β_2 , β_3 , γ^V and $R(T - \tau)$ represent the field envelope, linear loss, free-carrier contribution term, GVD, TOD, effective nonlinearity and Raman response function. In this simulation, we ignore the effect of free carrier absorption, two photon absorption and loss. The nonlinear response function $R(t)$ is defined by [12], $R(t) = (1 - f_R)\delta(t) + f_R h_R(t)$ with $f_R = 0.043$. The delayed Raman response $h_R(t)$ of silicon is expressed as: $h_R(t) = \Omega_R^2 \tau_1 \exp(\frac{-t}{\tau_2}) \sin(\frac{t}{\tau_1})$, where $\tau_1 = 10 \text{ fs}$ and $\tau_2 = 3 \text{ ps}$ correspond to the Raman shift and the bandwidth of the Raman gain spectrum, respectively and Ω_R related to τ_1 .

The pulse propagation in SN-PCF is studied by solving the hitherto mentioned NLS type equation using symmetrized split-step Fourier method. We analyze the pulse evolution of SC

by considering the hyperbolic secant profile as the input pulse and the same is given by [13]: $A(0, t) = N\sqrt{P_0}\text{sech}[\frac{t}{T_0}]$, where P_0 is the peak power and T_0 is the input soliton duration defined as $T_{FWHM}/1.763$. The soliton order N is defined as, $N^2 = \frac{\gamma P_0 T_0^2}{|\beta_2|}$. We point out that, in the simulation, we consider the minimum value of ellipticity (0.3) since the proposed SN-PCF meets the requirements (less GVD and high nonlinearity) of SC generation for this value only at 1.55 μm wavelength.

The SC evolution with the pump peak power increasing from 25 to 100 W at 1.55 μm wavelength is as shown in Fig. 5, where the input pulse width is 25 fs and the length of fiber is 2 mm. From the Fig. 5, one can observe that the SN-PCF exhibits a broad spectrum at high input power (100 W) due to the combined action of self-phase modulation, soliton fission and Raman effect. Therefore, the width of the SC depends on the incident power of the pulse. Fig. 6 shows the generation of SC of SN-PCF at 1.55 μm wavelength for various fiber lengths from 5 to 15 mm for a constant input peak power (25 W) and pulse width (25 fs). From Figs. 5 and 6, we observe that the intensity spectrum splits into number of solitons upon increasing the input power and length of the fiber. The proposed SN-PCF exhibits relatively a wider bandwidth of more than 1500 nm. This wider SC spectrum may be useful for ultrahigh-resolution optical coherence tomography system for dental imaging and optical communication systems.

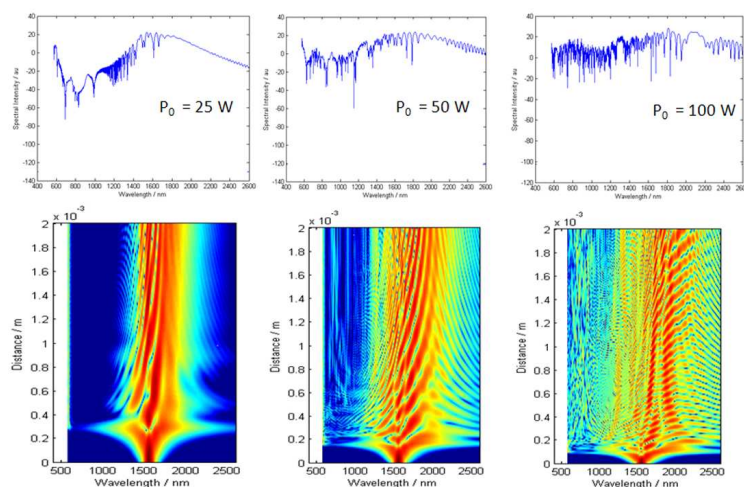


Figure 5: Spectral evolution and spectrum of supercontinuum for various input powers at 1.55 μm wavelength.

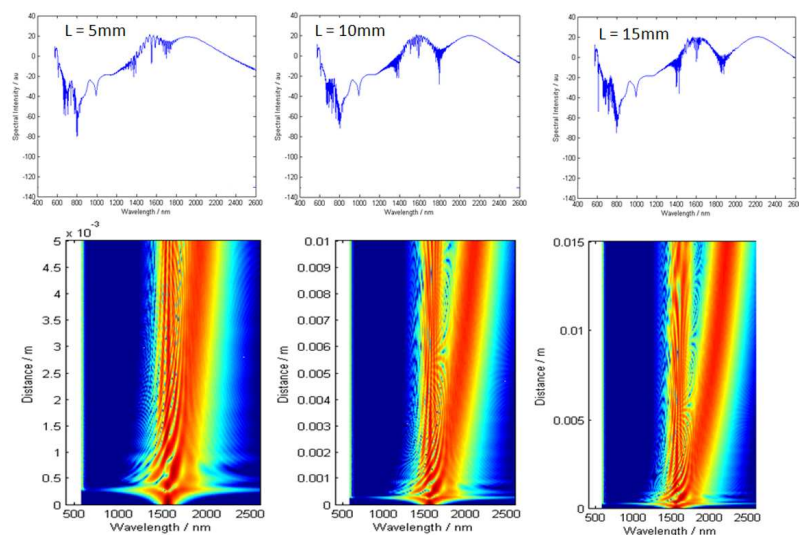


Figure 6: Spectral evolution and spectrum of supercontinuum for various length of SN-PCFs at 1.55 μm wavelength.

6. CONCLUSION

In this paper, we have proposed an elliptical core silicon nanowire embedded photonic crystal fiber and studied the optical properties for various ellipticities using a fully-vectorial finite element method. We have demonstrated the supercontinuum in SN-PCF for various input peak powers and fiber lengths with an input pulse of width 25 fs at 1.55 μm wavelength. We have noticed an enhanced bandwidth of 1800 nm. We envisage that the proposed SN-PCF would highly be useful in the field of medicine, especially, in dentistry, besides its applications in optical communication systems.

ACKNOWLEDGMENT

KSN wishes to thank CSIR [No.: 03(1264)/12/EMR-II] and DST [No.: SR/FTP/PS-66/2009], Government of India, for the financial support through the sponsored projects. SS wishes to thank DST [No.: SR/S2/LOP-0014/2012], Government of India, for the financial support through the sponsored project.

REFERENCES

1. Ranka, J. K., R. S. Windeler, and A. J. Stentz, "Visible continuum generation in air silica microstructure optical fibers with anomalous dispersion at 800 nm," *Opt. Lett.*, Vol. 25, No. 1, 25–27, 2000.
2. Dudley, J. M., G. Genty, and S. Coen, "Supercontinuum generation in photonic crystal fiber," *Rev. Mod. Phys.*, Vol. 78, No. 4, 1135–1184, 2006.
3. Kudlinski, A., G. Bouwmans, M. Douay, M. Taki, and A. Mussot, "Dispersion-engineered photonic crystal fibers for CW-pumped supercontinuum sources," *J. Lightwave Technol.*, Vol. 27, No. 11, 1556–1564, 2009.
4. Biancalana, F., T. X. Tran, S. Stark, M. A. Schmidt, and P. St. J. Russell, "Emergence of geometrical optical nonlinearities in photonic crystal fiber nanowires," *Phys. Rev. Lett.*, Vol. 105, No. 9, 093904–093907, 2010.
5. Gunasundari, E., K. Senthilnathan, S. Sivabalan, M. Abdosllam Abobaker, K. Nakkeeran, and P. Ramesh Babu, "Waveguiding properties of silicon nanowire embedded photonic crystal fiber," *Opt. Materials*, Vol. 36, No. 5, 958–964, 2014.
6. Tong, L., J. Lou, and E. Mazur, "Single-mode guiding properties of sub-wavelength diameter silica and silicon wire waveguides," *Opt. Express*, Vol. 12, No. 6, 1025–1035, 2004.
7. Foster, M., A. L. Gaeta, Q. Cao, and R. Trebino, "Soliton-effect compression of supercontinuum to few-cycle durations in photonic nanowires," *Opt. Express*, Vol. 13, No. 18, 6848–6855, 2005.
8. Salem, A. B., R. Cherif, and M. Zghal, "Low-energy single-optical-cycle soliton self-compression in photonic nanowires," *J. Nanophoton.*, Vol. 5, No. 1, 059506(1–6), 2011.
9. Salem, A. B., R. Cherif, and M. Zghal, "Soliton-self compression in highly nonlinear chalcogenide photonic nanowires with ultralow pulse energy," *Opt. Express*, Vol. 19, No. 21, 19955–19966, 2011.
10. Salem, A. B., R. Cherif, and M. Zghal, "Rigorous optical modelling of elliptical photonic nanowires," *J. Lightw. Technol.*, Vol. 30, No. 13, 2176–2180, 2012.
11. Afshar, S. V. and T. M. Monro, "A full vectorial model for pulse propagation in emerging waveguides with subwavelength structures part I: Kerr nonlinearity," *Opt. Express*, Vol. 17, No. 4, 2298–2318, 2009.
12. Yin, L., Q. Lin, and G. P. Agrawal, "Soliton fission and supercontinuum generation in silicon waveguides," *Opt. Lett.*, Vol. 32, No. 4, 391–393, 2007.
13. Agrawal, G. P., *Nonlinear Fiber Optics*, Academic Press, 2007.

Fractal Labyrinths: Path Matrices and Borders Topology

V. I. Grachev

Kotel'nikov Institute of Radio Engineering and Electronics, Russian Academy of Sciences, Russia

Abstract— In this paper some elements of the theory of fractal labyrinths are presented using fractional calculus mathematics and random walk model. A model of finitely ramified deterministic labyrinth fractal on a square grid is built, topology of its boundaries is defined, its pathways are calculated using the path matrices up to isomorphism accuracy with respect to rotation and flipping. The path matrices were calculated using the Jordan decomposition. For the constructed model of a fractal labyrinth there have been obtained numerical values of the labyrinth path's lengths before its exits, allowing obtaining the characteristics of the simulated fractal environment.

1. INTRODUCTION

Application of fractal formalism to the analysis of complex weakly formalized processes and systems, problems of stochastic image reconstruction of nanostructures [1], genetic and self-affine synthesis of antenna arrays [2], multidimensional signals, a rich variety of modes of transport etc. undergoes presently intensive development. In this paper we expand the class of fractal-scaling approaches by using self-similar (hierarchical) dendritic structures — fractal labyrinths.

2. ELEMENTS OF THE FRACTAL LABYRINTHS THEORY

Description of fractal structures and processes in fractal media does not fit into the traditional framework of differential equations of integer order. It is considered that the mathematical apparatus of fractal geometry is fractional calculus, which allows transition from ordinary differential equations to fractal equations. At the same time the standard methods of solving differential equations in partial derivatives or calculus of associated moments of transport are also applied to fractional equations. Physically, the operators of integro-differentiation of fractional order $D^\alpha[f(t)]$, where $-1 < \alpha < 1$, act as a kind of “filters” that emit only those components that are localized on the fractal (fractional) sets the process under investigation. The presence in the equations of fractional derivative is usually interpreted as a reflection of the special property of the process/system — memory, or non-Markovian (heredity).

Anomalous kinetics in fractal structures, including such as the labyrinthine fractals (or fractal labyrinths) — topologically connected dendritic (ramified) structures with fractal dimension $d_f > 1$, whose pathways have scaling, self-similar nature — adequately formulated in terms of a model of the continuous in time random walk, when transport events are subject to wide statistics [3]. Random walks in a fractal environment, i.e., chaotic motion with discontinuous trajectory on the bumps and potholes with abrupt change of direction — characterized by jump length $\lambda(x) = \int_0^\infty dt \psi(x, t)$

and waiting time (between two successive jumps, pauses) $w(t) = \int_{-\infty}^\infty dx \psi(x, t)$, where $\lambda(x)dx$ is the probability of jump length in the interval $(x, x + dx)$, and $w(t)dt$ — the probability of the waiting time in the interval $(t, t + dt)$. Here the probability density function $\psi(x, t) = \lambda(x)w(t)$, if $\lambda(x)$ and $w(t)$ — independent variables, i.e., random walks are determined by the characteristic waiting time $T = \int_0^\infty dt w(t)t$ and variance of the length of the jump $\Sigma^2 = \int_{-\infty}^\infty dx \lambda(x)x^2$.

Random walks are equivalent to the diffusion. In this connection the transport processes which in the limit of free force are slower than Brownian diffusion, treated as subdiffusion. The probability density function $W(x, t)$ to be in point x at the instant t obeys algebraic relation in the Fourier-Laplace space [4]

$$W(k, u) = \frac{1 - w(u)}{u} \frac{W_0(k)}{1 - \psi(k, u)}, \quad (1)$$

where $W_0(k)$ — Fourier-transformation of the initial condition $W_0(x)$. In the fractal time of random walk when T diverges (long pause), but the jump — Gaussian (with finite Σ^2), diffusion —

anomalous diffusion is described by the fractional diffusion equation (FDE) [3]:

$$\frac{\partial W}{\partial t} = {}_0D_t^{1-\alpha} K_\alpha \frac{\partial^2}{\partial x^2} W(x, t) \quad (2)$$

where $W(x, t)$ — propagator, which depends in general on the singularities of geometry of the interaction; α — anomalous diffusion index (the order parameter of the fractional derivative, fractal dimension of the environment); K_α — constant of the generalized diffusion (subdiffusion) which is defined as $K_\alpha \equiv \sigma^2/\tau^\alpha$ and in terms of scale σ and τ has the dimension $[K^\alpha] = \text{cm}^2\text{s}^{-\alpha}$; the operator ${}_0D_t^{1-\alpha} = \frac{\partial}{\partial t} {}_0D_t^{-\alpha}$ for $0 < \alpha < 1$ — Riemann-Liouville operator, defined by the integral relation

$${}_0D_t^{1-\alpha} W(x, t) = \frac{1}{\Gamma(\alpha)} \frac{\partial}{\partial t} \int_0^t dt' \frac{W(x, t')}{(t-t')^{1-\alpha}} \quad (3)$$

— direct continuation of the multiple integral Cauchy for an arbitrary complex α with $\text{Re}(\alpha) > 0$. Thus integrodifferential nature of fractional Riemann-Liouville operator ${}_0D_t^{1-\alpha}$ in accordance with (3), and with the integral kernel of the form $M(t) \propto t^{\alpha-1}$ provides non-Markovian nature of the subdiffusion process which is determined by FDE (2).

Rewriting (2) in the equivalent form

$${}_0D_t^\alpha W - \frac{t^{-\alpha}}{\Gamma(1-\alpha)} W_0(x) = K_\alpha \frac{\partial^2}{\partial x^2} W(x, t), \quad (4)$$

we obtain the initial value $W_0(x)$ in the form of the inverse power law $(t^{-\alpha}/\Gamma(1-\alpha))W_0(x)$, rather than exponential law, as for the standard diffusion [3]. At the same time, in the limit, $\alpha \rightarrow 1$ FDE (2) reduces to the second Fick's law, as it should be. The mean square displacement of a random walk is

$$\langle x^2(t) \rangle = \frac{2K_\alpha}{\Gamma(1-\alpha)} t^\alpha. \quad (5)$$

Thus, FDE concept is a real extension of the standard diffusion equation in the same sense in which the random walk model generalizes the Brownian motion.

Anomalous diffusion index α parameterizes several areas of anomalous transport: subdiffusion for $0 < \alpha < 1$, superdiffusion for $\alpha > 1$, the normal Brownian diffusion at the interface between the sub- and superdiffusion with $\alpha = 1$ and a ballistic motion at $\alpha = 2$. Kinetics in fractal labyrinths are based on the description of the phenomenon of subdiffusion, which corresponds to $0 < \alpha < 1$.

3. ALGORITHM CONSTRUCTION OF FRACTAL LABYRINTH

As a generating element of the model fractal let's use the construction of L. L. Christie [5]. Pre-fractal of the first order, $n = 1$ (see Figure 1(a)) is built in the unit square on a 4-node square $m \times m$ grid ($m = 4$) with a characteristic size L . Figure 1(b) — pre-fractal of the 2nd order ($n = 2$), shows the development of the generating element through the recursive branching and scaling.

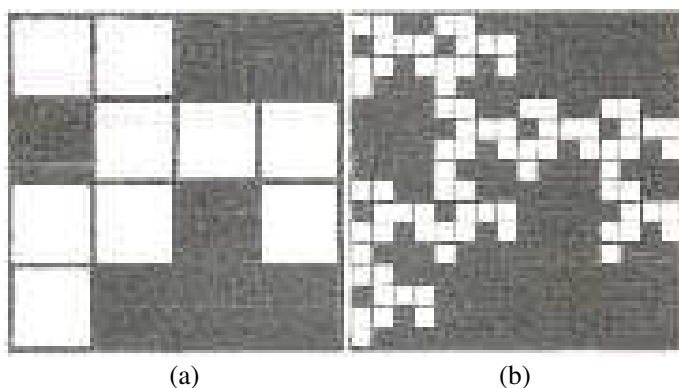


Figure 1: 4×4 -labyrinth fractals: (a) $n = 1$, (b) $n = 2$.

An iterative procedure for obtaining the fractal set of points $x, y \in [0, 1]$ on the unit square $[0, 1] \times [0, 1]$ for $m \geq 1$ is given by the relations

$$S_{i,j}^m = \left\{ (x, y) \left| \frac{i}{m} \leq x \leq \frac{i+1}{m}, \frac{j}{m} \leq y \leq \frac{j+1}{m} \right. \right\} \text{ and } S_m = \{S_{i,j}^m \mid 0 \leq i \leq m-1, 0 \leq j \leq m-1\}.$$

The set of white squares of the first order ($n = 1$) in Figure 1(a) denotes $W_1 \subset S_m$, then the set of black squares of the first order is $B_1 = S_m \setminus W_1$. Herewith

$$\forall (z_x, z_y) \in [0, 1] \times [0, 1] \exists P_Q(z_x, z_y) = (qz_x + x, qz_y + y).$$

For $n \geq 2$ we have

$$S_{m^n} = \{S_{i,j}^{m^n} \mid 0 \leq i \leq m^n - 1, 0 \leq j \leq m^n - 1\},$$

wherein respectively

$$W_n = \bigcup_{W_1 \in A_1, W_{n-1} \in W_{n-1}} \{P_{W_{n-1}}(W)\}$$

and $B_n = S_{m^n} \setminus W_n$. For $n \geq 1$, we define the associated graph $G(W_n)$ as a self-similar set, the vertices of which are the cells of Figure 1 — white squares, and the edges — the passages between adjacent cells, the sequence of vertices is a path in a graph. If this path is the only path and it is not a cycle, then such connected graph is a tree, a self-similar dendrite. We consider a finitely ramified deterministic fractal on a square grid. Topology of its borders is the following. The top row of order n , of sets W_n on the border of the dendrite is the set of all white squares in $\{S_{i,m^n-1,m^n} \mid 0 \leq i \leq m^n - 1\}$. The bottom row, left column, and right column are defined by analogy. A top exit in W_n is a white square in the top row of order n , such that there is a white square in the same column in the bottom row of order n . A bottom exit is defined by analogy. A left exit in W_n is a white square in the left column of order n , such that there is a white square in the same row in the right column of order n . A right exit is defined by analogy. Such dendritic set W_n with exits is called $m \times m$ -labyrinth set. Let us distinguish in W_n ($n \geq 1$) a sequence of compact sets $L_n = \bigcup_{W \in W_n} W$, then we obtain $\{L_n\}_{n=1}^\infty$ — monotonously decreasing sequence, whose limit is $L_\infty = \bigcap_{n=1}^\infty L_n$. The limit set L_∞ of a labyrinth set W_1 is called *labyrinth fractal*. The Hausdorff dimension of L_∞ is

$$\dim_H(L_\infty) = \frac{\log |W_1|}{\log m},$$

which one obtains from known results for self-similar sets [4]. Since in the case of labyrinth fractals, we have $|W_1| > m$, it follows that $\dim_H > 1$.

In the pre-fractals Figure 1 there are six possible options of paths: the path from vertex to base with the length p_{1n} , which leads to the exit of the W_n ; the paths from left to right, top to right, right to bottom, bottom to left and left to top, leading to the exits with lengths $p_{2n}, p_{3n}, p_{4n}, p_{5n}, p_{6n}$, respectively. Our model of labyrinth is limited, i.e., labyrinth is blocked horizontally and vertically: horizontally — if the series of squares from left to right is contained at least one black square and vertically — if a black square is contained in the column of the squares from top to bottom exit. Based on the existence and uniqueness theorems of curves of finite length in blocked labyrinth fractals [4], let's construct pathways of fractal tree using the path matrix, up to isomorphism accuracy with respect to rotation and flipping. There is a non-negative 6×6 matrix path M , so that for $n \geq 1$

$$\begin{pmatrix} p_{1n} \\ p_{2n} \\ p_{3n} \\ p_{4n} \\ p_{5n} \\ p_{6n} \end{pmatrix} = M \cdot \begin{pmatrix} p_{1n-1} \\ p_{2n-1} \\ p_{3n-1} \\ p_{4n-1} \\ p_{5n-1} \\ p_{6n-1} \end{pmatrix} = M^n \cdot \begin{pmatrix} 1 \\ 1 \\ 1 \\ 1 \\ 1 \\ 1 \end{pmatrix}.$$

Figure 1(a) shows the example of 4×4 -labyrinth set B that is horizontally and vertically blocked. Let M be the path matrix of the labyrinth set W_1 . In the Jordan decomposition $M = B \cdot J \cdot B^{-1}$,

we have

$$J = \begin{pmatrix} 000000 \\ 010000 \\ 001000 \\ 000200 \\ 000020 \\ 000005 \end{pmatrix}. \quad \text{Therefore, } M^n = B \cdot J^n \cdot B^{-1}, \quad \text{where } J^n = \begin{pmatrix} 000000 \\ 010000 \\ 001000 \\ 0002^n 00 \\ 00002^n 0 \\ 000005^n \end{pmatrix}.$$

After algebraic simplifications (explicit forms of B and B^{-1} are omitted) we obtain the numerical values of path lengths (unit is — cell-square) $p_{n1} = (4 \cdot 5^n - 2^n)1/3$, $p_{n2} = (4 \cdot 5^n - 2^n)1/3$, $p_{n3} = 5^n + 2^n - 1$, $p_{n4} = (5^{n+1} - 2^{n+1})1/3$, $p_{n5} = (5^n - 2^n + 3)1/3$, $p_{n6} = 5^n$. Herewith, the matrix J of Jordan decomposition is the same for all horizontal and vertical 4×4 -blocked labyrinth sets. For $n = 1$ we have 6, 6, 6, 7, 2, 5; for $n = 2$: 32, 32, 28, 39, 8, 25 — see Figure 1.

Knowing the values of the paths' lengths and of the mean square displacement of a random walk (5) allows us to determine the times of passing through fractal labyrinth, anomalous diffusion index and the fractal dimension of the medium.

4. CONCLUSION

This paper presents the basic relations of the anomalous transport with use of the continuous time random walk scheme as the starting point. These relations determines also the fractal kinetics. To investigate the properties of labyrinthine fractals we constructed the model of fractal labyrinth — dendritic fractal with exits at the boundaries. We formed the paths matrix for such labyrinth considering the topology of its borders. Using the Jordan decomposition, we calculated lengths of all possible paths in the constructed model. The proposed approach can be used to describe transport dynamics in complex systems, which are governed by anomalous diffusion and non-exponential relaxation patterns. Where approximation of processes or structures by dendritic graphs is possible, the calculation of pathways allows receiving fractal characteristics of the investigated medium.

REFERENCES

1. Grachev, V. I., A. A. Potapov, and V. A. German, "Fractal labyrinths and planar nanostructures," *PIERS Proceedings*, 122–125, Stockholm, Aug. 12–15, 2013.
2. Potapov, A. A. and V. I. Grachev, "The labyrinth structure in the synthesis of fractal antennas," *Progress In Electromagnetics Research Symposium Abstracts*, 169, Moscow, Russia, Aug. 19–23, 2012.
3. Metzler, R. and J. Klafter, "The random Walk's guide to anomalous diffusion: A fractional dynamics approach," *Phys. Rep.*, Vol. 339, 1–77, 2000.
4. Oldham, K. B. and J. Spanier, *The Fractional Calculus*, 234, Academic Press, NY, 1974.
5. Cristea, L. L. and B. Steinsky, "Curves of infinite lenght in 4×4 -labyrinth fractals," *Geom. Dedicata*, Vol. 141, 1–17, 2009.

Kd-tree Based Shooting and Bouncing Ray Method for Fast Computation of Near Field Scattering

P. C. Gao, Z. C. Liang, and W. Gao

Science and Technology on Electromagnetic Scattering Laboratory, China

Abstract— In this paper, we propose an efficient kd-tree based shooting and bouncing ray (SBR) method for solving near field scattering problems. The kd-tree is highly effective in handling the irregularly distribution of triangles of the target. It is utilized to accelerate the ray tube tracing in the SBR, especially for electrically large and complex targets. The SBR is based on the combination of the geometrical optics (GO) and the physical optics (PO). The far field assumption results in the decrease of the accuracy of the standard PO in the near field observation. By applying the locally expanded phase approximations together with surface partitioning, the refined PO can extend the region of validity of the SBR to near field scattering. Numerical examples demonstrate that the proposed method can efficiently handle the near field scattering problems of realistic complex targets with high accuracy.

1. INTRODUCTION

The efficient high frequency asymptotic methods have been widely used in computation of scattering from electrically large targets. The shooting and bouncing ray (SBR) method [1] is one of the most commonly adopted techniques for radar cross section (RCS) prediction of arbitrarily shaped targets. This is because it provides more accurate results by applying the ray-tube tracing to take into account the multiple bounces contribution.

The procedure of the SBR involves two steps: ray tube tracing and electromagnetic computing. In near field analysis, the incident field is approximated as a spherical wave, not a plane wave. Bundles of rays radiating from source instead of a grid of parallel rays are shot toward the target. The density of the rays on the virtual aperture should be greater than about ten rays per wavelength in view of the convergence. Thus, the ray tube tracing in the SBR is very time-consuming for electrically large and complex targets. Jin et al. [2] utilized the octree, recursively subdividing the box into eight equal children boxes using three axis-perpendicular planes, to reduce the number of intersection tests. It is based on the assumption that triangles are uniformly distributed in the target space. However, the hypothesis is hardly satisfied by realistic target. The kd-tree recursively split the target space into uneven axis-aligned boxes according to the ray tracing cost estimation model. It is highly effective in handling the irregularly distribution of triangles of the target and can significantly decrease the number of ray-triangle intersection tests. Tao et al. [3] presented the kd-tree based ray tube tracing to accelerate the SBR.

Most published work on high frequency scattering calculation is related to far field analysis. However, computation of near field scattering is crucial due to its military value, i.e., essential for radar-target end-game electromagnetic modeling. The SBR is based on the combination of the geometrical optics (GO) and the physical optics (PO). The standard PO utilizes the far field assumption to simplify the radiation integral for surface currents and makes possible practical closed-form solutions. Thus, the most straightforward way of refine the PO in the near field is to employ a more accurate representation of the Green's function. Pouliguen et al. [4] as well as Neto [5] applied the exact Green's function. This approach achieves excellent accuracy at the cost of requiring numerical integration of the surface currents, which reduces the performance especially for electrically large objects. Legault [6] overcomes the difficulty and preserves the simplicity of standard PO formulation by introducing a phase approximation with an expansion center used in conjunction with surface partitioning. Sui et al. [7] proposed the concept of distinct wave propagation vector (DWPV) to model incident wave with spherical wavefront for radar signature prediction of near field targets. The aforementioned approaches are based on the similar idea. It is dealing with each small piece of the target surface individually, and the observation point and the source point are in the far field zone of each small piece. Jeng [8] applied the same method to modify the SBR to handle near field scattering. Here, we apply the locally expanded phase approximations to refine the SBR in the near field, and utilize the kd-tree acceleration structure to make it efficient for the scattering from electrically large targets.

This paper is organized as follows. Section 2 introduces the kd-tree acceleration structure. Section 3 presents formulas of the near field SBR. In Section 4, numerical results are given with discussion, followed by the conclusions and future work.

2. KD-TREE CONSTRUCTION AND TRAVERSAL

The kd-tree has been publicly known the best space-partition data structure to accelerate ray tracing of the static scenes in computer graphics [9]. Recently, it has been successfully applied in RCS prediction with the SBR [3]. A kd-tree is constructed by recursively employing the axis-perpendicular plane to split the target space into uneven axis-aligned boxes. At each step of the procedure, a node, which contains a group of triangles that overlap the axis-aligned box of the node, is processed to be an interior node or a leaf node. The optimal splitting plane is searched based on the greedy surface area heuristic (SAH) [10] strategy, which minimizes the traversal time of interior nodes and the ray-triangles intersection time to construct the approximately optimal kd-tree. While the octree simply puts the splitting positions at the middle point of the extend in each axis, the kd-tree can provide faster ray tracing by taking into account the triangle distribution in the target space.

The depth-first kd-tree traversal starts with the root node of the kd-tree, and a stack is used as a priority queue of nodes left to visit according to how closer to the ray origin. In order to remove the unnecessary traversal steps of interior nodes, the kd-tree can be augmented with ropes in leaf nodes. The rope on each face of leaf nodes is a pointer to the adjacent leaf node, the smallest interior node or a nil node for leaf nodes on the border. Thus, the ray passing through a leaf node can efficiently continue the traversal with the rope, and it avoids the requirement of the stack to keep to-be-visited nodes. Figure 1 shows the traversal procedure of a 2D kd-tree with ropes.

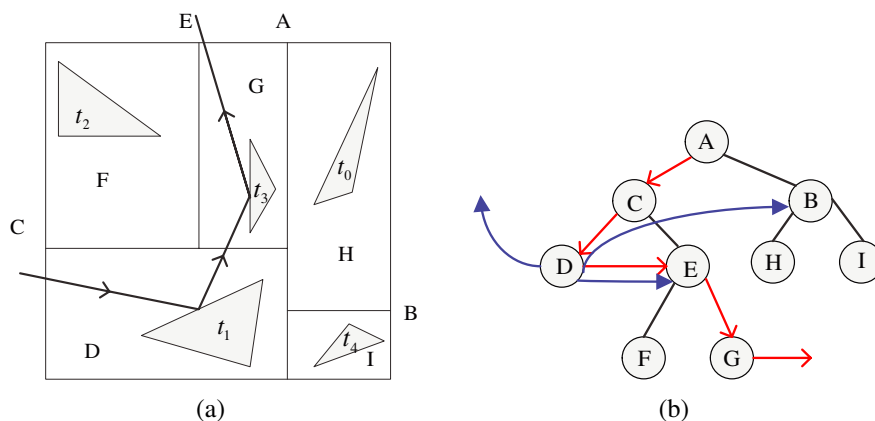


Figure 1: A 2D kd-tree and its traversal. (a) The interior nodes (B, C, E) of the kd-tree are labeled as their splitting planes and leaf nodes (D, F, G, H, I) are labeled in their boxes. The ray is recursively traced and has two intersections with the target. (b) The traversal path is shown as a red bold line. The traversal begins with the root node A, and proceeds down through the interior node C. Then an intersection is found in the leaf node D. With the help of the rope of D (the rope of D is marked with blue bold line), the generated reflected ray directly moves to the smallest interior node E including the leaf node F and G. Ray tracing ends with the second reflected ray exiting the leaf node G.

3. NEAR FIELD SBR

As seen in Figure 2, the incident spherical wave is modeled as a dense grid of ray tubes with distinct incident propagation vector, which radiate from source towards the target. With object geometrical center being the origin of the rectangular coordinates, where \mathbf{r}' is the position vector of a point on the target, and \mathbf{r} denote observation and source points. Given a finite observation range r , the accuracy of Green's function with far field assumption decreases with increasing \mathbf{r}' . A good way of removing the difficulty is to apply phase approximations with an arbitrary expansion centre as opposed to one essentially fixed at the origin. When \mathbf{r}' lies in the neighbourhood of the expansion centre \mathbf{r}_n^c , the Green's function can be approximated as

$$\frac{e^{-jk\hat{\mathbf{R}}\cdot(\mathbf{r}-\mathbf{r}')}}{R} \simeq \frac{e^{-jk\hat{\mathbf{k}}^{sn}\cdot(\mathbf{r}-\mathbf{r}')}}{r} \quad (1)$$

where $R = |\mathbf{R}| = |\mathbf{r} - \mathbf{r}'|$, and the unit vector

$$\hat{\mathbf{k}}^{\text{sn}} = \frac{\mathbf{R}_n}{|\mathbf{R}_n|} = \frac{\mathbf{r} - \mathbf{r}_n^c}{|\mathbf{r} - \mathbf{r}_n^c|} \quad (2)$$

where \mathbf{r}_n^c is the center of the projected footprint of n th ray tube, and \mathbf{R}_n is the position vector from \mathbf{r}_n^c to the observation point \mathbf{r} . The incident propagation vector of the n th ray tube is defined as $\hat{\mathbf{k}}^{\text{in}} = -\hat{\mathbf{k}}^{\text{sn}}$ in monostatic cases. The incident electric field \mathbf{E}^{in} for the n th ray tube is

$$\mathbf{E}^{\text{in}} = \left(E^{i\theta} \hat{\boldsymbol{\theta}} + E^{i\varphi} \hat{\boldsymbol{\varphi}} \right) e^{-jk\hat{\mathbf{k}}^{\text{in}} \cdot \mathbf{r}'_n} \quad (3)$$

where \mathbf{r}'_n is the position vector of a point on the footprint of the n th ray tube with footprint center being the origin. In respective, $\hat{\boldsymbol{\theta}}$ and $\hat{\boldsymbol{\varphi}}$ are the unit elevation vector and unit azimuth vector, $E^{i\theta}$ and $E^{i\varphi}$ are the scalar component of \mathbf{E}^{in} in $\hat{\boldsymbol{\theta}}$ and $\hat{\boldsymbol{\varphi}}$.

The near field PO integral is carried out on the four-sided polygon modeled by the exit position of ray tube. At an observation point, the formula of the scattered field of the n th ray tube is given

$$\mathbf{E}^{\text{sn}} = -\frac{j}{\lambda} \frac{e^{-jkR_n}}{R_n} \hat{\mathbf{n}} \times \left(E^{i\varphi} \hat{\boldsymbol{\theta}} - E^{i\theta} \hat{\boldsymbol{\varphi}} \right) \iint_{S'} e^{-jk(\hat{\mathbf{k}}^{\text{in}} - \hat{\mathbf{k}}^{\text{sn}}) \cdot \mathbf{r}'_n} ds' \quad (4)$$

The integral $\iint_{S'} e^{-jk(\hat{\mathbf{k}}^{\text{in}} - \hat{\mathbf{k}}^{\text{sn}}) \cdot \mathbf{r}'_n} ds'$ can be calculated with the well-known Gordon's contour integration [11].

4. NUMERICAL RESULT

Several numerical results are presented to evaluate the proposed near field SBR with the kd-tree acceleration structure. The results are derived on an Intel Core i5 2.6 GHz CPU without special declaration. The targets are perfect electric conductor (PEC) in this paper.

A square plate with dimension of 10 m, which is illuminated by a Hertzian dipole of 0.3 GHz located on x -axis at 33 m, lying in the y - z plane is used to verify the accuracy of the proposed method. For the plate, the corresponding maximum dimension is $D=10\sqrt{2}$ m, so that the far field limit is $r_{ff}(D) = 2D^2/\lambda = 400$ m. The scattering parameters are: $r = 33$ m, $\theta = 90^\circ$, $\varphi = 0^\circ \sim 60^\circ$. As shown in Figure 3, the result of the proposed kd-tree based near field SBR agrees well with FEKO's MLFMA result over angles of 0° to 30° , and the deviation is seen in the observation angles after 30° both for the proposed approach and FEKO's PO. This is in concordance with the widely accepted rule of thumb of restricting observation angles within 30° of boresight for accurate backscattering results using PO with planar structures.

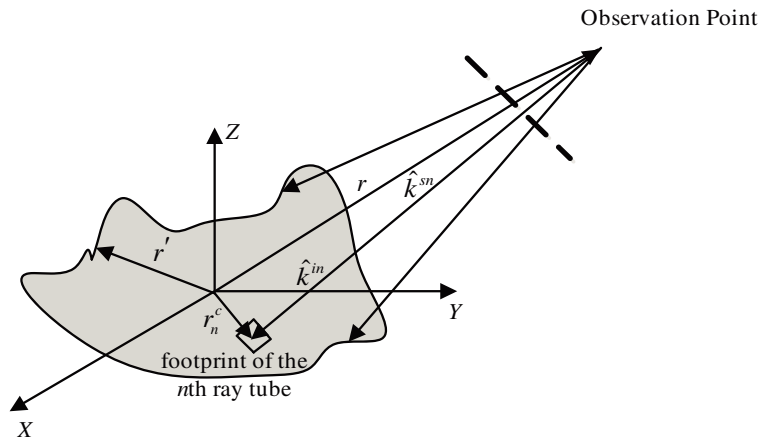


Figure 2: Geometry of near field scattering.

In order to demonstrate the efficiency of the proposed approach for scattering from electrically large targets, the RCS of a missile illustrated in Figure 4 at 10 GHz is calculated. The missile is $33\lambda \times 21\lambda \times 8\lambda$, and the corresponding far field limit is about 96 m. The Hertzian dipole is located at the position (10 m, 70° , 30°), and the scattering parameter is: φ from 0° to 90° on the $\theta = 70^\circ$ plane

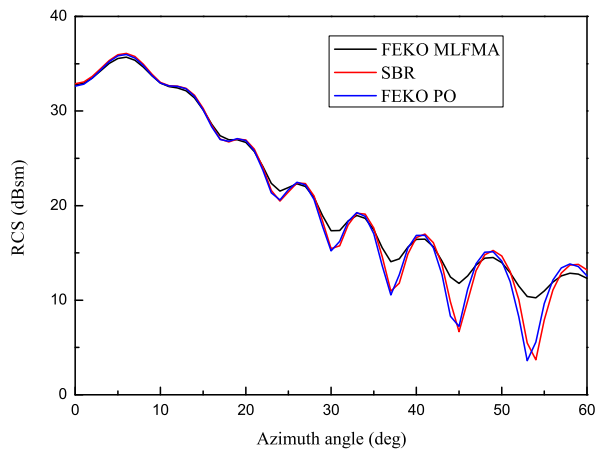


Figure 3: The near field RCS of a square plane with 10 m length as a function of azimuth angle in θ -polarization.

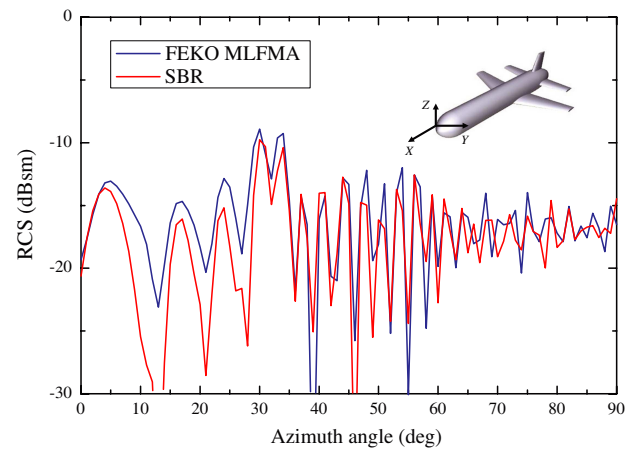


Figure 4: The near field RCS of a missile-like target as a function of azimuth angle in θ -polarization.

with an angular resolution 1° at $r = 10$ m. As can be seen clearly from Figure 4, a good agreement is observed between the proposed method result and the FEKO's MLFMA result, and the deviation may be partly due to the lack of the edge-diffraction effect. It has been proven that the kd-tree based SBR is more efficient than the one with other acceleration structures (e.g., octree) [3]. Thus, no comparison of efficiency is presented in this paper. The missile is composed of 11404 triangles, and 7037640 rays are shot toward it to ensure the convergence of result. The computation time for one observation point is 6.3 seconds, i.e., the kd-tree based near field SBR can process over a million rays per second including both ray tube tracing and electromagnetic computing with only one core. Parallel MLFMA of FEKO takes 132 seconds with 22 cores to solve the same problem. For the similar computational resource, the proposed algorithm can be parallelized to efficiently handle challenging realistic problems with a dimension of several hundreds wavelengths.

5. CONCLUSION

It has been shown that the SBR can efficiently handle the scattering from electrically large targets by employing the kd-tree acceleration structure constructed based on the distribution of triangles of the target. Additionally, the standard PO formulation is adapted to near field computations using locally expanded approximation in conjunction with surface partitioning. Numerical results show excellent agreement with the well-known commercial EM software FEKO, and demonstrate the efficiency of the kd-tree based near field SBR.

ACKNOWLEDGMENT

This work was supported in part by National Natural Science Foundation of China (No. 61302036).

REFERENCES

1. Ling, H., R. C. Chou, and S. W. Lee, "Shooting and bouncing rays: Calculating the RCS of an arbitrarily shaped cavity," *IEEE Trans. Antennas Propag.*, Vol. 37, No. 2, 194–205, 1989.
2. Jin, K. S., T. I. Suh, S. H. Suk, B. C. Kim, and H. T. Kim, "Fast ray tracing using a space-division algorithm for RCS prediction," *Journal of Electromagnetic Waves and Applications*, Vol. 20, No. 1, 119–126, 2006.
3. Tao, Y. B., H. Lin, and H. J. Bao, "Kd-tree based fast ray tracing for RCS prediction," *Progress In Electromagnetics Research*, Vol. 81, 329–341, 2008.
4. Pouliguen, P. and L. Desclos, "A physical optics approach to near field RCS computations," *Ann. Telecommun.*, Vol. 51, Nos. 5–6, 219–226, 1996.
5. Neto, A., "True physical optics for the accurate characterization of antenna radomes and lenses," *IEEE Antennas Propag. Symp. Dig.*, Vol. 4, 416–419, 2003.
6. Legault, S. R., "Refined physical optics for near-field computations," *Electron. Lett.*, Vol. 40, 71–72, 2004.
7. Sui, M. and X. J. Xu, "A novel procedure for high resolution radar signature prediction of near field targets," *IEEE Trans. Antennas Propag.*, Vol. 58, No. 9, 2981–2993, 2010.

8. Jeng, S. K., “Near-field scattering by physical theory of diffraction and shooting and bouncing rays,” *IEEE Trans. Antennas Propag.*, Vol. 46, No. 4, 551–558, 1998.
9. Havran, V., “Heuristic ray shooting algorithms,” Ph.D. Dissertation, University of Czech Technical, Prague, 2000.
10. Goldsmith, J. and J. Salmon, “Automatic creation of object hierarchies for ray tracing,” *IEEE Computer Graphics and Applications*, Vol. 7, No. 5, 14–20, 1989.
11. Gordon, W. B., “Far-field approximation to the Kirchhoff-Helmholtz representation of scattering fields,” *IEEE Trans. Antennas Propag.*, Vol. 23, 590–592, 1975.

Analysis of the Fluorescence Imaging of Surface Plasmon-coupled Emission Microscopy

X. Ji¹, T. Suyama², A. Matsushima¹, Y. Zhang³, and Y. Okuno⁴

¹Graduate School of Science and Technology, Kumamoto University, Kumamoto, Japan

²Akashi National College of Technology, Akashi, Japan

³Department of Physics and Electronic Information, Wenzhou University, Wenzhou, China

⁴South China Normal University, Guangzhou, China

Abstract— Surface plasmon-coupled emission microscopy (SPCEM) that makes use of a thin layer of metal deposited on glass slides to efficiently excite fluorophore and to collect the emission light is a widely used imaging technique that has found a number of applications in areas such as biotechnology and biological measurements. SPCEM is a relatively new imaging technique that potentially promises better detection sensitivity and higher signal-to-noise ratio than conventional total internal reflection fluorescence (TIRF) imaging. However, recent theoretical studies suggest that the sensitivity of SPCEM is actually reduced due to the metal layer. We have designed a metal-dielectric multilayer film structure which consists of Ag-Si₃N₄ layers, and we have analyzed the transmission of two counter-propagation lights from the multilayer film by using the characteristic matrix method in the film optics. In this paper, optimization is utilized in the design of the multilayer film structure. And it is coated on the glass slides to improve the quality of microscopic imaging. We mainly use the optimization method to design the thickness of the metal layer and the dielectric layer. We analyze the transmission coefficient of two counter-propagation lights from the multilayer film with different thickness and different number of layer. The refractive indexes with different number of the layer of multilayer film are also discussed.

1. INTRODUCTION

Metallic devices at the nanometer scale have stimulated a broad range of interests in nanophotonics and near-field microscopy. For instance, sharp aperture less metal tips have been used to enhance the signal-to-noise ratio and the spatial resolution in a wide range of experiments. Surface plasmon-coupled emission microscopy (SPCEM) was proposed as a high sensitivity technique that made use of a thin layer of metal deposited on glass slide to efficiently excite the fluorescence molecules and to collect the emission light. The SPCEM technique with the total internal reflection fluorescence microscopy (TIRFM) configuration is a widely used imaging technique that has found a number of applications in areas such as biotechnology and biological measurements. The SPCEM method was first proposed as a high sensitivity and efficient fluorescence detection method by Lakowicz et al. [1, 2]. They showed that, through imaging fluorophores near to a silver-coated glass substrate, that the fluorescence emission was highly directional and this increased the collection efficiency to nearly 50%, as well as contributed to low background noise. Experiments have also shown that the fluorescence of single molecules in the vicinity of a thin metallic film may appear enhanced up to a factor of 12 when detected through the metallic film [3, 4].

SPCEM is a relatively new imaging technique that potentially promises better detection sensitivity and higher signal-to-noise ratio than conventional total internal reflection fluorescence (TIRF) imaging. However, recent theoretical studies suggest that the sensitivity of SPCEM is actually reduced due to the metal layer. Duo to the SPCE, the single-layer metal film coated on the surface of glass slide in the TIRFM could intensify the transmission of the excitation light so that the emission of fluorescence molecules was enhanced. On the other hand, the metal film also collected the emission light which propagating direction was contrary to the propagating direction of the excitation light, so that the collection ability to the emission light was lower than that without the metal film. To overcome this disadvantage and further increase the intensity of fluorescent image, we have proposed a metal-dielectric multilayer film structure which consists of Ag-Si₃N₄ layers, and analyzed the transmission of two counter-propagation lights from the multilayer film by using the characteristic matrix method in the film optics. The transmissions of two counter-propagating lights can be enhanced by use of the proposed multilayer film and consequently the fluorescent imaging intensity is larger than that by use of a single-layer metal film in the TIRFM [5, 6]. In this paper, optimization is utilized in the design of the multilayer film structure. And it is coated on the glass slides to improve the quality of microscopic imaging. We mainly use the optimization method

to design the thickness of the metal layer and the dielectric layer. We analyze the transmission coefficient of two counter-propagation lights from the multilayer film with different thickness and different number of layer. The refractive indexes with different number of the layer of multilayer film are also discussed.

2. MODEL AND FORMULATE

For simplicity, we calculated the transmission coefficients of plane wave passing through the multilayer film using the transfer matrix method. For concreteness, we assumed that the composite film consists of a Si_3N_4 dielectric layer with the dielectric constant $\varepsilon_d = 4.08$ and an Ag metal-layer (as shown in Fig. 1) and the thickness of metal and dielectric layers were denoted as t and h respectively. Both metal and dielectric are assumed nonmagnetic (i.e., $\mu = 1$). The glass slide in the TIRFM was on top of the composite film and water is below the composite film, fluorescence molecule was in water and in the vicinity of the interface between the composite film and water. We assumed excitation light with 532 nm wavelength propagates along the route of glass→composite film→water, while emission light with 560 nm wavelength propagates along the route contrary to the excitation light. (n_g, n_w, n_m, n_d) denote the refractive indices of glass slide, water, metal, and dielectric, respectively.

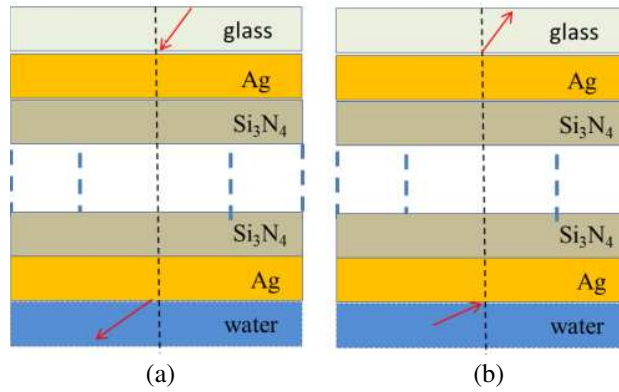


Figure 1: Metal-dielectric photonic crystal structure. (a) The incidence of excitation light from the glass and (b) the incidence of emission light from the glass.

According to the film optics, the electric-field transmission coefficient of the film can be written as

$$t_s = \frac{2p_g}{(m'_{11} + m'_{12}p_w)p_g + (m'_{21} + m'_{22}p_w)}, \quad (1)$$

where

$$p_g = n_g \cos \theta_g, \quad p_w = n_w \cos \theta_w, \quad p = n \cos \theta \quad (2)$$

$$M(z) = \begin{bmatrix} m'_{11} & m'_{12} \\ m'_{21} & m'_{22} \end{bmatrix} = \begin{bmatrix} \cos(k_0 n z \cos \theta) & -\frac{i}{p} \sin(k_0 n z \cos \theta) \\ -ip \sin(k_0 n z \cos \theta) & \cos(k_0 n z \cos \theta) \end{bmatrix} \quad (3)$$

for the TE-polarized wave incident on the composite film and

$$t_p = \frac{n_s}{n_l} \frac{2q_g}{(m'_{11} + m'_{12}q_w)q_g + (m'_{21} + m'_{22}q_w)} \quad (4)$$

where

$$q = \cos \theta/n, \quad q_g = \cos \theta_g/n_g, \quad q_w = \cos \theta_w/n_w \quad (5)$$

$$M(z) = \begin{bmatrix} m'_{11} & m'_{12} \\ m'_{21} & m'_{22} \end{bmatrix} = \begin{bmatrix} \cos(k_0 n z \cos \theta) & -\frac{i}{q} \sin(k_0 n z \cos \theta) \\ -iq \sin(k_0 n z \cos \theta) & \cos(k_0 n z \cos \theta) \end{bmatrix} \quad (6)$$

for the TM-polarized wave incident on the MDPC film. The superscripts s and p denote the components for the TE- and TM-polarized lights, respectively.

3. NUMERICAL RESULTS

It is well known that when the TE-polarized light is incident on a metal film, there is no the SPCE to come into being. Only for the TM-polarized light is incident on a metal film, the SPCE may be generated. Therefore, the TM-polarized light or radially polarized light are usually used in the TIRFM to effectively produce the SPCE. In the following calculations, we study only the TM-polarized light.

3.1. Single Layer Metal Film

As a starting point, we first calculate the transmission coefficients from a single-layer Ag film. Figure 2 presents the maximum amplitudes of transmission coefficients as a function versus the thickness of the metal film.

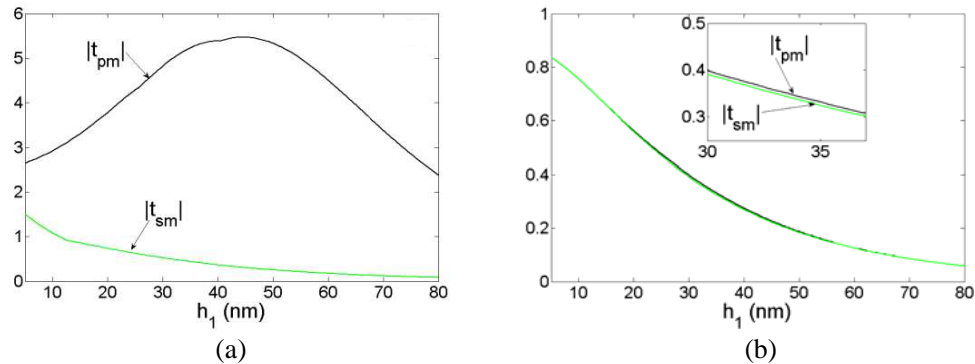


Figure 2: Maximum amplitudes of transmission coefficients as a function versus the thickness h_1 of the metal film. (a) For the excitation light propagating along the glass→metal→water direction; (b) for the emission light propagating along the water→metal→glass direction.

In the Figure 2(a), we can see that, when TM-polarized light is incident on the film, the size of peak value has a non-monotone behavior with the thickness of the film, and reaches its maximum value. When TE-polarized light is incident on the film, the peak value decreases with the thickness. In the Figure 2(b), the peak value decreases with the thickness and all are smaller for larger thickness.

3.2. Metal-dielectric-metal Composite Film

In Figure 3, we can see that, when the thickness of the metal film within a certain range, the transmission coefficients of two counter-propagating lights all are larger than 1, in another word, the transmissions of two counter-propagating lights are both enhanced.

Figure 4 presents the amplitudes of transmission coefficients and phases of the composite film as a function versus the incident angles. As is shown in the Figure 4, transmission coefficients of two counter-propagating lights all are larger when the incident angle is less than 74 degrees.

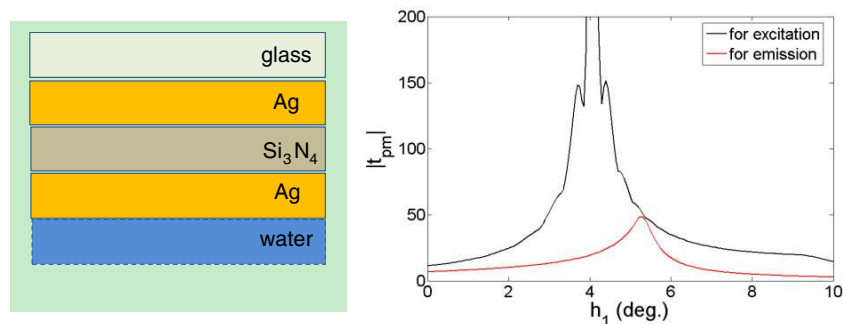


Figure 3: Maximum amplitudes of transmission coefficients of the metal-dielectric-metal sandwich film as a function versus the thickness h_1 of the metal film when $h_2 = 37$ nm. Black and red curves are the cases for the excitation light propagating along the glass→sandwich→water direction and for the emission light propagating along the water→sandwich→glass direction, respectively.

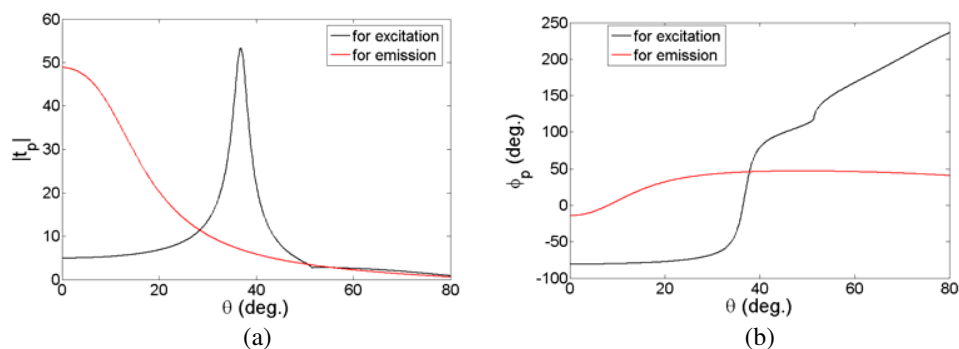


Figure 4: (a) Amplitude and (b) phase of transmission coefficients of light passing the sandwich versus the incident angle when $h_1 = 5.25$ nm and $h_2 = 37$ nm.

3.3. Multilayer Metal-dielectric Composite Film

Figure 5 presents the amplitudes of transmission coefficients of the composite film as a function versus the thickness of the metal film when the thickness of the dielectric film is 28 nm. When the thickness of the metal film is within a certain range, the bidirectional transmission coefficients are greater than 1. As shown as Figure 6, as $\theta < 70^\circ$, both the transmission coefficient of emission light and excitation light are very large. Compared to metal-dielectric-metal sandwich film, the maximum amplitudes of transmission coefficients decreased. However, as $\theta < 46.5^\circ$, transmission lights of both directions were strengthened at the same time. And in this incident Angle range, phase change is very small.

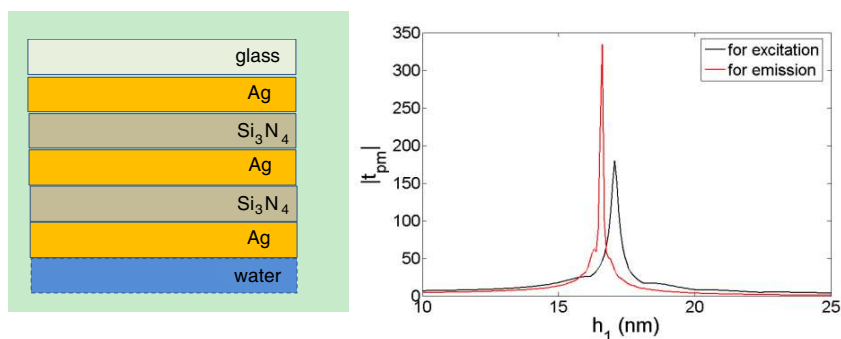


Figure 5: Maximum amplitudes of transmission coefficients of the composite film as a function versus the thickness h_1 of the metal film when $h_2 = 28$ nm. Black and red curves are the cases for the excitation light propagating along the glass→composite film→water direction and for the emission light propagating along the water→composite film→glass direction, respectively.

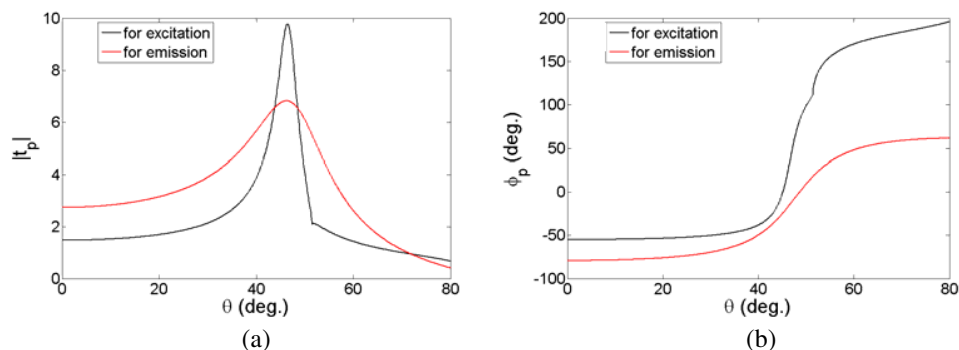


Figure 6: (a) Amplitude and (b) phase of transmission coefficients of light passing composite film versus the incident angle when $h_1 = 13$ nm and $h_2 = 27$ nm.

4. CONCLUSION

To enhance the image of single molecule fluorescence, one single-layer metal film is usually deposited on the glass slide in conventional localized TIRFMs. In this paper, we propose two kinds of metal-dielectric multilayer film, and it is coated on the glass slides to improve the quality of microscopic imaging. We analyze the transmission coefficient of two counter-propagation lights from the multilayer film with different thickness and different number of layer. The refractive indexes with different number of the layer of multilayer film are also discussed. It is clear that the transmissions of multilayer metal-dielectric composite film for two counter-propagating lights are both enhanced. The brightness of fluorescent imaging patterns will be increased remarkably if such multilayer metal-dielectric composite film is used in the total internal reflection fluorescence microscopy.

REFERENCES

1. Török, P., P. Varga, Z. Laczik, and G. R. Booker, "Electromagnetic diffraction of light focused through a planar interface between materials of mismatched refractive indices: An integral representation," *J. Opt. Soc. Am. A*, Vol. 12, 325–332, 1995.
2. Lakowicz, J. R., "Directional surface plasmon-coupled emission: A new method for high sensitivity detection," *Biochem. and Biophys. Res. Comm.*, Vol. 307, No. 3, 435–439, 2003.
3. Van de Nes, A., L. Billy, S. Pereira, and J. Braat, "Calculation of the vectorial field distribution in a stratified focal region of a high numerical aperture imaging system," *Opt. Express*, Vol. 12, 1281–1293, 2004.
4. Tang, W. T., E. Chung, Y. H. Kim, P. T. C. So, and C. J. R. Sheppard, "Investigation of the point spread function of surface plasmon-coupled emission microscopy," *Opt. Express*, Vol. 15, No. 8, 4634–4646, 2007.
5. Suyama, T., X. Ji, and Y. Zhang, "A metal-dielectric composited film applied to enhance the fluorescence imaging," *PIERS Proceedings*, 1409–1414, Stockholm, Aug. 12–15, 2013.
6. Suyama, T., X. Ji, and Y. Zhang, "Enhancement of fluorescent labeling via a composited thin film," *International Journal of Polymer Science*, No. 921489, 2014.

Analysis of Plasmon Resonance in a Multilayer-coated Bigrating

Xun Xu¹, Yoichi Okuno², and Taikei Suyama³

¹Kyushu Sangyo University, Fukuoka, Japan

²South China Normal University, Guangzhou, China

³Akashi National College of Technology, Akashi, Japan

Abstract— Periodically corrugated thin metal films have an interesting property such as the partial or total resonance absorption of incident light energy. The resonance absorption is associated with the excitation of the surface plasmons and is then termed the resonance absorption. Most of studies on the resonance absorption have mainly dealt with a thin metal film grating whose surfaces are periodic in one direction. We investigate the plasmon resonance of a multilayer-coated bigrating which consists of thin-films corrugated periodically in two directions. In solving the problem, we employed a computational technique based on modal expansion. Taking a sandwiched structure Vacuum/Ag/SiO₂/Ag/Vacuum for an example, we observed: (1) excitation of a SISP mode at the lit surface of the 1st Ag layer with strong field enhancement for thick enough Ag layer case; (2) excitation of coupled SPR modes (SRSP or LRSP) at each surface between vacuum and Ag layers with strong field enhancements for thin enough Ag layer cases no matter with the thickness of SiO₂ layers; (3) standing wave pattern of the electric field in the SiO₂ film. The coupled plasmon modes were resulted by the resonance waves excited on four surfaces in these cases.

1. INTRODUCTION

In our previous study we examined the excitation of coupled plasmon modes in a thin-film grating made of a metal [1]. When the metal is thick, e.g., more than ten times the skin depth, the plasmon can be excited on the lit surface alone. This is termed a single-interface surface plasmon (SISP). When the thickness is decreased, the plasmon can be seen also on the other surface of the film. The two plasmon waves interact with each other to form coupled plasmon modes called short-range and long-range surface plasmon (SRSP and LRSP) [2].

In the present research we consider a sandwiched structure: metal/dielectric/metal, which is interesting for a wide area of applications including biosensors [3].

2. FORMULATION AND METHOD OF SOLUTION

In this section we first formulate the problem of diffraction by multilayered bigratings shown in Fig. 1(a). After formulating the problem we state a method of solution based on a modal-expansion approach.

2.1. Incident Wave

The electric and magnetic field of an incident light are given by

$$\begin{bmatrix} \mathbf{E}^i \\ \mathbf{H}^i \end{bmatrix}(\mathbf{P}) = \begin{bmatrix} \mathbf{e}^i \\ \mathbf{h}^i \end{bmatrix} \exp(i\mathbf{k}^i \cdot \mathbf{P}) \quad (1)$$

where \mathbf{e}^i and \mathbf{h}^i are the electric- and magnetic-field amplitude; $\mathbf{k}^i = [\alpha, \beta, -\gamma]$ is the incident wavevector with $\alpha = n_1 k \sin \theta \cos \varphi$, $\beta = n_1 k \sin \theta \sin \varphi$, $\gamma = n_1 k \cos \theta$, $k = 2\pi/\lambda$ and n_1 is the relative refractive index of region V₁; $\mathbf{P} = (X, Y, Z)$ is an observation point; λ is the wavelength of the incident wave; θ is the incident angle between the Z -axis and the incident wave-vector; and φ is the azimuth angle between the X -axis and the plane of incidence.

The amplitude of the incident electric field can be decomposed into TE- and TM component, which means the electric (or magnetic) field is perpendicular to the plane of incidence. To do this, we define two unit vectors \mathbf{e}^{TE} and \mathbf{e}^{TM} that span a plane orthogonal to \mathbf{k}^i . Hence, the amplitude \mathbf{e}^i in (3) is decomposed as

$$\mathbf{e}^i = \mathbf{e}^{\text{TE}} \cos \delta + \mathbf{e}^{\text{TM}} \sin \delta \quad (2)$$

where δ is the polarization angle between \mathbf{e}^i and \mathbf{e}^{TE} as shown in Fig. 1(b).

2.2. Diffracted Wave

We seek for the diffracted fields $\mathbf{E}_\ell(\mathbf{P})$ and $\mathbf{H}_\ell(\mathbf{P})$ in each region, i.e., $\ell = 1, 2, \dots, L+1$. They should satisfy the following requirements:

- (C1) The Helmholtz equations in each region;
- (C2) Radiation conditions: The diffracted waves in V_1 (or V_{L+1}) should propagate or attenuate in the positive (or negative) Z -direction;
- (C3) Periodicity conditions: Each component of the diffracted electric and magnetic field should satisfy

$$f(X + d_X, Y, Z) = \exp(i\alpha d_X) f(X, Y, Z) \quad (3)$$

$$f(X, Y + d_Y, Z) = \exp(i\beta d_Y) f(X, Y, Z) \quad (4)$$

where α and β are the phase constants in X and Y .

- (C4) Boundary conditions: The tangential components of electric and magnetic fields are continuous across the boundaries S_ℓ ($\ell = 1, 2, \dots, L+1$).

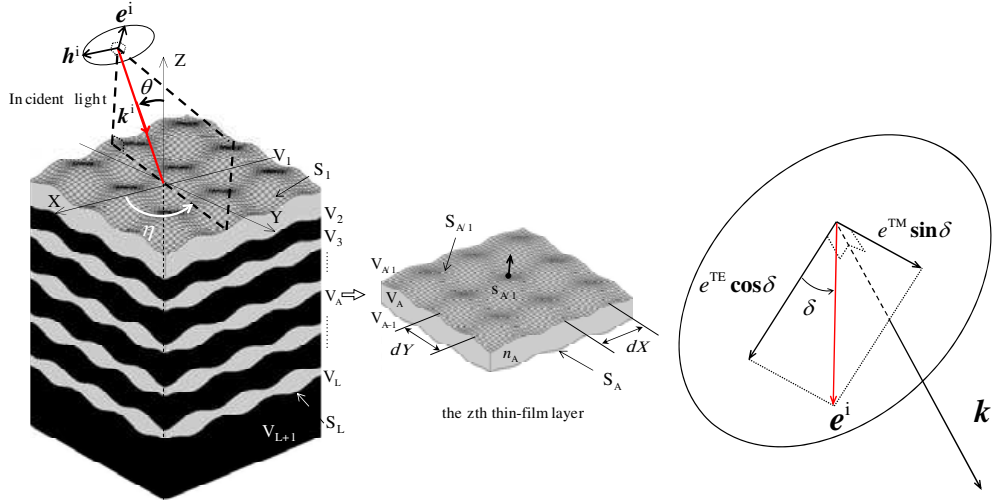


Figure 1: (a) Schematic representation of a multilayered bigrating with an incident light ($V_1: \{\mathbf{P}|Z > S_1(X, Y)\}$, $V_{L+1}: \{\mathbf{P}|Z < S_L(X, Y)\}$); (b) Definition of a polarization angle.

2.3. Method of Solution

We solve the problem above using Yasuura's method of modal expansion [4, 5]. To do this, we first define the sets of modal functions; next we construct approximate solutions in terms of finite modal expansions with unknown coefficients; and, finally we determine the coefficients applying the boundary conditions.

Modal functions: Because the diffracted waves have both TE- and TM-components, we need TE and TM vector modal functions in constructing the solutions. Here we employ the functions derived from the Floquet modes (separated solutions of the Helmholtz equations satisfying the periodicity (C3) and the radiation conditions (C2) if necessary). The modal functions for electric fields for each region are given by

$$\varphi_{\ell mn}^{\text{TE, TM}\pm}(\mathbf{P}) = \mathbf{e}_{\ell mn}^{\text{TE, TM}\pm} \exp(i\mathbf{k}_{\ell mn}^\pm \cdot \mathbf{P}) \quad (5)$$

where, $m, n = 0, \pm 1, \pm 2, \dots$, $\ell = 1, 2, \dots, L+1$, and unit vectors \mathbf{e} in (5) are defined by

$$\mathbf{e}_{\ell mn}^{\text{TE}\pm} = \frac{\mathbf{k}_{\ell mn}^\pm \times \mathbf{i}Z}{|\mathbf{k}_{\ell mn}^\pm \times \mathbf{i}Z|}, \quad \mathbf{e}_{\ell mn}^{\text{TM}\pm} = \frac{\mathbf{e}_{\ell mn}^{\text{TE}\pm} \times \mathbf{k}_{\ell mn}^\pm}{|\mathbf{e}_{\ell mn}^{\text{TE}\pm} \times \mathbf{k}_{\ell mn}^\pm|} \quad (6)$$

and

$$\mathbf{k}_{\ell mn}^\pm = [\alpha_m, \beta_n, \pm\gamma_{\ell mn}], \quad \alpha_m = \alpha + \frac{2m\pi}{d_x}, \quad \beta_n = \beta + \frac{2n\pi}{d_y}, \quad \gamma_{\ell mn} = (n_\ell^2 k^2 - \alpha_m^2 - \beta_n^2)^{1/2} \quad (7)$$

where $\text{Re}(\gamma_{\ell mn}) \geq 0$ and $\text{Im}(\gamma_{\ell mn}) \geq 0$. We use the modal functions defined in equations from (5) to (7) to construct approximations of diffracted electric fields. For the accompanying magnetic fields, we employ

$$\boldsymbol{\psi}_{\ell mn}^{\text{TE,TM}\pm}(\mathbf{P}) = \frac{1}{\omega\mu_0} \mathbf{k}_{\ell mn}^\pm \times \boldsymbol{\varphi}_{\ell mn}^{\text{TE,TM}\pm}(\mathbf{P}). \quad (8)$$

Approximate solutions: To satisfy the radiation condition (C2), the approximate solution in V_1 should have a form of finite linear combination of up-going modal functions with unknown coefficients. Likewise, the solution in V_{L+1} must be a linear combination of down-going modal functions. The solution in V_ℓ , however, must have both up- and down-going waves. To show the travelling direction of a modal function, we use superscripts + and – representing up- and down-going waves. Here, we form approximate solutions for the diffracted electric and magnetic fields in V_ℓ :

$$\begin{aligned} \begin{pmatrix} E_{\ell N}^d \\ H_{\ell N}^d \end{pmatrix}(\mathbf{P}) &= \sum_{m,n=-N}^N A_{\ell mn}^{\text{TE}+}(N) \begin{pmatrix} \varphi_{\ell mn}^{\text{TE}+} \\ \psi_{\ell mn}^{\text{TE}+} \end{pmatrix}(\mathbf{P}) + \sum_{m,n=-N}^N A_{\ell mn}^{\text{TM}+}(N) \begin{pmatrix} \varphi_{\ell mn}^{\text{TM}+} \\ \psi_{\ell mn}^{\text{TM}+} \end{pmatrix}(\mathbf{P}) \\ &+ \sum_{m,n=-N}^N A_{\ell mn}^{\text{TE}-}(N) \begin{pmatrix} \varphi_{\ell mn}^{\text{TE}-} \\ \psi_{\ell mn}^{\text{TE}-} \end{pmatrix}(\mathbf{P}) + \sum_{m,n=-N}^N A_{\ell mn}^{\text{TM}-}(N) \begin{pmatrix} \varphi_{\ell mn}^{\text{TM}-} \\ \psi_{\ell mn}^{\text{TM}-} \end{pmatrix}(\mathbf{P}) \\ &(\ell = 1, 2, \dots, L+1) \end{aligned} \quad (9)$$

where N denotes the number of truncation.

Boundary matching: Because the approximate solutions satisfy the requirements (C1), (C2), and (C3) by definition, the unknown coefficients $A_{\ell mn}^{\text{TE}\pm}(N)$ and $A_{\ell mn}^{\text{TM}\pm}(N)$ are determined such that the solutions satisfy the boundary conditions (C4) in an approximate sense. In the Yasuura's method [4], the least-squares method is employed to fit the solution to the boundary conditions. That is, we find the coefficients that minimize the weighted mean-square error by

$$\begin{aligned} I_N &= \int_{S'_\ell} \left| \mathbf{v} \times [\mathbf{E}_{1N}^d + \mathbf{E}^i - \mathbf{E}_{2N}^d](s_1) \right|^2 \mathbf{d}s_1 + |\Gamma_1|^2 \int_{S'_\ell} \left| \mathbf{v} \times [\mathbf{H}_{1N}^d + \mathbf{H}^i - \mathbf{H}_{2N}^d](s_1) \right|^2 \mathbf{d}s_1 \\ &+ \sum_{\ell=2}^L \left\{ \int_{S'_\ell} \left| \mathbf{v} \times [\mathbf{E}_{\ell N}^d - \mathbf{E}_{\ell+1,N}^d](s_\ell) \right|^2 \mathbf{d}s_\ell + |\Gamma_\ell|^2 \int_{S'_\ell} \left| \mathbf{v} \times [\mathbf{H}_{\ell N}^d - \mathbf{H}_{\ell+1,N}^d](s_\ell) \right|^2 \mathbf{d}s_\ell \right\} \end{aligned} \quad (10)$$

where S'_ℓ denotes one-period cells of the interface S_ℓ , Γ_ℓ is the intrinsic impedance of the medium in V_ℓ and \mathbf{v} is a unit normal vector of each boundary.

To solve the least-squares problem on a computer, we need a discretized form of the problem. We first discretize the weighted mean-square error I_N by applying a two-dimensional trapezoidal rule where the number of sampling points is chosen as $2(2N+1)$ [5, 6]. We then employ orthogonal decomposition methods [singular-value decomposition (SVD) and QR decomposition (QRD)] in solving the discretized problem [6].

3. NUMERICAL RESULTS

The multilayered bigrating is composed of three layers: Ag/SiO₂/Ag. The incident light is a TM-polarized plane wave with a 650 nm wavelength. The relative refractive index of vacuum is 1, $n_{\text{Ag}} = 0.07 + 4.2i$ and $n_{\text{SiO}_2} = 1.5$. The periods are set to be $d_x = d_y = 556$ nm. We consider three types of grating with different thickness pairs of each region: (A) $e_{\text{Ag}} = e_{\text{SiO}_2} = 27.8$ nm; (B) $e_{\text{Ag}} = 27.8$ nm, $e_{\text{SiO}_2} = 278$ nm; and (C) $e_{\text{Ag}} = 278$ nm $e_{\text{SiO}_2} = 27.8$ nm. We show the diffraction efficiency and field distributions of these gratings below.

Figure 2 shows the (0, 0)-th order reflection and transmission efficiency as functions of the incident angle θ for the three types of grating with the azimuth angle is set to be $\varphi = 45^\circ$.

Five dips are observed on the reflection curves throughout Figs. 2(a)–2(c). In type (A) shown in Fig. 2(a), two dips (dip 1 at $\theta = 10.6^\circ$ and dip 2 at $\theta = 12.5^\circ$) are observed; at the same points the transmission efficiency has small peaks. This shows that the plasmon surface wave is excited on the four surfaces of Ag films; and the surface wave at the bottom surface excites a propagating mode in V_5 . These surface waves are coupled modes SRSP or LRSP [1].

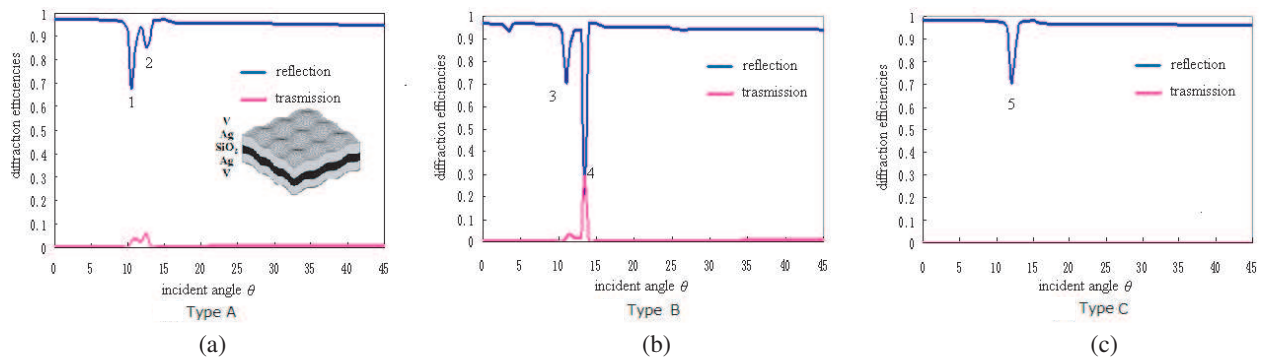


Figure 2: The $(0, 0)$ -th order reflection and transmission efficiency for 3-layered doubly periodic gratings (a) $e_{\text{Ag}} = e_{\text{SiO}_2} = 27.8$ nm; (b) $e_{\text{Ag}} = 27.8$ nm, $e_{\text{SiO}_2} = 278$ nm; and (c) $e_{\text{Ag}} = 278$ nm, $e_{\text{SiO}_2} = 27.8$ nm.

For type (B) shown in Fig. 2(b), two dips (dip 3 at $\theta = 11.1^\circ$ and dip 4 at $\theta = 13.5^\circ$) are observed on reflection curve and the transmission coefficient increases at the same time. Reflection at dip 4 is much lower than that of dips 1 and 2 accompanying change of the thickness of SiO_2 . The coupled plasmon modes are resulted by resonance waves excited at four surfaces [1].

In type (C) shown in Fig. 2(c), only one dip (dip 5 at $\theta = 12.0^\circ$) is observed on reflection curve and no transmission can be seen. This shows excitation of SISP [1].

Next, we investigated the field distributions of the total electric field E^{total} and the TM component of the $(0, 0)$ th-order diffracted electric field $E_{\ell(0,0)}^{\text{TM}}$ in the vicinity of the SiO_2 film. The magnitude of E^{total} and $E_{\ell(0,0)}^{\text{TM}}$ ($\ell = 1, 2, \dots, 5$) along the Z -axis are plotted in Fig. 3 where $\theta = 0^\circ$ and $e_{\text{SiO}_2} = 166.8$ nm. We observe in the figure that the field distributions of E^{total} inside the SiO_2 film indicates a standing wave pattern corresponding to the normal mode of a onedimensional cavity resonator, and that the distribution is almost close to that of $E_{3(0,0)}^{\text{TM}}$. We think that the field distribution is associated with resonance of the $(0, 0)$ th-order diffracted wave $E_{3(0,0)}^{\text{TM}}$ in the SiO_2 film sandwiched by a silver film grating.

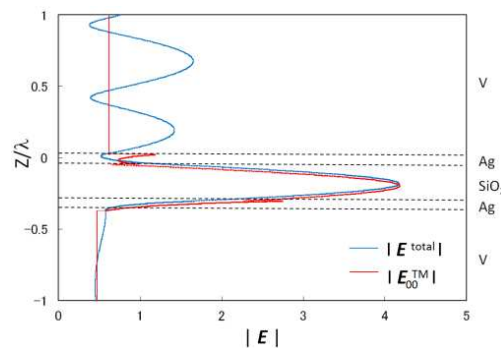


Figure 3: Standing wave pattern of the electric filed in the SiO_2 film.

4. CONCLUSIONS

We solved the problems for 3-layered bigratings. By calculating the diffraction efficiency and field distributions, we observed: (1) excitation of a SISP mode at the lit surface of the 1st Ag layer with strong field enhancement for a thickenough Ag layer case; (2) excitation of coupled SPR modes (SRSP or LRSP) at each surface between vacuum and Ag layers with strong field enhancements for thin enough Ag layer cases no matter with the thickness of SiO_2 layers; (3) standing wave pattern of the electric filed in the SiO_2 film. The coupled plasmon modes were resulted by the resonance waves excited on four surfaces in these cases We are planning to study the nature of the plasmon surface waves excited on the multilayered thin metal/dielectric gratings.

REFERENCES

1. Suyama, T., A. Matsushima, Y. Okuno, and T. Matsuda, “Resonant excitation of plasmons in bigrating,” *Plasmonics — Principles and Applications*, K. Kim (Ed.), Chap. 12, 313–334, INTECH, Rijeka, 2012.
2. Hibbins, A. P., W. A. Murray, J. Tyler, S. Wedge, W. L. Barnes, and J. R. Sambles, “Resonant absorption of electromagnetic fields by surface plasmons buried in a multilayered plasmonic nanostructure,” *Phys. Rev. B*, Vol. 74, No. 073408, 2006.
3. Ahn, J. H., T. Y. Seong, W. M. Kim, T. S. Lee, I. Kim, and K. S. Lee, “Fiber-optic waveguide coupled surface plasmon resonance sensor,” *Optics Express*, Vol. 20, No. 19, 21729–21738, 2012.
4. Okuno, Y., “Mode-matching Method,” *Analysis Methods for Electromagnetic Wave Problems*, E. Yamashita (Ed.), 107–138, Artech House, Boston, 1990
5. Yasuura, K. and T. Itakura, “Approximation method for wave functions (I), (II), and (III),” *Kyushu Univ. Tech. Rep.*, Vol. 38, 72–77, 1965; Vol. 38, 378–385, 1966; Vol. 39, 51–56, 1966.
6. Matsuda, T. and Y. Okuno, “Numerical evaluation of plane-wave diffraction by a doubly periodic grating,” *Radio Sci.*, Vol. 31, 1791–1798, 1996.

RCS Computation of 3D-wake Vortex Using Method of Moments

Venkat Prasad Padhy¹, N. Balakrishnan¹, and P. Srinivasa Murthy²

¹SERC, Indian Institute of Science, Bangalore 560012, India

²Aeronautical Development Establishment (ADE), Bangalore 60075, India

Abstract— An efficient and accurate 3D full wave numerical solution model for computing the radar cross section (RCS) of wake-vortex is presented, by solving Euler equation to compute the pressure in the aircraft wake region by computational fluid dynamics model and parallel integral equation (IE), based on method of moments (MoM) is used to compute the volume polarization currents, under the plane wave incidence. Then the currents are used to compute far-field from the vortex region.

1. INTRODUCTION

The scattering of radio waves in the atmosphere has drawn attention of many researchers in recent times, particularly in the areas of radio acoustic sounding system (RASS) [1–5] and wake-vortex studies [4–9]. In clear air, the radar reflectivity of wake vortex is mainly caused by Bragg scattering from the refractive index variations. Since wake turbulence is inevitable to all flying aircrafts, remote detection and tracking of wake vortices is important for hazard avoidance especially near airports during landing and take-off phases. Aircrafts that fly through these hazardous vortices experience sudden induced roll. In order to avoid the wake vortex encountering hazard, efforts have been made in the past to monitor and detect wake vortices, and the existing technologies include lidar, sodar and radar. Among them, the radar detection is considered to be the potential candidate for its long working range and under different weather conditions [10, 11].

In the past studies, aircraft wake is evolved by known vortex model derived from experiment based on aircraft geometry and inertial properties [6]. Also vortex wake is based on wing alone model; body and tail vortex effect are not considered and these models are confined to 2D cross sections in the wake region. And the RCS is computed using Born approximation with highly oscillatory integrand, with the aid of quadrature methods. The validity and applicability of Born approximation is well studied in the low frequency regime, and more recently even at high frequency regime [7].

However, there is still a need to improve the accuracy and efficiency of wake vortex scattering problem, which demands for a rigorous full wave solution method. Owing to huge disparity in EM and acoustic frequencies, a quasi-stationary approximation using an adiabatic approach enables EM propagation at different instants of acoustic-flow cycle to be posed as scattering problem of a frozen inhomogeneous media [8], which then can be effectively solved through integral equation using MoM.

2. FORMULATION

The Euler equations which are derived from conservation laws of mass, momentum and energy applicable for compressible inviscid flows are expressed in vector form in Cartesian coordinate system as follows [10]:

$$\frac{\partial \mathbf{m}}{\partial t} + \frac{\partial \mathbf{f}_x}{\partial x} + \frac{\partial \mathbf{f}_y}{\partial y} + \frac{\partial \mathbf{f}_z}{\partial z} = 0 \quad (1)$$

$$\mathbf{m} = \begin{pmatrix} \rho \\ \rho u \\ \rho v \\ \rho w \\ E \end{pmatrix}; \quad \mathbf{f}_x = \begin{pmatrix} \rho u \\ p + \rho u^2 \\ \rho uv \\ \rho uw \\ u(E + p) \end{pmatrix}; \quad \mathbf{f}_y = \begin{pmatrix} \rho v \\ \rho uv \\ p + \rho v^2 \\ \rho vw \\ v(E + p) \end{pmatrix}; \quad \mathbf{f}_z = \begin{pmatrix} \rho w \\ \rho vw \\ p + \rho w^2 \\ w(E + p) \end{pmatrix} \quad (2)$$

There are five equations and six unknowns. To close the system one more equation is required which is supplemented by equation of state:

$$p = \rho(\gamma - 1)e \quad (3)$$

Where \mathbf{m} is a vector of conservative variables, which are to be computed, \mathbf{f}_x , \mathbf{f}_y and \mathbf{f}_z are convective fluxes in x , y and z directions respectively, p is the pressure, ρ is the density, γ is the adiabatic

index and e is the internal energy per unit mass of the fluid, also we have total energy per unit volume, E as

$$E = \rho e + \frac{1}{2}\rho(u^2 + v^2 + w^2) \quad (4)$$

Let V be the inhomogeneous dielectric volume with relative permittivity $\epsilon_r(\vec{r})$ and relative permeability $\mu_r(\vec{r}) = 1$. The permittivity and permeability of free space are ϵ_0 and μ_0 respectively. Let \vec{E}^i be the incident field and \vec{E}^s be the scattered field; then the total field \vec{E} can be expressed as the sum of \vec{E}^i and \vec{E}^s [14]

$$\vec{E}(\vec{r}) = \vec{E}^i(\vec{r}) + \vec{E}^s(\vec{r}) \quad (5)$$

The scattered field due to the volume polarization current $\vec{J}_v(\vec{r}) = j\omega(\epsilon(\vec{r}) - \epsilon_0)\vec{E}(\vec{r})$ in V can be written as

$$\vec{E}(\vec{r}) = \vec{E}^i(\vec{r}) + j\omega\mu_0 \int_V \vec{G}(\vec{r}, \vec{r}') \cdot \vec{J}(\vec{r}') dv' \quad (6)$$

$$\text{where } \vec{G}(\vec{r}, \vec{r}') = \left(\vec{\bar{I}} + \frac{1}{k_0^2} \nabla \nabla \right) \cdot G(\vec{r}, \vec{r}') \quad (7)$$

$\vec{\bar{I}}$ is a unit dyad and $G(\vec{r}, \vec{r}')$ is the free space Green's function, with $k_0 = \omega\sqrt{\mu_0\epsilon_0} = \frac{2\pi}{\lambda_0}$.

The use of method of moments requires the total field $\vec{E}(\vec{r})$ or unknown electric current density $\vec{J}_v(\vec{r})$ inside domain to be expanded in terms of a set of N orthogonal basis functions \vec{f}_n which reduce Equation (6) into system of linear equations, of the form [15, 16]

$$\mathbf{ZI} = \mathbf{V} \quad (8)$$

3. NUMERICAL RESULTS

In this section, we present numerical results of dielectric constant variation due to pressure in the wake from a typical aircraft model of wing span 2.16 m and fuselage 2.5 m, and hence RCS computation. The flow parameters of density, pressure and velocity, around the aircraft are obtained by solving for inviscid compressible flow by a finite volume formulation using ANSYS FLUENT solver. The rectangular parallelepiped flow domain with embedded aircraft is discretized with unstructured tetrahedral mesh.

The case analysed is for the landing configuration with velocity 133 m/s, angle of attack of 10 degrees, so the boundary condition set at inlet is velocity prescribed at 133 m/s with $\alpha = 10$ degrees. Outlet Boundary condition is set as pressure boundary conditions and velocity is computed. Other four boundaries, two sides and top and bottom boundaries are set as characteristic boundary

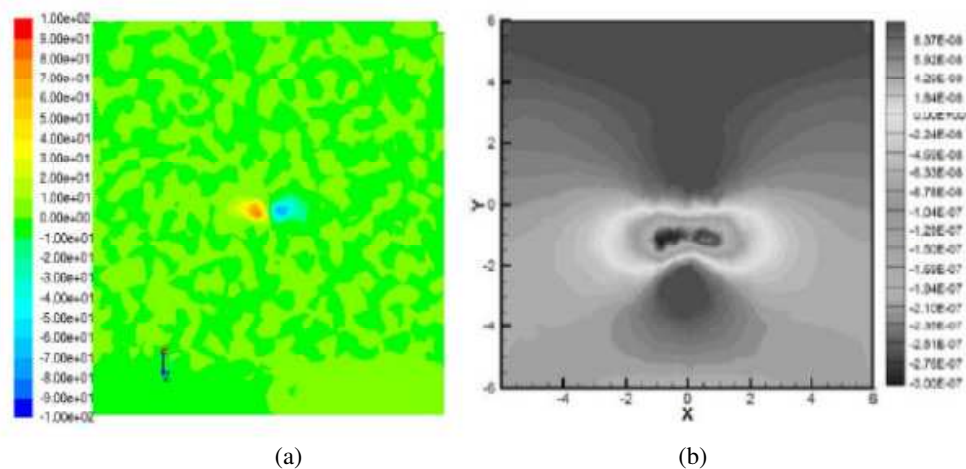


Figure 1: (a) X-Vorticity contour from flow solver. (b) Dielectric Constant variation due to pressure.

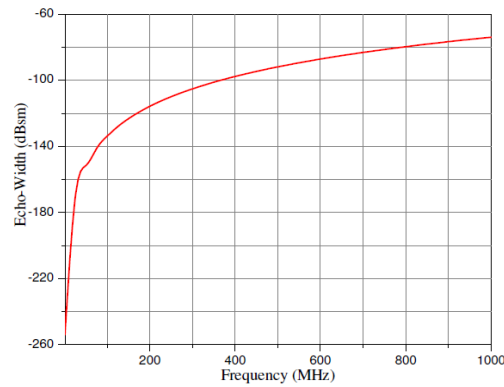


Figure 2: Echo width from the 2D wake profile

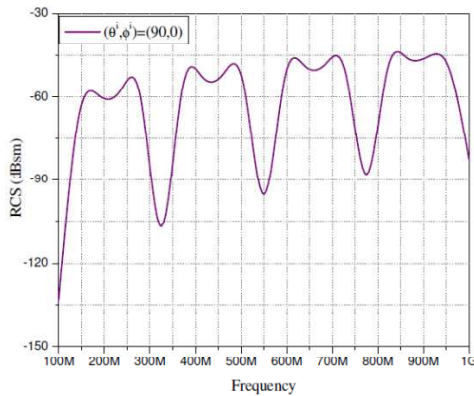


Figure 3: RCS vortex core of size 0.3 m × 6 m × 6 m.

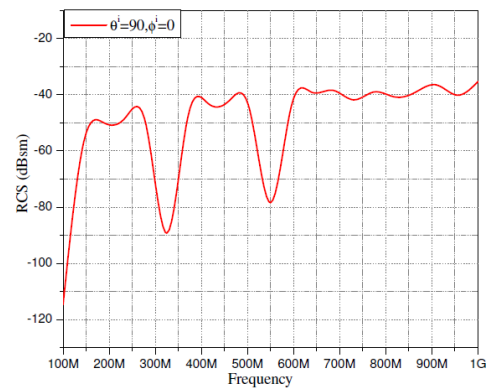


Figure 4: RCS from vortex core of size 0.9 m × 6 m × 6 m.

conditions which are nothing but inflow/outflow boundary condition depending on direction of characteristic waves.

The link between Maxwell and Euler equations is the relationship between the pressure perturbation and the permittivity fluctuations, i.e., the dielectric constant in the integral equation is function of pressure in the wake region. The pressure obtained from the flow solver is used to compute the dielectric constant by using [4]

$$\epsilon_r = 1 + 1.552 \times 10^{-6} P/T \quad (9)$$

And further interpolated over the MoM solver domain. The X-vorticity contour and dielectric constant variation due to pressure are shown in Figure 1. The 2D computational domain is of size 12 m × 12 m, discretized with respect to free space wavelength at highest frequency resulting into 160000 square grids. RCS of two 3D regions about the vortex core viz., near the tail of aircraft 0.3 m × 6 m × 6 m and the other far from tail 0.9 m × 6 m × 6 m are computed. The volume is discretized with cubical grids of equal volume. 8 cells per wavelength, with respect to the highest frequency of operation considered, resulting into 440000, 675000 grids and 1.32, 2.025 million unknowns. In both the cases pulse basis and point matching technique are used to convert the integral equations to the system of linear equations. The system of linear equations is solved using a parallel BiCG solver.

4. CONCLUSION

In the present work aircraft wake is computed by solving 3D Euler equations using ANSYS FLUENT solver with FVM method. Complete aircraft flow field is computed including vortex generated by all the components such as body, wing and tail units. CFD based wake flow computation is more accurate than the vortex model based computation. Also, the IE solution using MoM for RCS computation is a full wave method. Thus, for both flow as well as EM fields, accurate methodologies have been employed, enabling the solution to be more accurate than when models or approximations are used for the governing equations.

REFERENCES

1. Marshall, J. M., A. M. Peterson, and A. A. Barnes, “Combined radar-acoustic sounding system,” *Applied Optics*, Vol. 11, No. 1, 108–112, 1972.
2. May, P. T., R. G. Strauch, K. P. Moran, and W. L. Ecklund, “Temperature sounding by RASS with wind profiler radars: A preliminary study,” *IEEE Transactions on Geoscience and Remote Sensing*, Vol. 28, No. 1, 19–27, 1990.
3. Andreas, T., “Electro-acoustic scattering in an atmosphere with wind,” *IEEE Transactions on Antennas and Propagation*, Vol. 51, No. 6, 1242–1250, 2003.
4. Said, B., et al., “Two-dimensional simulations of wake vortex detection using RASS,” *AIAA Journal*, Vol. 40, No. 11, 2247–2256, 2002.
5. Marshall, R. E., et al., “Wing tip generated wake vortices as radar targets,” *IEEE AES Systems Magazine*, December 1996.
6. Shariff, K. and A. Wray, “Analysis of the radar reflectivity of aircraft vortex wakes,” *Journal of Fluid Mechanics*, Vol. 463, 121–161, 2002.
7. Li, J., X. Wang, and T. Wang, “Modeling of aircraft wake vortices’ dielectric constant distribution,” *IEEE Transactions on Aerospace and Electronics Systems*, Vol. 47, No. 2, 820–831, April 2011.
8. Saleh, B. E. A. and M. C. Teich, *Fundamentals of Photonics*, BJohn Wiley & Sons, Inc., 2009.
9. Barbaresco, F., “Airport radar monitoring of wake vortex in all weather conditions,” *Proceedings 7th European Radar Conference*, 85–88, 2010.
10. Danielle, V.-J., D. Kahina, and B. Frédéric, “Model for the calculation of the radar cross section of wake vortices of take-off and landing airplanes,” *9th European Radar Conference EuRAD*, 2012.
11. Liu, Z., et al., “Modeling the radar signature of raindrops in aircraft wake vortices,” *Journal of Atmospheric and Oceanic Technology*, Vol. 30, 470–484, 2013.
12. Wang, X., et al., “Temporal evolution of the RCS of aircraft wake vortices,” *Aerospace Science and Technology*, Vol. 24, 204–208, 2013.
13. Anderson, J. D., *Computational Fluid Dynamics, The Basics With Applications*.
14. Harrington, R. F., *Field computation by Moment Methods*, IEEE Press Series.
15. Richmond, J. H., “TE-wave scattering by a dielectric cylinder of arbitrary cross-section shape,” *IEEE Transactions on Antennas and Propagation*, Vol. 14, No. 4, 460–464, 1966.
16. Wang, J. J. H., *Generalized Moment Methods in Electromagnetics: Formulation and Computer Solution of Integral Equations*, John Willey, 1991.

A Compact Diplexer Composed of Quarter-wavelength Resonators for Ultra-wideband (UWB) System

Kai Wang¹, Zai-Cheng Guo¹, Yu-Fa Zheng¹, Jing-Yu Lin², Sai Wai Wong¹, and Qing-Xin Chu¹

¹School of Electronic and Information Engineering, South China University of Technology
Guangzhou, Guangdong 510641, China

²School of Information Science and Technology, Southwest Jiaotong University
Chengdu, Sichuan 611756, China

Abstract— A compact diplexer composed of quarter-wavelength resonators for ultra-wideband (UWB) system is proposed and implemented in this paper. The microstrip diplexer is mainly composed of two bandpass filters, which operates at 3.1–5.0 GHz (namely L-BPF) and 6.2–10.1 GHz (namely H-BPF), respectively. Each filter is composed of three shorted-circuit quarter-wavelength resonators. After optimizing the performance, the highest return loss of each filter in the desired passband is -14 dB and -16.8 dB, respectively. For both filters, the insertion loss is below 1 dB and the wide stopband rejection is greater than 20 dB. The isolation between two channels is more than 25 dB. The design concept is proposed in detail and has been verified by the experimental results of a fabricated diplexer. The size is compact with overall dimensions of $19.5 \times 19 \times 0.8$ mm³.

1. INTRODUCTION

In the existing communication systems, diplexer is one of the essential component building blocks that is widely used in transceiver and mixer applications to isolate two or more frequencies [1, 2]. Diplexers are three terminal devices that take two or more frequencies into one port and separate them to two output ports. Diplexers can be constructed by different filter configurations such as lowpass and highpass filters, two bandpass filters, and bandpass and bandstop filters [3]. In the composition of filters, resonator cell is the key part. In the past, numerous kinds of resonator cell have been proposed, such as open-loop ring resonator [4], stepped impedance coupled-line resonator [5], open-circuited periodic stubs [6], hairpin line resonator [7]. In [8], quarter-wavelength resonator is proposed to construct interdigital bandpass filter. In this way, quarter-wavelength resonator can be used to design diplexers with good performance.

On the other hand, to avoid the frequency use of 5–6 GHz for IEEE 802.11a wireless networks (WLANs), the direct sequence ultra-wideband (DS-UWB) specifications for wireless personal area network (WPANs) need to divide into a low band of 3.1–5.0 GHz and a high band of 6.1–10 GHz. Thus, designing diplexers satisfy the desired operation band is necessary.

In this paper, a compact diplexer composed of quarter-wavelength resonators is introduced. The diplexer is constructed by two bandpass filters and each bandpass filter is composed of three identical quarter-wavelength resonators. Each resonator is short-circuited at one end and open-circuited at the other end. The advantages of the diplexer is compact, low insertion loss, good out-of-band performance and covering the desired operation band in ultra-wideband (UWB) systems.

2. DESIGN OF DIPLEXER

Figure 1 shows the structure of the design diplexer. The primary structures are lower passband filter (L-BPF) operating at 3.1–5.0 GHz and higher passband filter (H-BPF) operating at 6.2–10.1 GHz, respectively. Each BPF is composed of three identical quarter-wavelength resonators (with respect to each central frequency at 4 GHz and 8 GHz, respectively). Each resonator is short-circuited at one end and open-circuited at the other end. Port 1 is the input port with impedance of 50Ω and the microstrip feed line is coupled to two resonators tightly. Each resonator is coupled tightly to each other to form strong coupling and compact structure. Two structure parameters, spacing (s) between resonators and gap (g) between I/O ports and resonator are extracted to control coupling coefficient and quality factor, respectively. The diplexer is designed on PCB with dielectric constant of 2.55, substrate thickness of 0.8 mm and loss tangent of 0.003.

An electromagnetic (EM) simulator Agilent Technologies' 2013 Advance Design System (ADS) is used to extract coupling coefficient (k) between two resonators. The coupling coefficient (k) is controlled by the resonator spacing (s) as shown in Fig. 2(a). The coupling between resonators can

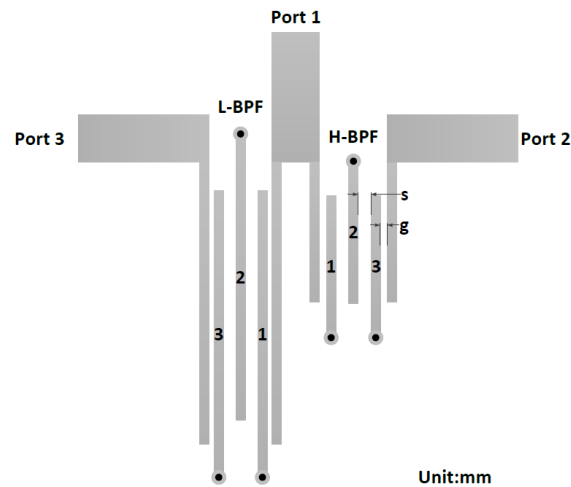
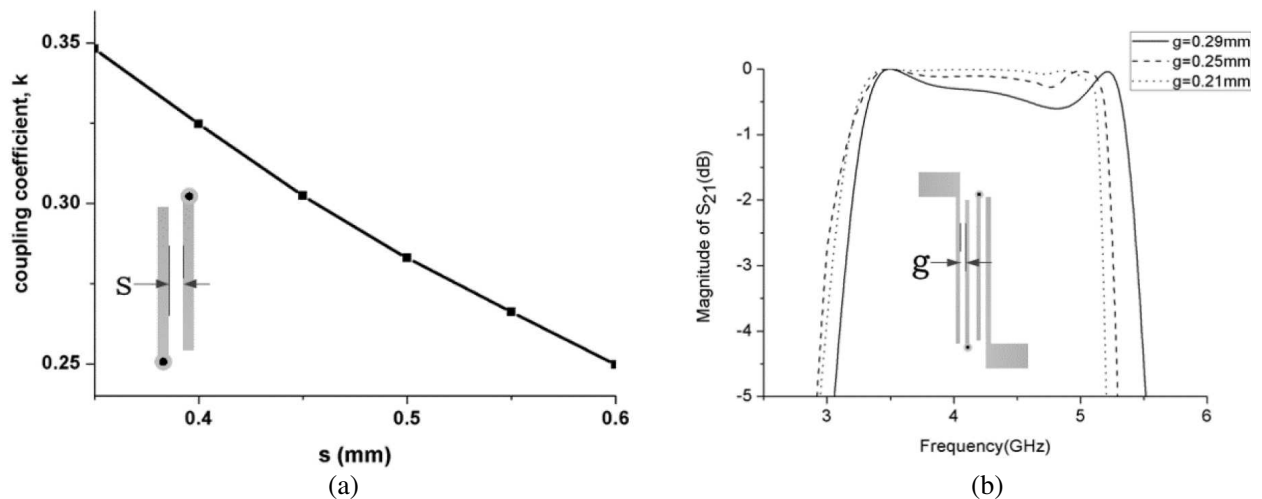


Figure 1: Practical layout of the design diplexer.

be specified by the two dominant resonant modes, which are split off from the resonance condition. The simulated coupling coefficient $K_{i,i+1}$ between the resonator i and $i+1$ ($i = 1, 2$) as functions of spacing (s) is calculated as [8]

$$K_{i,i+1} = \frac{f_H^2 - f_L^2}{f_H^2 + f_L^2} \quad (1)$$

where the f_H is the higher frequency of the two resonant modes, and f_L be the lower one. It is noted that K_{12} and K_{23} are all subjected to an offset s . When s value is reducing, the coupling coefficient would be increased, namely the two resonant modes can be largely separated.

Figure 2: (a) Calculated coupling coefficient between resonators with different spacing, (b) the simulated frequency response with different gaps between the resonator and the I/O ports ($s = 0.43$ mm).

On the other hand, to achieve the balanced passband behavior, namely without ripple in the passband, a strong coupling level between I/O ports and the resonators is needed. As shown in Fig. 2(b), the simulated performances of a pair of resonators are discussed as functions of different gap (g). As the spacing (s) is fixed at 0.43 mm and the gap is reduced, the coupling strength would be enhanced. The smaller the gap (g), the better the passband performance. When the gap (g) is reduced to 0.21 mm, the unbalanced passband level Δ_{dB} is less than 0.1 dB ($\Delta_{dB} = |S_{21(\max)}| - |S_{21(\min)}|$) in the passband), this implies a low passband ripple. Moreover, such small gap ($g = 0.21$ mm) is still available using the conventional carving machine, without using the expensive lithography process. Therefore, gap of $g = 0.21$ mm would be optimum design condition for both H-BPF and L-BPF in this paper.

The three-pole ($n = 3$) Chebyshev low pass prototype with a passband ripple of 3 dB is chosen for H-BPF and L-BPH, both with a FBW of 50% at center frequency 4 GHz and 8 GHz, respectively. The lowpass prototype parameters are $g_0 = g_4 = 1$, $g_1 = g_3 = 3.3487$, $g_2 = 0.7117$. Thus, theoretical coupling coefficient $M_{i,i+1}$ is obtained as $M_{1,2} = M_{2,3} = 0.324$, calculated by using [8]

$$M_{i,i+1} = \frac{FBW}{\sqrt{g_i g_{i+1}}} \quad (2)$$

According to Fig. 2(a), when the coupling coefficient is 0.324, then the spacing (s) is about 0.45 mm, so the theoretical spacing $s_{i,i+1}$ between resonator i and $i + 1$ is $s_{1,2} = s_{2,3} = 0.45$ mm. After optimizing the structure, the final design spacing is $s = 0.54$ mm for L-BPF and $s = 0.56$ mm for H-BPF, respectively. Moreover, the length of each resonator is 11.9 mm for L-BPF and 5.8 mm for H-BPF, respectively. The design input/output impedance are all 50Ω and the radius of via is 0.3 mm. The size is compact with overall dimensions of $19.5 \times 19 \times 0.8$ mm³.

3. SIMULATION AND EXPERIMENT RESULTS

The microstrip diplexer was fabricated using the carving machine and then measured by an Advantest R3770 vector network analyzer over the frequency range from 0 to 11 GHz. Figs. 3(a)–(d) show the simulated and measured results of the diplexer. As expected, there are three modes in each passband and the measured results show a good agreement with the simulated result. As shown in Fig. 3(c), for the lower passband filter, the center frequency is 4.1 GHz and 3 dB bandwidth is 3.17–5.06 GHz (FBW = 46.1%). The maximum return loss in the passband is -14 dB for the

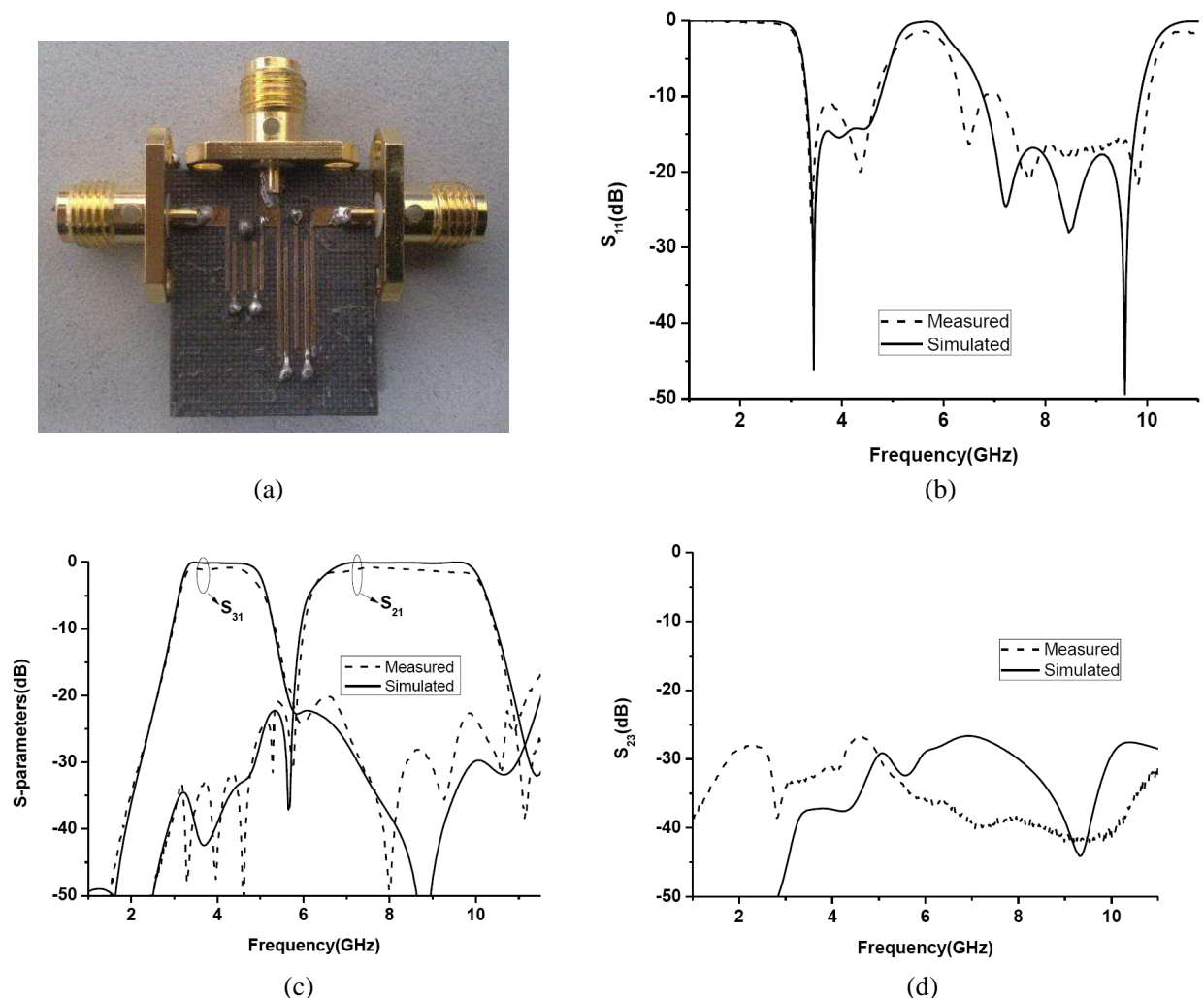


Figure 3: Measured and simulated results of the diplexer: (a) picture of fabricated diplexer, (b) S_{11} , (c) S_{21} and S_{31} , (d) S_{23} .

simulated result and -10.8 dB for the measured result, respectively. The measured insertion loss S_{21} is less than -1.2 dB and the wide stopband rejection is greater than 20 dB from 5.6–11 GHz. For the lower passband filter, the center frequency is 8.1 GHz and 3 dB bandwidth is 6.2–10.1 GHz (FBW = 48.1%), the maximum return loss in the passband is -16.8 dB for the simulated result and -9.4 dB for the measured result, respectively. The measured insertion loss S_{21} is less than -1.5 dB and the wide stopband rejection is greater than 20 dB from 1–5.8 GHz. From Fig. 3(d), it can be observed that the isolation between two channels is more than 25 dB. The measured results verified the proposed design concept. In addition, the overall dimension is $19.5 \times 19 \times 0.8$ mm³, which is compact and low cost to fabricate.

ACKNOWLEDGMENT

This work is supported by the National Natural Science Foundation of China (61101017), Program for New Century Excellent Talents in University (NCET-13-0214), the State Key Laboratory of Millimeter Waves (K201327) Southeast University and The Fundamental Research Funds for the Central Universities (2014ZZ0029).

REFERENCES

1. Yun, T.-Y., C. Wang, P. Zepeda, C. T. Rodenbeck, M. R. Coutant, M.-Y. Li, and K. Chang, "A 10- to 21 GHz, low-cost, multifrequency, and full-duplex phased-array antenna system," *IEEE Trans. Antennas Propaga.*, Vol. 50, No. 5, 641–650, May 2002.
2. Shimozawa, M., T. Katsura, N. Suematsu, K. Itoh, Y. Isota, and O. Ishida, "A passive-type even harmonic quadrature mixer using simplefilter configuration for direct conversion receiver," *IEEE MTT-S Int Microwave Symp.*, 11–16, Boston, MA, 2000.
3. Weber, R. J., *Introduction to Microwave Circuits Radio Frequency and Design Applications*, 248–252, IEEE Press, New York, 2001.
4. Hsieh, L.-H. and K. Chang, "New microstrip diplexer using open-loop ring resonators with two transmission zeros," *Microw. Opt. Technolo. Lett.*, Vol. 44, No. 5, 396–398, Mar. 5, 2005.
5. Srisathit, S., S. Patisang, R. Phromloungsri, S. Bunnjaweht, S. Kosulvit, and M. Chongcheawchamnan, "High isolation and compact size microstriphairpin line diplexer," *IEEE Microw. Wireless Compon. Lett.*, Vol. 15, No. 2, 101–103, Feb. 2005.
6. Strassner, B. and K. Chang, "Wide-band low-loss high-isolation microstripperiodic-stub diplexer for multiple-frequency applications," *IEEE Trans. Microw. Theory Tech.*, Vol. 49, No. 10, 1818–1820, Oct. 2001.
7. Weng, M. H., C. Y. Hung, and Y.-K. Su, "A Hairpin line diplexer for direct sequence ultra-wideband wireless communications," *IEEE Microw. Wireless Compon. Lett.*, Vol. 17, No. 7, 519–521, Jul. 2007.
8. Hong, J. S. and M. J. Lancaster, *Microstrip Filters for RF/Microwave Application*, Wiley, New York, 2001.

Design of High Isolation Diplexer with Source-load Coupling

Fu-Chang Chen, Hao-Tao Hu, Fu-Xiang Guo, and Qing-Xin Chu

School of Electronic and Information Engineering, South China University of Technology
Guangzhou, Guangdong 510640, China

Abstract— A microstrip diplexer with very high isolation is proposed. The diplexer comprises two third-order CT filters and a connecting line between them. The improved CT filter has three adjustable transmission zeros through leading in the coupling coefficient between the source and load. By locating the transmission zero of one channel at the passband of the other channel, very high isolation of the diplexer can be achieved. Good agreements are also achieved between measurement and simulation.

1. INTRODUCTION

Planar diplexer with compact circuit size, low insertion loss, high isolation and controllable channel frequencies is an important component in wireless communication systems. For the design of planar diplexers, the traditional approach is to design two different filters individually and then to design the matching network. The most straightforward method is to combine two bandpass filters with a T -junction Y -junction [1, 2]. The method, which features one filter an open-circuited line shunted to the other filter at the frequency of the latter, is adopted to reduce the mutual loading effect between the filters. In [3–5], the common resonator technology is proposed to remove the input junction in the diplexer designs and reduces the size to a great degree. Some novel diplexer designs without distribution networks have appeared in the recent literatures [6–9]. A new topology of the diplexer with common port directly connected to two filters was proposed and synthesized in [6]. A design procedure for coupled resonator diplexers that does not employ any external junctions was also proposed in [7].

In this paper we presented a novel type of microstrip diplexer structure with center frequencies at 1.8 and 2.3 GHz. High isolation large than 37 dB from 1 to 5 GHz is obtained. Two cascaded triplet (CT) filters are employed in parallel configurations to obtain the dual-channel response, and the center frequency and bandwidth of each passband can be controlled independently. The source-load coupling is also introduced to provide two additional transmission zeros, which improve the selectivity greatly.

2. DIPLEXER DESIGN

Figure 1 shows the structure of the proposed diplexer using quarter-wavelength resonators. The proposed diplexer consists of two cascaded triplet (CT) unit. Three quarter-wavelength resonators are combined together to form a typical CT unit. Some resonators are folded to reduce the size. The via holes that connect the microstrip line and the ground plane are denoted by circles. To improve the selectivity of the diplexer, the coupling between the source and load is introduced to add two

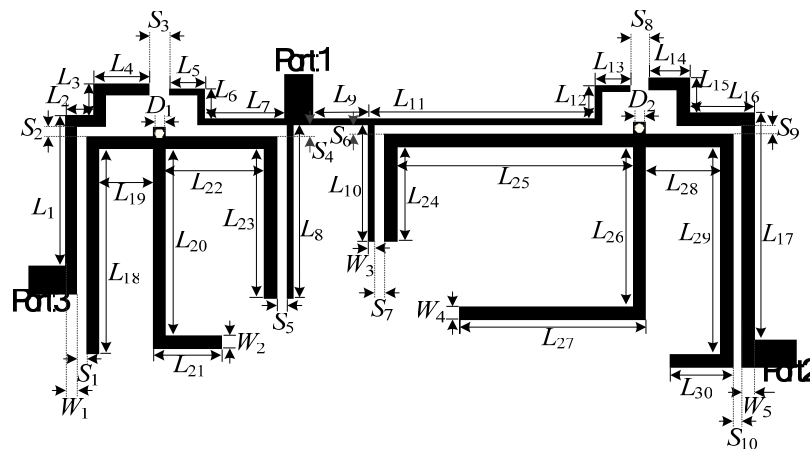


Figure 1: Layout of the proposed diplexer filter.

transmission zeros. Figure 2 shows the coupling diagram of the dual-band filter, which contain two CT filter with source-load coupling. Both the direct couplings between the adjacent resonators and cross coupling between the first and third resonators are magnetic, so the filter presented in this paper is a special case of CT filter. The cross-coupling is inductive, so one transmission zero can only be located at the upper stopband of each channel.

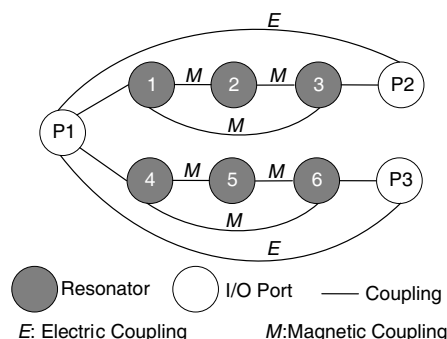


Figure 2: Coupling and routing scheme of the diplexer.

The proposed dual-band filter is to be designed on a substrate with dielectric constant = 2.55, loss tangent = 0.0029, and thickness $h = 0.8$ mm. In this study, IE3D is employed for simulating and optimizing the filter design. A trial diplexer centering at 1.8 and 2.3 GHz is design for demonstration. Figure 3 shows the simulated insertion loss responses under different situations. Each passband can be designed separately. To obtain a dual-channel response, a novel matching network with four open-circuited stubs is designed.

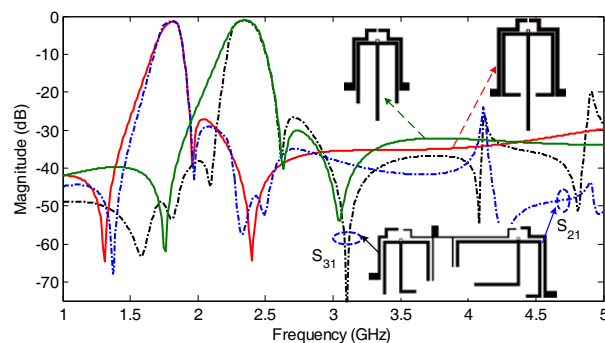


Figure 3: Diplexer design based on CT bandpass filters.

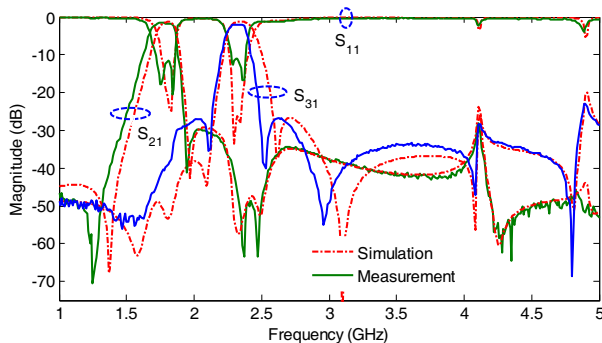


Figure 4: Simulated and measured reflection and transmission coefficients of the designed diplexer.

3. SIMULATION AND MEASUREMENT RESULTS

Based on the foregoing design process, a diplexer with high isolation is presented. The dimensions for the diplexer are: $S_1 = 0.2$ mm, $S_2 = 0.2$ mm, $S_3 = 0.5$ mm, $S_4 = 0.2$ mm, $S_5 = 0.2$ mm, $S_6 = 0.5$ mm, $S_7 = 0.35$ mm, $S_8 = 0.55$ mm, $S_9 = 0.2$ mm, $S_{10} = 0.2$ mm, $L_1 = 12.6$ mm, $L_2 = 3.5$ mm, $L_3 = 2.4$ mm, $L_4 = 3.15$ mm, $L_5 = 2.75$ mm, $L_6 = 2.3$ mm, $L_7 = 6.4$ mm, $L_8 = 11.4$ mm, $L_9 = 4.9$ mm, $L_{10} = 8.65$ mm, $L_{11} = 18.15$ mm, $L_{12} = 2.5$ mm, $L_{13} = 2.7$ mm, $L_{14} = 3.4$ mm, $L_{15} = 2.65$ mm, $L_{16} = 5.2$ mm, $L_{17} = 18.1$ mm, $L_{18} = 16.35$ mm, $L_{19} = 4.3$ mm, $L_{20} = 16.65$ mm, $L_{21} = 4.5$ mm, $L_{22} = 7.9$ mm, $L_{23} = 11.3$ mm, $L_{24} = 7.15$ mm, $L_{25} = 18.8$ mm, $L_{26} = 12.9$ mm, $L_{27} = 14.1$ mm, $L_{28} = 6$ mm, $L_{29} = 17$ mm, $L_{30} = 4.35$ mm, $W_1 = 0.9$ mm, $W_2 = 1$ mm, $W_3 = 0.5$ mm, $W_4 = 1$ mm, $W_5 = 1.15$ mm, $D_1 = D_2 = 0.8$ mm. The simulated and measured S parameters are shown in Figures 4 and 5. The full-wave simulation is carried out by IE3D, and the diplexer is measured using Agilent vector network analyzer 5230A. The center frequencies of the diplexer are 1.8 and 2.3 GHz. The insertion losses are 1.7 and 1.8 dB, and the isolations among channels are larger than 37.5 dB. The fractional bandwidths of the two passbands are 10% and 7%. The photograph of the proposed diplexer is shown in Figure 6, and the circuit size of the proposed diplexer is $58 \text{ mm} \times 25 \text{ mm} = 0.50\lambda_g \times 0.22\lambda_g$, where λ_g is the guided wavelength on the substrate at the center frequency of the first channel.

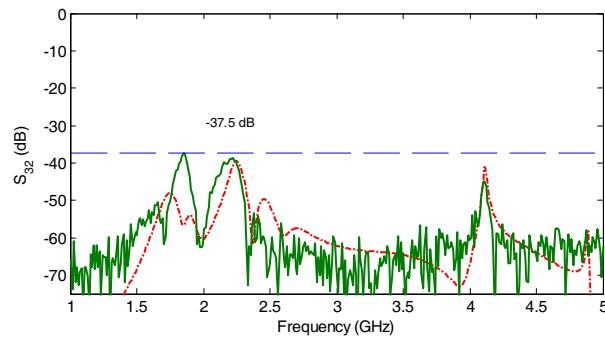


Figure 5: Simulated and measured isolation of the designed diplexer.

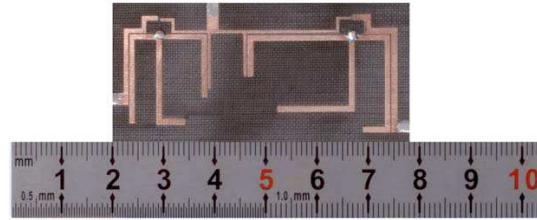


Figure 6: Photograph of the fabricated diplexer.

4. CONCLUSION

A new type of diplexer based on a microstrip CT filter with source-load coupling is presented. The implemented CT filter has the merits of compact size and high selectivity. The positions of the transmission zeros can be easily controlled by source-load coupling. This feature is applied to improve the isolation of the diplexer successfully. A trial diplexer centering at 1.8 and 2.3 GHz is presented to prove the efficiency of this design method.

ACKNOWLEDGMENT

This work was supported by the National Natural Science Foundation of China (61101016), the Specialized Research Fund for the Doctoral Program of Higher Education of China (20110172120009), the Fundamental Research Funds for the Central Universities (2013ZZ0038 and 2013ZZ0049).

REFERENCES

1. Yang, T., P. L. Chi, and T. Itoh, "High isolation and compact diplexer using the hybrid resonators," *IEEE Microstrip and Wireless Components Letters*, Vol. 20, No. 10, 551–553, 2010.
2. Zeng, H. Y., G. M. Wang, D. Z. Wei, and Y. W. Wang, "Planar diplexer using composite right-/left-handed transmission line under balanced condition," *Electronics Letters*, Vol. 48, No. 2, 104–106, 2012.
3. Chen, C. F., T. Y. Huang, C. P. Chou, and R. B. Wu, "Microstrip diplexers design with common resonator sections for compact size, but high isolation," *IEEE Transactions on Microwave Theory and Techniques*, Vol. 54, No. 5, 1945–1952, 2006.
4. Yang, T. P., L. Chi, and T. Itoh, "Compact quarter-wave resonator and its applications to miniaturized diplexer and triplexer," *IEEE Transactions on Microwave Theory and Techniques*, Vol. 59, No. 2, 260–269, 2011.
5. Chuang, M. L. and M. T. Wu, "Microstrip diplexer design using common T-shaped resonator," *IEEE Microwave and Wireless Components Letters*, Vol. 21, No. 11, 583–585, 2011.
6. Garcia-Lamperez, A., M. Salazar-Palma, and T. K. Sarkar, "Analytical synthesis of microwave multiport networks," *IEEE MTT-S Int. Microwave Symp. Digest*, 455–458, 2004.
7. Skaik, T. F., M. J. Lancaster, and F. Huang, "Synthesis of multiple output coupled resonator circuits using coupling matrix optimisation," *IET Microwaves, Antennas and Propagation*, Vol. 5, No. 9, 1081–1088, 2011.
8. An, J., G. M. Wang, C. X. Zhang, and P. Zhang, "Diplexer using composite right-/left-handed transmission line," *Electronics Letters*, Vol. 44, No. 11, 685–687, 2008.
9. Dong, Y. D. and T. Itoh, "Substrate integrated waveguide loaded by complementary splitting resonators for miniaturized diplexer design," *IEEE Microwave and Wireless Components Letters*, Vol. 21, No. 1, 10–12, 2011.

A Bandpass Filter Using HMSIW-DGS Cell

Y.-M. Huang, Z.-S. He, P.-K. Li, Z.-H. Shao, C.-J. You, and D. Jiang

School of Communication and Information Engineering

University of Electronic Science and Technology of China, Chengdu 611731, China

Abstract— In this paper, a half mode substrate integrated waveguide-to-defected ground structure (HMSIW-DGS) cell, and its embedded structure are proposed to miniaturize a bandpass filter. Both cells can purchase wideband frequency response and low insertion loss, as well as simple and easy fabrication. By cascading two of them according to design requirement, a X-band bandpass filter is designed and measured to meet compact size, low insertion loss, good return loss as well as second harmonic suppression.

1. INTRODUCTION

The half-mode substrate integrated waveguide (HMSIW), derived from substrate integrated waveguide (SIW) with similar high performance and half or so size reduction, has attracted lots of attention due to its merits of easy integration and been widely used in microwave passive components design [1–3]. However, compared with microstrip circuit, the physical size of HMSIW is not small enough, since it just cuts half along the longitudinal direction of SIW, that is to say, its length is still as long as SIW [4].

The defected ground structure (DGS), developed from the photonic bandgap (PBG) structure [5], but much different from the PBG since it needn't to be periodic [6]. As shown in [6], the DGS can change the distribution of the effective permittivity of the substrate, which brings in the change of the distributed capacitance and inductance of the guided wave structure based on this substrate, resulting in the bandgap performance. So the DGS can be used for the circuit size reduction. However, the DGS is etched on the ground plane of the circuit, which makes inconvenience for system integration, since the ground plane of the circuit should be conjunct with the metal shielding cavity. One solution for this drawback is to use the “coplanar DGS”, i.e., combining the DGS together with coplanar waveguide (CPW) and SIW [7, 8], which keeps the ground and the transmission line at the same plane. Besides, the complementary split ring resonator (CSR) [9], loaded on SIW, can be used to realize miniaturized filter since the SIW-CSR cell can resonate below the cutoff frequency of SIW. However, because of the cascaded coupling scheme of the filters reported in [9], their insertion losses are quite high.

In this paper, a HMSIW-DGS cell, with DGS etched on the top plane of SIW, and its embedded structure, are proposed. And the transmission responses with different parameters are discussed briefly, as well. Based on the proposed cells, a microwave bandpass filter is designed, fabricated and measured. According to the measured results, low insertion loss, good return loss, compact size and suppressed second harmonic are achieved.

2. HMSIW-DGS CELLS

Topologies of proposed HMSIW-DGS cell and its embedded structure are shown in Figures 1(a) and (b), respectively. It can be obtained from the topologies that the cells consist of two parts: the HMSIW section and the DGS section. So it can be expected that the transmission response of the HMSIW-DGS cell contains the inherent highpass characteristic of the HMSIW, which determine the lower sideband cutoff frequency, and the bandgap function of the DGS, which mainly affects the upper stopband, both the cutoff frequency and the rejection strength. As reported in [4], the highpass characteristic of the HMSIW is mainly determined by its width, aw , as shown in Figure 1. And to clarify the property of DGS better, influence of its different geometrical parameters is studied.

Figures 2 and 3 show some full wave simulated results of proposed HMSIW-DGS cell. On one hand, according to Figure 2, as the width of slots' terminal point, $w1$, becomes wider, and the transverse length of slots, $l2$, get longer, the upper sideband bandgap frequency shifts lower, while the lower sideband nearly keeps the same. So it can be predicted that the larger the size of DGS is, the lower the upper sideband bandgap frequency is. On the other hand, as $s1$, the space between two slots, gets wider, the upper sideband bandgap frequency shifts higher heavily, and the central

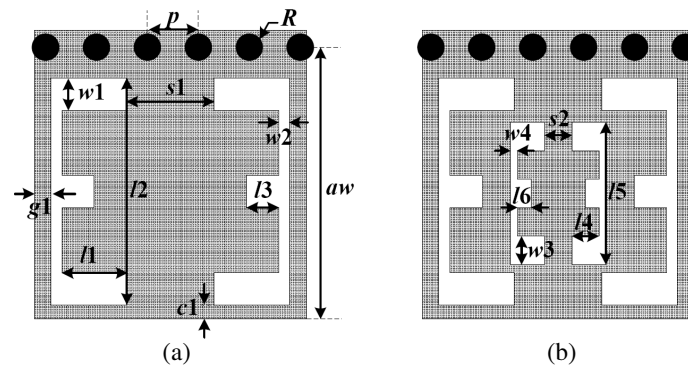


Figure 1: Topologies of (a) HMSIW-DGS cell and (b) embedded form. Black circles, grey zone and white zone represent the metalized via-holes, metal cover and DGS, respectively.

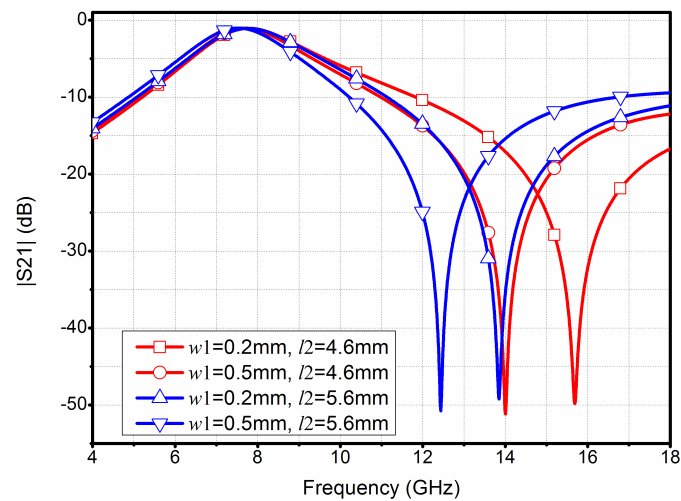


Figure 2: Simulated $|S_{21}|$ of proposed HMSIW-DGS cell with different l_2 and w_1 . Other geometrical parameters are: $aw = 6$ mm, $s_1 = 1$ mm, $c_1 = 0.2$ mm, $p = 0.8$ mm, $R = 0.2$ mm, $g_1 = 0.2$ mm, $l_3 = 0.5$ mm, $w_2 = 0.2$ mm and $l_1 = 1.5$ mm.

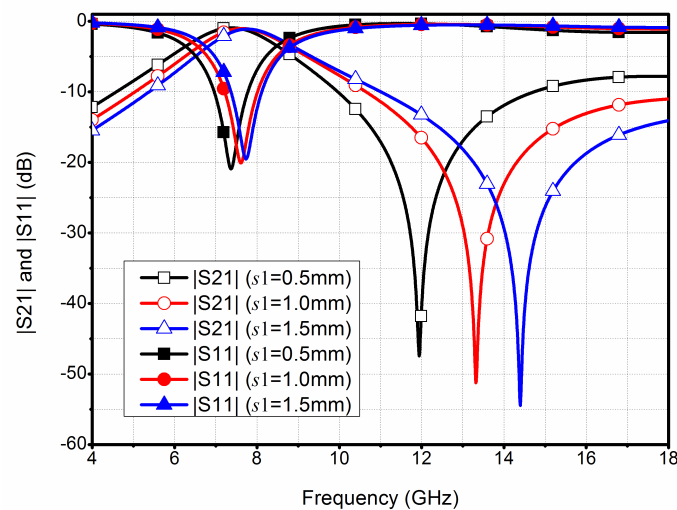


Figure 3: Simulated S -parameters of proposed HMSIW-DGS cell with different s_1 . Other geometrical parameters are: $aw = 6$ mm, $c_1 = 0.2$ mm, $p = 0.8$ mm, $R = 0.2$ mm, $g_1 = 0.2$ mm, $l_3 = 0.5$ mm, $w_2 = 0.2$ mm, $l_1 = 1.5$ mm, $w_1 = 0.5$ mm and $l_2 = 4.6$ mm.

operating frequency shifts higher a bit, as shown in Figure 3. All full wave simulation is done based on a substrate with a thickness of 0.254 mm, a relative permittivity of 2.2 and loss tangent of 0.001.

For these phenomena, it can be analyzed by the equivalent circuit model. As discussed in [6], the equivalent circuit model of the DGS can be set as a parallel LC resonator, where L and C represent the distributed inductance and capacitance of DGS, respectively. With this method, it can be obtained easily that: For proposed HMSIW-DGS cell, as w_1 gets wider or l_2 gets longer, the distributed inductance increases, so that the bandgap frequency shifts lower; as s_1 becomes wider, the distributed capacitance decreases, so that the bandgap frequency shifts higher. More accurately, the enlargement of DGS and the broadening of slots' space bring change to both the distributed inductance and capacitance. However, the enlargement of DGS makes the distributed inductance increase more heavily while the broadening of slots' space makes the distributed capacitance decrease more greatly.

3. FILTER DESIGN

Using the proposed HMSIW-DGS cell and its embedded structure as basic unit, a bandpass filter is designed on a RT/Duroid 5880 substrate with a thickness of 0.254 mm, a relative permittivity of 2.2 ± 0.2 , and a loss tangent of 0.0009, with its configuration shown in Figure 4. The filter consists of three HMSIW-SIW cells (two single and one embedded form), two half-tapered microstrip-to-SIW transitions and two 50 ohm microstrip transmission lines. Different from the conventional filter design based on resonance and coupling scheme, the filter here is designed by using the transmission scheme. Firstly, the HMSIW-DGS cell and its embedded structure are both operating in transmission form, instead of the resonance form. Secondly, the cascaded combination between

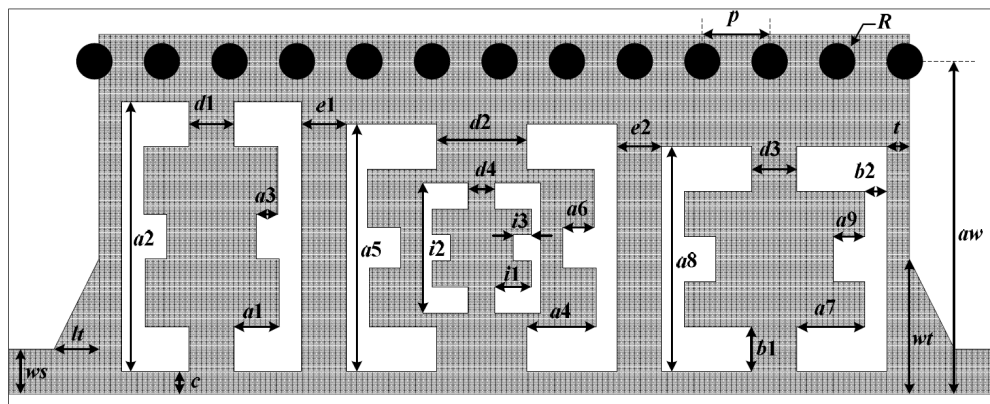


Figure 4: Configuration of the bandpass filter based on proposed HMSIW-DGS cells.

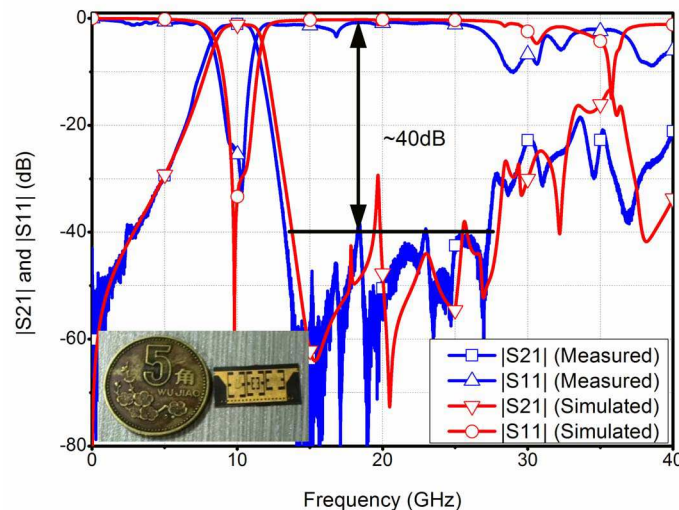


Figure 5: Comparison between measured and simulated results of the proposed HMSIW-DGS filter.

adjacent HMSIW-DGS cells also operates in transmission form. Another pivotal element for the filter design is the external quality factor (Q_e). In this filter design, two half-tapered microstrip-to-SIW transitions are used to achieve high Q_e , and it can be easily captured that the narrower the taper width “ wt ” is, the lower the Q_e is. With a wider wt , the Q_e is higher, so that the passband insertion loss is lower and the return loss is better. Based on proposed HMSIW-DGS cells with initial parameters operating at the requisite frequency, the filter is tuned and optimized by using a finite element method (FEM) full wave simulator. The optimized dimensions for fabrication are: $aw = 5.5$, $p = 0.8$, $R = 0.2$, $ws = 0.76$, $lt = 1.5$, $wt = 2.5$, $c = 0.2$, $d1 = d2 = d3 = 1$, $e1 = e2 = 0.22$, $t = 0.19$, $a1 = 1$, $a2 = 5.2$, $a3 = 0.5$, $a4 = 1$, $a5 = 5$, $a6 = 0.5$, $a7 = 1.1$, $a8 = 4.1$, $a9 = 0.6$, $i1 = 0.5$, $i2 = 2.4$, $i3 = 0.2$, $d4 = 0.32$, $b1 = 0.6$, $b2 = 0.2$ (unit: mm).

Using a single layer printed circuit board (PCB) process, the filter is fabricated and gold plated. The fabricated filter is measured by an Agilent PNA-X vector network analyzer N5245A. Comparison between measured and simulated results is shown in Figure 5, as well as the photograph of the fabricated filter. It can be obtained from the comparison that the measure results are in good agreement with the simulated ones. The filter is with a central frequency of 10 GHz, a fractional bandwidth of 25%, a return loss is better than 20 dB, and an insertion loss of 1.1 dB, including the loss of two 2.4-mm connectors and only about 0.2 dB higher than the simulated one. Its upper out-of-band rejection is better than 40 dB at the frequency range from 14 GHz to 28 GHz and better than 20 dB up to 40 GHz. That is to say, the filter has quite good second harmonic suppression performance. At last, the overall size of the filter is 15×7 mm, about $0.367\lambda_g^2$, which is quite compact. Table 1 shows some comparisons between proposed filter and some reported filters in references using similar technologies. According to Table 1, compared with filters represented in references, proposed filter is with lower insertion loss, better second harmonic suppression and compacter size. It can also be obtained that the insertion losses of HMSIW structure filters are probably larger than those of SIW structure. The reason for this is that the radiated loss of HMSIW is larger than that of SIW. Since HMSIW is a half closed structure with one radiated side, while SIW is a full closed structure with two column metalized viaholes.

Table 1: Comparison with filters represented in references.

Reference filter	Units number	Topology	f_c (GHz) and FBW^*	Insertion loss (dB)	2nd harmonic suppression (dB)	Size (λ_g^2)**
[3]-1	3	HMSIW-slot	7.8 and 22%	1.5	30	0.44
[3]-2	5	HMSIW-slot	8.79 and 40%	1.2	30	0.435
[10]	3	SIW-CSRR	8.15 and 23%	2.16	-	0.77
[11]	3	SIW-CSRR-slot (bottom)	9.4 and 30%	1	30	1.034
Proposed	3	HMSIW-DGS	10 and 25%	1.1	40	0.367

* f_c and FBW stand for central frequency and fractional bandwidth, respectively.

** λ_g stands for the guided wavelength at the central frequency.

4. CONCLUSION

A X-band bandpass filter based on the two proposed HMSIW-DGS cells is designed, fabricated and measured. The measured results show good agreement with the simulated ones. Compared with some reported filters using same technology and operating at similar frequency, the proposed filter has better performance in low insertion loss, compact size and good second harmonic suppression.

ACKNOWLEDGMENT

This work was supported in part by the Excellent Ph.D. Candidate Academic Foundation of UESTC under Grant YBXSZC20131054, the Fundamental Research Funds for the Central Universities under Grant ZYGX2013J006 and the Scientific Research Foundation of UESTC under Grant Y02002010101063.

REFERENCES

1. Hong, W., B. Liu, Y.-Q. Wang, Q.-H. Lai, H.-J. Tang, X.-X Yin, Y.-D. Dong, Y. Zhang, and K. Wu, “Half mode substrate integrated waveguide: A new guided wave structure for mi-

- crowave and millimeter wave application,” *Proceedings of Joint 31st International Conference on Infrared Millimeter Waves and 14th International Conference on Terahertz Electronics*, 219, Shanghai, China, May 2006.
2. Liu, B., W. Hong, Y.-Q. Wang, Q.-H. Lai, and K. Wu, “Half mode substrate integrated waveguide (HMSIW) 3-dB coupler,” *IEEE Microw. Compon. Lett.*, Vol. 54, No. 1, 22–24, 2007.
 3. Wang, Y.-Q., W. Hong, Y.-D. Dong, B. Liu, H.-J. Tang, J.-X. Chen, X.-X. Yin, and K. Wu, “Half mode substrate integrated waveguide (HMSIW) bandpass filter,” *IEEE Microw. Compon. Lett.*, Vol. 54, No. 4, 265–267, 2007.
 4. Lai, Q., C. Fumenaux, W. Hong, and R. Vahldieck, “Characterization of the propagation properties of the half-mode substrate integrated waveguide,” *IEEE Trans. Microw. Theory Tech.*, Vol. 57, No. 8, 1996–2004, 2009.
 5. Kim, C.-S., J.-S. Park, D. Ahn, and J.-B. Lim, “A novel 1-D periodic defected ground structure for planar circuits,” *IEEE Microw. Gui. Wave Lett.*, Vol. 10, No. 4, 131–133, 2000.
 6. Ahn, D., J.-S. Park, C.-S. Kim, J. Kim, Y.-X. Qian, and T. Itoh, “A design of the low-pass filter using the novel microstrip defected ground structure,” *IEEE Trans. Microw. Theory Tech.*, Vol. 49, 86–93, 2001.
 7. Shao, Z.-H. and M. Fujise, “Bandpass filter design based on LTCC and DGS,” *Proceedings of Asia-Pacific Microwave Conference*, 138–139, Soochow, China, December 2005.
 8. Huang, Y.-M., Z.-H. Shao, and L.-F. Liu, “A substrate integrated waveguide bandpass filter using novel defected ground structure shape,” *Progress In Electromagnetics Research*, Vol. 135, 201–213, 2013.
 9. Dong, Y.-D., T. Yang, and T. Itoh, “Substrate integrated waveguide loaded by complementary split-ring resonators and its applications to miniaturized waveguide filters,” *IEEE Trans. Microw. Theory Tech.*, Vol. 57, 2211–2223, 2009.
 10. Deng, K., Z. Guo, C. Li, and W. Che, “A compact planar bandpass filter with wide out-of-band rejection implemented by substrate-integrated waveguide and complementary split-ring resonator,” *Microw. Optical Tech. Lett.*, Vol. 53, No. 7, 1483–1487, 2011.
 11. Zhang, X.-C., Z.-Y. Yu, and J. Xu, “Novel band-pass substrate integrated waveguide (SIW) filter based on complementary split ring resonators (CSR),” *Progress In Electromagnetics Research*, Vol. 72, 39–46, 2007.

Compact and Sharp-rejection Dual-band Bandstop Filter Based on Transversal Signal-interaction Concept

Lei-Lei Qiu and Qing-Xin Chu

School of Electronic and Information Engineering
South China University of Technology, Guangzhou 510640, China

Abstract— A compact dual-band bandstop filter with sharp-rejection using transversal signal-interaction, consisting of a transmission line path and a cascaded coupled line path, is proposed. Folded structure is used to decrease the size. By tuning the coupling coefficient and length, the centre frequency and bandwidth can be controlled, respectively. Meanwhile the transmission line impedance and odd-mode impedance can be used to improve the return loss and to allocate the transmission poles to sharp the attenuation rate, independently. A compact dual-band bandstop filter centring at 2.4 GHz and 3.7 GHz prototype is designed and fabricated to verify the validity. The simulation and measurement results agree well.

1. INTRODUCTION

Compact dual-band bandstop filters (DBBSFs) are highly desired in wireless communication system applications for their effective double-sideband spectrum suppression, low passband insertion loss and group delay. Many different methods and structures have been proposed to design DBBSFs [1–7]. In [1], the two-step frequency-variable transformation to the low pass prototype was applied to perform a dual-stopband response. While in [2], composite shunt resonators were implemented. In [3], modified optimum bandstop filter with source-load coupled line was introduced to achieve wide dual stopband. For the purpose of miniaturizing and controlling the frequency ratio, SIRs [4, 5], short-[6] and open-circuited [6, 7] stub-loaded resonators were presented. Whereas, due to the single transmission zero in the stopband [1–6], the selectivity of the filters needed to be improved. Thus signal-interference technique [8] with more transmission zeros was used to design sharp-rejection DBBSF.

This letter proposes a novel and compact DBBSF with sharp-rejection using transversal signal-interaction concept, which can be implemented by inlaying two short-circuited resonators out of the two folding coupled stubs. The centre frequency and bandwidth can be controlled mainly by tuning the coupling coefficient and length, respectively. In addition, the return loss and selectivity out of the stopband can be improved by adjust the impedance of the transmission line path and coupled path. Detailed theoretical design, simulation, and experiment results for the proposed DBBSF are demonstrated and discussed.

2. FILTER ANALYSIS AND DESIGN

Figure 1 shows the configuration and ideal circuit of the proposed bandstop filter, which is composed of two main paths. Path 1 is a length of transmission line with the impedance Z_1 , while path 2 consists of cascaded short-/open-circuited coupled lines with different electrical length θ_2 and θ_3 . All coupled lines have the same odd-/even-mode impedance (Z_{oo} and Z_{oe}). All I/O lines are with the impedance of $50\ \Omega$.

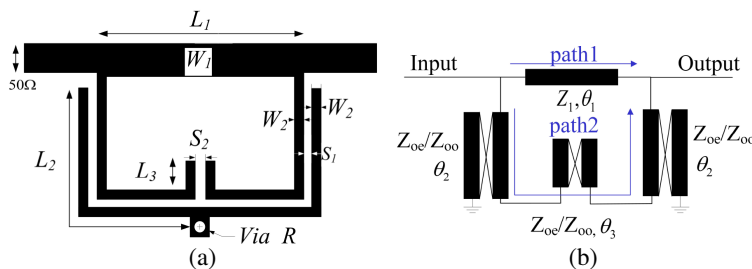


Figure 1: (a) The configuration and (b) ideal circuit of the proposed DBBSF.

According to [9], the $ABCD$ matrices of the shorted/open coupled lines (M_{s1}/M_{s2} and M_o) and two paths are

$$M_{s1} = \begin{bmatrix} A & B \\ C & D \end{bmatrix}, \quad M_{s2} = \begin{bmatrix} D & B \\ C & A \end{bmatrix} \quad (1)$$

$$A = \frac{2Z_{oe}Z_{oo}(1 + \cos^2 \theta_2) - \sin^2 \theta_2(Z_{oe} + Z_{oo})}{4Z_{oe}Z_{oo} \cos \theta_2}, \quad D = \cos \theta_2 \quad (2)$$

$$B = j \frac{(Z_{oe} + Z_{oo}) \sin \theta_2}{2}, \quad C = j \frac{(Z_{oe} + Z_{oo}) \sin \theta_2}{2Z_{oe}Z_{oo}} \quad (3)$$

$$M_o = \frac{1}{Z_{oe} - Z_{oo}} \begin{bmatrix} Z_{oe} + Z_{oo} & -j2Z_{oe}Z_{oo} \cot \theta_3 \\ j2 \tan \theta_3 & Z_{oe} + Z_{oo} \end{bmatrix} \quad (4)$$

$$\begin{bmatrix} A_1 & B_1 \\ C_1 & D_1 \end{bmatrix}_{\text{path1}} = \begin{bmatrix} \cos \theta_1 & jZ_1 \sin \theta_1 \\ j \sin \theta_1 / Z_1 & \cos \theta_1 \end{bmatrix}, \quad \begin{bmatrix} A_2 & B_2 \\ C_2 & D_2 \end{bmatrix}_{\text{path2}} = M_{s1} \times M_o \times M_{s2} \quad (5)$$

After $ABCD$ - and Y -parameter conversions, the S -parameters of the $DBBSF$ can be express as

$$S_{11} = \frac{Y_0^2 - Y_{11}^2 + Y_{21}^2}{(Y_0 + Y_{11})^2 - Y_{21}^2}, \quad S_{21} = j \frac{-2Y_{21}Y_0}{(Y_0 + Y_{11})^2 - Y_{21}^2} \quad (6)$$

where $Y_0 = 1/Z_0$ ($Z_0 = 50 \Omega$), $Y_{11} = D_1/B_1 + D_2/B_2$, $Y_{21} = -1/B_1 - 1/B_2$.

Transmission zeros can be obtained when $S_{21} = 0$. Fig. 3 plots the calculated transmission zeros (f_{tz1} , f_{tz2} , f_{tz3} and f_{tz4}) against K and θ_3 according to (6). When keep Z_{oo} and Z_1 constant, f_{tz1} and f_{tz2} decrease while f_{tz3} and f_{tz4} increase as the increasing of K . Therefore, the frequency ratio f_2/f_1 of the two stopbands can be controlled and larger K will obtain larger f_2/f_1 . When θ_3 is zero, the selectivity is poor as only one visible transmission zero is in each stopband. With the increasing of S , f_{tz1} and f_{tz2} (f_{tz3} and f_{tz4}) separate each other with a larger bandwidth.

To explain the characteristics of the filter, Variation of simulated filter characteristic with Z_{oo} and Z_1 are simulated by Agilent Advanced Design System (ADS) and plotted. As can be seen from Figs. 3(a) and (b), the changes of Z_{oo} and Z_1 have no significant effect on transmission zeros while have influence on the characteristic out of the band. The increase of Z_{oo} or decrease of Z_1 will result in the moving of transmission poles to transmission zeros thus sharps the selectivity. Moreover, it should be noted that the impedance Z_1 of the transmission line may be used to improve the return loss out of stopband.

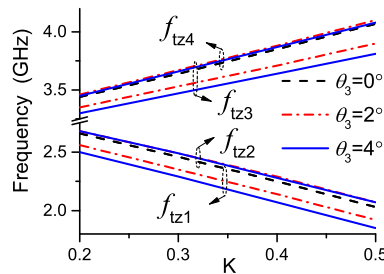


Figure 2: Variation of calculated transmission zeros with K and θ_3 ($Z_{oo} = 90 \Omega$, $Z_1 = 60 \Omega$).

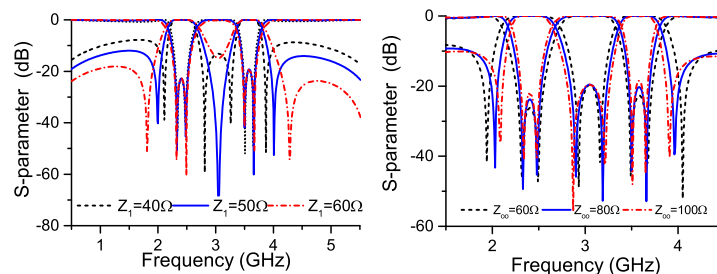


Figure 3: Variation of simulated filter characteristic with Z_{oo} , Z_1 ($K = 0.3$, $\theta_3 = 3$).

From above we know that since the introduction of proposed structure, the centre frequencies and bandwidths in the stopbands can be independently controlled through coupling strength K and electrical length θ_3 . In addition, the impedance of the transmission line and odd-impedance of the coupled line can be independently used to adjust the return loss and selectivity out of the stopband. All this make the design of the proposed filter more flexibility.

To clarify the proposed filter design, a proposed DBBSF centring at 2.4 GHz and 3.7 GHz with a relative fractional bandwidth BW_Z of 6% and 4.6%, is designed and implemented. Considering that $f_2/f_1 = 1.5417$ and the requirement of bandwidth, $f_{t1} = 2.33$ GHz, $f_{t2} = 2.47$ GHz, $f_{t3} = 3.65$ GHz and $f_{t4} = 3.8$ GHz. Through (6), we can obtain that $K = 0.33$ and $\theta_3 = 3$. Z_{oo} and Z_1 are 88Ω and 45.5Ω to achieve the isolation up to 20 dB. The configuration of the filter are demonstrated in Fig. 1(a) and the simulated results are shown in Fig. 4. Four transmission zeros are located at 2.33 GHz, 2.461 GHz, 3.67 GHz and 3.79 GHz. The two stopband have a relative 20 dB fabrication bandwidth (FBW) of 8.7% and 5.2%, respectively. The insertion loss is less than 0.35 dB, while the return loss is over 20 dB between the stopbands.

3. RESULTS

The proposed filter is fabricated on the substrate with a relative dielectric constant of 2.55, thickness of 0.8 mm and loss tangle of 0.0029. Fig. 4 illustrates the photograph and measurement result of the DBBSF, the filter has a compact size of only $0.22\lambda_g \times 0.15\lambda_g$ (λ_g is the free space wavelength at the centre frequency of the first stopband). The filter is measured by Agilent 5230 vector network analyzer.

It is shown that more than 25 dB rejection can be achieved in 2.41 GHz and 3.75 GHz with a relative 20 dB FBW of 8.8% and 5%, respectively. The return loss between the two stopbands is about 20 dB. The insertion loss is less than 0.7 dB up to 2.03 GHz while within 1 dB from 4 GHz to 7 GHz. The attenuation rates at the passband to stopband are 174 dB/GHz (measured attenuations being 5.062 dB and 19.96 dB at 2.21 and 2.3 GHz) and 168 dB/GHz (measured attenuations being 19.92 dB and 4.986 dB at 3.85 and 3.94 GHz). The variance between measurement and simulation mainly due to dielectric loss, fabrication tolerance and the loss of SMA connector. To further demonstrate the performances of this filter, the comparisons of measured results for several reported DBBSFs [2–8] are shown in Table 1. The proposed filter shows miniaturization and sharp skirt selectivity.

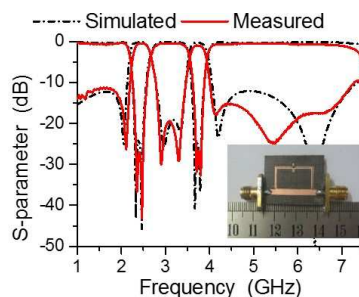


Figure 4: The simulated and measured response of the proposed DBBSF.

Table 1: Comparison with the reported DBBSFs.

Ref.	ILmax (dB)	RL (dB)	Attenuation Slope (dB/GHz)		TZ	Size ($\lambda_g * \lambda_g$)
			Lower	Upper		
[2]	3	15	139	110	1	0.71*0.59
[3]	3.5	23	79	93	1	0.46*0.21
[4]	3	20	90	112	1	0.29*0.25
[5]	1.5	20	67	72	1	0.24*0.23
[6]	1	20	143	87	1	0.85*0.3
	1	15	80	68	1	0.25*0.19
[7]	1	12	32	26	2	0.26*0.18
[8]	2	15	67	122	2	0.49*0.26
This Work	1	20	174	168	2	0.22*0.15

4. CONCLUSION

In this paper, a compact and sharp-rejection dual-band bandstop filter has been proposed using signal-interaction concept. The filter model has been introduced to analysis the transmission zeros and the effect of parameters on the filter characteristic. Due to four parameters independently control the frequency ratio, bandwidth, return loss and selectivity, the design of the filter is simple and flexible. Finally, the proposed DBBSF is designed, fabricated and measured. Agreement between simulation and measurement verifies the validation of the analyses.

ACKNOWLEDGMENT

This work was supported by the National Natural Science Foundation of China (61171029 and 61101016), the Fundamental Research Funds for the Central Universities (2013ZP0018) and the Guangzhou Science and Information Technology Project (201300000029).

REFERENCES

1. Uchida, H., H. Kamino, et al., “Dual-band-rejection filter for distortion reduction in RF transmitters,” *IEEE Trans. Microwave Theory Tech.*, Vol. 52, No. 11, 2550–2556, 2004.
2. Ma, Z., K. Kikuchi, et al., “Novel microstrip dual-band bandstop filter with controllable dual-stopband response,” *Proceedings of the AsiaCPacific Microwave Conference*, 1174–1177, 2006.
3. Guntupalli, A. B., V. K. Velidi, and S. Sanyal, “Compact Dual wide bandstop filter,” *Proceedings of the Applied Electromagnetics Conference (AEMC)*, 1–4, 2009.
4. Chin, K. S., J. H. Yeh, et al., “Compact dual-band bandstop filters using stepped-impedance resonators,” *IEEE Microw. Wireless Compon. Lett.*, Vol. 17, No. 12, 849–851, 2007.
5. Velidi, V. K., A. B. Guntupalli, et al., “Compact tapped stepped impedance open stub dual-band bandstop filters with sharp rejection characteristics,” *Microw. Opt. Technol. Lett.*, Vol. 51, No. 10, 2274–2277, 2009.
6. Gao, L., S. W. Cai, et al., “Dual-band bandstop filter using open and short stub-loaded resonators,” *Proceedings of the Microwave and Millimeter Wave Technology*, 1–3, 2012.
7. Chen, F. C., J. M. Qiu, and Q. X. Chu, “Dual-band bandstop filter using stub-loaded resonators with sharp rejection characteristic,” *Electron. Lett.*, Vol. 49, No. 5, 351–353, 2013.
8. Feng, W. J., W. Q. Che, S. Y. Shi, and Q. Xue, “Compact dual-wideband bandstop filters based on open-coupled lines and transversal signal-interaction concepts,” *IET Microw. Antennas Propag.*, Vol. 7, No. 2, 92–97, 2013.
9. Hong, J. S. and M. J. Lancaster, *Microstrip Filters for RF/Microwave Applications*, John Wiley & Sons, New York, 2001.

Wide-stopband Millimeter-wave Bandpass Filter Based on Discriminating Coupling on GaN MMIC

Jie Kai Lin¹, Xiu Yin Zhang¹, Qing Yi Guo¹, and Hsuan-Ling Kao²

¹School of Electronic and Information Engineering

South China University of Technology, Guangzhou 510640, China

²Department of Electronic Engineering, Chang Gung University, Taoyuan, Taiwan

Abstract— This paper presents a third harmonics up pressed bandpass filter on GaN MMIC (Monolithic Microwave Integrated Circuit). By analysing the voltage distribution at fundamental frequency and third harmonic of the resonators, suitable coupling region between the feeding lines and resonators can be selected. In this way, we make the coupling coefficient at third harmonic to be zero while the coupling coefficient at fundamental frequency is not zero. Therefore, the third harmonic can be suppressed by the discriminating coupling scheme while the fundamental mode responses are unaffected. Meanwhile, to improve the selectivity, source-load coupling is employed to introduce transmission zeros near the passband. For demonstration, a millimeter-wave filter with wide stopband is implemented. The filter is designed based on the technology of GaN MMIC with center frequency of 33.5 GHz and insertion loss of 3.2 dB. The circuit area of the filter is only $410 \mu\text{m} \times 210 \mu\text{m}$, featuring very compact size.

1. INTRODUCTION

Bandpass filter is one of the most important elements in wireless communication system. Among bandpass filter, parallel-coupled bandpass filter is widely used in RF front-ends because of their simple configuration and easy design procedures. However, most parallel-coupled filters suffer from harmonic responses, which degrade system performance. To suppress these spurious responses, various methods have been proposed [1–3]. In [1], the author introduces two different open stubs tapped on the input and output port with length of quarter length of harmonic wave creating two transmission zeros to suppress harmonic. In this design, more extra circuit should be added, which increases the size of the filter. By separately allocating the two different transmission zeros, the suppression of spurious response at the third harmonic frequency can be achieved in [2]. In [3], fractal shape is employed to improve harmonic suppression by a factor of 2. In [4], a new method that suppresses the harmonic response by tuning the coupling coefficient between the two transmission lines is introduced to us. However, these filters are fabricated at lower frequency.

In recent years, with the development of IC industry and the operating frequency in wireless communication system shifting to higher frequency, more and more traditional RF circuit have been transplanted to IC platform. In [5], a 4-stage on-chip open loop resonators band pass filter which operates at 60 GHz is proposed. In [6], the author introduces a compact multilayer CPW MMIC spiral directional couplers and bandpass filter to us. More and more bandpass filters have been fabricated at such high frequency. However, fewer bandpass filters with wide bandstop are complemented on IC platform. Since the method mentioned in [4] is useful and the size of the designed filter is compact, it is necessary and essential to transplant it to IC platform.

In this letter, bandpass filter with third harmonic suppression has been introduced to MMIC. It is based on discriminating coupling. Therefore, no more extra circuits are employed to suppress the harmonic. Although the third harmonic signal is suppressed, the fundamental one can pass without any influence. Base on the proposed idea, a two-order bandpass filter with third harmonic suppressed has been implemented using quarter wave length short-ended microstrip line. The design methodology and experimental results are also presented.

2. ANALYSIS OF DISCRIMINATING COUPLING

The harmonic suppression is based on discriminating coupling, so it is necessary to present the theory of coupling coefficient. The electric coupling coefficient between the transmission lines can be defined, i.e.,

$$k_e = \frac{\iiint \varepsilon \vec{E}_1 \cdot \vec{E}_2 dv}{\sqrt{\iiint \varepsilon |\vec{E}_1|^2 dv \cdot \iiint \varepsilon |\vec{E}_2|^2 dv}} \quad (1)$$

where \vec{E} represents the electric field vectors generated by the two lines and V is the volume. Since the dominant mode is quasi-TEM, the electric field can be replaced by corresponding voltage to evaluate the coupling coefficient, i.e.,

$$k_e = P \times \frac{\int_{-d/2}^{d/2} v_1(x)v_2(x)dx}{\sqrt{\int_{-d/2}^{d/2} |v_1(x)|^2 dx \times \int_{-d/2}^{d/2} |v_2(x)|^2 dx}} \quad (2)$$

where $V_1(x)$ and $V_2(x)$ represent the voltage-wave functions on the two coupling lines, p represents a constant and d is the length of the coupling region. In order to suppress harmonic, it is necessary to create a zero value of k_e upon the frequency. Letting the integrand in the numerator to be an odd function is one of the easy and efficient way to create a zero value. When one of the voltage-wave functions is odd and the other one is even, the integrand in the numerator will be an odd function, which implies that the electric coupling coefficient is zero.

According to the mechanism above, an instance of discriminating coupling and its application to filter design is shown in Fig. 1. There are two transmission lines in Fig. 1(a). In Fig. 1(b), the voltage-wave function on line1 is odd, while even on line2 at a specific frequency, which leads to an odd function of the integrand in the numerator. As a result, the value of k_e is zero at a specific frequency. Similarly, the value of the magnetic coupling coefficient is

$$k_m = 0 \quad (3)$$

Thus, the total coupling coefficient is

$$k = k_m + k_e = 0 \quad (4)$$

According to the instance, it is easy to observe that the coupling coefficient between the two transmission lines could be zero at specific frequencies. It means that the signal cannot pass across the coupling region and thus it will be suppressed.

3. FILTER DESIGN

Figure 2 shows the configuration of the wide-stopband millimeter-waveband pass filter based on discriminating coupling on GaN. The filter consists of two symmetric quarter-wavelength resonators and they are folded to reduce the size. The two feeding lines are coupled with the resonators and the ports are tapped at the middle of the feeding line. Meanwhile, source-load coupling is employed to introduce transmission zeros near the passband [7].

For quarter-wave length shorted-ended microstrip line, the voltage wave function at fundamental frequency can be described as

$$V_{f_0}(x) = \cos(\beta x) \quad x \in [0, L] \quad (5)$$

while third harmonic frequency

$$V_{3f_0}(x) = \cos(3\beta x) \quad x \in [0, L] \quad (6)$$

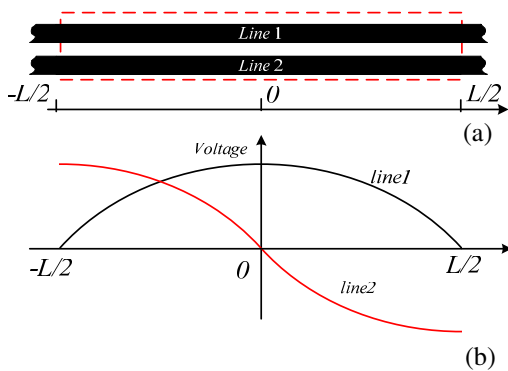


Figure 1: Coupling region with zero coupling coefficient. (a) Coupled microstrip lines. (b) Normalized voltage on the two lines.

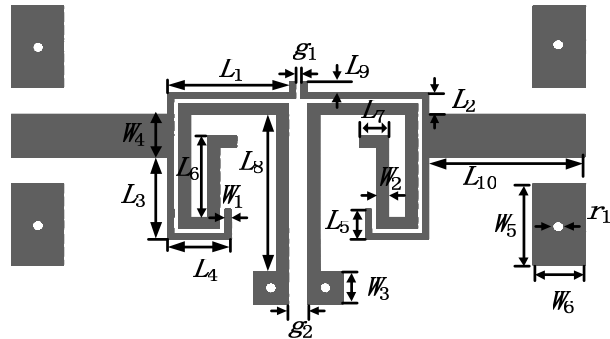


Figure 2: The configuration of the third harmonic suppression filter based on discriminating coupling on MMIC.

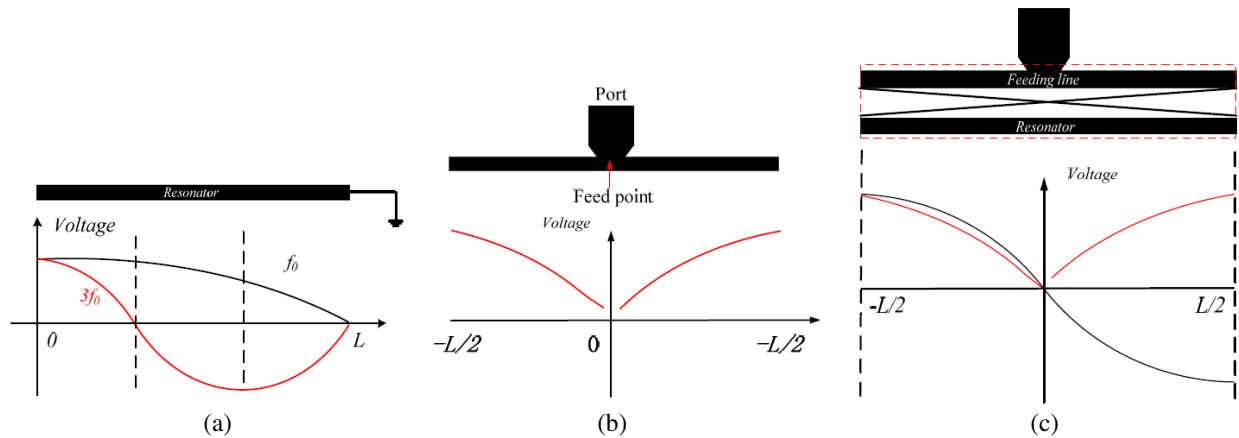


Figure 3: (a) The wave function of fundamental and third harmonic on quarter wave length shorted-ended microstrip line. (b) The wave function on feed line. (c) The wave function between the coupling regions.

where β represents the propagation constant at fundamental resonant frequency and L is the whole length of the transmission line. Fig. 3(a) shows this two voltage wave function.

For the feeding line, the voltage wave function on it is always even. In addition, it is kind of subsection function and can be described as

$$V(x) = \begin{cases} \sin(px) & x \in (0, L/2] \\ -\sin(px) & x \in [-L/2, 0) \end{cases} \quad (7)$$

where p represents a constant and L is the whole length ignoring the port. Fig. 3(b) shows its voltage wave function and the combination of voltage wave function between the coupling regions is shown in Fig. 3(c).

According to (1), we can easily draw a conclusion that the coupling coefficient of third-harmonic between this two transmission lines is zero, which implies that the third-harmonic can be suppressed. Based on this discriminating coupling mechanism, the BPF with the third-harmonic suppression and wide stopband can be implemented.

The filter is fabricated on GaNas shown in Fig. 4, which consists of three layers of substrates. The dimensions of the proposed filter are determined as follows: $L_1 = 212.5 \mu\text{m}$, $L_2 = 40 \mu\text{m}$, $L_3 = 152 \mu\text{m}$, $L_4 = 110 \mu\text{m}$, $L_5 = 55 \mu\text{m}$, $L_6 = 150 \mu\text{m}$, $L_7 = 20 \mu\text{m}$, $L_8 = 320 \mu\text{m}$, $L_9 = 20 \mu\text{m}$, $L_{10} = 272.5 \mu\text{m}$, $W_1 = 10 \mu\text{m}$, $W_2 = 20 \mu\text{m}$, $W_3 = 60 \mu\text{m}$, $W_4 = 78 \mu\text{m}$, $W_5 = 150 \mu\text{m}$, $W_6 = 90 \mu\text{m}$, $g_1 = 10 \mu\text{m}$, $g_2 = 35 \mu\text{m}$, $r_1 = 20 \mu\text{m}$.

Figure 5 depicts the simulated result of this filter. The passband is centered at 33.5 GHz with 3 dB fractional bandwidth of 27.5% and the insertion loss is 3.2 dB. Three transmission zeros can be observed. The lower transmission zero is caused by quarter-wave resonance that short out

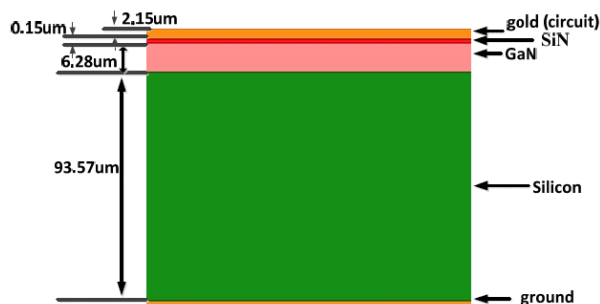


Figure 4: Configuration of the substrate.

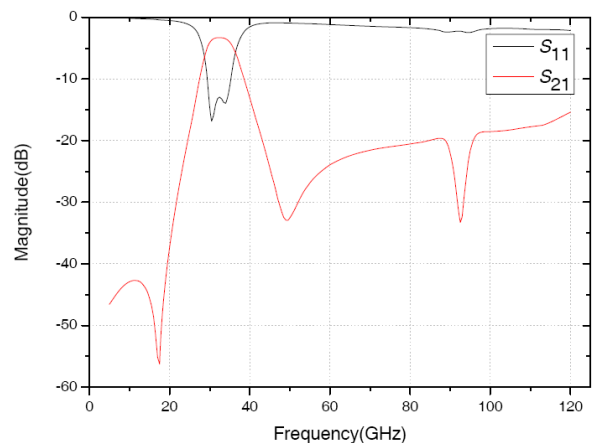


Figure 5: Simulated responses of the proposed filter.

the port at the frequency above the resonant frequency. The other one near the passband result from the source-load coupling. Another transmission zero is generated at about 95 GHz, which is introduced by discriminating coupling. The coupling coefficient at this frequency is zero, namely third harmonic. The rejection level reaches 35 dB, helping enhance the rejection level within the upper stopband. Due to these transmission zeros, high selectivity and wide-stopband is realized, which verifies the analysis.

4. CONCLUSION

In this letter, we have introduced a third harmonic suppressed bandpass filter on GaN MMIC. Discriminating coupling mechanism is introduced two suppress third harmonic on GaN MMIC with no extra circuit. The feeding lines and resonators can be folded to make the circuit miniaturization with no effect to discriminating coupling. It means the miniaturization and wide stopband of the filter can be both realized on MMIC circuit. Moreover electronic source-load coupling is employed to introduce transmission zeros near the passband, which contribute to the good selectivity of the filter. The experimental results show the demonstrated filter is applicable to wireless communication system.

REFERENCES

1. Gao, L., X. Y. Zhang, and B. J. Hu, "Tunable dual-band bandpass filter using varactor-loaded short-ended resonators," *2013 IEEE International Wireless Symposium (IWS)*, 1–3, Apr. 2013.
2. Gao, J. and L. Zhu, "Asymmetric parallel-coupled CPW stages for harmonic suppressed $\lambda/4$ bandpass filters," *Electronics Letters*, Vol. 40, No. 18, 1122–1123, Sep. 2004
3. Esa, M., N. Hassan, M. A. M. Abas, N. N. N. A. Malik, and N. Fisal, "Reduced size microstrip fractal filter with suppressed second harmonic," *Asia Pacific Microwave Conference, 2009, APMC 2009*, 1462–1464, Dec. 2009.
4. Zhang, X. Y. and Q. Xue, "Harmonic-suppressed bandpass filter based on discriminating coupling," *IEEE Microwave and Wireless Components Letters*, Vol. 19, No. 11, 695–697, Nov. 2009.
5. Pokharel, R. K., X. Liu, R. Dong, A. B. A. Dayang, H. Kanaya, and K. Yoshida, "A high selectivity, low insertion loss 60 GHz-band on-chip 4-pole band pass filter for millimeter wave CMOS SoC," *Proceedings of the 6th European Microwave Integrated Circuits Conference*, 660–663, Oct. 2011.
6. Sun, Q., J. Yuan, J. Lu, A. Rezazadeh, L. Krishnamuthy, and V. T. Vo, "A compact multilayer CPW MMIC spiral directional couplers and bandpass filter," *Proceedings of the 40th European Microwave Conference*, 561–564, Nov. 2010.
7. Liao, C. K. and C. Y. Chang, "Design of microstrip quadruplet filters with source-load coupling," *IEEE Trans. Microw. Theory Tech.*, Vol. 53, No. 7, 2302–2308, 2005.

Reconfigurable WIFI Filter with Isolation Enhancement

Yuan Jiang, Jiawei Yu, Xian Qi Lin, Fei Cheng, and Yong Fan

EHF Key Laboratory of Science, School of Engineering
University of Electronic Science and Technology of China, Chengdu 611731 China

Abstract— This paper presents a reconfigurable WIFI band filter with three switchable modes. Half wavelength resonators coupled with a microstrip transmission line are used to design the frequency of WIFI band. PIN switches mounted at the microstrip near the resonators are used to switch the working modes of the WIFI filter. This WIFI filter is able to work at both 2.45 GHz and 5.8 GHz with the resonators working at different modes. A dual-band band-stop mode is also available with the filter. A centrally loaded resonator technology is used to suppress the harmonic of 2.45 GHz which would interfere the performance at 5.8 GHz. The isolation is enhanced by more than 40 dB with the structure in this paper.

1. INTRODUCTION

Due to the requirements of multifunction and multiband reconfigurable, filters are more and more important in modern communication systems [1–9]. Most of the studies are focus on center frequency tuning and bandwidths tuning or constant bandwidths, there are also some researches about pass-stop mode reconfigurable, tunable rejection levels and so on.

A tunable band-pass filter with reconfigurable bandwidth by utilized a coupling reducer [3]. Young-Ho Cho et al. presented a 0.73–1.03-GHz tunable band-pass filter with a reconfigurable multi-pole response [4]. Abunjaileh et al. also presented a tunable filter design with tunable bandwidth and center frequency [5]. A high linearity miniaturized filter at 1.4–2.0 GHz was presented by El-Tanani et al. in [6]. A RF-MEMS tunable filter by high linearity anti-biased is presented in [7]. H. Wang et al. presented a reconfigurable notch bands UWB filter with Terminated Cross-Shaped Resonators [8]. In [9] a tunable parallel resonance between two resonators is used to present a filter with enhanced rejection level and tunable bandwidths.

In this paper, a three modes reconfigurable WIFI filter with isolation enhanced is presented. PIN switches and centrally loaded resonator are used to design the WIFI filter. The design and simulation are demonstrated in the following sections. In order to test the performance of the reconfigurable WIFI filter, substrate F4B with thickness of 0.8 mm and dielectric constant of 2.65 was used in the EM simulation with Ansys HFSS.

2. DESIGN OF THE PROPOSED WIFI FILTER

In this section, the WIFI filter is designed to have a reconfigurable property with half wavelength resonator and PIN switches.

In order to make the WIFI filter compact and simplify designs, half wavelength microstrip resonators, which are very popular on planar and compact microwave circuits, are used in this design. A half wavelength resonator coupled with a complete microstrip can compose a band-stop filter by forming a transmission pole at the resonator frequency. If the microstrip is broken and coupled by the folded resonator, this structure can compose a band-pass filter by forming a transmission zero at the resonator frequency similarly. A PIN switch is used to combine and reconfigurable the band-stop and band-pass filters as shown in Figure 1. The half wavelength resonator is designed to be folded to make the structure compact.

As shown in Figure 1, the simulation shows the reconfigurable property of the structure:

When PIN A is ON, the structure is working as a half wavelength resonator coupled with a complete microstrip. So, the structure is a band-stop filter.

When PIN A is OFF, the structure is working as a half wavelength resonator coupled with a broken microstrip. So, the structure is a band-pass filter.

The properties shown below is very interesting. If a 5.8 GHz similar structure is cascaded, its working mode can be controlled by setting the status of the PIN switches. Especially, when the two PIN switches are set different status, the isolation will be enhanced by each other. For example, if the 2.45 GHz PIN switch is ON, and the 5.8 GHz PIN switch is OFF, it is a 5.8 GHz filter, on the same time, the channel of 2.45 GHz is protected by working as a band-stop filter.

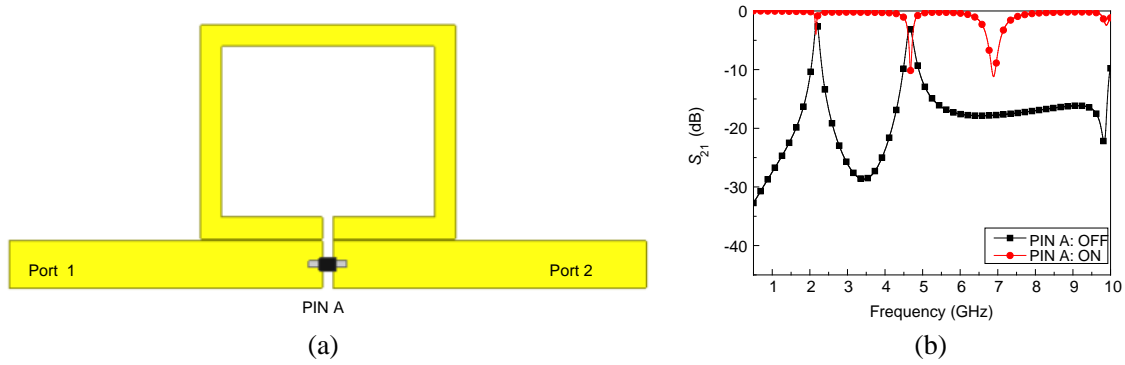


Figure 1: PIN switch working performance (2.45 GHz). (a) Reconfigurable cell with a half wavelength resonator and a PIN switch. (b) The performance of the PIN switch at ON and OFF modes.

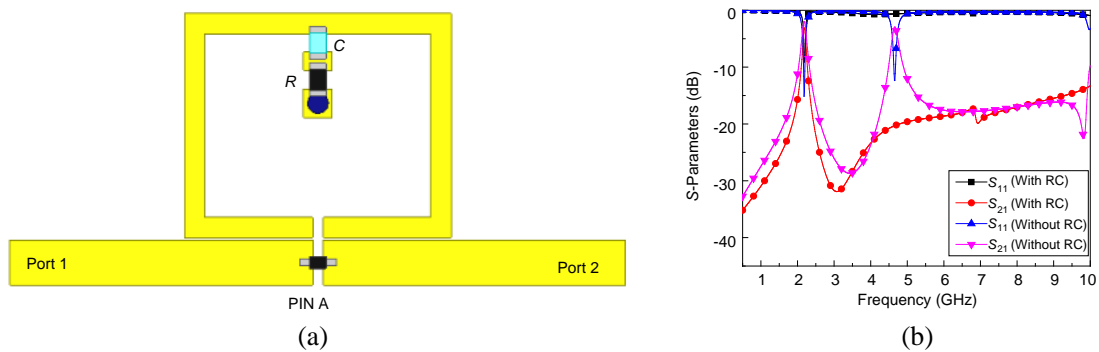


Figure 2: Harmonic suppression (RC: centrally loaded resistor and capacitor). (a) Reconfigurable cell utilized centrally loaded resonator. (b) The result of the harmonic suppression.

However, there is harmonic near 5.8 GHz forming by the 2.45 GHz resonator. The harmonic will decline the performance of a system. Therefore, a centrally loaded resonator is utilized to suppress the interference [11].

The harmonic is caused by the even mode of the resonator by an odd and even mode method. The even mode of a centrally loaded half wavelength resonator will be reflected and absorbed by the loaded resistor and capacitor, as shown in Figure 2, so as to be suppressed.

Figure 2 shows the structure and results of a reconfigurable cell with centrally loaded half wavelength resonator: the harmonic is vanished obviously. The harmonics of 5.8 GHz cell will no influence the 2.45 GHz cell, so, it is no necessary to design a centrally loaded resonator for 5.8 GHz.

3. SIMULATION RESULTS OF THE WIFI FILTER

In this section, the simulation results of a reconfigurable WIFI filter cascaded with a centrally loaded 2.45 GHz cell and a normal 5.8 GHz cell is described.

The proposed reconfigurable WIFI filter and simulation are shown in Figure 3: Resonator A works at 2.45 GHz and Resonator B works at 5.8 GHz. C0 is used to block DC caused by the Biases of the two PIN switches.

The reconfigurable properties can be seen as:

When PIN A is ON, and PIN B is OFF: 2.45 GHz cell is a stop band at 2.45 GHz and pass band at 5.8 GHz, 5.8 GHz cell is a stop band at 2.45 GHz and pass band at 5.8 GHz. It is working as a band-pass filter at 5.8 GHz with an isolation of more than 40 dB at 2.45 GHz.

When PIN A is ON, and PIN B is OFF: similarly, it is working as a band-pass filter at 2.45 GHz with an isolation of more than 40 dB at 5.8 GHz.

When PIN A is ON, and PIN B is ON: 2.45 GHz cell is a stop band at 2.45 GHz and pass band at 5.8 GHz, 5.8 GHz cell is a pass band at 2.45 GHz and stop band at 5.8 GHz. It is working at dual-band band-stop mode.

When PIN A is OFF, and PIN B is OFF: similarly, it is working at dual-band band-stop mode, however, its performance is bad than (ON, ON) status.

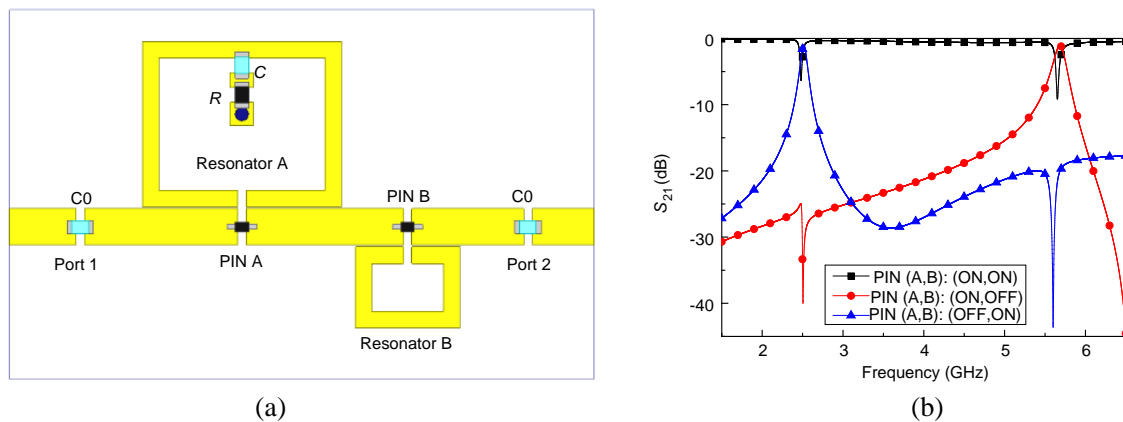


Figure 3: Simulation results of the proposed WIFI filter. (a) Reconfigurable WIFI filter. (b) The three working modes of the WIFI filter.

It is also can be seen that when the PIN switches shift their modes, the frequency will have a slight shift, which will limit the usage of the WIFI filter.

4. FUTURE WORK

The proposed WIFI filter can utilize varactors to resolve the problem by make the filter be continuously tunable. And it will combine mode shift at 2.45 GHz and 5.8 GHz and part continuously tunable at each frequency is more promising in WIFI systems.

5. CONCLUSION

In summary, a reconfigurable WIFI filter with three modes: dual-band band-stop filter, band-pass at 2.45 GHz and 5.8 GHz with a more than 40 dB protection at counterpart is proposed in this paper. A centrally loaded resonator is utilized to suppress the harmonic produced by the even mode of the normal resonator. It is very promising to using in modern WIFI systems.

ACKNOWLEDGMENT

This work was supported in part by the State Key Laboratory of CEMEE Foundation under Grant No. CEMEE2014Z0201A, in part by the Fundamental Research Funds for the Central Universities under Grant Nos. ZYGX2010J021 and ZYGX2012YB002, in part by the Program for New Century Excellent Talents in University under Grant No. NCET-13-****.

REFERENCES

1. Rebeiz, G. M., K. Entesari, I. C. Reines, S. J. Park, M. A. El-Tanani, A. Grichener, and A. R. Brown, "Tuning in to RF MEMS," *IEEE Microw. Mag.*, Vol. 10, No. 6, 55–72, Oct. 2009.
2. Zhu, L., S. Sun, and R. Li, *Microwave Band-pass Filters for Wideband Communications*, Wiley, New York, NY, USA, 2012.
3. Sanchez-Renedo, M., R. Gomez-Garcia, J. I. Alonso, and C. Briso-Rodriguez, "Tunable combline filter with continuous control of center frequency and bandwidth," *IEEE Trans. Microw. Theory Tech.*, Vol. 53, No. 1, 191–199, Jan. 2005.
4. Cho, Y. H. and G. M. Rebeiz, "0.73–1.03-GHz tunable band-pass filter with a reconfigurable 2/3/4-pole response," *IEEE Trans. Microw. Theory Tech.*, Vol. 62, No. 2, 252–265, Feb. 2014.
5. Abunjaileh, A. I. and I. C. Hunter, "Tunable band-pass and band-stop filters based on dual-band combline structures," *IEEE Trans. Microw. Theory Tech.*, Vol. 58, No. 12, 3710–3719, Dec. 2010.
6. El-Tanani, M. A. and G. M. Rebeiz, "A two-pole two-zero tunable filter with improved linearity," *IEEE Trans. Microw. Theory Tech.*, Vol. 57, No. 4, 830–839, Apr. 2009.
7. Chen, K., X. Liu, A. Kovacs, W. J. Chappell, and D. Peroulis, "Anti-biased electrostatic RFMEMS varactor and tunable filters," *IEEE Trans. Microw. Theory Tech.*, Vol. 58, No. 12, 3971–3981, Dec. 2010.

8. Wang, H., K. W. Tam, S. K. Ho, W. Kang, and W. Wu, “Design of ultra-wideband band-pass filters with fixed and reconfigurable notch bands using terminated cross-shaped resonators,” *IEEE Trans. Microw. Theory Tech.*, Vol. 62, No. 2, 290–296, Feb. 2014.
9. Chiou, Y.-C. and G. M. Rebeiz, “Tunable 1.55–2.1 GHz 4-pole elliptic band-pass filter with bandwidth control and 50 dB rejection for wireless systems,” *IEEE Trans. Microw. Theory Tech.*, Vol. 61, No. 1, 117–124, Jan. 2013.
10. Zhang, Y. X. and Q. Xue, “Novel centrally loaded resonators and their applications to band-pass filters,” *IEEE Trans. Microw. Theory Tech.*, Vol. 56, No. 4, 913–921, Apr. 2008.

Reconfigurable Substrate Integrated Waveguide

Yue Feng Hou, Yuan Jiang, Xian Qi Lin, Fei Cheng, and Yong Fan

EHF Key Laboratory of Science, School of Engineering
University of Electronic Science and Technology of China, Chengdu 611731, China

Abstract— In this paper, a new substrate integrated waveguide (SIW), which is called reconfigurable substrate integrated waveguide (RCSIW) is proposed. RCSIW is derived from SIW and tunable technology which is widely used in microwave system. It is realized by replacing the side-wall metal posts of SIW with several grounded varactors which are employed to make the SIW tunable. The cutoff frequency and propagation constant can be reconfigurable by controlling these varactors. A RCSIW is designed to test these properties with the input and output of microstrip line. Ansoft HFSS was used to get the characteristics of RCSIW. The results show the reconfiguration of RCSIW.

1. INTRODUCTION

Substrate integrated waveguide (SIW) has been interested by researchers around the world and widely used in microwave and millimeter wave circuit and system. A simple reason is that SIW, as a combination of waveguide and planar circuit, has a lot of attractive properties such as low cost, low profile, high power capacity and easy to integrate with planar circuits [1–4]. And there are some planar structures based on SIW, such as half-mode substrate integrated waveguide (HMSIW) [5], quarter-mode substrate integrated waveguide (QMSIW) [6], ridge substrate integrated waveguide (RSIW) [7], folded substrate integrated waveguide (FSIW) [8], corrugated substrate integrated waveguide (CSIW) [9] and so on.

Reconfigurable technologies are required in many microwave systems, such as multiband wireless communication and wideband radar systems. Varactors, micro-electromechanical systems (MEMS) and piezoelectric transducers and ferroelectric components are common reconfigurable technologies. Due to the high tuning speed and reliability, diode varactors are widely utilized in the design of reconfigurable devices [10–12].

HMSIW and QMSIW structures, due to their open side, are very suitable to place varactors, which makes them be employed with reconfiguration technologies conveniently. The concept of HMSIW which is forming by bisecting SIW along a fictitious quasi-magnetic wall was proposed in [7]. As an improved structure, HMSIW keeps most of the excellent performance of SIW, while both the waveguide width and the size of the structure are reduced by nearly a half compared with the SIW. Since its birth, the characterization of the propagation properties of HMSIW has been studied in [13]. Because the center symmetrical plane of the HMSIW can also be equivalently regarded as a quasi-magnetic wall for some particular modes, the HMSIW can be further bisected into two parts again along the symmetrical plane. Hence, a QMSIW is realized. The field distribution of the QMSIW is almost the same as the field distribution of the original SIW [6]. QMSIW has only 25% size of SIW, meanwhile, the advantages of SIW has been inherited.

In this paper, a new SIW structure with electrically tunable technology is been proposed, and we call it reconfigurable substrate integrated waveguide (RCSIW). It is realized by replacing the side-wall metal posts of SIW with several grounded varactors. The cutoff frequency and propagation constant of RCSIW can be tuned by changing the capacitance of the varactors. The characteristics of RCSIW are presented in Section 2, conclusions are presented in Section 3.

2. CHARACTERISTICS OF RCSIW

In this section, we investigate the electric field, modes, insertion loss, cutoff frequency and propagation constant of RCSIW. RCSIW is designed with substrate F4B, which $h = 0.764$ mm, $\epsilon_r = 2.55$, and $\tan \delta = 0.001$. Ansoft HFSS is used as an aided designer to simulate and explore the properties of SIW structures.

2.1. Dominant Mode of RCSIW

Figure 1 shows the configuration of RCSIW, microstrip line is employed to make the measurement convenient. Microstrip-RCSIW transition is used to match the RCSIW and microstrip line. To construct a RCSIW, first, two gaps are cut on the top of SIW, after that, several varactors are

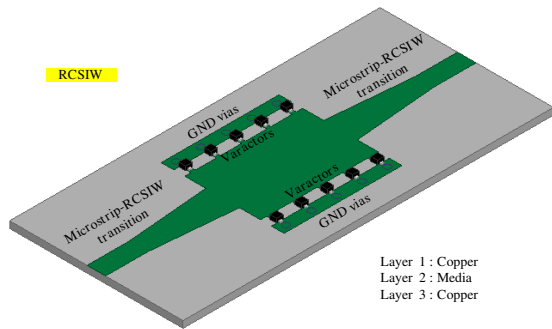


Figure 1: Configuration of the proposed RCSIW.

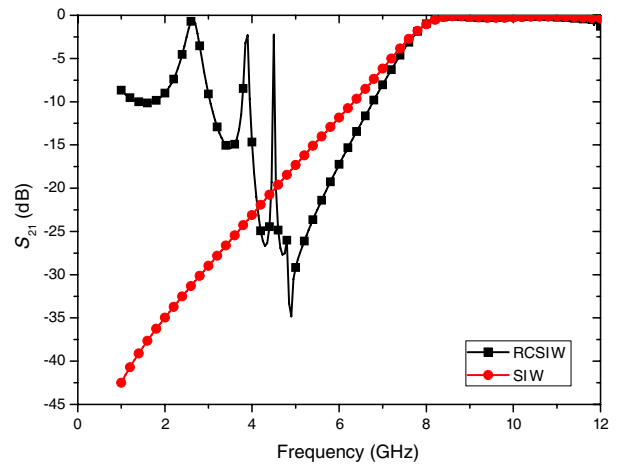


Figure 2: S_{21} of RCSIW and SIW.

placed on the gaps. In this case, there are five varactors on each side of the gap. A SIW is designed to compare with RCSIW and they have the same cutoff frequency.

Figure 2 shows the S_{21} of RCSIW and SIW. Comparing the two structures, it can be tell that, the insertion losses of SIW and RCSIW are on the same level about 0.3 dB, at the frequency of 8.2 GHz to 11 GHz. But the insertion loss of RCSIW is not so gentle compared with SIW, the insertion loss of RCSIW is 0.5 dB, at the frequency of 12 GHz. It also shows RCSIW has much more modes below the cutoff frequency, but it does not matter when the RCSIW is used to working at the waveguide dominant mode.

Figure 3 shows the electric fields of RCSIW and SIW at 8.2 GHz. The electric field of RCSIW is similar to that of SIW, when they work on dominant mode: TE_{10} mode, at the same frequency. It is shown that the width of RCSIW is a litter narrower than SIW, which is caused by the capacity

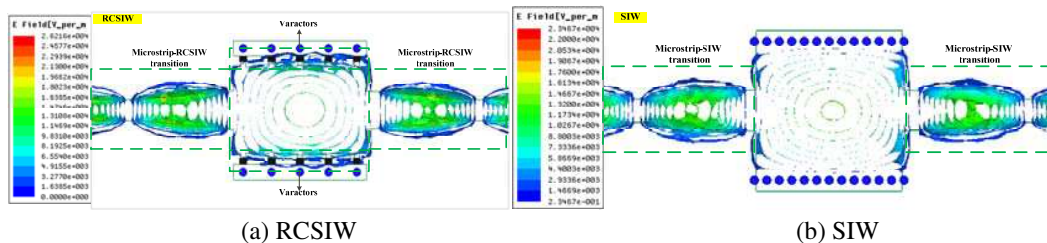


Figure 3: Electric field (dominant mode: TE_{10}) of RCSIW and SIW.

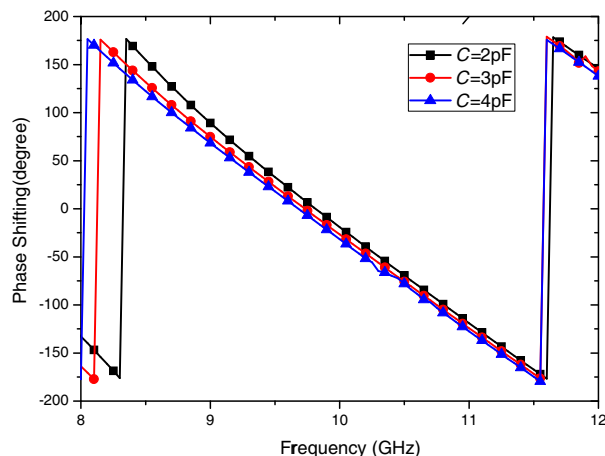


Figure 4: Phase shifting of RCSIW varied with the capacity of the loaded varactors.

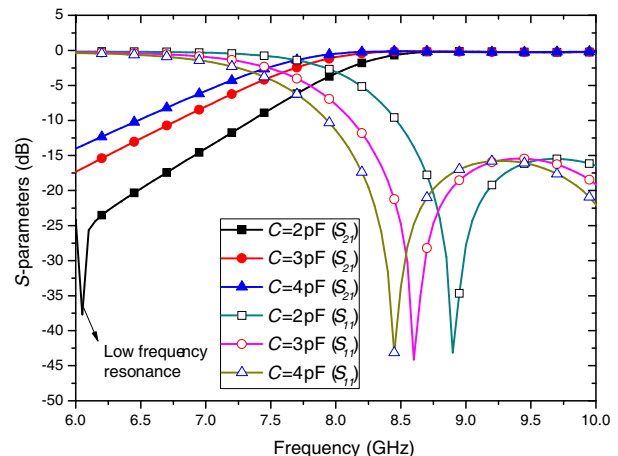


Figure 5: S -parameters of RCSIW varied with the capacity of the loaded varactors.

effect of varactors. And the varactors are placed in the two sides of the RCSIW with very low level electric field, which means the displacement current flowing through series resistance of the varactors is rather small leading a quite safe situation of the varactors.

2.2. Reconfiguration of RCSIW

In this subsection, the capacity of the varactors is tuned simultaneously to make the RCSIW reconfigurable. When the capacity of the varactors is varied from 2 pF to 4 pF, the phase of RCSIW changes 40.6 degree (shown in Figure 4). It is caused by the varactors changing the equivalence width of RCSIW, which makes the propagation constant of RCSIW reconfigurable. So RCSIW can be used in reconfigurable phase shifters.

Figure 5 shows the cutoff frequency can be tuned by controlling the capacity of the varactors. It is also caused by the changing the equivalence width of RCSIW. This property makes RCSIW to be promising in reconfigurable filters.

3. CONCLUSIONS

In this paper, a new reconfigurable substrate integrated waveguide is proposed. Varactors are employed to make the RCSIW tunable. The cutoff frequency and propagation constant of RCSIW can be tuned by changing the capacitance of the varactors, and these varactors are placed in a quite safe situation. The RCSIW structure is promising in microwave and millimeter circuits and systems.

ACKNOWLEDGMENT

This work was supported in part by the State Key Laboratory of CEMEE Foundation under Grant No. CEMEE2014Z0201A, in part by the Fundamental Research Funds for the Central Universities under Grant Nos. ZYGX2010J021 and ZYGX2012YB002, in part by the Program for New Century Excellent Talents in University under Grant No. NCET-13-****.

REFERENCES

1. Wu, K., D. Deslandes, and Y. Cassivi, "The substrate integrated circuits — A new concept for high-frequency electronics and optoelectronics," *2003 6th International Conference on TELSIKS*, Vol. 1, P-III-P-X, Oct. 2003.
2. Sekar, V. and M. Armendariz, "A 1.2-1.6-GHz substrate-integrated-waveguide RF MEMS tunable filter," *IEEE Transactions on Microwave Theory and Techniques*, Vol. 59, 866–876, 2011.
3. Jiang, C. Y. and C. Z. Ning, "Single-layered SIW post-loaded electric coupling-enhanced structure and its filter applications," *IEEE Transactions on Microwave Theory and Techniques*, Vol. 61, 125–130, 2013.
4. Ke, G. and H. Wei, "Substrate integrated waveguide quasi-elliptic filters with controllable electric and magnetic mixed coupling," *IEEE Transactions on Microwave Theory and Techniques*, Vol. 60, 3071–3078, 2012.
5. Hong, W., B. Liu, Y. Q. Wang, Q. H. Lai, and K. Wu, "Half mode substrate integrated waveguide: A new guided wave structure for microwave and millimeter wave application," *Proc. Joint 31st Int. Infrared Millimeter Wave Conf./14th Int. Terahertz Electron. Conf.*, 18–22, Shanghai, China, Sep. 2006.
6. Jin, C. and R. Li, "Quarter-mode substrate integrated waveguide and its application to antennas design," *IEEE Transactions on Antennas and Propagation*, Vol. 99, 1–1, 2013.
7. Yan, D. and W. Ke, "Miniaturization techniques of substrate integrated waveguide circuits," *IEEE MTT-S International Microwave Workshop Series on Art of Miniaturizing RF and Microwave Passive Components, IMWS 2008*, 63–66, 2008.
8. Grigoropoulos, N. and P. R. Young, "Compact folded waveguides," *34th European Microwave Conference*, 973–976, London, United Kingdom, Oct. 12–14, 2004.
9. Eccleston, K. W., "Mode analysis of the corrugated substrate integrated waveguide," *IEEE Transactions on Microwave Theory and Techniques*, Vol. 60, No. 10, 3004–3012, 2012.
10. Hunter, I. C. and J. D. Rhodes, "Electronically tunable microwave band-pass filters," *IEEE Trans. Microw. Theory Tech.*, Vol. 30, No. 9, 1354–1360, Sep. 1982.
11. Park, S.-J. and G. M. Rebeiz, "Low-loss two-pole tunable filters with three different predefined bandwidth characteristics," *IEEE Trans. Microw. Theory Tech.*, Vol. 56, No. 5, 1137–1148, May 2008.

12. Yin, Z. X. and X. Quan, “High-selectivity tunable bandpass filters with harmonic suppression,” *IEEE Transactions on Microwave Theory and Techniques*, Vol. 58, 964–969, 2010.
13. Lai, Q., C. Fumeaus, W. Hong, and R. Vahldieck, “Characterization of the propagation properties of the half-mode substrate integrated waveguide,” *IEEE Trans. Antennas Propag.*, Vol. 57, 1996–2004, 2009.

A Compact Substrate Integrated Waveguide Diplexer Using Dual-mode Filters

F. Cheng, X. Q. Lin, Y. Jiang, K. J. Song, and Y. Fan

EHF Key Lab of Fundamental Science, School of Electronic Engineering
University of Electronic Science and Technology of China, Chengdu 611731, China

Abstract— This paper presents a novel approach for designing compact integrated substrate waveguide diplexer fed by coplanar-waveguide. To reduce the size, conventional T -junction for impedance matching and isolation at the input port is replaced by the coplanar-waveguide-fed structure. It also contributes to size reduction of the diplexer. Two dual-mode integrated substrate waveguide filters are vertically stacked which results in further size reduction. A diplexer with lower and upper channels centered at 10 and 11 GHz, respectively, is designed to verify the proposed concept. Good agreements are achieved between measurement and simulation.

1. INTRODUCTION

Microwave diplexers are widely used in communication systems to allow two different devices to share a common communications channel [1]. For example, one application of diplexers is to allow two receivers working at different frequencies to share one antenna. Such a diplexer typically consists of two channel filters connected to the common input port through impedance transformers.

T -junction is the mostly common used impedance transformer in a diplexer design [2]. However, it occupies large area. It is a significant drawback for a communication system which has size requirements. Moreover, it would introduce extra insertion loss which increases with its length. Therefore, a lot of investigations have been carried out and various design approaches have been proposed to alleviate this problem [3, 4]. One approach is to use the reactance component to shorten the T -junction arms [3]. But some unwanted resonance would rise. And readjustment is required due to the short T -junction would affect the performance of each channel filter. In [4], common resonator sections were used to realize compact microstrip diplexers. By properly locating the fundamental and the first spurious resonant frequencies of the common resonators, these resonators can be shared by both filter channels. In this way, the T -junction was removed and the total number of resonators was reduced. Thus, the circuit size was dramatically reduced.

Substrate integrated waveguide (SIW) dual-mode resonators have the ability to reduce the total number of resonators. Meanwhile, the unloaded Q of the dual-mode is higher than that of the fundamental mode [5–8]. In this letter, these resonators are adopted in the channel filter design. The filters are fed by coplanar-waveguide (CPW) at the common port. On one hand, this feeding structure has a wider range of Q_e . On the other hand, the circuit size is dramatically reduced without the T -junction. The design procedure is simplified since no T -junction or common resonators are required. The diplexer size is further reduced by vertically stacking the two channel filters. To demonstrate, a diplexer centered at 10 GHz and 11 GHz is implemented.

2. CHARACTERISTICS OF THE DUAL-MODE SIW CAVITY

Figure 1 illustrates the structure of the dual-mode SIW resonator. Two perturbation vias with a diameter of d_1 are placed in the diagonal line of the square. Where, a is the width of the square cavity, h is thickness of the substrate, d is the diameter of the sidewall vias, p is the distance between two adjacent vias' center, and t is the distance from the perturbation vias to the sidewalls.

Dual-mode SIW resonator is adopted here for its high unloaded Q value which may lead to a low insertion loss of the diplexer. Table 1 compares the unloaded Q values of different resonant modes. All the cavities are squared-shaped. In the dual-mode cavity, two metallic perturbation vias with diameter of 0.8 mm are located along the diagonal line of the square cavity with 4 mm perpendicular to the sidewall. Table 1 demonstrates that diagonal TE_{201} and TE_{102} modes have higher unloaded Q values than the fundamental mode TE_{101} mode.

The first degenerate modes in a square cavity are diagonal TE_{102} and TE_{201} mode. When the two perturbation vias move along the diagonal line of the cavity, the resonant frequency of one degenerate mode stays the same, while the other one increases with t , as shown in Fig. 2. It is because the electrical field is zero in the diagonal line for the former one mode. Thus, the perturbation vias would not influence the electrical field distribution. On the other hand, the

Table 1: Comparison of different resonant modes in a square cavity.

Mode	Q_u and frequency
TE ₁₀₁	578 @ 9 GHz
diagonal TE ₂₀₁ /TE ₁₀₂	591 @ 9 GHz / 605 @ 9.62 GHz

where, the substrate thickness is 0.8 mm, relative permittivity is 2.65, loss tangent is 0.001, the foil is copper with a thickness of 0.018 mm.

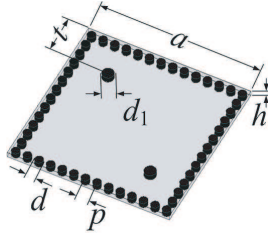


Figure 1: Structure of the dual-mode SIW resonator.

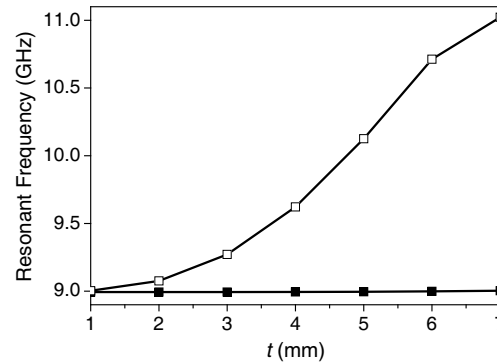


Figure 2: Variation of the resonant frequencies of diagonal TE₂₀₁ and TE₁₀₂ mode with respect to the position of the perturbation vias. ($a = 23.7$ mm, $h = 0.8$ mm, $p = 1$ mm, $d = d_1 = 0.8$ mm).

electrical field is not zero for the latter mode. So the resonant frequency changes with the location of the perturbation vias.

The resonant frequency of the TE_{*mnl*} mode is decided by [9]

$$f_{mnl} = \frac{c}{2\pi\sqrt{\mu_r\epsilon_r}} \sqrt{\left(\frac{m\pi}{a}\right)^2 + \left(\frac{n\pi}{h}\right)^2 + \left(\frac{l\pi}{b}\right)^2}, \quad (1)$$

where a , b , and h are the cavity's length, width and height respectively, c_0 is the light velocity in vacuum, μ_r and ϵ_r are the relative permeability and relative permittivity of the cavity substrate. According to (1), the effective length of the square cavity can be calculated by

$$a_{eff} = \frac{c_0}{2f_{201}} \sqrt{\frac{5}{\epsilon_r}}, \quad (2)$$

where, f_{201} is the resonant frequency of TE₂₀₁ mode. According to (2), we can get the length of the cavity, which can expressed as [10]

$$a = a_{eff} + \frac{d^2}{0.95p}. \quad (3)$$

Thus, according to the resonant frequency, we can decide the size of the cavity.

3. DESIGN OF THE PROPOSED DIPLEXER

As illustrated in Fig. 3, the diplexer consists of two substrates. On each substrate, there is a square cavity. On the metal layer II, a 50-Ω CPW feeding line is fabricated to feed the two channel filters. On the metal layer I and II, Port 2 and 3 are fed through microstrip to CPW transition. The design procedures of the two dual-mode filters are similar to that described in [5]. Each channel filter can be designed separately, but with the same CPW feeding structure at the input port. Then, combine them into a diplexer. No impedance match work is needed. Thus, the design procedure is simplified.

The CPW feeding line on metal layer II is dependent on the external quality factor of the two channel filters. In order to meet each channel filter's bandwidth specification, the common port is required to have wider tunable range of Q_e . For comparison, two dual-mode SIW resonators

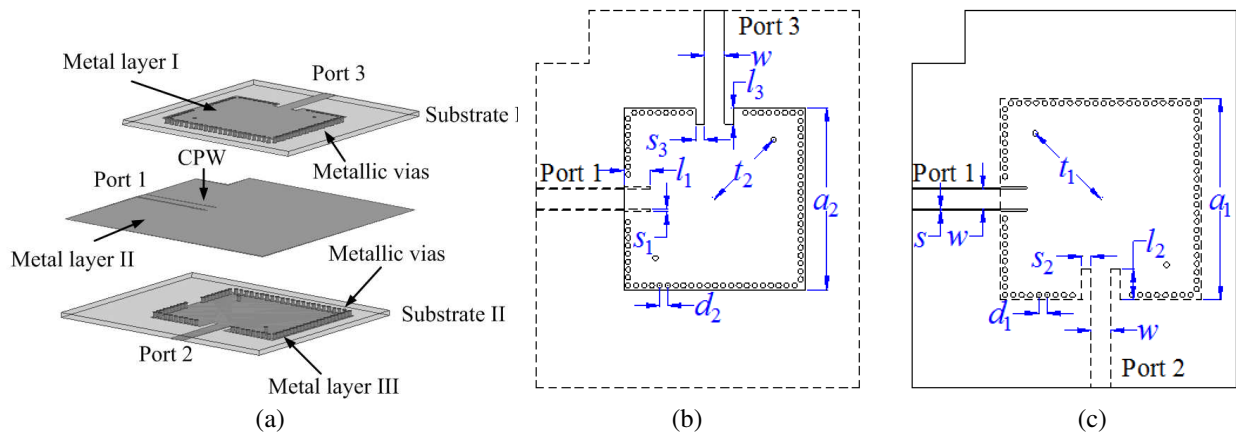


Figure 3: Structure of the proposed diplexer. (a) Exploded 3D view; (b) top view of Substrate I and (c) top view of Substrate II. ($w = 2.3$ mm, $l_1 = 3$ mm, $l_2 = 3.5$ mm, $l_3 = 1.8$ mm, $s = 0.1$ mm, $s_1 = 0.2$ mm, $s_2 = s_3 = 1$ mm, $t_1 = 10.55$ mm, $t_2 = 9.48$ mm, $d_1 = 0.96$ mm, $d_2 = 0.9$ mm, $a_1 = 22.8$ mm, $a_2 = 20.6$ mm).

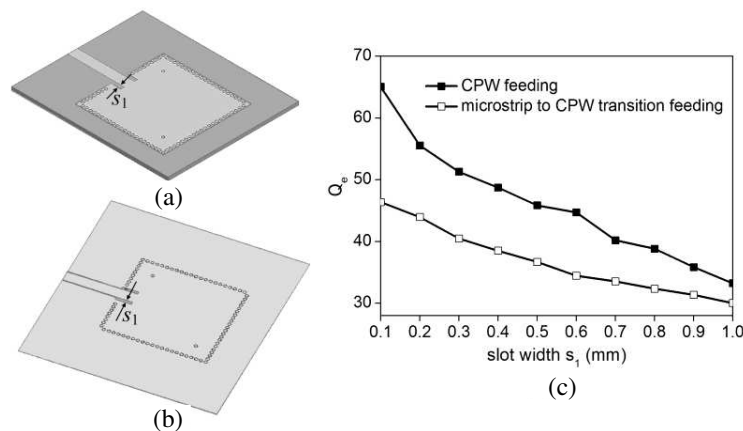


Figure 4: (a) Dual-mode resonator fed by microstrip to CPW transition structure; (b) Dual-mode resonator fed by CPW structure and (c) comparison of external quality factors between direct CPW feeding and microstrip to CPW transition feeding configurations. (Both the resonators have the same dimensions.)

with the same dimensions are fed by microstrip to CPW transition and CPW lines as shown in Figs. 4(a) and (b). A full-wave simulator is used to extract the Q_e of these two structures. Q_e can be extracted as

$$Q_e = \frac{f_0}{\Delta f_{\pm 90^\circ}}, \quad (4)$$

where f_0 denotes the resonant frequency, and $\Delta f_{\pm 90^\circ}$ is the bandwidth over which the phase shifts $\pm 90^\circ$ with respect to the absolute phase at f_0 [11]. The extracted Q_e with different slot width s_1 are compared in Fig. 4(c). As can be observed, the direct CPW feeding configuration obtains a wider range of Q_e , therefore, can be used to design filters with wider bandwidth ratio.

A SIW diplexer operating at 10 and 11 GHz is designed to demonstrate the above analysis. A F4B substrate with a relative dielectric constant of 2.65, a thickness of 0.8 mm, and a loss tangent of 0.001 is chosen for the diplexer design. Fig. 5 shows the photograph of the fabricated diplexer. The dimensions of the diplexer are illustrated in Fig. 3. The simulated and measured results are shown in Fig. 6. The simulated insertion loss at the two filter's center frequencies are 0.77 and 0.7 dB. The measured center frequencies of the lower and higher channel filters are 9.93 and 10.94 GHz respectively, and the corresponding insertion loss at the center frequencies is 2.31 and 1.75 dB. The simulated bandwidths for each filter are 0.52 and 0.59 GHz while the measured ones are 0.43 and 0.49 GHz. The simulated isolation is larger than 27 dB from 9 to 13 GHz while the measured one is larger than 29 dB in that band. The frequency shift is conjecturally caused by the errors of the substrate dielectric constant and the large insertion loss is conjecturally resulted from assembly

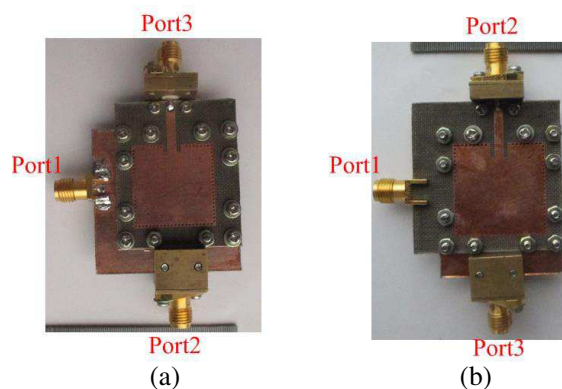


Figure 5: Photograph of the fabricated diplexer. (a) Top view and (b) bottom view.

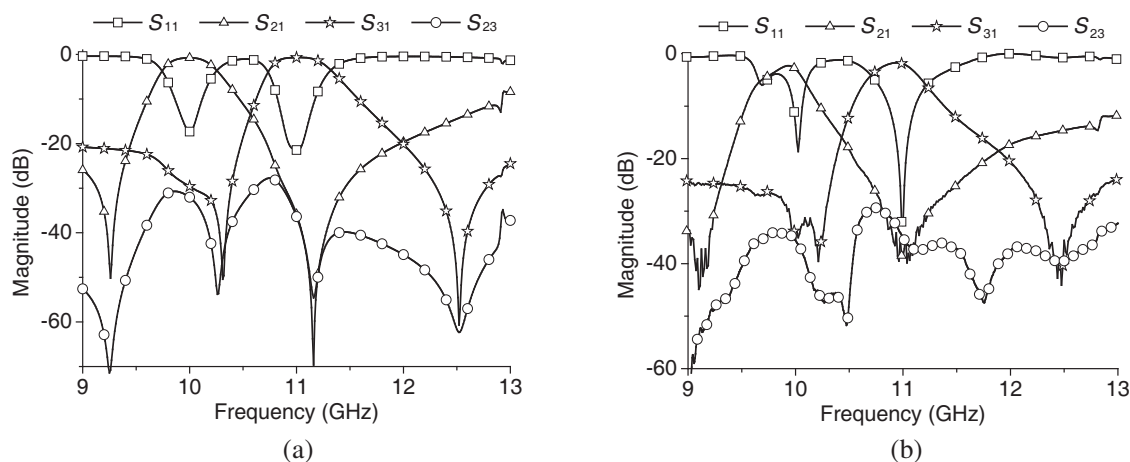


Figure 6: Simulated and measured results. (a) Simulation and (b) measurement.

errors and mismatch of the SMA connector.

4. CONCLUSIONS

A compact SIW diplexer using CPW-fed dual-mode filters has been studied in this letter. Extra combination circuits at the common port, as required in the conventional diplexer, are eliminated, which greatly simplifies the design procedures and reduces circuit size. Meanwhile, the multi-layer structure of the proposed diplexer allows further size reduction compared with planar diplexers. Good agreement between simulation and measurement has proved the validation of our concept.

ACKNOWLEDGMENT

This work was supported in part by China Scholarship Council, in part by NSFC (Nos. 61271026), in part by RFDP (No. 20090185120005), in part by the Fundamental Research Funds for the Central Universities (Nos. ZYGX2010J021 and ZYGX2012YB002), in part by the Program for New Century Excellent Talents in University (NCET-11-0066), and in part by the Research Fund of Shanghai Academy of Spaceflight Technology (SAST201243).

REFERENCES

1. Cameron, R. J. and M. Yu, "Design of manifold-coupled multiplexer," *IEEE Microwave Mag.*, Vol. 8, No. 5, 46–59, 2007.
2. Cheng, F., X. Q. Lin, Z. B. Zhu, L. Y. Wang, and Y. Fan, "High isolation diplexer using quarter-wavelength resonator filter," *IEE Electron. Lett.*, Vol. 48, No. 6, 302–303, 2012.
3. Tang, H. J., W. Hong, J.-X. Chen, G. Q. Luo, and K. Wu, "Development of millimeter-wave planar diplexers based on complementary characters of dual-mode substrate integrated waveguide filters with circular and elliptic cavities," *IEEE Trans. Microw. Theory Tech.*, Vol. 55, No. 4, 776–782, 2007.

4. Chuang, M.-L. and M.-T. Wu, “Microstrip diplexer design using common T-shaped resonator,” *IEEE Microw. Wirel. Compon. Lett.*, Vol. 21, No. 11, 583–585, 2011.
5. Chang, C.-Y. and W.-C. Hsu, “Novel planar, square-shaped, dielectric-waveguide, single-, and dual-mode filters,” *IEEE Trans. Microw. Theory Tech.*, Vol. 50, No. 11, 2527–2536, 2002.
6. Li, R. Q., X. Tang, and F. Xiao, “Substrate integrated waveguide dual-mode filter using slot lines perturbation,” *IEE Electron. Lett.*, Vol. 46, No. 12, 845–846, 2010.
7. Xu, Z. and H. Xia, “Miniaturized multilayer dual-mode substrate integrated waveguide filter with multiple transmission zeros,” *Progress In Electromagnetics Research*, Vol. 139, 627–642, 2013.
8. Xu, Z., Y. Shi, C. Xu, and P. Wang, “A novel dual mode substrate integrated waveguide filter with mixed source-load coupling (MSLC),” *Progress In Electromagnetics Research*, Vol. 136, 595–606, 2013.
9. Pozar, D. M., *Microwave Engineering*, Wiley, New York, 1998.
10. Cassivi, Y., L. Perregrini, P. Arcioni, M. Bressan, K. Wu, and G. Conciauro, “Dispersion characteristics of substrate integrated rectangular waveguide,” *IEEE Microw. Wireless Compon. Lett.*, Vol. 12, No. 9, 333–335, 2002.
11. Hong, J.-S. and M. J. Lancaster, *Microstrip Filter for RF/Microwave Applications*, Wiley, New York, 2001.

Ka-band Wideband Filter with a Reconfigurable Mode of Bandpass-bandstop Switching

Yuan Jiang, Jiawei Yu, Xian Qi Lin, Fei Cheng, and Yong Fan

EHF Key Laboratory of Science, School of Engineering
University of Electronic Science and Technology of China, Chengdu 611731, China

Abstract— In this paper, a Ka-band wideband filter with a reconfigurable mode of bandpass-bandstop switching is presented. As a low-Q resonator, a rectangle ring with a straight “tail” is inserted into the central E -plane of a waveguide to realize the wideband performance. With the “ON” or “OFF” state of the PIN diode, the EM field driving by the resonator may be the same direction with or suppress the TE_{10} of the waveguide, which makes the filter be reconfigurable. At the frequency of 33 GHz–37 GHz, the insertion loss is lower than 1 dB at band-pass mode, and when it is working as a band-stop filter, the insertion loss is more than 15 dB on the whole frequency band.

1. INTRODUCTION

Recently, reconfigurable filters are taking an increasing attention for their multi-functional and low-profile features in modern wireless and mobile communication systems [1]. Studies are focus on center frequency tuning [2] and bandwidths or constant bandwidths [3] are common, and pass-stop mode reconfigurable [4], tunable rejection levels and notch of UWB tunable [5] are also popular.

Metallic waveguide filter, widely used in millimeter wave systems, has advantages of high power capability and low loss. However, its size is much larger than that of planar one. Many miniaturization technologies have been investigated to design waveguide filters [6–9].

In this paper, a modes reconfigurable wideband filter with rectangle waveguide is presented. A PIN switch and rectangle ring resonator are used to design the WIFI filter. The design and simulation are demonstrated in the following sections. In order to test the performance of the reconfigurable WIFI filter, a standard Ka-band waveguide with a width of 7.112 mm and height of 3.556 mm. substrate F4B with thickness of 0.8 mm and dielectric constant of 2.65 was used in the EM simulation with Ansys HFSS.

2. DESIGN OF PROPOSED RECONFIGURABLE FILTER

In this section, the Ka-band filter is designed to have a reconfigurable property with rectangle ring resonator and a PIN switch.

A rectangle ring resonator is low-Q [10], which will have a wideband property. In order to test the properties of a rectangle ring resonator, two simulations are utilized. They are all using a substrate with a metal layer forming the rectangle ring resonator in standard Ka-band waveguide. The

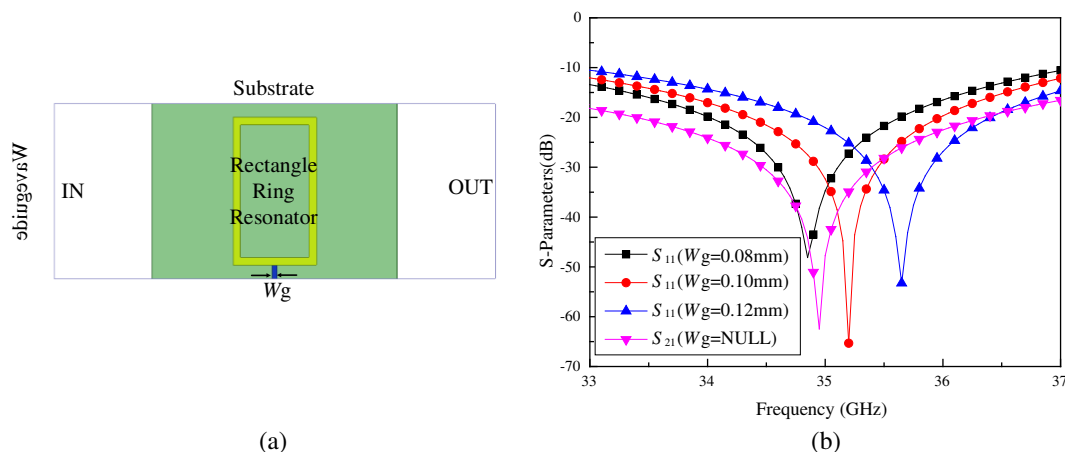


Figure 1: Performance of rectangle ring resonator. (a) Rectangle ring resonator. (b) The performance of the rectangle ring resonator.

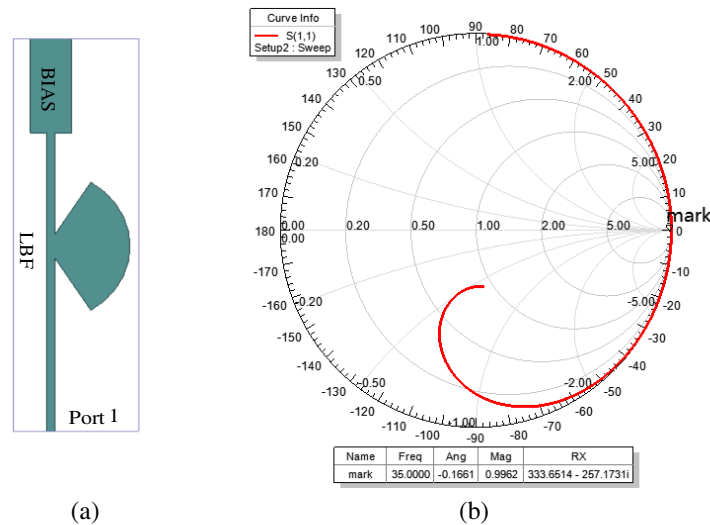


Figure 2: Bias of the PIN switch. (a) Model of the DC bias. (b) The Smith chart of the bias.

rectangle ring resonator plane is mounted along the center of wide side of the Ka-band waveguide with and without a straight “tail” ground to the waveguide, as shown in Fig. 1(a).

Figure 1(b) shows the simulation results of the tests:

When the rectangle ring resonator is alone without the “tail”, it is a band-stop filter, with a insertion loss of 65 dB at center frequency.

When the rectangle ring resonator is connect the wall of the waveguide with the “tail”, it is a band-pass filter, and has a deep reflection pole. If the width W_g can be tuned, the center frequency of the band-pass filter will be changed greatly. So, this property can be used to design a reconfigurable filter with a PIN switch changing the working state of filter.

To design the reconfigurable filter, three steps may be followed:

Firstly, make the rectangle ring resonator working at needed frequency. It can be achieved by adjusting the size of the rectangle ring resonator when it is alone without the “tail”.

Secondly, design the PIN switch position to make another mode working at center frequency. It can be achieved by adjusting the width of the “tail” W_g fixing the dimension of first step.

Lastly, design the DC bias of the PIN switch. A low-pass filter is necessary to make sure the PIN switch is working and the microwave signal would not entry the DC path. The bias circuit should be open to the microwave signal.

Figure 2 shows the model and performance of the low-pass filter: at port 1, the bias circuit is open at the center frequency which make sure the bias circuit would not influence the microwave signal or the performance of the rectangle ring resonator.

3. SIMULATION RESULTS OF THE PROPOSED FILTER

In this section, the entail model and the simulation results of a reconfigurable Ka-band filter is described.

As shown in Fig. 3(a), the PIN switch is mounted out of the waveguide, to enhance the pass-band performance and reduce the current passing the PIN switch. The blue circles are ground posts ground the PIN switch and prevent the resonance of the substrate.

Figure 3(b) shows the simulation results of the Ka-band filter:

When the PIN switch is ON: it is a pass band at the frequency range of 33 GHz to 37 GHz, with an insertion loss less than 1 dB.

When the PIN switch is OFF: it is a stop band at the frequency range of 33 GHz to 37 GHz. The insertion loss is more than 15 dB at the entail band. And at the center frequency of 35 GHz, the isolation of the input and output is about 65 dB.

The reconfigurable wideband filter is able to switching the mode of band-pass and band-stop.

4. FUTURE WORK

This technology can be combine with other reconfigurable or tunable technologies, for instance, the working frequency or bandwidth can be tuned with a varactor-based method.

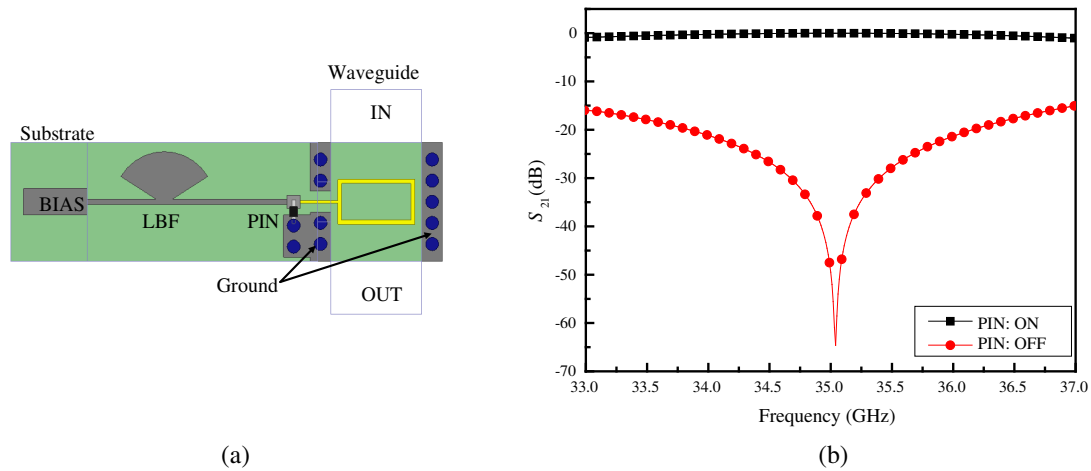


Figure 3: Simulation results of the proposed filter. (a) Entail model of the filter. (b) The simulation results of the filter with PIN switch working at different status.

5. CONCLUSION

This paper presents a Ka-band reconfigurable filter which has a function of switching band-pass and band-stop mode. A rectangle ring resonator is used to construct the resonator which will influence the EM field in the waveguide, so as to control the working state. The simulation shows At the frequency of 33 GHz–37 GHz, the insertion loss is lower than 1 dB at band-pass mode, and when it is working as a band-stop filter, the insertion loss is more than 15 dB on the whole frequency band, and at the center frequency of 35 GHz, the insertion loss is high to 65 dB. This technology can be used in microwave and millimeter wave systems.

ACKNOWLEDGMENT

This work was supported in part by the State Key Laboratory of CEMEE Foundation under Grant No. CEMEE2014Z0201A, in part by the Fundamental Research Funds for the Central Universities under Grant Nos. ZYGX2010J021 and ZYGX2012YB002, in part by the Program for New Century Excellent Talents in University under Grant No. NCET-13-****.

REFERENCES

1. Tsai, H. J., N. W. Chen, and S. K. Jeng, "Center frequency and bandwidth controllable microstrip bandpass filter design using loop-shaped dual-mode resonator," *IEEE Transactions on Microwave Theory and Techniques*, Vol. 61, 3590–3600, 2013.
2. Abunjaileh, A. I. and I. C. Hunter, "Tunable band-pass and band-stop filters based on dual-band combline structures," *IEEE Transactions on Microwave Theory and Techniques*, Vol. 58, No. 12, 3710–3719, Dec. 2010.
3. Sanchez-Renedo, M., R. Gomez-Garcia, J. I. Alonso, and C. Briso-Rodriguez, "Tunable combline filter with continuous control of center frequency and bandwidth," *IEEE Transactions on Microwave Theory and Techniques*, Vol. 53, No. 1, 191–199, Jan. 2005.
4. Cho, Y. H. and G. M. Rebeiz, "0.73–1.03-GHz tunable band-pass filter with a reconfigurable 2/3/4-pole response," *IEEE Transactions on Microwave Theory and Techniques*, Vol. 62, No. 2, 252–265, Feb. 2014.
5. Wang, H., K. W. Tam, S. K. Ho, W. Kang, and W. Wu, "Design of ultra-wideband band-pass filters with fixed and reconfigurable notch bands using terminated cross-shaped resonators," *IEEE Transactions on Microwave Theory and Techniques*, Vol. 62, No. 2, 290–296, Feb. 2014.
6. Bahrami, H., M. Hakkak, and A. Pirhadi, "Analysis and design of highly compact band-pass waveguide filter utilizing complementary split ring resonators (CSRR)," *Progress In Electromagnetics Research*, Vol. 80, 107–122, 2008.
7. Suntheralingam, N. and D. Budimir, "Compact S-shaped resonator loaded waveguide band-pass filters," *Antennas Propag. Society Intern. Symp.*, No. 1, 1–4, 2009.
8. Glubokov, O. and D. Budimir, "Compact *E*-plane doublet structures for modular filter design," *Eur. Microwave Conf.*, No. 1, 1253–1256, 2010.

9. Glubokov, O. and D. Budimir, “Novel inline waveguide E -plane filters using dual-mode extracted pole section,” *Eur. Microwave Conf.*, No. 1, 99–102, 2011.
10. Lin, X. Q., J. W. Yu, J. Yuan, J. Y. Jin, and F. Yong, “Electromagnetically induced transparencies in a closed waveguide with high efficiency and wide frequency band,” *Applied Physics Letters*, Vol. 101, 093502–093502-3, 2012.

Microstrip Filters with Adjustable Transmission Zeros Using Inductive-coupled Open Stub-loaded Resonators

F. Cheng, X. Q. Lin, Y. Jiang, K. J. Song, and Y. Fan

EHF Key Lab of Fundamental Science, School of Electronic Engineering
University of Electronic Science and Technology of China, Chengdu 611731, China

Abstract— This paper presents two compact microstrip bandpass filters using inductive-coupled open stub-loaded resonator. The character of the open stub-loaded resonator is studied. One adjustable transmission zero above the pass band of the filters is got by the open stub, which greatly improves the stopband rejection of the filter. The short-circuited stub is introduced to generate inductive-coupling between the resonators. In order to create more transmission zeros, cross-coupling between the source and load is introduced in the second filter design. The simulated and measured results agree very well which has demonstrated the validation of our design.

1. INTRODUCTION

Recent advances in wireless communication have created a need for filters with low insertion loss, good stopband rejection and high selectivity for the modern microwave communication system design [1]. It is usually favorable that a filter has several transmission zeros which can suppress the useless frequency near the passband or improve the stopband rejection. Several methods have been proposed to produce transmission zeros, such as adopting proper cross-coupling between nonadjacent resonators [1–3], tapping microstrip line resonators [4], establishing separate multi coupling paths for adjacent resonators [5, 6].

A filter consists of a quarter-wavelength open stub between quarter-wavelength resonators was first reported in Ref. [7]. The filter has one transmission zero which can be adjusted by changing the length of the open stub. However, the proposed filter suffers from bad stopband suppression and only two transmission poles are got with three quarter-wavelength sections. Moreover, the first harmonic passband occurs at about $2f_0$. In the following years, this type of filter is developed by many researchers [8–10]. However, the problems still do not have completely solved.

In this paper, the open stub-loaded resonator can create both a transmission zero and a transmission pole. The short-circuit stub which equals to a K -inverter is used to generate inductive-coupling between adjacent resonators [11, 12]. The merit is the coupling can be controlled by the length of the short-circuit stub. In order to improve the performance of the filter, another third-order filter with source-load coupling is introduced to create more transmission zeros. In all, the implemented filters have a better stopband rejection and harmonic suppression compared with the filter in [7].

2. ANALYSIS OF THE OPEN STUB-LOADED RESONATOR

The proposed resonator structure composed of two short lines and a shunt open stub is shown in Fig. 1(a), where Z_1 and Z_2 are the characteristic impedances of the microstrip sections and θ_1 and θ_2 are the respective electrical lengths. l_1 , l_2 are the corresponding physical lengths. The input

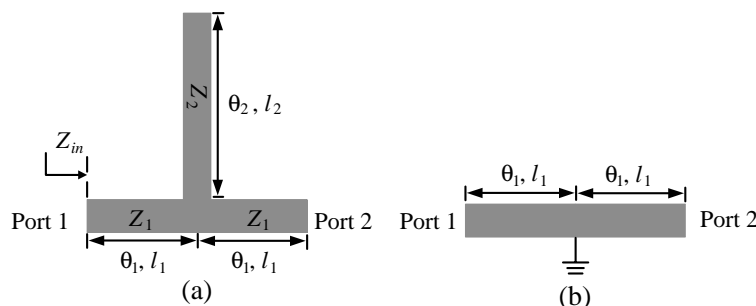


Figure 1: (a) Structure of the open stub-loaded resonator, (b) the equivalent circuit of the resonator when the open stub equals to a short circuit.

impedance of the resonator from port 1 is

$$Z_{in} = -jZ_1 \frac{Z_2 - \tan \theta_1 (Z_2 \tan \theta_1 + Z_1 \tan \theta_2)}{2Z_2 \tan \theta_1 + Z_1 \tan \theta_2}. \quad (1)$$

The resonance condition can be obtained by letting $Z_{in} = 0$,

$$Z_2 - \tan \theta_1 (Z_2 \tan \theta_1 + Z_1 \tan \theta_2) = 0. \quad (2)$$

It can be simplified as

$$\tan 2\theta_1 \tan \theta_2 = R_z, \quad (3)$$

where R_z is the impedance ratio, $R_z = 2Z_2/Z_1$. By solving the above equation, we can get the fundamental resonant frequency f_1 . On the other hand, an open circuit can equal to a short circuit by the open stub which plays a role as the $\lambda/4$ impedance inverter. If the center of the resonator is short-circuited as shown in Fig. 1(b), the energy from port 1 would be completely reflected and no energy would be transferred to port 2. Thus a transmission zero would be created. Let the open stub work as a $\lambda/4$ impedance inverter, we can get the frequency of the transmission zero which is expressed as

$$f_2 = \frac{c}{4\sqrt{\varepsilon_e}l_2}. \quad (4)$$

By changing l_2 , we can adjust the location of the transmission zero. Fig. 2 shows the $2l_1 + l_2$ under different l_2 and R_z when $f_1 = 2$ GHz. From the graph, for a certain l_2 , the smaller R_z is, the shorter total length $2l_1 + l_2$ is. When $R_z = 1$, the total length stay the same for different l_2 . Usually, l_2 is chosen a litter shorter than $\lambda/4$ at the filter's center frequency, to make the transmission zero near the passband. This would lead a good selectivity of the filter. On this condition, l_1 is very small as shown in Fig. 2. The total length $2l_1 + l_2$ would appropriate $\lambda/4$ at the filter's center frequency. Moreover, the open stub loaded resonator is very similar to a $\lambda/4$ SIR. When R_z is large, the first spurious response exhibits lower than $3f_1$, and vice versa. This phenomenon would be shown in the next section.

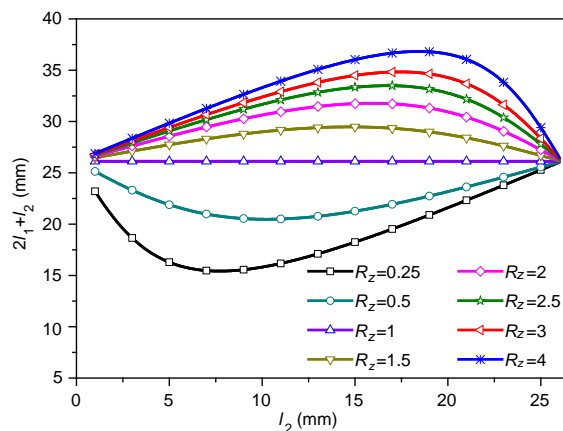


Figure 2: Solutions of $2l_1 + l_2$ for the given l_2 and R_z .

3. THIRD-ORDER FILTER REALIZATION

In this section, a third-order filter has been designed as shown in Fig. 3(a). The open stub-loaded resonator is connected to two quarter-wavelength resonator by two short-circuit stub. The short-circuit stub can be equaled to a K -inverter. The coupling coefficient can be adjusted by the length of the short-circuit stub or the radius of the via. Here, Z_1 and Z_2 are both 41.3Ω . l_2 is 21.8 mm to have a transmission zero at 2.26 GHz.

The third-order filter is designed to have 280 MHz bandwidth at a center frequency of 2 GHz. The measured and simulated frequency response of the proposed filter is given in Fig. 3(b). A F4B substrate with relative dielectric constant of 2.45, loss tangent of 0.001, and thickness of 0.8 mm is chosen for the filter fabrication. The measured results exhibit an absolute bandwidth of 260 MHz at the center frequency of 1.95 GHz and the measured minimum insertion loss is 1.1 dB. A transmission

zero is located at 2.22 GHz. The first spurious response is at about three times the center frequency. But the first spurious frequency of the open stub-loaded resonator is at 5.2 GHz which is lower than three times the center frequency 6 GHz. This is because its $R_z = 2 > 1$.

To validate the theory proposed in last section, other two filters using different open stub-loaded resonator are proposed. The filters have nearly the same bandpass response but different transmission zeros by choosing proper l_1 and l_2 . Fig. 4 shows the simulated response of these filters. It can be seen that the transmission zero can be adjusted by choosing different l_2 . The location of

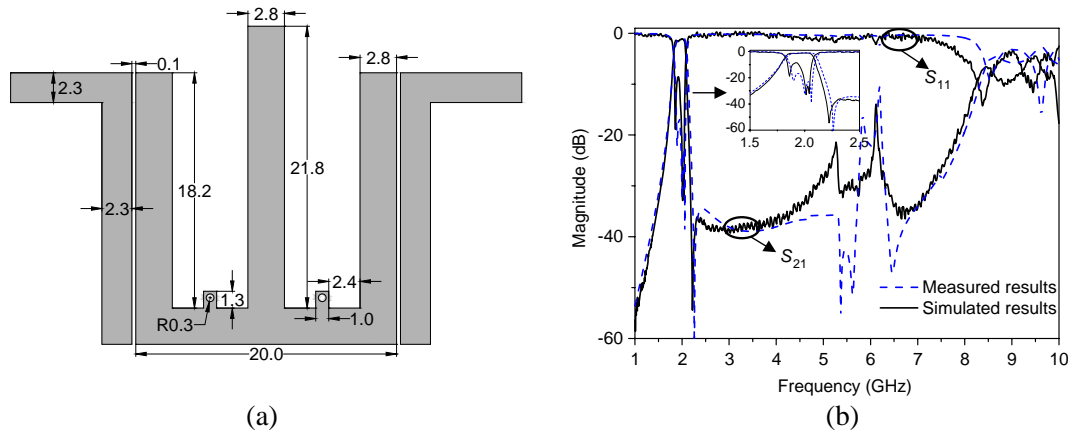


Figure 3: (a) Structure of the proposed third-order filter (unit: mm). (b) Simulated and measured results.

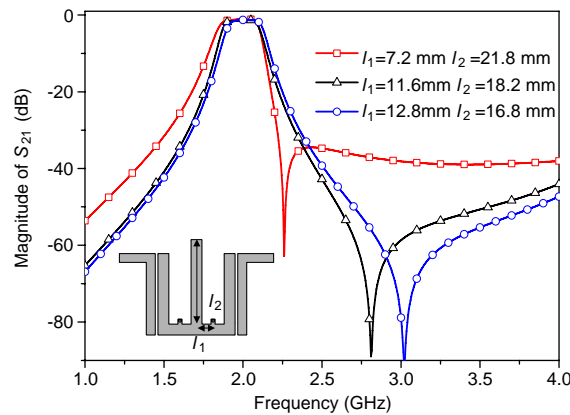


Figure 4: Filters' response with different l_1 and l_2 .

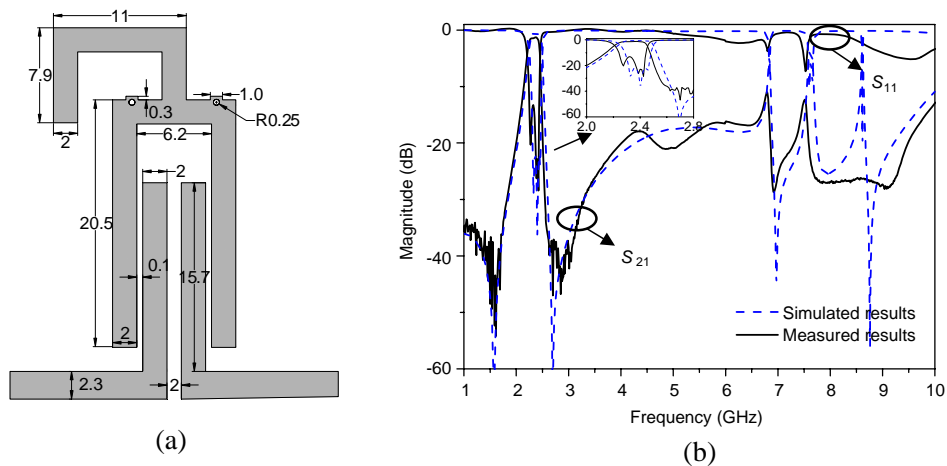


Figure 5: (a) Structure of the proposed third-order filter with source-load coupling (unit: mm). (b) Simulated and measured results.

the transmission zero is determined by Equation (4).

4. THIRD-ORDER FILTER WITH SOURCE-LOAD COUPLING

To produce more transmission zeros, another third-order cross-coupled filter is implemented as illustrated in Fig. 5(a). The input and output feedlines are capacitive-coupled to each other compared with the proposed filter structure in Section 3. The filter is designed to have a center frequency of 2.4 GHz and a fractional bandwidth of 10%. The measured and simulated results of the proposed filter are shown in Fig. 5(b). The implemented filter has a center frequency of 2.33 GHz, minimum insertion loss of 1.28 dB at 2.375 GHz, and 3-dB bandwidth of 10.2%. Two transmission zeros are located at about 1.6 GHz and 2.6 GHz respectively.

5. CONCLUSION

In this study, two novel microstrip bandpass filter using inductive-coupled open stub-loaded resonator has been proposed and carefully examined. By employing open stub-loaded resonator, the proposed filters exhibit one adjustable transmission zero at upper stopband which can be tuned by the length of the open stub. In addition, to produce more transmission zeros, the source-load coupling is added to the filter design. The proposed filters are useful for applications in the communication systems when low insertion loss and good stopband rejection are required.

ACKNOWLEDGMENT

This work was supported in part by China Scholarship Council, in part by NSFC (No. 61271026), in part by RFDP (No. 20090185120005), in part by the Fundamental Research Funds for the Central Universities (Nos. ZYGX2010J021 and ZYGX2012YB002), in part by the Program for New Century Excellent Talents in University (NCET-11-0066), and in part by the Research Fund of Shanghai Academy of Spaceflight Technology (SAST201243).

REFERENCES

1. Hong, J.-S. and M. J. Lancaster, *Microstrip Filter for RF/Microwave Applications*, Wiley, New York, 2001.
2. Lin, S.-C., Y.-S. Lin, and C. H. Chen, "Extended-stopband bandpass filter using both half- and quarter-wavelength resonators," *IEEE Microw. Wirel. Compon. Lett.*, Vol. 16, No. 1, 43–45, 2006.
3. Lu, J.-C., C.-K. Liao, and C.-Y. Chang, "Microstrip parallel-coupled filters with cascade trisection and quadruplet responses," *IEEE Trans. Microw. Theory Tech.*, Vol. 56, No. 9, 2101–2110, 2008.
4. Wang, C.-H., C.-K. Liao, C.-Y. Chang, P.-H. Deng, and C. H. Chen, "Coplanar-waveguide-fed microstrip bandpass filters with capacitively broadside-coupled structures for multiple spurious suppression," *IEEE Trans. Microw. Theory Tech.*, Vol. 55, No. 4, 768–775, 2007.
5. Hsieh, L.-H. and K. Chang, "Tunable microstrip bandpass filters with two transmission zeros," *IEEE Trans. Microw. Theory Tech.*, Vol. 51, No. 2, 520–525, 2003.
6. Ma, K.-X., J.-G. Ma, K.-S. Yeo, and M.-A. Do, "A compact size coupling controllable filter with separate electric and magnetic coupling paths," *IEEE Trans. Microw. Theory Tech.*, Vol. 54, No. 3, 1113–1119, 2006.
7. Lee, J.-R., J.-H. Cho, and S.-W. Yun, "New compact bandpass filter using microstrip $\lambda/4$ resonators with open stub inverter," *IEEE Microw. Wirel. Compon. Lett.*, Vol. 10, No. 12, 526–527, 2000.
8. Hong, J.-S., H. Shaman, and Y.-H. Chun, "Dual-mode microstrip open-loop resonators and filters," *IEEE Trans. Microw. Theory Tech.*, Vol. 55, No. 8, 1764–1770, 2007.
9. Zhang, X. Y., Z. Y. Yu, and J. Xu, "Design of microstrip dual-mode filters based on source-load coupling," *IEEE Microw. Wirel. Compon. Lett.*, Vol. 18, No. 10, 677–679, 2008.
10. Tu, W.-H., "Compact double-mode cross-coupled microstrip bandpass filter with tunable transmission zeros," *IET Microw. Antennas Propag.*, Vol. 2, No. 4, 373–377, 2008.
11. Chang, W.-S. and C.-Y. Chang, "Analytical design of microstrip short-circuit terminated stepped-impedance resonator dual-band filters," *IEEE Trans. Microw. Theory Tech.*, Vol. 59, No. 7, 1730–1739, 2011.
12. Cheng, F., X. Q. Lin, Z. B. Zhu, L.Y. Wang, and Y. Fan, "High isolation diplexer using quarter-wavelength resonator filter," *Electron. Lett.*, Vol. 48, No. 6, 330–331, 2012.

Design of Wideband Non-equiripple Filtering Response Using Genetic Algorithm Based Neural Network

Shiqing Cui¹, Sheng Sun¹, Shan Shan Gao², and Lei Zhu³

¹Department of EEE, The University of Hong Kong, Hong Kong, China

²Chengdu University, Chengdu, China

³Department of ECE, The University of Macau, Macau, China

Abstract— In this paper, the wideband multiple-mode-based bandpass filter with non-equiripple response is designed using genetic algorithm based neural network. The neural network is first employed to reduce the complexity in the design of wideband in-band equiripple response. Without deriving analytic solutions or solving non-linear equations, the coefficients of polynomials for the filters with non-equiripple responses can also be determined. Finally, the filters with both the five-pole equiripple and non-equiripple bandpass responses are designed and demonstrated. The accuracy of the proposed optimization method is also discussed in details.

1. INTRODUCTION

Ultra-wideband technology has been receiving much attention since the frequency range from 3.1–10.6 GHz was licensed for commercial communication applications by the Federal Communications Commission (FCC) in 2002. Thus, many researchers have explored different kinds of wideband bandpass filters with a fractional bandwidth of 110%. For the wideband filter design, some synthesis approaches have been developed based on the transmission line theory [1, 2]. However, these approaches were required to deal with the expressions of traditional *Chebyshev* functions and *ABCD* matrices. For the high-order filter with more transmission poles, the derivation becomes very complicated. In addition, the initial *em* simulated frequency responses of these synthesized filters are always poor and unpredictable, especially near the transition band due to the existing frequency dispersion and parasitic effects. This situation will probably get worse if the additional manufacturing errors are involved.

To remedy this issue, the *Chained-function* was employed as a transfer function in [3]. The insertion loss near the edge of the passband can be set to be smaller than that in the center of the passband, which is useful for reducing the sensitivity to the manufacturing errors. After that, a dome-shaped envelope filtering function in [4] provided an alternative solution to the *Chained-function* filter.

Very recently, a wide-band dome-shaped envelop filtering function was formulated. By computing the coefficients of the polynomials, a wide passband with non-equiripple response can be achieved [5, 6]. Nevertheless, this method still needs repetitive calculations of unknown coefficients for different specified ripple levels. To reduce the computational complexity, the numerical process based on neural network is proposed here to find these coefficients according to the filtering specifications. In general, the transfer functions for both equiripple and non-equiripple responses can be expanded as a polynomial with unknown coefficients. Thus, the forming transfer function becomes how to determine these coefficients.

In this paper, the genetic algorithm (GA) is used to optimize the learning process in the neural network [7], which can be trained to obtain the unknown coefficients for the required transfer function. This network is first trained to achieve equiripple *Chebyshev* response to prove its accuracy. Then, it can be extended to obtain the coefficients for the non-equiripple response, instead of solving the complicated non-linear equations in our previous study [5, 6]. The results show that this approach is accurate enough for the design of the wide-band bandpass filter and also efficient for the synthesis purpose.

2. DESIGN OF WIDEBAND FILTERING RESPONSES

To show the whole process for the proposed design approach, a single multiple-mode-resonator (MMR) bandpass filter with transmission poles is modeled. Fig. 1(a) shows the equivalent transmission line model of this filter. Here, the optimal design process has only one-step with neural network instead of the traditional two steps design approach with expressions of *ABCD* matrix and *Chebyshev* functions. The flow charts of the two design processes are shown in Fig. 1(b) and Fig. 1(c), respectively.

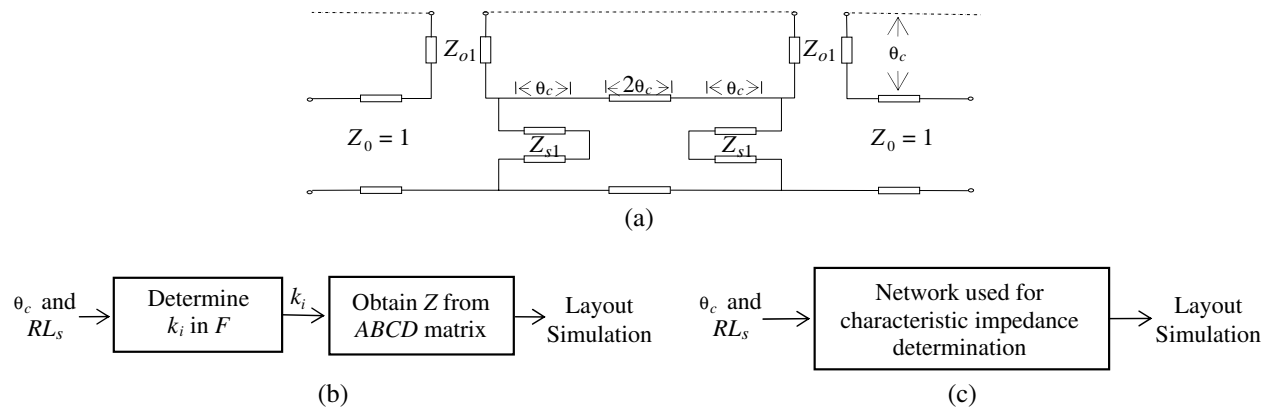


Figure 1: (a) Transmission-line model of a five-pole multiple-mode-based bandpass filter. (b) Flow chart of traditional design. (c) Flow chart of neural network based design.

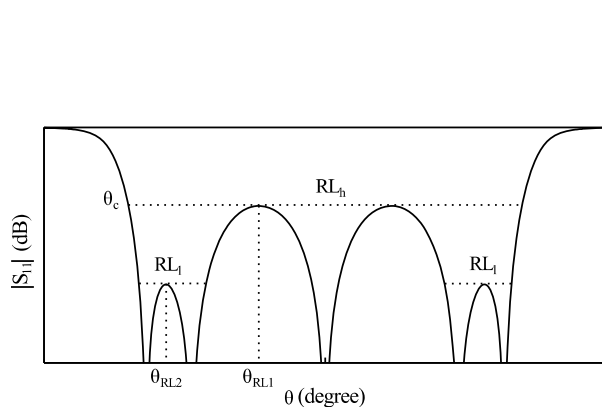


Figure 2: Reflection coefficients of a wideband bandpass filter with non-equiripple response.

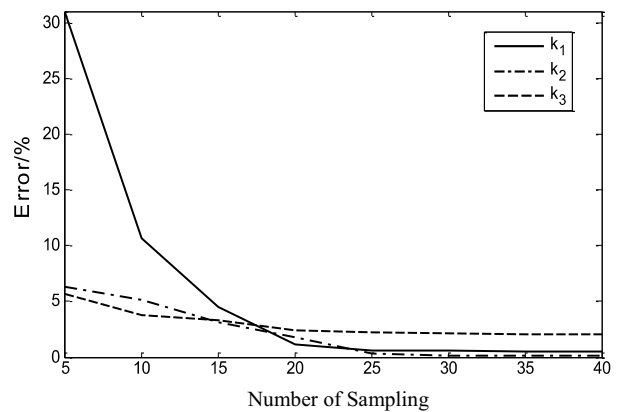


Figure 3: Training errors of network versus the number of sampling.

Traditionally, the characteristic impedances of each transmission line section can only be obtained from the $ABCD$ matrix after matching the coefficients of the transfer function F with *Chebyshev* function. Hence, the neural network can be trained to determine the coefficients. Next, we can also train the network to obtain the characteristic impedances.

According to the filter specifications, the cut-off frequency (θ_c) and the in-band reflection lobes (RL) as shown in Fig. 2 can be set as the samples of input vectors, while the coefficients k_i of filtering transfer function are set as the output vectors in the network training process. For all the network training process, the maximum training step is set to 2000 and the target error is zero. As shown in Fig. 3, the accuracy of the trained network can be enhanced by increasing of the number of the sampling data. It can also be noticed that the training error converges well when the number of the samples is larger than 25.

2.1. Equiripple Responses with Five Transmission Poles

For a five-pole *Chebyshev* bandpass filter with equiripple response, F can be derived as [1]

$$F = k_1 \frac{\cos^4 \theta}{\sin \theta} + k_2 \frac{\cos^2 \theta}{\sin \theta} + k_3 \frac{1}{\sin \theta} \quad (1)$$

Here, we can define the input vector according to the filter specifications as

$$P = \begin{bmatrix} \theta_c^1 & \theta_c^2 & \dots & \theta_c^{31} \\ RL^1 & RL^2 & \dots & RL^{31} \end{bmatrix} \quad (2)$$

where $\theta_c \in (10^\circ, 70^\circ)$ and $RL = -20$ dB. And the output vector is defined as

$$T = \begin{bmatrix} k_1^1 & k_1^2 & \dots & k_1^{31} \\ k_2^1 & k_2^2 & \dots & k_2^{31} \\ k_3^1 & k_3^2 & \dots & k_3^{31} \end{bmatrix} \quad (3)$$

where $n = 31$ in this case, and $k_{i=1,2,3}$ is the three unknowns of coefficients in (1). Table 1 shows the trained and analytically derived coefficients, and their relative errors. It can be noticed that the errors from the training are less than 2.1% in comparison with the results from the analytical solutions in [1]. It implies that the trained network can also achieve a good performance. Also, the frequency responses with the trained coefficients from the neural network have a good agreement with those obtained from analytical solutions.

Table 1: Trained results for five-pole bandpass filter with equiripple responses ($\theta_c = 45^\circ$ and $RL = -20$ dB).

Coefficients	Synthesis [1]	Trained	Errors
k_1	5.6284	5.5962	0.572%
k_2	-3.8799	-3.8808	0.023%
k_3	0.5828	0.5948	2.059%

2.2. Non-equiripple Responses with Five Transmission Poles

Different from the filter with equiripple responses, the unknown coefficients for the filter with non-equiripple responses cannot be derived analytically. Instead, we have to solve non-linear equations [6], where the design procedure becomes complicated. Thus, it would be interested to extend the aforementioned training process based on neural network to the filter design with non-equiripple responses. For this purpose, the coefficients for equiripple response filter can be adjusted within a small range to generate new sampling coefficients for the non-equiripple responses. With these new coefficients, the insertion loss and the return loss can also be determined. Subsequently, a set of cutoff frequency θ_c , the higher ripple constant RL_h and the lower ripple constant RL_l can be obtained as sampling points.

For the non-equiripple bandpass filter with five transmission poles, the input vector can be written as

$$P = \begin{bmatrix} \theta_c^1 & \theta_c^2 & \dots & \theta_c^{50} \\ RL_h^1 & RL_h^2 & \dots & RL_h^{50} \\ RL_l^1 & RL_l^2 & \dots & RL_l^{50} \end{bmatrix} \quad (4)$$

where the two reflection lobes may have different ripple-level constants RL_h and RL_l . Similarly, the output vector can be set as the same as (6), while the input vectors are the $\theta_c \in (10^\circ, 70^\circ)$, $RL_h \in (-21, -10)$ dB and $RL_l \in (-26, -20)$ dB. Fig. 4 shows the non-equiripple frequency responses of the designed filter based on the trained network.

The target and obtained network values for the parameters θ_c , RL_h , RL_l are tabulated in Table 2. The dotted lines indicate the target parameters θ_c , RL_h and RL_l . The error obtained from the trained network is about 3.68% for the ripples near the band edges, while the error near the center of band is about 0.20%, as shown in Table 2.

Table 2: Trained results for five-pole bandpass filter with non-equiripple responses.

Parameters	Target	Obtained	Errors
θ_c	0.5233	0.5292	1.13%
RL_h	-20.0000	-20.0394	0.20%
RL_l	-25.0000	-25.9212	3.68%

3. OPTIMIZATION FOR FILTER IMPLEMENTATION

Traditionally, in order to implement the above filter, the characteristic impedances of transmission line sections can then be determined via $ABCD$ matrices, as detailed in [1]. However, this synthesis procedure involves two steps: finding coefficients and determining the impedances. Based on the

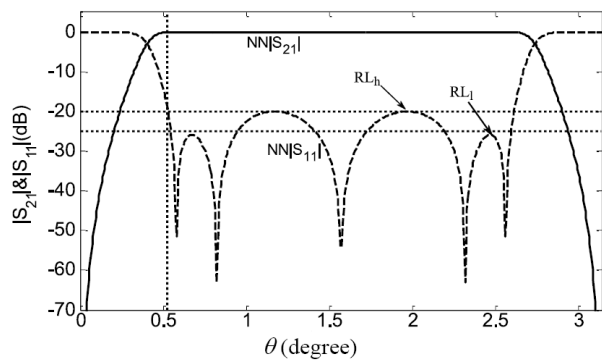


Figure 4: Frequency response $|S_{21}|$ and $|S_{11}|$ of the five-pole bandpass filter obtained from trained networks for non-equiripple responses, with $\theta_c = 30^\circ$, $RL_h = -20$ dB and $RL_l = -25$ dB.

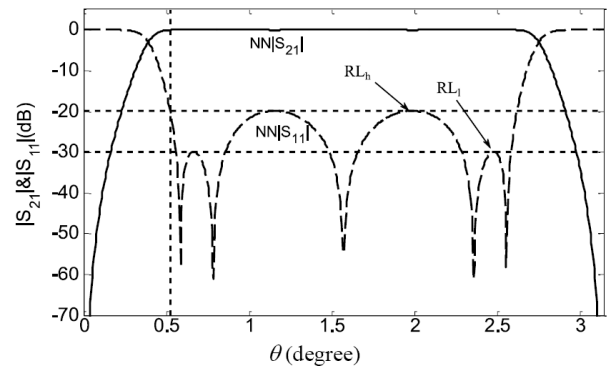


Figure 5: Frequency responses of the filter obtained from one-step training for non-equiripple responses ($\theta_c = 30^\circ$, $RL_h = -20$ dB and $RL_l = -30$ dB).

neural network optimization, this design procedure can also be simplified by omitting the first step with finding coefficients. Details of these two design procedures are shown in the flow chart of Figs. 1(b) and 1(c). Let's consider the filtering topology in [1] as an example. The input vector for the training initialization still contains three parameters, i.e., θ_c , RL_h and RL_l , as those defined in (7). The output vector of the training network can be set directly with the characteristic impedances in the transmission line model, i.e., z_{o1} , $z_{1,2}^1$, and z_{s1} , which is given by

$$T = \begin{bmatrix} z_{o1}^1 & z_{o1}^2 & \cdots & z_{o1}^{75} \\ z_{1,2}^{1,1} & z_{1,2}^{1,2} & \cdots & z_{1,2}^{1,75} \\ z_{s1}^1 & z_{s1}^2 & \cdots & z_{s1}^{75} \end{bmatrix} \quad (5)$$

Here, the sampling data with both the equiripple responses and non-equiripple responses are considered in the training process. Fig. 5 shows the trained results for filters with non-equiripple responses. As shown in Tables 3 and 4, the overall errors for the case with equiripple responses are less than 1.2%, while the errors are well controlled within 0.5% for the case with non-equiripple responses.

Table 3: Trained results for filter with equiripple responses.

Parameters	Target value	Network value	Error
θ_c	0.7850	0.7857	0.08%
RL_h	-20.0000	-19.8748	0.63%
RL_l	-20.0000	-20.2365	1.18%

Table 4: Trained results for filter with non-equiripple responses.

Parameters	Target value	Network value	Error
θ_c	0.5233	0.5234	0.01%
RL_h	-20.0000	-19.9051	0.47%
RL_l	-30.0000	-29.9713	0.10%

4. CONCLUSION

In this paper, the GA-based neural networks have been utilized in the design of the wideband bandpass filter. Instead of deriving complicated expressions in the traditional way, the design parameter can be easily obtained with a well robust control. In addition, the proposed method can be directly extended to obtain the design parameters for the filter with non-equiripple responses, where the traditional synthesis cannot be applied analytically. As shown in the given samples, the

overall errors for the final design are well controlled. Without any intermediate computation, the training process has been applied to obtain the characteristic impedances in the transmission line model.

REFERENCES

1. Li, R., S. Sun, and L. Zhu, "Synthesis design of ultra-wideband bandpassfilters with composite series and shunt stubs," *IEEE Trans. Microwave Theory & Tech.*, Vol. 57, No. 3, 684–692, Mar. 2009.
2. Chin, K.-S., L.-Y. Lin, and J.-T. Kuo, "New formulas for synthesizing microstrip bandpass filters with relatively wide bandwidths," *IEEE Microw. Wireless Compon. Lett.*, Vol. 14, No. 5, 231–233, May 2004.
3. Chrisostomidis, C. E. and S. Lucyszyn, "On the theory of chained-function filters," *IEEE Trans. Microwave Theory & Tech.*, Vol. 53, No. 10, 3142–3151, Oct. 2005.
4. Jayyousi, A. B., M. J. Lancaster, and F. Huang, "Filtering functions with reduced fabrication sensitivity," *IEEE Microw. Wireless Compon. Lett.*, Vol. 15, No. 5, 360–362, May 2005.
5. Sun, S. and S. S. Gao, "Design and implementation of wideband bandpassfilter with shunt short-circuited stubs and non-equiripple responses," *IEEE MTT-S Int. Microwave Symp.*, 2013.
6. Gao, S. S. and S. Sun, "Synthesis of wideband parallel-coupled linebandpassfilters with non-equiripple responses," submitted to *IEEE Microw. Wireless Compon. Lett.*, 2014.
7. Wilde, P. D., *Neural Network Models: Theory and Projects*, Springer, London, 1997.

Dual-polarized Unit-cell of Continuous Reflective Phase-shift for Reconfigurable Reflectarrays

M. T. Zhang^{1,2}, S. Gao¹, J. X. Wan², B. N. Tian², and C. B. Wu²

¹School of Engineering and Digital Arts, University of Kent, Canterbury, CT2 7NT, UK

²Xi'an Institute of Space Radio Technology, Xi'an, Shaanxi 710100, China

Abstract— This paper presents a Ku-band dual-polarized patch unit-cell of continuous phase shift for reconfigurable reflectarray antennas, which can twist the polarization of incident wave. This cross-polarized unit-cell can be applied in the folded reflectarray configuration for beam-scanning, and its performance is validated by the full-wave simulations under periodic boundary conditions. The scattered phase of the cross-polarized field varies continuously by approximate 300° as the capacitance in the varactor diodes is varied, and the magnitude of the cross-polarized field is higher than that of co-polarized field. The calculated results confirm that the dual-polarized multi-layer unit-cell consisting of dual-polarized H-shaped aperture coupled microstrips and varactor-based reflection-type phase-shifter can be used as a reconfigurable reflectarray unit-cell to reflect the incident wave with a continuous phase shift after polarization twist.

1. INTRODUCTION

Recently, as one approach for high-directivity antennas of flexible functions, reconfigurable reflectarrays are becoming increasingly important for future wireless system applications. In space applications, the antennas of high-directivity are generally employed, and reflectarray antennas as strong candidates can form highly-directive beams by spatial feeds without beamforming network. The architecture of reflectarrays provides low-cost and high-efficiency beamforming. Electronically reconfigurable reflectarrays [1] have been nominated and demonstrated for beamscanning or other agile performance. The reflectarray can utilize reconfigurable technologies, and the varactor diode that can govern the scattered field from the unit-cell, is preferred in the electronic tuning design because of its continuous tuning and easy integration. In the classic folded reflectarray [2] for fixed-beam, the cross-polarized unit-cell is generally used to realize polarization twist for low profile structure and convenient feeder line. For electronically beamscanning, the reconfigurable unit-cells [3] can be used and meanwhile the polarizing grid in the folded reflectarray that can implement polarization selection demands the unit-cell can twist the polarization of the plane wave incident broadside to the unit-cell. The reflected wave after polarization twist can pass through the polarizing grid, if the phase calibration is performed in the reflectarray aperture according to the expected beam direction, the power originating from feed and distributed directly by the polarizing grid can be focused into a coherent beam in free space.

So the electronically tunable phase-shift unit-cells of polarization twist are necessary for this reconfigurable reflectarray, and the model based guided-wave approach has advantages in the design. Reflection-type phase-shifter based on hybrid coupler and varactors can be integrated with dual-polarized radiator to absorb the incident power and then re-radiate the power with an arbitrary phase-shift. The varactor-loaded transmission line can reflect the wave with a continuous reflective phase shift [4, 5], and in the phase-shifter the reflected waves from two identical varactor-loaded transmission lines can cancel out at the input port, while can be aggregated at the output port, the phase of the transmission coefficient can be manipulated dynamically by the embedded varactors. By connecting the ports of the dual-polarized radiator to the ports of the phase-shifter with transmission lines, the dual-polarized unit-cell of continuous reflective phase-shift can be built for cross-polarized reflectarray design where the input and output polarizations are orthogonal, which ordinarily characterizes the folded reflectarray. This unit-cell designed at Ku-band frequencies here is suitable for the implementation in the dual-reflective configuration using the polarizing grid.

In this paper, a cross-polarized unit-cell consisting of dual-polarized H-shaped aperture coupled microstrip and reflective phase-shifters is proposed. The scattering characteristics for this proposed reflectarray unit-cell with tuning the varactors are obtained using HFSS simulation.

2. UNIT-CELL CONFIGURATION AND DESCRIPTION

The proposed unit-cell is composed of two parts, one is the dual-polarized radiation part, and another is the electronically tuning reflection-type phase-shifter.

2.1. Configuration of Dual-polarized Radiator

The radiator is a multi-layer PCB structure, and consists of square patches and the H-shaped coupling slots in the ground, which supply the microstrip-patch transitions for dual linearly polarized radiation. The two ports of $50\ \Omega$ transmission lines for orthogonal polarizations are defined in this dual-polarized radiator. The arrangement [6] of the slots in the ground is specially selected, and the design to optimize the slots is completed, which saves the space for the reflection-type phase-shifter, as shown in Fig. 1. The multi-layer structure consists of Rogers Duroid 5880 substrate of different thickness with relative permittivity $\epsilon_r = 2.20$ and low loss tangent and Rogers Duroid 6006 substrate of 0.254 mm thickness with $\epsilon_r = 6.15$, on which the square patches and the transmission-line network for reflection-type phase-shifter are etched. The substrates of different permittivity can improve the radiating ability of patches, meanwhile can restrain the edge field for network miniaturization, two no copper-cladding substrates of the 0.787-mm thickness with excavated central square vacuums cavity is sandwiched to enhance the coupling among patches and the coupling between patches and slots in the ground.

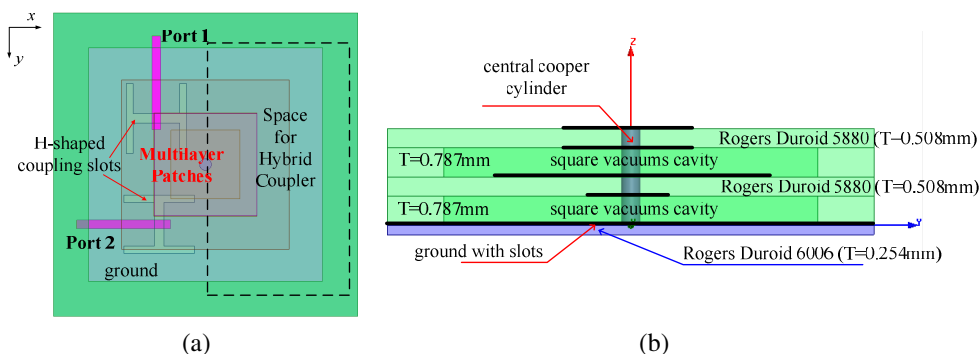


Figure 1: Configuration of dual-polarized H-slot coupled patch unit-cell for reconfigurable reflectarray. (a) Top view and (b) side view.

The performance of this radiator with the defined two ports is analyzed, and the scattering parameters are given in Fig. 2. It can be noticed that the broadband dual-polarized radiator can be matched in the range from 12.5 GHz to 14.5 GHz, and nearly 14% relative bandwidth (return loss ≤ -9 dB) is achieved, the decoupling level between two ports are approximate 20 dB. The scattering performance of this dual-polarized radiator is extremely important for the total unit-cell, cascading the radiator with the tunable phase-shifter will worsen the scattering parameters, and the dual-polarized radiator prescribe the potential limit for the total unit-cell.

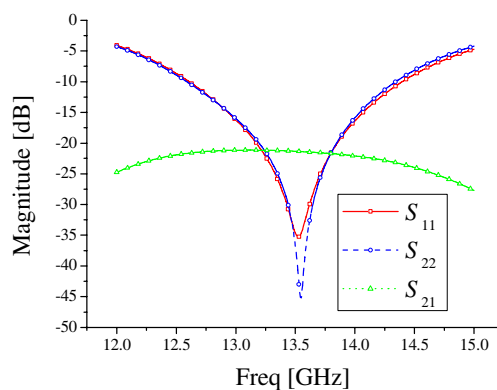


Figure 2: Scattering parameters of the designed dual-polarized radiator.

2.2. Configuration of Reflection-type Phase-shifter

As discussed above, the reflection-type phase-shifter should be designed for this unit-cell, and for the sake of stability in the operating Ku-band frequency range the 2-step 3 dB quadrature hybrid is chosen here, shown in Fig. 3, the diagram describes the basic working principle of reflection-type phase-shifter. When the excitation E_i exists at the Port 3, the reflected field can be eliminated if

the network is an ideal circuit, and Port 4 outputs a phase-tunable transmission field without loss. The network circuit is printed on the bottom side of Rogers Duroid 6006 substrate shown in Fig. 1, and the ground is same to the one in which the H-shaped slots are etched.

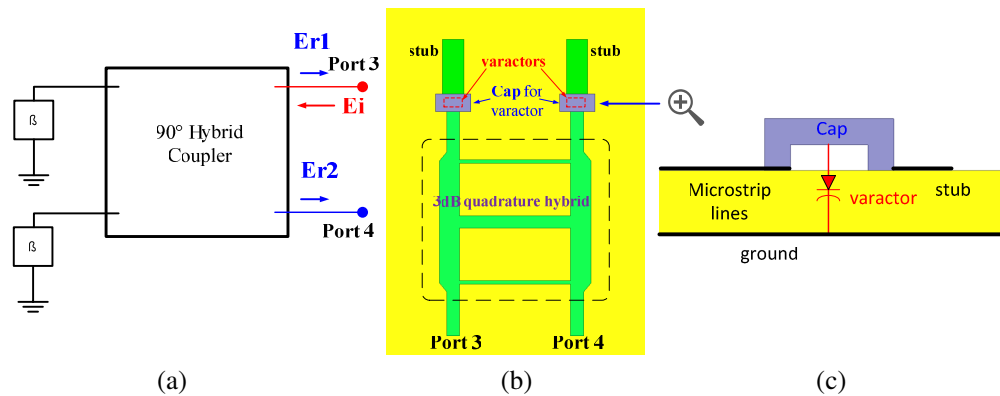


Figure 3: Diagram and Configuration of varactor-loaded reflection-type phase-shifter based on hybrid coupler for reconfigurable reflectarray unit-cell.

As shown in the Figs. 3(b) & (c), a pair of Microsemi GC15006-89 varactor diodes is used, which is silicon epitaxial mesa device. The junction capacity in the selected varactor diode, C_{var} , varies in the range between 2.2 pF and 0.2 pF when reverse-biased between 0 and 30 V. The equivalent circuits including package effects are considered and modelled in the simulation. The Microsemi GC15006-89 is preferred in the design thanks to its very high quality factor and high total capacitance ratio. In the design of varactor-loaded reflection-type phase-shifter, the cap for the varactor is added for integration, the Fig. 3(c) is a side view after zooming in for the varactor. Each varactor is connected to the microstrip and the ground by the cap, a strip bridge over the microstrip and the stub.

The width and the length of the stub can be adjusted for the tradeoff between the loss and the phase range. In [7], the tunable load consists of a series LC lumped circuit, and in my design the distributed component is used because of its ease for practice and flexibility. This reflection-type phase-shifter is analyzed by tuning the capacitance in varactors, and the results are given in Fig. 4. It can be noticed that the phase variation of about 300° is achieved, and the ports match well with a return loss of below -20 dB, and the maximum loss in the phase shift is about 1.5 dB at the frequency point 13.50 GHz. From the analysis, the design of the Ku-band reflection-type phase-shifter is confirmed, the performance is suitable for being integrated in the final reconfigurable reflectarray unit-cell based on guided-wave approach for continuous phase shift and polarization twist.

2.3. Integration for the Reconfigurable Reflectarray Unit-cell

After the design of the dual-polarized radiator and the reflection-type phase-shifter, the reconfigurable reflectarray unit-cell of continuous phase shift and polarization twist shown in Fig. 5 can be built by connecting Port 1 to Port 3 and Port 2 to Port 4 with transmission lines. The microstrip lines are assigned to maintain a decoupling of more than 30 dB between lines. It can be discovered

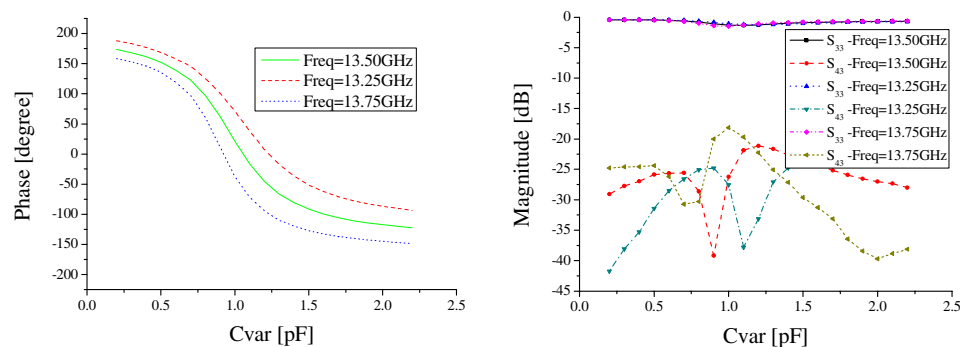


Figure 4: Phase and amplitude variation in the reflection-type phase-shifter with tuning capacitance in varactors.

that the special arrangement of the slots reserves enough space for the reflection-type phase-shifter's location. Due to the uncertainty of the output position and its stable performance, the dc biasing line connected to the network for controlling the varactors is hidden, that consists of a high impedance line with an open-ended radial stub, as a RF-chock in the operational frequency band, and thanks to the metal connectivity one dc biasing line can control the two varactors together.

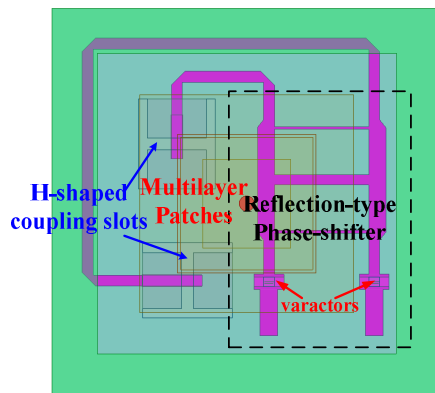


Figure 5: Configuration of the proposed reconfigurable reflectarray unit-cell.

3. SIMULATIONS AND DISCUSSIONS

The performance of the proposed topology has been assessed at the frequency point 13.50 GHz. Numerical characterisations with HFSS® commercial software have been carried out using Floquet Boundary approach for this square cell of size $13 \times 13 \text{ mm}^2$ with the consideration of coupling in the arrays. The cell is excited with the plane waves with the electric fields perpendicular to the grid of the array. In the simulations, results in the situations of the normal incidence (0°) and oblique incidence (30°) are calculated, and the phase and the amplitude variation in scattering parameters with tuning the varactors are illustrated in Fig. 6.

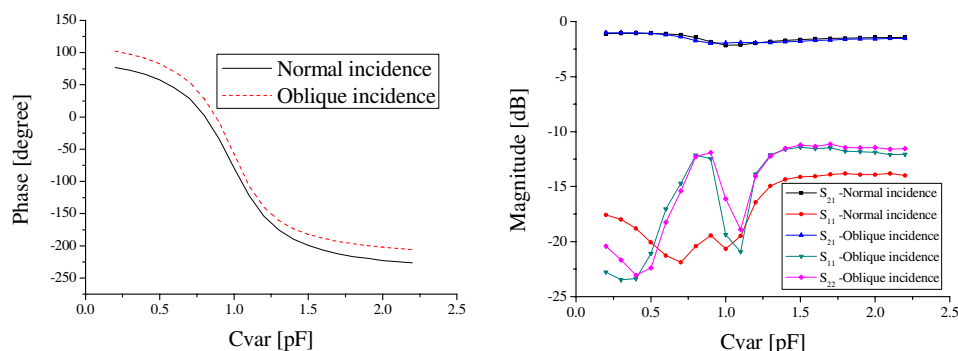


Figure 6: Phase and amplitude variation with tuning capacitance in varactors.

In the results, the phase of the cross-polarized component in the scattered field varies continuously by approximate 300° , and the magnitude of the cross-polarized component is higher than that of co-polarized component over the tuning range by 10 dB. It can be summarized that the continuous reflective phase-shift and the polarization twist are combined in the dual linearly polarized unit-cell for reconfigurable reflectarray antenna, and the unit-cell is preferred in the reconfigurable folded reflectarray antenna application.

4. CONCLUSIONS

For continuous phase tuning, the varactor-loaded unit-cell based on reflection-type phase-shifter and dual-polarized radiator is preferred and designed for the polarization twist in the reconfigurable folded reflectarray. The varactor's tuning in the reflection-type phase-shifter endow the unit-cell with a continuous reflective phase shift, further the cross-polarized unit-cell can transform

the incident linearly polarized wave into the reflected wave of orthogonal polarization with a continuous phase tuning, and the reciprocity of the unit-cell can be demonstrated by the dual-polarized reflective transition. This proposed reflectarray unit-cell is able to offer a wide continuous phase tuning range, which is of critical importance for the reconfigurable reflectarray antenna performance improvement, and its performance is verified by the total model full-wave simulations instead of the network-based approach in [7]. The continuous phase shift in the unit-cell of polarization twist is required necessarily for high performance realization, which ensures the high aperture efficiency in the antenna radiation. Therefore, this unit-cell gives a good option for advanced reconfigurable reflectarray antenna.

ACKNOWLEDGMENT

This research is funded by China Scholarship Council, Xi'an Institute of Space Radio Technology. Also the authors would like to thanks the staff from China Scholarship Council, Xi'an Institute of Space Radio Technology and University of Kent for the support and help. Professor Yongchang Jiao from Xidian University in China is acknowledged for the care and concern.

REFERENCES

1. Hum, S. V. and J. Perruisseau-Carrier, "Reconfigurable reflectarrays and array lenses for dynamic antenna beam control: A review," *IEEE Trans. Antennas Propag.*, Vol. 62, No. 1, 183–198, Jan. 2014.
2. Tarn, I. Y., Y. S. Wang, and S. J. Chung, "A dual-mode millimeter-wave folded microstrip reflectarray antenna," *IEEE Trans. Antennas Propag.*, Vol. 56, No. 6, 1510–1517, Jun. 2008.
3. Montori, S., R. V. Gatti, R. Sorrentino, S. Dieter, and W. Menzel, "Reconfigurable and dual-polarization folded reflectarray antenna," *42nd European Microwave Conf., (EuMC 2012)*, 735–738, Amsterdam, The Netherlands, 2012.
4. Venneri, F., S. Costanzo, and G. Di Massa, "Reconfigurable aperture-coupled reflectarray element tuned by single varactor diode," *Electronics Letters*, Vol. 48, No. 2, 68–69, Jan. 2012.
5. Venneri, F., S. Costanzo, and G. Di Massa, "Design and validation of a reconfigurable single varactor-tuned reflectarray," *IEEE Trans. Antennas Propag.*, Vol. 61, No. 2, 635–645, Oct. 2012.
6. Wong, K.-L., *Compact and Broadband Microstrip Antenna*, John Wiley & Sons, New York, 2004.
7. Kishor, K. K. and S. V. Hum, "Modeling of active reconfigurable reflectarray elements," *13th International Symposium on Antenna Technology and Applied Electromagnetics and the Canadian Radio Sciences Meeting, (ANTEM/URSI 2009)*, Toronto, Canada, 2009.

A Reconfigurable Folded Antenna for Mobile Phone Applications

Liu Hu, Ying Liu, Cao Yu, and Shuxi Gong

National Laboratory of Science and Technology on Antennas and Microwaves
Xidian University, Xi'an 710071, China

Abstract— A folded reconfigurable antenna using three PIN diodes is proposed for personal communication handset applications. In a compact volume of $60 \times 9 \times 8 \text{ mm}^3$, the antenna has a simple metal structure comprising a folded loop strip, a Y-shape folded strip and three PIN diodes. By independently controlling the on/off states of the three PIN diodes located on the radiating element, the proposed structure can operate in the inverted-F antenna (IFA) and loop modes, respectively. While operating in the IFA mode, the bandwidth is sufficient to cover the DCS (1710–1880 MHz), PCS (1850–1990 MHz) bands. Owing to the additional Y-shape folded strip, the bandwidth generated by multiple resonances of the loop mode covers GSM850 (824–894 MHz), GSM900 (880–960 MHz), GPS (1560–1590 MHz), UMTS (1920–2180 MHz), LTE2300 (2305–2400 MHz), WLAN (2400–2480 MHz) bands. Good radiation efficiency and antenna gain at frequencies over the desired operating bands are obtained. The proposed antenna is fabricated and all simulated results are confirmed with measured data.

1. INTRODUCTION

With the rapid progress in wireless communication, the requirement of a single compact antenna covering multi-wireless radiation bands is increasing. Many antennas with wide bandwidth and compact structure have been introduced in [1, 2]. However, these conventional antennas mentioned above have relatively narrow operation bandwidth and are too large to be integrated into mobile terminals. Recent studies showed that the loop antennas are promising candidates for mobile phone application [3, 4]. However, good impedance matching of loop antenna is not easy to be achieved at its resonant mode.

In this paper, a novel folded reconfigurable antenna is presented for multifunctional wireless personal communication devices. The performance of the antenna is reconfigured in the IFA and loop modes by adjusting the states of the three PIN diodes. The proposed antenna generates very wide bandwidth to cover the DCS and PCS bands in the IFA mode. An additional strip connected to the main radiating element is utilized in the loop mode to widen the operating bandwidth. The four desired resonance at about 900 MHz, 1575 MHz, 1850 MHz and 2450 MHz can be excited for the proposed antenna of loop mode to cover GSM850, GSM900, GPS, UMTS, LTE2300 and WLAN bands.

2. DESIGN OF THE PROPOSED RECONFIGURABLE ANTENNA

Figures 1(a) and 1(b) show the geometry of the proposed reconfigurable antenna. A 1 mm thick FR4 substrate of relative permittivity 4.4 is used as the printed circuit board (PCB). The broadside of folded metal strip is divided into two parts. The length of the left part which plays a major role in IFA mode is 4 mm, while the length of the rest part is 2 mm to maintain the performance of loop mode. The additional Y-shape folded strip is attached to the main radiating element with the same width.

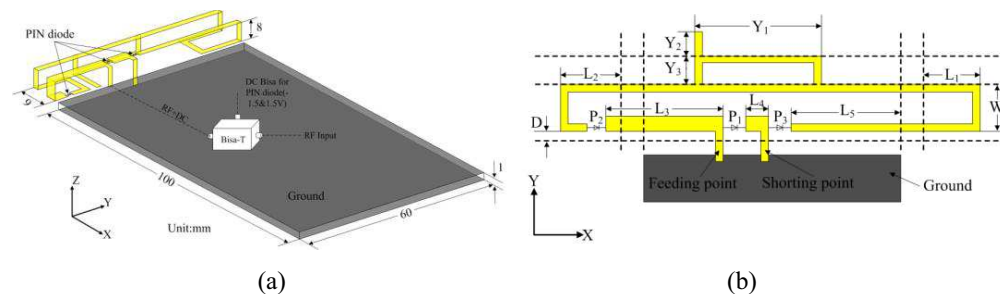


Table 1: Optimized dimensions of the proposed antenna (mm)..

parameter	L_1	L_2	L_3	L_4	L_5
value	13	12	34	6	32
parameter	Y_1	Y_2	Y_3	W	D
value	22	8	7	9	2

The positions of PIN diodes (P_1 , P_2 and P_3) are illustrated in Figs. 1(a) and 1(b). P_1 is located between the feed point and short point. P_2 and P_3 are placed on either end of the 4 mm-wide patch to adjust the length of the folded strip in IFA mode.

3. DISCUSSIONS AND OPTIMIZATION

The antenna is composed of a folded loop strip and a Y-shape folded strip when P_2 and P_3 are turned on and P_1 is turned off. The total length of the folded loop strip from the short point to the feed point is close to 0.5-wavelength of the frequency at 900 MHz, which makes it possible to generate a 0.5-wavelength resonant mode for GSM850/900 operation. Moreover, the loop antenna generates a 1.0-wavelength mode at about 1570 MHz. The 1.5-wavelength resonant mode is also excited at about 1950 MHz, which, however, cannot cover UMTS/LTE2300/WLAN operation for the antenna's upper band. By attaching an additional Y-shape folded strip to the main radiating element, the upper band can be formed together by the 1.5-wavelength resonant mode and the 2.0-wavelength resonant mode excited at about 2450 MHz.

Meanwhile when P_2 and P_3 are turned off and P_1 is turned on, the loop antenna can be divided to IFA by slicing the folded radiating element. For the inverted-L copper strip, the width is set to be 4 mm and the total length is about 40 mm which generates a 0.25-wavelength resonance at about 2000 MHz for DCS and PCS operations.

4. ANTENNA FABRICATION AND MEASUREMENT RESULTS

Antenna prototype was fabricated. In the bias circuit, the DC signal is isolated from the RF signal by an inductor and a chip capacitor. The blocking capacitor (C_b) is implemented between the port and main radiating element for DC blocking. On the other hand, an inductor (L_b) is located between DC signal and radiating element, which is used for RF choking.

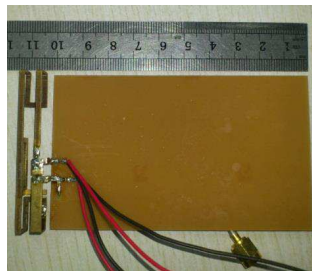


Figure 2: Photograph of the reconfigurable antenna.

Figure 3 shows the simulated and measured reflection coefficients of the proposed antenna in two operation modes. In the loop mode, the fabricated antenna covers the GSM850, GSM900 GPS, UMTS, LTE2300 and WLAN bands. For the IFA mode, the the measured bandwidth is 677 MHz which cover the DCS and PCS bands.

Figure 4 shows the gain radiation patterns of the reconfigurable antenna at 900 MHz, 1575 MHz, 1850 MHz, 2000 MHz and 2400 MHz, respectively. It is observed that the radiation patterns for the lower frequency band are similar to that of a conventional quarter-wavelength monopole antenna in the xy - and yz -planes, and omnidirectional radiation in the xz -plane. The main reason is that the antenna has a dominant operating current in the y -direction. The antenna radiation patterns cannot show complete omnidirectional pattern and linear polarization over the upper frequency bands for the existence of undesired weak surface currents in other directions. However, this is not a strict requirement for handheld devices antennas. The proposed antenna also has a high cross-polarization level of radiation patterns.

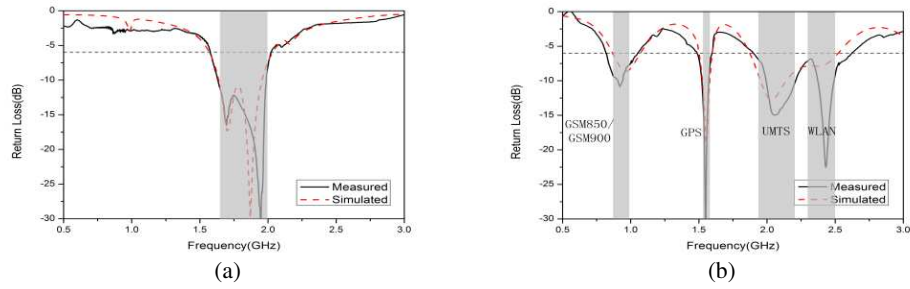


Figure 3: Simulated and measured reflection coefficients of (a) the IFA mode and (b) the loop mode.

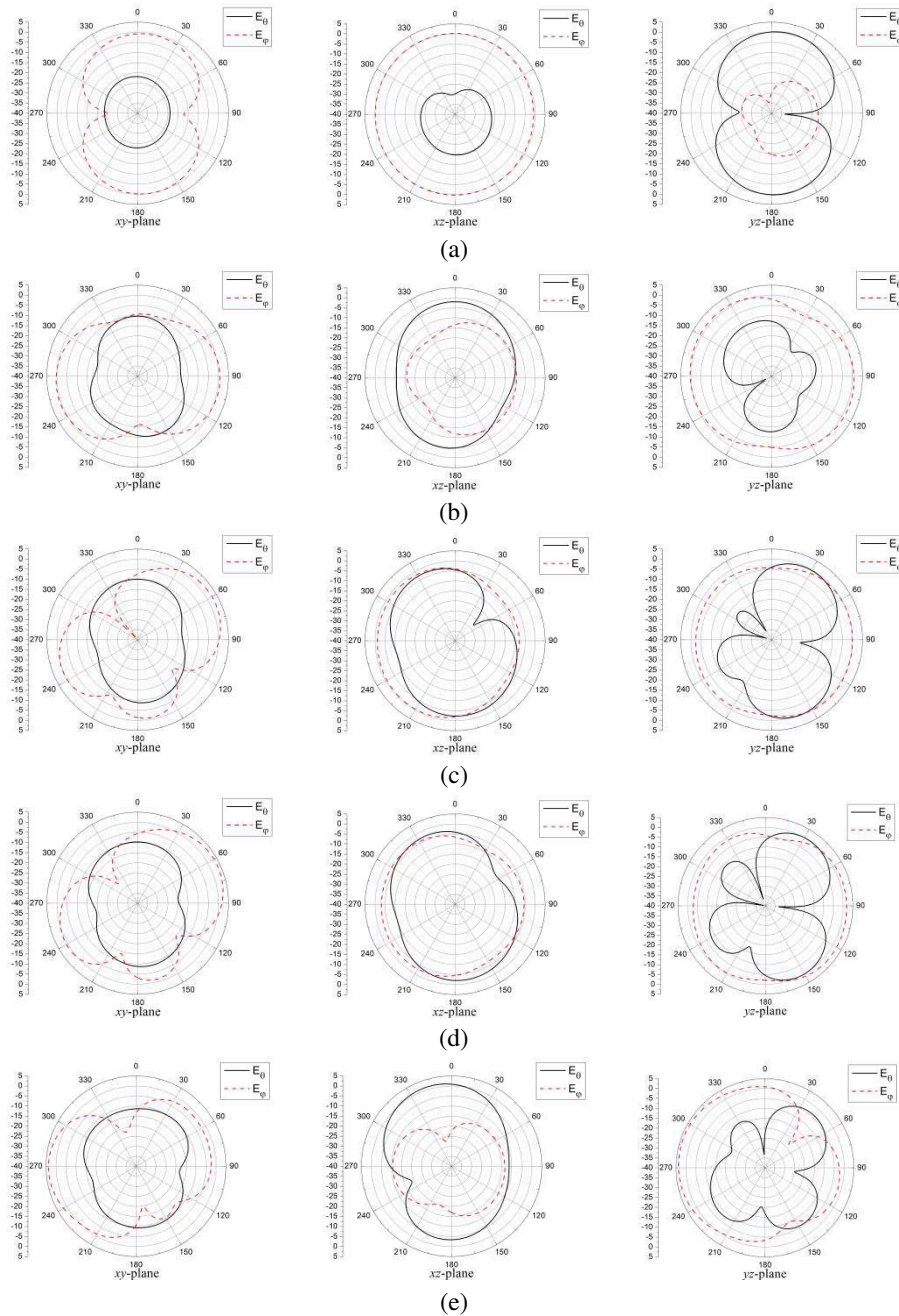


Figure 4: 2D-radiation pattern (co-polarization and cross-polarization) of the reconfigurable antenna in (a) 900 MHz, (b) 1575 MHz, (c) 1850 MHz, (d) 2000 MHz and (e) 2400 MHz.

Table 2 presents the simulated antenna gain and radiation efficiency for the proposed antenna in different frequency bands. The gains are about 0.66–0.84 dBi and the radiation efficiencies are higher than 50% over the GSM850/900 bands. Meanwhile, the gains for the GPS, DCS, PCS, UMTS, LTE2300 and WLAN bands range from 1.31 to 2.73 dBi and the radiation efficiencies are higher than 60%.

Table 2: The simulated gain and measured efficiency of the proposed antenna at different frequencies.

Band	GSM 850	GSM 900	GPS	DCS	PCS	UMTS	LTE 2300	WLAN
Frequency (GHz)	0.85	0.9	1.575	1.8	1.9	2.05	2.35	2.45
Gain (dBi)	0.66	0.84	1.31	2.59	2.73	2.61	1.76	2.28
Total Efficiency (%)	56.5	58.3	61.1	64.5	73	74.2	62.7	65.6

5. CONCLUSIONS

A folded loop antenna with reconfigurable characteristic for personal communication handset applications is presented. Wide bandwidth is achieved by merging the different working frequency bands generated in different operating modes. By adding a Y-shape folded strip, the impedance matching is improved for the upper bands in loop mode. The reconfigurable antenna can cover the following frequency bands: GSM850, GSM900, GPS, DCS, PCS, UMTS, LTE2300 and WLAN with a compact volume of $60 \times 9 \times 8 \text{ mm}^3$. Good radiation characteristics over the operating bands have been obtained.

ACKNOWLEDGMENT

This work is supported by Program for New Century Excellent Talents in University (NCET-11-0690) and the Fundamental Research funds for the Central Universities (K5051202049)

REFERENCES

1. Abutarboush, H. F., R. Nilavalan, and T. Peter, "Multiband inverted-F antenna with independent bands for small and slim cellular mobile handsets," *IEEE Transactions on Antennas and Propagation*, Vol. 59, No. 7, 2636–2645, 2011.
2. Lin, D. B., I. T. Tang, and M. Z. Hong, "A compact quad-band PIFA by tuning the defected ground structure for mobile phones," *Progress In Electromagnetics Research B*, Vol. 24, 173–189, 2007.
3. Wong, K.-L., W.-Y. Chen, and T.-W. Kang, "On-board printed coupled-fed loop antenna in close proximity to the surrounding ground plane for penta-band WWAN mobile phone," *IEEE Transactions on Antennas and Propagation*, Vol. 59, No. 3, 751–757, 2011.
4. Wong, K.-L. and C.-H. Huang, "Printed loop antenna with a perpendicular feed for penta-band mobile phone application," *IEEE Transactions on Antennas and Propagation*, Vol. 56, No. 7, 2138–2141, 2008.
5. Chi, Y.-W. and K.-L. Wong, "Compact multiband folded loop chip antenna for small-size mobile phone," *IEEE Transactions on Antennas and Propagation*, Vol. 56, No. 12, 3797–3803, 2008.

Pattern Reconfigurable Printed Antennas with High Gain and Broadband

Xue-Xia Yang, Zhong-Liang Lu, Guan-Nan Tan, and Yong-Jin Zhou
 School of Communication and Information Engineering, Shanghai University
 Shanghai 200072, China

Abstract— This paper presents a wideband printed tapered slot antenna with pattern reconfigurability. The antenna consists of four tapered slots, a reconfigurable microstrip-to-slotline transition, and four PIN diodes. Four agile endfire radiation patterns are realized with the measured relative impedance bandwidth of 71.3%. The gains for the four directions are all higher than 6.4 dBi at the center frequency of 2.4 GHz. Good patterns are maintained at the four reconfigurable directions in a wideband. To further enhance the gain, the zero-index-metamaterial (ZIM) units are loaded in the tapered slot. The simulation results show that extra gains of 1.4 to 1.7 dBi can be obtained within the center band from 2.2 GHz to 2.6 GHz.

1. INTRODUCTION

Reconfigurable antennas with adjusting beams are demanded in the wireless communication systems such as small base stations. Adjusting beam antenna can provide pattern diversity, which results in improving signal to noise ratio and the capacity of the wireless communication systems. Planar printed antennas are preferred because of the low cost, low profile and easiness to be integrated with switches of PIN diodes and RF-MEMS.

Most of the reported pattern reconfigurable antennas have narrow bandwidth which could not satisfy the rapidly growing bandwidth requirement of the modern communication systems. In [1–3], broadband pattern reconfigurable monopoles antennas are proposed, and the relative bandwidths are 29%, 55.7% and 66.7%, respectively. However, there are only two or three reconfigurable radiation patterns and the gains are no more than 6 dBi. Ref. [4] presents a printed Yagi antenna with six adjustable beam directions. A tie-shape dipole with the two arms being printed on the opposite side of the dielectric-slab is adopted as the driven element to extend the bandwidth. Six PIN diode switches are attached between the ground and the driven dipole on the ground to control the radiation directions. The bandwidth of the reflection coefficient less than 10 dB is 400 MHz, and the gains are all 7.5 dBi on the six adjustable radiation directions.

Wideband pattern reconfigurable Vivaldi tapered slot antennas are proposed in [5–7]. Three different radiation patterns, including one omnidirectional and two endfire patterns are realized. The relative bandwidths are about 50% to 60% and the gains are less than 6.5 dBi. Most of the above mentioned designs include extra DC isolation structures, which add the complexity to the antennas.

In this paper, a broadband pattern reconfigurable tapered slot antenna is designed with four adjustable endfire directions. The antenna is coupling fed by a microstrip feedline. The four beam directions around 360° are controlled by four PIN diodes without extra bias circuits being required. This pattern reconfigurable antenna has wideband from 1.5 GHz to 3.3 GHz and high gain of 6.8 dBi at the center frequency of 2.4 GHz. The further approaches of gain enhancement are discussed by using zero-index metamaterial (ZIM).

2. PATTERN RECONFIGURABLE TAPERED SLOT ANTENNA

2.1. Antenna Structure

The antenna is printed on both sides of a square substrate with the relative permittivity of 2.65 and the depth of 0.8 mm. The side and top views are shown in Figs. 1(a) and (b). There are four metal sheets with the same sizes denoted as M_1 , M_2 , M_3 and M_4 on the top layer, which form four identical tapered slots denoted as S_1 , S_2 , S_3 and S_4 . The antenna is fed by a $50\ \Omega$ microstrip line on the bottom layer, and the metal sheet M_1 acts as the ground plane.

Firstly, an original tapered slot antenna element with the length of L_s and the maximal slot width of W_{s2} is designed, whose bandwidth ($S_{11} < -10$ dB) is from 1.5 GHz to 3.3 GHz. A reconfigurable microstrip-to-slotline transition structure is elaborately designed to feed the four tapered slot radiators. Details of the transition dotted in Fig. 1(b) are enlarged in Fig. 1(c). It consists of

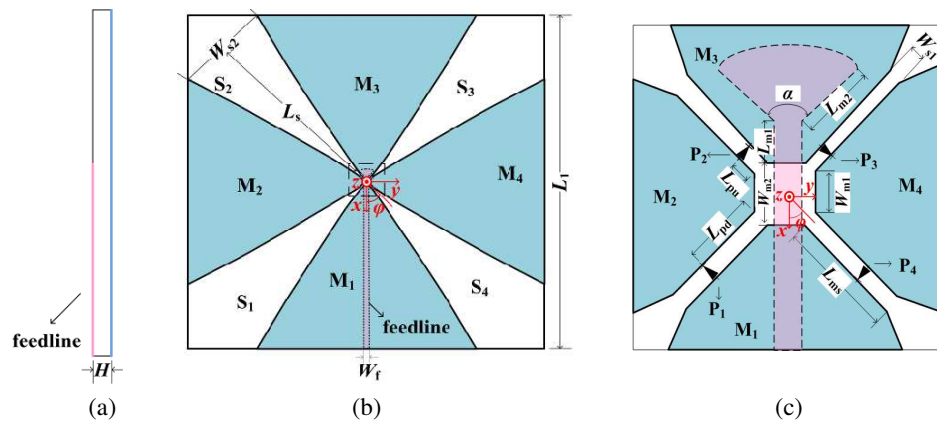


Figure 1: Antenna structure. (a) Side view. (b) Top view. (c) Detailed view.

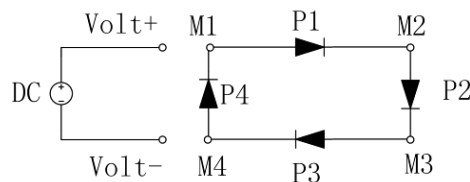


Figure 2: Schematic diagram of the bias circuit.

a microstrip feedline on the bottom layer, a square slot with the width of W_{m2} at the center on the top layer, and four rectangle slots with the length of L_{ms} and width of W_{s1} . The microwave on the microstrip line is coupled by the square slot, and then guided by four rectangles to the tapered slot radiators. A PIN diode is placed across each rectangle slot at an appropriate position. The dimensions are optimized using the software HFSS and the final sizes are (unit: mm): $H = 1.5$ mm, $W_f = 4.1$, $W_{s2} = 83.6$, $L_s = 169.6$, $W_{s1} = 1.5$, $W_{m1} = 4.2$, $W_{m2} = 6.3$, $L_{ms} = 3.5$, $L_{m1} = 2.5$, $L_{pu} = 2.3$, $L_{pd} = 0.9$, $L_{m2} = 5.9$, $\alpha = 80^\circ$.

The selected PIN diode is Infineon BAR64-02V with the working frequency band from 0.1 GHz to 6 GHz. This diode can be equivalent to a resistance of 2.1Ω on the forward-bias state and a capacitance of 0.17 pF on the reverse-bias one according to the datasheet. The polarities of the four PIN diodes are arranged clockwise as shown in Fig. 1(c). The simplified bias circuit is illustrated in Fig. 2. If one of the four tapered slots is chosen as the radiator, for example, S_1 , the DC bias voltage should be added to the two adjacent metal sheets of M_1 and M_2 . When one diode is on ‘Off’ state, the corresponding tapered slot radiates endfire pattern. At the same time, other three diodes are on ‘On’ state and the corresponding slots are shorted and do not work.

2.2. Simulation and Measurement Results

An antenna prototype with the bias circuit is fabricated and tested. The photograph of the fabricated prototype is shown in Fig. 3. Due to the symmetrical characteristic, the results of the directions of 315° and 225° chosen to be given here which are identified as ‘down’ and ‘up’ modes, respectively.

The reflection coefficients are measured by the Agilent 8722ES network analyzer. The measured and simulated reflection coefficients are illustrated in Fig. 4. It can be seen that the measured common bandwidth of $S_{11} < -10$ dB is of both modes is from 1.57 GHz to 3.31 GHz and the relative bandwidth is 71.3%.

The simulated and measured normalized radiation patterns at the center frequency are illustrated in Fig. 5. It shows that the mainlobe directs to $\varphi = 315^\circ$ and $\varphi = 225^\circ$ in the xoy plane respectively. The measured cross polarization of the antenna is below 12 dBi at the mainlobe direction. The front to back ratio is more than 1 dBi at the center frequency.

3. GAIN ENHANCEMENT WITH ZIM

To enhance the antenna gain, the Zero-index metamaterial (ZIM) is designed. Meander-line resonator structure is chosen as the unit cell of the metamaterials which is shown in Fig. 6(a). The

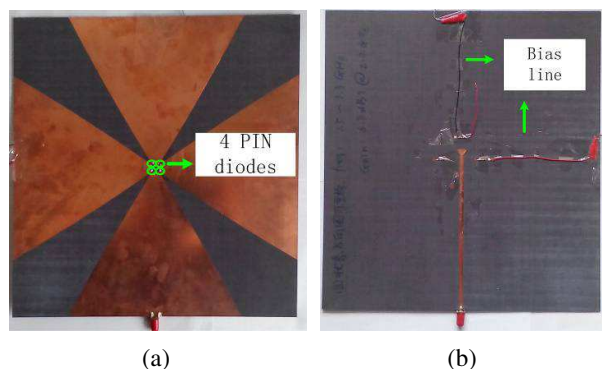


Figure 3: Photograph of the proposed reconfigurable antenna. (a) Front view. (b) Bottom view.

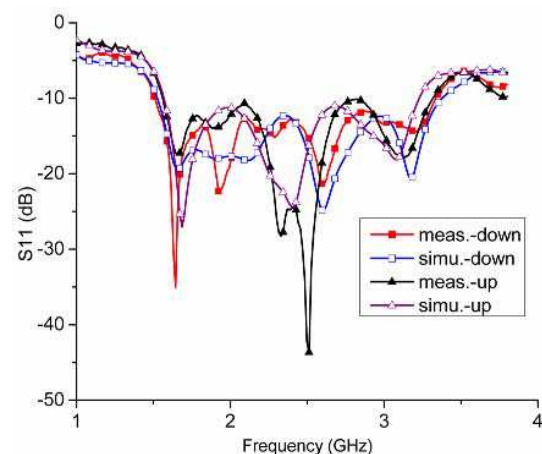


Figure 4: Simulated and measured reflection coefficient.

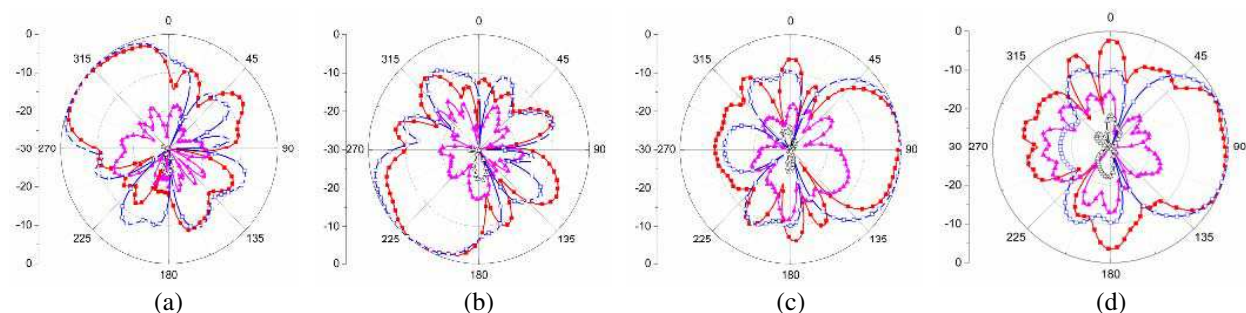


Figure 5: Normalized radiation patterns at center frequency. (a) E plane of 'down' mode. (b) E plane of 'up' mode. (c) H plane of 'down' mode. (d) H plane of 'up' mode. (-■-: measured co-polarization; -▲-: measured cross-polarization; -□-: simulated co-polarization; -△-: simulated cross-polarization).

optimized dimensions are (in mm): $L_x = 13$, $L_y = 16$, $W = 0.8$, $A_x = 10.7$, $A_y = 1.2$. The effective permittivity and permeability are obtained using standard retrieval procedure, as shown in Fig. 6(b). It can be seen that the effective permittivity is about zero at around the 2.4 GHz. The bandwidth of $|\text{Re}(\epsilon)| \leq 1$ is from 2.2 GHz to 2.8 GHz.

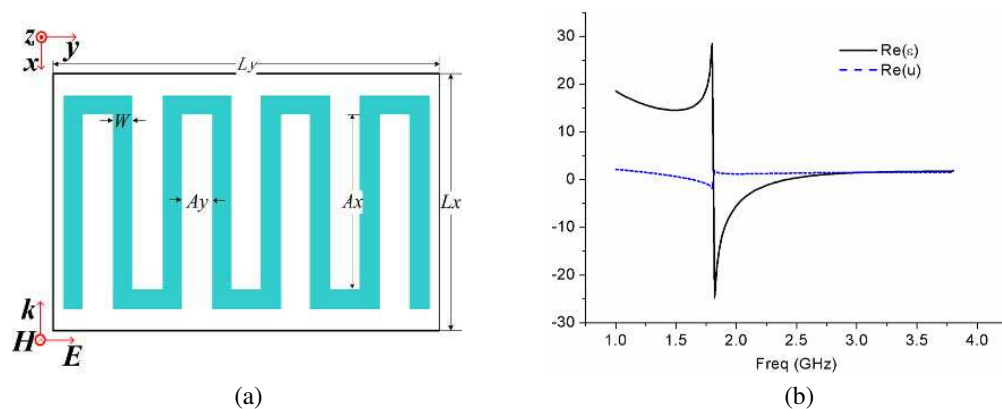


Figure 6: Meander-line unit cell. (a) Structure and dimensions. (b) Retrieved results of the permittivity and permeability.

The ZIM unit cells are added to the tapered slots of the proposed antenna as shown in Fig. 7(a). The field distribution of the down mode at 2.4 GHz without and with ZIM is shown in Figs. 7(b) and (c), respectively. It can be seen that the field are mainly distributed in the slot S_1 on both cases. The ZIM cells make the field distribution more uniform than the antenna without ZIM,

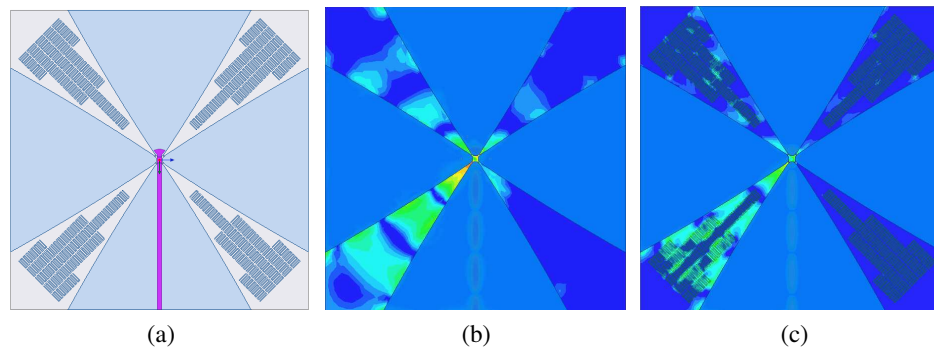


Figure 7: Antenna with ZIM. (a) Layout. (b) Field distribution at 2.4 GHz (a) without zim and (b) with ZIM.

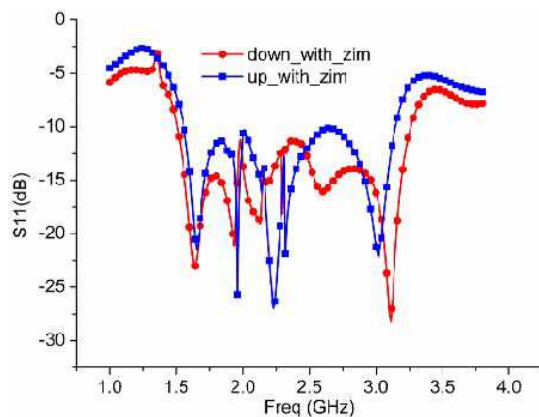


Figure 8: Simulated S_{11} of two directions with ZIM.

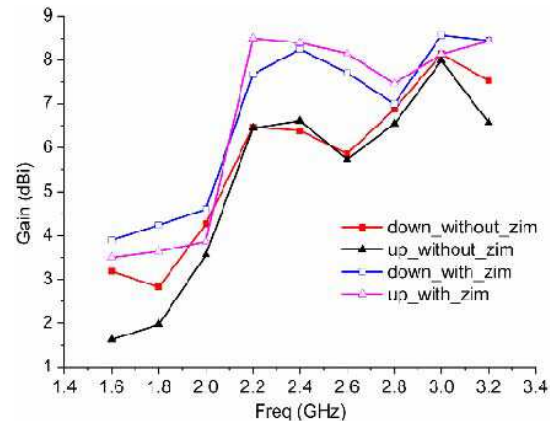


Figure 9: Gain response of two directions with and without ZIM.

which causes the gain enhancement. The reflection coefficients of both modes are illustrated in Fig. 8. Compared with Fig. 4, it can be seen that the impedance bandwidth of each directions are almost unchanged. The gain responses with and without the ZIM are compared in Fig. 9. The gains are improved about 1.4 to 1.7 dBi within the operation band from 2.2 GHz to 2.6 GHz. The gains with and without ZIM for the ‘down’ mode at the center frequency of 2.4 GHz are 8.2 dBi, and 6.6 dBi, respectively. Those for the ‘up’ mode are 8.4 dBi, and 6.4 dBi, respectively. A maximum improvement of 2 dBi has been obtained at the center frequency.

4. CONCLUSIONS

A novel wideband printed pattern reconfigurable antenna based on tapered slots is proposed. The antenna can switch its maximum radiation directions among four endfire directions within a broad bandwidth from 1.57 GHz to 3.31 GHz. ZIM of meander-line unit cells are designed and loaded on the tapered slot for gain enhancement. The gains increase about 1.4 to 1.7 dBi in the operation band from 2.2 to 2.6 GHz. The gains high than 8.2 dBi are achieved for different modes of the reconfigurable antenna.

REFERENCES

1. Ding, X. and B. Z. Wang, “A novel wideband antenna with reconfigurable broadside and endfire patterns,” *IEEE Antennas Wireless Propag. Lett.*, Vol. 12, 995–998, 2013.
2. Zhang, G. M., J. S. Hong, G. Song, et al., “Design and analysis of a compact wideband pattern reconfigurable antenna with alternate reflector and radiator,” *IET Microw. Antennas Propag.*, Vol. 6, No. 15, 1629–1635, Dec. 2012.
3. Aboufoul, T., C. Parini, X. Chen, et al., “Pattern-reconfigurable planar circular ultra-wideband monopole antenna,” *IEEE Trans. Antennas Propagat.*, Vol. 61, No. 10, 4973–4980, Oct. 2013.
4. Gong, B. and X.-X. Yang, “A planar printed Yagi antenna with adjustable beam,” *Journal of Shanghai University (Natural Science)*, Vol. 20, No. 1, 83–91, 2014.

5. Wu, S. J. and T. G. Ma, “A wideband slotted bow-tie antenna with reconfigurable CPW-to-slotline transition for pattern diversity,” *IEEE Trans. Antennas Propagat.*, Vol. 56, No. 2, 327–334, Feb. 2008.
6. Li, Y., Z. Zhang, J. Zheng, Z. Feng, and M. F. Iskander, “Experimental analysis of a wideband pattern diversity antenna with compact reconfigurable CPW-to-slotline transition feed,” *IEEE Trans. Antennas Propagat.*, Vol. 59, No. 22, 4222–4228, Nov. 2011.
7. Zhang, G. M., J. S. Hong, B. Z. Wang, G. B. Song, and P. Li, “Design and time-domain analysis for a novel pattern reconfigurable antenna,” *IEEE Antennas Wireless Propag. Lett.*, Vol. 10, 365–368, 2011.

A Thin Planar Antenna Based on Gradient Metasurface

Bo Chen, Hongyu Shi, Anxue Zhang, and Juan Chen

School of Electronic and Information Engineering, Xi'an Jiaotong University, China

Abstract— Gradient metasurface (GM) can have a pre-defined large wave vector along its surface. It has shining attributes as field enhancement and sub-wavelength transmission. In former works, GMs were excited mostly by plane waves illuminated from high above, and experts concentrated on waveform converting or anomalous reflection. This letter analyses electromagnetic field distribution above GM with some plane waves vertically illuminating. Then it provides a new way to excite GM on one of its edges using parallel plate waveguide, from which we can get an escaping plane wave towards above, and this is the inverse process of plane wave vertical incidence. After a delicate parameter sweep, the simulation shows our design has comparatively high directivity and efficiency within a bandwidth of 0.6 GHz (7.7 GHz to 8.3 GHz). The impact of some important size parameters to the antenna performance is discussed in the letter. On account of the fact that GMs are usually constructed by a mass of unit cells, their shapes are variable and they can cover many facilities, which have great potential in both civil and military use. With the development of metasurfaces, the unit cells will become smaller, and the adjustability of the antennae shapes will rise. To excite GMs with the same unit cells but different shapes, it is possible that we only need to tune their matching structure but not the unit cells. Then a new way to design reconfigurable antennae presents. And with the help of metasurfaces, reconfigurable antennae will be more various and flexible and will have better performance.

1. INTRODUCTION

Surface plasmon polaritons (SPPs) refers to some combining mode of EM waves and electron density that can hardly escape from a surface [1]. As the research on SPPs goes deeper and many devices have been tested successfully, SPPs shows great potential in optics application. Spoof plasmon polaritons [2], similar to SPPs, have attributes as field enhancement [3, 4] and sub-wavelength transmission [5–8], but in THz or microwave band. Spoof plasmon polaritons act as surface wave in free space, and can be realized by using gratings, prisms [9–11] and gradient metasurfaces (GMs) [2].

However in former works, experts mainly concentrated on how GM can transform incident plane wave into surface wave or realization of anomalous reflection [12–14], which means the sources were always hanging above. In order to extend the range of GMs' application, new ways to excite GMs should be discovered.

This letter analysis field distribution of the surface wave above GM and then gives a new way to excite GM on one of its edges. Our simulation successfully proves GM can radiate energy with comparatively high directivity if it is properly excited. Our simulation was run in HFSS and CST.

2. PROPERTIES OF GM

GM is usually constructed by several kinds of unit cells. When certain plane wave illuminating onto, neighboring unit cells show gradient reflection index phases, which can provide a large horizontal wave vector. In this way can GM transform the plane wave into a surface wave with high efficiency. Obviously, GM supports surface wave propagating. If we exert an EM-field on one edge of the GM, whose field distribution is similar to that of a surface wave but propagating direction is opposite, we may get an escaping plane wave. It is similar to the reversibility of optical path, making the whole structure as an antenna.

We choose a typical super cell as shown in Figure 1(a) with its size $3.3\text{ mm} \times 33\text{ mm}$. It is constructed by metallic split ring resonators etched on substrate of FR4. There is a metallic sheet on the back of substrate as in Ref. [2]. Its working frequency is 7.87 GHz. Being placed periodically along x and y directions, super cells construct an infinite GM. A y -polarized plane wave vertically incidents onto GM. Power flow at 7.87 GHz is shown in Figure 1(b), in which it shows energy flows along the surface towards $-y$ direction. Magnitude of E -field in x , y and z directions at 7.87 GHz are shown in Figures 2(a) to (c). E -field mainly lies in y and z directions but little in x direction.

3. SIMULATION OF ANTENNA AND PARAMETER DISCUSSION

If we want to excite this GM on one of its edges, we must do it on the side where the former plane wave is propagating to. We need a kind of EM-field whose E -field mainly lies in y and z directions

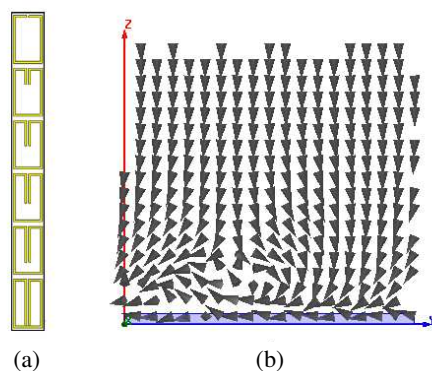


Figure 1: Design and property of super cell: (a) overall structure of supercell; (b) power flow on yOz plane at 7.87 GHz.

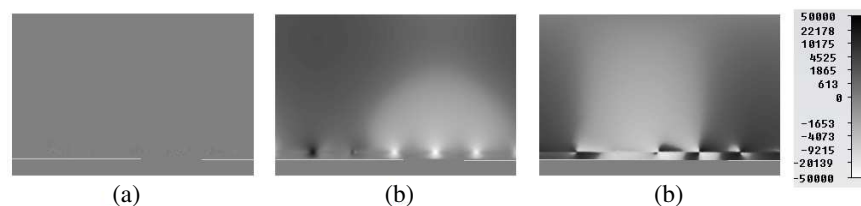


Figure 2: Snap shot of E -field distribution at 7.87 GHz: (a) E -field in x direction; (b) E -field in y direction; (c) E -field in z direction.

but not x direction, and it should propagate to $+y$ direction. Parallel plate waveguide filled with FR-4 is adopted, because the E -field on its edge is just suit to this situation. We construct our GM by 15×6 super cells. GM and the feed structure is connected as shown in Figure 3(a), and the parameters are set as shown in Figure 3(b). Here Port 1 is set to be lumped port. After a delicate parameter sweep, we fix $d = 7$, $h = 5$ and $t = 2$ Magnitude of S_{11} over frequency is shown in Figure 4. It keeps lower than -10 dB from 7.7 GHz to 8.35 GHz. Total gain in yOz plane (i.e., $\varphi = 90^\circ$) at 7.9 GHz, 8.1 GHz and 8.3 GHz is shown in Figure 5(a). At 8.1 GHz, total gain in yOz plane reaches its peak as 11.7 dB. More anecdotally, as frequency increases from 7.7 GHz to 8.3 GHz, the maximum gain angle changes from $\theta = -6^\circ$ to $\theta = 4^\circ$. Gain distribution in x , y and z directions at 8.1GHz is shown in Figure 5(b). It is clear the radiated E -field mainly lies in y direction, which is similar to the reverse of y -polarized plane wave vertically illuminating. E -field on port 1 at 8.1 GHz is shown in Figure 6. On wave guide's edge, direction of E -field keeps the same, which makes the direction of surface current on unit cell in parallel to be the same, ensuring the whole antenna's high directivity.

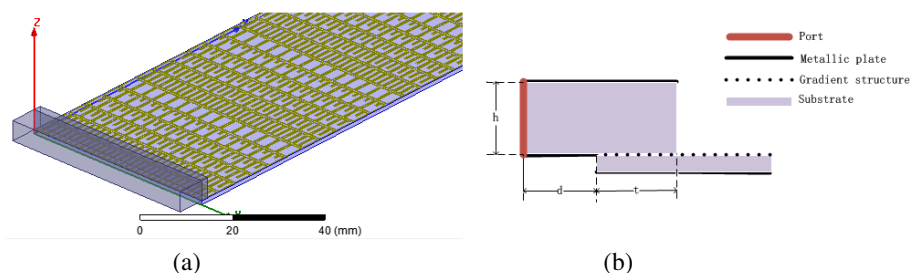
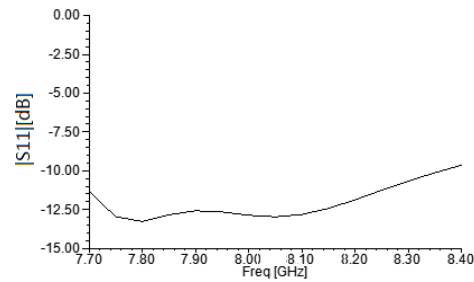
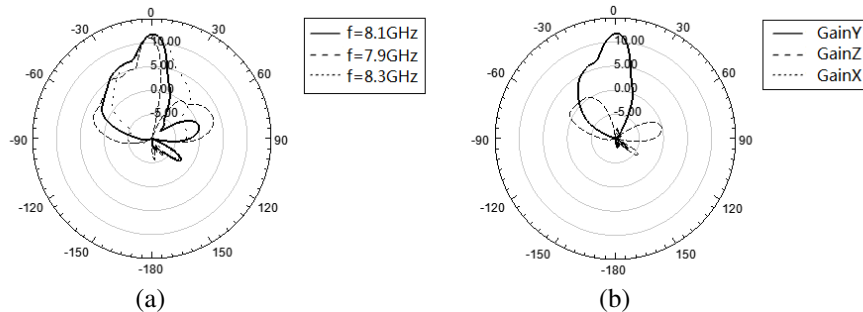
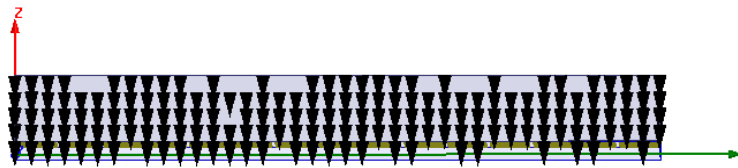


Figure 3: Structure of antenna: (a) overall structure of antenna, (b) parameters setting.

The working frequency of the former infinite GM is 7.87 GHz, while our antenna achieves its maximum gain at 8.1 GHz. This frequency shift is mainly caused by the fact that the environment of the first and second rows of the super cells has changed. The former infinite GM is constructed by super cells being placed periodically. So to each of the super cell, its environment is the same. But in our antenna, it is the parallel plate wave guild that being placed next to it, and what's more, it has a finite size. The attributes of some super cells change, and it leads to the shift.

In the simulation, Port 1 is set to be lumped port with its width of 49.5 mm. At 8.1GHz,

Figure 4: Magnitude of S_{11} over frequency.Figure 5: Radiation pattern in dB: (a) Total gain at different frequencies; (b) Total gain distribution in x , y and z directions at 8.1 GHz.Figure 6: E -field on Port 1 at 8.1 GHz.

wavelength of TEM mode EM-wave propagating in FR-4 is 17.86 mm. The width of Port 1 is 2.77 times as that of the wavelength. However, in practice we usually need to transmit signal from coaxial cable to parallel plate waveguide, while the former can be seen a point source. It is difficult to get a plane wave from a point source within a short distance. This will lead to the inconformity of the phase along the edge of waveguide and the reduction of antenna's gain. To solve this problem, two methods are presented: using narrower super cells or using fewer super cells in parallel. The minimum width of the super cell depends on machining accuracy. More importantly, if the feed structure and GM are cut narrow enough, the result will turn to be destructive. The super cells along the edges of GM can be considered “on the edge”, while their attributes have changed a lot as we mentioned. Therefore when designing antenna of this kind, we should take gain, realization method and number of super cells in parallel into consideration.

If we want to change the shape of antenna, we can add or cut some unit cells and tune the parameter of feed structure. Unit cells being made removable, the shape of antenna will be flexible. With the development of GM, unit cells will be smaller, and then the antenna will have higher reconfigurability.

4. CONCLUSION

To sum up, this letter analyses the EM-field above GM when some plane wave vertically illuminates, according to which it gives a new way to excite GM at one of its edges to form an antenna. In the simulation, the antenna shows high directivity and low return loss. The influence of some parameters on antenna is discussed. Due to the fact that GM is usually constructed by small unit cells, this letter provides a new way to design reconfigurable antenna.

ACKNOWLEDGMENT

The authors are grateful to the supports from the National Natural Science Foundation of China under Grant Nos. 61331005, 61001039 and 41390454.

REFERENCES

1. Kawata, S., *Top. Appl. Phys.*, Vol. 81, 1, 2001.
2. Wang, J., S. Qu, H. Ma, Z. Xu, and A. Zhang, *Appl. Phys. Lett.*, Vol. 101, 201104, 2012.
3. OHara, J. F., R. D. Averitt, and A. J. Taylor, *Opt. Express*, Vol. 12, 6397, 2004.
4. Saxler., J. G. Rivas, C. Janke, H. P. M. Pellemans, P. H. Bolivar, and H. Kurz, *Phys. Rev. B*, Vol. 69, 155427, 2004.
5. Pendry, J. B., L. Martin-Moreno, and F. J. Garcia-Vidal, *Science*, Vol. 305, 847, 2004.
6. Hibbins, A. P., B. R. Evans, and J. R. Sambles, *Science*, Vol. 308, 670, 2005.
7. Acuna, G., S. F. Heucke, F. Kuchler, H.-T. Chen, A. J. Taylor, and R. Kersting, *Opt. Express*, Vol. 16, 18745, 2008.
8. Gollub, J. N., D. R. Smith, D. C. Vier, T. Perram, and J. J. Mock, *Phys. Rev. B*, Vol. 71, 195402, 2005.
9. Lockyear, M. J., A. P. Hibbins, and J. R. Sambles, *Phys. Rev. Lett.*, Vol. 102, 073901, 2009.
10. Hibbins, A. P., J. R. Sambles, and C. R. Lawrence, *J. Appl. Phys.*, Vol. 86, 1791, 1999.
11. Hibbins, A. P., J. R. Sambles, and C. R. Lawrence, *Phys. Rev. E*, Vol. 61, 5900, 2000.
12. Yu, N. F., P. Genevet, M. A. Kats, F. Aieta, J.-P. Tetienne, F. Capasso, and Z. Gaburro, *Science*, Vol. 334, 333, 2011.
13. Ni, X. J., N. K. Emani, A. V. Kildishev, A. Boltasseva, and V. M. Shalaev, *Science*, Vol. 335, 427, 2012.
14. Aieta, F., P. Genevet, N. F. Yu, M. A. Kats, Z. Gaburro, and F. Capasso, *Nano Lett.*, Vol. 12, 1702, 2012.

Wideband RCS Reduction of Microstrip Antenna by Frequency Reconfigurable Electromagnetic Band Gap

Y. Liu, Y.-W. Hao, Y.-T. Jia, and S.-X. Gong
Xidian University, China

Abstract— In this paper, a novel frequency configurable electromagnetic band-gap (EBG) structure is designed to achieve microstrip antenna's RCS reduction in a wide frequency range. The compact frequency configurable EBG element is comprised of spiral inductors and two diodes. By turning the diodes on or off, the frequency configurable EBG element can operate at different frequency. And then it can work in a wide frequency band. Based on the cancellation of the reflection from the EBG structure and the perfect conductor of the antennas, RCS reduction can be realized over the frequency range of 6 GHz–12 GHz.

1. INTRODUCTION

With the development of stealth technique, more and more attention has been paid to radar cross section (RCS) reduction. And antenna's scattering makes the main contribution to the total RCS of low-observable platform [1]. In recent years, many methods have been proposed to reduce the antenna's RCS. For example, the structural modification [2] and the use of frequency select surface (FSS) are both effective solutions to achieve RCS reduction. However, FSS can only reduce out-band RCS reduction. Based on passive cancellation theory, the EBG structure is applied to RCS reduction. The mushroom-like EBG structure is a classical EBG structure proposed by Sievenpiper [3]. In reference [4], RCS reduction is realized in a narrowband. However, a wideband RCS reduction is usually required in modern battleground environment.

Reconfigurable antennas have a unique advantage in modern wireless communication system, because it can be applied to multiple systems and has a multifunctional role. In reference [5], a frequency reconfigurable EBG structure is designed and used for a microstrip antenna to shift the resonance frequency of the antenna. Moreover, a novel reconfigurable EBG structure is proposed to switch its own resonance frequency in reference [6]. The above researches prove the significance of reconfigurable EBG structure. However, almost no research on loading reconfigurable EBG structures to accomplish RCS reduction has been done.

In this paper, 40 EBG elements are used to cover the partial substrate around the patch of the antenna. And each element is comprised of spiral inductors and two diodes. The dimensions of the EBG element and antennas are optimized by using Ansoft's HFSS software. As a result, RCS can be reduced over the frequency range of 6 GHz–12 GHz by turning the diodes on or off.

2. DESIGN OF THE ANTENNA AND THE RECONFIGURABLE EBG STRUCTURE

In order to load more reconfigurable EBG elements, each cell should be miniaturized. Figure 1 shows the geometry of the miniaturized EBG element, which is comprised of spiral inductors. And the resonance frequency of each element is able to shift by changing the length of the spiral. Furthermore, the principle of its operation is based on the cancellation of the reflection from the EBG structure and the perfect conductor of antennas. When the reflection phase of the EBG is less than $\pm 90^\circ$, the effect of RCS reduction can be achieved.

Figure 2 shows a novel reconfigurable EBG element based the element in Figure 1. And the dimension is $4.6 \text{ mm} \times 4.6 \text{ mm}$. Besides, each element covers the partial FR-4 substrate with the thickness of 2.5 mm and relative permittivity of 4.4. In order to change the length of the spiral, two diodes are added to each element.

In theory, there are four kinds of state for each EBG element. However, significant RCS reduction can be realized in only three states. As shown in Table 1, these three states are defined as three modes.

Based on the above analysis, the antenna with reconfigurable EBG elements is able to operate in three different modes. And the geometry of the antenna operating in different modes is shown in Figure 3. The reference antenna consists of one metal ground with the dimension of $36 \text{ mm} \times 36 \text{ mm}$ and one metal patch with the dimension of $10 \text{ mm} \times 10 \text{ mm}$. Furthermore, the distance between the coaxial probe and the center of the patch is 2 mm.

Table 1: States of two switches in different modes.

switch \ mode	mode1	mode2	mode3
switch1	on-state	off-state	off-state
switch2	on-state	off-state	on-state



Figure 1: Simulative demonstration and geometry of the EBG element.

Figure 2: Simulative demonstration and geometry of the reconfigurable EBG element with two diodes.

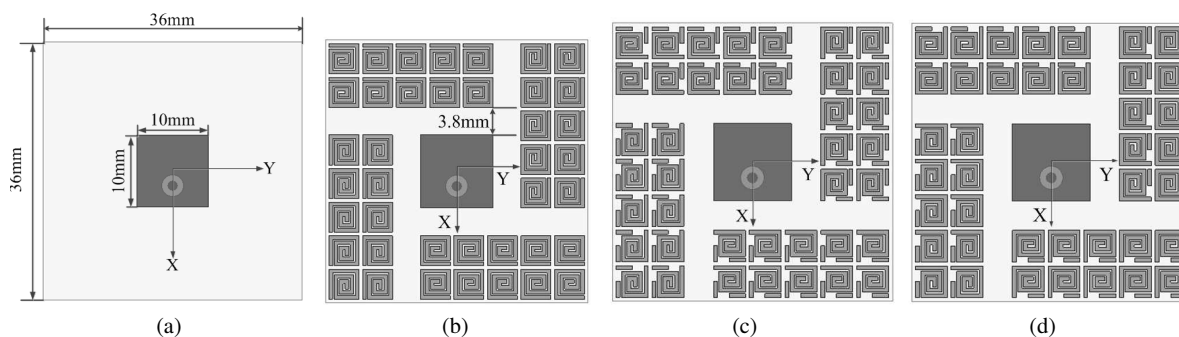


Figure 3: The geometry of the antenna operating in different modes, (a) reference, (b) mode1, (c) mode2, (d) mode3.

3. SIMULATION RESULTS

All radiation characteristics including S_{11} and radiation patterns are shown in Figure 4 and Figure 5. As shown in Figure 4, it can be seen that the antenna with and without reconfigurable EBG elements operate at same frequency. Moreover, EBG elements have almost no impact on radiation patterns, which can be seen in Figure 5. The simulated gain of the reference antenna is 5.67 dB in normal direction (z -axis). Besides, the gain of the antenna operating in mode1, mode2 and mode3 is 5.56 dB, 5.54 dB and 5.60 dB respectively. So, the max gain loss is less than 0.13 dB.

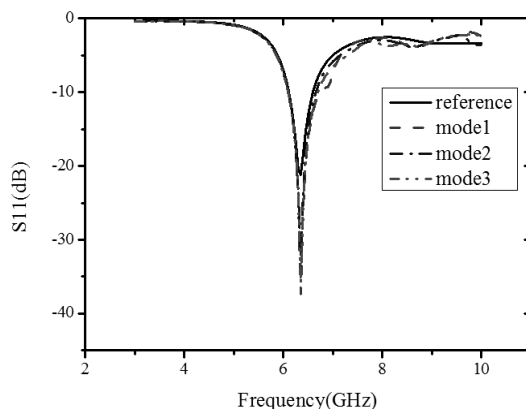


Figure 4: Comparison of S_{11} of antennas in different modes.

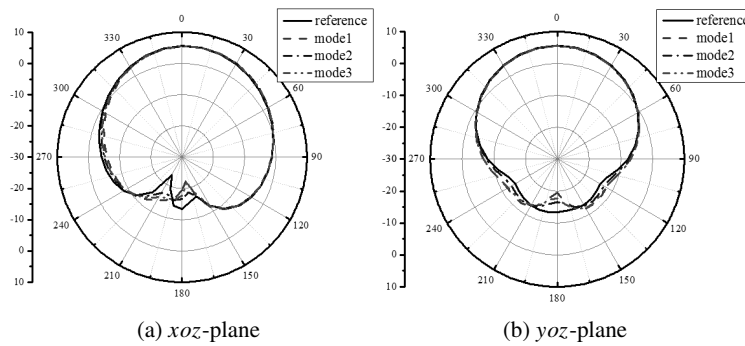


Figure 5: Comparison of radiation patterns of antennas in different modes.

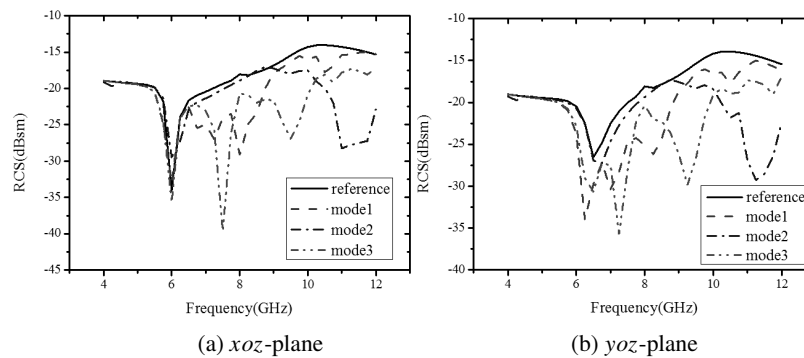


Figure 6: Comparison of monostatic RCS of antennas in different modes.

As shown in Figure 6, RCS reduction is achieved in different range of frequency by controlling the operating mode of the antenna. As a result, the antenna is able to operate in a state of low RCS from 6 GHz to 12 GHz.

4. CONCLUSION

A frequency EBG structure is designed and simulated to apply to RCS reduction of the antenna. By using some PIN diodes to change the effective length of spirals, the resonance frequency of EBG elements can be shifted. As a result, the antenna with reconfigurable EBG structures can remain a state of low RCS over a wide frequency range.

REFERENCES

1. Liu, Y., S. X. Gong, and H. B. Zhang, "A novel fractal slot microstrip antenna with low RCS," *IEEE Antennas and Propagation Society International Symposium*, 2006.
2. Jia, Y., Y. Liu, S.-X. Gong, T. Hong, and D. Yu, "Printed UWB end-fire Vivaldi antenna with low RCS," *Progress In Electromagnetics Research Letters*, Vol. 37, 11–20, 2013.
3. Sievenpiper, D., L. Z. Romulo, F. J. Broas, N. G. Alexopoulos, and E. Yablonovitch, "High-impedance electromagnetic surfaces with a forbidden frequency band," *IEEE Transactions on Microwave Theory and Techniques*, Vol. 47, No. 11, 2059–2074, 1999.
4. Li, Y. Q., "RCS reduction of ridged waveguide slot antenna array using EBG radar absorbing material," *IEEE Antennas and Wireless Propagation Letters*, Vol. 7, 473–476, 2008.
5. Liang, J. and H. Y. Yang, "Microstrip patch antennas on tunable electromagnetic band-gap substrates," *IEEE Transactions on Antennas and Propagation*, Vol. 57, No. 6, 1612–1617, 2009.
6. Kern, D. J., J. A. Bossard, and D. H. Werner, "Design of reconfigurable electromagnetic bandgap surfaces as artificial magnetic conducting ground planes and absorbers," *IEEE Antennas and Propagation Society International Symposium*, 2006.

Frequency Reconfigurable Narrow-frame Antenna for WWAN/LTE Smartphone Applications

Zhong-Xiang Chen and Yong-Ling Ban

Institute of Electromagnetics, University of Electronic Science and Technology of China
2006 Xi-Yuan Avenue, Western High-Tech District, Chengdu, Sichuan 611731, China

Abstract— A compact narrow-frame antenna loaded a PIN diode for hepta-band smartphone applications is presented. The greatest highlight is that the edge of the no-ground planet is quite narrow of only 5 mm, which meets the requirements of the popular narrow-frame smartphone designs with larger touch-screens. Furthermore, the reconfigurable technology is applied to realize a wide coverage with a small volume and a compact structure. The hepta-band operation is successfully achieved by combining the two working states. Detailed considerations of the design are studied in this paper and the proposed antenna is successfully simulated, fabricated, and measured.

1. INTRODUCTION

For smartphone applications, larger touch-screens with narrow-frames have been widely pursued for not only the appearance design but also the user experience. Therefore, besides the fundamental demands of multi-band operation, the antenna should also be miniaturized, compact and narrow-frame for smartphone applications. However, when applied to the antennas with a narrow frame of 5 mm for multi-band smartphone applications, most of these antenna patterns have poor coverage due to the close space between the antenna and the system planet which leads to the high value of Q. Moreover, the troubles in multi-band narrow-frame antenna design for smartphone applications in a limited area occur not only for the lower-band but also for the upper-band.

Recently, antennas with narrow-frames for hepta-band smartphone applications have been presented and studied in [1, 2]. The narrow-frame antenna proposed in [1] employs a band-stop matching circuit structure to obtain wideband operation with a small size of $5 \times 40 \times 3 \text{ mm}^3$, while the other narrow-frame antenna presented in [2] applies a loaded chip capacitor to realize the hepta-band operation with a size of $5 \times 60 \times 5 \text{ mm}^3$.

To further reduce the sizes of the antennas, the reconfigurable antennas [4–10] which have been proposed and widely studied are considered to be an efficient solution. In this paper, a folded coupled-fed narrow-frame antenna for hepta-band WWAN/LTE smartphone applications is proposed and studied. The proposed antenna can be reconfigured by employing a PIN diode, which changes its resonant modes by modifying the electrical length for the lower-band in two working states, and exerts little effect on the upper-band. With outstanding merits of a narrow frame of only 5 mm and a compact structure of $5 \times 5 \times 35 \text{ mm}^3$, the proposed antenna is quite practical for smartphone applications with larger touch-screens. The proposed PIN diode loaded antenna has also been proved applicable with simple structures, acceptable insertion loss and low cost. The prototype with the PIN diode and the bias circuit was built, while the measured results including radiation efficiencies and gains are acceptable.

2. PROPOSED ANTENNA CONFIGURATION

Figure 1 shows the geometry of the proposed compact frequency-reconfigurable narrow-frame antenna, which is mounted on the bottom edge of the FR4 ($\epsilon_r = 4.4$, $\tan \delta = 0.02$) printed circuit board and has a whole volume of $35 \times 5 \times 5 \text{ mm}^3$ of no-ground area. On the back side of the FR4 printed circuit board, a ground plane of $110 \times 60 \text{ mm}^2$ is printed to serve as the system ground of the mobile phone with the protruded ground of $25 \times 5 \text{ mm}^2$ connected to the system ground. A $50\text{-}\Omega$ mini coaxial feed line is employed to excite the antenna and it is connected to the feeding point (point A) and the PCB shorting point (point C). In the study, a 1-mm thick plastic slab ($\epsilon_r = 3$, $\sigma = 0.02 \text{ S/m}$) is also employed to build a plastic case to simulate the handset housing in practical applications. In addition, detailed dimensions of the proposed antenna are shown in Fig. 1(b).

The proposed compact antenna mainly comprises two folded strips (strip1 and strip2 with a lumped inductor of 3 nH), which are designed to generate upper-frequency resonant mode at about

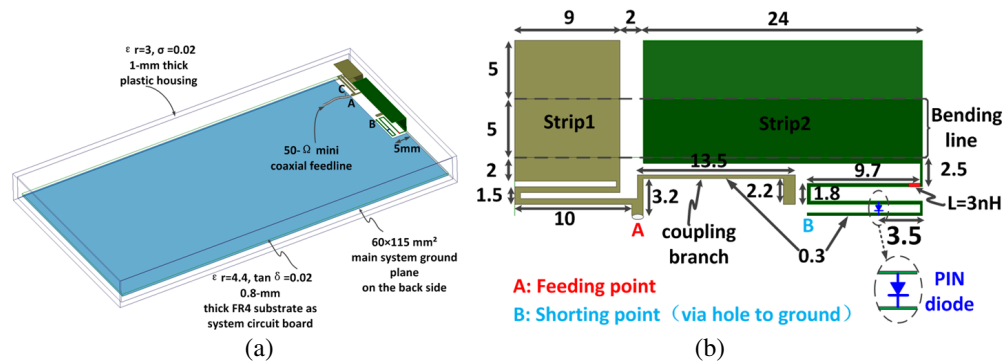


Figure 1: Proposed antenna array configuration. (a) Geometry of proposed narrow-frame antenna. (b) Detailed dimensions of the proposed antenna. (Unit: mm).

2000 MHz and lower-frequency resonant mode at about 910 MHz, respectively. However, higher-order mode generated by strip2 leads to failure in widening the bandwidth for the upper-band, which is mostly in coincidence with the resonant mode generated by strip1 at about 2000 MHz. To solve this trouble, a coupling branch is employed to generate the other upper-frequency resonant mode at about 2400 MHz, and reduce the capacitance of strip1 to generate a lower-frequency resonant mode at about 850 MHz. In addition, the introduction of the coupling branch also forms a coupled loop together with the system ground and part of the strip2, which contributes a half-wavelength upper-frequency resonant mode at about 2900 MHz, covering the GSM850/1800/1900/UMTS/LTE 2300/2500 operation. To further meet the multi-band requirements, the reconfigurable technology is employed to cover the GSM900 band by modifying the electrical length for the lower-band, which is realized by a PIN diode and has little effect on the upper-band.

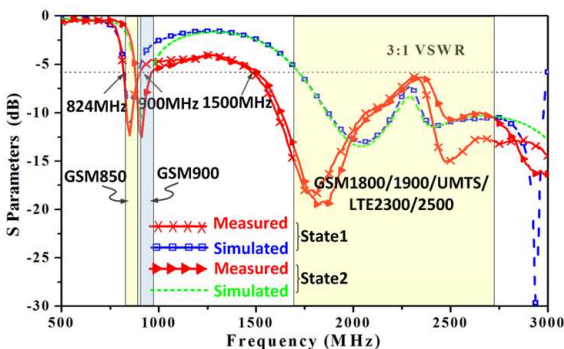


Figure 2: Measured and simulated S parameters.

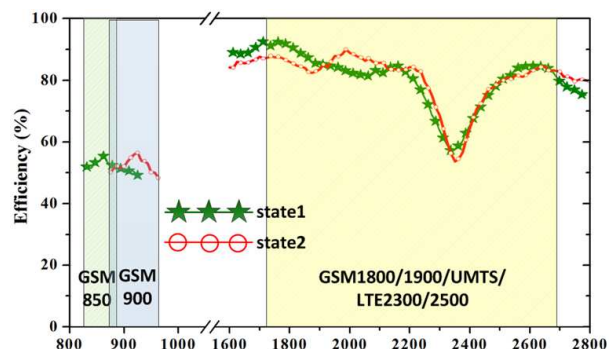


Figure 3: Measured radiation efficiency.

The PIN diode loaded reconfigurable antenna works in two different states, namely state1 (the PIN diode is OFF) and state2 (the PIN diode is ON). When the antenna works in state1, the operating bands of GSM850/1800/1900/UMTS/LTE2300/2500 are covered. The specified position of the PIN diode is optimized to meet the requirements of covering the operating band of GSM900. When the antenna works in state2, the electrical length is reduced by about 7 mm, which shifts the lower-frequency resonant mode from about 870 MHz to about 910 MHz, covering the GSM900/1800/1900/UMTS/LTE2300/2500 operation. In addition, the insertion of the PIN diode brings little influence on the upper-band. Consequently, the proposed narrow-frame antenna has finally covered the GSM850/900/1800/1900/UMTS/LTE2300/2500 operation by combining the two working states.

3. RESULTS AND DISCUSSION

The proposed narrow-frame antenna with the PIN diode was successfully fabricated and tested. The type of the PIN diode is selected as Siemens BAR65-02W with low capacitance and loss. The simulated results of both working states are obtained by Ansoft HFSS version 13, while the measured results are tested by using an Agilent N5247A vector network analyzer. Measured and simulated reflection coefficients presented in Fig. 2 with good agreement between them for the

lower-band. The measured impedance matching bandwidth is based on 3 : 1 VSWR. For state1, the obtained bands are 824–900 and 1500–2690 MHz. For state2, the achieved bands are 880–960 and 1520–2690 MHz. Therefore, by combining two working states, the hepta-band WWAN/LTE operation is successfully covered. The measured radiation efficiency is depicted in Fig. 3.

4. CONCLUSION

A compact frequency-reconfigurable narrow-frame antenna for hepta-band WWAN/LTE smartphone applications is proposed and studied. The edge of the no-ground planet to support the antenna is only 5 mm, which is quite promising for narrow-frame smartphone applications. By combining two working states of the PIN diode, hepta-band including GSM/850/900/1800/1900/UMTS-LTE2300/2500 can be successfully covered with a compact volume of $35 \times 5 \times 5 \text{ mm}^3$, which is much smaller than the previous designs. In addition, the measured results including reflection coefficients, antenna efficiencies and gains are presented and can meet the requirements of smartphone systems.

REFERENCES

1. Ban, Y. L., Y. F. Qiang, L. W. Li, et al., “Low-profile narrow-frame antenna for seven-band WWAN/LTE smartphone applications,” *IEEE Antennas Wireless Propag. Lett.*, Vol. 13, 463–466, 2014.
2. Chen, Z.-X., Y.-L. Ban, Z. Chen, K. Kang, and J. L.-W. Li, “Two-strip narrow-frame monopole antenna with a capacitor loaded for hepta-band smartphone applications,” *Progress In Electromagnetics Research*, Vol. 145, 31–38, 2014.
3. Zhu, H. L., X. H. Liu, S. W. Cheung, et al., “Frequency-reconfigurable antenna using metasurface,” *IEEE Trans. Antennas Propag.*, Vol. 62, No. 1, 80–85, 2014.
4. Tawk, Y., J. Costantine, C. G. Christodoulou, et al., “Reconfigurable filtennas and MIMO in cognitive radio applications,” *IEEE Trans. Antennas Propag.*, Vol. 62, No. 3, 1074–1083, 2014.
5. Ban, Y. L., S. C. Sun, P. P. Li, et al., “Compact eight-band frequency reconfigurable antenna for LTE/WWAN table computer applications,” *IEEE Trans. Antennas Propag.*, Vol. 62, No. 1, 471–475, 2014.
6. Shi, Z., R. P. Zheng, J. Ding, et al., “A novel pattern-reconfigurable antenna using switched printed elements,” *IEEE Antennas Wirel. Propag. Lett.*, Vol. 11, 1100–1103, 2012.
7. Li, Y., Z. J. Zhang, J. F. Zheng, et al., “Compact heptaband reconfigurable loop antenna for mobile handset,” *IEEE Antennas Wirel. Propag. Lett.*, Vol. 10, 1162–1165, 2011.
8. Li, H., J. Xiong, Y. F. Yu, and S. He, “A simple compact reconfigurable slot antenna with a very wide tuning range,” *IEEE Trans. Antennas Propag.*, Vol. 58, No. 11, 3725–3728, Nov. 2010.
9. Augustin, G., B. P. Chacko, and T. A. Denidni, “Electronically reconfigurable uniplanar antenna for cognitive radio applications,” *IET Microwave, Antenna & Propag.*, Vol. 8, No. 5, 367–376, 2014.
10. Kumar, A., A. Patnaik, and C. G. Christodoulou, “Design and testing of a multifrequency antenna with a reconfigurable feed,” *IEEE Antennas Wireless Propag. Lett.*, 2014 (appear).